

Handbook of terahertz technology for imaging, sensing and communications

Edited by Daryoosh Saeedkia

Handbook of terahertz technology for imaging, sensing and communications

Related titles:

Semiconductor lasers: Fundamentals and applications
(ISBN 978-0-85709-121-5)

Handbook of solid-state lasers: Materials, systems and applications
(ISBN 978-0-85709 272-4)

Laser spectroscopy for sensing: Fundamentals, techniques and applications
(ISBN 978-0-85709-273-1)

Details of these books and a complete list of titles from Woodhead Publishing can be obtained by:

- visiting our web site at www.woodheadpublishing.com
- contacting Customer Services (e-mail: sales@woodheadpublishing.com; fax: +44 (0) 1223 832819; tel: +44 (0) 1223 499140 ext. 130; address: Woodhead Publishing Limited, 80, High Street, Sawston, Cambridge CB22 3HJ, UK)
- in North America, contacting our US office (e-mail: usmarketing@woodheadpublishing.com; tel.: (215) 928 9112; address: Woodhead Publishing, 1518 Walnut Street, Suite 1100, Philadelphia, PA 19102-3406, USA)

If you would like e-versions of our content, please visit our online platform: www.woodheadpublishingonline.com. Please recommend it to your librarian so that everyone in your institution can benefit from the wealth of content on the site.

We are always happy to receive suggestions for new books from potential editors. To enquire about contributing to our Electronic and Optical Materials series, please send your name, contact address and details of the topic/s you are interested in to Laura.Pugh@woodheadpublishing.com. We look forward to hearing from you.

The Woodhead team responsible for publishing this book:

Commissioning Editor: Laura Pugh

Publications Coordinator: Anneka Hess

Project Editor: Rachel Cox

Editorial and Production Manager: Mary Campbell

Production Editor: Mandy Kingsmill

Project Manager: Vedhapriya Badrinarayanan, Newgen Knowledge Works Pvt Ltd

Freelance Copyeditor: Dick Hill

Proof reader: Suma George, Newgen Knowledge Works Pvt Ltd

Cover designer: Terry Callanan

Woodhead Publishing Series in Electronic and Optical Materials:
Number 34

Handbook of terahertz technology for imaging, sensing and communications

Edited by
Daryoosh Saeedkia



Oxford Cambridge Philadelphia New Delhi

Published by Woodhead Publishing Limited,
80 High Street, Sawston, Cambridge CB22 3HJ, UK
www.woodheadpublishing.com
www.woodheadpublishingonline.com

Woodhead Publishing, 1518 Walnut Street, Suite 1100, Philadelphia,
PA 19102-3406, USA

Woodhead Publishing India Private Limited, G-2, Vardaan House, 7/28 Ansari Road,
Daryaganj, New Delhi – 110002, India
www.woodheadpublishingindia.com

First published 2013, Woodhead Publishing Limited

© Woodhead Publishing Limited, 2013. Note: the publisher has made every effort to ensure that permission for copyright material has been obtained by authors wishing to use such material. The authors and the publisher will be glad to hear from any copyright holder it has not been possible to contact.

The authors have asserted their moral rights.

This book contains information obtained from authentic and highly regarded sources. Reprinted material is quoted with permission, and sources are indicated. Reasonable efforts have been made to publish reliable data and information, but the authors and the publisher cannot assume responsibility for the validity of all materials. Neither the authors nor the publisher, nor anyone else associated with this publication, shall be liable for any loss, damage or liability directly or indirectly caused or alleged to be caused by this book.

Neither this book nor any part may be reproduced or transmitted in any form or by any means, electronic or mechanical, including photocopying, microfilming and recording, or by any information storage or retrieval system, without permission in writing from Woodhead Publishing Limited.

The consent of Woodhead Publishing Limited does not extend to copying for general distribution, for promotion, for creating new works, or for resale. Specific permission must be obtained in writing from Woodhead Publishing Limited for such copying.

Trademark notice: Product or corporate names may be trademarks or registered trademarks, and are used only for identification and explanation, without intent to infringe.

British Library Cataloguing in Publication Data

A catalogue record for this book is available from the British Library.

Library of Congress Control Number: 2012953435

ISBN 978-0-85709-235-9 (print)

ISBN 978-0-85709-649-4 (online)

ISSN 2050-1501 Woodhead Publishing Series in Electronic and Optical Materials (print)

ISSN 2050-151X Woodhead Publishing Series in Electronic and Optical Materials (online)

The publisher's policy is to use permanent paper from mills that operate a sustainable forestry policy, and which has been manufactured from pulp which is processed using acid-free and elemental chlorine-free practices. Furthermore, the publisher ensures that the text paper and cover board used have met acceptable environmental accreditation standards.

Typeset by Newgen Knowledge Works Pvt Ltd

Printed and bound in the UK by the MPG Books Group

Contents

<i>Contributor contact details</i>	<i>xiii</i>
<i>Woodhead Publishing Series in Electronic and Optical Materials</i>	<i>xvii</i>
<i>Preface</i>	<i>xxi</i>
Part I Fundamentals of terahertz technology for imaging, sensing and communications	1
1 Optoelectronic techniques for the generation and detection of terahertz waves	3
D. SAEEDKIA, TeTechS Inc., Canada	
1.1 Introduction	3
1.2 Terahertz detector technologies	6
1.3 Terahertz signal generation in terahertz photoconductive antennas (THz-PCAs)	8
1.4 Terahertz signal detection with terahertz photoconductive antennas (THz-PCAs)	15
1.5 Parametric interaction in nonlinear crystals	18
1.6 Difference frequency mixing in nonlinear crystals	19
1.7 Conclusion	22
1.8 References	22
2 Transmission and propagation of terahertz waves in plastic waveguides	28
B. UNG and M. SKOROBOGATIY, École Polytechnique de Montréal, Canada	
2.1 Introduction	28
2.2 Main challenges of the plastic-based terahertz fiber optics	29
2.3 Devices based on subwavelength fibers	39
2.4 Hollow-core fibers	45
2.5 Composite terahertz materials	51

2.6	Experimental characterization of terahertz waveguides	54
2.7	Conclusions	56
2.8	Acknowledgments	58
2.9	References	58
3	Fundamental aspects of surface plasmon polaritons at terahertz frequencies	62
	J. GÓMEZ RIVAS, AMOLF and Eindhoven University of Technology, The Netherlands and Y. ZHANG and A. BERRIER, AMOLF, The Netherlands	
3.1	Introduction	62
3.2	The Drude model	64
3.3	Surface plasmon polaritons on planar surfaces	67
3.4	Multilayered structures	76
3.5	New trends in terahertz plasmonics	81
3.6	Acknowledgments	84
3.7	References	84
4	Fundamental aspects of terahertz near-field imaging and sensing	91
	D.-S. KIM and Y.-M. BAHK, Seoul National University, Republic of Korea and P. C. M. PLANKEN, Delft University of Technology, The Netherlands	
4.1	Introduction	91
4.2	Terahertz near-field measurements	95
4.3	Near-fields of various subwavelength holes	99
4.4	Kirchhoff formalism for near-field estimate	110
4.5	Conclusions	116
4.6	References	117
5	Field effect transistors for terahertz applications	121
	W. KNAP and M. I. DYAKONOV, Laboratoire Charles Coulomb, Université Montpellier 2 and CNRS, France	
5.1	Introduction	121
5.2	Plasma waves in low-dimensional structures	122
5.3	Instability of the steady state with a dc current in field effect transistors (FETs)	125
5.4	Detection of terahertz radiation by an FET	128
5.5	Studies of terahertz emission from FETs	135
5.6	Experimental studies of terahertz detection by FETs	141

5.7	Conclusions	152
5.8	Acknowledgements	152
5.9	References	152
6	Terahertz wireless communications	156
J. F. FEDERICI, New Jersey Institute of Technology, USA, L. MOELLER, Bell Laboratories, Alcatel-Lucent, USA and K. SU, New Jersey Institute of Technology, USA		
6.1	Introduction	156
6.2	Motivation for terahertz wireless communications	157
6.3	Atmospheric propagation for communications	159
6.4	Modeling of terahertz communication channels	165
6.5	Hardware for terahertz communications: sources and detectors	177
6.6	Modulators for terahertz waves	184
6.7	Modulation formats for terahertz signals	190
6.8	Examples of terahertz communication systems	192
6.9	Experimental characterization of rain, fog and scintillations on terahertz communication links	200
6.10	Future trends	206
6.11	Sources of further information	208
6.12	Acknowledgments	208
6.13	References	208
Part II	Recent progress and novel techniques in terahertz technology	215
7	Terahertz bio-sensing techniques	217
J.-H. SON, University of Seoul, Republic of Korea		
7.1	Introduction	217
7.2	Sensing of water dynamics by terahertz waves	218
7.3	Sensing of proteins	219
7.4	Binding-state dependent sensing	222
7.5	Characteristic resonances of biomolecules in the terahertz range	223
7.6	Water-mediated terahertz molecular imaging	225
7.7	Conclusion	227
7.8	Acknowledgements	227
7.9	References	227

8	Terahertz array imagers: towards the implementation of terahertz cameras with plasma-wave-based silicon MOSFET detectors	231
	S. BOPPEL, A. LISAUSKAS and H. G. ROSKOS, Johann Wolfgang Goethe-Universität, Germany	
8.1	Introduction	231
8.2	Resistive mixing – a quasi-static analysis	233
8.3	Plasmonic mixing – a hydrodynamic analysis	235
8.4	Technology, design and implementation of complementary metal oxide semiconductor (CMOS) field effect transistors as terahertz detectors	243
8.5	Characterization and optimization of field effect transistor (FET) detectors	249
8.6	Developments towards a terahertz camera	260
8.7	Overview of other focal-plane technologies for terahertz imaging	266
8.8	Acknowledgements	267
8.9	References	267
9	Resonant field enhancement of terahertz waves in subwavelength plasmonic structures	272
	R. SINGH and A. K. AZAD, Los Alamos National Laboratory, USA and W. ZHANG, Oklahoma State University, USA	
9.1	Introduction	272
9.2	Fundamentals of surface plasmon polaritons at terahertz frequencies	273
9.3	Extraordinary transmission of terahertz waves through metallic hole arrays	274
9.4	Active control of terahertz surface plasmon polaritons	282
9.5	Conclusion	293
9.6	References	293
10	Fiber-coupled terahertz time-domain spectroscopy (THz-TDS) systems	295
	M. THEUER and F. ELLRICH, Fraunhofer-Institute for Physical Measurement Techniques IPM, Germany and D. MOLTER and R. BEIGANG, University of Kaiserslautern, Germany	
10.1	Introduction	295
10.2	Fiber guiding	300
10.3	Experimental layout and system characterization	303

10.4	Measurement results of fiber-based terahertz systems	312
10.5	Comparison of THz-TDS with other systems and techniques	318
10.6	Future trends and conclusions	324
10.7	References	324
11	State-of-the-art in terahertz continuous-wave photomixer systems	327
	A. DENINGER, Toptica Photonics AG, Germany	
11.1	Introduction	327
11.2	Continuous-wave emitter and detector technologies	329
11.3	Coherent signal detection	344
11.4	Laser sources	350
11.5	Selected applications of photomixing continuous-wave terahertz systems	358
11.6	Conclusion	364
11.7	Acknowledgements	364
11.8	References	365
12	Novel techniques in terahertz near-field imaging and sensing	374
	M. NAGEL, AMO GmbH, Germany, C. MATHEISEN, RWTH Aachen University, Germany and H. KURZ, AMO GmbH, Germany	
12.1	Introduction	374
12.2	State-of-the-art terahertz near-field approaches	375
12.3	Novel micro-machined terahertz near-field probe-tips	377
12.4	Analysis of nanophotonic second-order nonlinear-optic waveguides with terahertz near-field probing	382
12.5	Failure analysis in integrated electronic structures based on terahertz time-domain reflectometry	386
12.6	High-resolution imaging of free-carrier concentrations for photovoltaic material inspection	392
12.7	Conclusion and future trends	396
12.8	References	397
13	Terahertz nano-devices and nano-systems	403
	Y. KAWANO, Tokyo Institute of Technology, Japan	
13.1	Introduction	403
13.2	Nanoscale terahertz detector	404

x Contents

13.3	Near-field terahertz imager	412
13.4	Conclusion	419
13.5	Acknowledgments	419
13.6	References	419
14	Terahertz integrated devices and systems	423
	T. OUCHI, Canon Inc., Japan	
14.1	Integrated terahertz biosensor chip	423
14.2	Terahertz oscillators integrated with patch antennas	429
14.3	Results and discussion of fabricated resonant tunneling diodes	431
14.4	References	434
15	Terahertz frequency metrology based on frequency comb techniques	436
	T. YASUI, The University of Tokushima, Japan	
15.1	Introduction	436
15.2	Coherent frequency linking with a frequency comb	437
15.3	Terahertz-comb-referenced spectrum analyzer	439
15.4	Optical-comb-referenced terahertz synthesizer	447
15.5	Terahertz-comb-referenced spectrometer	456
15.6	Conclusions and future trends	460
15.7	References	462
16	Semiconductor material development for terahertz applications	464
	M. MISSOUS, The University of Manchester, UK	
16.1	Introduction	464
16.2	Generation and detection of broadband pulsed terahertz radiation	466
16.3	Generation of continuous wave terahertz radiation using photomixing	469
16.4	Photoconductive semiconductor materials	470
16.5	Conclusions	485
16.6	Acknowledgements	486
16.7	References	486

Part III Applications of terahertz technology	491
17 Terahertz applications in tomographic imaging and material spectroscopy: a review	493
T. SHIBUYA and K. KAWASE, Nagoya University and RIKEN, Japan	
17.1 Introduction	493
17.2 Tomographic imaging applications	494
17.3 Quantitative analysis of powdered chemicals	501
17.4 Conclusion	508
17.5 References	508
18 Terahertz applications in the aerospace industry	510
M. J. BOHN, Air Force Institute of Technology, USA and D. T. PETKIE, Wright State University, USA	
18.1 Introduction	510
18.2 Non-destructive evaluation of aircraft composites using transmissive terahertz time domain spectroscopy	513
18.3 Non-destructive evaluation of aircraft composites using reflective terahertz time domain spectroscopy	520
18.4 Continuous-wave non-destructive terahertz imaging for aerospace applications	532
18.5 Comparison of non-destructive imaging for glass fiber reinforced plastics	537
18.6 Conclusion	542
18.7 References	545
19 Terahertz applications in the wood products industry	547
M. E. REID, I. D. HARTLEY and T. M. TODORUK, University of Northern British Columbia, Canada	
19.1 Introduction	547
19.2 Applications of terahertz technology in the wood products industry	549
19.3 Wood structure and morphology	552
19.4 Far infrared properties of wood	556
19.5 Probing wood characteristics at terahertz frequencies	565
19.6 Terahertz sensing in the oriented strand board industry	569
19.7 Future trends	574
19.8 References	576

20	Terahertz applications in the pharmaceutical industry	579
	Y.-C. SHEN, University of Liverpool, UK and B. B. JIN, Nanjing University, China	
20.1	Introduction	579
20.2	Terahertz time-domain spectroscopy (THz-TDS): spectroscopy set-up and analysis	581
20.3	Terahertz time-domain spectroscopy (THz-TDS): identification, quantification and analysis	589
20.4	Terahertz time-domain imaging (THz-TDI): imaging set-up and analysis	594
20.5	Terahertz time-domain imaging (THz-TDI): process monitoring, spectroscopic imaging and chemical mapping	601
20.6	Conclusions and future trends	607
20.7	Acknowledgement	609
20.8	References	609
21	Terahertz applications in art conservation	615
	K. FUKUNAGA, National Institute of Information and Communications Technology, Japan	
21.1	Introduction	615
21.2	Material analysis using terahertz waves	617
21.3	Observation of the internal structure of artworks using terahertz waves	620
21.4	Prospective development of terahertz technology as a tool for heritage science	621
21.5	References	622
22	Applications of terahertz technology in the semiconductor industry	624
	Y. CAI, Z. WANG and D. GOYAL, Intel Corporation, USA	
22.1	Introduction	624
22.2	Characterizations of electro-optical terahertz pulse reflectometry (EOTPR)	629
22.3	Examples of failure analysis using electro-optical terahertz pulse reflectometry (EOTPR)	633
22.4	Conclusions and future trends	638
22.5	References	639
	<i>Index</i>	641

Contributor contact details

(* = main contact)

Editor and Chapter 1

Daryoosh Saeedkia
TeTechS Inc.
595 Bay St, Suite 1204
P.O. Box 7
Toronto
Ontario M5G 2C2
Canada
E-mail: daryoosh@tetechs.com

Chapter 2

B. Ung and Prof. Maksim Skorobogatiy*
Department of Engineering Physics
École Polytechnique de Montréal
C.P. 6079, succ. Centre-ville
Montréal
Québec H3C 3A7
Canada
E-mail: maksim.skorobogatiy@polymtl.ca

Chapter 3

Prof. Jaime Gómez Rivas*
FOM Institute for Atomic and
Molecular Physics, AMOLF
c/o Philips Research
High-Tech Campus 4

5656 AE Eindhoven
The Netherlands

E-mail: rivas@amolf.nl
Y. Zhang and A. Berrier
AMOLF
The Netherlands

Chapter 4

D.-S. Kim* and Y.-M. Bahk
Center for Subwavelength Optics
and Department of Physics and
Astronomy
Seoul National University
Seoul 151-747
Republic of Korea
E-mail: dsk@phya.snu.ac.kr
P. C. M. Planken
Delft University of Technology
Faculty of Applied Sciences
Department of Imaging Science and
Technology
Lorentzweg 1
2628 CJ Delft
The Netherlands

Chapter 5

Prof. Wojciech Knap* and Michel
Dyakonov
Laboratoire Charles Coulomb
Université Montpellier 2 and
CNRS

France

E-mail: Knap.wojciech@gmail.com;
michel.dyakonov@gmail.com

Chapter 6

John F. Federici*
Department of Physics
New Jersey Institute
of Technology
323 Martin Luther King Blvd.
Newark
New Jersey 07102
USA

E-mail: federici@adm.njit.edu

Lothar Moeller
Bell Laboratories
Alcatel-Lucent
Holmdel
New Jersey 07733
USA

E-mail: lothar.moeller@
alcatel-lucent.com

Ke Su
Department of Physics
New Jersey Institute of Technology
323 Martin Luther King Blvd
Newark
New Jersey 07102
USA

E-mail: ks265@njit.edu

Chapter 7

Prof. Joo-Hiuk Son
Department of Physics
University of Seoul
Seoul 130-743
Republic of Korea
E-mail: joohiuk@uos.ac.kr

Chapter 8

S. Boppel, Dr A. Lisauskas and
Prof. Hartmut Roskos*

Physikalisches Institut
Johann Wolfgang
Goethe-Universität
Max-von-Laue-Strasse 1
Frankfurt 60438
Germany

E-mail: roskos@physik.
uni-frankfurt.de

Chapter 9

R. Singh and A. K. Azad
Los Alamos National Laboratory
USA

Prof. Weili Zhang*
School of Electrical and Computer
Engineering
Oklahoma State University
Stillwater
Oklahoma 74078
USA

E-mail: weili.zhang@okstate.edu

Chapter 10

Dr Michael Theuer and Dr Frank
Ellrich
Fraunhofer-Institute for Physical
Measurement Techniques IPM
Department of Terahertz
Measurement and Systems
Kaiserslautern 67663
Rhineland-Palatinate
Germany

Dr Daniel Molter and Prof.
Dr René Beigang*
University of Kaiserslautern
Department of Physics

Kaiserslautern 67663
Rhineland-Palatinate
Germany
E-mail: rene.beigang@ipm.
fraunhofer.de

Chapter 11

Dr Anselm Deninger
Toptica Photonics AG
Lochhamer Schlag 19
D-82166 Gräfelfing
Germany
E-mail: anselm.deninger@toptica.
com

Chapter 12

Dr Michael Nagel* and
Prof. H. Kurz
AMO GmbH
Otto-Blumenthal-Straße 25
Aachen 52074
Germany
E-mail: nagel@amo.de

C. Matheisen
RWTH Aachen University
Sommerfeldstraße 24
Aachen 52074
Germany

Chapter 13

Prof. Yukio Kawano
Quantum Nanoelectronics
Research Center
Department of Physical Electronics
Tokyo Institute of Technology
2-12-1 Ookayama
Meguro-ku
Tokyo 152-8552
Japan
E-mail: kawano@pe.titech.ac.jp

Chapter 14

Dr Toshihiko Ouchi
Corporate R&D Headquarters
Canon Inc.
3-30-2, Shimomaruko
Ohta-ku
Tokyo 146-8501
Japan
E-mail: ouchi.toshihiko@canon.co.jp

Chapter 15

Prof. Takeshi Yasui
Institute of Technology and Science
The University of Tokushima
2-1 Minami-Josanjima
Tokushima
Tokushima 770-8506
Japan
E-mail: yasui.takeshi@tokushima-u.
ac.jp

Chapter 16

Prof. Mohamed Missous
School of Electrical and Electronic
Engineering
The University of Manchester
Manchester M13 9PL
UK

E-mail: m.missous@manchester.ac.uk

Chapter 17

Dr Takayuki Shibuya* and Prof.
Kodo Kawase
Nagoya University
Furocho
Nagoya 464-8603
Japan

and

RIKEN
519-1399 Aramaki-aoba
Sendai 980-0845
Japan

E-mail: shibuya.takayuki@iri-tokyo.jp; kawase@nuee.nagoya-u.ac.jp

Chapter 18

Dr Matthew J. Bohn*
Adjunct Professor of Physics
Department of Engineering Physics
Air Force Institute of Technology/
ENP BLDG 640
2950 Hobson Way
Wright-Patterson AFB
Ohio
USA

E-mail: matthew.bohn@gmail.com

Prof. Douglas T. Petkie
Department of Physics
Wright State University
Dayton
Ohio 45419
USA

E-mail: doug.petkie@wright.edu

Chapter 19

Prof. Matthew Reid*, I. D. Hartley
and T. M. Todoruk
Department of Physics
University of Northern British
Columbia
Prince George
British Columbia
V2N 4Z9
Canada

E-mail: mreid@unbc.ca

Chapter 20

Dr Yao-Chun Shen*
Department of Electrical
Engineering and Electronics

University of Liverpool
Brownlow Hill
Liverpool L69 3GJ
UK

E-mail: y.c.shen@liverpool.ac.uk;

Prof. Biaobing B. Jin
School of Electronic Science and
Engineering
Nanjing University
Nanjing 210093
P. R. China

E-mail: bbjin@nju.edu.cn

Chapter 21

Dr Kaori Fukunaga
Electromagnetic Compatibility
Laboratory
National Institute of Information
and Communications Technology
4-2-1 Nukui-Kita
Koganei
Tokyo 184-8795
Japan

E-mail: kaori@nict.go.jp

Chapter 22

Dr Yongming Cai, Dr Zhiyong
Wang and Dr Deepak Goyal*
Intel Corporation
CH5-263, 5000 W. Chandler Blvd.
Chandler
Arizona 85226
USA

E-mail: deepak.goyal@intel.com

Woodhead Publishing Series in Electronic and Optical Materials

1 Circuit analysis

J. E. Whitehouse

2 Signal processing in electronic communications: For engineers and mathematicians

M. J. Chapman, D. P. Goodall and N. C. Steele

3 Pattern recognition and image processing

D. Luo

4 Digital filters and signal processing in electronic engineering: Theory, applications, architecture, code

S. M. Bozic and R. J. Chance

5 Cable engineering for local area networks

B. J. Elliott

6 Designing a structured cabling system to ISO 11801: Cross-referenced to European CENELEC and American Standards

Second edition

B. J. Elliott

7 Microscopy techniques for materials science

A. Clarke and C. Eberhardt

8 Materials for energy conversion devices

Edited by C. C. Sorrell, J. Nowotny and S. Sugihara

9 Digital image processing: Mathematical and computational methods

Second edition

J. M. Blackledge

10 Nanolithography and patterning techniques in microelectronics

Edited by D. Bucknall

11 Digital signal processing: Mathematical and computational methods, software development and applications

Second edition

J. M. Blackledge

- 12 **Handbook of advanced dielectric, piezoelectric and ferroelectric materials: Synthesis, properties and applications**
Edited by Z.-G. Ye
- 13 **Materials for fuel cells**
Edited by M. Gasik
- 14 **Solid-state hydrogen storage: Materials and chemistry**
Edited by G. Walker
- 15 **Laser cooling of solids**
S. V. Petrushkin and V. V. Samartsev
- 16 **Polymer electrolytes: Fundamentals and applications**
Edited by C. A. C. Sequeira and D. A. F. Santos
- 17 **Advanced piezoelectric materials: Science and technology**
Edited by K. Uchino
- 18 **Optical switches: Materials and design**
Edited by S. J. Chua and B. Li
- 19 **Advanced adhesives in electronics: Materials, properties and applications**
Edited by M. O. Alam and C. Bailey
- 20 **Thin film growth: Physics, materials science and applications**
Edited by Z. Cao
- 21 **Electromigration in thin films and electronic devices: Materials and reliability**
Edited by C.-U. Kim
- 22 **In situ characterization of thin film growth**
Edited by G. Koster and G. Rijnders
- 23 **Silicon-germanium (SiGe) nanostructures: Production, properties and applications in electronics**
Edited by Y. Shiraki and N. Usami
- 24 **High-temperature superconductors**
Edited by X. G. Qiu
- 25 **Introduction to the physics of nanoelectronics**
S. G. Tan and M. B. A. Jalil
- 26 **Printed films: Materials science and applications in sensors, electronics and photonics**
Edited by M. Prudenziati and J. Hormadaly
- 27 **Laser growth and processing of photonic devices**
Edited by N. A. Vainos
- 28 **Quantum optics with semiconductor nanostructures**
Edited by F. Jahnke

- 29 **Ultrasonic transducers: Materials and design for sensors, actuators and medical applications**
Edited by K. Nakamura
- 30 **Waste electrical and electronic equipment (WEEE) handbook**
Edited by V. Goodship and A. Stevles
- 31 **Applications of ATILA FEM software to smart materials: Case studies in designing devices**
Edited by K. Uchino and J.-C. Debus
- 32 **MEMS for automotive and aerospace applications**
Edited by M. Kraft and N. M. White
- 33 **Semiconductor lasers: Fundamentals and applications**
Edited by A. Baranov and E. Tournie
- 34 **Handbook of terahertz technology for imaging, sensing and communications**
Edited by D. Saeedkia
- 35 **Handbook of solid-state lasers: Materials, systems and applications**
Edited by B. Denker and E. Shklovsky
- 36 **Organic light-emitting diodes: Materials, devices and applications**
Edited by A. Buckley
- 37 **Lasers for medical applications: Diagnostics, therapy and surgery**
Edited by H. Jelíneková
- 38 **Semiconductor gas sensors**
Edited by R. Jaaniso and O. K. Tan
- 39 **Handbook of organic materials for optical and optoelectronic devices: Properties and applications**
Edited by O. Ostroverkhova
- 40 **Metallic films for electronic, optical and magnetic applications: Structure, processing and properties**
Edited by K. Barmak and K. Coffey
- 41 **Handbook of laser welding technologies**
Edited by S. Katayama
- 42 **Nanolithography: The art of fabricating nanoelectronics, nanophotonics and nanobiology devices and systems**
Edited by M. Feldman
- 43 **Laser spectroscopy for sensing: Fundamentals, techniques and applications**
Edited by M. Baudelet
- 44 **Chalcogenide glasses: Preparation, properties and applications**
Edited by J.-L. Adam and X. Zhang

45 Handbook of MEMS for wireless and mobile applications

Edited by D. Uttamchandani

46 Subsea optics and imaging

Edited by J. Watson and O. Zielinski

47 Carbon nanotubes and graphene for photonic applications

Edited by S. Yamashita, Y. Saito and J. H. Choi

48 Optical biomimetics: Materials and applications

Edited by M. Large

Preface

The last two decades have witnessed an impressive and unprecedented advance in the field of terahertz science and technology. Bulky and expensive terahertz laboratory instruments, traditionally used for radio astronomy and plasma diagnostics applications, have evolved into commercially available turn-key systems available to scientists and technologists to revisit their scientific problems in the light of terahertz waves. Terahertz sensing and imaging systems are now commercially available, and terahertz wireless communication is on the foreseeable horizon. We celebrate the emergence of a new era: the Tera Era.

Compact terahertz sources and detectors have been developed to generate, detect, and manipulate coherent terahertz signals. Terahertz sources such as quantum-cascade lasers, frequency multipliers and photoconductive photomixers have seen unprecedented improvement in their efficiencies and fabrication and packaging techniques. Advancements in uncooled sensitive terahertz detector arrays have made room-temperature video-rate terahertz imaging a reality. Terahertz surface plasmon and near-field sensors have been deeply investigated and their applications in bio-sensing and terahertz integrated circuits have been demonstrated. Terahertz imaging systems are being deployed on the factory floor for real-time process and quality control in production lines, while several other industrial applications have been investigated as potential markets for terahertz technology.

This book is meant to serve those who are interested in knowing more about one of the most exciting and fastest growing research fields, as well as those who have been contributing to the terahertz technology advance over the past few years. For the latter group of readers, this book can be used as a collection of review articles on the latest developments in the field of terahertz technology, as well as a reference book on the fundamental theories of terahertz science. For the newcomers to the terahertz community, each chapter introduces an area of terahertz science and technology, and provides a comprehensive list of references for further reading.

I would like to thank the authors for their fascinating contributions. I hope the readers enjoy the book.

*Daryoosh Saeedkia
Waterloo, Ontario, Canada*

Optoelectronic techniques for the generation and detection of terahertz waves

D. SAEEDKIA, TeTechS Inc., Canada

DOI: 10.1533/9780857096494.1.3

Abstract: In this chapter, terahertz source and detector technologies are reviewed. Terahertz signal generation and detection in terahertz photoconductive antennas are studied, and their performances under continuous-wave and pulsed mode operation are compared. Terahertz signal generation in nonlinear crystals by parametric interaction and difference frequency mixing techniques are studied.

Key words: terahertz sources, terahertz detectors, photoconductive antennas, parametric sources, nonlinear crystals.

1.1 Introduction

Technology advancement in photonics, electronics and communications has entered a new realm: the Tera Era (T-Era). Today's transistors function at teraflops per second, wireless-data communications is reaching to Tb/s speed, and terabyte hard-drive memories are now a reality. Over the past two decades, intense research and development activities in academia and industry have closed the gap between the microwave and infrared spectra. Compact terahertz (THz) sources and detectors have been developed to generate, detect and manipulate coherent terahertz signals. Terahertz sensing and imaging systems are now commercially available, and terahertz wireless communication is on the horizon. Recent innovations offering both powerful and reliable terahertz sources, together with high performance terahertz spectroscopy and imaging systems, have opened remarkable new opportunities in science and technology. Although major gains in performance and functionality are still anticipated, commercially available terahertz devices and systems have already made the terahertz spectrum accessible to many scientists and technologists in diverse areas, ranging from biology and medicine to chemical, pharmaceutical and environmental sciences to revisit their scientific problems under the light of terahertz waves.

1.1.1 Terahertz source technologies

Terahertz sources can be divided into two major categories: electronic and photonic sources. Terahertz electronic sources that are widely used include electron beam and solid-state sources, and frequency multipliers. The common terahertz photonic sources include terahertz semiconductor and gas lasers and terahertz optoelectronic sources.

Electron beam sources

Gyrotrons,¹ free electron lasers (FELs),² and backward wave oscillators (BWOs)³ are electron beam sources that generate relatively high-power signals at the terahertz frequency range. The operation of these devices is based on the interaction of a high-energy electron beam with a strong magnetic field inside resonant cavities or waveguides, which results in an energy transfer between the electron beam and an electromagnetic wave. Gyrotrons with 1 MW power at 140 GHz have been successfully developed.⁴ An FEL is a gyrotron with very high operating frequencies and wider frequency tuning range.⁵

BWOs can be electrically tuned over a bandwidth of more than 50% of their operational frequencies, and can generate up to 50 mW of power at 300 GHz going down to a few mW at 1 THz.⁶ Complete systems are heavy and large and need high bias voltage and usually a water-cooling system.⁷ Micro-fabrication and micro-assembly technologies are promising approaches to reduce the size of these devices and to make them more suitable for terahertz applications.⁸

Solid-state sources

Solid-state sources include resonant tunnelling diodes (RTD),⁹ Gunn or transferred electron devices (TED),^{10,11} and transit time devices such as impact avalanche transit time (IMPATT) diodes and tunnel injection transit time (TUNNETT) diodes. Gunn devices generating 0.2–5 µW power at 400–560 GHz frequency range are now feasible.¹² TUNNETT diodes with operational frequency as high as 355 GHz with 140 µW output power have been reported.¹³

Frequency multipliers

In a terahertz frequency multiplier, the frequency of a driver source is multiplied in a nonlinear device to generate higher-order harmonic frequencies. Planar Schottky varactor diodes are commonly used in frequency multipliers, taking the advantage of GaAs substrateless technology to reduce substrate loss. The drive sources can be BWOs or solid-state sources

such as Gunn and IMPATT oscillators, with relatively high output power in the range of 50 GHz to 150 GHz. Microwave frequency synthesizers in combination with high-gain power amplifiers fabricated by the monolithic microwave integrated circuit (MMIC) technology can generate high output power above 100 GHz.¹⁴ The most efficient terahertz frequency multipliers are realized by series chains of frequency doublers and frequency triplers.¹⁵ Signals up to 2 THz are achievable from frequency multipliers.^{16,17} However, using a hybrid system consisting of a BWO and a chain of frequency multipliers, it is possible to generate terahertz signals with frequencies of more than 2.5 THz.¹⁸

Terahertz semiconductor lasers

The most promising terahertz semiconductor lasers are quantum cascade lasers.^{19,20} A quantum cascade laser is a unipolar laser, in which the conduction band or the valence band is divided into few sub-bands. The carrier transition occurs between these discrete energy levels within the same band. The discrete energy levels are created in a semiconductor heterostructure containing several coupled quantum wells. Quantum cascade lasers with around 10 mW output power at 2 THz have been demonstrated. Operational temperatures as high as 93 K have been reported for a terahertz quantum cascade laser at 3.2 THz.²¹

Optically pumped far-infrared gas lasers

These terahertz sources consist of a pump laser radiating into a cavity filled with a gas that lases at the terahertz frequency range.^{22,23} The lasing frequency is dictated by the filling gas. Power levels of 1–20 mW are common for 20–100 W laser-pump power.

1.1.2 Terahertz optoelectronic sources

Terahertz photoconductive antennas (THz-PCAs) are widely used to generate terahertz broadband pulses and terahertz narrowband continuous-wave (cw) signals.²⁴ Since their demonstration as practical THz sources and detectors, THz-PCAs have been the subject of a vast number of scientific and industrial reports investigating their application as terahertz wave transmitters and receivers. In continuous-wave mode, two cw laser beams, with their frequency difference in the THz range, combined either inside an optical fibre or properly overlapped in space, are mixed in a photo-absorbing medium (photomixer) and generate a beat frequency signal.²⁵ Terahertz signals with the frequency linewidth as low as a few kHz can be generated by photomixers. The frequency of the terahertz signal can be tuned by tuning

the wavelengths of the lasers. The output power in conventional photomixers falls from 2 μW at 1 THz to below 0.1 μW at 3 THz.

Broadband terahertz pulses can be generated by exciting THz-PCAs with a femto-second short pulse laser. Using a femto-second laser with \sim 100 fs optical pulse duration, terahertz pulses with their frequency content extended up to around 5 THz and an average power of a few μW can be achieved.²⁶ Broadband terahertz pulses can also be generated in electro-optic crystals excited by femto-second short pulse lasers.²⁷ Terahertz signals can be generated via parametric interaction of near-infrared photons and optical vibration modes inside an optical crystal. Using this technique, generation of a quasi-cw terahertz signal with pulse duration of 3.6 ns, an average power 9 nW and a frequency tuning range of 0.7 to 2.4 THz has been reported.²⁸

1.2 Terahertz detector technologies

Highly sensitive cooled terahertz detectors have been traditionally developed for radio astronomy applications. However, developing highly sensitive room temperature terahertz detectors has been challenging. In this section, we review the common terahertz detection techniques.

1.2.1 Homodyne detectors

In homodyne (or direct) detection techniques, the incident terahertz wave on a detector is converted into a measurable electrical signal. Thermal detectors form a large class of the homodyne detectors. The incident terahertz signal on a thermal detector is absorbed by a material whose physical properties such as volume, electric conductivity and dielectric properties change with temperature. Thermal detectors are square-law devices, whose output signals are proportional to the square of the incident field. The phase information of the incident signal is not directly measured by thermal detectors. Most of the thermal detectors have relaxed intrinsic-frequency limitation due to their purely thermal sensing principle, and they are usually slow-response devices. The figure of merit for thermal detectors is their noise equivalent power (NEP, in $\text{W}\text{Hz}^{-1/2}$), defined as the input signal power required to deliver an output signal-to-noise ratio equal to unity in 1 Hz bandwidth, or noise equivalent temperature difference (NETD or NEAT, in deg K), which is defined as the equivalent temperature difference on the object that results in a signal-to-noise ratio of unity at the detector output. Golay cells, pyroelectric detectors, thermoelectric detectors or thermopiles, and bolometers are among the most widely used thermal detectors. In Golay cells, the incident power is absorbed by a thin absorber membrane which

heats up a sealed volume of gas. The change of the gas volume can be measured either by a sensitive microphone or by changing the angle of a mirror in an optical amplifier. Their typical responsivity at 1 THz with 10 Hz modulation frequency is around 10^5 V/W with the NEP of around 10^{-10} WHz $^{-1/2}$. In pyroelectric detectors, the incident signal changes the dielectric constant of a material inside a voltage biased capacitor, and consequently generates a measurable current proportional to the rate of the change in the dielectric constant of the absorbing material. Pyroelectric detectors are mostly used as the infrared detectors with typical NEP of 5×10^{-10} WHz $^{-1/2}$ at 1 MHz modulation frequency and $\lambda = 10$ μm wavelength range. Their sensitivity drops at far-infrared and terahertz frequencies.

Bolometers form a large class of the thermal detectors.^{29,30} In a bolometer, a resistance thermometer is thermally attached to an absorber material and measures the temperature change of the absorber due to the incident radiation. The absorber material has a large absorptivity and a low heat capacity, and can be made of a normal metal, a doped semiconductor, or a superconductor film. NEP for room temperature bolometers with normal metal absorbers is in the range of 5×10^{-10} WHz $^{-1/2}$ with responsivity of 100 V/W and 1 s response time. For liquid nitrogen cooled bolometers, the NEP can be as low as 2.5×10^{-12} WHz $^{-1/2}$ with responsivity of 4000 V/W and 200 ns response time. The most sensitive bolometers are liquid helium cooled with their NEP in the range of 1×10^{-18} WHz $^{-1/2}$ with responsivity of 10^9 V/W and 1 s response time. Another class of room temperature homodyne terahertz detectors is demonstrated based on plasma wave oscillation in field effect transistors³¹ with typical NEP around 1×10^{-10} WHz $^{-1/2}$ and responsivity of 200 V/W.^{32–34} The resonance absorption frequency can be tuned over a wide range by tuning the gate voltage. Devices compatible with standard complementary metal oxide semiconductor (CMOS) technology have been demonstrated and are promising candidates for low-cost terahertz array detector technologies.³²

1.2.2 Heterodyne detectors

In a heterodyne detection scheme,^{35,36} the input terahertz signal is multiplied by a signal from a local oscillator in a nonlinear mixer device such as a Schottky mixer, a hot electron bolometer (HEB) mixer or a superconductor–insulator–superconductor (SIS) mixer, and the resulting intermediate frequency (IF) signal containing both amplitude and phase information of the input terahertz signal is amplified, filtered and processed in the back-end IF electronic stages.³⁷ The figure of merit for heterodyne detectors is their noise temperature (NT, in deg K). The Schottky mixers can operate at room temperature with 104 K NT at 1.5 THz and need relatively high local oscillator power in the range of 1–10 mW. HEB mixers operating at liquid

nitrogen temperature can work at frequencies up to 3 THz, where the SIS mixers fail to operate, and need very low local oscillator power in the region of 10 nW. The SIS mixers with 1 μ W local oscillator power working at liquid helium temperature exhibit the highest sensitivity among the heterodyne mixers with NT in the order of 400 K at 1 THz.

1.2.3 Optoelectronic detectors

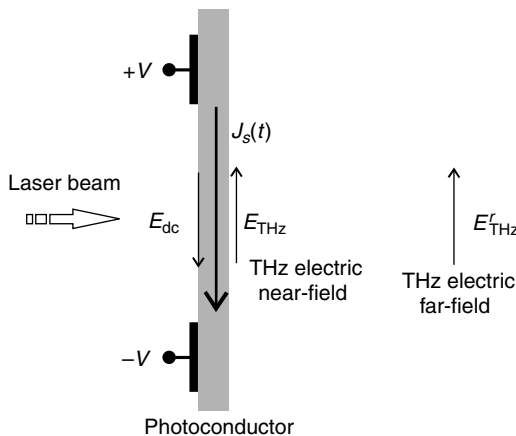
Optoelectronic techniques exhibit alternative solutions for extracting both amplitude and phase information of a terahertz signal incident on an optically gated terahertz photoconductive antenna³⁸ or a nonlinear electro-optic crystal.²⁷ The gating laser beam can come from a short pulse laser or from a pair of continuous-wave lasers with their frequency difference being equal to the frequency of the incident continuous-wave terahertz signal.³⁹ In the photoconductive antenna detection scheme, the amplitude of the generated photocurrent on the receiver antenna is proportional to the amplitude of the incident terahertz electric field. In the case of electro-optic detection scheme, the incident terahertz wave co-propagates with the gating laser beam inside an electro-optic crystal and induces a change in the polarization state of the linearly polarized laser beam. The change in the polarization state of the gating laser beam is proportional to the amplitude of the terahertz electric field, which can be detected as a voltage at the output of a pair of balanced photodiode detectors. In both photoconductive antenna and electro-optic detection schemes, the phase information of the received terahertz signal can be extracted by controlling the arrival time of the gating laser beam with respect to the arrival time of the incident terahertz signal.

1.3 Terahertz signal generation in terahertz photoconductive antennas (THz-PCAs)

Figure 1.1 shows a d.c. biased aperture THz-PCA illuminated by a laser beam (pulse or cw). In the presence of the applied d.c. bias and the incident laser beam, an induced current is generated, which radiates a terahertz wave into free space. One can use the electromagnetic potential theory⁴⁰ to find the terahertz far-field radiation, $E_{\text{THz}}^r(r, t)$, as

$$E_{\text{THz}}^r(r, t) = -\frac{A}{4\pi r \epsilon_0 c^2} \frac{d}{dt} J_s(t) \quad [1.1]$$

where A is the area of illumination, r is the distance between the observation point and the centre of the aperture and $J_s(t)$ is the induced surface current.



1.1 An aperture THz-PCA illuminated by a laser beam. The thickness of the photoconductor is assumed to be much less than the terahertz radiation wavelength.

The induced surface current is related to the sheet conductivity, $\sigma_s(t)$, as

$$J_s(t) = \sigma_s(t)(E_{dc} + E_{THz}(t)) \quad [1.2]$$

where E_{dc} is the applied d.c. electric field and $E_{THz}(t)$ is the terahertz near-field radiation.

The sheet conductivity is related to the free carrier density, $N(t)$, as

$$\sigma_s(t) = \frac{1}{\alpha} e \mu N(t) \quad [1.3]$$

where α is the optical absorption coefficient and μ is the carrier mobility. The free carrier density can be calculated from the following continuity equation

$$\frac{d}{dt} N(t) = \frac{\alpha(1-R)}{hv} I(t) - \frac{1}{\tau} N(t) \quad [1.4]$$

where R is the optical reflection coefficient at the air-photoconductor interface, h is the Planck's constant, v is the optical frequency, $I(t)$ is the optical illumination intensity and τ is the carrier recombination time. When the size of the illumination area is greater than the wavelength of the radiation,

using the boundary condition on the magnetic field, the electric near-field radiation can be approximated as⁴¹

$$E_{\text{THz}}(t) = -\frac{\eta_0}{1+\sqrt{\epsilon_r}} J_s(t) \quad [1.5]$$

where η_0 is the intrinsic impedance of free space and ϵ_r is the relative dielectric constant of the photoconductor. When the illumination area is less than the radiation wavelength, a more rigorous calculation is needed to find the electric near-field radiation. From Equations [1.1], [1.2] and [1.5] the terahertz far-field radiation can be expressed as

$$E_{\text{THz}}^r(r,t) = -\frac{A}{4\pi r \epsilon_0 c^2} \frac{E_{\text{dc}}}{\left[1 + \sigma_s(t)/\sigma_d\right]^2} \frac{d}{dt} \sigma_s(t) \quad [1.6]$$

where $\sigma_d = \frac{1+\sqrt{\epsilon_r}}{\eta_0}$ is defined as conductivity threshold (12 mS for GaAs),

and the sheet conductivity can be calculated from

$$\frac{d}{dt} \sigma_s(t) = \frac{e\mu(1-R)}{hv} I(t) - \frac{1}{\tau} \sigma_s(t) \quad [1.7]$$

A solution to Equation [1.7] for $\sigma_s(t)$ can be written as^{41,42}

$$\sigma_s(t) = \frac{e\mu(1-R)}{hv} \int_{-\infty}^t I(t') \exp\left(\frac{-(t-t')}{\tau}\right) dt' \quad [1.8]$$

For a given pulse or cw optical illumination intensity, $I(t)$, one can calculate $\sigma_s(t)$ from Equation [1.8] and then find the terahertz far-field radiation from Equation [1.6].

1.3.1 Continuous-wave mode

In continuous-wave operation mode, the optical illumination intensity can be written as

$$I(t) = I_0 [1 + \cos(\omega t)] \quad [1.9]$$

where I_0 is the average of the total optical illumination intensity in W/m² and ω is the terahertz beat frequency. The steady-state

solution to Equation [1.7] for the optical illumination density given by Equation [1.9] is

$$\sigma_s(t) = \frac{e\mu\tau(1-R)I_0}{hv} \left[1 + \frac{1}{\sqrt{1+(\omega\tau)^2}} \sin(\omega t + \varphi) \right] \quad [1.10]$$

where $\phi = \tan^{-1}(1/\omega\tau)$. For typical LT-GaAs photomixers, the maximum sustainable optical intensity before thermal failure is around $1 \text{ mW}/\mu\text{m}^2$.⁴³ Assuming $I_0 = 1 \text{ mW}/\mu\text{m}^2$, for an LT-GaAs photomixer working at $\lambda = 800 \text{ nm}$ wavelength range and with $\tau = 0.4 \text{ ps}$, $\mu = 400 \text{ cm}^2/\text{Vs}$ and $R = 0.3$, one can calculate $v_{s,\max} = e\mu\tau(1 - R)I_0/hv = 7.22 \mu\text{S}$, which is equivalent to the maximum carrier density of $N_{\max} = 1.13 \times 10^{15} \text{ cm}^{-3}$. Hence, under normal operation condition $\sigma_{s,\max} \ll \sigma_d$, and one can approximate Equation [1.6] as

$$E_{\text{THz}}^r(r,t) = -\frac{A}{4\pi r\varepsilon_0 c^2} E_{\text{dc}} \frac{d}{dt} \sigma_s(t) \quad [1.11]$$

In other words, under cw operation and for optical illumination intensity below device thermal failure, the near-field radiation screening effect is negligible in THz-PCAs. From Equations [1.7] and [1.11], one can calculate the terahertz far-field radiation as

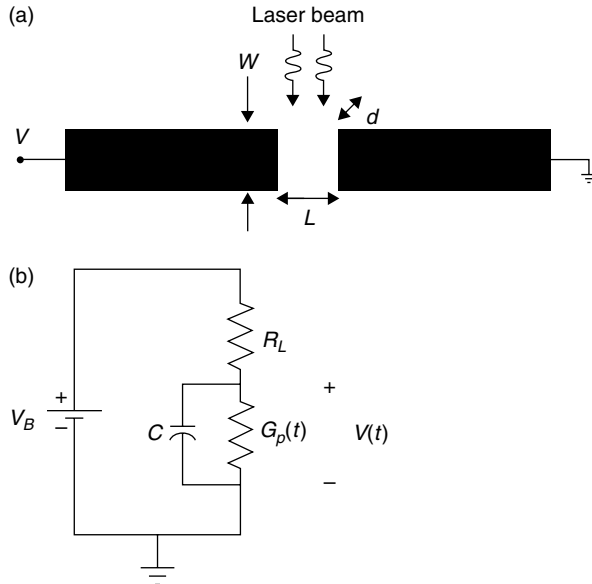
$$E_{\text{THz}}^r(r,t) = -\frac{e\mu(1-R)P_0}{4\pi h\nu\varepsilon_0 c^2 r} E_{\text{dc}} \frac{\omega\tau}{\sqrt{1+(\omega\tau)^2}} \cos(\omega t + \varphi) \quad [1.12]$$

where $P_0 = AI_0$ is the total optical illumination power in watts.

The above analysis is valid for the aperture THz-PCAs, where the induced surface current directly radiates the terahertz wave into free space. However, for the THz-PCAs with a small active area acting as a feed point for a radiating antenna (e.g., dipoles, bow-ties, spirals etc.), one has to find the current distribution over the antenna and then calculate the radiation field for the new current distribution. For these antennas, an equivalent circuit analysis can be used to find the delivered terahertz power from the feed point to the antenna with radiation resistance R_L .⁴⁴

Figure 1.2 shows a THz-PCA with a small active area and its equivalent circuit model. The conductance of the active area upon laser illumination can be written as

$$G_p(t) = e\mu \frac{w_g}{l_g} \frac{1}{\alpha} N(t) \quad [1.13]$$



1.2 (a) A THz-PCA with small active area connected to a radiating antenna. (b) Equivalent circuit model for the THz-PCA.

where $N(t)$ is the carrier density and can be calculated from Equations [1.4] and [1.9] as

$$N(t) = \frac{\alpha\tau(1-R)I_0}{hv} \left[1 + \frac{1}{\sqrt{1+(\omega\tau)^2}} \sin(\omega t + \varphi) \right] \quad [1.14]$$

The conductance, $G_p(t)$, can be written in the form

$$G_p(t) = G_0 \left[1 + \beta \sin(\omega t + \varphi) \right] \quad [1.15]$$

where $G_0 = \frac{e\mu\tau(1-R)}{hv} \frac{w_g}{l_g} I_0$ and $\beta = \frac{1}{\sqrt{1+(\omega\tau)^2}}$.

In Fig. 1.2b the voltage across the THz-PCA, $v(t)$, is the solution to the following differential equation

$$(R_L C) \frac{d}{dt} v(t) + [1 + R_L G_p(t)] v(t) = V_B \quad [1.16]$$

The steady-state first harmonic solution to the Equation [1.16] can be written as

$$v(t) = v_0 + v_1 \sin(\omega t + \varphi) + v_2 \cos(\omega t + \varphi) \quad [1.17]$$

$$v_0 = \frac{\left[(1+G_0R_L)^2 + (\omega R_L C)^2 \right]}{(1+G_0R_L)\left[(1+G_0R_L)^2 + (\omega R_L C)^2 - \frac{1}{2}(G_0R_L\beta)^2 \right]} V_B \quad [1.18]$$

$$v_1 = -\frac{G_0R_L\beta}{(1+G_0R_L)^2 + (\omega R_L C)^2 - \frac{1}{2}(G_0R_L\beta)^2} V_B \quad [1.19]$$

$$v_2 = \frac{(\omega R_L C)(G_0R_L\beta)}{(1+G_0R_L)\left[(1+G_0R_L)^2 + (\omega R_L C)^2 - \frac{1}{2}(G_0R_L\beta)^2 \right]} V_B \quad [1.20]$$

The delivered terahertz power to the antenna is⁴⁴

$$P_{\text{THz}} = \frac{1}{2R_L} [v_1^2 + v_2^2] = \frac{\frac{1}{2}(V_B G_0 \beta)^2 R_L \left[(1+G_0R_L)^2 + (\omega R_L C)^2 \right]}{(1+G_0R_L)^2 \left[(1+G_0R_L)^2 + (\omega R_L C)^2 - \frac{1}{2}(G_0R_L\beta)^2 \right]^2} \quad [1.21]$$

When $G_0R_L \ll 1$, Equation [1.21] reduces to⁴⁴

$$P_{\text{THz}} = \frac{1}{2} V_B^2 \frac{G_0^2 R_L}{1 + (\omega R_L C)^2} \frac{1}{1 + (\omega \tau)^2} \quad [1.22]$$

Assuming $I_0 = 1 \text{ mW}/\mu\text{m}^2$, $W_g = l_g$, $\tau = 0.4 \text{ ps}$, $\mu = 400 \text{ cm}^2/\text{Vs}$ and $R = 0.3$, the condition $G_0R_L \ll 1$ implies that $R_L \ll 140 \text{ K}\Omega$, which is valid for many practical THz-PCA designs.

In the low frequency limit, where $\omega\tau \ll 1$ and $\omega R_L C \ll 1$, the delivered terahertz power to the antenna is $P_{\text{THz}} = \frac{1}{2}(V_B G_0)^2 R_L = \frac{1}{2} I_{\text{dc}}^2 R_L$, and can be

estimated from the d.c. photocurrent, I_{dc} . In the high frequency limit, where $\omega\tau \gg 1$ and $\omega R_L C \gg 1$, the delivered terahertz power to the antenna is

$$P_{\text{THz}} = \frac{1}{2R_L} V_B^2 \left[\frac{e\mu(1-R)}{hv} \right]^2 \frac{P_0^2}{\omega^4 C^2 l_g^4} \quad [1.23]$$

1.3.2 Pulsed mode

In pulsed mode operation, the optical illumination intensity can be represented by a Gaussian function as

$$I(t) = I_0 \exp\left(-t/\delta_t^2\right) \quad [1.24]$$

Unlike cw operation mode, in pulsed operation mode maximum sheet conductivity can exceed σ_d , which can cause terahertz field saturation with optical intensity due to the near-field screening effect. For example, for an average optical pulse intensity $I_{ave} = 0.5 \text{ mW}/\mu\text{m}^2$, for an LT-GaAs aperture THz-PCA with $\tau = 0.4 \text{ ps}$, $\mu = 400 \text{ cm}^2/\text{Vs}$ and $R = 0.3$, illuminated by a fs pulse laser working at $\lambda = 800 \text{ nm}$ wavelength range with 100 fs pulse duration and 100 MHz pulse repetition rate, the peak optical pulse intensity is $I_{peak} = 5 \text{ W}/\mu\text{m}^2$ which results in $\sigma_{s,peak} = 36.1 \mu\text{S}$ equivalent to the carrier density of $N = 5.6 \times 10^{18} \text{ cm}^{-3}$. For THz-PCAs made of S.I. GaAs with longer carrier life time and larger carrier mobility, the near-field screening saturation effect occurs at even smaller optical intensities. For $\sigma_{s,peak} \gg \sigma_d$, one can approximate Equation [1.6] as

$$E_{\text{THz}}^r(r,t) = -\frac{A\sigma_d^2}{4\pi r\varepsilon_0 c^2} \frac{E_{dc}}{\sigma_s^2(t)} \frac{d}{dt} \sigma_s(t) \quad [1.25]$$

At high optical intensities, the terahertz radiation field becomes inversely proportional to the square of the sheet conductivity and saturates with optical intensity due to the near-field screening effect.

1.3.3 Coulomb and radiation screening effect

There are two types of field screening effects in THz-PCAs, namely the radiation and Coulomb screening effects. The radiation screening effect is due to the terahertz near-field radiation partially screening the applied bias field, as

discussed in previous sections. The radiation screening effect becomes negligible for typical THz-PCAs in cw operation mode.⁴⁶ However, the effect can be noticeable in pulsed mode operation, where the peak optical pulse intensity is high.⁴⁷

The origin of the Coulomb screening effect is from the space-charge field generated by the photo-excited electron–hole pairs.⁴⁸ As the free carriers move under the influence of applied bias field, they generate a static field that partially screens the applied bias field. It has been shown that for a d.c. biased aperture THz-PCA excited by a short pulse laser with the carrier density around 10^{17} cm^{-3} , the Coulomb screening effect is dominant for optical excitation spot sizes less than $100 \mu\text{m}$, but for larger spot sizes, the radiation screening effect becomes dominant.⁴⁸ From the results discussed in^{47,49} one can expect the Coulomb screening effect to be negligible in typical THz-PCAs working in cw mode, where the carrier density is in the range of 10^{15} cm^{-3} . It has been shown that for a given optical power the radiated terahertz power increases by increasing the laser excitation spot size.⁴⁹ For smaller excitation area and hence higher optical intensity, the Coulomb screening effect is stronger, which reduces the radiated terahertz power.⁴⁷

1.4 Terahertz signal detection with terahertz photoconductive antennas (THz-PCAs)

In detection mode, the incident terahertz field on the THz-PCA induces a time-varying voltage across the active region of the antenna, which induces a photocurrent through the receiving antenna in the presence of a laser excitation. The amplitude of the induced photocurrent is proportional to the amplitude of the incident terahertz field. By measuring the induced photocurrent, one can extract the amplitude and phase information of the incident terahertz field. THz-PCAs have been used for coherent terahertz wave detection in both pulsed and cw modes.

1.4.1 Continuous-wave mode

Assuming the incident cw terahertz field on the THz-PCA shown in Fig. 1.2 is

$$E_{\text{THz}}(t) = E_0 \cos(\omega t + \phi) \quad [1.26]$$

the induced time-varying voltage across the antenna gap can be simply expressed as

$$V_{\text{THz}}(t) = V_0 \cos(\omega t + \phi) \quad [1.27]$$

where $V_0 = E_0 l_a$, with l_a being the length of the antenna. One can use more rigorous analysis to find the induced voltage across the gap of the receiving antenna. Here, as the first order approximation, we simply assume the induced voltage is the integral of the incident field over the antenna length, and we also assume that the incident terahertz field is uniform over the antenna. This is a reasonable assumption when the length of the antenna is much less than the spot size of the incident terahertz field. Assuming the same pair of laser beams that generate the incident terahertz wave excite the receiving antenna, the conductance at the antenna gap upon the laser excitation can be written as

$$G_p(t) = G_0 \left[1 + \beta \cos(\omega(t - t_d) + \phi') \right] \quad [1.28]$$

where t_d is the optical time delay between the transmitter and the receiver and G_0 and β are the same parameters given in Equation [1.15]. The d.c. component of the photocurrent flowing through the antenna is

$$I_{dc}(t_d) = av \{ V_{THz}(t) G_p(t) \} = I_0 \cos(\omega t_d + \psi) \quad [1.29]$$

where $I_0 = V_0 G_0 \beta \propto E_0$, and ψ is a constant phase independent of t_d . By changing the time delay t_d and measuring the d.c. component of the photocurrent, one can map the measured photocurrent and extract both amplitude and phase information of the incident terahertz field.³⁹

1.4.2 Pulsed mode

In pulsed mode detection scheme, the optical gating pulse arrives at the antenna gap with a time delay t_a relative to the incident terahertz pulse and generates a photocurrent proportional to the amplitude of the incident terahertz pulse. The average d.c. photocurrent flowing through the receiving antenna can be written as⁴¹

$$I_{dc}(t_d) = \frac{2}{\sqrt{\epsilon_r} + 1} \frac{l_a w_g}{l_g \alpha} \frac{1}{T} \int_0^T E_{THz}(t + t_d) \sigma_s(t) dt \quad [1.30]$$

where $E_{THz}(t)$ is the incident terahertz pulse electric field coming from the substrate side, $\sigma_s(t)$ is the sheet conductivity at the antenna gap given by Equation [1.8], and T is the period between optical gating pulses. For the limit when the carrier lifetime is too short resulting in the surface conductance acting as a delta function, from Equation [1.30], the amplitude of the detected d.c. photocurrent will be proportional to the amplitude of the

incident terahertz pulse at $t = t_d$ ($I_{dc}(t_d) \propto E_{\text{THz}}(t_d)$). By varying the arrival time between the incident terahertz pulse and the optical gating pulse and using an antenna made of an ultrafast photoconductor material, one can map the measured d.c. photocurrent and extract both amplitude and phase information of the incident terahertz pulse wave.

1.4.3 Continuous-wave versus pulsed mode

For a cw terahertz wave detected by a THz-PCA, the average incident terahertz power versus the measured photocurrent on the receiver antenna can be written as

$$P_{\text{av}}^{\text{cw}} = \frac{1}{2} \eta_0 |E_{\text{THz}}^{\text{cw}}|^2 \propto \frac{1}{2} I_{\text{cw}}^2 \quad [1.31]$$

where $|E_{\text{THz}}^{\text{cw}}|$ is the amplitude of the incident cw terahertz electric field and η_0 is the impedance of free space. For a pulse terahertz wave detected by a THz-PCA, the average incident terahertz power versus the measured photocurrent on the receiver antenna can be written as

$$P_{\text{av}}^{\text{pulse}} = \frac{\Delta t}{T} \eta_0 |E_{\text{THz}}^{\text{pulse}}|^2 \propto \frac{\Delta t}{T} I_{\text{pulse}}^2 \quad [1.32]$$

where Δt is the terahertz pulse duration, T is the period between terahertz pulses, and $|E_{\text{THz}}^{\text{pulse}}|$ is the amplitude of the incident pulse terahertz electric field. From Equations [1.31] and [1.32] one can find

$$\frac{P_{\text{av}}^{\text{pulse}}}{P_{\text{av}}^{\text{cw}}} = \frac{2\Delta t}{T} \frac{I_{\text{pulse}}^2}{I_{\text{cw}}^2} \quad [1.33]$$

For an equal incident average power of pulse and cw terahertz waves, the measured photocurrents on the receiver antenna for the pulsed and cw modes are related by

$$I_{\text{cw}} = \left(\frac{2\Delta t}{T} \right)^{\frac{1}{2}} I_{\text{pulse}} \quad [1.34]$$

For example, for $\Delta t = 1\text{ps}$ and $T = 10\text{ns}$, $I_{\text{cw}} \approx 0.01 I_{\text{pulse}}$, which means that the measured photocurrent (and the signal-to-noise ratio) on the receiver antenna for the pulsed mode detection is much higher than that in cw mode.

1.5 Parametric interaction in nonlinear crystals

Terahertz wave generation via interaction of near-infrared photons and optical vibration modes inside a nonlinear optical crystal was observed for the first time in 1969.⁵⁰ In this process, the energy of an input pump photon with frequency ν_p is partially depleted through parametric interaction with the optical vibration modes inside the crystal and produces a Raman-shifted Stokes photon with frequency ν_s .⁵¹ Consequently, the difference frequency generation (DFG) process between the pump and the Stokes photons inside the nonlinear crystal generates a terahertz signal with frequency ν_t , such that $\nu_t = \nu_p - \nu_s$ to fulfil the law of conservation of energy. Conservation of the momentum manifests the phase matching condition on wave vectors as $\vec{k}_p = \vec{k}_s + \vec{k}_t$, where \vec{k}_p , \vec{k}_s and \vec{k}_t are the wave vectors of pump, Stokes and THz beams, respectively. Using LiNbO₃ as the nonlinear crystal working in the vicinity of its A₁-symmetry 248 cm⁻¹ polariton mode, the polarization of the pump beam, the Stokes beam and the THz beam all become parallel to the crystal's c-axis, and hence their wave vectors make a triangle to satisfy the phase matching condition.^{50,51} In this arrangement, the angle between the pump and the Stokes beam, φ , is less than a few degrees. The frequency of the generated THz wave changes by the angle between the pump and the

Stokes beams as $\nu_t = \nu_p \phi \left[\left(n_t / n_p \right)^2 - 1 \right]^{-0.5}$, where n_t and n_p are the refractive indices of the crystal at the THz and near-infrared wavelengths, respectively.⁵² The THz frequency can be tuned over a wide range by changing the incident angle of the input pump beam. The non-collinear phase matching condition is satisfied for a large number of the values of φ , resulting in a spatially dispersed THz wave with a wide spectral linewidth in the order of hundreds of GHz.

Using two 6.5 cm long MgO-doped LiNbO₃ crystal pumped by a flashlamp-pumped Q-switched Nd:YAG laser working at 1064 nm wavelength with 5 ns pulse width, a THz signal with 2.9 THz spectrum linewidth (0.9–3.8 THz) has been generated with 105 pJ/pulse energy (62 mW peak power) at 66 mJ/pulse pump energy.⁵³ An average THz power around 32.6 pW with 267 mW average pump power has been generated with a similar system and detected by a 4K Si bolometer.⁵⁴

Spectral linewidths in the order of tens of GHz can be achieved by polishing the input and output facets of the crystal and using it as a resonator for the Stokes beam,^{50,55} or by putting the crystal inside an external cavity such as a Fabry–Perot resonator.^{28,52,56} A THz signal with 20 GHz linewidth, continuously tunable between 1 and 2.14 THz frequency range, with 10 ns pulse duration and with average power of 9.6 nW, has been generated using a 6.5 cm long LiNbO₃ crystal pumped with a Q-switched Nd:YAG laser

(wavelength: 1064 nm, pulse width: 25 ns, pulse repetition rate: 50 Hz) with average pump power of 1.7 W. The frequency of the generated THz signal was tuned by putting the cavity mirrors and the crystal on a precise rotation stage and changing the incident angle of the pump beam from 2.1° to 0.9° by rotating the stage. By rotating the stage, the angle between the THz beam and the Stokes beam inside the crystal changed from 66° to 65°. The THz signal was coupled out into the free space using an array of Si prisms and was detected by a 4 K Si bolometer.

A narrow band THz signal with the spectrum linewidth less than 200 MHz was generated using a pair of 6.5 cm long undoped and MgO-doped LiNbO₃ crystals pumped by a Q-switched Nd:YAG laser (wavelength: 1064 nm, pulse width: 15 ns, pulse repetition rate: 10 Hz, spectral linewidth: 40 MHz) and a continuous-wave single mode Yb-fibre laser (wavelength: 1070 nm, spectral linewidth: 1 MHz) as a ‘seeder’ for the Stokes beam.⁵⁷ By introducing the seeder beam, the energy of the Stokes beam with the wavelength equal to that of the seeder beam increased from 7 µJ/pulse to more than 1 mJ/pulse and its spectral linewidth decreased from around 800 GHz to less than 1 GHz.²⁸ The average THz power was 9 nW for the average pump power of 450 mW and for a seed power of 250 mW. The THz pulse duration was 3.6 ns. By using a tunable diode laser as a seeder, the THz frequency was tuned from 0.7 to 2.4 THz with the THz pulse energy varying between 10 pJ/pulse and 1.3 nJ/pulse over the tuning range with its maximum at 1.5 THz.²⁸ Using this technique, a table top terahertz gas spectrometer has been developed which is capable of fast scan over the 0.6–2.4 THz frequency range with frequency resolution better than 100 MHz and scanning rate of 3 GHz/s to 47 GHz/s in 6 MHz to 100 MHz steps, respectively.⁵⁸ A two-channel balanced He-cooled Si bolometer was used for THz detection. Using this system, real-time monitoring of the absorption lines of water molecules and their rotational transitions has been demonstrated.

1.6 Difference frequency mixing in nonlinear crystals

Solution of the wave equation inside a nonlinear crystal with a large second-order susceptibility, $\chi^{(2)}$, and in the presence of two electromagnetic waves propagating inside the crystal with frequencies and wave vectors (ω_1, \vec{k}_1) and (ω_2, \vec{k}_2) results in an electromagnetic wave with frequency and wave vector (ω_3, \vec{k}_3) with $\omega_3 = \omega_1 - \omega_2$ and $\vec{k}_3 = \vec{k}_1 - \vec{k}_2$. This is based on the conservation of energy and momentum. Narrowband THz signals can be generated in this way by mixing two frequency detuned narrow linewidth laser beams inside a nonlinear crystal.^{59–63} This method is different from the technique explained in the previous section, where a Stokes beam

is generated inside the crystal due to the parametric interaction between an input laser beam and crystal's optical vibration modes, and the generated Stokes beam mixes with the input beam to generate the difference frequency signal. Here, both input laser beams are generated outside the crystal and are coupled into it for mixing purposes. The input laser beams can be delivered by: (1) two separate Q-switched lasers (Nd:YAG or Yb-fibre lasers); (2) a Q-switched laser and an optical parametric oscillator (OPO) which is pumped by the second- or third-harmonic of either the same Q-switched laser or a different one; (3) two separate OPO pumped by one Q-switched laser; (4) a dual-mode OPO pumped by a Q-switched laser.

The propagation of the two input laser beams inside the crystal can be either collinear⁶³ or non-collinear,⁶⁴ leading to different forms of phase matching conditions on wave vectors. In the case of the collinear propagation scheme, the phase matching condition reduces to the following scalar equations

$$\left| \frac{n(\lambda_1)}{\lambda_1} - \frac{n(\lambda_2)}{\lambda_2} \right| = \frac{n(\lambda_t)}{\lambda_t} \quad [1.35]$$

where $n(\lambda_1)$, $n(\lambda_2)$ and $n(\lambda_t)$ are the refractive indices of the input laser beams and the THz beam at their respective wavelengths λ_1 , λ_2 and λ_t , which can be calculated using Sellmeier equations. In a nonlinear crystal with small birefringence effect such as GaP, the phase matching condition given by Refs 35 and 36 can be satisfied by properly choosing the input wavelengths of the two laser beams.^{65,66} For a given THz frequency, one can find a wavelength range for the input laser beams for which the phase matching condition is

satisfied and the coherence length $L_c = \frac{1}{2} \left| \frac{n(\lambda_1)}{\lambda_1} - \frac{n(\lambda_2)}{\lambda_2} - \frac{n(\lambda_t)}{\lambda_t} \right|^{-1}$ is long

enough in the order of a few mm up to a few cm.⁶⁵ By aligning the polarization of the input beams along the crystal's axis with the highest second-order susceptibility and rotating the crystal to have an optimum incident angle for the input beams, one can efficiently generate a THz signal whose frequency is equal to the frequency difference of the two laser beams.⁶⁶ The frequency of the generated THz signal can be tuned by fine tuning the wavelengths of the input lasers; however, by tuning the wavelengths of the lasers, the phase matching condition will not be fully satisfied and the efficiency will decrease.

A THz signal with 0.106 µW average power (0.66 W peak power) with 90 GHz spectrum linewidth was generated using a semi-insulating 20 mm long GaP crystal pumped by a dual-wavelength OPO with two 15 mm long KTiOPO₄ (KTP) crystals as the nonlinear medium located inside a 150 mm resonant cavity with its mirrors being highly reflective for idler waves and

highly transmissive for the signal waves.⁶⁵ The wavelengths of the two output beams were tuned from 930 to 980 nm for the first beam and from 930 to 1000 nm for the second one by rotating the corresponding KTP crystals. The OPO was pumped by a diode-pumped, frequency-doubled, Q-switched Nd:YAG laser with 10 ns pulse duration, 10 mJ energy per pulse and 20 Hz repetition rate. The THz frequency was tuned from 0.5 to 4.5 THz by rotating both KTP crystals to tune both optical wavelengths. A 0.8 THz tuning range was possible by rotating only one of the KTP crystals.

The polarization of both incident beams was perpendicular to the <100> direction of the GaP crystal and collinearly propagated inside the crystal.

The absorption coefficient of the GaP rapidly increases above 5 THz due to the optical phonon absorption.⁶⁷ As an alternative crystal for high THz frequency generation, the organic nonlinear crystal trans-4-[4-(dimethylamino)-N-methylstilbazonium] p-tosylate (DAST) has shown to be a promising material.^{68–70} Although DAST shows strong absorption below 2 THz, a THz signal with 2.2 µW average power at 19 THz has been generated using a 1 mm thick crystal pumped by a dual-mode OPO with 0.55–0.7 mJ energy per pulse over 1300–1450 nm wavelength range.⁶⁹ The spectrum linewidth of the THz signal was 60 GHz and the average power was more than 0.1 µW over 2 THz–20 THz frequency range, which was detected by a deuterated triglycine sulfate (DTGS) pyroelectric detector. Using an improved dual-mode KTP based OPO with 21 mJ available energy at 1300 nm, a THz signal with 25 µW average power was generated at 27 THz.⁷⁰

The phase matching condition for two collinear laser beams propagating inside a nonlinear crystal with strong birefringence effect, such as GaSe and ZnGeP₂, can be satisfied by aligning the polarization of one of the incident laser beams along the ordinary axis of the crystal and that of the second beam along the extraordinary axis of the crystal.^{63,71–73}

The extraordinary refractive index of a nonlinear crystal effectively changes by the incident angle, the property that one can use to re-establish the phase matching condition after tuning the THz frequency, and increase the frequency tuning range of the system. The effective nonlinear coefficient of the crystal is also a function of the incident angle, and its maximum does not necessarily occur at the optimum angle for the perfect phase matching, and hence there is a trade-off between the phase matching condition and the maximum nonlinear efficiency of the crystal. Using a highly birefringent nonlinear crystal, one can potentially increase the efficiency of the tunable THz signal generation mechanism. However, the need for the crystal rotation after frequency tuning makes the system more complicated.

Mixing a dual-wavelength polarization maintaining Yb-fibre laser working at 1064.2 nm and 1055–1061.2 nm with a pulse duration of 1 ns and repetition rate of 100 kHz in a 15 mm long ZnGeP₂ crystal, 2 mW average THz power was generated at 2.45 THz.⁷⁴ The conversion efficiency has

been reported as 0.00137, which implies that the average incident power on the crystal was around 1.46 W. The THz frequency was tuned from 0.8 to 2.45 THz with the maximum output power at 2.45 THz. A THz signal with 0.43 µW average power (0.53 mW peak power) at 1.5 THz has been generated using a 15 mm thick GaSe crystal pumped with two Er/Yb-fibre lasers, working at 1550.67 nm and 1538.74 nm wavelengths and simultaneously Q-switched by a single lead zirconate titanate (PZT) piezo. The developed fibre laser system generated pulses with duration from 15 to 70 ns, repetition rate of 50 Hz to 650 kHz, average power of 3 to 56 mW, and the spectral linewidth of 35 MHz.⁷¹

Difference frequency mixing of two collinearly propagating optical beams inside quasi-phase-matched periodically poled or periodically inverted electro-optic crystals such as LiNbO₃,^{72,75} GaAs,^{73,76,77} and GaP⁷⁸ can be used to generate cw THz signals. Using a quasi-phase-matched GaAs structure with an OPO with periodically poled lithium niobate (PPLN) as its gain medium pumped by a mode-locked Nd: yttrium orthovanadate (YVO₄) laser working at 1064 nm with 7 ps pulse width, 50 MHz repetition rate and 10 W average power, the generation of a 2.8 THz signal with 1 mW average power and 300 GHz spectrum linewidth has been recently reported.⁷³

1.7 Conclusion

Terahertz optoelectronic techniques play an essential role in future THz components and systems because of their unique capabilities in generation and detection of coherent THz signals.

New optoelectronic devices will pave the way for all optoelectronic compact THz systems for high performance THz imaging and spectroscopy applications with dramatically reduced size and cost.

1.8 References

1. K. Flech, B. G. Danly, H. R. Jory, K. E. Kreischer, W. Lawson, B. Levush, and R. J. Temkin, ‘Characteristics and applications of fast-wave gyrodevices’, *Proceedings of IEEE*, **87**(5), 752–781, 1999.
2. S. Krishnagopal and V. Kumar, ‘Free-electron lasers’, *Radiation Physics and Chemistry*, **70**(4–5), 559–569, 2004.
3. R. Kompfner and N. T. Williams, ‘Backward-wave tubes’, *Proceedings of IRE*, **41**, 1602–1610, 1953.
4. G. Dammertz, S. Alberti, A. Arnold, E. Borie, V. Erckmann, G. Gantenbein, E. Giguet, R. Heidinger, J. P. Hogge, S. P. Illy, W. Kasperek, K. Koppenburg, M. Kuntze, H. P. Laqua, G. P. LeCloarec, Y. LeGoff, W. Leonhardt, C. Lievin, R. Magne, G. Michel, G. Müller, G. Neffe, B. Piosczyk, M. Schmid, K. Schwörer, M. K. Thumm and M. Q. Tran, ‘Development of a 140-GHz 1-MW continuous

- wave gyrotron for the W7-X stellarator', *IEEE Transactions on Plasma Science*, **30**(3), 808–818, 2002.
- 5. L. Granatstein, R. K. Parker, and C. M. Armstrong, 'Vacuum electronics at the dawn of the twenty-first century', *Proceedings of IEEE*, **87**(5), 702–716, 1999.
 - 6. L. P. Schmidt, S. Biber, G. Rehm, and K. Huber, 'THz measurement technologies and applications', *14th International Conference on Microwaves, Radar and Wireless Communications*, **2**, 581–587, 2002.
 - 7. R. L. Ives, D. Marsden, M. Caplan, C. Kory, J. Neilson, and S. Schwartzkopf, 'Advanced terahertz backward wave oscillators', in *4th IEEE International Conference on Vacuum Electronics*, May 2003, 20–21.
 - 8. R. L. Ives, 'Microfabrication of high-frequency vacuum electron devices', *IEEE Transactions on Plasma Science*, **32**(3), 1277–1291, 2004.
 - 9. E. R. Brown and C. D. Parker, 'Resonant tunnel diodes as submillimetre-wave sources', *Philosophical Transactions of the Royal Society of London*, **354**, 2365–2381, 1996.
 - 10. H. Eisele and R. Kamoua, 'Submillimeter-wave InP Gunn devices', *IEEE Transactions on Microwave Theory and Techniques*, **52**(10), 2371–2378, 2004.
 - 11. L. Wandinger, 'mm-wave InP Gunn devices: status and trends', *Microwave Journal*, **24**(3), 71–78, 1981.
 - 12. H. Eisele, M. Naftaly, and R. Kamoua, 'Generation of submillimeter-wave radiation with GaAs TUNNETT diodes and InP Gunn devices in a second or higher harmonic mode', *International Journal of Infrared and Millimeter Waves*, **26**(1), 1–14, 2005.
 - 13. H. Eisele, '355 GHz oscillator with GaAs TUNNETT diode', *Electronics Letters*, **41**(6), 55–56, 2005.
 - 14. L. A. Samoska, T. C. Gaier, A. Peralta, S. Weibre, J. Bruston, I. Mehdi, Y. Chen, H. H. Liao, M. Nishimoto, R. Lai, H. Wang, and Y. C. Leong, 'MMIC power amplifiers as local oscillator drivers for FIRST', in *The Proceedings of SPIE Conference*, **4013**, 275–284, 2000.
 - 15. P. H. Siegel, 'Terahertz technology', *IEEE Transactions on Microwave Theory Techniques*, **50**(3), 910–928, 2002.
 - 16. J. Ward, E. Schlecht, G. Chattopadhyay, A. Maestrini, J. Gill, F. Maiwald, H. Javadi, and I. Mehdi, 'Capability of THz sources based on Schottky diode frequency multiplier chains', in *IEEE MTT-S International Microwave Symposium Digest*, **3**, 1587–1590, 2004.
 - 17. V. Krozer, G. Loata, J. Grajal de la Fuente, and P. Sanz, 'Limitations in THz power generation with Schottky diode varactor frequency multipliers', in *Proceedings of IEEE Tenth International Conference on Terahertz Electronics*, 109–112, 2002.
 - 18. C.P. Endres, H.S.P. Muller, S. Brunken, D.G. Paveliev, T.F. Giesen, S. Schlemmer, and F. Lewen, 'High resolution rotation inversion spectroscopy on doubly deuterated ammonia, ND₂H, up to 2.6 THz', *Journal of Molecular Structure*, **795**(1), 242–255, 2006.
 - 19. J. Faist, F. Capasso, D. L. Sivco, C. Sirtori, A. L. Hutchinson, and A. Y. Cho, 'Quantum cascade laser,' *Science*, **264**(5158), 553–556, 1994.
 - 20. F. Capasso, R. Paiella, R. Martini, R. Colombelli, C. Gmachl, T. L. Myers, M. S. Taubman, R. M. Williams, C. G. Bethea, K. Unterrainer, H. Y. Hwang, D. L. Sivco, A. Y. Cho, A. M. Sergent, H. C. Liu and E. A. Whittaker, 'Quantum

- cascade lasers: ultrahigh-speed operation, optical wireless communication, narrow linewidth, and far-infrared emission', *IEEE Journal of Quantum Electronics*, **38**(6), 511–532, 2002.
- 21. S. Kumar, B. S. Williams, S. Kohen, Q. Hu, and J. L. Reno, 'Continuous-wave operation of terahertz quantum-cascade lasers above liquid-nitrogen temperature', *Applied Physics Letters*, **84**(14), 2494–2496, 2004.
 - 22. T. Y. Chang and T. J. Bridges, 'Laser action at 452, 496, and 541 μm in optically pumped CH₃F', *Optics Communications*, **1**, 423–426, 1970.
 - 23. M. Inguscio, G. Moruzzi, K. M. Evenson, and D. A. Jennings, 'A review of frequency measurements of optically pumped lasers from 0.1 to 8 THz', *Journal of Applied Physics*, **60**(12), R161–R192, 1986.
 - 24. D. Saeedkia and S. Safavi-Naeini, 'Terahertz photonics: optoelectronic techniques for generation and detection of terahertz waves', *IEEE/OSA Journal of Lightwave Technology*, **26**(15), 2409–2423, 2008.
 - 25. D. Saeedkia, S. Safavi-Naeini, and R. R. Mansour, 'The interaction of laser and photoconductor in a continuous-wave terahertz photomixer', *IEEE Journal of Quantum Electronics*, **41**(9), 1188–1196, 2005.
 - 26. D. Saeedkia, 'Resonantly enhanced terahertz power spectrum in terahertz photoconductive antennas', *Proceedings of the 34th International Conference on Infrared, Millimeter, and Terahertz Waves*, 2009.
 - 27. I. Wilke and S. Sengupta, 'Nonlinear optical techniques for terahertz pulse generation and detection – optical rectification and electrooptic sampling', in S. L. Dexheimer (ed.), *Terahertz Spectroscopy: Principles and Applications*. New York: CRC Press, chapter 2, pp. 41–72, 2008.
 - 28. K. Kawase, J. Shikata, and H. Ito, 'Terahertz wave parametric source', *Journal of Physics D: Applied Physics*, **34**, R1–R14, 2001.
 - 29. P. L. Richards, 'Bolometers for infrared and millimetre waves', *Journal of Applied Physics*, **76**(1), 1–24, 1994.
 - 30. A. J. Kreisler and A. Gaugue, 'Recent progress in high-temperature superconductor bolometric detectors: from the mid-infrared to the far-infrared (THz) range', *Superconductor Science and Technology*, **13**, 1235–1245, 2000.
 - 31. M. Shur and V. Ryzhii, 'Plasma wave electronics', in D. L. Woolard, W. R. Loerop and M. S. Shur (eds), *Terahertz Sensing Technology, Volume 1: Electronic Devices and Advanced Systems Technology*. Singapore: World Scientific, pp. 225–250, 2003.
 - 32. R. Tauk, F. Teppe, S. Boubanga, D. Coquillat, W. Knap, Y. M. Meziani, C. Gallon, F. Boeuf, T. Skotnicki, C. Fenouillet-Beranger, D. K. Maude, S. Rumyantsev, and M. S. Shur, 'Plasma wave detection of terahertz radiation by silicon field effects transistors: Responsivity and noise equivalent power', *Applied Physics Letters*, **89**, 253 511, 2006.
 - 33. A. Lisauskas, W. von Spiegel, S. Boubanga-Tombet, A. El Fatimy, D. Coquillat, F. Teppe, N. Dyakonova, W. Knap, and H.G. Roskos, 'Terahertz imaging with GaAs field-effect Transistors', *Electronics Letters*, **44**(6), 408–409, 2008.
 - 34. A. El Fatimy, J.C. Delagnes, A. Younus, E. Nguema, F. Teppe, W. Knap, E. Abraham, and P. Mounaix, 'Plasma wave field effect transistor as a resonant detector for 1 terahertz imaging applications', *Optics Communications*, **282**(15), 3055–3058, 2009.
 - 35. H.-W. Hubers, 'Terahertz heterodyne receivers', *IEEE Journal of Selected Topics Quantum Electronics*, **14**(2), 378–391, 2008.

36. P. H. Siegel and R. J. Dengler, 'Terahertz heterodyne imaging part I: introduction and techniques', *International Journal of Infrared and Millimeter Waves*, **27**(4), 465–480, 2006.
37. P. H. Siegel, 'THz technology: an overview', in D. L. Woolard, W. R. Loerop and M. S. Shur (eds), *Terahertz Sensing Technology, Volume 1: Electronic Devices and Advanced Systems Technology*. Singapore: World Scientific, pp. 1–44, 2003.
38. R. A. Cheville, 'Terahertz time-domain spectroscopy with photoconductive antennas', in S. L. Dexheimer (ed.), *Terahertz Spectroscopy: Principles and Applications*. New York: CRC Press, pp. 1–39, 2008.
39. S. Verghese, K. A. McIntosh, S. Calawa, W. F. Dinatale, E. K. Duerr, and K. A. Molvar, 'Generation and detection of coherent terahertz waves using two photomixers', *Applied Physics Letters*, **73**(26), 3824–3826, 1998.
40. P. K. Benicewicz, J. P. Roberts, and A. J. Taylor, 'Scaling of terahertz radiation from large-aperture biased photoconductors', *Journal of Optical Society of America B*, **11**(12), 2533–2546, 1994.
41. J. T. Darrow, X.-C. Zhang, D. H. Auston, and J. D. Morse, 'Saturation properties of large-aperture photoconducting antennas', *IEEE Journal of Quantum Electronics*, **28**(6), 1607–1616, 1992.
42. D. Grischkowsky and N. Katzenellenbogen, 'Femtosecond pulses of terahertz radiation: physics and applications', *OSA Proceedings on Picosecond Electronics and Optoelectronics*, **9**, 9–14, 1991.
43. S. Verghese, K. A. McIntosh, and E. R. Brown, 'Optical and terahertz power limits in the low-temperature-grown GaAs photomixers', *Applied Physics Letters*, **71**(19), 2743–2745, 1997.
44. E. R. Brown, F. W. Smith, and K. A. McIntosh, 'Coherent millimeter-wave generation by heterodyne conversion in low-temperature-grown GaAs photoconductors', *Journal of Applied Physics*, **73**(3), 1480–1484, 1993.
45. M. Neshat, D. Saeedkia, and S. Safavi-Naeini, 'On the behavior of the radiation field from large-aperture terahertz photoconductive antenna under impulsive excitation', *IEEE Proceedings on Antenna Technology: Small and Smart Antennas Metamaterials and Applications*, 495–498, 2007.
46. D. Saeedkia and S. Safavi-Naeini, 'A comprehensive model for photomixing in ultrafast photoconductors', *IEEE Photonics Technology Letters*, **18**(13), 1457–1459, 2006.
47. H. Tiedje, D. Saeedkia, M. Nagel, and H. Haugen, 'Optical scanning techniques for characterization of terahertz photoconductive antennas', *IEEE Transactions on Microwave Theory and Techniques*, **58**(7), 2040–2045, 2010.
48. D. S. Kim and D. S. Citrin, 'Coulomb and radiation screening in photoconductive terahertz sources', *Applied Physics Letters*, **88**, 161117, 2006.
49. J. H. Kim, A. Polley, and S. E. Ralph, 'Efficient photoconductive terahertz source using line excitation', *Optics Letters*, **30**(18), 2490–2492, 2005.
50. J. M. Yarborough, S. S. Sussman, H. E. Purhoff, R. H. Pantell, and B. C. Johnson, 'Efficient, tunable optical emission from LiNbO₃ without a resonator', *Applied Physics Letters*, **15**(3), 102–105, 1969.
51. H. E. Puthoff, R. H. Pantell, B. G. Huth, and M. A. Chacon, 'Near-forward Raman scattering in LiNbO₃', *Journal of Applied Physics*, **39**(4), 2144–2146, 1968.
52. M. A. Piestrup, R. N. Fleming, and R. H. Pantell, 'Continuously tunable submillimeter wave source', *Applied Physics Letters*, **26**(8), 418–421, 1975.

53. S. Hayashi, H. Minamide, T. Ikari, Y. Ogawa, J. Shikata, H. Ito, C. Otani, and K. Kawase, ‘Output power enhancement of a palmtop terahertz-wave parametric generator’, *Applied Optics*, **46**(1), 117–123, 2007.
54. J. Shikata, K. Kawase, T. Taniuchi, and H. Ito, ‘Fourier-transform spectrometer with a terahertz-wave parametric generator’, *Japanese Journal of Applied Physics*, **41**(1), 134–138, 2002.
55. B. C. Johnson, H. E. Purhoff, J. SooHoo, and S. S. Sussman, ‘Power and linewidth of tunable stimulated far-infrared emission in LiNbO₃’, *Applied Physics Letters*, **18**(5), 181–183, 1971.
56. T. Ikari, X. Zhang, and H. Minamide, ‘THz-wave parametric oscillator with a surface-emitted configuration’, *Optics Express*, **14**(4), 1604–1610, 2006.
57. K. Kawase, J. Shikata, K. Imai, and H. Ito, ‘Transform-limited, narrow-linewidth, terahertz-wave parametric generator’, *Applied Physics Letters*, **78**(19), 2819–2821, 2001.
58. R. Guo, K. Akiyama, H. Minamide, and H. Ito, ‘Frequency-agile terahertz-wave spectrometer for high-resolution gas sensing’, *Applied Physics Letters*, **90**(12), 121127, 2007.
59. F. Zernike and P. R. Berman, ‘Generation of far infrared as a difference frequency’, *Physical Review Letters*, **15**(26), 999–1001, 1965.
60. D. W. Faries, K. A. Gehring, P. L. Richards, and Y. R. Shen, ‘Tunable far-infrared radiation generated from the difference frequency between two ruby lasers’, *Physical Review*, **180**(2), 363–365, 1969.
61. T. J. Bridges and A. R. Strnad, ‘Submillimeter wave generation by difference-frequency mixing in GaAs’, *Applied Physics Letters*, **20**(10), 382–384, 1972.
62. B. Lax, R. L. Aggarwal, and G. Favrot, ‘Far-infrared step-tunable coherent radiation source: 70 μm to 2 mm’, *Applied Physics Letters*, **23**(12), 679–681, 1973.
63. Y.J. Ding, ‘High-power tunable terahertz sources based on parametric processes and applications’, *IEEE Journal of Selected Topics in Quantum Electronics*, **13**(3), 705–720, 2007.
64. T. Tanabe, K. Suto, J. Nishizawa, T. Kimura, and K. Saito, ‘Frequency-tunable high-power terahertz wave generation from GaP’, *Journal of Applied Physics*, **93**(8), 4610–4615, 2003.
65. T. Taniuchi and H. Nakanishi, ‘Collinear phase-matched terahertz-wave generation in GaP crystal using a dual-wavelength optical parametric oscillator’, *Journal of Applied Physics*, **95**(12), 7588–7591, 2004.
66. W. Shi and Y. J. Ding, ‘Tunable terahertz waves generated by mixing two copropagating infrared beams in GaP’, *Optics Letters*, **30**(9), 1030–1032, 2005.
67. E. D. Palik, Ed., *Handbook of Optical Constants of Solids*, Vol. I, 1985; Vol. II, 1991; Vol. III. Academic Press, 1998.
68. T. Taniuchi, J. Shikata, and H. Ito, ‘Tunable terahertz-wave generation in DAST crystal with dual-wavelength KTP optical parametric oscillator’, *Electronics Letters*, **36**(16), 1414–1416, 2000.
69. T. Taniuchi, S. Okada, and H. Nakanishi, ‘Widely tunable terahertz-wave generation in an organic crystal and its spectroscopic application’, *Journal of Applied Physics*, **95**(11), 5984–5988, 2004.
70. K. Suizu, K. Miyamoto, T. Yamashita, and H. Ito, ‘High-power terahertz-wave generation using DAST crystal and detection using mid-infrared powermeter’, *32*(19), 2885–2887, 2007.

71. W. Shi, M. Leigh, J. Zong, and S. Jiang, ‘Single-frequency terahertz source pumped by Q-switched fiber lasers based on difference-frequency generation in GaSe crystal’, **32**(8), 949–951, 2007.
72. J.A. L’huillier, G.Torosyan, M.Theuer, Y.Avetisyan, and R.Beigang, ‘Generation of THz radiation using bulk, periodically and aperiodically poled lithium niobate’, *Applied Physics B*, **86**, 185–208, 2007.
73. J. E. Schaar, K. L. Vodopyanov, and M.M. Fejer, ‘Intracavity terahertz-wave generation in a synchronously pumped optical parametric oscillator using quasi-phase-matched GaAs’, *Optics Letters*, **32**(10), 1284–1286, 2007.
74. D. Creeden, J. C. McCarthy, P. A. Ketteridge, T. Southward, P. G. Schunemann, J. J. Komiak, W. Dove, and E. P. Chicklis, ‘Compact fiber-pumped terahertz source based on difference frequency mixing in ZGP’, *IEEE Journal of Selected Topics in Quantum Electronics*, **13**(3), 732–737, 2007.
75. Y.-S. Lee, T. Meade, V. Perlin, H. Winful, T. B. Norris, and A. Galvanauskas, ‘Generation of narrow-band terahertz radiation via optical rectification of femtosecond pulses in periodically poled lithium niobate’, *Applied Physics Letters*, **76**(18), 2505–2507, 2000.
76. G. Imeshev, M. E. Fermann, K. L. Vodopyanov, M. M. Fejer, X. Yu, J. S. Harris, D. Bliss, and C. Lynch, ‘High-power source of THz radiation based on orientation-patterned GaAs pumped by a fiber laser’, *Optics Express*, **14**(10), 4439–4444, 2006.
77. L. A. Eyres, P. J. Tourreau, T. J. Pinguet, C. B. Ebert, J. S. Harris, M. M. Fejer, L. Becouarn, B. Gerard, and E. Lallier, ‘All-epitaxial fabrication of thick, orientation-patterned GaAs films for nonlinear optical frequency conversion’, *Applied Physics Letters*, **79**(7), 904–906, 2001.
78. I. Tomita, H. Suzuki, H. Ito, H. Takenouchi, K. Ajito, R. Rungsawang, and Y. Ueno, ‘Terahertz-wave generation from quasi-phase-matched GaP for 1.55 μm pumping’, *Applied Physics Letters*, **88**, 071118, 2006.

Transmission and propagation of terahertz waves in plastic waveguides

B. UNG and M. SKOROBOGATIY,
École Polytechnique de Montréal, Canada

DOI: 10.1533/9780857096494.1.28

Abstract: Polymer optical fibers provide a versatile solution for guiding terahertz (THz) radiation. The key benefits of this technology include: the abundance of the low-cost relatively low-absorption-loss polymers; the ease of fiber preform fabrication by molding, drilling, stacking and the use of other standard polymer processing techniques; and finally the advantage of simple fabrication method by fiber drawing at relatively low temperatures. In this chapter we review the latest developments in the design, fabrication and characterization of plastic-based optical fibers for guiding of THz light.

Key words: terahertz waveguides, optical fiber design and fabrication, microstructured optical fibers, polymer optical fibers, terahertz spectroscopy.

2.1 Introduction

In the last decade, technological advances in the generation (Imeshev *et al.*, 2006; Shi *et al.*, 2009; Tang *et al.*, 2010) and the detection (Cai *et al.*, 1998; Karpowicz *et al.*, 2008) of terahertz (THz) signals have come a long way. Both pulsed and continuous-wave THz sources are now commercially available, and complete THz imaging/spectroscopy turnkey systems based on free-space optics are getting close to market introduction (Hoshina *et al.*, 2009; Jansen *et al.*, 2010a; Wilmink *et al.*, 2011; Zhong *et al.*, 2011). As is the case with most free-space-optics-based systems, their size is large, and the constituent optical subcomponents require careful alignment, thus rendering such systems bulky and difficult to service and reconfigure. In the near-infrared spectral range, the use of flexible optical fibers as links between individual optical components has resulted in a dramatic increase in the reliability of system performance, reduction in the system size, and high level of integration. We believe that the same can be achieved with THz systems if only the low-loss, low-dispersion, broadband fibers were

to be available. In this respect, development of the THz fibers constitutes an important milestone towards successful commercialization of the THz technology.

In this chapter we give an assessment of the latest technological progress in the design, fabrication and characterization of polymer microstructured optical fibers (MOFs) and polymer photonic bandgap (PBG) fibers for THz waveguiding. We argue that polymers possess several key properties desirable for THz waveguides: cheap and widely accessible materials, facile low-temperature processing, and relatively low losses compared to those of other dielectrics in the THz spectral range. We then outline the main challenges currently facing THz waveguide technology in general, and how they apply to polymer-based fibers in particular. We present a selection of plastic MOFs and PBG fibers of various types that demonstrate promising results. Future areas of improvement and research are proposed. Finally, we provide an overview of some niche applications in the THz waveband, where plastic MOFs can be an enabling and cost-effective technology.

2.2 Main challenges of the plastic-based terahertz fiber optics

Currently, the main obstacle in the design of THz dielectric waveguides resides in the large material losses that significantly limit the waveguide transmission efficiency. In what follows, we present several innovative designs of the porous, subwavelength, and hollow-core plastic fibers that effectively circumvent this problem, albeit within somewhat limited spectral regions.

Another key obstacle which pertains to the efficient transmission of the broadband THz pulses is presented by the need of low waveguide dispersion. In this respect, we will show that relatively large effective bandwidths can be achieved by the same porous dielectric fibers and the hollow-core fibers where modal propagation primarily occurs within the low-loss low-dispersion gaseous core.

2.2.1 Losses

Most of the solid materials exhibit large losses $\sim \text{cm}^{-1}$ in the THz frequency range (Jin *et al.*, 2006). Therefore, the first challenge in designing the THz waveguides is to minimize their propagation losses. Since dry air (and some other dry gases) possesses negligible THz absorption, one successful strategy for reducing modal propagation loss is to maximize the fraction of power that is guided outside the lossy material and within low-loss gaseous region. The ratio of the modal loss to bulk material losses can then be evaluated

to first-order approximation using the following (Skorobogatiy and Yang, 2009, Chapter 5.2.1) expression:

$$f_\alpha = \frac{\alpha_{\text{mode}}}{\alpha_{\text{mat}}} = c \epsilon_0 \frac{\text{Re}(n_{\text{mat}}) \cdot \int_{\text{mat}} |E|^2 dA}{\int_{\text{total}} S_z dA} \quad [2.1]$$

$$S_z = \frac{1}{2} \text{Re}(E \times H^*) \cdot \hat{z}$$

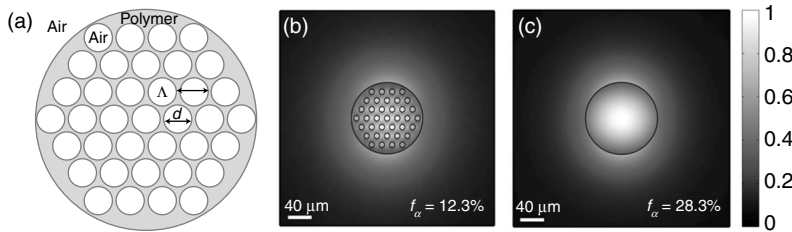
where c denotes the light velocity in vacuum.

Solid core subwavelength fibers

One of the simplest plastic fibers that provide for a high fraction of power in the low-loss regions is the subwavelength core fiber introduced by Chen *et al.* (2006) and used extensively in power transmission and imaging applications (Lu *et al.*, 2008a, 2008b; Chiu *et al.*, 2009). The fiber is a simple plastic wire having circular cross-section of subwavelength diameter. This step-index fiber allows single-mode HE₁₁ operation via total internal reflection guiding mechanism. Due to the subwavelength diameter of the solid core, the fundamental guided mode has a strong presence in the low-loss air cladding (see Fig. 2.1c).

Porous core subwavelength fibers

It was demonstrated by Nagel *et al.* (2006) that inserting a subwavelength-sized hole in the middle of an otherwise solid dielectric core leads to a significant enhancement of the modal fields in the gas-filled hole, and as a consequence, reduction in the waveguide losses. The authors explained the strong field presence in the subwavelength hole using the continuity of transverse component of the electric displacement field at the air/dielectric interface. Taking one step further, it was recently proposed theoretically by Hassani *et al.* (2008a, 2008b), and then demonstrated experimentally (Atakaramians *et al.*, 2009; Dupuis *et al.*, 2009, 2010) that incorporation of an array of deeply subwavelength holes in the core of a subwavelength fiber (see Fig. 2.1a) allows further reduction of the fiber propagation losses compared to those of a solid core fiber of similar diameter. In Fig. 2.1b and c we present distribution of the energy flux along the fiber direction S_z in the porous polyethylene (PE) fiber and solid core PE fiber of the same outer diameter ($d_{\text{fiber}} = 120 \mu\text{m}$). A full-vector finite-element method was used (COMSOL Multiphysics) to compute the fiber modes at 1 THz. In the case of a porous fiber we observe strong presence of the modal fields in the low-loss holes, while in the case of a solid core fiber the modal fields are mostly concentrated in the lossy dielectric.



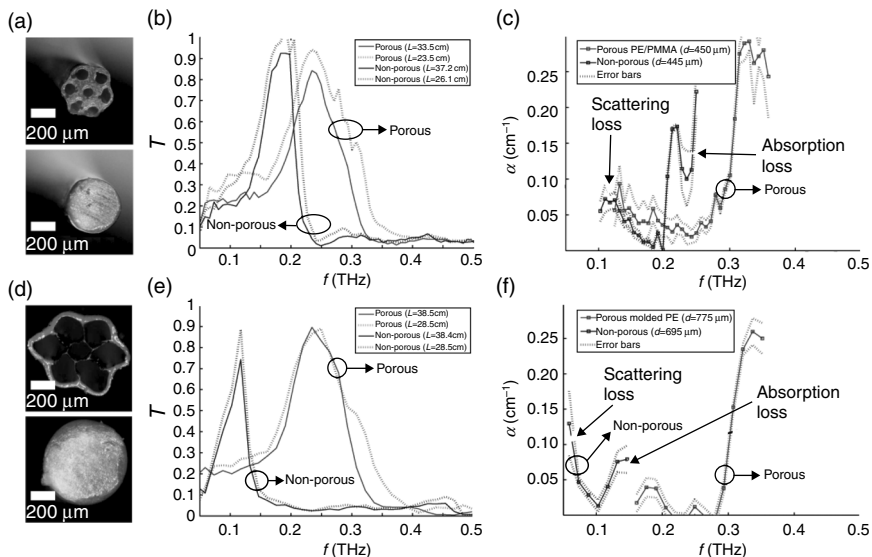
2.1 (a) Schematic of the cross-section of a porous fiber with $N=3$ layers of holes. (Λ represents the period (that is the pitch) of the holes.) (b) Fundamental mode profile at 1 THz in a subwavelength porous core PE fiber ($d_{\text{fiber}} = 120 \mu\text{m}$, $d_{\text{hole}} = 9 \mu\text{m}$), and (c) in a subwavelength solid core PE fiber ($d_{\text{fiber}} = 120 \mu\text{m}$).

It is not surprising that a porous fiber shows lower modal losses than a solid rod fiber of comparable diameter. This is due to the lower fraction of the modal power – as calculated with Equation [2.1] – in the lossy material region for the porous fiber ($f_\alpha = 12.3\%$ in Fig. 2.1b), when compared to that for the solid core fiber ($f_\alpha = 28.3\%$ in Fig. 2.1c). Cutback measurements of the propagation losses (Fig. 2.2c and f) demonstrate that propagation losses as low as $0.01\text{--}0.02 \text{ cm}^{-1}$ can be consistently achieved with porous and solid core fibers, even when bulk material loss is as large as 0.2 cm^{-1} . Although not explicitly shown in Fig. 2.2, one indeed typically observes that the minimal transmission loss of a porous fiber is smaller than that of a solid core fiber of a comparable diameter.

We note that at low frequencies, modal losses of both fibers show strong increase due to onset of the scattering loss on the fiber microstructure defects and longitudinal fiber diameter fluctuations. At higher frequencies, the modal loss shows a sharp rise due to onset of the material absorption loss stemming from the stronger modal confinement inside the lossy dielectric region.

Additionally, it was demonstrated that porous fibers allow both broadening and shifting the transmission window towards higher THz frequencies compared to non-porous fibers of equal diameter (Dupuis *et al.*, 2010), as is also revealed in the transmission spectra presented in Fig. 2.2b and e.

To summarize, there are several benefits in using highly porous fibers compared to solid core fibers. First of all, addition of an array of subwavelength holes into the cross-section of a subwavelength fiber not only increases the fraction of power guided in the air (thus leading to lower absorption losses), but also allows concentrating more light within the porous core itself, thus dramatically reducing the proximity cross-talk of the fiber mode with the environment. Moreover, it can be shown that porous fibers exhibit a much smaller bending loss compared to the non-porous fibers of comparable transverse dimensions, which again can be explained by stronger modal confinement inside the porous core (Hassani *et al.*, 2008b). Finally, porous



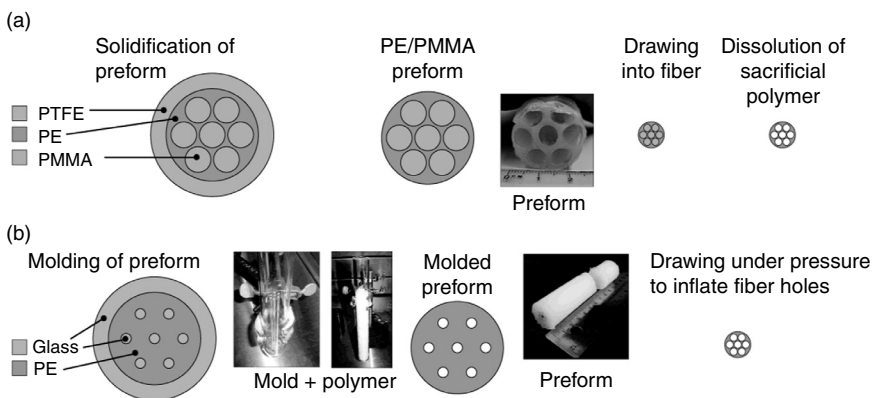
2.2 Transmission and cutback loss measurements of porous and non-porous subwavelength PE fibers of (a)–(b)–(c) small diameter fibers ($d \sim 450 \mu\text{m}$), and (d)–(e)–(f) larger diameter fibers ($d \sim 700 \mu\text{m}$). (From Dupuis *et al.*, 2010.)

fibers with outer diameters much larger than the wavelength of light can be designed, while still operating in a single-mode regime and exhibiting low propagation and bending losses. This is particularly useful when trying to couple into such fibers using THz sources featuring relatively large beam sizes >1 mm, which is typical for many practical THz systems.

Fabrication of the porous core subwavelength fibers

Solid core subwavelength fibers can be produced by drawing a cylindrical preform of a plastic material into a fiber. Similarly, porous fibers are created by drawing into a fiber a cylindrical preform with holes. The main challenge in the fabrication of porous fibers lies in preventing the holes from collapsing or getting partially obstructed during fiber drawing. In what follows, we describe two different approaches for fabricating porous fibers that were successfully demonstrated: the sacrificial polymer technique, and the microstructured molding technique, as schematically presented in Fig. 2.3a and Fig. 2.3b, respectively.

In the sacrificial polymer technique (Fig. 2.3a), rods of the sacrificial polymer (in this case PMMA plastic) are first stacked in a triangular lattice inside a polymer tube (here PTFE plastic) while ensuring the rods do not touch each other (Dupuis *et al.*, 2009, 2010). All the remaining interstices



2.3 Schematics of the fabrication procedures of porous subwavelength fibers via (a) the sacrificial polymer technique and (b) the microstructured molding technique. (From Dupuis *et al.*, 2010.)

in the tube preform are filled with granules of the fiber core polymer (in this example, low-density PE). It is important that the sacrificial polymer (PMMA) should possess a higher glass transition temperature than the fiber core polymer (PE) in order for the PE granules to melt and fill out the interstitial space between the PMMA rods. The ensuing all-polymer preform is then drawn at a temperature of 210°C. Finally, the drawn fiber is placed into a solvent bath to dissolve all the PMMA from the fiber and reveal the holes. Drawing of the porous fibers is greatly simplified when the sacrificial polymer technique is used, since the resultant preform is fully solid and hole collapse is not an issue during the process. However, a post-processing step is required to remove the sacrificial polymer, which limits the length of porous fibers that could readily be fabricated to several meters. Moreover, the sacrificial polymer method usually produces smaller porosity fibers (<35%) compared to the microstructured molding followed by drawing under pressure technique where porosity as high as 86% was demonstrated.

Porous fibers can also be fabricated using the microstructured molding technique (Fig. 2.3b) where the fiber preform is cast in a microstructured mold (Dupuis *et al.*, 2010). The resulting preform features air holes which have to be pressurized during drawing to prevent hole collapse. A schematic of the fabrication steps is shown in Fig. 2.3b. First, a microstructured mold featuring suitably aligned capillaries (or rods) made from silica glass is fabricated, and PE granules are added to fill the entire preform. The tubular preform is then heated in a furnace in order to melt all the PE, and left to cool down. The bulk glass structure is removed from the preform by hand, and any glass residues are dissolved in hydrofluoric acid, which has no effect on the PE preform. The preform is subsequently drawn under pressure. A

proper choice of pressure is necessary to prevent holes from collapsing or to further inflate the holes. This enables fabrication of fibers with porosities higher than porosity of a preform.

In passing, we also note that an alternative method – not discussed here – for fabricating porous fibers is through an extrusion process. Complex pre-forms have been demonstrated with this method (Ebendorff-Heidepriem and Monro, 2007).

2.2.2 Dispersion

Many of the currently used THz sources emit broadband picosecond pulses. Efficient waveguide delivery of such pulses requires low transmission losses in the whole spectral window covered by the pulse, as well as low group velocity dispersion (GVD) to prevent degradation of the pulse shape. The main impact of the waveguide dispersion is in the pulse spreading, leading to a significant decrease in the peak pulse amplitude and, as a consequence, a significant decrease in the signal-to-noise ratio. Moreover, every THz system has a fundamental limit on the maximal duration of a pulse, which is either by the finite length of the delay line or the appearance of secondary reflections in the detection antennae assembly. In principle, for linear systems dispersion compensation can be used to counteract the effects of waveguide dispersion and to reconstruct the original pulse shape; however, this approach has not yet been explored in the THz frequency range. Chromatic dispersion of the group velocity is typically quantified using the coefficient β_2 (in ps/THz/cm) corresponding to the second-order term in the Taylor expansion of the modal propagation constant β with respect to the frequency of operation:

$$\beta_2 = \frac{2}{c} \frac{dn_{\text{eff}}}{d\omega} + \frac{\omega}{c} \frac{d^2n_{\text{eff}}}{d\omega^2} \quad [2.2]$$

where $\omega = 2\pi f$ and $n_{\text{eff}} = \text{Re}(\beta) \cdot c/\omega$ denotes the real part of the effective refractive index of the mode. If the initial pulse is Gaussian with the pulse width τ_0 , after propagating along the length L of a dispersive waveguide, the output pulse is a broadened Gaussian with a new width $\Delta\tau \sim LD/\tau_0$. Assuming that the average pulse power stays the same, spectral power density will thus decrease inversely proportional to the temporal pulse width $\Delta\tau$. This in turn will result in the decrease of a signal-to-noise ratio by $-10 \log_2(\tau_0/\Delta\tau)$ [dB].

Typical dispersion values for the fundamental mode of a solid core subwavelength fiber are presented in Fig. 2.4a for various values of the fiber core diameter. As seen from this figure, the calculated GVD for the

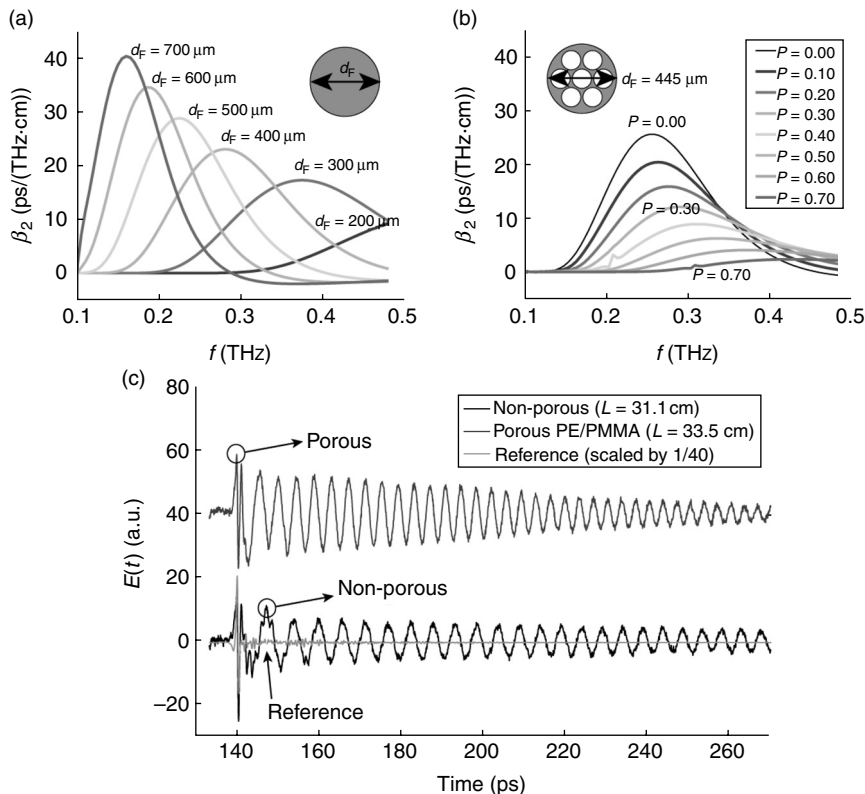
fundamental mode of a solid core subwavelength PE fiber can be quite high, reaching ~ 40 ps/THz/cm between 0.1 and 0.5 THz (Dupuis *et al.*, 2010). As an example, for a $\tau_0 = 1$ ps-long THz input pulse, the output pulse width after propagation over $L = 1$ cm of a fiber with 10 ps/THz/cm dispersion will be 10 ps, thus resulting in a decrease of a signal-to-noise ratio by $-10 \log_{10}(\tau_0/\Delta\tau) = 10$ dB. With a typical ~ 30 dB power budget of a THz set-up, this constitutes a considerable reduction of the signal-to-noise ratio after propagation even over a short length, and limiting the total propagation distance to less than 10 cm.

For a given fiber diameter, GVD of the fundamental mode can be reduced by introducing porosity into the fiber core. In Fig. 2.4b, waveguide dispersion is presented for the fundamental mode of a fiber of 450 μm diameter as a function of the fiber porosity. Porosity is defined as a ratio of the net surface of all the air regions to the area of the fiber cross-section. By increasing porosity, the modal field becomes more and more delocalized in the air region. As a result, the corresponding modal effective refractive index becomes close to that of air, which is the main reason for the reduced GVD of the fundamental mode in porous fibers. In Fig. 2.4c, we present the shapes of the THz pulses transmitted through ~ 30 cm-long section of porous and non-porous fibers. The two fibers have comparable outer diameters of ~ 450 μm . As a reference, we also present the shape of a THz Gaussian pulse source in the absence of fibers. It is clear from Fig. 2.4c that the porous fiber has lower dispersion since the envelope of the THz pulse is decaying more rapidly than that of the non-porous fiber; however, the guided pulse envelope is still significantly wider than that of the original pulse, thus corroborating the large dispersion predicted in the simulations (Fig. 2.4b).

We believe that GVD of less than 1 ps/THz/cm can be achieved in the low-loss porous fibers without sacrificing too many fiber guidance properties such as resilience to bending losses. We also mention in passing that a solid core fiber using Topas® copolymer was recently demonstrated to have low GVD in the range of ~ 2 ps/THz/cm for frequencies between 0.2 and 1.4 THz (Nielsen *et al.*, 2009). This is achieved by using material with relatively low material dispersion, as well as through active dispersion engineering of the fundamental mode.

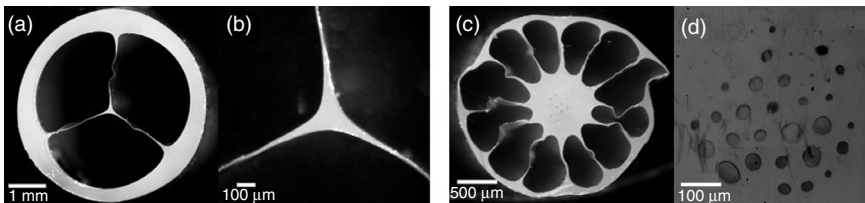
2.2.3 Packaging of subwavelength fibers

While a highly delocalized field is favorable for lowering absorption losses in the material, it is a major inconvenience when handling the fiber during normal operation, because of the strong perturbation induced to the mode through direct manipulation of the fiber or via holders (such as strings and other apparatus) used for maintaining the fiber in the position (Rozé *et al.*, 2011). Therefore, the issue of core encapsulation is crucial



2.4 Dispersion parameter of (a) non-porous and (b) porous PE fibers based on finite-element simulations. (c) Temporal evolution of the output signal in $d = 450 \mu\text{m}$ porous fiber (top curve) and $d = 445 \mu\text{m}$ non-porous fiber (bottom dark curve), compared with the reference pulse (bottom light curve). The porous fiber time scan is offset vertically by +40; while the reference pulse is scaled by a factor 1/40 for clarity. (From Dupuis *et al.*, 2010.)

for subwavelength dielectric fibers. There are two principal incentives for encapsulating the solid/porous core of a fiber within an outer polymer tube as shown in Fig. 2.5a and Fig. 2.5c. First, the solid tubular cladding confers greater mechanical stability and shielding for the subwavelength-sized core, thus allowing smaller bending radii and protection against the accumulation of dust and other surface contaminants. Second, the outer tube cladding prevents the highly delocalized core-guided mode from interacting with the surrounding environment, thus eliminating cross-talk noise with adjacent waveguides, and perturbation-induced losses incurred by direct manipulation of the fibers or due to fiber holders. Moreover, core encapsulation opens the way for the easy and economical purging of the low volume tube



2.5 (a) Cross-section of the suspended core fiber ($OD = 5.1\text{ mm}$) and (b) close-up view of the suspended core region ($d_{\text{core}} = 150\text{ }\mu\text{m}$). (c) Cross-section of the porous core fiber ($OD = 3\text{ mm}$) and (d) close-up view of the suspended large porous core ($d_{\text{core}} = 900\text{ }\mu\text{m}$). (From Rozé *et al.*, 2011.)

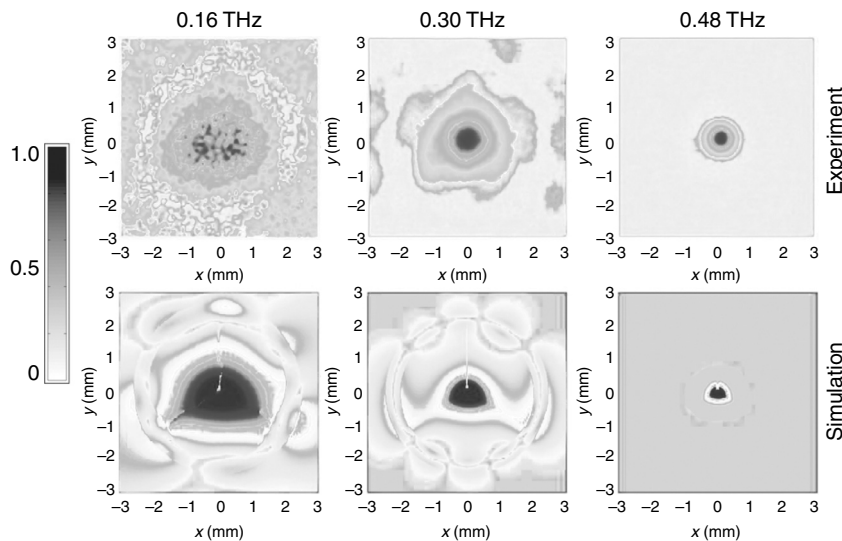
cladding with dry air so as to eliminate losses due to water vapor typically present in the ambient environment. In other words, core encapsulation allows forgoing the use of large purged or vacuumed enclosures that are typically required for guiding THz light over long distances, as the porous fiber cladding becomes the enclosure.

Figure 2.5 presents two types of suspended core fibers that were both fabricated using low-density polyethylene (PE) and demonstrated propagation losses as low as 0.02 cm^{-1} (Rozé *et al.*, 2011). A combination of drilling and stacking techniques were used to fabricate a solid suspended core fiber (Fig. 2.5a–b) featuring a $150\text{ }\mu\text{m}$ core suspended in the middle of a 5.1 mm outer diameter (OD) fiber; along with a suspended porous core fiber (Fig. 2.5c–d) having a $900\text{ }\mu\text{m}$ diameter core with ~10% porosity inside a 3 mm OD fiber.

Images of the output Ex -polarized near-field profiles from both fibers were obtained using a THz near-field imaging system that utilizes a scanning photoconductive antenna as a polarization-sensitive near-field probe. This powerful characterization technique provides subwavelength spatial resolution ($\sim\lambda/20$) images with time-frames of sub-picosecond temporal precision. More details on the utilized near-field microscopy set-up can be found in (Bitzer *et al.*, 2010; Walther and Bitzer, 2011).

Two-dimensional profile maps (x - y distribution) of the transverse $|Ex|$ -field were captured by raster scanning of the fiber cross-section with the probe detector yielding a 60×60 pixels resolution in a 6 mm^2 area that covered the whole output facet of the fibers. Figure 2.6 presents the output field profiles at selected frequencies as measured experimentally (top row) and via simulations (bottom row) based on the full-vector finite-element method, for the case of the small suspended core fiber in Fig. 2.5a–b.

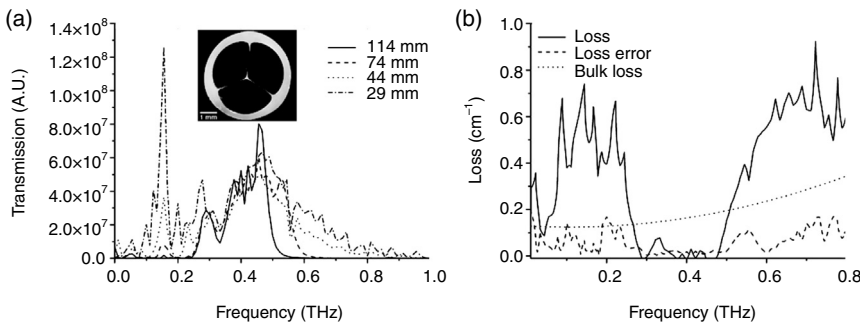
The complex modal structure pictured in Fig. 2.6 stems from the various guiding mechanisms that coexist in this waveguide depending on the excitation frequency. For example: core-guided modes, cladding modes, surface



2.6 Near-field microscopy images (top row) and corresponding simulations (bottom row) of the output $|Ex|$ -field profile of the suspended solid core fiber at 0.16, 0.30 and 0.48 THz. (Adapted from Rozé *et al.*, 2011.)

modes, and bridge-guided modes can be excited at various frequencies. We here identify two main regimes of light propagation in such fibers. The first guidance regime, which occurs near 0.16 THz, is due to anti-resonant (ARROW) guidance by the encapsulating tube. In this regime, the mode is essentially insensitive to the structure of the suspended core. Instead, the guided field is strongly delocalized and fills completely the inner tube region, while the efficiency of mode propagation is dictated by the Fabry–Pérot resonant conditions in the tubular cladding of finite thickness. As a result, a narrow transmission peak at 0.16 THz can be seen in the transmission spectrum of the fiber (Fig. 2.7a).

The second propagation regime (see modal field distributions at 0.30 THz and 0.48 THz in Fig. 2.6) represents the main regime of interest where the mode is guided by the total internal reflection in the suspended-in-air high-refractive-index core. The propagation is effectively single-mode if care is taken not to excite peripheral modes in the tubular cladding. The suspended core fiber shows low-loss single-mode guidance in the 0.28–0.48 THz spectral region, as revealed by the cutback measurements shown in Fig. 2.7b. A propagation loss value of less than 0.02 cm^{-1} is estimated in this region. Near-field imaging of the modal profiles (Fig. 2.6) reveals that a large fraction of power is guided within the low-loss air regions and well inside the tubular jacket. At frequencies higher than 0.50 THz, modal field confinement



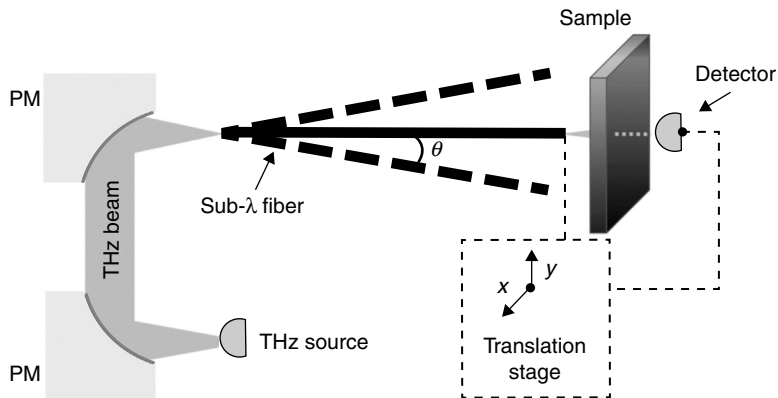
2.7 (a) Amplitude transmission spectra measured for varying lengths of suspended solid core fiber and (b) corresponding average power attenuation losses. (From Rozé *et al.*, 2011.)

becomes so strong that almost all the guided power propagates within the lossy solid core, thus explaining the rapid increase of the modal propagation loss. Additionally, higher-order modes appear at higher frequencies (Rozé *et al.*, 2011).

2.3 Devices based on subwavelength fibers

A number of spectroscopic and imaging systems have been recently reported in the THz spectral region for non-destructive testing applications in the manufacturing, security, food industries (Jansen *et al.*, 2010a), biology and medicine (Siegel, 2004), and many other areas where the non-ionizing and slightly penetrating THz radiation can be exploited (Tonouchi, 2007). The potential for THz spectroscopy in the petrochemical (Jin *et al.*, 2008) and pharmaceutical (Zeitler *et al.*, 2007) industries, as well as in biochemistry (Ebbinghaus *et al.*, 2008) and remote gas spectroscopy (Liu *et al.*, 2010), have also been identified. However, most of these THz systems rely on the bulky free-space optics and require a large nitrogen-purged or evacuated cage to minimize ambient water vapor absorption, which significantly limits the convenience of operation and portability of these systems.

In this respect, we believe that fully encapsulated low-loss polymer waveguides for THz delivery have strong potential to simplify realization of the compact and easy-to-use THz systems. Particularly, by purging the fiber microstructure with dry gas one can forgo the bulky nitrogen-filled cage. At the same time, standoff distance between the THz source and target sample, and hence convenience of operation, can be greatly increased by using fibers for THz wave delivery. In what follows we present two examples in which subwavelength dielectric fibers have been integrated into practical THz systems.



2.8 Schematic of the THz fiber-based scanning imaging system.
PM, parabolic mirror.

2.3.1 Fiber-based terahertz imaging

A THz fiber endoscope (Lu *et al.*, 2008a), a fiber-based THz imaging system (Lu *et al.*, 2008b) and a fiber-scanning THz near-field microscope (Chiu *et al.*, 2009) have been demonstrated using subwavelength polymer fibers. These systems used small deflections of one end of the fiber ($\theta \leq 2^\circ$) for scanning, while keeping the other end fixed. The schematic diagram in Fig. 2.8 illustrates the basic approach of the THz fiber-scanning imaging technique.

Set-up in Fig. 2.8 is designed to measure the THz transmission through THz-transparent samples (Lu *et al.*, 2008b). A modification of this set-up enables THz near-field imaging by attaching a metallic bull's-eye structure at the output fiber end, whose role is to lower the divergence angle of the output THz beam, so as to tightly focus the light onto the thinly sliced (20 μm thick) biological samples. The THz signal transmitted through the samples is collected with the help of a light concentrator (in this case, a Winston cone) and then imaged on the detector cell (Chiu *et al.*, 2009). Yet another modification of this set-up (which uses two subwavelength fibers in a directional coupler configuration) creates a fiber endoscope that allows detection and imaging of the reflected THz signal from a biological sample (Lu *et al.*, 2008a). Moreover, the authors demonstrated that it is possible with this technique to also retrieve the depth profile of the samples by slowly moving the endoscope away from the sample while recording the amplitude of the reflected signal. The resulting signal amplitude as a function of longitudinal (z -axis) distance shows clear Fabry-Pérot fringes – yielded by the multiple reflections of the THz signal between the sample surface and the output end of the imaging fiber – which can be used to reconstruct the transverse depth information of the samples.

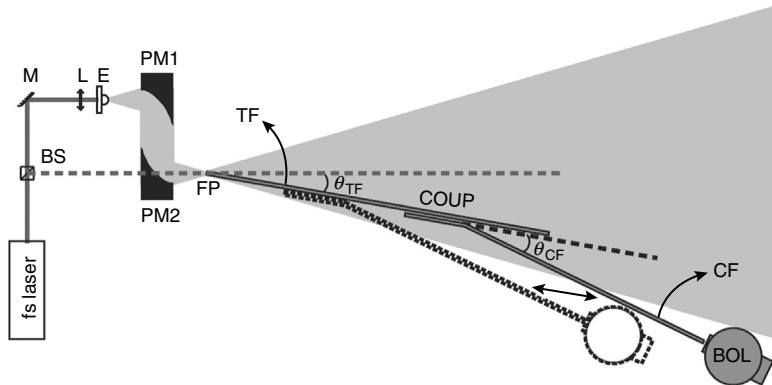
2.3.2 Directional couplers and non-destructive cutback technique

Transmission losses incurred by the THz signal propagating inside subwavelength fibers are generally evaluated through the standard cutback method in which one measures the output power of a fiber that is cleaved to yield progressively shorter fiber segments, and subsequently inferring the average losses. The cutback method is therefore a destructive technique which is susceptible to errors, due to irregular cleaving and realignment of the fiber output end, for each fiber segment.

Since the mode propagating in a bare subwavelength fiber typically possesses a highly delocalized field (see Fig. 2.1c), one can exploit the large modal lateral extension by using another fiber to probe the evanescent field on the surface of the test fiber under study. This approach described in Dupuis *et al.* (2009), called *directional coupler method*, provides a non-destructive procedure to evaluate the transmission losses of a subwavelength fiber.

The directional coupler method consists of using a second subwavelength fiber (henceforth referred as the *coupler fiber* (CF)) to form a directional coupler with the subwavelength fiber under study (referred to as the *test fiber*). As shown on the diagram (Fig. 2.9), the output end of the CF remains fixed with respect to the bolometer's input aperture. The ensuing apparatus (CF and bolometer) forms a directional coupler that is mounted on a rail and then translated along the length of the test fiber (TF) in order to directly probe the power attenuation as a function of propagation distance. In this set-up (Fig. 2.9), the two ends of the TF are individually positioned with 3-axis mounts; where the input end can be accurately aligned with the optical axis of the THz beam by using a Ti:Sapphire laser line which passes through a small hole in the second parabolic mirror (PM2). The directional coupler consists of a straight 7 cm-long segment of the CF (total fiber length is 29 cm) which was brought in parallel to, and nearly touching, the TF. The two angles $\theta_{TF} = 10^\circ$ and $\theta_{CF} = 16^\circ$ are suitably chosen such that the bolometer remains at all times outside the cone of divergence of the input THz light. This procedure enables elimination of all background noise encountered in the cutback method when measuring short fiber segments during which the detector is located close to the emitter and thus within the divergence cone of the THz source.

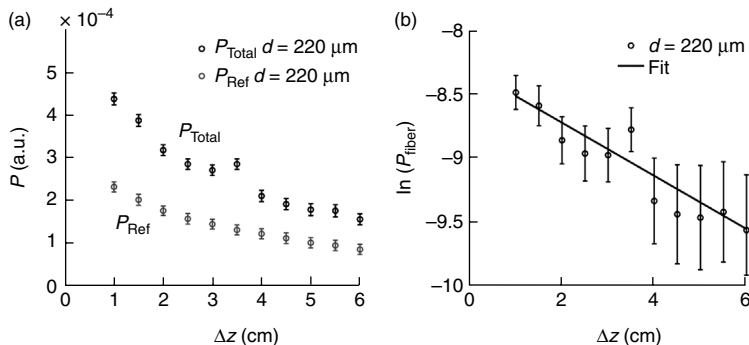
Figure 2.10a plots the variation of power as a function of displacement (Δz) along the length of a TF. We note that the horizontal axis in Fig. 2.10 does not represent the absolute position with respect to the input end of the TF, but rather the relative distance traveled by the coupler along the TF from an initial point. The reference signal in Fig. 2.10a, is obtained by translating the coupler in the absence of the TF, and thus measures the fraction of THz light (from the divergent cone) that directly couples into the CF.



2.9 Schematic of the set-up used for measuring fiber transmission losses using the directional coupler method. The directional coupler assembly (COUP) which consists of a coupling fiber (CF) and a bolometer (BOL), is translated along the length of a TF. The TF is placed at a $\theta_{TF} = 10^\circ$ angle with respect to the axes of a focusing parabolic mirror (PM2), while the CF is placed at $\theta_{CF} = 16^\circ$ angle with respect to the TF. Other elements include a beam splitter (BS), mirror (M), lens (L) and a THz emitter (E). (From Dupuis *et al.*, 2009.)

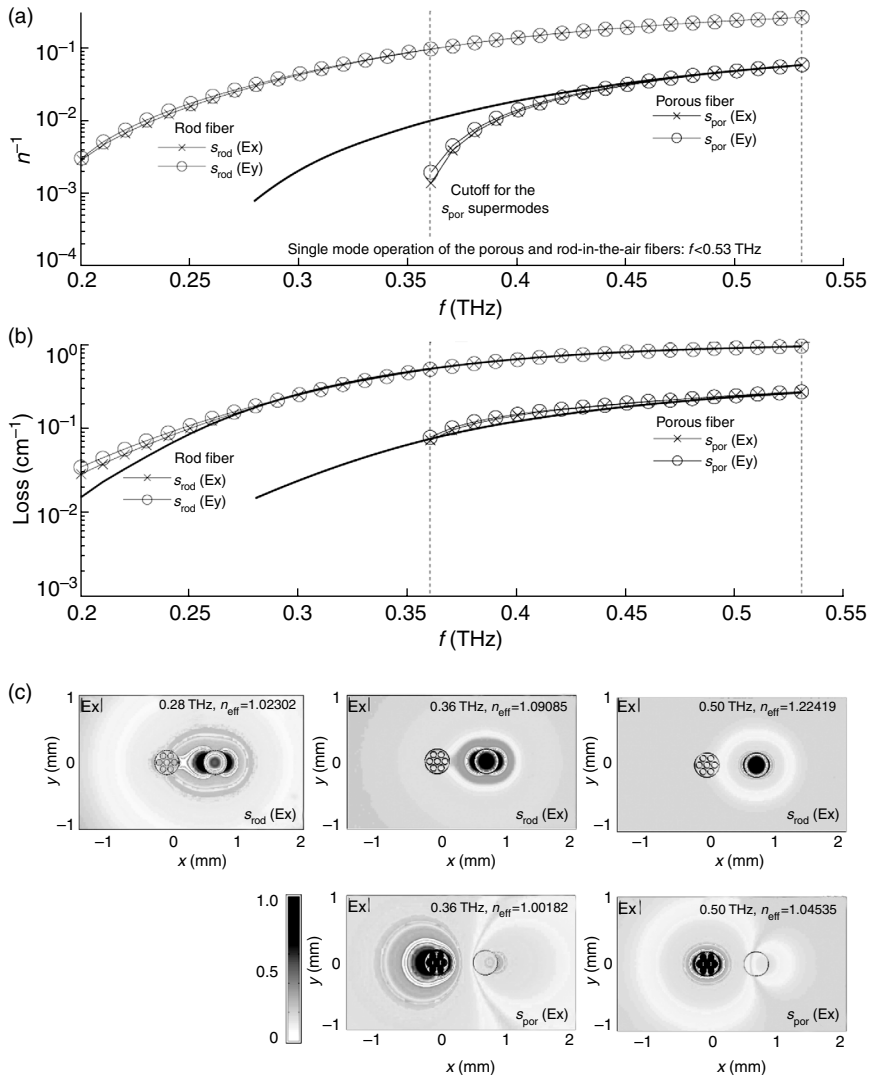
The fiber transmission is obtained by subtracting the reference signal from the total signal measured with the TF. Figure 2.10b plots the power attenuation (on a logarithmic scale) as a function of displacement along the TF. The slope of the least-squares fit ($P_{\text{fiber}}(\Delta z) \sim e^{-\alpha_{\text{TF}} \Delta z}$) provides an estimate of the attenuation coefficient: $0.21 \pm 0.05 \text{ cm}^{-1}$. We note that in these measurements we assume the power coupling efficiency between the two fibers remains constant for all measurements taken along the TF.

We have further investigated the coupling mechanisms occurring in the directional coupler composed of a subwavelength solid core fiber and a subwavelength porous core fiber (with seven air holes of $95 \mu\text{m}$ diameter) separated by a small $380 \mu\text{m}$ air gap, by performing eigenmode calculations based on the finite-element method (COMSOL Multiphysics). Both fibers are assumed to have ODs of $380 \mu\text{m}$ with the refractive index and absorption of polyethylene: $n_{\text{PE}} = 1.516$ and $\alpha_{\text{PE}} = 1 \text{ cm}^{-1}$ respectively. Preliminary simulations performed separately on each fiber first indicated that both subwavelength fibers are single-moded at smaller frequencies $f \leq 0.53 \text{ THz}$. The calculated fundamental mode dispersion relation ($n_{\text{eff}} - 1$) and propagation losses are plotted for the porous and non-porous fibers in Fig. 2.11a–b. We note in Fig. 2.11b that losses of a subwavelength porous fiber are consistently and significantly lower than those of a similar non-porous fiber.



2.10 (a) Power (in arbitrary units) as a function of a relative displacement (Δz) along the TF (220 μm average diameter). Total and reference signals are measured with and without the TF, respectively. (b) Fit of the fiber attenuation data ($P_{\text{fiber}} = P_{\text{Total}} - P_{\text{Ref}}$). (From Dupuis *et al.*, 2009.)

For the coupler configuration, due to mirror symmetry with respect to the x -axis, the coupler supermodes can be labeled as x or y -polarized depending on whether the dominant component of their electric field is E_x or E_y . In Fig. 2.11a we note that two of the four coupler supermodes have a cut-off frequency of $f = 0.36$ THz; therefore, below this frequency all individual fibers and the coupler are single-moded. We further note that their dispersion relations and losses remain very similar; therefore only the field distribution of the x -polarized coupler supermodes are presented in Fig. 2.11c. We identify two types of supermodes inside the frequency range $0.36 \text{ THz} < f < 0.53 \text{ THz}$: one supermode labeled s_{por} has a profile with most of its field localized in the vicinity of the porous fiber (see bottom row of Fig. 2.11c) while the other type labeled s_{rod} has most of its field localized near the non-porous fiber (i.e., rod) (see top row of Fig. 2.11c). Figure 2.11a indicates that the rod-type supermode (s_{rod}) is a fundamental mode of the coupler and does not have a cut-off. From the top row of Fig. 2.11(c) we can establish that in going to lower frequencies, the field of the s_{rod} supermode gets strongly expelled from the core of the non-porous fiber and as a result the field begins to have a substantial overlap with the adjacent porous fiber, thus leading to strong hybridization of the supermode. In fact, the subwavelength fibers couple strongly (at least 50% by power) only at frequencies lower than 0.3 THz. Moreover, propagation losses for the non-porous CF become sufficiently low (0.1 cm^{-1}) only at frequencies below 0.3 THz. Based on the above considerations, we concluded that the CF and evanescent coupler considered in that work acted as low-pass filters with a cut-off frequency near 0.3 THz.



2.11 Finite-element calculated modal properties of a directional coupler made of two subwavelength fibers (porous and non-porous) of $380 \mu\text{m}$ diameter separated by a $380 \mu\text{m}$ air gap. (a) Effective refractive indices and (b) propagation losses of the individual fiber modes (solid lines) and corresponding x -polarized (crosses) and y -polarized (open circles) coupler supermodes. (c) $|\text{Ex}|$ -field distributions in the fundamental modes of porous and non-porous fibers, as well as for coupler supermodes at various frequencies. (Adapted from Dupuis *et al.*, 2009.)

2.4 Hollow-core fibers

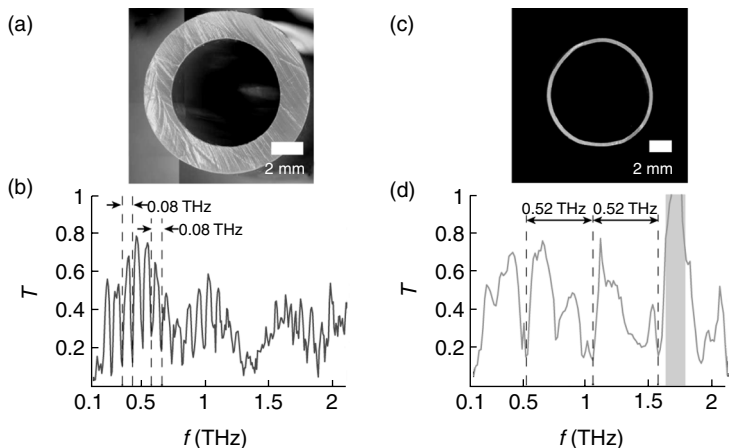
2.4.1 Anti-resonant reflecting optical fibers

Another interesting approach to low-loss guiding is presented by guiding THz radiation in the hollow-core fibers. A classical result for guiding in straight capillaries predicts propagation losses scaling as λ^2/a^3 with the bore radius a . Therefore in principle, propagation losses can be set arbitrarily low just by enlarging the bore diameter. However, the downside of increasing the bore diameter is in increased bending losses and in the highly multi-mode nature of capillary guidance resulting in the low spatial quality of the guided beams.

Another type of hollow-core fiber is presented by a thin tube that guides using anti-resonant reflections from its walls to confine the light in the hollow core. Such fibers are typically referred as ARROW waveguide for ‘anti-resonant reflecting optical waveguide’ (Lai *et al.*, 2009, 2010). Making use of a simple Fabry–Pérot resonator model, one can predict the periodic spacing between two adjacent resonant frequencies in the fiber transmission spectrum (Lai *et al.*, 2010):

$$\Delta f = \frac{c}{2t\sqrt{n_{\text{clad}}^2 - n_{\text{core}}^2}}, \quad [2.3]$$

where n_{core} and n_{clad} respectively designate the refractive indices of the gaseous core (usually air) and that of the polymer tube cladding, while t stands for the wall thickness of the tube cladding. From Equation [2.3] we note that the periodic spacing between two resonant frequencies is inversely proportional to the wall thickness. Hence, in an ARROW fiber, in order to obtain the widest spectral separation between two resonant frequencies (and consequently the widest transmission windows), it is necessary to have the thinnest possible wall, often below sub-millimeter dimensions. ARROW guidance is demonstrated in Fig. 2.12 where the transmission spectra of two polymer tubes, one 1.6 mm thick polyethylene (PE) tube and a 0.30 mm thick Teflon (PTFE) tube, are compared. We note that the refractive index values of bulk PE and PTFE remain relatively constant, at 1.534 and 1.560 respectively, inside the investigated range of frequencies. The output spectrum of the thick-wall tube (Fig. 2.12b) exhibits many narrowly spaced transmission windows of roughly 0.08 THz bandwidth; while that of the thinner tube (Fig. 2.12d) has wider transmission windows of nearly 0.52 THz bandwidth.



2.12 Images of cross-sections of (a) 1.6 mm thick PE tube and (c) 0.30 mm thin PTFE tube. Transmission intensity through the (b) thick-walled and (d) thin-walled ARROW fibers. (Images taken from Dupuis (2010) with permission.)

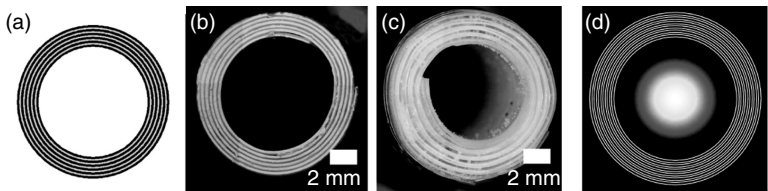
2.4.2 Bragg fibers

The biggest problem with the thin-walled tubes is that they are challenging to fabricate, highly fragile, and thus inconvenient to handle. An alternative solution to the light confinement in the hollow core exploits resonant reflections from the periodic multilayer reflector surrounding the hollow-core region. Fibers featuring periodic reflectors are commonly referred to as Bragg fibers. Periodic reflectors in Bragg fibers are typically composed of two alternating dielectrics featuring high-refractive-index contrast (example in Fig. 2.13a) in order to maximize fiber transmission bandwidth (Johnson *et al.*, 2001). This approach was proven to be effective for the low-loss delivery of mid-infrared CO₂ laser light (Temelkuran *et al.*, 2002) and at visible frequencies (Dupuis *et al.*, 2007; Gauvreau *et al.*, 2008). Moreover, the potential of bandgap guiding in all-polymer Bragg fibers for the transmission of THz light was identified (Skorobogatiy 2005; Skorobogatiy and Dupuis, 2007).

Transmission characteristics of the Bragg fibers are mostly determined by the first few layers in the reflector adjacent to the fiber core. Bragg fibers can therefore have a thicker cladding that confers greater mechanical stability and lower sensitivity to the environment compared to the thin-walled ARROW fibers.

Fabrication of the Bragg fibers based on high-index composite materials

Two types of the high-refractive-index contrast polymer Bragg fibers for THz waveguiding have been recently fabricated and characterized in our



2.13 (a) Schematic of hollow Bragg fiber with $N=5$ bilayers of high-index and low-index layers. (b) Fabricated Bragg fiber with high-index TiO_2 doped layers and low-index PE layers. (c) Fabricated Bragg fiber with high-index PE layers separated by PMMA particles from the low-index air layers. (d) Fundamental HE_{11} mode profile at 1 THz inside the TiO_2 -doped Bragg fiber of panel (b) with $d_{core}=6.63$ mm, $d_h=135\ \mu m$ and $d_l=100\ \mu m$. (Panels (b) and (c) reprinted from Dupuis *et al.* (2011) with permission.)

research group (Dupuis *et al.*, 2011). In Fig. 2.13b–c we show the fiber cross-sections and in Fig. 2.13d we present theoretical energy flux distribution in the fundamental HE_{11} mode propagating in such fibers. The first type of Bragg fiber (Fig. 2.13b) comprises a reflector made of the low-refractive-index ($n_L=1.567$) pure PE layers and high-refractive-index ($n_H=2.985$) 80 wt% TiO_2 -doped PE layers.

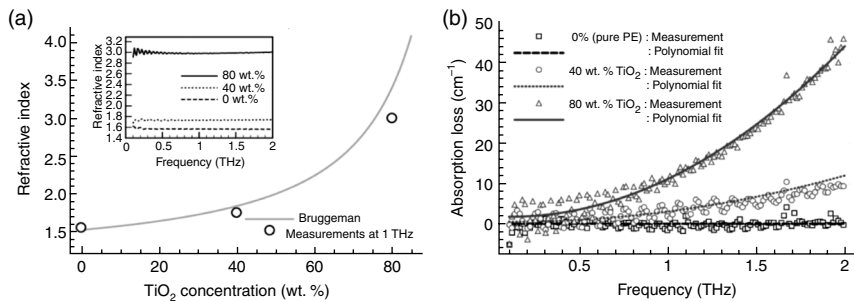
The availability of the high-refractive-index dielectric materials is notably scarce in the THz range, and as a result many polymers exhibit similar and small values of the refractive index. For this reason, we used high-refractive-index titania (TiO_2) microparticles (Jansen *et al.*, 2010b) to dope the host polymer, which in our case consists of pure PE. The refractive index and absorption coefficient of the composite TiO_2 -PE material were measured using a standard THz time-domain spectroscopy set-up (THz-TDS); and the results are displayed in Fig. 2.14.

The Bruggeman model for the effective random media provides a good approximation of the compound's refractive index as a function of concentration of subwavelength-sized spherical doping microparticles (Scheller *et al.*, 2009):

$$1 - f_v = \frac{\varepsilon_p - \varepsilon_m}{\varepsilon_p - \varepsilon_h} \sqrt[3]{\frac{\varepsilon_h}{\varepsilon_m}} \quad [2.4]$$

where f_v denotes the volume fraction ($0 < f_v < 1$) of doping particles, and ε_p , ε_h and ε_m denote the respective permittivities of the dielectric particles, host and mixture. The absorption coefficient can be well fitted with a second-order polynomial function as demonstrated by the curves in Fig. 2.14b.

The second type of fabricated Bragg fiber is made of air–polymer bilayers. In this case, fine PMMA powder particles are used as spacers in order



2.14 (a) Refractive index of a PE-based polymer compound as a function of weight concentration of TiO₂ dopants: Bruggeman model fit (solid curve) and measurements at 1 THz (circles). Inset: THz-TDS measurements that show the refractive index of the composite material remains fairly constant inside the 0.01–2.0 THz range for all weight concentrations of TiO₂. (b) Power absorption loss of the doped PE-based polymer compound as a function of frequency (THz) for various levels of TiO₂ doping concentrations. (From Ung *et al.*, 2011.)

to maintain a certain air gap between each PE layer. The fabrication procedures of both types of Bragg fibers are presented schematically in Fig. 2.15.

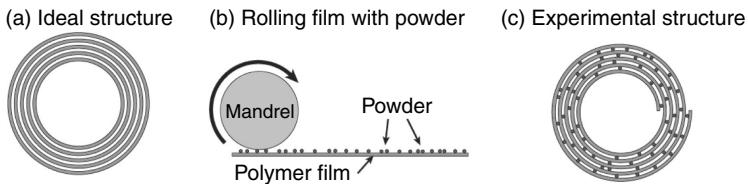
For the air–polymer Bragg fiber, a PMMA powder, with an average particle size of 150 µm, was randomly laid out on top of two touching 127 µm thick PTFE films. The films were subsequently rolled around a mandrel to form the Bragg fiber. The resulting air–polymer Bragg fiber had an inner diameter (ID) of 6.73 mm and a reflector composed of five bilayers consisting of 254 µm PTFE and 150 µm thick air layers. For the titania-doped PE Bragg fiber, a mixture of 80 wt% TiO₂ powder and PE was prepared using a twin-screw extruder. The extrudate was cut into pellets and subsequently extruded into film. An all-solid bilayer was formed by pressing doped and undoped films together with a hot press, yielding high-index doped PE layers and low-index undoped PE layers of 135 µm and 100 µm thickness, respectively. The bilayer was then rolled into a Bragg fiber with ID of 6.63 mm.

Modal properties in high-index-contrast polymer Bragg fibers

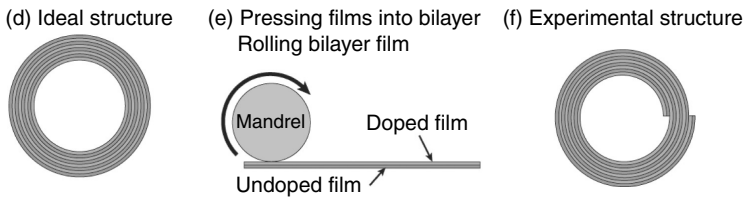
Experimentally measured transmissions (T) through the two fibers, as well as the upper bounds for the fiber propagation losses (calculated as $-2 \ln(|T|)/L$), are presented in Fig. 2.16. We remark that both types of Bragg fibers feature relatively broad transmission windows and relatively small transmission losses $\sim 0.05 \text{ cm}^{-1}$ inside their corresponding bandgaps.

The effects of the losses in the composite material on the fiber bandgaps were further studied in detail in Ung *et al.* (2011). The authors first assumed a Bragg fiber composed of $N = 14$ bilayers of 135 µm 80 wt% TiO₂-doped PE

Air-polymer Bragg fiber:

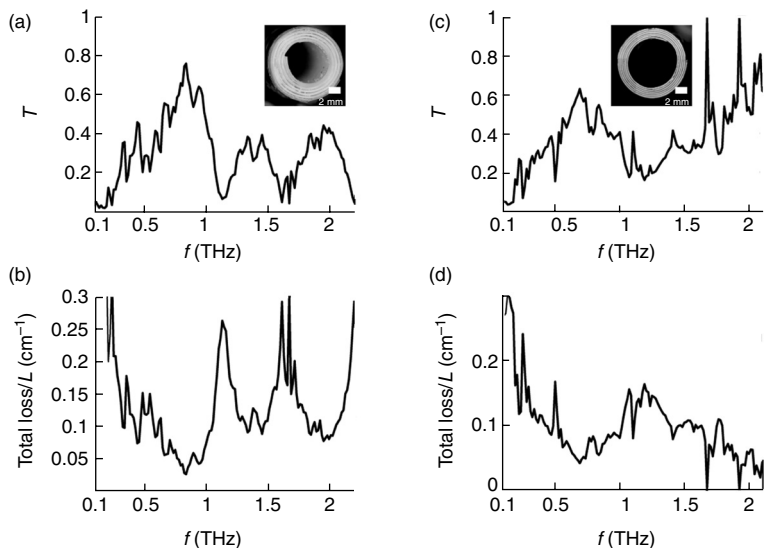


Doped-polymer Bragg fiber:



2.15 Fabrication procedure of polymer Bragg fibers. (a–c) Air-polymer Bragg fiber. (d–f) TiO_2 -doped Bragg fiber. We note that the ideal geometry is circularly symmetric; however, the rolling of films creates a spiral defect that breaks the symmetry. (From Dupuis *et al.*, 2011.)

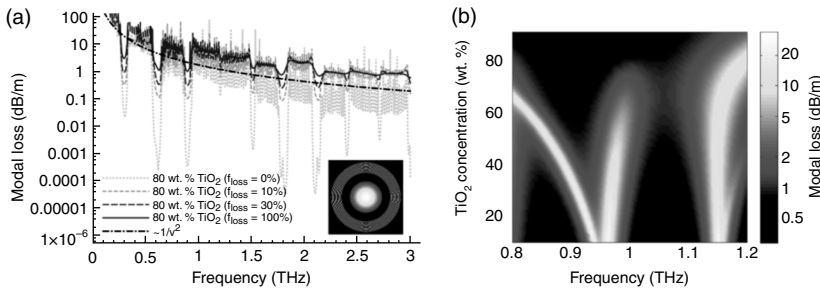
and 100 μm undoped PE layers, and kept the refractive index of the doped PE layers fixed at $n_{\text{H}} = 2.985$, while gradually increasing the fraction (f_{loss}) of the applied material absorption (α_{mat}) within the doped PE layers ($\alpha = f_{\text{loss}} \alpha_{\text{mat}}$) from 0% up to its nominal value (100%) at 80 wt% doping concentration. The numerically computed absorption spectra of this system (Fig. 2.17a), based on vectorial transfer-matrix simulations, reveal ten distinct bandgaps inside the 0.1–3.0 THz range, with the widest being the fundamental bandgap located at 0.3 THz. Two main effects of material absorption were identified. First, for frequencies outside the bandgaps, large material losses led to the flattening of the rapid oscillations (due to resonances in the fiber cladding region) in the fundamental mode loss. This was rationalized by noting that larger material losses cause strong attenuation of the outward traveling waves in the fiber cladding region, thus suppressing the interference effects responsible for variations in the fiber transmission. The second notable effect is that bandgaps, while persisting, become smaller for fairly high material losses (dashed, long-dashed and solid curves in Fig. 2.17a), or can even completely disappear. Particularly, for frequencies within the bandgap, the modal fields decay exponentially into the reflector region; thus field penetration is usually limited to only the first few bilayers. Appearance of the bandgap regions in the transmission spectrum of the fiber is actually due to destructive interference of the counter-propagating waves of comparable amplitudes within the first few bilayers closest to the core/reflector



2.16 (a) and (c) Normalized amplitude transmission spectra; (b) and (d) upper bound on propagation loss given by the ratio of the total loss divided by the waveguide length, for the two fabricated Bragg polymer fibers. (From Dupuis *et al.*, 2011.)

interface. At higher frequencies ($f > 1.0$ THz) for which material losses are very large (solid curve in Fig. 2.17a), the destructive interference within the first few reflector layers can suffer significantly as the backward propagating waves (reflected waves) can have much smaller amplitudes than the forward propagating waves due to absorption. Thus, in the regime of high material losses in the reflector materials, the Bragg fiber guides predominantly via Fresnel reflections at the inner air/reflector interface, and not via resonant reflections from the multilayer reflector. This also means that there is a trade-off in doping a host polymer with high refractive index and high-loss additives for building periodic reflectors. Particularly, while high refraction dopants can enhance the refractive index of a composite material – which would have a positive impact on the bandgap size – it will also increase the intrinsic material loss which may eventually result in the bandgap destruction.

An additional study was performed with the aim of finding an optimum balance between the high-refractive index and material losses by gradually increasing the concentration of TiO_2 dopants in the polymeric compound (Ung *et al.*, 2011). Transmission through a Bragg fiber with $N = 5$ bilayers was modeled with the individual layer thicknesses satisfying the ‘ideal reflector’ quarter-wave condition (Skorobogatiy and Yang, 2009, chapter 4.1): $d_{\text{H}}\tilde{n}_{\text{H}} = d_{\text{L}}\tilde{n}_{\text{L}} = \lambda_c/4$, $\tilde{n}_i = \sqrt{n_i^2 - n_c^2}$, where n_c is the refractive index of the



2.17 (a) Fundamental mode loss in TiO_2 -doped PE/PE hollow-core Bragg fibers ($N = 14$ bilayers) as a function of frequency and for various levels of fractional nominal loss (f_{loss}) inside the dielectric layers. Inset: calculated fundamental HE_{11} mode power profile at 1 THz. (b) Modal loss (dB/m) as a function of TiO_2 doping concentration of high-index layers and frequency, for an ideal Bragg fiber (five bilayers) whose reflector layer thicknesses are tuned to obey the quarter-wave condition around the center frequency (1 THz) of interest. (From Ung *et al.*, 2011.)

hollow core, and λ_c is the center wavelength of the fundamental bandgap, which in our case was chosen to correspond to $f_c = 1$ THz. The results of simulations are presented in Fig. 2.17(b) where we can identify two main regimes of modal propagation. First, at low TiO_2 doping concentrations (≤ 20 wt%), the refractive-index contrast of the multi-layered reflector is too low to sustain Bragg-reflection-induced bandgaps. Instead in that regime, the fiber acts as an ARROW fiber exhibiting closely and periodically spaced narrow bandgaps (bandwidth ~ 0.1 THz). The other regime of interest observed in Fig. 2.17b occurs at high doping concentration levels (~ 85 wt%) resulting in a high-refractive-index-contrast reflector yielding a broad transmission window (bandwidth ~ 0.35 THz) via Bragg reflection. We thus deduce that it is possible to tune the individual layer thicknesses and doping concentration of the lossy high-refractive-index composite materials of the Bragg reflector in order to create very wide bandgaps with relatively low losses. However, this may be achieved only in some range of frequencies for which the absorption losses of the composite material is not so large as to effectively destroy the bandgap confinement mechanism of the Bragg reflector.

2.5 Composite terahertz materials

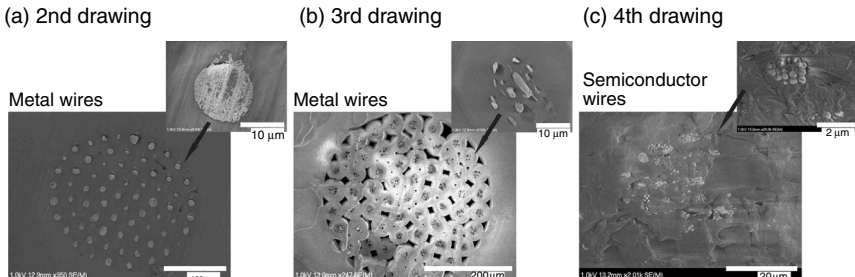
Because of the scarcity of the high-refractive-index dielectrics in the THz spectral region and their imperative need as building blocks for the THz optical components, design and fabrication of high-refractive-index composite materials (dielectric compounds, metal–dielectric and semiconductor–dielectric compounds) is currently a fertile area of research. As

demonstrated in the previous section, one approach for enhancing the refractive index of a bulk polymer is to incorporate high-refractive-index dopants (such as TiO_2 , CaCO_3 , Mg(OH)_2 , glass fibers, powdered silicon, etc.) within the low-refractive-index matrix (Wietzke *et al.*, 2007; Scheller *et al.*, 2009; Jansen *et al.*, 2010b; Dupuis *et al.*, 2011; Ung *et al.*, 2011).

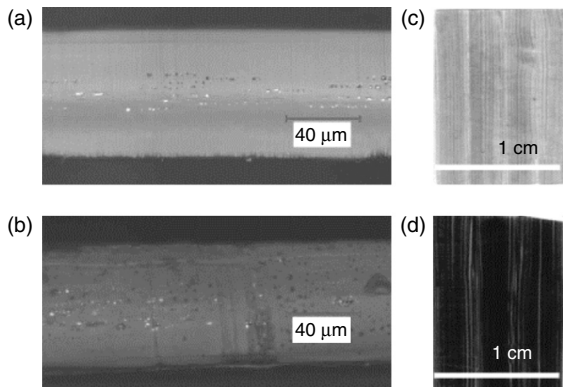
Another method, which could also provide additional control over the polarization of the incoming THz radiation, is to incorporate metallic (or semiconductor) microwires aligned along a certain direction inside the host polymer. This approach was recently demonstrated experimentally (Mazhorova *et al.*, 2010) using low-temperature-melting Tin-Bismuth (Sn-Bi) alloy microwires and amorphous chalcogenide (As_2Se_3) semiconductor microwires embedded in polycarbonate (PC). To create these composite materials, a novel fabrication technique was developed which uses consecutive stack-and-draw steps to progressively reduce the size of the embedded microwires. The fabrication procedure is simple: a PC tube is filled with liquid-phase metal alloy (42% Bi, 58% Sn) and then left to cool and solidify. The preform is then drawn at 190°C to produce metallic polymer-clad microwires of 260 μm average diameter. After the first drawing, several hundreds of microwires are stacked together and subsequently put inside a new PC tube to perform a second drawing. By repeating the stack-and-draw process multiple times, one can produce ordered wire arrays with sub-micron-size wires. We note that a relatively thick polymer cladding around the metal wire is needed so as to prevent the individual wires from coalescing during the drawing steps.

Figure 2.18a shows that after the second drawing, the size of individual Sn-Bi wires is around 10 μm. After the third drawing, the size of Sn-Bi wires is between 0.5 and 4.0 μm. Sub-micron semiconductor (As_2Se_3) wire dimensions on the order of 200 nm have also been demonstrated with this technique after four consecutive drawings (Fig. 2.18c). A planar film of a composite THz material was then fabricated by compressing the fibers fabricated after three consecutive drawings. In particular, the fibers were first placed on a flat surface parallel to each other and then pressed into thin films (Fig. 2.19) by a hot press with several tons of pressure at 195°C.

Transmission through the metamaterial film in the THz range (0.10–1.00 THz) was then measured using THz-TDS. The linear optical properties (refractive index and absorption values) were subsequently extracted by fitting the predictions of a full-vector transfer-matrix model on the complex transmission data (amplitude and phase). Finally, the refractive index and absorption values (i.e., the real and imaginary parts of the permittivity) of the metamaterial film were retrieved and are presented in Fig. 2.20.

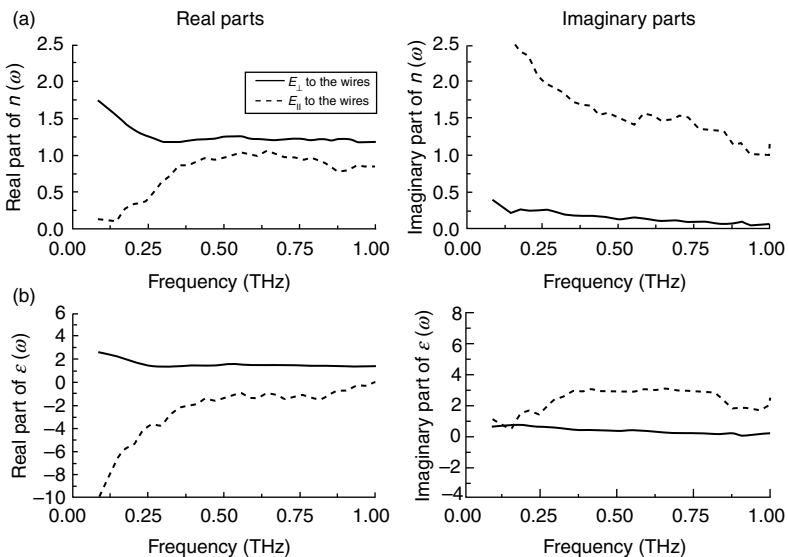


2.18 SEM pictures of the cross-sections of fabricated wire-array fibers. (a) Sn-Bi metal wire fiber after 2nd drawing, (b) Sn-Bi metal wire fiber after 3rd drawing, (c) As₂Se₃ semiconductor wire fiber after 4th drawing. Inset of (c) shows cluster of nanowires with individual diameters as small as 200 nm. (From Mazhorova *et al.*, 2010.)



2.19 Optical micrographs of the compound films containing (a) metal and (b) semiconductor microwire arrays. Metamaterial layer is sandwiched between the two polymer layers. Panels (c) and (d) present top views of the films where metal and semiconductor wires can be seen to be highly oriented and traversing the entire film. (From Mazhorova *et al.*, 2010.)

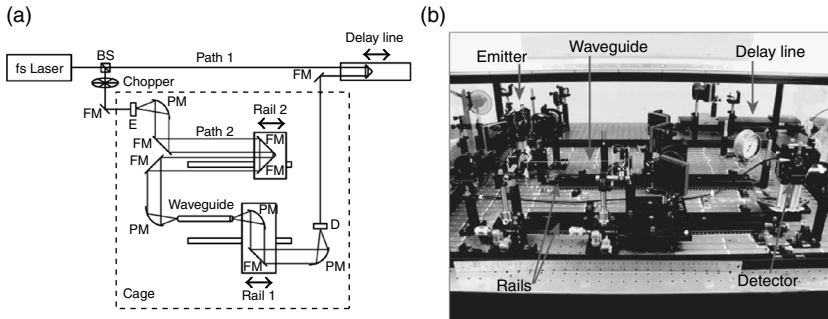
We first note in Fig. 2.20 the strong polarization anisotropy in the real permittivity of the metamaterial when the electric field vector of a THz wave is directed parallel to the metallic wires in the film. This acute polarization sensitivity and birefringence across a relatively wide THz bandwidth could make such composite materials useful in the design of THz linear polarizers and filters, birefringent devices and other passive and active THz devices. In other works, a polymer-based volumetric one-dimensional photonic crystal element exhibiting pronounced THz form birefringence was also reported recently (Scheller *et al.*, 2010).



2.20 Extracted (a) refractive index and (b) permittivity of metamaterial film containing metallic (Sn-Bi) wires. (From Mazhorova *et al.*, 2010.)

2.6 Experimental characterization of terahertz waveguides

Contrary to standard THz-TDS set-ups that are tuned for pointwise measurements of samples in the focal-point-to-focal-point configuration (using off-axis parabolic mirrors), elongated waveguides require a different set-up in order to accommodate waveguides of widely different lengths. To this end, we here describe a reconfigurable set-up featuring an adaptable path length capable of accommodating waveguides of different lengths (Dupuis *et al.*, 2010). A schematic of the set-up is presented in Fig. 2.21a and a photo of the experimental set-up is shown in Fig. 2.21b. The set-up features two mirror assemblies mounted on two independent sets of rails so as to allow quick and easy adjustment of the THz optical path (Rail 2), and to allow insertion of a waveguide (Rail 1). In this scheme, a fixed parabolic mirror (PM) focuses the THz radiation into the waveguide, therefore the in-coupling plane remains fixed; while the output of the waveguide is positioned at the focal point of another PM mounted on Rail 1, which can be appropriately translated in order to adapt to the varying lengths of different waveguides. This approach successfully measured THz waveguides of up to 50 cm in length (Dupuis *et al.*, 2010). We also note that the same set-up may be used for pointwise sample measurements by simply displacing the PM mounted on Rail 1 such that its focal point coincides with that of the first



2.21 (a) Schematic of the THz-TDS set-up for waveguide measurements. E: emitter, D: detector, PM: parabolic mirror, BS: beam splitter, FM: flat mirror. (b) Photograph of the actual set-up capable of accommodating a waveguide of up to 50 cm in length. (From Dupuis *et al.*, 2010.)

PM (on the left). Rail 2 provides additional optical path length compensation for the cases where the optical path length difference between the set-up with and without a waveguide is so large that the maximal pulse delay of a computer-controlled variable delay line is insufficient to compensate for it. The latter may be necessary for THz waveguides exhibiting effective refractive indices much larger than 1.

The pump source consisted of a frequency-doubled ($\lambda = 780$ nm) C-fiber laser while two low-temperature-grown GaAs photoconductive antennas – all from Menlo Systems GmbH – acted as the emitter and detector, respectively. A Stanford Research Systems lock-in amplifier was used together with a chopper for measuring the detected signal. The entire assembly was housed in a nitrogen-purged cage to minimize the detrimental effects of water vapor on the measurements’ quality. Using this set-up, the frequency-dependent transmission (T) through a waveguide of length L may be modeled as:

$$T(\omega) = \frac{E_{\text{wavg}}(\omega)}{E_{\text{ref}}(\omega)} = C_{\text{in}} \cdot C_{\text{out}} \cdot e^{i\omega(n_{\text{eff}}-1)L/c} e^{-\alpha L/2} \quad [2.5]$$

where

$$E_{\text{wavg}}(\omega) = E_{\text{source}}(\omega) \cdot C_{\text{in}} \cdot C_{\text{out}} \cdot e^{i\omega[n_{\text{eff}}L + (L_{\text{ref}} - L)]/c} e^{-\alpha L/2} \quad [2.6]$$

and

$$E_{\text{ref}}(\omega) = E_{\text{source}}(\omega) \cdot e^{i\omega L_{\text{ref}}/c} \quad [2.7]$$

E_{wavg} represents the output field from the waveguide of length L , while E_{ref} is the reference signal measured with no waveguide present, and $E_{\text{source}}(\omega)$ is the amplitude spectrum of the THz source. The total distance between the source emitter and the detector in the absence of a waveguide is denoted L_{ref} . The variables n_{eff} and α respectively designate the modal effective refractive index and power propagation loss, while the scalars C_{in} and C_{out} denote respectively the normalized input and output coupling coefficients (of the waveguide) which by symmetry arguments are assumed to be equal ($C_{\text{out}} \approx C_{\text{in}} = C$) and defined by the overlap integral of the modal field and the field of the input beam:

$$C = \frac{\int (E_{\text{mode}}^* \times H_{\text{beam}} + E_{\text{beam}} \times H_{\text{mode}}^*) dA}{\sqrt{2 \int \text{Re}(E_{\text{mode}} \times H_{\text{mode}}^*) dA} \cdot \sqrt{2 \int \text{Re}(E_{\text{beam}} \times H_{\text{beam}}^*) dA}} \quad [2.8]$$

We note in Equation [2.5] that the waveguide's output transmission exhibits a time delay of $(n_{\text{eff}} - 1)L/c$ with respect to the reference signal. In the case of highly porous fibers for which $n_{\text{eff}} \sim 1$, this time delay is rather small.

2.7 Conclusions

In this chapter, we have described the principal challenges (losses, chromatic dispersion, fabrication, packaging and characterization) for the THz polymer-based waveguides, and presented several types of polymer MOFs that successfully address some of these challenges. Table 2.1 lists different types of fabricated polymer-based microstructured fibers along with their reported minimum propagation loss and operation bandwidth.

The following are the brief conclusions of the various chapter sections. At the beginning of the chapter, in Section 2.2.1, we emphasized the importance of material losses (including polymers) in the THz range, and pointed out that to alleviate the magnitude of losses the most effective approach is to minimize the fraction of power guided in lossy material regions. We then showed that this could be achieved in subwavelength polymer fibers, with either a porous or a plain solid core. We also demonstrated that, compared to a solid core subwavelength fiber of same diameter, a porous subwavelength fiber enables increasing the fraction of power guided in low-loss air regions, while allowing broadening and shifting the transmission window to higher frequencies. Two fabrication methods of porous subwavelength fibers were outlined: the sacrificial polymer technique and the microstructured molding technique. Furthermore, we showed in Section 2.2.2 that core porosity also assists in reducing the magnitude of GVD in such waveguides towards wideband THz pulse propagation.

Table 2.1 Summary of the polymer microstructured optical fibers (MOFs) surveyed in this chapter

Type of fiber	Min. loss (cm ⁻¹)	Bandwidth Δf (THz)	References
Subwavelength solid core fiber	0.01	0.30	Chen <i>et al.</i> , 2006
	0.04	0.12	Dupuis <i>et al.</i> , 2010
Porous subwavelength fiber	0.012	0.25	Dupuis <i>et al.</i> , 2009, 2010
			Rozé <i>et al.</i> , 2011
Suspended subwavelength solid core fiber	0.02	0.28–0.48	Rozé <i>et al.</i> , 2011
Suspended subwavelength porous core fiber	0.05	0.10	Rozé <i>et al.</i> , 2011
Photonic crystal fiber (Topas copolymer)	0.035	0.50–0.60	Nielsen <i>et al.</i> , 2009
Anti-resonant reflecting tube ('ARROW' fiber)	0.005	0.38	Lai <i>et al.</i> , 2009
Hollow-core Bragg fiber (air–polymer)	0.028	0.82	Dupuis <i>et al.</i> , 2010
Hollow-core Bragg fiber (TiO ₂ -doped polymer)	0.042	0.69	Dupuis <i>et al.</i> , 2010

Then, in Section 2.2.3, we discussed the role of packaging for the subwavelength fibers, in which the modal fields are highly delocalized and thus susceptible to interactions with the surrounding environment. To that end, we presented a practical solution in the form of subwavelength fibers suspended in the middle of an outer tubular cladding. We showed that the role of the tubular cladding in this case is to isolate the core from outside perturbations, thus enabling direct and convenient manipulation of the fibers without inducing modal distortions. The latter was confirmed through the output near-field characterization of the fabricated suspended subwavelength fibers performed with THz near-field microscopy.

We then presented in Section 2.3 a number of practical devices that utilized subwavelength polymer fibers as the chief enabling components. In particular, we showed that subwavelength fibers may be used in fiber-based THz imaging systems, and for non-destructive and continuous measurement of propagation losses along the length of a TF.

Another category of polymer optical fibers was introduced in Section 2.4: hollow-core fibers, where the mode is confined and guided within the lossless hollow core. The first type of hollow-core fiber discussed in Section 2.4.1 was the simple thin capillary tube (also known as ARROW fiber) where mode propagation proceeds through anti-resonant guidance. We showed that the thinner the tube, the wider are the transmission windows present in this fiber. The second type of hollow-core fiber is the Bragg fiber (Section 2.4.2), presenting a periodic multilayer reflector cladding, and where modal

field confinement and propagation occurs through bandgap guidance. Since the transmission efficiency of a Bragg fiber scales with the number of layers present in the reflector, Bragg fibers can therefore have a thick cladding that not only confers greater mechanical stability compared to the thin-walled ARROW fibers, but also provides stronger modal confinement, and consequently, lower bending losses and reduced sensitivity to the environment. Moreover, it was demonstrated that it is possible to obtain very wide bandgaps with Bragg fibers provided that a high-refractive-index contrast is present in the bilayers of the periodic reflector. The latter can be achieved using composite materials, and this approach was experimentally demonstrated by doping a low-index polymer host with high-index titania microparticles. Furthermore, pertaining to bandgap size, a theoretical analysis showed there exists a trade-off between the high-refractive index and the accompanying elevated material losses when increasing the doping concentration of the host polymer with titania particles.

Due to the scarcity of high-refractive-index and low-loss materials for the THz range, in Section 2.5 we discussed the momentous interest in the design and fabrication of novel THz materials, and in particular, composite materials based on embedded metallic/semiconductor nanowires. We showed experimentally that metallic nanowire media, in particular, enables design of artificial materials with tunable refractive index and remarkable polarization properties.

Finally in Section 2.6, we presented an innovative THz time-domain spectroscopy set-up offering a fast and simple reconfiguration capability for accommodating and measuring the transmission of THz waveguides up to 50 cm in length.

2.8 Acknowledgments

We would like to thank members of our research group for their instrumental contribution to the theory and experiments on THz waveguides: Alexandre Dupuis, Anna Mazhorova, Mathieu Rozé, as well as Prof. D. Morris from the University of Sherbrooke who helped us with the first measurements of THz fibers, and Prof. Markus Walther from the University of Freiburg (Germany) who hosted Prof. Skorobogatiy during his sabbatical leave and who contributed to the near-field characterization of the sub-wavelength fibers.

2.9 References

- Atakaramians S, Afshar V S, Ebendorff-Heidepriem H, Nagel M, Fischer B M, Abbott D, and Monro T M (2009), ‘THz porous fibers: design, fabrication and experimental characterization’, *Opt Express*, **17**, 14053–14062.

- Bitzer A, Ortner A, and Walther M (2010), ‘Terahertz near-field microscopy with subwavelength spatial resolution based on photoconductive antennas’, *Appl Opt*, **49**, E1–E6.
- Cai Y, Brener I, Lopata J, Wynn J, Pfeiffer L, Stark J B, Wu Q, Zhang X C, and Federici J F (1998), ‘Coherent terahertz radiation detection: Direct comparison between free-space electro-optic sampling and antenna detection’, *Appl Phys Lett*, **73**, 444–446.
- Chen L J, Chen H W, Kao T F, Lu J Y, and Sun C K (2006), ‘Low-loss subwavelength plastic fiber for terahertz waveguiding’, *Opt Lett*, **31**, 308–310.
- Chiu C M, Chen H W, Huang Y R, Hwang Y J, Lee W J, Huang H Y, and Sun C K (2009), ‘All-terahertz fiber-scanning near-field microscopy’, *Opt Lett*, **34**, 1084–1086.
- Dupuis A, Guo N, Gauvreau B, Hassani A, Pone E, Boismenu F, and Skorobogatiy M (2007), ‘Guiding in the visible with “colorful” solid-core Bragg fibers’, *Opt Lett*, **32**, 2882–2884.
- Dupuis A, Allard J F, Morris D, Stoeffler K, Dubois C, and Skorobogatiy M (2009), ‘Fabrication and THz loss measurements of porous subwavelength fibers using a directional coupler method’, *Opt Express*, **17**, 8012–8028.
- Dupuis A, Mazhorova A, Désévédavy F, Rozé M, and Skorobogatiy M (2010), ‘Spectral characterization of porous dielectric subwavelength THz fibers fabricated using a microstructured molding technique’, *Opt Express*, **18**, 13813–13828.
- Dupuis A (2010), ‘Dielectric THz waveguides’, *Ph.D. thesis*, Ecole Polytechnique de Montréal, Department of engineering physics.
- Dupuis A, Stoeffler K, Ung B, Dubois C, and Skorobogatiy M (2011), ‘Transmission measurements of hollow-core THz Bragg fibers’, *J Opt Soc Am B*, **28**, 896–907.
- Ebendorff-Heidepriem H and Monro T M (2007), ‘Extrusion of complex preforms for microstructured optical fibers’, *Opt Express*, **15**, 15086–15092.
- Ebbinghaus S, Kim S J, Heyden M, Yu X, Gruebele M, Leitner D M, and Havenith M (2008), ‘Protein Sequence- and pH-Dependent Hydration Probed by Terahertz Spectroscopy’, *J Am Chem Soc*, **130**, 2374–2375.
- Gauvreau B, Guo N, Schicker K, Stoeffler K, Boismenu F, Ajji A, Wingfield R, Dubois C, and Skorobogatiy M (2008), ‘Color-changing and color-tunable photonic bandgap fiber textiles’, *Opt Express*, **16**, 15677–15693.
- Hassani A, Dupuis A, and Skorobogatiy M (2008a), ‘Low loss porous terahertz fibers containing multiple subwavelength holes’, *Appl Phys Lett*, **92**, 071101.
- Hassani A, Dupuis A, and Skorobogatiy M (2008b), ‘Porous polymer fibers for low-loss Terahertz guiding’, *Opt Express*, **16**, 6340–6351.
- Hoshina H, Sasaki Y, Hayashi A, Otani C, and Kawase K (2009), ‘Noninvasive Mail Inspection System with Terahertz Radiation’, *Appl Spectrosc*, **63**, 81–86.
- Imeshev G, Fermann M E, Vodopyanov K L, Fejer M M, Yu X, Harris J S, Bliss D and Lynch C (2006), ‘High-power source of THz radiation based on orientation-patterned GaAs pumped by a fiber laser’, *Opt Express*, **14**, 4439–4444.
- Jansen C, Wietzke S, Peters O, Scheller M, Vieweg N, Salhi M, Krumbholz N, Jördens C, Hochrein T, and Koch M (2010a), ‘Terahertz imaging: applications and perspectives’, *Appl Opt*, **49**, E48–E57.

- Jansen C, Wietzke S, Astley V, Mittleman D M, and Koch M (2010b), ‘Mechanically flexible polymeric compound one-dimensional photonic crystals for terahertz frequencies’, *Appl Phys Lett*, **96**, 111108.
- Jin Y S, Kim G J, and Jeon S G (2006), ‘Terahertz dielectric properties of polymers’, *J Korean Phys Soc*, **49**, 513–517.
- Jin Y S, Kim G J, Shon C H, Jeon S, and Kim J I (2008), ‘Analysis of petroleum products and their mixtures by using terahertz time domain spectroscopy’, *J Korean Phys Soc*, **53**, 1879–1885.
- Johnson S G, Ibanescu M, Skorobogatiy M, Weisberg O, Engeness T D, Soljacic M, Jacobs S A, Joannopoulos J D, and Fink Y (2001), ‘Low-loss asymptotically single-mode propagation in large-core OmniGuide fibers’, *Opt Express*, **9**, 748–779.
- Karpowicz N E, Chen J, Tongue T, and Zhang X C (2008), ‘Coherent millimetre wave to mid-infrared measurements with continuous bandwidth reaching 40 THz’, *Electron Lett*, **44**, 544–545.
- Lai C H, Hsueh Y C, Chen H W, Huang Y J, Chang H C, and Sun C K (2009), ‘Low-index terahertz pipe waveguides’, *Opt Lett*, **34**, 3457–3459.
- Lai C H, You B, Lu J Y, Liu T A, Peng J L, Sun C K, and Chang H C (2010), ‘Modal characteristics of antiresonant reflecting pipe waveguides for terahertz wave-guiding’, *Opt Express*, **18**, 309–322.
- Liu J, Dai J, Chin S L, and Zhang X C (2010), ‘Broadband terahertz wave remote sensing using coherent manipulation of fluorescence from asymmetrically ionized gases’, *Nat Photonics*, **4**, 627–631.
- Lu J Y, Kuo C C, Chiu C M, Chen H W, Hwang Y J, Pan C L, and Sun C K (2008a), ‘THz interferometric imaging using subwavelength plastic fiber based THz endoscopes’, *Opt Express*, **16**, 2494–2501.
- Lu J Y, Chiu C M, Kuo C C, Lai C H, Chang H C, Hwang Y J, Pan C L, and Sun C K (2008b), ‘Terahertz scanning imaging with a subwavelength plastic fiber’, *Appl Phys Lett*, **92**, 084102.
- Mazhorova A, Gu J F, Dupuis A, Peccianti M, Tsuneyuki O, Morandotti R, Minamide H, Tang M, Wang Y, Ito H, and Skorobogatiy M (2010), ‘Composite THz materials using aligned metallic and semiconductor microwires, experiments and interpretation’, *Opt Express*, **18**, 24632–24647.
- Nagel M, Marchewka A, and Kurz H (2006), ‘Low-index discontinuity terahertz waveguides’, *Opt Express*, **17**, 8592–9954.
- Nielsen K, Rasmussen H K, Adam A J L, Planken P C M, Bang O, and Jepsen P U (2009), ‘Bendable, low-loss Topas fibers for the terahertz frequency range’, *Opt Express*, **17**, 8592–8601.
- Rozé M, Ung B, Mazhorova A, Walther M, and Skorobogatiy M (2011), ‘Suspended core subwavelength fibers: towards practical designs for low-loss terahertz guidance’, *Opt Express*, **19**, 9127–9138.
- Scheller M, Wietzke S, Jansen C, and Koch M (2009), ‘Modelling heterogeneous dielectric mixtures in the terahertz regime: a quasi-static effective medium theory’, *J Phys D: Appl Phys*, **42**, 065415.
- Scheller M, Jördens C C, and Koch M (2010), ‘Terahertz form birefringence’, *Opt Express*, **18**, 10137–10142.
- Shi W, Hou L, Lui Z, and Tongue T (2009), ‘Terahertz generation from SI-GaAs stripline antenna with different structural parameters’, *J Opt Soc Am B*, **26**, A107–A112.

- Siegel P H (2004), ‘Terahertz technology in biology and medicine’, *IEEE Trans Microw Theory Tech*, **52**, 2438–2447.
- Skorobogatiy M (2005), ‘Efficient antiguideing of TE and TM polarizations in low-index core waveguides without the need for an omnidirectional reflector’, *Opt Lett*, **30**, 2991–2993.
- Skorobogatiy M, and Dupuis A (2007), ‘Ferroelectric all-polymer hollow Bragg fibers for terahertz guidance’, *Appl Phys Lett*, **90**, 113514.
- Skorobogatiy M, and Yang J (2009), *Fundamentals of Photonic Crystal Guiding*, New York, Cambridge University Press.
- Tang M, Minamide M, Wang Y, Notake T, Ohno S, and Ito H (2010), ‘Dual-wavelength single-crystal double-pass KTP optical parametric oscillator and its application in terahertz wave generation’, *Opt Lett*, **35**, 1698–1700.
- Temelkuran B, Hart S D, Benoit G, Joannopoulos J D, and Fink Y (2002), ‘Wavelength-scalable hollow optical fibres with large photonic bandgaps for CO₂ laser transmission’, *Nature*, **420**, 650–653.
- Tonouchi M (2007), ‘Cutting-edge terahertz technology’, *Nat Photonics*, **1**, 97–105.
- Ung B, Dupuis A, Stoeffler K, Dubois C, and Skorobogatiy M (2011), ‘High-refractive-index composite materials for terahertz waveguides: trade-off between index contrast and absorption loss’, *J Opt Soc Am B*, **28**, 917–921.
- Walther M, and Bitzer A (2011), ‘Electromagnetic wave propagation close to microstructures studied by time and phase-resolved THz near-field imaging’, *J Infrared Millim Te*, **32**, 1020–1030.
- Wietzke S, Jansen C, Rutza F, Mittleman D M, and Koch M (2007), ‘Determination of additive content in polymeric compounds with terahertz time-domain spectroscopy’, *Polym Test*, **26**, 614–618.
- Wilminck G J, Ibey B L, Tongue T, Schulkin B, Laman N, Peralta X G, Roth C C, Cerna C Z, Rivest B D, Grundt J E, and Roach W P (2011), ‘Development of a compact terahertz time-domain spectrometer for the measurement of the optical properties of biological tissues’, *J Biomed Opt*, **16**, 047006.
- Zeitler J A, Taday P F, Newnham D A, Pepper M, Gordon K C, and Rades T (2007), ‘Non-destructive quantification of pharmaceutical tablet coatings using terahertz pulsed imaging and optical coherence tomography’, *J Pharm Pharmacol*, **59**, 209–223.
- Zhong S, Shen Y C, Ho L, May R K, Zeitler J A, Evans M, Taday P F, Pepper M, Rades T, Gordon K C, Müller R, and Kleinebudde P (2011), ‘Non-destructive quantification of pharmaceutical tablet coatings using terahertz pulsed imaging and optical coherence tomography’, *Opt Laser Eng*, **49**, 361–365.

Fundamental aspects of surface plasmon polaritons at terahertz frequencies

J. GÓMEZ RIVAS, AMOLF and Eindhoven University of Technology, The Netherlands and Y. ZHANG and A. BERRIER, AMOLF, The Netherlands

DOI: 10.1533/9780857096494.1.62

Abstract: We present in this chapter an introduction to the field of terahertz (THz) plasmonics. The characteristics of surface plasmon polaritons (SPPs) are determined by the complex permittivity of conductors. Therefore, we introduce the Drude model to describe the permittivity of conductors at THz frequencies. The large absolute value of the permittivity of metals leads to a weaker confinement of SPPs in these materials compared to semiconductors. We illustrate the characteristic lengths of SPPs on flat surfaces by calculating them on an InSb–SiO₂ interface at different temperatures. These characteristic lengths are the wavelength, propagation and confinement lengths. The tunability of the permittivity of semiconductors by controlling the free charge carrier concentration, for example, with temperature, opens the possibility of active THz plasmonic components. We also describe long-range and short-range SPPs in thin layers of semiconductors surrounded by a homogeneous dielectric. These surface modes arise from the coupling of SPPs at the opposite sides of the thin film. New trends in the field of THz plasmonics, comprising designed and localized surface plasmon polaritons, are also discussed in this chapter.

Key words: plasmonics, surface waves, localized resonances, conductors, Drude permittivity.

3.1 Introduction

Methods for confining and guiding electromagnetic radiation into the smallest possible volume have been investigated for many decades. Transmission lines, optical fibers and waveguides are some examples of instruments developed for this purpose. As the demand for compact devices increases, this research has been strengthened in the past few years. A compact approach for guiding electromagnetic waves is to couple them to the collective oscillation of free charge carriers at the interface between a conductor and a dielectric. This interaction is called surface plasmon polaritons (SPPs).¹

SPPs can propagate along the interface tens to hundreds of wavelengths, decaying evanescently in the perpendicular direction into the two media. SPPs give rise to resonances, known as localized surface plasmon polaritons, when the conductor is not spatially extended but forms a particle of small dimension.² These resonances lead to large local field enhancements in the vicinity of the particles.

Most of the work in plasmonics has focused on optical frequencies by using noble metals.^{3,4} The reason for this focus lies in the strength of coupling between the radiation and the free charges, which is determined by the permittivity of the metal. The coupling is optimum at frequencies close to the plasma frequency, which for metals is typically in the visible and UV regions of the electromagnetic spectrum. At these frequencies, the absolute value of the permittivity of the conductor is small and the electromagnetic field can penetrate into the material. This large field penetration leads to an efficient coupling of the field to the free electrons at optical frequencies. Moreover, ohmic losses in metals are low. These losses are associated with decoherence of the free charge oscillation by carrier scattering.

Metals have very large permittivities at THz frequencies, typically five to six orders of magnitude larger than at optical frequencies. This large permittivity reduces the penetration of the electromagnetic field into the metal and minimizes its coupling to the free charges. The weak coupling also leads to a weak confinement of the field to the surface and the concomitant increase of the propagation length of the surface mode as ohmic losses in the metal are reduced. SPPs evolve from highly confined modes at the surface of a metal propagating moderate distances at optical and infrared (IR) wavelengths to weakly confined surface waves propagating very long distances at THz frequencies. The latter situation corresponds to Sommerfeld-Zenneck waves at low frequencies.⁵ Two major approaches have been employed to increase the confinement of SPPs at THz frequencies: either electromagnetic waves bounded to metal surfaces are obtained by perforating these surfaces with periodic arrays of holes or grooves;⁶ or SPPs are excited on semiconductor surfaces.⁷

The THz time-domain measurements of SPPs on single metallic interfaces^{8–12} and on structured films^{7,13–18} has led to a quick expansion of the field of THz plasmonics. Some remarkable results are the experimental demonstration of the enhanced THz transmission through arrays of sub-wavelength apertures assisted by surface waves,^{13–15} the excitation of surface modes on cylindrical waveguides,^{19–23} the active control of plasmonic resonances,^{24,25} and the observation of designed surface modes in microstructured surfaces.^{18,26}

In this chapter, we present an introduction to SPPs at THz frequencies. The characteristic lengths, such as wavelength, propagation and confinement

lengths, of SPPs on a flat interface separating a dielectric from a conductor are solely determined by the permittivities of the two materials. Therefore, we start the chapter with a description of the Drude permittivity of conductors. In Section 3.3, we derive the dispersion relation of SPPs on flat surfaces and discuss the characteristics lengths of SPPs. For this discussion we consider an interface separating InSb from SiO₂. Semiconductors such as InSb allow the modulation of the free charge carrier density, which influences the characteristics of SPPs. We illustrate this influence by considering InSb at different temperatures, that is, with different density of thermally excited carriers across the semiconductor band-gap. In Section 3.4, we discuss coupled SPPs across thin layers of conductors. These modes are known as long- and short-range SPPs, since their mutual coupling leads to a longer propagation length and a weaker confinement for the former and to a shorter propagation length and a stronger confinement for the latter. We finish the chapter by presenting new trends in the field of THz plasmonics. These trends include designed surface waves in structured surfaces and localized SPPs in particles. We do not discuss the very fast evolving field of graphene plasmonics at IR and THz frequencies.

3.2 The Drude model

In order to determine the response of a material to an external electric field, we need to know its dielectric function or permittivity. The permittivity is a complex quantity with an imaginary component defining the losses. In the case of a conductor, these losses are related to its resistivity. We can use the Drude model describing the response of free charge carriers to define the complex permittivity of conductors at THz frequencies. The Drude permittivity is calculated by solving the equation of motion of the charges when they are driven in oscillation by the harmonic electric field of an electromagnetic wave. This permittivity is given in terms of the plasma frequency of the material ω_p and the angular frequency ω by²⁷

$$\varepsilon_c(\omega) = \varepsilon'_c(\omega) + i\varepsilon''_c(\omega) = \varepsilon_l - \frac{\omega_p^2}{\omega^2 + i\omega\Gamma}, \quad [3.1]$$

with

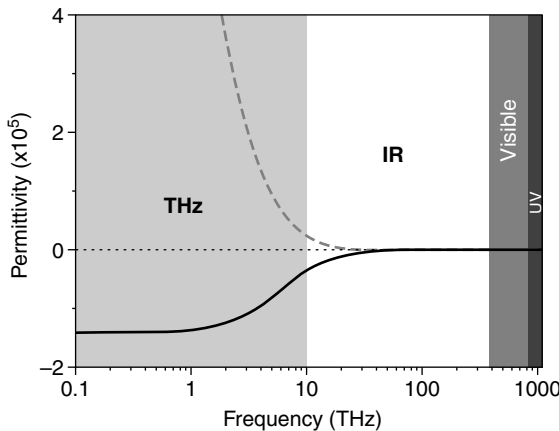
$$\omega_p^2 = \frac{e^2 N}{\varepsilon_0 m^*}, \quad [3.2]$$

$$\Gamma = \frac{e}{m^* \mu}. \quad [3.3]$$

where ϵ_l is the contribution of bound charges to the permittivity, e the elementary charge, N the free charge carrier concentration, ϵ_0 the vacuum permittivity, and m^* and μ the effective mass and mobility of the free charge carriers. The parameter Γ defines the scattering rate of the free charge carriers. This scattering rate corresponds to the inverse of the relaxation time or the mean-free time between carrier collisions. The complex permittivity (Equation [3.1]) scales with the square of ω_p , and it is inversely proportional to the square of ω and the scattering rate of the charge carriers Γ . The material parameters of significance in the Drude model are thus the carrier concentration, and the effective mass and mobility of the carriers.

Figure 3.1 displays the permittivity of gold (real and imaginary components with black and gray curves, respectively) through the electromagnetic spectrum from low frequencies THz to the UV. This permittivity has been calculated using the Drude model with $\epsilon_l = 1$, $\omega_p/2\pi = 2.18 \times 10^3$ THz and $\Gamma/2\pi = 6.45$ THz.²⁸ The plasma frequency of metals is typically in the UV region of the electromagnetic spectrum. This high plasma frequency is mainly caused by the large free carrier concentration in metals, in the order of $N \sim 10^{28} \text{ m}^{-3}$. The values of both the real and imaginary components of the permittivity of gold in the visible are low. As explained in Section 3.3.2, these values determine the confinement and propagation of SPPs. The permittivity of metals has very large absolute values at low frequencies as a consequence of its ω^2 dependence. In the case of gold at 1 THz, $\epsilon_r \sim -10^5 + 7 \times 10^5 i$ and its behavior approaches that of a perfect electrical conductor at lower frequencies. (A perfect conductor is characterized by $\epsilon_r = -\infty$. The skin depth of perfect conductors is nil and they cannot support surface plasmon polaritons.) The large value of the permittivity of metals at THz frequencies leads to a large optical impedance at interfaces with dielectrics. This impedance translates into a weak penetration of the electromagnetic field into the metal and a long propagation length of surface waves along the interface, despite the large values of the imaginary component of the permittivity. The field is also weakly bounded to the interface, extending a long distance into the dielectric.

Semiconductors have much lower free carrier densities than metals, which are determined by their doping level. The plasma frequency of semiconductors is typically in the IR and THz range. THz SPPs on semiconductors have been investigated in *n*- and *p*-doped silicon,^{7,13,29–32} GaAs,³³ InAs⁹ and InSb.^{34–37} A key material property for THz plasmonics is the free carrier mobility determining the propagation length of surface waves. This mobility is higher for electrons than that for holes and depends on the semiconductor crystal structure, defect density, temperature and carrier concentration. The electron mobility in single crystalline Si is low, with typical values of $\mu \sim 1500 \text{ cm}^2/\text{V}\cdot\text{s}$. The mobility is significantly higher in GaAs ($\mu \sim 9000 \text{ cm}^2/\text{V}\cdot\text{s}$) and InAs ($\mu \sim 3 \cdot 10^4 \text{ cm}^2/\text{V}\cdot\text{s}$). The best semiconductor for THz plasmonics is InSb. InSb is a narrow band semiconductor with a band-gap energy of

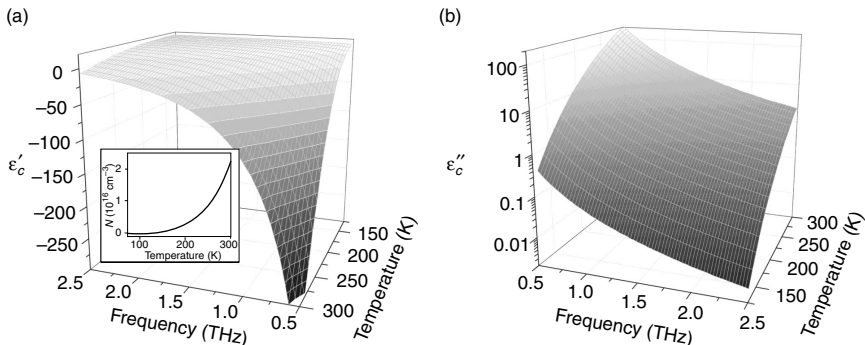


3.1 Real (black curve) and imaginary (gray dashed curve) components of the permittivity of gold as a function of the frequency.

0.16 eV. At room temperature, there are a significant number of electrons thermally excited into the conduction band, $N \sim 2 \times 10^{16} \text{ cm}^{-3}$, which determine the free carrier concentration in intrinsic InSb. The mobility of the electrons in single crystalline InSb at 300 K is $\mu \sim 7.7 \times 10^4 \text{ cm}^2/\text{V}\cdot\text{s}$, outperforming other semiconductors.

Semiconductors are versatile electronic materials in which the carrier concentration is controlled by the doping. This carrier concentration can be also actively modified, which can be exploited to modify the characteristics of SPPs. The modification of the carrier concentration can be realized with magnetic fields,^{38–41} by photo-generation of carriers^{42–45} and by thermal excitation of carriers.^{33,46–48} Also SPPs in metallic structures on top of semiconductor or phase change materials substrates can be tuned by acting on the permittivity of the substrate.^{49–52}

Figure 3.2 displays the (a) real ϵ'_c , and (b) imaginary components ϵ''_c of the permittivity of InSb as a function of the temperature and the frequency. This figure illustrates the tunability of the permittivity of semiconductors. The permittivity has been calculated using Equation [3.1] with $\epsilon_l = 15.7, m^* = 0.013 m_0$, where m_0 is the rest mass of the electron, and a temperature dependent carrier concentration and mobility given in reference 53. When compared to the permittivity of Au of Fig. 3.1, we notice that the absolute values of the permittivity of InSb are much smaller at THz frequencies. This large difference is the result of the much lower carrier concentration in InSb that gives rise to a plasma frequency in the THz region instead of in the UV. The permittivity of InSb can be tuned in a wide range of values by varying the temperature. This tunability is the result of the temperature dependence of the density of thermally excited carriers, which is illustrated in the inset of Fig. 3.2a.



3.2 (a) Real and (b) imaginary components of the permittivity of single crystalline bulk InSb as a function of the temperature and frequency. The inset of (a) displays the temperature dependence of the free charge carrier concentration in InSb.

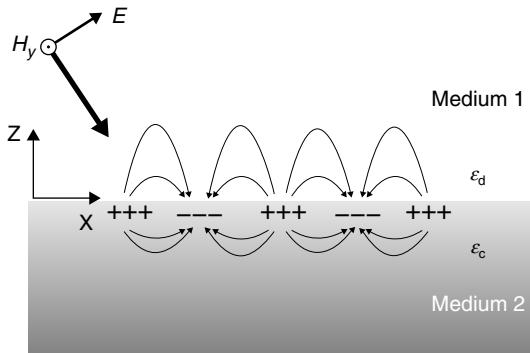
In the next section, we discuss the dispersion relation of SPPs on planar interfaces and derive their characteristic lengths. To illustrate these characteristic lengths with an example, we consider an interface separating InSb from SiO_2 at different temperatures.

3.3 Surface plasmon polaritons on planar surfaces

Surface plasmon polaritons are electromagnetic waves coupled to the free charge carriers at the interface separating a conductor from a dielectric. These surface waves represent the coherent oscillation of the free charges at the interface driven by the electric field of the electromagnetic wave. The coupling of the field to the charges leads to longitudinal surface charge density oscillations that propagate along the surface and to an electromagnetic field with an amplitude that decays evanescently away from the interface. Figure 3.3 displays a schematic representation of SPPs at the interface between a dielectric with permittivity ϵ_d (medium 1) and a conductor with permittivity ϵ_c (medium 2). The free charges at the interface as well as the electric field lines are indicated in the figure. In this section, we calculate the dispersion and characteristic lengths of SPPs.

3.3.1 Dispersion

Surface plasmon polaritons are longitudinal waves, that is, polarized along their propagation direction. The dispersion relation of SPPs can be derived from Maxwell equations and the electromagnetic boundary conditions. In this section, we describe the simplest geometry supporting surface modes,



3.3 Schematic representation of the surface charge and electric field lines of SPPs at the interface between a conductor with permittivity ϵ_c (medium 2) and a dielectric with permittivity ϵ_d (medium 1). Also indicated are the electric and magnetic field components of an incident plane wave with a k-vector given by the larger arrow.

namely, a single interface separating two media with different permittivities. Later, in Section 3.4, we discuss the case of SPPs in thin layers resulting from the coupling of surface modes across the layer. Let us consider a p-polarized plane wave incident onto the interface (see Fig. 3.3). An electric field component perpendicular to the interface is necessary to build a surface polarization. Therefore, only p-polarized light can excite SPPs. Surface modes are characterized by a real wavenumber along the propagation direction (or complex in the case of losses in the metal or dielectric) and an imaginary wavenumber in the direction normal to the surface. These wavenumber components correspond to those of a wave propagating along the surface and decaying evanescently from it. The wavenumber along the propagation direction (k_x) is related to the wavenumber components in the perpendicular direction inside the dielectric (k_{z_1}) and the conductor (k_{z_2}) by

$$k_x^2 + k_{z_1}^2 = \epsilon_d k_0^2, \quad [3.4]$$

$$k_x^2 + k_{z_2}^2 = \epsilon_c k_0^2, \quad [3.5]$$

where $k_0 = 2\pi/\lambda_0$ is the wavenumber of the electromagnetic radiation in vacuum. The equations for the magnetic and electric field in the dielectric (medium 1) are given by

$$\begin{aligned}
 H_{y_1} &= Ae^{-i(k_{x_1}x+k_{z_1}z)} + Be^{i(-k_{x_1}x+k_{z_1}z)} \\
 E_{x_1} &= \frac{k_{z_1}}{\omega\epsilon_0\epsilon_d} \left[Ae^{-i(k_{x_1}x+k_{z_1}z)} - Be^{i(-k_{x_1}x+k_{z_1}z)} \right] \\
 E_{z_1} &= \frac{k_{x_1}}{\omega\epsilon_0\epsilon_d} \left[Ae^{-i(k_{x_1}x+k_{z_1}z)} + Be^{i(-k_{x_1}x+k_{z_1}z)} \right]
 \end{aligned} \quad [3.6]$$

whereas in the conductor (medium 2) these are given by

$$\begin{aligned}
 H_{y_2} &= Ce^{-i(k_{x_2}x+k_{z_2}z)} \\
 E_{x_2} &= \frac{k_{z_2}}{\omega\epsilon_0\epsilon_c} Ce^{-i(k_{x_2}x+k_{z_2}z)} \\
 E_{z_2} &= -\frac{k_{z_2}}{\omega\epsilon_0\epsilon_c} Ce^{-i(k_{x_2}x+k_{z_2}z)}
 \end{aligned} \quad [3.7]$$

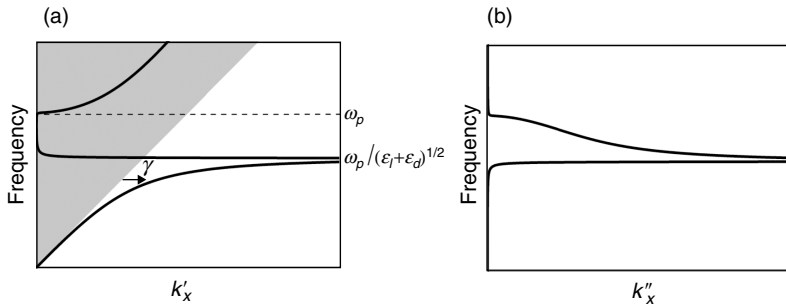
A , B and C are the amplitudes of the incident, reflected and transmitted waves, respectively. To determine the surface eigenmodes in this system, we set the amplitude of the incident wave to 0, that is, $A = 0$, and the amplitude of the fields exponentially decaying functions in the z -direction. The electromagnetic boundary condition establishing the conservation of the field components parallel to the interface, H_y and E_x at $z = 0$, is satisfied when $B = C$ and

$$\frac{k_{z_1}}{\epsilon_d} = -\frac{k_{z_2}}{\epsilon_c}. \quad [3.8]$$

Equation [3.8] constitutes the dispersion relation of SPPs on a flat interface separating a dielectric from a conductor. Using Equations [3.4] and [3.5], the dispersion relation can be written as

$$k_x = k_0 \sqrt{\frac{\epsilon_c \epsilon_d}{\epsilon_c + \epsilon_d}} = \frac{\omega}{c_0} \sqrt{\frac{\epsilon_c \epsilon_d}{\epsilon_c + \epsilon_d}}. \quad [3.9]$$

This expression relates the wavenumber of the SPP along the propagation direction with the wavenumber of electromagnetic waves in vacuum k_0 . The complex value of ϵ_c makes the wavenumber a complex quantity, with a real component k'_x that defines the dispersion of SPPs and an imaginary component k''_x that is proportional to the SPP losses. Figure 3.4 displays the (a) real and (b) imaginary components of the wavenumber as a function of the frequency. For this calculation, we assume a Drude-like behavior for the



3.4 (a) Real and (b) imaginary components of the wavenumber of SPPs (horizontal axis) versus frequency (vertical axis).

conductor with low losses, that is, $\Gamma \ll \omega$. Under this assumption the components of the wavenumber can be approximated by

$$k'_x \approx \frac{\omega}{c_0} \sqrt{\frac{\epsilon'_c \epsilon_d}{\epsilon'_c + \epsilon_d}}; \quad k''_x \approx \frac{\omega}{c_0} \left(\frac{\epsilon'_c \epsilon_d}{\epsilon'_c + \epsilon_d} \right)^{3/2} \frac{\epsilon''_c}{2 \epsilon'^2_c}. \quad [3.10]$$

The gray area in Fig. 3.4a represents the light cone, that is, the range of frequencies and wavenumbers at which electromagnetic radiation can propagate in the dielectric. The edge of the light cone defines the light line, with a dispersion relation given by

$$k = \frac{\omega}{c_0} n_d = k_0 n_d, \quad [3.11]$$

where $n_d = \sqrt{\epsilon_d}$ is the refractive index of the dielectric. An electromagnetic surface mode is characterized by an evanescently decaying field away from the surface, that is, it has an imaginary wavenumber in the direction normal to the surface. In the limit of low losses and using Equations [3.4] and [3.11], this wavenumber in the dielectric can be written as

$$k_{z_1} = \sqrt{k^2 - k'^2_x} = i \sqrt{\gamma(\gamma + 2k)} = k''_x, \quad [3.12]$$

where $\gamma = k'_x - k$ defines the confinement parameter of the SPPs to the interface. SPPs bounded to the surface are characterized by wavenumbers k'_x larger than the wavenumber of free-space radiation in the dielectric, that is, wavenumbers outside the light cone for which $\gamma > 0$. This condition is met when $\epsilon'_c < 0$ and $|\epsilon'_c| \geq \epsilon_d$, that is, for frequencies lower than the so-called

surface plasmon polariton frequency. For weakly absorbing conductors, this frequency is given by

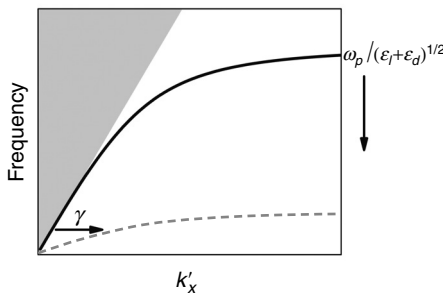
$$\omega_{\text{spp}} = \frac{\omega_p}{\sqrt{\epsilon_l + \epsilon_d}}. \quad [3.13]$$

At this point it is worth noting that it is impossible to excite SPPs by illuminating a flat interface. For this excitation to take place, it is necessary to increase the wavenumber of the incident radiation to match that of the SPPs. The increase in wavenumber can be achieved by scattering with a grating,⁵³ with single scatterers,⁸ and by total internal reflection at the interface of a high index prism.⁹

As can be seen in Fig. 3.4a, the real component of the wavenumber of SPPs is close to the light cone at low frequencies. SPPs have light-like characteristics at these frequencies, that is they are weakly bounded to the surface and propagate a long distance. This situation corresponds to the aforementioned case of Sommerfeld-Zenneck surface waves. The real wavenumber of the SPPs deviates from the light cone as the frequency increases, increasing also the confinement of the field to the interface. The wavenumber approaches an asymptotic limit at ω_{spp} . The divergence of k'_x is limited by the losses in the conductor. The imaginary component of the wavenumber and the SPPs losses increase as the frequency approaches ω_{spp} (see Fig. 3.4b). Losses are dominant in the frequency range between the surface plasmon polariton frequency and the conductor plasma frequency. In this frequency range the dispersion of SPPs is anomalous, that is, the group velocity defined as $v_g = d\omega/dk'_x$ has negative values. At higher frequencies, the SPP wavenumber is inside the light cone. The mode has in this case a real value of k_{z_1} and it is not bounded to the interface. At these frequencies, the material behaves as a dielectric with a positive permittivity.

Based on the explanations above, we can intuitively define possible ways to increase the confinement of SPPs to the surface. This confinement can be increased at a certain frequency by approaching the ω_{spp} to that frequency. This concept is illustrated in Fig. 3.5. The surface plasmon polariton frequency can be lowered by reducing ω_p or by increasing ϵ_d . This second possibility has been measured at THz frequencies by depositing thin layers of dielectric on top of gold surfaces.⁸ As we have discussed in Section 3.2, ω_p is reduced by lowering the free carrier concentration of the conductor.

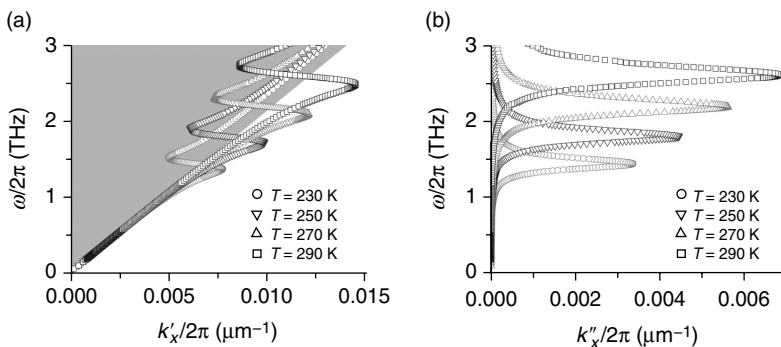
In the next section, we discuss in detail the characteristic lengths of SPPs by looking to the specific case of SPPs on an InSb–SiO₂ surface at different temperatures, that is, with different carrier concentrations.



3.5 Dispersion relation of SPPs with different values of $\omega_{\text{spp}} = \omega_p / \sqrt{\epsilon_i + \epsilon_d}$. The confinement parameter γ increases at a fixed frequency as ω_{spp} approaches this frequency.

3.3.2 Characteristic lengths of surface plasmon polaritons: wavelength, propagation length and decay lengths

Surface plasmon polaritons are described by four characteristic lengths, namely, the surface plasmon polariton wavelength, the propagation length, the decay length into the dielectric, and the decay length into the conductor. These characteristic lengths are mutually related and can be derived from the complex dispersion relation. We have presented a general description of the dispersion of SPPs at a single interface in Section 3.3.1. We will now derive the characteristic lengths of SPPs at the interface between intrinsic InSb at different temperatures and silica (SiO_2) with a permittivity $\epsilon_d = 2$. We choose InSb to illustrate the characteristic lengths of SPPs because of its superior properties for THz plasmonics. These properties are associated with its large carrier mobility and the ease in tuning the characteristic lengths of SPPs by active control of the material permittivity. Figure 3.6 displays the (a) dispersion relation and (b) the imaginary component of the wavenumber of SPPs on an InSb– SiO_2 interface for different temperatures. Lowering the temperature of InSb reduces the density of thermally excited electron–holes pairs. The carrier concentration is consequently reduced as it is illustrated in the inset of Fig. 3.2a, leading to a red-shift of ω_p and ω_{spp} , and the concomitant changes in the permittivity. Also the carrier mobility increases as the temperature is lowered, due to the reduction of e^- phonon scattering.



3.6 (a) Real and (b) imaginary components of the wavenumber of SPPs (horizontal axis) versus frequency (vertical axis) of SPPs on a InSb–SiO₂ interface at different temperatures.

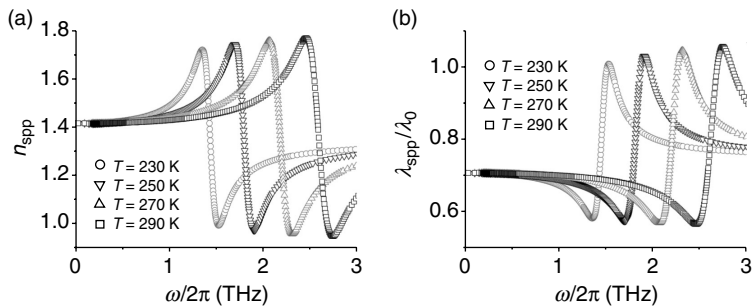
The SPP wavelength is obtained from the real component of its wavenumber along the propagation direction

$$\lambda_{\text{spp}} = \frac{2\pi}{k_x'} = \frac{\lambda_0}{n_{\text{spp}}}, \quad [3.14]$$

where λ_0 is the vacuum wavelength and n_{spp} is the index of refraction of the SPPs. Figure 3.7a displays the values of n_{spp} for the SPPs on the InSb–SiO₂ interface at different temperatures as function of the frequency. The index of refraction of the SPPs has a resonant behavior, increasing as the frequency approaches ω_{spp} . At slightly higher frequencies, the dispersion is anomalous with a negative slope of the frequency dependent index of refraction. At higher frequencies n_{spp} is smaller than the index of refraction of free-space radiation in the dielectric, which in our example is $n_d = \sqrt{\epsilon_d} = 1.41$. For these frequencies, SPPs are not bounded to the interface and they leak into the dielectric. Figure 3.7(b) displays λ_{spp} normalized to the wavelength in vacuum, as a function of the frequency for different temperatures. The reduction of the SPP wavelength close to the surface plasmon polariton resonance is the reason why SPPs are being thoroughly investigated as a way to achieve subwavelength two-dimensional optics.^{3,4}

The propagation length of SPPs along the interface represents the distance over which the intensity of the surface mode decreases by a factor $1/e$. The propagation length can be derived from the imaginary component of the wavenumber along this direction

$$L_x = \frac{1}{2k_x''}. \quad [3.15]$$



3.7 (a) Index of refraction of SPPs at the InSb–SiO₂ interface and (b) SPPs wavelength normalized to the vacuum wavelength, as a function of the frequency and for different temperatures.

Note that the expression of k_x'' given in the previous section is valid for a perfectly flat surface in which losses are ohmic, that is, they are entirely due to the complex permittivity of the material. Radiative losses due to scattering at imperfections onto the surface are not considered, although these losses can be dominant when the size of the imperfections becomes comparable to λ_{spp} .

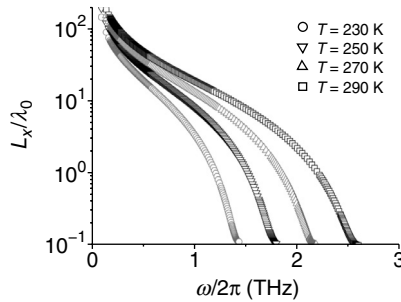
Figure 3.8 displays the propagation length of SPPs for the InSb–SiO₂ interface at different temperatures. The propagation lengths are normalized to the wavelength in vacuum and represented as a function of the frequency only at frequencies lower than ω_{spp} , that is, at frequencies at which the SPPs are surface modes bounded to the interface. The propagation length has large values of several tens to hundreds of wavelengths at low frequencies. As the frequency approaches ω_{spp} , the propagation length is drastically reduced and SPPs become overdamped surface modes.

With the expression of k_x'' derived for weakly absorbing conductors and given in Equation [3.10], the propagation length is inversely proportional to ϵ_c'' . This dependence describes the ohmic losses in the propagation of SPPs. Ohmic losses are limited by the quadratic dependence of the propagation length with the real component of the permittivity. Therefore, surface waves can propagate very long distances at low frequencies at which ϵ_c' has large values, even though at these frequencies ϵ_c'' is also large.

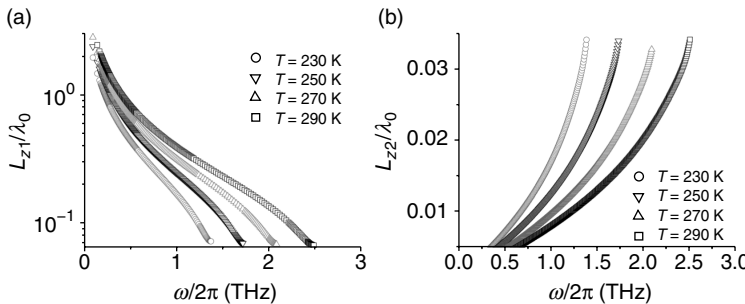
The imaginary component of the wavenumber in the direction normal to the interface in the dielectric defines the confinement length of the SPPs. With Equation [3.12], the intensity confinement length reduces to

$$L_{z_1} = \frac{1}{2|k_{z_1}''|} = \frac{1}{2\sqrt{\gamma(\gamma + 2k)}}. \quad [3.16]$$

The confinement length decreases with the inverse of the confinement parameter. As discussed in the previous section, and as can be appreciated



3.8 Propagation length of SPPs on an InSb–SiO₂ interface normalized to the wavelength in vacuum as a function of the frequency and for different temperatures.



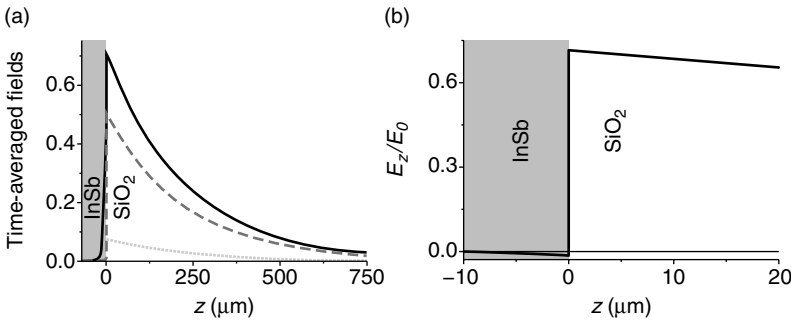
3.9 Decay lengths of SPPs on an InSb–SiO₂ interface (a) into SiO₂ and (b) into InSb at different temperatures. The decay lengths are normalized to the wavelength in vacuum and are represented as a function of frequency.

in Fig. 3.9a, the confinement parameter increases for frequencies close to ω_{spp} , leading to a reduction of L_{z_1} .

The decrease in the decay length of the SPP inside the dielectric is paired with an increase in the decay length inside the conductor. This decay length defines the last characteristic length of SPPs on planar interfaces:

$$L_{z_2} = \frac{1}{2|k''_{z_2}|}, \quad [3.17]$$

and it is displayed in Fig. 3.9b for the case of the InSb–SiO₂ interface at different temperatures. The larger penetration of the field in the conductor at higher frequencies is caused by the reduction of the permittivity of the conductor. This reduction leads to a low optical impedance mismatch at the interface, which facilitates the penetration of the field. As a consequence



3.10 (a) Time-averaged field profiles of SPPs at the interface between SiO_2 and $InSb$ at 290 K and at a frequency of 1 THz, normalized to the incident field. The black, dashed and dotted curves correspond to the H_y , E_z , and E_x components, respectively. (b) E_z instantaneous field profile normalized by the incident field.

of the larger penetration of the field in the conductor, the coupling to the charge carriers becomes stronger leading to the aforementioned reduction of L_{z_1} .

To illustrate the decay of the field inside both media, we have calculated the time-averaged field profiles using Equations [3.6] and [3.7]. These fields are defined as

$$|\mathbb{F}| = \frac{1}{\sqrt{2}} \left[(\mathbb{F}')^2 + (\mathbb{F}'')^2 \right]^{\frac{1}{2}}, \quad [3.18]$$

where \mathbb{F}' and \mathbb{F}'' stand for the real and imaginary components of the field component \mathbb{F} . The field profiles, normalized to the incident fields, are displayed in Fig. 3.10(a) as a function of the distance to the interface, which is located at $z = 0$. In that figure we can appreciate the exponential decay of the fields away from the interface. We also see the shorter decay of the field inside the conductor with respect to the decay into the dielectric. Figure 3.10(b) displays the instantaneous field profile of the E_z component. The electromagnetic boundary conditions impose the conservation of the perpendicular component of the displacement field, $D_z = \epsilon E_z$, at the interface. The different sign of the permittivity between the conductor and the dielectric leads to the discontinuous and asymmetric E_z field profile with respect to the interface.

3.4 Multilayered structures

In the previous sections, we have described the dispersion and the characteristic lengths of SPPs on single interfaces. The next step of complexity

can be made by considering double interfaces. The system formed by a conductor–dielectric–dielectric multilayer is interesting, since thin layers of high index materials on top of metals lead to an increased confinement of the SPPs.^{8,54–59} Also conductor–dielectric–conductor multilayers can have very large field confinement.^{60–63} Slot conductor–dielectric–conductor cavities based on semiconductors,^{35,64} and parallel plate waveguides in metals^{65–67} and semiconductors^{36,68,76} have been investigated at THz frequencies. In the case of a perfect conductor, the last system corresponds to parallel plate waveguide and it has been thoroughly treated in literature.⁷⁰

In this section, we are going to discuss SPPs on a dielectric-conductor–dielectric multilayer. In the case where thickness of the conductor is smaller than the penetration length of SPPs, and when the permittivity of the dielectric materials on both sides is similar, the SPPs at the opposite sides of the thin film can couple with each other. As a result of this coupling, their degeneracy is lifted and long-range and short-range SPPs are formed. As it is shown next, these SPPs have pronouncedly different characteristics.

3.4.1 Long-range and short-range surface plasmon polaritons in a slab

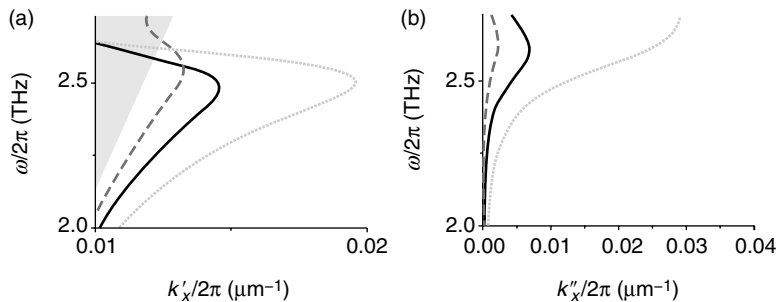
The dispersion of surface modes guided in multilayered structures can be derived in a similar way as it was done for SPPs on single interfaces in Section 3.3.1, but now considering two interfaces that delimit a layer of thickness d . These interfaces separate three media with different permittivities. We have nine field components in this system, three in each medium. By applying the electromagnetic boundary conditions to the fields at the interfaces, we obtain the following dispersion relation for transverse magnetic (TM) polarized surface modes⁷¹

$$\exp(-2ik_{z_2}d) = \left(\frac{k_{z_2} + k_{z_1}}{\frac{\varepsilon_2}{k_{z_2}} + \frac{\varepsilon_1}{k_{z_1}}} \right) \cdot \left(\frac{k_{z_2} + k_{z_3}}{\frac{\varepsilon_2}{k_{z_2}} + \frac{\varepsilon_3}{k_{z_3}}} \right). \quad [3.19]$$

In this expression the thin film corresponds to the medium labeled with the sub-index 2. As in Section 3.3.1, k_{z_j} are the wavenumber components perpendicular to the interfaces inside each medium and are defined as

$$k_x^2 + k_{z_j}^2 = \varepsilon_j k_0^2, \quad [3.20]$$

where $j = 1, 2, 3$ and k_x is the propagation constant of the surface mode or the wavenumber along the propagation direction. In the case of a thin



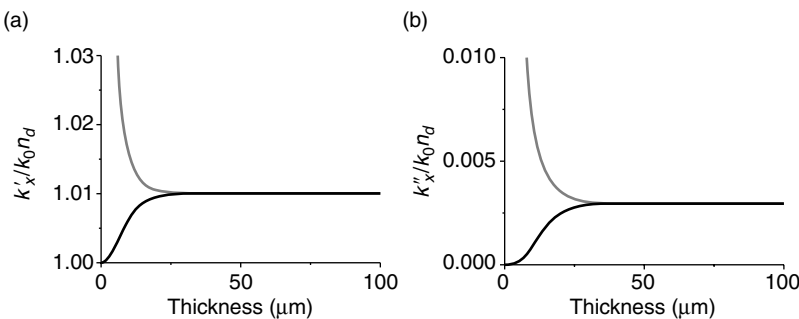
3.11 (a) Real and (b) imaginary components of the wavenumber of LRSPPs (dashed curves) and SRSPPs (dotted curves) in a 10 μm thick layer of InSb at 290 K surrounded by SiO_2 versus frequency (vertical axis). The black curves correspond to the real and imaginary components of the wavenumber of SPPs on a single InSb– SiO_2 interface at 290 K. The gray shaded area represents the light cone.

conducting layer symmetrically surrounded by the same dielectric, we have $\epsilon_1 = \epsilon_3 = \epsilon_{\text{d}}$, $\epsilon_2 = \epsilon_{\text{c}}$ and $k_{z_1} = k_{z_3}$. In this system, Equation [3.18] splits into two equations:

$$\tanh\left(ik_{z_2}d/2\right) = -\frac{\epsilon_2 k_{z_1}}{\epsilon_1 k_{z_2}}, \quad [3.21]$$

$$\tanh\left(ik_{z_2}d/2\right) = -\frac{\epsilon_1 k_{z_2}}{\epsilon_2 k_{z_1}}. \quad [3.22]$$

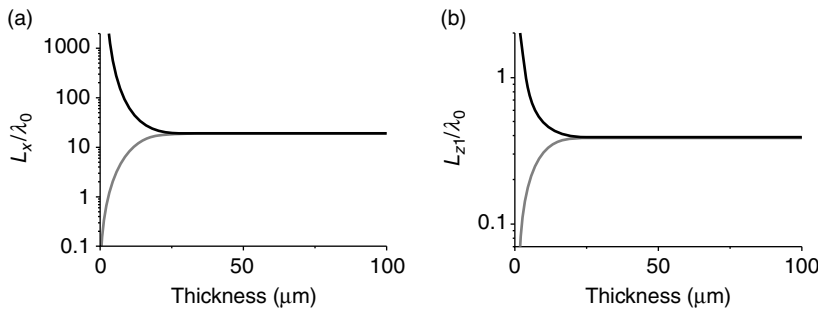
Equations [3.21] and [3.22] with Equation [3.19] represent the dispersion relations of surface modes known as long-range surface plasmon polaritons (LRSPPs) and short-range surface plasmon polaritons (SRSPPs), respectively. LRSPPs and SRSPPs result from the coupling of SPPs at the opposite sides of the thin conducting layer. The coupling lifts the degeneracy of the SPPs at the two sides, leading to two modes with different dispersion. The real wavenumbers of LRSPPs and SRSPPs in a 10 μm thick layer of InSb at room temperature embedded in SiO_2 are plotted in Fig. 3.11a with dashed and dotted curves, respectively. Also the wavenumber of SPPs on an InSb– SiO_2 single interface is plotted in the same figure with a black curve. The imaginary components of the wavenumber along the propagation direction are plotted in Fig. 3.11b. Following the explanation of Section 3.3.2, at a given frequency, the confinement parameter of SRSPPs is larger than that of LRSPPs. This stronger confinement of the mode to the thin layer leads also to a larger penetration of the electromagnetic field inside



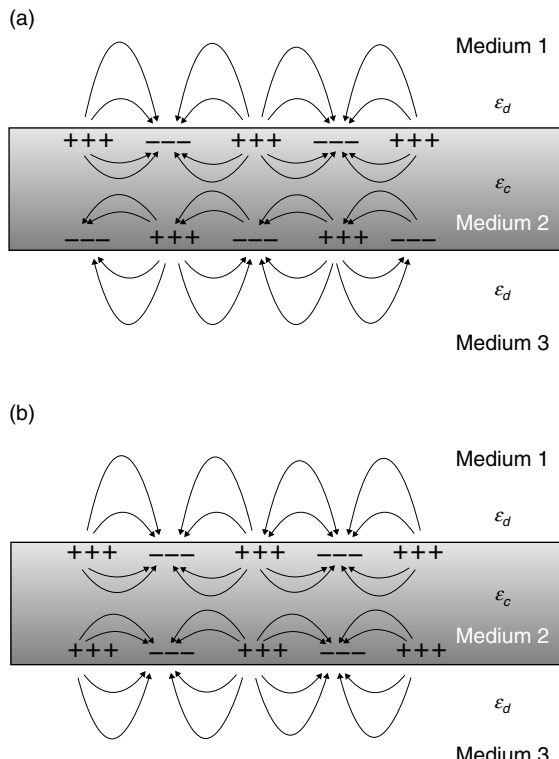
3.12 (a) Real and (b) imaginary components of the wavenumber of LRSPPs (black curves) and SRSPPs (gray curves), normalized to the wavenumber of free-space radiation in the surrounding dielectric, versus the thickness of the layer. The calculations are done at 1 THz in an InSb layer at a temperature of 290 K and surrounded by SiO_2 .

the conducting layer and the concomitant increase of the ohmic losses. The increase of the losses can be appreciated by the larger value of k_x'' for SRSPPs seen in Fig. 3.11b.

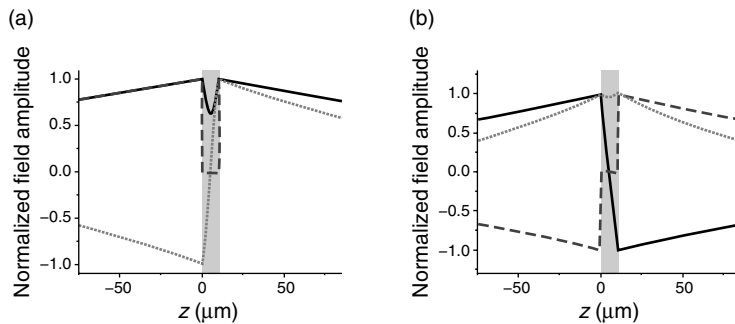
To illustrate the effect of the coupling of SPPs across the thin film, we have calculated the real and imaginary components of the wavenumber k_x of LRSPPs and SRSPPs as a function of the thickness of the film. These calculations are shown in Fig. 3.12 for the case of a layer of InSb at a temperature of 290 K embedded in SiO_2 and at a frequency of 1 THz. For a thickness greater than 25 μm the wavenumbers of LRSPPs and SRSPPs converge to the same value. For these thicknesses, the coupling of SPPs across the layer becomes negligible and the SPPs at opposite sides are degenerate. As the thickness of the film is reduced, the coupling strength between the two SPPs increases, leading to the splitting into the two modes with different energies and wavenumbers. The real wavenumber of the LRSPPs converges to the wavenumber of free-space radiation in the surrounding dielectric and its imaginary component vanishes as the thickness of the layer goes to zero (black curves in Fig. 3.12). On the other hand, the real and imaginary components of the wavenumber of SRSPPs (light-gray curves in Fig. 3.12) diverge for very thin layers. This behavior is consistent with the explanation that LRSPPs are less confined to the thin layer, extending a greater distance inside the dielectric than SRSPPs and propagating a longer distance, that is, they have smaller k_x . Using Equations [3.16] and [3.17], we can derive the propagation and the confinement lengths of LRSPPs and SRPPs. These calculations are displayed in Fig. 3.13a and b, respectively as a function of the thickness of the thin film. The propagation and decay lengths of LRSPPs increase as the thickness of the layer decreases, while the opposite behavior is observed for SRSPPs.



3.13 (a) Propagation length and (b) decay length into the surrounding dielectric, normalized to the wavelength in vacuum, of LRSPPs (black curves) and SRSPPs (gray curves) at 1 THz in an InSb layer at a temperature of 290 K and surrounded by SiO_2 , versus the thickness of the layer.



3.14 Schematic representation of the surface charges and electric field lines of (a) LRSPPs and (b) SRSPPs in a thin conducting layer (medium 2) surrounded by dielectric (media 1 and 3).



3.15 Time-averaged field profiles of (a) LRSPPs and (b) SRSPPs in a 10 μm thick layer of InSb at 290 K surrounded by SiO_2 normalized by the maximum field at the interfaces. The black curves correspond to H_y , while the dashed and dotted curves are E_z and E_y , respectively.

The microscopic origin of the different characteristics of LRSPPs and SRSPPs can be found in the different symmetry of the charges across the thin layer and the associated field symmetries. These differences are schematically represented in Fig. 3.14, where the charges at both interfaces of the thin film and the electric field lines are displayed. LRSPPs are characterized by an asymmetric charge distribution across the thin film, while the charge distribution is symmetric for SRSPPs. As a consequence of the charge distributions, the fields also exhibit different symmetries with respect to the middle plane of the thin film. These symmetries are visible in Fig. 3.15a and b where the time-averaged field amplitudes normalized by the maximum field amplitude at the interfaces are represented for the case of LRSPPs and SRSPPs, respectively. The calculations correspond to a frequency of 1 THz in a 10 μm thick layer of InSb at a temperature of 290 K and surrounded by SiO_2 .

3.5 New trends in terahertz plasmonics

So far, we have discussed SPPs propagating on flat surfaces separating a conductor from a dielectric. In this section, we introduce the concept of spoof plasmons or surface waves propagating on structured surfaces. We also discuss SPPs confined to single conducting particles or localized SPPs.

3.5.1 Designed surface plasmon polaritons in perforated metals

Terahertz surface waves can be supported by structured surfaces.⁷² This phenomenon was first investigated in thin meshes of metallic wires,⁷³ and

extended to infinitely thick perfect conductors perforated with arrays of subwavelength holes.⁶ Measurements have been performed at microwave⁷⁴ and THz¹⁸ frequencies. Perfect conductors cannot support SPPs due to the complete screening of the electromagnetic field. However, the perforated surface allows the penetration of the field in the effective medium defined by the holes in the conductor. The penetration of the field can be described by considering a hollow waveguide. If we consider a square waveguide of size L , the cut-off wavelength is given by $\lambda_c = 2L$. There are no guided modes at longer wavelengths than λ_c . In this range, the electromagnetic field penetrates evanescently into the waveguide. The evanescent penetration of the field in a perforated perfect metal resembles the penetration of the field in a real conductor. Therefore, surface modes on perforated metals have dispersion characteristics similar to SPPs and, consequently, they have been named spoof SPPs.⁶ A crucial difference between SPPs and spoof SPPs is that ω_{spp} in the latter is determined by geometrical parameters, for example, L , whereas for the former it is determined by material properties, that is, the permittivity of the conductor. In the case of square holes the effective plasma frequency is given by⁶

$$\omega_p = \frac{\pi c_0}{\sqrt{\epsilon_d} L}, \quad [3.23]$$

where ϵ_d is the permittivity of the material filling the holes. Note that Equation [3.23] corresponds to the cut-off frequency of the waveguide. The geometrical dependence of the effective plasma frequency allows the design of the characteristic lengths and propagation of surface waves.^{17,75–78} Complementary to spoof SPPs on perforated conductors, it has recently proposed a system of metallic parallelepipeds standing on top of a metallic surface. This system supports guided modes with superior characteristics than those of SPPs in terms of field confinement and low losses.⁷⁹ The guided modes have been named domino SPPs because of the resemblance of the guiding structure to a chain of domino pieces.

3.5.2 Localized surface plasmon polaritons

This chapter has focused so far on propagating modes on extended surfaces. It is also possible to excite SPPs in small conducting particles. These localized excitations are known as localized SPPs or localized surface plasmon resonances (LSPRs). LSPRs are the result of the oscillation of the free charges in a conducting particle, coherently driven by an external electromagnetic field. The response of a particle to an external field is described by its polarizability, which is a function of the permittivity of the materials

forming the particle and its surrounding, its shape and size. In the quasi-static limit, that is, when $\lambda \ll a$, where a is the size (e.g., radius) of the particle, the field is homogeneously distributed over the entire volume of the particle and the polarizability can be derived from the electrostatic potential.⁸⁰ The polarizability per unit volume in this limit is given by

$$\frac{\alpha}{V} = 3 \frac{\epsilon_d - \epsilon_c}{\epsilon_d - 2\epsilon_c}. \quad [3.24]$$

Note that to simplify the notation, we have labeled the permittivity of the material surrounding the sphere as ϵ_d and the one forming the sphere as ϵ_c . Equation [3.24] is general and thus the material forming the sphere can be a dielectric or a conductor. In the case of a loss-less conductor ϵ_c is a real and negative number and α/V has a pole at the frequency at which ϵ_d equals $-2\epsilon_c$. This frequency is known as the localized surface plasmon polariton frequency or the Fröhlich frequency and can be associated with the frequency of the dipolar oscillation of the free charge carriers in the particle. The polarizability of the particle diverges at the localized surface plasmon polariton frequency as the incident field is in resonance with the charges in the particle. Real metals have ohmic losses, which define their complex permittivity. Moreover, a correct description of the scattering of an electromagnetic field with a particle needs to include radiative losses, which represent the emitted radiation by the oscillating charges. These two loss mechanisms lead to a complex α that reaches a maximum value at the localized surface plasmon polariton frequency.

The resonance frequency in the quasi-static limit is determined by the permittivities of the particle and its surrounding. As the size of the particle is increased, optical retardation of the electromagnetic field over the particle becomes important. The quasi-static approximation is not valid in this situation and retardation leads to red-shift of the resonance. This red-shift can be controlled by the size and shape of the particle. Structures supporting designed plasmonic resonances have been named optical or plasmonics antennas because of their similarities with radio antennas.^{2,81} However, there are fundamental differences between radio antennas and plasmonic antennas, the most pronounced one originating from the penetration of the field inside the conductor in plasmonic antennas. This penetration is negligible in metals at radio frequencies due to their large values of the permittivity. In this limit, multipolar resonant frequencies are solely determined by the size and geometry of the antenna, and the surrounding dielectric. In the case of a metallic rod in vacuum, the resonant frequencies are $\omega = \pi c_0 (2n+1)/a$, where $n = 0, 1, 2, \dots$.

The penetration of the field inside the metal at frequencies close to the plasma frequency leads to a red-shift of the resonances.⁸² Resonances in plasmonic antennas are thus pronouncedly red-shifted with respect to their analogs in radio antennas. THz resonances in particles and antennas have been demonstrated with metals^{83–86} and semiconductor structures.^{87–89} Also localized THz resonances in hole arrays⁹⁰ and slits⁹¹ have been reported.

One of the most important features of plasmonic antennas is the possibility to focus and enhance locally the electromagnetic field in subwavelength volumes. These local field enhancements are being thoroughly investigated at optical frequencies as a means to enhance the sensitivity of optical sensors.⁹² Plasmonic structures have been also recently proposed for the strong local enhancement of THz fields.^{59,93} Calculations have predicted this enhancement to be larger at THz frequencies in semiconductor antennas when compared to similar antennas of metals.⁹⁴ The recent observation of localized surface plasmon polaritons in semiconductor particles and the possibility of switching these resonances by control of the carrier concentration⁸⁸ has opened new possibilities in the field of THz plasmonic antennas.

3.6 Acknowledgments

JGR acknowledges the European Research Council (ERC) for financial support through the ERC starting grant number 259272-THz Plasmon. This work was also supported by the European Commission Seventh Framework Programme (FP7) under grant agreement no FP7-224189 and is part of the research program of the ‘Stichting voor Fundamenteel Onderzoek der Materie (FOM),’ which is financially supported by the ‘Nederlandse Organisatie voor Wetenschappelijk Onderzoek (NWO)’.

3.7 References

1. H. Raether, *Surface Plasmons*. Berlin: Springer-Verlag, 1988.
2. P. Muhlschlegel, H.-J. Eisler, O.J.F. Martin, B. Hecht, and D.W. Pohl, Resonant optical antennas, *Science*, **308**, 1607–1609 (2005).
3. W.L. Barnes, A. Dereux, and T.W. Ebbesen, Surface plasmon subwavelength optics, *Nature*, **424**, 824–830 (2003).
4. E. Ozbay, Plasmonics: merging photonics and electronics at nanoscale dimensions, *Science*, **311**, 189–193 (2006).
5. G.J. Goubau, Surface waves and their application to transmission lines, *J. Appl. Phys.*, **21**, 1119–1128 (1950).
6. J.B. Pendry, L. Martín-Moreno, and F.J. García-Vidal, Mimicking surface plasmons with structured surfaces, *Science*, **305**, 847 (2004).

7. J. Gómez Rivas, M. Kuttge, P.H. Bolivar, H. Kurz and J.A. Sánchez Gil, Propagation of surface plasmon polaritons on semiconductor gratings, *Phys. Rev. Lett.*, **93**, 256804 (2004).
8. J. Saxler, J. Gómez Rivas, C. Janke, H. P.M. Pellemans, P. Haring Bolívar, and H. Kurz, Time-domain measurements of surface plasmon polaritons in the terahertz frequency range, *Phys. Rev. B*, **69**, 155427 (2004).
9. H. Hirori, K. Yamashita, M. Nagai, and K. Tanaka, Attenuated total reflection in time domain using terahertz coherent pulses, *Jap. J. Appl. Phys.*, **43**, L1287–L1289 (2004).
10. J.F. O'Hara, R.D. Averitt, and A.J. Taylor, Prism coupling to terahertz surface plasmon polaritons, *Opt. Express*, **13**, 6117–6126 (2005).
11. T.-I. Jeon and D. Grischkowsky, THz Zenneck surface wave (THz surface plasmon) propagation on a metal sheet, *Appl. Phys. Lett.*, **86**, 161904 (2005).
12. L.S. Mukina, M.M. Nazarov, and A.P. Shkurinov, Propagation of THz plasmon pulse on corrugated and flat metal surface, *Surf. Sci.*, **600**, 4771–4776 (2006).
13. J. Gómez Rivas, C. Schotsch, P. Haring Bolívar, and H. Kurz, Enhanced transmission of THz radiation through subwavelength holes, *Phys. Rev. B*, **68**, 201306 (2003).
14. D. Qu, D. Grischkowsky, and W. Zhang, Terahertz transmission properties of thin, subwavelength metallic hole arrays, *Opt. Lett.*, **29**, 896 (2004).
15. H. Cao and A. Nahata, Resonantly enhanced transmission of terahertz radiation through a periodic array of subwavelength apertures, *Opt. Express*, **12**, 1004 (2004).
16. J.F. O'Hara, R.D. Averitt, and A. J. Taylor, Terahertz surface plasmon polariton coupling on metallic gratings, *Opt. Express*, **12**, 6397–6402 (2004).
17. W. Zhu, A. Agrawal, and A. Nahata, Planar plasmonic terahertz guided-wave devices, *Opt. Express*, **16**, 6216–6226 (2008).
18. C. R. Williams, S. R. Andrews, S. A. Maier, A. I. Fernández-Domínguez, L. Martín-Moreno, and F. J. García-Vidal, Highly confined guiding of terahertz surface plasmon polaritons on structured metal surfaces, *Nat. Photonics*, **2**, 175–179 (2008).
19. K. Wang and D.M. Mittleman, Metal wires for terahertz wave-guiding, *Nature*, **432**, 376–379 (2004).
20. T.-I. Jeon, J. Zhang, and D. Grischkowsky, THz Sommerfeld wave propagation on a single metal wire, *Appl. Phys. Lett.*, **86**, 161904 (2005).
21. M. Wachter, M. Nagel, and H. Kurz, Frequency-dependent characterization of THz Sommerfeld wave propagation on single wires, *Opt. Express*, **13**, 10815–10822 (2005).
22. H. Cao and A. Nahata, Coupling of terahertz pulses onto a single metal wire waveguide using milled groove, *Opt. Express*, **13**, 7028–7034 (2005).
23. K. Wang and D.M. Mittleman, Dispersion of surface plasmon polaritons on metal wires in the Terahertz frequency range, *Phys. Rev. Lett.*, **96**, 157401 (2006).
24. J. Gómez Rivas, C. Janke, P.H. Bolívar, and H. Kurz, Transmission of THz radiation through InSb gratings of subwavelength apertures, *Opt. Express*, **13**, 847–859 (2005).

25. E. Hendry, F.J. Garcia-Vidal, L. Martin-Moreno, J. Gómez Rivas, M. Bonn, A.P. Hibbins, and M.J. Lockyear, Optical control over surface-plasmon-polariton-assisted THz transmission through a slit aperture, *Phys. Rev. Lett.*, **100**, 123901 (2008).
26. S.A. Maier, S.R. Andrews, L. Martin-Moreno, and F.J. Garcia-Vidal, Terahertz surface plasmon-polariton propagation and focusing on periodically corrugated metal wires, *Phys. Rev. Lett.*, **97**, 176805 (2006).
27. N.W. Ashcroft and N.D. Mermin, *Solid State Physics* (Thomson Learning Inc., USA, 1976).
28. M. A. Ordal, Robert J. Bell, R. W. Alexander, Jr, L. L. Long, and M. R. Querry, Optical properties of fourteen metals in the infrared and far infrared: Al, Co, Cu, Au, Fe, Pb, Mo, Ni, Pd, Pt, Ag, Ti, V, and W, *Appl. Optics*, **24**(24), 4493–4499 (1985).
29. J. Allen, D.C. Tsui, and R.A. Logan, Observation of the two dimensional plasmon in silicon inversion layers, *Phys. Rev. Lett.*, **38**, 980–983 (1977).
30. C. Janke, J. Gómez Rivas, C. Schotsch, L. Beckmann, P. Haring Bolivar, and H. Kurz, Optimization of enhanced terahertz transmission through arrays of subwavelength apertures, *Phys. Rev. B*, **69**, 205314 (2004).
31. A.K. Azad, Y. Zhao, and W. Zhang, Transmission properties of terahertz pulses through an ultrathin subwavelength silicon hole array, *Appl. Phys. Lett.*, **86**, 141102 (2005).
32. W. Zhang, A.K. Azad, J. Han, J. Xu, J. Chen, and X.-C. Zhang, Direct observation of a transition of a surface plasmon resonance from a photonic crystal effect, *Phys. Rev. Lett.*, **98**, 183901 (2007).
33. A.K. Azad, H.-T. Chen, S.R. Kasarla, A.J. Taylor, Z. Tian, X. Lu, W. Zhang, H. Lu, A.C. Gossard, and J.F. O'Hara, Ultrafast optical control of terahertz surface plasmons in subwavelength hole arrays at room temperature, *Appl. Phys. Lett.*, **95**, 011105 (2009).
34. J. Gómez Rivas, C. Janke, P.H. Bolivar, H. Kurz, Transmission of THz radiation through InSb gratings of subwavelength apertures, *Opt. Express*, **13**, 847–859 (2005).
35. B. Gelmont, R. Parthasarathy, T. Globus, A. Bykhovski, N. Swami, Terahertz (THz) electromagnetic field enhancement in periodic subwavelength structures, *IEEE Sens. J.*, **8**, 791–796 (2008).
36. R. Parthasarathy, A. Bykhovski, B. Gelmont, T. Globus, N. Swami, and D. Woolard, Enhanced coupling of subterahertz radiation with semiconductor periodic slot arrays, *Phys. Rev. Lett.*, **98**, 153906 (2007).
37. X.-Y. He, Numerical analysis of the propagation properties of subwavelength semiconductor slit in the terahertz region, *Opt. Express*, **17**, 15359–15371 (2009).
38. Y.-C. Lan, Y.-C. Chang, and P.-H. Lee, Manipulation of tunneling frequencies using magnetic fields for resonant tunneling effects of surface plasmons, *Appl. Phys. Lett.*, **90**, 171114 (2007).
39. B. Hu, B.-Y. Gu, B.-Z. Dong, Y. Zhang, Optical transmission resonances tuned by external static magnetic field in an n-doped semiconductor grating with subwavelength slits, *Opt. Comm.*, **281**, 6120–6123 (2008).
40. J. Han, A. Lakthatakia, Z. Tian, X. Lu, and W. Zhang, Magnetic and magneto-thermal tunabilities of subwavelength-hole arrays in a semiconductor sheet, *Opt. Lett.*, **9**, 1465–1467 (2009).

41. H. Yin and P.M. Hui, Controlling enhanced transmission through semiconductor gratings with subwavelength slits by a magnetic field, *Appl. Phys. Lett.*, **95**, 011115 (2009).
42. C. Janke, J. Gómez Rivas, Peter Haring-Bolívar, and H. Kurz, All-optical switching of the transmission of electromagnetic radiation through subwavelength apertures, *Opt. Lett.*, **30**, 2357–2359 (2005).
43. J. Gómez Rivas, J.A. Sánchez-Gil, Peter Haring-Bolívar, and H. Kurz, Optically switchable mirrors for surface plasmon polaritons propagating on semiconductor surfaces, *Phys. Rev. B*, **74**, 245324 (2006).
44. T. Okada, S. Tsuji, K. Tanaka, K. Hirao, and K. Tanaka, Transmission properties of surface plasmon polaritons and localized resonance in semiconductor hole arrays, *Appl. Phys. Lett.*, **97**, 261111 (2010).
45. E. Hendry, F. J. Garcia-Vidal, L. Martin-Moreno, J. Gómez Rivas, M. Bonn, A.P. Hibbins, and M.J. Lockyear, Optical control over surface plasmon polariton-assisted THz transmission through a slit aperture, *Phys. Rev. Lett.*, **100**, 12390 (2008).
46. J. Gómez Rivas, M. Kuttge, H. Kurz, P. Haring-Bolívar, and J.A. Sánchez-Gil, Low-frequency active surface plasmon optics on semiconductors, *Appl. Phys. Lett.*, **88**, 082106 (2006).
47. J.A. Sánchez-Gil and J. Gómez Rivas, Thermal switching of the scattering coefficients of terahertz surface plasmon polaritons impinging on a finite array of subwavelength grooves on semiconductor surfaces, *Phys. Rev. B*, **73**, 205410 (2006).
48. M.-K. Chen, Y.-C. Chang, C.-E. Yang, Y. Guo, J. Mazurowski, S. Yin, P. Ruffin, C. Brantley, E. Edwards, and C. Luo, Tunable terahertz plasmonic lenses based on semiconductor microslits, *Microw. Opt. Tech. Lett.*, **52**, 979–981 (2010).
49. E. Hendry, M.J. Lockyear, J. Gómez Rivas, L. Kuipers, and M. Bonn, Ultrafast optical switching of the THz transmission through metallic subwavelength hole arrays, *Phys. Rev. B*, **75**, 235305 (2007).
50. H.-T. Chen, H. Lu, A.K. Azad, R.D. Averitt, A.C. Gossard, S.A. Trugman, J.F. O’Hara, and A.J. Taylor, Electronic control of extraordinary terahertz transmission through subwavelength metal hole arrays, *Opt. Express*, **16**, 7641 (2008).
51. H.-T. Chen, W.J. Padilla, J.M.O. Zide, A.C. Gossard, A.J. Taylor, and R.D. Averitt, Active terahertz metamaterial devices, *Nature*, **444**, 597–600 (2006).
52. S.B. Choi, J.S. Kyoung, H.S. Kim, H.R. Park, D.J. Park, D.-J. Kim, Y.H. Ahn, F. Rotermund, H.-T. Kim, K.J. Ahn, and D.S. Kim, Nanopattern enabled terahertz all-optical switching on vanadium dioxide thin film, *Appl. Phys. Lett.*, **98**, 071105 (2011).
53. S. Adachi, *Handbook on physical properties of semiconductors*, vol. 2 (Springer, Berlin, 2004).
54. R.J. Seymour, E.S. Koteles, and G.I. Stegeman, Far-infrared surface plasmon coupling with overcoated gratings, *Appl. Phys. Lett.*, **41**, 1013–1015 (1982).
55. S.-Z.A. Lo and T.E. Murphy, Terahertz surface plasmon propagation in nanoporous silicon layers, *Appl. Phys. Lett.*, **96**, 201104 (2010).

56. N.C.J. van de Valk and P.C.M. Planken, Effect of a dielectric coating on terahertz surface plasmon polaritons on metal wires, *Appl. Phys. Lett.*, **87**, 071106 (2005).
57. M. Gong, T.-I. Jeon, and D. Grischkowsky, THz surface wave collapse on coated metal surfaces, *Opt. Express*, **17**, 17088–17100 (2009).
58. T.H. Isaac, W.L. Barnes, and E. Hendry, Determining the terahertz optical properties of subwavelength films using semiconductor surface plasmons, *Appl. Phys. Lett.*, **93**, 241115 (2008).
59. R. Salvador, A. Martínez, G. García-Meca, R. Ortunio, and J. Martí, Analysis of hybrid dielectric plasmonic waveguides, *IEEE J. Sel. Top. Quantum Elec.*, **14**, 1077–1501 (2008).
60. A. Rusina, M. Durach, K.A. Nelson, and M.I. Stockman, Nanoconcentration of terahertz radiation in plasmonic waveguides, *Opt. Express*, **16**, 18576–18589 (2008).
61. M.A. Seo, H.R. Park, S.M. Koo, D.J. Park, J.H. Kang, O.K. Suwal, S.S. Choi, P.C.M. Planken, G.S. Park, N.H. Park, Q.H. Park, D.S. Kim, Terahertz field enhancement by a metallic nano slit operating beyond the skin-depth limit, *Nat. Photonics*, **3**, 152–156 (2009).
62. D.J. Park, S.B. Choi, Y.H. Ahn, F. Rotermund, I.B. Sohn, C. Kang, M.S. Jeong, and D.S. Kim, Terahertz near-field enhancement in narrow rectangular apertures on metal film, *Opt. Express*, **17**, 12493–12501 (2009).
63. H. Merbold and T. Feurer, Slit waveguide based terahertz near-field microscopy: Prospects and limitations, *J. Appl. Phys.*, **107**, 033504 (2010).
64. J. Li and K.J. Webb, Terahertz field enhancement in doped semiconductor slot cavities, *J. Appl. Phys.*, **106**, 124901 (2009).
65. G. Gallot, S.P. Jamison, R.W. McGowan, and D. Grischkowsky, Terahertz waveguides, *J. Opt. Soc. Am. B*, **17**, 851–863 (2000).
66. J. Zhang and D. Grischkowsky, Waveguide terahertz time-domain spectroscopy of nanometer water layers, *Opt. Lett.*, **29**, 1617–1619 (2004).
67. J. Liu, R. Mendis, and D.M. Mittleman, The transition from a TEM-like mode to a plasmonic mode in parallel-plate waveguides, *Appl. Phys. Lett.*, **98**, 231113 (2011).
68. T.H. Isaac, J. Gómez Rivas, J.R. Sambles, W.L. Barnes, and E. Hendry, Surface plasmon mediated transmission of subwavelength slits at THz frequencies, *Phys. Rev. B*, **77**, 113411 (2008).
69. X. He, R. Li, G. Cai, and J. Cui, Investigation of the propagation properties of terahertz waves through a semiconductor subwavelength slit, *Opt. Comm.*, **284**, 3534–3538 (2011).
70. D. M. Pozar, *Microwave Engineering* (John Wiley & Sons, Inc., USA, 2005).
71. R. Fuchs, K.L. Kliewer, and W.J. Pardee, Optical properties of an Ionic crystal slab, *Phys. Rev.*, **150**, 589–596 (1966).
72. F.J. García de Abajo and J.J. Sáenz, Electromagnetic surface modes in structured perfect-conductor surfaces, *Phys. Rev. Lett.*, **95**, 233901 (2005).
73. R. Ulrich and M. Tacke, Submillimeter waveguiding on periodic metal structure, *Appl. Phys. Lett.*, **22**, 251–253 (1973).
74. A.P. Hibbins, B.R. Evans, and J.R. Sambles, Experimental verification of designer surface plasmons, *Science*, **308**, 670–672 (2005).

75. S.-H Kim, T.-T. Kim, S.S. Oh, J.-E. Kim, H.Y. Park, and C.-S. Kee, Experimental demonstration of self-collimation of spoof surface plasmons, *Phys. Rev. B*, **83**, 165109 (2011).
76. B.K. Juluri, Sz.-C.S. Lin, T.R. Walker, L. Jensen, and T.J. Huang, Propagation of designer surface plasmons in structured conductor surfaces with parabolic gradient index, *Opt. Express*, **17**, 2997–3006 (2009).
77. A.I. Fernández-Domínguez, E. Moreno, L. Martín-Moreno, and F.J. García-Vidal, Guiding terahertz waves along subwavelength channels, *Phys. Rev. B*, **79**, 233104 (2009).
78. N. Yu, Q.J. Wang, M.A. Kats, J.A. Fan, S.P. Khanna, L. Li, A.G. Davies, E.H. Linfield, and F. Capasso, Designer spoof-surface-plasmon structures collimate terahertz laser beams, *Nature Mater.*, **9**, 730–735 (2010).
79. D. Martin-Cano, M.L. Nesterov, A.I. Fernandez-Dominguez, F.J. Garcia-Vidal, L. Martin-Moreno, and L. Moreno Esteban, Domino plasmons for subwavelength terahertz circuitry, *Opt. Express*, **18**, 754–764 (2010).
80. J.D. Jackson, *Classical Electrodynamics, third edition* (John Wiley & Sons, Inc., New York, 1999).
81. J.-J. Greffet, Nanoantennas for light emission, *Science*, **308**, 1561–1563 (2005).
82. L. Novotny, Effective wavelength scaling for optical antennas, *Phys. Rev. Lett.*, **98**, 266802 (2007).
83. K.J. Chau, K.M. Rieckmann, and A.Y. Elezzabi, Subsurface probing of terahertz particle plasmons, *Appl. Phys. Lett.*, **90**, 131114 (2007).
84. X. Lu and W. Zhang, Terahertz localized plasmonic properties of subwavelength ring and coaxial geometries, *Appl. Phys. Lett.*, **94**, 181106 (2009).
85. Z. Tian, A.K. Azad, X. Lu, J. Gu, J. Han, Q. Xing, A.J. Taylor, J.F. O'Hara, and W. Zhang, Large dynamic resonance transition between surface plasmon and localized surface plasmon modes, *Opt. Express*, **18**, 12482–12488 (2010).
86. C.J.E. Straatsma, M.A. Startsev, and A.Y. Elezzabi, An investigation of terahertz particle plasmons: Effect of particle size on the transparency of a metallic particle ensemble, *J. Infrared Milli. Terahz. Waves*, **31**, 659–666 (2010).
87. X. Shi, A. Cleary, A. Khalid, and D.R.S. Cumming, Multiple plasmon resonances at terahertz frequencies from arrays of arsenic doped silicon dots, *Microelec. Eng.*, **86**, 1111–1113 (2009).
88. J. Grant, X. Shi, J. Alton, and D.R.S. Cumming, Terahertz localized surface plasmon resonance of periodic silicon microring arrays, *J. Appl. Phys.*, **109**, 054903 (2011).
89. A. Berrier, R. Ulbricht, M. Bonn, and J. Gómez Rivas, Ultrafast active control of localized surface plasmon resonances in silicon bowtie antennas, *Opt. Express*, **18**, 23226–23235 (2010).
90. T. Okada, S. Tsuji, K. Tanaka, K. Hirao, and K. Tanaka, Transmission properties of surface plasmon polaritons and localized resonance in semiconductor hole arrays, *Appl. Phys. Lett.*, **97**, 261111 (2010).
91. J. Kyung, M. Seo, H. Park, S. Koo, H.-S Kim, Y. Park, B.-J. Kim, K. Ahn, N. Park, H.-T. Kim, and D.-S. Kim, Giant nonlinear response of terahertz nanoresonators on VO₂ thin film, *Opt. Express*, **18**, 16452 (2010).
92. J.N. Anker, W.P. Hall, O. Lyandres, N.C. Shah, J. Zhao, and R.P. Van Duyne, Biosensing with plasmonic nanosensors, *Nat. Mater.*, **7**, 442–453 (2008).

93. A. Berrier, R. Ulbricht, M. Bonn, and J. Gómez Rivas, Ultrafast active control of localized surface plasmon resonances in silicon bowtie antennas, *Opt. Express*, **18**, 23226–23235 (2010).
94. V. Giannini, A. Berrier, S.A. Maier, J.A. Sanchez-Gil, and J. Gómez Rivas, Scattering efficiency and near field enhancement of active semiconductor plasmonic antennas at terahertz frequencies, *Opt. Express*, **18**(3), 2797–2807 (2010).

Fundamental aspects of terahertz near-field imaging and sensing

D.-S. KIM and Y.-M. BAHK, Seoul National University,
Republic of Korea and P. C. M. PLANKEN,
Delft University of Technology, The Netherlands

DOI: 10.1533/9780857096494.1.91

Abstract: The terahertz (THz) frequency range lies between optics and electronics, and THz frequencies are the lowest frequencies in which free space conventional optics can still be used before microwave components take over. Owing to its large wavelength, deep subwavelength phenomena of $\lambda/100$ are experimentally accessible even with a few microns of spatial resolution. In this chapter, a number of different imaging techniques to overcome the diffraction limit in the THz frequency will be reviewed. Particular emphasis will be given to the giant field enhancements associated with sharp edges and antenna structures and how to estimate these field enhancements directly from imaging or from the diffraction formalism.

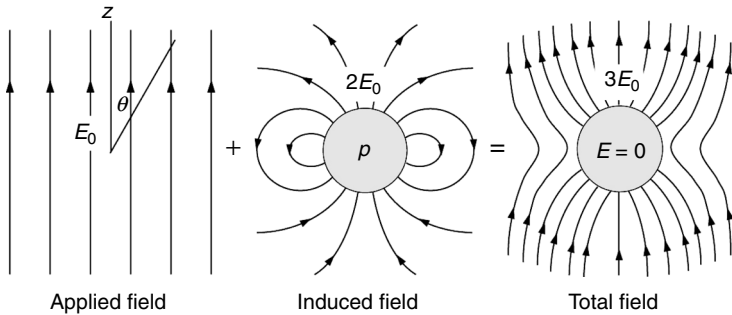
Key words: terahertz near-field measurement, terahertz spectroscopy, field enhancement, nanogap slot antenna, subwavelength optics.

4.1 Introduction

In this chapter, we proceed to discuss the properties of electromagnetic fields in the near- and far-field zones around a subwavelength object that serves as a source for the field. Near-field behavior with subwavelength distance from the source can have physical properties that are drastically different from the far-field. To understand the near-field behavior, we consider the simple system in which electric-dipole and magnetic-dipole are induced by the static ‘incident’ field. Furthermore, we examine the radiation of the induced electric- and magnetic-dipoles.

4.1.1 Near-field and far-field

For the purpose of this chapter, it suffices to say that all near-field components are created by light impinging upon small, subwavelength objects. To illustrate this point, let us consider a static case applicable to the deep



4.1 Total enhanced electric field (E) near a perfectly conducting sphere as a vector summation of the applied field, E_0 , added to the electric field by the induced electric-dipole moment, p .

subwavelength regime: a perfectly conducting sphere of radius a placed in an initially uniform electric field E_0 . This static field induces surface charge distribution with a dipole moment of $p = 4\pi a^3 \epsilon_0 E_0$ which makes the inside-electric field zero, while creating a dipole field of

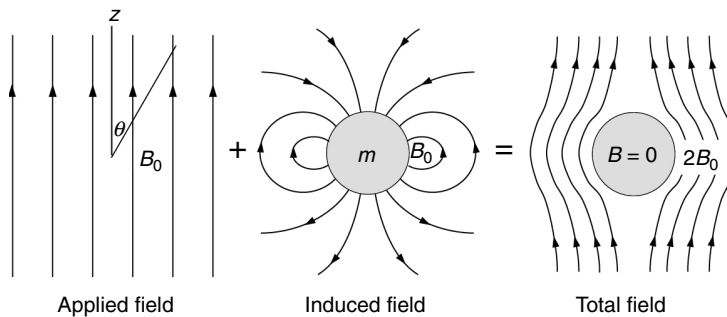
$$\vec{E} = \frac{1}{4\pi\epsilon_0} \frac{3(\hat{n} \cdot \vec{p})\hat{n} - \vec{p}}{r^3}$$

so that at the north and south poles, the induced field is twice that of the applied field. The sum of the applied field and the induced near-field gives rise to the total near-field $3E_0$ found at the north and the south poles of the perfect electrical conductor (PEC) sphere (see Fig. 4.1):

$$\vec{E}_{\text{near}}(r = a; \theta = 0) = E_0 \hat{z} + \frac{1}{4\pi\epsilon_0} \frac{(3-1)4\pi a^3 \epsilon_0}{a^3} \hat{z} = E_0 \hat{z} + 2E_0 \hat{z} = 3E_0 \hat{z}.$$

For the magnetic field, in the optical regime, the magnetic-dipole moment m induced by the incident magnetic field B_0 is much smaller than its electric-dipole counterpart: $m \ll pc$ so that it is generally ignored. However, in the terahertz (THz) regime where the metals can be considered perfect in the quasi-static sense ($\lambda \gg a \gg \delta$ (skin depth)), the magnetic-dipole effect can be comparable to that of the electric-dipole. To see this, we consider the effect of a time-varying magnetic field on a metallic sphere of radius a . The magnetic-dipole moment created by the induced currents should oppose the incident field inside the sphere. Knowing that the magnetic field of a magnetic dipole m is given by:

$$\vec{B} = \frac{\mu_0}{4\pi} \frac{3(\hat{n} \cdot \vec{m})\hat{n} - \vec{m}}{r^3},$$



4.2 Total magnetic field (B) distribution near a metallic sphere as a vector summation of the incident field, B_0 , and the magnetic field by the induced magnetic-dipole moment, m .

we have the induced magnetic moment of $m = -2\pi a^3 (B_0/c)$ which will create a zero-field inside the sphere as well as at the north and south poles, while at the equator the incident and induced magnetic fields add to make the total field of $2B_0$ (Fig. 4.2).

To summarize, the near-field is frequently associated with (1) new vector components non-existing on the incident field, and (2) a certain field enhancement.

4.1.2 Radiation of the induced electric and magnetic-dipole moment

The induced electric-dipole creates electromagnetic fields of

$$\vec{H} = \frac{ck^2}{4\pi} (\hat{n} \times \vec{p}) \frac{e^{ikr}}{r} \left[1 - \frac{1}{ikr} \right] \quad [4.1]$$

$$\vec{E} = \frac{1}{4\pi\epsilon_0} \left\{ k^2 (\hat{n} \times \vec{p}) \times \hat{n} \frac{e^{ikr}}{r} + \left[3\hat{n}(\hat{n} \cdot \vec{p}) - \vec{p} \right] \left(\frac{1}{r^3} - \frac{ik}{r^2} \right) e^{ikr} \right\}, \quad [4.2]$$

where k is the wave vector and \hat{n} is a unit vector in the direction of the observation point.

We note that the magnetic field is transverse to the radial vector at all positions, but that the electric field has components both parallel and perpendicular to \hat{n} .

In the radiation zone ($r \gg \lambda$), the fields can be written as

$$\vec{H}_{\text{far}} = \frac{ck^2}{4\pi} (\hat{n} \times \vec{p}) \frac{e^{ikr}}{r} \quad [4.3]$$

$$\vec{E}_{\text{far}} = \frac{1}{4\pi\epsilon_0} \left\{ k^2 (\hat{n} \times \vec{p}) \times \hat{n} \frac{e^{ikr}}{r} \right\}. \quad [4.4]$$

In the near-field zone ($r \ll \lambda$), on the other hand, induced fields take on the limiting forms,

$$\vec{H} = \frac{i\omega}{4\pi} (\hat{n} \times \vec{p}) \frac{1}{r^2} \quad [4.5]$$

$$\vec{E} = \frac{1}{4\pi\epsilon_0} \frac{3\hat{n}(\hat{n} \cdot \vec{p}) - \vec{p}}{r^3}. \quad [4.6]$$

It is interesting to note that the electric-dipole induced magnetic field is much weaker than the incident magnetic field at all distances: in the perfect conductor case, the induced magnetic field is at most $(2\pi a/\lambda)H_0 \ll H_0$ even for $r = a$, in contrast to the induced electric field that can reach a maximum value of $2E_0$ at the near-zone.

The magnetic field for an induced magnetic-dipole source is equal to $1/Z_0$ (Z_0 is the impedance of free space, $(\mu_0/\epsilon_0)^{1/2}$) times the electric field for the electric-dipole, with the substitution $\vec{p} \rightarrow \vec{m}/c$. Similarly, the electric field for the magnetic-dipole source is the negative of Z_0 times the magnetic field for an electric-dipole. Thus, we obtain the dipole fields

$$\vec{H} = \frac{1}{4\pi} \left\{ k^2 (\hat{n} \times \vec{m}) \times \hat{n} \frac{e^{ikr}}{r} + \left[3\hat{n}(\hat{n} \cdot \vec{m}) - \vec{m} \right] \left(\frac{1}{r^3} - \frac{ik}{r^2} \right) e^{ikr} \right\} \quad [4.7]$$

$$\vec{E} = -\frac{Z_0}{4\pi} k^2 (\hat{n} \times \vec{m}) \frac{e^{ikr}}{r} \left(1 - \frac{1}{ikr} \right). \quad [4.8]$$

In the near-zone, the magnetic-dipole induced fields are approximated as

$$\vec{H} = \frac{1}{4\pi} \frac{3\hat{n}(\hat{n} \cdot \vec{m}) - \vec{m}}{r^3} \quad [4.9]$$

$$\vec{E} = \frac{iZ_0}{4\pi} k (\hat{n} \times \vec{m}) \frac{1}{r^2}. \quad [4.10]$$

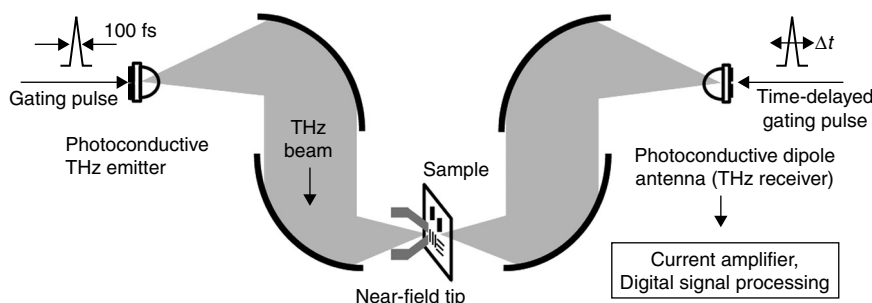
Needless to say, the magnetic field of the induced magnetic-dipole moment can be stronger than the incident magnetic field in case of the PEC case: the

electric field by the induced magnetic-dipole moment tends to be smaller than the incident electric field. It is noted that the fields in the near-zone are not only stronger, but contain more complex vector components than the far-fields, as shown in Figs 4.1 and 4.2. These fields are important in sensing subwavelength objects, such as single molecules, thin films, and biological features such as membranes.^{1–5}

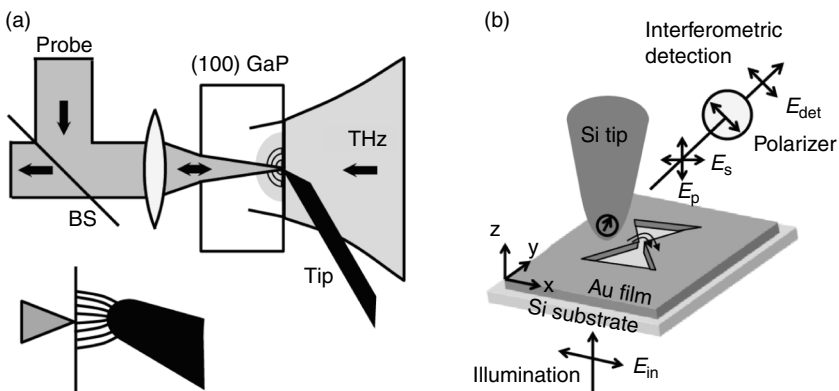
4.2 Terahertz near-field measurements

Near-field imaging with a subwavelength spatial resolution is obtained using different techniques in a wide spectral range from the visible to the THz frequency regime.⁶ One way to improve the spatial resolution is to use an aperture made from a hole in a metal.^{7–14} In 1998, the first demonstration of THz imaging with a spatial resolution about $\lambda/4$ was reported by Hunsche *et al.*¹⁵ As shown in Fig. 4.3, they focused the radiation into a tapered metal tip with a small aperture ($d < 100 \mu\text{m}$) and scanned a sample in the near-field of this aperture.

Apertureless scanning near-field optical microscopy (ASNOM) is another near-field measurement technique, based on the idea that a subwavelength-sized metal tip can scatter light.^{16–18} van der Valk *et al.* achieved a spatial resolution of $18 \mu\text{m}$, which corresponds to about $\lambda/110$ for a wavelength of 2 mm. The THz pulses are focused onto a copper tip, which has been sharpened in a FeCl etch bath. The sharp copper tip locally distorts and concentrates the THz electric field (Fig. 4.4a).¹⁹ Apertureless near-field imaging was originally developed at visible and mid-infrared wavelengths Schnell *et al.* also obtained the local near-field vector by scattering-type scanning near-field optical microscopy (SNOM) with a spatial resolution of about 10 nm in the mid-infrared regime (Fig. 4.4b).^{20,21}



4.3 Experimental set-up for THz near-field scanning optical microscopes using a subwavelength aperture (adapted from Reference 15).

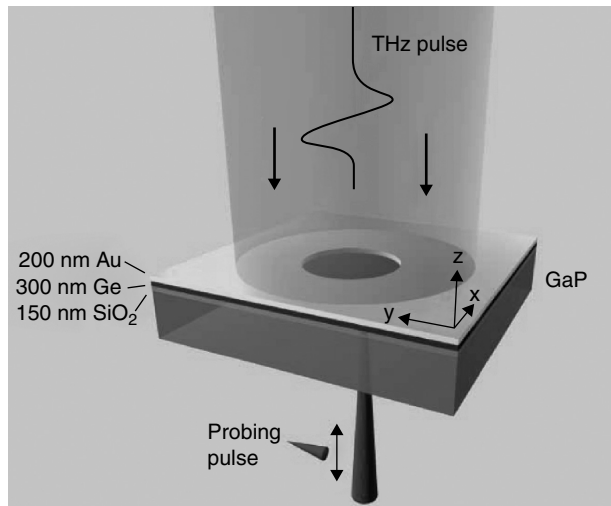


4.4 (a) Schematic of ASNOM technique for THz imaging (adapted from Reference 19). (b) Scattering-type SNOM for a vectorial near-field mapping in mid-infrared frequency range (adapted from Reference 20). BS, beam splitter.

In both the aperture and the apertureless cases, the spatial resolution is determined by the aperture size or the tip radius curvature. For the aperture of radius a , the signal goes down as a^6/λ^4 , which limits its effectiveness.²² For the scattering off a sharp tip, to isolate scattering from the near-field only, high frequency tapping and heterodyne detection is needed.^{20,21} In addition, there is the inevitable disturbance of the large tip affecting the environment. A more direct approach is to use an optical beam focused onto the near-field, to take advantage of (1) the naturally small spot size of the optical beam relative to the THz wavelength, and (2) the large wavelength separation between the optical regime and the THz regime, which limits interference and artifacts. For the optical beam to ‘see’ the THz field, the sample needs to be grown onto an electro-optic (EO) crystal such as GaP or ZnTe.

P. C. M. Planken’s group reported on the measurement of the THz electric near-field behind a subwavelength-sized hole, which was directly integrated onto an EO detection crystal.^{23–25} Figure 4.5 schematically shows the EO near-field imaging set-up when the sample is grown on GaP crystal. A quasi-near-field imaging can be achieved by the EO crystal being in mechanical contact with the sample, by pressing the sample gently on the crystal. This method has the advantage of being able to probe the evolution from the near-field to the far-field.

EO detection is based on a second-order nonlinear response of polarization in an EO material to an applied electric field.^{26,27} A refractive index of the EO material is proportionally changed by the THz electric field. The birefringence causes a polarization change of the optical probe pulse that travels through the EO detection crystal. After the detection crystal, the probe beam passes through a quarter-wave plate which is oriented such that

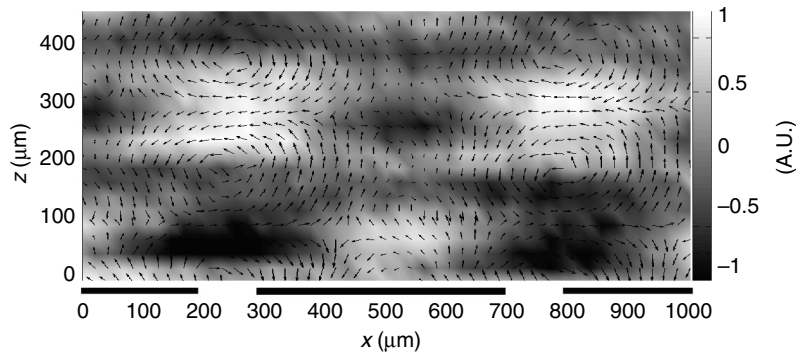


4.5 THz near-field microscopy set-up. EO sampling is used to measure the electric near-field of a subwavelength hole at each point. The local electric field is measured using the synchronized femtosecond optical probe beam. A germanium (Ge) and a SiO_2 layer prevent the probe beam from reflecting off the gold layer (adapted from Reference 28).

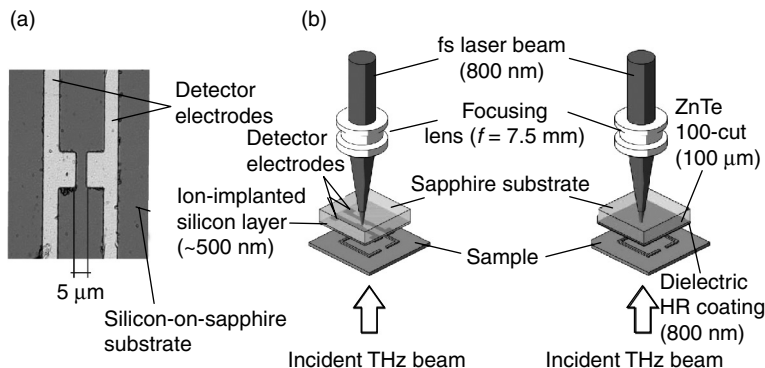
the originally linear polarization of the probe beam becomes circular. A signal proportional to the THz electric field is obtained by measuring the difference in the energy of two orthogonal polarization direction beams with a Wollaston prism and two photodiodes. For EO detection, zincblende crystals such as ZnTe and GaP are often used. By selecting the orientation of the detection crystal, it is possible to choose which component of the THz electric field vector the EO detection set-up is sensitive to. The x - and y -components of THz electric field are measured by a (110) or (111) crystal orientation, and the vertical component E_z by a (001) oriented crystal. From the measurement of the three components of the electric field, measured as we move the sample away from the EO crystal, in this case GaP, one can calculate also the magnetic near-field, via the Maxwell's equations,

$$\nabla \times \vec{E} = -\frac{\partial \vec{B}}{\partial t}. \quad [4.11]$$

Figure 4.6 shows THz electric near-field vectors measured behind a metallic slit array with a width of 100 μm and a period of 500 μm when the incident beam comes from below.²⁸ The background grey color scale represents the y -component magnetic field, calculated from the measured electric field



4.6 THz electric field and magnetic near-field profile at 1 THz for the slit array. The black line represents the electric field, E_x and E_z , and the background color denotes the magnetic field, B_y , calculated from the electric field. The measurements were performed as we moved the sample away from the crystal, defining z (adapted from Reference 28).



4.7 (a) Electrode structure of the detector antenna used as a THz near-field probe (from Reference 29). (b) Two different near-field detection techniques. Photoconductive antenna as polarization sensitive near-field probe (left) and nonlinear crystal as near-field probe (right) (adapted from Reference 30).

vectors by using Equation [4.11]. The black and white indicate negative and positive magnetic field amplitudes, respectively. This operational method has been adopted both in THz and in infrared (Andreas Bitzer and Markus B. Raschke).^{29–31}

An alternative method is to use a small subwavelength-sized photoconductive antenna as a near-field probe, gated by a femtosecond optical pulse.^{29,30,32} The detector antenna consists of an H -shaped electrode structure as shown in Fig. 4.7a deposited on a 500-nm-thick ion-implanted silicon-on-sapphire substrate. The system allows us to measure the in-plane electric and out-of-

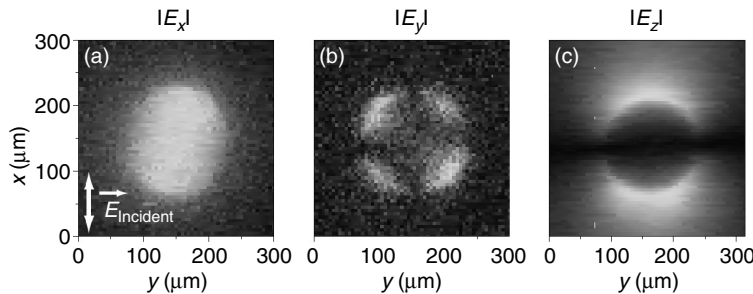
plane magnetic fields close to the sample with a spatial resolution on the micrometer scale ($\sim\lambda/20$) at 0.5 THz (Fig. 4.7b, left). Out-of-plane electric field component can be measured using a detection scheme based on EO sampling in a nonlinear crystal (Fig. 4.7b, right). In the following chapters, we mainly focus on the EO sampling technique described in Fig. 4.5.

4.3 Near-fields of various subwavelength holes

Electromagnetic waves generally transmit through a single deep subwavelength hole with an efficiency below unity. This low transmission efficiency is due to poor coupling of subwavelength holes with radiative electromagnetic modes and the evanescent decay of the electromagnetic fields inside the holes.^{22,33} However, the enhanced transmission in a single hole could be achieved by a bound cavity mode that couples resonantly to incident light or periodic corrugations of holes.^{34–37} The transmission characteristics of light through various subwavelength holes and hole arrays in a metallic film have been the focus of much research activity around the world,^{37–42} and it has been proved that the hole shape influences the optical transmission properties.^{43–49} The near-field measurements can illustrate in detail how light interacts with the subwavelength hole and emerges from the hole. In this section, we will investigate the near-field characteristics for various subwavelength holes.

4.3.1 Near-field imaging of circular holes

The electric fields, both in amplitude and in phase, passing through various holes are measured by the THz near-field time-domain spectroscopy (TDS) techniques. In 2009, Adam *et al.* reported on the measurement of all three electric field components, $E_x(t)$, $E_y(t)$ and $E_z(t)$, underneath subwavelength-sized circular holes.^{23,24} These three components were measured by choosing a suitable probe-beam polarization and EO detection crystal orientation. They measured the x - and y -components by a (111) crystal orientation, and the z -component by a (100) crystal. The circular hole was fabricated in a 200-nm-thick gold layer deposited onto a GaP detection crystal with a thickness of 300 μm . The results can be seen in Fig. 4.8 with amplitude images of the x -, y - and z -components of the measured THz electric near-field at 0.2 THz for a single circular hole, with a diameter of 150 μm . The scan area is 315 μm by 315 μm and the spatial resolution is about 10 μm . The figure shows that the x -component of electric field is strongest in the middle of the hole. The y -component of the field exhibits a quadrupole mode consisting of four lobes, in which adjacent lobes are out of phase. Finally, the z -component of the field is concentrated at the top and bottom edges of the hole, which are out of phase of each other.



4.8 THz electric near-field for a single circular hole with a diameter of 150 μm at 0.2 THz. Figures (a)–(c): $|E_x|$, $|E_y|$ and $|E_z|$ (adapted from Reference 24).

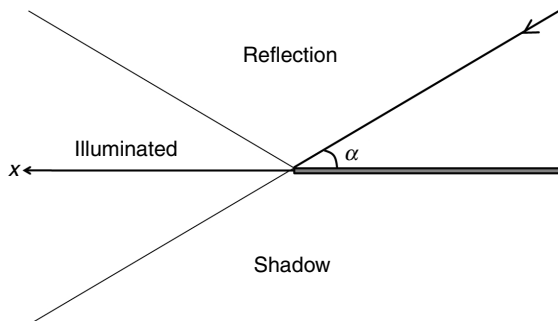
These results can be understood by the predictions made by Bouwkamp because metals act as perfect conductors in THz frequency regime.^{22,50} The diffraction of electromagnetic radiation by a subwavelength hole was first treated by Bethe.²² He studied the electromagnetic coupling through a very small hole in the idealized case of a zero-thickness perfect conductor film perforated with a circular hole of radius a . However, some important details of the field distribution in the near-zone cannot be explained by his model: subsequent higher-order corrections were calculated by Bouwkamp. From his calculations, we see that, inside the hole ($\rho < a$) at normal incidence, the tangential components of E vary rapidly over the surface of the hole,

$$E_x = -\frac{4ik}{3\pi} \frac{2a^2 - \rho^2(1 + \sin^2 \phi)}{(a^2 - \rho^2)^{1/2}} E_{\text{inc}}, \quad E_y = -\frac{2ik}{3\pi} \frac{\rho^2 \sin 2\phi}{(a^2 - \rho^2)^{1/2}} E_{\text{inc}}, \quad E_z = 0 \quad (\rho < a). \quad [4.12]$$

He also calculated the field on either face of the screen in the vicinity of the hole. In his model, the electric near-field of a hole at the shadow is written as

$$E_x = 0 \quad E_y = 0 \quad E_z = \frac{4ika^3}{3\pi} \frac{\cos \phi}{\rho(\rho^2 - a^2)^{1/2}} E_{\text{inc}} \quad (\rho > a). \quad [4.13]$$

Near the boundary $\rho = a$, the normal component of E has weak singularities. This is analogous to a weak, integrable singularity occurring frequently at two-dimensional sharp edges for example, in Sommerfeld's solution of the diffraction by a half-plane. In 1896, Sommerfeld treated the two-dimensional case of a plane wave incident on an infinitely thin,



4.9 Diffraction of a plane wave by a perfectly conducting half-plane (adapted from Reference 51).

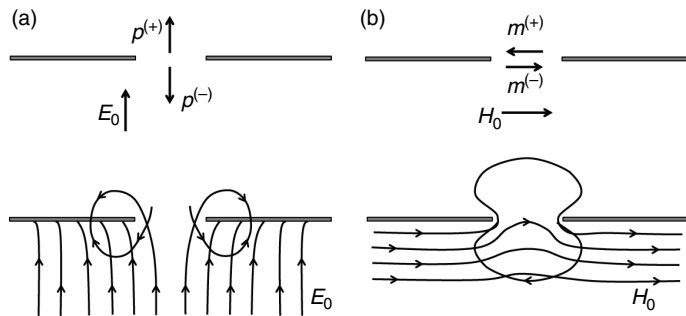
perfectly conducting half-plane, as shown in Fig. 4.9. He theoretically discussed the diffraction by a narrow slit when the magnetic field vector is parallel to the edges of the slit. The following equation shows that the electromagnetic fields have singularities occurring at a sharp edge with a normal incident light ($\alpha = 90^\circ$):

$$E_x(x,t) = \frac{E_0}{\sqrt{2\pi}} \sqrt{\frac{\lambda}{x}} e^{-i\omega t} e^{-\frac{i\pi}{4}}, \quad [4.14]$$

where ϵ_0 is the vacuum permittivity, E_0 the incident electric field, ω the angular frequency, and x the distance from the edge, respectively. The field singularity at $x = 0$ for this half-plane is the origin of the weak singularities at the edge of the circular hole.

4.3.2 Effective dipole moments of circular holes

The near-fields described in the previous section are closely related to the surface currents and surface charges around the hole, which constitute the source of the far-field radiation. Closer examination reveals that these sources mimic pseudo-electric and magnetic-dipoles, as shall be shown. When the hole is small compared to wavelength, the problem of radiation from the hole can be described as a quasi-static boundary value problem. The boundary value problem is specified by the *normal* electric field $E_{0,\text{nor}}$ and the *tangential* magnetic field $H_{0,\text{tan}}$ that would exist in the absence of the aperture. This is not surprising, since the tangential magnetic field and the normal electric fields are what survive at the metal interface with their amplitudes *twice* the incident fields by reflection. When solving the mixed boundary condition problems, the near-fields are represented by a multipole expansion.⁵² The field lines shown in Fig. 4.10a and b are the sum of the



4.10 The effective (a) electric- and (b) magnetic-dipole moments, as viewed from above and below the surface (top). The field lines can be described by fictitious dipoles added to the initial fields without the hole (bottom) (adapted from Reference 52).

straight field lines in the absence of the hole, and the fictitious dipoles of the magnitudes

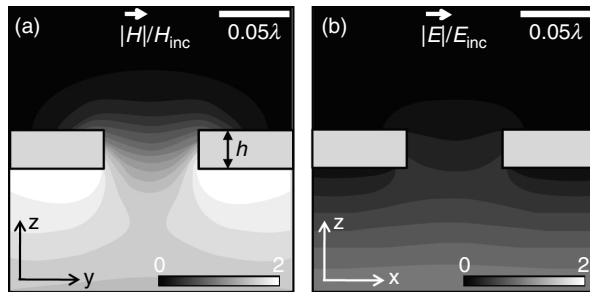
$$\vec{p}_{\text{eff}} = \pm \frac{4\epsilon_0 a^3}{3} \vec{E}_{0,\text{nor}}, \vec{m}_{\text{eff}} = \mp \frac{8a^3}{3} \vec{H}_{0,\tan}, \quad [4.15]$$

where the plus and minus signs are chosen according to whether we are describing the field lines above the hole or below. Figure 4.10 shows how the electric and magnetic field lines distort to give rise to the dipole field.

The concept of effective dipole moments to describe the electromagnetic properties of small holes was developed by Bethe.²² From his calculation of the first-order diffracted field, the diffraction cross-section is proportional to

$$\begin{aligned} \pi a^2 \left(\frac{64}{27\pi^2} k^4 a^4 \right) \left(1 + \frac{1}{4} \sin^2 \theta \right) &= \pi a^2 \left(\frac{1024}{27} \pi^2 \frac{a^4}{\lambda^4} \right) \left(1 + \frac{1}{4} \sin^2 \theta \right) \\ &\approx \pi a^2 \left[374 \left(\frac{a}{\lambda} \right)^4 \right] \left(1 + \frac{1}{4} \sin^2 \theta \right) \end{aligned}$$

where a is the radius, λ the wavelength, $k = 2\pi/\lambda$, θ the incidence angle, and TM (transverse magnetic) polarization is assumed. Note the large factor of 374 in front of the well known $(a/\lambda)^4$ term, which softens somewhat the rapid decrease of the cross-section with decreasing size for subwavelength holes.

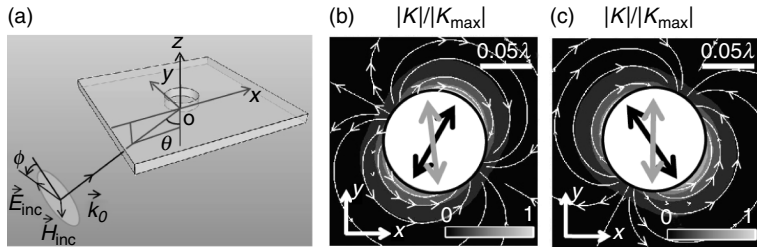


4.11 Normalized (a) tangential magnetic and (b) tangential electric field distributions for the normal incidence, for a finite-thickness PEC film calculated by the finite-difference-time-domain (FDTD) technique. The results are essentially the same for normal incidence and oblique incidences (adapted from Reference 53).

Experimentally, it is meaningful to devise a means to test whether the Bethe's concept holds for realistic subwavelength holes. To this end, we briefly examine subwavelength holes at optical frequency. Recently, Kihm *et al.* studied near- and far-field radiation of a subwavelength circular hole on a *finite-thickness* PEC plane.⁵³ While the singularities are largely softened by the finite thickness some salient features remain. The tangential magnetic field enters the subwavelength hole with a certain distortion (Fig. 4.11a), with its amplitude at the center of the aperture equal to that of the incident field. In contrast, the tangential electric field is primarily reflected, its influence being much weaker on both sides of the plane and inside the hole (Fig. 4.11b). Therefore, the scattering properties of an aperture in a metal film are mainly determined by the incident magnetic field-induced surface currents, which in turn function as a source for the far-field radiation.

The best way to separate the effects of the incident electric and magnetic fields on the metallic hole is to probe the structure with light at oblique-incidence angles, having an asymmetric polarization that is neither purely transverse electric (TE, $\phi = 0^\circ$) nor transverse magnetic (TM, $\phi = 90^\circ$), where ϕ is the polarization angle (Fig. 4.12a). In this case, the incident electric and magnetic fields projected onto the reflecting plane, $\vec{E}_t = \vec{E}_{\text{inc}} - (\hat{z} \cdot \vec{E}_{\text{inc}}) \hat{z} = E_{\text{inc}} (-\cos \theta \sin \phi, \cos \phi, 0)$ and $\vec{H}_t = H_{\text{inc}} (-\cos \theta \cos \phi, -\sin \phi, 0)$ are, in general, not orthogonal, which creates an ideal situation to discriminate the electric and magnetic nature of the scattering.

Figure 4.12b and c show finite-difference-time-domain (FDTD) calculations of surface currents on the scattering side of the structure, for the case of an oblique incident angle ($\theta = 80^\circ$) with two polarization states,



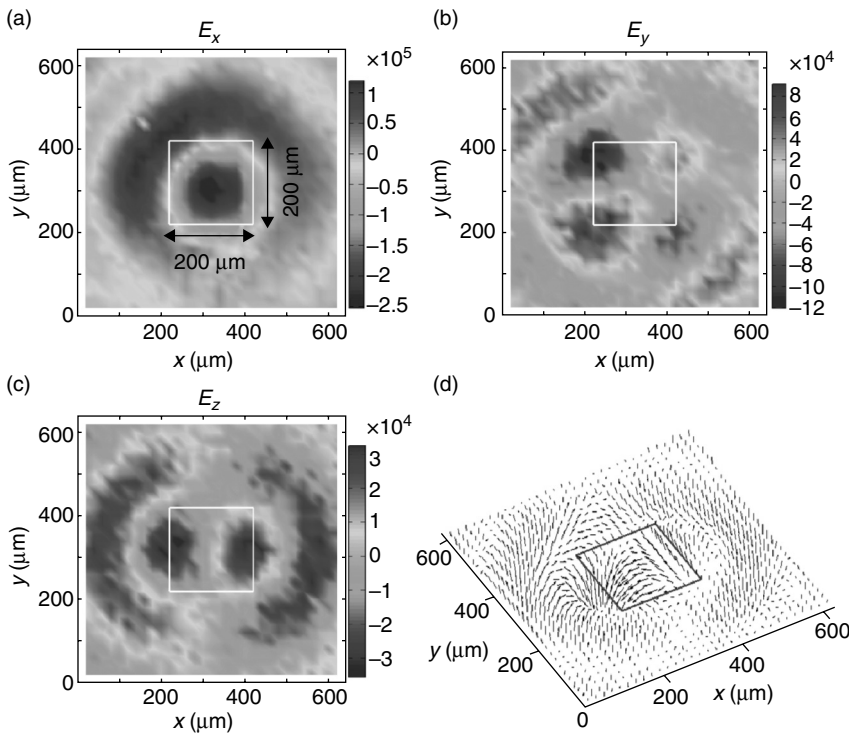
4.12 (a) Schematic of set-up with an oblique incidence. (b, c) Surface current distribution on the exit side of the hole for $\phi = 21^\circ$ and 159° with fixed $\theta = 80^\circ$, respectively. \vec{E}_t and \vec{H}_t are depicted as gray and black arrows inside the hole, respectively. The white arrows represent the direction of the surface current (adapted from Reference 53).

$\phi = 21^\circ$ and 159° , respectively. \vec{E}_t and \vec{H}_t are depicted by gray and black arrows, respectively. For both cases, the surface current \vec{K} profile is aligned perpendicularly to the tangential magnetic field, with the incident electric field direction being essentially irrelevant. Continuous changing of the electric field direction while maintaining the magnetic field direction can be achieved by varying the wave vector of the incident light with almost no effect on the surface current distribution. These observations strongly suggest that the surface currents on the scattering side of the structure are of an induced nature, with symmetric axis determined by the incident magnetic field direction $\hat{n} \times \vec{H}_t$, where \hat{n} is the unit vector normal to the plane, in this case \hat{z} .

With the surface current profile on the scattering side determined primarily by the incident magnetic field, the far-field radiation polarization also reflects the magnetic field orientation. As its far-field polarization is largely invariant with respect to changes in the incident electric field, the subwavelength aperture, when combined with far-field polarization analysis, senses the orientation of the magnetic vector field. The incident magnetic field direction can be obtained simply by rotating the polarization of the scattered light by 90° . It is expected that oblique-incidence, non-TM/TE polarization THz imaging will reveal the same trends.

4.3.3 Near-field imaging of square holes

Hole shapes are obviously important in terms of near-field enhancements. In terms of symmetry, the square hole most closely resembles a circular hole, and Fig. 4.13a, b, and c represent x -, y -, and z -components of electric field distribution for a single square hole at 1.44 THz, when the incident field

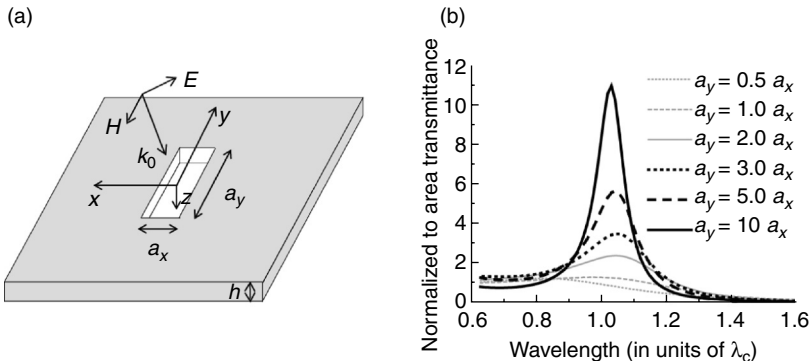


4.13 (a) x - (b) y - and (c) z -components of electric field distribution for single square hole at 1.44 THz are represented. (d) Three-dimensional vector mapping of the electric field distribution. The size of square hole is about 200 μm punctured on 80- μm -thick Al plate, and an EO sampling was performed with the crystal in close contact.

polarization is along the x -direction. The size of the square hole is about 200 μm deposited on 80- μm -thick Al plate. In Fig. 4.13d, the black arrows denote a three dimensional vector mapping of the electric field for the single square hole. The figure demonstrates that the E_x component is mostly localized inside the square hole, whereas the y - and z -components of the field are mostly confined to the edges of the hole, closely resembling the images for the circular hole.

4.3.4 Near-field imaging of rectangular holes

Both the square hole and circular hole are poor antennas and their singularities are of an integrable kind, which limits the field enhancements. One way to dramatically increase the field enhancement is to make the aperture a strongly asymmetric rectangle, which supports a well-defined transmission



4.14 (a) Schematic of a single rectangular hole of sides a_x and a_y perforated on a metal film of thickness h . (b) Normalized-to-area transmittance versus wavelength (in units of the cut-off wavelength $\lambda_c = 2a_y$), for a normal incident plane wave impinging on a rectangular hole, for different ratios a_y/a_x (adapted from Reference 34).

resonance for light polarized along its short side. F. J. Garcia-Vidal *et al.* have shown numerically that a single rectangular hole exhibits strong transmission resonances near their cut-off wavelengths³⁴. Figure 4.14a shows schematically the system: a rectangular hole of sides a_x and a_y perforated on a metallic film of thickness h . The structure is illuminated by p -polarized light and the metal is treated as a PEC, a good approximation in the THz frequency regime. Figure 4.14b depicts the calculated normalized-to-area transmission spectra for rectangles in which the aspect ratio (a_y/a_x) is varied between 1 (square hole) and 10. The thickness of the metallic film is fixed in all cases at $h = a_y/3$. As the ratio a_y/a_x is increased, a transmission peak develops close to the cut-off wavelength ($\lambda_c = 2a_y$), with increasing maximum transmittance and decreasing linewidth. The physical origin of the transmission resonances appearing at $\lambda_{\text{res}} = \lambda_c$ stems from the excitation of a Fabry-Pérot resonance in which the propagation constant is zero. An analytical approximation for the transmittance at resonance T_{res} can be obtained by

$$T_{\text{res}} \approx \frac{3}{4\pi} \frac{\lambda_{\text{res}}^2}{a_x a_y} \approx \frac{3}{\pi} \frac{a_y}{a_x}. \quad [4.16]$$

It is noted that the transmission cross-section of a rectangular hole is given by the square of the long (a_y) sides of the rectangle at the resonance, so that it is proportional to λ_{res}^2 , $\sigma_{\text{res}} \approx 3/4\pi\lambda_{\text{res}}^2$. A close analogy is found in bound charges with losses only through radiation (radiation damping),

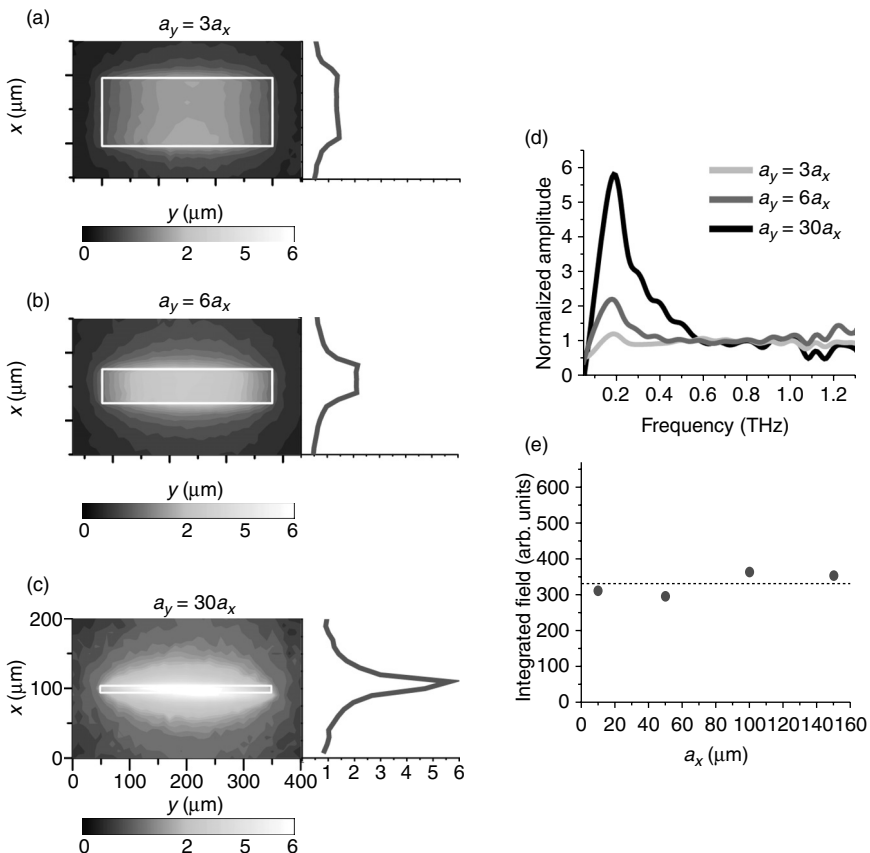
whose resonant cross-section is also proportional to λ_{res}^2 , $\sigma_{\text{res}} \approx (3/2\pi)\lambda_{\text{res}}^2$. The cross-section of the rectangle is half this value because we are only looking at the transmittance, not reflection. The electric field enhancement has also the form resembling Equation [4.16], because both energy and amplitude enhancements are essentially the same, the magnetic field amplitude being almost identical to the incident one. The electric field enhancement can be verified by near-field imaging experiments.

In 2007, Seo *et al.* experimentally verified the occurrence of a large field enhancement through the rectangular hole in the THz frequency range, using THz Fourier-transform near-field imaging with $\sim\lambda/100$ resolution.⁵⁴ They could measure the component parallel to the short side of rectangle, that is, the main near-field component. Figure 4.15a, b and c are images for samples with $a_x = 100, 50$ and $10 \mu\text{m}$ respectively for a fixed length of $a_y = 300 \mu\text{m}$ at 0.2 THz , which is the approximated resonant frequency. These figures show that the near-field amplitude becomes proportionally stronger as the rectangular hole becomes narrower. The field enhancement increases with the increasing aspect ratio of the rectangular hole, a_y/a_x , and therefore with decreasing width of the rectangle (Fig. 4.15d). Figure 4.15e shows that the area-integrated field amplitude remains nearly constant for different rectangle widths. It strongly suggests that the same amount of the energy passes through a narrow rectangular hole, confirming the funneling of energy in the near-field.

4.3.5 Near-field imaging of rectangular holes with nano-sized width

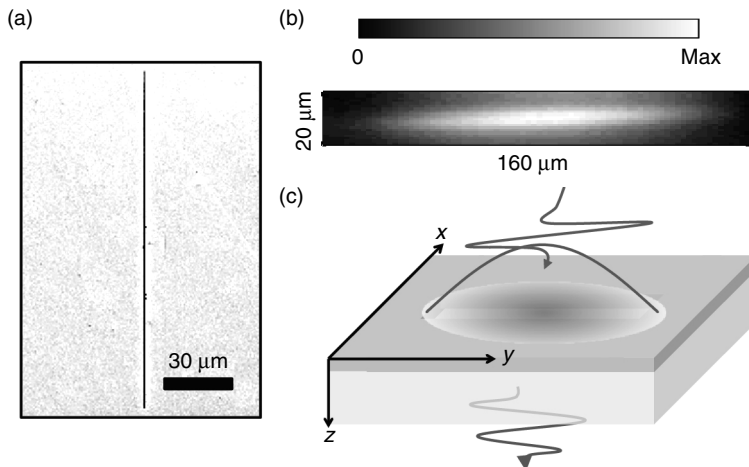
In the previous section, the rectangular hole structures had micron-sized widths. In this regime, it has been shown, theoretically and experimentally, that the field enhancement inside holes increases as the width decreases. A natural question is whether this field enhancement will keep going up as we decrease the width to nanoscale.

In this section, we will image long rectangular holes with nano-sized widths, called THz nanoantennas or THz nanoresonators, with a spatial resolution of $10 \mu\text{m}$. The samples were fabricated by Dai-Sik Kim's group and THz near-field imaging experiments were performed by A. J. L. Adam at TU-Delft. This structure was shown to induce field enhancement in the range of a few hundred for the fundamental resonance,⁵⁵ estimated by the Kirchhoff integral formalism (Section 4.4). These THz nanoantennas with a striking aspect ratio funnel THz electromagnetic waves through, accompanied by a large field enhancement unavailable for micron-sized width. THz nanoantennas with giant field enhancement open a strong possibility of potential applications, such as broadband field enhancement and nonlinear devices, filters, detectors and active switching device.^{56–60}



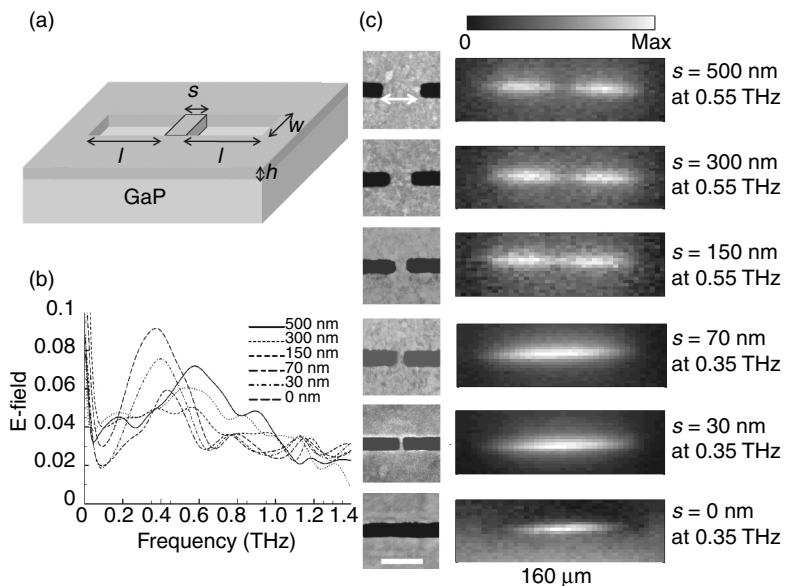
4.15 x-component of electric near-fields around single rectangles of different widths for fixed length, patterned on top of the EO crystal (GaP). The plotted images are shown for (a) $a_x = 100 \mu\text{m}$, (b) $a_x = 50 \mu\text{m}$ and (c) $a_x = 10 \mu\text{m}$. The length is fixed at 300 μm . The black line on the right side is cut through the center of the rectangular hole. (d) The spectra at the center of the rectangle for various aspect ratios are shown. (e) The integrated field amplitude over the area of the rectangle versus the width of the rectangle is shown (adapted from Reference 54).

Figure 4.16a shows a scanning electronic microscope (SEM) image of a THz nanoantenna with a length of 150 μm and a width of 120 nm. The samples are grown on a 300- μm -thick (110) oriented GaP EO detection crystal to measure the x-component of the electric near-field. Figure 4.16b shows the electric near-field imaging at resonance frequency, showing a fundamental mode at the frequency of 0.35 THz. These modes are schematically described in Fig. 4.16c.



4.16 (a) SEM image of THz nanoantenna with a length of 150 μm and a width of 120 nm. (b) x-component of electric near-field at resonance frequency of 0.35 THz. (c) Schematic of the fundamental mode.

Using this THz near-field method, we can also see a coupling between two THz nanoantennas separated by sub-skin depth barriers. Shown in Fig. 4.17a, two THz nanoantennas are vertically aligned with a metallic nanoscale barrier. Normally, the coupling between two vertically aligned nanoantennas has been ignored, because the coupling between parallelized dipoles is relatively weak compared to that between serialized dipoles. Hyeong-Ryeol Park *et al.*, however, have shown that the coupling between the paired nanoantennas changes drastically, as the width of the metallic barrier decreases below the skin depth, about 100 nm in the THz regime.⁶¹ The resonance is expected to change from ω to $\omega/2$ as the nanobarrier widths fall below the skin depth (ω corresponds to the fundamental mode of each resonator with length l , but influenced also by the index of refraction of GaP). This is because the strongly enhanced resonant electric field inside each nanoantenna can penetrate through the sub-skin depth barrier, coupling the adjacent modes, and generating a new resonant mode. Shown in Fig. 4.17b are the near-field spectra of two equal-length THz nanoantennas with a length of 75 μm and width of 120 nm, taken at the center point. Nanobarriers with widths of $s = 0, 30, 70, 150, 300$ and 500 nm separate the two nanoantennas. We start to see significant red-shift in the resonant transmission peak at the barrier width 150 nm, close to the skin depth of gold. For the thinnest 30 nm wide nanobarrier, it is noted that indeed, the resonance frequency converges to $\omega/2$. It can also be confirmed by THz near-field imaging, as shown in Fig. 4.17c.



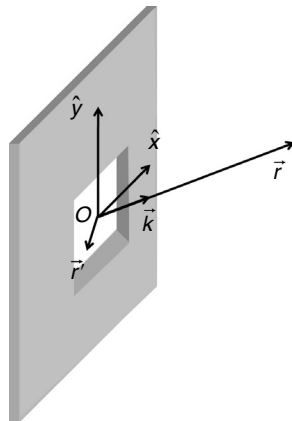
4.17 (a) Schematic of a metallic nanobarrier with width s between the two THz nanoantennas with a length l and a width w fabricated on a thin gold film with a thickness of h . GaP crystal is used as substrate for THz near-field measurement. (b) Spectra of electric fields measured at the metallic barrier region of the coupled THz nanoantennas ($l = 75 \mu\text{m}$ and $w = 120 \text{ nm}$). The barrier widths (s) are 0, 30, 70, 150, 300 and 500 nm. (c) SEM images (left) and x-component of electric near-fields (right) for six cases of the paired THz nanoantennas considered in (b). The scale bar is 500 nm.

4.4 Kirchhoff formalism for near-field estimate

Far-field transmissions exceeding the areal coverage, caused by strong near-field enhancements of subwavelength holes have been reported in a wide spectral range from the visible to the THz frequency regime. The estimation of near-field enhancement via the far-field transmission is achieved without direct near-field measurements.⁶²

4.4.1 Kirchhoff formalism and the relation between near- and far-fields

The relation between the near- and the far-field is derived from the Kirchhoff integral formalism. When an observation point is located far



4.18 Diffraction geometry for a screen with a square aperture (adapted from Reference 62).

from the hole, the diffracted electric field can be approximated by the Kirchhoff integral,

$$\vec{E}(\vec{r}) = \frac{ie^{i\vec{k}\cdot\vec{r}}}{2\pi r} \vec{k} \times \int_A \hat{n} \times \vec{E}(\vec{r}') e^{-i\vec{k}\cdot\vec{r}'} d\alpha' \quad [4.17]$$

where \vec{r}' is the coordinate of the element of the surface area of the hole, A ; \vec{r} is the distance from origin, O, to the observation point; \hat{n} is the surface normal and \vec{k} is the wave vector in the direction of the observation point, as indicated in Fig. 4.18.

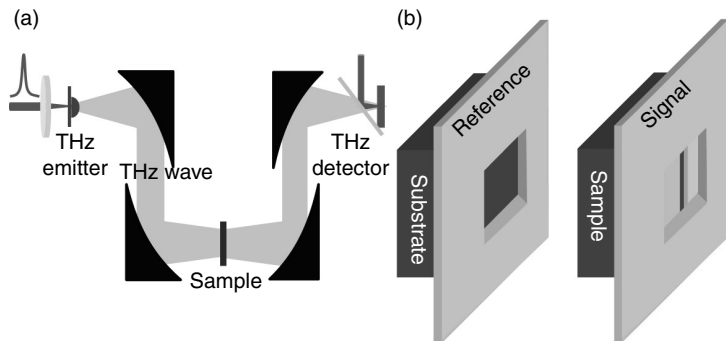
For an incident beam polarized in the horizontal direction and impinging upon the hole at the normal incidence, we can use the scalar expression and define the diffracted horizontal component of electric fields,

$$E_{\text{far}} = \frac{e^{ikr}}{i\lambda r} \int_A E_{\text{near}}(r') d\alpha' = \frac{e^{ikr}}{i\lambda r} \langle E_{\text{near}} \rangle A, \quad [4.18]$$

where the bracket means the averaged near-field over the aperture area, that is,

$$\langle E_{\text{near}} \rangle = \frac{1}{A} \int_A E_{\text{near}}(r') d\alpha'. \quad [4.19]$$

According to this formalism, the transmitted far-field through the hole is proportional to the near-field distribution inside the hole.



4.19 (a) Typical THz far-field set-up. (b) Schematics of a reference aperture with substrate (typically Si, quartz, sapphire or SiN membrane) only (left), and with a metallic sample grown on the same substrate (right).

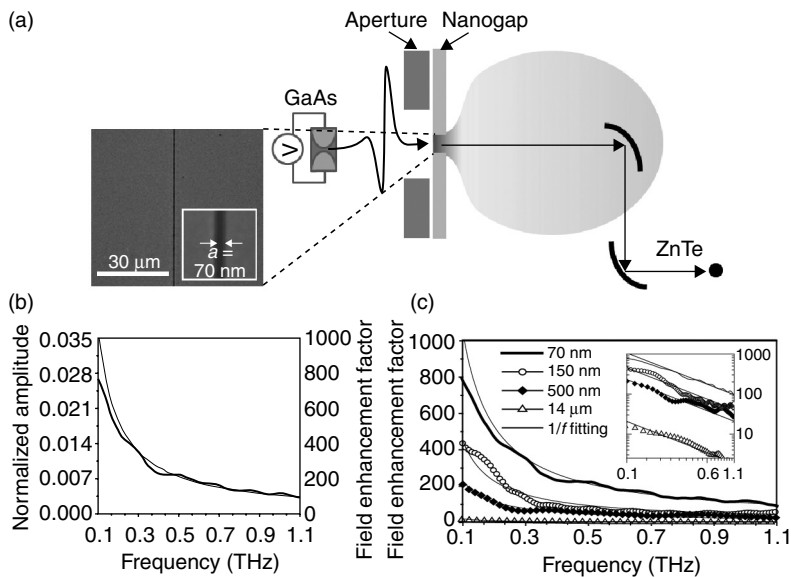
Figure 4.19a shows the typical set-up for the measurement of the transmitted far-field THz wave.^{55,63} The transmission through the sample is experimentally characterized by the normalized amplitude, $\alpha(\omega)$, defined as the ratio between the transmitted amplitude through the substrate only on the reference aperture, and that through the sample (Fig. 4.19b).

$$\alpha(\omega) = \frac{|E_{\text{far}}^{\text{signal}}(\omega)|}{|E_{\text{far}}^{\text{reference}}(\omega)|} = \frac{|\langle E_{\text{near}}^{\text{reference}}(\omega) \cdot w \cdot l \rangle|}{|\langle E_{\text{near}}^{\text{reference}}(\omega) \cdot A \rangle|} = \frac{|\langle E_{\text{near}}^{\text{signal}}(\omega) \rangle|}{|\langle E_{\text{inc}}(\omega) \rangle|} \cdot \beta \quad [4.20]$$

It follows therefore that the near-field enhancement can be estimated from the far-field measurement, corresponding to $\alpha(\omega)/\beta$, where β is the hole-to-aperture area ratio.

4.4.2 Near-field estimate of nanoslit and nanoantenna

In 2009, a 10^3 field enhancement inside a very narrow slit was demonstrated by measuring the transmitted far-field in the THz regime.⁶³ Figure 4.20a presents a schematic of the experiment set-up. The sample consisted of a nanoslit (width $w = 70$ nm) fabricated using a focused ion beam on the 60-nm-thick gold film. To obtain a normalized transmitted amplitude through the nanoslit, they performed THz far-field TDS with single-cycle THz source generated from a 2 kV/cm biased semi-insulating GaAs emitter. The emitter was illuminated by a femtosecond Ti:sapphire laser pulse train with center-wavelength 780 nm, a 76 MHz repetition rate and a 130 fs pulse width. An EO sampling method was used to detect the transmitted THz waves in the time domain, in which an optical probe pulse underwent

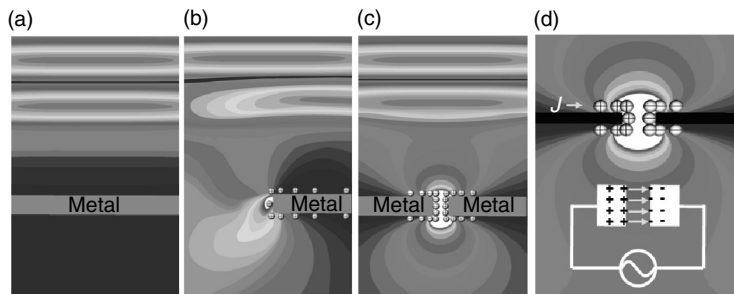


4.20 (a) SEM image of a 70-nm-width nanogap perforated on gold film and THz-TDS using EO sampling for detection of far-field transmitted amplitudes. (b) Normalized amplitude and field enhancement shown on the right-hand axis. (c) Field enhancement through samples with various gap widths: $a = 70, 150, 500$ nm and $14 \mu\text{m}$, where $h = 60, 150, 60$ nm and $17 \mu\text{m}$, respectively (inset: a log-log plot) (adapted from Reference 63).

a slight polarization rotation by the synchronized THz beam in a (110) oriented ZnTe crystal, detecting the horizontal electric field.

The transmitted far-field amplitude is connected to the enhanced near-field amplitude at the gap through Kirchhoff integral formalism, described in the previous section. Figure 4.20b shows $\alpha(\omega)$ for the nanogap sample, reaching 2.7% at the lowest frequency of 0.1 THz. The nanogap-to-aperture area ratio, $\beta = \text{width(nanogap)}/\text{width(aperture)}$, is only $0.0035\% = 70 \text{ nm}/2 \text{ mm}$. From these results, they could obtain the near-field enhancement inside the gap, a factor of 800. They also proved that the electric field increases with decreasing slit width (Fig. 4.20c). This field enhancement is caused by two Sommerfeld half-planes closely approaching, creating a steeper singularity.

When an electromagnetic wave impinges on a perfect electrically conducting plane at normal incidence, current is induced on the surface, with no charge accumulating anywhere. When this plane is cut into Sommerfeld half-planes, charges accumulate at the edges within a scale length of one wavelength, so that the surface charge density has a singularity at $x = 0$. When the two metallic half-planes are brought back together, charges at both sides

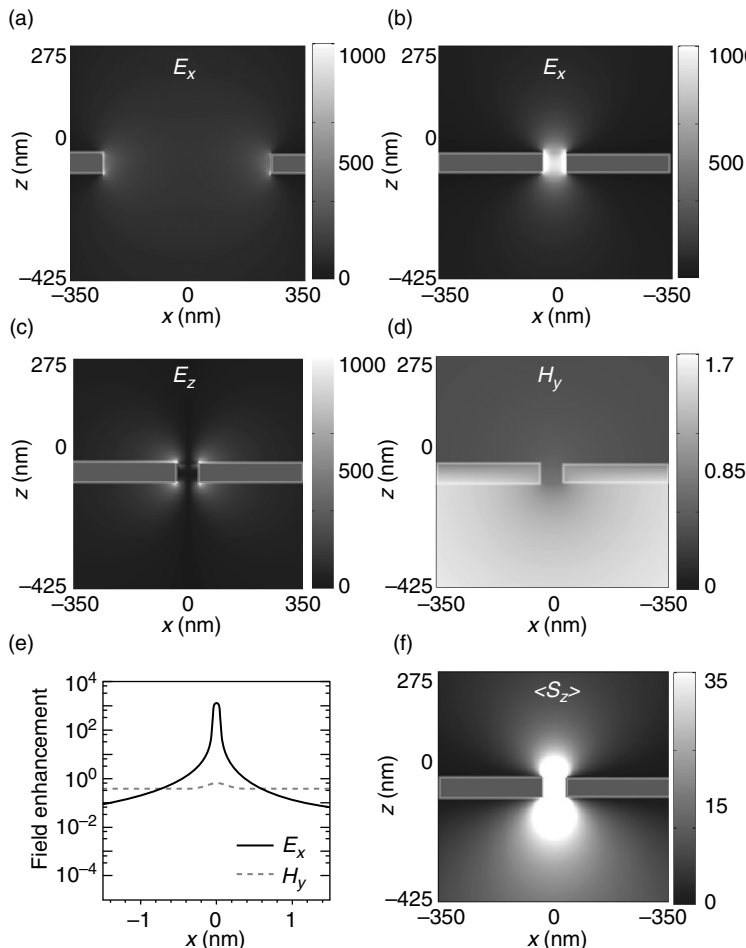


4.21 THz nanogap concept. (a) A conducting plane excited by normal incidence light. (b) A half-plane. (c) A nanogap. (d) A capacitor-like charging of the nanogap.

attract each other with increasing strength as the slit width decreases. This implies a capacitor-like charging of the nanogap (Fig. 4.21).

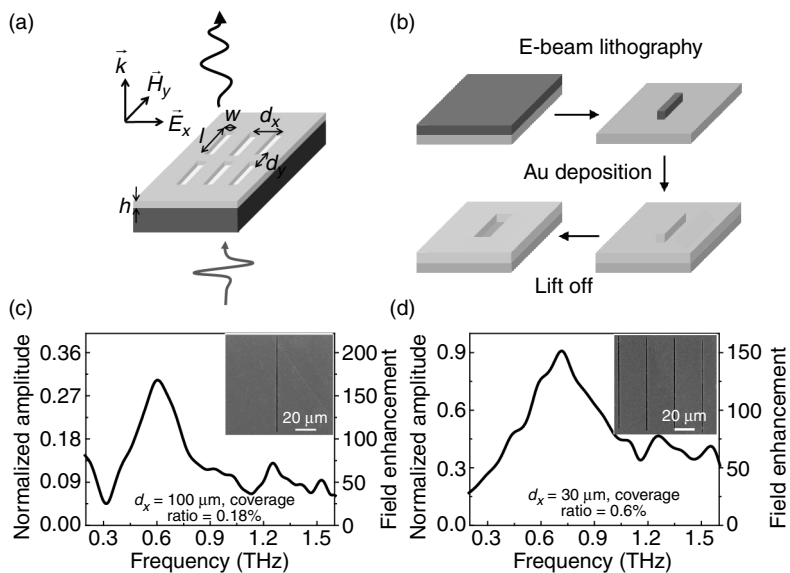
To understand these phenomena occurring near the nanoslit, a two-dimensional FDTD analysis was carried out. Figure 4.22a and b show an increasing field enhancement with a decreasing gap beyond the skin depth regime. It is in close agreement with the experimental results. While the horizontal electric field at the gap is orders of magnitudes stronger, the magnetic field stays mostly on the order of 1, but with a very small radius of curvature resulting in an enormous curl. To see the energy flow through the nanoslit, Fig. 4.22f plots the time-averaged Poynting vector $\langle S_z \rangle$ where concentration of light energy at the sub-skin depth gap is apparent. What is striking is that the Poynting vector enhancement is much smaller than what simple multiplication of electric and magnetic fields suggests, indicating that the phase difference between the enhanced electric field and impinging magnetic fields is close to 90° in this quasi-static regime.

Field enhancements in rectangular holes can also be better estimated by Kirchhoff formalism than by direct imaging described in Section 4.3, where the high frequency plateau was assumed to have the same amplitude as the incident field. Park *et al.* present a giant field enhancement of the THz electric component through THz nanoantennas which are hundreds of microns in length and have nano-sized widths,⁵⁵ using Kirchhoff formalism. They considered an array of rectangular holes with $w = 200$ nm and $l = 100$ μm in a metallic film with thickness $h = 100$ nm on a dielectric substrate of 450- μm -thick undoped silicon, as shown in Fig. 4.23a. These THz nanoantennas, acting as resonators in THz frequency range, have the maximum field enhancement of about 150 at the resonance frequency of 0.6 THz, which is $\sim c/(2n_{\text{eff}}l)$, where n_{eff} is the effective refractive index of the air-substrate composite.⁶³ The samples were fabricated by electron beam lithography using a negative photoresist and a single-layer lift-off process



4.22 The FDTD analysis of fields around nanoslits. (a) Simulated horizontal electric field around a 500-nm width at 0.1 THz. (b) Horizontal electric field around a 70-nm width. (c) Vertical electric field around the 70-nm width. (d) Simulated magnetic field around the 70-nm width. (e) Cross-sectional plot of the horizontal electric and magnetic fields at the exit side. (f) Time-averaged Poynting vector component $\langle S_z \rangle$ (adapted from Reference 63).

(Fig. 4.23b). Shown in Fig. 4.23c and d are normalized amplitude spectra for two periods of 100 μm and 30 μm . For the 30 μm period sample, the normalized amplitude increased to over 90% at the resonance with the hole coverage ratio of only 0.6%. The field enhancement was therefore over 150, calculated by the Kirchhoff integral formalism. Increasing the period to 100 μm , increased the field enhancement only slightly, suggesting that the



4.23 (a) Schematic of an array of rectangular holes. (b) THz nanoantennas are fabricated by electron beam lithography using negative type of photoresist patterning. (c) Normalized transmitted amplitude through an array of nanoantennas with $l = 100 \mu\text{m}$, $w = 200 \text{ nm}$, and $d_x = 100 \mu\text{m}$ and $d_y = 110 \mu\text{m}$. (d) The same as (c) except $d_x = 30 \mu\text{m}$. Inset displays SEM images of the samples. (adapted from Reference 55).

antenna cross-section of each slot antenna on Si substrate was about 100 μm by 30 μm.

4.5 Conclusions

We have investigated how light emerges from holes with dimensions much smaller than the wavelength of the incident light in the THz frequency regime. THz near-field images directly show that subwavelength holes in metal film have salient features such as highly enhanced electromagnetic fields near the edges for strongly asymmetric apertures. In addition, near-field enhancement can be estimated by measuring only the far-field transmission, using the Kirchhoff formalism. This is particularly useful for nano-width apertures accompanied by enormous field enhancements, where the limited spatial resolution of the near-field imaging renders direct measurement of the enhancements difficult. We have shown that the combination of near-field imaging and far-field transmission measurements provide vital insights in such new frontier problems as the sub-skin depth barrier separating THz nanoslot antennas.

4.6 References

- Ambrose, W. P., Goodwin, P. M., Martin, J. C. and Keller, R. A. Single-molecule detection and photochemistry on a surface using near-field optical-excitation. *Physical Review Letters* **72**, 160–163 (1994).
- Nie, S. M. and Emery, S. R. Probing single molecules and single nanoparticles by surface-enhanced Raman scattering. *Science* **275**, 1102–1106 (1997).
- Kuhn, S., Hakanson, U., Rogobete, L. and Sandoghdar, V. Enhancement of single-molecule fluorescence using a gold nanoparticle as an optical nanoantenna. *Physical Review Letters* **97**, doi:10.1103/PhysRevLett.97.017402 (2006).
- Novotny, L., Anger, P. and Bharadwaj, P. Enhancement and quenching of single-molecule fluorescence. *Physical Review Letters* **96**, doi:10.1103/PhysRevLett.96.113002 (2006).
- Vanden Bout, D. A., Kerimo, J., Higgins, D. A. and Barbara, P. F. Near-field optical studies of thin-film mesostructured organic materials. *Accounts of Chemical Research* **30**, 204–212, doi:10.1021/ar960274k (1997).
- Betzig, E. and Trautman, J. K. Near-field optics: microscopy, spectroscopy, and surface modification beyond the diffraction limit. *Science* **257**, 189–195, doi:10.1126/science.257.5067.189 (1992).
- Keilmann, F. FIR microscopy. *Infrared Physics and Technology* **36**, 217–224, doi:10.1016/1350-4495(94)00066-t (1995).
- Ash, E. A. and Nicholls, G. Super-resolution aperture scanning microscope. *Nature* **237**, 510–512 (1972).
- Mitrofanov, O., Brener, I., Harel, R., Wynn, J. D., Pfeiffer, L. N., West, K. W. and Federici, J. Terahertz near-field microscopy based on a collection mode detector. *Applied Physics Letters* **77**, 3496–3498 (2000).
- Lee, M., Hsu, J.W.P., Pfeiffer, L.N., West, K.W., Wynn, J.D. and Federici, J.F. Terahertz pulse propagation through small apertures. *Applied Physics Letters* **79**, 907–909 (2001).
- Nguyen, T. D., Vardeny, Z. V. and Nahata, A. Concentration of terahertz radiation through a conically tapered aperture. *Optics Express*, **18**, 25441–25448 (2010).
- Zhan, H., Mendis, R. and Mittleman, D. M. Superfocusing terahertz waves below lambda/250 using plasmonic parallel-plate waveguides. *Optics Express* **18**, 9643–9650 (2010).
- Chen, Q., Jiang, Z. P., Xu, G. X. and Zhang, X. C. Near-field terahertz imaging with a dynamic aperture. *Optics Letters* **25**, 1122–1124 (2000).
- Mittleman, D. M., Jacobsen, R. H. and Nuss, M. C. T-ray imaging. *IEEE Journal of Selected Topics in Quantum Electronics* **2**, 679–692 (1996).
- Hunsche, S., Koch, M., Brener, I. and Nuss, M. C. THz near-field imaging. *Optics Communications* **150**, 22–26, doi: 10.1016/s0030-4018(98)00044-3 (1998).
- Hillenbrand, R., Taubner, T. and Keilmann, F. Phonon-enhanced light-matter interaction at the nanometre scale. *Nature* **418**, 159–162 (2002).
- Knoll, B. and Keilmann, F. Near-field probing of vibrational absorption for chemical microscopy. *Nature* **399**, 134–137 (1999).
- Wang, K. L., Mittleman, D. M., van der Valk, N. C. J. and Planken, P. C. M. Antenna effects in terahertz apertureless near-field optical microscopy. *Applied Physics Letters* **85**, 2715–2717, doi:10.1063/1.1797554 (2004).

19. van der Valk, N. C. J. and Planken, P. C. M. Electro-optic detection of subwavelength terahertz spot sizes in the near field of a metal tip. *Applied Physics Letters* **81**, 1558–1560, doi:10.1063/1.1503404 (2002).
20. Hillenbrand, R., Schnell, M., Garcia-Etxarri, A., Alkorta, J. and Aizpurua, J. Phase-resolved mapping of the near-field vector and polarization state in nanoscale antenna gaps. *Nano Letters* **10**, 3524–3528, doi:10.1021/nl101693a (2010).
21. Schnell, M., García-Etxarri, A., Huber, A. J., Crozier, K., Aizpurua, J., and Hillenbrand, R. Controlling the near-field oscillations of loaded plasmonic nanoantennas. *Nature Photonics* **3**, 287–291, doi:http://www.nature.com/nphoton/journal/v3/n5/supplinfo/nphoton.2009.46_S1.html (2009).
22. Bethe, H. A. Theory of diffraction by small holes. *Physical Review* **66**, 163 (1944).
23. Adam, A. J. L., Brok, J. M., Seo, M. A., Ahn, K. J., Kim, D. S., Kang, J. H., Park, Q. H., Nagel, M. and Planken, P. C. M. Advanced terahertz electric near-field measurements at sub-wavelength diameter metallic apertures. *Opt. Express* **16**, 7407–7417 (2008).
24. Knab, J. R., Adam, A. J. L., Nagel, M., Shaner, E., Seo, M. A., Kim, D. S. and Planken, P. C. M. Terahertz near-field vectorial imaging of subwavelength apertures and aperture arrays. *Optics Express* **17**, 15072–15086 (2009).
25. Adam, A. J. L., Guestin, L., Knab, J. R., Nagel, M. and Planken, P. C. M. Influence of the dielectric substrate on the terahertz electric near-field of a hole in a metal. *Optics Express* **17**, 17412–17425 (2009).
26. Planken, P. C. M., Nienhuys, H.-K., Bakker, H. J. and Wenckebach, T. Measurement and calculation of the orientation dependence of terahertz pulse detection in ZnTe. *Journal of the Optical Society of America B* **18**, 313–317 (2001).
27. van der Valk, N. C. J., Wenckebach, T. and Planken, P. C. M. Full mathematical description of electro-optic detection in optically isotropic crystals. *Journal of the Optical Society of America B* **21**, 622–631 (2004).
28. Seo, M. A., Adam, A. J. L., Kang, J. H., Lee, J. W., Jeoung, S. C., Park, Q. H., Planken, P. C. M. and Kim, D. S. Fourier-transform terahertz near-field imaging of one-dimensional slit arrays: mapping of electric-field-, magnetic-field-, and Poynting vectors. *Optics Express* **15**, 11781–11789 (2007).
29. Walther, M., Bitzer, A. and Ortner, A. Terahertz near-field microscopy with subwavelength spatial resolution based on photoconductive antennas. *Applied Optics* **49**, E1–E6 (2010).
30. Bitzer, A., Ortner, A., Merbold, H., Feurer, T. and Walther, M. Terahertz near-field microscopy of complementary planar metamaterials: Babinet's principle. *Optics Express* **19**, 2537–2545 (2011).
31. Olmon, R. L., Rang, M., Krenz, P. M., Lail, B. A., Saraf, L. V., Boreman, G. D. and Raschke, M. B. Determination of electric-field, magnetic-field, and electric-current distributions of infrared optical antennas: a near-field optical vector network analyzer. *Physical Review Letters* **105**, 167403 (2010).
32. Bitzer, A. and Walther, M. Terahertz near-field imaging of metallic subwavelength holes and hole arrays. *Applied Physics Letters* **92**, doi:10.1063/1.2936303 (2008).
33. Roberts, A. Electromagnetic theory of diffraction by a circular aperture in a thick, perfectly conducting screen. *Journal of the optical society of America A* **4**, 1970–1983 (1987).

34. Garcia-Vidal, F. J., Moreno, Esteban, Porto, J. A. and Martin-Moreno, L. Transmission of light through a single rectangular hole. *Physical Review Letters* **95**, 103901 (2005).
35. Webb, K. J. and Li, J. Analysis of transmission through small apertures in conducting films. *Physical Review B* **73**, doi:10.1103/PhysRevB.73.033401 (2006).
36. de Abajo, F. J. G. I. Light transmission through a single cylindrical hole in a metallic film. *Opt Express* **10**, 1475–1484 (2002).
37. Lezec, H. J., Degiron, A., Devaux, E., Linke, R. A., Martin-Moreno, L., Garcia-Vidal, F. J. and Ebbesen, T. W. Beaming light from a subwavelength aperture. *Science* **297**, 820–822, doi:10.1126/science.1071895 (2002).
38. Ebbesen, T. W., Lezec, H. J., Ghaemi, H. F., Thio, T. and Wolff, P. A. Extraordinary optical transmission through sub-wavelength hole arrays. *Nature* **391**, 667–669 (1998).
39. Genet, C. and Ebbesen, T. W. Light in tiny holes. *Nature* **445**, 39–46 (2007).
40. Garcia-Vidal, F. J., Martin-Moreno, M., Ebbesen, T. W. and Kuipers, L. Light passing through subwavelength apertures. *Reviews of Modern Physics* **82**, 729–787, doi:citeulike-article-id:6969700 (2010).
41. Pendry, J. B., Martín-Moreno, L. and Garcia-Vidal, F. J. Mimicking surface plasmons with structured surfaces. *Science* **305**, 847–848 (2004).
42. Degiron, A., Lezec, H. J., Yamamoto, N. and Ebbesen, T. W. Optical transmission properties of a single subwavelength aperture in a real metal. *Optics Communications* **239**, 61–66, doi:DOI: 10.1016/j.optcom.2004.05.058 (2004).
43. Cao, H. and Nahata, A. Resonantly enhanced transmission of terahertz radiation through a periodic array of subwavelength apertures. *Optics Express* **12**, 1004–1010 (2004).
44. Koerkamp, K. J. K., Enoch, S., Segerink, F. B., van Hulst, N. F. and Kuipers, L. Strong influence of hole shape on extraordinary transmission through periodic arrays of subwavelength holes. *Physical Review Letters* **92**, 183901 (2004).
45. Gordon, R., Brolo, A. G., McKinnon, A., Rajora, A., Leathem, B. and Kavanagh, K. L. Strong polarization in the optical transmission through elliptical nanohole arrays. *Physical Review Letters* **92**, 037401 (2004).
46. Degiron, A. and Ebbesen, T. W. The role of localized surface plasmon modes in the enhanced transmission of periodic subwavelength apertures. *Journal of Optics A: Pure and Applied Optics* **7**, S90 (2005).
47. Ruan, Z. and Qiu, M. Enhanced transmission through periodic arrays of subwavelength holes: the role of localized waveguide resonances. *Physical Review Letters* **96**, 233901 (2006).
48. Lee, J. W., Seo, M. A., Kang, D. H., Khim, K. S., Jeoung, S. C. and Kim, D. S. Terahertz electromagnetic wave transmission through random arrays of single rectangular holes and slits in thin metallic sheets. *Physical Review Letters* **99**, 137401 (2007).
49. Lee, J. W., Seo, M. A., Park, D. J. and Kim, D. S., Jeoung, S. C., Lienau, Ch., Park, Q. H. and Planken, P. C. M. Shape resonance omni-directional terahertz filters with near-unity transmittance. *Opt. Express* **14**, 1253–1259 (2006).
50. Bouwkamp, C. J. Diffraction theory. *Reports on Progress in Physics* **17**, 35 (1954).
51. Born, M. and Wolf, E. *Principles of Optics*. (Cambridge University Press, 1999).
52. Jackson, J. D. *Classical Electrodynamics*. (John Wiley & Sons, Inc., 2001).

53. Kihm, H. W., Koo, S. M., Kim, Q. H., Bao, K., Kihm, J. E., Bak, W. S., Eah, S. H., Lienau, C., Kim, H., Nordlander, P., Halas, N. J., Park, N. K. and Kim, D.-S. Bethe-hole polarization analyser for the magnetic vector of light. *Nat Commun* **2**, 451, doi:http://www.nature.com/ncomms/journal/v2/n8/supplinfo/10.1038-nco-mms1430-unlocked-60x70_S1.html (2011).
54. Seo, M. A., Adam, A. J. L., Kang, J. H., Lee, J. W., Ahn, K. J., Park, Q. H., Planken, P. C. M. and Kim, D. S. Near field imaging of terahertz focusing onto rectangular apertures. *Optics Express* **16**, 20484–20489 (2008).
55. Park, H. R., Park, Y. M., Kim, H. S., Kyoung, J. S., Seo, M. A., Park, D. J., Ahn, Y. H., Ahn, K. J. and Kim, D. S. Terahertz nanoresonators: giant field enhancement and ultrabroadband performance. *Applied Physics Letters* **96**, 121106–121103, doi:10.1063/1.3368690 (2010).
56. Bahk, Y. M., Park, H. R., Ahn, K. J., Kim, H. S., Ahn, Y. H., Kim, D. S., Bravo-Abad, J., Martin-Moreno, L. and Garcia-Vidal, F. J. Anomalous band formation in arrays of terahertz nanoresonators. *Physical Review Letters* **106**, 013902 (2011).
57. Seo, M., Kyoung, J., Park, H., Koo, S., Kim, H. S., Bernien, H., Kim, B. J., Choe, J. H., Ahn, Y. H., Kim, H. T., Park, N., Park., Q. H., Ahn, K. and Kim, D. S. Active Terahertz nanoantennas based on VO₂ phase transition. *Nano Lett* **10**, 2064–2068, doi:10.1021/nl1002153 (2010).
58. Kyoung, J., Seo, M., Park, H., Koo, S., Kim, H. S., Park, Y., Kim, B. J., Ahn, K., Park, N., Kim, H. T. and Kim, D. S. Giant nonlinear response of terahertz nanoresonators on VO₂ thin film. *Optics Express* **18**, 16452–16459 (2010).
59. Choi, S. B., Kyoung, J. S., Kim, H. S., Park, H. R., Park, D. J., Kim, B.-J., Ahn, Y. H., Rotermund, F., Kim, H.-T., Ahn, K. J. and Kim, D. S. Nanopattern enabled terahertz all-optical switching on vanadium dioxide thin film. *Applied Physics Letters* **98**, 071105–071103, doi:10.1063/1.3553504 (2011).
60. Jeong, Y.-G., Bernien, H., Kyoung, J. S., Park, H. R., Kim, H. S., Choi, J. W., Kim, B. J., Kim, H. T., Ahn, K. J. and Kim, D. S. Electrical control of terahertz nano antennas on VO₂ thin film. *Optics Express* **19**, 21211–21215 (2011).
61. Park, H.-R., Bahk, Y. M., Ahn, K. J., Park, Q. H., Kim, D. S., Martín-Moreno, L., García-Vidal, F. J. and Bravo-Abad, J. Controlling terahertz radiation with nanoscale metal barriers embedded in nano slot antennas. *ACS Nano* **5**, 8340–8345, doi:10.1021/nn2031885 (2011).
62. Kyoung, J. S., Seo, M. A., Park, H. R., Ahn, K. J. and Kim, D. S. Far field detection of terahertz near field enhancement of sub-wavelength slits using Kirchhoff integral formalism. *Optics Communications* **283**, 4907–4910, doi: 10.1016/j.optcom.2010.08.008 (2010).
63. Seo, M. A., Park, H. R., Koo, S. M., Park, D. J., Kang, J. H., Suwal, O. K., Choi, S. S., Planken, P. C. M., Park, G. S., Park, N. K., Park, Q. H. and Kim, D. S. Terahertz field enhancement by a metallic nano slit operating beyond the skin-depth limit. *Nat Photon* **3**, 152–156 (2009).
64. Park, H. R., Koo, S. M., Suwal, O. K., Park, Y. M., Kyoung, J. S., Seo, M. A., Choi, S. S., Park, N. K., Kim, D. S. and Ahn, K. J. Resonance behavior of single ultra-thin slot antennas on finite dielectric substrates in terahertz regime. *Applied Physics Letters* **96**, 211109–211103, doi:10.1063/1.3437091 (2010).

5

Field effect transistors for terahertz applications

W. KNAP and M. I. DYAKONOV,
Laboratoire Charles Coulomb, Université
Montpellier 2 and CNRS, France

DOI: 10.1533/9780857096494.1.121

Abstract: This chapter gives an overview of the main physical ideas and experimental results concerning the application of field effect transistors (FETs) for the generation and detection of terahertz (THz) radiation. Resonant frequencies of the two-dimensional plasma oscillations in FETs increase with the reduction of the channel dimensions and for submicron gate length reach the THz range. When the mobility is high enough, the dynamics of a short channel FET at THz frequencies is dominated by plasma waves. This may result, on the one hand, in a direct current (dc) induced spontaneous generation of plasma waves and THz emission and, on the other hand, in a resonant photoresponse to incoming radiation. In other cases, when plasma oscillations are overdamped, the FET can operate as an efficient broadband THz detector.

Key words: semiconductors, field effect transistors, terahertz radiation, plasma waves, low-dimensional systems.

5.1 Introduction

The channel of a field effect transistor (FET) can act as a resonator for plasma waves with a typical wave velocity $s \sim 10^8$ cm/s. The fundamental frequency f of this resonator depends on its dimensions and, for gate length L of a micron or less, can reach the terahertz (THz) range, since $f \sim s/L$. The interest in using FETs for THz applications was initiated at the beginning of 1990s by the theoretical work of Dyakonov and Shur¹ who predicted that a steady current flow in an asymmetric FET channel can lead to instability against the spontaneous generation of plasma waves. This can in turn produce the emission of electromagnetic radiation at the plasma wave frequency. Later, it was shown² that the nonlinear properties of the 2D plasma in the transistor channel can also be used for detection and mixing of THz radiation. The detection may be efficient not only in the resonant case of high electron mobility, when plasma oscillation modes are excited in the channel, but also in the non-resonant case of low mobility, where plasma oscillations are overdamped (non-existent).

Both THz emission^{3–6} and detection, resonant^{7–9} and non-resonant,^{10–11} were observed experimentally at cryogenic as well as at room temperatures, clearly demonstrating effects related to the excitation of plasma waves. Currently, the most promising application appears to be the broadband THz detection and imaging in the non-resonant regime. However, resonant THz emission and detection by excitation of plasma waves are also interesting phenomena that deserve further exploration.

5.2 Plasma waves in low-dimensional structures

Plasma waves are oscillations of the electron density. Generally, they can be obtained from the continuity equation:

$$\frac{\partial \rho}{\partial t} + \operatorname{div} \mathbf{j} = 0, \quad [5.1]$$

where ρ is the charge density and \mathbf{j} is the current density, related to the local electric field \mathbf{E} by Ohm's law

$$\mathbf{j} = \sigma \mathbf{E}, \quad [5.2]$$

where σ is the conductivity. These equations must be complemented by the relation between the electric field and the charge density. Bold symbols denote vector quantities. In three dimensions, this relation is simply $\operatorname{div} \mathbf{E} = 4\pi\rho/\epsilon$, where ϵ is the background dielectric constant (we use Gaussian units throughout). In two-dimensional (2D) and one-dimensional (1D) structures, while this equation obviously remains true, it does not help because the field entering Equation [5.2] is *not* the total electric field, but rather its component that drives the current, for example, for a 2D electron it is the electric field component that lies in the 2D plane. (The $\operatorname{div} \mathbf{j}$ term in Equation [5.1] should be also understood as divergence in two dimensions.)

It should be taken into account that plasma waves exist in the high frequency limit $\omega\tau > 1$, where ω is the frequency and τ is the damping time for plasma waves, normally equal to the momentum relaxation time. Accordingly, if damping is completely ignored, we should use the high frequency limit for the complex conductivity: $\sigma(\omega) = ine^2/m\omega$, where n is the electron concentration, and e and m are the electron charge and effective mass, respectively. This formula can be derived by writing the Drude equation for the mean electron velocity as $\partial \mathbf{v}/\partial t = e\mathbf{E}/m$ and neglecting the 'friction' term \mathbf{v}/τ . Equivalently, one can use the following equation for the current density $\mathbf{j} = env$:

$$\frac{\partial \mathbf{j}}{\partial t} = \frac{ne^2}{m} \mathbf{E}. \quad [5.3]$$

Combining Equations [5.1] and [5.3], we obtain

$$\frac{\partial^2 \rho}{\partial t^2} + \frac{ne^2}{m} \operatorname{div} \mathbf{E} = 0. \quad [5.4]$$

The electric field \mathbf{E} should be expressed through the charge density ρ , and this is where the difference lies between the three-dimensional (3D) case and various low-dimensional structures (gated or ungated 2D electrons, wires, etc.).

5.2.1 Bulk plasma waves

For this case we have simply $\operatorname{div} \mathbf{E} = 4\pi\rho/\epsilon$, and Equation [5.4] describes a harmonic oscillator with a resonant frequency

$$\omega_p = \sqrt{\frac{4\pi ne^2}{m\epsilon}}, \quad [5.5]$$

which is the famous formula for the plasma frequency in three dimensions (Langmuir waves).

5.2.2 Two-dimensional (2D) electron gas

We must express the electric field in the plane through the 2D charge density. This relation is given by an integral describing the Coulomb law. It may be significantly simplified if one introduces the Fourier transforms for the charge density and the electric field, ρ_k and \mathbf{E}_k . Then it can be found that $\mathbf{E}_k = -2\pi i k \rho_k / \epsilon k$, $(\operatorname{div} \mathbf{E})_k = 2\pi k \rho_k / \epsilon$, and the Fourier transformed Equation [5.5] becomes:

$$\frac{\partial^2 \rho_k}{\partial t^2} + \frac{2\pi n e^2 k}{m\epsilon} \rho_k = 0. \quad [5.6]$$

Thus for a given wave-vector k the plasma wave frequency is given by the square root law:

$$\omega(k) = \sqrt{\frac{2\pi n e^2 k}{m\epsilon}}, \quad [5.7]$$

where now n is the 2D electron concentration. Interestingly, a similar dispersion law $\omega \sim k^{1/2}$ describes surface waves in deep water (when the depth is much greater than the wavelength).

5.2.3 Gated 2D electron gas

This is the case of an FET, which is the main object of our interest here. The relation between the charge density and the electric field in the channel is readily obtained from the plane capacitor formula:

$$\rho = en = CU, \quad [5.8]$$

where C is the gate-to-channel capacitance per unit area, and U is the so-called gate voltage swing: $U = V_g - V_{th}$ (V_g is the gate voltage and V_{th} is the threshold voltage, at which the channel becomes completely depleted). From Equation [5.8] we obtain:

$$\mathbf{E} = -\nabla U = -\frac{1}{C}\nabla\rho. \quad [5.9]$$

Note, that in contrast to the 3D case, where $\partial E_x / \partial x \sim \rho$, for gated 2D electrons we have $E_x \sim \partial \rho / \partial x$! It is important to understand that Equations [5.8] and [5.9] hold not only when U is a constant, but also when the scale of the spatial variation of U is large compared to the gate-to-channel separation (the gradual channel approximation). Equation [5.4] now gives a linear dispersion relation for plasma waves:

$$\omega(k) = sk. \quad [5.10]$$

The plasma wave velocity s is given by

$$s = \sqrt{\frac{ne^2}{mC}} = \sqrt{\frac{eU_0}{m}}, \quad [5.11]$$

where U_0 is the direct current (dc) part of the gate voltage swing related to the electron concentration n by Equation [5.8]. The fundamental frequency of the resonator formed by the FET channel with gate length L is given by $f = \omega/2\pi \sim s/L$ (up to a numerical factor depending on the boundary conditions).

It was shown in Reference 1 that the nonlinear hydrodynamic equations describing the electrons in the channel of an FET are exactly the same as the shallow water equations in conventional hydrodynamics (the term ‘shallow water’ refers to a situation when the wavelength or, more generally the spatial scale of variation of the water level is much greater than the depth h). The only modification is that for the case of an FET one should replace gh (g is the free-fall acceleration) by eU/m . Thus plasma waves in the FET channel are analogous to shallow water waves, whose velocity is $(gh)^{1/2}$ (compare with Equation [5.11]).

It should be recalled that the considerations in this subsection are based on Equation [5.8], which is valid when the wavelength is much greater than the gate-to-channel separation d , or $kd \ll 1$. In the opposite case of short wavelengths ($kd \gg 1$) the existence of the gate is of no importance, and plasma waves are described by Equation [5.7], similar to the ‘deep water’ case.

Historically, plasma waves in two-dimensional structures were considered theoretically in References 12–15, the first experimental observations were reported in References 16 and 17. The general formula describing plasma waves in a gated 2D electron gas for arbitrary values of the parameter kd was obtained by Nakayama.¹⁴ In the limiting cases $kd \gg 1$ and $kd \ll 1$ this formula reduces to Equation [5.7] and Equation [5.10], respectively.

5.2.4 Plasma waves in wires

The dispersion law for plasma waves in this case is very similar to that of the previous case. The Fourier transforms of the electrostatic potential ϕ and the *linear* charge density ρ are related by:

$$\varphi_k = \left(\frac{\rho_k}{\varepsilon} \right) \ln \left(\frac{1}{kr} \right). \quad [5.12]$$

The wavelength is assumed to be large compared to the wire radius r ($kr \ll 1$). Using this relation, and calculating $(\text{div } \mathbf{E})_k$ as above, one easily obtains from Equation [5.4] a nearly linear dispersion law:

$$\omega(k) = sk \ln(1/kr), \quad s = \sqrt{\frac{ne^2}{m\varepsilon}}, \quad [5.13]$$

where for this case n is the 1D concentration and ε is the dielectric constant of the surrounding medium.

5.3 Instability of the steady state with a dc current in field effect transistors (FETs)

This instability was predicted in Reference 1. The conditions for instability are:

- (a) The plasma wave damping is small, $\omega\tau > 1$, where ω is the plasma oscillation frequency on the order of s/L , L is the channel length and τ is the momentum relaxation time defining the electron mobility.

- (b) The boundary conditions at the source and the drain are asymmetric. An extreme case of such asymmetry, considered in Reference 1, consists in the open circuit condition at the source and the short circuit condition at the drain.
- (c) The steady state electron drift velocity v must exceed a threshold value depending on the damping time τ . For $\omega\tau \gg 1$, the threshold value of the drift velocity is *much smaller* than the plasma wave velocity s .

The physical origin of this instability is related to the difference in velocities of plasma waves propagating upstream ($s - v$) and downstream ($s + v$). Because of this difference, the reflection coefficients at the boundaries may be *greater than 1*. It can be shown that for the boundary conditions mentioned above the net amplification due to plasma wave reflections during a round trip is equal to $(s + v)/(s - v)$. The time t_0 needed to make a round trip is obviously

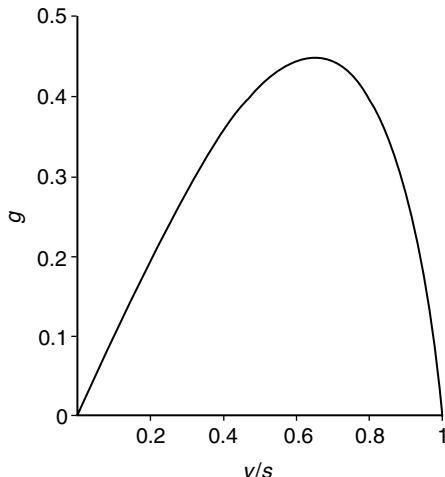
$$t_0 = \frac{L}{s - v} + \frac{L}{s + v}. \quad [5.14]$$

For $t \gg t_0$ the number of round trips can be estimated as t/t_0 , and the total increase of the plasma wave amplitude during time t can be written as $[(s + v)/(s - v)]^{t/t_0}$. We can now rewrite this expression as $\exp(\gamma t)$, where the instability increment γ is given by the formula:

$$\gamma = \frac{s}{2L} \left(1 - \frac{v^2}{s^2} \right) \ln \left(\frac{s + v}{s - v} \right). \quad [5.15]$$

This is the result obtained in Reference 1 by the standard method of studying what happens to small perturbations of the steady state with a given drift velocity v . The dependence of the increment γ on the ratio v/s is presented in Fig. 5.1. For low drift velocities, $v \ll s$, Equation [5.15] reduces to $\gamma = v/L$. In the absence of damping, the steady state is unstable for arbitrarily small values of the drift velocity v ; however, if damping is taken into account, the instability occurs when $\gamma > 1/\tau$ and this condition defines the threshold value of the drift velocity. If τ is small enough, the steady state is stable.

The instability of the current-carrying steady state results in the generation of plasma waves at the resonator modes. Essentially, the device operates like a laser, with an interesting difference: contrary to what happens in a laser, the gain is due to amplification *during reflections* from the ‘mirrors’, while the losses occur during the propagation of the plasma wave between the mirrors.



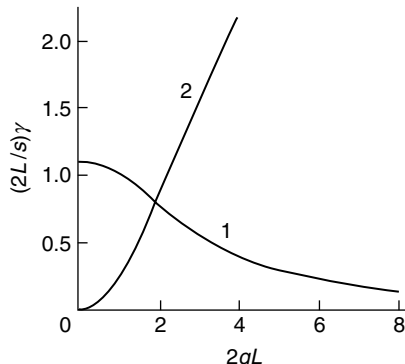
5.1 The dimensionless instability increment $g = \gamma L / s$ as a function of v/s , Equation [5.15].

The instability results in strong stationary nonlinear plasma oscillations in the channel. This was demonstrated in Reference 18 by a numerical solution of the non-linearized ‘shallow water’ equations. It was also shown that a similar instability may exist in an ungated 2D electron gas.¹⁹

5.3.1 Oblique modes and edge emission

The experimental results regarding THz emission from FETs in References 3–6 and other works cannot be directly compared with the theory¹ because the experimental geometry is very different from the 1D model adopted in Reference 1. In the standard experimental situation, the width W of the gate is much greater than the gate length L – typically W/L varies from 10 to 100. Under such conditions the 1D model, where the plasma density and velocity depend on the coordinate x only, is not appropriate, since *oblique plasma waves* with a non-zero component, q , of the wave vector in the y direction can propagate. In such geometry, the gated region is not a resonator, but rather a waveguide with a continuous spectrum of plasma waves. The spectrum of the plasma modes is given by the formula $\omega_n(q) = [\omega_{0n}^2 + (sq)^2]^{1/2}$, where n is the mode number and ω_{0n} is the mode frequency for the 1D problem ($q = 0$).

In Reference 20, the analysis of stability was extended to the more realistic case when $W \gg L$, and it was shown that, somewhat unexpectedly, in such a geometry an additional new mode of instability dominates, which is



5.2 Calculated instability increments (1) for the normal fundamental mode and (2) for the boundary mode as function of the transverse wave-vector q , for $v/s = 0.5$.²⁰ The mode localized at the boundaries becomes more unstable.

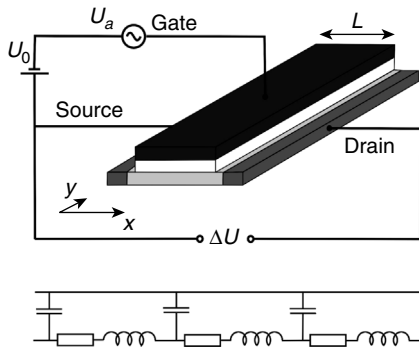
localized near the gate boundaries. A similar instability should exist near a single boundary of current-carrying 2D plasma.

Figure 5.2 shows the calculated increments γ for different modes and $v/s = 0.5$ as a function of the transverse wave-vector q . It can be seen that for large enough values of q the new boundary mode becomes more unstable, which means that it should dominate.

Certainly, the linear theory cannot predict the outcome of this instability. However, since the spectrum of plasma waves is continuous, it seems likely that the instability will result in a turbulent motion of the electron fluid near the boundary of the gated region. The spectrum of the plasma oscillations should be broad, as is observed in experiments. This is similar to that which one can see in a river, when the water flows with sufficient velocity across an abrupt step in the waterbed: waves with wave vectors perpendicular to the flow are excited, while the wave vectors in the direction of the flow are purely imaginary, which accounts for the localization of the turbulent region near the step. It would be interesting to verify these predictions experimentally.

5.4 Detection of terahertz radiation by an FET

The idea of using an FET for detection of THz radiation was put forward in Reference 2. The possibility of the detection is due to nonlinear properties of the transistor, which lead to the rectification of an alternating current (ac) induced by the incoming radiation. As a result, a photoresponse appears in the form of dc voltage between source and drain which is proportional to the radiation power (photovoltaic effect).



5.3 Schematics of an FET as a THz detector (above) and the equivalent circuit (below).

Obviously, some asymmetry between the source and drain is needed to induce such a voltage. There may be various reasons for such asymmetry. One of them is the difference in the source and drain boundary conditions due to external (parasitic) capacitances. Another one is the asymmetry in feeding the incoming radiation, which can be achieved either by using a special antenna, or by an asymmetric design of the source and drain contact pads. Thus the radiation may predominantly create an ac voltage between the source and the gate. Finally, the asymmetry can naturally arise if a dc current is passed between source and drain, creating a depletion of the electron density on the drain side of the channel.

Theoretically, we will consider the case of an extreme asymmetry, where the incoming radiation creates an ac voltage with amplitude U_a only between the source and the gate, see Fig. 5.3. We will also assume that there is no dc current between the source and drain. The influence of such a current was studied in References 21 and 22.

Generally, the FET may be described by an equivalent circuit presented in Fig. 5.3. The obvious elements are the distributed gate-to-channel capacitance and the channel resistance, which depends on the gate voltage through the electron concentration in the channel, according to Equation [5.8].

As mentioned above, this equation is valid locally, so long as the scale of the spatial variation of $U(x)$ is greater than the gate-to-channel separation d (the gradual channel approximation). Under static conditions and in the absence of the drain current, $U = U_0 = V_g - V_{th}$, where U_0 is the static voltage swing. The inductances in Fig. 5.3 represent the so-called *kinetic* inductances, which are due to the electron inertia and are proportional to m , the electron effective mass. Depending on the frequency ω , one can distinguish two regimes of operation, and each of them can be further divided into two sub-regimes depending on the gate length L .¹¹

5.4.1 High frequency regime

The high frequency regime occurs when $\omega\tau > 1$, where τ is the electron momentum relaxation time, determining the conductivity in the channel $\sigma = ne^2\tau/m$. In this case, the kinetic inductances in Fig. 5.3 are of primordial importance, and the plasma waves, analogous to the waves in a resistance, inductance, capacitance (RLC) transmission line like in Fig. 5.3, will be excited. The plasma waves have a velocity $s = (eU_0/m)^{1/2}$ and a damping time τ . Thus their propagation distance is $s\tau$.

Regime 1a. Short gate, $L < s\tau$

The plasma wave reaches the drain side of the channel, is reflected, and forms a standing wave with enhanced amplitude, so that the channel serves as a high quality resonator for plasma oscillations. The fundamental mode has the frequency $\sim s/L$, with a numerical coefficient depending on the boundary conditions.

Regime 1b. Long gate, $L \gg s\tau$

The plasma waves excited at the source will decay before reaching the drain, so that the ac current will exist only in a small part of the channel adjacent to the source.

5.4.2 Low frequency regime

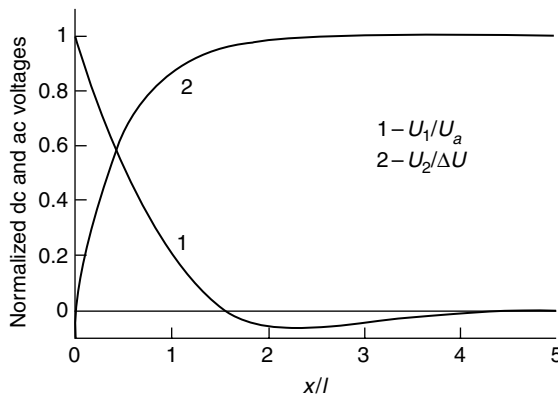
Low frequency regime, $\omega\tau \ll 1$. Now, the plasma waves cannot exist because of overdamping. At these low frequencies, the inductances in Fig. 5.1 become short-circuited which leads to an RC line. Its properties further depend on the gate length, the relevant parameter being $\omega\tau_{RC}$, where τ_{RC} is the RC time constant of the whole transistor. Since the total channel resistance is $L\rho/W$, and the total capacitance is CWL (where W is the gate width and $\rho = 1/\sigma$ is the channel resistivity), one finds $\tau_{RC} = L^2\rho C$.

Regime 2a. Short gate, $L < (\rho C\omega)^{-1/2}$

Short gate, $L < (\rho C\omega)^{-1/2}$, means that $\omega\tau_{RC} < 1$, so that the ac current goes through the gate-to-channel capacitance practically uniformly across the whole length of the gate. This is the so-called ‘resistive mixer’ regime.²³ For the THz frequencies this regime can apply only for transistors with extremely short gates.

Regime 2b. Long gate, $L \gg (\rho C\omega)^{-1/2}$

Now $\omega\tau_{RC} \gg 1$, and the induced ac current will leak to the gate at a small distance l from the source, such that the resistance $R(l)$ and the capacitance



5.4 Dependence of the ac voltage U_1/U_a at $\omega t = 2\pi n$ and of the dc photo-induced voltage $U_2/\Delta U$ on the distance from the source x for a long gate.

$C(l)$ of this piece of the transistor channel satisfy the condition $\omega\tau_{RC}(l) = 1$, where $\tau_{RC}(l) = R(l)C(l) = l\rho C$. This condition gives the value of the ‘leakage length’ l on the order of $(\rho C\omega)^{-1/2}$ (which can also be rewritten as $s(\tau/\omega)^{1/2}$). If $l \ll L$, then neither ac voltage nor ac current will exist in the channel at distances beyond l from the source, see Fig. 5.4.

More detailed analysis of different detection regimes can be found in the review paper.¹¹

5.4.3 Characteristic length

The characteristic length across which the ac exists is $l = s\tau$ for the high-frequency regime ($\omega\tau > 1$), and $l = s(\tau/\omega)^{1/2}$ for the low-frequency regime ($\omega\tau < 1$).² Let us now make some estimations of the characteristic length for the different cases presented above. For $\tau = 30$ fs ($\mu = 300$ cm²/(Vs) in Si MOSFET) and $s = 10^8$ cm/s, regime 1 will be achieved for radiation frequencies f greater than 5 THz; the regime 1a corresponds to $l < 30$ nm. For $f = 0.5$ THz (regime 2), one finds the characteristic gate length distinguishing regimes 2a and 2b to be around 100 nm. If the conditions of the case 1a are satisfied, the photoresponse will be resonant, corresponding to the excitation of discrete plasma oscillation modes in the channel. In all the other cases (regimes 1b, 2a, 2b), the FET will operate as a broadband detector.

For a long gate, there is no qualitative difference between the low frequency regime ($\omega\tau \ll 1$), when plasma waves do not exist (the case 2b) and the high frequency regime ($\omega\tau \gg 1$), where plasma oscillations are excited (regime 1b). There are, however, some quantitative differences, see Equation [5.16]. The excitation of plasma waves in the high frequency for the case of

a long gate (1b) has been clearly confirmed by the recent detection experiments in magnetic field.²¹

In magnetic field the dispersion law for plasma waves reads: $\omega = [\omega_c^2 + (sk)^2]^{1/2}$, where ω_c is the cyclotron frequency (for $\omega_c = 0$, this reduces to Equation [5.10]). Thus plasma waves cannot propagate below the cyclotron frequency, since $\omega < \omega_c$ is possible only for imaginary values of the wave vector k . Therefore, in experiments with a fixed radiation frequency, the photoresponse is strongly reduced when the magnetic field increases above the cyclotron resonance.²⁵ This is probably the most striking manifestation of the importance of plasma waves in THz detection by FETs and will be presented in more detail in Section 5.6.

Another interesting feature appearing in magnetic fields at low temperatures is related to Shubnikov-de Haas oscillations of the mobility. This provides an additional mechanism for the nonlinearity producing the photoresponse.

5.4.4 Mechanism of the nonlinearity

The most important mechanism is the modulation of the electron concentration in the channel, and hence of the channel resistance, by the local ac gate-to-channel voltage, as described by Equation [5.8]. Because of this, in the expression for the electric current $j = env$, both the concentration n and the drift velocity v will be modulated at the radiation frequency. As a result, a dc current will appear: $j_{dc} = e\langle n_1(t)v_1(t)\rangle$, where $n_1(t)$ and $v_1(t)$ are the modulated components of n and v , and the angular brackets denote averaging over the oscillation period $2\pi/\omega$. Under open circuit conditions a compensating dc electric field will arise, resulting in the photo-induced source-drain voltage ΔU .

5.4.5 Simplified theory

So far, the most relevant case is that of a long gate (the regimes 1b and 2b) when, independently of the value of the parameter $\omega\tau$, the ac current excited by the incoming radiation at the source cannot reach the drain side of the channel. For this case within the hydrodynamic approach, the following result for the photo-induced voltage has been derived:²

$$\Delta U = \frac{U_a^2}{4U_0} \left(1 + \frac{2\omega\tau}{\sqrt{1+(\omega\tau)^2}} \right). \quad [5.16]$$

As can be seen from this formula, the photoresponse changes by only a factor of 3 as the parameter $\omega\tau$ increases from low to high values, despite

the significant change of the underlying physics (for $\omega\tau > 1$ plasma waves are excited, while for $\omega\tau < 1$ they are not).

For the latter case (2b), the basic equations may be written as:^{1,2}

$$\frac{\partial U}{\partial t} + \frac{\partial}{\partial x}(Uv) = 0, \quad [5.17]$$

$$\frac{\partial v}{\partial t} = -\frac{e}{m} \frac{\partial U}{\partial x} - \frac{v}{\tau}. \quad [5.18]$$

Here Equation [5.17] is the continuity equation, in which the concentration n is replaced by U using Equation [5.8], while Equation [5.18] is the Drude equation for the drift velocity v . (Within the hydrodynamic approach,¹ the lhs of Equation [5.18] contains an additional ‘convective’ nonlinear term $v(\partial v/\partial x)$. The hydrodynamic approach is valid when the collisions between electrons are more frequent than collisions with impurities and phonons.) The boundary condition for gate-to-channel voltage at the source side of the channel ($x = 0$) is: $U(0,t) = U_0 + U_a \cos(\omega t)$. For a long gate, the boundary condition at the drain is $v(\infty) = 0$. The inertial term $\partial v/\partial t$ is accounted for by the kinetic inductances in Fig. 5.2. Here, we will consider only the simple case $\omega\tau < 1$, when the inertial term can be neglected. Then $v = -\mu \partial U / \partial x$, and

$$\frac{\partial U}{\partial t} = \mu \frac{\partial}{\partial x} \left(U \frac{\partial U}{\partial x} \right), \quad [5.19]$$

where $\mu = e\tau/m$ is the electron mobility. We search for the solution of the nonlinear Equation [5.19] as an expansion in powers of U_a : $U = U_0 + U_1 + U_2$. Here, U_1 is the ac voltage, proportional to U_a , and U_2 is the time-independent contribution proportional to U_a^2 (the photovoltage). In the first order in U_a we obtain the diffusion equation for U_1 :²⁶

$$\frac{\partial U_1}{\partial t} = s^2 \tau \frac{\partial^2 U_1}{\partial x^2}, \quad [5.20]$$

with the boundary conditions $U_1(0,t) = U_a \cos(\omega t)$, $U_1(\infty,t) = 0$. The solution of this equation is

$$U_1(x,t) = U_a \exp(-x/l) \cos(\omega t - x/l), \quad [5.21]$$

where the characteristic length l for the decay of the ac voltage (and current) away from the source is given by:

$$l = s \left(\frac{2\tau}{\omega} \right)^{1/2}. \quad [5.22]$$

This length defines the size of the part of the transistor adjacent to the source, whose resistance and the capacitance are such that $\omega\tau_{RC}(l) \sim 1$, as explained above.

In the second order in U_a , Equation [5.5] yields:

$$U_0 \frac{\partial U_2}{\partial x} + \left\langle U_1 \frac{\partial U_1}{\partial x} \right\rangle = 0, \quad [5.23]$$

which indicates simply the absence of the dc current. Integrating this equation, one obtains:

$$U_2(x) = \frac{1}{2U_0} \left[\langle U_1^2(0,t) \rangle - \langle U_1^2(x,t) \rangle \right] = \frac{U_a^2}{4U_0} \left[1 - \exp\left(\frac{-2x}{l}\right) \right], \quad [5.24]$$

where the time averaged quantity $\langle U_1^2(x,t) \rangle = (1/2)U_a^2 \exp(-2x/l)$ is found from Equation [5.21]. Thus the photovoltage $\Delta U = U_2(\infty)$ coincides with Equation [5.16], provided that $\omega\tau \ll 1$. Figure 5.4 shows the ac voltage U_1 and the build-up of the dc voltage U_2 as functions of the distance from the source.

The maximal photovoltage is achieved at $U_0 \approx 0$, where the relative ac modulation of the electron concentration in the channel is the strongest (note that Equation [5.8] is not valid in the near vicinity of $U_0 = 0$!). A theoretical study of the photoresponse in this region is presented in Reference 27.

5.4.6 Phenomenological approach

For low frequency and long gate (case 2b) a phenomenological approach was recently developed^{28,29} that relates the expected detector signal with the channel conductivity $\sigma(U)$. The resulting simple formula reads:

$$\Delta U = \frac{U_a^2}{4} \left[\frac{1}{\sigma} \frac{d\sigma}{dU} \right]_{U=U_0}. \quad [5.25]$$

In the simplest case considered above, when $n \sim U$ and the mobility μ is constant, this formula gives the same result as Equation [5.24] for $x \gg l$.

However, Equation [5.25] is more general: it takes into account the possible dependence of the mobility on gate voltage, and it remains valid even for $U_0 < 0$. This approach allows calculating the expected photoresponse by a simple differentiation of the transfer characteristic. This formula also describes the observed contribution of Shubnikov-de Haas oscillations of the mobility to the photoresponse: these oscillations depend on the Fermi energy, and hence on electron concentration, which is governed by the gate voltage. The derivative in Equation [5.25] explains the observed 90° phase difference between the photoresponse oscillations and the resistance oscillations (see Section 5.6.13).

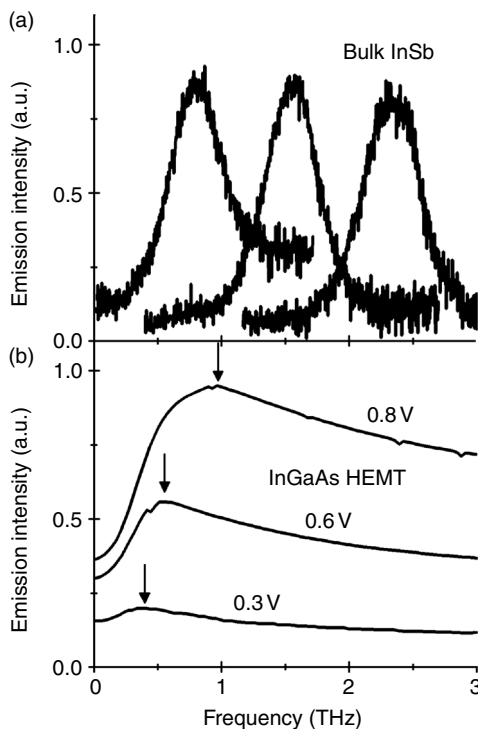
We will now describe the main results of the experimental studies stimulated by the theoretical predictions outlined in Sections 5.2–5.4. We will first describe the main experiments concerning THz emission (Section 5.5) and then we will concentrate on THz detection and imaging (Section 5.6).

5.5 Studies of terahertz emission from FETs

To measure a weak emission ($\ll 1$ nW) in the THz range, one needs a highly sensitive measurement system in which the background radiation and water vapour absorption can be avoided or compensated. Below we describe two such systems that were used in our experiments.

5.5.1 The cyclotron resonance spectrometer

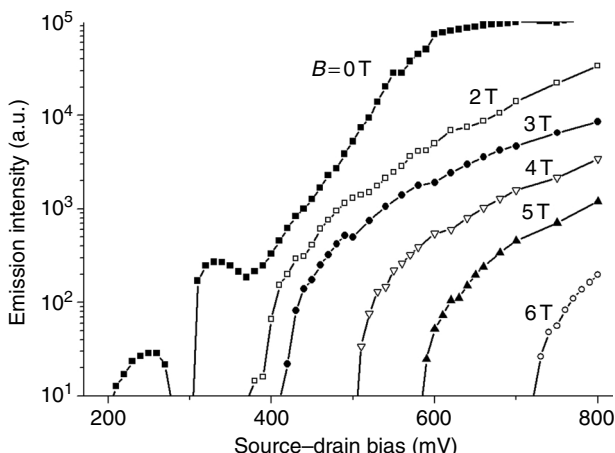
The cyclotron resonance spectrometer was originally conceived to investigate a weak THz cyclotron resonance emission from bulk semiconductors and their heterojunctions.^{30,31} It consisted of two superconducting coils mounted in the same helium cryostat. Two samples: a source of radiation and a detector were mounted in a copper waveguide and placed in the spectrometer at the centres of corresponding coils. In this way a high sensitivity was achieved because the system was immersed in the liquid helium and perfectly screened from the background radiation. The emitted radiation was analysed by a narrow band, magnetically tuneable InSb cyclotron detector calibrated with conventional bulk (GaAs or InSb) cyclotron resonance emitters. In Fig. 5.5a we show results of calibration experiments. The cyclotron radiation from bulk InSb emitter placed in magnetic field (0.4 T, 0.8 T and 1.2 T) was analysed by an InSb detector. The signal was registered as a function of the magnetic field in the detector coil. It showed maxima each time the cyclotron frequency of the detector corresponded to the frequency of emitted radiation: ~0.8 THz, 1.6 THz and 2.4 THz, respectively.



5.5 Spectra of a cyclotron resonance (a) InSb bulk emitter and (b) an InGaAs HEMT (high-electron mobility transistor) emitter. The curves in (a) correspond to different values of the emitter magnetic field: 0.4 T, 0.8 T and 1.2 T (from left to right). In (b) the emission spectra for InGaAs HEMT correspond to different source–drain voltages equal to 0.3 V, 0.6 V and 0.8 V.³

5.5.2 The Fourier-transform spectrometer

The Fourier-transform spectrometer operating under the vacuum was used in some cases (mainly for GaN-based devices) when the emission was strong enough to overcome the 300 K background. A fast scan and/or step scan operating spectrometer equipped with an ultra-sensitive Si-bolometer was used in the 0.3–10 THz range. The emission signal was excited by square-like voltage/current pulses with frequency of a few tens of Hz and a duty cycle from 0.1 to 0.5. The experimental procedure was as follows: first, the reference spectrum with the unbiased transistor inside the vacuum chamber (without any applied voltage) was measured in a fast scan mode, providing information about the 300 K emission background. Then the spectra were measured with a biased transistor. To analyse only the transistor emission,



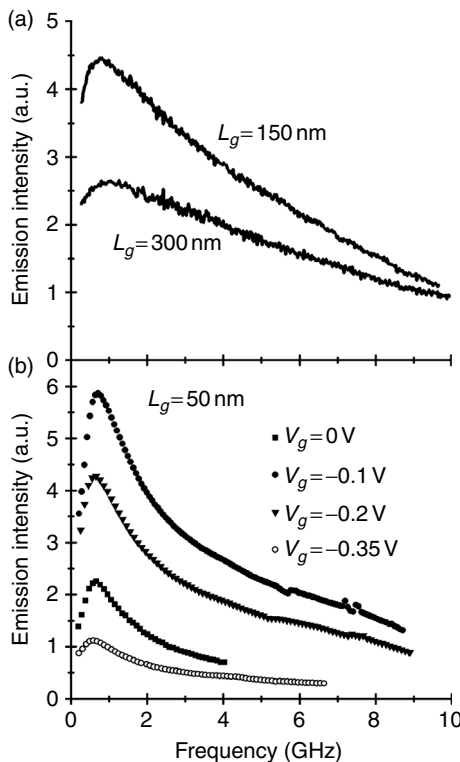
5.6 Emission intensity as a function of source–drain bias in a magnetic field from 0 to 6 T.⁴

the spectrometer was operating in the step scan mode and lock-in detection of the signal was synchronized to the voltage pulses. The final results were obtained by normalizing the spectra from the biased transistor by the reference spectrum.

5.5.3 Terahertz emission threshold

In one of the first emission experiments, lattice-matched nanometer gate lengths InGaAs/InP high-electron mobility transistors (HEMTs) were used. The gate length was 60 nm, and the drain–source separation was 1.3 μm . An InGaAs/InP HEMT was chosen for its high carrier mobility (resulting in high quality factor values). Typical results are shown in Fig. 5.5b. The emission spectrum was relatively broad but it displayed a maximum that shifted from ~ 0.4 THz to ~ 1.2 THz with increasing drain voltage. This emission appeared only above a certain threshold value of the drain voltage and sharply increased (by orders of magnitude) with increasing the bias.³ We used the second superconducting coil, at the transistor side, to change the conditions of the emission. The threshold voltage increased with applied magnetic field due to the increase of the channel resistance in a magnetic field.⁴

The threshold behaviour for different magnetic fields is shown in Fig. 5.6. It served as the main argument for interpreting the observed emission due to plasma wave instability.

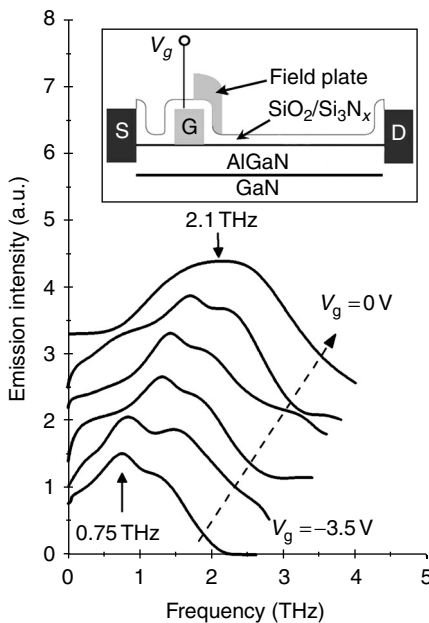


5.7 Spectra of emission from InGaAs HEMTs with (a) different gate lengths and (b) different gate voltages.

5.5.4 Edge emission

The experimental results obtained for GaInAs transistors have indeed demonstrated that THz emission appears when the drain current exceeds a certain threshold. Also, the radiation frequencies are in a reasonable agreement with estimates for fundamental plasma modes. However, some other features predicted in Reference 1, such as a strong dependence of the radiation frequency on the gate length and the gate bias, has not been observed. This is illustrated in Fig. 5.7 showing the emission spectra from an InGaAs HEMTs with gate lengths varying from 50 nm to 100 nm. One can see that emission occurs always in the same frequency range and does not noticeably depend on the gate length.

We believe that the edge instability²⁰ discussed in Section 5.3.1 can explain most of the observed broadband emission spectra which are not influenced by gate voltage and gate length.

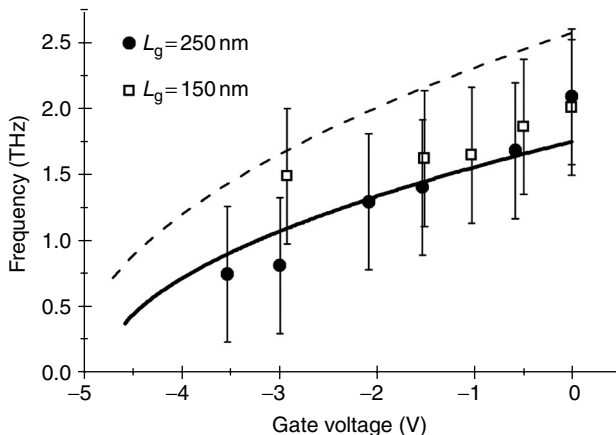


5.8 The emission spectra for a GaN/AlGaN transistor ($L = 250$ nm) at drain voltage 4 V and different gate voltages. Inset: schematic of AlGaN/GaN HEMT with a field plate covering the gate.⁶ (S – source, D – drain, G – gate.)

5.5.5 Tuneable emission

Only recently, THz emission tuneable by the gate bias has been observed in AlGaN/GaN-based HEMTs.⁶ It persisted from cryogenic up to room temperatures. The Fourier-transform spectrometer method described above was used. Unlike previous experiments, the emission peak was found to be tuneable by the gate voltage between 0.75 and 2.1 THz. The highest emission was obtained from transistors with a modified architecture which included the so-called field plate – an additional metal layer deposited between the gate and the drain terminals (see inset Fig. 5.8). The emission appeared in a threshold manner indicating plasma instability as its origin. Figure 5.8 presents the emission spectra for one of the samples and Fig. 5.9 shows the position of the maxima of the emission as a function of the gate voltage. The solid line shows the dependence of the fundamental frequency on the gate bias calculated according to the theory.^{1,32}

The THz emission results obtained using the field plate GaN/AlGaN HEMTs show three main features: (i) the emission appears at a certain drain bias in a threshold-like manner; (ii) the radiation frequency corresponds to the lowest fundamental plasma mode in the gated region of the transistor



5.9 Experimental data (points), and calculations (lines) of emission frequency as a function of gate bias for transistors with gate lengths 150 nm (upper dashed line) and 250 nm (lower continuous line).⁶

and (iii) the radiation frequency is tuned by the gate bias which modifies the velocity s of plasma waves. These features are inherent attributes of the Dyakonov–Shur plasma wave instability in a gated 2D electron gas, and their presence provides a convincing argument that we are observing this phenomenon.

5.5.6 Discussion

Summarizing the current experimental state of the art concerning plasma wave instabilities and THz emission from HEMTs, one can state that different types of instabilities with threshold-like behaviour of the emission intensity have been observed. Broadband gate length and gate voltage independent THz emission can be attributed to the edge instability.²⁰ The broadband edge emission often dominates.

Although the results on field plate HEMTs are very promising, much more experimental research is necessary to establish the architecture of the best gate-voltage-controlled THz emitters. The power levels currently registered are typically of the order of $\sim 0.1\text{ }\mu\text{W}$. This power is relatively small when compared with other existing sources. The real importance of FET based emitters comes from the fact that using modern electronics technology many of these elements could be easily integrated into matrices to make high power sources.

5.6 Experimental studies of terahertz detection by FETs

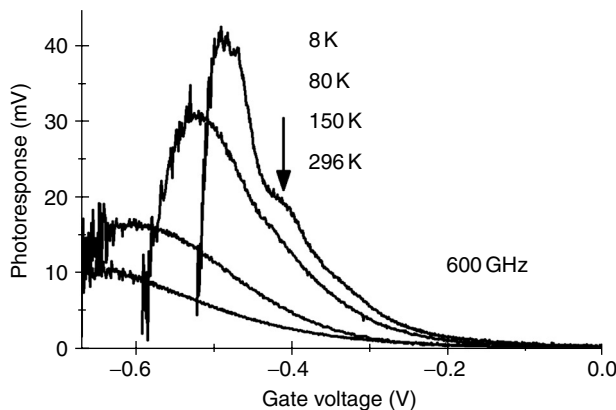
Below we describe *the* most significant experimental results on detection of sub-THz radiation by FETs.

5.6.1 The experimental set up

The experimental set up for detection experiments is usually designed using monochromatic sources. The radiation is generated either by an electronic source (e.g., a Gunn diode), a backward wave oscillator (BWO), or a CO₂-pumped molecular THz laser. THz radiation is guided using mirrors or light pipes and coupled to the FET by contact pads and bonding wires or specially designed antennas. The experiments with polarized radiation usually show a well-defined preferential orientation of the electric field of the incident radiation related to the geometry of the antennas (or that of the bonding wires playing the role of antennas).³³

Typical results of detection experiments are shown in Fig. 5.10.

A photovoltaic signal between source and drain is recorded as a function of the gate voltage, that is, versus the carrier density in the channel. For a high carrier density (open channel) the signal is relatively small. The signal increases and saturates when the gate voltage approaches the threshold and rapidly decreases in the sub-threshold region.²⁷



5.10 Photoresponse of the GaAs/AlGaAs 0.15 μm FET to 600 GHz radiation. The radiation-induced source-drain voltage is shown as a function of the gate voltage for different temperatures. The arrow marks feature corresponding to the resonant detection observed at the lowest temperature.²⁷

5.6.2 Modelling of the photoresponse

Modelling of the photoresponse by FETs uses the theoretical approach presented in Section 5.4.^{2,9} In the case of a non-resonant detection, the signal should increase with the decreasing carrier density, n , as $1/n$. However, as discussed in Section 5.4.5, this conclusion is valid only well above the threshold. As shown in Fig. 5.10, for voltages close to the threshold the signal saturates and decreases in the sub-threshold region. The main reasons behind this discrepancy are: (i) the assumption of a linear dependence of the carrier density on the gate voltage; (ii) neglecting the leakage currents; and (iii) neglecting loading effects. The linear dependence of the carrier density on the gate voltage is applicable to the open state of the transistor (i.e., well above the threshold) but is not valid in the sub-threshold region. The analytical expressions describing the signal versus gate voltage in the case of a realistic carrier density dependence were given in Reference 27. It was shown that in the case of an exponential carrier versus gate voltage dependence (which is a standard approximation below threshold), the photoresponse saturates at a constant value

$$\Delta U = \frac{U_a^2}{4U^*} \quad [5.26]$$

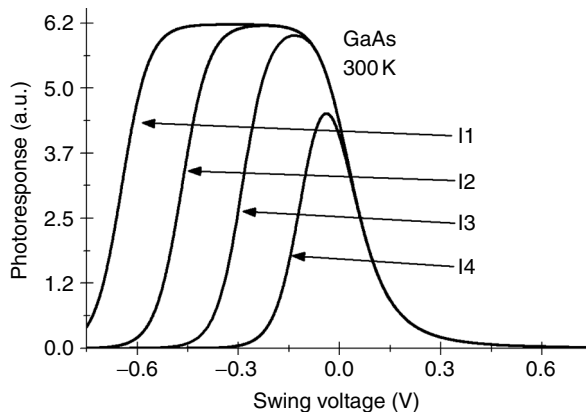
where U_a is the voltage induced between source and gate by incoming radiation and U^* is the voltage that defines the exponential decay of the carrier density in the sub-threshold range. This voltage can be written as $U^* = \eta kT/e$, where η is so-called ideality factor of the transistor.

5.6.3 The gate leakage current

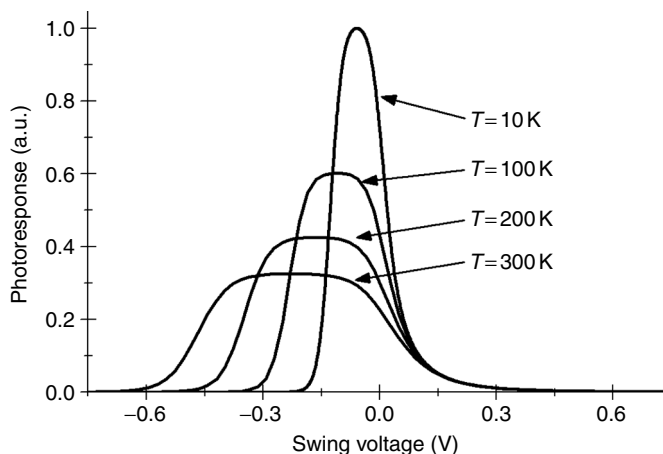
The gate leakage current was found to be one of the possible causes for the signal drop often observed close to the threshold. Results of calculations²⁷ for different values of leakage currents are shown in Fig. 5.11. One can see that for a low leakage current the signal increases and reaches the same saturation value. This value is given by Equation [5.26]. For higher leakage currents, the signal does not reach the saturation value and a well-defined maximum near the threshold voltage is seen. Figure 5.11 illustrates that an increase of the gate leakage current suppresses the detector performance resulting in a bell-shaped photoresponse.

5.6.4 Temperature dependence

Temperature dependence of the non-resonant signal was also calculated in Reference 27 and presented in Fig. 5.12.



5.11 Calculated room temperature photoresponse of the GaAs/AlGaAs FET at 600 GHz for different gate leakage currents I₁, I₂, I₃, I₄ corresponding to 10^{-10} A, 10^{-8} A, 10^{-6} A, 10^{-4} A, respectively.²⁷

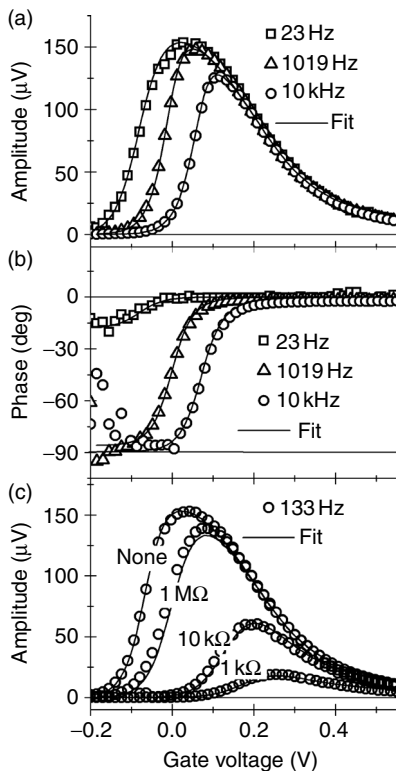


5.12 Calculated photoresponse of the GaAs/AlGaAs FET at 600 GHz at four different temperatures.²⁷

One can see that the temperature evolution of the calculated width and the amplitude of the photoresponse in Fig. 5.12 agree qualitatively with the experimental results in Fig. 5.10.

5.6.5 Loading effects

A full quantitative interpretation of the experimental results is not possible without taking into account the loading effects of the external circuit. They become important because of the exponential increase of the channel

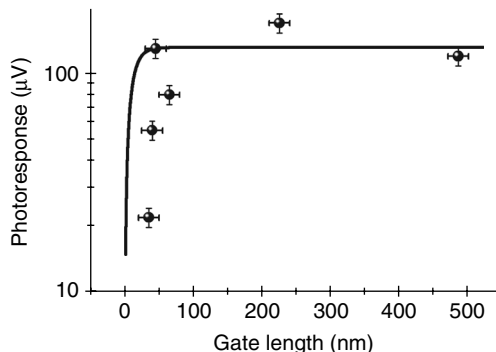


5.13 (a) Amplitude and (b) phase of the registered signal for different frequencies. The influence of the loading resistances on the amplitude of the signal is shown in panel (c).³⁴

resistance below threshold. Due to loading effects, the signal below threshold will decrease even in the absence of a leakage current.

The most complete approach to the quantitative interpretation of the experimental results was recently presented in Reference 34. It was shown that to reproduce the experimental results one should begin by calculating the maximum expected signal ΔU by differentiation of the transfer characteristics using Equation [5.25] – see Section 5.4.6. Then one has to divide ΔU by a factor $(1 + R_{\text{CH}}/Z)$, where R_{CH} is the channel resistance and Z is the complex load impedance of the read-out set-up. It is important that Z contains not only the load resistance of the preamplifiers but also all the parasitic capacitances. The inductance component can usually be ignored.

The experimental and theoretical results are compared in Fig. 5.13. The parasitic read-out circuit capacitances were determined by independent measurement with an RLC bridge and found to be ~ 150 pF. The measured



5.14 Photoresponse of Si-MOSFETs versus gate length.^{34,35}

amplitude and phase of the signal are presented for different load resistances and modulation frequencies.

One can see that by changing the modulation frequency or loading resistance we change the loading impedance and thus shift the height and position of the photoresponse maxima.

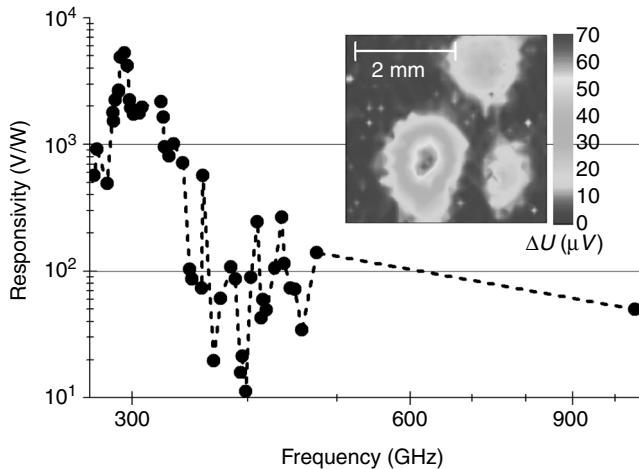
5.6.6 Choice of the optimal length

As in the case of silicon FETs, at room temperature, plasma waves are usually overdamped and incoming THz radiation leads only to a carrier density perturbation that decays exponentially with the distance with a characteristic length l that is typically of the order of a few tens of nanometers. Equation [5.24] allows one to determine the optimal length of the MOSFET gate. For gate lengths much shorter than the characteristic length l , one expects a decrease of the photoresponse. Figure 5.14 shows the photoresponse of FETs as a function of gate lengths. Black points are experimental values. The solid line in Fig. 5.14 was calculated using Equation [5.24] with $l = 100 \text{ nm}$. One can see that this simple theoretical estimate gives a relatively good description of the observed signal reduction.^{34,35}

For optimal detection, the gate length of the transistor should be chosen on the order of the leakage length l , so that the channel length is limited to the region which contributes to rectification.

5.6.7 THz detection by Silicon FETs

THz detection by Silicon FETs represents the most promising application of this technological domain. This is because Silicon MOSFETs offer the advantages of room temperature operation, together with easy on-chip integration with read-out electronics and high reproducibility. The first



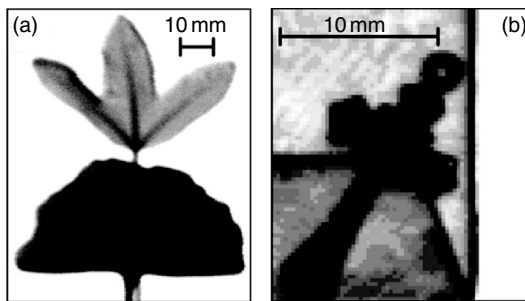
5.15 Responsivity as a function of frequency f for gate voltage 0.2 V. Filled circles: measured points, dashed line: guide for the eye. Inset: raster scan image of the source beam at 1.05 THz. ΔU is the photo-induced drain-source voltage.³⁸

demonstration of sub-THz and THz detection by CMOS FETs in silicon dates back to 2004.³⁶ Tauk *et al.* in 2006 have shown that CMOS FETs at room temperature can reach a noise equivalent power competitive with the best conventional room temperature THz detectors.³⁷ The first focal plane arrays in silicon technology have been designed for imaging at 300 GHz and 600 GHz by Schuster *et al.*^{38,39} and Öjefors *et al.*⁴⁰

Recently it has been demonstrated that by using an appropriate antenna and transistor design one can reach a record responsivity of up to ~ 5 kV/W and a noise equivalent power (NEP) below 10 pW/Hz $^{0.5}$ for detectors operating in the atmospheric window around 300 GHz, which is an important result for potential applications. The record responsivity and NEP were obtained; thanks to the careful design of the antenna. Also FET gate length was chosen to be close to the leakage length – see Equation [5.22]. Thus the channel was limited to the actively rectifying region, avoiding the series resistance of the passive part.

5.6.8 Room temperature imaging

Room temperature imaging with FETs was demonstrated in many works. However, until now, most of the results were obtained in the sub-THz range. There are only very few results on imaging with FETs at frequencies above 1 THz. This is because in the broadband detection regime, the photovoltaic signal decreases strongly with the increase of radiation frequency either



5.16 (a) Images of tree leaves at 300 GHz (a) and a metallic cross in the envelope at 1.6 THz (b) obtained in the transmission mode at room temperature.⁴¹

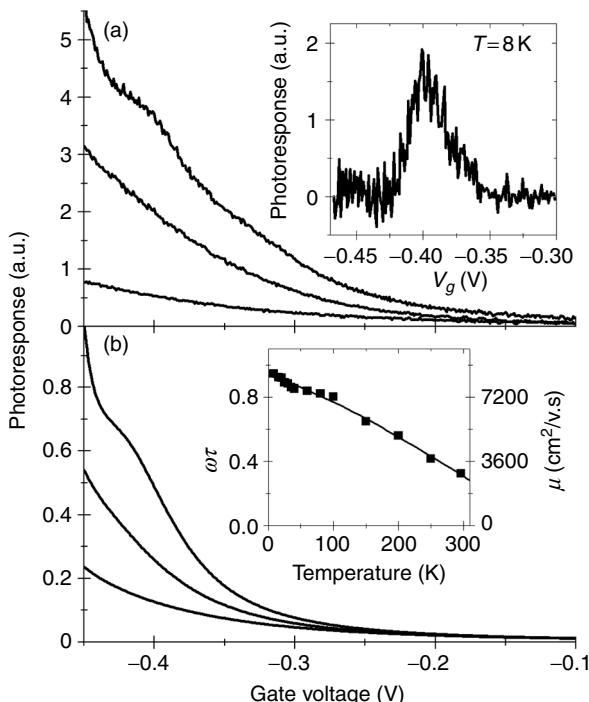
because of the reduction in coupling efficiency or because of water vapour absorption. In Fig. 5.16, images of leaves obtained with a 300 GHz source and silicon MOSFET (Fig. 5.16a) are compared with an image of a metallic object in the envelope obtained with CO₂ pumped far infrared laser (1.6 THz) and GaAs FET (Fig. 5.16b).

The images were recorded in a transmission mode by mechanical raster scanning the sample in X and Y directions. The good resolution, contrast, and an acquisition rate high enough for video-rate imaging systems were obtained. Generally, FETs are excellent candidates for fast room temperature THz imaging at sub-THz and THz frequencies.⁴¹

5.6.9 Resonant detection

When $\omega\tau > 1$ the condition for resonant detection is satisfied. In Fig. 5.17 one can clearly see that for the lowest temperature an additional peak appears. This is a signature of the resonant detection. As mentioned above, in a majority of experiments, the incoming radiation is a monochromatic beam and the source–drain voltage is recorded versus the gate voltage. The gate voltage controls the carrier density in the channel and tunes the resonant plasma frequency. A resonant enhancement of the registered voltage is observed once the resonant plasma frequency coincides with the frequency of the incoming THz radiation and the quality factor condition $Q = \omega\tau > 1$ is fulfilled. The resonance appears at low temperatures when the relaxation time becomes long enough (lower scattering rate). In Fig. 5.17 the results of experiments are compared with calculations according to the theory of Reference 2 (regime 1a discussed in Section 5.4.1).

The higher quality factor condition (Q from 2 to 4) can be obtained in high carrier mobility InGaAs transistors⁹ where well-defined resonances were measured. An example of resonant detection is shown in Fig. 5.18.

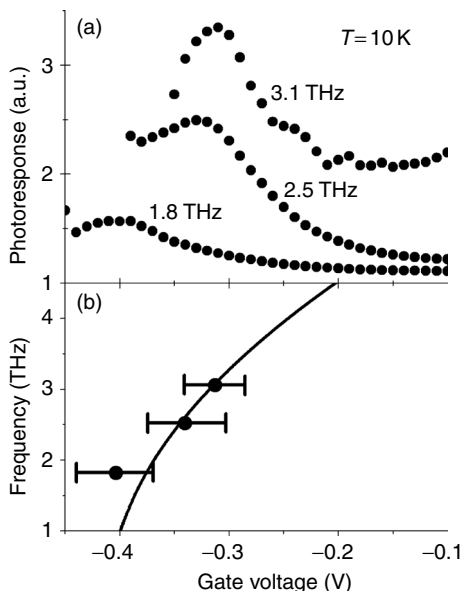


5.17 The photoresponse versus gate voltage: (a) experiment and (b) theory. The evolution of the photoresponse with temperature (300 K, 180 K, and 8 K, bottom to top). Inset in (a) shows the resonant signal after subtraction of the background. Inset in (b) shows the evolution of the carrier mobility and the corresponding quality factor at 600 GHz.⁹

In Fig. 5.18b, the position of the resonant maximum is shown. As the excitation frequency increases from 1.8 THz to 3.1 THz, the plasma resonance moves to higher swing voltages in an approximate agreement with theoretical predictions (solid line).

5.6.10 Broadening

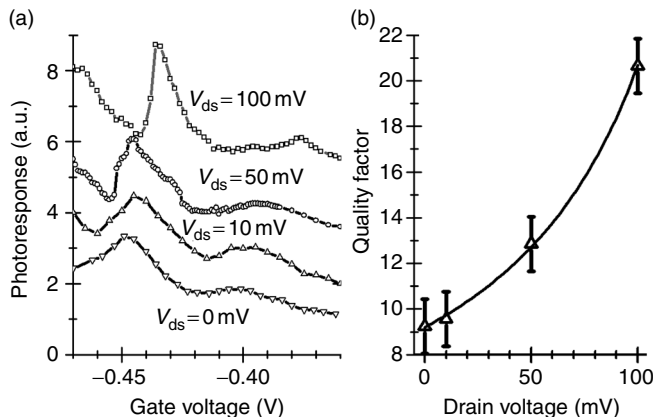
The resonances observed in all of the experiments were broader than theoretically expected. A significant plasma resonance broadening appears to be one of the main unresolved problems of the resonant THz detection by FETs. The main motivation behind changing the transistor material system from GaAs/GaAlAs, as used in first experiments,⁹ to InGaAs/InP¹⁰ and using higher excitation frequencies (up to 3 THz instead of 0.6 THz) was to improve the quality factor of the response resonance. However, the experimentally observed plasma resonances remained broad. Even at 3 THz the



5.18 (a) Photoresponse of high mobility InGaAs/InAlAs transistors at 1.8 THz, 2.5 THz and 3.1 THz registered at 10 K. (b) Position of the signal maximum versus the gate voltage. Solid line is a result of calculations.¹⁰

experimental quality factor Q was in the range of 2 to 4, while the theory predicted the quality factor higher by at least one order of magnitude. Understanding the origin of the broadening, and minimizing it, is one of the most important current experimental and theoretical challenges.

The two main hypotheses concerning broadening are: (i) the existence of oblique plasma modes²⁰ and (ii) an additional damping due to the leakage of gated plasmons to ungated parts of the transistor channel.⁴² The first hypothesis was discussed in Section 5.3.1. In the devices with the gate width much greater than the gate length, plasma waves can propagate not only in the source–drain direction but also in oblique directions. The frequency of oblique modes depends on the direction of the propagation vector and the spectrum of plasma waves is continuous. The second hypothesis, a leakage of gated plasmons to ungated parts of the channel,⁴² considers the fact that in the investigated HEMTs the gate covers only a small part of the source–drain distance. Therefore, the plasma under the gate cannot be treated independently of the plasma in ungated parts. An interaction between the two plasma regions can lead not only to a modification of the resonant frequency,³² but also to a mode leakage followed by a shortening of the gated plasmon lifetimes and hence in line broadening.



5.19 (a) Photoresponse at 10 K as a function of the gate voltage. Curves were obtained at 540 GHz with a multichannel InGaAs HEMT for different drain voltages V_{ds} from 0 mV to 100 mV. Curves are vertically shifted. (b) Quality factor of the resonance as a function of the drain voltage.^{43,44}

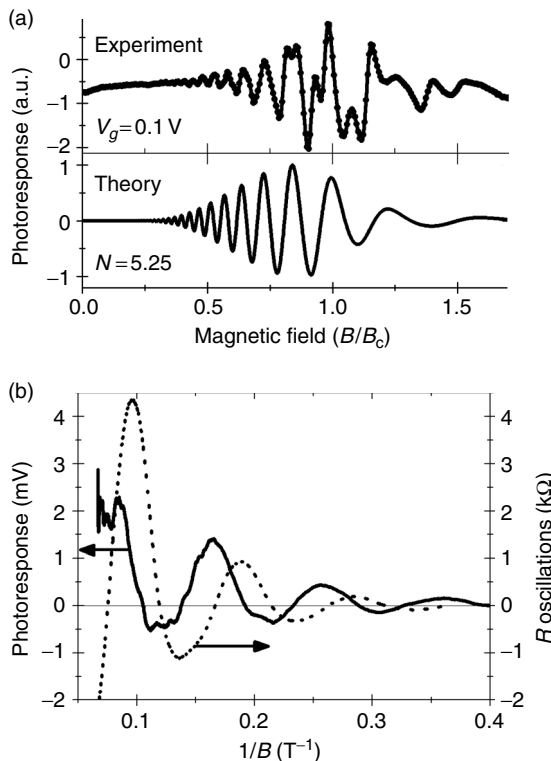
5.6.11 Narrowing of the channel

To decrease the role of oblique modes, one has to change the geometry of the channel. One can, for example, replace a wide single channel by a series of many narrow channels. Transistors with narrow channels were investigated in References 43 and 44.

In Fig. 5.19a we present the photoresponse at 540 GHz of a narrow multichannel transistor at 540 GHz. One can clearly see the narrowing plasma resonant lines. With increase of the drain voltage/current the lines become narrower. The quality factor shown in Fig. 5.19b increases from 9 up to 21. This result clearly shows that using FETs with narrow channels is a good way to improve the quality factor.

5.6.12 Current narrowing

Another way to decrease the broadening of the plasma resonances is to apply a drain current. The drain current affects the plasma relaxation rate by driving the 2D plasma in the transistor channel towards the Dyakonov–Shur plasma wave instability. As shown in Reference 13, the resonant response in the presence of a drain current has an effective width $1/\tau_{\text{eff}}$ that depends on carrier drift velocity v according to equation $1/\tau_{\text{eff}} = 1/\tau - \gamma$, where γ is the instability increment (see Section 5.3), which depends on the drift velocity v . For $v \ll s$, $\gamma = v/L$. Here L is the channel length. With increasing the current, the electron drift velocity increases, leading to the increase of the quality



5.20 (a) Top: experimental photoresponse as a function of the magnetic field for gate voltage 0.1 V – high carrier density. Bottom: calculations using Equation [5.1] of Reference 23. (b) Comparison of the magnetoresistance – dotted line – and 300 GHz photoresponse oscillations – solid line.

factor $Q = \omega\tau_{\text{eff}}$. The effect of the current-driven line narrowing is illustrated in Fig. 5.19. Curve 3 (triangles) was measured in the current-driven detection regime with the applied drain-to-source voltage $V_d = 100$ mV. A comparison of curves 2 and 3 shows that the line width clearly decreases with an increasing applied current. Systematic studies have shown that the quality factor could thus be increased by more than an order of magnitude.^{43,44} The good agreement between the experimental data and calculations (solid line in Fig. 5.19) confirms the model and clearly indicates that a dc current may be used to decrease the broadening of the plasma resonances.

5.6.13 High magnetic field studies

High magnetic field studies were performed at cryogenic temperatures on long InGaAs transistors with high mobility. These conditions correspond to

regime 1b described in Section 5.4.1, that is, $L \gg st$. The plasma waves are excited at the source and decay before reaching the drain. Oscillations analogous to Shubnikov-de Haas oscillations were observed. As already discussed in Section 5.4.3, the plasma waves can propagate only if the cyclotron resonance frequency is lower than the radiation frequency. In the opposite case, the plasma wave-vector becomes imaginary and thus the plasma oscillations are rapidly damped.^{24,25}

Figure 5.20a (top panel) shows the FET signal as a function of the magnetic field. The experiment shows an oscillatory character of the signal. Lower panel in Fig. 5.20a shows the calculated photoresponse.²⁴ The theory correctly describes oscillations of the photoresponse. Also the plasma wave damping in the post cyclotron resonance region is reproduced. In Fig. 5.20b the Shubnikov-de Hass oscillations of magnetoresistance are presented together with photoresponse oscillations.⁴⁵ One can see the 90° shift. This shift is due to the fact that the photoresponse is proportional to the derivative of the conductivity – see Equation [5.25]. The results in magnetic fields are spectacular manifestation of the importance of plasma waves in THz detection by FETs.

5.7 Conclusions

We have presented an overview of the main physical ideas and experimental results concerning the THz plasma oscillations in FETs for the generation and detection of THz radiation. Both THz emission and detection, resonant and non-resonant, were observed experimentally at cryogenic, as well as at room temperatures, clearly demonstrating effects related to the excitation of plasma oscillations. Currently, the most promising application appears to be the broadband THz detection and imaging in the non-resonant regime. However, resonant THz emission and detection by excitation of plasma waves with high-quality factors are still not achieved and deserve further exploration.

5.8 Acknowledgements

This work was supported in part by French-Japanese (ANR-JST) project WITH and GDR-I ‘Semiconductor Sources and Detectors of Terahertz Radiation’.

5.9 References

1. M. I. Dyakonov and M. S. Shur, ‘Shallow water analogy for a ballistic field effect transistor: New mechanism of plasma wave generation by dc current’, *Phys. Rev. Lett.* **71**, 2465 (1993).

2. M. I. Dyakonov and M. S. Shur, 'Plasma wave electronics: novel terahertz devices using two dimensional electron fluid', *IEEE Trans. Electron Devices* **43**, 380 (1996).
3. W. Knap, J. Łusakowski, T. Parenty, S. Bollaert, A. Cappy, V.V. Popov and M. S. Shur, 'Terahertz emission by plasma waves in 60 nm gate high electron mobility transistors', *Appl. Phys. Lett.* **84**, 3523 (2004).
4. N. Dyakonova, F. Teppé, J. Łusakowski, W. Knap, M. Levinstein, A. P. Dmitriev, M. S. Shur, S. Bollaert and A. Cappy, 'Magnetic field effect on the terahertz emission from nanometer InGaAs/AlInAs high electron mobility transistors', *J. Appl. Phys.* **97**, 4313 (2005).
5. N. Dyakonova, A. El Fatimy, J. Łusakowski, W. Knap, M. I. Dyakonov, M. A. Poisson, E. Morvan, S. Bollaert, A. Shchepetov, Y. Roelens, Ch. Gaquiere, D. Theron and A. Cappy, 'Room temperature terahertz emission from nanometer field-effect transistors', *Appl. Phys. Lett.* **88**, 141906 (2006).
6. A. El Fatimy, N. Dyakonova, Y. Meziani, T. Otsuji, W. Knap, S. Vandenbrouk, K. Madjour, D. Théron, C. Gaquiere, M. A. Poisson, S. Delage, P. Pristawko, C. Skierbiszewski, 'AlGaN/GaN high electron mobility transistors as a voltage-tunable room temperature terahertz sources', *J. Appl. Phys.* **107**, 024504 (2010).
7. J.-Q. Lu, M. S. Shur, J. L. Hesler, L. Sun and R. Weikle, 'Terahertz detector utilizing two-dimensional electronic fluid', *IEEE Electron Device Lett.* **19**, 373 (1998).
8. J.-Q. Lu and M. S. Shur, 'Terahertz detection by high-electron-mobility transistor: enhancement by drain bias', *Appl. Phys. Lett.* **78**, 2587 (2001).
9. W. Knap, Y. Deng, S. Rumyantsev and M. S. Shur, 'Resonant detection of sub-terahertz and terahertz radiation by plasma waves in submicron field-effect transistors', *Appl. Phys. Lett.* **81**, 4637 (2002) and *Appl. Phys. Lett.* **80**, 3434 (2002).
10. A. El Fatimy, F. Teppe, N. Dyakonova, W. Knap, D. Seliuta, G. Valušis, A. Schchepetov, Y. Roelens, S. Bollaert, A. Cappy and S. Rumyantsev, 'Resonant and voltage-tunable terahertz detection in InGaAs/InP nanometer transistors', *Appl. Phys. Lett.* **89**, 131926 (2006).
11. W. Knap, M. Dyakonov, D. Coquillat, F. Teppe, N. Dyakonova, J. Łusakowski, K. Karpierz, G. Valusis, D. Seliuta, I. Kasalynas, A. El Fatimy and T. Otsuji, 'Field effect transistors for terahertz detection: physics and first imaging applications', *J. Infrared Milli Terahz Waves* **30**, 1319 (2009).
12. F. Stern, 'Polarizability of a two-dimensional electron gas', *Phys. Rev. Lett.* **18**, 546 (1967).
13. A. V. Chaplik, 'Energy spectrum and electron scattering processes in inversion layers', *Zh. Eksp. Teor. Fiz.* **60**, 1845 (1971); [*Sov. Phys. JETP* **33**, 997 (1971)].
14. M. Nakayama, 'Theory of surface waves coupled to surface carriers', *J. Phys. Soc. Jpn.* **36**, 393 (1974).
15. A. Eduiluz, T.K. Lee, J.J. Quinn and K.W. Chiu, *Phys. Rev. B* **11** 4989 (1975).
16. S.J. Allen, D.C. Tsui and R.A. Logan, 'Observation of the two-dimensional plasmon in silicon inversion layers', *Phys. Rev. Lett.* **38**, 980 (1977).
17. D.C. Tsui, E. Gornik and R.A. Logan, 'Far infrared emission from plasma oscillations of Si inversion layers', *Solid State Commun.* **35**, 875 (1980).

18. A. P. Dmitriev, A. S. Furman, V. Yu. Kachorovskii, G. G. Samsonidze and Ge. G. Samsonidze, 'Numerical study of the current instability in a two-dimensional electron fluid', *Phys. Rev. B* **55**, 10319 (1997).
19. M. Dyakonov and M.S. Shur, 'Current instability and plasma waves generation in ungated two-dimensional electron layers', *Appl. Phys. Lett.* **87**, 111501 (2005).
20. M.I. Dyakonov, 'Boundary instability of a two-dimensional plasma', *Semiconductors* **42**, 984 (2008).
21. D. Veksler, F. Teppe, A. P. Dmitriev, V. Yu. Kachorovskii, W. Knap and M. S. Shur, 'Detection of terahertz radiation in gated two-dimensional structures governed by dc current' *Phys. Rev. B* **73**, 125328 (2006) – Published March 21, 2006
22. T. A. Elkhatib, V. Yu. Kachorovskii, W. J. Stillman, S. Rumyantsev, X.-C. Zhang and M. S. Shur, 'Terahertz response of field-effect transistors in saturation regime', *Appl. Phys. Lett.* **98**, 243505 (2011).
23. A. Lisauskas, U. Pfeiffer, E. Öjefors, P. H. Bolívar, D. Glaab and H.G. Roskos, 'Rational design of high-responsivity detectors of terahertz radiation based on distributed self-mixing in silicon field-effect transistors', *J. Appl. Phys.* **105**, 114511 (2009).
24. S. Boubanga-Tombet, M. Sakowicz, D. Coquillat, F. Teppe, W. Knap, M. I. Dyakonov, K. Karpierz, J. Łusakowski and M. Grynberg, 'Terahertz radiation detection by field effect transistor in magnetic field', *Appl. Phys. Lett.* **95**, 072106 (2009).
25. M.B. Lifshits and M.I. Dyakonov, *Phys. Rev. B* **80**, 121304(R) (2009).
26. M. I. Dyakonov and A. S. Furman, 'Charge relaxation in an anisotropic medium and in low-dimensional media', *Zh. Eksp. Teor. Fiz.* **92**, (1987) 1012 [*Sov. Phys. JETP* **65**, (1987) 574].
27. W. Knap, V. Kachorovskii, Y. Deng, S. Rumyantsev, J.-Q. Lü, R. Gaska, M. S. Shur, G. Simin, X. Hu, M. Asif Khan, C.A. Saylor and L. C. Brunel, *J. Appl. Phys.* **91**, 9346 (2002).
28. M. B. Lifshits, 'Terahertz photoresponse of field effect transistors near the threshold', *31st International Conference on the Physics of Semiconductors*, Zurich, 2012, Book of Abstracts, p. 242.
29. M. Sakowicz, M. B. Lifshits, O. A. Klimenko, F. Schuster, D. Coquillat, F. Teppe and W. Knap, 'Terahertz responsivity of field effect transistors versus their static channel conductivity and loading effects', *J. Appl. Phys.* **110**, 054512 (2011).
30. W. Knap, D. Dur, A. Raymond, C. Meny, J. Leotin, S. Huant and B. Etienne, 'A far infrared spectrometer based on cyclotron-resonance emission sources', *Rev. Sci. Instrum.* **63**(6), 3293–3297 (1992).
31. W. Chaubet, C. A. Raymond, W. Knap, J.Y. Muiot, M. Baj and J.P. Andre, 'Pressure dependence of cyclotron mass in GaAs/GaAlAs heterojunctions by far infrared emission and transport experiments', *Semicond. Sci. Tech.* **6**(3), 160–164 (1991)
32. V. Ryzhii, A. Satou, W. Knap and M. S. Shur 'Plasma oscillations in high-electron-mobility transistors with recessed gate', *J. Appl. Phys.* **99**, 084507 (2006).
33. M. Sakowicz, J. Lusakowski, K. Karpierz, M. Grynberg, W. Knap and W. Gwarek, 'Polarization sensitive detection of 100 GHz radiation by high mobility field-effect transistors', *J. Appl. Phys.* **104**, 024519 (2008).
34. H. Videlier, S. Nadar, M. Sakowicz, T. Trinhvandam, D. Coquillat, F. Teppe, N. Dyakonova, W. Knap and T. Skotnicki, 'Terahertz broadband detection using

- silicon MOSFET', *16th International Conference on Electron Dynamics in Semiconductors Optoelectronics and Nanostructures (EDISON 16)*, 24–28 August 2009, Montpellier, France. *J. Phys.: Conf. Ser.* **193**, 012095 (2009).
- 35. R. Tauk, J. Łusakowski, W. Knap, A. Tiberj, Z. Bougrioua, M. Azize, P. Lorenzini, M. Sakowicz, K. Karpierz, C. Fenouillet-Beranger, M. Cassé, C. Gallon, F. Boeuf and T. Skotnicki, 'Low electron mobility of field-effect transistor determined by modulated magnetoresistance', *J. Appl. Phys.* **102**, 103701 (2007).
 - 36. W. Knap, F. Teppe, Y. Meziani, N. Dyakonova, N. Lusakowski, F. Boeuf, T. Skotnicki, D. Maude, S. Rumyantsev and M. S. Shur, 'Plasma wave detection of sub-terahertz and terahertz radiation by silicon field-effect transistors', *Appl. Phys. Lett.* **85**(4), 675, (2004).
 - 37. R. Tauk, F. Teppe, S. Boubanga, D. Coquillat, W. Knap, Y. M. Meziani, C. Gallon, F. Boeuf, T. Skotnicki, C. Fenouillet-Beranger, D. K. Maude, S. Rumyantsev and M. S. Shur, 'Plasma wave detection of terahertz radiation by silicon field effect transistors: responsivity and noise equivalent power', *Appl. Phys. Lett.*, **89**, 253511, (2006).
 - 38. F. Schuster, D. Coquillat, H. Videlier, M. Sakowicz, F. Teppe, L. Dussopt, B. Giffard, T. Skotnicki and W. Knap, 'Broadband terahertz imaging with highly sensitive silicon CMOS detectors', *Opt. Express* **19**, 7828 (2011).
 - 39. F. Schuster, W. Knap and V. Nguyen, 'Terahertz imaging achieved with low-cost CMOS detectors', *Laser Focus World*, **47**(7), 37–41, (2011).
 - 40. E. Oje fors, U. Pfeiffer, A. Lisauskas and H. Roskos, 'A 0.65 THz focal-plane array in a quarter-micron CMOS process technology', *IEEE J. Solid-St. Circ.* **44**, 1968–1976 (2009).
 - 41. S. Nadar, H. Videlier, D. Coquillat, F. Teppe, M. Sakowicz, N. Dyakonova, W. Knap, D. Seliuta, I. Kašalynas and G. Valušis, 'Room temperature imaging at 1.63 and 2.54 terahertz with field effect transistor detectors', *J. Appl. Phys.* **108**, 054508 (2010).
 - 42. V. V. Popov, O. V. Polischuk, W. Knap and A. El Fatimy, 'Broadening of the plasmon resonance due to plasmon-plasmon intermode scattering in terahertz high-electron-mobility transistors', *Appl. Phys. Lett.* **93**, 263503 (2008).
 - 43. A. Shchepetov, C. Gardès, Y. Roelens, A. Cappy, S. Bollaert, S. Boubanga-Tombet, F. Teppe, D. Coquillat, S. Nadar, N. Dyakonova, H. Videlier, W. Knap, D. Seliuta, R. Vadoklis and G. Valušis, 'Oblique modes effect on terahertz plasma wave resonant detection in InGaAs/InAlAs multichannel transistors', *Appl. Phys. Lett.* **92**, 242105 (2008).
 - 44. S. Boubanga-Tombet, F. Teppe, D. Coquillat, S. Nadar, N. Dyakonova, H. Videlier, W. Knap, A. Shchepetov, C. Gardès, Y. Roelens, A. Cappy, S. Bollaert, D. Seliuta, R. Vadoklis and G. Valušis, 'Current driven resonant plasma wave detection of terahertz radiation: Toward the Dyakonov–Shur instability', *Appl. Phys. Lett.* **92**, 212101 (2008).
 - 45. O. A. Klimenko, Yu. A. Mityagin, H. Videlier, F. Teppe, N. V. Dyakonova, C. Consejo, S. Bollaert, V. N. Murzin and W. Knap, 'Terahertz response of InGaAs field effect transistors in quantizing magnetic fields', *Appl. Phys. Lett.* **97**, 022111 (2010).

Terahertz wireless communications

J. F. FEDERICI, New Jersey Institute of Technology, USA,
L. MOELLER, Bell Laboratories, Alcatel-Lucent, USA and
K. SU, New Jersey Institute of Technology, USA

DOI: 10.1533/9780857096494.1.156

Abstract: The rapidly increasing demand for higher bandwidth and data rates in wireless communication systems over the past several decades is well known. Over the last 12 years, terahertz (10^{12} Hz) frequency systems have emerged as a new paradigm to transmit data wirelessly. The goal of this chapter is to provide a comprehensive review of wireless terahertz communications for which terahertz waves are the free-space carrier of data. This chapter describes the motivation for terahertz wireless communications, the effect of atmospheric propagation, modeling of communications channels, and hardware.

Key words: terahertz wireless communication, atmospheric effects, channel modeling, bit-error rate, scintillations.

6.1 Introduction

The rapidly increasing demand for higher bandwidth and data rates in wireless communication systems over the past several decades is well known. According to Edholm's law, the demand for point-to-point bandwidth in wireless short-range communications has doubled every 18 months over the last 25 years. It can be predicted that data rates of around 5–10 Gb/s will be required in ten years. Some of the reported advantages of THz communications links compared to millimeter-wave links are inherently higher utilizable bandwidth relative to the higher carrier frequency, less susceptibility to scintillation effects than infrared wireless links, and the ability to use THz links for secure communications. Over the past 12 years, several groups have considered the prospects of using THz waves as a means to transmit data, and numerous papers covering various aspects of the topic – THz sources and detectors, modulation schemes, wireless communication measurements – have been reported. The goal of this chapter is to provide a comprehensive review of wireless THz communications for which THz waves as the free-space carrier of data. This chapter describes the motivation for THz wireless communications (Section 6.2), the effect

of atmospheric propagation on THz communications (Section 6.3), modeling of THz communications channels (Section 6.4), hardware (Section 6.5), THz modulators (Section 6.6), modulator formats (Section 6.7) and demonstrated examples of THz communication systems (Section 6.8). Future trends are summarized in Section 6.10.

6.2 Motivation for terahertz wireless communications

Commercial wireless point-to-point microwave communications systems currently operate at carrier frequencies as high as 18–30 GHz (K band and Ka band). Several research projects in the fields of electronics and fiber optics have focused in the past on developing devices for communication systems running at 60 GHz signals. The high oxygen-absorption peak in these frequency bands strongly attenuates radio signals, allowing the design of low interference pico cell mobile communication systems with ultra-high capacity.^{1,2} Even at higher frequencies up to 300 GHz, the Federal Communications Commission (FCC) has started to allocate frequency bands for mobile, satellite and wireless links.³

Historically, individual (point-to-point) and aggregate (within a volume of space) bandwidth demands for wireless networking have increased rapidly over the last two decades. One way of meeting these bandwidth demands is to increase the spectral utilization efficiency by applying advanced modulation techniques, which enable increased point-to-point data rates, increased sharing of a given band of frequencies, and increased amounts of frequency reuse within a volume of space. However, it is recognized that there is a limit to employing advanced modulation and signal processing techniques.⁴ Shannon's channel capacity formula, even when extended to wireless networking in a shared volume of space through the use of multi-input/multi-output (MIMO) approaches, shows an upper limit for this strategy. Beyond this limit transmission bands at higher carrier frequencies have to be accessed to provide sufficient transmission capacity. According to Edholm's law of bandwidth,⁵ the demand for bandwidth in wireless short-range communications has doubled every 18 months over the last 25 years. From this recent trend, it can be predicted that data rates of around 5–10 Gbit/s will be required in 10 years. As reported in Reference 6, a compound annual growth rate of around 71% for mobile traffic in Japan from 2007 to 2017 is predicted. At that rate, the mobile traffic in 2017 in Japan will be 220 times higher than in 2007. In the United States,⁶ mobile traffic is expected to be 40 times higher in 2015 than in 2010. Britz⁷ reports a growing industry consensus that today's cellular networks may be approaching a critical conjuncture due to mass consumer use of 'smart' portable devices which is driving the

need to dramatically increase capacity. A review by Koch⁸ in 2007 suggests that THz based communications systems will replace or supplement wireless LAN systems during 2017–23.

In the latest United States Federal Strategic Spectrum Plan,⁹ it is recognized that Federal agencies universally have an increased demand for higher data throughput and bandwidth – in particular for wireless broadband applications. The 30–300 GHz (or extremely high frequency (EHF)) portion of the spectrum is anticipated to be used for radiolocation (radar) services, in particular near 35, 90, 140 and 240 GHz for which there are atmospheric windows for transmission. According to this report, the National Science Foundation believes that new allocations in the 0.275–1 THz region may be needed within a decade for radio astronomy and other science services. Currently, the main thrust is to use the higher frequency bands (275–2400 GHz) for radio-astronomy research. One can anticipate that as research and development applications above 300 GHz emerge, the spectrum requirements will be updated, and frequency bands allocated. However, a recent review of THz communications⁶ suggests a near-term conflict in the allocation of THz bandwidth between radio astronomy and wireless communication. It is expected that THz communication transmitters will interfere with the sensitive detectors which are used in radio astronomy.

A number of papers have highlighted different applications for THz communication. As will be discussed in Section 6.3, in conjunction with the high-bandwidth potential, THz links will exhibit an intrinsically short path length and line-of-sight communication. In his discussion of future THz communication systems, Mann¹⁰ suggests that the commercial application of THz communication links would be a niche in which very high data rates are required over short distances on a multi-point-to-point/multi-point basis (i.e., the ‘first’ and ‘last mile’ problem). The ‘last’ and ‘first’ mile problem^{11,12} refers to establishing broadband, multi-user local wireless connections to high-speed networks (i.e., fiber-optical). As an example, THz wireless links could be used as part of the ‘last mile’ transmission of multiple channel HDTV signals.¹³ THz communication systems with gigabit or higher data rates could enable a wide variety of high-bandwidth applications including¹¹ wireless extensions of broadband access fiber-optical networks, wireless extension of high-speed wired local networks,¹³ a wireless bridge between lower data-rate wireless local networks and high-speed fiber-optical networks, high-definition television (HDTV),¹⁴ and broadband indoor pico-cells to handle high demand from a number of mobile users. Applications of indoor THz communications to wireless local area network (WLAN) and wireless personal area network (WPAN) systems have been detailed.⁴ Typical in-home uses of these

networks with THz links might include wireless displays, in-home HDTV distribution, rapid wireless connections to/from a fiber-optic backbone high-speed network.

For future outdoor wireless systems, David Britz proposed a Triple-Stack Nanocellular Architecture.⁷ Conceptually, this proposal is a logical progression of cell splitting. However, the driving force behind the rapid splitting of wireless cells results from the opening of cellular networks to the Internet and broadband data. Britz argues that cell sizes will have to shrink dramatically to cope with this data influx. The end results are much smaller cells and a precipitous increase in their number. The Triple-Stack Architecture includes existing cellular and Wi-Fi for slower real-time communications while THz communications provide extremely high throughputs via localized (sub-kilometer) nanocells. Britz recommends that the THz spectrum be exploited to provide Gigabit Ethernet-like wireless throughputs.

The intrinsic advantage of THz communication systems compared to microwave or millimeter-wave systems is that of higher bandwidth. However, what about the other competing frequency limit, namely free-space infrared (IR) communications? IR free-space communication links at 1.5 μm wavelength are the most common optical transmission vehicle for short reach (up to 10 km). As previously noted by Koch,⁸ wireless IR systems are 30 years old, yet until recently the highest data rates reported were 155 Mb/s.¹⁵ A 2007 review of the field in Reference 16 shows no improvement beyond the 155 Mb/s data rate reported in 2001. Only recently has a 10 Gb/s data rate been demonstrated in a simulated atmospheric environment.¹⁶ The key to increasing the IR wireless data rate to 10 Gb/s was advanced modulation formats such as orthogonal frequency division multiplexing.

Two of the most important issues with IR free-space communications are transceiver misalignment due to atmospheric turbulence and/or humidity fluctuations in the beam path (i.e., scintillation) as well as atmospheric absorbance of the IR signal.¹⁷ Atmospheric turbulence and humidity fluctuations cause temporally and spatially dependent variations in the atmospheric real refractive index. Consequently, the location of the IR beam on the receiver tends to vary in time leading to scintillation effects. This effect will be discussed in Section 6.3.2.

6.3 Atmospheric propagation for communications

In this section, basic considerations of THz communications are considered including directionality, scintillations, and atmospheric and free-space damping including fog, rain, and dust/ smoke.

6.3.1 Directionality of THz radiation

THz communications are inherently more directional at the same transmitter aperture than microwave or millimeter (MMW) links due to less free-space diffraction of the waves, and therefore line-of-sight detection is required. The importance of the diffractive effects in free-space THz systems can be explored using the Friis formula. Following the analysis of Brown,¹⁸ the power supplied to the load of the receiving antenna is given by

$$P_{\text{out}} = P_{\text{in}} \left(\frac{\lambda}{4\pi d} \right)^2 G_r \cdot G_t \cdot F_r(\theta_r, \phi_r) \cdot F_t(\theta_t, \phi_t) \cdot \tau \cdot \epsilon_p \quad [6.1]$$

where P_{in} is the input power to the transmitting antenna, G is the antenna gain, F is the normalized intensity pattern function, τ is the path power transmission factor, ϵ_p is the polarization coupling efficiency, λ is the wavelength of the radiation, and d is the distance between the transmitting (t) and receiving (r) antenna. The angles θ and ϕ refer to spherical coordinates at either the receiver or transmitter. The free-space loss factor $(\lambda/4\pi d)^2$ arises from two effects: (1) the assumption that the receiving antenna is detecting the far-field radiation of the transmitting antenna leads to treating the source as emitting a spherical-like wave whose power decreases as $1/d^2$ with distance; (2) the factor of λ^2 arises from the diffraction limited directivity (D_{\max}) or alternatively the solid angle which defines the extent of the diffracting intensity pattern function: $D_{\max} = 4\pi/\Omega = 4\pi A_{\text{eff}}/\lambda^2$, for which A_{eff} is the effective area of the detector.

The antenna gain and directivity are related by

$$G_t = \frac{P_{\text{rad}}}{P_{\text{in}}} D_t \quad [6.2]$$

where P_{rad} is the power radiated by the antenna. If we assume that the radiation and input powers are matched, then the gain of the antenna is equal to the directivity. In this case, Equation [6.1] can be rewritten as

$$P_{\text{out}} = P_{\text{in}} \frac{A_t A_r}{d^2 \lambda^2} F_r(\theta_r, \phi_r) \cdot F_t(\theta_t, \phi_t) \cdot \tau \cdot \epsilon_p \quad [6.3]$$

where A_t and A_r refer to the effective apertures of the transmitter and receiver, respectively. According to Equation [6.3], the power received at a detector varies as $1/\lambda^2$ so the efficiency of detection improves as the wavelength decreases or the THz frequency increases. This implies that THz communications are inherently more directional than microwave or MMW

links due to less free-space diffraction of the waves. Consequently, THz communication systems will typically be line-of-sight systems.

For a more detailed analysis of typical THz power link budgets, which include other factors such as the noise power spectral density, noise bandwidth, system margin, etc., the reader is referred to several examples.^{4,10,19}

6.3.2 Scintillations as link degradation

Real refractive index fluctuations can destroy the flat phase front of an IR light beam when it passes through a few kilometers of air. Local temperature, pressure, or humidity gradients, which are generated by thermals and turbulence near ground level, cause small refractive index variations across the wave front of the beam. Even if a single local refractive index fluctuation only slightly distorts the wave's phase front, the effect can accumulate over a few kilometers of propagation distance resulting in a complete or almost complete destruction of the phase front. As a consequence, on the receiver side the beam cross-section appears as a speckle pattern (Fig. 6.1) with huge local and temporal intensity variations preventing detection of constantly sufficient signal power.²⁰ These scintillation effects are the main link length limitation in IR communication systems under clear weather conditions. Complex equalizer schemes for phase front correction based on mirror arrays were proposed as a counter measure but could not so far show a convincing performance. As will be shown below, THz beams are much less susceptible to scintillation compared to IR beams.

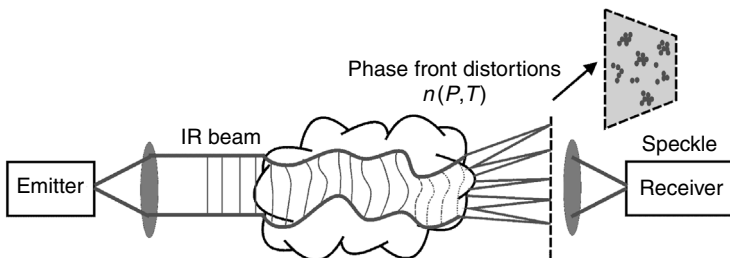
The refractive index of air in the millimeter-wave band up to a few hundred GHz can be well approximated as function of temperature and pressure by:

$$n_{\text{mmW}} \approx 1 + \frac{7.76}{T} \left[P_a + 4810 \frac{P_v}{T} \right] \times 10^{-6} \quad [6.4]$$

where T , P_a , P_v stand for the temperature in Kelvin, the atmospheric pressure in kPa, and the water vapor pressure in kPa, respectively.²¹ Similarly, for IR wavelengths the refractive index of air can be written as:

$$n_{\text{IR}} \approx 1 + 7.76 \times 10^{-6} \left[1 + 7.52 \times 10^{-3} \lambda^{-2} \right] \frac{P_a}{T} \equiv 1 + 7.76 \times 10^{-6} \frac{P_a}{T} \quad [6.5]$$

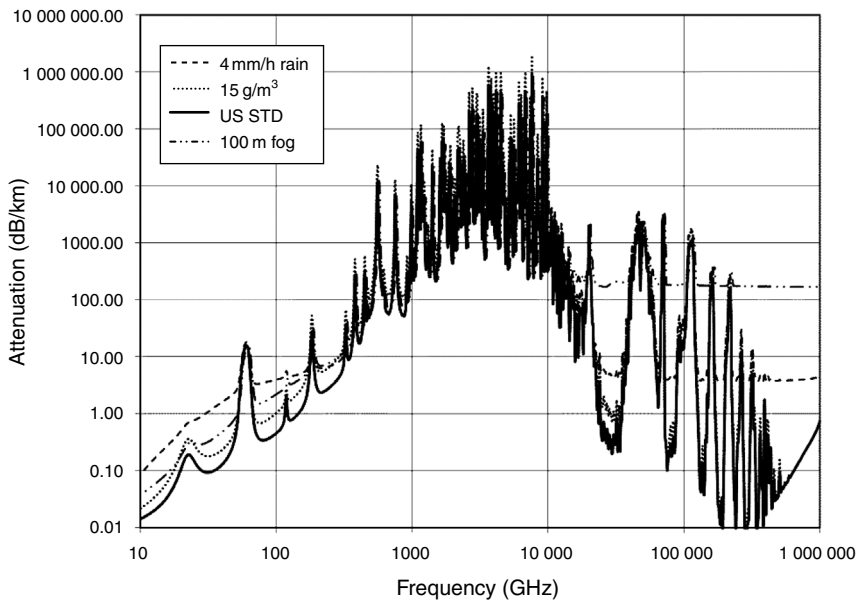
where λ stands for the wavelength in μm .²² The formula does not consider humidity as it only insignificantly degrades IR propagation. Under the assumption of relevant air parameters, a numerical comparison of both



6.1 Air turbulence causes refractive index fluctuations resulting in speckles (intensity variations at the receiver) that limit the reach of IR systems. $n(P,T)$ describes how the local refractive index ' n ' varies with local pressure ' P ' and temperature ' T '. (Reprinted with permission from J. Federici and L. Moeller, 'Review of terahertz and subterahertz wireless communications', *J. Appl. Phys.* **107**, 111101 (2010). ©2010, American Institute of Physics.)

formulas shows that even at high levels of water vapor pressure, the refractive index changes in both the THz and IR bands are comparable. Since scintillation effects are driven by variations in phase, the relevant parameter is the variation in the optical path length relative to the electromagnetic wavelength. Since the variation in the optical path length for both the IR and THz are comparable (the changes in refractive index are commensurate), the relative magnitudes of the phase variations are predominately determined by the electromagnetic wavelength. But, the wavelength of THz at ~ 200 GHz is approximately 1000 times longer than the wavelength of $1.5\text{ }\mu\text{m}$ light. In summary, while time-varying fluctuations in the real refractive index of the atmospheric path leads to scintillation effects in wireless communications, these effects are much smaller for THz compared to IR wireless links.

There have been some measurements of scintillation effects at 97 GHz which showed that the long-term probability distribution of scintillation amplitudes due to rain could be modeled by the Mousley-Vilar equation.²³ Knowledge of the scintillation amplitude distribution can be used to predict the degradation of the communication link due to scintillation. Experimental evidence that has been published concerning the effect of scintillation on THz communication includes brief comments in References 24 and 25 and a more detailed analysis in Reference 26. Yamaguchi *et al.*²⁴ describe the effect of wind on the THz communication measurements at 125 GHz. As wind velocity increased, the lateral deviation of the THz beam from the receiver axis also increased which caused the input power to the receiver to decrease. However, since the detected power was greater than the minimum required, the authors did not observe any increase in bit-error rate. Reference 25, which characterizes the effect of rain, suggests that scintillations may be the cause of a



6.2 Calculated atmospheric attenuation in THz and IR band. ITU recommendations are used from 10 to 1000 GHz. MODTRAN 4 is used from 0.3 to 30 microns. A code for the 1–10 THz region was developed by MMW Concepts LLL.²⁰ The dashed line corresponds to 4 mm/h of rain. The dash-dot line corresponds to 100 m visibility of fog, and the solid line corresponds to US standard atmospheric conditions at sea level (59% relative humidity = 7.5 g/m³ water content). The dotted line corresponds to 15 g/m³ of water content. A wavelength of 1.5 μm corresponds to 2 × 10⁵ GHz. (Reprinted with permission from J. Federici and L. Moeller, ‘Review of terahertz and subterahertz wireless communications’, *J. Appl. Phys.* **107**, 111101 (2010). ©2010, American Institute of Physics.)

discrepancy between the measured and predicted bit-error-rate in a THz link. Reference 26 will be discussed in detail in Section 6.9.

6.3.3 Atmospheric and free-space damping including fog, rain and snow

Atmospheric attenuation of THz and IR communication links are impacted differently by weather conditions such as fog, rain, snow and humidity. Figure 6.2 compares the absorption coefficient of millimeter waves, THz and IR waves at sea level for different weather conditions. Under fog conditions, the THz absorption at ~240 GHz is around 8 dB/km which is considerably lower than the 200 dB/km that the 1.5 μm wavelength suffers. The maximum

reach of THz radiation in fog can be much larger than that of usual IR based systems when assuming comparable output powers. Thus THz based communication systems could serve as a back-up for foggy weather when IR signaling fails. It should also be noted that above 200 GHz and below 10 THz, the attenuation is dominated by atmospheric water vapor, with attenuation due to rain and fog playing a minor role. In the IR, fog and smoke will cause significant attenuation. As noted by Brown¹⁸ in his extensive consideration of MMW and THz remote sensing systems, there is little or no experimental data on THz scattering by fog, rain, particulates etc. Brown attributes the limited experimental data to a lack of calibrated THz instrumentation and the general difficulty in distinguishing absorption from scattering effects.

With the advancement of THz remote sensing and communications, the modeling and experimental studies of the atmospheric propagation in the THz range has seen renewed scientific interest.²⁷ The basic processes in atmosphere of importance in the THz range should include Beer-Lambert law absorption for example by water vapor, Mie scattering by dust, ice, rain etc., atmospheric refraction and turbulence (leading to scintillation effects), and background radiation either from the 3 K cosmic radiation or emission from the earth's surface. Recent measurements of THz propagation through a humid atmosphere²⁸ show higher attenuation than previously measured or predicted in the THz transmission windows between 0.2 and 2 THz. While experimental data at 97 GHz²³ indicates a reasonable agreement between measured rain attenuation values and those predicted by different models, differences between the measured and predicted values suggest that further measurements are required to fully validate rain attenuation models at the higher MMW or sub-THz frequency range. Recent measurements, which characterize the effect of fog on a 625 GHz THz communication link as well as rain on a 120 GHz link, are described in Section 6.9.

Due to the relatively small size of atmospheric particulates, such as dust and smoke, compared to the THz wavelength, one would expect minimal THz attenuation due to airborne particulates. Mann had predicted that fog and smoke has little or no effect up to 1 THz.¹⁰ A rough estimate of the attenuation can be made assuming that the particulates act as spherical Mie scattering centers. Following a simple Mie scattering formalism²⁹ that was used previously to study attenuation of THz radiation due to particle grains,³⁰ one can estimate the attenuation at IR, THz and sub-THz frequencies using known particles sizes and concentrations. The extinction coefficient takes on the following form:

$$\mu_{th}(v) = N \frac{c^2}{2\pi v^2} \sum_{m=1}^{\infty} (2m+1) \operatorname{Re}(a_m + b_m) \quad [6.6]$$

where N is the number of particles per unit volume, c is the speed of light, ν is the electromagnetic frequency, and a_m and b_m are the coefficients in the infinite summation such that,

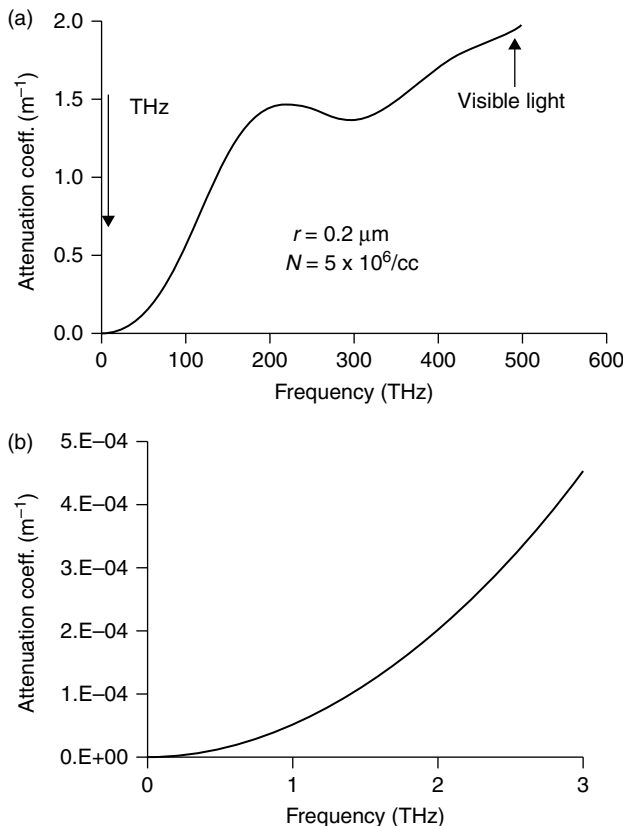
$$\begin{cases} a_m = \frac{\psi'_m(y)\psi_m(x) - n\psi_m(y)\psi'_m(x)}{\psi'_m(y)\zeta_m(x) - n\psi_m(y)\zeta'_m(x)} \\ b_m = \frac{n\psi'_m(y)\psi_m(x) - \psi_m(y)\psi'_m(x)}{n\psi'_m(y)\zeta_m(x) - \psi_m(y)\zeta'_m(x)} \end{cases} \quad \text{where } \begin{cases} \psi_m(z) = zj_m(z) \\ \zeta_m(z) = zh_m^{(2)}(z) \end{cases} \quad [6.7]$$

Here $j_m(z)$ and $h_m^{(2)}(z)$ are spherical Bessel functions of the first kind and third kind, respectively. The parameter z can be either $x = 2\pi\nu r/c$ or $y = 2\pi\nu nr/c$, where r is the radius of the spherical particle and n is the frequency independent refractive index of the particle.

As an example, Federici and Moeller^{20,31} estimated the attenuation due to battlefield³² or wildfire particulates and smoke³³ using Equations [20.6] and [20.7]. (By comparison, the attenuation coefficient due to Rayleigh scattering is many orders of magnitude smaller.) As shown in Fig. 6.3, IR wavelengths are strongly attenuated while THz and sub-THz wavelengths would enable communications through a much longer link distance, since there is lower attenuation of THz radiation compared to IR under certain atmospheric conditions (e.g., dust, fog). Under certain weather conditions and for specific link length requirements THz can enable reliable communication where IR based systems would fail.

6.4 Modeling of terahertz communication channels

In considering the atmospheric attenuation of THz waves, clearly certain spectral ‘windows’ are available for THz communication such as the 200–300 GHz window of Fig. 6.2. Based on the strong atmospheric attenuation, Koch⁸ concludes that practical THz communication distances are limited to several tens of meters. Therefore, he concludes that THz wireless systems will be limited to medium-link and short-link *indoor* applications since outdoor scenarios are much less likely unless adverse weather conditions are rare. Since both indoor and outdoor THz systems exhibit smaller diffractive effects at THz frequencies compared to microwave frequencies, one would expect that any THz system would require line-of-sight connection between transmitter and receiver. For outdoor systems, this restriction is less of a problem, for example, if the transmitter and receivers were placed on roof-tops of buildings. For indoor systems, one would have to rely on non-line-of-sight paths including reflections from walls. Clearly objects or people moving in the beam path will severely disrupt the communication channel.



6.3 Predicted IR (a) THz and (b) sub-THz attenuation due to spherical airborne particles. For the calculation, parameters comparable to battlefield fog oil particles are used: particle density $5 \times 10^6/\text{cc}$, 0.2 micron particle radius, and a real index of 1.5. (Reprinted with permission from J. Federici and L. Moeller, 'Review of terahertz and subterahertz wireless communications', *J. Appl. Phys.* **107**, 111101 (2010). ©2010, American Institute of Physics.)

6.4.1 Indoor

As discussed in Reference 4 and Section 6.2, there are several potential applications of THz communication links to wireless long range and personal area network systems. However, severe technical hurdles need to be addressed for a viable indoor solution. For example, since THz systems are required to be highly directional, how does the wireless signal get rerouted if an obstacle, such as a person, temporarily blocks the path between a THz transmitter and receiver which are transferring data – for example – from a wireless router to a handheld computing tablet. It is important to note

that this modality of a THz wireless data link is very different from today's indoor wireless communication systems. Consequently, implementation of an indoor THz communications links cannot be just an extension of existing technology, but must involve the development of new concepts and ideas to make it feasible.⁸

As a further example of the need for new ideas, objects can block line-of-sight (people moving around in a room) such that alternative non-line-of-sight routes, such as reflections from walls, are required for a THz communications link. However, since the reflection from typical building materials³⁴ would introduce substantial additional losses in the links, highly reflecting mirrors are needed. In addition, steerable high-gain antennas are required to connect from another path in case the primary path is blocked.

A key hardware component towards implementing indoor THz communications is reflective 'wall paper' that increases the THz reflection³⁵ from walls in the event of a non-line-of-sight path in a room. The first version of the reflecting paper³⁶ used alternating layers of plastics (real refractive indices 1.7 and 1.59). Stacked alternative layers produced a relatively high reflectivity (76%) at 187 GHz with ~16 GHz bandwidth. One advantage of these dielectric mirrors is that they are flexible since they can be fabricated with flexible plastics. However, the maximum reflectivity is limited by the index difference between the different layers. An improved version of the mirrors, described in Reference 37, consists of alternating stacks of polypropylene ($n = 1.53$) and high resistivity silicon ($n = 3.418$). These mirrors, due to the large index difference between adjacent layers, have high reflectivity (>95%) for both S and P polarization regardless of incident angle. The bandwidth of the mirrors is limited to ~56 GHz due to the shifting of the P polarization reflection band with incident angle. Measurements of the dispersive properties of the mirror show that the group delay is on the order of five picoseconds³⁸ with some variation in both the THz frequency (between 0.25 and 0.4 THz) and polarization. Unfortunately, the 63 micron thick crystalline silicon layers are not flexible. However, a flexible high-index dielectric has been fabricated by mixing highly refractive TiO₂ powder either with polypropylene or polyvinylidene fluoride (PVDF). The mixture can be either drop cast or extruded.³⁹ A five layer structure of alternating PVDF and PVDF/TiO₂ layers exhibits a high reflectivity between 0.25 and 0.35 THz. Moreover, since the structure is flexible, one can conceivably deform the layer into a focusing THz optic, suggesting the possibility of integrating beam shaping and filtering functionality in to the same component. Alternative composite layers (e.g., tellurium and polystyrene) have been proposed, but not experimentally demonstrated, for omnidirectional broadband THz dielectric mirrors.⁴⁰

In order to characterize an indoor THz communication channel, ray-tracing and Monte Carlo simulations were performed.⁸ Ray-tracing techniques can be used since the THz wavelength is small compared to the

geometric size of typical indoor scatterers. Consequently, the THz communication channel can be described using basic parameters such as free-space attenuation, reflection coefficients from objects in the room, antenna gains, and the power delay profile. The power delay profile refers to the path length difference between the direct line of sight and once- or twice-reflected THz radiation. Clearly, there will be a time delay in the data at the receiving antenna depending on which path is taken. If the data rate were too high, there would be Inter-Symbol Interference (ISI) between data traveling along the multiple paths.

In the simulation environment, models are included for people and objects. They are placed randomly in a ‘cell’ or room and geometrically modeled with planes of appropriate dimensions and THz reflectivity. People are considered to be totally absorbing. Metallic surfaces are considered to reflect THz radiation perfectly. Reflection of smooth objects is modeled with Fresnel equations using the known complex indices of refraction and angles of incidence as input data. In some of the earlier simulations, it was shown that high-gain antennas are required for indoor THz communication links. In addition, the placement of people was considered to be static. The simulations have been improved¹¹ to consider motion of people including their speed of movement, direction of motion, and changes in direction. The simulation allows people to be moving in room for 30 s. The THz transmitter is positioned on the ceiling while the receiver is located on a desktop in the room. Monte Carlo ray-tracing from transmitter to receiver establishes THz communication channel statistical properties.

The simulation calculates the THz power at the receiver from direct line-of-sight paths, once-reflected paths, and twice-reflected paths. The assumed sensitivity limit for detection is –110 dBm. Thirty percent of all simulated paths are interrupted by interfering objects. Shadowing effects are observed predominately near static objects such as furniture and walls. While only direct line of sight is not feasible due to moving objects, these early modeling results suggest that twice-reflected power should be avoided: more than –100 dBm of power from the twice-reflected path is available only 30% of time. The once-reflected path provides more than –95 dBm of the power 65% of the time.

If the data rate were too high, there would be ISI between the multiple paths. Consequently, the data rate must be slow enough to eliminate ISI. For the simulated channels, 90% have a time delay spread of less than 10 ns. From this maximum time delay, Piesiewicz *et al.*¹¹ estimate a maximum data rate of 5 Mb/s on a given binary channel. Multiple channels would be required to achieve Gb/s data rates. Since the THz beams are highly directional, Piesiewicz *et al.* suggest that ‘smart’ (steerable) antennas could utilize one propagation path at a time and therefore eliminate ISI.

References 41 and 42 describe the latest simulations of wireless THz communication links using highly directive antennas in realistic indoor environments. The simulation models a transceiver front end with available components which employs heterodyne detection methods. The simulated room includes walls made from a variety of materials (plaster, wood, plastics, bricks, etc.), windows, and office furniture. Reflections from optically thick, smooth and rough surfaces⁴³ are included, as well as multilayer reflections from optically thin materials. The ray-tracing model, following previous work, assumes direct line-of-sight, once-reflected, and twice-reflected THz beams. The THz antennas are assumed to be very high gain (i.e., highly directional) and controlled with a signal tracking system so that data streams can be easily passed from one path to another. The signal tracking system in conjunction with the high-gain antennas reduces the contribution of multiple paths to the THz receiver so that ISI would not be a concern. The walls of the room are assumed to have omni-directional dielectric mirrors covering the walls and ceiling. In a realistically furnished office room, data rates of ~20 Gb/s and 8 Gb/s, for single and double-bounce paths, should be feasible. However, such an antenna system still needs to be developed and evaluated.

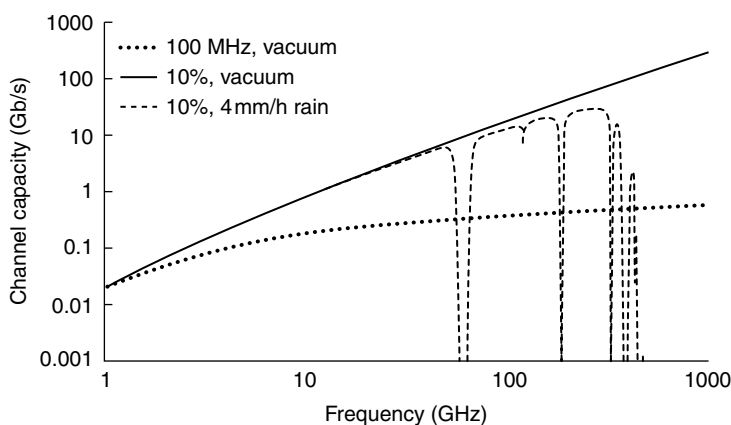
In summary, from these simulations it is concluded that: (a) alternative routes are needed in which THz reflects off walls to make the system robust against obstacles blocking a primary line-of-sight path of the THz beam. Only direct line of sight, once- and twice-reflected beams should be utilized; (b) dielectric mirrors improve indoor THz communications by increasing the reflectivity of the walls and ceiling for non-line-of-sight links; (c) interference (ISI) among the various beam paths limits the maximum data rate; and (d) lastly, high-gain and ‘smart’ steerable THz antennas are needed to switch between different link paths to minimum ISI and achieve multigiga-bit operation.

Some of the predictions of the simulations have been tested under laboratory conditions.⁴⁴ For example, it is shown that as an object partially blocks the THz line-of-sight beam, the interference between the direct and diffracted THz beams seriously deteriorates the signal-to-noise ratio. Consequently, fast switching from a direct line-of-sight to an alternative bounced path is essential even for marginal obstruction of the line-of-sight path. Severe loss penalties are observed if the transmitter and receiver antennas are misaligned, supporting the modeling requirement for highly directive and accurately aligned antennas. Experimental measurements, mimicking a mobile device on a desktop connected wirelessly to a fixed access point in the middle of a room, show that once- and twice-reflected THz beam paths can be utilized for communication links albeit at the cost of higher attenuation with reflected paths compared to direct line-of-site.

6.4.2 Satellite-to-satellite/satellite-to-ground

The attenuation of THz radiation is a function of altitude and temperature. At higher altitudes, the humidity decreases leading to a large increase in the maximum distance for THz communication.

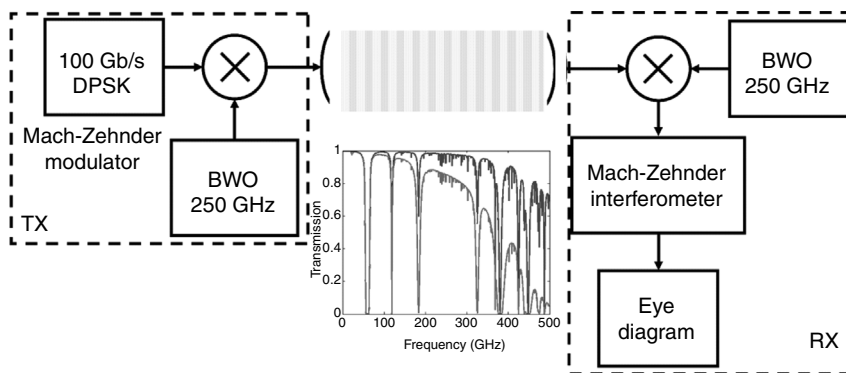
Figure 6.4 illustrates the predicted channel capacity as a function of frequency for a link from the ground to an aerial vehicle at 5 km altitude (from H. B. Wallace²⁰). The model assumes a linear channel which is distorted by white Gaussian noise and atmospheric absorption. It calculates the channel capacity based on the Shannon-Hartley theorem and the system parameters are shown in the legend of Fig. 6.4. Three cases are compared: (a) the channel bandwidth is fixed at 100 MHz (dotted curve), and (b) the channel bandwidth equals 10% of the carrier frequency (solid curve). In both cases signal propagation under vacuum conditions (no absorption) is assumed. To visualize the atmospheric effects on the communication link, it is assumed in case (c) the channel bandwidth to be again 10% of the carrier frequency but also moderate rain with 4 mm/h precipitation across the signal-propagation path. Due to strong attenuation at higher THz frequencies, the effective



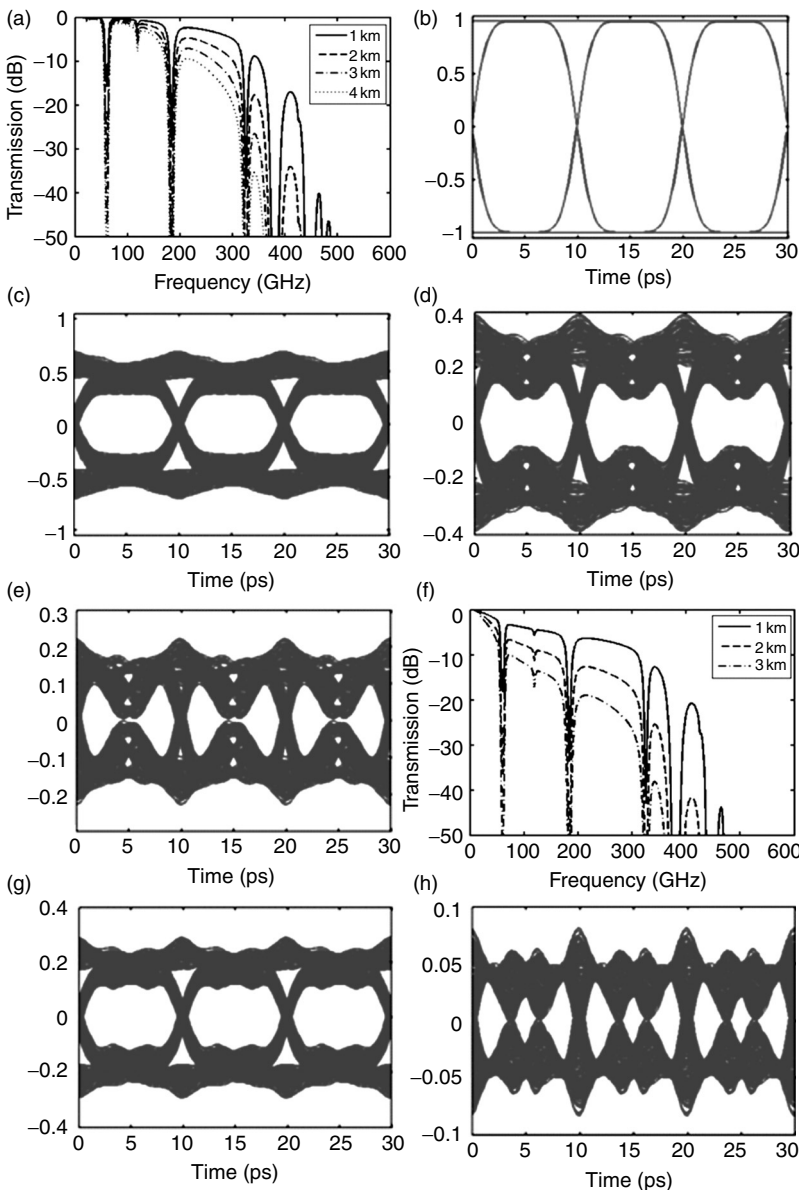
6.4 Channel capacity versus frequency for a link between the ground and an airborne vehicle at 5 km altitude. The communications channel follows a line-of-sight path from the ground to the vehicle at an angle of 30° relative to the horizontal. The dotted line corresponds to a fixed bandwidth of 100 MHz, the solid line corresponds to a 10% bandwidth in vacuum, while the dashed line corresponds to 10% bandwidth in rain at a rate of 4 mm/h. For this calculation, the transmitter power is assumed to be 0.5 W. The diameter of both the transmitter and receiver antennas is 7.5 cm, the noise figure is 8 dB, and the antenna loss is 3 dB. (Reprinted with permission from J. Federici and L. Moeller, 'Review of terahertz and subterahertz wireless communications', *J. Appl. Phys.* **107**, 111101 (2010). ©2010, American Institute of Physics.)

channel capacity is reduced. Above about 500 GHz the channel capacity drops sharply about five orders of magnitude. From this one can conclude that ultra-high capacity channels (>10 Gb/s) with transmission distances of over several kilometers have to operate in the frequency range between approximately 100 and 300 GHz.

As an example of how humidity and other weather conditions affect THz systems, a communication link operating around 250 GHz (Fig. 6.5) was theoretically modeled by H. B. Wallace.²⁰ As illustrated in the figure inset, 250 GHz was chosen because it is roughly in the middle of the 200–300 GHz atmospheric transmission window. A 100 Gb/s DPSK signal was encoded on the 250 GHz carrier on the transmitter side by means of a Mach-Zehnder modulator, driving in push–pull operation. The sub-THz signal propagated through a channel whose water content can be varied. The inlay in Fig. 6.5 shows qualitatively the impact of humidity on the transmission band. Clearly, the channel attenuation increased but also the passband was tilted with increasing water content. The resulting bandwidth limitation caused significant distortions which we visualized by simulating the baseband eye diagram of the received signal (Fig. 6.6). The baseband signal was generated by down mixing the received signal and launching it through a Mach-Zehnder interferometer to convert its phase coding into an amplitude modulation. In the first case, we assumed standard weather conditions and plotted the eye diagram for back-to-back, 1 km, 2 km, and 3 km transmission distances (Fig. 6.6b–e). To highlight the impairment by channel bandwidth reduction, we normalized the received signal power (no attenuation by absorption). After about 3 km the eye diagram was completely closed, preventing high quality



6.5 Simulating distortions to eye diagrams from atmospheric attenuation. (BWO – backward wave oscillator, TX – transmitter, RX – receiver, DPSK – differential phase shift keying.) (Reprinted with permission from J. Federici and L. Moeller, 'Review of terahertz and subterahertz wireless communications', *J. Appl. Phys.* **107**, 111101 (2010). ©2010, American Institute of Physics.)



6.6 (a) Simulated transmission as a function of frequency and link distance for standard weather conditions. Simulated eye diagrams for transmission distances of (b) 0 km, (c) 1 km, (d) 2 km and (e) 3 km. Equivalent transmission (f) and eye diagrams for rain at a rate of 4 mm/h at link distances of (g) 1 km and (h) 2 km. For panels (b)–(e), (g) and (h), the y-axis represents THz signal (a.u.). (Reprinted with permission from J. Federici and L. Moeller, ‘Review of terahertz and subterahertz wireless communications’, *J. Appl. Phys.* **107**, 111101 (2010). ©2010, American Institute of Physics.)

data communication. In the second case (Fig. 6.6f–h) rain at a rate of 4 mm/h was assumed across the free-space propagation area. As expected the impairments were even stronger than in the case of standard weather conditions. The eye diagram was already completely closed after 2 km transmission. This simulation shows that weather conditions have to be considered during the system design. To mitigate eye distortions, it could be better to split the 100 Gb/s data load onto ten 10 Gb/s channels which are frequency spaced. Another alternative could be to apply more bandwidth efficient modulation formats for example, quadrature phase shift keying (QPSK) or signal equalization on the receiver side.

6.4.3 Covert battlefield

Several papers in the THz scientific literature – whether they discuss THz sources, detectors, components, or communication – typically motivate their work by rightfully claiming that THz can be used for ‘secure’ communications. Scenarios for secure links might include stealthy short-distance communications between vehicles (manned or unmanned) and personnel. Unmanned vehicles may require short-distance secure and protected communications links so that they can receive instructions/transmit data before dispersing to conduct their remote controlled or autonomous mission. In order for the link to be secure, unauthorized personnel should not be able to identify either the data via eavesdropping on communication channels or the presence of a communication link.

A major driving force within the United States Department of Defense (DOD) for secure wireless THz communications may result from plans⁹ for broadband mobile-on-the-move technologies using both terrestrial and satellite units. DOD expects that its requirements beyond 2014 will be driven by a transition to wideband networks. This shift in technology mirrors the DOD’s desire to shift from a manual spectrum management plan to an autonomous electromagnetic spectrum management regime. Beyond 2014, DOD’s spectrum use will be driven by the transition to Wideband Network Waveform (WNW) wireless networks that contribute to DOD’s Network Centric Warfare model. Through such new technology, DOD plans a combat system that can link ground, maritime, aeronautical and space operations with layered redundancy, constant connectivity and situational awareness. Clearly for such a system high bandwidth and secure communications are essential. As part of a complete system, THz communication links could provide both of these important features.

Some of the characteristics of THz systems which enable them to operate as secure communication links are (a) highly directional beams compared to microwave communications at the same transmitter aperture; (b) less scattering of radiation compared to IR wireless; (c) limited propagation

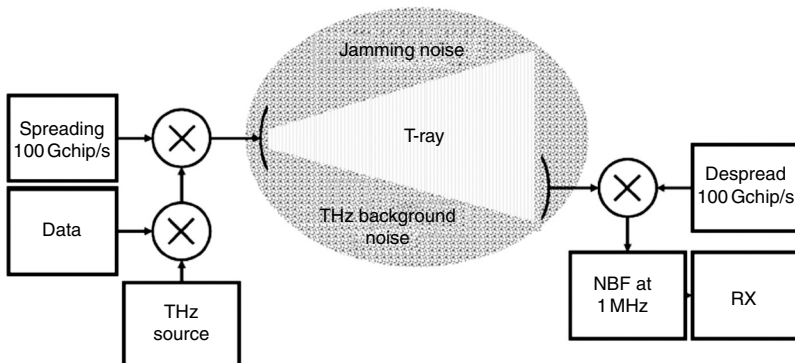
distance due to atmospheric attenuation; (d) large channel bandwidth for spread spectrum techniques which enable anti-jamming and low probability of detection systems; and (e) hidden THz signals in the background noise.

Since the frequency of THz radiation is larger than that of microwaves, beams of THz radiation will diffract less during free-space propagation. Consequently, as discussed previously, THz communication is typically line-of-sight. Since the THz communication beams are highly directional, it is possible to minimize the area over which THz radiation can be detected. Microwave wireless communication is less directional; the side-lobes of microwave radiation could be more easily detected by unauthorized personnel. On the other extreme of frequency, IR wireless communications are more highly directional than THz due to the higher carrier frequency and smaller potential beam diameter. However, IR radiation is more easily scattered by airborne particles. Scattered IR radiation from airborne particles could be detected thereby compromising the communication channel.

Intrinsic atmospheric attenuation of THz radiation, while limiting the maximum distance for wireless communications, could also be a benefit for secure links. Atmospheric absorption controls signal spreading and limits the detection range. Attenuation in the IR band (5–7 microns) can be used for secure communications.¹⁷ For short distances, data transmission to the intended target detector can be facilitated since the radiation is highly directional. However, the link is secure over longer distances as the radiation is absorbed by the atmosphere. Similarly for THz radiation, outside of a limited propagation distance the THz radiation is difficult to detect. The communication of such systems can be limited by absorption to certain geographic areas, thus it will be much more difficult to detect and intercept the signals outside of these areas by eavesdropping even when the system is running in a broadcasting mode.

In addition to the intrinsic propagation properties that enable THz ‘secure’ communication, the technological advantage of an ultra-wide-bandwidth communication system can reduce an adversary’s chances for successful attacks on a secure link. For example, the large channel bandwidth of THz systems allows for specific protection measures for channels against various standoff attacks such as jamming. In a recent review, Federici and Moeller²⁰ proposed a novel form of secure THz communication: an ultra-wide bandwidth THz channel allowing for low probability of detection communication such that the communication links could in principle be completely hidden, so that a third party would not even notice a signal exchange.

As an example, consider a THz link centered at 240 GHz which can utilize the entire ~100 GHz bandwidth in this atmospheric transparency window. Spreading the data throughout the 100 GHz bandwidth makes the system difficult to jam, because an adversary would need to generate high power to overwhelm the THz receiver. The key to this anti-jamming technique is to



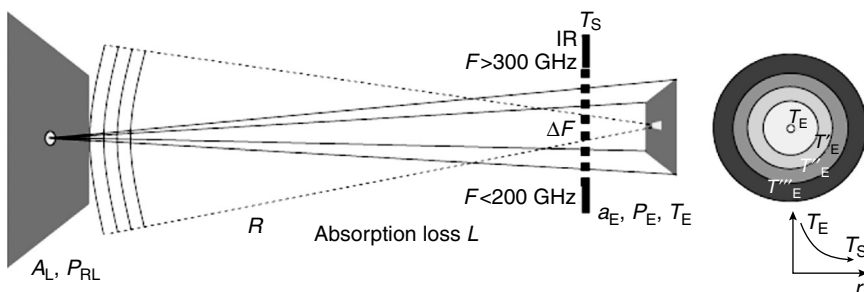
6.7 Schematic of hidden THz communication link utilizing ultra-wide THz bandwidth. The spreading factor is 10^5 (100 Gb/s: 1 Mb/s). (T-ray – THz radiation, NBF – noise band filter, RX – receiver.) (Reprinted with permission from J. Federici and L. Moeller, 'Review of terahertz and subterahertz wireless communications', *J. Appl. Phys.* **107**, 111101 (2010). ©2010, American Institute of Physics.)

spread the data throughout the available THz bandwidth using high-speed modulators and demodulators. While it will take still some time before ultra-wide bandwidth modulators and demodulators for THz signaling are available, technology for designing multiplexers and de-multiplexers to perform logic data processing at 100 Gb/s already exists for ultra-high-speed fiber communication at $1.5 \mu\text{m}$ wavelengths. Figure 6.7 illustrates the operational principle of the frequency spreading system. A 1 Mb/s data signal, modulated on a carrier of a THz source, is encrypted using a long code sequence at a chip rate of 100 Gb/s. A signal from a jamming attack that does not carry the correct codeword but possesses the right carrier frequency and chip rate will get further spectrally broadened in the decoder by approximately a factor of $\sqrt{2}$ depending on the chosen modulation format. Assuming that the transmitter signal is perfectly deconvoluted and has a spectral efficiency of about 1 bit/s/Hz, then narrow bandwidth post filtering at the decoder output results in a rejection ratio for jamming attacks of about 40 dB, that is, a potential jammer must possess a technology advantage allowing for building sources that output several orders of magnitude and more power in order to prevent communication. However, it will probably be extremely challenging to modulate 100 Gb/s data signals on a carrier at 240 GHz due to the required unusually high bandwidth-to-carrier-frequency ratios.

As an example of the frequency spreading, consider a broadcast configuration in which the THz signal is emitted at a power level of -14 dBm (which can be reached, for example, with an integrated multiplied microwave source), and intensity-wise evenly radiated across an area of 10 km^2 size. A receiver antenna with an effective aperture of 1 m^2 would collect

about -104 dBm power. This level is sufficient to detect the data at high quality if the decoding can be assumed to be lossless and a 20 dB link margin can account for atmospheric propagation losses. A 20 dB power margin to compensate for coding and decoding losses can be achieved by increasing the emitter power to about 4 mW. In principle, the receiver noise is limited by the thermal noise of the antenna. At room temperature and a signal bandwidth of $\Delta B_{\text{sig}} \sim 1$ MHz, the antenna noise after narrow bandwidth filtering accumulates to $N_o = K_B T \Delta B_{\text{sig}} = 4fW$ leading to a signal-to-noise ratio of approximately 10 dB. If a loop finder, used to locate a hidden sender, is steering directly in the direction of the emitter but does not have the right code sequence to decode the signal then it would measure the emitted signal as a slightly enhanced antenna noise. More quantitatively, the detected ultra-wide bandwidth signal would appear as an antenna temperature enhancement of $\Delta T \sim -104$ dBm/ $(K_B \cdot 100 \text{ GHz}) \sim 30$ mK.

Although this amount is very small compared to possible natural environmental sources, the signal spectrum could in principle be completely hidden in the thermal noise by using ‘channel cooling’ (Fig. 6.8). The aperture of the THz emitter is surrounded by a mounted cooled plate and radiates into the area where a receiver and a possible loop finder is located. It can be shown that if the loop finder were far enough, such that its spatial resolution is not high enough to selectively detect the emitter aperture and the cooled plate, it would measure only an average antenna noise that could be chosen to be adjusted to the environment level. Hence, the emitter would be in its active frequency range spectrally invisible. This example is just intended to illustrate the main idea behind ‘channel cooling’ for concealing



6.8 Channel cooling together with spread spectrum techniques result in a spectrally invisible emitter. (A_L – area of the loop finder, P_{RL} – arriving power at loop finder, T_S – temperature of the cooled shield plate, a_E – effective area of emitter, P_E – power emitted by emitter, T_E – equivalent emitter temperature, ΔF – the frequency band over which energy of transmission is spread, R – distance to loop finder.) (Reprinted with permission from J. Federici and L. Moeller, ‘Review of terahertz and subterahertz wireless communications’, *J. Appl. Phys.* **107**, 111101 (2010). ©2010, American Institute of Physics.)

the emitter. The amount of cooling depends on several system parameters like, distance, plate size, received power, apertures of the loop finder and emitter. However, we expect that under assumption of reasonable system parameters, a cooling of a few degrees Kelvin for a plate with size comparable to the emitter aperture is sufficient to hide the sender.

6.5 Hardware for terahertz communications: sources and detectors

In this section, the basic hardware for THz communications links including methods of THz generation, THz detection, and modulation are described. Four types of source and detector hardware will be discussed: opto-electronic, THz integrated circuits, multiplied microwave components, and quantum cascade lasers.

6.5.1 Opto-electronic

Using opto-electronic generation (Chapter 1 and Reference 45), one has a variety of options to convert beat frequencies from visible/near-infrared laser beams to THz signals including via photodetection (e.g., uni-traveling carrier photodetector (UTC-PD), comb frequency generators (Chapter 15)), continuous-wave (CW) photomixing (Chapter 11), and of course time-domain THz generation. Since opto-electronic THz sources are extensively covered in other chapters, we focus only on issues that are relevant for THz communications. This section highlights THz generation by ultrafast pulsed lasers, rectification in fast photodiodes (eg. UTC-PD and optical frequency comb generators), and CW photomixing.

One of the older methods for the generation and detection of THz radiation utilizes photoconductive antenna structures (Chapter 1), used extensively in THz time-domain spectroscopy (THz-TDS).⁴⁶ The technology has been sufficiently developed so that photoconductive THz sources and detectors, as well as CW photomixers, are commercially available from companies such as Toptica Photonics and GigaOptics. Related to the photoconductive antenna structures for THz-TDS are CW photomixers for THz radiation (Chapter 16, and References 47 and 48). In the literature, photomixing is sometimes called optical heterodyne conversion in a photoconductive switch. In the photomixing process, two co-linear optical or near-infrared beams illuminate the photomixing structure. The two beams are typically narrow optical bandwidth laser sources which are frequency stabilized. The photomixing process produces a THz beam at the difference frequency of the two laser beams. The THz frequency is adjusted by tuning the difference frequency of the two infrared laser sources. Whereas the time-domain method produces a THz pulse that is spectrally broad, the CW

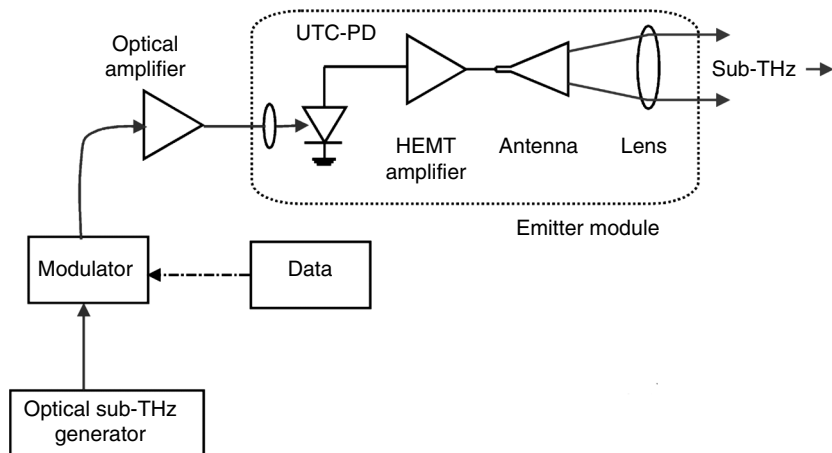
mixing method generates a narrowband THz signal which is typically limited by the linewidth of the lasers to roughly 1–2 MHz.

As described in the scientific literature, THz detection methods typically are intimately linked to the THz generation method. For example, systems in which the THz is generated opto-electronically, as in THz time-domain or CW photomixing, use the same physical principles as well as laser sources to detect the THz radiation. Systems in which THz is generated by frequency multiplied microwave sources are typically detected using the same or similar microwave components. However, this is not necessarily the case. For example, Loffler *et al.*⁴⁹ used a multiplied Gunn emitter as the 0.6 THz source and a mode-locked Ti:Sapphire laser in conjunction with a ZnTe crystal for electro-optic detection of the THz radiation. Su *et al.*⁵⁰ demonstrated detection of a 94 GHz millimeter-wave source using CW THz photomixer detectors, while THz radiation from photonics based UTC-PD generators have been detected with a variety of modalities.

A detailed description of microwave and millimeter-wave generation by optical comb techniques can be found in Chapter 15. An optical frequency comb refers to the optical spectrum of a pulse train. Typically the pulse train is generated either by a pulsed mode-locked laser system or by modulation of a continuous laser beam. Ideally, the spectrum consists of a set of discrete frequencies which are separated in frequency by a stable pulse repetition rate. When the optical frequency comb illuminates a high-speed photodiode detector, the optical signal is converted to an electronic (i.e., terahertz) output signal within the electronic bandwidth of the photodiode detector. The electrical output is produced at the frequency interval of the comb and its harmonics. A key feature of the high-speed detector is that it must have an electronic bandwidth in the THz range.

Over the past dozen years, the unidirectional-carrier photodiode (UTC-PD) has emerged as a viable high-bandwidth device for optical generation of MMW and sub-THz radiation.⁵¹ UTC-PDs have been developed for both 1.5 micron light using InP/InGaAs^{52,53} as well as 800 nm light using GaAs/AlGaAs.⁵⁴ The UTC-PD is a hetero-junction photodiode with a p-type absorptive region. An electron-hole pair is generated in the absorption layer when a photon is absorbed. The photogenerated electron moves through a non-light-absorbing collection layer and into the n-layer at high velocity. Since the hole carrier moves very slowly in the p-type region due to a diffusion blocking layer, the response of the device – which is in the sub-THz band – is determined by the electron's velocity. Alternative photodiode structures, such as the Separated-Transport Recombination photodiode (STR-PD), have been demonstrated as THz emitters as well.⁵⁵ A recent review of high-power radiofrequency and THz photodiodes can be found in Reference 56.

Variations in the optical frequency comb technique enable the generation of either multiple sub-THz frequencies or single frequencies. For example, a



6.9 Schematic diagram of sub-THz generation using optical frequency comb in combination with a UTC-PD. (Reprinted with permission from J. Federici and L. Moeller, 'Review of terahertz and subterahertz wireless communications', *J. Appl. Phys.* **107**, 111101 (2010). ©2010, American Institute of Physics.)

photomixing geometry can be used. Two single-frequency $1.5\text{ }\mu\text{m}$ lasers beams can be combined, amplified, and then illuminate the UTC-PD to generate tunable THz radiation.^{53,56,57} In another embodiment, by splitting the output of an optical comb frequency generator, one can then use injection-locked lasers to each select out a single optical frequency. By combining and amplifying the two selected frequencies, and then illuminating a UTC-PD, power is generated at the difference frequency of the two optical signals corresponding to an integral multiple of the combs frequency interval.⁵⁸

Using an optical frequency comb in combination with the UTC-PD, the Microsystem Integration and Photonics Laboratories group at NTT Corporation has demonstrated THz data transmission at ~ 120 GHz and more recently in the 300–400 GHz band.^{6,57} The photonic sub-THz emitter⁵⁹ at 120 GHz comprised of an optical comb frequency generator and UTC-PD which converts an optical frequency comb to a sub-THz electrical signal. A schematic of the THz source is shown in Fig. 6.9. The key features of the source are the optical sub-THz generator (the optical frequency comb) and the photonic emitter. The photonic emitter consists of a UTC-PD which converts modulated optical frequencies in the comb to the sub-THz range, an amplifier, and an antenna structure to launch the sub-THz. The NTT group has used various methods⁵⁶ to generate the optical frequency comb.

The output of the UTC-PD can be amplified by a broadband high electron mobility transistor (HEMT) amplifier, while a planar-circuit-to-waveguide substrate transitions the amplified sub-THz signal to an antenna. A high-gain

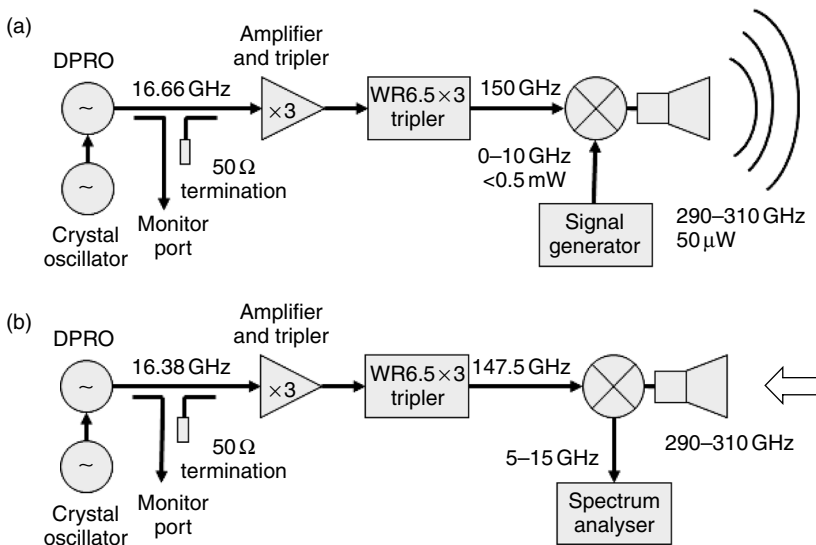
Gaussian optic lens collimates the sub-THz radiation making the photonic emitter highly directional. The HEMT amplifier boosts the sub-THz power that is launched, thereby reducing the input optical power necessary for error-free data transmission. With the HEMT amplifier, the photonic sub-THz emitter delivers approximately 8 dBm of 120 GHz power to the launch antenna.⁵⁹ Using photodiode technologies, the maximum output power which has been demonstrated in the 0.4–1 THz range is about 10 µW. Output power levels approaching 1 mW might be possible⁵⁶ if (a) the limitations in photodiode saturation current and dissipation of thermal energy can be circumvented, (b) optimal and efficient coupling between the photodiode and launch antenna can be realized, and (c) arrays of antennas can be used to combine the THz power from many photodiodes into a more powerful THz source.

Hirata *et al.*'s experiments with 120 GHz sub-THz communication systems used a variety of detection systems including Schottky diodes,⁵⁹ mixers, and all-electronic InP millimeter-wave integrated circuits (MMIC).^{24,60} The MMIC chipset which is used for the all-electronic transmitters and receivers has an on-wafer measured BER (bit error ratio) of 10^{-12} at 11 Gb/s. It is interesting to note that unlike THz time-domain, CW photomixing detection, Jastrow *et al.*'s work^{61,62} in which the THz transmitter and receiver operate on the same physical principles (i.e., PDAs, THz photomixers, or Schottky devices), Hirata *et al.* can use their Schottky diode detectors with a variety of THz sources including optical millimeter-wave sources (e.g., optical frequency comb/UTC-PD). Since the THz source and MMIC receivers are independent of each other, the receiver unit must include a clock recovery circuit.²⁰ Other examples of THz links based on 1.5 µm UTC-PD sources include Reference 63. In that reference, Ducournau *et al.*'s system is similar to that of Hirata's group, except that the THz receiver is based on a microwave frequency multiplier that mixes with the incoming THz signal in a sub-harmonic mixer to produce an intermediate frequency output at 10.3 GHz.

The 300–400 GHz band system⁶ is similar to the 120 GHz system except that the HEMT amplifier is absent, which limits the link distance to ~0.5 m. The receiver is a Schottky Barrier Detector which is mounted on a receiving antenna. Typical output power levels for the UTC-PD optimized for 300–400 GHz are ~110 microwatts for a photocurrent of 10 mA operating at 380 GHz. Higher power levels of up to 400 microwatts are possible if the photocurrent is increased to 20 mA.

6.5.2 Microwave frequency multipliers

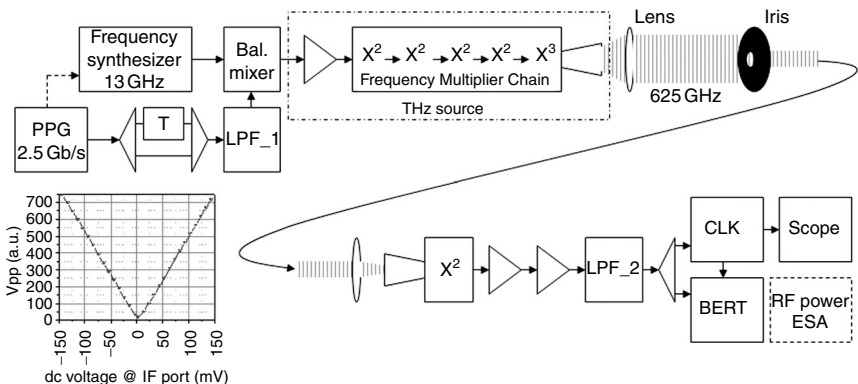
Rather than using optical sources and mixing down the frequency to access the THz range, conceptually one can begin with a lower frequency that is, microwave sources and upconvert the frequency into the THz range. One method of fabricating microwave frequency multipliers is to use Schottky



6.10 Microwave frequency multiplier THz (a) source and (b) receiver from Reference 62 (C. Jastrow, K. Munter, R. Piesiewicz, T. Kurner, M. Koch, and T. Kleine-Ostmann, '300 GHz transmission system', *Electron. Lett.* **44**, 213 (2008), ©IET).

diode based components.⁶⁴ For example, Virginia Diodes Inc. has fabricated autarkic transmitter and receiver units. These transmitter and receiver units (schematic shown in Fig. 6.10) were used by Jastrow *et al.*^{62,65} to demonstrate the feasibility of THz communications. A 16.66 GHz source consisting of a dielectric phase-locked resonator oscillator (DPRO) with a 10 MHz reference crystal oscillator is frequency tripled, amplified, and then tripled again. The resulting 150 GHz signal is combined with a local oscillator (LO) from a DC-10 GHz signal generator in a subharmonic mixer. The subharmonic mixer mixes the second harmonic of the 150 GHz input signal with the 0–10 GHz LO signal. Virginia Diode Inc. uses a symmetrical diode combination to achieve the mixing with high efficiency. This configuration also requires that the input (150 GHz) and output sub-THz signal frequencies differ by a factor of about two, so they can be coupled through different waveguides without the need for a diplexer.⁶⁴ A feedhorn for the sub-THz radiation is directly attached to mixer block. The authors report that the 50 µW of power is launched at 300 GHz. The newest sources from Virginia Diode Inc. produce several milliwatts of power at 300 GHz.

Piesiewicz *et al.* had suggested Schottky diodes as THz heterodyne mixer detectors.¹¹ Applying this concept, Jastrow *et al.*⁶² used a similar design for the microwave multiplier receiver to mix down the incoming THz radiation to an intermediate frequency of 5 GHz (Fig. 6.9). Note that on the receiver side, the



6.11 Schematic of THz transmission link and balanced mixer characteristics at 625 GHz. (PPG – programmable pulse generator, T – phase delay equivalent to the time duration of 1 bit, LPF – low pass filter, CLK – clock, BERT – bit error rate tester, RF – radio frequency, ESA – electrical spectrum analyzer.) (From L. Moeller, J. Federici, and K. Su, ‘2.5 Gbit/s duobinary signalling with narrow bandwidth 0.625 terahertz source’, *Electron. Lett.* **47**(15), 856–858 (2011). ©IET.)

fundamental microwave oscillator is tuned to 16.38 GHz compared to 16.66 GHz on the transmitter. Consequently, the high frequency signal inputted to the Schottky diode subharmonic receiver mixer is 147.5 GHz rather than 150 GHz as in the transmitter. The intermediate frequency from the subharmonic mixer is then $2 \times (150 - 147.5) = 5$ GHz. The factor of two in the calculation results from the fact that the second harmonic of the input is used in the mixing process. While the microwave oscillators for both the transmitter and receiver are freely running independent of each other, their frequencies need to be stabilized such that the intermediate frequency is fixed.

Another approach for a multiplied microwave source for THz communication experiments at 625 GHz has been recently reported.⁶⁶ The transmitter, a commercially available 1 mW (CW operation) source, consists of four cascaded frequency doublers followed by a frequency tripler, all based on biased Schottky diodes, which feed a horn antenna with 2.4 mm aperture (Fig. 6.11). A launched tone within the frequency acceptance band between 12.2 and 13.6 GHz saturates the 2 W input amplifier at about 5 dBm and gets up-converted into a frequency band between 585 and 653 GHz. The receiver horn is connected to a zero biased Schottky diode, which functions in the low power regime (input power <10 µW) as square law detector with large baseband bandwidth and a responsivity of about 2500 V/W. The optimal frequency position of the carrier is 12.933 GHz, corresponding to THz frequency at ~625 GHz and best system performance. On the receiver side the output of a Schottky diode detector is amplified by about 42 dB using two amplifiers (80 kHz – 7 GHz passband, 6 dB noise figure, maximum output

power ~19 dBm) and filtered by a quasi-Gaussian low-pass filter (LPF_2) with 3 GHz 3 dB-bandwidth. A 6 dB electrical power splitter launches one output ($V_{pp} \sim 500$ mV) to a high-speed scope or a bit-error-rate tester (BERT) and the other to a 2.5 Gb/s non-return-to-zero (NRZ) clock recovery circuit that synchronizes the measurement equipment. One advantage of this architecture, compared to Fig. 6.10, is that the data is encoded in the base band, which eliminates the need for a mixer in the THz band and enabling higher output THz power.

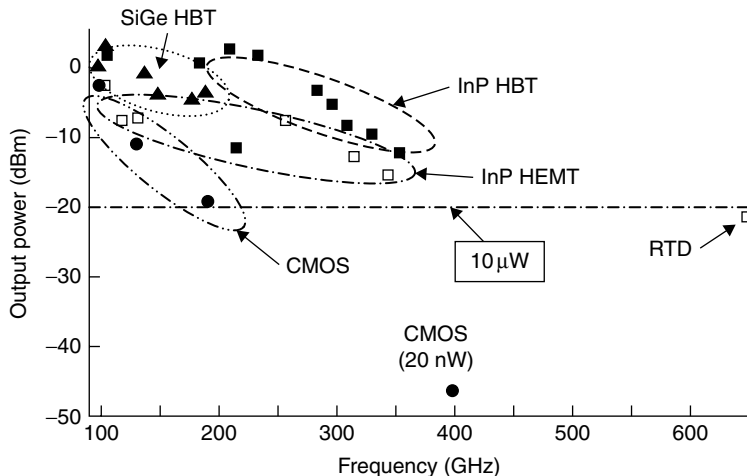
6.5.3 Quantum cascade lasers

Chapter 1, as well as recent reviews,^{67,68} extensively details the operation and development of THz quantum cascade lasers (QCLs). This section will focus on details related to the THz communication. What is clear from the literature is that THz QCLs operating below 1.5 THz and at room temperature will probably not be available in the near future. In fact, THz QCLs require low temperatures (< 40 K) to achieve lasing below 1 THz.⁶⁸ Based on the frequency dependence of the atmosphere (see Fig. 6.2 and Fig. 6.4), one would not expect QCLs to play a significant role in terrestrially-based THz communication components (except perhaps as a LO for a heterodyne receiver) since the expected frequency of a THz system would be ~300 GHz. However, QCL satellite-to-satellite communication systems might be possible due to the reduced atmospheric attenuation of THz beams. One should also note that limited THz communication demonstrations have been performed with 3.8 THz QCLs.⁶⁹

6.5.4 THz integrated circuits

Compared to opto-electronic sources, which can require sophisticated lasers and sensitive optical alignment, and microwave multiplier sources, which use delicate Schottky diode components, the concept of using a robust, solid-state integrated circuit as a THz source or detector is alluring. The progress in the development of THz semiconductor-based oscillator integrated circuits has been dramatic.^{4,6} Figure 6.12 shows the output power versus frequency for several semiconductor-based integrated circuits. The 10 μ W power level is highlighted as a typical minimum required power level for indoor communications.⁶ Outdoor systems will probably require 10 to 100 times more power to overcome atmospheric attenuation.

Figure 6.12 shows that InP technology is further advanced compared to SiGe and CMOS approaches in regards to high power levels in the ~300 GHz frequency range which is expected for terrestrial THz communication. Resonant tunneling diodes (RTDs) could also be competitive if their output power were increased. Most of the THz communications measurements



6.12 Comparison of output power versus frequency from several semiconductor-based integrated circuits. (PPG – programmable pulse generator, T – phase delay equivalent to the time duration of 1 bit, LPF – low pass filter, CLK – clock, BERT – bit error rate tester, RF – radio frequency, ESA – electrical spectrum analyzer.) (From T. Kleine-Ostmann and T. Nagatsuma, 'A review on terahertz communications research', *J. Infrared, Millimeter, and THz Waves*, 2011. **32**: 143–171. © 2011, Springer Science and Business Media, LLC. With kind permission from Springer Science and Business Media.)

performed to date (Section 6.8) have used microwave mixers and opto-electronic generation rather than THz integrated circuits. This in part is due to the fact that the required compact components for communication systems (like planar integrated circuits, amplifiers and antenna arrays), while actively under development, generally do not exist above 125 GHz. The exceptions are integrated millimeter-wave integrated circuit (MMIC) chip sets which have been developed at 125 GHz and utilized in a 10 Gb/s 800 m long wireless link experiment.²⁴ Recent technological progress in key technologies such as SiGe, BiCMOS, and InP suggests THz integrated circuits for communication will be available in a few years. For example, simple components like integrated voltage-controlled oscillators were demonstrated by Bell Labs in InP heterojunction bipolar transistor (HBT) technology with output power of -5 dBm at 350 GHz. Likely, fully electronic THz communications systems running at carrier frequencies of a few 100 GHz will become reality in the near future when sufficiently fast and powerful integrated circuit electronics are available.

6.6 Modulators for terahertz waves

In order to encode a THz carrier with data, clearly some sort of modulation scheme is required. The modulation scheme could either be a direct

modulation of a THz source, which is intimately tied to its operational principles, or an external modulator which in principle could be used on a variety of THz sources. This section briefly reviews a variety of modulation methods that can impress arbitrary bit patterns on THz carrier. First, modulator schemes that are specific to a particular method of THz generation are treated. Second, modulator methods that are independent of the particular choice of a THz source are reviewed. In addition to wireless communication, data modulation on THz signals could find application in sensing. When imprinting code sequences on pulse trains, ranging information from far distance scattering objects can be obtained to define selective measurement intervals. This technique is known from M-sequence radar where digital beam modulation enhances the system's unambiguous range.^{70,71}

6.6.1 THz generator specific modulation schemes

One method for directly modulating the THz beam from a photoconductive THz antenna is to directly modulate the bias voltage that is applied to the device.^{72,73} Since the generated THz field is directly proportional to the applied voltage across the photoconductive gap in these devices, a modulation of the applied voltage directly modulates the output power of the THz source. Modulation at rates of ~1 MHz and with 100% depth of modulation have been demonstrated with this method.⁷² The data rate in these types of modulation experiments, however, is limited to the detection bandwidth of the photoconductive THz detectors to ~1 MHz. An alternative method for modulating CW THz beams, which are generated by the optical mixing of two infrared beams in a photoconductive THz antenna, is to modulate the phase (or amplitude) of one of the infrared beams.⁷⁴ For this method, the phase (or amplitude) of one of the infrared beams is modulated at high speeds using a lithium niobate modulator. Moreover, arbitrary waveforms or bit patterns can be generated by applying the appropriate voltage waveform to the Lithium Niobate modulator. Since the speed of such modulators can be as high as the gigahertz range, one can in principle generate multi-Gb/s data patterns with this method. The current limitation with this method arises from the bandwidth of the photoconductive THz receivers.

For CW photomixing, the phase modulation of the THz beam depends on the phase difference modulations of the two infrared beams which mix to generate the THz beam. If both beams were phase modulated in unison, there would be no phase shift imposed on the THz beam. Consequently, for the CW photomixer modulation described in Reference 74, the phase of only one of the infrared beams that generates the THz radiation is modulated. The detection of THz by CW photomixers is a phase sensitive measurement: the output of the mixer depends on the relative phase between an incoming THz and the two infrared beams which act as a LO for the

mixer. Consequently, the signal from the photomixer not only depends on the amplitude of the THz signal, but also on the phase of the incoming THz signal, which could be altered due to a changing separation between the THz transmitter and receiver. If the phase of the THz beam were unimportant, alternatively one could amplitude modulate one or both of the optical beams. This approach of amplitude modulating the optical beams is used to data encode the optical frequency comb/UTC-PD THz generator (Section 6.5.1). As illustrated in Fig. 6.13, the optical frequency comb is modulated by data signals via a lithium niobate modulator and then amplified by a second erbium doped fiber amplifier.⁷⁵

Direct modulation of a 2.8 THz QCL has been achieved by modulating the bias voltage of the lasers double-metal waveguide. Continuously tunable modulations rates up to 13 GHz are demonstrated by the appearance of multiple gigahertz sidebands in the QCL's emission spectrum.⁷⁶

6.6.2 Schottky diode mixer systems

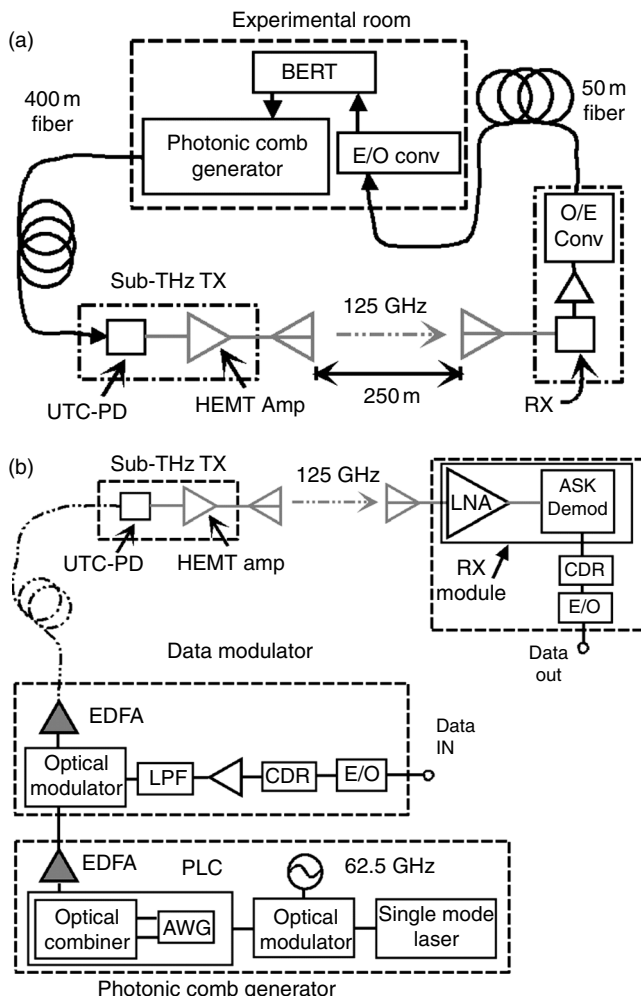
Improvements to Schottky mixer technology have enabled electronic modulation of THz carrier signals. As illustrated in Fig. 6.10, the modulated data can be introduced through the intermediate frequency port of the mixer (labeled signal generator in the figure). The modulator method used by Jastrow *et al.*⁶² to both modulate and detect the frequency multiplied microwave sources is based on GaAs Schottky barrier diodes⁶⁴ as the nonlinear elements in the THz frequency mixers and multipliers. Crowe *et al.* attribute the success of these THz components to three areas of technological innovation:

- The development of advanced fabrication technologies enabling precise fabrication of terahertz diodes and integrated diode circuits.
- The use of advanced computer aided design tools to simulate and optimize both the linear and nonlinear portions of the circuit.
- The development of innovative circuit designs. In particular, the inclusion of planar diodes enables the removal of the whisker-contact, which is by far the most difficult and irreproducible part of the component assembly.

Planar diode chips enable the integration of multiple diodes in the circuit design incorporating more complicated circuit designs and higher power throughput. Moreover, the planar diodes enable the circuits to operate over an entire waveguide band eliminating the need for mechanical tuning.

6.6.3 THz generator independent modulation schemes

Several approaches for external THz modulators have been discussed⁷⁷ including acousto-optic,⁷⁸ ferroelectric materials, liquid crystals,^{79,80} and optically



6.13 (a) Schematic of experimental set-up for outdoor data communication (adapted from Reference 60). (b) Details of the various subsystems (adapted from Reference 60). (E/O – electrical to optical conversion, O/E – optical to electrical conversion, LNA – linear amplifier, ASK – amplitude-shift keying, CDR – clock and data recovery unit, EDFA – erbium doped fiber amplifier, PLC – planar lightwave circuit, AWG – array waveguide grating.) (Reprinted with permission from J. Federici and L. Moeller, 'Review of terahertz and subterahertz wireless communications', *J. Appl. Phys.* **107**, 111101 (2010). ©2010, American Institute of Physics.)

or electronically free carriers in semiconductor structures.^{81,82} Optically or electrically driven external intensity and phase modulators based on active metamaterials have been demonstrated.⁸³ However, all of these methods show limited carrier frequency, modulation bandwidth or modulation index.

Several THz modulators are based on the absorption of THz radiation by either optically or electrically injected free carriers. Encoding of data on the THz beam is achieved by controllably modulating the free-carrier concentration in the device. One approach for the direct modulation of THz radiation was demonstrated⁸¹ using an optically controlled mixed type-I/type-II GaAs/AlAs multiple quantum well structure. The long photocarrier lifetimes (0.91 ms) in the structure enables sizeable photoinduced carrier densities for low optical pumping power. When the device is illuminated with visible or near-infrared light, the increase in free-carrier density results in absorption of THz radiation, which passes through the sample. The device requires low (40 K) temperatures for operation and does not exhibit better than a 72% reduction in THz transmission upon illumination.

Another electronic modulator, but one that still required low operating temperatures, utilized five identical parabolic quantum wells with equally spaced electron sub-bands.⁸² An applied electric field was used to control the electron occupation of the quantum wells and thus the THz absorption of the low temperature device. Room temperature operation of an electrically driven THz modulator was achieved by confining a 2-dimensional electron gas at a GaAs/AlGaAs heterointerface.⁸⁴ Using fabrication technology for producing HEMTs, the electron density of the electron gas can be controlled by the application of an external gate voltage. Unfortunately, the maximum depth of modulation for the device was only 3%. The data rate of the modulation was ~10 kHz.

A silicon waveguide has also been used as a THz modulator. The waveguide is coated with optically transparent films enabling illumination of the waveguide and optical injection of free carriers in the waveguide to modulate THz transmission. The waveguide required 240 mW of average power at 980 nm to achieve 70% modulation.⁸⁵ Further improvements to an optically injected free-carrier absorption THz modulator can be achieved by integrating the nonlinear element (e.g., the photodoping region) into a photonic bandgap or metamaterial structure.⁷⁷ A photonic bandgap or metamaterial structure – for example fabricated by alternating layers of high and low refractive index – exhibits spectral bands of high or low photonic transmission. The introduction of a nonlinear layer into the otherwise repetitive structure has two effects: (a) introduction of a defect mode by breaking the periodicity of the photonic crystal structure, and (b) potentially strong enhancement of the optical nonlinearity of the defect layer due to high localization of the electric field at the defect mode frequency. One structure constructed from alternating layers of crystalline SiO₂ and MgO with a semi-insulating GaAs wafer as a defect layer exhibited a 600 GHz defect band with a full width half maximum (FWHM) bandwidth of 5–16 GHz. The authors measured the free electron lifetime in the GaAs to be 170 ps. Based on this lifetime, they estimate a maximum switching rate (by optical

illumination) to be 5 GHz. They estimate a 50% amplitude modulation corresponding to a 10^{15} – 10^{16} cm³ concentration of optically induced carriers in a 1 micron thick photoexcited layer. While no experimental results verifying these predictions were presented, a low speed, optically switchable metamaterial has been demonstrated, as discussed below.

6.6.4 Modulators for THz beam shaping and steering

While data encoding of THz beams for communication will require modulators which operate in the GHz range, lower speed modulators will be important for THz beam shaping and manipulation in THz communication links. A simple example could be a dynamically controllable THz lens which is activated by mechanically pumping THz transparent liquid into an inflatable lens enclosure to change its focal length.⁸⁶ Liquid crystals, as another practical example, can be used for slow switching applications,^{79,80,87} such as electronically controllable beam shaping and steering. For example, THz liquid crystals with 2π radian phase shifts have been demonstrated. Wilk *et al.* have demonstrated an electrically switchable Bragg structure using liquid crystal layers.⁸⁸ The structure can function as both a stop-band filter and a mirror. By controlling the orientation of the liquid crystals with an applied voltage, a 60 GHz wide stop-band around 300 GHz can be programmatically removed or inserted.

Active and dynamic metamaterials components (Reference 89) also show promise as THz modulators. A viable approach for metamaterial modulators is to dynamically alter either the embedded resonator elements themselves or the surrounding substrate material via a thermal, optical, electronic, or magnetic external stimulus. Thermally tunable metamaterials are fabricated with materials such as ferroelectrics whose permittivity in the THz range depend on temperature.⁸⁹ The shortest switching times have been demonstrated using short-pulsed optical stimuli. For these devices, optical pulses generate photocarriers in the metamaterial structures which change their transmission properties. In principle, the optical switching of THz metamaterials can be as short as 20 ps.⁹⁰ While this switching time could be applicable to data encoding of the THz beam, the cost, complexity, and size requirements of the short-pulse optical systems will restrict the adaption of this approach as a practical high-speed modulator. Thus, electronically switchable metamaterials are quite attractive⁸⁹ especially for beam shaping, steering, and spectral filtering in THz communication systems, rather than modulators for data encoding of the THz beam.

One example for a metamaterial structure of an electronically controllable THz modulator is based on a 2-dimensional split ring resonator (SRR) structure.⁹¹ The resonators are fabricated on a 1 micron thick epitaxial layer of n-doped GaAs. The SRR and GaAs layer form a Schottky diode structure.

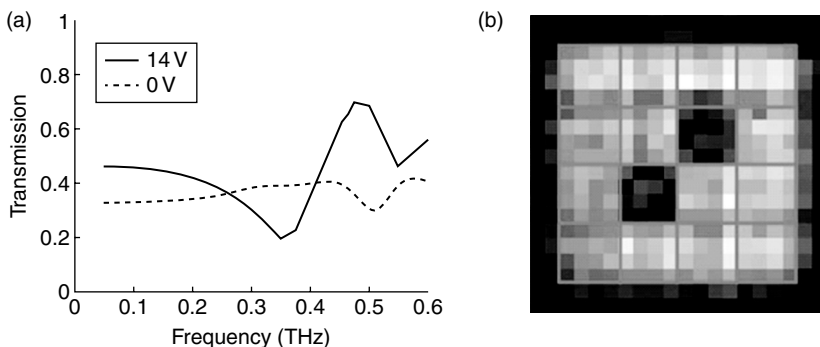
The application of a voltage to the diode structure modifies the free-carrier concentration in the depletion zone and consequently varies the tuning of the dielectric properties near the optical bandgaps of the SRRs, resulting in a voltage-controlled change in the THz transmission. At zero voltage bias the photonic bandgap THz transmission resonances are weak because the intrinsic free carriers shunt the metamaterial's capacitive gaps, leading to relatively small THz absorption at resonance. When a reverse bias voltage is applied to the device, the depletion region increases in size, thereby causing an enhancement in oscillator strength, and THz absorbance, for both resonances. The modulation characteristics of the metamaterial structure are complicated by the fact that the change in transmission amplitude and phase are strongly frequency dependent. If this metamaterial modulator were used for a modulator in a THz communication system, in general *both* the phase and amplitude of the THz signal would be modulated. The maximum transmission intensity change in the device is 80% while the maximum modulation rate is approximately 2 MHz.

An external, electrically driven active metamaterials modulator for 2.4 THz and 2.8 THz QCLs has been designed, fabricated and characterized. Modulation is achieved by applying a voltage to the metamaterial layer, which changes the attenuation and frequency location of the metamaterial response by actively displacing carriers from the n-doped layer. A maximum modulation depth of 60% with a large degree of modulation linearity is demonstrated.⁹² While the modulation speed of the device was not measured, it is expected to be in the MHz range.

An example of a spatial light modulator⁹³ which demonstrates the future potential for THz beam shaping by electronically programmable metamaterials is shown in Fig. 6.14. The modulator is a 4×4 pixel array in where each pixel is an individually addressable SRR metamaterial. The transmission modulation depth is roughly 40% at 0.36 THz. Figure 6.14b illustrates the ability to selectively turn on/off pixels to spatially control a THz beam. In addition to electronic switching of metamaterial structures, micro-electro mechanical systems (MEMS) technology has been utilized to demonstrate reconfigurable THz metamaterials. As an example, MEMS structures enable a programmable change in the orientation of SRR within the unit cell for tunable structures.⁸⁹

6.7 Modulation formats for terahertz signals

Early demonstrations of THz communication links employed only simple modulation formats (amplitude modulation). But it can be expected that THz communication will follow a similar path to that of radio communication, that is, more advanced modulation formats, for example, FM (frequency modulation) or QAM (quadrature amplitude modulation), will be



6.14 (a) Measured THz transmission spectra for one of sixteen pixels from a spatial light modulator with 0 and 14 V applied bias. (b) THz transmission image at 0.36 THz with two pixels turned off while the rest are on. (From W. L. Chan, H.-T. Chen, A. J. Taylor, I. Brener, M. J. Cich, and D. M. Mittleman, 'A spatial light modulator for terahertz beams', *Appl. Phys. Lett.* **94**, 213511 (2009). ©American Institute of Physics.)

applied to achieve modulation gain, or a higher spectral efficiency and less dispersion penalties. The advantages of such more complex modulation formats are known and the challenges reside in the realization of the required modulator hardware.

Several approaches for THz communications which are discussed in Section 6.6 show the progress in device design towards higher modulation rates. However, to simultaneously obtain high output power and large transmitter bandwidth at high carrier frequency remains in general challenging. But often THz sources are operating in resonance to efficiently generate output power which can reduce their effective bandwidth to a few hundreds of MHz. Thus when using narrow bandwidth signals that spectrally pass through the source, both goals – high output power and high data rate – can be simultaneously achieved.

One approach⁶⁶ takes advantages of this principle using a format similar to duobinary modulation – a technique known from wire line and optical communications^{94,95} that leads to a narrow signal spectrum – which a 625 GHz frequency multiplier chain based THz source (Fig. 6.11) can support. On the receiver side, a Schottky diode operates in direct detection mode, converting the THz signal into baseband. Pre-coding the data reduces the signal bandwidth but keeps its payload the same. As shown in Fig. 6.11, the pulse pattern generator (PPG) produces a 2.5 Gb/s NRZ signal that gets split into two branches using a wideband 6 dB electrical power splitter. One version is delayed by the duration of a bit (400 ps) before both replicas are combined using another wideband 6 dB power splitter. The resulting signal possesses three amplitude levels (-1, 0, 1) and an advantageous phase coding, which significantly shrinks its bandwidth compared to

its corresponding NRZ format. A following quasi-Gaussian low-pass filter (LPF_1) with about 1700 MHz 3 dB-bandwidth reduces further the signal spectrum, mainly by cutting off its tail, which drives as baseband signal a balanced mixer to imprint its data on a carrier at a frequency according to the acceptance band of the THz source. It is a specific feature of the balanced mixer that negative amplitudes of the driving signal result in a 180° phase shift of the carrier. A high-speed scope can conveniently be triggered to visualize the output of the balanced mixer as eye diagram when the product of carrier frequency and bit duration equals an integer. Therefore, a 12.5 GHz carrier frequency is chosen for eye recording, which is close to the operational frequency of 12.933 GHz, where the system performs best. Duobinary baseband modulation on the transmitter side generates a signal with a sufficiently narrow spectral bandwidth to pass an up-converting frequency multiplier chain.

6.8 Examples of terahertz communication systems

In this section, we summarize THz communication experiments to date. As shown in Table 6.1, almost all of the experiments to date have been done in the lower THz region in the range of 100–400 GHz. A variety of THz sources – THz time-domain, UTC-PD opto-electronic, monolithic microwave integrated circuits (MMIC), and microwave multiplication – were used. The two exceptions are a short link (2 m) operating at 3.8 THz using a QCLs and a multiplied microwave system operating at 625 GHz.

6.8.1 Opto-electronic THz communication systems

In this section, the two predominant opto-electronic-based THz communication systems are described. The first type is based on THz time-domain instrumentation whereas the second utilizes the conversion of beat frequencies from visible/near-IR laser beams to THz signals using a uni-traveling carrier photodetector (UTC-PD).

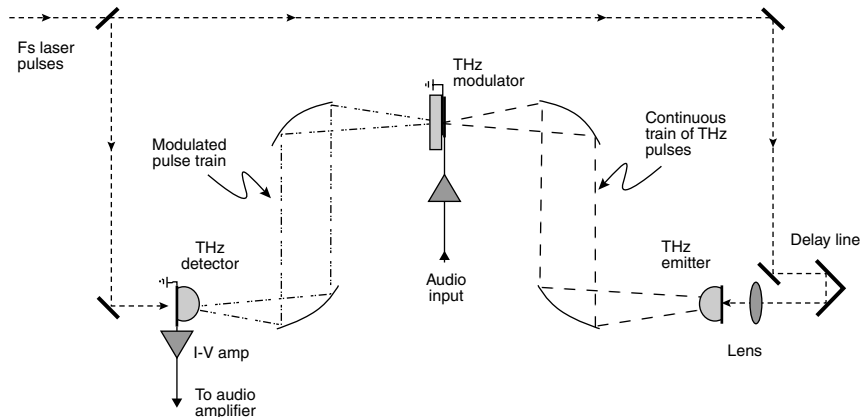
Time-domain systems as communication links

The first set of examples listed in Table 6.1 are based on THz time-domain systems which utilize photoconductive antenna (PDA) structures as the THz transmitter and receiver. All three of these examples have some common characteristics: (a) the center frequency of the THz pulse is roughly 0.3 THz; (b) the absolute maximum possible data rate of the THz time-domain systems is limited by the repetition rate of the Ti:Sapphire laser (typically ~80 MHz); (c) the electronic bandwidth of the PDA electronics potentially limits the data rate to <1 MHz; and (d) the transmitter-to-receiver distance and

Table 6.1 Summary of THz communication link measurements.

THz carrier frequency	Modulation hardware	Maximum distance	Modulation format	Modulation BW	BER	Reference number
<i>THz time-domain</i>						
300 GHz	External modulator	0.48 m	Analog	6 kHz	96	
300 GHz	Voltage modulation of PDA	1 m	Analog	5 kb/s	73	
300 GHz	Voltage modulation of PDA	1 m	PRBS	1 MHz	<10 ⁻⁸	72
<i>Opto-electronic/UTC-PD</i>						
120 GHz	Optical Mach-Zender modulator	100 m	PRBS	10 Gb/s	10 ⁻¹⁰	59
120 GHz	Optical modulator	250 m, 450 m	ASK	3 Gb/s	10 ⁻¹⁰	60, 14
200 GHz	Optical Mach-Zender modulator	2.6 m	ASK	1.06 Gb/s	<10 ⁻⁹	63
250 GHz	Electro-optic modulator	0.5 m	ASK	8 Gb/s	10 ⁻¹⁰	97, 98
300–400 GHz	Optical modulator	0.5 m	ASK	2 Gb/s, 12.5 Gb/s	10 ⁻¹²	6,57
<i>Millimeter-wave integrated circuit (MMIC)</i>						
120 GHz	MMIC	800 m	ASK	10 Gb/s	10 ⁻¹²	23
120 GHz	MMIC	5800 m	ASK	10 Gb/s	10 ⁻¹² with FEC	99
<i>Microwave multiplication</i>						
300 GHz	Subharmonic mixer	22 m	Analog	6 MHz	62	
300 GHz	Subharmonic mixer	52 m	Digital video broadcasting (DVB-S2)	96 Mb/s with FEC	~10 ⁻⁸ at 30 cm	61
625 GHz	Frequency multiplier chain	1 m	8-PSK Input signal Duobinary/ PRBS	2.5 Gb/s	10 ⁻¹⁰	66
<i>Quantum cascade laser (QCL)</i>						
3800 GHz	Electronic modulation of QCL	2 m	Analog	10 kHz	69	

Notes: BER, bit-error-rate; PDA, photoconductive antenna; PRBS, pseudo random bit sequence; ASK, amplitude shift keying; PSK, phase shift keying. FEC designates that forward error correction algorithms were employed.



6.15 Experimental set-up for analog THz communication link using an external THz modulator. (Adapted from Reference 96; Reprinted with permission from J. Federici and L. Moeller, 'Review of terahertz and subterahertz wireless communications', *J. Appl. Phys.* **107**, 111101 (2010). ©2010, American Institute of Physics.)

timing of the gating pulses are adjusted so that maximum THz signal power is detected, at peak of THz pulse. Consequently, timing jitter of the laser or variations in the optical path length degrades the quality of the link.

One of the first demonstrated THz communication links used a THz time-domain system to transmit analog audio signals⁹⁶ on a THz carrier using an external modulator. The transmission distance was 0.48 m and the maximum bandwidth of the modulation (Section 6.5.2) was ~10 kHz. While audio signals up to 25 kHz could be transmitted, the 3 dB point was ~1 kHz. Reliable data could be transmitted up to about 6 kHz. The bandwidth of THz detection was limited not only by the time-constant of the lock-in used to extract the detected signal, but also by a 7 kHz cutoff of the transimpedance amplifier that was used to amplify the small current signals from the THz detector modules. A schematic of the system is shown in Fig. 6.15.

Another analog THz link used LT:GaAs dipole antennas as a THz transmitter and receiver.⁷³ A Ti:Sapphire laser is used to generate and detect THz. Audio signals were impressed upon the THz carrier by directly modulating the bias voltage of the THz transmitter. Reference 73 demonstrated transmission of a six-channel analog and burst audio signal over a distance of 1 m. Peak-to-peak fluctuations of integrated signal at receiving antenna over 3 min was about 10%, while the signal-to-noise ratio of the detected THz time-domain waveform was around 1000 for frequencies up to 1 THz. The 3 dB frequency response of the transmission channel was about 20 kHz. The photoconductive dipole antennas that were used in the experiment were not designed for high FM. Consequently, the maximum data rate was limited by the RC

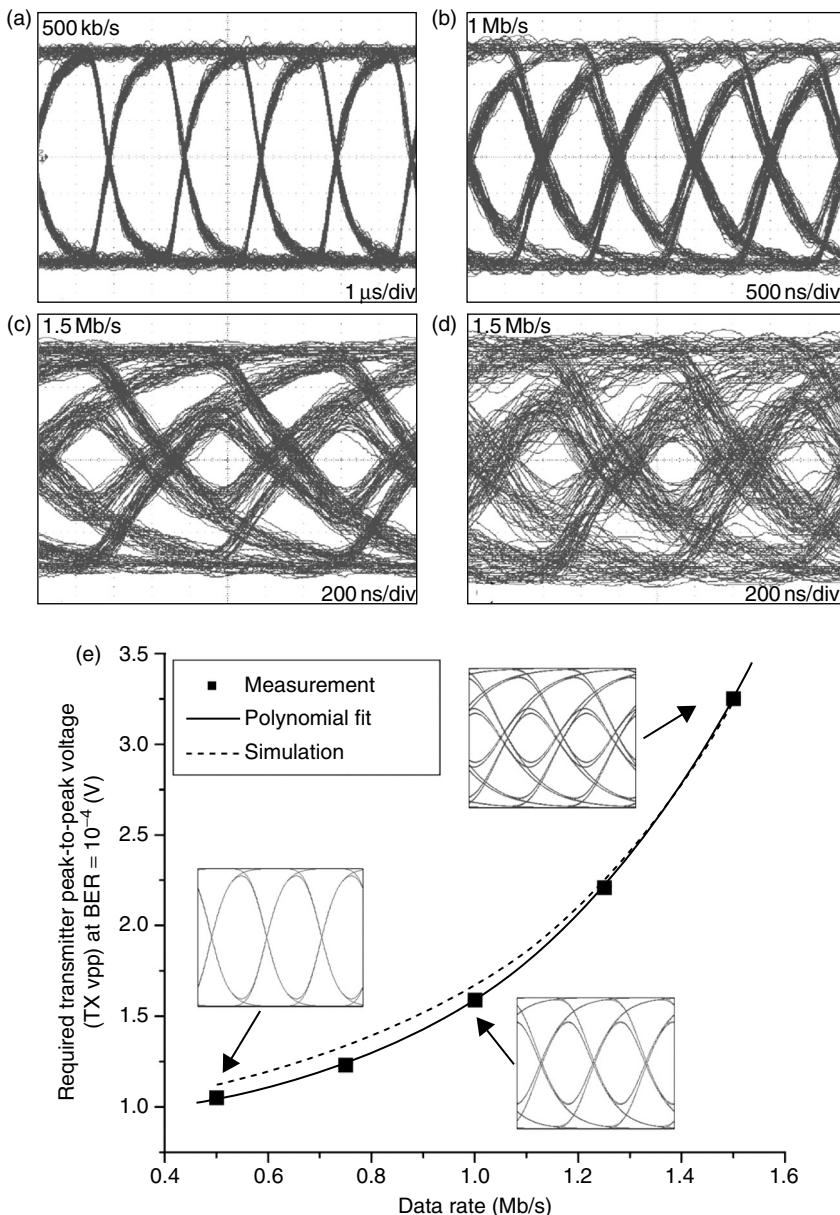
time-constant of the receiver. The authors demonstrated transmission of 5 kb/s data bursts. To demonstrate the fidelity of data transmission, they transmitted music through the data channel by using the electronic output from a computer's speaker to modulate the electronic bias to the THz transmitter. They observed good fidelity of their system up to ~ 2 kHz in the frequency domain.

Moeller *et al.*⁷² reported bipolar and on/off keying of THz pulses with maximum modulation index by direct data encoding the bias voltage of the photoconductive emitter antenna, enabling data rates almost three orders of magnitude higher than described in References 73, 96. Digital data transmission was characterized by BER measurements. The experimental set-up consisted mainly of a commercially available THz-TDS system which is electrically connected to a data source and BER tester. The THz transmitter (TX) is connected to a pseudo random bit sequence (PRBS) generator and instead of a constant bias, and the emitter antenna is electrically driven by a digital signal carrying the data. A d.c.-coupled amplifier can increase the voltage at the antenna input to about 20 V. A d.c.-offset between 0 V and half of the maximum bit voltage can be added to the pattern generator output, to allow switching of the signal format between bipolar and on/off modulation. As the electrical field of the THz pulse directly depends on the sign and the amount of the applied antenna bias, the PRBS data are linearly mapped onto the THz signal and form its envelope.

At error-free operation ($\text{BER} < 10^{-8}$) a high impedance sampling scope recorded 0.5 Mb/s, 1 Mb/s, and 1.5 Mb/s eye diagrams (Fig. 6.16b–d) at the preamplifier output, showing the data rate dependent ISI caused by limited receiver bandwidth. Eye diagrams of bipolar and on/off modulation with the same transmitter voltage swing (TVS) look similar. This is expected since the a.c.-coupled detector blocks offsets and saturation effects appear to be small at relevant swing levels. At low TVS, receiver noise (Fig. 6.16d) limits the $\text{BER} = 1 \times 10^{-4}$, which is manageable using forward error correcting codes. At this BER level we determined the minimal required TVS for different data rates to quantify ISI caused performance degradations (Fig. 6.16e). A comparison with second order LP filter simulations of the receiver shows good agreement with the measurement. Increasing the TVS widens the eye, which results in a reduced BER. Tests showed that long (i.e. $2^{23} - 1$ bits) and short (i.e. $2^7 - 1$ bits) PRBSs yield the same BER performance.

Photonic MMW/UTC-PD opto-electronic systems

The NTT group in Japan has been developing sub-THz communication links for the past several years,⁵⁶ leading to substantial innovations in the hardware components. Their contributions listed in Table 6.1 focus on three types of systems: (a) photonic UTC-PD THz source with Schottky diode detectors;⁵⁹ (b) the same UTC-PD source with MMIC receivers;⁶⁰ and (c) an integrated MMIC



6.16 Eye diagrams at different data rates and error-free operation (a–c) and at 1.5 Mb/s with $\text{BER} = 10^{-4}$ (d); (e) measured and simulated required TVS at different data rates, simulated eye diagrams show good agreement with Fig. 6.16(a–c) from Reference 72. (L. Moeller, J. Federici, A. Sinyukov, C. Xie, H. C. Lim, and R. C. Giles, ‘Data encoding on terahertz signals for communication and sensing’, *Opt. Lett.* **33**, 393 (2008). ©2008.)

transmitter and receiver.²⁴ The first two are radio-over-fiber (RoF) systems. RoF systems⁶⁰ refer to modulating optical carrier signals at millimeter-wave frequencies. The optical signals can be routed to a sub-THz transmitter module using low loss optical fiber. Within the THz transmitter module, the modulated optical beam is converted to a sub-THz signal using a UTC-PD and then launched into free-space using a feed horn. The details of the hardware are discussed in Section 6.5.1. The motivation for RoF technology, as opposed to a conventional millimeter-wave communication link, are several fold. While a rooftop-to-rooftop link would be conceptually straight forward, delivering the MMW signal from the interior of a building, for example, to the roof could be problematic due to attenuating obstacles. Therefore, the available locations for setting up wireless equipment are limited. A RoF system could be an attractive solution to this problem because the millimeter-wave signals can be transmitted over long distances by using optical fibers as an optical frequency comb as discussed in Section 6.5.1. Conceptually, one can generate the optical frequency comb, encode the data on the optical carrier using an optical modulator, and then route the optical signals through a building to a sub-THz transmitter located on a rooftop. Since a high-gain sub-THz antenna requires highly precise alignment, scintillation effects due to wind or even the motion of the buildings will cause variations in the received power. Figure 6.13 shows a possible configuration for a RoF system which would first transmit optical carriers through fiber (say through building) and then convert to wireless sub-THz radiation and then back to optical fiber. Another motivation and advantage of the RoF system is that it can easily be integrated into a high-speed optical fiber communication link as part of a ‘first mile’ and ‘last mile’ solution.^{11,12} Conceptually, optical communication systems can provide high-speed (typically 40 Gb/s per wavelength per channel), long distance point-to-point communication via optical fiber. However, in order to distribute data from a node to the end users, one needs to maintain the high data rate as the data branches off to multiple mobile users.

Figure 6.13 shows a schematic of a RoF wireless link system. The transmitter is composed of a low-phase-noise photonic millimeter-wave generator (described in Section 6.5.1) which outputs an optical frequency comb: an optical carrier upon which a sub-THz signal is impressed. The output of the photonic millimeter-wave generator passes through the data modulator. At this point, the digital data (which is generated by a bit-error-rate test set) is encoded onto the optical/sub-THz carrier. When the data modulated optical frequency comb illuminates the UTC-PD module, the optical frequency comb is electro-optically converted and amplified by the UTC-PD module to a sub-THz signal. The generated sub-THz signal (with data) is then transmitted from a high-gain antenna. In Hirata’s earlier work, the received sub-THz signal can be detected by either a Schottky

diode detector or mixer. The Schottky diode detection system exhibited a 10^{-10} bit error rate with a projected maximum distance of 100 m. For the RoF system described in Reference 60, the received sub-THz signal is detected, amplified and demodulated by a receiver module using a receiver MMIC chip.⁹⁷ The demodulated data signals are then converted to an optical signal by an electro-optic converter and launched into a fiber-optic cable. Finally, the optical signal is converted into an electronic signal and connected to a bit-error-rate test set. A bit-error-rate below 10^{-12} at 10 Gb/s is reported for a wireless link distance of 250 m. The estimated maximum transmission distance is about 2 km.¹⁴

6.8.2 Integrated circuit systems with MMIC

While the 1.5 μm fiber-optical components of the RoF systems enable easy integration with high-speed optical communications systems, there is a drawback of the photonic approach in terms of additional optical components, system size, total cost and added power consumption. Clearly, replacing the opto-electronic THz source with an integrated electronic device – which would work in concert with the MMIC receiver chip – could eliminate many of these issues. Yamaguchi *et al.*²⁴ implemented a flexible coplanar waveguide MMIC chipset,⁹⁸ which included amplifiers, modulators and demodulators, as the THz transmitter and receiver in a 10 Gb/s wireless link. The link exhibited a 10^{-12} BER over 800 m distance. Improvements to the 120 GHz transmitter as well as implementation of forward error correction algorithms have extended the link distance to 5.8 km with an error-free transmission of 10 Gb/s data.⁹⁹

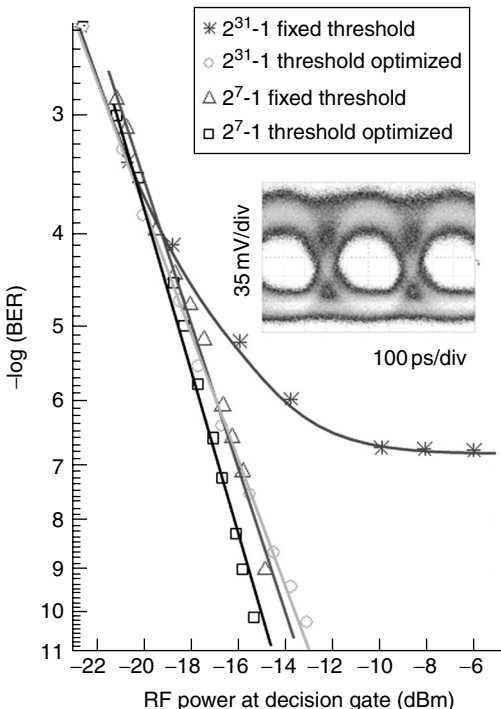
6.8.3 Quantum cascade laser systems

The QCL THz free-space communication system consists of a 3.8 THZ QCL laser in conjunction with a cryogenically cooled (12 K) quantum well photodetector.⁶⁹ Analog audio data is transmitted over a 2 m path length. Under normal operation, a custom-made pulse generator generates 8 ns pulses at a repetition rate of 455 kHz. On top of this constant modulation, an audio FM is applied. The resulting combined signal electronically modulates the QCL. The quantum well photodetector is sufficiently fast to measure the 455 kHz pulse repetition rate as well as the sidebands generated by the audio modulation. The electronic output of the photodetector is amplified and passed through a 10 kHz low-pass filter. Finally, the signal is passed to the antenna input of an AM radio to recover the audio signal. No information or metrics are presented as to the recovered audio signal quality.

6.8.4 Multiplied microwave systems

Analog⁶² and digital⁶¹ video signal transmission has been demonstrated at 300 GHz using a microwave multiplier system. The system, described in Fig. 6.10, consists of a frequency multiplied (6X) 16.66 GHz LO. The resulting 150 GHz signal is converted to a 290–310 GHz signal using a subharmonic mixer and a DC-10 GHz signal generator. The receiver LO is 16.38 GHz so that the intermediate frequency (IF) of the receiver (5 GHz) is detected using heterodyne detection. To demonstrate data transmission, Jastrow *et al.* transmit a color video baseband signal with 6 MHz bandwidth modulated on an ultra high frequency (UHF) carrier (855.25 MHz) acting as the ‘signal generator’ to be transmitted over THz link. At the receiver, the 5 GHz IF is mixed down to baseband and fed to a standard TV card. The TV card input requires a minimum signal-to-noise ratio of 40 dB. The image quality is viewed on computer screen. Using just the THz feed horns, excellent picture quality is reported up to 0.5 m with significant degradation observable at transmission distances of 0.8 m. When lenses are used to collimate the THz radiation, a maximum link distance of 22 m is achieved. The system of Reference 62 has been used for digital transmission.⁶⁵ The system is capable of transmitting digital video broadcast (DVB) data at a rate of 96 Mb/s over a distance of 52 m using forward error correction codes.

Power, BER, and signal-to-noise ratio (SNR) measurements on the receiver side describe the signal performance of a 625 GHz link (Fig. 6.11) with duobinary modulation format.⁶⁶ As shown in Fig. 6.11, two identical THz lenses with short focal lengths (~32 mm) allow source beam transmissions over distances of a few meters (beam diameter ~ 20 mm) followed by refocusing the beam on the receiver side into a horn antenna that is identical to the one used in the transmitter. Transmission losses are emulated by reducing the detected T-ray power with an iris inserted concentrically into the THz beam to limit its effective diameter. The total receiver output power is measured with a RF power meter while the corresponding BER, with and without threshold optimization, are recorded (Fig. 6.17). After optimizing the data decision threshold at a BER of about 1×10^{-3} , increasing the detected THz power leads to smaller BER up to 2.5×10^{-7} where further power enhancement does not reduce the error count (error floor) for long PRBS ($2^{31}-1$). The impact of the PRBS length was investigated by performing similar BER measurements with shorter patterns. A short PRBS does not show error floors, as exemplified by a 2^7-1 pattern in both cases with and without decision threshold adjustment. The reason for this could be saturation effects of the receiver Schottky diode and bandwidth limitations of the receiver amplifiers.

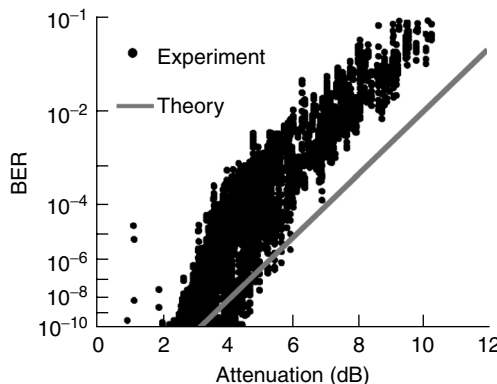


6.17 BER curves for long and short PRBSs with and without decision threshold optimization. Eye diagram at $\text{BER} = 10^{-9}$ at decision gate input for a $2^{31}-1$ PRBS. (From L. Moeller, J. Federici, and K. Su, '2.5 Gbit/s duobinary signalling with narrow bandwidth 0.625 terahertz source', *Electron. Lett.* **47**(15), 856–858 (2011). ©IET.)

6.9 Experimental characterization of rain, fog and scintillations on terahertz communication links

The 120 GHz link measurements from Yamaguchi *et al.*²⁴ contain an interesting observation that scintillation due to the effect of wind on the propagating 125 GHz radiation was measureable. As wind velocity increased, the receiver axis deviation also increased, which caused the input power to decrease. However, since the input power, even in the presence of the wind, was greater than the minimum required, the authors did observe a small increase in BER due to the wind.

In the THz range above 100 GHz, the effect of rain has been characterized only at 103 GHz¹⁰⁰ and 120 GHz.²⁵ The dependence of the attenuation coefficient A (in dB/km) on rain droplet size can be estimated from

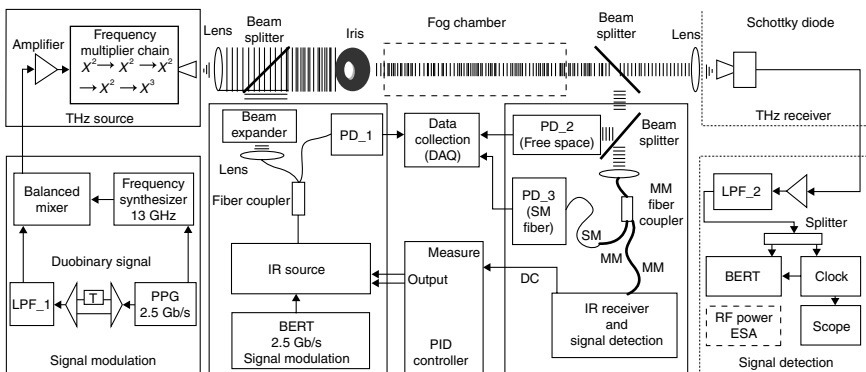


6.18 Measured BER for 120 GHz wireless link (10.3 Gb/s data rate) versus rain attenuation.²⁵ (© IEEE. All rights reserved. Reprinted, with permission, from A. Hirata, R. Yamaguchi, H. Takahashi, T. Kosugi, K. Murata, N. Kukutsu, and Y. Kado, 'Effect of rain attenuation for a 10-Gb/s 120-GHz-band millimeter-wave wireless link', *IEEE Transactions on Microwave Theory and Techniques*, **57**(12), 3099–3105 (2009).)

$$A = 4.343 \int Q(D, v, n) N(D) dD \quad [6.8]$$

where $Q = \mu_{th}/N$ is the attenuation cross-section as determined by Mie scattering in Equation [6.6], n is the refractive index of liquid water, and $N(D)$ represents the drop-size distribution function as a function of droplet diameter D . The attenuation A in dB/km is related to the rainfall rate R in mm/h by $A = aR^b$ in which a and b are constants determined by the particular raindrop-size distribution model. For rain rates averaged over 60 s, Reference 25 finds that both the Laws-Parsons as well as the ITU-specific attenuation models accurately predict the measured attenuation coefficient due to rain. In comparing the measured BER with rain attenuation, Hirata *et al.*²⁵ observe an interesting discrepancy between the experimental measurements and predicted theory. As shown in Fig. 6.18, as rain attenuation increases, the BER increases relative to the theoretical predictions from random noise theory. Hirata *et al.* suggests two possible explanations: wave-front distortions (i.e., scintillations as discussed in Section 6.3.2) or the difference in the measurement cycle for rain attenuation (averaged over 1 s) and BER (averaged over a much shorter time-period).

The first direct experimental performance comparison between THz and IR communication links, meaning both signals passing the same weather conditions, has been recently reported.²⁶ Most of the predictions regarding



6.19 Schematic of co-propagating THz and IR links for the study of atmospheric effects on both communication channels. (From K. Su, L. Moeller, R. B. Barat, and J. F. Federici, 'Experimental comparison of performance degradation from terahertz and infrared wireless links in fog', *Journal of the Optical Society of America* **29, 179–184 (2012) (©OSA 2012).)**

advantageous propagation features of THz beams are based on theoretical investigations (Sections 6.3.2 and 6.3.3) originally developed to support radio astronomy. As discussed in Section 6.3.3, only a few experimental measurements on the degradation of THz signals, by fog, rain, particulars and other weather, are available. In this section, the impact of fog on THz channels is described.

Using the 625 GHz THz link described in Fig. 6.11,²⁶ a co-propagating infrared (IR) free-space link is added (Fig. 6.19). Both the THz and an IR beam at 1.5 μm wavelength carrying same data load co-propagate through the same weather conditions. The IR channel is modulated with a normal NRZ format while duobinary coding drives the THz source. Both beams pass the same channel perturbations and their degradations are recorded simultaneously. Scintillation and fog attenuation effects are measured for the THz and IR signals by measuring BER, signal power, and phase front distortions.

The IR transmitter module (wavelength $\sim 1550 \text{ nm}$) includes a Mach-Zehnder optical modulator which is driven by the same 2.5 Gb/s NRZ signal as the THz transmitter. The EDFA amplifies the modulator output to about 25 dBm, the maximum input power of the bandpass filter, which reduces the detection of spontaneous emission on the receiver side. After passing through a variable optical attenuation, controlled by a proportional-integral-derivative (PID) controller, the IR signal is launched into a 90:10 single mode (SM) fiber coupler. Its weaker output, launched to photo detector PD_1, serves as monitor for the power entering the fog chamber. A fiber collimator expands the stronger IR beam to about 20 mm diameter, which is comparable to THz

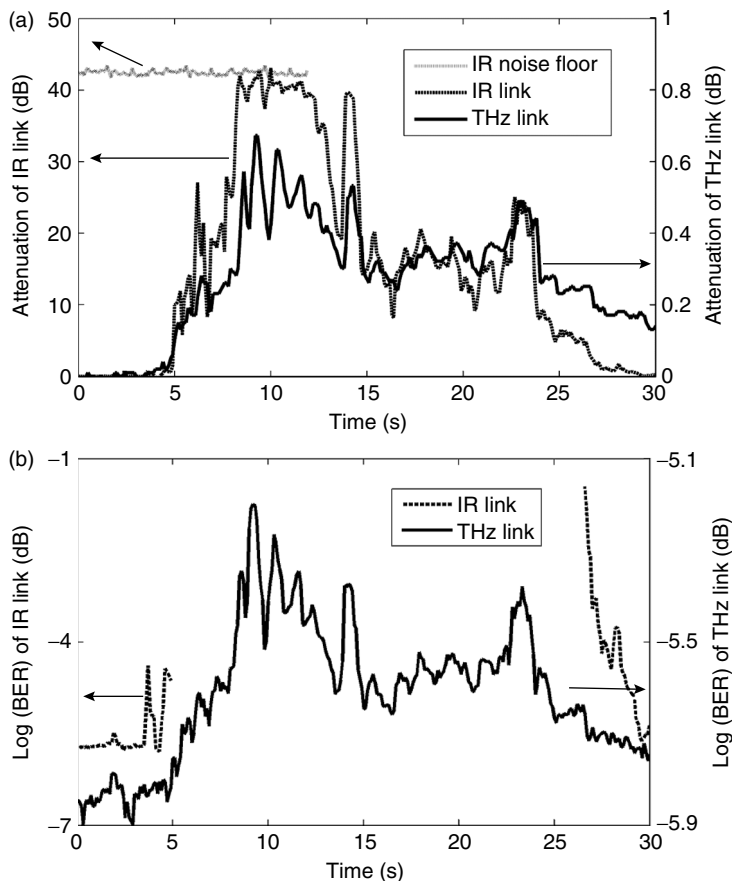
beam size. The collimated IR beam is superposed with the THz beam using a beam combiner and transmitted through the fog chamber. After the chamber, the IR beam is separated from the THz using another beam splitter and then further split into two parts. One beam illuminates a large area (effective area 19.6 mm^2) photo diode of detector PD_2, which in combination with PD_1 is used to determine the power loss caused by the chamber load. The remaining beam power is focused into an optical fiber and then directed to another photo detector (PD_3) through a 1 m long SSMF input fiber. Details of the IR link and PID are given in Reference 26.

Since higher attenuation levels are expected for the IR signal than for the THz beam when passing through fog (Fig. 6.3), one needs to actively control the dynamic range of the IR system for BER recording using a PID controller to adjust the launched power into the chamber such that the IR receiver power remains constant. For an unloaded chamber (i.e., no fog), the IR power in the chamber and the aperture of the iris are adjusted such that a BER of around 10^{-6} is obtained for both channels. Fog is generated by dripping liquid nitrogen into a cup filled with hot water (temperature about $\sim 80^\circ\text{C}$) and displaced inside the chamber from the beams. The fog diffuses into the chamber, flooding it typically in a few tens of seconds.

The measured attenuation of the THz and IR link through the fog (with PID controller disabled) is shown in Fig. 6.20a. Note that the THz absorbance is typically much less than that of the IR. Five seconds after the introduction of the fog, the THz absorption coefficient is ~ 60 times less than that of the IR. Usually, even ‘small’ amounts of fog are sufficient to block the IR beam after a few seconds of diffusion into the beam path. As a result the IR signal collapses, its BER is no longer measurable, but returns at ~ 27 s when the fog dissipates into the lab environment.

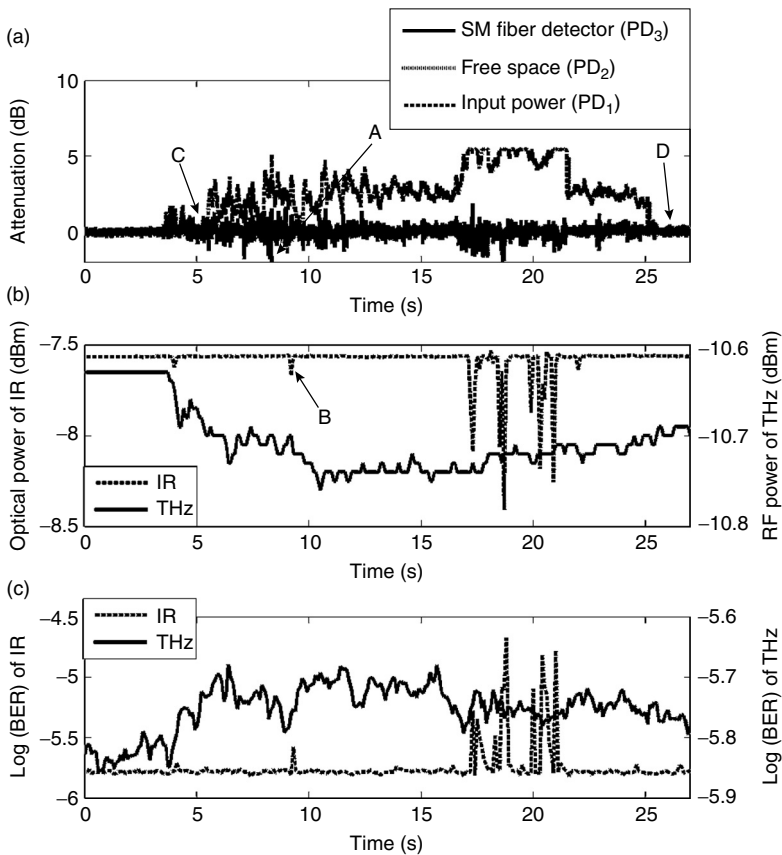
Two effects caused by fog contribute to the IR power reduction at the receiver side: a Beer-Lambert law power attenuation, and scintillation (Section 6.3.2). Scintillation can cause phase front distortions of the IR optical mode that is coupled into the detector fiber. If the mode of the IR beam were to be only attenuated in the fog chamber due to intrinsic absorbance and scattering by the fog particles but not phase front degraded, then the IR power coupled into the receiver fiber should be in good approximation proportional to the IR power detected by PD_2. However, if phase front distortions of the IR beam occur, one can expect a smaller couple efficiency especially into the small aperture SSMF and consequently lower detected power by photodetector PD_3.

The optical power at the IR data receiver’s input is kept constant with the PID controller when fog enters the beam. If the measured BER were only due to fluctuations in the received IR power, then the PID controller should eliminate those fluctuations and keep the BER of the IR channel constant. In the presence of fog and with the PID controller activated, the



6.20 (a) Attenuation of THz link and IR link with time, (b) log(BER) of THz link and IR link with time when the PID circuit is inactive. (From K. Su, L. Moeller, R. B. Barat, and J. F. Federici, 'Experimental comparison of performance degradation from terahertz and infrared wireless links in fog', *Journal of the Optical Society of America* **29**, 179–184 (2012) (©OSA 2012).)

outputs of all photodetectors are simultaneously recorded, along with the BER of the IR channel. When fog diffuses into the IR beam after about 3 s recording time (Fig. 6.21a), the PID controller increases the IR power launched into the chamber and measured by photodetector PD₁. Up to about 17 s recording time, the control loop can compensate the power loss inside the chamber. Thereafter, the maximum transmitter output power is insufficient to further equalize the losses of the link until the attenuation of the link drops back at about 22 s recording time to level within the power margin of the system. While the detected optical power at the data receiver



6.21 (a) Outputs of all IR photodetectors (PD₁, PD₂, PD₃) from Figure 6.19 in units of dB. (b) Log(BER) of IR and (c) log(BER) of THz due to fog. Small kinks in the received power of the data receiver (pointer 'B') could be caused by rapidly changing signal attenuation and noise, which affects the stable operation of the PID controller for short time. Interestingly, at pointer 'C' and 'D' the chamber attenuation for the IR beam is almost zero whereas the attenuation of the THz signal is about 0.1 dB. Likely, at these recording times fog was converted into humidity, which impacts the IR signal comparably less than the THz signal. (From K. Su, L. Moeller, R. B. Barat, and J. F. Federici, 'Experimental comparison of performance degradation from terahertz and infrared wireless links in fog', *Journal of the Optical Society of America* **29**, 179–184 (2012) (©OSA 2012).)

(not shown) stays almost constant (for $t < 16$ s), small changes of the output of PD₂ are observed. Around point 'A' in Fig. 6.21, these variations are less than ± 0.15 dB but show that receiver power (PD₃) and detected power of PD₂ are not always exactly proportional to each other. But the variations

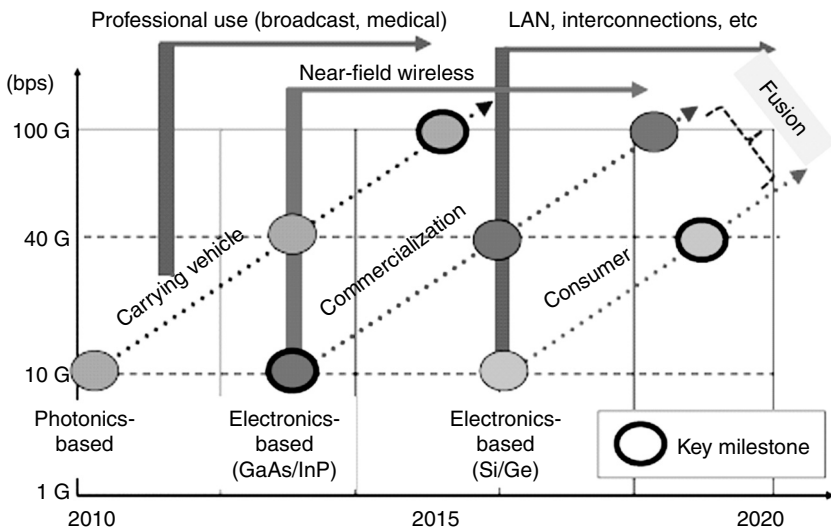
of the power coupled into the SSMF (PD_3) are more pronounced (up to ± 2 dB). The differences in the outputs of PD_2 and PD_3 indicate that scintillation effects impair the IR beam. However, possible scintillation in the THz beam is below the limits of detection.

In summary, the attenuation levels for the IR beam are typically several orders of magnitude higher than those for the THz beam when both signals are propagating over a distance of about 1 m and through the same fog. The IR signal is impaired by both attenuation and scintillation effects, whereas the THz signal experiences just attenuation.

6.10 Future trends

A technology roadmap of THz wireless communications (Fig. 6.22) was recently presented in Reference 4. Several key challenges remain. First and foremost is the development of high-power THz sources within the THz atmospheric transmission windows, as well as compatible high sensitivity detectors and modulation hardware. Recent technological progress in key technologies such as SiGe, BiCMOS and InP suggests that THz integrated circuits for communication will be available in a few years. While future THz communications links will probably utilize THz integrated circuits due to their inherently lower-cost compared to opto-electronic systems, near-term systems utilizing microwave multipliers can provide milliwatts of THz power and several GHz of bandwidth which should be suitable for reasonable (several hundreds of meters) link distances. Opto-electronic based systems, such as RoF systems, may find niche applications in which direct coupling of wireless THz links to high-speed fiber-optical systems is the major consideration. Since one of the potentially major benefits of THz communications is the wide bandwidth, hardware systems that can take efficient advantage of 100 GHz should be developed over the next several years. In addition to the development of the source/detector hardware itself, packaging of THz components is another challenging issue.⁴ Since metal packaging induces significant signal loss and is relatively heavy, breakthroughs in packaging of THz integrated circuits will be required.

Due to the highly directional nature of THz wireless communications, it is widely recognized^{4,7,8} that beam steering and tracking techniques need to be developed. Not only are these required for indoor system links, but also for outdoor mobile communications for which the effective coverage area is limited not only by the directionality of line-of-sight THz systems, but also by atmospheric attenuation. Systems are required which are capable of switching from one path or source to another if the direct line-of-sight were blocked or highly attenuated. Possible approaches could be phased-array antennas (i.e., a microwave approach) or lenses and mirrors (an optical



6.22 Technology road map of THz communications. (Copyright IEEE. All rights reserved. Reprinted, with permission, from H.-J. Song and T. Nagatsuma, 'Present and future of terahertz communications', *IEEE Transactions on Terahertz Science and Technology* **1**, 256–263 (2011).)

approach). Lenses, mirrors and filters using MEMS or metamaterials look promising.

As discussed in this chapter, there have been relatively few experimental studies on the attenuation and scintillation properties of the atmosphere – that is, the effect of fog, rain, and smoke – and their possible effects on THz communications. While some studies of rain²⁵ and fog²⁶ have been reported, more experiments are required to fully understand the physical processes of importance in the THz range, and to qualify atmospheric propagation models. Lastly, analogous to the development of radio communication, advanced modulation formats need to be applied to the THz links to achieve modulation gain or a higher spectral efficiency.

In the future, there may be a competition among various technology groups for a slice of the THz frequency spectrum. Currently, the THz frequency range is largely unregulated.⁸ In the United States, 275–300 GHz is reserved¹⁰¹ for mobile communications, while in Europe, above 275 GHz is available for communications. Reference 4 predicts that there will be a frequency conflict between the needs of THz wireless communications systems and astronomical applications. Radio-astronomy receivers in the 100–3000 GHz range are used to sense molecules many light years away. Terrestrial and satellite THz communications systems may interfere with these highly sensitive receivers. In a report issued by a study group,¹⁰² near worst-case assumptions show that a communications link at ~300 GHz would need to

be ~55 km away from radio observatories in order to avoid interference. The distance requirement decreases to 6 km above 450 GHz.

6.11 Sources of further information

The International Wireless Industry Consortium working group Mobile Multi Gigabit (MoGIG) Wireless Networks and Terminals website can be found at <http://www.iwpc.org/WorkingGroups.aspx>. The mission of this working group is to answer this question: what will happen to mobile wireless networks in the coming years when they run out of spectrum to support the massive increases in data demand?

IEEE802.15 Terahertz Interest Group web site: <http://www.ieee802.org/15/pub/IGthz.html>. Formed in 2007, the goal of this working group is to explore the feasibility of THz communications.

Recent reviews on THz wireless communications include References 4, 6, 8, 20.

- Spectrum Management for the 21st Century The President's Spectrum Policy Initiative, Federal Strategic Spectrum Plan, March 2008. <http://www.ntia.doc.gov/reports/2008/FederalStrategicSpectrumPlan2008.pdf>
- <http://www.ntia.doc.gov/files/ntia/publications/2003-allochrt.pdf>
– United States allocation chart of the radio spectrum
- FCC radio spectrum home page <http://www.fcc.gov/oet/spectrum/>

6.12 Acknowledgments

This material is based upon work supported by the National Science Foundation under Grant No. ECCS-1102222.

6.13 References

1. Reynolds, S. K., B.A. Floyd, U.R. Pfeiffer, T. Beukema, J. Grzyb, C. Haymes, B. Gaucher, and M. Soyuer, A silicon 60-GHz receiver and transmitter chipset for broadband communications. *IEEE Journal of Solid-State Circuits*, 2006. **41**(12): 2820–2829.
2. Heidemann, R., R. Hofstetter, and H. Schmuck, Fibre-optic technologies for 30/60 GHz pico-cellular PCN and mobile systems. *IEEE MTT-S International Microwave Symposium Digest*, 1994. **1**: 483–485.
3. Federal Communications Commission (FCC) Encyclopedia - Radio Spectrum Allocation. Available from: <http://www.fcc.gov/encyclopedia/radio-spectrum-allocation>
4. Song, H. -J. and T. Nagatsuma, Present and future of terahertz communications. *IEEE Transactions on Terahertz Science and Technology*, 2011. **1**: 256–263.
5. Cherry, S., Edholm's law of bandwidth. *IEEE Spectrum*, 2004. **41**(7): 50.

6. Kleine-Ostmann, T. and T. Nagatsuma, A review on terahertz communications research. *Journal of Infrared, Millimeter, and THz Waves*, 2011. **32**: 143–171.
7. Britz, D. M. Evolution of extreme bandwidth personal and local area terahertz wireless networks. IEEE 802.15 WPAN™ Terahertz Interest Group (IGthz) 2009; Available from: <http://www.ieee802.org/15/pub/IGthz.html>.
8. Koch, M. THz communications: A 2020 vision. In: *Terahertz Frequency Detection and Identification of Materials and Objects, Nato Science for Peace and Security Series-B: Physics and Biophysics*. 2007. Springer Verlag. 325–338.
9. *Spectrum Management for the 21st Century The President's Spectrum Policy Initiative, Federal Strategic Spectrum Plan, March 2008*. 2008; Available from: <http://www.ntia.doc.gov/reports/2008/FederalStrategicSpectrumPlan2008.pdf>.
10. Mann, C. M., Towards terahertz communications systems. In: *Terahertz Sources and Systems*, R. Miles, Editor. 2001. Kluwer Academic: Netherlands. 261–267.
11. Piesiewicz, R., J. Jemai, M. Koch, and T. Kurner, THz channel characterization for future wireless gigabit indoor communication systems. *Proceedings of SPIE – The International Society for Optical Engineering*, 2005. **5727**: 166–176.
12. Nagatsuma, T., Exploring sub-terahertz waves for future wireless communications. In: *Conference Digest of the 2006 Joint 31st International Conference on IR and MMW*. 2006. p. 4.
13. Hirata, A., M. Harada, and T. Nagatsuma, 120-GHz wireless link using photonic techniques for generation, modulation, and emission of millimeter-wave signals. *Journal of Lightwave Technology*, 2003. **21**(10): 2145–2153.
14. Hirata, A., T. Nagatsuma, T. Kosugi, H. Takahashi, R. Yamaguchi, N. Shimizu, N. Kukutsu, K. Murata, Y. Kado, H. Ikegawa, H. Nishikawa and T. Nakayama, 10Gbit/s wireless communications technology using sub-terahertz waves. *Proceedings SPIE*, 2007. **6772**: 67720B.
15. Jungnickel, V., T. Haustein, A. Forck and C. von Helmolt, 155Mbit/s wireless transmission with imaging infrared receiver. *Electronics Letters*, 2001. **37**(5): 314–315.
16. Langer, K.D. and J. Grubor. Recent developments in optical wireless communications using infrared and visible light. *9th International Conference on Transparent Optical Networks, 2007. ICTON '07*, 2007. **3**: 146–151.
17. Kedar, D. and S. Arnon, Urban optical wireless communication networks: The main challenges and possible solutions. *IEEE Communications Magazine*, 2004. **42**(5): S2–S7.
18. Brown, E.R., Fundamentals of terrestrial millimeter-wave and THz remote sensing. *International Journal of High Speed Electronics and Systems*, 2003. **13**: 995–1097.
19. Piesiewicz, R., T. Kleine-Ostmann, N. Krumbholz, D. Mittleman, M. Koch, J. Schoebel, and T. Kurner, Short-range ultra-broadband terahertz communications: concepts and perspectives. *IEEE Antennas and Propagation Magazine*, 2007. **49**(6): 24–39.
20. Federici, J. and L. Moeller, Review of terahertz and subterahertz wireless communications. *Journal of Applied Physics*, 2010. **107**(11): 111101.
21. Freeman, R. L., *Radio Systems Design for Telecommunications*. Second Edition. 1997. New Jersey: Wiley.
22. Andrews, L.C. and R.L. Phillips, *Laser Beam Propagation Through Random Media*. 1998. Washington: SPIE Press.

23. Khan, S. A., A.N. Tawfik, C.J. Gibbins and B.C. Gremont, Extra-high frequency line-of-sight propagation for future urban communications. *IEEE Transactions on Antennas and Propagation*, 2003. **51**(11): 3109–3121.
24. Yamaguchi, R., A. Hirata, T. Kosugi, H. Takahashi, N. Kukutsu, T. Nagatsuma, Y. Kado, H. Ikegawa, H. Nishikawa and T. Nakayama, 10-Gbit/s MMIC wireless link exceeding 800 meters. In: *RWS 2008* 2008. p. 695.
25. Hirata, A., R. Yamaguchi, H. Takahashi, T. Kosugi, K. Murata, N. Kukutsu and Y. Kado, Effect of rain attenuation for a 10-Gb/s 120-GHz-band millimeter-wave wireless link. *IEEE Transactions on Microwave Theory and Techniques*, 2009. **57**(12): 3099–3105.
26. Su, K., L. Moeller, R. Barat and J.F. Federici, Experimental comparison of performance degradation from terahertz and infrared wireless link in fog. *Journal of the Optical Society of America A*, 2012. **29**(2): 179–184.
27. Wang, R., J.Q. Yao, D.G. Xu, J.L. Wang and P. Wang, The physical theory and propagation model of Thz atmospheric propagation. *Journal of Physics: Conference Series*, 2011. **276**: 012223.
28. Yang, Y., A. Shutler and D. Grischkowsky, Measurement of the transmission of the atmosphere from 0.2 to 2 THz. *Optics Express*, 2011. **19**(9): 8830–8838.
29. Bohren, C. F. and D.R. Huffman, *Absorption and Scattering of Light by Small Particles*. 1983, New York: Wiley.
30. Bandyopadhyay, A., A. Sengupta, R.B. Barat, D.E. Gary, J.F. Federici, M. Chen and D.B. Tanner, Effects of scattering on THz spectra of granular solids. *International Journal of Infrared and Millimeter Waves*, 2007. **28**(11): 969–978.
31. Rosker, M. J. and H.B. Wallace, Imaging through the atmosphere at terahertz frequencies in microwave symposium, 2007. *IEEE/MTT-S International 2007*. 773–776.
32. Wu, B., B. Marchant, and M. Kavehrad, Channel modeling of light signals propagating through a battlefield environment: Analysis of channel spatial, angular, and temporal dispersion. *Applied Optics*, 2007. **46**(25): 6442–6448.
33. Noh, Y.M., D. Müller, D. H. Shina, H. Leea, J.S. Junga, K.H. Leec, M. Cribbc, Z. Lic and Y.J. Kim, Optical and microphysical properties of severe haze and smoke aerosol measured by integrated remote sensing techniques in Gwangju, Korea. *Atmospheric Environment*, 2009. **43**(4): 879–888.
34. Piesiewicz, R., T. Kleine-Ostmann, N. Krumbholz, D. Mittleman, M. Koch and T. Kürner, Terahertz characterisation of building materials. *Electronics Letters*, 2005. **41**(18): 1002–1004.
35. Wietzke, S., C. Jansen, and M. Koch, Mirrors for electromagnetic waves. *Kunststoffe International*, 2009. **99**(12): 37–40.
36. Turchinovich, D., A. Kammoun, P. Knobloch, T. Dobbertin and M. Koch, Flexible all-plastic mirrors for the THz range. *Applied Physics A: Materials Science and Processing*, 2002. **74**(2): 291–293.
37. Krumbholz, N., K. Gerlach, F. Rutz, M. Koch, R. Piesiewicz, T. Kürner and D. Mittleman, Omnidirectional terahertz mirrors: a key element for future terahertz communication systems. *Applied Physics Letters*, 2006. **88**(20): 202905.
38. Ibraheem, I. A., N. Krumbholz, D. Mittleman and M. Koch, Low-dispersive dielectric mirrors for future wireless terahertz communication systems. *IEEE Microwave and Wireless Components Letters*, 2008. **18**(1): 67–69.
39. Jansen, C., S. Wietzke, V. Astley, D.M. Mittleman and M. Koch. Mechanically flexible polymeric compound one-dimentional photonic crystals for terahertz frequencies. *Applied Physics Letters*, 2010. **96**: 111108.

40. Li, J. S., Terahertz wave omnidirectional dielectric mirror. *Optics and Laser Technology*, 2011. **43**(6): 989–991.
41. Kurner, T., M. Jacob, R. Piesiewicz and J. Schoebel, An integrated simulation environment for the investigation of future indoor Thz communication systems. *Simulation*, 2008. **84**: 123–130.
42. Piesiewicz, R., M. Jacob, M. Koch, J. Schoebel and T. Kurner, Performance analysis of future multigigabit wireless communication systems at THz frequencies with highly directive antennas in realistic indoor environments. *IEEE Journal of Selected Topics Quantum Electronics*, 2008. **14**(2): 421–430.
43. Jansen, C., S. Priebe, C. Moller, M. Jacob, H. Dierke, M. Koch and T. Kurner, Diffuse scattering from rough surfaces in THz communication channels. *IEEE Transactions on Terahertz Science and Technology*, 2011. **1**(2): 462–472.
44. Priebe, S., C. Jastrow, M. Jacob, T. Kleine-Ostmann, T. Schrader and T. Kürner, Channel and propagation measurements at 300 GHz. *IEEE Transactions on Antennas and Propagation*, 2011. **59**(5): 1688–1698.
45. Saeedkia, D. and S. Safavi-Naeini, Terahertz photonics: optoelectronic techniques for generation and detection of Terahertz waves. *Journal of Lightwave Technology*, 2008. **26**(15): 2409–2423.
46. Mittleman, D., Terahertz imaging. In: *Sensing with THz Radiation*, D. Mittleman, Editor. 2003, Springer.
47. Duffy, S. M., S. Verghese and K.A. McIntosh, Photomixers for continuous-wave terahertz radiation. In: *Sensing with Terahertz Radiation*. D. Mittleman, Editor. 2003, Springer.
48. Brown, E. R., THz generation by photomixing in ultrafast photoconductors. In: *Terahertz Sensing Technology Volume 1: Electronic Devices and Advanced Systems Technology*, D.L. Woolard, W.R. Loerop, and M.S. Shur, Editors. 2003.
49. Löffler, T., et al., Continuous-wave terahertz imaging with a hybrid system. *Applied Physics Letters*, 2007. **90**(9): Article number 091111.
50. Su, K., Z. Liu, R.B. Barat, D.E. Gary, Z.H. Michalopoulou and J.F. Federici, Two-dimensional interferometric and synthetic aperture imaging with a hybrid terahertz/millimeter wave system. *Applied Optics*, 2010. **49**(19): E13–9.
51. Nagatsuma, T., H. Ito and T. Ishibashi, High power RF photodiodes and their applications. *Laser and Photonics Review*, 2009. **3**: 123–137.
52. Beck, A., G. Ducournau, M. Zaknoune, E. Peytavit, T. Akalin, J.F. Lampin, F. Mollot, F. Hindle, C. Yang and G. Mouret, High-efficiency uni-travelling-carrier photomixer at 1.55 m and spectroscopy application up to 1.4 THz. *Electronics Letters*, 2008. **44**(22): 1320–1322.
53. Ito, H., Y. Hirota, A. Hirata, T. Nagatsuma and T. Ishibashi, 11 dBm photonic millimetre-wave generation at 100 GHz using uni-travelling-carrier photodiodes. *Electronics Letters*, 2001. **37**(20): 1225–1226.
54. Li, Y.T., J.-W. Shi, C.-Y. Huang, N.-W. Chen, S.-H. Chen, J.-I. Chyi and C.-L. Pan, Characterization of sub-THz photonic-transmitters based on GaAs-AlGaAs uni-traveling-carrier photodiodes and substrate-removed broadband antennas for impulse-radio communication. *IEEE Photonics Technology Letters*, 2008. **20**(16): 1342–1344.
55. Li, Y.T., J.-W. Shi, C.-Y. Huang, N.-W. Chen, S.-H. Chen, J.-I. Chyi, Y.-C. Wang, C.-S. Yang and C.-L. Pan, Characterization and comparison of GaAs/AlGaAs uni-traveling carrier and separated-transport-recombination photodiode based high-power sub-THz photonic transmitters. *IEEE Journal of Quantum Electronics*, 2010. **46**(1): 19–27.

56. Nagatsuma, T., H. Ito, and T. Ishibashi, High-power RF photodiodes and their applications. *Laser and Photonics Reviews*, 2009. **3**(1–2): 123–137.
57. Nagatsuma, T., H.-J. Song, Y. Fujimoto, K. Miyake, A. Hirata, K. Ajito, A. Wakatsuki, T. Furuta, N. Kukutsu, Y. Kado, Giga-bit wireless link using 300–400 GHz bands. In: *MWP09 – 2009 International Topical Meeting on Microwave Photonics 2009*, Article number 5342723. *MWP09 – 2009 International Topical Meeting on Microwave Photonics*, Valencia, 14 October 2009–16 October 2009; Category number CFP09756-USB; Code 78946.
58. Fukushima, S., C. F. C. Silva, Y. Muramoto and A.J. Seeds, Optoelectronic millimeter-wave synthesis using an optical frequency comb generator, optically injection locked lasers, and a unitraveling-carrier photodiode. *Journal of Lightwave Technology*, 2003. **21**(12): 3043–3051.
59. Hirata, A., T. Kosugi, N. Meisl, T. Shibata and T. Nagatsuma, High-directivity photonic emitter using photodiode module integrated with HEMT amplifier for 10-Gbit/s wireless link. *IEEE Transactions on Microwave Theory and Techniques*, 2004. **52**: 1843–1850.
60. Hirata, A., H. Takahashi, R. Yamaguchi, T. Kosugi, K. Murata, T. Nagatsuma, N. Kukutsu and Y. Kado , Transmission characteristics of 120-GHz-band wireless link using radio-on-fiber technologies. *Journal of Lightwave Technology*, 2008. **26**: 2338–2344.
61. Jastrow, C., S. Priebe, B. Spitschan, J. Hartmann, M. Jacob, T. Kurner, T. Schrader and T. Kleine-Ostmann, Wireless digital data transmission at 300 GHz. *Electronics Letters*, 2010. **46**(9): 661–663.
62. Jastrow, C., K. Munter, R. Piesiewicz, T. Kurner, M. Koch and T. Kleine-Ostmann, 300 GHz transmission system. *Electronics Letters*, 2008. **44**(3): 213–214.
63. Ducournau, G., P. Sriftgiser, D. Bacquet, A. Beck, T. Akalin, E. Peytavit, M. Zaknoune and J.F. Lampin, Optically power supplied Gbit/s wireless hotspot using 1.55 m THz photomixer and heterodyne detection at 200 GHz. *Electronics Letters*, 2010. **46**(19): 1349–1351.
64. Crowe, T.W., D.W. Porterfield, J.L. Hesler, W.L. Bishop, Submillimeter-wave and terahertz diodes, components and subsystems. In: *IRMMW-THz 2006 - 31st International Conference on Infrared and Millimeter Waves and 14th International Conference on Terahertz Electronics 2006*, Article number 4222338, 396.
65. Jastrow, C., S. Priebe, B. Spitschan, J. Hartmann, M. Jacob, T. Kurner, T. Schrader and T. Kleine-Ostmann, Wireless digital data transmission at 300 GHz. *Electronics Letters*, 2010. **46**: 661–663.
66. Moeller, L., J. Federici and K. Su, 2.5Gbit/s duobinary signalling with narrow bandwidth 0.625 terahertz source. *Electronics Letters*, 2011. **47**(15): 856–858.
67. Kumar, S. and A. W. M. Lee, Resonant-phonon terahertz quantum-cascade lasers and video-rate terahertz imaging. *IEEE Journal on Selected Topics in Quantum Electronics*, 2008. **14**(2): 333–344.
68. Williams, B. S. Terahertz quantum-cascade lasers. *Nature Photonics*, 2007. **1**(9): 517–525.
69. Grant, P. D., S.R. Laframboise, R. Dudek, M. Graf, A. Bezinger and H.C. Liu, Terahertz free space communications demonstration with quantum cascade laser and quantum well photodetector. *Electronics Letters*, 2009. **45**(18): 952–954.
70. Sachs, J., P. Peyerl and M. Rossberg, New UWB-principle for sensor-array application. *Conference Record – IEEE Instrumentation and Measurement Technology Conference*, 1999. **3**: 1390–1395.

71. Daniels, D. J., *Ground Penetrating Radar*. 2nd Edition, David J. Daniels, Editor, IEE Radar, Sonar and Navigation series 15, 2004, IEE.
72. Möller, L., J. Federici, A. Sinyukov, C. Xie, H.C. Lim and R.C. Giles, Data encoding on terahertz signals for communication and sensing. *Optics Letters*, 2008. **33**(4): 393–395.
73. Liu, T. A., G. -R. Lin, Y. -C. Chang and C. -L. Pan, Wireless audio and burst communication link with directly modulated THz photoconductive antenna. *Optics Express*, 2005. **13**(25): 10416–10423.
74. Sinyukov, A. M., Z. Liu, Y.L. Hor, K. Su, R.B. Barat, D.E. Gary, Z. -H. Michalopoulou, I. Zorych, J.F. Federici and D. Zimdar, Rapid-phase modulation of terahertz radiation for high-speed terahertz imaging and spectroscopy. *Optics Letters*, 2008. **33**(14): 1593–1595.
75. Hirata, A., T. Kosugi, H. Takahashi, R. Yamaguchi, F. Nakajima, T. Furuta, H. Ito, H. Sugahara, Y. Sato and T. Nagatsuma, 120-GHz-band millimeter-wave photonic wireless link for 10-Gb/s data transmission. *IEEE Transactions on Microwave Theory and Techniques*, 2006. **54**(5): 1937–1942.
76. Barbieri, S., W. Maineult, S.S. Dhillon, C. Sirtori1, J. Alton, N. Breuil, H.E. Beere and D.A. Ritchie, 13 GHz direct modulation of terahertz quantum cascade lasers. *Applied Physics Letters*, 2007. **91**(14): 143510.
77. Kužel, P. and F. Kadlec, Tunable structures and modulators for THz light. *Comptes Rendus Physique*, 2008. **9**(2): 197–214.
78. Ma, Y., S.C. Saha, A.L. Bernassau and D. R. S. Cumming, Terahertz free space communication based on acoustic optical modulation and heterodyne detection. *Electronics Letters*, 2011. **47**(15): 868–870.
79. Wilk, R., N. Vieweg, O. Kopschinski and M. Koch, Liquid crystal based electrically switchable Bragg structure for THz waves. *Optics Express*, 2009. **17**(9): 7377–7382.
80. Ghattan, Z., T. Hasek, R. Wilk, M. Shahabadi and M. Koch, Sub-terahertz on-off switch based on a two-dimensional photonic crystal infiltrated by liquid crystals. *Optics Communications*, 2009. **281**(18): 2623–4625.
81. Libon, I. H., S. Baumgärtner, M. Hempel, N.E. Hecker, J. Feldmann, M. Koch and P. Dawson, An optically controllable terahertz filter. *Applied Physics Letters*, 2000. **76**(20): 2821–2823.
82. Kersting, R., G. Strasser and K. Unterrainer, Terahertz phase modulator. *Electronics Letters*, 2000. **36**(13): 1156–1158.
83. Chen, H.-T., W.J. Padilla, J.M.O. Zide, A.C. Gossard, A.J. Taylor and R.D. Averitt, Active terahertz metamaterial devices. *Nature*, 2006. **444**(7119): 597–600.
84. Kleine-Ostmann, T. , P. Dawson, K. Pierz, G. Hein and M. Koch, Room-temperature operation of an electrically driven terahertz modulator. *Applied Physics Letters*, 2004. **84**(18): 3555–3557.
85. Cooke, D. G. and P.U. Jepsen, Optical modulation of terahertz pulses in a parallel plate waveguide. *Optics Express*, 2008. **16**(19): 15123–15129.
86. Scherger, B., C. Jördens and M. Koch, Variable-focus terahertz lens. *Optics Express*, 2011. **19**(5): 4528–4535.
87. Wu, H. Y., C. -F. Hsieh, T. -T. Tang, R. -P. Pan and C. -L. Pan, Electrically tunable room-temperature 2π liquid crystal terahertz phase shifter. *IEEE Photonics Technology Letters*, 2006. **18**(14): 1488–1490.
88. Wilk, R., N. Vieweg, O. Kopschinski and M. Koch, Liquid crystal based electrically switchable Bragg structure for THz waves. *Optics Express*, 2009. **17**: 7377.

89. Chen, H. -T., J.F. O'Hara, A.K. Azad and A.J. Taylor, Manipulation of terahertz radiation using metamaterials. *Laser Photonics Review*, 2011. **5**(4): 513–533.
90. Chen, H. T., W.J. Padilla, J. M. O. Zide, S.R. Bank, A.C. Gossard, A.J. Taylor and R.D. Averitt, Ultrafast optical switching of terahertz metamaterials fabricated on ErAs/GaAs nanoisland superlattices. *Optics Letters*, 2007. **32**(12): 1620–1622.
91. Chen, H. -T., W.J. Padilla, M.J. Cich, A.K. Azad, R.D. Averitt and A.J. Taylor, A metamaterial solid-state terahertz phase modulator. *Nature Photonics*, 2009. **3**(3): 148–151.
92. Peralta, X. G., I. Brener, W.J. Padilla, E.W. Young, A.J. Hoffman, M.J. Cich, R.D. Averitt, M.C. Wanke, J.B. Wright, H. -T. Chen, J.F. O'Hara, A.J. Taylor, J. Waldman, W.D. Goodhue, J. Li and J. Reno, External modulators for TeraHertz Quantum Cascade Lasers based on electrically-driven active metamaterials. *Metamaterials*, 2010. **4**(2–3): 83–88.
93. Chan, W. L., H. -T. Chen, A.J. Taylor, I. Brener, M.J. Cich and D.M. Mittleman, A spatial light modulator for terahertz beams. *Applied Physics Letters*, 2009. **94**(21): 213511.
94. Lender, A., The duobinary technique for high-speed data transmission. *IEEE Transactions on Communications and Electronics*, 1963. **82**: 214–218.
95. Penninckx, D., M. Chbat, L. Pierre and J. -P. Thiery, The phase-shaped binary transmission (PSBT): a new technique to transmit far beyond the chromatic dispersion limit. *IEEE Photonics Technology Letters*, 1997. **9**(2): 259–261.
96. Kleine-Ostmann, K., Pierz, G. Hein, P. Dawson and M. Kochw, Audio signal transmission over THz communication channel using semiconductor modulator. *Electronics Letters*, 2004. **40**: 124–126.
97. Kosugi, T., T. Shibata, T. Enoki, M. Muraguchi, A. Hirata, T. Nagatsuma and H. Kyuragi, A 120-GHz millimeter-wave MMIC chipset for future broadband wireless access applications. *IEEE MTT-S International Microwave Symposium Digest*, 2003. **1**: 129–132.
98. Kosugi, T., M. Tokumitsu, T. Enoki, M. Muraguchi, A. Hirata and T. Nagatsuma, 120-GHz Tx/Rx chipset for 10-Gbit/s wireless applications using 0.1- μ m-gate InP HEMTs. *IEEE Compound Semiconductor Integrated Circuit Symposium*, 2004, 2004: 171–174.
99. Hirata, A., T. Kosugi, H. Takahashi, J. Takeuchi, K. Murata, N. Kukutsu, Y. Kado, S. Okabe, T. Ikeda, F. Suginosita, K. Shogen, H. Nishikawa, A. Irino, T. Nakayama and N. Sudo, 5.8-km 10-Gbps data transmission over a 120-GHz-band wireless link. in *2010 IEEE International Conference on Wireless Information Technology and Systems, ICWITS 2010*. 2010.
100. Utsunomiya, T. and M. Sekine, Rain attenuation at 103 GHz in millimeter wave ranges. *International Journal of Infrared and Millimeter Waves*, 2005. **26**(11): 1651–1660.
101. Available from: <http://www.ntia.doc.gov/osmhome/allocrpt.pdf>.
102. Sharing between the radio astronomy service and active services in the frequency range 275–3 000 GHz. Report ITU-R RA.2189. October 2010. Available from: http://www.itu.int/dms_pub/itu-r/opb/rep/R-REP-RA.2189-2010-PDF-E.pdf

Terahertz bio-sensing techniques

J.-H. SON, University of Seoul, Republic of Korea

DOI: 10.1533/9780857096494.2.217

Abstract: This chapter reviews research involving the sensing and analysis of biological materials using terahertz (THz) waves. Because the characteristic energy of biological materials, generated by molecular motions such as rotation and vibration, lies in the THz frequency range, THz spectroscopy is the best tool for the direct sensing of biological molecules and the associated techniques. This review begins with water, outlining its bulk dielectric property and the temperature dependence thereof, and its solvation dynamics in the presence of various solutes including proteins. THz techniques have also been used to study the dynamic behaviour of proteins, as well as to sense ligand binding to proteins. Through the measurement of dielectric functions in the THz range, the binding-state dependence of molecules such as DNA and triple-strand β (beta)-glucans can be characterized. For molecules, such as DNA, RNA, nucleobases, nucleosides and polypeptides, resonant features arising from their characteristic motions are reviewed along with the identification of peaks using density functional theory. The temperature-dependent dielectric property of water has led to the invention of a THz molecular imaging technique using nanoparticles, the principle of which is briefly described with an outline of its potential applications, such as cancer diagnosis and drug delivery monitoring.

Key words: terahertz, bio-sensing, molecular imaging, water dynamics, biological molecules, cancer diagnosis.

7.1 Introduction

Terahertz (THz) waves have been utilized for the study of biological and medical materials, revealing many new phenomena and demonstrating the feasibility of their further use in diagnosing diseases such as cancer (Pickwell and Wallace, 2006; Son, 2009). Investigating biological characteristics and dynamics using THz techniques has both advantages and disadvantages. One of the most important advantages is the low energy of THz waves, corresponding to a few meV, which is well below the ionization energies of atoms and molecules. This means that we can study materials with THz waves without disturbing the system under study, unless enough power is applied to cause a significant increase in temperature. The other major

advantage is that the characteristic energy of the hydrogen bond, which is the most dominant bond in biological molecules, lies in the THz frequency range and, therefore, THz waves can directly detect spectral features such as resonances and motions of molecules. However, a serious disadvantage is the high absorption of THz waves by the water in which biological molecules reside. This water absorption can mask the characteristic features of samples, even though biological dynamics naturally occur in water.

This review begins with the microscopic and macroscopic dynamics of water probed by THz waves. Water molecules affect the dynamics of biomolecules in cells. For example, the interactions between water and proteins cause hydrogen bonds to adjust during the formation of a hydration layer. Macroscopic characteristics of water, such as high absorption around 6 THz and temperature dependence, are also discussed in the next section. In Section 7.3, the study of protein dynamics and ligand binding to proteins by THz dielectric function measurement is reviewed. Binding-state dependencies of DNA and triple-stranded β -glucans are discussed in Section 7.4. Dramatic resonant features of biomolecules such as nucleobases and polypeptides, originating from their characteristic motions, are described in Section 7.5, and the theoretical methods to identify these features are also discussed. On the basis of the THz dynamics of water, a novel molecular imaging technique using nanoparticles, THz molecular imaging (TMI), has been developed, the principle of which is presented in Section 7.6, along with its potential applications in medicine such as cancer diagnosis and drug delivery monitoring. The chapter is summarized in Section 7.7.

7.2 Sensing of water dynamics by terahertz waves

A water molecule consists of two hydrogen atoms and one oxygen atom, and the molecules are bound to each other by hydrogen bonds to form structures of tetrahedral shape. Water is essential in biological systems, as it plays a key role as the solvent in molecular reactions, conformational changes and functions. Water shows characteristic absorption features mainly in the infrared and THz regions, because its resonance is related to symmetric stretch, asymmetric stretch, bending, libration and rotation, which are modified by hydrogen bonding in the liquid state (Pickwell and Wallace, 2006). The combinations of those motions produce complex absorption spectra (Praprotnik *et al.*, 2004). The relaxational response of water is also found in the THz region, and is related to the breakage and formation of a hydrogen bonding network. The dielectric response of liquid water in the THz range can be described by the Debye model, which proposes two distinct processes of relaxation: slow (8 ps) and fast (170 fs) (Kindt and Schmuttenmaer, 1996; Ronne *et al.*, 1997; Ronne *et al.*, 1999; Oh *et al.*, 2007). The slow relaxation

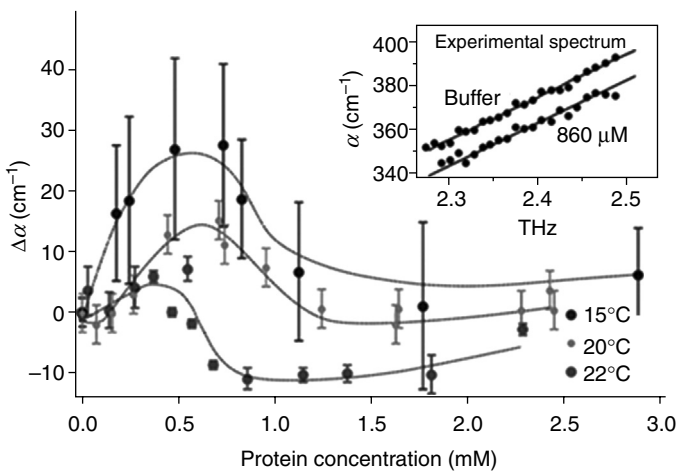
is related to the rotational dynamics of water, but the physical origin of fast relaxation remains unclear. Around a frequency of 6 THz (200 cm^{-1}), a broad shoulder is seen due to the intermolecular vibrational mode caused by the hydrogen bond, and the response to oscillating fields is no longer overdamped but becomes resonant (Zelmann, 1995). Because of the typical timescale of intermolecular vibrations of water, hydrogen bonding network and these relaxation processes is in the picosecond range; THz spectroscopy is a powerful tool for studying the dynamics of water molecules (Kindt and Schmuttenmaer, 1996).

The electromagnetic absorption by water in the THz range is highly dependent on temperature, because the aforementioned motion of water molecules and the hydrogen bonds between them are sensitive to temperature change. The power absorption and refractive index, measured by THz time-domain spectroscopy, show increased values as the temperature is raised (Son, 2009). The power absorption at 367 K is four times larger than that at 271 K at a frequency of 1 THz (Kindt and Schmuttenmaer, 1996). This temperature-dependent change in the absorption properties of water is a basis for the principle of TMI, as explained in Section 7.6.

As well as the dynamics of bulk water, the interaction of water with biological molecules, proteins for example, has drawn much attention, as it can provide clues to the understanding of biological events. Heugen *et al.* observed an increase in the THz absorption of the water in the hydration layer surrounding lactose, which was explained by the coherent oscillations between the water and solute (Heugen *et al.*, 2006). Ebbinghaus *et al.* directly probed the solvation dynamics around proteins by using THz spectroscopy to measure the width of the dynamic hydration layer. The solute concentration dependence of solvation dynamics was also investigated, as shown in Fig. 7.1, and a non-monotonic trend was observed, which was explained by the existence of overlapping solvation layers around proteins (Ebbinghaus *et al.*, 2007). The influence of water on proteins and sugars is well summarized in a report by Born and Havenith (2009). This study found that the dynamic hydration layer of saccharides is composed of several hundred water molecules, while that of proteins contains up to a thousand water molecules (Born and Havenith, 2009).

7.3 Sensing of proteins

Solvation dynamics also affect protein flexibility and protein folding dynamics, as investigated in a previous study using the so-called kinetic THz absorption (KITA) technique. Because the THz absorption and refractive indices of folded protein solutions are different from those of unfolded protein solutions, a change in the THz field was observed (Kim *et al.*, 2008).

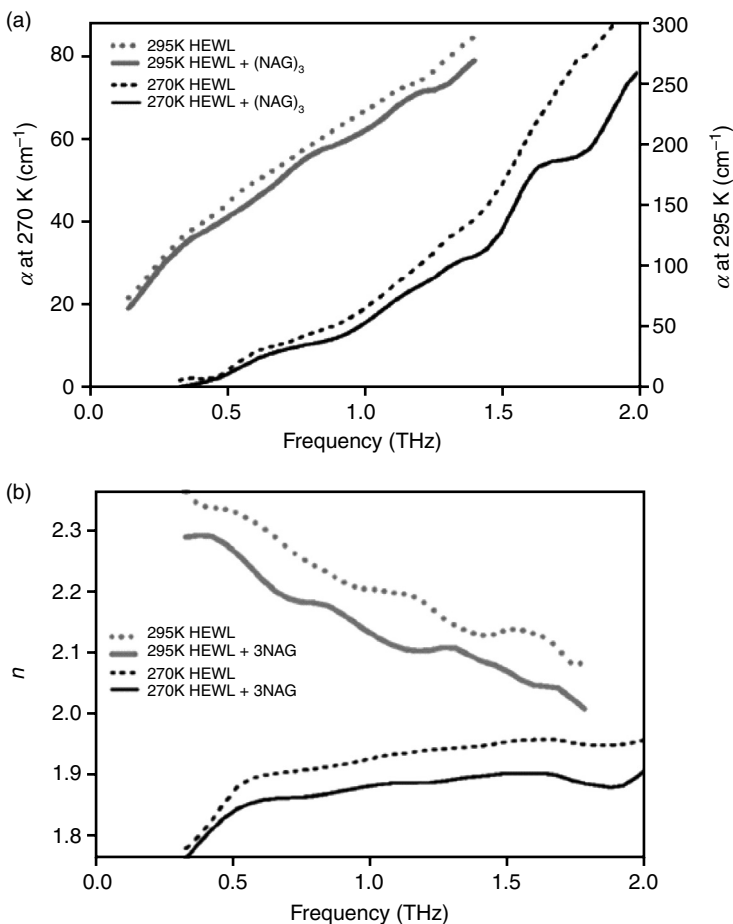


7.1 Difference in absorption of protein at 2.25 THz plotted with respect to concentration. The inset shows the frequency dependence of the absorption coefficient. From Ebbinghaus *et al.* (2007). Copyright © 2007 by The National Academy of Sciences of the USA. Reprinted by permission of The National Academy of Sciences of the USA.

Another protein folding study using the KITA technique revealed that solvent dynamics are related to protein secondary structure formation. The protein folds into its native state within seconds, following the dynamic rearrangement of the solvent water network, which occurs in milliseconds (Born and Havenith, 2009).

The THz molar absorption of solvated bovine serum albumin (BSA) was successfully extracted from the much stronger attenuation of water by Xu *et al.*, and they observed a densely overlapping spectrum of vibrational modes, increasing monotonically with a frequency increment. There was no evidence of distinct spectral features, implying that no specific collective vibrations dominate the protein's spectrum of motions (Xu *et al.*, 2007).

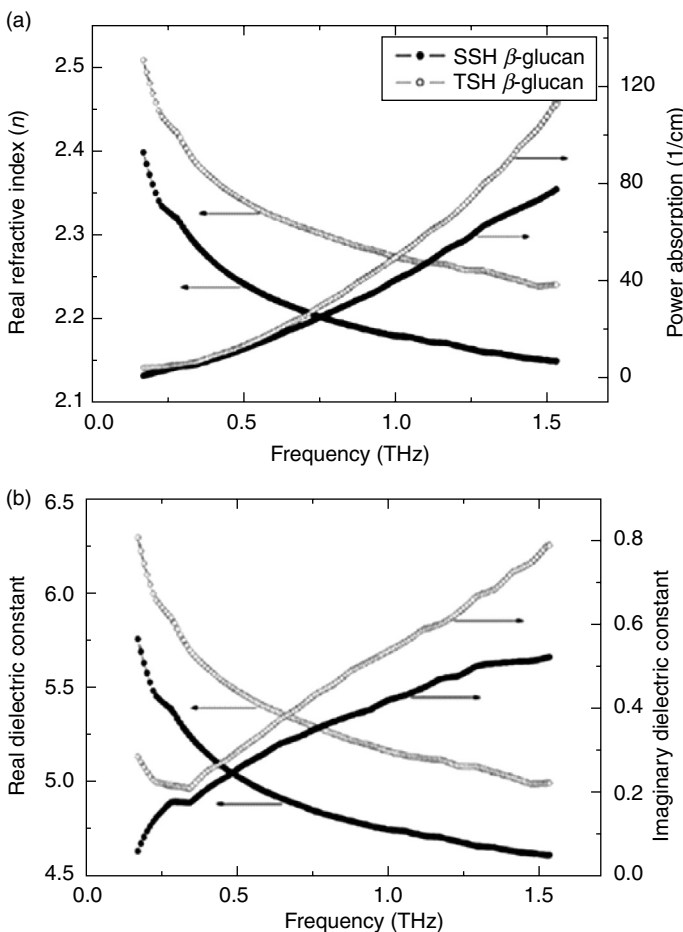
The origin of dynamic transition, a strong temperature dependence of molecular flexibility around 200 K for proteins and polynucleotides above a certain hydration level, has been considered in several studies, being a fundamental question in protein dynamics (He *et al.*, 2008). Although various experimental techniques have been employed by many researchers, these studies have been inconclusive (Bauminger *et al.*, 1983; Doster *et al.*, 1989; Rasmussen *et al.*, 1992; Zaccai, 2000). However, by measuring the dielectric properties of short-chain alanine peptides using THz time-domain spectroscopy, Markelz and her colleagues determined that the strong temperature dependence of molecular flexibility is a result of the interaction of the



7.2 (a) Measured absorption coefficients of HEWL and HEWL + triacetylglucosamine (3NAG) and (b) measured indices of refraction. From Chen *et al.* (2007). Copyright © 2007 by American Institute of Physics. Reprinted by permission of American Institute of Physics.

protein side chains with water, rather than the overall structural motions of the proteins (He *et al.*, 2008; Knab *et al.*, 2007).

It was also observed that protein-ligand binding in the solution phase could be sensitively identified by THz spectroscopy. A ligand, triacetylglucosamine, showed a decrease in absorption and refractive indices upon binding to hen egg white lysozyme (HEWL), as displayed in Fig. 7.2, both at room temperature and below the liquid–solid transition for water. This phenomenon can be exploited in bio-sensing without the need for probe immobilization (Chen *et al.*, 2007).



7.3 (a) Frequency-dependent refractive indices and power absorption, and (b) dielectric constants, of triple-stranded helix (TSH) and single-stranded helix (SSH) β -glucans. From Shin *et al.* (2009). Copyright © 2009 by American Institute of Physics. Reprinted by permission of American Institute of Physics.

7.4 Binding-state dependent sensing

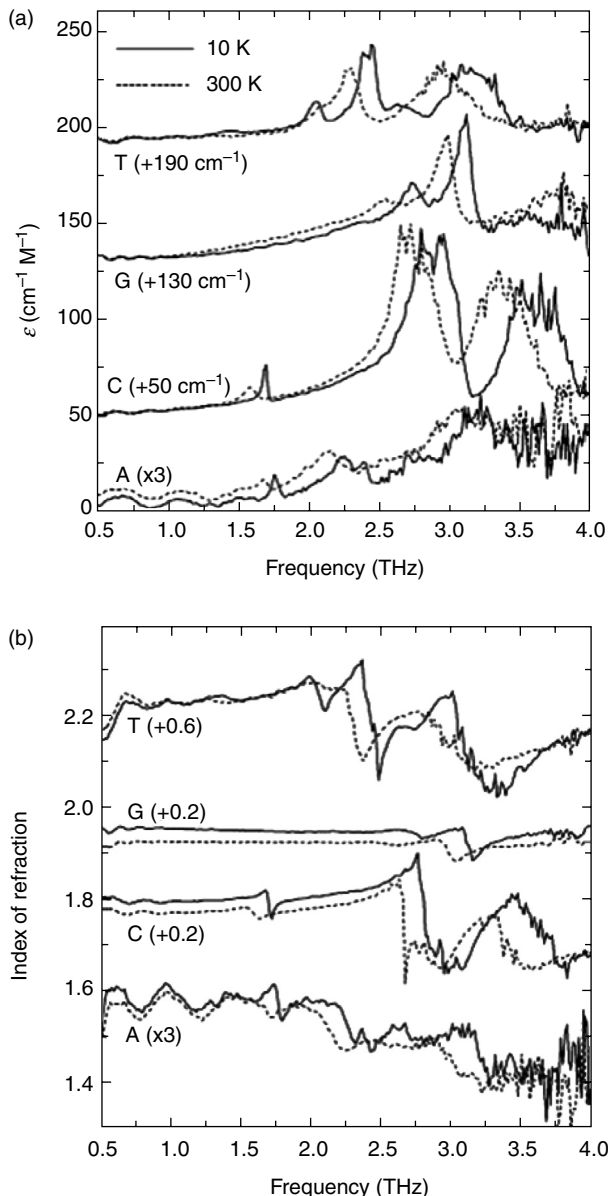
As well as the detection of ligand binding, dielectric function measurement using THz spectroscopy can sense conformational changes in macromolecules. This type of analysis was first attempted with DNA films in order to achieve label-free determination of the binding states of polynucleotides. Brucherseifer *et al.* measured the transmission through hybridized and denatured DNA and found that the denatured form caused less change

in transmission, resulting in a smaller index of refraction (Brucherseifer *et al.*, 2000). Using asynchronous optical sampling THz spectroscopy, the state change of oriented DNA films from hydration to dehydration was measured, and the B to A conformational transition was corroborated by Raman spectroscopy (Kistner *et al.*, 2007). Two different types of artificially synthesized single-stranded RNA, polyadenylic acid (poly-A) and polycytidylic acid (poly-C), were also distinguished by THz dielectric measurements (Fischer *et al.*, 2005).

In addition to DNA and RNA, the conformational state transition of polysaccharides was characterized using the THz-TDS technique (Shin *et al.*, 2009). The polysaccharides used in the study were β -glucans, well-known anti-tumour agents that are widely distributed in algae, fungi and mushrooms. They usually exist as triple-stranded helix (TSH) structures with intermolecular O–H hydrogen bonds. Single-stranded helix (SSH) β -glucans, known to have different immunological activities, can be obtained from the TSH structure by a chemical treatment with NaOH solution. The binding-state dependent conformational change was clearly detectable by THz measurement in terms of refractive index, power absorption and dielectric constant, as shown in Fig. 7.3.

7.5 Characteristic resonances of biomolecules in the terahertz range

The studies described in the previous section showed only the binding-state dependence without displaying the characteristic peaks of DNA and RNA in the THz region, although resonant modes are expected because DNA molecules have twist and H-bond motions at 0–2 THz. Only a few studies were able to observe the distinct resonant features from DNA and RNA by using a sample with a thickness less than 10 μm (Globus *et al.*, 2003; Globus *et al.*, 2006). Measurements of such macromolecules performed on thicker samples have not shown any resonant peaks because of the inhomogeneous broadening caused by neighbouring molecules (Fischer *et al.*, 2005). However, nucleobases, smaller molecules that are the constituents of DNA and RNA, clearly display their vibrational modes in THz transmission measurements (Nishizawa *et al.*, 2005). As can be seen in Fig. 7.4, many distinct spectral features were found for the adenine (A), guanine (G), cytosine (C) and thymine (T) nucleobases in both their frequency-dependent molar absorption coefficients and refractive indices. The corresponding nucleosides, dA, dG, dC and dT (d = deoxyribose), hydrogen bonding between which is known to be essential for the formation and stability of the double-helix structure of DNA, also showed distinct spectral peaks. The spectra of the nucleosides can be characterized by the combination of the



7.4 (a) Molar absorption coefficient and (b) refractive index of the nucleobases A, C, G and T, recorded at 10 K (solid lines) and 300 K (dashed lines). From Fischer *et al.* (2002). Copyright © 2002 by Institute of Physics Publishing. Reprinted by permission of Institute of Physics Publishing.

resonance coming from nucleobases, which is relatively broad and intense in the frequency region above 1.5 THz, and the narrow and asymmetric low-frequency wing, which is located between 1 and 2 THz and stems from vibrational modes involving the sugar groups attached to the nucleobases (Fischer *et al.*, 2002).

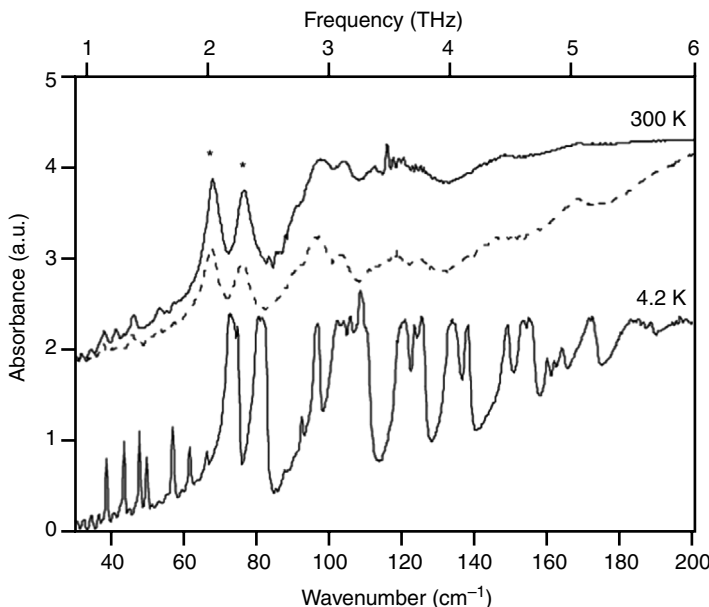
Polypeptides, the constituents of protein, also display resonant features, and their THz absorption spectra can reveal dramatic shape changes according to the combinations of components, although proteins do not show resonant peaks, as explained in the previous sections (Kutteruf *et al.*, 2003). Kutteruf *et al.* measured the THz spectra of various dipeptides (e.g., glycine–alanine) and tripeptides (e.g., valine–glycine–glycine) and observed many distinct features. These features were found to be sequence-dependent, implying that THz absorption spectra are potentially sensitive to amino-acid chain sequence, peptide composition, intermolecular hydrogen bonding and crystal structure packing.

It is usually difficult to identify the sources of measured resonant features either theoretically or experimentally. Nagai *et al.* carefully designed an experiment to distinguish whether these features come from intermolecular or intramolecular vibrations. They spotted water onto L-(+)-arginine mono-hydrochloride and found that the resonant peak at 1.34 THz disappeared. This was due to the decreased molecular interaction between arginine and HCl because HCl is well dissolved in water (Nagai *et al.*, 2005).

Theoretical analysis using density functional theory (DFT) calculations has been applied to identify the sources of resonant peaks. Fischer *et al.* determined the origin of vibrational modes of thymine using DFT, finding that the four lowest-frequency modes occur from intermolecular motion in the form of out-of-plane and in-plane vibrations of hydrogen bonds (Fischer *et al.*, 2002). Low-frequency vibrations of a non-reducing disaccharide, α, α -trehalose dihydrate, were measured below 6 THz at 4 K and 300 K as shown in Fig. 7.5. The two strong peaks at 67.7 and 75.9 cm^{-1} , marked with asterisks in the figure, were ascribed to the torsion modes of two hydroxymethyl groups associated with the hydrogen torsional motion of two water molecules by DFT calculations. A sharp peak at 49.3 cm^{-1} appearing at 4 K is due to the translational motion of water molecules (Takahashi *et al.*, 2006).

7.6 Water-mediated terahertz molecular imaging

As we have reviewed in the previous sections, THz spectroscopy has been widely utilized for the scientific study of biological materials and phenomena. In addition to this, many THz researchers have searched for applications in medicine in order to commercialize THz technology. Wallace and



7.5 Absorption spectra of α,α -trehalose dehydrate in polycrystalline powder form at 300 K (upper) and 4.2 K (lower). The dashed and solid lines represent spectra at 5% and 10% mass concentration, respectively. From Takahashi *et al.* (2006). Copyright © 2006 by Elsevier. Reprinted by permission of Elsevier.

his colleagues tested various tumours of breast and skin cancers *in vivo* and *ex vivo* and found that cancerous tumours can be distinguished from healthy tissues by THz waves (Woodward *et al.*, 2003; Wallace *et al.*, 2004; Fitzgerald *et al.*, 2006). Although their results showed reasonably good agreement with histology, the sensitivity of THz spectroscopy measurements for medical diagnosis can be dramatically improved by using nanoparticle contrast agents, as used in other medical imaging techniques such as magnetic resonance imaging (MRI) and X-ray computed tomography (CT) (Lee *et al.*, 2007; Lee *et al.*, 2008; Oh *et al.*, 2009; Lee *et al.*, 2011).

Nanoparticle probes, such as gold nano-rods, can be delivered or targeted to tumours, organs or cells by antibody conjugation (Weissleder *et al.*, 2000; Weissleder and Ntziachristos, 2003). As the nanoparticles are irradiated with a near infrared (NIR) laser beam, the ambient temperature in the target cell is raised due to the resonance of surface plasma polaritons. This temperature rise changes the optical properties of the water in the cell, such as its absorption and refractive index, particularly in the THz frequency range because there is a characteristic resonance of water molecules at around 6 THz, as explained in Section 7.2. Therefore, the THz

absorbance and reflectance are dramatically changed by the illumination of nanoparticles with an NIR beam (Oh *et al.*, 2009). Based on this principle, water-mediated molecular imaging using THz waves was demonstrated using a highly sensitive differential measurement technique. Issues such as sensitivity, resolution and quantification were also addressed. The sensitivity of the TMI technique is much higher than that of NIR absorption imaging, which is the conventional method for imaging nanoparticles. The quantifiability is also excellent, as the output is linearly proportional to the concentration of nanoparticles. The spatial resolution is limited by the wavelength of the NIR beam but not by that of THz waves, at least in principle. Thus, as examples of its use in medical diagnosis, the TMI technique has been applied for the target-specific sensing of cancers and the molecular monitoring of nanoparticle drug delivery to organs *in vivo* and *ex vivo* (Oh *et al.*, 2011).

7.7 Conclusion

As reviewed in the previous sections, with examples from various biological molecules, THz technology is unique in biological study in having the capacity to provide real-time chemical recognition of characteristic bonds without ionizing them. This valuable property leads to numerous applications including medical diagnosis. Such medical applications are further improved by the TMI technique in combination with nanoparticle probes to result in the sensitive diagnosis of cancers.

7.8 Acknowledgements

The author thanks Mr Hyeongmoon Kim, Mr Heejun Shin and Mr Dong-Kyu Lee for their assistance in the preparation of this paper. This study was supported by a grant from the Korean Health Technology R&D Project of the Ministry for Health, Welfare & Family Affairs, Republic of Korea (A101954) and National Research Foundation of Korea (NRF) grants funded by the Korean government (MEST) under Grant Nos. 20100020647, 20100001979, 20100015989, 20100011934 and 20090054519.

7.9 References

- Bauminger ER, Cohen SG, Nowik I, Ofer S and Yariv J (1983), Dynamics of heme iron in crystals of metmyoglobin and deoxymyoglobin. *Proc. Nat. Acad. Sci.* **80**: 736–740.
Born B and Haverith M (2009), Terahertz dance of proteins and sugars with water. *J Infrared Milli. Terahz. Waves* **30**: 1245–1254.

- Brucherseifer M, Nagel M, Haring Bolivar P, Kurz H, Bosserhof A and Buttner R (2000), Label-free probing of the binding state of DNA by time-domain terahertz sensing. *Appl. Phys. Lett.* **77**: 4049–4051.
- Chen JY, Knab JR, Ye S, He Y and Markelz AG (2007), Terahertz dielectric assay of solution phase protein binding. *Appl. Phys. Lett.* **90**: 243901–1–3.
- Doster W, Cusack S and Petry W (1989), Dynamical transition of myoglobin revealed by inelastic neutron scattering. *Nature* **337**: 754–756.
- Ebbinghaus S, Kim SJ, Heyden M, Yu X, Heugen U, Gruebele M, Leitner DM and Havenith M (2007), An extended dynamical hydration shell around proteins. *Proc. Natl. Acad. Sci. USA* **104**: 20749–20752.
- Fischer BM, Hoffman M, Helm H, Wilk R, Rutz F, Klein-Ostmann, Koch M and Uhd Jepsen P (2005), Terahertz time-domain spectroscopy and imaging of artificial RNA. *Opt. Exp.* **13**: 5205–5215.
- Fischer BM, Walther M and Uhd Jepsen P (2002), Far-infrared vibrational modes of DNA components studied by terahertz time-domain spectroscopy. *Phys. Med. Biol.* **47**: 3807–3814.
- Fitzgerald AJ, Wallace VP, Jimenez-Linan M, Bobrow L, Pye RJ, Prushotham AD and Arnone DD (2006), Terahertz pulsed imaging of human breast tumors. *Radiology* **239**: 533–540.
- Globus T, Bykhovskaya, Woolard D and Gelmont B (2003), Sub-millimetre wave absorption spectra of artificial RNA molecules. *J. Phys. D: Appl. Phys.* **36**: 1314–1322.
- Globus T, Woolard D, Crowe TW, Khromova T, Gelmont B and Hesler J (2006), Terahertz Fourier transform characterization of biological materials in a liquid phase. *J. Phys. D: Appl. Phys.* **39**: 3405–3413.
- He Y, Ku PI, Knab JR, Chen JY and Markelz A (2008), Protein dynamical transition does not require protein structure. *Phys. Rev. Lett.* **101**: 178103–1–4.
- Heugen U, Schwaab G, Brundermann E, Heyden M, Yu X, Leitner DM and Havenith M (2006), Solute-induced retardation of water dynamics probed directly by terahertz spectroscopy. *Proc. Natl. Acad. Sci. USA* **103**: 12301–12306.
- Kim SJ, Born B, Havenith M and Gruebele M (2008), Real-time detection of protein-water dynamics upon protein folding by terahertz absorption spectroscopy. *Angew. Chem. Int. Ed.* **47**: 6486–6489.
- Kindt JT and Schmuttenmaer CA (1996), Far-infrared dielectric properties of polar liquids probed by femtosecond terahertz pulse spectroscopy. *J. Phys. Chem.* **100**: 10373–10379.
- Kistner C, Andre A, Fischer T, Thoma A, Janke C, Bartels A and Gisler T (2007), Hydration dynamics of oriented DNA films investigated by time-domain terahertz spectroscopy. *Appl. Phys. Lett.* **90**: 233902–1–3.
- Knab JR, Chen JY, He Y and Markelz A (2007), Terahertz measurements of protein relaxational dynamics. *Proc. IEEE* **95**: 1605–1610.
- Kutteruf MR, Brown CM, Iwaki LK, Campbell MB, Korter TM and Heiweil EJ (2003), Terahertz spectroscopy of short chain polypeptides. *Chem. Phys. Lett.* **375**: 337–343.
- Lee DK, Kim H, Kim T, Cho B, Lee K and Son JH (2011), Characteristics of gadolinium oxide nanoparticles as contrast agents for terahertz imaging. *J. Infrared Milli. Terahz. Waves* **32**: 506–512.

- Lee J, Yang J, Ko H, Oh SJ, Kang J, Son JH, Lee K, Lee SW, Yoon HG, Suh JS, Huh YM and Haam S (2008), Multifunctional magnetic gold nanocomposites: Human epithelial cancer detection via magnetic resonance imaging and localized synchronous therapy. *Adv. Func. Mat.* **18**: 258–264.
- Lee JH, Huh YM, Jun YW, Seo JW, Jang JT, Song HT, Kim S, Cho EJ, Yoon HG, Suh JS and Cheon J (2007), Artificially engineered magnetic nanoparticles for ultra-sensitive molecular imaging. *Nature Med.* **13**: 95–99.
- Nagai N, Kumazawa R and Fukasawa R (2005), Direct evidence of inter-molecular vibrations by THz spectroscopy. *Chem. Phys. Lett.* **413**: 495–500.
- Nishizawa JI, Sasaki T, Suto K, Tanabe T, Saito K, Yamada T and Kimura T (2005), THz transmittance measurements of nucleobases and related molecules in the 0.4- to 5.8-THz region using a GaP THz wave generator. *Opt. Comm.* **246**: 229–239.
- Oh SJ, Choi J, Meang I, Park JY, Lee K, Huh YM, Suh JS, Haam S and Son JH (2011), Molecular imaging with terahertz waves. *Opt. Express* **19**: 4009–4016.
- Oh SJ, Kang J, Meang I, Suh JS, Huh YM, Haam S and Son JH (2009), Nanoparticle-enabled terahertz imaging for cancer diagnosis. *Opt. Express* **17**: 3469–3475.
- Oh SJ, Son J, Yoo O and Lee DH (2007), Terahertz characteristics of electrolytes in aqueous Luria-Bertani media. *J. Appl. Phys.* **102**: 074702-1–5.
- Pickwell E and Wallace VP (2006), Biomedical applications of terahertz technology. *J. Phys. D* **39**: R301–R310.
- Praprotnik M, Janezic D and Mavri J (2004), Temperature dependence of water vibrational spectrum: a molecular dynamics simulation study. *J. Phys. Chem. A* **108**: 11056–11062.
- Rasmussen BF, Stock AM, Ringe D and Petsko GA (1992), Crystalline ribonuclease A loses function below the dynamical transition at 220 K. *Nature*. **357**: 423–424.
- Ronne C, Astrand PO and Keiding SR (1999), THz spectroscopy of liquid H₂O and D₂O. *Phys. Rev. Lett.* **82**: 2888–2891.
- Ronne C, Thrane L, Astrand PO, Wallquist A, Mikkelsen KV and Keiding SR (1997), Investigation of the temperature dependence of dielectric relaxation in liquid water by THz reflection spectroscopy and molecular dynamics simulation. *J. Chem. Phys.* **107**: 5319–5331.
- Shin HJ, Oh SJ, Kim SI, Kim HW and Son JH (2009), Conformational characteristics of β-glucan in laminarin probed by terahertz spectroscopy. *Appl. Phys. Lett.* **94**: 111911-1–3.
- Son JH (2009), Terahertz electromagnetic interactions with biological matter and their applications. *J. Appl. Phys.* **105**: 102033-1–10.
- Takahashi M, Kawazoe Y, Ishikawa Y and Ito H (2006), Low-frequency vibrations of crystalline α,α-trehalose dehydrate. *Chem. Phys. Lett.* **429**: 371–377.
- Wallace VP, Fitzgerald AJ, Shankar S, Flanagan N, Pye R, Cluff J and Arnone DD (2004), Terahertz pulsed imaging of basal cell carcinoma *ex vivo* and *in vivo*. *British J. Dermatol.* **151**: 424–432.
- Weissleder R, Moore A, Mahmood U, Bhorade R, Benveniste H, Chiocca EA and Basilion JP (2000), *In vivo* magnetic resonance imaging of transgene expression. *Nature Med.* **6**: 351–355.

- Weissleder R and Ntziachristos V (2003), Shedding light onto live molecular targets. *Nature Med.* **9**: 123–128.
- Woodward RM, Wallace VP, Pye RJ, Cole BE, Arnone DD, Linfield EH and Pepper M (2003), Terahertz pulse imaging of *ex vivo* basal cell carcinoma. *J. Invest. Dermatol.* **120**: 72–78.
- Xu J, Plaxco KW and Allen SJ (2007), Probing the collective vibrational dynamics of a protein in liquid water by terahertz absorption spectroscopy. *Protein Science* **15**: 1175–1181.
- Zaccai G (2000), How soft is a protein? A protein dynamics force constant measured by neutron scattering. *Science* **288**: 1604–1607
- Zelmann HR (1995), Temperature dependence of the optical constants for liquid H₂O and D₂O in the far IR region. *J. Mol. Struct.* **350**: 95–114.

Terahertz array imagers: towards the implementation of terahertz cameras with plasma-wave-based silicon MOSFET detectors

S. BOPPEL, A. LISAUSKAS and H. G. ROSKOS,
Johann Wolfgang Goethe-Universität, Germany

DOI: 10.1533/9780857096494.2.231

Abstract: This chapter deals with plasma-wave-based detection of THz radiation with metal–oxide–semiconductor field-effect transistors (MOSFETs). Building on the general presentation of the subject in Chapter 5, the focus is now on room-temperature detectors and focal-plane arrays in Si complementary metal oxide semiconductor (CMOS) technology. A review of the detection principle emphasizes the close relationship with resistive mixing at low radiation/signal frequencies, which develops into distributed resistive mixing above the transistors' cut-off frequency, and then into full plasmonic mixing. Detector design, implementation and characterization are discussed for frequencies from 200 GHz to beyond 4 THz. A 10-kilopixel array is emulated experimentally, and imaging in power-detection and heterodyne mode are presented.

Key words: complementary metal oxide semiconductor (CMOS), terahertz (THz) camera, field effect transistor (FET)-based rectification, resistive mixing, plasmonic mixing.

8.1 Introduction

While many potential applications of terahertz (THz) sensing and imaging have been identified, wide commercial success continues to be limited due to the lack of suitable components in the spectral range from 300 GHz to 10 THz. This is especially true for THz imaging, potentially the largest market for THz technology as a whole. Cost-efficient, real-time THz imaging remains a challenge, despite major research efforts on sources and detectors. With regard to sources, the difficulty in providing sufficient radiation power with sufficiently compact emitter systems still represents a major hurdle. Passive imaging (detecting thermal radiation emitted, or ambient radiation reflected, by the object under investigation itself) is usually not an

alternative because thermal and ambient radiation power levels are much lower at THz frequencies than in the infrared and visible spectral ranges. Opto-electronic approaches, which are based on lasers operating in the near-infrared or visible and employ coherent optoelectronic conversion to and from THz frequencies, may spawn fast imaging systems (Kawase *et al.*, 2005; Malcolm, 2007; Friederich *et al.*, 2010; Meng *et al.*, 2010) but existing systems do not provide enough power or are too bulky and usually much too expensive to represent a good solution (Jiang and Zhang, 1999; Oda, 2010).

With regard to research on detectors, the last few years have been an exciting time. A wide range of thermal, photonic and electronic detection concepts have been explored and very promising routes for sensitive detection have been identified. Novel detectors and focal-plane arrays have emerged. Section 8.5 briefly summarizes the current status of those detectors which are available – or could be so soon – for real-time imaging under non-cryogenic conditions.

Interestingly, it is a combination of new detection concepts, or at least new aspects thereof, and the projection of these concepts onto well-established device implementation and fabrication platforms (such as complementary metal oxide semiconductor (CMOS) or bipolar complementary metal oxide semiconductor (BICMOS) for silicon, or comparably mature technologies for III/V semiconductors), which together mark out the success of these device developments. The linking of THz technology with technologies from mainstream electronics benefits tasks which require a high level of precision and reproducibility, such as the monolithic fabrication of focal-plane arrays. To a degree, this common trend to build as much as possible on existing platform solutions is a reversal of the approach of former years where it was more the ambition of researchers to come up with new detector concepts or new detector materials.

The CMOS-based detector, which is at the centre of this contribution, provides a study in case. The concept of the detection of radiation deep in the THz range (up to several THz) by using FETs is novel, because it overcomes the bandwidth-restricting transport-time limitations of the charge carriers by utilizing non-quasi-static phenomena in the transistor's channel. The mechanism is explained in terms of rectification mediated by plasma waves in the channel (Dyakonov and Shur, 1996). Details of the physical concept and of the pioneering experimental work to prove and explore plasma-wave-related phenomena in FETs can be found in Chapter 5 by W. Knap and M. I. Dyakonov. From this scientific foundation, a viable THz sensing and imaging technology is developing rapidly at this time by the projection of the concept onto mainstream silicon electronics, which not only includes the foundry-based fabrication of the entire devices, but also the use of the library of functional and read-out solutions which the technology

platform offers. This brings with it significant advantages with respect to costs, scalability, device uniformity, reliability and function integration.

This chapter gives a detailed description of the detection principle, moving from an intuitive quasi-static picture to a more advanced plasma-wave description, in order to derive practical device quantities useful for the description of detector performance and the discussion of detector optimization. Special emphasis is given to practical aspects of device realization in CMOS technology, to focal-plane implementation, and to detector and focal-plane characterization. Multi-pixel imaging by direct-power detection as well as heterodyne detection is presented for a 10-kilopixel ‘quasi-camera’ which emulates a real-time imaging system.

8.2 Resistive mixing – a quasi-static analysis

Before discussing the detection principle at THz frequencies, we will explain detection in terms of classical resistive mixing to provide an intuitive understanding of the underlying detection mechanism and to introduce different modalities of signal coupling and readout. Even though resistive mixing relies on a quasi-static analysis and thus is not applicable to the THz frequency range, it reproduces the detector response of the full non-quasi-static treatment to quite a large extent (Lisauskas *et al.*, 2009; Öjefors *et al.*, 2009).

In the following and throughout the whole chapter, we repeatedly consider the strong-inversion regime, where $U_{\text{gs}} - U_{\text{th}} > \eta k_B T/q$ (U_{gs} is the gate-to-source voltage, U_{th} the threshold voltage, η the non-ideality factor, k_B the Boltzmann constant, T the temperature and q the electron charge). Although actual device operation is usually close to the threshold voltage and hence below the strong-inversion regime, the analytical expressions obtained for the latter are very useful and yield good quantitative approximations.

In the strong-inversion regime, the drain current of an FET is determined by the well-known textbook equation describing quasi-static device operation (Öjefors *et al.*, 2009):

$$I_d = G_{\text{ds}} U_{\text{ds}} = \mu C_{\text{ox}} \frac{W}{L} \left((U_{\text{gs}} - U_{\text{th}}) - \frac{U_{\text{ds}}}{2} \right) U_{\text{ds}}, \quad [8.1]$$

where W and L denote the channel width and length, respectively, C_{ox} the oxide (gate-to-channel) capacitance per unit area, and μ the mobility. If an a.c. signal $U_{\text{RF}} \sin(\omega_{\text{RF}} t)$ is used to simultaneously modulate the channel conductance G_{ds} as well as the drain–source voltage U_{ds} , the drain current I_d , being the product of both quantities, shows a $\sin^2(\omega_{\text{RF}} t)$ -dependence. Therefore, it contains a rectified response which is proportional to U_{RF}^2 and hence is also proportional to the power of the incoming a.c. signal. Power

detection based on this $\sin^2(\omega_{\text{RF}}t)$ -dependent rectification is commonly referred to as *square-law detection*.

Equation [8.1] shows that two signal coupling approaches are in principle possible for square-law detection with FETs: (i) Gate–source coupling: If an a.c. signal is applied across the gate–source contacts, $U_{\text{gs}} = U_g + U_{\text{RF}}\sin(\omega_{\text{RF}}t)$, in order to modulate the channel conductance, rectification in the quasi-static regime requires simultaneous application of the a.c. signal to the drain–source contact $U_{\text{ds}} = U_{\text{RF}}\sin(\omega_{\text{RF}}t)$. U_g denotes the d.c. bias voltage, which controls the d.c. channel conductance. This simultaneous application of the oscillatory signal may be realized by using an external a.c.-signal-shunting capacitor connecting the gate and drain contacts. Additional enhancement of rectification can be achieved by introducing a phase shift of π between the oscillations of the gate–source and drain–source contacts (Krekels *et al.*, 1992). (ii) Drain–source coupling: rectification can also be achieved by an a.c. signal solely applied to the drain contact, $U_{\text{ds}} = U_{\text{RF}}\sin(\omega_{\text{RF}}t)$, and the gate contact remains only d.c.-biased, $U_{\text{gs}} = U_g$. One has principally two options to handle drain–source coupling practically. Either the source contact or the drain contact is on a.c. ground (the source is – by definition – always where d.c. ground is). Because there is usually no fundamental difference between the two cases, we will not explicitly discuss the situation that the source contact is not a.c.-grounded, but its potential is modulated by the a.c. signal. We will assume that source and gate are jointly a.c.-grounded.

The gate-voltage source can be utilized as an a.c. shunt. In this case, only the second term on the right side of Equation [8.1] contributes. Because the conductance also depends on the drain–source voltage, mixing is achieved without additional external shunting.

For both case – gate–source coupling and drain–source coupling – one determines from Equation [8.1] the magnitude of the d.c.-current response (Öjefors *et al.*, 2009):

$$I_{\text{det}} = \langle I_d \rangle = G_{\text{ds}} \frac{U_{\text{RF}}^2}{4(U_g - U_{\text{th}})}, \quad [8.2]$$

where $\langle \dots \rangle$ denotes the time average. This form of readout will be referred to as current readout mode. The detector can also be read out in voltage mode by a high-impedance voltmeter connected between source and drain. Then the d.c. current of Equation [8.2] builds up a potential difference between source and drain:

$$U_{\text{det}} = \langle U_{\text{ds}} \rangle = \frac{\langle I_d \rangle}{G_{\text{ds}}} = \frac{U_{\text{RF}}^2}{4(U_g - U_{\text{th}})}. \quad [8.3]$$

The quasi-static treatment presented in this paragraph applies to FETs operated below the transistors' cut-off frequency. The cut-off frequency is defined as the frequency of unity gain (Sze and Ng, 2007). Describing a specific technology, this value is usually specified in the deep-inversion regime. In contrast, FET-based detectors work close to the threshold. Here the cut-off is reached at considerably lower frequencies. See also the discussion of Fig. 8.3. Resistive mixing has been known for a very long time in the electronics community, and it has been used to implement incoherent broadband power detectors, which includes detectors for the range of 10 to 500 MHz using junction-gate field-effect transistors (JFETs) (Barrett, 1987), and detectors for the 0.1–3 GHz range using GaAs metal-semiconductor FETs (MESFETs) (Krekels *et al.*, 1992). For higher frequencies, the description of the current-voltage dependence of Equation [8.1] breaks down. In contrast to transport-time-limited phenomena, such as amplification or switching in logic circuits, the detection mechanism of a.c. signals via rectification survives non-quasi-static conditions.

Resistive mixing is not limited to FETs. It also works with other kinds of transistors such as bipolar ones (Pfeiffer *et al.*, 2008b).

8.3 Plasmonic mixing – a hydrodynamic analysis

In the following sections, we consider the FET's electronic response and notably the mixing behaviour without the limitation of the a.c. signal's frequency to the quasi-static regime. If the transit-time-limited cut-off frequency is reached or exceeded, one can no longer consider the FET as a lumped element, but it rather has to adopt a waveguide picture in order to describe the spatio-temporal behaviour of the electrical potential and the charge-density in the FET's channel. In this section, we analyse the FET's response on the basis of the hydrodynamic transport model, which has proven to be highly useful to tackle this task.

8.3.1 The device model

In order to describe rectification in FETs under high-frequency excitation, the electron transport along the transistor channel is modelled by the hydrodynamic equations for the charge density n and the drift velocity v according to Dyakonov and Shur (1993, 1996):

$$\frac{\partial v}{\partial t} + v \frac{\partial v}{\partial x} + \frac{q}{m} \frac{\partial U}{\partial x} + \frac{v}{\tau} = 0, \quad [8.4]$$

$$\frac{\partial n}{\partial t} + \frac{\partial(nv)}{\partial x} = 0. \quad [8.5]$$

Here, $U = U(x) = U_{\text{gs}}(x) - U_{\text{th}}$ denotes the gate-to-channel voltage swing along the channel, which is defined as the difference between local gate-to-channel voltage and threshold voltage, q is the electron charge m the effective electron mass and τ the effective scattering time. Additionally, we assume an instantaneous dependence of the local carrier density $n = n(x)$ on the local gate-to-channel voltage swing $U(x)$ (Shur *et al.*, 1992; Knap *et al.*, 2002):

$$n = \frac{C_{\text{ox}} \eta k_B T}{q^2} \ln \left(1 + \frac{1}{2} \exp \left[\frac{qU}{\eta k_B T} \right] \right). \quad [8.6]$$

Note that the corresponding expression in Knap *et al.* (2002), in contrast to Shur *et al.* (1992), does not have the factor $1/2$ in front of the exponent. Equation [8.6] is a semi-empirical expression (evident already from the fact that it contains the fit factor η), and its approximative nature makes it fairly tolerant to parameter changes. For reasons of consistency, note however that all expressions which use Equation [8.6] in the following hence differ by this factor $1/2$ from corresponding expressions in Knap *et al.* (2002).

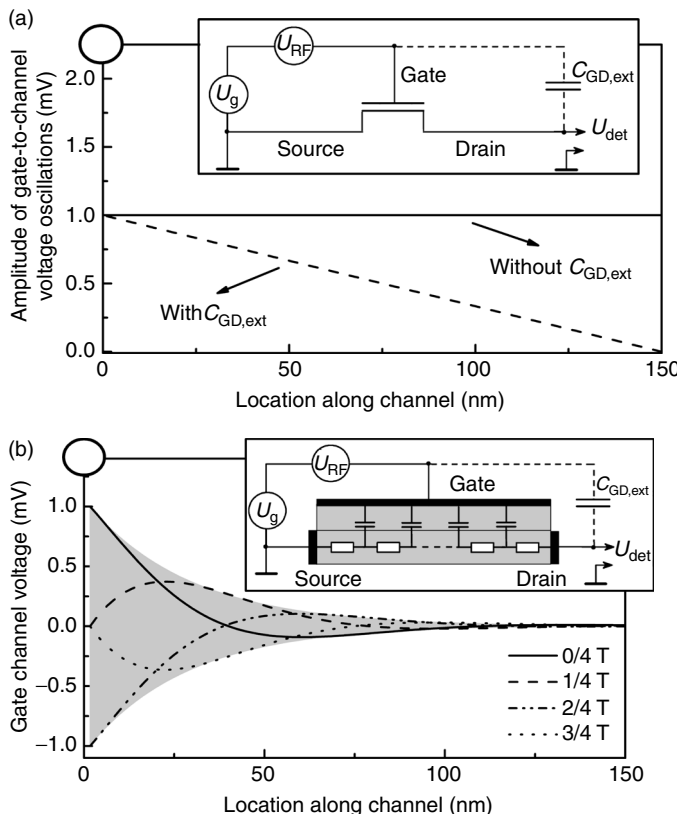
In the strong-inversion regime, $U_{\text{gs}} - U_{\text{th}} > \eta k_B T/q$, Equation [8.6] can be approximated by:

$$n = \frac{C_{\text{ox}}}{qU}. \quad [8.7]$$

In the hydrodynamic equations, the mechanism of rectification by classical resistive mixing finds an extension as a local phenomenon which is expressed in the second term of the continuity equation (Equation [8.5]), the gradient of the product of the local carrier density n , and the local carrier velocity v . As both quantities depend on the external a.c. signal(s), the product term represents a mixing operation of two oscillatory signals which produce a time-independent (rectified) contribution. Its value critically depends on the boundary conditions at the three terminals of the transistor. The fundamentally new aspect is that externally introduced voltage modulations generate oscillations of the potential and charge carrier density, which propagate as plasma waves through the channel.

8.3.2 The resistive mixing regime

In order to demonstrate that classical resistive mixing is contained in the Dyakonov–Shur equations, one can solve them for the quasi-static limit and reproduce the results of resistive mixing. Neglecting the time-dependent



8.1 Spatial distribution of gate-to-channel voltage oscillations with and without external capacitive shunting. (a) Amplitude of oscillations in the quasi-static regime, in which rectification only occurs with external capacitance. (b) Gate-to-channel voltage for distributed resistive self-mixing, depicted at four different time points (fractions of the oscillation period T). External shunting does not affect the oscillations, as the function of the external shunt is taken over by the residual distributed capacitance along the channel.

terms $\partial v / \partial t$, $\partial n / \partial t$ along with the convective term $v (\partial v / \partial x)$, and also assuming strong inversion, reduces Equations [8.4] and [8.5] to the form $\partial^2 U^2 / \partial x^2 = 0$. Its solution at the boundaries is that of Equation [8.1]. We now assume an oscillatory gate-source voltage $U_{gs} = U_g + U_{RF} \sin(\omega_{RF} t)$. Figure 8.1a shows the spatial distribution of the amplitude of the resulting gate-to-channel voltage oscillations. The solid line represents the result obtained without an external shunt between gate and drain (see inset of Fig. 8.1a), showing that the oscillations are of uniform amplitude along the channel. The uniformity prohibits a d.c. response across the

channel. An external shunt capacitor breaks this uniformity (see dashed line in Fig. 8.1a) because it pins the drain potential to the gate potential. The amplitude of the voltage oscillations introduced at the source linearly decreases along the channel to vanish at the drain. This decrease implies that an electric field is generated along the channel which now interacts with the gate-modulated channel conductivity to produce a rectified signal.

8.3.3 The distributed resistive-self-mixing regime

If the frequency is raised, the quasi-static conditions gradually break down and oscillations begin to propagate in the form of plasma waves along the channel. One enters the regime of distributed resistive self-mixing. The frequency is still low enough that $\omega_{\text{RF}}\tau \ll 1$. In the Dyakonov–Shur equations, $\partial v/\partial t$ can be assumed to be negligibly small compared to v/τ . The convective term $v(\partial v/\partial x)$ can be neglected for gate–source voltages U_{gs} close to the threshold voltage U_{th} (Knap *et al.*, 2002). Then, Equations [8.4], [8.5] and [8.7] reduce to the following second-order differential equation:

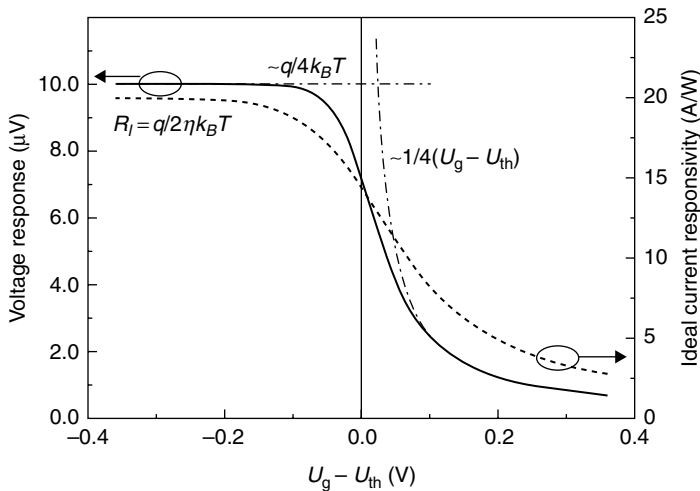
$$\frac{\partial U}{\partial t} - \mu \frac{1}{2} \frac{\partial^2 U^2}{\partial x^2} = 0 \quad [8.8]$$

For sufficiently long channels, the plasma waves, which are excited at the boundaries, fully decay along the channel. Numerical simulations with parameters typical for metal oxide semiconductor field effect transistors (MOSFETs) at room temperature show that, at 600 GHz, the decay length of the plasma waves is 42 nm (Lisauskas *et al.*, 2009b) (decay length: the distance after which the relative amplitude has decreased to $1/e$ of its initial value; for III/V materials, see Preu *et al.* 2012). With increasing frequency, the decay length decreases.

We now come to an expression for the detector response for gate–source coupling, with $U(x=0,t) = U_{\text{gs}} - U_{\text{th}} = U_g + U_{\text{RF}}\sin(\omega_{\text{RF}}t) - U_{\text{th}}$, remarking that the response for drain–source coupling is identical, except for a change of sign.

Assuming a solution of the channel potential of the form $U(x,t) = U_0(x) + U_1(x)\exp(-i\omega t)/2 + U_1^*(x)\exp(i\omega t)/2$, thus considering harmonic coupling only to the first order, the small-signal ($U_{\text{RF}} \ll k_B T/q$) d.c. voltage response across the channel U_{det} is given by Knap *et al.* (2002) (note remark at Equation [8.6]):

$$U_{\text{det}} = \frac{qU_{\text{RF}}^2}{4\eta k_B T} \frac{1}{1 + 2 \exp\left[-\frac{q(U_g - U_{\text{th}})}{\eta k_B T}\right]} \frac{1}{\ln\left(1 + \frac{1}{2} \exp\left[\frac{q(U_g - U_{\text{th}})}{\eta k_B T}\right]\right)}. \quad [8.9]$$



8.2 Voltage response (continuous line) and the ideal current responsivity (dashed line) as a function of the gate bias voltage for an ideality factor $\eta = 1$. Dashed-dotted lines indicate approximations of the voltage response for the deep-sub-threshold regime (left) and for strong inversion (right). The ideal current responsivity assumes full power conversion by ideal impedance matching for all gate voltages applied.

Figure 8.2 displays a plot of the voltage response as a function of the d.c. gate bias voltage U_g for an applied signal amplitude of $U_{\text{RF}} = 1 \text{ mV}$, an ideality factor $\eta = 1$, and assuming room temperature. In the deep-sub-threshold regime, where $U_g - U_{\text{th}} < 0$ and $|U_g - U_{\text{th}}| \gg k_B T / q$, the voltage response becomes maximal and can be approximated by a constant value of

$$U_{\text{det}} = \frac{q U_{\text{RF}}^2}{4 \eta k_B T} \quad [8.10]$$

The detector behaviour can also be expressed as ideal current responsivity \Re_I (see also Section 8.5.1), a quantity independent of the applied signal and independent of the detectors' input resistance. The current responsivity is normalized to the incident power and full power conversion is assumed.

\Re_I is displayed by the dashed line in Fig. 8.2. It is fundamentally limited by $q/2\eta k_B T$ (yielding a value of 20 A/W for $U_{\text{RF}} = 1 \text{ mV}$ at room temperature and with an ideality factor $\eta = 1$).

The voltage response of Equation [8.9] can be approximated in the strong-inversion regime by

$$U_{\text{det}} = \frac{U_{\text{RF}}^2}{4(U_g - U_{\text{th}})}. \quad [8.11]$$

Equation [8.11] is identical to the lumped-element solution of resistive mixing as given by Equation [8.3]. This implies that the derived self-mixing response in this regime of strongly damped plasma waves ($\omega_{\text{RF}} \tau \ll 1$) is independent of the channel length, which is remarkable for the THz range, as it implies that arbitrarily large FETs can in principle be used for THz detection, as long as one neglects noise, parasitic effects, and impedance matching aspects. Rectification of a continuous-wave signal at THz frequencies is not transit-time limited because it is mediated by decaying plasma waves, which do not depend on the transport of charge carriers. For long devices, the rectification takes place only close to the boundary at which the oscillatory signal is injected (compare Fig. 8.1b). The residual part of the transistor can be considered itself as a capacitive shunt, thus intrinsically providing the non-uniformity of the charge-density oscillations needed for rectification by shorting the gate and drain contacts in the case of gate-source coupling, respectively shorting the source and gate contacts for drain coupling. Therefore, in comparison to resistive mixing, the rectification is self-induced, through the plasma wave. An external shunt capacitor is not needed anymore.

Rectification in this frequency regime can also be understood by modelling the transistor as a waveguide consisting of a discrete series of resistive mixers (Lisauskas *et al.*, 2009b) (see inset of Fig. 8.1b). Therefore this description was termed *distributed resistive self-mixing*. The channel is divided into discrete segments. Each segment i consists of a resistor with a resistance R_i and a capacitor with capacitance C_i . This is equivalent to a nonlinear RC-transmission-line description, however with R_i being dependent on the gate-to-channel voltage U_i . The voltage difference between the i th segment and its neighbour is equal to the current I_i through the i th resistor times its resistance R_i : $\Delta U_i = U_{i+1} - U_i = I_i R_i$. Employing the definition of resistance $R_i = \rho_i \Delta x / A$ with $\rho_i = 1/(-qn\mu)$ being the specific resistance, Δx the length of each segment, and A the effective cross-section, one obtains:

$$\frac{\Delta U_i}{\Delta x} = \frac{1}{-en\mu} \frac{I_i}{A}, \quad [8.12]$$

with $\mu = -q\tau/m$, $I_i = -qnvA$ and applying the continuum limit $\Delta x \rightarrow 0$, we reproduce Equation [8.4] without time-dependent and convective terms, thus yielding:

$$\frac{q}{m} \frac{\partial U}{\partial x} + \frac{v}{\tau} = 0. \quad [8.13]$$

The current law states $I_i = I_{i+1} + I_{ci}$, thus the difference of currents $\Delta I = I_{i+1} - I_i = \Delta(-qnvA)$ is equal to the current flow through the i th capacitor

$I_{ci} = \partial Q_{ci}/\partial t = -eA^{\Delta x}\partial n/\partial t$. The continuum limit $\Delta x \rightarrow 0$ yields the continuity equation,

$$\frac{\partial n}{\partial t} + \frac{\partial(nv)}{\partial x} = 0. \quad [8.14]$$

The model of distributed resistive self-mixing is not only helpful to understand the connection between resistive mixing and the Dyakonov–Shur description, but can also be useful for modelling with circuit design tools. Simulations of the FET response can be found in Öjefors *et al.* (2009).

8.3.4 The plasmonic mixing regime

With increasing frequency, one reaches $\omega_{RF}\tau \approx 1$, and the approximations made to the Dyakonov–Shur equations in order to describe distributed resistive self-mixing becomes invalid. The full equations must be considered without approximations.

High-frequency enhancement of the sensitivity

Solving the set of Equations [8.4–8.6], one arrives at an expression for the rectified voltage which can be written in the form $U_{\text{det}} = \frac{U_{\text{RF}}^2}{4(U_g - U_{\text{th}})} \cdot f(L, \tau, s, \omega)$. This corresponds to Equation [8.11] with the additional dimensionless efficiency factor $f(L, \tau, s, \omega)$, which depends, in addition to the channel length L and the scattering time τ , on the radiation frequency and the velocity s of the plasma wave (Dyakonov and Shur, 1996). An evaluation of $f(L, \tau, s, \omega)$ in the long-channel approximation (plasma wave decays before the other channel contact is reached) is shown in Fig. 8.3 for the mobility parameters of CMOS transistors at room temperature (Boppel *et al.*, 2012c). The τ channel length is assumed to be $L = 150$ nm. The mobility value μ_1 of $110 \text{ cm}^2/\text{Vs}$ (yielding $\tau_1 = 17$ fs, obtained

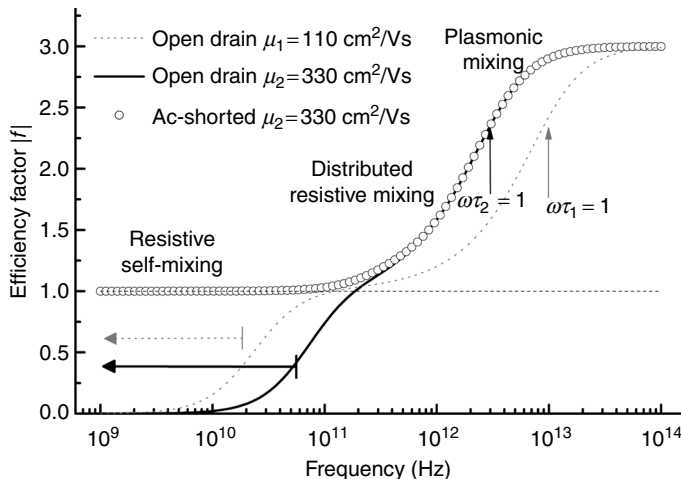
with $m = 0.26 m_0$) is a typical value obtained from experiments with our devices described later. The mobility of $330 \text{ cm}^2/\text{Vs}$ ($\tau_2 = 50 \text{ fs}$) is a typical literature value. An efficiency factor of $f = 1$ corresponds to the response of Equation [8.11] obtained in the resistive self-mixing regime. The solid line and the dashed line show the efficiency for μ_1 and μ_2 , respectively, for gate–source coupling without external shunt to the drain contact. The circles depict the efficiency for μ_2 for the case with external shunt. The same result is obtained for drain–source coupling. Considering uns-hunted gate–source coupling, mixing is absent at low frequencies, in the regime of classical resistive mixing. With rising frequency, mixing sets in and becomes more efficient as the regime of distributed resistive mixing is approached. The latter is formally reached when the signal frequency exceeds $\omega \geq 2s^2\tau/L^2$ (Boppel *et al.*, 2012c). This boundary is marked in Fig. 8.3 by short vertical lines at 20 GHz for μ_1 , respectively 60 GHz for μ_2 . Distributed resistive self-mixing is fully developed at about 100 GHz. With increasing frequency, one then enters a broad transition region to full plasmonic mixing. This transition is characterized by a continuous rise of the efficiency factor $f(L, \tau, s, \omega)$ up to a value of three. The condition $\omega_{\text{RF}}\tau = 1$ is fulfilled at 9.6 THz for μ_1 , respectively 3.2 THz for μ_2 , more than half-way up the rise in this transition region. The rise finally levels off at several THz reaching a plateau. Mathematically, this corresponds to reaching conditions where the scattering term v/τ in Equation [8.4] can be neglected against the time-derivative term $\partial v/\partial t$. Hence, at very high frequencies, electron scattering plays no role any more, and maximal rectification efficiency is reached. The Dyakonov–Shur model contains no mechanism for a decrease of the rectification efficiency thereafter.

Regarding drain–source coupling, respectively drain-shunted gate–source coupling, the high-frequency behaviour is the same as discussed for uns-hunted gate–source coupling. At low frequencies, this is different. One starts out with $f = 1$, which only changes with the transition to full plasmonic mixing. While the efficiency factor hence stays nearly constant in the transition region from classical resistive mixing to distributed resistive self-mixing, the role of the external shunt is taken over gradually by the residual capacitance of the channel. This is reflected in Fig. 8.3 in the black curve coming nearer the circles until they finally merge.

An analysis of the plasmonic mixing regime in the waveguide picture is given in Preu *et al.* (2012).

Resonant mixing

When the decay length of the plasma waves becomes larger than the channel length, $s\tau/L > 1$, the long-channel approximation breaks down and one



8.3 Frequency dependence of the efficiency factor $f(L,\tau,s,\omega)$ over all three frequency regimes for a MOSFET with a gate length of 150 nm. Circles: drain–source coupling or equivalently gate–source coupling with an external capacitive shunt to the drain. Solid and dashed curves: unshunted gate–source coupling for two mobility values. The dashed curve uses an experimentally determined mobility value whereas the solid line is based on a typical literature-specified CMOS mobility. The horizontal dashed line marks the unity efficiency characteristic for classical resistive self-mixing. (Adapted from Fig. 4.b, Boppel *et al.*, 2012c.)

enters the regime of *resonant mixing*. Plasma waves will be reflected at the contacts, and wave interference (leading to etalon-like effects) becomes important. Theory predicts a large enhancement of the responsivity of the FETs at the resonance frequencies with constructive wave interference (Dyakonov and Shur, 1996). While indications of resonant mixing have been observed with high-mobility III/V FETs at cryogenic temperatures (see Chapter 7), this is not the case for silicon transistors.

8.4 Technology, design and implementation of complementary metal oxide semiconductor (CMOS) field effect transistors as terahertz detectors

Having reviewed the principle of operation, this section is devoted to providing details on how the detection concept can be implemented with standard silicon CMOS technology.

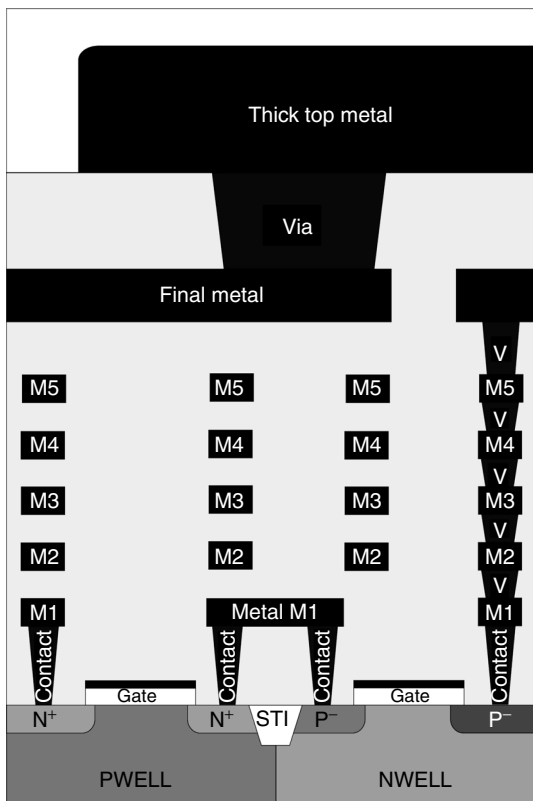
8.4.1 CMOS technology with respect to THz focal-plane arrays

The CMOS process has become the dominant technology in modern integrated circuit manufacturing due to its advantages of low power dissipation and its possibility of an overwhelmingly large transistor count per chip. This technology offers mature, cost-efficient and highly reliable fabrication processes. These properties are of paramount importance, which explains why the success of CMOS technology is not limited to logic circuitry but also extends to modern monolithically-integrated digital camera chips, readout integrated circuitry (ROIC) and data post-processing circuitry. Linking the fabrication of THz detectors and focal-plane arrays to CMOS technology is highly desirable.

That antenna-coupled FET detectors (including amplifiers for the rectified signal, if desired) can be fully integrated into silicon CMOS technology was first shown in Pfeiffer *et al.* (2008a), Lissauskas *et al.* (2009b) and Öjefors *et al.* (2009) for a frequency of 645 GHz. Since then, a number of groups have worked on an improvement of the detectors – also extending the approach to more sophisticated silicon-based technologies – and on the development of focal-plane arrays (Öjefors *et al.*, 2010; Kopyt *et al.*, 2011; Schuster *et al.*, 2011; Sherry *et al.*, 2011). All-silicon integration (even monolithic) of focal-plane arrays with ROICs is foreseen.

Figure 8.4 shows a schematic view illustrating the basic architecture of CMOS process technology. FETs are commonly processed on doped silicon substrate. In order to achieve the high circuit complexity of modern micro-chips, the CMOS process provides a large back-end of up to ten metal layers for the electrical connection of transistors and other elements. This back-end can be utilized for antenna integration. The properties and allowed thicknesses of the materials used for both metallization and electrical insulation are well suited for patch antennas in the THz frequency range (see the following text) (Boppel *et al.*, 2012c).

Because of the large wavelength and correspondingly large size of the antennas, THz detector pixels require considerably more space than pixels in the optical range. On the other hand, pixels can be realized with a large filling factor, because unlike CMOS detectors in the optical range, the electronic functions can be easily placed in the detector array. If THz focal-plane arrays with a large number of pixels (albeit certainly lower than the multi-million number of pixels possible with arrays for the visible or near-infrared range) are to be fabricated, the ultimate size limit for a monolithically-integrated CMOS sensor array is determined by the wafer size, which is 300 mm in diameter for a standard CMOS processes. However, the small feature size of CMOS electronics limits the maximum area that



8.4 Cross-sectional view through the back-end of a CMOS chip. At the bottom n-type metal oxide semiconductors (NMOS) and p-type metal oxide semiconductors (PMOS) transistors are depicted, which have been processed on a silicon wafer. Above, metal layers M1 to M5, final metal and the thick top metal are shown, which are commonly used for connecting transistors to large circuitry. V denotes the vertical interconnects (vias), STI denotes shallow trench isolation. (Adapted from www.lfoundry.com.)

can be exposed in one photolithographic step to usually $22 \times 22 \text{ mm}^2$ (this area may vary, as it is determined by the optical system used). Monolithic integration beyond this area requires stitching (Yamashita *et al.*, 2011). For lower-volume production, the price of a wafer of a few hundred dollars is negligible in comparison with the production costs of a set of photolithography masks, which ranges approximately from \$50 000 for a multi-layer mask set to \$300 000 for the full set of masks (prices refer to the year 2011). In order to reduce costs, some foundries offer a multi-layer mask run. The number of masks required for a process is reduced by dividing a mask into segments and using these segments for the individual processing steps. The

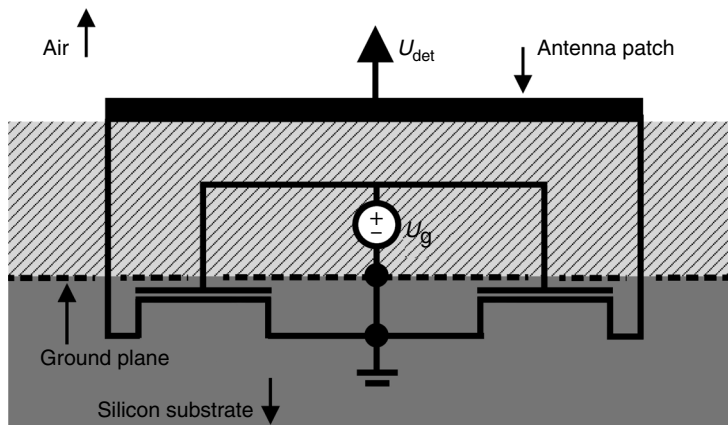
costs for masks can be reduced strongly through mask sharing with other research projects in a multi-project wafer run. If this is possible in a specific fabrication situation, the CMOS process can be cost-efficient even at low volume production. The processing costs for the small imaging arrays, which have been fabricated in a 150-nm technology offered by LFoundry, Germany, with our mask designs and which will be presented in this section, are in the order of \$200 per multi-pixel detector chip with an area of 4 mm². The costs include commercial wire bonding and packaging.

8.4.2 CMOS antenna integration

The efficient, reliable and predictable implementation of plasmonic-mixing-based detectors requires coupling of the transistors to antennas. If cost is important, then one should stay entirely within the bounds of standard CMOS technology. This entails certain constraints for the design of the antennas, the most important one arising from the fact that standard CMOS technology uses doped silicon substrates. This leads to absorption losses if the THz radiation interacts with the substrate. The losses can be avoided to a large degree with microstrip antennas realized in the back-end of the CMOS process. The limited thickness of the back-end insulator layers makes this approach, which will be discussed in the following, viable for frequencies of several hundred GHz and upwards.

Microstrip antennas, which consist of a planar metal structure on top of an antenna ground plane, are suitable for the integration into the CMOS back-end. The modes build up between the metal patch and the ground plane. The insulator of the back-end takes on the role of the antenna dielectric. The ground plane shields the modes from the lossy silicon substrate.

CMOS THz detectors for frequencies from 220 GHz to 4.25 THz have been realized using rectangular patch antennas (Öjefors *et al.*, 2009; Boppel *et al.*, 2012c). Implementation is illustrated for the example of the 150-nm CMOS process provided by LFoundry GmbH. FETs are fabricated on p-doped silicon. In the back-end, the process offers seven metal layers embedded in silicon-based (SiO_2 , Si_3N_4) dielectric material. The metal layers can be connected by vertical interconnects (vias), see Figs 8.4 and 8.5. The separation between the first metal layer ‘M1’ and the last metal layer ‘Top Metal’ is approximately 7 μm and is fixed. The ground plane of the antenna is usually implemented in the metal layer M1. One of the upper metal layers can then be utilized for the formation of the antenna patch. For lower THz frequencies, this would be the Top Metal layer, for higher frequencies, impedance considerations may provide more favourable conditions with one of the intermediate metal layers. On the lower THz frequency side, the restricted thickness available for the dielectric material limits antenna



8.5 Cross-section of a THz detector with patch antenna differentially coupled to a transistor pair through their drain contacts. Dimensions are not to scale. For a 590-GHz design, the complete 7- μm thick insulator layer (hatched area) is used as antenna dielectric. U_g denotes the d.c. bias voltage of the FETs, the arrow marked by U_{det} indicates that readout of the rectified signal occurs through the antenna metallization. (Adapted from Fig. 2, Boppel *et al.*, 2012c.)

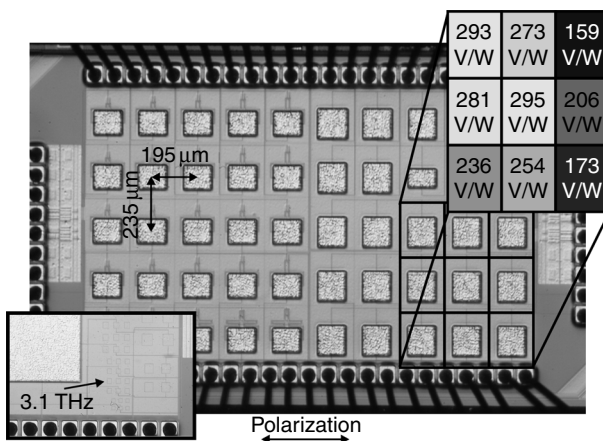
efficiency and impedance. The ratio between the separation of patch and ground plane on one hand, and the wavelength in the dielectric material on the other hand is below an unfavourable 1% for frequencies lower than 200 GHz. However, going to larger frequencies, this design constraint gradually relaxes. At 4 THz, a thickness-to-wavelength ratio of 20% is reached, if one uses M1 and Top Metal. Thus, at larger frequencies, antennas not only require less area, but there is also an increased design freedom, allowing the implementation of efficient antenna structures.

Using a ground plane for shielding purposes is not feasible for many other types of antennas because they would lose their desired characteristics. Antennas without shielding of the silicon substrate have been demonstrated using folded-dipole (Pfeiffer *et al.*, 2008a) and bow-tie antennas (Schuster *et al.*, 2011). However, antenna modes penetrate into the low-resistivity (ca. $10 \Omega\text{cm}$) substrate, which causes significant losses. For antennas without shielding of the silicon substrate, it is desirable to use non-standard CMOS silicon-on-insulator (SOI) technology or to employ high-resistivity silicon (with a specific resistance which can exceed $10\,000 \Omega\text{cm}$) to avoid substrate losses, distorted antenna patterns and possible interaction and cross-talk between neighbouring antenna structures in an array arrangement. Radiation in-coupling through the substrate offers the (potentially important) advantage that a substrate lens can be employed for focusing the

radiation, whereas tight focusing of radiation entering from the front-side (as in the case of patch antennas) is more challenging because of the presence of the electrical interconnects on this side.

8.4.3 Detector design and implementation

In this section, we do not review the various implementations of silicon-based detectors which can be found at present in the literature, but rather focus on an exemplary dual-band detector solution by Boppel *et al.* (2012c) implemented in a LFoundry process. The drain–source coupling approach enables detection both in the THz range with a full width at half maximum (FWHM) bandwidth of approximately 8% and in a band spanning from d.c. to several hundred MHz. Figure 8.5 schematically shows the implementation of a detector pixel. It consists of a rectangular patch antenna, which was designed for 590 GHz and is via-connected to the drain contacts of a pair of NMOS FETs (320-nm gate width and 150-nm gate length) in differential-operation configuration. The rectangular patch is implemented in the top metal layer and the ground plane in M1. The connectors to the antenna are located at the edges of the patch to achieve a simulated antenna impedance of $300\ \Omega$ (CST Microwave Studio), and the THz signal is directly (vertically) coupled to the drain terminals without the use of waveguides. The rectified signal is read out at the centre of the patch antenna, which acts as virtual a.c. ground. The gate contacts of both transistors are connected to an external d.c. bias-voltage source (marked in Fig. 8.5 as U_g). The gate wiring is implemented in M2 and provides an external gate-to-source capacitance relative to the ground plane in M1 which acts as an a.c. shunt between gate and source contacts. This design exhibits a couple of advantages: (i) by reading out the detector at the antenna centre (a.c. ground), the antenna itself acts as a low-pass filter and, therefore, additional lossy filter structures can be avoided; (ii) the transistors are placed in proximity to the antenna feed, therefore transmission line losses can be reduced. The simplification and the avoidance of additional structures contribute to achieve low performance variations among different detectors (to be discussed later); (iii) the design readily allows testing and calibration of the detectors. This is achieved with the help of low-frequency a.c. signals which are applied electronically to the readout port. They are detected by classical resistive mixing, with the gate and source being on a.c. ground via both the gate-to-source capacitance and the external gate-voltage source. The a.c. signal and the d.c. rectified signal are separated using an external bias tee. A disadvantage of this design is that the possibility of applying a low-frequency signal complicates the implementation of an on-chip amplifier and buffers. Therefore, for the better determination of the detector performance, we used bare FET detectors.



8.6 Array of 50 patch-antenna-coupled detectors for a frequency of 590 GHz. The detectors on the chip exhibit design variations, but the nine detectors in the square array in the lower right corner of the photograph are nominally identical to each other. The numbers in the inset in the upper right corner specify the measured responsivity values. The inset in the lower left corner displays a view onto another chip containing devices designed for frequencies above 1 THz. The patch antennas are buried in the dielectric. The large patch on the surface of the chip, visible on the left side, is an antenna for 220 GHz. (Adapted from Fig. 1, Boppel *et al.*, 2011.)

This design was implemented in a focal-plane array with 5×10 pixels (see Fig. 8.6). Except for a 3×3 matrix, all pixels were varied in important design parameters. In a second implementation (see inset on the lower left of Fig. 8.6), detectors were realized for frequency bands from 200 GHz up to 4.25 THz. The antennas were rescaled implementing the patch structure for higher frequencies in lower metal layers to maintain approximately the same antenna characteristics and impedance. These detectors are discussed further below.

8.5 Characterization and optimization of field effect transistor (FET) detectors

This section considers operation of the MOSFET detectors. Sections 8.5.1 and 8.5.2 define the electrical and optical responsivities and the noise-equivalent power as appropriate figures of merit. Section 8.5.3 addresses limiting factors for the response time of the detectors, while Section 8.5.4 discusses the challenges of impedance matching. Our approach towards the determination of the optical responsivity is described in Section 8.5.5, and Section 8.5.6 presents measured result. Finally, Section 8.5.7 addresses the enhancement of the sensitivity by a source-drain current bias, and the price to be paid by the increased noise.

8.5.1 Electrical and optical responsivity

The detector voltage response per incident power P_{RF} defines the voltage responsivity

$$\mathfrak{R}_V = \frac{U_{\text{det}}}{P_{\text{RF}}}, \quad [8.15]$$

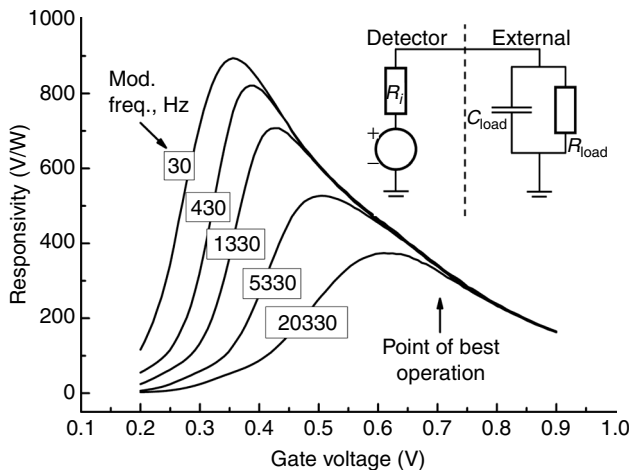
while the current response per incident power P_{RF} defines the current responsivity \mathfrak{R}_I .

When the responsivity is used for detector comparison, special attention should be devoted to the definition of the incident power. For FET detectors, the *electrical responsivity* can be defined by referring to the electrically applied power, which is absorbed by the transistor with input impedance R_{in} in the case of matched impedance and excluding the influence of the feeding network. The voltage amplitude of the applied signal is given by $U_{\text{RF}} = \sqrt{2P_{\text{RF}}R_{\text{in}}}$. Together with Equation [8.9], this yields an electrical responsivity of

$$\mathfrak{R}_V = \frac{qR_{\text{in}}}{2\eta k_B T} \frac{1}{1 + 2 \exp\left[-\frac{q(U_g - U_{\text{th}})}{\eta k_B T}\right]} \frac{1}{\ln\left(1 + \frac{1}{2} \exp\left[\frac{q(U_g - U_{\text{th}})}{\eta k_B T}\right]\right)}. \quad [8.16]$$

The *optical responsivity* refers to radiative coupling and includes antenna losses, losses of the feeding network, and impedance mismatch between antenna and transistor. P_{RF} is defined as the power incident on the effective cross-section of the antenna. The corresponding equation has been discussed (Boppel *et al.*, 2012c). A third quantity, the *optical array responsivity*, is defined as the response per radiative power subjected to the pixel area, which itself is defined by the pixel pitch (periodicity).

In real systems, the responsivity discussed above is often modified by the electrical readout electronics (Stillman *et al.*, 2007). This effect is illustrated by experimental data in Fig. 8.7. In this experiment, the responsivity \mathfrak{R}_V determined at different signal chopping frequencies is displayed as a function of the gate voltage U_g (compare similar data in Lisauskas *et al.*, 2009b). At low U_g , the responsivity, measured across the external load resistance, vanishes because the internal resistance R_i of the FET becomes infinitely large and is shunted by the impedance of the applied readout electronics. With the gate voltage increasing towards and beyond the threshold voltage of 0.6 V, the external responsivity initially rises as R_i decreases (for equations describing the channel impedance, see Boppel *et al.*, 2012c). It then peaks and falls because of the decrease of the intrinsic responsivity with



8.7 Measured voltage responsivity R_V versus gate voltage for different modulation frequencies for a detector operated at 555 GHz. Inset: The detector represented as a perfect voltage source with an internal resistance R_i in series with an external load consisting of a resistance R_{load} and a capacitance C_{load} . In this example, C_{load} is dominated by the parasitic capacitance of the readout cables.

rising gate voltage as predicted by Equation [8.11] (see Fig. 8.2). The load resistance hence influences both the values and the peak position of the measured responsivity.

8.5.2 Noise-equivalent power (NEP)

Amplification of the rectified signal results in a better value of the detector's responsivity. This, however, has a limited meaning, because the noise is amplified as well. Therefore, the responsivity should be related to the detector noise. For cold FETs (without source-to-drain bias), the noise of the transistor is determined by the thermal noise for sufficiently high modulation frequencies. The thermal spectral voltage-noise density is given by (von Haartman and Östling, 2007):

$$\sqrt{\mathcal{S}_V} = \sqrt{\frac{4k_B T}{G_{DS}}}, \quad [8.17]$$

where the d.c. channel conductance in the cold-operation regime is found from Equations [8.4]–[8.6] to be

$$G_{DS} \Big|_{U_{DS}=0} = \lim_{U_{DS} \rightarrow 0} \frac{\partial I_D}{\partial U_{DS}} = \mu C_{ox} \frac{W}{L} \frac{\eta k_B T}{q} \ln \left(1 + \frac{1}{2} \exp \left[\frac{q(U_g - U_{th})}{\eta k_B T} \right] \right). \quad [8.18]$$

The *electrical noise-equivalent power* (NEP_e) is defined as the electrical voltage responsivity divided by the thermal spectral voltage-noise density. One obtains

$$\begin{aligned} \text{NEP}_e = \frac{\sqrt{\mathcal{S}_V}}{\mathfrak{R}_V} &= \frac{2k_B T}{R_{\text{in}}} \left(1 + 2 \exp \left[-\frac{q(U_g - U_{\text{th}})}{\eta k_B T} \right] \right) \\ &\times \sqrt{\frac{L}{\mu C_{\text{ox}} W} \frac{4\eta}{q} \ln \left(1 + \frac{1}{2} \exp \left[\frac{q(U_g - U_{\text{th}})}{\eta k_B T} \right] \right)} \end{aligned} \quad [8.19]$$

When the current-related NEP is derived, exactly the same equation is obtained.

Figure 8.8 illustrates the typical dependence of the NEP_e of an FET detector on the applied gate voltage for distributed resistive self-mixing under cold-operation conditions. The minimum NEP_e is obtained, when the gate voltage U_g slightly exceeds the threshold voltage U_{th} . For comparison, the current responsivity of Fig. 8.2 is also displayed.

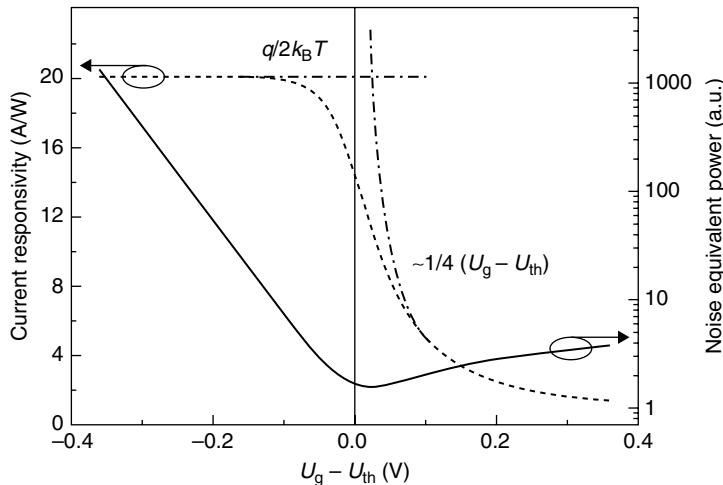
The *optical noise-equivalent power* (NEP_o) is defined correspondingly as the optical responsivity divided by the thermal spectral voltage-noise density.

8.5.3 Response time

The response time is the time it takes for the transistor to respond to a change of amplitude, frequency or phase of the applied signal.

The intrinsic response-time limit is determined by the charge-carrier transit time and represents the theoretical limit of the detector's response time. It strongly depends on the length of the FET's channel as well as on the applied gate bias voltage. In practice, the transit time is also determined by the CMOS technological processes. The transistors with a gate length of 150 nm made by the LFoundry process exhibit a cut-off frequency of approximately 35 GHz at transistor threshold. This value then represents the fundamental limit of the detector's modulation bandwidth.

Practically, the voltage response time and hence the modulation bandwidth are limited by capacitive loading. For example, a transistor with an internal low-frequency resistance $R_i = 14 \text{ k}\Omega$ connected to a cable with a capacitance of 100 pF will exhibit an RC-limited modulation bandwidth of 0.11 MHz. In order to increase the modulation bandwidth of a detector in voltage detection mode, a trans-impedance amplifier is required for reducing the detector impedance R_i and, with it, the capacitive loading effects. In current mode, the response time is limited by the cable capacitively

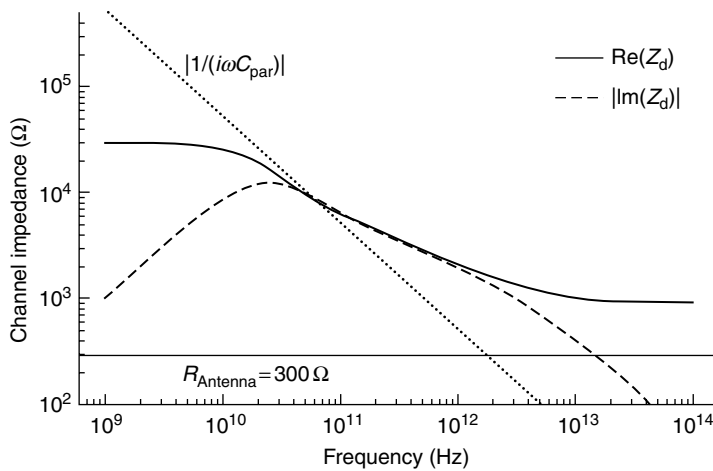


8.8 NEP (continuous line) as a function of gate voltage, calculated with Equation [8.19]. For comparison, the calculated ideal current responsivity of Fig. 8.2 is also displayed (dashed line).

shunting the ammeter (capacitive current leakage) which will occur if the cable's impedance is lower than the ammeter's impedance. Assuming a cable's capacitance of 100 pF and a 50- Ω input impedance of the ammeter, shunting sets in at approximately 32 MHz. It should be noted that capacitive loading or capacitive leakage reduce the responsivity and transistor noise in the same way, and the NEP may be limited by the noise of the readout devices.

8.5.4 Limitations for impedance matching and tuning

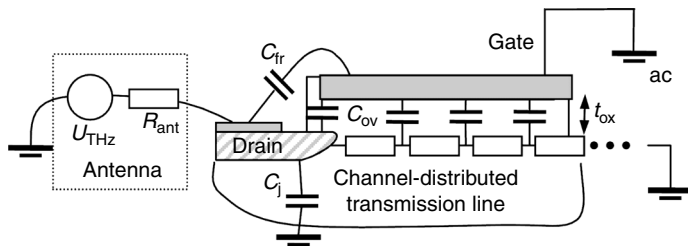
For optimum performance, the detector should be antenna-coupled with a perfect match of the transistor input impedance with the antenna impedance. However, the transistor, operated rather close to threshold voltage for optimum detector performance, is a high-impedance device which makes matching one of the main challenges of device optimization. (Note that our devices have a quite narrow channel in order to keep parasitic capacitances low. This comes at the price of an even higher impedance.) From the hydrodynamic device model, the intrinsic transistor impedance can be calculated (Boppel *et al.*, 2012c). Data for a MOSFET with a channel length (width) of 150 nm (320 nm) are displayed in Fig. 8.9 for a gate voltage $U_g - U_{th}$ of 0.1 V. In the low-frequency regime, the transistor exhibits high resistance in the tens-of-k Ω range. Approaching the regime of distributed resistive self-mixing, the reactance rises and reaches the value of



8.9 Calculated resistance (solid black curve) and reactance (dashed curve) of an FET with an electron mobility of 110 cm²/Vs. Also shown: impedance of parasitic capacitance C_{par} (dot-dash line) and antenna impedance at resonance of 300 Ω (horizontal line).

the resistance. In the distributed resistive self-mixing regime, the resistance and reactance jointly decrease gradually. In the plasmonic mixing regime, the reactance loses importance and the resistance levels off to a value in the kΩ range. It should be stressed that these intrinsic impedances are not included in standard circuit simulation tools.

Depending on the technology used, the detector impedance may, however, be dominated by parasitic impedances of the transistors. The origin of three of them is illustrated in Fig. 8.10: the fringing capacitance C_{fr} between gate and drain contacts, the overlap capacitance C_{ov} resulting from the spatial overlap of the gate electrode with a portion of the highly doped drain region, and the junction capacitance C_j between drain and silicon substrate. With increasing frequency, conductor losses and parasitic capacitances gain importance and it is likely that they rather than the device physics limit the high-frequency performance of rectification. For MOSFETs designed for 590 GHz, we determine from optical responsivity data measured with devices with different gate widths that the total parasitic capacitance C_{par} is about 0.3 fF for a gate width of 320 nm. The frequency-dependent impedance resulting from this value of C_{par} is plotted in Fig. 8.9 where it is found to be comparable with the intrinsic resistance and reactance of the transistor in the distributed resistive self-mixing regime. Knowledge of the high-frequency impedance is important for impedance matching of antenna and transistor. In general, the device impedance is significantly higher than the patch antenna's impedance which – according to simulations – amounts to



8.10 Schematic illustration of drain coupling and the most relevant parasitic equivalent-circuit components which limit detector performance at high frequencies: the fringe capacitance C_{fr} , the junction capacitance C_j and the overlap capacitance C_{ov} .

about $300\ \Omega$ for the specific design of the 590 GHz devices addressed above, but can be considerably lower for different antenna designs and at different frequencies (Boppel *et al.*, 2012c).

8.5.5 A method for device characterization

The optical responsivity and the NEP of a pixel in a periodic array can be determined with the following self-referenced method (Lisauskas *et al.*, 2009a). At first, the beam profile of the THz radiation is scanned with a 2D-translational stage using the detector pixel to be characterized itself as sensor. The voltage responsivity is defined by the ratio between measured peak-to-peak voltage signal divided by peak-to-peak power. Therefore the voltage responsivity can be determined by

$$\Re_V = \frac{\pi/\sqrt{2}}{P_{RF}A_D} \int V_{det}(x,y) dx dy, \quad [8.20]$$

where $V_{det}(x,y)$ is the detected voltage response at the position (x,y) , and P_{RF} is the total radiation power of the THz beam determined, for example, by a large-area power-meter. A_D is the effective area of the detector pixel. The factor $\pi/\sqrt{2} \approx 2.2$ results from the temporal modulation of the beam required for lock-in detection. Here, a square-wave-type chopping of the beam is assumed. The factor 2.2 originates from the fact that the lock-in amplifier gives the root-mean-square value of the sine-wave component, but the THz beam is assumed to be modulated with square-wave functional dependence. For this method to produce reliable results, it is important to avoid standing waves at the detectors and feedback to the source.

8.5.6 Results for MOSFET THz detectors

In the following, various results obtained with FET detectors of the kind displayed in Fig. 8.5 are summarized. We begin with patch-antenna-coupled detectors designed for 590 GHz (Boppel *et al.*, 2011). Samples were subjected to a focused beam of continuous-wave radiation delivered by a synthesizer-controlled millimetre-wave signal source at 590 GHz, and the beam power was determined with a calibrated large-area Thomas Keating power-meter. The responsivity was determined by the self-referenced procedure described in the previous section and in Lissauskas *et al.* (2009a), taking the product of the detector pitch of 195 μm horizontally and 235 μm vertically as the effective detector area. With a modulation of the beam at 330 Hz for lock-in detection, capacitive loading effects were found to be significant at gate bias values around 0.39 V (maximal responsivity), but negligible above 0.5 V (and hence also at the minimal-NEP point at 0.7 V). NEP data were derived from the responsivity and thermal noise calculations based on d.c.-resistance measurements. Calculated thermal noise values were experimentally confirmed for a small set of samples by direct noise measurements in the voltage regime where loading effects can be neglected. To minimize spurious cavity effects, the standing wave ratio (SWR) was reduced to less than 1.04.

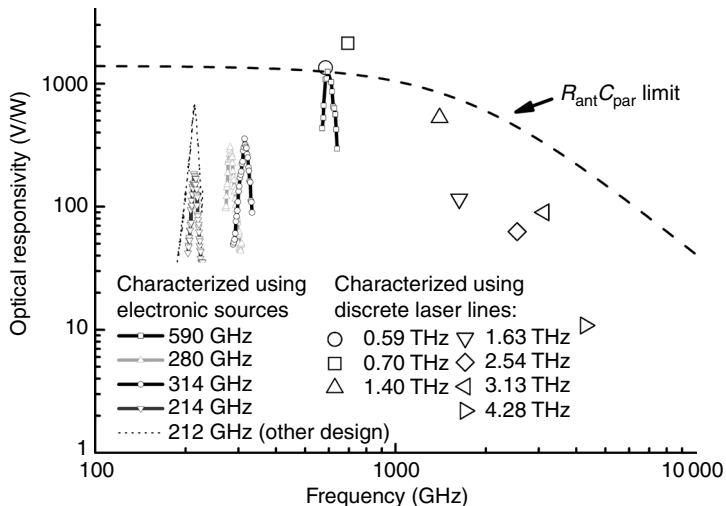
A series of detectors were carefully characterized showing a maximum (capacitive-loading-limited) optical responsivity of 970 V/W and a minimum optical NEP of 43 pW/ $\sqrt{\text{Hz}}$ at room temperature (both values averaged over 15 samples on different chips). Both the NEP and responsivity of the detectors were found to exhibit a low standard deviation of less than 8%. Referred to an effective antenna area of the microstrip patches equal to their physical size of 115 $\mu\text{m} \times$ 125 μm instead of the pitch area, the maximum responsivity amounts to 3.1 kV/W, the minimum NEP to 13.5 pW/ $\sqrt{\text{Hz}}$. Finally, we address the electrical performance of the detectors. Assuming the effective antenna area to be equal to the physical area of the patches, and further assuming a simulated antenna efficiency of 65%, the electrical responsivity can be estimated from the measured optical responsivity of 340 V/W to be 1.7 kV/W, and the electrical NEP to be 9 pW/ $\sqrt{\text{Hz}}$ (optical NEP: 43 pW/ $\sqrt{\text{Hz}}$), both at 0.7 V gate bias and in resonance. These values are in good agreement with our simulations predicting 1.5 kV/W and 11 pW/ $\sqrt{\text{Hz}}$, correspondingly. The detector performance can be further improved by cryogenic cooling until charge-carrier freeze-out is reached. This improvement occurs because of two reasons: (i) with the decrease of temperature, the amplitude of thermal noise also decreases and (ii) the nonlinear dependence between carrier density and local electric field increases. At 20 K, detectors with an antenna resonant at 590 GHz can reach a maximum

responsivity of 3.47 kV/W and a NEP as low as 3 pW/ $\sqrt{\text{Hz}}$ at this frequency (values related to the detector pitch; with respect to the patch size, they are 11.06 kV/W and less than 1 pW/ $\sqrt{\text{Hz}}$).

Having determined the performance of detectors with antennas optimized for the 600-GHz regime, we now turn to an investigation of the frequency dependence of detector performance (Boppel *et al.*, 2012c). This is done mainly with a view towards the identification of factors which limit the performance at high frequencies, deep in the THz regime. The reader is reminded that the intrinsic response of the FETs should rather improve than decline (see Fig. 8.3), but that parasitic effects are expected to become influential.

Detectors so far were arranged in focal-plane arrays and the pitch of neighbouring antennas was used to define the active detector area, as is often done for focal-plane arrays and camera applications. For the experimental study of the frequency dependence, we use the areas of the antenna patches as active area, because the patch size is clearly defined for all pixels implemented and scales more precisely with frequency than the antenna pitch. Figure 8.11 displays the optical responsivities derived thus for a considerable number of detectors designed to be resonant with various electronic emitters, which we own, respectively with emission lines of a molecular-gas laser at the Center for Physical Sciences and Technology, Vilnius, where the corresponding measurements were performed. Details about the devices, all fabricated with the LFoundry process, are found in Boppel *et al.* (2012c). Detectors designed for 220, 225, 295, 320, 630 and 735 GHz, all use the metal layers M1 and Top Metal, and hence exhibit the same thickness of the dielectric layer of 7 μm between patch and ground plane. Detectors designed for 1.475, 1.810, 2.770, 3.290 and 4.330 THz use lower metal layers M4 down to M2 for the patches, M1 for the ground plane, with correspondingly thinner dielectric layers. The inset of Fig. 8.6 displays a view on a chip where buried antennas can be seen through the dielectric.

The measurements performed with electronic sources (up to 0.6 THz) reveal antenna responses peaked at the frequencies as stated in the legend of Fig. 8.11. The deviations between design frequencies and measured peaks are less than 10%. Starting from the low-frequency side, and going from 220 GHz up to 735 GHz, the peak responsivity of the detectors is found to gradually increase by a factor of ten. Patch antennas made from an ideal metal should have a constant performance over this frequency range. However, the simulations show that the limited thickness of the dielectric layer between patch and ground plane in conjunction with the limited conductivity of the metal layers result in a substantial decrease of both the antenna efficiency and impedance when the thickness of the dielectric layer is reduced while keeping the composition and thickness of the metal layers



8.11 Optical responsivity of detectors designed for discrete emission frequencies. Note: the optical responsivity is determined with regard to the area of the respective antenna patch rather than the detector patch. Up to 0.6 THz, the devices were characterized with electronic sources; the frequency values specified in the legend denote the peak frequencies of the displayed response curves. Above 0.6 THz, molecular-gas laser lines were used; the fixed emission frequencies are listed in the legend. The dashed line illustrates a theoretical, purely RC-time-controlled frequency dependence normalized to the responsivity measured at 590 GHz. (Adapted from Fig. 7, Boppel *et al.*, 2012c.)

constant (and only changing the aerial size of the patch). Conversely, for a fixed thickness of the dielectric layer, the performance of detectors made for ever lower frequency declines. The highest responsivity of 2126 V/W was observed at 735 GHz.

Continuing to higher frequencies, the performances of the detectors measured at 1.40, 1.63, 2.54, 3.13 and 4.28 THz gradually decrease, exhibiting optical responsivities of 528, 115, 69, 90 and 11 V/W, respectively. The measurements prove that the detection mechanism is still active even at 4.28 THz. At the present time, the origin of the decrease in responsivity observed with rising frequency cannot be identified unambiguously. Parasitic influences should play an important role. The dashed line in Fig. 8.11 indicates the *RC* roll-off expected for an antenna impedance R_{ant} of 300 Ω and a parasitic capacitance C_{par} of 0.3 fF (parameters determined for devices at 590 GHz, see above; for simulated antenna impedances at other frequencies, see Boppel *et al.*, 2012c), assuming that neither the antenna nor the device properties change with frequency (hence also neglecting that the mixing

efficiency of the detectors slightly increases in this frequency range). If the detectors were to behave according to this *RC* trend, then the responsivity in the vicinity of 4.3 THz could reach values above 100 V/W. The measured roll-off is somewhat stronger. One cannot conclude yet, however, that this is evidence for additional limiting effects to play a role, because the measurements suffer from a slight mismatch of the design frequencies of the detectors and the laser frequencies. Considering the limited FWHM bandwidth of the patch antennas of typically 8%, the measurements could well have missed the peak frequencies of the antenna response. Spectrally resolved measurements at THz frequencies are presently being carried out with the free-electron laser, named FELBE, at the Helmholtz-Zentrum Dresden-Rossendorf (HZDR), Germany.

8.5.7 Enhancement of the responsivity by a current bias

We finally address an interesting approach for the enhancement of the responsivity of the detectors, which is to apply a bias current to the channel. It was shown both theoretically and experimentally in the literature that the responsivity of high-electron-mobility transistors can be enhanced hugely by the application of a drain bias current close to the saturation value (Lisauskas *et al.*, 2012b). The mechanism is explained in Veksler *et al.* (2006) as an enhanced sensitivity of the detector resulting from a low density of charge carriers near the drain at saturation. Small external fields can then affect the density in a very pronounced manner.

For our CMOS detectors, we also measured an enormous enhancement of the responsivity when a drain bias current was applied (Lisauskas *et al.*, 2011, 2012b). Expecting also increased noise in such a field-sensitive device, we extended our study to a theoretical and experimental investigation of the noise performance. Detailed results are reported in Lisauskas *et al.* (2011, 2012b). Summarizing the results, it was found experimentally that both the responsivity and the spectral density of the voltage fluctuations significantly increase with the bias current, with the consequence that the signal-to-noise ratio (SNR) at any given gate voltage increases at most by a small amount. The hydrodynamic transport model indeed predicts a possible absolute SNR enhancement by a factor of 1.35 close to the saturation current. Our experimental data did not reveal even this modest enhancement. We did not observe an absolute improvement beyond the best SNR value obtained without bias current. Based on these findings, we come to the conclusion that the responsivity enhancement by a bias current is not practically relevant when the SNR is the key quantity of the measurements – as for THz imaging – and not the responsivity itself. Current-enhancement of the responsivity may be useful though in some applications in the context of a first amplification stage.

8.6 Developments towards a terahertz camera

Detectors such as those characterized in the previous section were analysed with regard to their applicability in focal-plane arrays for the realization of THz cameras.

8.6.1 A 50-pixel array

An important issue for a focal-plane array is pixel uniformity. In order to perform a first test on performance variations of nominally identical detectors, we tested the nine pixels of the array marked in the photograph displayed in Fig. 8.6 (Boppel *et al.*, 2011). All devices were measured at a gate voltage of 0.7 V (optimum bias with respect to NEP). For each pixel, the responsivity values of four different chips were averaged. Central detector pixels show similar responsivities of 293, 273, 281, and 295 V/W, exhibiting a low variation between chips as expressed by relative standard deviations of 4%, 8%, 6%, and 7%. Pixels which are very close to the bonding pads show slightly reduced average responsivity values of 236 V/W and 254 V/W, and an increased relative standard deviation of 11% and 15%, respectively. Pixels at the vertical edge of the detector show notably reduced responsivities of 159, 206 and 172 V/W, with relative standard deviations of 18%, 9%, and 20%. We attribute the reduction mainly to the broken symmetry caused by the end of the ground plane, which modifies the antenna radiation pattern and gain. Results for the inner group of detectors indicate that the responsivity values are remarkably uniform for non-edge pixels benefiting from the low variability of the CMOS technological processes.

With a pitch of $195\text{ }\mu\text{m} \times 235\text{ }\mu\text{m}$, the pixel dimensions are below the free-space wavelength of the radiation of approximately 500 μm . When the Shannon–Nyquist sampling theorem is considered, images should be acquired with a spatial resolution which are at least two times smaller than the diffraction limit of the optical system in order not to lose information. As not all assumptions of the theorem are fulfilled in real imaging situations, the factor should be even larger. In the following experiments, images were sampled with five times the optical resolution (which is a value used in common optical sensors as well).

For THz radiation, where beam power is scarce, it can be advisable to trade optical resolution for sensitivity, for example, by the binning of pixels. One should remember, however, that each detector contributes its noise, therefore a theoretically superior approach is to effectively increase the active area of a single pixel by either applying a silicon substrate lens or using suitable antenna concepts.

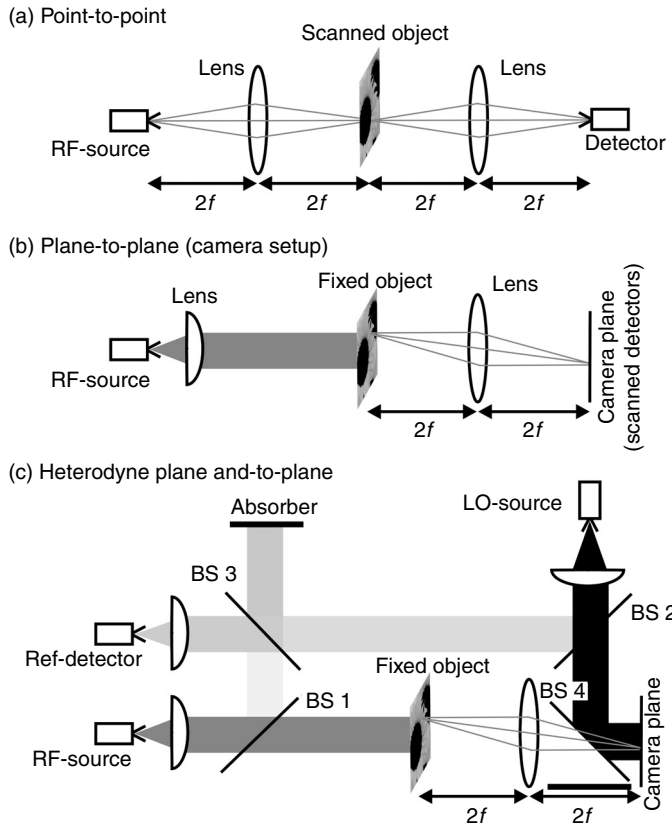
8.6.2 Emulation of real-time direct imaging with a 10-kilopixel virtual camera

A central aim of THz imaging is the development of cameras which can be operated in real-time mode. With the CMOS detectors considered here, the finite responsivity necessitates active illumination of the scene. In the following, a study is described which explores the potential of active real-time imaging for realistic illumination conditions (Boppel *et al.*, 2012a, 2012b). This section considers direct detection (i.e., measuring the beam power), while the next section explores coherent (heterodyne) field detection with the same CMOS detectors.

Figure 8.12 specifies various options for imaging in transmission mode. Figure 8.12a shows a point-to-point setup often used in the THz field. It employs a single source and a single-pixel THz detector. The radiated power is focused onto an object located at the intermediate focus, and the transmitted radiation is then refocused onto the detector. For raster-scan imaging, the object is translated in one, two or three dimensions through the intermediate focus.

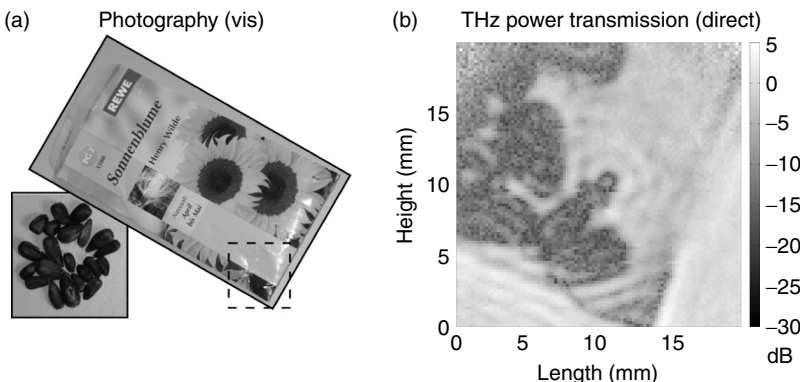
The illumination conditions, which correspond to parallel imaging with a multi-pixel sensor array and are suited for real-time imaging, are displayed in Fig. 8.12b. In this plane-to-plane imaging configuration, a certain area of the object, or the object as a whole, is illuminated by a THz beam (in the figure, this is a collimated beam, but other configurations are possible). The transmitted power is imaged onto the camera plane by the use of standard optical components. There, the image can be recorded with an appropriate multi-pixel sensor. The main challenge of plane-to-plane imaging in the THz field is to cope with the limited beam power usually available for object illumination.

A transmission setup for plane-to-plane imaging was investigated experimentally in direct-detection mode. A 432- μW beam at 591.4 GHz delivered from a synthesizer-driven multiplier chain was used as RF source and collimated to a beam width of approximately 15 mm by a Picarin lens (focal length: 100 mm). The beam illuminated the object plane with 331 μW of power. The object was imaged by a bi-aspheric Teflon lens, which was designed in-house for good off-axis performance using the ZEMAX simulation tool. Instead of a fully integrated THz camera, not available at the time, a room-temperature virtual camera with 100×100 effective pixels and an area of $20 \times 20 \text{ mm}^2$ was emulated by raster-scanning a single pixel or a few pixels from the 50-pixel MOSFET detector array presented before through the image plane. Images were recorded using a lock-in amplifier with an integration time of 20 ms and with a 6-dB/octave filter, which would correspond to an effective frame rate of 17 Hz of a real-time camera system.



8.12 Three modalities of THz imaging in transmission mode:
 (a) point-to-point imaging, suitable if a single emitter and a single power detector are employed; (b) plane-to-plane imaging for detection with a power detector array; (c) plane-to-plane imaging in heterodyne mode. (Adapted from Fig. 1, Boppel *et al.*, 2012a.)

Imaging tests were performed with objects such as the package of sunflower seeds shown in Fig. 8.13. The right side of the figure displays the recorded single-scan THz image. Analysing the image data, one finds that direct imaging achieves a dynamic range of 20 dB at the image centre, which gradually degrades with increasing distance from the optical axis. The dynamic range on a circle of 9 mm diameter is approximately 15 dB. These data lead to the conclusion that real-time imaging with power detection is feasible. The beam power available for illumination restricts the area to be imaged with sufficient dynamic range to a few cm².



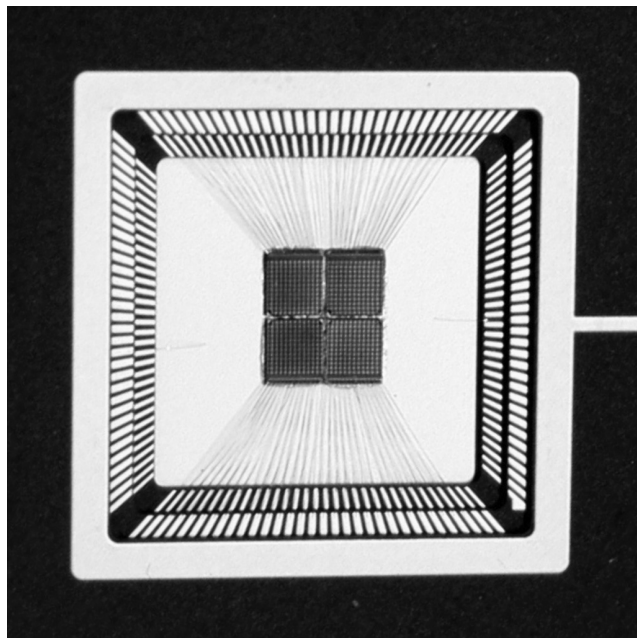
8.13 Package with sunflower seeds used for the THz imaging demonstration. (a) Photograph of the package and some seeds – the dashed lines indicate the imaged area. (b) Transmission image measured in power-detection mode at 590 GHz. Raw image data were divided by the intensity distribution of the beam. (Adapted from Fig. 2, Boppel *et al.*, 2012a.)

Note: While finalizing this manuscript, a CMOS FET THz camera with a 1-kilo-pixel focal-plane array has been reported (Sherry *et al.*, 2012). Also recently, we reported on real-time imaging with a 12×12 -pixel CMOS THz array (Lisauskas *et al.*, 2012c), which is part of the 24×24 pixel camera shown in Fig. 8.14. The latter camera is capable of heterodyne operation, which is experimentally simulated in the next section.

8.6.3 Emulation of real-time coherent imaging with a 10-kilopixel virtual camera

The high cut-off frequency of the FETs and their ensuing fast response allow enhancing the sensitivity of the detectors by heterodyne operation (Glaab *et al.*, 2010). Usually in heterodyning, a weak RF-signal is mixed in a detector with a very strong signal from a local oscillator (LO). If this concept is to be applied unchanged to multi-pixel imaging, one would need a large amount of LO power to feed all detectors of the array. This amount of power is, at hundreds of GHz, usually not available at acceptable cost. The following therefore presents a study focusing on the question of whether heterodyning can be advantageous and also if each detector pixel receives only a small amount of LO power, as is the case if the radiation from a THz LO source is distributed over all detectors of the array (Boppel *et al.*, 2012a, 2012b).

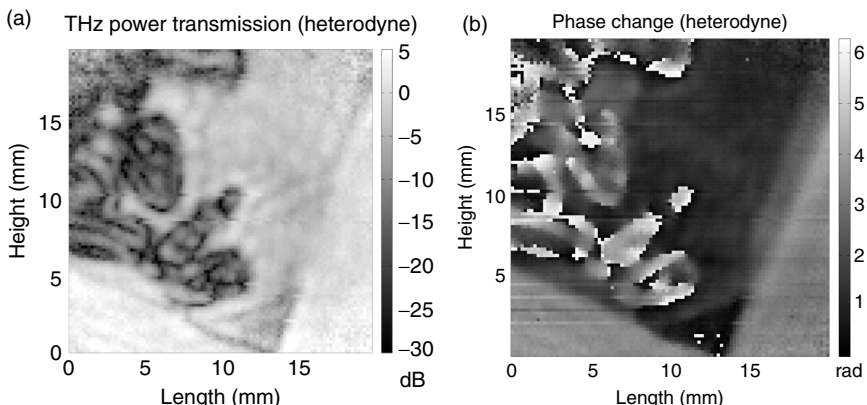
The experimental setup for this study is shown schematically in Fig. 8.12c. The THz wave from a continuous-wave electronic emitter (termed



8.14 A photograph of the packaged camera chip, consisting of four die implemented in 150-nm CMOS technology each consisting of a monolithically integrated 12×12 pixel array with patch-antenna-coupled detectors for 590 GHz.

RF source) was used for object illumination. The transmitted radiation was optically superimposed with the radiation from a second electronic source (termed LO source) on the image plane. The LO radiation was coupled onto the RF beam-path after the imaging lens with beam-splitter BS4. The radiation for object illumination was derived from the same emitter used for direct-detection imaging in the preceding section. It delivered a beam power of $432 \mu\text{W}$ at 591.4 GHz. The LO source was frequency-offset by 15 kHz and delivered a power of $247 \mu\text{W}$. The LO beam was not focused, but rather spread over the whole effective area of the hypothetical focal-plane array. By the beam attenuation at all optical components and the spreading of the power, the 100×100 pixels were pumped on average by 5 nW of LO power each.

Figure 8.15 displays the single-scan transmission image of the package with sunflower seeds in heterodyne mode for the same lock-in integration time as used in direct-detection mode. The left side shows the transmitted-power data, the right side shows the phase information. Despite the low LO power, the evaluation of the image data revealed that heterodyne imaging was advantageous with regard to the dynamic range achieved. The



8.15 Example for THz heterodyne imaging with a 150-nm-gate-length MOSFET using plane-to-plane imaging. (a) Transmitted power and (b) phase contour. (Adapted from Fig. 2, Boppel *et al.*, 2012a.)

heterodyne image displayed a dynamic range of about 30 dB at the centre, which reduced to 20 dB along a circular path at a distance of 9 mm from the centre. This performance has to be compared with that obtained in the case of direct-power imaging. Here, the data exhibited a dynamic range of 20 dB at the image centre, which gradually fell off with increasing distance from the optical axis to approximately 15 dB on a circle of 9 mm radius. The heterodyne approach brings with it the additional information of the phase-change profile not accessible with direct-power detection.

Finally, we would like to point out that the LO source necessary for heterodyne imaging could well be placed directly onto the detector chip. As can be clearly seen from our results, only a moderate LO power is required to improve the dynamic range of the detection considerably compared with direct-power detection. If groups of detectors would be integrated with an oscillator which would directly supply them with an LO power of 1 μ W per detector (which also does not need to be out-coupled from the chip), then this LO power would boost the dynamic range of the system by 26 dB compared with the present external pumping by 5 nW. 23 dB (corresponding to the ratio 1 μ W/5 nW) of this increase comes from the enhanced LO power and an additional 3 dB from the avoidance of the beam-splitter.

Providing LO power at the fundamental frequency becomes more and more difficult with rising frequency. An alternative is subharmonic mixing. It was demonstrated recently with MOSFETs at 639 GHz with LO radiation at 213 GHz (Lisauskas *et al.*, 2012a). With regard to future integrated system, it appears feasible to generate the LO signal on-chip or on-board, even if signals at the fundamental frequency cannot be provided because of amplification-gain limitations of the semiconductor technology employed.

8.7 Overview of other focal-plane technologies for terahertz imaging

As mentioned in the Introduction, THz imaging has experienced impressive progress over the last few years. One driving force is the perceived need for standoff scanners for security screening purposes. Short-distance imaging for the detection of concealed objects and chemical compounds (such as drugs and explosives) can now be performed with impressive resolution at microwave frequencies below 100 GHz, and various imaging systems – for example, as portal solutions at entrance gates – are on the market. Larger screening distances in the order of many metres require higher frequencies to maintain sufficient spatial image resolution. Two approaches have been identified by research as probably viable in the near future: passive (thermal) imaging with superconducting detectors (May and Meyer, 2007; Grossman *et al.*, 2010), and active, coherent imaging with commercially available horn-antenna-coupled multiplier emitters and Schottky-diode detectors (Cooper *et al.*, 2011; Friederich *et al.*, 2011). Both approaches work in the 300 to 800 GHz range. Higher frequencies are not only more difficult to access, but also do not provide better image quality because the all-important penetration through fabrics, leather and many other materials deteriorates with increasing frequency (Appleby and Wallace, 2007). Multi-pixel detector arrays (which are unlikely to come about in monolithic form because of diffraction limitation issues) are very difficult and expensive to fabricate; images therefore are generated with the help of scanning mirrors, with frame rates coming close to real-time.

The other macro-trend in THz imaging is device-technology driven, aiming at integrated multi-pixel (kilopixel and more) detector arrays for real-time operation at room temperature or at least at non-cryogenic conditions. An impressive variety of promising technologies – at different stages of maturity – has emerged, as shown in the list which does not claim completeness:

- Pyroelectric cameras are already on the market for a considerable time, e.g. by Ophir Optronics Ltd., but their sensitivity ($NEP \sim 45 \text{ nW}/\sqrt{\text{Hz}}$) is often not sufficient.
- Microbolometer arrays, adapted from commercially available camera solutions for infrared thermal imaging after the discovery that the latter work also around 4 THz (Lee *et al.*, 2006), have recently become available commercially and the number of vendors is expected to increase soon. The focal-plane arrays are optimized for 2–5 THz, fabricated in a CMOS-compatible technology allowing for integration of CMOS-readout electronics, and exhibit impressive NEP values of $40 \text{ pW}/\sqrt{\text{Hz}}$ (Oda, 2010), $20 \text{ pW}/\sqrt{\text{Hz}}$ (Nguyen *et al.*, 2012), and $70 \text{ pW}/\sqrt{\text{Hz}}$ (Bolduc *et al.*, 2011).

- A novel microbolometric approach uses (silicon) FETs and exploits the dependence of the channel's conductance on temperature (Corcos *et al.*, 2011).

Both, the pyroelectric and the microbolometer cameras – with pixel numbers up to 320×240 – are power detectors with detector response times roughly in the millisecond time range. They are not suited for heterodyne operation. This is different for the following technologies:

- Schottky diodes, both as power detectors and heterodyne mixers, have been the workhorse of THz technology for many decades. Surprisingly, however, it appears that the production of monolithically-integrated detector arrays encounters so many technological problems that the device-to-device performance variations and even the percentage of non-functional detectors per chip tend to be unacceptably high. To our knowledge, Schottky-diode-based focal-plane arrays are not yet available commercially, although a number of research groups and companies are working to solve the problems.
- III/V-tunnelling-diode arrays have appeared on the market very recently (Burdette *et al.*, 2011). Focal-plane arrays with a size up to 120×120 pixels, are specified with an NEP of $5 \text{ nW}/\sqrt{\text{Hz}}$. The detectors are antenna-coupled and specified for the frequency range 0.6–1.2 THz.
- Thermoelectric devices: asymmetrically-necked planar diodes for frequencies mainly up to 1.5 THz are investigated on the device-technology level (Seliuta *et al.*, 2006). NEP values of the latter, are on the order of $4 \text{ nW}/\sqrt{\text{Hz}}$ with considerable room for improvement (Minkevičius *et al.*, 2011). Their conceptual simplicity makes them interesting for monolithic array fabrication.

8.8 Acknowledgements

The authors acknowledge funding by BMBF (project LiveDetect3D), WI Bank Hessen, Alexander-von-Humboldt Foundation (institute partnership with the Center for Physical Sciences and Technology, Vilnius) and Oerlikon AG.

8.9 References

- Appleby, R. and Wallace, H.B., 2007. Standoff detection of weapons and contraband in the 100 GHz to 1 THz region. *IEEE Transactions on Antennas and Propagation* **55**, 2944–2956.
- Barrett, R., 1987. Broadband RF power detector using FET. *US Patent* 4,647,848.

- Bolduc, M., Terroux, M., Tremblay, B., Marchese, L., Savard, E., Doucet, M., Oulachgar, H., Alain, C., Jerominek, H. and Bergeron, A., 2011. Noise-equivalent power characterization of an uncooled microbolometer-based THz imaging camera. 80230C-80230C-10.
- Boppel, S., Lisauskas, A., Krozer, V. and Roskos, H.G., 2011. Performance and performance variations of sub-1 THz detectors fabricated with 0.15 μ m CMOS foundry process. *Electronics Letters* **47**, 661.
- Boppel, S., Lisauskas, A., Krozer, V. and Roskos, H.G., 2012a. Towards monolithically integrated CMOS cameras for active imaging with 600 GHz radiation, in: *Proceedings of SPIE* 8261. 826106–0–10.
- Boppel, S., Lisauskas, A., Max, A., Krozer, V. and Roskos, H.G., 2012b. CMOS detector arrays in a virtual 10-kilopixel camera for coherent terahertz real-time imaging. *Optics Letters* **37**, 536.
- Boppel, S., Lisauskas, A., Mundt, M., Seliuta, D., Minkevičius, L., Kašalynas, I., Valušis, G., Mittendorff, M., Winnerl, S., Krozer, V. and Roskos, H.G., 2012c. CMOS integrated antenna-coupled field-effect-transistors for the detection of radiation from 0.2 to 4.3 THz. *IEEE Transactions on Microwave Theory and Techniques*, accepted DOI:10.1109/TMTT.2012.2221732.
- Burdette, D.J., Alverbro, J., Zhang, Z., Fay, P., Ni, Y., Potet, P., Sertel, K., Trichopoulos, G., Topalli, K., Volakis, J. and Mosbacher, H.L., 2011. Development of an 80 \times 64 pixel, broadband, real-time THz imager. *Proceedings of SPIE* 8023. 80230F-80230F-12.
- Cooper, K.B., Dengler, R.J., Llombart, N., Thomas, B., Chattopadhyay, G. and Siegel, P.H., 2011. THz imaging radar for standoff personnel screening. *IEEE Transactions on Terahertz Science and Technology* **1**, 169–182.
- Corcos, D., Brouk, I., Malits, M., Svetlitza, A., Stolyarova, S., Abramovich, A., Farber, E., Bachar, N., Elad, D. and Nemirovsky, Y., 2011. The TeraMOS sensor for monolithic passive THz imagers, in: *2011 IEEE International Conference on Microwaves, Communications, Antennas and Electronic Systems (COMCAS 2011)*. IEEE, pp. 1–4.
- Dyakonov, M. and Shur, M., 1993. Shallow water analogy for a ballistic field effect transistor: New mechanism of plasma wave generation by dc current. *Physical Review Letters* **71**, 2465–2468.
- Dyakonov, M. and Shur, M., 1996. Detection, mixing, and frequency multiplication of terahertz radiation by two-dimensional electronic fluid. *IEEE Transactions on Electron Devices* **43**, 380–387.
- Friederich, F., Spickermann, G., Roggenbuck, A., Deninger, A., Am Weg, C., von Spiegel, W., Lison, F., Bolivar, P.H. and Roskos, H.G., 2010. Hybrid continuous-wave demodulating multipixel terahertz imaging systems. *IEEE Transactions on Microwave Theory and Techniques* **58**, 2022–2026.
- Friederich, F., von Spiegel, W., Bauer, M., Meng, F., Thomson, M.D., Boppel, S., Lisauskas, A., Hils, B., Krozer, V., Keil, A., Loffler, T., Henneberger, R., Huhn, A.K., Spickermann, G., Bolivar, P.H. and Roskos, H.G., 2011. THz active imaging systems with real-time capabilities. *IEEE Transactions on Terahertz Science and Technology* **1**, 183–200.
- Glaab, D., Boppel, S., Lisauskas, A., Pfeiffer, U., Öjefors, E. and Roskos, H.G., 2010. Terahertz heterodyne detection with silicon field-effect transistors. *Applied Physics Letters* **96**, 042106.

- Grossman, E., Dietlein, C., Ala-Laurinaho, J., Leivo, M., Gronberg, L., Gronholm, M., Lappalainen, P., Rautiainen, A., Tamminen, A. and Luukanen, A., 2010. Passive terahertz camera for standoff security screening. *Applied Optics* **49**, E106.
- von Haartman, M. and Östling, M., 2007. *Low-frequency Noise in Advanced MOS Devices*. Dordrecht, Springer.
- Jiang, Z. and Zhang, X.-C., 1999. Terahertz imaging via electrooptic effect. *IEEE Transactions on Microwave Theory and Techniques* **47**, 2644–2650.
- Kawase, K., Ogawa, Y., Minamide, H. and Ito, H., 2005. Terahertz parametric sources and imaging applications. *Semiconductor Science and Technology* **20**, S258–S265.
- Knap, W., Kachorovskii, V.Y., Deng, Y., Rumyantsev, S., Lü, J.-Q., Gaska, R., Shur, M.S., Simin, G., Hu, X., Khan, M. A., Saylor, C. A. and Brunel, L. C., 2002. Nonresonant detection of terahertz radiation in field effect transistors. *Journal of Applied Physics* **91**, 9346.
- Kopyt, P., Marczewski, J., Kucharski, K., Lusakowski, J. and Gwarek, W.K., 2011. Planar antennas for THz radiation detector based on a MOSFET, in: *2011 International Conference on Infrared, Millimeter, and Terahertz Waves. IEEE*, 1–2.
- Krekels, H.G., Schiek, B. and Menzel, E., 1992. Power detector with GaAs field effect transistors, in: *European Microwave Conference*, 1992. 22nd. 174–179.
- Lee, A.W.M., Williams, B.S., Kumar, S., Hu, Q. and Reno, J.L., 2006. Real-time imaging using a 4.3-THz quantum cascade laser and a 320 /spl times/ 240 microbolometer focal-plane array. *IEEE Photonics Technology Letters* **18**, 1415–1417.
- Lisauskas, A., Boppel, S., Mundt, M., Krozer, V. and Roskos, H.G., 2012a. Subharmonic mixing with field-effect transistors: theory and experiment at 639 GHz high above f_T . *IEEE Sensors Journal*, DOI:10.1109/JSEN.2012.2223668.
- Lisauskas, A., Boppel, S., Matukas, J., Palenskis, V., Valusis, G., Haring Bolivar, P. and Roskos, H.G., 2012b. Terahertz responsivity and low-frequency noise in biased silicon CMOS detectors. Submitted.
- Lisauskas, A., Boppel, S., Matukas, J., Palenskis, V., Minkevičius, L., Valusis, G. and Haring Bolivar, P., 2011. Terahertz responsivity enhancement and low-frequency noise study in silicon CMOS detectors using a drain current bias, in: *Noise and Fluctuations (ICNF), 2011, 21st International Conference On. IEEE*, 297–300.
- Lisauskas, A., Boppel, S., Saphar, M., Krozer, V., Minkevičius, L., Venckevičius, R., Seliuta, D., Kašalynas, I., Tamošiūnas, V., Valušis, G. and Roskos, H. G., 2012c, Detectors for terahertz multi-pixel coherent imaging and demonstration of real-time imaging with a 12×12-pixel CMOS array. *SPIE Optics and Photonics*, Paper 8496–18, in print.
- Lisauskas, A., Glaab, D., Roskos, H.G., Öjefors, E. and Pfeiffer, U.R., 2009a. Terahertz imaging with Si MOSFET focal-plane arrays, in: *Proceedings of SPIE. SPIE*, 72150J-72150J-11.
- Lisauskas, A., Pfeiffer, U.R., Öjefors, E., Bolívar, P.H., Glaab, D. and Roskos, H.G., 2009b. Rational design of high-responsivity detectors of terahertz radiation based on distributed self-mixing in silicon field-effect transistors. *Journal of Applied Physics* **105**, 114511.
- Malcolm, G., 2007. New laser sources benefit terahertz and mid-infrared remote sensing. *SPIE Newsroom*, DOI: 10.1117/2.1200710.0842.

- May, T. and Meyer, H.G., 2007. Der enttarnte Terrorist. *Optik and Photonik* **2**, 34–37.
- Meng, F.Z., Thomson, M.D., Molter, D., Löffler, T., Jonuscheit, J., Beigang, R., Bartschke, J., Bauer, T., Nittmann, M. and Roskos, H.G., 2010. Coherent electro-optical detection of terahertz radiation from an optical parametric oscillator. *Optics Express* **18**, 11316–26.
- Minkevičius, L., Tamšiūnas, V., Kašalynas, I., Seliuta, D., Valušis, G., Lisauskas, A., Boppel, S., Roskos, H.G. and Köhler, K., 2011. Terahertz heterodyne imaging with InGaAs-based bow-tie diodes. *Applied Physics Letters* **99**, 131101.
- Nguyen, D.-Thong, Simoens, F., Ouvrier-Buffet, J.-L., Meilhan, J. and Coutaz, J., 2012. Broadband THz uncooled antenna-coupled microbolometer array—electromagnetic design, simulations and measurements. *IEEE Transactions on Terahertz Science and Technology* **2** (3), 299–305.
- Oda, N., 2010. Uncooled bolometer-type terahertz focal-plane array and camera for real-time imaging. *Comptes Rendus Physique* **11**, 496–509.
- Öjefors, E., Baktash, N., Zhao, Y., Hadi, R.A., Sherry, H. and Pfeiffer, U.R., 2010. Terahertz imaging detectors in a 65-nm CMOS SOI technology, in: *2010 Proceedings of ESSCIRC*. IEEE, 486–489.
- Öjefors, E., Pfeiffer, U.R., Lisauskas, A., Roskos, H.G., 2009. A 0.65 THz focal-plane array in a quarter-micron CMOS process technology. *IEEE Journal of Solid-State Circuits* **44**, 1968–1976.
- Pfeiffer, U.R., Öjefors, E., Lisauskas, A., Glaab, D., Voltolina, F., Fonkwe Nzogang, V.M., Haring Bolivar, P. and Roskos, H.G., 2008a. A CMOS focal-plane array for terahertz imaging, in: *2008 33rd International Conference on Infrared, Millimeter and Terahertz Waves*. IEEE, 1–3.
- Pfeiffer, U.R., Öjefors, E., Lisauskas, A. and Roskos, H.G., 2008b. Opportunities for silicon at mmWave and Terahertz frequencies, in: *2008 IEEE Bipolar/BiCMOS Circuits and Technology Meeting*. IEEE, 149–156.
- Preu, S., Kim, S., Verma, R., Burke, P.G., Sherwin, M.S. and Gossard, A.C., 2012. An improved model for non-resonant terahertz detection in field-effect transistors. *Journal of Applied Physics* **111**, 024502.
- Schuster, F., Coquillat, D., Videlier, H., Sakowicz, M., Teppe, F., Dussopt, L., Giffard, B., Skotnicki, T. and Knap, W., 2011. Broadband terahertz imaging with highly sensitive silicon CMOS detectors. *Optics Express* **19**, 7827–7832.
- Seliuta, D., Kašalynas, I., Tamšiūnas, V., Balakauskas, S., Martūnas, Z., Ašmontas, S., Valušis, G., Lisauskas, A., Roskos, H.G. and Köhler, K., 2006. Silicon lens-coupled bow-tie InGaAs-based broadband terahertz sensor operating at room temperature. *Electronics Letters* **42**, 825.
- Sherry, H., Al Hadi, R., Grzyb, J., Öjefors, E., Cathelin, A., Kaiser, A. and Pfeiffer, U.R., 2011. Lens-integrated THz imaging arrays in 65nm CMOS technologies, in: *IEEE Radio Frequency Integrated Circuits Symposium (RFIC)*. IEEE, 1–4.
- Sherry, H., Grzyb, J., Zhao, Y., Al Hadi, R., Cathelin, A., Kaiser, A. and Pfeiffer, U., 2012. A 1kPixel CMOS camera chip for 25fps real-time terahertz imaging applications, in: *IEEE International Solid-State Circuits Conference*, 252–253.
- Shur, M., Fjeldly, T., Ytterdal, T. and Lee, K., 1992. Unified MOSFET model. *Solid-State Electronics* **35**, 1795–1802.
- Stillman, W., Shur, M.S., Veksler, D., Rumyantsev, S. and Guarin, F., 2007. Device loading effects on nonresonant detection of terahertz radiation by silicon MOSFETs. *Electronics Letters* **43**, 7–8.

- Sze, S.M. and Ng, K.K., 2007. *Physics of Semiconductor Devices*, 3rd ed. John Wiley & Sons, New Jersey.
- Veksler, D., Teppe, F., Dmitriev, A.P., Kachorovskii, V.Y., Knap, W. and Shur, M.S., 2006. Detection of terahertz radiation in gated two-dimensional structures governed by d.c. current. *Physical Review B* **73**, 1–10.
- Yamashita, Y., Takahashi, H., Kikuchi, S., Ota, K., Fujita, M., Hirayama, S., Kanou, T., Hashimoto, S., Momma and G., Inoue, S., 2011. A 300mm wafer-size CMOS image sensor with in-pixel voltage-gain amplifier and column-level differential readout circuitry, in: *2011 IEEE International Solid-State Circuits Conference*. IEEE, 408–410.

Resonant field enhancement of terahertz waves in subwavelength plasmonic structures

R. SINGH and A. K. AZAD, Los Alamos National Laboratory,
USA and W. ZHANG, Oklahoma State University, USA

DOI: 10.1533/9780857096494.2.272

Abstract: Resonant terahertz field enhancement is investigated in arrays of subwavelength holes patterned on metals, semiconductors and superconductors. The effects of array film thickness, the dielectric function of metals, and a dielectric overlayer were investigated by the state-of-the-art terahertz spectroscopy. Extraordinary terahertz transmission was demonstrated in arrays of subwavelength holes made even from Pb, generally a poor metal, and having optically thin thicknesses less than one-third of a skin depth. We also demonstrate active control of surface plasmons at terahertz frequencies. Direct transitions of surface plasmon modes from a photonic crystal minimum or an inductive-capacitive metamaterial resonance in photo-doped semiconductor arrays are observed. In addition, we demonstrate a superconducting plasmonic array of subwavelength holes with active thermal control over the resonant transmission. Such plasmonic structures are promising in terahertz imaging, biomedical sensing, subwavelength terahertz spectroscopy and integrated terahertz devices.

Key words: terahertz waves, surface plasmon polaritons, subwavelength, field enhancement.

9.1 Introduction

The passage of light through holes much smaller than its wavelength has proved to be a surprising phenomenon.^{1–3} When light passes through the subwavelength aperture, we think about the distribution of transmitted wave amplitude, its direction and its phase. This seemingly simple thought has been the subject of studies, discussions and further investigations over past several decades and has given rise to a whole new field of plasmonics. Recently, plasmonics has become one of the most interesting and active research areas in micro-nanotechnology, enabling numerous fundamental studies and applications in a variety of scientific disciplines.⁴ A plasmon oscillation can be described as the collective motion of conduction band electrons relative to fixed positive ions (i.e., atoms) in a metal that is driven

by the electric field component of incident light.⁵ Surface plasmon polaritons (SPPs) are surface waves that result from the coupling of light to collective free electron modes at an interface of a metal and a dielectric.^{6,7} This excitation is an electromagnetic wave which is trapped close to the interface because of the presence of free charge carriers provided by the metal. Therefore, inside the metal this excitation has a plasma-like character while inside the dielectric it resembles a free electromagnetic wave. The most interesting feature of SPPs is that their electromagnetic field is maximum at the interface and decays exponentially inside both media. However, the freely propagating light does not readily interact with SPPs because of their momentum mismatching, which often requires various techniques, such as prism coupling, aperture coupling, subwavelength periodic structures coupling, etc. When excited in subwavelength structures, these SPP oscillations allow extraordinary transmission, confinement and manipulation of light at extremely short length scales.

9.2 Fundamentals of surface plasmon polaritons at terahertz frequencies

SPPs have been intensively investigated in the last two decades, but the focus has been primarily on the visible and near-infrared regimes. In dealing with terahertz (THz) or lower frequency radiation, the following important question arises: are there *real* surface plasmons at such long wavelengths? At THz frequencies, does the key property of strong confinement typical of surface plasmons at visible and near-infrared frequencies exist?

It is well known that the in-plane vector of SPPs on a planar metal–dielectric interface is given by $\beta(\omega) = k_0 \sqrt{\epsilon_d \epsilon_m(\omega) / (\epsilon_d + \epsilon_m(\omega))}$ where k_0 is the free space wave vector, ω is angular frequency, ϵ_d and ϵ_m are the complex permittivity of dielectric and the metal at the interface. At THz frequencies, the real part of metal permittivity is two to three orders of magnitude higher than the real part of the dielectric permittivity and it allows the SPP dispersion curve to be approximated by the light line, and the expression simplifies to $\beta(\omega) \approx k_0 \sqrt{\epsilon_d}$. Due to this simplification, the value of out-of-plane wave-vector, $|\kappa| = \sqrt{\beta^2(\omega) - k_0^2 \epsilon_d}$ that determines the decay rate of SPPs perpendicular to the interface becomes very small, leading to poor confinement of surface waves.^{5,7} This type of surface wave was first studied by Zenneck in 1907 at radio frequencies, so they are also known as Zenneck waves.⁸ Due to the poor confinement of the SPP waves, it is still argued vehemently whether there exists a real surface plasmon wave at THz and lower frequencies.

In this chapter, we discuss the recent finding on two-dimensional array of subwavelength micro-sized holes, which enables extraordinary transmission of electromagnetic waves via SPPs and has become a unique component in integrated micro-photonics.^{9–22} Understanding the physical origin of resonant properties in such plasmonic structures has attracted significant interest in a broad spectrum of electromagnetic waves and special interest in the THz regime. Thus, in subsequent sections, we discuss the different types of THz metallic hole arrays mainly fabricated from metals, semiconductors and superconductors to realize SPP-enhanced extraordinary transmissions, their active and passive controls, and applications.

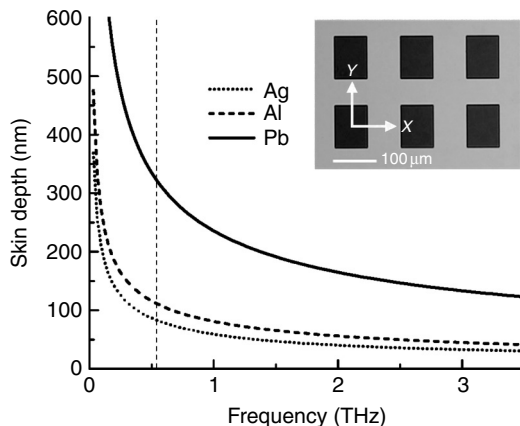
9.3 Extraordinary transmission of terahertz waves through metallic hole arrays

Metals are used for construction of waveguides and resonators for electromagnetic radiation at microwave and THz frequencies; since at these frequencies, they act as perfect conductors and the impinging electromagnetic waves penetrate only a negligible fraction into the metal. At higher frequencies, towards infrared and optical, the electromagnetic field penetration increases leading to increased losses and dissipation, thus not allowing a simple size scaling of photonic devices that work efficiently at low frequencies to infrared and optical regime. In this section, we will focus on metal plasmonic devices that work well at the THz frequencies due to their high conductivity.

Experimental results on transmission properties of light in metallic structures have indicated that SPP-enhanced transmission is normally achieved in metals with large ratio of the real to the imaginary dielectric constant, $-\epsilon_{\text{rm}}/\epsilon_{\text{im}} \gg 1$.^{19,20} In the THz regime, however, this ratio becomes $-\epsilon_{\text{rm}}/\epsilon_{\text{im}} < 1$ for non-transition metals, such as Ag, Au, Cu and Al.²³ This was considered a limitation to realizing resonant excitation of THz SPPs in the periodic subwavelength structures. Recent studies, however, have demonstrated that an appropriate surface corrugation provided by the subwavelength structures could facilitate the resonant excitation of SPPs. SPP-enhanced THz transmission has been experimentally observed in subwavelength hole arrays patterned in metal films made from both good and generally poor metals.^{21,22}

9.3.1 Resonant transmission through optically thin metallic hole arrays

In this section, we describe the resonant THz transmission through subwavelength hole arrays patterned on metallic films with thicknesses less than a skin depth. The experimental results have revealed a critical array



9.1 Frequency-dependent skin depth of metals Ag, Al and Pb. The vertical dashed line represents the $[\pm 1,0]$ SPP mode at 0.55 THz for the Pb–silicon interface. Inset: optical image of the array of periodic holes.

thickness, above which the SPP resonance begin to establish.²¹ The maximum amplitude transmission was achieved when the thickness of metal film approaches skin depth. However, enhanced THz transmission of up to 90% of the maximum transmission was realized with a film thickness of only one-third of the skin depth at the metal–silicon $[\pm 1,0]$ SPP mode at 0.55 THz.

Several sets of metallic arrays of subwavelength rectangular holes made from Pb film were deposited on the silicon wafer. The rectangular holes have physical dimensions of $100\text{ }\mu\text{m} \times 80\text{ }\mu\text{m}$, with a periodicity of $160\text{ }\mu\text{m}$, as shown in the inset of Fig. 9.1. Pb was chosen as the constituent metal of the arrays mainly for two reasons. First, extraordinary THz transmission in Pb subwavelength hole arrays has been demonstrated with an amplitude efficiency of up to 82% at 0.55 THz, which is close to the performance of arrays made from good conducting metal such as Ag, Al or Au.²³ Second, the skin depth of Pb at 0.55 THz is 320 nm, nearly three times that of Ag and Al. It thus provided a large dynamic thickness range to characterize the evolution of SPP resonance at the sub-skin-depth thickness limit.

The value of skin depth of electromagnetic waves in metal is determined by the penetration distance at which the electric field falls to $1/e$ of its maximum. The SPPs, which propagate along the metal–dielectric interface, decay exponentially in both media. At THz frequencies, the complex wave-vector inside the metal perpendicular to the interface is approximately given as⁹

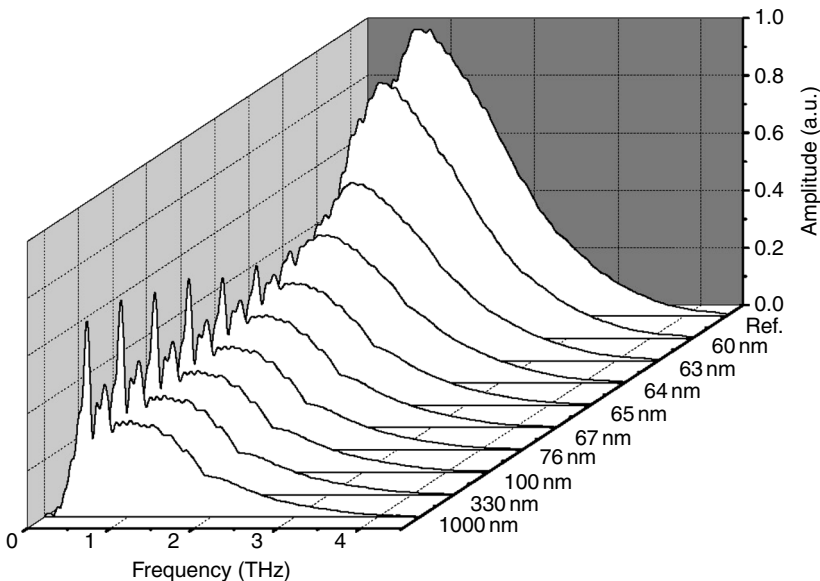
$$k_z = \frac{\omega}{c} \varepsilon_m^{1/2}, \quad [9.1]$$

where ω is the angular frequency and c is the speed of light in vacuum. Since only the imaginary part of k_z causes the exponential decay of electric fields, the skin depth can be defined as²⁴

$$\delta = \frac{1}{\text{Im}(k_z)} = \frac{c}{\omega} \frac{1}{\text{Im}(\epsilon_m^{1/2})} = \left(\frac{2}{\omega \mu_0 \sigma_{dc}} \right)^{1/2}. \quad [9.2]$$

where μ_0 is the vacuum permeability and σ_{dc} is the d.c. conductivity of metal. Based on this relation, frequency-dependent skin depths of various metals are plotted in the THz regime in Fig. 9.1. As can be seen, the skin depths for Pb, Al and Ag at 0.55 THz, the primary SPP $[\pm 1, 0]$ resonance, are estimated to be 320, 110 and 83 nm, respectively.

Pb arrays with various thicknesses ranging from 60 to 1000 nm were prepared. In the THz-TDS measurements,^{25,26} the input THz radiation was linearly polarized along the minor axes (80 μm) of the rectangular holes and penetrated the array at normal incidence. In Fig. 9.2, evolution of the SPP resonance as a function of the array film's thickness is depicted in the Fourier-transformed spectra of the reference and the samples. When the array film was thin, the spectrum showed no resonance but similar features to the reference spectrum with additional attenuation. At 64 nm, which was observed as a critical thickness for the Pb array, the SPP resonance excited

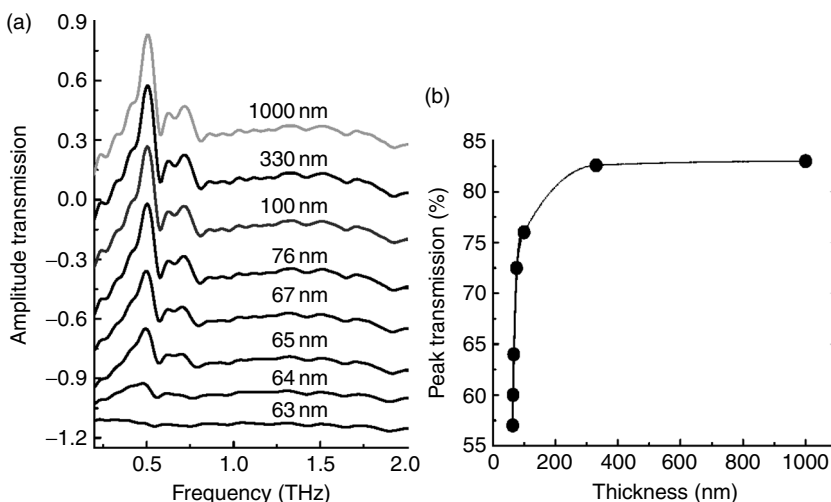


9.2 Fourier-transformed spectra of the transmitted THz pulses through reference (blank substrate) and the subwavelength Pb hole arrays with different film thicknesses.

at the Pb–Si interface appeared in the spectrum. Above this critical thickness, the resonance peak was enhanced with thicker array film.²¹

In Fig. 9.3a, evolution of SPP resonance as a function of array film thickness is depicted in the amplitude transmission spectra of various arrays. It clearly reveals two regions of thickness dependence. Below the critical thickness, 64 nm, the frequency-dependent transmission is nearly flat, showing no resonance peak. Above the critical thickness, a resonance at 0.55 THz appears in the transmission, with amplitude that increases with array thickness while the background transmission reduces. This resonance is attributed to the excitation of SPPs at the Pb–Si interface. Immediately above the critical thickness, the resonance amplitude is very sensitive to the thickness of arrays. The dependence of peak transmission on array thickness above the critical thickness is shown in Fig. 9.3b. The amplitude transmission efficiency increases exponentially when the array thickness is below 100 nm. It then saturates gradually and approaches the maximum at one skin depth.²¹

It is worth noting that a transmission efficiency as high as 76% was achieved at array thickness of 100 nm, only one-third of skin depth. This value is more than 90% of the maximum transmission efficiency achieved at one skin depth. For comparison, it was also shown that two additional arrays of same structure but made from Ag and Al of one-third of skin depth. The



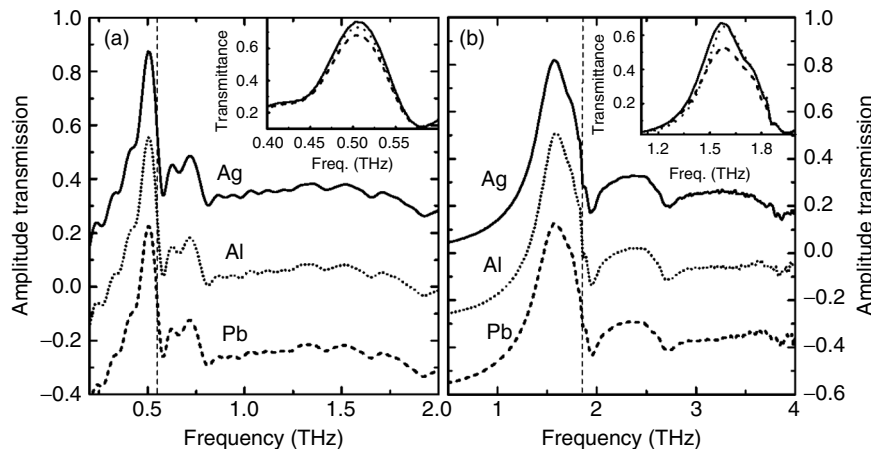
9.3 (a) Measured amplitude transmission of the Pb arrays with different thicknesses; the curves are vertically displaced for clarity; and (b) measured peak amplitude of the $[\pm 1, 0]$ SPP mode at 0.55 THz as a function of the Pb thickness (circles), connected by a thin curve to guide the eye. The solid curve is an exponential fit for the region of array thicknesses below 100 nm.

measured transmission efficiencies are all above 90% of their maximum amplitude transmission. This finding may extensively reduce the metal thickness of plasmonic components for applications in photonic, optoelectronic and sensing devices.

9.3.2 Metallic permittivity dependent transmission of surface waves

In this subsection, we focus on highlighting the conductivity dependent behavior of THz plasmonic hole arrays. The conductivity and the dispersive complex dielectric constant of constituent metals was found to play an essential role in the extraordinary transmission of light in 2D subwavelength metallic hole arrays. Owing to the different ratio of the real to imaginary dielectric function, $-\epsilon_{\text{rm}}/\epsilon_{\text{im}}$, transmission properties of light showed a large difference in the arrays made from Ag, Au and Cr.^{19,20} The SPP-enhanced transmission efficiency of light was found to be increased with higher ratio $-\epsilon_{\text{rm}}/\epsilon_{\text{im}}$; for example, the transmission efficiency of Ag arrays was several times higher than that of Ni arrays of the same structure. To explore dielectric function dependent THz transmission properties of metal arrays at different resonance frequencies, two types of array samples were lithographically fabricated: array-on-silicon samples with patterned optically thick metal film on blank silicon substrate for the metal–silicon [$\pm 1,0$] mode at 0.55 THz^{9,22} and freestanding metallic arrays for the metal–air [$\pm 1,0$] mode at 1.60 THz. The THz-TDS measurements have shown that the resonant THz transmission was increased with the higher ratio of $-\epsilon_{\text{rm}}/\epsilon_{\text{im}}$ for metals with dielectric function following the Drude model. This result is consistent with the observation at optical frequencies.^{19,20} However, due to significant increase in the values of dielectric function, the difference in the resonance peaks between arrays made from different metals was narrowed down extensively compared to the resonant transmission of light.

At 0.55 THz, the ratios $-\epsilon_{\text{rm}}/\epsilon_{\text{im}}$ for Ag, Al and Pb are 0.12, 0.03 and 0.01, respectively, indicating that Ag is still a better metal than others, and was expected to show resonance with higher amplitude transmission. Practically, as shown in Fig. 9.4a, the Ag array indeed showed the highest amplitude transmission 87%, while the Al and Pb arrays followed with small attenuation, giving 85.5% and 82%, respectively. Even though the amplitude transmission of these arrays revealed small differences, it indeed increased with higher ratio $-\epsilon_{\text{rm}}/\epsilon_{\text{im}}$. This showed good consistency with those observed at visible frequencies. Compared to excellent metals, Pb is generally considered a poor electrical conductor. However, the drastic increase in dielectric constant enables Pb to behave as a better metal towards the establishment of SPP-enhanced transmission at THz frequencies. In Fig. 9.4b, the measured

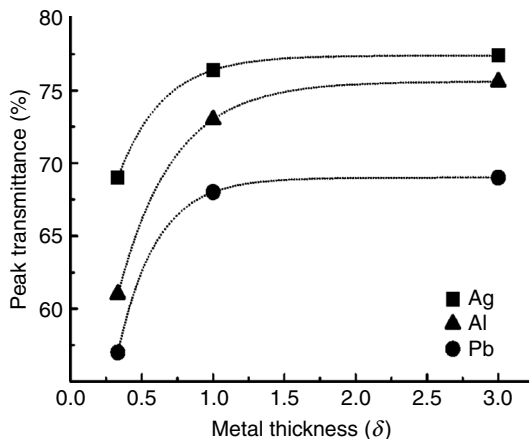


9.4 (a) Measured amplitude transmission of the array-on-silicon samples made from Ag, Al and Pb. For clarity, the spectra of Al and Pb arrays are moved down by 0.3 and 0.6, respectively. The vertical dashed line indicates the calculated $[\pm 1,0]$ metal–Si SPP mode at 0.55 THz.
 (b) Metal–air SP mode at 1.85 THz. The insets show the corresponding transmittances.

peak transmissions at the SPP $[\pm 1,0]$ resonance at 1.60 THz for Ag, Al and Pb are 82%, 81% and 72.5%, respectively, showing similar properties to those observed at the SPP $[\pm 1,0]$ metal–Si resonance at 0.55 THz.²² The difference in amplitude transmission for arrays made from these metals has arisen from the difference in effective propagation length of SPPs.

We have also fabricated array-on-silicon samples with various thicknesses to verify the experimental results. Figure 9.5 illustrates the peak transmittance measured at the 0.55 $[\pm 1,0]$ THz SPP mode for the Ag, Al and Pb arrays. With metal thicknesses of one-third and three times skin depth, the comparison of peak transmittance for these metals maintains the same trend as observed with one skin-depth thickness, demonstrating the generality of the concept.

The difference in resonant transmission for arrays made from different metals has primarily arisen from the difference in effective propagation length of SPPs determined primarily by internal damping, radiation and scattering damping. At THz frequencies, the imaginary propagation vector along the metal–dielectric interface approximately given as $k_i = k_0 \varepsilon_d^{3/2} / (2\varepsilon_{im})$ ⁹ governs the internal damping, where k_0 is the wave-vector of electromagnetic wave in vacuum. The measured transmission of the metal arrays shows a decreasing trend with increasing k . On a rough metal surface, besides the internal absorption, radiation and scattering damping also modify the propagation length. As a result, the effective



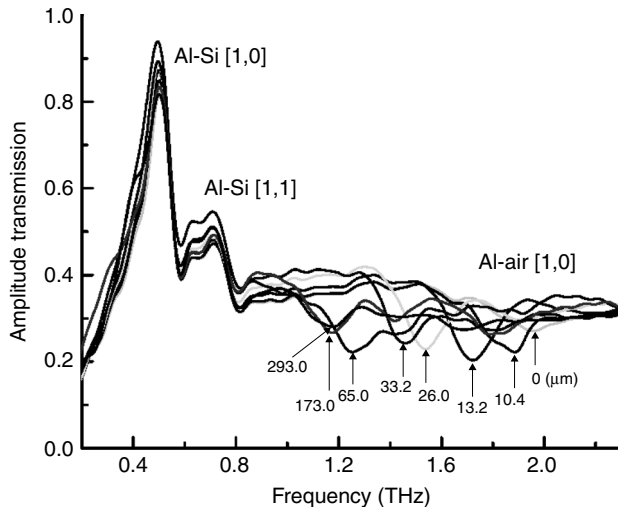
9.5 Peak transmittance at the 0.55 [$\pm 1, 0$] THz metal–Si SPP mode for arrays made from different metals, Ag, Al and Pb and different thicknesses. The dotted curves are to guide the eye.

propagation lengths for different metals can be extensively reduced, leading to the difference in the resonant transmission.

9.3.3 Surface plasmonic sensors: effect of dielectric layer on metallic hole arrays

SPPs have the characteristic of good confinement near the metal–dielectric interface. This makes their resonant properties, such as amplitude, frequency and propagation length, extremely sensitive to the dielectric function of the medium adjacent to the metal surface. This has made such plasmonic hole arrays very promising for sensing applications.^{27–30} In particular, arrays with asymmetric metal–dielectric interfaces on both sides, such as an air–metal–substrate system, provide improved sensitivity because the analytes ($\epsilon > 1$) applied on the array not only replace air as a dielectric medium at the metal surface, but also easily fill up the hole cavities against the substrate. Significant modifications of resonant transmission at the SP modes were observed by coating dielectric overlayer on the plasmonic device. The shift in the resonant frequencies shows that these devices act as a dielectric sensor.

The metal–air SPP [$\pm 1, 0$] mode at 1.95 THz exhibited up to 0.80 THz remarkable tuning range, while the peak amplitude transmission of the metal–Si SPP [$\pm 1, 0$] mode at 0.5 THz was enhanced from 0.82 to 0.94, owing to resultant change in wave vectors of the SPP modes.²⁹ A dielectric layer made from photoresist ($\epsilon_2 = 2.2 \pm 0.1$ at 1.1 THz, Futurrex, Inc.) was

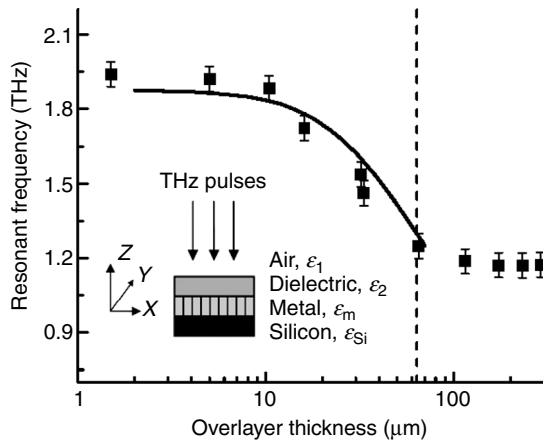


9.6 Amplitude transmission of THz pulses in the Al hole array with a dielectric overlayer of different thicknesses varying from 0 to 293 μm .

spin-coated on a 180 nm thick Al hole-array-on-Si sample by a single-wafer spin processor (Laurell WS-400 A). The array comprised 80 μm (x -axis) \times 100 μm (y -axis)-sized rectangular holes with a periodicity of 160 μm . The extracted frequency-dependent amplitude transmission of the array with a dielectric overlayer of various thicknesses d , from 0 to 293 μm , is illustrated in Fig. 9.6. As indicated by the arrows, the SPP resonance of the Al-air [$\pm 1,0$] mode shifted remarkably to lower frequencies with increasing d . Without the dielectric layer, the resonance of the Al-air [$\pm 1,0$] mode occurred at 1.95 THz, while it shifted to 1.87 THz with a layer thickness of 10.3 μm . When the dielectric layer thickness was increased to 65 μm , this resonance redshifted significantly to 1.25 THz. Further increase in layer thickness, however, led to little variation at this resonance mode and it was eventually saturated at 1.17 THz with layer thicknesses varying from 173 to 293 μm . At the resonance frequency of the Al-Si [$\pm 1,0$] mode, only minor redshifts were observed due to the overlayer effect, however, the peak amplitude transmission was essentially enhanced with increasing overlayer thickness.²⁹

The resonance shift due to the overlayer at the Al-air [$\pm 1,0$] SPP mode can be understood through the dispersion relation of the SP modes at normal incidence,⁵

$$k_{\text{sp}} = \frac{\omega}{c} \text{Re} \left(\frac{\epsilon_d \epsilon_m}{\epsilon_d + \epsilon_m} \right)^{1/2}. \quad [9.3]$$



9.7 Resonance frequencies of the Al-air [$\pm 1,0$] SPP mode as a function of the thickness of the overlayer dielectric film. Experimental data: squares, numerical calculation: solid curve. Inset: schematic diagram of the array sample.

In this case, without the dielectric layer, the adjacent medium is air, giving $\epsilon_d = \epsilon_1 = 1$. When the dielectric film was applied on metal surface and if the film thickness $d > \lambda$ was fulfilled, with λ the resonance wavelength, the dispersion in Equation [9.3] can be modified from ($\epsilon_d = \epsilon_1$) to ($\epsilon_d = \epsilon_2$), where ϵ_2 is the dielectric function of the overlayer film, as shown in the inset of Fig. 9.7.

Thus, the resonant frequency shifted due to modification of the dielectric function of the adjacent medium. When the overlayer thickness was less than the resonance wavelength $d < \lambda$, however, the dielectric layer ϵ_2 , along with the ambient air ϵ_1 , served as an effective adjacent medium to the metal. The shift in SPP resonance arose from the modification of the SP wave-vector due to thickness change of the overlayer. This demonstration showed that the THz SPP on a metallic hole array could lead to plasmonic sensing application.

9.4 Active control of terahertz surface plasmon polaritons

The previous section gives an overview of resonant excitation of THz SPPs, which exhibit extraordinary transmission in two-dimensional metallic subwavelength hole arrays. The SPPs are excited by the in-plane electromagnetic wave scattering provided by these periodic gratings, and SPPs can propagate along the metal–dielectric interfaces. The excitation of surface waves leads to a field enhancement at the metal–dielectric interface and a large transmission through subwavelength apertures at

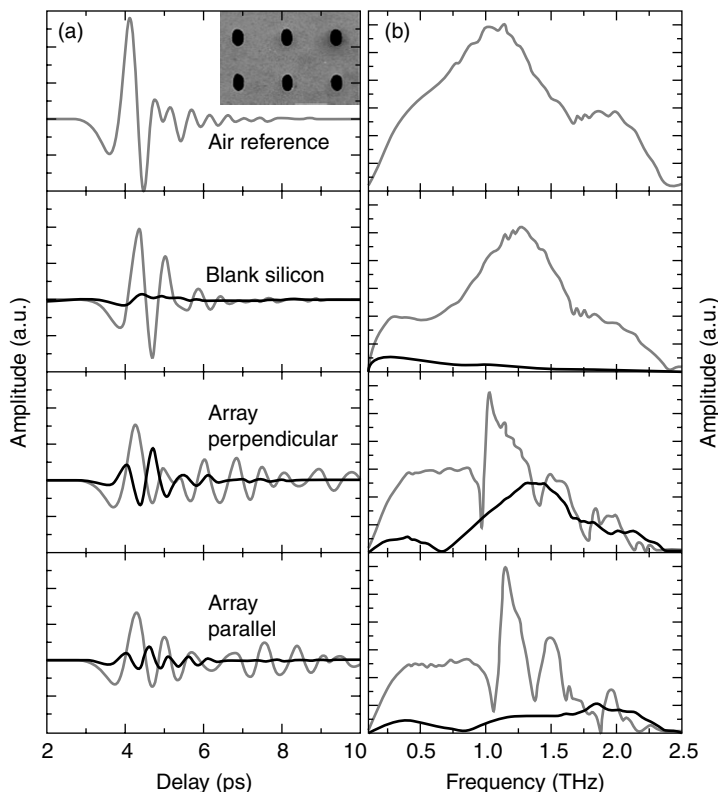
distinct wavelengths associated with the period of the array. The highly frequency-dependent transmission, as well as the localized electric field strengths at the metal–dielectric interface, means that hole arrays are finding applications in sensing, spectroscopy, subwavelength optics, nonlinear optics and photolithography. Metals are excellent for fabricating passive plasmonics devices, the only problem being that once these devices are fabricated, we cannot tune their response or their functionalities. At THz frequencies, there is a need for active devices in which the resonant transmission can be switched in short time scales. In this section, we discuss some techniques to actively control resonant THz transmission. The active control was achieved either by using a dielectric whose conductivity was actively tuned by photoexcitation, or by using high temperature superconductors that undergo a phase transition upon cooling and have the ability to switch the plasmonic resonances off and on depending on the thermal environment.^{31–37}

9.4.1 Active transition from a silicon photonic crystal to a metallic hole array

A doped semiconductor, such as silicon, behaves like a metal, and enables excitation of SPPs at THz frequencies if the doping is sufficiently high. Enhanced THz transmission in highly doped semiconductor hole arrays was recently demonstrated and the resonant amplitude was found to be controllable by the doping level.^{10,31–36} In this subsection we study an interesting question on how SPP resonance behaves when the real part of dielectric function of the constituent medium is altered actively from positive, across zero, to negative? In an effort to address this question, we have observed a characteristic evolution of an SPP resonance in a semiconductor subwavelength hole array by use of optical pump–THz probe measurements.^{32,38} The purpose of optical pumping was to change the dielectric properties of silicon sample by introducing and controlling photo-induced free carriers remotely. The plasmonic array sample was made from lightly doped silicon, a fairly transparent medium to THz radiation. Its relatively low carrier density is insufficient to support SPP resonance. The experimental results revealed that the THz transmission properties of the static array were dominated by the out-of-plane two-dimensional photonic crystal effect. When optical excitation was applied to the array, the photo-generated free carriers altered the dielectric properties of Si; the real part of dielectric constant changed from positive to negative with increasing excitation intensity. As a result, the signature of photonic crystal effect gradually disappeared and SPP resonance emerged and was developed into extraordinary THz transmission.

The array sample was fabricated from commercially available 30- μm thick n-type Si with 10- $\Omega\text{ cm}$ resistivity and $4\times 10^{14}\text{cm}^{-3}$ carrier concentration. The sample was a 10 mm \times 10 mm-sized array of 80 μm \times 40 μm elliptical holes in a square lattice with a periodicity of 160 μm . During measurements THz electric field was aligned along the minor (major) axis of the elliptical holes, which we labeled perpendicular (parallel) orientation.

Figure 9.8a illustrates the transmitted THz pulses through air reference, blank Si and the array of both perpendicular and parallel orientations before and after the optical excitation of a 111 mW average power. The perpendicular (parallel) orientation of the array is defined with the longer axis of the elliptical hole perpendicular (parallel) to THz electric field. The transmitted THz pulse through the unexcited blank Si showed a ~85% amplitude transmission if surface reflections are taken into account. The Si became

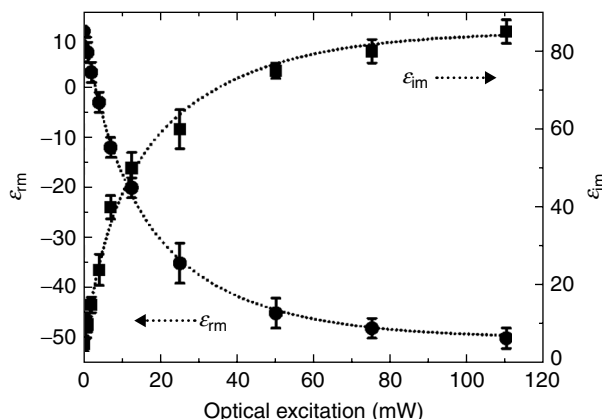


9.8 (a) Measured transmitted THz pulses and (b) the corresponding Fourier-transformed spectra through air reference, blank Si, Si array of perpendicular and parallel orientations with (black curves) and without (gray curves) optical excitation at an 111 mW average power. The inset shows the SEM image of the Si array of elliptical holes.

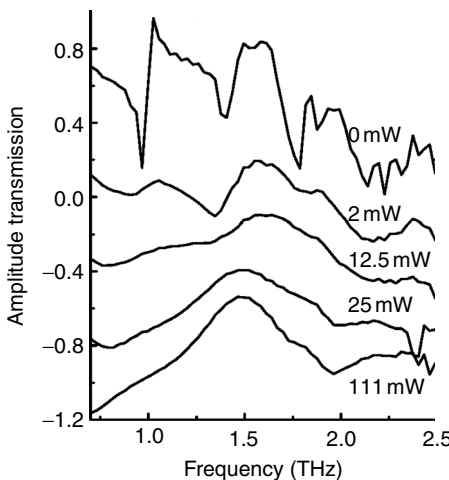
nearly opaque to THz radiation under intense optical excitation due to strong absorption of photo-generated free carriers. The corresponding Fourier-transformed spectra are shown in Fig. 9.8b. In the absence of optical excitation the array can be considered as a two-dimensional out-of-plane photonic crystal slab that has shown complicated spectral structures instead of stopgaps.³⁹ Under intense optical excitation, however, the transmission spectra exhibited totally different features; the photonic crystal resonances disappeared and SP resonance peaks occurred at different frequencies.

The metallic behavior of the array is mainly determined by the negative value of the real dielectric constant $\epsilon_{rm} < 0$. Under intense optical excitation, the Si array became a complex multilayer medium, composing a stack of photo-excited Si and unexcited Si layers. At THz frequencies, ϵ_{rm} of the photo-excited layer may become negative from positive under appropriate optical excitation and hence the sample behaved as a metallic grating that favored the formation of SPPs. The thickness of the photo-excited layer depends on the penetration depth δ_L at the excitation laser wavelength, here $\delta_L = 10\mu\text{m}$ for Si at $\lambda = 800\text{ nm}$. In contrast, the penetration depth for THz radiation in the photo-excited Si is $\delta_{\text{THz}} = 3\mu\text{m}$ at 1.50 THz under 111 mW excitation, corresponding to a carrier density $N = 0.99 \times 10^{18}\text{ cm}^{-3}$. δ_{THz} can be controlled by laser intensity and it became thinner with increasing optical excitation.

Figure 9.9 shows the dependence of the complex dielectric constant of the photo-excited Si layer at 1.50 THz, the $[\pm 1, 0]$ SPP mode, on laser excitation power. The dielectric function was measured from the reference Si slab, where the power absorption α and the refractive index n of the photo-excited Si layer were determined by comparing the transmitted THz pulses



9.9 Measured dielectric function of the photo-excited Si at 1.50 THz as a function of optical excitation. The dotted curves are to guide the eye.



9.10 Frequency-dependent THz transmission of the array with the electric field along the shorter axis of the holes under various laser excitations ranging from 0 to 111 mW. The measurements for different optical excitations are vertically shifted for clarity.

through the photo-excited and unexcited slab. The dielectric constant was obtained from measured α and n using the relations $\epsilon_{\text{rm}} = n^2 - k^2$ and $\epsilon_{\text{im}} = 2nk$, where $k = ac/(2\omega)$. As expected, the real dielectric constant ϵ_{rm} was evolutionally tuned from positive, across zero, to negative with increasing optical power. Above 3 mW, the photo-excited Si layer began to exhibit metallic properties and had potential to support SPPs.

To explore the characteristic evolution of the photo-induced SPP resonance, the frequency-dependent THz transmission of the array under varying power from 0 to 111 mW optical excitation is measured and plotted for THz electric field along the shorter axis of the holes in Fig. 9.10.

Transmission enhancement was observed at the fundamental SPP 1.50 [$\pm 1,0$] THz mode at silicon–air interface. At low excitation, the transmission was dominated by complex out-of-plane photonic crystal resonances near 0.97, 1.40 and 1.78 THz. When the laser power was increased to 12.5 mW, the photonic crystal effect nearly disappeared and a new resonance peak appeared at 1.60 THz due to the excitation of SPPs. The further increase in excitation power gave rise to an enhanced THz transmission and a red-shift of resonance peak to 1.50 THz. The transmission efficiency at the SPP resonance 1.50 THz was found to increase with increasing power of laser excitation. At 25 mW, the maximum THz transmittance was 25.5%, while it was increased to 45% at 111 mW, corresponding to a 340% transmittance when normalized to the areas of the holes. From the pump-dependent dielectric function shown in Fig. 9.9, this phenomenon can be seen that the

photo-excited Si layer showed improved metallic properties with increasing optical excitation and hence favored the establishment of SPs.

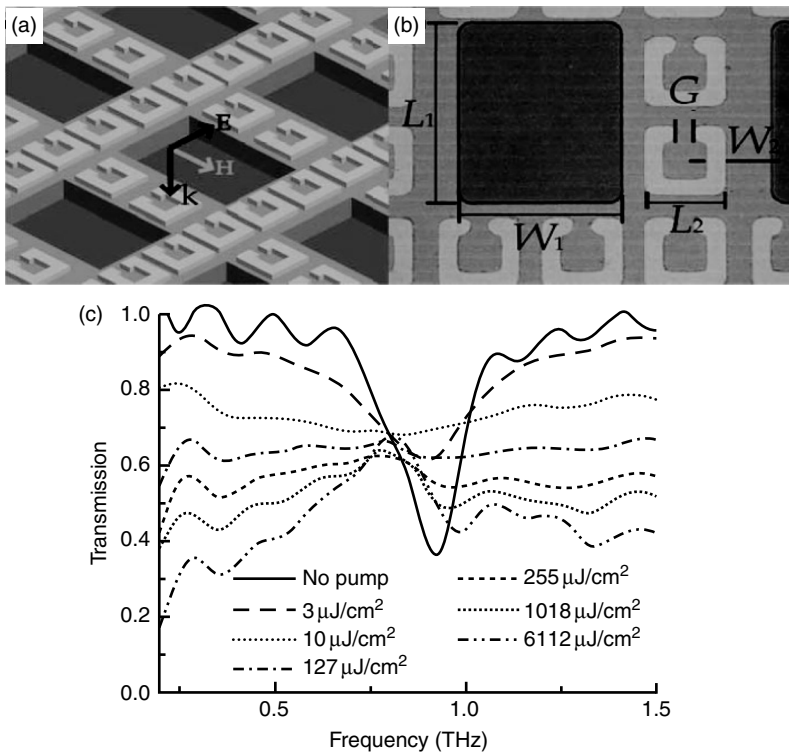
9.4.2 Hybrid plasmonic switching devices with metamaterial properties

In this subsection, we discuss a unique hybrid active metamaterial consisting of an engineered composite film that dynamically switches resonant transmission behavior of THz radiation from band-stop to band-pass under appropriate optical excitation. In the absence of optical excitation, a resonant band-stop behavior is observed arising from metallic split-ring-resonators fabricated on an epitaxial silicon film that was already patterned into a periodic hole array. Pumping with external infrared light, the silicon film becomes quasi-metallic, damping the metamaterial response and enabling a band-pass surface plasmon resonance through the photo-conducting hole array.

Active control is employed to alter the fundamental inductive-capacitive (LC) resonance of the split-ring-resonator (SRR) structure, which natively exhibits a band-stop behavior in the transmission spectra.^{40–42} However, if this band-stop mode could be dynamically switched to a band-pass resonance at the same frequency, the resulting metamaterials could be promising in active THz applications.

Figure 9.11a shows the schematic and a microscopic image of the fabricated structure. The aluminum SRR array was patterned on the silicon film using a conventional photolithography process. This was followed by reactive ion etching to form the hole array in the silicon film. Each of the unit cells comprise five SRRs and a silicon hole, with dimensions of $33 \times 33 \mu\text{m}^2$ and $65 \times 50 \mu\text{m}^2$ respectively, as shown in Fig. 9.11a, which have a periodicity of $100 \times 100 \mu\text{m}^2$. The gap-bearing arm of the SRR was designed to be parallel with the width of the holes. These dimensions and orientations of the SRRs and holes were designed such that the fundamental SRR resonance and the [1,0] SPP resonance occur at the same frequency. Figure 9.11b shows the actual microscopic image of the sample.

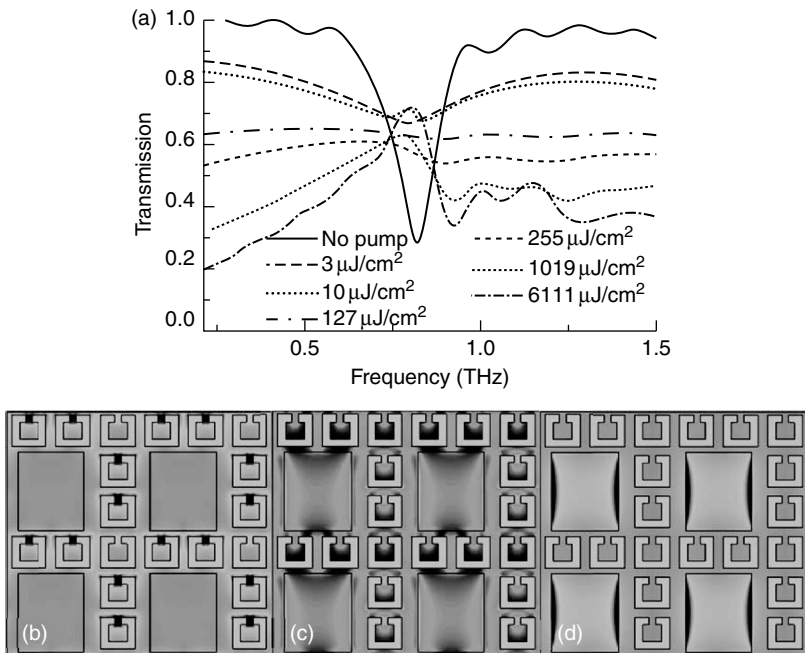
The measured transmitted spectra of the composite plasmonic film at various pump fluences are plotted in Fig. 9.11c. Without optical excitation the THz spectrum shows a well-defined resonance feature, which is due to the LC resonance arising from the SRRs. Thus, the spectrum for the unpumped sample shows the strongest LC resonance with band-stop transmission amplitude as low as 0.36. When the optical excitation fluence is gradually increased from 0 to $10 \mu\text{J}/\text{cm}^2$, the LC resonance eventually disappears and the transmission amplitude increases from 0.36 to 0.7. Under $10 \mu\text{J}/\text{cm}^2$ excitation, the LC resonance completely disappears and the transmission



9.11 (a) Schematic and (b) microscopic image of the plasmonic metamaterial (silicon, aluminum and sapphire are marked by gray, white and black colors, respectively). The geometrical dimensions of the metamaterial are $L_1 = 65 \mu\text{m}$, $W_1 = 50 \mu\text{m}$, $L_2 = 33 \mu\text{m}$, $W_2 = 6 \mu\text{m}$ and $G = 5 \mu\text{m}$ (c) Measured transmission spectra at different pump fluence.

spectrum shows a flat attenuation. Further increase of the optical fluence up to $255 \mu\text{J}/\text{cm}^2$ only reduces the flat amplitude transmission from 0.68 to 0.62 due to increasing photo-carriers in the silicon layer. As the fluence is increased above $255 \mu\text{J}/\text{cm}^2$, a resonance peak appears in the transmission spectrum, whose amplitude increases with excitation power. The measured peak is attributed to the SPP resonance excited by the metallic silicon hole arrays.

In order to gain an insight into the pump-dependent behavior of the plasmonic metamaterial, we performed full wave electromagnetic simulations (CST Microwave Studio) of THz transmission through the sample.⁴³ Since the tunable response arises from the change in conductivity of the silicon layer, we employed different conductivities in the numerical simulation to represent different pump powers.³⁶ The simulated amplitude transmissions



9.12 (a) Simulated spectra at different pump fluences. Simulated electric fields at different pump fluences: (b) no pump, (c) $127 \mu\text{J}/\text{cm}^2$ and (d) $6.11 \text{ mJ}/\text{cm}^2$.

are shown in Fig. 9.12a, which agree well with the measurements. The electric field distributions at the resonance frequency were simulated for three different conductivities of 0 (no pump), 7.6×10^3 ($127 \mu\text{J}/\text{cm}^2$) and $2.94 \times 10^5 \text{ S/m}$ ($6112 \mu\text{J}/\text{cm}^2$), as shown in Figs 9.12b–d, respectively. We clearly observe the transition from high electric field concentration in the SRR gaps with no pump, to intense fields at the edge of the hole arrays with maximum pumping.

At the maximum pump fluence the conductivity of the silicon film is high enough to support a SPP resonance. At this pump level the metal SRRs are effectively shorted against the metallic silicon film. The hole array builds up a strong SPP band-pass transmission resonance, wherein the electric field is mainly focused along the length of the holes. Interestingly, for moderate pump fluences neither the LC nor the SPP resonance feature was observed in Fig. 9.12c since the electric field appears to be fairly uniform across the entire sample. The reason is that the conductivity of the silicon layer was enough to damp the SRR resonance but not enough to support the propagation of surface waves, which normally requires some minimum threshold of both metal conductivity and thickness.

9.4.3 Superconducting plasmonics

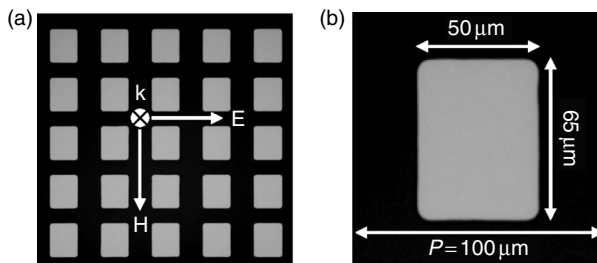
In this subsection, we review the superconductor array of subwavelength holes with active thermal control over the resonant transmission induced by SPPs. The array was fabricated by patterning high temperature yttrium barium copper oxide (YBCO) superconducting film and we observed a strong switching from a virtual excitation of the surface plasmon mode to a real surface plasmon mode. The highly controllable superconducting plasmonic hole arrays could be applied in the design of low loss, large dynamic range amplitude modulation and surface plasmon based THz devices. At THz frequencies, semiconductors are efficient materials for active plasmonics. Thermal, electrical, magnetic and optical switching of THz SPPs has been extensively demonstrated in recent years, allowing active control of the surface plasmon resonance. The semiconductor and the metal used in fabricating plasmonic devices suffer from the limitation of higher losses. This drawback can be mitigated by the use of high transition temperature (T_c) superconductor (HTS) thin films, which uniquely work only at THz or lower frequencies due to the small pseudo gap between the Cooper pairs.

The sample is made from a commercial 280 nm thick YBCO film, which typically has a $T_c = 86$ K and 2.3 MA/cm^2 critical current density grown on a 500 μm thick sapphire substrate. The superconductor hole array was fabricated using photolithography followed by a wet etching of superconducting film in 0.04% nitric acid.³⁷ The optical images of the hole array are illustrated in Fig. 9.13. The dimension of a unit hole is $65 \times 50 \mu\text{m}^2$ with a lattice constant of 100 μm .

The measurements were performed at room temperature and then gradually cooled down to 51.4 K in a helium cryo-assisted THz-TDS system. Figure 9.14a illustrates the measured normalized transmission response of the YBCO array under normal incidence at 297, 183, 133, 86 and 51.4 K, respectively. At 297K, we observed two resonance modes at 0.85 and 1.16 THz with peak amplitudes of 0.69 and 0.51, respectively, which correspond to the $[\pm 1, 0]$ and $[\pm 1, \pm 1]$ modes of the surface wave. As the hole array was cooled down, both resonances gradually became prominent with an increase in their respective peak amplitudes. Finally, at 51.4 K, a temperature well below T_c , the $[\pm 1, 0]$ resonance mode showed a clear switching effect when the peak transmission value was switched to 0.97.

Since YBCO is a highly anisotropic material, the dispersion relation of surface polaritons can be expressed as:⁴⁴

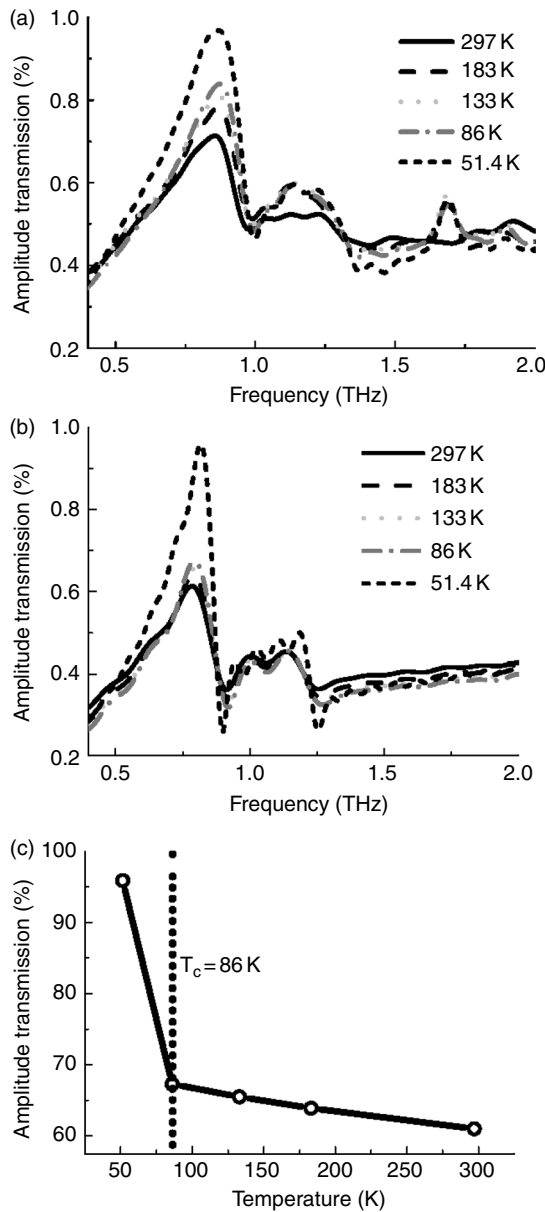
$$k^2 = \frac{\omega^2}{c^2} \epsilon_s \epsilon_c \frac{\epsilon_{ab} - \epsilon_s}{\epsilon_{ab} \epsilon_c - \epsilon_s^2} \quad [9.4]$$



9.13 Optical images of (a) a periodic subwavelength YBCO hole array on sapphire substrate, where k , E , and H denote the wave propagation vector, direction of electric field, and direction of magnetic field, respectively and (b) a unit cell with geometric dimensions.

where ϵ_s is the dielectric constant of the surrounding substrate, ϵ_{ab} and ϵ_c are the dielectric function of YBCO along the a - b plane and c -axis, respectively. This dispersion relation is consistent with that in the isotropic material if $\epsilon_{ab} = \epsilon_c$. For YBCO, however, $\epsilon_{ab} \neq \epsilon_c$, thus two cases arise. When the temperature is lower than the critical temperature of 86 K, $\epsilon_{ab} < 0$, $\epsilon_c < 0$ and $|\epsilon_{ab}| \gg |\epsilon_c|$, the dispersion relation can be simplified as $k^2 = (\omega^2/c^2) \times \epsilon_s$. In this case, the THz wave can be coupled to the real SPP mode, which is similar to the case in the metallic hole array. As the temperature rises above the critical transition, $\epsilon_{ab} < 0$, $\epsilon_c > 0$ and $|\epsilon_{ab}| \gg \epsilon_c$, the dispersion relation again simplifies to the same expression, $k^2 = (\omega^2/c^2) \times \epsilon_s$, but the surface mode excited here is a *virtual* SPP mode, which occurs only for small magnitude of wave-vector. Figure 9.14a clearly reveals that all the measured transmission resonances above $T_c = 86$ K are caused by the virtual excitation of SPPs, and a strong enhancement at 51.4 K is mainly due to resonant excitation of a real SPP mode.

In order to confirm the experimental results at temperatures above and well below T_c , finite-element simulations using CST Microwave Studio were carried out in which we used measured real and imaginary conductivity values for unpatterned YBCO film at 297, 183, 133 and 86 K. The conductivity at 51.4 K was taken from Reference 45. As shown in Fig. 9.14a, due to increase in the ratio of the real to the imaginary dielectric constant,⁴⁶ the peak amplitude transmission caused by the virtual excitation type SPP became gradually larger, and at superconducting state the transmission peak caused by a real SPP nearly reached 100%, demonstrating extremely low loss. The frequency blue-shift is caused by the increase in real part of dielectric function. The dramatic change in amplitude transmission can be seen in Fig. 9.14b, where the transmission at resonance suddenly increases by almost 30% due to the formation of superconducting Cooper pairs below the transition temperature. This switching behavior in the simulation matches reasonably well with our measurements. The slight difference between the simulated and the measured data can be attributed to defects in the YBCO film and changes in the superconductor film thickness while processing the hole array sample.



9.14 (a) Measured and (b) simulated amplitude transmission response of the YBCO hole array at 297, 183, 133, 86 and 51.4 K, respectively, at normal incidence; (c) amplitude transmission peak percentage at varying temperatures.

Before the superconductor reaches its transition temperature, the change in transmission from room temperature up to the critical temperature is only $\sim 5\%$, as evident from Fig. 9.14c.

9.5 Conclusion

We would like to propose that multifunctional THz devices can be built by exploiting the unique characteristics of SPPs with semiconductors and the low-loss properties of metals in this frequency range. We also propose creating reconfigurable active SPP based semiconductor, as well as superconductor, switches, filters, waveguides and beam splitters for THz light. The SPPs in metallic hole arrays can be efficiently used as sensors due to the close proximity of the analytes with the surface wave. Using plasmonic devices capable of concentrating THz light into subwavelength spots will provide a wealth of possibilities to THz science and technology.

9.6 References

1. T. W. Ebbesen, H. J. Lezec, H. F. Ghaemi, T. Thio, and P. A. Wolff, *Nature* **391**, 667 (1998).
2. W. L. Barnes, A. Dereux, and T. W. Ebbesen, *Nature* **424**, 824 (2003).
3. C. Genet, and T. W. Ebbesen, *Nature* **445**, 39 (2007).
4. H. Atwater, *Sci. Am.* **296**, 56 (2007).
5. H. Raether, *Surface plasmons on smooth and rough surfaces and on gratings*. (Springer-Verlag, Berlin, 1988).
6. A. D. Boardman, *Electromagnetic surface modes* (Wiley, New York, 1982).
7. S. A. Maier, *Plasmonics: fundamentals and applications* (Springer-Verlag, New York, LLC, 2007).
8. T.-I. Jeon, and D. Grischkowsky, *Appl. Phys. Lett.* **88**, 061113 (2006).
9. D. Qu, D. Grischkowsky, and W. Zhang, *Opt. Lett.* **29**, 896 (2004).
10. A. K. Azad, Y. Zhao, and W. Zhang, *Appl. Phys. Lett.* **86**, 141102 (2005).
11. H. Cao and A. Nahata, *Opt. Express* **12**, 1004 (2007).
12. F. Miyamaru and M. Hangyo, *Appl. Phys. Lett.* **84**, 2742 (2004).
13. J. O'Hara, R. D. Averitt, and A. J. Taylor, *Opt. Express* **12**, 6397 (2004).
14. D. Qu and D. Grischkowsky, *Phys. Rev. Lett.* **93**, 196804 (2004).
15. G. Torosyan, C. Rau, B. Pradarutti, and R. Beigang, *Appl. Phys. Lett.* **85**, 3372 (2004).
16. J. B. Masson and G. Gallot, *Phys. Rev. B* **73**, 121401 (2006).
17. J. W. Lee, M. A. Seo, D. J. Park, D. S. Kim, S. C. Jeoung, C. Lienau, Q. H. Park and P. C. M. Planken, *Opt. Express* **14**, 1253 (2006).
18. T. Matsui, A. Agrawal, A. Nahata, and Z. V. Vardeny, *Nature* **446**, 517 (2007).
19. T. Thio, H. F. Ghaemi, H. J. Lezec, P. A. Wolff, and T. W. Ebbesen, *J. Opt. Soc. Am. B* **16**, 1743 (1999).
20. D. E. Grupp, H. J. Lezec, T. W. Ebbesen, K. M. Pellerin, and T. Thio, *Appl. Phys. Lett.* **77**, 1569 (2000).
21. A. K. Azad and W. Zhang, *Opt. Lett.* **30**, 2945 (2005).

22. A. K. Azad, M. He, Y. Zhao, and W. Zhang, *Opt. Lett.* **31**, 2637 (2006).
23. M. A. Ordal, L. L. Long, R. J. Bell, S. E. Bell, R. R. Bell, R. W. Alexander, Jr., and C. A. Ward, *Appl. Opt.* **22**, 1099 (1983).
24. S. Ramo and J. R. Whinnery, *Fields and waves in modern radio* (Wiley, New York, 1953), Chap. 6, p. 239.
25. D. Grischkowsky, S. Keiding, M. Van Exter, and Ch. Fattinger, *J. Opt. Soc. Am. B* **7**, 2006 (1990).
26. M. He, A. K. Azad, S. Ye, and W. Zhang, *Opt. Commun.* **259**, 389 (2006).
27. A. G. Brolo, R. Gordon, B. Leathem, and K. K. Kavanagh, *Langmuir* **20**, 4813 (2004).
28. J. Dintinger, S. Klein, F. Bustos, W. L. Barnes, and T. W. Ebbesen, *Phys. Rev. B* **71**, 035424 (2005).
29. J. Han, X. Lu, and W. Zhang, *J. Appl. Phys.* **103**, 033108 (2008).
30. J. F. O'Hara, R. Singh, I. Brener, E. Smirnova, J. Han, A. J. Taylor, and W. Zhang, *Opt. Express* **16**, 1786 (2008).
31. C. Janke, J. G. Rivas, C. Schotsch, L. Beckmann, P. H. Bolivar, and H. Kurz, *Phys. Rev. B* **69**, 205314 (2004).
32. W. Zhang, A. K. Azad, J. Han, J. Xu, J. Chen, and X.-C. Zhang, *Phys. Rev. Lett.* **98**, 183901 (2007).
33. E. Hendry, F. J. Garcia-Vidal, L. Martin-Moreno, J. G. Rivas, M. Bonn, A. P. Hibbins, and M. J. Lockyear, *Phys. Rev. Lett.* **100**, 123901 (2008).
34. E. Hendry, M. J. Lockyear, J. Gomez Rivas, L. Kuipers, and M. Bonn, *Phys. Rev. B* **75**, 235305 (2007).
35. A. K. Azad, H.-T. Chen, S. R. Kasarla, A. J. Taylor, Z. Tian, X. Lu, W. Zhang, H. Lu, A. C. Gossard, and J. F. O'Hara, *Appl. Phys. Lett.* **95**, 011105 (2009).
36. Z. Tian, A. K. Azad, X. Lu, J. Gu, J. Han, Q. Xing, A. J. Taylor, J. F. O'Hara, and W. Zhang, *Opt. Express* **18**, 12482 (2010).
37. Z. Tian, R. Singh, J. Han, J. Gu, Q. Xing, J. Wu, and W. Zhang, *Opt. Lett.* **35**, 3586 (2010).
38. B. I. Greene, John F. Federici, D. R. Dykaar, A. F. J. Levi, and L. Pfeiffer, *Opt. Lett.* **16**, 48 (1991).
39. Z. Jian and D. Mittleman, *Appl. Phys. Lett.* **87**, 191113 (2005).
40. A. K. Azad, J. Dai, and W. Zhang, *Opt. Lett.* **31**, 634 (2006).
41. W. J. Padilla, A. J. Taylor, C. Highstrete, M. Lee, and R. D. Averitt, *Phys. Rev. Lett.* **96**, 107401 (2006).
42. R. Singh, E. Smirnova, A. J. Taylor, J. F. O'Hara, and W. Zhang, *Opt. Express* **16**, 6537 (2008).
43. Computer Simulation Technology (CST), Darmstadt, Germany. www.cst.com.
44. A. Hartstein, E. Burstein, J. J. Brion, and R. F. Wallis, *Surface Sci.* **34**, 81 (1973).
45. M. Khazan, *Time-domain terahertz spectroscopy and its application to the study of high-T_c superconductor thin films* (Ph.D. Dissertation, University Hamburg, 2002).
46. R. Singh, A. K. Azad, J. F. O'Hara, A. J. Taylor, and W. Zhang, *Opt. Lett.* **33**, 1506 (2008).

Fiber-coupled terahertz time-domain spectroscopy (THz-TDS) systems

M. THEUER and F. ELLRICH, Fraunhofer-Institute for Physical Measurement Techniques IPM, Germany and D. MOLTER and R. BEIGANG, University of Kaiserslautern, Germany

DOI: 10.1533/9780857096494.2.295

Abstract: In this chapter we review the possibilities and design criteria of fiber-coupled terahertz spectroscopy systems. To obtain broadband terahertz radiation the coherent detection using time-domain spectroscopy offers many advantages. In fiber-coupled systems the transmission of ultrashort broadband laser pulses within fibers has to be controlled in terms of dispersion and nonlinear effects. The distortionless transmission of femtosecond pulses is crucial for a good performance of the entire terahertz system. The system layout and components are discussed, and scientific and industrial applications are presented.

Key words: terahertz, time-domain, broadband spectroscopy, femtosecond pulses, fiber-coupling, measurement heads, angle-dependent measurements.

10.1 Introduction

The frequency band in the electromagnetic spectrum between microwaves and infrared is called terahertz (THz) radiation. Formerly also known as the far infrared (FIR), this range covers frequencies between 100 GHz and 10 THz. These frequencies correspond to wavelengths between 3 mm and 30 μ m in vacuum. A wide field of applications in fundamental science and in industry can be addressed by using THz radiation (Jepsen *et al.*, 2011; Theuer *et al.*, 2011). The need for reliable and flexible THz systems drives the development of fiber-based systems.

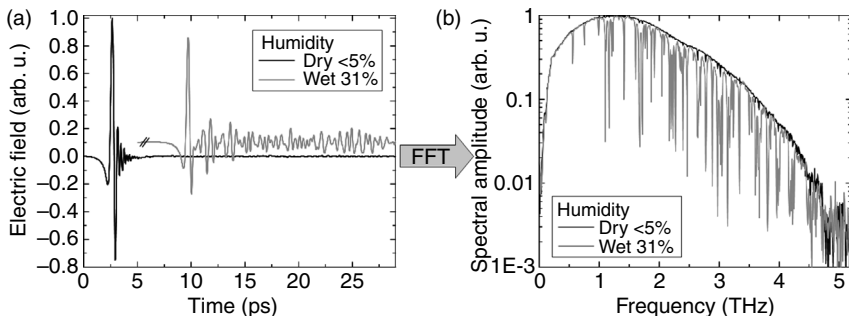
As an electromagnetic wave with a frequency of 1 THz has the cycle duration of 1 ps, it is obvious that the generation and detection of such ultrashort pulses are close to the high-frequency limit of the state-of-the-art electronics (Lin *et al.*, 2011). Using multiplier chains it also became possible to obtain emission above 2 THz, but with an output power strongly reduced compared to the lower fundamental oscillator frequency of 90 GHz (Ward *et al.*, 2004). However, it was proved possible to access these frequencies above

100 GHz with a good signal-to-noise ratio (SNR) by combining laser optics and high-frequency electronics in the new field of electro-optics.

Ultrafast charge carrier dynamics are exploited to obtain emission at THz frequencies. Methods such as carrier separation and recombination on the surface of semiconductors or in biased semiconducting antennas are applied. In this electro-optic approach, the laser pulse excites the charge carrier dynamics and thereby starts the THz emission. Depending on the laser pulse duration, narrowband or broadband THz emission is obtained. Pumped by nanosecond lasers, parametric generators or oscillators (Molter *et al.*, 2009) emit THz waves with a linewidth below 100 MHz (Kawase *et al.*, 2002). On the other hand, broadband emission gated by femtosecond lasers can be obtained by optical rectification in nonlinear media. Especially on the detection side, the availability of femtosecond laser sources improved the system performance significantly. For this reason, in the following an emphasis is given to such femtosecond laser based systems.

The principle applied is the technique of THz time-domain spectroscopy (THz-TDS) (Grischkowsky *et al.*, 1990). This photonic approach is based on the coherent detection of THz pulses by sampling the electric field as a function of delay. To probe a sub-ps transient it is important to have an even shorter gating pulse. The required shorter event is supplied by an ultra-fast femtosecond laser source. This approach is comparable to stroboscopic sampling of a periodic signal. Ti:Sapphire or fiber lasers are typically used to deliver pulses of sub-100 fs duration. These are well suited to sample the THz transient due to their high pulse-to-pulse stability. Experimentally this is achieved by splitting up the laser pulse into two fractions, one to pump the transmitter and one to gate the receiver. By changing the timing between these two, the detection gate is relatively moved over the THz pulse as a function of delay. Typically, the delay is generated using a retro-reflective mirror on top of a linear stage in one of the laser beams and changing the relative distances in space (time-domain). As in a pump-probe experiment, the time-dependent THz pulse is detected. This coherent detection scheme results in a high SNR as well as the possibility to detect the phase of the pulse. Recent systems even use two synchronized lasers with a slightly detuned repetition rate for sampling the THz pulses. This technique is called ‘asynchronous optical sampling’ (ASOPS) (Klatt *et al.*, 2011). Despite the fast data acquisition in this scheme, due to the two lasers and peripheral electronics needed, these systems are not yet ready for industrial portable systems, but are expected to be available in the future.

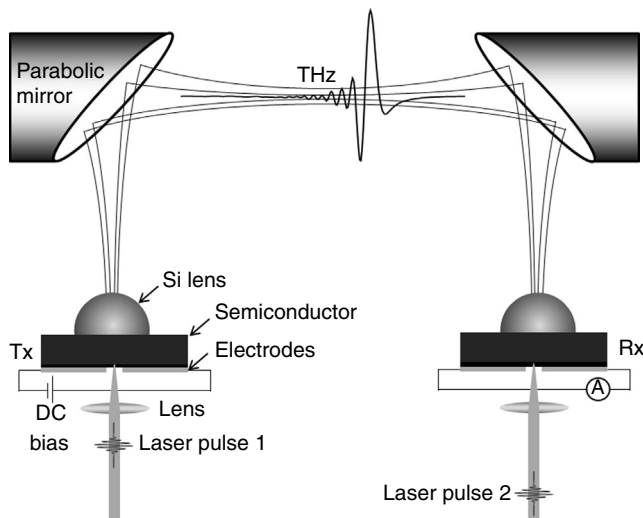
By that means, not only is the intensity measured, but also the electric field of the THz pulse is resolved in the coherent detection scheme, which contains much more information on the sample under investigation. The result of a typical measurement under laboratory conditions can be seen in Fig. 10.1. This shows the reference electric field, acquired under dry air



10.1 (a) Recorded electric field in the time domain and (b) the spectral amplitude in the frequency domain obtained by applying a FFT. The reference is an empty chamber flooded with dry air, while the grey data correspond to an atmosphere of 31% humidity. Fringing after the main pulse can be clearly seen, giving rise to narrow band absorption lines in the frequency domain.

conditions. The transient consists of a single-cycle pulse with a duration of less than 1 ps. If a sample, for example a gas cell with humid air (see grey curve, 31% relative humidity), is inserted in the beam, the pulse is delayed due to the slightly higher refractive index of the sample (even after taking account of the windows of the cell). The pulse peak amplitude is also reduced and fringing echo modulations can be seen after the main peak. Using a fast Fourier transform (FFT) to convert the time-domain raw data into the frequency domain, the THz spectrum is revealed. The smooth reference amplitude extends from 100 GHz to well above 4 THz. If now air moisture is present in the THz beam path, the polar water molecules absorb some discrete narrowband frequencies in their rotational modes. Characteristic minima can be detected, which can be assigned to the particular molecular mode. Knowing the length of the sample, the spectrally resolved absorption coefficient can be calculated. Data on various samples are reported, especially on gases (Cheville and Grischkowsky, 1999; Weiss *et al.*, 2001) as well as crystalline solids (Melinger *et al.*, 2007; Leahy-Hoppa *et al.*, 2009).

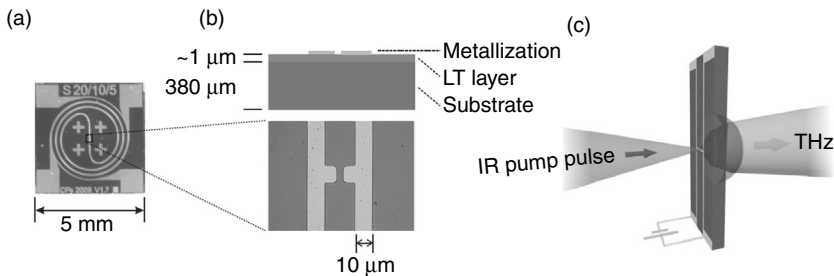
Standard laboratory THz-TDS systems use free-space propagation of pump pulses between bulky mirrors guiding the gating pulses to the transmitter and receiver. They enable easy alignment and do not need dispersion control. This is a reasonable solution for most fundamental THz applications; however, it is very space consuming and lacks THz optical flexibility. The laser source, mirrors, electro-optic components and THz optics are mounted on a work bench. Also in terms of eye safety, precautionary measures have to be taken against the laser light. Even if such systems offer a good performance with a high SNR for an electric field of 80 dB and a bandwidth of up to 5 THz, its experimental layout is mostly limited to geometries



10.2 Experimental layout of a laboratory THz time-domain spectroscopy system (Grischkowsky *et al.*, 1990). The transceiver (Tx) and receiver (Rx) are gated by free-space femtosecond laser pulses. Silicon lenses and off-axis parabolic mirrors are used to guide the THz beam.

working in transmission or reflection under one particular fixed angle. For angular-resolved measurements, which are required for example, for investigating scattering samples, a tremendous realignment effort is necessary, leading to errors which cause results that are not perfectly reproducible. On the other hand, fiber-coupled measurement modules would offer a huge advantage in flexibility. As the laser pulses are guided in glass fibers, the system is inherently eye-safe. Less free-space propagation also increases the system's mechanical and thermal stability.

In the optical approach to the THz spectral range, the key question is how to transfer radiation from the visible or infrared (IR) into THz frequencies (FIR) with a high conversion efficiency. For pulsed broadband spectroscopy, various types of emitter can be used. Among them, the most prominent ones are based either on nonlinear optics (optical rectification, difference frequency generation (Lhuillier *et al.*, 2007a, 2007b)) or photoconductive effects (Zhang and Auston, 1992). Depending on the available laser (output center wavelength, peak and average power) and application, the appropriate combination of transmitter (Tx) and receiver (Rx) is chosen. Given the fact that industrial THz systems need to be eye-safe and reasonably priced, only a combination of low average power fiber lasers with subsequent fiber-guided pump beam delivery is possible. This limits the potential transmitter and receiver components to photoconductive antennae (Grischkowsky *et al.*, 1990). A typical system using photoconductive antennae is shown in Fig. 10.2.



10.3 Photoconductive antenna (PCA, or Auston switch), consisting of a semiconductor substrate with short carrier lifetime and a resonant metallized structure on top. (a) PCA with contact pads at the edges and circular wended feed wires. (b) Zoom to the center of the H-shaped dipole and the profile of the device. (c) Optical geometry used with excitation laser pulse and silicon lens to couple the generated THz radiation out of the semiconductor.

These photoconductive antennas (PCAs), also named Auston switches (Auston *et al.*, 1984), already start to operate efficiently at a few milliwatts of average laser power. Their efficiency is based on the semiconductor and resonant structure used. In the simplest geometry, the PCA consists of an H-shaped metallization on top of a semi-insulating substrate (typically gallium arsenide, GaAs). A sketch of a PCA can be seen in Fig. 10.3. The shining metallization has contact pads at the chip edges with a spiral-shaped parallel feed line to the center gap. This layout offers echo-free performance for an entire footprint of the PCA restricted to $5 \times 5 \text{ mm}^2$ (Fig. 10.3a). A microscope image of the center shows the gap between the two lines, the so-called H-shaped dipole (Fig. 10.3b). If a laser pulse illuminates the gap, free charge carriers are injected and the antenna becomes conductive. Together with an electric bias on the feed wires, a THz wave is generated and coupled out into free space by a silicon lens (Fig. 10.3c). The identical antenna serves as receiver Rx, if the bias is replaced by a sensitive ammeter or transimpedance amplifier. So the tiny current of nano-amperes can be detected which is proportional to the THz electric field.

As the semiconductor has a high dark resistivity, there is nearly no current in the unilluminated cycle. To obtain a short switching time, the carrier lifetime of the semiconductor also has to be as short as possible. Thus the top layer of the semiconductor is made of low-temperature grown GaAs (LT-GaAs). This roughly $1 \mu\text{m}$ thick layer has a carrier lifetime below 1 ps, which again is necessary for the effective gate width of the detection scheme. The semiconducting substrate of GaAs used has a bandgap of 1.43 eV, corresponding to a wavelength of 870 nm. So available solid-state Ti:Sapphire and frequency-doubled fiber lasers around 800 nm wavelength can be applied.

The particular shape of the metallization defines the output characteristics in terms of THz polarization, spectral distribution and power. For example, finger-type emitters are designed as arrays of strip lines to enhance the output, at the cost of more required pump power (Dreyhaupt *et al.*, 2005) or circular antennas are used if a circularly polarized mode is needed (Deibel *et al.*, 2005).

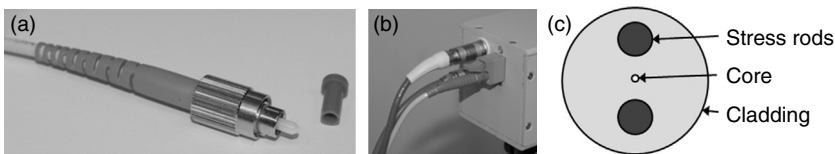
The aim to obtain as short carrier lifetimes as possible, along with the application of ultrashort laser pump pulses, is related to the maximum achievable bandwidth. For example, by using 10 fs long pump pulses, frequency components up to 50 THz were detected (Huber *et al.*, 2000) using an instantaneously responding THz detector based on electro-optical sampling (Wu and Zhang, 1995). The gating laser pulses can be regarded as averaging windows for the electric field. If a 10 fs long laser pulse (= 3 μm length in free space, ‘envelope frequency’ of 100 THz) is used for sampling, the corresponding Nyquist-frequency is exactly 50 THz.

The signal quality of this coherent detection scheme is already sufficient as the high repetition rate laser (typically 100 fs long pulses at a repetition rate of 100 MHz), and so the detector has a duty cycle of 10^5 . This is why no environmental electromagnetic noise is integrated during the off-time of the PCA, even close to strong thermal THz emitters like hot flames (Cheville and Grischkowsky, 1995). Additionally, the lock-in technique can also be applied to reduce the noise level even further.

10.2 Fiber guiding

Since the discovery of the first low-loss optical fiber by Keck *et al.* at Corning in 1973 (Keck *et al.*, 1973), glass fiber started to influence our everyday life. Inventions extending from simple light delivery (endoscope), to long-distance data transmission leading to transatlantic phone calls or recent fiber-to-the-home technology, would not have been possible without this technology. In this work, we use glass fibers as waveguides for the transmission of ultrashort laser pulses to the PCA.

Unlike long-distance continuous-wave (cw) light power transmission, where the total loss during transmission is the limiting factor, for femtosecond applications it is rather the pulse disturbing effects and their influence on the shape, duration and spectral distribution of frequencies within the pulse that have to be considered. Assuming a Fourier-limited Gaussian pump pulse with a pulse duration of 100 fs at a center wavelength of 800 nm, a spectral bandwidth of 9.4 nm corresponding to a spectral bandwidth of 4.4 THz is needed according to the time-bandwidth product. So spectrally broadband pulses have to be transmitted in the fiber, which leads to chromatic and nonlinear effects.



10.4 Fiber patch cord used to guide the laser pulses to the measurement head. (a) Standard polarization-maintaining single-mode fiber. (b) Eye-safe E2000 connector on the rear panel of the measurement head. (c) Cross section of a polarization-maintaining fiber using stress rods, a so-called PANDA structure.

Optical fibers in general are waveguides for electromagnetic radiation, mostly visible or infrared light (Agrawal, 1997). Once coupled into the fiber, the propagating mode is guided by total internal reflection in the core, which is covered by a cladding with smaller index of refraction. The propagation loss can be ignored for all applications described here as the propagation distance of a couple of meters does not contribute to considerable intensity reduction. The loss for a typical polarization-maintaining single-mode fiber is 40% per kilometer (< 4 dB/km at 850 nm). In contrast, the coupling into the optical fiber is a lossy process, as the pump intensity distribution and the fiber mode do not perfectly match. Also Fresnel surface losses, and scattering particles at the interface, reduce the coupling ratio. Typical values for the coupling ratio from free space to a single-mode fiber are 50–75% of intensity. So it is advantageous to minimize the number of coupling transitions. Additionally, the fiber has a plastic coating to make it mechanically resistant to external forces and chemicals while retaining mechanical flexibility. Fiber connections can be easily made by using fiber connectors that are screwed together (see Fig. 10.4a). Also self-locking integrated shutters are available, to make the fiber guiding completely eye-safe, even if the fiber becomes unplugged (E2000 connector, see Fig. 10.4b).

In the following, the transmission of pulses through the fiber will be described. An optimization with respect to the shortest possible output pulses is presented, aiming for a distortionless and dispersion-free transmission. The particular fiber used is a polarization-maintaining (pm) single-mode (sm) fiber. This already eliminates two major contributions to the dispersion within the fiber, that is, polarization mode dispersion, and modal dispersion. Polarization mode dispersion is caused by deviation from the perfect circular shape, or by asymmetry of the fiber core. This makes the fiber birefringent, so different polarization states experience different effective refractive indices. Also external stress, which is impressed if the fiber is moved or bent, results in an induced birefringence. In sum, two orthogonal polarization states will propagate at different velocities, resulting in

a double-pulse output at the fiber end. For TDS-systems this is unacceptable, as the THz bandwidth would be reduced by the pump pulse extension, or disturbing echoes would be observed in the THz signal. Technologically, polarization preservation is achieved by building in two stress rods next to the fiber core (see Fig. 10.4c). This breaks the symmetry. If now only one linear principal polarization is coupled into the fiber, the linear polarization will be maintained (comparable to an extended wave plate).

The property of the fiber to guide the used wavelength in only one single transversal mode is also important in keeping the pulse duration short. In multi-mode fibers various transverse modes are excited. Due to the different mode field distribution, more or less intensity is propagated in the refractive index shifted cladding. So each mode has its own integrated average effective refractive index. Thus again at the output, a pulse train of different modes would be observed. This is avoided by reducing the core diameter and thereby shifting the cutoff frequency to remove the higher order modes until only the fundamental HE_{11} mode remains. By choosing the correct polarization-maintaining single-mode fiber for the particular pump wavelength range, these two intermodal effects of waveguide dispersion are negligible. Among all remaining intramodal dispersion mechanisms, chromatic dispersion has the strongest negative influence on pulse shape and thus has to be compensated for.

Chromatic dispersion describes the fact that different frequencies within the fiber propagate at different group velocities. While the group velocity v_g describes the propagation of the pulse envelope, the spectral distribution under the envelope and the temporal broadening mechanism has to be considered. This is the group velocity dispersion (GVD), which for the fiber is caused by waveguide and material dispersion (fused silica). The dispersion parameter quantifies the GVD

$$D = \frac{d}{d\lambda} \left(\frac{1}{v_g} \right) = -\frac{2\pi c}{\lambda^2} \beta_2 \quad [10.1]$$

The specific value of β_2 of the used fiber is 117614.1 fs²/m, mostly caused by material dispersion. Transmitting laser pulses with a pulse duration of T_0 over a glass fiber link, the GVD broadens the pulse to a duration of $\sqrt{2} T_0$ for the dispersion length of

$$L_D = \frac{T_0^2}{|\beta_2|} \quad [10.2]$$

For the system presented here, the dispersion length L_D is 8.5 cm. So for fiber-coupled THz measurement heads, which require some meters of fiber

for an adequate positioning of the modules close to the object to be measured, the dispersion has to be compensated for. As β_2 is positive, as for most regular natural materials, the dispersion is called normal. So to compensate for $\beta_2 > 0$, abnormal dispersion ($\beta_2 < 0$) is needed. This is typically achieved by angular dispersion.

Besides the linear effects of material dispersion, nonlinear effects also occur in the fiber as a high peak power P_0 is guided within a tiny area (mode field diameter of 5 μm). The length, after which the pulse has temporally broadened by a factor of $\sqrt{2}$, is called nonlinear length

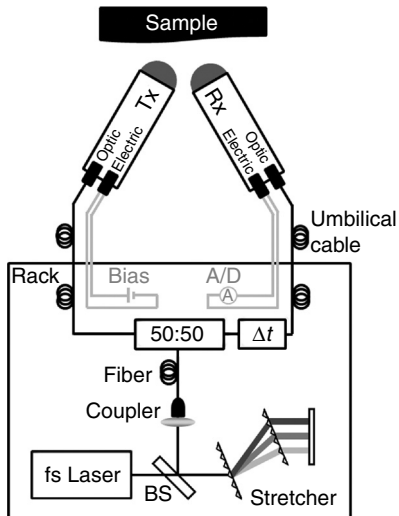
$$L_{\text{NL}} = \frac{1}{\gamma P_0} = \frac{f_{\text{rep}} T_0}{\gamma \bar{P}} \quad [10.3]$$

For the used fiber, the value of the parameter γ is $2.623 \times 10^{-3} (\text{m W})^{-1}$. Transmitting typical gating pulses delivered by a high repetition rate laser oscillator (100 fs at 100 MHz), the peak power P_0 for 5 mW of average optical power \bar{P} used is 0.5 kW, resulting in a nonlinear length L_{NL} of 76 cm. Again, the value of the nonlinear length is in the range of needed fiber length of the THz system. Looking at the ratio L_D/L_{NL} one can see whether the dispersion or the nonlinearity is the dominating broadening mechanism. In the case of fiber-coupled femtosecond THz systems, the dispersion is much more critical than the nonlinear effects while the nonlinear effects have to be considered when coming to long fiber lengths or higher peak powers (Lee *et al.*, 2007).

10.3 Experimental layout and system characterization

The design of the entire THz spectroscopy system has to offer the positioning flexibility of fiber-coupled measurement heads (Tx, Rx) at a high stability. The general layout of the fiber-coupled system can be seen in Fig. 10.5. It consists of a 19" rack containing all the optics and electronics. Only an umbilical cable feeds the Tx and Rx heads. Of course, the THz signal has to be broadband with the shortest possible pulses. This requires a mechanically rigid housing and electronically independent and shielded electronics. The corresponding certificates and eye safety (laser class 1) are mandatory. Finally, the price of the system, which is mostly related to the incorporated femtosecond laser source, should be reasonable. Keeping these main decision criteria in mind, the system layout will be discussed in the following section (Agrawal, 1997; Ellrich *et al.*, 2008, 2011).

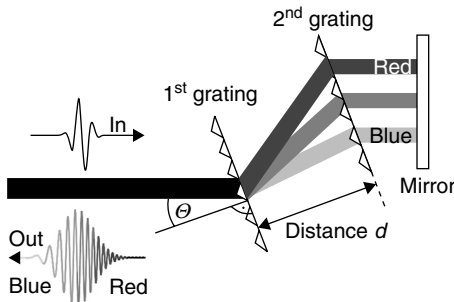
Among the solid-state lasers, either Ti:Sapphire or frequency-doubled fiber lasers are in principle suited for this purpose. The latter have the advantage that they are compact, do not require water cooling, and are cheaper than



10.5 Experimental layout of fiber-coupled THz-TDS system. Only an umbilical cable leaves the 19" rack to the transmitter and receiver.

Ti:Sapphire lasers. The obtainable output power of a frequency-doubled fiber laser is approximately 100 mW at an operating wavelength of 780 nm. In principle fiber lasers, emitting at their fundamental wavelength of 1550 nm, would also be applicable. Unfortunately, the best-performing photoconductive semiconductor (GaAs) has a band gap of 870 nm, which is too large to be excited by that wavelength. Therefore, external frequency-doubling units have to be integrated, reducing the average output power due to their limited conversion efficiency in the nonlinear second harmonic generation process. But the investigation of new semiconductor materials is an ongoing process, with first results already indicating the application of telecom standard components at 1550 nm (Sartorius *et al.*, 2008).

Working with a center wavelength of 780 nm and a spectral bandwidth of 10 nm, close to the Fourier-limit, the particular polarization-maintaining single-mode fiber can be chosen. But still, the chromatic dispersion broadens the 100 fs long input pulse to 1 ps within the first meters of fiber. So the linear GVD related to β_2 , the apparent difference in propagation time for different wavelengths, has to be compensated by angular dispersion. The spectral spread can be achieved by prisms or gratings. Typically, the optical sequence of components of the so-called compressor is as follows: the first spectrally-selective component splits the colors, while a second makes the rays parallel again. To obtain a collimated beam with a small diameter again, the identical two devices are used in the opposite direction. Due to the symmetrical geometry, a mirror can also be placed in the symmetry plane, to use the first set of components twice and reduce cost and dimensions. Also the

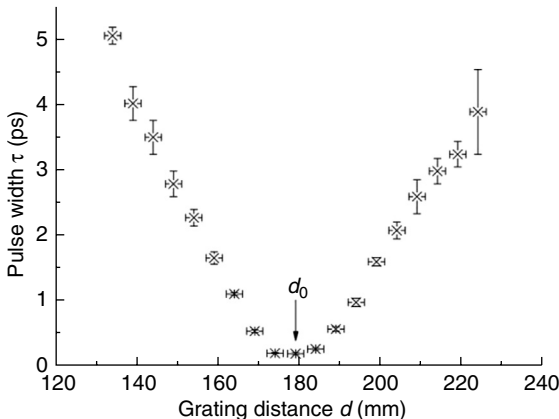


10.6 Stretcher based on angular dispersion. Two transmission gratings in a double-pass geometry cause a negative dispersion depending on the grating distance d .

adjustment is easier as a change in dispersion or distance d only requires a movement of the second grating and the mirror.

As can be seen in Fig. 10.6, the geometry chosen here is based on gratings. Compared to prisms, gratings show a much larger angular dispersion, so the grating compressor has smaller dimensions. Also, by using transmission gratings, the overall transmission loss can be reduced considerably, due to their higher efficiency of 72% ($= 0.92^4$) compared to 24% ($= 0.70^4$) for the entire stretcher. In principle it makes no difference to the linear dispersion whether the positive GVD of the fiber or the negative GVD of the grating compressor are prior in the optical sequence. But for practical application, it is advantageous to use the grating compressor first (then rather named stretcher) as then the losses occur first. The pulse is pre-chirped negatively, until it is finally recompressed at the end of the fiber. At each diffraction a fraction of the laser power is lost (higher order diffraction, optical properties, imperfections, beam quality) so the grating stretcher is a rather lossy optical device. To reduce nonlinear effects during propagation, the optical power in the fiber should be minimized, which is achieved by this design scheme.

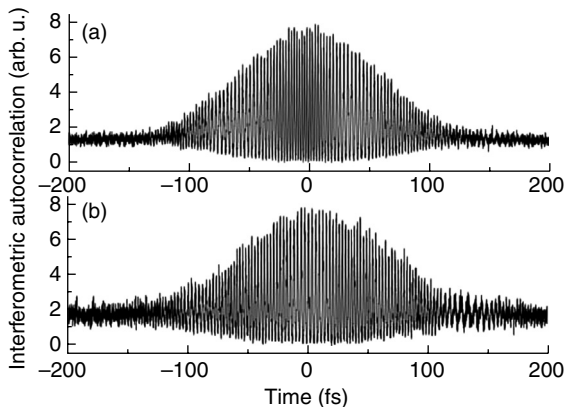
By changing the distance d between the gratings in the diverging part of the stretcher (see Fig. 10.6), the GVD can be controlled linearly. Hence the compressor can be adjusted to perfectly match the fiber GVD but having the opposite sign of dispersion. So only for one particular distance d_0 the effective GVD is nearly zero. This working point is determined by measuring the laser pulse duration behind the combination of grating pair and fiber link as a function of the grating distance d . A typical measurement is shown in Fig. 10.7 for a fiber length of 15 m and 6 mW of optical power. Already for a deviation of some millimeters, the output pulse undergoes a tremendous pulse broadening. At shorter and longer distances, it will be under- or over-compensated, respectively, resulting in a chirped extended output pulse.



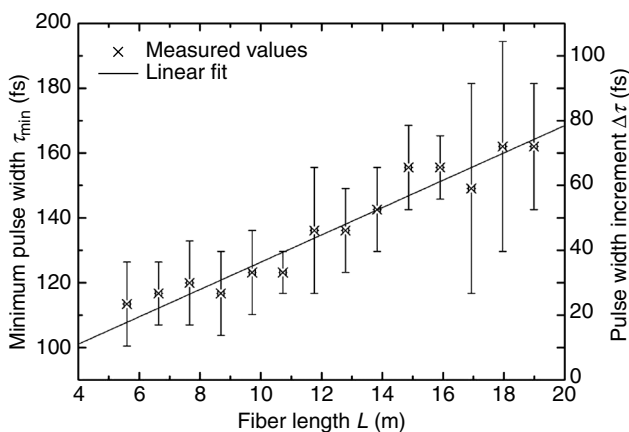
10.7 Laser pulse width after propagation through the fiber stretcher and 15 m of fiber. The average optical power was 6 mW. The grating distance d is adjusted to d_0 to obtain the minimum output pulse width. For other grating distances the dispersion is under- or over-compensated, leading to pulse extension. (Reprinted with permission from Ellrich *et al.*, 2011. © 2011 American Institute of Physics.)

To characterize the quality of a pulse transmission, the optical output power and the pulse duration have to be monitored. As a measurement tool, interferometric autocorrelations are used to determine the pulse duration (with some pulse-shape dependent assumptions). This scheme is based on overlapping two replicas of the laser pulse within a nonlinear crystal in space and time. By changing the delay between these two, the laser pulse gates itself, and some pulse parameters can be retrieved. To demonstrate the nearly distortionless transmission of sub-100 fs pulses, interferometric autocorrelations are presented in Fig. 10.8. The upper trace is the interferometric autocorrelation of the laser pulse as it leaves the laser resonator. As the autocorrelation is a symmetric convolution of the pulse with itself, the full-width-at-half maximum (FWHM) is corrected via a pulse-shape dependent factor. This results in a pulse duration of 93 fs. After passing through the adjusted grating stretcher and 2 m fiber compression, the interferometric autocorrelation does not indicate any remarkable change of the pulse shape nor pulse duration (95 fs). It appears to be noisier than the original one, but this is rather related to the lower available optical power at that point.

As the GVD is only a linear approximation of the dispersion, higher order dispersion also starts to play a role if the fiber link becomes significantly longer. Starting with the third order dispersion TOD (β_3) the sign of the quartz-glass fiber dispersion and the grating-compressor dispersion are identical ($\beta_3 > 0$). This means that only a large fraction of the dispersion, that is, the linear GVD, can be compensated while the fraction of the TOD remains distorting the pulse. This limits the possibility to extend the fiber

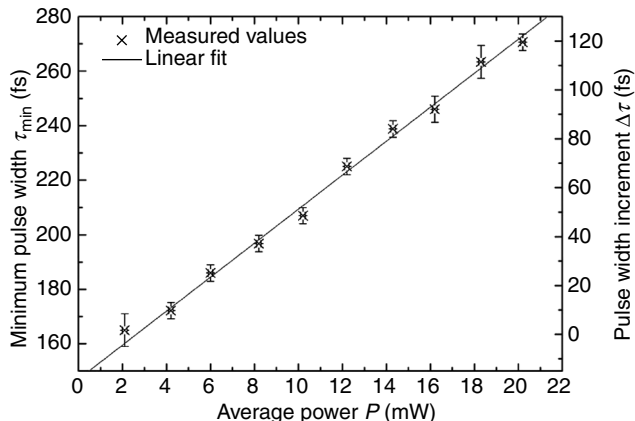


10.8 Interferometric autocorrelation of the laser pulses as they exit the laser and at the end of the fiber. (a) Before stretcher and (b) after stretcher and 2 m of fiber. The pulse transmission is nearly distortionless. (Reprinted with permission from Ellrich *et al.*, 2011. © 2011 American Institute of Physics.)



10.9 Dependency of the minimally obtainable laser pulse duration after propagation through fibers of different lengths. The longer the fiber is, the larger is the remaining uncompensated higher order dispersion, leading to pump pulse extension. (Reprinted with permission from Ellrich *et al.*, 2011. © 2011 American Institute of Physics.)

link to much longer lengths. The minimum output pulse width for different fiber lengths is shown in Fig. 10.9. At each position the grating stretcher was readjusted to a new distance d_0 to obtain the shortest possible pulse. But due to the TOD, the minimum pulse width has a linearly inclining slope as a function of fiber length. If fiber links that long are needed, other dispersion correcting elements (e.g., different types of fiber, additional prisms, chirped mirrors, etc.) will have to be used.



10.10 Average power dependent pulse length after propagation through the compensated fiber link. The high peak power leads to nonlinearities which increase the pulse duration. (Reprinted with permission from Ellrich *et al.*, 2011. © 2011 American Institute of Physics.)

10.3.1 Nonlinear effects

The strongest effect contributing to the nonlinear fiber length L_{NL} is self-phase-modulation (SPM). It is caused by the intensity-dependent refractive index of the fiber material, which leads to an intensity-dependent phase term for the pulse evolution. In the time-domain, this corresponds to a generation of red spectral components at the leading edge of the pulse and blue components at the tail. This results in a linear up-chirp in the center of the pulse which needs to be compensated. To some extent this can be compensated by readjusting the grating distance d of the stretcher, but some residual pulse broadening remains, as can be seen in Fig. 10.10 where the effect of pump power dependent pulse broadening is shown as an example for a fiber of 15 m length.

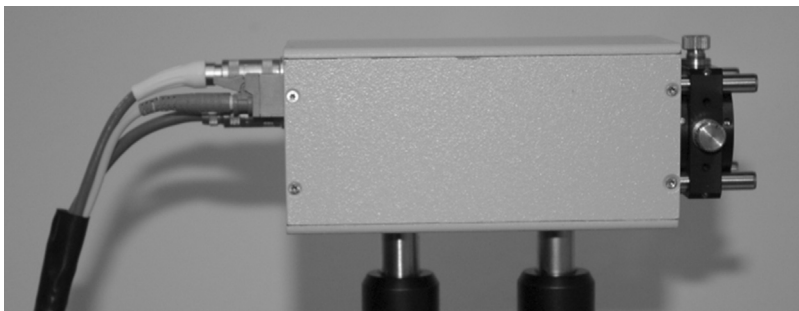
Generally speaking, chromatic dispersion and nonlinear effects temporally broaden the pump pulses. So the THz bandwidth is reduced correspondingly, as the gate width of the sampling process is widened (Crooker, 2002). This limits the optical parameters of the fiber link and so affects the possibilities of intended spectroscopic applications (SNR, bandwidth, maximum frequency, steepness of pulse slope). Therefore the general intention is to work with the shortest reasonable fiber lengths, as well as to keep the required laser power as low as possible.

10.3.2 Components, heads and system

The measurement heads (transmitter Tx, receiver Rx) are the key components of the system. They are connected via an umbilical cable to the 19" supply rack. The mechanically stable housing contains the PCA for the generation and detection of THz pulses. One of the problems to be solved is the laser pulse propagation at the final connection between the end of the fiber and the PCA. Its gap to be illuminated is only 5 µm wide, so a tiny focus is needed. One approach is to collimate the divergent beam leaving the fiber, and refocus it down as in standard free-space geometry. But this layout is subject to strong thermal drifts, as the needed positioning accuracy of the laser spot on the PCA is very high. Another method relies on the fact that the fiber's mode field diameter of 5 µm has the same dimensions as the gap of the PCA. So if one could optically and mechanically attach the fiber to the correct position, no free-space coupling would be necessary. This is a technologically demanding process, but has big advantages, such as higher opto-mechanical stability, less space consumption and fewer optical transitions. For the system presented here, these fiber-to-chip connections are fabricated via an automated online alignment procedure which keeps track of the signal during the drying process. A special type of glue guarantees long-term mechanical and optical stability.

Figure 10.11 shows a photograph of a Rx module, while the Tx has the identical layout. The main sections are the patch panel on the rear, the opto-mechanical unit in the center, and the optional THz optics in the front. The size is roughly 6 cm × 6 cm × 14 cm. The Tx module consists of a 60 µm dipole PCA to obtain a large THz output amplitude. In the Rx head, a 20 µm dipole is used to obtain a broadband signal. Depending on the application, aiming for large bandwidth or high pulse peak amplitude, other combinations are possible, too. Further on, the transimpedance amplifier, which converts the measured current to a recordable voltage, is integrated in the Rx head, too. So high signal levels are generated before leaving the Rx head, reducing environmental influences as no significant noise is superimposed on the amplified signal during electric transmission on the metal wire.

The power supply and drivers are mounted within a 19" rack. The rack contains an optic module and an electronic module including an uninterruptible power supply. The patch panel can be seen in the front along, with the umbilical cable to the two heads (see Fig. 10.12). Not shown here is the laptop PC, which is used to operate the system. The software monitors all system parameters and controls the measurement process. A Labview™ program is used to synchronously read out the delay position and the detected voltage at each data point. Material parameters such as absorption



10.11 Photograph of one of the measurement heads.

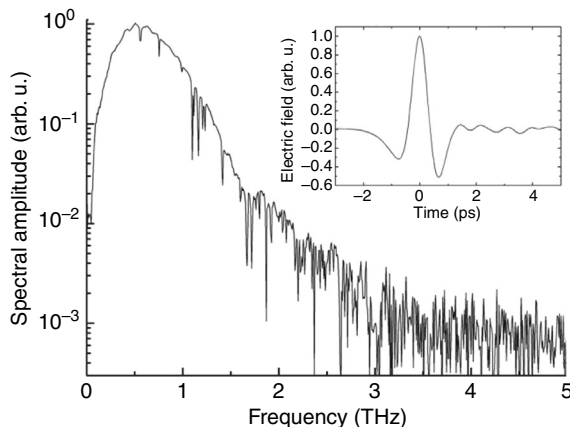


10.12 A 19" rack containing all electronics and optics with attached fiber-coupled measurement heads on top. Only a 110/220 V wall plug is needed to operate the system.

coefficient, refractive index and thickness can be easily calculated and displayed.

10.3.3 System characterization

Depending on the laser pulse duration, semiconductor quality and THz optical alignment, the optimum system reference may differ. While the laboratory-based system and laser pulse durations below 80 fs at the PCA allowed



10.13 Recorded reference pulse measured in transmission (inset). The lock-in integration time was 30 ms at a relative humidity of ~35%. The spectrum of the pulse shows a dynamic range of more than 60 dB at around 0.5 THz. The overall bandwidth is about 3 THz. (Reprinted with permission from Ellrich *et al.*, 2011. © 2011 American Institute of Physics.)

for spectroscopic investigations up to 4.5 THz (see Fig. 10.1), the maximum frequency drops for longer pump pulses and so depends on the accumulated pulse distortion in the fiber link. The reference for a fiber-coupled system in transmission geometry is shown in Fig. 10.13. No dry air purging was used, so water vapor absorptions reduce the amplitude at discrete frequencies. These lines can be resolved in the frequency interval between 100 GHz and 3 THz. At the maximum spectral amplitude of 500 GHz the system has a dynamic range of more than 60 dB. This data was recorded with a lock-in amplifier at an integration time of 30 ms. If no lock-in technique is used and a direct AD-signal is measured (also resulting in an increased scanning speed) the SNR drops. This is often used for imaging applications and makes the alignment procedure easier. A built-in rapid scanning delay line (shaker) operates in parallel in the system, so the acquisition of 100 ps long traces at a frequency of 40 Hz is possible. Talking about imaging, this corresponds to a data acquisition time of 25 ms per pixel. Further approaches to improve the scanning speed will be introduced later.

The THz spotsize is determined by the beam pattern of the emitter, the optics (lenses vs. mirrors) and geometry (transmission and reflection). Typical spotsizes for a lens-focused THz beam are below 5 mm, which can be improved by using off-axis parabolic mirrors as in the laboratory-based systems. Another point which is of particular interest, especially for rough and curved surfaces, is the collection angle of the detector. Having 1 inch standard optics, the tolerance of alignment is approximately $\pm 5^\circ$, which can be increased by using larger optics.

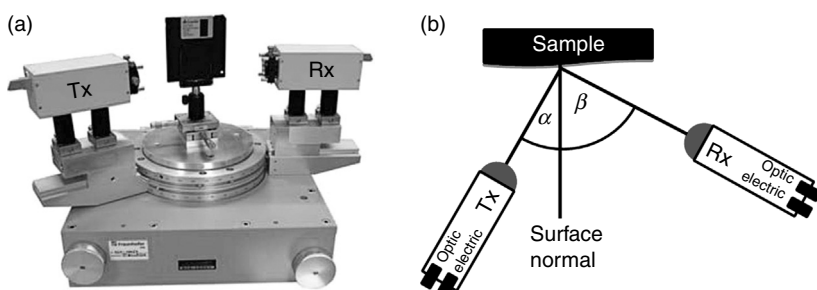
10.4 Measurement results of fiber-based terahertz systems

In this section, typical results obtained with fiber-coupled THz systems will be presented that demonstrate particular advantages of such fiber-coupled THz spectrometer. First of all, the independent positioning of emitter and detector are utilized for angle dependent investigations of scattering and reflection processes. In the second example, the fiber coupling is combined with a fast delay line in order to perform measurements with a high-data acquisition rate. The fiber coupling is required to do measurements in a strong magnetic field at cryogenic temperatures. In the last example, the fiber coupling is combined with an attenuated total reflection (ATR) measurement head for spectroscopic investigations of liquids via total internal reflection.

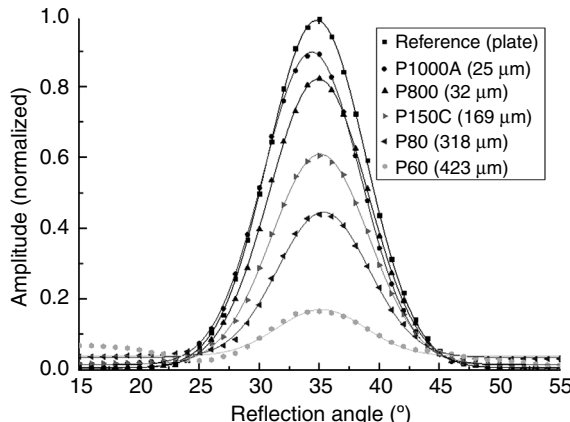
10.4.1 Angle dependent measurements

One of the biggest advantages of fiber-based THz systems is the possibility to carry out angular-resolved measurements. In that case, no realignment of the laser optical path is necessary, unlike the standard free-space THz systems (Zhan *et al.*, 2010). Keeping, for example, the THz emitter at a constant position, by rotating the sample and/or the detector, the spectral amplitude (transmission, reflection, absorption, etc.) of the sample under a particular angle can be measured (Robine *et al.*, 2010). With the help of a goniometer (see Fig. 10.14), also the alignment of the THz part can be reproduced in an easy and standardized way.

In Fig. 10.15, scattering objects were measured using the goniometer setup in Fig. 10.14. The incident THz beam direction holds an angle α of 35° with respect to the surface normal. Hence the maximum of the specular reflection is expected also around $\beta = 35^\circ$. The reflected peak amplitude is plotted as a function of the reflection angle (symbols) along with theory curves (lines). The particular samples were pieces of sand paper whose surfaces were metallized to increase the overall reflectivity while keeping the surface



10.14 (a) Photograph of goniometer with Tx/Rx modules for angular-resolved measurements. (b) Schematic (top view).



10.15 Angular-resolved reflection measurement of metallized sandpaper. The finer the grid, the larger is the reflected amplitude. The bell-shaped curve has a width of approximately 10° for all samples.

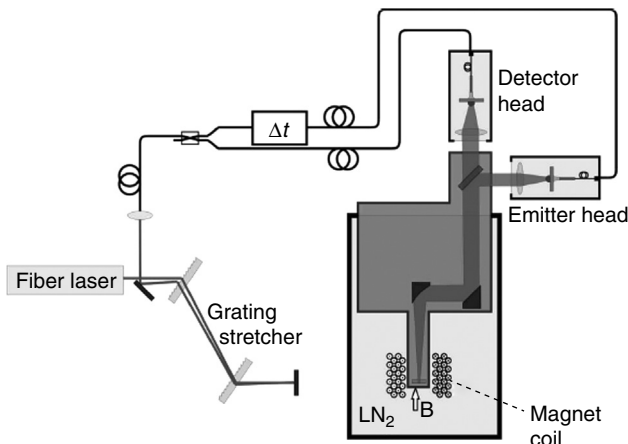
roughness at a defined level. Grid P1000A is the finest one (particle size $25\text{ }\mu\text{m}$), while the P60 corresponds to a rough surface with $423\text{ }\mu\text{m}$ particles. As reference, a flat and polished aluminum plate was taken.

The FWHM of the bell-shaped curves is roughly 10° for the reference as well as for the sand paper. Regarding the measured amplitudes, it becomes obvious that the rougher the surface gets (smaller numbers of sand paper), the less amplitude is reflected due to interference at the surface. The fine sandpaper (P1000a) still has 80% of the reflected amplitude compared to the reference, while the rough one (P60) only shows a reflectivity of 20%. The surface roughness can be regarded as small steps which change the delay (phase) and so the superposition of the laterally averaged signal. As the particle size is in the order of magnitude of the THz wavelength, this effect is obvious.

Interestingly, the measured FWHM is not changed by the surface roughness. This means that the scattering into larger or smaller angles (diffuse reflection) is much weaker than the direct reflection (specular reflection). In fact, what this setup rather detects is the collection angle of the used THz imaging optics. Also, spectroscopic applications are possible, keeping in mind that the directly reflected beam still hits the detection optics. Working with the diffuse reflection is tricky, as the THz power levels are much lower than for the specular geometry.

10.4.2 High-speed measurement of cyclotron resonance in pulsed magnetic field

Due to the flexible positioning of the Tx and Rx modules, measurements under various angles, from normal transmission via grazing incidence to

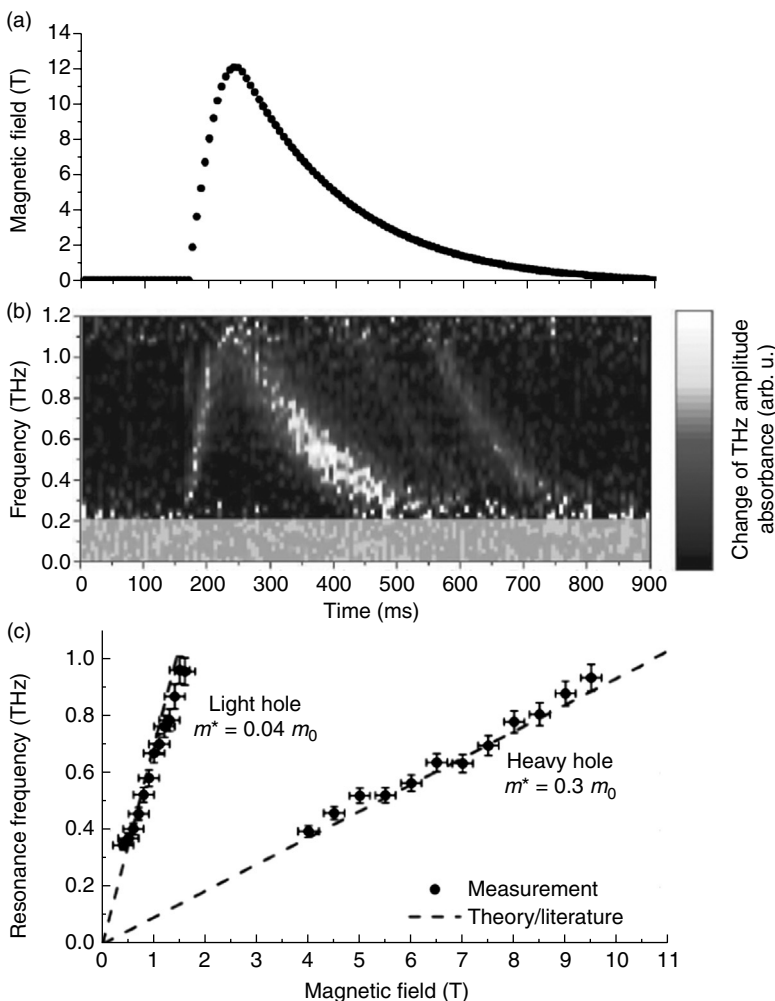


10.16 Experimental layout of fiber-based THz-TDS system with new fast delay line (Δt). The chosen THz geometry is operating in perpendicular reflection to investigate the time-resolved response of semiconducting samples on a magnetic pulse. (Reprinted with permission from Molter *et al.*, 2010. © 2010 Optical Society of America.)

(nearly) normal reflection, can be measured. But the perfectly perpendicular reflection can only be measured using additional THz optics as the modules cannot be aligned that close for geometrical reasons. Also the integrated version of Tx/Rx combinations called transceivers are reported (Jördens *et al.*, 2008), but the typical way is to use a high resistivity silicon wafer ($n_{\text{Si}} = 3.41$) as beam splitter and combiner. Figure 10.16 shows the system layout with the detector and emitter head mounted at an angle of 90°. In between, perfectly aligned to 45°, is the 10 mm thick silicon wafer. Additional parabolic mirrors focus the THz beam down to the sample, dependent on the application.

The setup presented here has the additional capability of scanning at higher speeds. Therefore, a rotational delay line is implemented, based on helicoid reflecting surfaces. The rotational movement is much faster than the one offered by commercially available linear stages or shakers. No mass has to be accelerated between individual scans, and so high rotational speed is obtained, corresponding to a repetition rate of 250 Hz (Molter *et al.*, 2010). To handle the large amount of rapidly changing analog data, the lock-in amplifier is replaced by a fast A/D-card and a personal computer.

This rapid THz pulse sampling is important for example, for imaging applications to increase the amount of data points and thereby to improve the resolution or reduce the measurement time. Additionally, it allows for detecting time-resolved physical processes without the need to sample a triggered periodic signal. The measurement task described here is the detection



10.17 (a) Time-dependent magnetic field applied to the p-Ge sample. (b) Measured THz spectral absorbance for different times. (c) Calculated resonance frequencies as a function of the magnetic field (evaluation of panels a and b). (Reprinted with permission from Molter *et al.*, 2010. © 2010 Optical Society of America.)

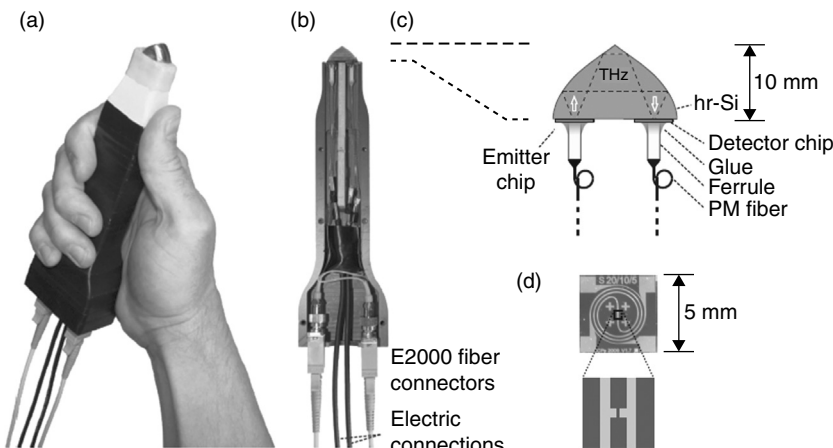
of THz absorption by light and heavy holes in a p-doped Germanium (p-Ge) crystal as a function of applied magnetic field (Molter *et al.*, 2010). The pulse is a 300 ms long burst of magnetic field, with a slope, given by switching time and exponential decay (see Fig. 10.17a). To detect the THz response of the sample on the magnetic field, as many THz traces as possible need to be recorded within this short period.

Using the fast delay line it is possible to detect a THz transient every 6.6 ms. So in the interesting time frame of the magnetic burst, enough data can be recorded within one single pulse. The measured THz absorption for the evolving magnetic field is plotted in Fig. 10.17b. If now the absorption frequencies for different magnetic field strengths are extracted, one can clearly identify the features caused by light and heavy holes, respectively (Fig. 10.17c) (Molter *et al.*, 2010). For this type of measurement, the advantages of the high flexibility of alignment, the portability of the system, and the fast data acquisition are the decision criteria for the system of choice. This allows for further experiments on semiconductor characterization providing insight in charge carrier dynamics and magneto-optics.

10.4.3 Fiber-coupled monolithic attenuated total reflection (ATR) sensor

Another interesting possibility is offered by the modularity of the fiber-based system. As the optic and electronic part of the system (19" rack) is independent of the Tx/Rx modules, the same supply system can be used for different measurement tasks. The only requirement is the pulse re-compression in the fiber. This defines the length of the fiber link to be attached between rack and module. Otherwise the grating stretcher has to be readjusted. So using the correct fiber length along with the same rack, a very compact sensor for attenuated total reflection (ATR) spectroscopy is reported (Molter, 2011). ATR is a means to explore the evanescent field decaying exponentially in space at a facet of total internal reflection. This technique allows one for example, to investigate high-loss samples, such as water or other polar liquids (Cheng *et al.*, 2008). The absorption length is given by the evanescent field extent, and thus does not change if too much sample is applied on top of the sensor.

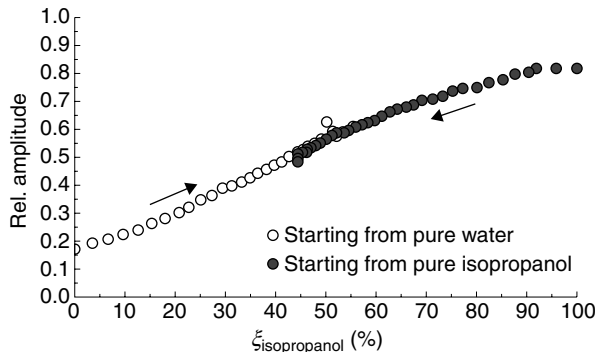
Combining the fiber-coupled photoconductive transmitter and receiver chip with the high-refractive index silicon optical element, a monolithically integrated sensor is created (see Fig. 10.18a). The shape of the silicon piece is designed and fabricated to imitate the 4f geometry of typical free-space THz systems. The bulk silicon piece is directly free-form machined into the off-axis parabolic geometry needed for an optimal collectivity. The totally internally reflecting surface forms the sensitive area of the sensor. The PCAs are glued to the silicon piece without any remaining adjustable parts. No further alignment is needed. If now a sample is in direct contact with the curved silicon surface, the evanescent wave will interact with the sample and carry the spectroscopic information. This all-solid-state sensor without any free-space propagation of neither THz nor laser radiation is mechanically very stable, even water proof.



10.18 A compact and monolithic sensor for ATR spectroscopy.
 (a) Photograph of fiber-coupled ATR sensor. (b) Opened housing with fiber connectors and wirings. The sensitive silicon piece is shown on the top. (c) THz beam path within the silicon piece with glued photoconductive switches. (d) Chip layout of the used antennas.
 (Molter, 2011.)

As water is a polar molecule, its absorption coefficient is large in the THz range. So single-pass transmission measurements are tricky to perform (Kindt and Schmuttenmaer, 1996) or even impossible in the THz frequency range. In contrast, using the ATR sensor, quantitative measurements are possible (Dobroiu *et al.*, 2005). The measurement result of an aqueous solution of varying isopropanol concentration is presented as an example in Fig. 10.19. Starting from a pure water or pure isopropanol sample, the ATR sensor detects the transmitted amplitude. Clearly, for pure water, the transmission is smaller because the evanescent THz wave ‘sees’ the high losses. As a function of concentration, a monotonic calibration curve is obtained which can be used to quantitatively determine the concentration of a mixture if the two individual constituents are independently measured for calibration.

These ATR measurements were carried out with the same THz system as before, but with only the fiber-coupled sensor being exchanged. This proves the high flexibility and modularity of the system. On the laser side there is more laser power available in the fiber than needed to gate a pair of photoconductive switches; the layout would even be easily scalable to a multi-pixel system without an enormous increase of cost or equipment. Other pairs of sensors, for example, to monitor different parameters at various positions of a production process, are possible.



10.19 Relative transmitted THz amplitude of the ATR sensor put within different liquids. The sample is a mixture of isopropanol and water. The concentration is determined by the onset of the large absorption caused by the polar water. (Molter, 2011.)

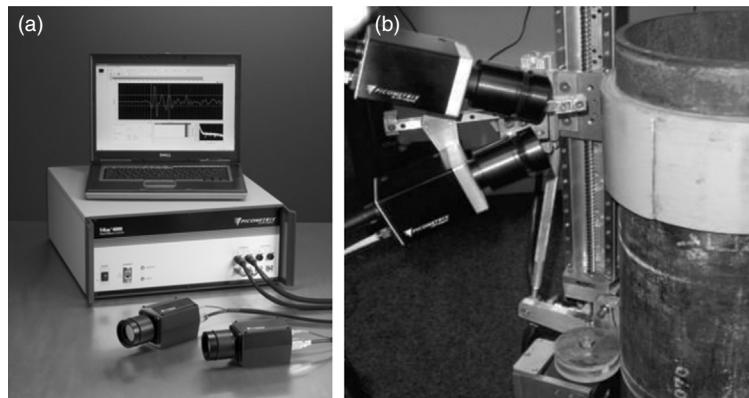
10.5 Comparison of THz-TDS with other systems and techniques

There are a number of fiber-coupled systems on the market all having their own specific properties that make them useful for different applications including tunable cw systems. In particular, systems pumped by a fs laser operating at 1.5 μm are of interest. The dispersion control of these systems required for fiber delivery has certain advantages compared with systems operating with an 800 nm laser. On the other hand, photoconductive switches are still more complex compared with GaAs emitters and detectors. Typical examples are discussed in this section.

10.5.1 Fiber-based pulsed systems – Picometrix Inc.

Intense experimental work is being carried out using fiber-based detectors to have the higher flexibility for the THz beam path, for example, for testing the beam profile of waveguides, (Zhan *et al.*, 2010) raster scanning imaging, (Inoue *et al.*, 2006) angular-resolved THz ranging (McClatchey *et al.*, 2001) and the characterization of building materials in transmission and reflection geometry (Piesiewicz *et al.*, 2005).

In principle, the fiber-based THz systems can be divided into femtosecond-pulsed and cw systems. On the pulsed side, systems applying different pump laser wavelengths are reported. Besides the system described above, other broadband fiber-based systems operating with lasers around 800 nm wavelength (e.g., frequency-doubled fiber laser or solid-state Ti: Sapphire laser) are also available.



10.20 System layout of Picometrix Inc. fiber-coupled modules. (a) Photograph of the system. (b) Arrangement to investigate the integrity of a pipeline. In reflection geometry, the rotationally symmetric sample is scanned to identify breaks or delamination. (© 2009. Reprinted by permission from Macmillan Publishers Ltd: *nature photonics*; Duling and Zimdars, 2009.)

Already in 2000, Rudd *et al.* at Picometrix Inc. reported on a fiber-coupled TDS system (Rudd *et al.*, 2000). At that time, it was rather fiber-coupled laboratory equipment than a system for industrial purposes, as an optical table was still necessary. But since then the development was enormous, as today a scanning window of 320 ps at a repetition rate of 100 Hz with a SNR > 70 dB is available using their system. Their particular components and techniques can be found in US Patent 6,320,191 and US Patent 6,816,647. Various investigations were reported in the field of non-destructive testing. Among them, the most prominent application is the inspection of sprayed-on-foam insulation used in space shuttles (Zimdars *et al.*, 2004). Looking for voids and intrusions, reflective THz imaging was able to resolve the failures.

Another possible application of THz-TDS is the determination of coating thickness by evaluating the time delay between different THz pulses. The separation between the arising echoes is proportional to the coating thickness and the refractive index of the sample. A possible application is the integrity check of pipelines, as can be seen in Fig. 10.20b. A fiber-coupled emitter-detector combination operating in THz refection geometry is circulating around the pipeline to obtain an entire image. Thereby defects such as voids, intrusions or delamination areas can be identified.

10.5.2 Pulsed systems at 1.5 microns pump wavelength

A big technological advantage is expected once the operating wavelength of the femtosecond pump laser can be shifted to 1.5 μm , the telecommunication

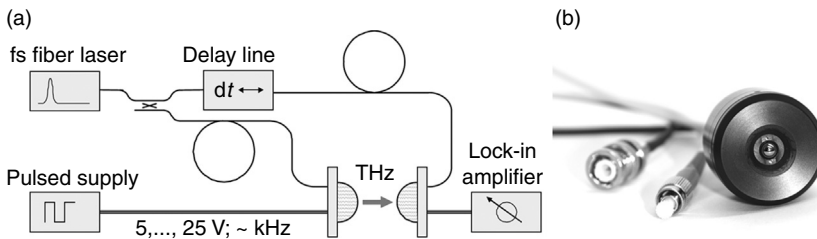
band. The optical components for these wavelengths are already available and well developed. This has the potential to increase the reliability and reduce the price of the THz system. Unfortunately, the typically used semiconductor GaAs cannot be gated by a 1.5 μm laser as the photon energy is not sufficient to overcome the band gap. So special attention has to be placed on the semiconductor to have a PCA with a good performance even if gated by 1.5 μm wavelength.

In general, indium gallium arsenide (InGaAs) is a potential semiconductor with an appropriate band gap. But to come to comparable performance of InGaAs with respect to LT-GaAs, first the technique of low temperature growth of InGaAs on lattice-matched InP using molecular beam epitaxy (MBE) needs to be understood to have the required ultrafast response. But to really explore the short carrier lifetime, the dark resistivity also has to be increased to use the device as photoconductive substrate. Various approaches are reported to reduce the dark current, such as Fe implantation (Suzuki and Tonouchi, 2005), heavy-ion Br⁺-irradiation (Chimot *et al.*, 2005), ErAs:InGaAs super-lattices (Schwagmann *et al.*, 2010) or InGaAs/InAlAs multilayer trapping patterns (Sartorius *et al.*, 2008). As the latter ones, along with subtle mesa-structuring, Roehle *et al.*, (2010) have shown the best performance at 1.5 μm wavelength, and as they were already integrated into an all-fiber system, the results will be presented here.

For the telecommunication wavelength of 1.55 μm well developed fs fiber lasers are available. They can be designed so that their output is pre-chirped for a particular length of fiber to be attached. The dispersion compensation is therefore already realized in the laser itself. This makes the system even more compact and increases mechanical stability due to the reduced free-space propagation of the laser pulses. Sartorius *et al.* reported the first all-fiber system operating at 1.5 μm in 2008 (Sartorius, *et al.*, 2008). All-fiber in this case means that the light is guided in a fiber between the particular functional components. The delay line is still realized by free-space propagation of pulses within a device having fiber input and output connectors. But other fiber-coupled delay lines based on piezo-driven fiber expansion are under investigation (Krumbholz *et al.*, 2008).

The experimental layout of the 1.5 μm pumped system can be seen in Fig. 10.21a. It consists of a pre-chirped fiber laser and two InGaAs/InAlAs multilayer PCAs. The laser pulses are guided via fibers from the laser to the Tx and Rx, which are mounted within a solid housing (see Fig. 10.21b). Measurements through ambient air were performed resolving water lines from 0.25 to 2 THz.

The problem of the planar multilayer system arises in the heterostructure of up to 100 individual layers itself: the effect of the decreasing in-plane electrical bias field is considerably increased. Further on, in the large area between the electrodes of the H-shaped dipoles, the dark resistivity is still



10.21 Fiber-coupled system using $1.5 \mu\text{m}$ pump wavelength as reported by Sartorius *et al.* (2008). (a) Layout of all-fiber TDS system (Sartorius *et al.*, 2008; © 2008 Optical Society of America). (b) Housing of PCA (© 2012 Fraunhofer Heinrich Hertz Institute).

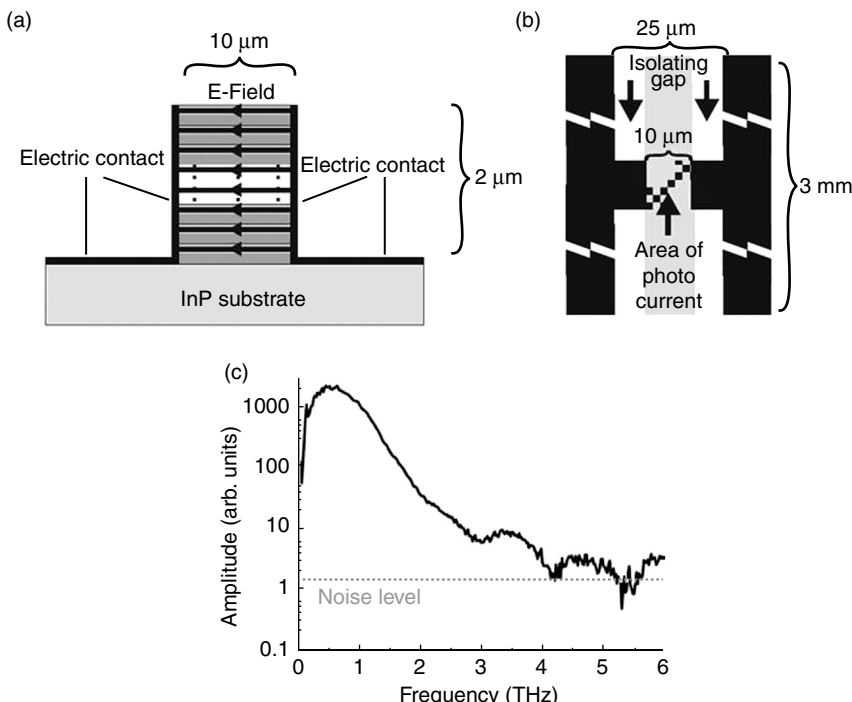
not as high as for LT-GaAs. Therefore, a considerable improvement was achieved by mesa-structuring of the photoactive area. To laterally narrow the photoactive area, steep flanks are produced in the multilayer structure by chemically assisted ion-beam etching. After metallization of the side walls, the electric field can be applied in-plane along the layers (see Fig. 10.22a). This results in a homogeneous distribution of the bias field in the heterostructure. Additionally, an active area with better electrical isolation is formed between the metallized lines of the dipole (Fig. 10.22b). Both effects improve the photocurrent (to a factor of 5) while minimizing the dark current (to a factor of 23), making these devices superior to the planar devices.

A combination of two PCAs of the described type was measured in a $1.5 \mu\text{m}$ TDS system. The obtained spectrum can be seen in Fig. 10.22c. It extends well to 4 THz, which indicates a short carrier lifetime and a good SNR of the detector, directly scaling with the dark resistivity. Despite the reported good performance of the devices, the difficulty in production of the mesa-multilayer system is still high, as also are the costs. Progress in the field of new ultrafast semiconductors is expected to gain even more impact on the THz field in the future.

10.5.3 Fiber-based continuous wave (cw) systems

For completeness, it should not be omitted that there are also cw laser-pumped fiber-coupled THz systems available (Deninger *et al.*, 2008). Even if it is a different method from the fs-TDS approach, depending on the application, the cw systems do have advantages such as reduced cost, high-frequency selectivity and narrow linewidths. So the following system reported by Roggenbuck *et al.* (Roggenbuck *et al.*, 2010) will now be presented (see Fig. 10.23).

Starting from the system side, the expensive femtosecond laser is replaced by two distributed feedback (DFB) cw lasers emitting at slightly different frequencies v_1 and v_2 , respectively. Each of the individual lasers is actively

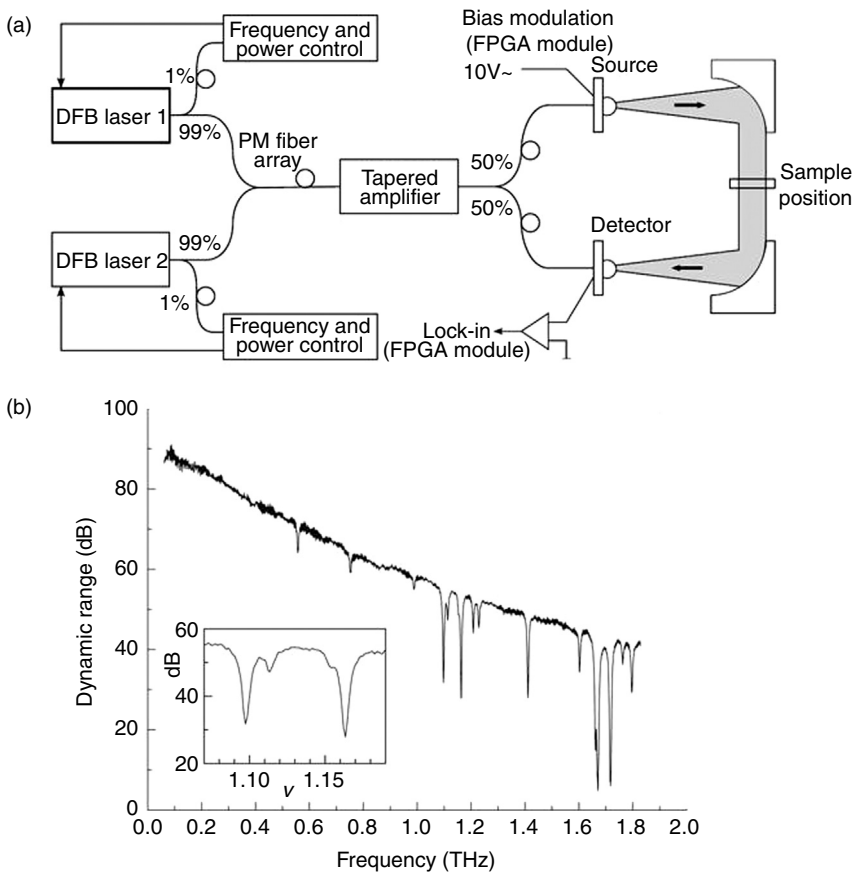


10.22 Mesa-structured InGaAs/InAlAs PCAs for 1.5 μm operation.
 (a) Side view of the multilayer system with electric contacts at the flanks. (b) Top view of the photoconductive switch. (c) Obtained spectrum with mesa PCAs Tx and Rx. (Roehle *et al.*, 2010; © 2010 Optical Society of America.)

stabilized via an interferometer for high frequency and output power stability which is required for high resolution spectroscopy. The THz radiation is generated in a photomixer (Tx) in which the two laser beams overlap. Due to their slightly different frequencies, a beat corresponding to a frequency in the THz range $v_{\text{THz}} = |v_1 - v_2|$ is generated (Brown *et al.*, 1993). This beat on top of cw laser illumination produces a modulation of charge carriers in the biased photomixer, which as a result emits a cw THz wave. In the optical heterodyne detection scheme, the THz wave produces a current in the detector gated by the same optical beat. The generated photocurrent is proportional to the THz electric field E_{THz} and the cosine of the phase difference $\Delta\phi$ between laser beat and THz signal

$$I_{\text{photo}} \propto E_{\text{THz}} \cos(\Delta\phi).$$

So for a fixed frequency it is necessary to optimize the phase $\Delta\phi$ to obtain a large photocurrent. This can be done by inserting a delay stage in one arm



10.23 (a) Layout of a cw THz system consisting of two cw lasers whose wavelengths are slightly detuned at an emission wavelength of around 855 nm. The frequency difference corresponds to an optical beat which has a frequency in the THz range. It can be used to pump the photomixer (Tx) and to coherently detect THz waves (Rx) by tuning the frequency. (b) Dynamic range covering frequencies from 60 GHz to 1.8 THz. Narrowband absorption features caused by rotational water vapor absorption lines can be seen. (Roggenbuck *et al.*, 2010; © 2010 IOP Publishing Ltd.)

(Deninger *et al.*, 2008). Alternatively, one scans the THz frequencies and thereby changes the phase difference. The obtained interference pattern can be evaluated to extract material parameters such as refractive index or absorption.

The dynamic range in Fig. 10.23b was measured with interdigitated photomixers made out of ion-implanted GaAs, on which a self-complementary log-periodic spiral antenna was processed as resonant structure. More than

100 mW of optical power was used to illuminate the fiber-coupled photomixers. The tuning range starts at 60 GHz, due to the efficiency of the photomixers, and reaches up to 1.8 THz, limited by the temperature tuning curve of the two lasers. At the maximum of 100 GHz a dynamic range of 90 dB is demonstrated. This measurement has a high spectral resolution and does not require any moving mechanical components. So high system stability with fiber-coupled PCAs is obtained. The time constant of such a measurement is given by the laser-tuning response and the needed integration constant of the lock-in amplifier. If only a limited band of the THz spectrum has to be scanned, the frequency window can be chosen accordingly. Especially for the narrow band rotational transitions in polar gases the high-frequency resolution is useful to determine the line center and line width. This has the potential to be used for trace gas detection. The ongoing development also pushes the pump wavelength towards the telecommunication band of 1.5 μm for the cw systems (Stanze *et al.*, 2011).

10.6 Future trends and conclusions

We reviewed the current state-of-the-art of fiber-coupled THz spectroscopy systems. The evolution of pulsed TDS systems coming from bulky Ti:Sapphire lasers via frequency-doubled fiber lasers to systems operating at the telecommunication wavelength of 1.5 μm were presented. Exemplarily, the problems and solutions of the design for a broadband fiber-coupled THz-TDS system based on a femtosecond frequency-doubled fiber laser were discussed in detail. The fiber transmission link with respect to modal selection, dispersion and nonlinearities was explained. A comparison to other systems and techniques including laser-pumped cw THz spectroscopy is given.

The ongoing development shows that THz radiation based on a fiber-coupled spectrometer has the potential to extend the applicable electromagnetic spectral range into the far infrared. Thus new fundamental and industrial applications can be accessed based on this type of fiber optical approach. In the future new compact and cheaper laser sources can considerably reduce the prices of such systems. This will increase the availability of such systems in laboratories as well as in real-world applications.

10.7 References

- G. P. Agrawal, Wiley & Sons, New York, 2nd ed. (1997).
D. H. Auston, K. P. Cheung, and P. R. Smith, *Appl. Phys. Lett.* **45**, 284 (1984).
E. R. Brown, F. W. Smith, and K. A. McIntosh, *Appl. Phys. Lett.* **73**, 1480 (1993).
L. Cheng, S. Hayashi, A. Dobroiu, C. Otani, K. Kawase, T. Miyazawa, and Y. Ogawa, *Appl. Phys. Lett.* **92**, 181104 (2008)

- R. A. Cheville and D. Grischkowsky, *Opt. Lett.* **20**, 1646 (1995).
- R. A. Cheville and D. Grischkowsky, *J. Opt. Soc. Am. B* **16**, 317 (1999).
- N. Chimot, J. Mangeney, L. Joulaud, P. Crozat, H. Bernas, K. Blary, and J. F. Lampin, *Appl. Phys. Lett.* **87**, 193510 (2005).
- S. A. Crooker, *Rev. Sci. Instrum.* **73**, 3258 (2002).
- J. A. Deibel, M. D. Escarra, and D. M.ittleman, *Electron. Lett.* **41**, 226 (2005).
- A. J. Deninger, T. Göbel, D. Schönher, T. Kinder, A. Roggenbuck, M. Köberle, F. Lison, T. Müller-Wirts, and P. Meissner, *Rev. Sci. Instrum.* **79**, 044702 (2008).
- A. Dobroiu, R. Beigang, C. Otani, and K. Kawase, *Appl. Phys. Lett.* **86**, 261107 (2005).
- A. Dreyhaupt, S. Winnerl, T. Dekorsy, and M. Helm, *Appl. Phys. Lett.* **86**, 121114 (2005).
- I. Duling and D. Zimdars, *Nat. Photonics* **3**, 630 (2009).
- F. Ellrich, T. Weinland, M. Theuer, J. Jonuscheit, and R. Beigang, *Tech. Mess.* **75**, 14 (2008).
- F. Ellrich, T. Weinland, D. Molter, J. Jonuscheit, and R. Beigang, *Rev. Sci. Instrum.* **82**, 053102 (2011).
- D. Grischkowsky, S. Keiding, M. van Exter, and C. Fattinger, *J. Opt. Soc. Am. B* **7**, 2006 (1990).
- R. Huber, A. Brodschelm, F. Tauser, and A. Leitenstorfer, *Appl. Phys. Lett.* **76**, 3191 (2000).
- R. Inoue, Y. Ohno, and M. Tonouchi, *Jpn. J. Appl. Phys.* **45**, 7928 (2006).
- P. U. Jepsen, D. G. Cooke, and M. Koch, *Laser Photonics Rev.* **5**, 124 (2011).
- C. Jördens, N. Krumbholz, T. Hasek, N. Vieweg, B. Scherger, L. Bahr, M. Mikulics, and M. Koch, *Electron. Lett.* **44**, 1473 (2008).
- K. Kawase, J. Shikata, and H. Ito, *J. Phys. D Appl. Phys.* **35**, R1 (2002).
- D. B. Keck, R. D. Maurer, and P. C. Schultz, *Appl. Phys. Lett.* **22**, 307 (1973).
- J. T. Kindt and C. A. Schmuttenmaer, *J. Phys. Chem.* **100**, 10373 (1996).
- G. Klatt, R. Gebs, H. Schäfer, M. Nagel, C. Janke, A. Bartels, and T. Dekorsy, *IEEE J. Sel. Top. Quant.* **17**, 159 (2011).
- N. Krumbholz, M. Schwerdtfeger, T. Hasek, B. Scherger, and M. Koch, in 33rd International Conference on Infrared, Millimeter and Terahertz Waves IRMMW-THz 2008 (2008).
- M. R. Leahy-Hoppa, M. J. Fitch, and R. Osiander, *Anal. Bioanal. Chem.* **395**, 247 (2009).
- Y. Lee, S. Tanaka, N. Uetake, S. Fujisaki, R. Inoue, and M. Tonouchi, *Appl. Phys. B-Lasers O.* **87**, 405 (2007).
- J. L'huillier, G. Torosyan, M. Theuer, Y. Avetisyan, and R. Beigang, *Appl. Phys. B-Lasers O.* **86**, 185 (2007a).
- J. L'huillier, G. Torosyan, M. Theuer, C. Rau, Y. Avetisyan, and R. Beigang, *Appl. Phys. B-Lasers O.* **86**, 197 (2007b).
- Y. M. Lin, A. Valdes-Garcia, S. J. Han, D. B. Farmer, I. Meric, Y. Sun, Y. Wu, C. Dimitrakopoulos, A. Grill, P. Avouris, and K. A. Jenkins, *Science* **332**, 1294 (2011).
- K. McClatchey, M. T. Reiten, and R. A. Cheville, *Appl. Phys. Lett.* **79**, 4485 (2001).
- J. S. Melinger, N. Laman, S. S. Harsha, S. F. Cheng, and D. Grischkowsky, *J. Phys. Chem. A* **111**, 10977 (2007).
- D. Molter, M. Theuer, and R. Beigang, *Opt. Express* **17**, 6623 (2009).

- D. Molter, F. Ellrich, T. Weinland, S. George, M. Goiran, F. Keilmann, R. Beigang, and J. Léotin, *Opt. Express* **18**, 26163 (2010).
- D. Molter, *Novel Approaches in Coherent Terahertz Measurement Techniques*. Verlag Dr. Hut, München, ISBN 9783843902168 (2011).
- R. Piesiewicz, T. Kleine-Ostmann, N. Krumbholz, D. Mittleman, M. Koch, and T. Kurner, *Electron. Lett.* **41**, 1002 (2005).
- C. D. Robiné, C. Wiegand, K. Rühle, F. Ellrich, T. Weinland, and R. Beigang, in Conference on Lasers and Electro-Optics (Optical Society of America, 2010), p. JWA114.
- H. Roehle, R. J. B. Dietz, H. J. Hensel, J. Böttcher, H. Künzel, D. Stanze, M. Schell, and B. Sartorius, *Opt. Express* **18**, 2296 (2010).
- A. Roggenbuck, H. Schmitz, A. Deninger, I. C. Mágorga, J. Hemberger, R. Güsten, and M. Grüninger, *New J. Phys.* **12**, 043017 (2010).
- J. Rudd, Dispersive precompensator for use in an electromagnetic radiation generation and detection system (2001), US Patent 6,320,191.
- J. V. Rudd, M. W. Warmuth, S. L. Williamson, and D. A. Zimdars, Compact fiber pigtailed terahertz modules (2004), US Patent 6,816,647.
- J. V. Rudd, D. A. Zimdars, and M. W. Warmuth, *Proc. SPIE* **3934**, 27 (2000).
- B. Sartorius, H. Roehle, H. Künzel, J. Böttcher, M. Schlak, D. Stanze, H. Venghaus, and M. Schell, *Opt. Express* **16**, 9565 (2008).
- A. Schwagmann, Z.-Y. Zhao, F. Ospald, H. Lu, D. C. Driscoll, M. P. Hanson, A. C. Gossard, and J. H. Smet, *Appl. Phys. Lett.* **96**, 141108 (2010).
- D. Stanze, A. Deninger, A. Roggenbuck, S. Schindler, M. Schlak, and B. Sartorius, *J. Infrared Millim. Te.* **32**, 225 (2011).
- M. Suzuki and M. Tonouchi, *Appl. Phys. Lett.* **86**, 163504 (2005).
- M. Theuer, S. S. Harsha, D. Molter, G. Torosyan, and R. Beigang, *ChemPhysChem* **12**, 2695 (2011).
- J. Ward, E. Schlecht, G. Chattopadhyay, A. Maestrini, J. Gill, F. Maiwald, H. Javadi, and I. Mehdi, in IEEE MTT-S (2004), **3**, 1587.
- C. Weiss, E. Viehl, C. Theiss, G. Torosyan, M. Weinacht, R. Beigang, and R. Wallenstein, *Tech. Mess.* **68**, 388 (2001).
- Q. Wu and X.-C. Zhang, *Appl. Phys. Lett.* **67**, 3523 (1995).
- H. Zhan, R. Mendis, and D. M. Mittleman, *Opt. Express* **18**, 9643 (2010).
- X.-C. Zhang and D. H. Auston, *Appl. Phys. Lett.* **71**, 326 (1992).
- D. Zimdars, J. A. Valdmanis, J. S. White, G. Stuk, W. P. Winfree, and E. I. Madaras, in Conference on Lasers and Electro-Optics (Optical Society of America, 2004), p. CThN4.

State-of-the-art in terahertz continuous-wave photomixer systems

A. DENINGER, Toptica Photonics AG, Germany

DOI: 10.1533/9780857096494.2.327

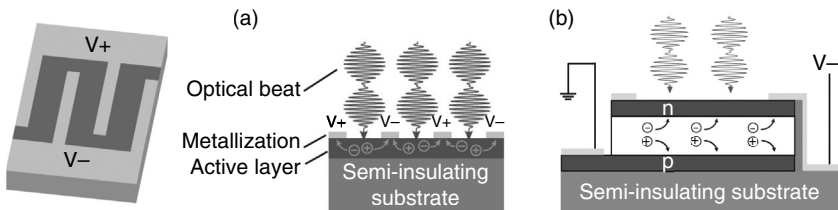
Abstract: This chapter reviews terahertz generation via heterodyne difference frequency generation, or ‘photomixing’. Key aspects of photomixer and antenna design are summarized, considering both photoconductive emitters and p-i-n diodes. The most common photoconductor material, GaAs, requires laser excitation below 870 nm, and ‘defect engineering’ is applied to maximize the terahertz bandwidth. p-i-n diodes, by contrast, are based on InGaAs/InP and are driven at 1.5 μm , taking advantage of compact laser sources developed for optical communication systems. The chapter further includes a discussion of two-color lasers and coherent detection techniques, and concludes with a presentation of selected applications, that have sufficiently matured for first industrial implementations.

Key words: frequency-domain terahertz, photomixing, photoconductor, p-i-n diode, GaAs, InGaAs, coherent detection, two-color laser, trace gas detection, spectroscopy, imaging.

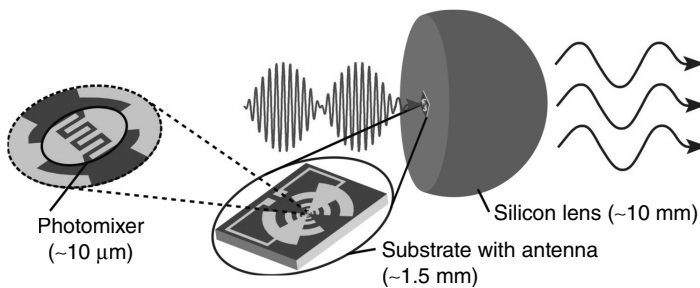
11.1 Introduction

The term ‘photomixing’ refers to heterodyne difference frequency generation in high-bandwidth photoconductors. The output of two continuous-wave (cw) lasers with adjacent frequencies is converted into cw terahertz radiation at exactly the difference frequency of the lasers.

In this chapter, a ‘photomixer’ denotes either a photoconductive element with a micrometer-sized metal-semiconductor-metal (MSM) interface (Fig. 11.1a), or a p-i-n photodiode with an intrinsic layer embedded between p-doped and n-doped semiconductor layers (Fig. 11.1b). The first configuration is commonly used for GaAs-based terahertz emitters, and the two-color laser is focused on the MSM interface (Brown *et al.*, 1993a). The p-i-n structure, on the other hand, is usually realized with InGaAs/InP devices (Ishibashi *et al.*, 1997a), and the laser beam is coupled into the intrinsic



11.1 (a) Top view (left) and cross-section (right) of a planar photomixer with interdigitated finger structure. (b) Cross-section of a p-i-n photodiode. V+ and V- denotes the applied bias voltage. (After Göbel, 2010 and Preu *et al.*, 2011.)



11.2 Terahertz emitter with planar photomixer, log-periodic antenna and silicon lens, with typical dimensions. (After Göbel, 2010.)

layer either through one of the cover layers or from the side, employing waveguide geometry.

In both cases, electron-hole pairs are created in the semiconductor, provided that the photon energy is greater than the bandgap. When a bias voltage is applied to the metal electrodes, a photocurrent is generated, which oscillates at the optical beat frequency. An antenna structure surrounding the photomixer (Fig. 11.2) converts the photocurrent into a new electromagnetic wave, again at the terahertz beat frequency. Commonly, a complete emitter module also includes a Silicon lens to couple the terahertz radiation into free space. The lens serves to reduce the refractive index step between the semiconductor and air, minimizing reflection losses. Often, it also shapes or pre-collimates the terahertz beam.

Theoretically explored in the 1960s (Pantell and Solymar, 1965; Teich, 1969), photomixing was pioneered at MIT (Boston, USA) (Brown *et al.*, 1993a, 1993b, 1995; Vergheese *et al.*, 1993; McIntosh *et al.*, 1995) and soon afterwards realized at Kansai Advanced Research Center (Kobe, Japan) (Hyodo *et al.*, 1996; Matsuura *et al.*, 1997) and then at the Universities of Braunschweig (Germany) (Kleine-Ostmann *et al.*, 2001), Frankfurt

(Germany) (Siebert *et al.*, 2002a), Lille (France) (Peytavit *et al.*, 2002) and Cambridge (UK) (Gregory *et al.*, 2003).

Today, photomixer-based cw terahertz systems are commercially available¹ and – as Section 11.5 of this review will show – are finding their way into first industrial installations.

As there are already several excellent review articles (Brown, 2003; Duffy *et al.*, 2003; Ito *et al.*, 2005; Matsuura and Ito, 2005; Saeedkia and Safavi-Naeini, 2008; Preu *et al.*, 2011), this chapter does not attempt to provide an exhaustive summary of the history of photomixing, nor a full-length theoretical description. The focus rather lies on recent achievements – devices, detection techniques and laser systems employed: instruments that have sufficiently matured to take the step out of the lab and into ‘real-world’ applications. Specifically, Section 11.2 will look at the state-of-the-art in photomixing. Different options for photomixer and antenna design are described, and the benefits and challenges of both GaAs and InGaAs emitters are discussed. Section 11.3 explains the usage of photomixers as coherent receivers, which offers a particularly sensitive detection scheme for terahertz radiation. Section 11.4 presents various ways of realizing the required two-color laser source. Finally, Section 11.5 highlights some exemplary applications that benefit from the advantages of continuous-wave, or ‘frequency-domain’ terahertz technologies: wide tuning, high spectral resolution, large dynamic range, compact footprint, and the possibility of realizing a portable terahertz spectrometer.

11.2 Continuous-wave emitter and detector technologies

For a photomixer-based terahertz emitter, the terahertz power P_{THz} can be expressed as (Saeedkia, 2005; Preu *et al.*, 2011)

$$P_{\text{THz}} \propto I_{\text{ph}}^2 \frac{1}{1 + (2\pi\nu)^2 \tau^2} \frac{R_A}{1 + (2\pi\nu)^2 R_A^2 C^2}. \quad [11.1]$$

Here I_{ph} is the photocurrent in the emitter, ν is the terahertz frequency, τ is the charge carrier lifetime, R_A is the antenna impedance, and C the capacitance of the photomixer. The photocurrent can be related to the applied bias voltage V_{bias} and the laser output power P_{opt} by

$$I_{\text{ph}} \propto V_{\text{bias}} P_{\text{opt}}, \quad [11.2]$$

¹ Companies include TeraView (Cambridge, UK), Toptica Photonics (Munich, Germany) and Emcore (Alhambra, USA).

where equal power levels and an ideal overlap of both laser beams have been assumed.

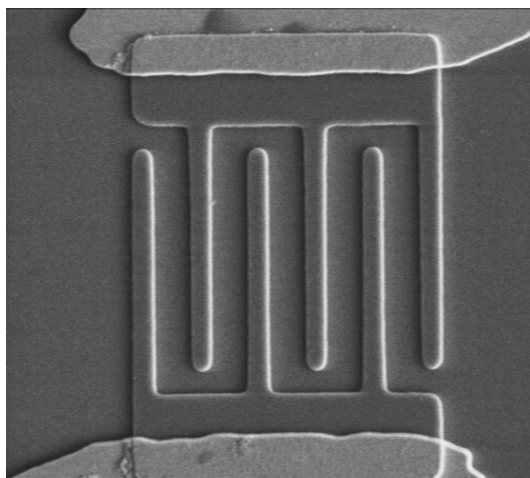
Taking a closer look, the parameter τ in Equation [11.1] has two subtly different meanings, depending on the type of photomixer. In planar photoconductors, $\tau = \tau_{\text{rec}}$ denotes the electron–hole recombination time, which must be short compared to the inverse terahertz frequency. Otherwise, the contributions from carriers generated at different times interfere destructively at the contact electrodes. On the other hand, carrier recombination is negligible in p-i-n-type emitters, as basically all photogenerated charge carriers reach the electrodes (Preu *et al.*, 2011). In this scenario, $\tau = \tau_{\text{tr}}$ is the transit time to the contact pads.

It is instructive to look at some of the implications of Equations [11.1] and [11.2]. First, the terahertz output is expected to scale with the square of the laser power. In practice, this dependence becomes sub-quadratic at high optical power levels, due to device heating (Brown *et al.*, 1993a, 1993b). Second, given the proportionality of I_{ph} and V_{bias} (this is Ohm's law), Equation [11.1] predicts a quadratic dependence of the terahertz output on the bias voltage. In reality again, this is valid only for moderate bias fields (approximately 10 V for GaAs (Jackson, 1999)). A further increase of the bias voltage leads to an augmented photocarrier lifetime, with two consequences: the photocurrent rises in a superlinear way (Brown *et al.*, 1994; Zamdmer *et al.*, 1999), and the terahertz bandwidth is reduced. The latter effect is seen in the saturation behavior of the terahertz output power (bias voltage ≥ 15 V for GaAs (Jackson, 1999)).

Finally, Equation [11.1] predicts two frequency ‘roll-off’ effects: the influence of the carrier recombination/transit time, and the contribution of the photomixer capacitance. In the high-frequency limit, with $(2\pi\nu)^2 \tau^2 \gg 1$ and $(2\pi\nu)^2 R_A^2 C^2 \gg 1$, the power decreases $\propto \nu^{-4}$, that is, with 12 dB per octave, and 40 dB per decade. In photomixer design, a short carrier lifetime and a low capacitance are thus of particular relevance.

11.2.1 GaAs devices

The bandgap of GaAs is 1.42 eV at room temperature, requiring laser excitation below 870 nm. Sub-picosecond carrier recombination times are attained by means of ‘defect engineering’: The carrier lifetime is artificially reduced by introducing recombination centers into the semiconductor. This is realized by low-temperature (LT) growth of GaAs with non-stoichiometric excess Arsenic, ion bombardement with Nitrogen or Oxygen, or the usage of nano-composite materials such as ErAs:GaAs. These techniques will be described



11.3 SEM image of a photomixer with interdigitated finger electrodes. The finger length is 9 μm . The bright material on the top and bottom is the titanium/gold antenna metallization. (From Göbel, 2010, reprinted with permission from Cuvillier Verlag.)

in sub-sections ‘Low-temperature-grown GaAs’ to ‘Nanocomposite GaAs’ below.

The highest power levels reported with GaAs photomixers are in the μW range at frequencies around 1 THz. With LT-GaAs and a resonant dipole antenna, 2 μW were achieved at 1.05 THz (Jackson, 1999; Duffy *et al.*, 2001). Comparable values were reported more recently with ErAs:GaAs photomixers too (Demers *et al.*, 2007).

Photomixer design

A planar photomixer usually features an interdigitated structure, onto which the two laser beams are focused (Fig. 11.3). This structure, which is much smaller than the terahertz wavelength, not only enlarges the metal–semiconductor interface, but also helps achieve a more uniform field distribution, thus increasing the optoelectronic conversion efficiency (Gregory *et al.*, 2007).

The performance of a photomixer depends on a variety of design parameters, with respect to both its geometry and material composition. Relevant dimensions are the finger spacing (= the horizontal distance between adjacent fingers in Fig. 11.3), the finger width, and the overall size of the active area.

A large *finger spacing* minimizes the capacitance, but on the other hand, increases the traveling time of the photoelectrons to the finger electrodes.

This reduces the responsivity of the photomixer, that is, the ratio between the number of carriers collected at the contacts (the effective photocurrent) vs the number of photocarriers generated. A practicable value of the finger spacing is 1–2 μm (Kadow *et al.*, 2000; Gregory *et al.*, 2004a; Mikulics *et al.*, 2005; Peytavit *et al.*, 2008).

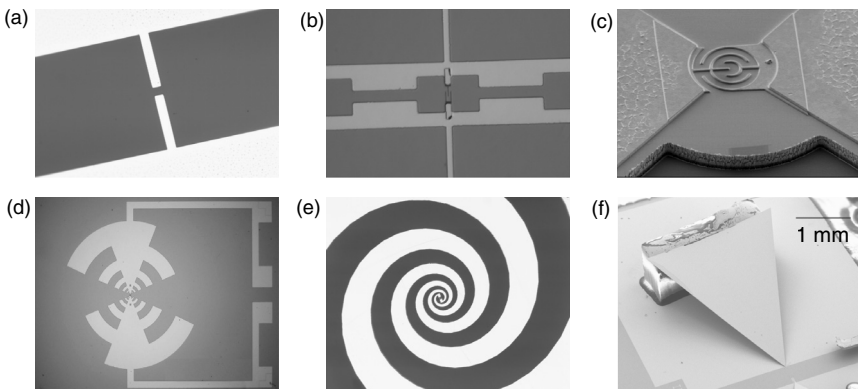
A narrow *finger width* is beneficial as it reduces the capacitance and increases the responsivity. Common values are in the range of 200–300 nm (Jackson, 1999; Gregory *et al.*, 2003; Cámara Mayorga *et al.*, 2007; Göbel, 2010). Finally, for a given laser intensity, a small *active area* maximizes the terahertz output. However, the current and power density resulting from the tight laser focus imposes a damage threshold and thus a practical limit on the device size. Typical dimensions are approximately $10 \times 10 \mu\text{m}^2$ (McIntosh *et al.*, 1995; Gregory *et al.*, 2004a; Mikulics *et al.*, 2005; Göbel, 2010). Recessed finger contacts, which are partially buried in 200–300 nm deep trenches in the active layer, further increase the output power compared to surface-electrode MSM structures (Mikulics *et al.*, 2006b; Kordos *et al.*, 2007).

Besides the geometric considerations, success criteria for GaAs photomixers are:

- a short carrier recombination time of 200–500 fs (Brown *et al.*, 1995; McIntosh *et al.*, 1995; Peytavit *et al.*, 2002),
- a high carrier mobility, typically $200 \text{ cm}^2/(\text{V s})$ (Brown *et al.*, 1993b; Verghese *et al.*, 1993),
- a high optical damage threshold of 50–100 mW (Verghese *et al.*, 1997a, 1997b),
- a high breakdown field threshold, ideally 500–1000 kV/cm (Brown, 2003; Awad *et al.*, 2007).

The electric breakdown tolerance is relevant as space charge screening attenuates the applied external bias (Pedersen *et al.*, 1993; Loata *et al.*, 2007b). The screening effect results from the separation of electrons and holes in the active region, which leads to an accumulation of space charges. The electric field then becomes very high near the contact electrodes, but weak in the active region itself. The effect is aggravated by trapped charge carriers, which contribute to the space charge screening but not to the terahertz current (Loata *et al.*, 2007a, 2007b). The external bias then has to be increased to overcome the effect, yet without risking device breakdown.

Thermal failure occurs when the temperature difference between the active region and the substrate exceeds approximately 110°C, independent of the absolute temperature of the active region (Verghese *et al.*, 1997a, 1997b). With typical mixer geometries as above, this corresponds to a



11.4 Microscope images of different antenna designs: (a) end-feed dipole (Toptica Photonics, previously unpublished), (b) center-feed dipole with choke elements (© I. Gregory, TeraView), (c) bow-tie with interdigitated fingers (Stanze *et al.*, 2011, courtesy of Springer Publishing), (d) log-periodic (Göbel, 2010, courtesy of Cuvillier Verlag), (e) log-spiral (Toptica Photonics, previously unpublished), and (f) horn antenna (© E. Peytavit, University Lille). Panels (a) and (b) are resonant designs whereas panels (c)–(f) are broadband antennas. The choke elements in (b) increase the impedance of the connecting leads at the resonance frequency.

maximum laser intensity of 50–100 mW. This limit, determined more than a decade ago, still applies today.

Antenna design

The antenna transforms the terahertz photocurrent into a free-space electromagnetic wave – ideally, with frequency-independent polarization, emission geometry and impedance. In reality, these parameters depend strongly on the shape of the antenna, which therefore has a profound impact on the useable frequency range of a photomixer emitter. A multitude of antenna geometries (Fig. 11.4) has been proposed, the most common planar forms being dipoles, bow-ties, log-spiral and log-periodic shapes. By contrast, a horn antenna is a 3-dimensional structure with a flared waveguide, which provides a gradual impedance change from the source into free space.

Notwithstanding the design, there exists a significant impedance mismatch between the photomixer and the load circuit of the antenna: the impedance of an illuminated photomixer = bias voltage/photocurrent is $\sim 10\text{ k}\Omega$ (Verghese *et al.*, 1998), whereas the antenna has a typical impedance of 50–200 Ω (Matsuura and Ito, 2005; Cámera Mayorga *et al.*, 2006). Thus, a significant fraction of the terahertz power is not coupled into the antenna at all but is lost in the photomixer.

Resonant antennas enhance the terahertz power within a narrow frequency range. The simplest form is a dipole structure (McIntosh *et al.*, 1996; Matsuura *et al.*, 1997), which can be tailored to a desired target frequency. End-feed and center-feed antennas (Fig. 11.4a and b) act as half-wave and full-wave dipoles, respectively (Gregory *et al.*, 2004a), and are resonant when the dipole length equals one half (or the full) effective terahertz wavelength.² The main advantage of a dipole antenna is its high impedance, which improves the coupling of the electrical circuit and the free-space terahertz field. At resonance, the terahertz output is about five times higher than that of a broadband design patterned on an identical substrate (Gregory *et al.*, 2004a). It is noteworthy that the *peak power* is not limited by any RC time constant, and the frequency roll-off behavior of appropriately designed dipoles follows a 6 dB/octave slope, rather than 12 dB/octave (Duffy *et al.*, 2001). A dipole antenna has a bandwidth of approximately 10% of its center frequency (Matsuura and Ito, 2005). The output polarization is linear and extinction ratios (ER) better than 650:1 have been measured (Gregory *et al.*, 2005b).

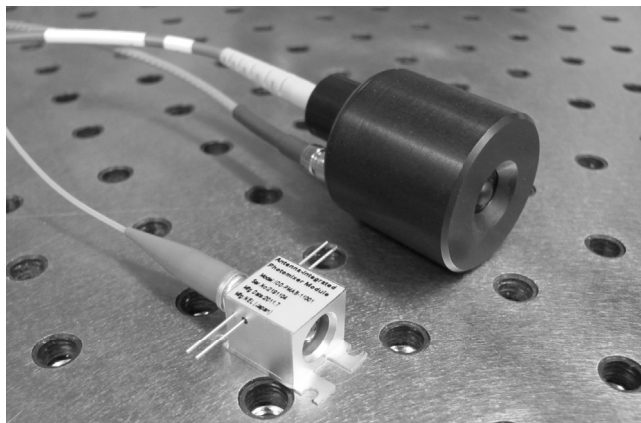
In contrast to resonant structures, broadband antennas such as bow-ties or spirals operate over a large frequency range (Brown *et al.*, 1995; McIntosh *et al.*, 1995). The advantage of a bow-tie is its simple design and a frequency-independent linear polarization. The ER is approximately 20:1 (Gregory *et al.*, 2005b).

A log-spiral shape has a near-constant impedance over a wide frequency range (Cámara Mayorga *et al.*, 2007) and thus very smooth frequency characteristics (see Fig. 11.11 later). On the other hand, the output polarization exhibits a more complex frequency dependence. At frequencies beneath a lower cutoff, when the effective wavelength exceeds the maximum arm length, the terahertz output is elliptically polarized (Preu *et al.*, 2011). As the frequency increases, the polarization changes to circular, only to become elliptical again above ~200 GHz (Gregory *et al.*, 2005b), owing to the contribution of the interdigitated fingers. A mainly linear polarization regime prevails between ~600 and 1100 GHz, with the polarization axis oriented parallel to the fingers. At even higher frequencies, a perpendicular polarization component develops, as the spacing between adjacent fingers becomes the relevant length scale (Gregory *et al.*, 2005b).

A compromise between a bow-tie and a log-spiral structure is the log-periodic geometry. A log-periodic antenna is resonant whenever one of its fingers has an electrical length of $\lambda/4$. As the impedance varies with frequency (Mendis *et al.*, 2005), intermediate frequencies are attenuated (see e.g., Deninger *et al.*,

² The term ‘effective wavelength’ takes the refractive index change at the semiconductor–air interface into account. GaAs has a permittivity of $\epsilon = 12.8$, and for a GaAs/air dielectric half-space, the wavelength decreases by a factor

$$\sqrt{(\epsilon + 1)/2} = 2.63.$$



11.5 Examples of fiber-pigtailed photomixers. Front: Uni-traveling-carrier photodiode from NTT Laboratories; back: p-i-n diode from Fraunhofer Heinrich Hertz-Institute Berlin (Toptica Photonics, previously unpublished).

2008). The polarization is linear at the resonances but undergoes a periodic tilting when the frequency is scanned (Mendis *et al.*, 2005).

A challenge for any planar design is the positioning of the Silicon lens on the output side, which requires careful alignment. Moreover, as broadband anti-reflection coatings are not yet available at terahertz wavelengths, the lens gives rise to parasitic interference effects due to multiple reflections of the terahertz beam. The advantage of horn antennas (Peytavit *et al.*, 2007; Beck *et al.*, 2008; Mangeney *et al.*, 2010) is that they alleviate the need for any lens on the output side. Horn antennas, too, are broadband and provide linearly polarized terahertz radiations, with an ER better than 60:1 (Peytavit *et al.*, 2008).

Flexible handling of a terahertz emitter is realized by equipping the module with a permanently installed ('pigtailed') single-mode fiber. One possibility to achieve the required alignment precision is the usage of a three-axis positioning stage with piezoelectric control. The air gap between the fiber and the semiconductor substrate – another potential source of unwanted interference effects – is filled with an optical adhesive with a refraction index similar to the fiber core (Cámara Mayorga *et al.*, 2006). Figure 11.5 shows examples of fiber-pigtailed terahertz emitter modules.

GaAs photomixers function not only as terahertz emitters, but also as coherent receivers – a situation that is different for the InGaAs diode devices described below. Although there is some evidence that optimum performance requires different antenna designs for the emitter and receiver (Gregory *et al.*, 2007), excellent dynamic ranges were achieved

with symmetric configurations too (Demers *et al.*, 2007; Roggenbuck *et al.*, 2010).

Low-temperature-grown GaAs

LT-GaAs was the first semiconductor employed for photomixing (Brown *et al.*, 1993a, 1993b; Verghese *et al.*, 1993) and has remained the most widely used material to-date (e.g., Cámará Mayorga *et al.*, 2006; Gregory *et al.*, 2007; Deninger *et al.*, 2008; Peytavit *et al.*, 2009; Scheller *et al.*, 2011).

The growth process usually involves a semi-insulating GaAs substrate, onto which the LT-GaAs film is grown by means of molecular beam epitaxy. The term ‘low temperature’ refers to a growth temperature around 200°C (McIntosh *et al.*, 1995; Siebert *et al.*, 2002a; Gregory *et al.*, 2003), rather than 600°C for standard GaAs. Combined with Arsenic overpressure (McIntosh *et al.*, 1995), this leads to a non-stoichiometric growth with 1–2% of excess Arsenic. The As antisite defects – As atoms located at Ga sites (Gregory *et al.*, 2005b) – act as mid-bandgap traps (Smith *et al.*, 1988) and thus shorten the electron–hole recombination time to approximately 0.1 ps (Gregory *et al.*, 2003). Unfortunately, the dark resistance of as-grown LT-GaAs is about 1 MΩ and thus far too low for photomixing applications. Therefore, the material is subsequently annealed at 500–600°C for ~10 min (McIntosh *et al.*, 1995; Göbel, 2010). Annealing creates quasimetallic As clusters (Preu *et al.*, 2011) that act as carrier traps, thus increasing the resistance of the semiconductor by several orders of magnitude (Luo *et al.*, 1996). On the other hand, this step also enlarges the photocarrier lifetime again, which calls for very careful balancing of the annealing conditions (McIntosh *et al.*, 1997; Gregory *et al.*, 2003). A reasonable compromise is found for carrier lifetimes of 0.2–0.3 ps (McIntosh *et al.*, 1995; Peytavit *et al.*, 2002; Gregory *et al.*, 2005b).

Further layers are usually included between the LT-GaAs and the substrate, for example, to realize an etch stop (Peytavit *et al.*, 2002; Deninger *et al.*, 2008) or to increase the thermal conductivity of the device and thus reduce the risk of thermal failure (Jackson, 1999).

Although bandwidths above 3 THz have been achieved with LT-GaAs photomixers (Brown *et al.*, 1995; McIntosh *et al.*, 1995; Matsuura *et al.*, 1997; Peytavit *et al.*, 2009), device manufacturing has remained a challenge, due to the sensitive dependence on the aforementioned growth conditions. Alternative materials that permit a more reproducible production process are presented in the next two sections.

Ion-implanted GaAs

Ion implantation in GaAs films produces significant lattice defects (Chen *et al.*, 2000). While a variety of ions including Arsenic (Liu *et al.*, 2003) and protons (Salem *et al.*, 2006) have been assessed for pulsed photoconductive

switches, Nitrogen (Mikulics *et al.*, 2003, 2005; Michael *et al.*, 2007) and Oxygen implantation (Cámará Mayorga *et al.*, 2007) have produced the best results for cw photomixers.

Implantation is performed in a linear accelerator, with doses between 10^{12} – 10^{16} ions/cm² (Mikulics *et al.*, 2006c; Michael *et al.*, 2007) and ion energies ranging from 0.5 MeV to 3 MeV (Mikulics *et al.*, 2005, 2006a). The ions penetrate 2–3 μm into the GaAs substrate, that is, deeper than the optical absorption length of ~1 μm (Cámará Mayorga *et al.*, 2007). The ion bombardment creates various types of defects in the lattice – vacancies, interstitials, antisites (Cámará Mayorga *et al.*, 2007) – which act as carrier traps much in the same way as the defects in LT-GaAs. Recombination times as short as 110 fs have been obtained with 880 keV Nitrogen ions (Mikulics *et al.*, 2005).

The advantage of ion implantation lies in the possibility to precisely engineer the semiconductor with the desired properties, and thus achieve a highly reproducible photoconductive material. A terahertz output of 2.6 μW at 850 GHz was measured with Nitrogen-implanted GaAs material, with a traveling-wave photomixer and a bow-tie antenna (Mikulics *et al.*, 2006a). This value is comparable to the best results obtained with LT-GaAs or nanocomposite GaAs.

Nanocomposite GaAs

The growth of thin layers of ErAs in GaAs leads to the spontaneous formation of nanometer-scale ErAs ‘islands’ (Kadow *et al.*, 1999, 2000), as the ErAs layers disintegrate into isolated ErAs nanoparticles, with a typical diameter of 1–2 nm (Kadow *et al.*, 2000). The quasimetallic behavior of the ErAs islands results in sub-picosecond carrier recombination times, making the material suitable for photomixing.

An ErAs:GaAs nanocomposite photomixer consists of a multilayer ‘superlattice’ structure, with up to 60 iterations of an ErAs monolayer on ~20 nm of GaAs (Kadow *et al.*, 2000). The GaAs is grown under standard (not LT) conditions. The ErAs layers are deposited at the same temperature, by closing the respective Ga and As shutters, opening the Er inlet and exploiting the background As pressure in the growth chamber. Increasing the temperature yields larger ErAs islands (Kadow *et al.*, 1999).

The well-defined superlattice period determines the recombination time: the larger the lattice spacing, the longer τ_{rec} (Kadow *et al.*, 1999). The carrier lifetime can thus be fine-tuned by controlling the lattice period (Matsuura and Ito, 2005), to reproducibly obtain the desired material performance.

Recombination times of 120 fs and breakdown fields above 200 kV/cm have been achieved with ErAs:GaAs photomixers (Kadow *et al.*, 2000). Terahertz power values of 12 μW at 90 GHz (Bjarnason *et al.*, 2004) and 2 μW at 1 THz (Demers *et al.*, 2007) have been reported.

It is worth noting that all of the GaAs variants discussed here have found their way into commercial cw terahertz systems, with comparable performance.³

11.2.2 InGaAs/InP devices

The lure of InGaAs-based terahertz emitters lies in the simplicity of the laser system. Wavelengths around 1.5 μm are well established in optical communication systems, and a multitude of highly integrated lasers and optical components has been developed (see Section 11.4.1). InGaAs, or precisely: In_{0.53}Ga_{0.47}As, is usually grown on InP substrates and, in this composition, has a band gap of 0.74 eV or 1.68 μm. Telecom-band lasers thus seem to be the perfect match.

Cw terahertz generation with InGaAs-based devices is the realm of p-i-n photodiodes, despite their more complex production process as compared to photoconductors. Photoconductive sources have been attempted, but even though all of the tricks developed with GaAs have been played on InGaAs as well – LT growth (Baker *et al.*, 2005; Kim *et al.*, 2011), ion implantation (Mangeney *et al.*, 2007, 2010) and the usage of ErAs:InGaAs nanocomposites (Sukhotin *et al.*, 2003) – these approaches have been limited to sub-μW power levels. P-i-n diode emitters thus outperform planar photoconductors by several orders of magnitude.

There are distinct differences between GaAs photomixers and InGaAs p-i-n diodes. In the latter case, the device structure is not planar; rather, the bias voltage is applied to differently doped semiconductor layers (Fig. 11.1b). Processing thus commonly comprises etching a mesa structure on epitaxially grown p-i-n layers (Preu *et al.*, 2011). The photoelectrons and holes are generated in (or close to) the intrinsic layer and propagate to the n- and p-doped layers, respectively. Consequently, the critical parameter that determines the high-frequency roll-off is the transit time τ_{tr} of the photocarriers through the intrinsic layer. From a practical perspective, the (reverse) bias voltage required to drive a p-i-n emitter is three to ten times smaller than that of a GaAs photoconductor, that is, 2–3 V vs 10–30 V (Kadow *et al.*, 2000; Ito *et al.*, 2005; Roggenbuck *et al.*, 2010; Stanze *et al.*, 2011).

The quest for a short τ_{tr} seems to favor thin intrinsic layers, but this needs to be counterbalanced against the inevitable increase in device capacitance. Three different approaches to tackle this challenge are described in the section ‘Photodiode emitters: nipnip, WIN and UTC designs’. The section on ‘Receiver photomixers’ returns to InGaAs photoconductors and explains how they have proven themselves as sensitive terahertz detectors. Finally,

³ The TeraView CW Spectra 400 uses LT-GaAs, Toptica’s TeraScan 850 is based on ion-implanted GaAs, whereas the Emcore PB7100 employs ErAs:GaAs photomixers.

the section on ‘Receiver photodiodes’ subsumes recent work that has shown how UTC diodes do indeed work on the detection side, too.

Photodiode emitters: nippnip, WIN and UTC designs

This section presents three advanced designs that aim to increase the output power and efficiency of InGaAs-based photodiode emitters: stacked p-i-n superlattice (‘nippnip’) structures (Döhler *et al.*, 2005; Preu *et al.*, 2007), waveguide-integrated (WIN) photodiodes (Bach *et al.*, 2004), and uni-traveling carrier (UTC) diodes (Ishibashi *et al.*, 1997a, 1997b). Of all those, UTC diodes hold the present world record for optoelectronically generated cw terahertz output: NTT Laboratories (Kanagawa, Japan) demonstrated 20.8 mW at 100 GHz (Ito *et al.*, 2003), and researchers at University College London achieved 25 µW at 900 GHz, combining a waveguide-UTC diode and a resonant antenna design (Renaud *et al.*, 2006; Rouvalis *et al.*, 2010).

Nippnip photodiodes

A ‘nippnip’ structure consists of a superlattice of N stacked p-i-n diodes (Döhler *et al.*, 2005; Preu *et al.*, 2007). Each individual p-i-n diode is optimized for short transit times, yet the capacitance C_{total} of the complete device scales inversely with N :

$$C_{\text{total}} = C_{\text{p-i-n}} / N,$$

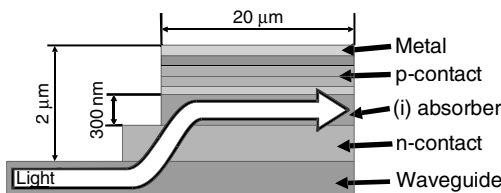
where $C_{\text{p-i-n}}$ is the capacitance of an individual p-i-n element. This design thus elegantly decouples the optimization of transit time and RC roll-off. A typical value for N is $\sim 3\text{--}4$ (S. Preu, personal communication, 2011).

The band structure of a nippnip photodiode can be optimized so that (i) charge carrier generation is restricted to a region close to the p-layers, and consequently only the electrons contribute to the photocurrent (this is also exploited in the case of UTC diodes, see Fig. 11.7 in subsection on UTC photodiodes); and (ii) electron transport is fully ballistic, that is, unimpeded by inter-valley scattering (Preu *et al.*, 2007, 2011). Ballistic transport results in an electron velocity that exceeds the saturation velocity ($\sim 10^7$ cm/s) by as much as one order of magnitude (Preu *et al.*, 2011), thus further decreasing τ_{tr} .

To-date, nippnip diodes have reached power levels of 150 µW at 120 GHz, 4 µW at 500 GHz and 0.65 µW at 1 THz (S. Preu, personal communication, 2011).

WIN photodiodes

Waveguide-integrated photodiodes were originally designed for high-bandwidth telecommunication (Bach *et al.*, 2004, Beling *et al.*, 2005).



11.6 Cross-section of a waveguide-integrated photodiode. (© D. Stanze, Fraunhofer Heinrich Hertz-Institute Berlin.)

Equipped with a suitable antenna, these devices yield efficient terahertz emitters (Sartorius *et al.*, 2009; Stanze *et al.*, 2011), despite their conventional p-i-n design.

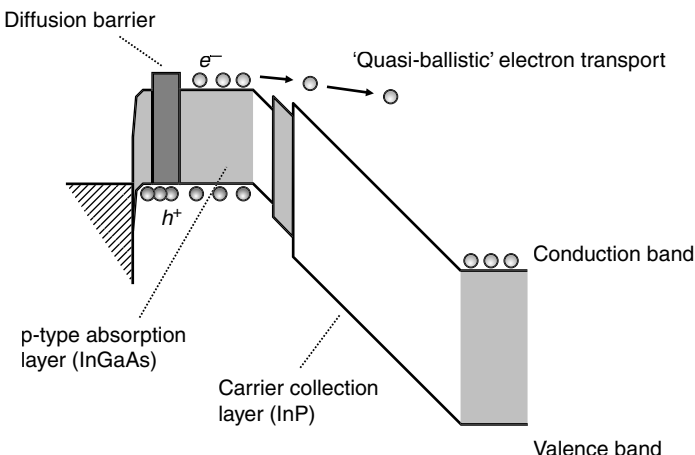
The advantage of the waveguide design is a long absorption length for the laser light, yet a (relatively) thin intrinsic layer. In the design shown in Fig. 11.6, the absorbing layer lies on top of the waveguide, and the light couples evanescently into the absorbing layer. The latter has a thickness of ~ 300 nm, whereas the length of the waveguide is ~ 65 times greater.

With an integrated bow-tie antenna, WIN photodiodes have attained bandwidths above 2 THz (Stanze *et al.*, 2010), and power levels of 10 μW and 5 μW have been demonstrated at 200 GHz and 500 GHz, respectively (Sartorius *et al.*, 2009; Stanze *et al.*, 2011).

UTC photodiodes

Uni-traveling-carrier photodiodes, pioneered by NTT in Japan (Ishibashi *et al.*, 1997a, 1997b, 2001; Ito *et al.*, 2003), offer what might be the most promising approach to unite high-bandwidth and high-power terahertz output. A UTC diode features a moderately p-doped InGaAs absorption layer and a depleted, undoped or lightly n-doped InP carrier collection layer (Fig. 11.7) (Ishibashi *et al.*, 2001; Ito *et al.*, 2004). Photocarriers are generated in the absorption layer, close to the p-contact. The electrons diffuse/drift into the (higher-bandgap) collection layer but, due to an additional diffusion block, not to the p-contact layer. The holes, by contrast, travel to the p-contact but do not enter the collection layer. Thus, only the electrons cross the collection layer – hence the ‘uni-traveling-carrier’ denomination. This type of carrier transport is substantially different from conventional p-i-n diodes, where both electrons and holes contribute to the high-frequency photocurrent.

The UTC design allows for independent optimization of the absorption and collection layers. For instance, the absorption layer can be kept thin, pushing the transit-time roll-off to high frequencies, without walking straight into the capacitance roll-off trap (Ito *et al.*, 2005). The high electron velocity counteracts space charge effects in the depletion layer, which allows for reaching high current outputs before saturation occurs. This is



11.7 Schematic band diagram of a uni-traveling-carrier photodiode.
(© NTT Laboratories.)

a favorable condition to achieve a high-power terahertz output, as the terahertz power scales with the square of the photocurrent (Equation [11.1]).

The high electron mobility is maintained even at a weak bias voltage. In fact, as the hole current itself induces an electric field in the absorption layer, the photogenerated electrons are accelerated even without an external bias voltage applied (Ito *et al.*, 2004). Zero-bias operation of a UTC diode has indeed been demonstrated (Ito *et al.*, 2000).

UTC photodiodes have set the bar high for any optoelectronic cw terahertz emitter. A recent addition to the record values mentioned above was an RF output of 530 μ W at 350 GHz, at a photocurrent of 20 mA and a reverse bias of 2.5 V (Wakatsuki *et al.*, 2008). On the other hand, GaAs photomixers still lead the field in terms of bandwidth, and deliver higher output power above \sim 1.5 THz (Ito *et al.*, 2005).

Of the three approaches presented in this chapter, only WIN photodiodes are commercially available at the time of writing, at least for the low to medium-sized volumes required for present-day terahertz instrumentation.⁴

Receiver photomixers

Even though the terahertz output from (non-p-i-n) InGaAs photomixers has been limited, these devices have performed well as heterodyne receivers (Baker *et al.*, 2005; Ducournau *et al.*, 2009; Sartorius *et al.*, 2009; Kiessling

⁴ WIN diodes are manufactured by Heinrich Hertz-Institute, Berlin/Germany. Toptica Photonics offers terahertz spectroscopy systems based on these modules. NTT's UTC photodiodes are presently not available in small quantities.

et al., 2011; Kim *et al.*, 2011; Stanze *et al.*, 2011). In a coherent emitter–receiver configuration (Section 11.3), a dynamic range up to ~ 80 dB has been measured for the terahertz power (Sartorius *et al.*, 2009; Stanze *et al.*, 2011). This value is already close to the state-of-the-art in GaAs photomixers (Fig. 11.11, see also Demers *et al.* (2007) and Roggenbuck *et al.* (2010)).

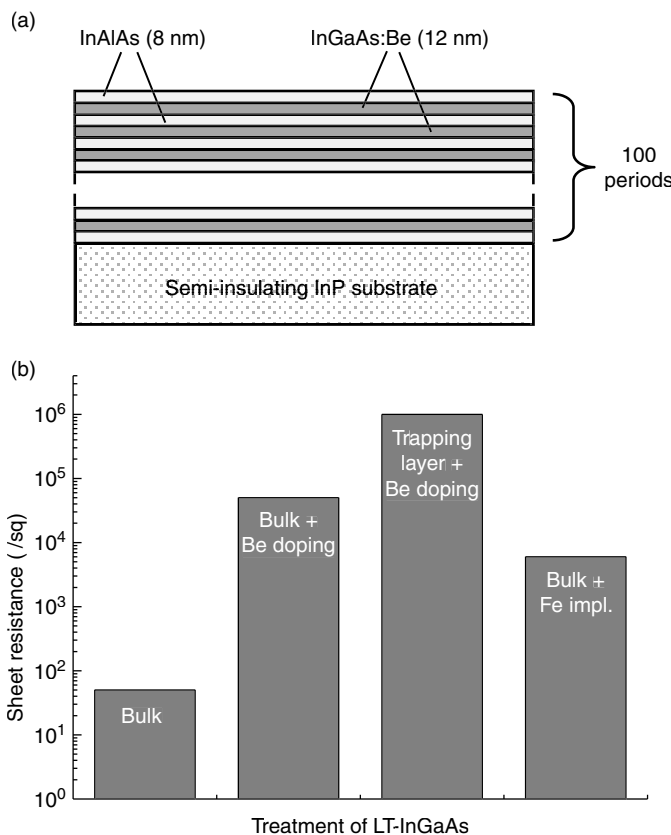
Highly efficient terahertz receivers, developed at Fraunhofer Heinrich Hertz-Institute, Berlin (Sartorius *et al.*, 2008), are based on LT ($< 200^\circ\text{C}$) grown InGaAs, yet the preparation involves two clever design tricks. The LT growth process, while creating the As antisites mandatory for short recombination times, results in a low resistance and thus high dark conductivity (Fig. 11.8b), which would render the bulk semiconductor unsuitable for terahertz applications. In order to increase the resistance, the first design modification involves co-doping with Beryllium, which acts as additional acceptor. The second measure consists of embedding the photoconductive InGaAs layers between InAlAs layers (Fig. 11.8a). InAlAs is transparent for the $1.5\ \mu\text{m}$ pump light and thus does not contribute to the photoconductivity, but the InAlAs–InGaAs interface provides a high concentration of deep electron traps. Given a sufficiently thin photoconductive layer ($\sim 10\ \text{nm}$), electrons can tunnel out and are captured in the traps. Best results are attained with a multi-stack design of alternating photoconductive (12 nm) and trapping layers (8 nm). This design enhances the absorption of the pump light and significantly increases the efficiency of the device. Equipped with an appropriately matched antenna, these photoconductors have been used for pulsed terahertz generation and detection (Sartorius *et al.*, 2008), and as cw terahertz receivers (Sartorius *et al.*, 2009; Stanze *et al.*, 2010).

Receiver photodiodes

It was long believed that p-i-n diodes did not work as terahertz receivers, following the argument that an illuminated photodiode exhibits a current output, no matter whether a terahertz field is present or not. However, a collaboration between NTT Laboratories and the University of Osaka (Japan) recently demonstrated that a pair of UTC diodes can, in fact, be utilized in an emitter–receiver configuration (Nagatsuma *et al.*, 2010).

Nagatsuma *et al.* describe two different ways of employing a UTC diode for terahertz detection (Fig. 11.9): with a forward bias applied, the receiver UTC diode acted as power detector, the output signal being proportional to the square of the incident terahertz intensity. Alternatively, reverse biasing yielded a phase-sensitive detector similar to a classical photomixer receiver, where the output signal is proportional to the amplitude of the terahertz field.

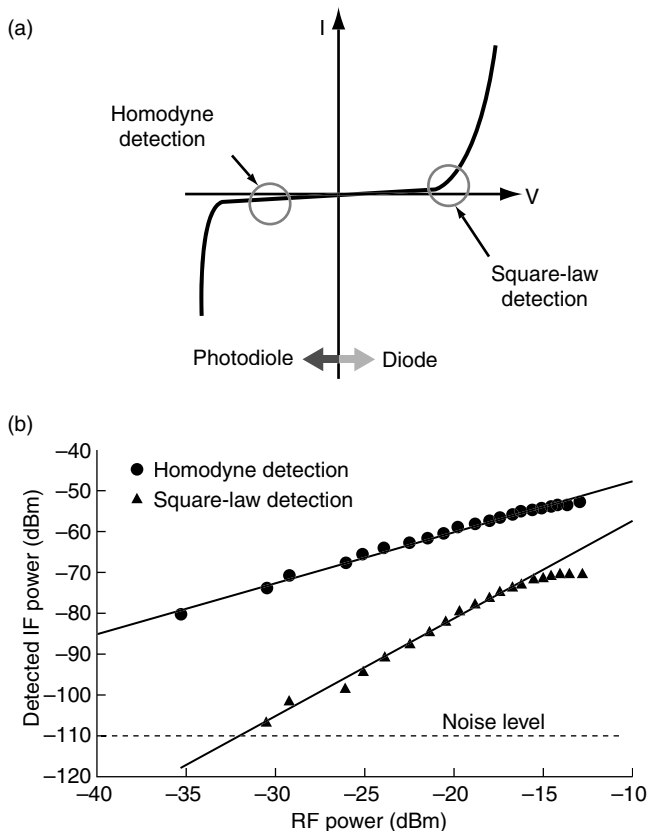
The effect exploited here is based on electron-dominated space charge phenomena. Under a low bias voltage, negative space charges accumulate



11.8 (a) Multilayer structure of an LT-InGaAs receiver module.
 (b) Resistance of differently treated LT-InGaAs. The combination of Beryllium doping and the inclusion of InAlAs trapping layers yields the highest resistance. Iron-implanted LT-InGaAs is shown for comparison.
 (After Sartorius *et al.*, 2008.)

between the absorption layer and the collection layer. This creates a potential barrier at the layer interface, which blocks the current flow into the collection layer. The potential barrier thus gives rise to a ‘dynamic capacitance’ (Fushimi *et al.*, 2004) and a prolonged carrier transit time. The entire scenario depends sensitively on the applied bias – and hence, even the minute voltage changes induced by the terahertz field can be measured.

Nagatsuma *et al.* (2010) determined a dynamic range of their emitter-receiver configuration of 40 dB in power detection mode and 60 dB in the photomixer receiver mode, at a frequency of 350 GHz. This is still less than that of the ‘real’ InGaAs/InAlAs photoconductive receivers described in the previous section (Stanze *et al.*, 2011). Advantages of the twin-UTC approach are the restored symmetry of emitter and receiver,



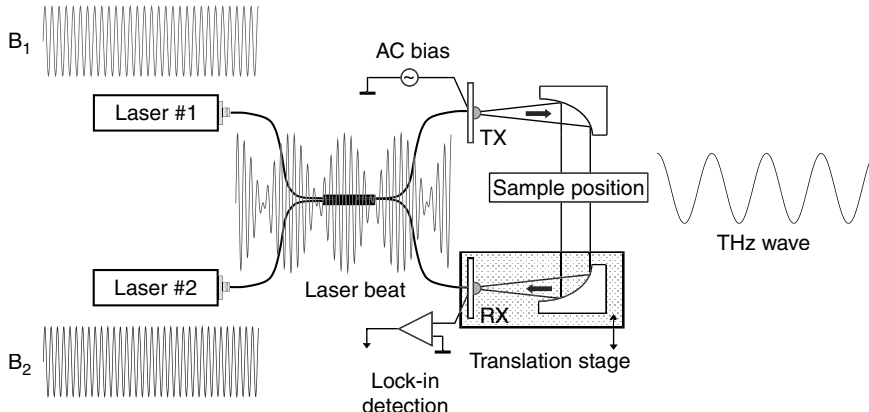
11.9 (a) Operation modes of a UTC diode as terahertz receiver. The circles indicate the operation points under reverse and forward bias.
 (b) Receiver signal under reverse bias (circles, 'homodyne detection') and forward bias (triangles, 'square-law detection'). (From Nagatsuma *et al.*, 2010, reproduced courtesy of EMW Publishing.)

and in particular the possibility to toggle between coherent and incoherent detection techniques.

11.3 Coherent signal detection

Coherent detection involves the acquisition of both amplitude and phase of the terahertz wave. First demonstrated by the MIT group in 1998 (Verghese *et al.*, 1998; Verghese and McIntosh, 2002), the technique has since found widespread use as a particularly sensitive measurement scheme.

A coherent measurement utilizes a pair of photomixers (Fig. 11.10), with one device acting as terahertz emitter, the second as receiver. Both are optically pumped by the same two-color laser source. The beat signal of the two optical



11.10 Continuous-wave spectroscopy set-up with coherent signal detection. TX = terahertz transmitter, RX = receiver.

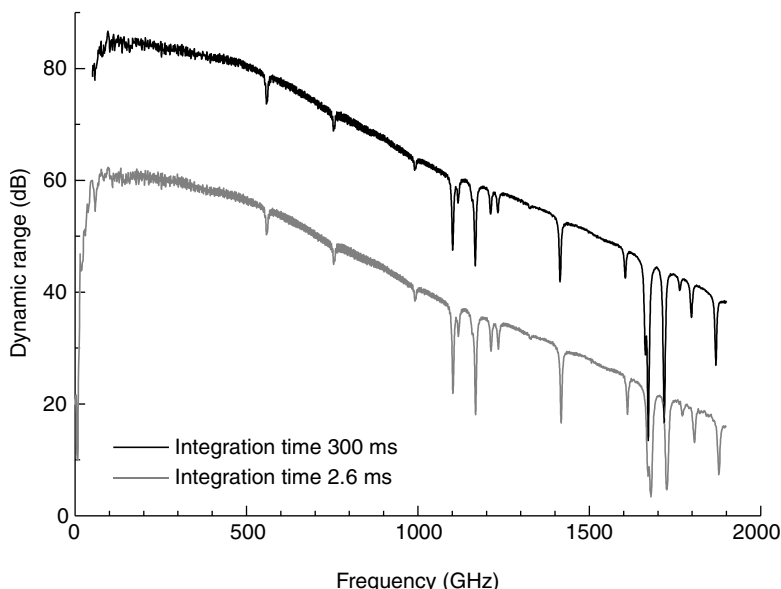
frequencies periodically modulates the photoconductance of the receiver photomixer. When an incident terahertz wave generates a voltage in the antenna, the MSM junction is biased and a small photocurrent flows into a transimpedance amplifier. Since typical photocurrent levels are in the nA to μ A range, one commonly employs lock-in detection. The required signal modulation can either be realized by including a mechanical chopper in the optical or terahertz beam, or electronically by feeding an AC bias to the emitter.

Due to the high detection sensitivity, a dynamic range in excess of 80 dB can be attained (Fig. 11.11). Given a maximum emitter power of $\sim 1 \mu\text{W}$, and rescaling to an integration time of 1 s, the noise-equivalent power (NEP) is approximately $30 \text{ pW/Hz}^{1/2}$. This is below the NEP of present-day Golay cells ($\sim 100 \text{ pW/Hz}^{1/2}$ (http://www.tydexoptics.com/products/thz_optics/golay_cell/)) and in fact close to that of Helium-cooled bolometers ($\sim 10 \text{ pW/ Hz}^{1/2}$ (Chen *et al.*, 1997; Matsuura and Ito, 2005)), yet without the complexity of the latter.

The photocurrent I_R in the receiver photomixer is proportional to the amplitude of the incident terahertz electric field, E_{THz} , and furthermore depends on the phase difference $\Delta\phi$ between the terahertz wave and the optical beat (Vergheze *et al.*, 1998; Roggenbuck *et al.*, 2010):

$$I_R \propto E_{\text{THz}} \cos(\Delta\phi) = E_{\text{THz}} \cos(2\pi v \Delta L/c). \quad [11.3]$$

Here, v is the terahertz frequency, c is the speed of light, and ΔL is the deviation from zero path difference at the receiver, that is, the difference between the length of the receiver arm, and the length of the emitter arm including the terahertz path.

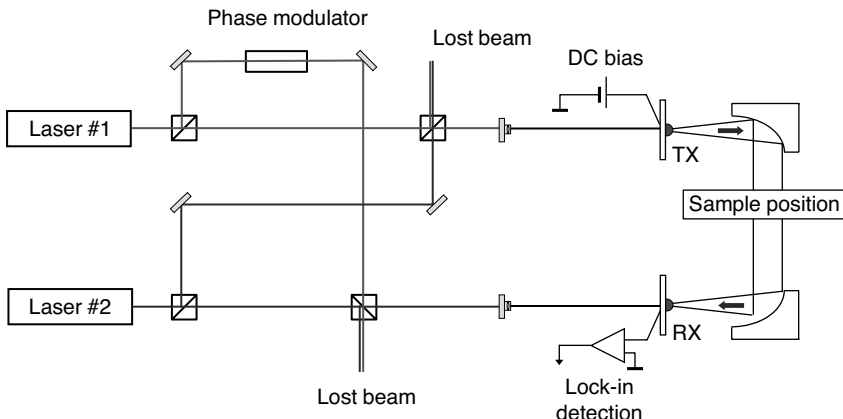


11.11 Dynamic range of a frequency-domain spectroscopy set-up using ion-implanted GaAs photomixers with log-spiral antennas. The dynamic range in dB is computed via $20 \times \log(I_{\text{Signal}}/I_{\text{Noise}})$, where I_{Signal} is the signal photocurrent and I_{Noise} is the noise current, measured with a blocked beam. Two curves are shown, acquired with lock-in integration times of 300 ms and 2.6 ms per frequency point. As expected, a factor of 100 in the integration time corresponds to 20 dB in the dynamic range. The dips are absorption lines of water vapor (Toptica Photonics, previously unpublished).

Extracting the amplitude information E_{THz} therefore requires a variation of $\Delta\phi$. In the set-up of Fig. 11.10, this is accomplished by a delay stage in the terahertz beam path (Deninger *et al.*, 2008). This implementation, though easily aligned, is rather slow, as the velocity of a mechanical translation stage is limited to a few mm per second. Three – faster – alternatives will be presented in Sections 11.3.1–11.3.3.

11.3.1 Phase variation with electro-optic modulator

Particularly fast phase modulation is achieved by means of an electro-optic modulator (EOM) (Sinyukov *et al.*, 2008; Göbel *et al.*, 2008, 2009). In the set-up sketched in Fig. 11.12, both laser outputs are evenly split, and one of the four generated beams passes the EOM, for example, a $\text{MgO}: \text{LiNbO}_3$ phase modulator. The beams are combined again and fed to the terahertz emitter and receiver modules.



11.12 Frequency-domain set-up with electro-optic phase modulator in the laser beam path. Note that at the terahertz emitter, the AC bias of Fig. 11.10 has been replaced by a DC voltage. (After Sinyukov *et al.*, 2008.)

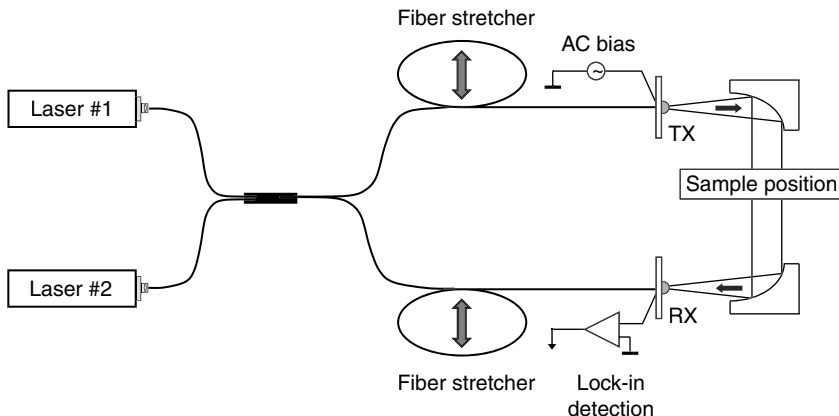
In contrast to a delay stage in the terahertz path, where a stroke of several hundred microns is required to scan the full terahertz wavelength, the EOM approach requires a path length change by no more than the laser wavelength ($\sim 1 \mu\text{m}$) in order to achieve a 2π phase variation. This is easily accomplished by the EOM, where the applied voltage changes the refractive index and thus, the optical length of the crystal.

It is even possible to use the phase modulation ramp as driving signal for the lock-in detection, eliminating the need for further mechanical or electronic chopping of the terahertz wave. To this end, modulation rates of 100 kHz have already been employed (Sinyukov *et al.*, 2008) – five to six orders of magnitude faster than a motor-driven translation stage.

One drawback of this approach is that 50% of the laser power is lost in the second set of beam splitters (see Fig. 11.12), and thus additional laser amplifiers may be required to provide the required optical power on the photomixer. Further, the sensitivity of the terahertz phase on the optical path length can turn into a curse, as path length jitter on the order of $\sim 1 \mu\text{m}$ results in a complete loss of phase information, even though the terahertz amplitude is still measured accurately (Göbel, 2010).

11.3.2 Phase variation with fiber stretcher

Fiber stretchers offer another possibility of rapid phase modulation in the optical beam path (Gregory *et al.*, 2007). Polarization-maintaining fiber extensions of several tens of meters are wound around a piezoelectric



11.13 Frequency-domain set-up with a pair of fiber stretchers. (After Roggenbuck *et al.*, 2011.)

actuator, which is driven by an AC voltage with an amplitude of typically 100–400 V (Roggenbuck *et al.*, 2011).

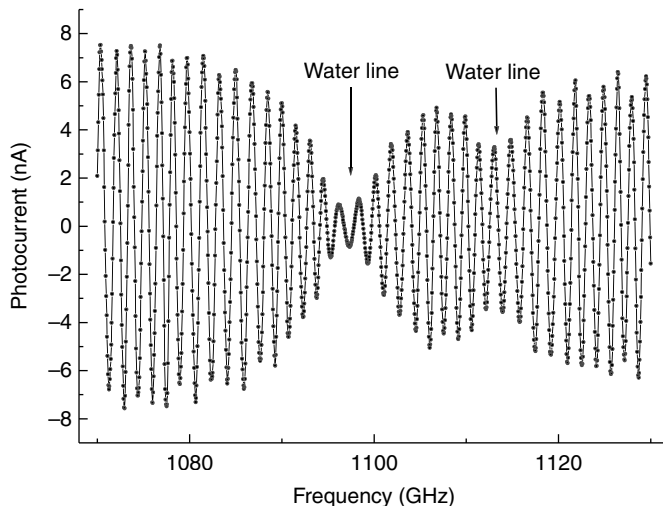
Roggenbuck *et al.* describe the usage of two identical fiber stretchers – one in the transmitter arm and the second one, operated with inverted voltage, in the receiver arm (Fig. 11.13). Compared to a single-stretcher assembly, the two-fiber approach reduces the sensitivity to thermal drifts, as common drifts, for example, of the ambient temperature which equally affect the length of both arms. The total path length modulation is as large as 1.4 cm at a modulation frequency of 300 Hz, or 3 mm at 1400 Hz.

In Fig. 11.13, the terahertz emitter is once again AC-biased, which is necessary to eliminate disturbances such as optical power variations resulting from the length change of the optical fiber. Switching the emitter voltage inverts the terahertz signal, but not the disturbance, which is thus cancelled out.

Benefits of a fiber modulator are fast data rates up to kHz ranges, the compactness of an all-fiber set-up, and an efficient use of the available laser power (no lost beams). Demerits are the significant costs for the fiber assembly and the high-voltage driver.

11.3.3 Phase variation in controlled frequency steps

Rather than modulating the path length ΔL , the terahertz phase can equally be varied by scanning the frequency in small steps (cf. Equation [11.3]). The effect is similar to scanning an interference pattern in frequency (Fig. 11.14), and has been exploited for thickness and distance measurements (Mouret *et al.*, 2007), and for spectroscopy of solid-state samples (Roggenbuck *et al.*, 2010).



11.14 Frequency scan across two water vapor absorption lines. Scan range is 1070–1130 GHz at 50 MHz step size. The fringe spacing is approximately 1.6 GHz, which corresponds to a path length difference ΔL of approximately 20 cm. Note the variation of the fringe period at the line center (Toptica Photonics, previously unpublished).

In the absence of a sample, the spacing $\delta\nu$ of two adjacent ‘fringes’ (subsequent maxima of the receiver photocurrent) is obtained from Equation [11.3]:

$$\delta\nu = c/\Delta L. \quad [11.4]$$

Phase information is gathered from the extrema and zero crossings of the photocurrent oscillation. The *effective frequency resolution* of the phase data is thus $\delta\nu/4 = c/4\Delta L$. The resolution of the amplitude data is a factor of two lower ($c/2\Delta L$), because only the extrema are used for the amplitude analysis (Roggenbuck *et al.*, 2010).

For spectroscopy, this measurement technique is both promising and challenging. The spectral resolution is under experimental control, simply by adjusting the terahertz path length. In contrast to the approaches of Section 11.3.1 and 11.3.2, no further hardware is required. A first challenge is the need for accurate frequency control: a frequency step has to be much smaller than the fringe pattern spacing $\delta\nu$, which in turn should be chosen much smaller than the signature of interest. One solution for high-precision frequency control is presented in Section 11.4.1, subsection ‘Excursion: a quadrature interferometer for frequency control’.

A second challenge arises from the large density of data points, which increases the total measurement time. A 2 THz scan with 40 MHz step size

consists of no less than 50 000 data points! Completing a scan in a few minutes then calls for lock-in times in the single-ms range. This is only possible if the dynamic range of the spectrometer is sufficiently high, or put differently: with ‘premium’ photomixers.

11.4 Laser sources

In the early days of photomixing, continuous-wave Ti:Sapphire lasers were employed (Brown *et al.*, 1993b; Siebert *et al.*, 2002a), soon to be replaced by distributed Bragg reflector (DBR) diode lasers (McIntosh *et al.*, 1995). However, for high-resolution measurements, the large DBR linewidth (40 MHz on a 10 ms scale) required complex stabilization schemes (Chen *et al.*, 1997).

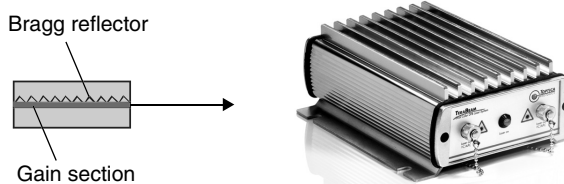
Today, distributed feedback (DFB) diodes have become the workhorses for photomixing (Demers *et al.*, 2007; Gregory *et al.*, 2007; Wilk *et al.*, 2007; Deninger *et al.*, 2008; Wilk *et al.*, 2008; Roggenbuck *et al.*, 2010; Scheller *et al.*, 2010; Stanze *et al.*, 2011). DFB lasers offer robust mono-mode operation, wide continuous tuning, convenient frequency control and a very compact footprint. Fiber-optic beam combination facilitates the beam overlap on the photomixer.

Section 11.4.1 portrays DFB laser sources, with an excursion into means for precise frequency control. Sections 11.4.2 and 11.4.3 look at alternative approaches: lasers that emit two wavelengths simultaneously, from one device.

11.4.1 Twin-distributed feedback (DFB) lasers

DFB diodes were originally developed for telecommunication, at wavelengths around 1.5 μm (Tohmori *et al.*, 1993). Today, DFBs are commercially available at literally any wavelength between 750 nm and 3500 nm. Driven by applications in alkaline spectroscopy, high-power devices (>100 mW) have been developed near 780 nm (Rubidium D₂ line) and 850 nm (Cesium D₂ line). These wavelengths match the excitation requirements of GaAs-based photomixers, while the 1.5 μm lasers are well suited for InGaAs terahertz emitters.

The key element of a DFB diode is a grating structure (Bragg reflector) embedded within the gain section of the semiconductor (Fig. 11.15). Changing the grating pitch, either electrically or thermally, tunes the lasing wavelength. Electric tuning works on time scales as short as microseconds, yet the tuning range is limited by the current span from laser threshold to maximum power – a few 10 GHz, if one is willing to accept a 100% power



11.15 Left: schematic of a DFB laser diode. Right: commercial two-color DFB laser head. The two diodes, fiber-inline optical isolators and fiber-optic beam combiners are contained in the housing, which has a footprint of 16 × 13 × 6 cm.

variation. Thermal tuning, by contrast, is comparatively slow – due to thermal inertia, a temperature step of, for example, 40 K takes 10–20 s – but on the other hand, covers a huge frequency span. Typical thermal tuning coefficients $\Delta\nu/\Delta T$ are

$$\Delta\nu/\Delta T \sim -25 \text{ GHz/K} \text{ at } 780 \text{ nm and } 850 \text{ nm} \quad [11.5]$$

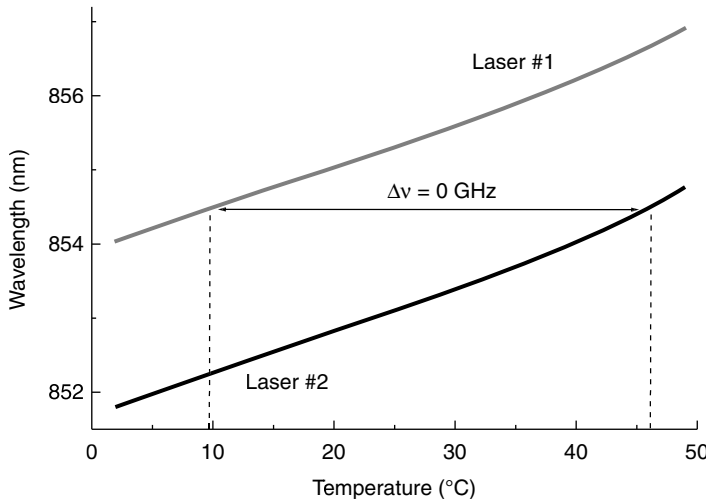
$$\Delta\nu/\Delta T \sim -10 \text{ GHz/K} \text{ at } 1550 \text{ nm} \quad [11.6]$$

and consequently, the 40 K temperature step sweeps the laser frequency across 400–1000 GHz (Fig. 11.16).⁵

This scan is usually mode-hop free, that is, without any discontinuities in frequency or output power. In photomixing systems, thermal tuning is the most widely used mechanism for laser frequency control.

Both wavelength regimes – 780/850 nm on one side, 1.5 μm on the other side – have their advantages. Shorter wavelengths offer a wider scan range, due to the larger tuning coefficient (Equations [11.5] and [11.6]). However, these diodes are not (yet) mass-produced, plus require customized optical components, such as free-space optical isolators with Terbium Gallium Garnet crystals, or non-standard fiber-optic arrays. All of these elements drive up the cost of the lasers. Telecom-band diodes, on the other hand, are available in highly integrated ‘butterfly’ packages, with miniaturized optics and fiber pigtail, and a two-color laser at 1.5 μm can thus be realized in a very compact set-up (Fig. 11.15).

⁵ Ultimately, the tuning range of a DFB laser is limited by the fact that the gain profile of the semiconductor shifts about five times more than the grating-selected laser line, when a temperature step is applied. Eventually, when gain profile and grating line no longer match, the diode starts lasing at the gain maximum, in an uncontrolled way.



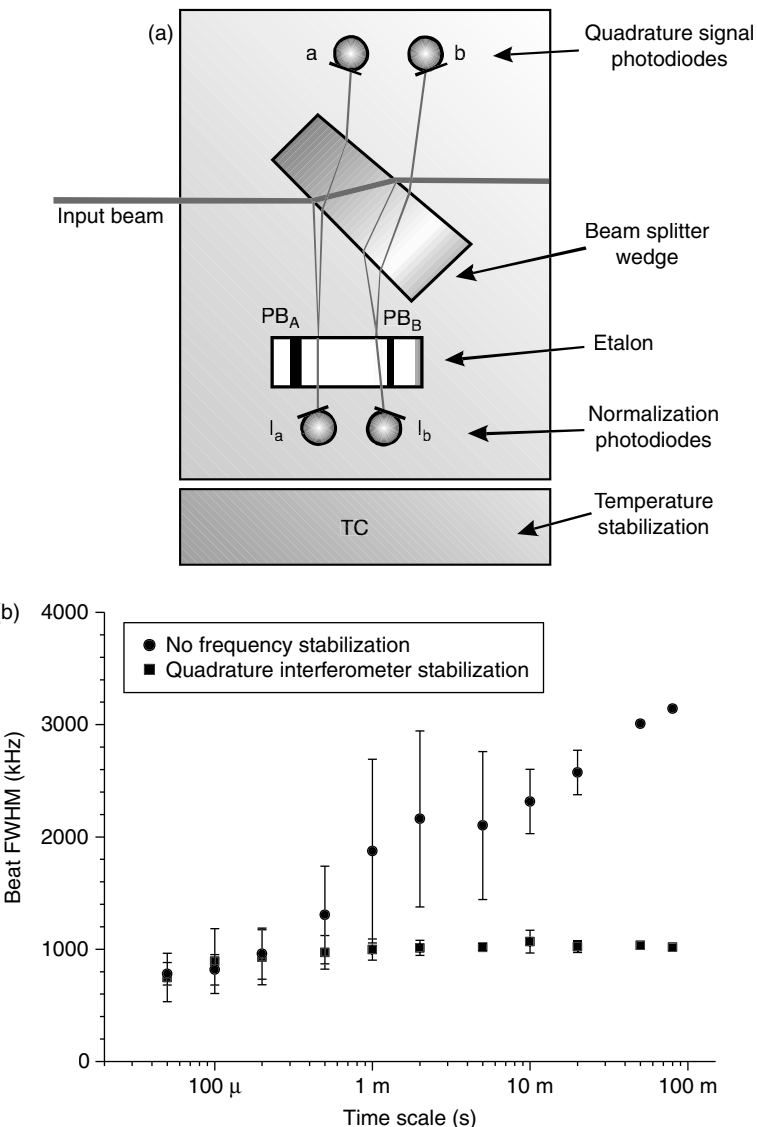
11.16 Temperature tuning of DFB lasers. The wavelengths of laser #1 and laser #2 match at temperatures of $T_1 = 10^\circ\text{C}$ and $T_2 = 46^\circ\text{C}$. Heating laser #1 and cooling laser #2 increases the terahertz difference frequency, to a maximum value of 2.08 THz (Toptica Photonics, previously unpublished).

The frequency resolution of a cw terahertz system is only limited by the frequency stability and linewidth of the utilized laser source. This comes as a curse or a blessing. Given a highly stable laser system, the desired terahertz frequency can be addressed with single-Megahertz resolution – but vice versa, this requires thermal control in the sub-Millikelvin range.

The two degrees of freedom for frequency control (temperature and current) open the possibility to fine-tune not only the emission wavelength, but also the laser power during a frequency scan. One device designed to accomplish this is described in the following Excursion.

Excursion: a quadrature interferometer for frequency control

A quadrature interferometer offers an elegant way to stabilize both frequency and power of the DFB seed lasers. The principle is based on quadrature signal generation within a low-finesse Fabry-Perot etalon (Müller-Wirts, 2001; Kinder, 2004; Deninger *et al.*, 2008). From each laser, a probe beam is tapped off and fed to the interferometer head (Fig. 11.17, top), where a wedge-shaped beam splitter generates two further probe beams PB_A and PB_B . The probe beams enter the etalon under slightly different angles, which gives rise to a pair of interference signals with a relative phase of $\pi/2 = 90^\circ$. These signals are detected by two photodiodes (*a*, *b*) and combined into a quadrature signal (resembling the components of a vector in polar coordinates), the phase of which is a linear function of the optical



11.17 (a) Quadrature interferometer. (b) Beat signal linewidth of two DFB lasers with and without frequency stabilization, for time scales from 50 μ s to 80 ms. (From Deninger *et al.*, 2008, reprinted with permission from American Institute of Physics.)

frequency. The measured phase is compared with, and stabilized to, a set-point phase which represents the target frequency. The resolution of this frequency control loop is approximately 1/10 000 of the etalon free spectral

range (FSR). An FSR of, for example, 8 GHz thus translates into sub-MHz frequency control.

Two additional photodiodes in the interferometer head (I_a and I_b in Fig. 11.17a) monitor the laser intensity. An additional feedback loop then corrects the laser current, in order to maintain a constant optical output over the entire tuning range of the lasers.

The linewidth of the terahertz wave is given by the convolution of the linewidths of the two seed lasers. Figure 11.17b shows linewidth measurements on time scales between 50 μ s and 80 ms, with and without active frequency control. In the unregulated case, the beat linewidth amounts to > 3 MHz at 80 ms integration time. With the feedback loop in place, the linewidth remains at approximately 1 MHz, independent of the integration time.

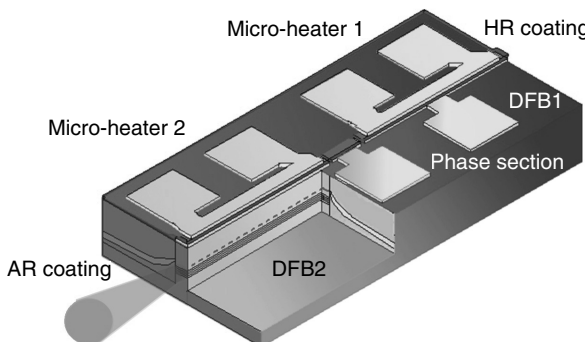
While not every cw terahertz study requires this extreme frequency resolution, there are applications that benefit from this approach, such as precision spectroscopy of low-pressure gas samples (Section 11.5.1) or experiments that require a high-frequency repeatability, for example, when comparing spectra with and without a sample in place (Section 11.5.2).

11.4.2 Dual-mode and multi-mode laser diodes

The complexity of the laser set-up would be greatly reduced if both laser colors were to be produced simultaneously in a single source. Laser diodes with two longitudinal modes have indeed been used for cw terahertz generation (Gu *et al.*, 1998; Wilk *et al.*, 2007; Klehr *et al.*, 2008; Osborne *et al.*, 2008). One possibility is to employ both the fundamental and the first order lateral mode (Wilk *et al.*, 2007). Alternatively, non-adjacent laser modes can be selected by micro-structuring the ridge waveguide of the emitter (Osborne *et al.*, 2008). However, while the mode spacing of these emitters is typically in the range of a few hundred GHz, the terahertz difference frequency can hardly, if at all, be frequency tuned.

A tunable dual-mode DFB laser was realized by Kim *et al.* (2009). The laser consists of two separate DFB sections and a reversely biased phase section (Fig. 11.18) that serves to suppress unwanted side modes in the emission spectrum. Two micro-heaters, one on top of each DFB section, allow for individual control of the two laser lines ($\lambda \sim 1.57$ μ m). Thus, the frequency spacing can be tuned continuously up to ~ 1 THz (Kim *et al.*, 2011). In proof-of-principle experiments, photomixers made of Fe⁺ implanted InGaAs (Kim *et al.*, 2009) or LT-InGaAs (Kim *et al.*, 2011) converted the optical beat into monochromatic terahertz radiation.

Drawing on the plethora of miniature optoelectronic components based on InP technologies, even higher integration levels can be envisaged. These include additional on-chip semiconductor amplifiers, EOMs for phase



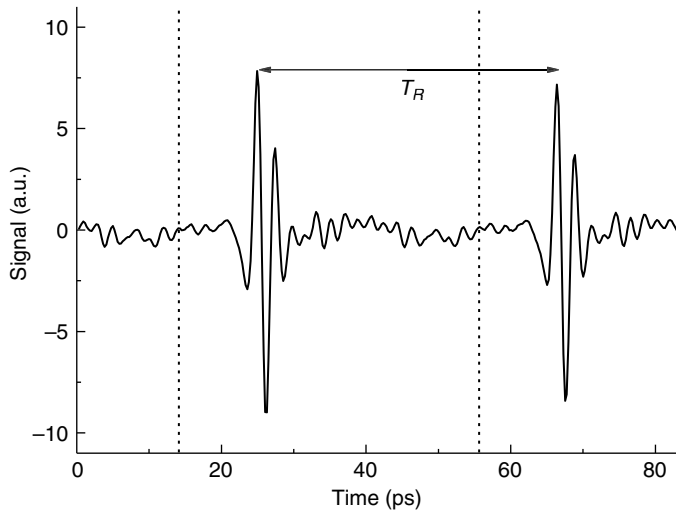
11.18 Dual-mode distributed feedback laser diode. (From Kim *et al.*, 2009, reprinted with permission of the Optical Society of America.)

variation, or even a monolithic set-up that incorporates a waveguide-type terahertz emitter as well.

The idea of using multiple emission lines from a single diode is not restricted to two lasing modes only. Taken to the extreme, the entire gain spectrum of a multi-mode laser diode can be converted into terahertz radiation. Pioneered as early as 1997 (Tani *et al.*, 1997), the concept was explored in detail by Scheller and Koch (2009). The equidistant mode spacing of a standard Fabry-Perot laser diode produces a comb-like terahertz spectrum. When the terahertz signal is sampled with a moving delay stage, the time-domain detector photocurrent indeed exhibits a pulse-like shape (Fig. 11.19), with a repetition time equal to the inverse mode spacing of the laser chip. A Fourier transform of the time trace yields a terahertz spectrum, the bandwidth of which is determined by the gain profile of the laser (~ 600 GHz in the example of Fig. 11.19). This technique has been dubbed ‘quasi-time-domain spectroscopy’ (QTDS).

Compared to twin-DFB systems, the charm of QTDS is that low-cost, multi-mode laser diodes can be used, with a price tag about an order of magnitude lower than that of a DFB diode. Vice versa, the single-line systems of Section 11.4.1 have advantages in terms of spectral resolution and dynamic range. Since the multi-mode diode is not tunable, the spectral resolution is limited by the mode spacing, which is typically on the order of several tens of GHz. Also, the amplitude of any frequency component is proportional to $(\text{laser power})^2/(\text{number of modes})^2$, and therefore broader spectral information is paid for in terms of dynamic range.

Different groups have therefore combined the QTDS concept with the twin-laser approach (Brenner *et al.*, 2010; Scheller *et al.*, 2010). Such a hybrid system unites the spectral brightness of monochromatic terahertz radiation



11.19 Quasi-time-domain spectroscopy. The emitter and receiver photomixer are illuminated by a multi-mode laser diode, and the terahertz signal is sampled via a moving delay stage. The signal period T_R of the time-domain waveform is the reciprocal mode spacing of the diode laser ($T_R = 41 \text{ ps} = (24 \text{ GHz})^{-1}$). (From Scheller and Koch, 2009, reprinted with permission of the Optical Society of America.)

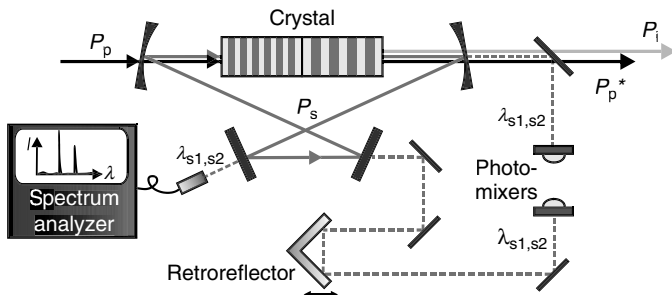
and the possibility to determine unambiguous depth profiles via QTDS ‘time-of-flight’ measurements (Scheller *et al.*, 2010).

11.4.3 Dual-wavelength optical parametric oscillators (OPOs)

In an optical parametric oscillator (OPO), a nonlinear crystal placed in a resonator configuration converts pump light of frequency ω_p into signal and idler waves of frequencies ω_s and ω_i , respectively (Harris, 1969), with

$$\omega_p = \omega_s + \omega_i \quad [11.7]$$

The pump laser is usually a high-power solid-state laser, for example, a Ti:Sapphire or Yb:YAG source. Three-wave interaction within the crystal amplifies the signal and idler wave, at the cost of the pump wave amplitude. A key advantage of an OPO is the wide tuning range of signal and idler wavelengths – tens to hundreds of nanometers (Vainio *et al.*, 2008) – which is realized by scanning the pump wavelength, changing the crystal temperature, and/or the usage of crystals with different poling periods (Breunig



11.20 Two-color OPO, with a segmented periodically poled crystal. P_p , P_s , P_i and P_p^* denote the pump light, signal wave, idler and residual pump light, respectively. (From Breunig *et al.*, 2008.)

et al., 2008). In the special case of a degenerate OPO, the frequencies of signal and idler are equal.

One might naively expect that a near-degenerate OPO readily provides two laser lines spaced apart at terahertz frequencies. Unfortunately, near-degenerate OPOs have a tendency to mode hops and thus, unstable operation, though recent results indicate that this problem can be overcome by including additional intracavity optics, such as a spectrally selective grating (Vainio and Halonen, 2011).

Figure 11.20 depicts a cw terahertz set-up based on a two-color OPO. The nonlinear element – a MgO-doped, periodically poled Lithium Niobate (PPLN) crystal – features two sections: the former has a fixed poling period while the latter consists of five different periods. Thus, two signal waves are generated, with a difference frequency tunable from 0.64–0.85 THz and 1.4–5.3 THz. Fine-tuning over approximately 200–1000 GHz is accomplished via the crystal temperature. Partially transmissive mirrors couple out a fraction of the signal waves, and ion-implanted InGaAs photomixers convert the optical beat into cw terahertz radiation. The required overlap of both laser colors on the antenna is automatically secured, as both wavelengths circulate in the resonator.

It should be noted that the OPO concept can be extended to direct intracavity terahertz generation, without involving any photomixing. This scenario comprises a two-stage process: the nonlinear crystal converts the pump light to a first signal wave, which in turn drives a second parametric process that yields terahertz light. Power levels above 1 μ W have been demonstrated at a frequency of 1.4 THz (Sowade *et al.*, 2009; Kiessling *et al.*, 2011).

Table 11.1 compares the spectral properties of the laser sources described in this chapter, along with the accessible terahertz frequency range and the spectral resolution of the terahertz signal.

Table 11.1 Comparison of laser sources

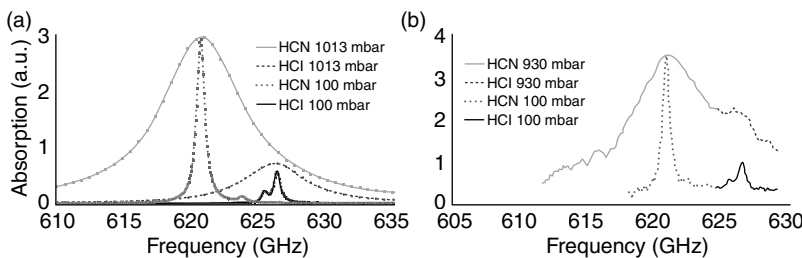
Specification	DFB lasers at 850 nm	DFB lasers at 1550 nm	Multi-mode diode	Dual-wavelength OPO
Laser wavelength	853 nm + 855 nm	1546 nm + 1550 nm	660 nm	1400–1470 nm
Laser power	2 × 50 mW (fiber output)	2 × 30 mW, up to 80 mW (fiber output)	100 mW (free space)	2 × 40 mW, up to 1 W (free space)
Laser tuning range	±1.3 nm	±2.2 nm	–	70 nm
THz frequency range	0–2.0 THz (tunable)	0–1.1 THz (tunable)	0.6 THz (broadband)	0.64–5.3 THz (tunable)
Frequency accuracy	2 GHz absolute, 10 MHz relative (100 MHz absolute, < 1 MHz relative with quadrature interferometer)	–	25 GHz (resonator mode spacing)	700 MHz (resonator mode spacing)
Reference	Our work	Our work	Scheller and Koch, 2009	Breunig <i>et al.</i> , 2008

11.5 Selected applications of photomixing continuous-wave terahertz systems

As applications of terahertz radiations are covered in several other chapters of this compendium, this section, rather than providing a research review, picks a few personal highlights – measurement tasks on the verge of industrial implementation, that might benefit from the particular advantages of photomixing systems. The topics considered here are high-resolution gas spectroscopy (Section 11.5.1), solid-state spectroscopy and measurements of a sample's complex dielectric constant (Section 11.5.2), and imaging (Section 11.5.3). The latter is particularly interesting as alternative techniques, for example, all-electronic emitters, have also matured over the last years, and I will discuss where photomixing approaches have their merits and limits.

11.5.1 Trace gas detection

Many polar gas molecules possess distinct rotational transitions in the terahertz frequency range. At room temperature and standard pressure, absorption linewidths appear pressure-broadened to a few GHz (Preu *et al.*, 2011). At low (sub-mbar) pressures, however, transition lines narrow to single-MHz widths (Matsuura and Ito, 2005). This opens the possibility to identify individual gases by their spectral ‘fingerprint’, even in a cluttered environment. While trace gas detection is also possible in the near-IR, infrared lasers



11.21 Terahertz spectra of a mixture of hydrocyanic acid and hydrochloric acid, at two different gas pressures; (a) simulation, (b) measurement. (© A. Majewski, Goodrich Corp.)

generally have a limited tuning range, and in the extreme case, every gas species to be measured may require an individual laser set-up. Moreover, gas compounds within a cluttered environment – taken to the extreme, in flames and smoke – might be hard to diagnose if the scene is opaque to near-IR light. Unique benefits of cw terahertz spectroscopy are thus chemical specificity (a single terahertz spectrometer is able to detect and identify a large number of different gases) a decade-spanning bandwidth, MHz-level resolution, and the ability to be used in hitherto inaccessible settings, such as a full-scale fire (Shimizu *et al.*, 2011). Sensitivities down to the parts-per-million range were demonstrated using a time-domain set-up and a multipass cell (Harmon and Cheville, 2004).

Frequency-domain techniques were exploited for high-precision spectroscopy of SO₂, CH₃CN and CO back in the early days of photomixing (Pine *et al.*, 1996; Chen *et al.*, 1997; Matsuura *et al.*, 1998). A decade later, a mobile gas-phase terahertz spectrometer has already passed first field tests.⁶ The system uses an onboard pump to transfer a gas sample into a multipass absorption cell. The cell is evacuated to ~ 70 torr in less than one minute. A frequency scan of 1 THz, at a step size of 500 MHz, is completed in about two minutes. The reported frequency resolution and repeatability are 1.4 MHz and 4 MHz, respectively (Majewski, 2008). Figure 11.21 shows results obtained with a mixture of hydrocyanic acid (HCN) and hydrochloric acid (HCl).

Prospective applications include both industrial process control, and threat detection in public institutions. Demands are high: a chemical detection system in, say, a subway station must be able to unambiguously identify hazardous substances, against a background of cleaning agents, glues, engine fumes, perfumes and paint – without risking any false alarm.

⁶ Model TMS-1000, Goodrich ISR Systems, Danbury/USA.

11.5.2 Spectroscopy of solids

Not only gases, but also non-polar organic solids, including a number of explosives, show absorption signatures between 500 GHz–3 THz (Kemp *et al.*, 2003; Federici *et al.*, 2005). The absorption peaks result from either molecular vibrational modes or from the interaction between molecules. An example for the latter is the well-known 0.8 THz line in the plastic explosive RDX (Kemp *et al.*, 2003; Huang *et al.*, 2004). Complementing the information gained from amplitude spectra, phase measurements and consequently, refractive index data reveal precise insights into the properties of samples. In the case of polymers, the change of the refractive index with temperature can be used to detect minute structural changes (Wietzke *et al.*, 2009). For fiber-reinforced plastics, the refractive index yields information on the orientation of the fibers (Jördens *et al.*, 2010).

Most of the work in the field of terahertz-aided material characterization has been accomplished with time-domain techniques. In this case, the refractive index is computed from the time delay introduced when the sample is placed into the beam. However, cw techniques, too, allow for determining both the transmittance and the refractive index of a sample, or equivalently, the complex dielectric coefficient, with simple arithmetics.

As outlined in Section 11.3, amplitude and phase data of a frequency-domain measurement are readily accessible if a coherent detection scheme is used. As the raw data are commonly affected by a multitude of system-inherent or environmental side effects – frequency-dependent antenna response, parasitic interferences, water vapor absorption lines, etc. – an established approach involves comparing a sample spectrum with a reference run, which is recorded with an empty aperture and otherwise identical settings. This normalization requires a high repeatability of the signal, that is, a highly stable terahertz amplitude and reproducible frequency settings.

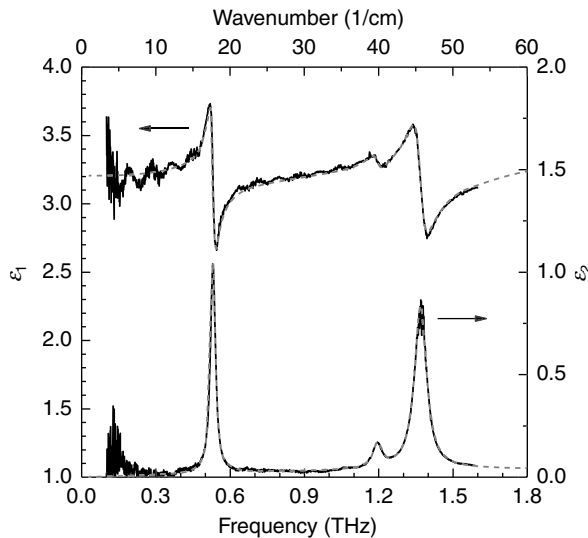
From the frequency-dependent amplitude values of sample and reference, $A_s(v)$ and $A_{\text{ref}}(v)$, the sample transmittance $T(v)$ is computed by taking the ratio

$$T(v) = [A_s(v)/A_{\text{ref}}(v)]^2. \quad [11.8]$$

Similarly, subtracting the respective phase values of sample and reference, $\phi_s(v)$ and $\phi_{\text{ref}}(v)$ yields the phase shift $\delta\phi$ introduced by the sample:

$$\delta\phi(v) = \phi_s(v) - \phi_{\text{ref}}(v) + 2\pi \cdot m(v), \quad [11.9]$$

with an integer number $m(v)$. The ambiguity in m can be resolved in a broadband measurement. Neglecting multiple reflections within the sample, one finds



11.22 Real part $\epsilon_1(\omega)$ (left axis) and imaginary part $\epsilon_2(\omega)$ (right axis) of the dielectric constant of α -lactose monohydrate. The dashed lines depict a Drude-Lorentz model fit of the transmission $T(\omega)$ and refractive index $n(\omega)$. (From Roggenbuck *et al.*, 2010, reprinted with permission from IOP Publishing.)

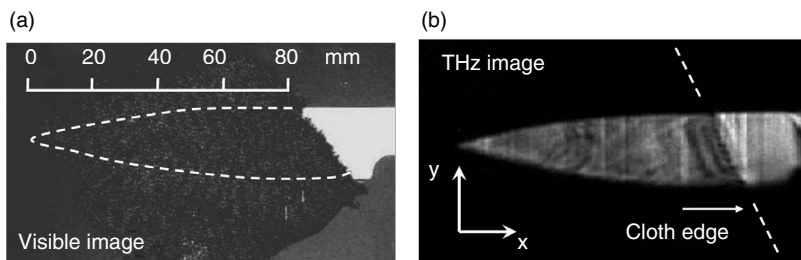
$$\delta\phi(v) \approx 2\pi(n - 1) d \cdot v/c, \quad [11.10]$$

where d is the sample thickness and n the refractive index. Thus, $\delta\phi$ approaches zero for $v \rightarrow 0$ and increases linearly with v in a frequency range with constant refractive index. Once $T(v)$, $\delta\phi(v)$ and the sample thickness are known, one can compute the dielectric constant (for a detailed description see Roggenbuck *et al.*, 2010).

Figure 11.22 depicts the real part ϵ_1 and imaginary part ϵ_2 of the dielectric constant for the example of α -lactose monohydrate, at frequencies from 100 GHz to 1.6 THz. Note that the data do not show any more water vapor signatures, even though the measurements were performed in room air. Normalizing the lactose data to the reference scan completely eliminated the water absorption lines, despite the > 15 dB signal attenuation at 1097 GHz and 1163 GHz (cf. Fig. 11.11).

11.5.3 Imaging

Since its first demonstration at AT&T Bell Laboratories in 1995 (Hu and Nuss, 1995), terahertz imaging has gained an ever-increasing momentum (Chan *et al.*, 2007; Tonouchi, 2007; Jansen *et al.*, 2010). Admittedly, most of



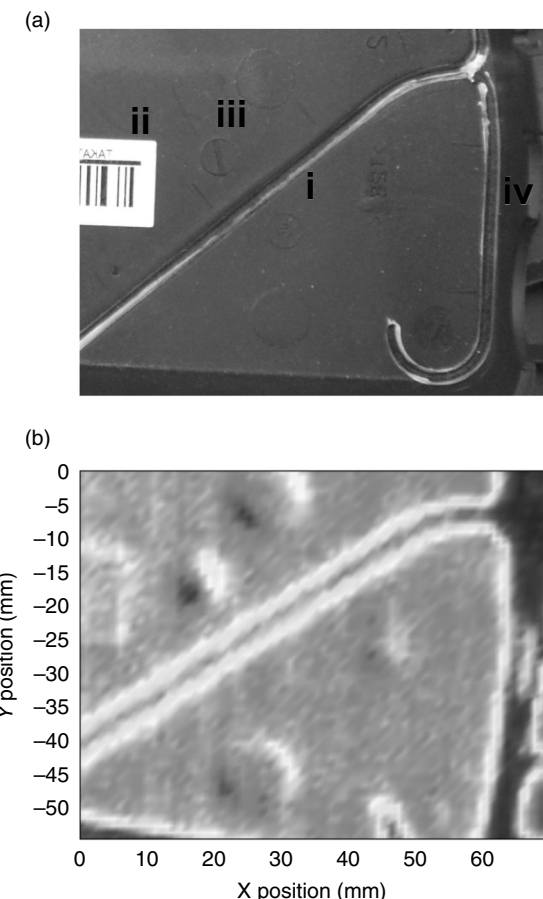
11.23 Photograph of (a) 500 GHz image and (b) a ceramic knife blade hidden behind 1 mm of black denim. (© I. Gregory, TeraView.)

the research in this field has been carried out with time-domain techniques, which – via time-of-flight-techniques – provide information on an object's thickness, absorption coefficient and refractive index, even in the case of multi-layered samples. This section focuses on results obtained with photomixing instruments, and attempts to highlight how cw systems might help to face the inherent challenges of any terahertz imaging apparatus: signal quality, imaging speed and cost.

Photomixing-based imaging was pioneered at the universities of Braunschweig (Kleine-Ostmann *et al.*, 2001) and Frankfurt (Siebert *et al.*, 2002a, 2002b) (both in Germany), and first commercialized by TeraView Ltd. (Cambridge, UK) (Gregory *et al.*, 2004b, 2005a). An example of a cw terahertz image is shown in Fig. 11.23, where a ceramic scalpel blade was placed behind black denim, to simulate a knife hidden in a pocket of a bag or jeans. The cloth is impenetrable to visible light, but at 0.5 THz the blade is clearly seen.

Data acquisition time is one of the key issues to be addressed if terahertz imaging is to succeed in a real-world scenario. While acquisition times of ~10 min per image were demonstrated as early as 2002 (Siebert *et al.*, 2002a), this might still be unacceptable for online monitoring tasks, for example, in industrial process control. Employing parallelized emitter/receiver configurations generates new challenges in terms of cost and laser power. An interesting proposal is the usage of interferometric imaging (Liu *et al.*, 2009), where radiation from a single terahertz source is received by an array of several detectors, and *correlations* between all possible detector pairs are exploited to obtain video-rate (16 ms/frame) images.

Since photomixing systems generally use lock-in detection, sampling speed is always paid for in terms of dynamic range. In the future, high-power emitters like the UTC photodiodes described in Section 11.2.2 could represent another leap forward. On the other hand, if spectral information can be sacrificed, all-electronic sources such as voltage-controlled oscillators with subsequent frequency multipliers might be the more



11.24 QTDS imaging of an airbag cover. (a) Photograph with positions of (i) intended break line, (ii) identification label, (iii) stampings within the polymer, and (iv) retainer bars. (b) Corresponding terahertz image. The peak-to-peak value of the signal is used as contrast mechanism. All of the features (i)–(iv) are recognized. (From Scheller *et al.*, 2011, reprinted with permission of the Optical Society of America.)

preferred choice. With these devices, dynamic ranges above 40 dB have already been demonstrated, at 40 μ s acquisition time per pixel (Quast and Löffler, 2009).

With respect to the third challenge, system cost, the quasi-time-domain approach outlined in Section 11.4.2 is certainly at the cutting edge. Besides the price advantage of the multi-line laser diode, QTDS imaging also resolves the 2π ambiguity of depth profile measurements (Scheller *et al.*, 2010), which monochromatic cw imaging has to face. Figure 11.24 depicts

the QTDS terahertz image of a polymeric airbag cover (Scheller *et al.*, 2011), which features a break line of reduced thickness. Utilizing the time-domain waveform data allows for extracting the thickness of the break line with submillimeter resolution. The example highlights the potential of this method for a contact-free, non-destructive testing routine.

11.6 Conclusion

Photomixing terahertz systems have undergone a considerable development over the past two decades and have come a long way from the initial, Ti:Sapphire-driven laboratory setups to compact and portable spectrometers that are already employed in first industrial implementations. Present-day photomixers are packaged with single-mode fiber pigtails that offer convenient operation and flexible handling.

GaAs and InGaAs/InP emitters each have their merits. Advances in material growth such as ErAs:GaAs nanocomposites, or ion-implanted GaAs, allow for reproducible manufacturing of GaAs photomixers with very short (~ 0.1 ps) carrier recombination times. GaAs emitters with broadband antennas have achieved record bandwidths above 3 THz, which compares favorably with InGaAs-based sources (≤ 2 THz). Vice versa, the InGaAs p-i-n diodes hold the prime position in terms of absolute output power. Uni-traveling-carrier diodes, in particular, have demonstrated RF outputs on the milliwatt level at 0.1 THz, and two-digit μW numbers at 1 THz, which is 1–2 orders of magnitude larger than GaAs photomixers. InGaAs devices also benefit from the availability of highly integrated, telecom-proven 1.5 μm laser technology.

On the receiver side, InGaAs/InAlAs superlattice structures have been successfully used as coherent detectors, even though the dynamic range is still 10–20 dB below that of GaAs spectrometers. An interesting innovation is the usage of UTC photodiodes for both coherent and incoherent detection by applying a forward or reverse bias, respectively.

Presently, the price for a fully-fledged cw terahertz system is on the US\$ 50–100 k level. This is still prohibitively high for broadband industrial use. On the other hand, it is generally agreed that prices will drop significantly if only the volume grows large enough – which seems to create some sort of ‘chicken and egg’ problem. At least, photomixing systems have the *potential* to become a widespread, inexpensive technology, and the possibility to use low-end multi-mode diodes is already a promising step in this direction.

11.7 Acknowledgements

I want to express my gratitude to Stephanie Schindler and Axel Roggenbuck (Toptica Photonics) who performed most of the measurements presented

in this chapter. I also want to thank Dennis Stanze and Thorsten Göbel (Fraunhofer Heinrich Hertz-Institute Berlin) for valuable discussions. Thanks to all of the researchers who provided figures for this chapter: Ingo Breunig (University of Freiburg), Ian Gregory (TeraView Ltd.), Markus Grüninger (University of Cologne), Namje Kim and Kyung Hyun Park (ETRI, Korea), Alexander Majewski (Goodrich Corp.), Emilien Peytavit (University of Lille), Tadao Nagatsuma (University of Osaka), Maik Scheller (University of Arizona), Makoto Shimizu and Tadao Ishibashi (NTT Laboratories).

11.8 References

- M. Awad, M. Nagel, H. Kurz, J. Herfort, K. Ploog : Characterization of low temperature GaAs antenna array terahertz emitters; *Appl. Phys. Lett.* **91**(18) (2007) 181124–181126.
- H.-G. Bach, A. Beling, G.G. Mekonnen, R. Kunkel, D. Schmidt, W. Ebert, A. Seeger, M. Stollberg, W. Schlaak : InP-based waveguide-integrated photodetector with 100-GHz bandwidth; *IEEE J. Quantum Electron.* **10**(4) (2004) 668–672.
- C. Baker, I. Gregory, M. Evans, W. Tribe, E. Linfield, M. Missous : All-optoelectronic terahertz system using low-temperature-grown InGaAs photomixers; *Opt. Express* **13**(23) (2005) 9639–9644.
- A. Beck, G. Ducournau, M. Zaknoune, E. Peytavit, T. Akalin, J.F. Lampin, F. Mollot, F. Hindle, C. Yang, G. Mouret : High-efficiency uni-travelling-carrier photomixer at 1.55 μm and spectroscopy application up to 1.4 THz; *Electron. Lett.* **44**(22) (2008) 1320–1321.
- A. Beling, H.-G. Bach, G.G. Mekonnen, R. Kunkel, D. Schmidt : Miniaturized waveguide-integrated p-i-n photodetector with 120-GHz bandwidth and high responsivity; *IEEE Photon. Technology Lett.* **17**(10) (2005) 2152–2154.
- J.E. Bjarnason, T.L.J.Chan, A.W.M. Lee, E.R. Brown, D.C. Driscoll, M. Hanson, A.C. Gossard, R.E. Muller: ErAs:GaAs photomixer with two-decade tunability and 12 μW peak output power; *Appl. Phys. Lett.* **85**(18) (2004) 3983–3985.
- C. Brenner, M. Hofmann, M. Scheller, M. Khaled Shakfa, M. Koch, I. Cámera Mayorga, A. Klehr, G. Erbert, G. Tränkle : Compact diode-laser-based system for continuous-wave and quasi-time-domain terahertz spectroscopy; *Opt. Lett.* **35**(23) (2010) 3859–3861.
- I. Breunig, J. Kiessling, R. Sowade, B. Knabe, K. Buse : Generation of tunable continuous-wave terahertz radiation by photomixing the signal waves of a dual-crystal optical parametric oscillator; *New J. Phys.* **10** (2008) 73003–73008.
- E.R. Brown, F.W. Smith, K.A. McIntosh: Coherent millimeter-wave generation by heterodyne conversion in low-temperature-grown GaAs photoconductors; *J. Appl. Phys.* **73**(3) (1993a) 1480–1484.
- E.R. Brown, K.A. McIntosh, F.W. Smith, M.J. Manfra, C.L. Dennis: Measurements of optical-heterodyne conversion in low-temperature-grown GaAs; *Appl. Phys. Lett.* **62**(11) (1993b) 1206–1208.
- E.R. Brown, K.A. McIntosh, F.W. Smith, K.B. Nichols, M.J. Manfra, C.L. Dennis, J.P. Mattia: Milliwatt output levels and superquadratic bias dependence in a low-temperature-grown GaAs photomixer; *Appl. Phys. Lett.* **64**(24) (1994) 3311–3313.

- E. R. Brown, K. A. McIntosh, K. B. Nichols, C. L. Dennis : Photomixing up to 3.8 THz in low temperature grown GaAs; *Appl. Phys. Lett.* **66**(3) (1995) 285–287.
- E.R. Brown: THz generation by photomixing in ultrafast photoconductors; *Int. J. High Speed Electron. Syst.* **13**:2 (2003) 497–545.
- W.L. Chan, J. Deibel, D.M. Mittleman: Imaging with terahertz radiation; *Rep. Prog. Phys.* **70** (2007) 1325–1379.
- P. Chen, G.A. Blake, M.C. Gaidis, E.R. Brown, K.A. McIntosh, S.Y. Chou, M.I. Nathan, F. Williamson : Spectroscopic applications and frequency locking of THz photomixing with distributed-Bragg-reflector diode lasers in low-temperature-grown GaAs; *Appl. Phys. Lett.* **71**(12) (1997) 1601–1603.
- J.F. Chen, J.S. Wang, M.M. Huang, N.C. Chen: Annealing dynamics of nitrogen-implanted GaAs films investigated by current–voltage and deep-level transient spectroscopy; *Appl. Phys. Lett.* **76**(16) (2000) 2283–2285.
- A.J. Deninger, T. Göbel, D. Schönherr, T. Kinder, A. Roggenbuck, M. Köberle, F. Lison, T. Müller-Wirts, P. Meissner : Precisely tunable continuous-wave terahertz source with interferometric frequency control; *Rev. Sci. Inst.* **79**(4) (2008) 44702–44707.
- J.R. Demers, R.T. Logan Jr., E.R. Brown: An optically integrated coherent frequency-domain THz spectrometer with signal-to-noise ratio up to 80 dB; *Microwave Photonics Tech. Digest*, Victoria, Canada (2007), pp. 92–95.
- G.H. Döhler, F. Renner, O. Klar, M. Eckardt, A. Schwahnhäuser, S. Malzer, D. Driscoll, M. Hanson, A.C. Gossard, G. Loata, T. Löffler, H. Roskos : THz-photomixer based on quasi-ballistic transport; *Semicond. Sci. Technol.* **20**(7) (2005) 178–190.
- G. Ducournau, A. Beck, K. Blary, E. Peytavit, M. Zaknoune, T. Akalin, J.-F. Lampin, M. Martin, J. Mangeney : All-fiber continuous wave coherent homodyne terahertz spectrometer operating at 1.55 μm wavelengths; *Proc. IRMMW-THz 2009*, Busan / Korea (2009).
- S. Duffy, S. Verghese, K. McIntosh, A. Jackson, A. Gossard, S. Matsuura : Accurate modeling of dual dipole and slot elements used with photomixers for coherent terahertz output power; *IEEE Trans. Microwave Theory and Tech.* **49**(6) (2001) 1032–1038.
- S.M. Duffy, S. Verghese, K.A. McIntosh: Photomixers for continuous-wave terahertz radiation; in D. Mittleman (Ed.): *Sensing with terahertz radiation*; Springer-Verlag Berlin Heidelberg (2003) 193–236.
- J.F. Federici, B. Schulkin, F. Huang, D. Gary, R. Barat, F. Oliveira, D. Zimdars : THz imaging and sensing for security applications – explosives, weapons and drugs; *Semicond. Sci. Technol.* **20** (2005) 266–280.
- H. Fushimi, T. Furuta, T. Ishibashi, H. Ito : Photoresponse nonlinearity of a uni-traveling-carrier photodiode and its application to optoelectronic millimeter-wave mixing in 60 GHz band; *Jap. J. Appl. Phys.* **43**(7B) (2004) 966–968.
- T. Göbel, D. Schönherr, C. Sydlo, M. Feiginov, P. Meissner, H.L. Hartnagel: Continuous-wave terahertz system with electro-optical terahertz phase control; *Electron. Lett.* **44**(14) (2008) 863–864.
- T. Göbel, D. Schönherr, C. Sydlo, M. Feiginov, P. Meissner, H.L. Hartnagel: Single-sampling-point coherent detection in continuous-wave photomixing terahertz systems; *Electron. Lett.* **45**(1) (2009) 65–66.

- T. Göbel : *Systeme, Verfahren und Komponenten zur hochauflösenden Dauerstrich-Terahertz-Spektroskopie*; PhD thesis, University of Darmstadt, Germany (2010).
- I.S. Gregory, C. Baker, W.R. Tribe, M.J. Evans, H.E. Beere, E.H. Linfield, A.G. Davies, M. Missous : High resistivity annealed low-temperature GaAs with 100 fs lifetimes; *Appl. Phys. Lett.* **83**(20) (2003) 4199–4201.
- I.S. Gregory, W.R. Tribe, B.E. Cole, M.J. Evans, E.H. Linfield, A.G. Davies, M. Missous : Resonant dipole antennas for continuous-wave terahertz photomixers; *Appl. Phys. Lett.* **85**(9) (2004a) 1622–1624.
- I.S. Gregory, W.R. Tribe, B.E. Cole, C. Baker, M.J. Evans, I.V. Bradley, E.H. Linfield, A.G. Davies; M. Missous : Phase sensitive continuous-wave THz imaging using diode lasers; *Electron. Lett.* **40**(2) (2004b) 143–145.
- I.S. Gregory, W.R. Tribe, C. Baker, B.E. Cole, M.J. Evans, L. Spencer, M. Pepper, M. Missous : Continuous-wave terahertz system with a 60 dB dynamic range; *Appl. Phys. Lett.* **86**(20) (2005a) 204104–204106.
- I.S. Gregory, C. Baker, W.R. Tribe, I.V. Bradley, M.J. Evans, E.H. Linfield, A.G. Davies, M. Missous : Optimization of photomixers and antennas for continuous-wave terahertz emission; *IEEE J. Quantum Electron.* **41**:5 (2005b) 717–728.
- I.S. Gregory, M.J. Evans, H. Page, S. Malik, I. Farrer, H.E. Beere: Analysis of photomixer receivers for continuous-wave terahertz radiation; *Appl. Phys. Lett.* **91**:15 (2007) 154103–154105.
- P. Gu, M. Tani, M. Hyodo, K. Sakai, and T. Hidaka : Generation of cw-terahertz radiation using a two-longitudinal-mode laser diode; *Jpn. J. Appl. Phys.* **37**, Part 2:8B (1998) 976–978.
- S.A. Harmon, R.A. Cheville: Part-per-million gas detection from long-baseline THz spectroscopy; *Appl. Phys. Lett.* **85**(11) (2004) 2128–2130.
- S.E. Harris: Tunable optical parametric oscillators; *Proc. IEEE* **57**:12 (1969) 2096–2113.
- B.B. Hu, M.C. Nuss: Imaging with terahertz waves; *Opt. Lett.* **20**:16 (1995) 1716–1720.
- F. Huang, B. Schuklin, H. Altan, J.F. Federici, D. Gary, R. Barat, D. Zimdars, M. Chen, D.B. Tanner: Terahertz study of 1,3,5-trinitro-s-triazine by time-domain and Fourier transform infrared spectroscopy; *Appl. Phys. Lett.* **85**:23 (2004) 5535–5537.
- M. Hyodo, M. Tani, S. Matsuura, N. Onodera, K. Sakai : Generation of millimetre-wave radiation using a dual-longitudinal-mode microchip laser; *Electron. Lett.* **32**:17 (1996) 1589–1591.
- T. Ishibashi, N. Shimizu, S. Kodama, H. Ito, T. Nagatsuma, T. Furuta : Uni-traveling-carrier photodiodes; in: *Ultrafast Electronics and Optoelectronics*, M. Nuss and J. Bowers, eds., **Vol. 13** of OSA Trends in Optics and Photonics Series (1997a), paper UC3.
- T. Ishibashi, S. Kodama, N. Shimizu, T. Furuta : High-speed response of uni-traveling-carrier photodiodes; *Jpn. J. Appl. Phys.* **36** (1997b) 6263–6268.
- T. Ishibashi, T. Furuta, H. Fushimi, H. Ito : Photoresponse characteristics of uni-traveling-carrier photodiodes; *Proc. SPIE* Vol. **4283** (2001) 469–478.
- H. Ito, T. Furuta, S. Kodama, T. Ishibashi : Zero-bias high-speed and high-output-voltage operation of cascade-twin uni-travelling-carrier photodiode; *Electron. Lett.* **36**:24 (2000) 2034–2036.

- H. Ito, T. Nagatsuma, A. Hirata, T. Minotani, A. Sasaki, Y. Hirota, T. Ishibashi: High-power photonic millimeter-wave generation at 100 GHz using matching-circuit-integrated uni-travelling-carrier photodiodes; *Proc. Inst. Elect. Eng. Optoelectron.* **150** (2003) 138–142.
- H. Ito, S. Kodama, Y. Muramoto, T. Furuta, T. Nagatsuma, T. Ishibashi : High-speed and high-output InP-InGaAs unidirectional uni-travelling-carrier photodiodes; *IEEE J. Quantum Electron.* **10**(4) (2004) 709–727.
- H. Ito, F. Nakajima, T. Furuta, T. Ishibashi : Continuous THz-wave generation using antenna-integrated uni-travelling-carrier photodiodes; *Semicond. Sci. Technol.* **20**(7) (2005) 191–198.
- A. Jackson : *Low-temperature grown GaAs photomixers designed for increased terahertz output power*; PhD thesis, University of California, Santa Barbara (1999).
- C. Jansen, S. Wietzke, O. Peters, M. Scheller, N. Vieweg, M. Salhi, N. Krumbholz, C. Jördens, T. Hochrein, M. Koch : Terahertz imaging: applications and perspectives; *Appl. Opt.* **49**(19) (2010) E48–E57.
- C. Jördens, M. Scheller, S. Wietzke, D. Romeike, C. Jansen, T. Zentgraf, K. Wiesauer, V. Reisecker, M. Koch : Terahertz spectroscopy to study the orientation of glass fibres in reinforced plastics; *Compos. Sci. Technol.* **70**(3) (2010) 472–477.
- C. Kadow, S.B. Fleischer, J.P. Ibbetson, J.E. Bowers, A.C. Gossard, J.W. Dong, and C.J. Palmstrøm: Self-assembled ErAs islands in GaAs: Growth and subpicosecond carrier dynamics; *Appl. Phys. Lett.* **75**(22), (1999) 3548–3550.
- C. Kadow, A.W. Jackson, A.C. Gossard, S. Matsuura, G.A. Blake: Self-assembled ErAs islands in GaAs for optical-heterodyne THz generation; *Appl. Phys. Lett.* **76**(24) (2000) 3510–3512.
- M.C. Kemp, P.F. Taday, B.E. Cole, J.A. Cluff, A.J. Fitzgerald, W.R. Tribe: Security applications of terahertz technology; in: *Terahertz for Military and Security Applications*, R.J. Hwu and D.L. Woolard, (eds), Proc. of SPIE Vol. **5070** (2003) 44–52.
- J. Kiessling, R. Sowade, I. Cámara Mayorga, K. Buse, I. Breunig: Coherent detection of terahertz radiation employing a continuous wave optical parametric source; *Rev. Sci. Inst.* **82**(2) (2011) 26108–26110.
- N. Kim, J. Shin, E. Sim, C.W. Lee, D.-S.Yee, M.Y. Jeon, Y. Jang, K.H. Park: Monolithic dual-mode distributed feedback semiconductor laser for tunable continuous-wave terahertz generation; *Opt. Express* **17**(16) (2009) 13851–13859.
- N. Kim, S.-P. Han, H. Ko, Y.A. Leem, H.-C. Ryu, C.W. Lee, D. Lee, M.Y. Jeon, S.K. Noh, K.H. Park: Tunable continuous-wave terahertz generation/detection with compact 1.55 μm detuned dual-mode laser diode and InGaAs based photomixer; *Opt. Express* **19**(16) (2011) 15397–15403.
- T. Kinder : *Beiträge zur absoluten Distanzinterferometrie mit variabler synthetischer Wellenlänge*; PhD thesis, University of Greifswald, Germany (2004).
- A. Klehr, J. Fricke, A. Knauer, G. Erbert, M. Walther, R. Wilk, M. Mikulics, M. Koch: High-power monolithic two-mode DFB laser diode for the generation of THz radiation; *IEEE J. Quantum Electron.* **14**(2) (2008) 289–294.
- T. Kleine-Ostmann, P. Knobloch, M. Koch, S. Hoffmann, M. Breede, M. Hofmann, G. Hein, K. Pierz, M. Sperling, K. Donnhuijsen: Continuous-wave THz imaging; *Electron. Lett.* **37**(24) (2001) 1461–1463.

- P. Kordoš, M. Marso, M. Mikulics: Performance optimization of GaAs-based photomixers as sources of THz radiation; *Appl. Phys. A* **87**:3 (2007) 563–567.
- T.-A. Liu, M. Tani, M. Nakajima, M. Hangyo, C.-L. Pan: Ultrabroadband terahertz field detection by photoconductive antennas based on multi-energy arsenic-ion-implanted GaAs and semi-insulating GaAs; *Appl. Phys. Lett.* **83**:7 (2003) 1322–1325.
- Z. Liu, K. Su, D.E. Gary, J.F. Federici, R.B. Barat, Z.-H. Michalopoulou: Video-rate terahertz interferometric and synthetic aperture imaging; *Appl. Opt.* **48**:19 (2009) 3788–3795.
- G.C. Loata, T. Löffler, H.G. Roskos: Evidence for long-living charge carriers in electrically biased low-temperature-grown GaAs photoconductive switches; *Appl. Phys. Lett.* **90**:5 (2007a) 52101–52103.
- G.C. Loata, M.D. Thomson, T. Löffler, H.G. Roskos: Radiation field screening in photoconductive antennae studied via pulsed terahertz emission spectroscopy; *Appl. Phys. Lett.* **91**:23 (2007b) 232506–232508.
- J.K. Luo, H. Thomas, D.V. Morgan, D. Westwood: Thermal annealing effect on low temperature molecular beam epitaxy grown GaAs: Arsenic precipitation and the change of resistivity; *Appl. Phys. Lett.* **64**(26) (1996) 3614–3616.
- A. Majewski: Terahertz spectroscopy: High-resolution terahertz spectrometer sniffs out chemicals; *Laser Focus World* **44**(4) (2008).
- J. Mangeney, A. Merigault, N. Zerounian, P. Crozat, K. Blary, J.F. Lampin: Continuous wave terahertz generation up to 2 THz by photomixing on ion-irradiated InGaAs at 1.55 μm wavelengths; *Appl. Phys. Lett.* **91**(24) (2007) 241102–241104.
- J. Mangeney, F. Meng, D. Gacemi, E. Peytavit, J.F. Lampin, T. Akalin : *Terahertz generation and power limits in $In_{0.53}Ga_{0.47}As$ photomixer coupled to transverse-electromagnetic-horn antenna driven at 1.55 μm wavelengths*; *Appl. Phys. Lett.* **97**(16) (2010) 161109–161111.
- S. Matsuura, M. Tani, K. Sakai : Generation of coherent terahertz radiation by photomixing in dipole photoconductive antennas; *Appl. Phys. Lett.* **70**(5) (1997) 559–561.
- S. Matsuura, M. Tani, H. Abe, K. Sakai, H. Ozeki, S. Saito : High-resolution terahertz spectroscopy by a compact radiation source based on photomixing with diode lasers in a photoconductive antenna; *J. Molecular Spectr.* **187**(1) (1998) 97–101.
- S. Matsuura, H. Ito : Generation of cw terahertz radiation with photomixing; in: K. Sakai (Ed.): *Terahertz Optoelectronics*; Springer-Verlag Berlin Heidelberg (2005) 157–202.
- I. Cámará Mayorga, P. Muñoz Pradas, E.A. Michael, M. Mikulics, A. Schmitz, P. van der Wal, C. Kaseman, R. Güsten, K. Jacobs, M. Marso, H. Lüth, P. Kordos : Terahertz photonic mixers as local oscillators for hot electron bolometer and superconductor-insulator-superconductor astronomical receivers; *J. Appl. Phys.* **100**:4 (2006), 43116–43119.
- I. Cámará Mayorga, E.A. Michael, A. Schmitz, P. van der Wal, R. Güsten, K. Maier, A. Dewald : Terahertz photomixing in high energy oxygen- and nitrogen-ion-implanted GaAs; *Appl. Phys. Lett.* **91**(3) (2007) 31107–31109.
- K.A. McIntosh, E.R. Brown, K.B. Nichols, O.B. McMahon, W.F. di Natale, T.M. Lyszczarz: Terahertz photomixing with diode lasers in low-temperature-grown GaAs; *Appl. Phys. Lett.* **67**(26) (1995) 3844–3846.

- K.A. McIntosh, E.R. Brown, K.B. Nichols, O.B. McMahon, W.F. DiNatale, T.M. Lyszczarz: Terahertz measurements of resonant planar antennas coupled to low temperature grown GaAs photomixers; *Appl. Phys. Lett.* **69**(24) (1996) 3632–3634.
- K.A. McIntosh, K.B. Nichols, S. Verghese, E.R. Brown: Investigation of ultrashort photocarrier relaxation times in low-temperature-grown GaAs; *Appl. Phys. Lett.* **70**(3) (1997) 354–356.
- R. Mendis, C. Sydlo, J. Sigmund, M. Feiginov, P. Meissner, H.L. Hartnagel: Spectral characterization of broadband THz antennas by photoconductive mixing: Toward optimal antenna design; *IEEE Antennas and Wireless Propagation Lett.* **4** (2005) 85–88.
- E.A. Michael, I. Cámera Mayorga, R. Güsten, A. Dewald, R. Schieder : Terahertz continuous-wave large-area traveling-wave photomixers on high-energy low-dose ion-implanted GaAs; *Appl. Phys. Lett.* **90**(17) (2007) 171109–171111.
- M. Mikulics, M. Marso, P. Kordoš, S. Stanek, P. Kováč, X. Zheng, S. Qu, R. Sobolewski: Ultrafast and highly sensitive photodetectors fabricated on high-energy nitrogen-implanted GaAs; *Appl. Phys. Lett.* **83**(9) (2003) 1719–1721.
- M. Mikulics, M. Marso, I. Cámera Mayorga, R. Güsten, S. Stanek, P. Kováč, S. Wu, X. Li, M. Khafizov, R. Sobolewski, E.A. Michael, R. Schieder, M. Wolter, D. Buca, A. Förster, P. Kordoš, H. Lüth : Photomixers fabricated on nitrogen-ion-implanted GaAs; *Appl. Phys. Lett.* **87**(4) (2005) 41106–41108.
- M. Mikulics, E.A. Michael, M. Marso, M. Lepsa, A. van der Hart, H. Lüth, A. Dewald, S. Stanek, M. Mozolik, P. Kordoš : Traveling-wave photomixers fabricated on high energy nitrogen-ion-implanted GaAs; *Appl. Phys. Lett.* **89**(7) (2006a) 71103–71105.
- M. Mikulics, E.A. Michael, R. Schieder, J. Stutzki, R. Güsten, M. Marso, A. van der Hart, H.P. Bochem, H. Lüth, P. Kordoš : Traveling-wave photomixer with recessed interdigitated contacts on low-temperature-grown GaAs; *Appl. Phys. Lett.* **88**(4) (2006b) 41118–41120.
- M. Mikulics, M. Marso, S. Mantl, H. Lüth, P. Kordoš : GaAs photodetectors prepared by high-energy and high-dose nitrogen implantation; *Appl. Phys. Lett.* **89**(9) (2006c) 91103–91105.
- G. Mouret, S. Matton, R. Bocquet, D. Bigourd, F. Hindle, A. Cuisset, J.F. Lampin, K. Blary, D. Lippens : THz media characterization by means of coherent homodyne detection, results and potential applications; *Appl. Phys. B* **89**(2–3) (2007) 395–399.
- T. Müller-Wirts : *Method and device for measuring and stabilization using signals from a Fabry-Perot*; Patent US 6,178,002, filed Dec. 3, 1998, issued Jan. 23, 2001.
- T. Nagatsuma, A. Kaino, S. Hisatake, K. Ajito, H.-J. Song, A. Wakatsuki, Y. Muramoto, N. Kukutsu, Y. Kado : Continuous-wave terahertz spectroscopy system based on photodiodes; *Piers Online* **6**(4) (2010) 390–394.
- S. Osborne, S. o'Brien, E. P. o'Reilly, P.G. Huggard, B.N. Ellison : Generation of cw 0.5 THz radiation by photomixing the output of a two-colour 1.49 μm Fabry-Perot diode laser; *Electron. Lett.* **44**(4) (2008) 296–297.
- R. H. Pantell, L. Solymar: Optical frequency mixing in semiconductors; *Intern. J. Electron.* **18**(1) (1965) 23–31.
- J.E. Pedersen, V.G. Lyssenko, J.M. Hvam, P. Uhd Jepsen, S.R. Keiding, C.B. Sorensen, P.E. Lindelof: Ultrafast local field dynamics in photoconductive THz antennas; *Appl. Phys. Lett.* **62**(11) (1993) 1265–1267.

- E. Peytavit, S. Arscott, D. Lippens, G. Mouret, S. Matton, P. Masselin, R. Bocquet, J.F. Lampin, L. Desplanque, F. Mollot : Terahertz frequency difference from vertically integrated low-temperature-grown GaAs photodetector; *Appl. Phys. Lett.* **81**(7) (2002) 1174–1176.
- E. Peytavit, J.-F. Lampin, T. Akalin, L. Desplanque : integrated terahertz horn antenna; *Electron. Lett.* **43**(2) (2007) 73–75.
- E. Peytavit, A. Beck, T. Akalin, J.-F. Lampin, F. Hindle, C. Yang, G. Mouret : Continuous terahertz-wave generation using a monolithically integrated horn antenna; *Appl. Phys. Lett.* **93**(11) (2008), 111108–111110.
- E. Peytavit, J.-F. Lampin, F. Hindle, C. Yang, G. Mouret : Wide-band continuous-wave terahertz source with a vertically integrated photomixer; *Appl. Phys. Lett.* **95**(16) (2009), 161102–161104.
- A.S. Pine, R.D. Suenram, E.R. Brown, K.A. McIntosh: A terahertz photomixing spectrometer: Application to SO₂ self broadening; *J. Mol. Spectrosc.* **175**(1) (1996) 37–47.
- S. Preu, F.H. Renner, S. Malzer, G.H. Döhler, L.J. Wang, M. Hanson, A.C. Gossard, T.L.J. Wilkinson, E.R. Brown: Efficient terahertz emission from ballistic transport enhanced n-i-p-n-i-p superlattice photomixers; *Appl. Phys. Lett.* **90**(21) (2007), 212115–212117.
- S. Preu, G.H. Döhler, S. Malzer, L.J. Wang, A.C. Gossard: Tunable, continuous-wave terahertz photomixer sources and applications; *J. Appl. Phys.* **109**(6) (2011) 61301–61356.
- S. Preu, Personal communication (2011).
- H. Quast, T. Löffler : 3D-terahertz-tomography for material inspection and security; *Proc. IRMMW-THz*, Busan/Korea (2009).
- C.C. Renaud, M. Robertson, D. Rogers, R. Firth, P.J. Cannard, R. Moore, A.J. Seeds: A high responsivity, broadband waveguide uni-travelling carrier photodiode; *Proc. SPIE 6194*, Strasbourg (2006) 61940C1–61940C8.
- A. Roggenbuck, H. Schmitz, A. Deninger, I. Cámera Mayorga, J. Hemberger, R. Güsten, M. Grüninger : Coherent broadband continuous-wave terahertz spectroscopy on solid-state samples, *New J. Phys.* **12** (2010) 43017–43029.
- A. Roggenbuck, A. Deninger, K. Thirunavukkumarasu, H. Schmitz, J. Marx, E. Vidal, M. Langenbach, J. Hemberger, M. Grüninger : A fast cw-THz spectrometer using fiber stretchers; *Proc. IRMMW-THz*, Houston/USA (2011).
- E. Rouvalis, C.C. Renaud, D.G. Moodie, M.J. Robertson, A.J. Seeds: Traveling-wave uni-traveling carrier photodiodes for continuous wave THz generation; *Opt. Express* **18**(11) (2010) 11105–11110.
- D. Saeedkia : *Modeling and design of photoconductive and superconductive terahertz photomixer sources*; PhD thesis, University of Waterloo, Canada (2005).
- D. Saeedkia, S. Safavi-Naeini : Terahertz photonics: optoelectronic techniques for generation and detection of terahertz waves; *J. Lightwave Technol.* **26**:15 (2008) 2409–2423.
- B. Salem, D. Morris, V. Aimez, J. Beauvais, D. Houde : Improved characteristics of a terahertz set-up built with an emitter and a detector made on proton-bombarded GaAs photoconductive materials; *Semicond. Sci. Technol.* **21**(3) (2006) 283–286.
- B. Sartorius, H. Roehle, H. Künzel, J. Böttcher, M. Schlak, D. Stanze, H. Venghaus, M. Schell : All-fiber terahertz time-domain spectrometer operating at 1.5 μm telecom wavelengths; *Opt. Express* **16**(13) (2008) 9565–9570.

- B. Sartorius, M. Schlak, D. Stanze, H. Roehle, H. Künzel, D. Schmidt, H.-G. Bach, R. Kunkel, M. Schell : Continuous wave terahertz systems exploiting 1.5 μm telecom technologies; *Opt. Express* **17**(17) (2009) 15001–15007.
- M. Scheller, M. Koch : Terahertz quasi time domain spectroscopy; *Opt. Express* **17**(20) (2009) 17723–17733.
- M. Scheller, M. Stecher, M. Gerhard, M. Koch : Hybrid continuous wave terahertz spectroscopy; *Opt. Express* **18**(15) (2010) 15887–15892.
- M. Scheller, S.F. Dürrschmidt, M. Stecher, M. Koch : Terahertz quasi-time-domain spectroscopy imaging; *Appl. Opt.* **50**(13) (2011) 1884–1888.
- N. Shimizu, T. Ikari, K. Kikuchi, K. Matsuyama, A. Wakatsuki, S. Kohjiro, R. Fukasawa: Remote gas sensing in full-scale fire with sub-terahertz waves; *Microwave Symposium Digest (MTT), IEEE MTT-S International*, Baltimore / USA (2011) 1–4.
- K.J. Siebert, H. Quast, R. Leonhardt, T. Löffler, M. Thomson, T. Bauer, H.G. Roskos, S. Czasch : Continuous-wave all-optoelectronic terahertz imaging; *Appl. Phys. Lett.* **80**(16) (2002a) 3003–3005.
- K.J. Siebert, T. Löffler, H. Quast, M. Thomson, T. Bauer, R. Leonhardt, S. Czasch, H.G. Roskos: All-optoelectronic continuous wave THz imaging for biomedical applications; *Phys. Med. Biol.* **47**(21) (2002b) 3743–3748.
- A.M. Sinyukov, Z. Liu, Y.L. Hor, K. Su, R.B. Barat, D.E. Gary, Z.-H. Michalopoulou, I. Zorych, J.F. Federici, D. Zimdars : Rapid-phase modulation of terahertz radiation for high-speed terahertz imaging and spectroscopy, *Opt. Lett.* **33**(14) (2008) 1593–1595.
- F.W. Smith, H.Q. Le, V. Diadiuk, M.A. Hollis, A.R. Calawa, S. Gupta, M. Frankel, D.R. Dykaar, G.A. Mourou, T.Y. Hsiang: Picosecond GaAs-based photoconductive optoelectronic photodetector; *Appl. Phys. Lett.* **54**(10) (1988) 890–892.
- R. Sowade, I. Breunig, I. Cámera Mayorga, J. Kiessling, C. Tulea, V. Dierolf, K. Buse: Continuous-wave optical parametric terahertz source; *Opt. Express* **17**(25) (2009) 22303–22310.
- D. Stanze, H. Roehle, R.J.B. Dietz, H.J. Hensel, D. Schmidt, H.-G. Bach, M. Schell, B. Sartorius : Improving photoconductive receivers for 1.5 μm CW THz systems; *Proc. IRMMW-THz 2010*, Rome / Italy (2010).
- D. Stanze, A. Deninger, A. Roggenbuck, S. Schindler, M. Schlak, B. Sartorius : Compact cw terahertz spectrometer pumped at 1.5 μm wavelength; *J Infrared Milli. Terahz. Waves* **32**(2) (2011) 225–232.
- M. Sukhotin, E.R. Brown, A.C. Gossard, D. Driscoll, M. Hanson, P. Maker, R. Muller: Photomixing and photoconductor measurements on ErAs/InGaAs at 1.55 μm ; *Appl. Phys. Lett.* **82**(18) (2003) 3116–3118.
- M. Tani, S. Matsuura, K. Sakai, M. Hangyo : Multiple-frequency generation of sub-terahertz radiation by multimode LD excitation of photoconductive antenna; *IEEE Microw. Guide. Wave Lett.* **7**(9) (1997) 282–284.
- M.C. Teich: Field-theoretical treatment of photomixing; *Appl. Phys. Lett.* **14**(6) (1969) 201–203.
- Y. Tohmori, F. Kano, H. Ishii, Y. Yoshikuni, Y. Kondo : Wide tuning with narrow linewidth in DFB lasers with superstructure grating (SSG); *Electron. Lett.* **29**(15) (1993) 1350–1352.
- M. Tonouchi : Cutting-edge terahertz technology; *Nat. Photonics* **1** (2007) 97–105.

- M. Vainio, J. Peltola, S. Persijn, F. J. M. Harren, L. Halonen : Singly resonant cw OPO with simple wavelength tuning; *Opt. Express* **16**(15) (2008) 11141–11146.
- M. Vainio, L. Halonen : Stable operation of a cw optical parametric oscillator near the signal-idler degeneracy; *Opt. Lett.* **36**(4) (2011) 475–477.
- S. Verghese, K.A. McIntosh, E.R. Brown: Optical and terahertz power limits in the low-temperature-grown GaAs photomixer; *Appl. Phys. Lett.* **71**(19) (1993) 2743–2745.
- S. Verghese, K. McIntosh, E. Brown : Highly tunable fiber-coupled photomixers with coherent terahertz output power; *IEEE Trans. Microwave Theory and Tech.* **45**(8) (1997a) 1301–1309.
- S. Verghese, K. McIntosh, E.R. Brown: Optical and terahertz power limits in the low-temperature-grown GaAs photomixers; *Appl. Phys. Lett.* **71**(19) (1997b) 2743–2745.
- S. Verghese, K.A. McIntosh: *Quasi-optical transceiver having an antenna with time varying voltage*; Patent US 6,348,683, filed May 4, 1998, issued Feb. 19, 2002.
- S. Verghese, K.A. McIntosh, S. Calawa, W.F. Dinatale, E.K. Duerr, K.A. Molvar: Generation and detection of coherent terahertz waves using two photomixers; *Appl. Phys. Lett.* **73**(26) (1998) 3824–3826.
- A. Wakatsuki, T. Furuta, Y. Muramoto, T. Yoshimatsu, H. Ito : High-power and broadband sub-terahertz wave generation using a J-band photomixer module with rectangular-waveguide-output port, Proc. IRMMW-THz, Pasadena / USA (2008).
- S. Wietzke, C. Jansen, T. Jung, M. Reuter, B. Baudrit, M. Bastian, S. Chatterjee, M. Koch : Terahertz time-domain spectroscopy as a tool to monitor the glass transition in polymers; *Opt. Express* **17**(21) (2009) 19006–19014.
- R. Wilk, A. Klehr, M. Mikulics, T. Hasek, M. Walther, M. Koch : Terahertz generation with 1064 nm DFB laser diode; *Elettron. Lett.* **43**(2) (2007) 108–110.
- R. Wilk, F. Breitfeld, M. Mikulics, M. Koch : Continuous wave terahertz spectrometer as a noncontact thickness measuring device; *Appl. Opt.* **47**(16) (2008) 3023–3026.
- N. Zamdmer, Q. Hu, K.A. McIntosh, S. Verghese : Increase in response time of low-temperature-grown GaAs photoconductive switches at high voltage bias; *Appl. Phys. Lett.* **75**(15) (1999) 2313–2315.

Novel techniques in terahertz near-field imaging and sensing

M. NAGEL, AMO GmbH, Germany, C. MATHEISEN,
RWTH Aachen University, Germany and
H. KURZ, AMO GmbH, Germany

DOI: 10.1533/9780857096494.2.374

Abstract: In this chapter, novel active optoelectronic probe-tips fabricated by micromachining techniques are introduced. These devices are highly attractive for a broad range of applications requiring micron-scale resolution and terahertz (THz) range operation. Using planar waveguide designing modalities they are the first devices combining THz generation, detection, transmission and focussing elements in a single self-contained cantilever microstructure. At the beginning of the chapter a brief overview of current near-field (NF) probing approaches and their applications is given. Passive focussing components such as apertures, metal tips or waveguides are discussed, as well as active (electro-optic and photoconductive) components are able to internally generate and detect THz signals on sub-wavelength scales. Then the new concept is explained and applications in the fields of nonlinear nanophotonic device characterization, failure location in integrated circuits (ICs) and photovoltaic material analysis are demonstrated.

Key words: terahertz (THz), near-field, imaging, sensing, non-destructive, contactless, material inspection, failure location, time-domain reflectometry.

12.1 Introduction

Over the last years the technological importance of the terahertz (THz) frequency range has strongly increased (Tonouchi, 2007) and it can be assumed that this trend will further continue. Electronic and photonic integration technologies have started to converge and both technologies are targeting operation frequencies in the THz range (MONA, 2008). Graphene is one of the drivers in this field. Graphene-based nanoelectronic devices, for example, have been envisaged as a next generation integrated circuit (IC) technology with transistors having THz range switching speed (Lin *et al.*, 2010) or THz plasma-wave oscillators (Rana, 2008). For application in the optical domain graphene-based THz lasers (Ryzhii *et al.*,

2009) and detectors (Ryzhii *et al.*, 2010) have been proposed. Silicon is a further good example of converging technology platforms targeting THz operation frequencies: silicon CMOS-based transistors have been demonstrated as rectifying detector elements (Sankaran and O, 2005) in high sensitivity focal plane arrays for THz imaging at room temperature (Boppel *et al.*, 2011; Schuster *et al.*, 2011). On the other hand, silicon nanophotonic devices have been suggested as optically pumped THz sources and detectors (Baehr-Jones *et al.*, 2008).

Most of these elementary devices have geometrical feature sizes which are much smaller than the corresponding THz free-space wavelengths. In order to accompany and foster the efficient development of future THz-range nanoelectronic and nanophotonic technologies, a THz near-field (NF) metrology which is capable to provide sub- μm and sub-ps spatio-temporal resolution is urgently needed. Beside this, many analytic THz applications are facing similar wavelength-to-sample mismatching problems as well. For example, marker-free biomolecular sensing based on the transmission of THz free-space radiation and diffraction-limited focussing is known to require extremely large amounts of sample material, typically in the μl -range (Brucherseifer *et al.*, 2000; Hoffmann *et al.*, 2005). However, by using sub-wavelength field-confining planar waveguides structures a sample volume reduction of more than five orders of magnitude can be easily achieved (Nagel *et al.*, 2006). The idea of using THz NF probing for this application appears very attractive since it could allow a direct use of standard biochips (Schena *et al.*, 1996) – instead of more costly THz waveguide chips (Debus *et al.*, 2009) – for marker-free biomolecule detection. Another example of a THz application that will strongly benefit from sub-wavelength resolution is given by carrier-dynamic investigations in nanoscale systems. Standard THz systems can probe ensemble properties but do not provide direct information about local charge-carrier behaviour (Ulbricht *et al.*, 2011). For instance, in next generation organic solar cells (Esenturk *et al.*, 2009) photo-generated charge transport is suspected to be strongly dependent on the active layer nanomorphology as a result of phase segregation (Hamadani *et al.*, 2010). Future THz NF probing techniques should render possible the spatio-temporal resolution of such local charge-carrier processes. In the following sections we will review recent progress in this field and introduce micro-machined NF probing devices with integrated active THz generation and detection entities.

12.2 State-of-the-art terahertz near-field approaches

Many different THz NF measurement approaches have been developed over the last years and overviews have been given in several review articles (Pfeiffer *et al.*, 1996; Yuan *et al.*, 2004; Chan *et al.*, 2007; Withayachumnankul

et al., 2007). The most recent review article about THz NF measurement methods and applications is the work from Adam (2011) which is especially recommended to the interested reader. A prominent classification criterion in THz NF technology is given by the use (or avoidance) of an aperture element to restrict the size of the THz illumination spot to sub-wavelength dimensions. An early demonstration of aperture-based THz NF imaging was presented by Hunsche *et al.* (1998). Unfortunately, a main draw-back of aperture-based imaging is the immense loss of THz light intensity at deep sub-wavelength resolutions ($< \lambda/10$) caused by the low-frequency cut-off behaviour of the aperture (Adam *et al.*, 2008) and optical coupling loss. The latter can be reduced (in certain cases) by placing a small detector or emitter element directly behind the aperture, as demonstrated by Mitrofanov *et al.* (2000) and Iwami *et al.* (2008), respectively, or by including periodic corrugations around the aperture (Cao *et al.*, 2005) to generate frequency-selective transmission enhancement. Apertureless approaches, on the other hand, are much better set to achieve deep sub-wavelength resolutions because frequency cut-offs are effectively avoided. Structures used for apertureless NF imaging include sharp metallic tips for local field enhancement and scattering light generation at the tip apex (Keilmann and Hillenbrand, 2004) or small detector (Adam *et al.*, 2008; Bitzer *et al.*, 2010) or source (Lecaque *et al.*, 2006) elements with sub-wavelength dimensions placed in the vicinity of the sample surface.

Highest spatial resolutions down to a few tens of nanometres have been reported for scattering-type (ST) metal-tip-based imaging. With this method a light beam from an external source is focussed on a metallic tip held in close proximity to a sample surface. The tip picks up a part of the incident light, which is then locally enhanced at the tip apex. As a consequence, a locally enhanced field interaction between the sample and the metal tip is achieved. This process generates scattering light, which is picked up by an external detector. The resolution of this method is practically only limited by the size of the tip diameter and applicable within a broad spectrum from infrared to microwaves (Keilmann and Hillenbrand, 2004). However, optical coupling loss between the discrete main components – emitter, detector and passive metal tip – is still one of the biggest contrast limiting problems of ST systems. This is because the electromagnetic energy transfer between these components is typically based on standard diffraction-limited optics rendering the excitation of the metal tip as well as the collection of the undirected scattering light very inefficient. In order to increase the signal-to-noise ratio (SNR) in such ST THz NF microscopes with far-field detection to useful levels multiple dynamic modulation procedures (such as tip/sample distance and emitter amplitude modulation), in conjunction with lock-in amplifier based detection, are necessarily required. Furthermore, for the same reason high intensity mW-range THz sources such as continuous-wave gas lasers or quantum cascade lasers are preferred (Huber *et al.*, 2008), in comparison

to low power nW-range semiconductor surface emitters as used for pulsed time-domain measurements (Cho *et al.*, 2005). An intensity loss on the order of 60 dB between input and demodulated output light was recently measured in a THz ST microscope (von Ribbeck *et al.*, 2008).

Opposed to far-field excitation/detection, using active excitation and/or detection instead – directly at the NF position of interest – are evident options to strongly increase the NF imaging contrast by minimizing coupling losses. In this case the NF probe becomes an active transducer device. With reference to this characteristic difference we will categorize both approaches as passive or active NF probing in the following. The idea of using an electro-optic (EO) crystal placed in close distance to a device under test (DUT) to measure its electrical response with ‘micrometre spatial resolution and a temporal response of a fraction of a picosecond’ dates back to the mid-1980s (Meyer and Mourou, 1985). In the following years, EO probes have been extensively developed and investigated by several groups (e.g. Shinagawa and Nagatsuma, 1990). These probes have been applied for the characterization of integrated planar circuits at GHz (Pfeifer *et al.*, 1996; Yang *et al.* 2000) and THz (Nagel *et al.*, 1999) frequencies. An ST THz microscope with active EO detection was first demonstrated by van der Valk and Planken (2002). Active EO (quasi-) NF spectroscopy including both THz pulse excitation and detection was later presented by Chakkittakandy *et al.* (2008) using two closely spaced EO crystals. Even without lock-in detection time-domain scans with a high SNR of 450 have been achieved in less than a minute of averaging time. Using single EO crystals for THz wave excitation and detection Feurer *et al.* (2007) and Blanchard *et al.* (2011) impressively demonstrated imaging of crystal internal THz waves and their NF interaction with surface deposited planar dipole antennas in real-time. However, some of the disadvantages still inherent to EO NF probing using bulk materials include relatively weak sensitivity to the evanescent electric fields of externally approached objects, a spatial resolution not better than 5–15 µm, technical difficulties preventing sufficient EO probe miniaturization as well as the very restricted means to guide and confine electro-optically generated THz waves within EO probes. These difficulties, which are highly relevant for a broad range of applications, can be tackled by micro-machined photoconductive probes, which will be discussed in the following.

12.3 Novel micro-machined terahertz near-field probe-tips

For more than three decades ultrafast photoconductive (PC) switches (Auston *et al.*, 1984) have been used for the generation and detection of electromagnetic pulses with ps or sub-ps duration, thereby covering a spectrum in the THz range. Today PC switches embedded in dipole antennas (as, for example, described in a previous review article by Dragoman and

Dragoman, 2004) are probably still the most widely used structures for the generation and detection of THz radiation. A PC switch capable in this sense is usually based on a semiconductor material with ultra-short lifetimes (also in the sub-ps range) of optically excited charge carriers and a pair of electrodes for electrical connection. THz pulses are generated at biased PC switches through short pulse optical excitation. The optical excitation triggers a photocurrent pulse within the PC switch, which generates an electromagnetic THz pulse. This pulse is partly guided along the connected electrode structures and partly radiated into free space. In order to utilize and optimize either on-chip pulse guidance or free-space radiation planar waveguide designs as principally known from microwave monolithic integrated circuit (MMIC) technology (Hoffmann, 1987) can be applied. So far, the plethora of field-confining and guiding structures known from MMIC technology is still barely utilized for THz NF imaging. As will be shown in the following, with MMIC semiconductor and micromachining technology a new class of THz NF measuring devices can be realized offering highly increased functionality and efficiency.

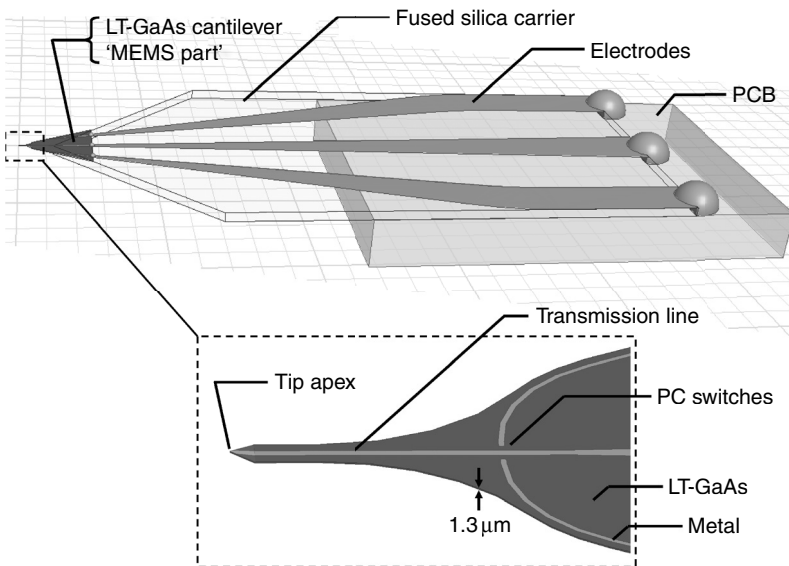
PC antenna devices have been used as active THz NF detectors by several groups (Lee *et al.*, 2002; Bitzer *et al.*, 2009). So far these devices have been limited to only moderate spatial resolutions (not better than 25 µm) which is mainly caused by the wavelength-dependent resonant antenna dimensions. Also the presence of a rigid carrier substrate below the detecting antenna element being several hundreds of µms thick often impedes a close approach between detector and sample surface, which has further negative influence on spatial resolution and signal contrast. A noteworthy improvement to better than 5 µm of spatial resolution for PC NF detection was recently introduced by Wächter *et al.* (2009) by displacing the resonant antenna element through a pair of tapered electrodes and using a micro-machined ultra-thin cantilever structure as PC NF probe. The cantilever is based on LT-GaAs grown by molecular beam epitaxy at low temperature (Gupta *et al.*, 1991) with a charge-carrier lifetime of 250 fs and a thickness of only 1.3 µm. It has favourable electronic properties such as high electron mobility and high breakdown voltage, as well as good mechanical properties for high durability and flexibility. First efforts in using micro-machined PC probes based on ultra-thin LT-GaAs layers were restricted to optical fibre-mounted detectors (Lai *et al.*, 1996; Lee *et al.*, 2002). While the attachment of the PC structure to an optical fibre has the advantage of a fixed alignment of the optical excitation beam to the PC switch, it has also some very undesirable disadvantages. For example, only one PC switch per probing device can be linked to a fibre-transmitted optical excitation beam in practice. Hence, pulse generation and detection cannot be realized in a single device. Also the electromagnetic behaviour of the PC probe is strongly disturbed by a directly attached fibre structure which is finally becoming noticeable in a strongly

reduced bandwidth. Last but not least, fabrication of fibre-mounted PC probes is very laborious since planar structuring methods cannot be applied throughout (e.g., for external electric connection). Overall, functionality, performance and manufacturability can be seriously affected by direct fibre coupling. For these reasons direct fibre coupling was avoided within the latest developments of LT-GaAs cantilever-based NF probing devices which will be discussed in the following.

A representative set of the main front-end components of our active PC NF measuring devices is shown in Fig. 12.1. Each component can be easily tailored to the specific requirements of the designated application. At the very tip of the device the micro-machined LT-GaAs cantilever is placed. Within the dashed box a zoom to the cantilever section with an example design is shown. This section contains the main functional structures (such as PC switches or waveguides) required for THz pulse generation, detection, transmission and field-confinement. Usually it is preferred to place all of the functional components within the free-standing area of the cantilever in order to avoid any performance limiting influence from the fused silica carrier substrate which is following next. The carrier substrate is needed as a mechanical and electrical connection with intermediate size and sufficient flatness between the ultra-thin LT-GaAs microstructure and a standard printed circuit board (PCB). The PCB provides the required robustness to handle the device (by hand) and lock it to a fixture within the set-up. Further electrical connections from the PCB to external devices, such as voltage sources or current amplifiers, are done through on-board plug and coaxial cables.

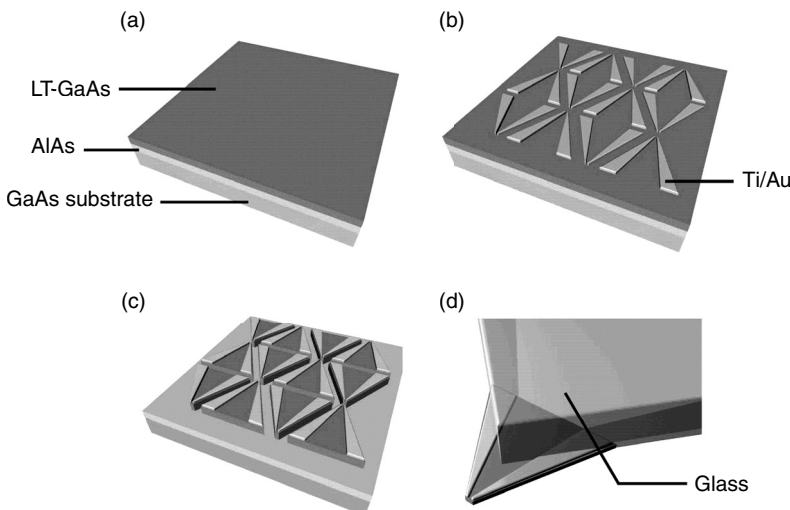
The fabrication of the LT-GaAs-based cantilever is illustrated in Fig. 12.2. The fabrication starts from a multilayer material featuring a 100 nm AlAs sacrificial layer and a 1.3 μm thick layer of LT-GaAs epitaxially grown on a GaAs host substrate. Electrode structures (Cr: 10 nm, Au: 200 nm) are then patterned on top of the LT-GaAs using optical lithography of a photo-resist masking layer, metal deposition and lift-off in acetone. Next, the shape of the LT-GaAs cantilever is patterned using optical lithography of a photo-resist masking layer and chemical wet etching of the unmasked LT-GaAs areas in a piranha solution until the underlying AlAs layer is exposed. Then, the AlAs sacrificial layer is etched off completely in 10% HF solution, thereby releasing the LT-GaAs-based chips from the host substrate. Finally, the chip is bonded onto a 180 μm thick carrier substrate of fused silica so that it extends a few hundred micrometres over the edge of the carrier substrate. Electrical contacts between LT-GaAs chip and carrier substrate are made by needle-printed dots of electrically conducting epoxy.

One of the most important attribute of our active PC probing devices is the capability for fabrication by planar semiconductor and micromachining techniques. This capability has given us direct access to a quasi-infinity choice of probe designs and functionalities, which are currently



12.1 Schematic drawing of a representative set of front-end components of an active cantilever-based PC NF probing device including a zoom to the LT-GaAs cantilever area with PC switch and transmission line components.

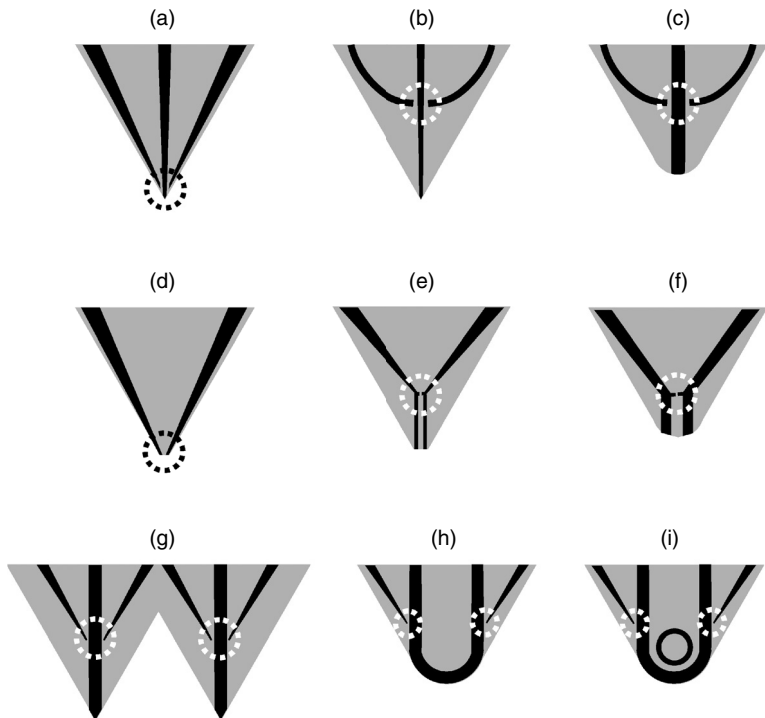
not available in such scale by any other THz NF technology. To give the reader a flavour of the possibilities, a few design options for cantilever structures are illustrated in Fig. 12.3. Planar electrodes, LT-GaAs, and areas of optical excitation around PC switches are represented by black, grey, and dashed line bordered areas, respectively. The featured designs come either with one integrated PC switch applicable for pulse generation *or* detection (Fig. 12.3a–f) or with two PC switches for THz pulse generation *and* detection within a single device (Fig. 12.3g–i). The shown probe designs with a single PC switch contain either a single-wire (a–c) or twin-wire (d,f) transmission line arrangement. This difference causes a fundamentally different tip-to-sample NF coupling behaviour, and can be utilized (as will be shown later) for the detection of field vector components with vertical or horizontal orientation to the sample surface by either using the single-wire or twin-wire design, respectively. This is demonstrated in Section 12.4. Samples with high parasitic sensitivity to optical excitation should be predominantly investigated using probe designs with PC switches that are laterally displaced from the tip apex, as shown by all designs except for Fig. 12.3 a and d. The latter versions contain a PC switch directly at the tip apex which can be helpful to achieve highest possible spatial resolution and signal contrast, however, also comes with a partial



12.2 Basic fabrication steps of the active PC probing devices.

(a) Multilayer material with AlAs sacrificial layer and LT-GaAs layer on a GaAs substrate. (b) Patterning and deposition of planar electrode structures. (c) Patterning and etching of LT-GaAs layer. (d) Etching of sacrificial layer and structure bonding to glass carrier.

illumination of the probed sample region. Of course, the shape of the LT-GaAs cantilever and the tip apex can also be easily tailored as required by the specific application. By choosing a larger tip radius – as shown by the designs c and f in comparison to the sharper tips b and d – it is possible to increase the tip/sample interaction at the expense of a decreased spatial resolution. Further, the shaping of the LT-GaAs cantilever determines also its mechanical properties, which need to be controlled for applications requiring a static tip/sample contact or a dynamic modulation of the tip/sample distance. The designs capable of THz pulse excitation and detection are especially useful for analytic and sensing applications which often profit from a compact single probe head. Figure 12.3h displays a probe design with a u-shaped single-wire transmission line connecting an emitter and a detector switch. A sample material placed near the tip region will alter the amplitude and phase of the signal transmitted along the single-wire according to its dielectric properties and the tip/sample distance. In order to increase the tip/sample interaction at defined frequencies, a resonating element (as sketched in terms of a ring resonator in Fig. 12.3i) may be added and coupled to the transmission line within the tip region. So far, such resonantly enhanced dielectric material sensing has been mainly realized at THz frequencies using chip-based structures (Nagel *et al.*, 2002, 2006; Cunningham *et al.*, 2006; Miyamaru *et al.*, 2006; Cunningham *et al.*,



12.3 Exemplary designs of active PC NF cantilever structures in top-view. Black regions are planar electrodes; grey regions represent LT-GaAs. Dashed circular areas show optical excitation spots at PC switches. Exhibited designs include single-wire probes (a–c), twin-wire probes (d–f) and transceiver probes (g–i).

2008; Debus *et al.*, 2009) but not as part of a micro-machined NF probe. The design of Fig. 12.3g is showing a combination of two single-wire probe which can be applied for THz pump/probe measurements and sample-based signal transmission. A typical application in this sense is given by time-domain reflectometry (TDR) based fault location in chip structures, which is described in Section 12.5.

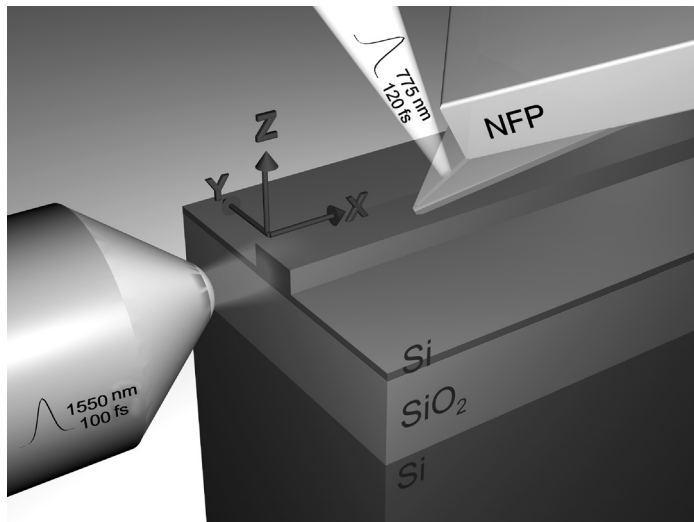
12.4 Analysis of nanophotonic second-order nonlinear-optic waveguides with terahertz near-field probing

Silicon-based nanophotonic devices have seen a rapid development in recent years. Due to the strong field-confinement that can be achieved in such devices, nonlinear optical processes are visible at relatively low pump

powers. Unfortunately, second-order nonlinearities ($\chi^{(2)}$) are absent in bulk silicon due to its centrosymmetric crystalline structure. Hence, second-order nonlinear-optic THz-field generation is not directly possible. Recent efforts aiming at the realization of silicon photonic structures with second-order nonlinearity rely on the addition of an EO cladding layer (Baehr-Jones and Hochberg, 2008), the application of mechanical strain from highly braced cladding layers (Jacobsen *et al.*, 2006; Chmielak *et al.*, 2011), or externally applied electric fields (Chen *et al.*, 2008). A recently developed novel approach based on a simple CMOS-compatible plasma-activated process induces significant increase of the second-order nonlinearity caused by a chemical modification of the silicon waveguide surface (Wächter *et al.*, 2010). The resulting EO activity has been applied for the generation of a broadband THz pulse via EO difference frequency generation (DFG) within a silicon nanophotonic waveguide using telecom wavelength pump pulses. Concurrently, active THz NF measurement techniques can be applied to monitor local second-order nonlinearity in such optical waveguides through the same DFG process as will be demonstrated below. The experimental set-up is sketched in Fig. 12.4. The silicon nanophotonic THz emitter is excited by infrared laser pulses with 100 fs duration, a wavelength of 1550 nm and a repetition rate of 100 MHz. The infrared light is coupled via a tapered fibre (on the left side in Fig. 12.4) into the silicon waveguide. In order to keep nonlinear losses within the waveguide small the injected average optical power is limited to 50 μ W. A NF probe (on the upper right side in Fig. 12.4) is placed directly above the waveguide and is optically excited by a frequency-doubled laser pulse with a variable time-delay corresponding to the time-domain measurement scheme. The NF probe-tip is freely positionable with respect to the silicon device. Spatially and temporally resolved measurements of vectorial field components depending on the design of the NF probe can be acquired. In this study probe-tips of type (b) (shown in Fig. 12.3) are positioned perpendicular to the silicon surface, while probe-tips of type (d) are aligned to have an angle of 30° to the silicon surface. This case is sketched in Fig. 12.4.

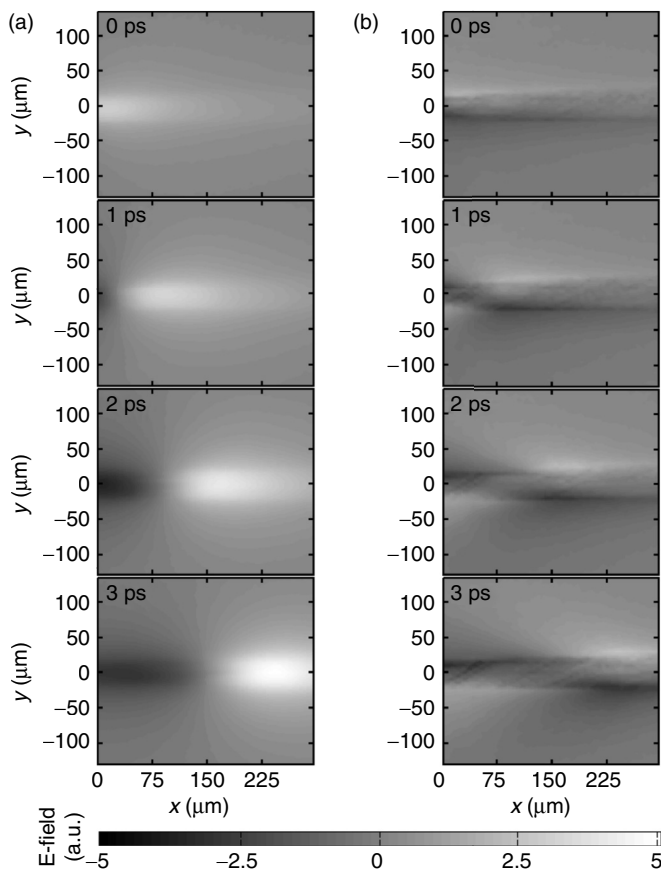
The access to the NF data is essential for the device development and analysis of the induced $\chi^{(2)}$ and its tensor nature. To demonstrate the amount of information enclosed in the NF a spatio-temporally resolved measurement of a plasma-activated silicon device is shown in the following.

Figure 12.5 shows the spatial field distribution of a waveguide with 50 μ m width and 220 nm top silicon thickness for different points of time and two polarizations. In the case of Fig. 12.5a the measurement is acquired with a NF probe of type (b) (see Fig. 12.3). The deployed NF probe is mainly sensitive for a field component polarized along the z -axis. The zero position of the graphs indicates the position where the optical excitation pulse



12.4 Schematic measurement set-up for spatio-temporal NF measurements of nanophotonic silicon devices. NFP, near-field probe.

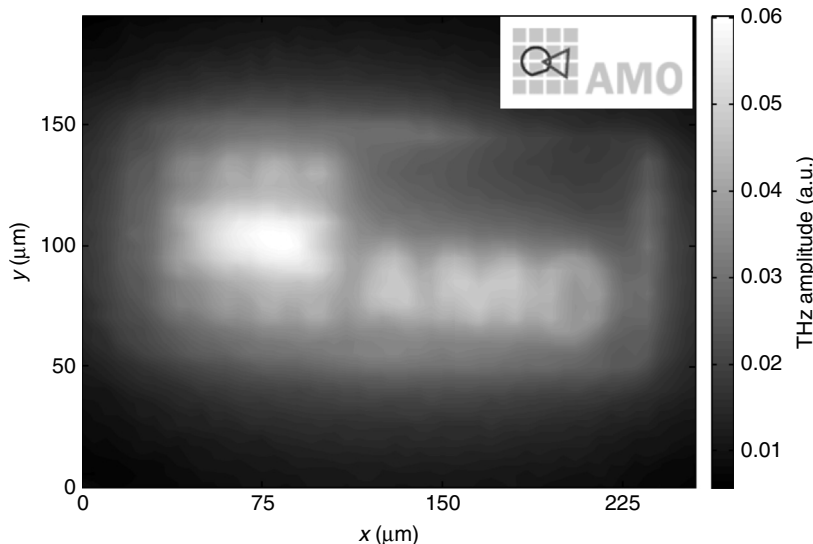
is coupled into the device, so the optical waveguide is located along the zero position of the y -axis. The graphs one below the other are taken at different points of time with a temporal displacement of 1 ps. A maximum of field amplitude can be observed in a y -position of zero which is temporally propagating along the x -axis. The temporal progress shows that the positive field is followed by a longer negative field indicating asymmetric single-cycle pulse propagation along the waveguide. The spatial analysis reveals a field component with a polarization normal to the silicon surface directly above the waveguide and above the optically excited area, respectively. Figure 12.5b is acquired under same conditions but with a different type of probe. Here a probe-tip of type (d) is used to achieve highest sensitivity for electrical fields polarized along the y -axis. The measurement at the first point of time exhibits a positive and a negative field located axially symmetric to the x -axis. The region directly above the waveguide, where the normal field component has its maximum, appears to have no in-plane field. The temporal evolution shows that the two amplitude maxima are co-propagating with the positive part of the z -field component. The negative part of the z -field pulse entering measurement frame at 2 ps is accompanied by an in-plane field distribution with inverted signs compared to the 0 ps case. In conclusion the in-plane field and normal field are symmetrically coupled. These measurements allow a conclusion of the three-dimensional field distribution in vicinity of the sample surface. The generated THz radiation is polarized along the z -axis, while the field contribution along the



12.5 Spatio-temporal field distribution of a plasma-activated silicon waveguide in (a) z-polarization and (b) y-polarization.

y-axis which is located beneath the optical excited area has its origin in the radiated dipole field of the optically excited area.

Under emitter engineering aspects the approach of nanophotonic devices with chemical surface modification offers multiple degrees of freedom in terms of design. Beside the most common variations of waveguide dimensions the plasma activation can be masked by lithography. Therefore the nonlinear active area can be freely defined, which is an important step towards a quasi phase-matching device structure (Hon *et al.*, 2009). To demonstrate the design capability a locally activated device featuring the company logo of AMO (see inset of Fig. 12.6) is measured spatio-temporally resolved with a NF probe of type (b). The waveguide has a width of 100 μm , a top silicon thickness of 220 nm and the length of the logo is 220 μm . Due to the spatial limitation along the propagation



12.6 Spatial resolved measurement of a locally activated silicon waveguide featuring the company logo of AMO GmbH. Inset: original company logo.

direction of the area that is excited by the short optical pulse at a given point of time – only a part of the device appears to be active. Therefore, the data of Fig. 12.6 is acquired by accumulation of the THz amplitude over several discrete points of time with 1 ps interval and a spatial resolution of 5 microns is acquired. The typical feature size of the logo elements is around 10 microns. One can easily identify the logo structures in the measurement. Even small features such as the quadrates on the left side of the logo with a size of 12 microns and a spacing of 7 microns are clearly separable. This indicates on the one hand the strikingly high contrast between activated and non-activated areas as well as the high spatial resolution of the NF probe. The realization of this ‘THz fluorescent writing’ demonstrates the high design capabilities of silicon nanophotonic devices with chemically modified surface for THz generation and the necessity of a high-resolution NF measurement device.

12.5 Failure analysis in integrated electronic structures based on terahertz time-domain reflectometry

The importance of non-destructive analysis techniques for fault location in electronic packages is continuously increasing. Due to the steadily growing complexity of IC technology, for example, 3D through silicon

via (3D-TSV) technology (Lau, 2011), inspection technologies such as TDR (Chen *et al.*, 2006), X-ray (Zschech *et al.*, 2009) or scanning acoustic microscopy (Harsányi *et al.*, 2000) need to keep up with these developments in terms of sensitivity, resolution and measurement speed. Among the non-destructive approaches TDR is considered an exceptionally fast method for fault detection. Currently all-electronic TDR systems – also dubbed as ‘closed-loop radar’ (Agilent Technologies, 2000) – employ as the main components of a step or pulse generator and a high-bandwidth oscilloscope. The electromagnetic signal is transmitted through a coaxial cable and a probe-tip to the DUT. Every impedance discontinuity in the DUT causes a part of the injected signal to be reflected. By monitoring these reflections in the time-domain, it is possible to detect structural defects and distinguish functional structures from defective structures very quickly. In simple (linear) DUT structures it is also straightforward to determine the spatial location of the defect by signal velocity considerations. Initially, TDR had been developed for fault location in large electrical systems such as cables, but it was quickly adopted for failure analysis in smaller structures at PCB level, in packages and interconnects.

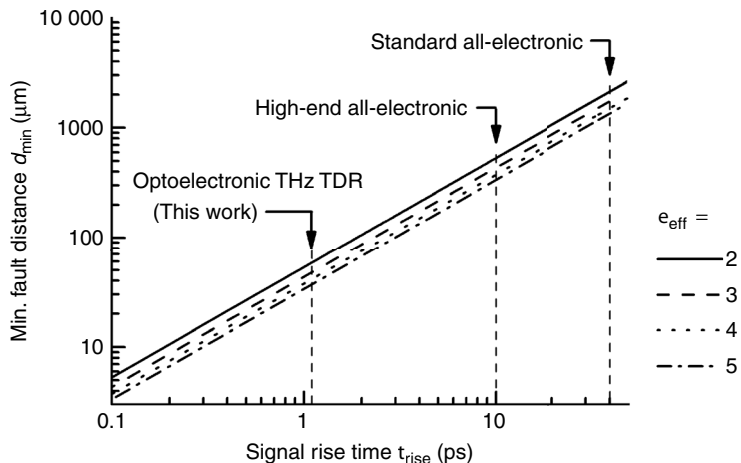
The spatial resolution of a TDR system in terms of the minimum distance d_{\min} required between two objects for their discrimination is directly linked to the rise time τ_{rise} of the injected signal by the relation (McGibney and Barrett, 2006)

$$d_{\min} = \tau_{\text{rise}} \cdot c / 4\sqrt{\epsilon_{r,\text{eff}}} \quad [12.1]$$

with c being the speed of light and $\epsilon_{r,\text{eff}}$ is the relative effective permittivity of the transmission line. As visualized by the diagram in Fig. 12.7, the maximum resolution of currently available high-end all-electronic systems with a measured $\tau_{\text{rise}} = 11.1$ ps is limited to approx. 365 μm for $\epsilon_{r,\text{eff}} = 5$ (Schoen, 2004). In order to go considerably beyond this limit and to allow the inspection of smaller scale chip-level structures alternative optoelectronic approaches are required.

The large potential of femtosecond (fs) laser-driven optoelectronic measurement techniques for the characterization of high-frequency devices was recognized very early – more than two-decades ago (Valdmanis *et al.*, 1982, 1986). Over the past years fs-lasers have become increasingly robust, compact, user-friendly and cost-efficient, which is now fostering an increased technology transfer from laboratory to real-world applications.

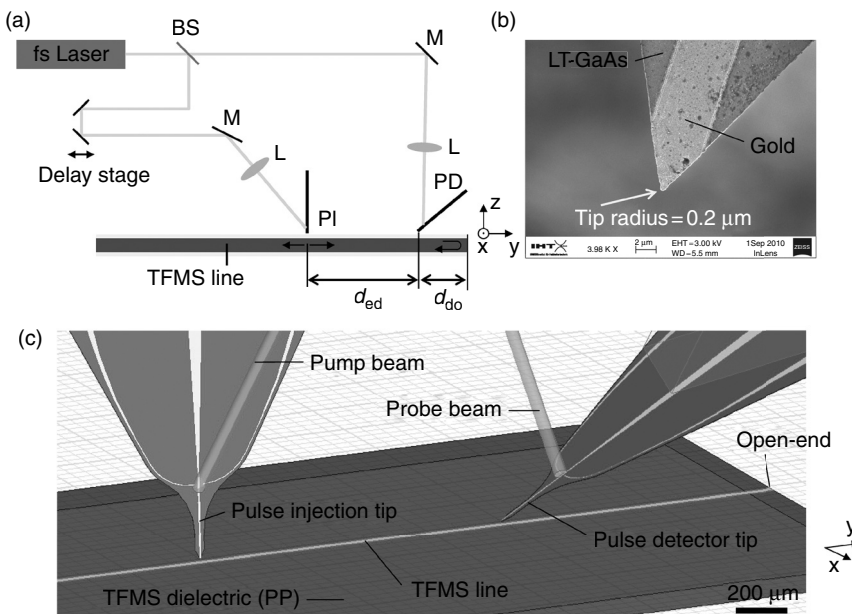
TDR-based fault isolation using a fs-laser-driven optoelectronic system was recently highlighted by the Intel Corp. (Cai *et al.*, 2010). With this system a $\tau_{\text{rise}} = 5.7$ ps has been achieved, leading to a substantial improvement over all-electronic systems. However, the main bottleneck within this



12.7 Minimum distance d_{\min} between neighbouring still resolvable discontinuities versus signal rise time τ_{rise} .

system – still preventing taking full advantage of the principally available sub-ps optoelectronic switching speeds – is given by the components interconnected between the optoelectronic chip and the DUT: a waveguide and a probe-tip having a bandwidth of only 110 GHz. In the following, a recent technical solution (Nagel *et al.*, 2011) for the effective elimination of this bottleneck is presented. Using advanced micro-machined photoconductive probes the optoelectronic TDR-based localization of a waveguide discontinuity with an unprecedented rise time of $\tau_{\text{rise}} = 1.1$ ps measured for the reflected signal after 5.8 mm of DUT-internal propagation is achieved. In contrast to standard configurations, the presented TDR measurements are made in a contact-free mode using capacitive probe/waveguide coupling. This approach appears not only attractive under device protection and automation considerations, but also for direct fault localization through spatio-temporally resolved field mappings of suspicious chip regions. Our approach can therefore be considered as a multidimensional extension of the standard TDR analysis concept.

The optoelectronic system, schematically sketched in Fig. 12.8a, is again based on a classic time-domain pump/probe set-up. The main components are a Ti:Sapphire fs-laser with a centre wavelength of 780 nm, 150 fs pulse width full width at half maximum (FWHM) and 78 MHz repetition rate and two micro-machined identical PC probe-tips according to the design scheme sketched in Fig. 12.3b. A thin-film microstrip (TFMS) line is used as DUT. The TDR measurements are conducted with 4 mW of average power for pump and probe beam, respectively. The pump beam is focussed on the active region of the first probe used for pulse injection (PI) into the DUT.



12.8 (a) Schematic of the applied optical pump/probe set-up for terahertz time-domain measurements. (b) SEM image of the tip region of the probe-tips used. (c) Detailed to-scale model of the applied probe configuration and orientation used for the measurements.

The active region contains a pair of biased PC switches made of two 5 μm wide gaps between two Ti/Au-based branch lines and a continuous centre line running to the tip apex. The planar electrode structures are integrated on the LT-GaAs cantilever. Fabrication processes are in accordance with the description given in Section 12.3. An SEM image of the tip apex and a drawing to scale of the geometrical design and the configuration of the probe-tips on the DUT during the measurement are shown in Fig. 12.8b and c, respectively.

Both probe-tips are positioned 10 μm above the TFMS line. The probe-to-probe tip distance $d_{\text{ed}} = 1$ mm is kept fixed throughout all measurements. Pulses generated at the pair of PC switches (which are symmetrically biased against the centre line) are guided along the centre line with a Sommerfeld-mode-like radial field distribution (Wächter *et al.*, 2005). The signal is then coupled from the probe-tip to the TFMS line. From the coupling position the pulse propagates in two anti-parallel directions along the TFMS line. The second probe-tip (marked PD for ‘pulse detection’ in Fig. 12.8a) is placed above the TFMS line section being shorter in distance to an open-end. With this probe the injected and reflected signal is sampled in time-domain. A linear mechanical stage controlling the optical length of the

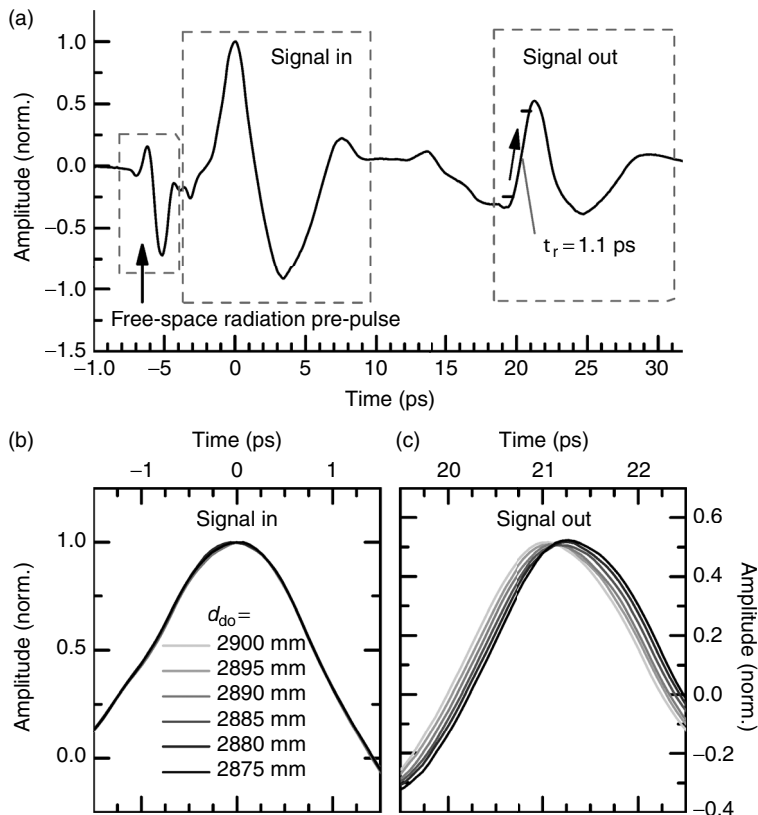
probe beam is used to sweep the time-delay of the optical probe pulses. The sampling process is the reverse analogue of the pulse excitation process: a part of the signal propagating along the TFMS line is coupled to the detection probe-tip. It is guided along the centre line to the pair of PC switches. The detected photocurrent across the PC switches is linear proportional to the electric field sampled by the PC elements. To increase the SNR a rectangular modulated bias voltage (3 V peak-to-peak, $f = 700$ Hz) and lock-in amplifier detection is used.

In order to investigate the capability of the system for TDR-based fault isolation we consider as the DUT a TFMS line with known THz transmission characteristics, as has been investigated in a prior work (Nagel *et al.*, 2001). This TFMS design was also previously applied for THz bio-sensing applications (Nagel *et al.*, 2003). It is fabricated on a silicon substrate covered by a 500-nm-thick Ti/Au-based ground layer and a 57 μm thick polypropylene/co-polymer acrylate film as dielectric layer. The signal line on top of the dielectric has a width of 31 μm and is made of the same metal layer system as used for the ground layer.

Figure 12.9a shows a time-domain signal recorded for a probe to open-end distance $d_{\text{do}} = 2.9$ mm. Using numerical field simulations, the coupling loss α_c for a vertical probe-to-sample distance $d_{\text{pp}} = 1\text{--}10 \mu\text{m}$ is calculated to be in the range of 18–22 dB. Still, a surprisingly large signal-to-noise amplitude ratio of the time-domain signal of approximately 900:1 is obtained for a lock-in amplifier averaging time of 30 ms. The signal trace can be divided in three characteristic parts: for $t < -4$ ps a pre-pulse caused by free-space radiation from the PI probe is detected; in the range of $t = -4\text{--}18$ ps a pulse with increased amplitude is observed which represents the guided incoming signal propagating from the PI probe towards the open-end (signal in); for $t > 18$ ps the detected signal is dominated by the reflection from the open-end (signal out). As expected for an open-end reflection the polarities of the incoming and the reflected signal are identical. The peak amplitude of the reflected signal is around 51% (−6 dB) of the incoming peak amplitude. Considering the waveguide attenuation of ca. 1.0 dB/mm at 0.5 THz measured earlier (Nagel *et al.*, 2001), this result indicates a nearly ideal reflection behaviour with negligible radiation loss.

An ultra-short rise time of $\tau_{\text{rise}} = 1.1$ ps (determined at the 10–90% levels of the rising signal edge) is measured. This is an order of magnitude shorter than achievable with state-of-the-art all-electronic systems and should allow the differentiation of discontinuities separated by less than 36 μm (for $\epsilon_{r,\text{eff}} = 5$).

Besides the ability to resolve neighbouring defects, even more important in many situations is the ability to accurately locate the position of a single defect. Beside short rise-times this also requires time jitter effects to be as low as possible. The latter point is a particular strength of optical coherent



12.9 (a) Measured time-domain signal for a vertical probe-tip to sample distance of 10 μm . The detection tip is placed at a distance of 2.9 mm from the open-end of the waveguide. (b) Time-domain data of the incoming and (c) the reflected pulse peaks measured at different probe-to-discontinuity distances d_{do} as listed.

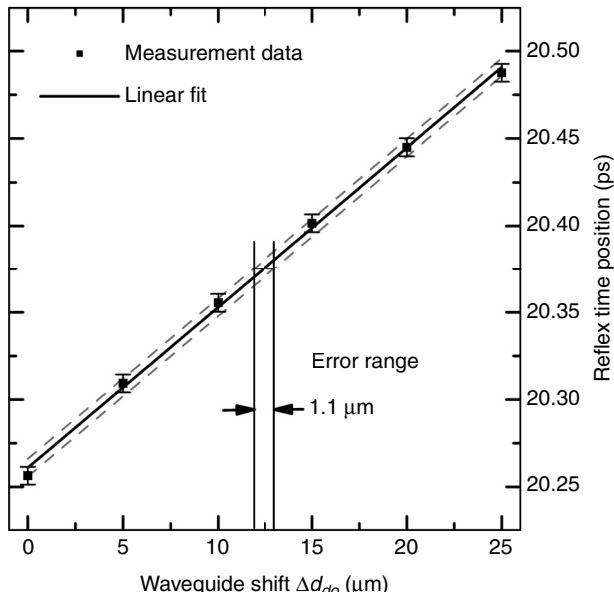
pump-probe measurement schemes (Pfeifer *et al.*, 1996) over all-electronic sampling systems, where time jitter values on the order of a few ps are common. We have quantified the location accuracy of our system by taking TDR scans at varying probe-to-end distances in a range of $d_{do} = 2875\text{--}2900 \mu\text{m}$ using 5 μm steps. As visualized by the data in Fig. 12.9b, the time position and slope of the incoming signal are virtually constant. This is expected since the transmission path between PI and detection in forward direction is constant in this comparison, as long as microscopic material or structure defects can be neglected. We determine a residual time base error of approx. ± 5 fs for the incoming signal. For the reflected signals (signal out) shown in Fig. 12.9c, very uniform signal slopes are registered which are, however, shifted towards earlier times for decreasing d_{do} . Within the

monitored relatively small range of propagation length variations ($2 \Delta d_{\text{do}} = 50 \mu\text{m}$), dispersion or attenuation effects are negligible and a linear dependency between the temporal position of the reflected signal and Δd_{do} can be assumed.

In Fig. 12.10, this correlation is plotted considering the half maximum position of the rising signal edge versus Δd_{do} . Here, the standard deviation from a linear dependence is found to be 2.6 fs and the maximum deviation is ± 5.1 fs, corresponding to a spatial location accuracy of $\pm 0.55 \mu\text{m}$. Since the observed jitter of the incoming and the reflected signals is almost equally large, we conclude that the accuracy of the mechanical translation stage used for the positioning of the DUT is sufficient, and that the observed residual jitter must be dominantly caused by laser intensity fluctuations. The average group velocity and effective permittivity which can be further extracted from the data set of Fig. 12.10 are $v_g = 216.5 \mu\text{m/ps}$ and $\epsilon_{r,\text{eff}} = 1.92$, respectively, which are also in excellent agreement with literature data (Nagel *et al.*, 2001).

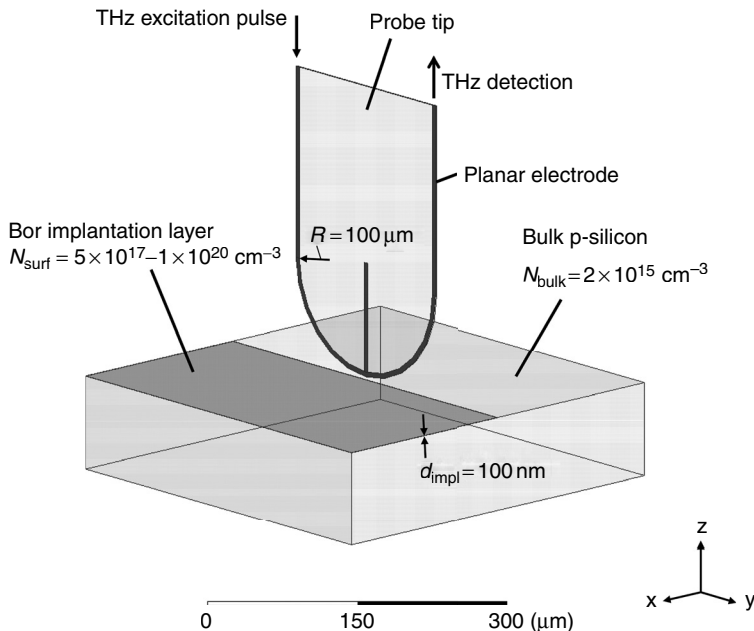
12.6 High-resolution imaging of free-carrier concentrations for photovoltaic material inspection

Local doping of semiconductor materials is routinely applied for a large number of semiconductor-based applications. In solar cells, for example, locally limited areas of increased carrier concentration are employed right below emitter electrodes in order to increase the conversion efficiency of the cell. The formation of such so called selective emitter structures can be accomplished through different kinds of doping technique, including laser-induced doping (Hameiri *et al.* 2011 and references therein), doping by doping-paste attached by screen printing (Mingirulli *et al.* 2011), or ion implantation (Chason *et al.* 1997). Laser-induced doping has recently gained increased attention because of its high cost efficiency. However, microscopic data of free-carrier concentrations, for example, induced by single or multiple focussed laser-pulse treatment, are not available in literature so far (although of high importance in terms of device performance). Severe roughness of laser treated or otherwise textured surfaces on the order of a few microns is one reason for the difficulties encountered using classic surface scanning techniques, such as resonant electron tunnelling microscopy, (Bolotov *et al.* 2008) or contactless optical techniques such as infrared lock-in thermography (Isenberg *et al.* 2004). THz active probing devices, as shown in the following, are optimally suited to be scaled for such applications requiring micron-scale spatial resolution on rough surfaces.



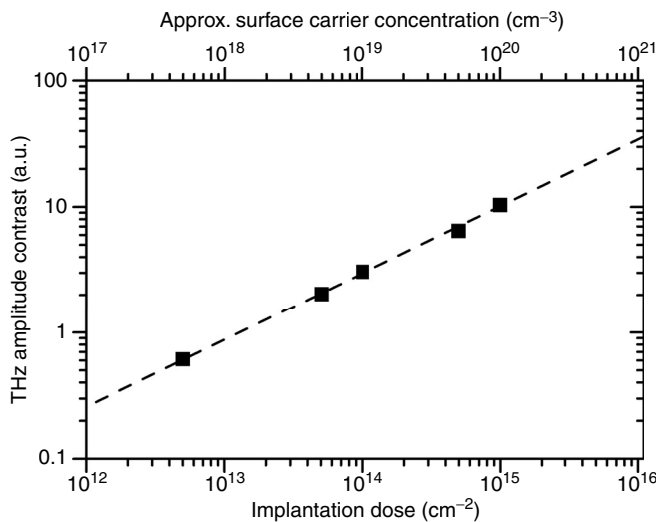
12.10 Measured time position of the reflected signal against waveguide shift from the open-end discontinuity. Fitting against a linear evolution reveals a location accuracy of $\pm 0.55 \mu\text{m}$.

The probe design used for the next application example is shown in Fig. 12.11. It is based on the concept sketched in Fig. 12.3i and includes a single-wire transmission line and a resonant element at the apex position for local field enhancement. In order to investigate the sensitivity of the probe to varying free-carrier concentrations, silicon wafers (p-Si, Bor, bulk carrier concentration $N_{\text{bulk}} = 2 \times 10^{15} \text{ cm}^{-3}$) have been prepared using ion implantation. As shown in Fig. 12.11 one half of the sample surface has been treated by ion (Bor) implantation and subsequent annealing at 1100°C . The acceleration energy was kept at 35 keV and the implantation dose was varied in a range of $5 \times 10^{12} \text{ cm}^{-2}$ to $1 \times 10^{15} \text{ cm}^{-2}$. Five samples with a surface carrier concentration N_{surf} of approximately $5 \times 10^{17} \text{ cm}^{-3}$, $5 \times 10^{18} \text{ cm}^{-3}$, $1 \times 10^{19} \text{ cm}^{-3}$, $5 \times 10^{19} \text{ cm}^{-3}$ and $1 \times 10^{20} \text{ cm}^{-3}$ were obtained from this processing. The thickness d_{impl} of the doping layer is about 100 nm. Similar ion-implanted silicon samples have been investigated using transmission of free-space THz radiation, however, yielding only diffraction-limited spatial resolution of 1 mm (Herrmann *et al.*, 2002). During our measurements the probe was kept in a distance of 2–4 μm above the sample surface while THz transmission through the probe was recorded. For increasing free-carrier concentration at the sample surface the amplitude of the THz transmission signal through the probe decreases.



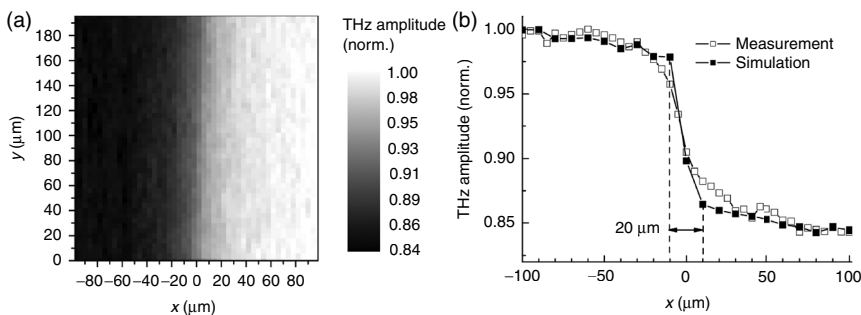
12.11 Probe and sample design applied for carrier concentration measurements at ion-implanted silicon samples. THz excitation and detection is accomplished by integrated PC switches.

This is shown through the measured peak amplitude contrast between unprocessed and ion-implanted areas as plotted in Fig. 12.12 for varying surface carrier concentration. In accordance to earlier free-space transmission experiments (Herrmann *et al.*, 2002), we see a linear relationship between surface carrier concentration and THz amplitude reduction in the considered range of $N_{\text{surf}} = 5 \times 10^{17} \text{ cm}^{-3}$ to $1 \times 10^{20} \text{ cm}^{-3}$. As also expected from free-space transmission results, phase shifts are not observed, hence carrier concentration measurements can be conducted solely at a fixed pump/probe time-delay where maximum amplitude contrast is obtained. Exemplary raster scanning data from a measurement across the boundary between a doped ($N_{\text{surf}} = 1 \times 10^{20} \text{ cm}^{-3}$) and an undoped area ($N_{\text{bulk}} = 2 \times 10^{15} \text{ cm}^{-3}$) are shown in Fig. 12.13 a and b in a two-dimensional mapping and a line scan, respectively. Although the probe-tip radius is as large as 100 μm , a spatial resolution of approximately 20 μm is still observed, which is in good agreement with the expected resolution predicted by numerical simulation using three-dimensional electromagnetic field modelling based on the finite element method (Fig. 12.13b). It is expected, that resolution and contrast can be further increased by probe design modification or sample/probe-distance modulation.



12.12 THz amplitude contrast between unprocessed ($N_{\text{bulk}} = 10^{16} \text{ cm}^{-3}$) and doped regions against implantation dose and surface carrier concentration of ion-implanted regions.

While the previous measurements were conducted with polished surfaces we now introduce further measurements with a rough surface of a multi-crystalline silicon solar cell structure. The sample surface was textured for improved light absorption with a peak-to-peak surface roughness amplitude of 10 μm . For these samples a probe design in accordance with Fig. 12.3g was applied with a tip-to-tip spacing of 300 μm and a vertical probe-to-sample distance of 20 μm . This probe design has a lower spatial resolution (basically limited to the tip-to-tip spacing), but comes with the important advantages of reduced sensitivity to surface topography and increased sensitivity to free-carrier concentration variations, which is attributed to wave transmission along the sample surface from emitter to detector tip. In contrast to the first ion-implanted sample, this typical solar cell structure has a constant high *n*-type free-carrier concentration ($N_{\text{surf}} = 1 \times 10^{20} \text{ cm}^{-3}$) directly at the surface; however, this value is kept to a depth of 100 nm or 200 nm in the case of the optically active or the selective emitter areas, respectively. The resulting sheet resistances for these areas are 100 Ω/sq . and 30 Ω/sq . respectively, and the bulk carrier concentration is 10^{16} cm^{-3} (*p*-type). Further details of the fabrication of these structures and comparative lock-in thermography measurements can be found in a publication by Mayer *et al.* (2010). As shown in Fig. 12.14a the selective emitter regions featuring a 1.6 mm wide bus bar and 300 μm wide finger structures are clearly resolved as regions of strongly reduced THz amplitude. Figure 12.14b shows a line

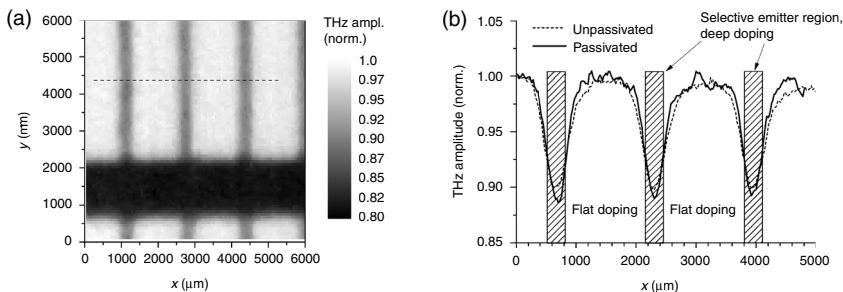


12.13 (a) Two-dimensional THz NF raster scan of the edge region between unprocessed ($N_{\text{bulk}} = 10^{16} \text{ cm}^{-3}$) and ion-implanted ($N_{\text{surf}} = 1 \times 10^{20} \text{ cm}^{-3}$) areas. The used raster step size is 4 μm . (b) Comparison of measured and simulated data at a line scan in x-direction.

scan across the finger structures (along the dashed line in Fig. 12.14a) as well as a comparison between the initial unpassivated sample and after passivation through application of a 60-nm-thin a-SiN_x:H layer (Janßen *et al.*, 2007). As can be seen, passivation has a negligible influence on our THz probe response opposed to light-induced LIT which is concurrently sensitive to carrier lifetime and carrier concentration variations (Mayer *et al.*, 2010). LIT-based carrier density imaging is also strongly impaired by parasitic signal contributions from the bulk material. As a result, measurements on inhomogenous mc-Si material (Mayer *et al.*, 2010) are nowhere nearly as clear as demonstrated here by THz NF probing.

12.7 Conclusion and future trends

Active optoelectronic probe-tips fabricated by micromachining techniques have been introduced as attractive new tools for a broad range of THz NF imaging applications. They are the first devices combining THz generation, detection, transmission and focussing elements in a single self-contained cantilever microstructure. This concept not only enables the build-up of very compact analysis systems, but also helps to reduce the enormous transmission losses observed with many other THz NF approaches. As a result, optical power requirements are so low (< 4 mW per emitter/detector) that cost-efficient fs-laser devices can be utilized as optical sources. It has been shown at several application examples that planar waveguide designing provides a broad basis of options to ideally equip and adapt the functionality, size and performance of the probes to the specific requirements of diverse application tasks. Besides the applications presented in the fields of nonlinear nanophotonic device characterization, failure location in ICs, and photovoltaic material/process analysis we see also a large potential for



12.14 (a) Two-dimensional THz NF raster scan showing the extension of a typical highly doped selective emitter region against lower doped regions on an unpassivated textured mc-Si surface. (b) Line scans along the dashed line in panel (a) across 300 μm wide selective emitter lines at passivated and unpassivated surfaces.

high-frequency electronic device characterization, label-free biomolecular sensing, and other (semiconductor) material inspection applications. Future developments will aim to continue application-targeted design improvements and to implement further applications. There is also large room for further technological improvements within the arrangement of the system environment. CW instead of pulsed-mode operation is straightforward, feasible, and maybe advantageous for certain applications. Also mechanic-free high-speed time-domain scanning approaches should be very effective in further improving system performance.

12.8 References

- Adam A J L, Brok J M, Seo M A, Ahn K J, Kim D S, Kang J H, Park Q H, Nagel M and Planken P C M (2008), ‘Advanced terahertz electric near-field measurements at sub-wavelength diameter metallic apertures’, *Opt Express*, **16**(10), 7407–7417.
- Adam A J L (2011), ‘Review of near-field terahertz measurement methods and their applications’, *J Infr Millim Terah Waves*, **32**(8–9), 1–44.
- Agilent Technologies (2000), ‘Evaluating microstrip with time domain reflectometry’, Application Note 1304-1, Available from: <http://www.agilent.com>.
- Auston D H, Cheung K P and Smith P R (1984), ‘Picosecond photoconducting Hertzian dipoles’, *Appl Phys Lett*, **45**, 284–286.
- Baehr-Jones T, Hochberg M, Soref R and Scherer A (2008), ‘Design of a tunable, room temperature, continuous-wave terahertz source and detector using silicon waveguides’, *J Opt Soc Am B*, **25**(2), 261–268.
- Baehr-Jones T and Hochberg M J (2008), ‘Polymer silicon hybrid systems: a platform for practical nonlinear optics’, *J Phys Chem C*, **112**, 8085–8090.
- Bitzer A, Merbold H, Thoman A, Feurer T, Helm HP and Walther M (2009), ‘Terahertz near-field imaging of electric and magnetic resonances of a planar metamaterial’, *Opt Express*, **17**(5), 3826–3834.

- Bitzer A, Ortner A and Walther M (2010), 'Terahertz near-field microscopy with subwavelength spatial resolution based on photoconductive antennas', *Appl Opt*, **49**(19), E1–E6.
- Blanchard F, Doi A, Tanaka T, Hirori H, Tanaka H, Kadoya Y and Tanaka K (2011), 'Real-time terahertz near-field microscope', *Opt Express*, **19**(9), 8277–8284.
- Bolotov L, Nishizawa M, Kanayama T and Miura Y (2008), 'Carrier concentration profiling on oxidized surfaces of Si device cross sections by resonant electron tunneling scanning probe spectroscopy', *J Vac Sci Technol B*, **26**, 415–419.
- Boppel S, Lisauskas A, Krozer V and Roskos HG (2011), 'Performance and performance variations of sub-1 THz detectors fabricated with 0.15 μ m CMOS foundry process', *Elec Lett*, **47**, 661–662.
- Brucherseifer M, Nagel M, Haring Bolivar P, Kurz H, Bosserhoff A and Büttner R (2000) 'Label-free probing of the binding state of DNA by time-domain terahertz sensing', *App Phys Lett*, **77**, 4049–4051.
- Cai YM, Wang ZY, Dias R and Goyal D (2010), 'Electro optical terahertz pulse reflectometry – an innovative fault isolation tool', *IEEE Proc 60th Electr Comp and Technol Conf (ECTC)* Las Vegas, NV, 1309–1315
- Cao H, Agrawal A and Nahata A (2005), 'Controlling the transmission resonance lineshape of a single subwavelength aperture', *Opt Express*, **13**, 763–769.
- Chakkittakandy R, Corver J and Planken P C M (2008), 'Quasi-near field terahertz generation and detection', *Opt Express*, **16**(17), 12794–12805.
- Chan W L, Deibel J and Mittleman D M (2007), 'Imaging with terahertz radiation', *Rep Prog Phys*, **70**, 1325–1379.
- Chason E, Picraux S T, Poate J M, Borland J O, Current M I, delaRubia T D, Eaglesham D J, Holland O W, Law M E, Magee C W, Mayer J W, Melngailis J and Tasch A F (1997), 'Ion beams in silicon processing and characterization', *J Appl Phys*, **81**(10), 6513–6561.
- Chen M K, Tai C C and Huang Y J (2006), 'Nondestructive analysis of interconnection in two-die BGA using TDR', *IEEE Trans on Instr and Meas*, **55**(2), 400–405.
- Chen Z, Zhao J, Zhang Y, Jia G, Liu X, Ren C, Wu W, Sun J, Cao K, Wang S and Shi B (2008), 'Pockel's effect and optical rectification in (111)-cut near-intrinsic silicon crystals', *Appl Phys Lett*, **92**, 251111.
- Chmielak B, Waldow M, Matheisen C, Ripperda C, Bolten J, Wahlbrink T, Nagel M, Merget F and Kurz H (2011), 'Pockels-effect based fully integrated, strained silicon electro-optic modulator', *Opt Express*, **19**, 17212–17219.
- Cho G C, Chen H T, Kraatz S, Karpowicz N and Kersting R (2005), 'Apertureless terahertz near-field microscopy', *Sem Sc Techn*, **20**(7), 286–292.
- Cunningham J, Wood C, Davies A G, Tiang C K, Tosch, P, Evans D A, Linfield E H, Hunter IC and Missous M (2006), 'Multiple-frequency terahertz pulsed sensing of dielectric films', *Appl Phys Lett*, **88**, 071112.
- Cunningham J, Byrne M, Upadhyaya P, Lachab M, Linfield E H and Davies A G (2008), 'Terahertz evanescent field microscopy of dielectric materials using on-chip waveguides', *Appl Phys Lett*, **92**, 032903.
- Debus C, Bolivar P H, Awad M and Nagel M (2009) 'Terahertz biochip technology: toward high-sensitivity label-free DNA sensors', *American Biotechnology Laboratory*, **27**(6), 8, 10–11.
- Dragoman D and Dragoman M (2004), 'Terahertz fields and applications', *Progress Quant Electr*, **28**, 1–66.

- Esenturk O, Melinger J S, Lane P A and Heilweil E J (2009), 'Relative photon-to-carrier efficiencies of alternating nanolayers of zinc phthalocyanine and C-60 films assessed by time-resolved terahertz spectroscopy', *J Phys Chem C*, **113**, 18842–18850.
- Feurer T, Stoyanov N S, Ward D W, Vaughan J C, Statz E R and Nelson K A (2007), 'Terahertz polaritonics', *Ann Rev Mat Res*, **37**, 317–350.
- Gupta S, Frankel M Y, Valdmanis J A, Whitaker J F, Mourou G A, Smith F W and Calawa A R (1991) 'Subpicosecond carrier lifetime in GaAs grown by molecular-beam epitaxy at low-temperatures', *Appl Phys Lett*, **59**, 3276–3278.
- Hamadani B H, Jung S Y, Haney P M, Richter L J and Zhitenev N B (2010), 'Origin of nanoscale variations in photoresponse of an organic solar cell', *Nano Lett*, **10**(5), 1611–1617.
- Hameiri Z, Mai L, Puzzer T and Wenham S R (2011), 'Influence of laser power on the properties of laser doped solar cells', *Sol Ener Mat and Sol Cells*, **95**(4), 1085–1094.
- Harsányi G, Semmens J E and Martell S R (2000), 'A new application of acoustic micro imaging: screening MCM-C multilayer defects', *Microel Reliab*, **40**(3), 477–484.
- Herrmann M, Tani M, Sakai K and Fukasawa R (2002), 'Terahertz imaging of silicon wafers', *J Appl Phys*, **91**(3), 1247–1250.
- Hoffmann M, Fischer B M and Jepsen P U (2005), 'Terahertz Spectroscopy of RNA and DNA and Spot Array Imaging', in Optical Terahertz Science and Technology, *Technical Digest* (CD) (Optical Society of America, 2005), paper WB2.
- Hoffmann R K (1987) 'Handbook of Microwave Integrated Circuits', Artech House.
- Hon N K, Tsia K K, Solli D R and Jalali B (2009), 'Periodically poled silicon', *Appl Phys Lett*, **94**, 091116.
- Huber A J, Keilmann F, Wittborn J, Aizpurua J and Hillenbrand R (2008), 'Terahertz near-field nanoscopy of mobile carriers in single semiconductor nanodevices', *Nano Lett*, **8**(11), 3766–3770.
- Hunsche S, Koch M, Brener I and Nuss M C (1998), 'THz near-field imaging', *Opt Commun*, **150**, 22–26.
- Isenberg J, Biro D and Warta W (2004), 'Fast, contactless and spatially resolved measurement of sheet resistance by an infrared method', *Prog Photovolt: Res Appl*, **12**, 539–552.
- Iwami K, Ono T and Esashi M (2008), 'A new approach to terahertz local spectroscopy using microfabricated scanning near-field probe', *Jap J Appl Phys*, **47**(10), 8095–8097.
- Jacobsen R S, Andersen K N, Borel P I, Fage-Pedersen J, Frandsen L H, Hansen O, Kristensen M, Lavrinenko A V, Moulin G, Ou H, Peucheret C, Zsigri B and Bjarklev A (2006), 'Strained silicon as a new electro-optic material', *Nature*, **441**, 199–202.
- Janßen L, Rinio M, Borchert D, Windgassen H, Bätzner D L and Kurz H (2007), 'Passivating thin bifacial silicon solar cells for industrial production', *Prog Photovolt*, **15**(6), 1540–1543.
- Keilmann F and Hillenbrand R (2004) 'Near-field microscopy by elastic light scattering from a tip', *Phil Trans Royal Soc Of London Series A – Math Phys Engin Scienc*, **362**(1817), 787–805.

- Lai R K, Hwang JR, Nees J, Norris T B and Whitaker J F (1996), 'A fiber-mounted, micromachined photoconductive probe with 15 nV/Hz^{1/2} sensitivity', *Appl Phys Lett*, **69**(13), 1843–1845.
- Lau J H (2011) 'Evolution, Challenge, and Outlook of TSV (Through-Silicon Via) and 3D IC/Si Integration', *IEEE International Conference on Electronics Packaging ICEP*, Nara, Japan, April 13–15.
- Lecaque R, Gresillon S, Barbev N, Peretti R, Rivoal J C and Boccara C (2006), 'THz near-field optical imaging by a local source', *Opt Commun*, **262**(1), 125–128.
- Lee J, Yu S and Kim J (2002), 'Characterization of picosecond electric-pulse propagation on CPW components by transient near-field mapping', *IEEE Trans on Adv Pack*, **25**(3), 459–466.
- Lin Y M, Dimitrakopoulos C, Jenkins K A, Farmer D B, Chiu H Y, Grill A and Avouris P (2010), '100-GHz Transistors from Wafer-Scale Epitaxial Graphene', *Science*, **327**, 662.
- Mayer B, Pletzer T M, Windgassen H, Bleidiessel R and Kurz H (2010), 'Characterisation of selective emitter solar cells by spatially-resolved light-induced lock-in thermography', 25th European Photovoltaic Solar Energy Conference and Exhibition / 5th World Conference on Photovoltaic Energy Conversion, 6–10 September 2010, Valencia, Spain, 2051–2054.
- McGibney E and Barrett J (2006), 'An overview of electrical characterization techniques and theory for IC packages and interconnects', *IEEE Trans On Adv Pack*, **29**(1), 131–139.
- Meyer K E and Mourou G A (1985), 'Two-dimensional E-field mapping with subpicosecond temporal resolution', *Electron Lett*, **21**(13), 568–569.
- Mingirulli N, Stuwe D, Specht J, Fallisch A and Biro D (2011), 'Screen-printed emitter-wrap-through solar cell with single step side selective emitter with 18.8% efficiency', *Prog Photovolt*, **19**(3), 366–374.
- Mitrofanov O, Brener I, Harel R, Wynn J D, Pfeiffer L N, West K W and Federici J (2000), 'Terahertz near-field microscopy based on a collection mode detector', *Appl Phys Lett*, **77**, 3496–3498.
- Miyamaru F, Hayashi S, Otani C, Kawase K, Ogawa Y, Yoshida H and Kato E (2006), 'Terahertz surface-wave resonant sensor with a metal hole array', *Opt Lett*, **31**(8), 1118–1120.
- MONA Consortium (2008), 'A European roadmap for photonics and nanotechnologies', Available from: www.ist-MONA.org.
- Nagel M, Bolivar P H, Brucherseifer M, Kurz H, Bosserhoff A and Büttner R (2002), 'Integrated THz technology for label-free genetic diagnostics', *Appl Phys Lett*, **80**, 154.
- Nagel M, Dekorsy T and Kurz H (1999), 'Spatially resolved optical measurements of electric terahertz signals on passive devices', in Chamberlain J M, ed. *Terahertz Spectroscopy and Applications* **11**, 263–265.
- Nagel M, Dekorsy T, Brucherseifer M, Haring-Bolivar P and Kurz H (2001) 'Characterization of polypropylene thin-film microstrip lines at millimeter and submillimeter wavelengths', *Microwave Opt Technol Lett*, **29**(2), 97–100.
- Nagel M, Richter F, Haring-Bolivar P and Kurz H (2003), 'A functionalized THz sensor for marker-free DNA analysis', *Phys Med Biol*, **48**, 3625–3636.
- Nagel M, Forst M and Kurz H (2006), 'THz biosensing devices: fundamentals and technology', *J Phys-Cond Matt*, **18**, 601–618.

- Nagel M, Michalski A and Kurz H (2011), ‘Contact-free fault location and imaging with on-chip terahertz time-domain reflectometry’, *Opt Express*, **19**, 12509–12514.
- Pfeifer T, Heiliger H M, Loffler T, Ohlhoff C, Meyer C, Lupke G, Roskos H G and Kurz H (1996) ‘Optoelectronic on-chip characterization of ultrafast electric devices: Measurement techniques and applications’, *IEEE J Sel Top Quant Electr*, **2**(3), 586–604.
- Rana F (2008), ‘Graphene terahertz plasmon oscillators’, *IEEE Trans on Nanotechnol*, **7**, 91–99.
- Ryzhii V, Ryzhii M, Satou A, Otsuji T, Dubinov A A and Aleshkin V Y (2009), ‘Feasibility of terahertz lasing in optically pumped epitaxial multiple graphene layer structures’, *J Appl Phys*, **106**, 084507.
- Ryzhii V, Ryzhii M, Mitin V and Otsuji T (2010), ‘Terahertz and infrared photo-detection using p-i-n multiple-graphene-layer structures’, *J Appl Phys*, **107**, 054512.
- Sankaran S and O K K (2005), ‘Schottky barrier diodes for millimeter wave detection in a foundry CMOS process’, *IEEE Electr Dev Lett*, **26**(7), 492–494.
- Schena M, Shalon D, Heller R, Chai A, Brown P O and Davis R W (1996), ‘Parallel human genome analysis: Microarray-based expression monitoring of 1000 genes’, *Proc Natl Acad Sci USA*, **93**(20), 10614–10619.
- Schoen K (2004), ‘High resolution TDR measurements using the PSPL model 4020 and model 4022 9 ps TDR source enhancement modules’, Picosecond Pulse Labs, Available from: <http://www.picosecond.com>.
- Schuster F, Coquillat D, Videlier H, Sakowicz M, Teppe F, Dussopt L, Giffard B, Skotnicki T and Knap W (2011), ‘Broadband terahertz imaging with highly sensitive silicon CMOS detectors’, *Opt Express*, **19**, 7827–7832.
- Shinagawa M and Nagatsuma T (1990) ‘Electrooptic sampling using an external GaAs probe tip’, *Electr Lett*, **26**(17), 1341–1343.
- Tonouchi M (2007), ‘Cutting-edge terahertz technology’, *Nature Photonics*, **1**, 97–105.
- Ulbricht R, Hendry E, Shan J, Heinz T F and Bonn M (2011), ‘Carrier dynamics in semiconductors studied with time-resolved terahertz spectroscopy’, *Rev Mod Phys*, **83**(2), 543–586.
- Valdmanis J A, Mourou G and Gabel C W (1982), ‘Picosecond electrooptic sampling system’, *Appl Phys Lett*, **41**(3), 211–212.
- Valdmanis J A and Mourou G (1986), ‘Subpicosecond electrooptic sampling – principles and applications’, *IEEE J Quant Electr*, **22**(1), 69–78.
- van der Valk N C J and Planken P C M (2002), ‘Electro-optic detection of subwavelength terahertz spot sizes in the near field of a metal tip’, *Appl Phys Lett*, **81**(9), 1558–1560.
- von Ribbeck H G, Brehm M, van der Weide D W, Winnerl S, Drachenko O, Helm M and Keilmann F (2008), ‘Spectroscopic THz near-field microscope’, *Opt Express*, **16**(5), 3430–3438.
- Wächter M, Nagel M and Kurz H (2005), ‘Frequency-dependent characterization of THz Sommerfeld wave propagation on single-wires’, *Opt Express*, **13**, 10815–10822.
- Wächter M, Nagel M and Kurz H (2009), ‘Tapered photoconductive terahertz field probe tip with subwavelength spatial resolution’, *Appl Phys Lett*, **95**, 041112.

- Wächter M, Matheisen C, Waldow M, Wahlbrink T, Bolten J, Nagel M and Kurz H (2010), ‘Optical generation of terahertz and second-harmonic light in plasma-activated silicon nanophotonic structures’, *Appl Phys Lett*, **97**, 161107.
- Withayachumnankul W, Png G M, Yin X X, Atakaramians S, Jones I, Lin H Y, Ung B S Y, Balakrishnan J, Ng B W H, Ferguson B, Mickan S P, Fischer B M and Abbott D (2007), ‘T-ray sensing and imaging’, *Proc IEEE*, **95**(8), 1528–1558.
- Yang K, David G, Yook J G, Papapolymerou I, Katehi L P B and Whitaker J F (2000), ‘Electrooptic mapping and finite-element modeling of the near-field pattern of a microstrip patch antenna’, *IEEE Trans Microw Th Techn*, **48**(2), 288–294.
- Yuan T, Xu J Z and Zhang X C (2004), ‘Development of terahertz wave microscopes’, *Infrared Phys Techn*, **45**(5–6), 417–425.
- Zschech E, Huebner R, Chumakov D, Aubel O, Friedrich D, Guttmann P, Heim S and Schneider G (2009), ‘Stress-induced phenomena in nanosized copper interconnect structures studied by x-ray and electron microscopy’, *J Appl Phys*, **106**, 093711.

DOI: 10.1533/9780857096494.2.403

Abstract: Sensing the terahertz (THz) waves in micro and nanometer regions is key for highly sensitive detection and high resolution imaging. For this purpose, the applications of nanoscale materials and devices are opening doors to new THz sensing and imaging technologies. This chapter gives an overview of nanoscale THz sensors, and then describes highly sensitive and frequency-tunable THz detectors and near-field THz imagers based on carbon nanotubes and semiconductor heterostructures.

Key words: terahertz, carbon nanotube, semiconductor heterostructure, two-dimensional electron gas, near-field imaging.

13.1 Introduction

Terahertz (THz) technology is nowadays in great demand in a wide variety of fields, ranging from basic science such as biochemical spectroscopy, astronomy, and nano-materials science, to practical areas such as environmental science, medicine, agriculture and security.^{1,2} The advantages of the THz wave are that it can be transmitted through objects opaque to visible light, and that the corresponding photon energy, 1–100 meV, is in the important energy spectrum for various materials and biomolecules. Moreover, the THz wave is much safer and does not damage objects much, when compared with X-rays. These features allow various applications of imaging and spectroscopy with THz waves, and hence make THz measurements a strong tool for non-destructive inspection.

However, when compared with other frequency regions, generation and detection of THz waves have not been technically well established. From the aspect of high frequency electronics, the frequency of the THz wave is too high to be handled with conventional semiconductor technology. From the aspect of optics/photonics, the photon energy of the THz wave is much lower than that of visible and near-infrared light, and, therefore, it is not easy to control and manipulate the THz wave with existing electronics and optics/photonics technologies, which is often referred to as the ‘THz gap’.

The applications of nanoscale materials and devices, however, are opening up new opportunities to overcome such difficulties. Nanostructured devices based on superconductors, semiconductors and carbon materials have enabled breakthroughs in THz technologies, for example quantum cascade lasers,³ semiconductor quantum dot (QD) detectors,⁴ nanoscale superconductor bolometers,⁵ coherent emitters with high-temperature superconductors,⁶ and so on. Such THz nano-devices are also closely related to the improvement in spatial resolution of THz imaging. From this viewpoint, I will present micro- and nanoscale THz detectors and imagers in the sections that follow.

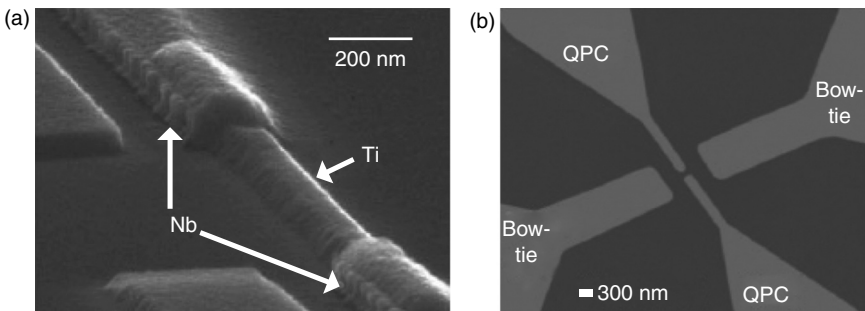
13.2 Nanoscale terahertz detector

In this section, I explain how the use of nanoscale devices leads to high-performance THz detectors. First I review several types of superconductor- and semiconductor-based THz detectors and then introduce another promising device – THz detectors with carbon nanotubes (CNT). The CNT THz detector has three types of detection mechanism: bolometric detection, photon-assisted tunneling (PAT), and single photon-electron converter. A performance comparison in terms of the noise equivalent power (NEP) is presented.

13.2.1 Superconductor and semiconductor

Superconductor THz detectors generally are of two types: bolometers and photoconductors. The bolometer is based on temperature increase induced by THz absorption. Wei *et al.*⁵ reported that a nanoscale superconducting bolometer (Fig. 13.1a) has the capability of detecting individual THz photons. On the other hand, THz detection by superconductor tunnel junctions utilizes electron tunneling through the junction via THz absorption. The typical NEP of this detector is $\sim 10^{-16}$ W/Hz $^{1/2}$ at 0.8 K.⁷

THz detectors based on semiconductors are also roughly categorized into bolometers and photoconductors. A representative device of the former type is the silicon bolometer, which has NEP $\sim 10^{-15}$ W/Hz $^{1/2}$ at 4.2 K. Also, a quantum point contact device with one-dimensional electron channel (Fig. 13.1b) has been shown to work as a THz bolometer.⁸ In this device, the THz-detected signal is generated as a result of temperature-dependent transmission through a saddle potential at the point contact region. As a photoconductor type, a Ge:Ga device is well known. When this crystal is subject to uniaxial compression, the detectable wavelength region extends from 50–110 μm to 110–220 μm and NEP reaches $\sim 10^{-17}$ W/Hz $^{1/2}$ at 2 K. The use of nanoscale islands connected to electrodes, or semiconductor QDs, have been demonstrated to enable single photon detection at very low temperature environment (< 0.3 K), showing NEP of $\sim 10^{-22}$ W/Hz $^{1/2}$ at 0.05 K.⁴



13.1 (a) Nanoscale superconductor THz bolometer. (Reprinted with permission from Reference 5.) (b) Semiconductor quantum point contact (QPC) THz detector. (Reprinted with permission from Reference 8.)

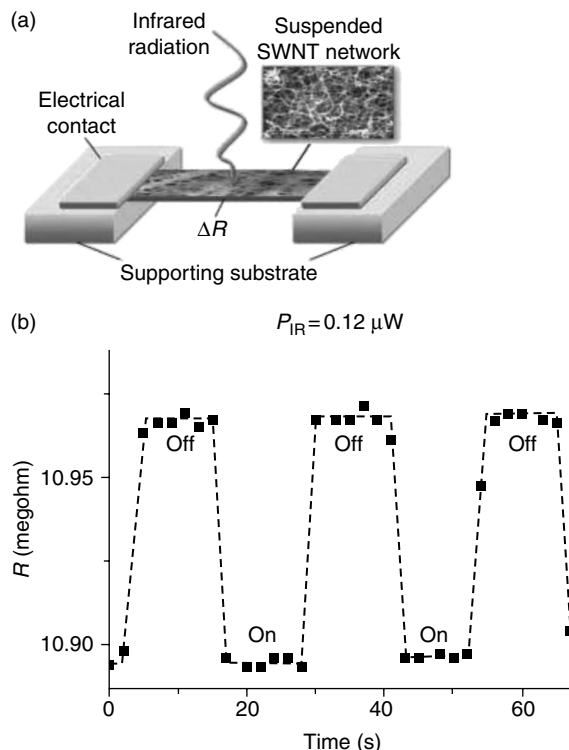
Another detection mechanism is heterodyne (frequency conversion) detection. Schottky-barrier diodes, GaAs/AlGaAs heterostructures,⁹ superconductors,¹⁰ etc. are used as frequency mixers. Here, a beat signal arising from the frequency difference with a local oscillator is measured. This type of detector is often used in the fields of astronomy and environmental science.

13.2.2 Carbon nanotubes

Bolometric THz detection

The CNT is another promising technology for high-performance THz detectors, owing to its unique one-dimensional structure.¹¹ In the near-infrared region, a sensor using the CNT transistor has been successfully developed.¹² The sensing mechanism is based on bolometric detection, in which the near-infrared illumination causes a rise in temperature of the CNT film (Fig. 13.2). They reported a responsivity of ~ 1000 V/W and a response time of ~ 50 ms. In the THz region, the photon energy becomes much smaller, thus making highly sensitive THz detection a difficult task. By using CNT bundles with an antenna and a silicon lens, Fu *et al.*¹³ demonstrated the bolometric THz detection ranging from 0.69 to 2.54 THz (Fig. 13.3), responsivity of ~ 10 V/W.

Although these groups opened up new possibilities for the CNT-based infrared/THz detection, much higher performance has not been achieved to date, compared to the detectors based on superconductors and semiconductors. This suggests that a new detection mechanism and/or device structure are required. In the following two sections, I will introduce other types of the CNT-based THz detectors.^{14,15} Unlike bolometric detection, these detectors are based on THz photon detection, which has two detection mechanisms: PAT¹⁴ and current peak shift.¹⁵ The use of the former has allowed frequency-tunable detection by sweeping the gate voltage. For the latter,

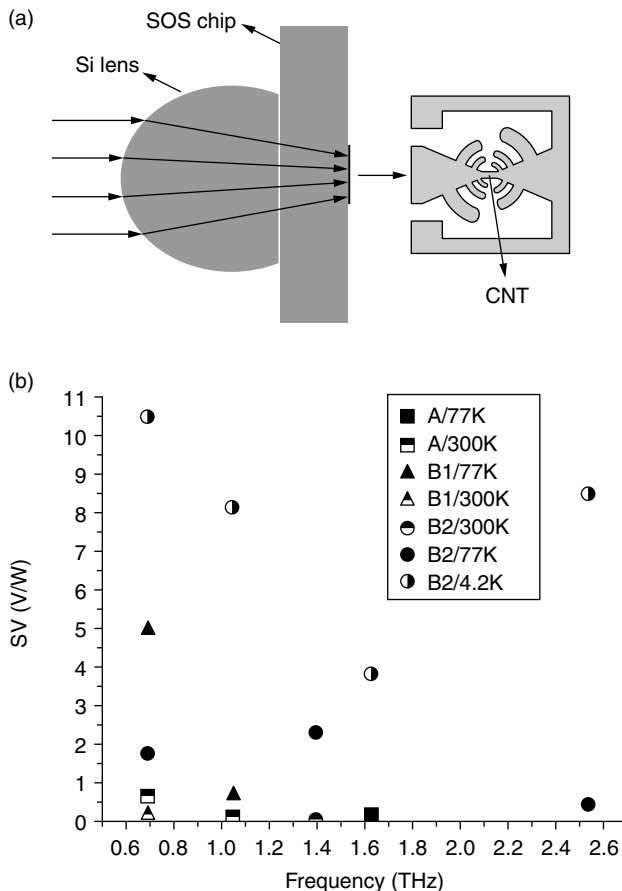


13.2 Near-infrared detector with carbon nanotube films. (a) Single-wall CNT network suspended between electrical electrodes. The thickness of the CNT film is 100 nm. (b) Modulation of electrical resistance of the CNT film at 50 K when square-wave pulses of infrared radiation were applied. The power of the infrared wave is $0.12 \mu\text{W}$. (Reprinted with permission from Reference 12.)

THz irradiation causes peak shift of CNT currents relative to gate voltage, leading to the realization of ultra-high sensitivity.

THz photon-assisted tunneling

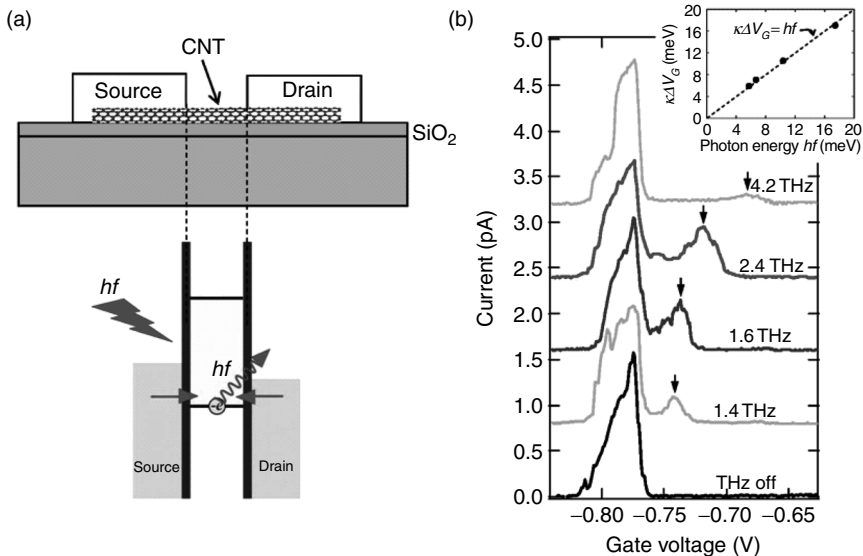
PAT is based on the theory proposed by Tien and Gordon in 1963.¹⁶ They discussed the interaction of a nanoscale island with an electromagnetic wave, and showed that new energy bands, the so-called photon sidebands, are formed by the a.c. electric potential of the electromagnetic wave at intervals of nhf (n , integer number; h , Plank's constant; f , frequency of the electromagnetic wave). This phenomenon has been previously observed for superconductor tunneling devices^{17,18} and semiconductor QDs^{19,20} with microwave irradiation. Tucker and Feldman²¹ called this phenomenon 'quantum detection' and discussed the application to an electromagnetic wave detector. However, most of the earlier work for the QDs was done in



13.3 THz detector with carbon nanotube transistors. (a) CNT device coupled with silicon lens and antenna. (b) Responsivities of the CNTTHz detectors in terms of voltage sensitivity SV vs. frequency. (Reprinted with permission from Reference 13.)

the microwave region. In order to realize THz-PAT in the QD, we used a CNT-QD. Compared to conventional QDs based on superconductors and semiconductors, the CNT-QD has higher charging energy and energy level spacing due to quantum electron confinement. These values typically reach ~ 10 meV, corresponding to a THz frequency (~ 2.4 THz). This property suggests a potential application of CNT-QDs to THz detectors. For this reason we studied THz response of the CNT-QDs.¹⁴

The upper panel of Fig. 13.4a shows a sketch of the lithographically-fabricated CNT-QD. We used metallic single-wall CNTs with a diameter of ~ 1 nm. The CNT-QD has source and drain electrodes with an interval of ~ 600 nm and side-gate electrodes. In this device, electrons are confined to a very small area of 1×600 nm 2 , thus forming a QD.

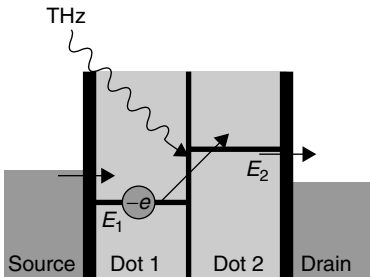


13.4 (a) Upper panel: schematic of a carbon nanotube quantum dot (CNT-QD). Lower panel: schematic view of electron tunneling processes in a QD under the electromagnetic wave irradiation. (b) Source-drain current I_{SD} versus gate voltage V_G for the frequency of the incident THz wave, $f = 1.4, 1.6, 2.4$ and 4.2 THz . The experimental curves for the THz irradiation are offset by multiples of 0.8 pA for clarity. The inset shows the energy spacing, $\kappa\Delta V_G$, between the original peaks and the satellite peaks as a function of the photon energy, hf , of the THz wave. The dashed line in the inset is a guide to the eye corresponding to $\kappa\Delta V_G = hf$.

Such a QD device with source, drain and gate electrodes works as a single-electron transistor (SET). By sweeping the gate voltage and measuring the source–drain current, periodic current oscillation is generated (Coulomb oscillation). The PAT in the QD can be thus observed as the generation of new current signals via inelastic electron tunnel when electrons exchange photons (lower panel of Fig. 13.4a).

The CNT-QD device was mounted in a ${}^4\text{He}$ cryostat at a temperature of 1.5 K , and the device was irradiated with THz waves through a THz transparent window made from a mylar sheet. As a THz illumination source, a THz gas laser pumped by a CO_2 -gas laser was used.

Figure 13.4b shows the data for the THz response of the CNT-QD. In contrast to the data without THz irradiation (black curve), when the THz wave is illuminated, new satellite current peaks are generated. It is also seen that its peak position relative to the gate voltage shifts in the positive direction with increasing the frequency, f , of the THz wave. As displayed in the inset of Fig. 13.4b, the energy spacing, $\kappa\Delta V_G$, between the original peaks and



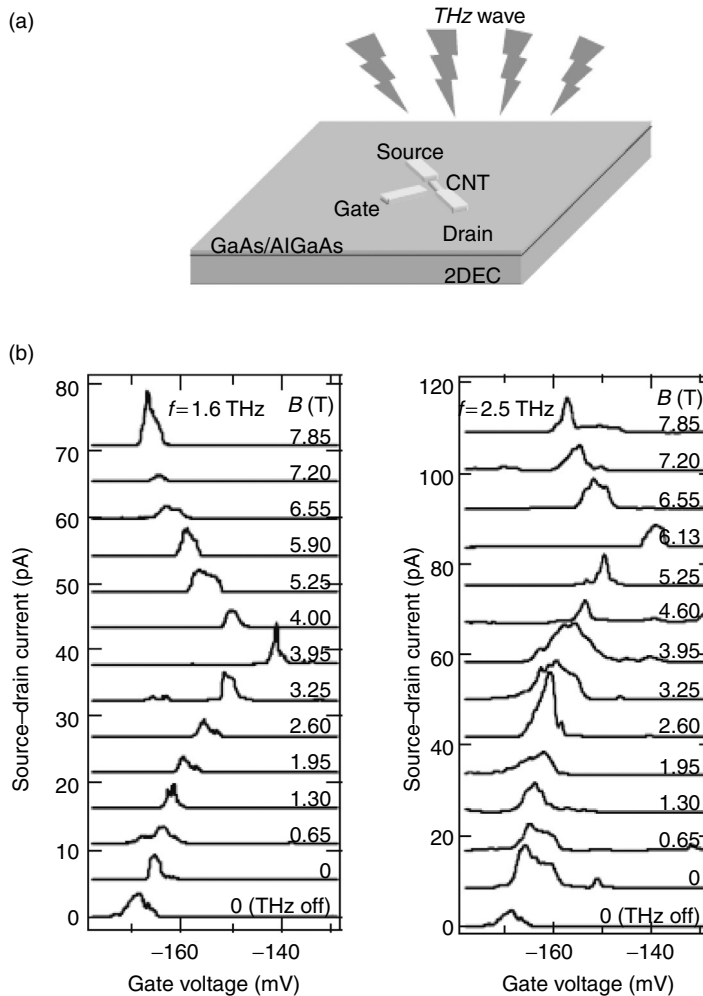
13.5 Schematic of the PAT process for the double-coupled QD.

the satellite peaks is in good agreement with the photon energy, hf , of the THz wave. This provides clear evidence for the THz-PAT in the CNT-QD. From the viewpoint of the THz detector, this result means that the CNT-QD was demonstrated to work as a frequency-tunable THz detector. Assuming a coupling efficiency of 1% between the CNT-QD and the THz wave, the NEP is estimated to be $\sim 10^{-14}$ W/Hz $^{1/2}$.

With respect to frequency selectivity, at present, the frequency resolution, or the width of the satellite current peak, is determined by the fact that electrons tunnel between the electron reservoir of the electrode and the discrete energy level of the QD. In order to improve the frequency selectivity, we plan to use a double-coupled CNT-QD, in which the PAT occurs as a consequence of electron transitions between two well-defined discrete levels, as depicted in Fig. 13.5.

Ultra-sensitive readout of THz-excited carriers (photon-electron converter)

For THz detector based on PAT, though frequency-tunable THz detection has been achieved, the detection sensitivity is insufficient. This is because within this detection mechanism, the absorption of one photon leads to the generation of only one electron, even if quantum efficiency of 100% is assumed. In order to obtain a measurable current, pA–fA, it is necessary to absorb 10^5 – 10^6 photons per second. This limits the detection sensitivity. To resolve this problem, we have created a new designed device:¹⁵ a CNT-SET is integrated with a GaAs/AlGaAs heterostructure containing a two-dimensional electron gas (2DEG) layer (Fig. 13.6a). This hybrid device has two separate roles: THz absorption in the 2DEG and signal readout in the CNT-SET. A basic idea of the THz detection with this device is that the CNT-SET senses electrical polarization induced by THz-excited electron-hole pairs in the 2DEG. Since the SET has the detection sensitivity of single electron, the CNT/2DEG device is expected to exhibit ultra-high sensitivity.



13.6 (a) THz detector with the CNT/2DEG hybrid structure. (Reprinted with permission from Reference 15.) (b) Source-drain current I_{SD} versus gate voltage V_G of the CNT-SET under the THz irradiation. The magnetic field B was applied to the detector perpendicular to the 2DEG plane, and the B values in units of Tesla (T) are given on the right-hand side of the figures. The data with the THz irradiation are offset for clarity. (Reprinted with permission from Reference 15.) (c) Time response of the THz-detected signal (the CNT-SET current I_{SD}) as the THz irradiation was cycled on and off. In this measurement, the intensity of the THz emitter based on another 2DEG was as low as $\sim 0.1 \text{ fW}$. (Reprinted with permission from Reference 15.)

(Continued)

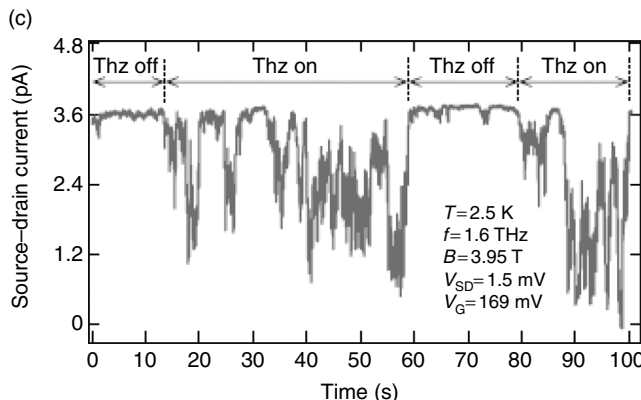


Fig. 13.6 Continued.

Figure 13.6b displays the THz response of the 2DEG/CNT device. We applied magnetic field, B , in the direction perpendicular to the 2DEG plane. The experimental setup for the THz measurements here is similar to that for the THz-PAT in the previous section. The laser intensity was reduced with THz attenuating filters and the intensity of the THz irradiation on the sample is estimated to be 0.75 nW/mm^2 .

The data of Fig. 13.6b shows that the THz illumination caused a shift in the current peak position in the direction of positive V_G . It is also found that for the irradiation at 1.6 THz, the shift was monotonically enhanced by increasing B up to 3.95 T, then decreased when B was further raised beyond $B = 3.95\text{ T}$. On the other hand, in case of the 2.5-THz irradiation, the B value for the maximum of the peak shift changed to 6.13 T.

Let me discuss the physical meaning behind the above features. When the 2DEG is subject to a perpendicular magnetic field, its energy state splits into discrete Landau levels. When the photon energy, hf , of the THz wave matches the Landau-level separation eB/m^* , the 2DEG absorbs the THz wave (cyclotron resonance) well. Here, e is the elementary charge, and m^* is the cyclotron effective mass for the crystal where the 2DEG is embedded. The above experimental data ($B = 3.95\text{ T}$ for $f = 1.6\text{ THz}$ and $B = 6.13\text{ T}$ for $f = 2.5\text{ THz}$) reveal that the f value is proportional to the B value for the maximum of the peak shift, which is consistent with the cyclotron resonance. In addition, from these data, the associated m^* value is derived to be $0.067m_0$, where m_0 is the free electron mass. This m^* value agrees with the cyclotron effective mass for a GaAs-based 2DEG.²² These facts indicate that the current peak shift of the CNT-SET arises from the THz absorption of the 2DEG.

How does the THz absorption of the 2DEG cause the current peak shift of the CNT-SET? Based on the above experimental facts, the microscopic dynamics of the THz-excited carriers can be understood as follows. The 2DEG is known to have a random impurity potential with a typical period

of 20–100 nm.²³ Accordingly, the THz-excited electrons and holes drift in opposite directions owing to the local electric field gradient arising from the random potential.²⁴ As a result, they are spatially separated from each other. Such separation of electron–hole pairs generates electrical polarization within the 2DEG. This situation is equivalent to the application of an additional gate voltage to the CNT-SET, resulting in the current peak shift.

Based on the above, we expect that when an extremely weak THz wave is illuminated onto the 2DEG, the current of the CNT-SET will switch on and off, according to the excitation and recombination of the electron and hole pairs. We then studied the temporal behavior of the THz-detected signal (the I_{SD} change associated with the current peak shift) as the THz irradiation was cycled on and off. We here used cyclotron radiation^{25,26} from another 2DEG device fabricated on a different GaAs/AlGaAs chip. We reduced its intensity to an extremely low level, in the order of 0.1 fW. We mounted, face to face, the CNT/2DEG detector and the 2DEG-based THz emitter in the same superconducting magnet, so that the two 2DEGs were both in cyclotron resonance. Figure 13.6c displays time trace of I_{SD} for an on/off sequence of the THz irradiation at $V_G = -169$ mV, $V_{SD} = 1.5$ mV, $B = 3.95$ T, and $f = 1.6$ THz. This result shows that the CNT-SET current was stable for the THz-off, whereas it repeatedly switched during the THz irradiation. This feature means that the CNT-SET detects temporal processes of the generation and relaxation of the THz-excited carriers in the 2DEG, namely ultra-sensitive readout of the THz-detected signal has been achieved and the resulting photon-electron converter has been developed.

Considering that the detection area of the CNT-SET is approximately determined by the wavelength (184 μm at $f = 1.6$ THz) and taking into account the radiation area, 3 mm², of the THz wave, the NEP is estimated to be 10^{-18} – 10^{-19} W/Hz^{1/2} at 2.5 K. This value is superior to other THz detectors operating at 2–4K, for example, Ge:Ga photoconductive detector (NEP $\sim 10^{-17}$ W/Hz^{1/2} at 2K) and Si bolometer (NEP $\sim 10^{-15}$ W/Hz^{1/2} at 4.2 K). Our strategy for further NEP improvement is to efficiently concentrate the THz electric field onto the CNT-SET. Implementing a metamaterial structure will be a promising method for realizing this. Reference 27 reported that when the THz wave is illuminated onto a metal–hole array, the THz electric field is concentrated in the edge region of the metal hole. By integrating such arrayed metal–hole structure with the CNT/2DEG detector, we expect to obtain an NEP enhancement of at least one order.

13.3 Near-field terahertz imager

One important application of the THz detector is THz imaging, in which the intensity distribution of reflected or transmitted THz waves is mapped out. Simultaneous measurements of frequency spectra allow characterizing physical/chemical properties. The technique therefore can be used

in non-destructive inspection, in a safer manner than the X-ray imaging. However, one concern of the THz imaging is low spatial resolution, which comes from the much longer wavelength compared to that of the visible light. A powerful method for overcoming the diffraction limit of the resolution is to use near-field imaging technology.^{28,29} Nevertheless, establishing near-field imaging in the THz region is a formidable task, because basic necessary components, such as high-transmission wave line suitable for near-field imaging, have not been well developed compared to other frequency regions.

In the next section, I review briefly the current status of near-field THz imaging and then describe high resolution THz imager based on micro/nano-sized THz detectors.

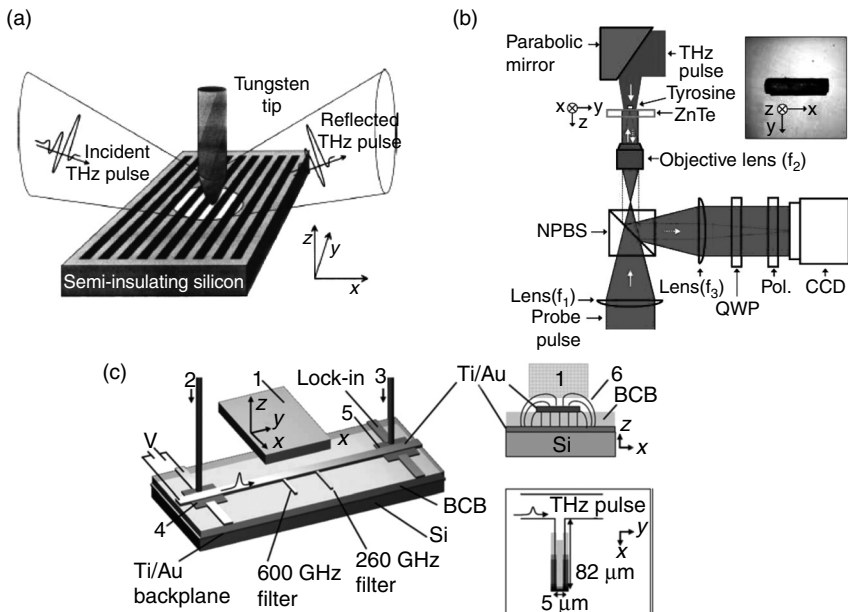
13.3.1 Near-field THz imaging

A basic principle of near-field imaging is that when an electromagnetic wave is illuminated onto an aperture smaller than a wavelength, a localized evanescent field (near-field) is generated just behind the aperture. The size of the evanescent field is determined only by the aperture size, and not the wavelength. By illuminating and/or detecting the evanescent field, it is possible to obtain high resolution beyond the diffraction limit.

Conventional systems for near-field imaging are generally categorized as an aperture type and an aperture-less (tip) type. In the visible and near-infrared regions, either a tapered, metal-coated optical fiber (aperture type)³⁰ or a metal tip (aperture-less type)³¹ is used. In the microwave region, either a sharpened waveguide (aperture type)³² or a coaxial cable (aperture-less type)³³ is used. Because the intensity of the evanescent field is very weak, the realization of near-field imaging needs a highly sensitive detection scheme, such as a high-transmission wave line and a highly sensitive detector.

Several methods for near-field imaging in the THz region have been presented. In the aperture type, a metal hole is used to obtain a resolution better than $\lambda/4$.³⁴ This method, however, has the drawback of low wave transmission through the small aperture, which requires detecting very weak waves. Mitrofanov *et al.* fabricated a GaAs pyramid-like structure protruding through the aperture and enhanced coupling between the incident THz waves and the aperture.³⁵

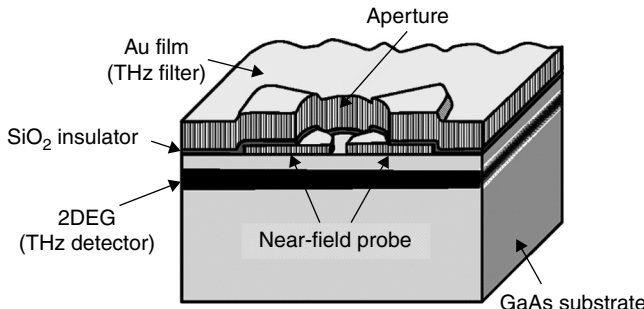
For the aperture-less type, a sharpened antenna,³⁶ a metal tip³⁷ (Fig. 13.7a) and a cantilever³⁸ have been reported. Although the aperture-less technique enables high spatial resolution, it has the problem of separation from a far-field component of an incident wave, which generates a large background signal. For this reason, in most instances, the probe position is modulated and the synchronously detected signal is measured. However, this scheme makes the whole system and its operation complicated.



13.7 Three types of near-field THz imaging systems: (a) metal tip (reprinted with permission from Reference 37), (b) surface of nonlinear optical crystal (NPBS, non-polarized beam splitter) (reprinted with permission from Reference 41) and (c) surface of BCB (benzocyclobutene) waveguide ((1) GaAs dielectric sample; (2) near-infrared excitation pulsed laser; (3) time-delayed detection pulsed laser; (4) low-temperature-grown GaAs THz emitter, integrated into the microstrip line; (5) low-temperature-grown GaAs THz detector, integrated into the microstrip line and (6) THz evanescent field around the microstrip line) (reprinted with permission from Reference 42).

Another method is to use a THz emission spot of size smaller than the wavelength. When an optical beam illuminates a nonlinear optical crystal such as ZnTe, it generates THz emission. If the incident optical beam is tightly focused, the radiation region of the THz emission in the close vicinity of the crystal surface (in the near-field zone) is reduced to the sub-wavelength size. By placing a sample directly on the crystal surface and scanning the focused optical beam relative to the crystal surface, it is possible to obtain near-field THz images^{39–41} (Fig. 13.7b).

There is an alternative method of this type, in which the surface of a THz waveguide made from dielectric materials is used as a sub-wavelength THz source. It is known that the evanescent field is generated in the near-field region close to the outside surface of dielectric materials, such as a Si waveguide. By illuminating the THz evanescent field onto a sample and scanning the sample across the dielectric materials, near-field THz imaging is possible. Figure 13.7c shows an example of such a method, in which Benzocyclobutene (low loss dielectric material) was used.⁴²



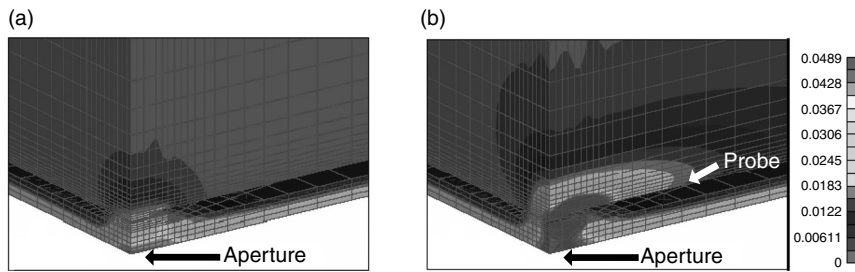
13.8 Schematic representation of the integrated near-field THz imager.

13.3.2 Integrated near-field THz imager

In contrast with the above methods, our basic idea for achieving near-field THz imaging is that a micro/nano-sized THz detector is directly coupled with the THz evanescent field in a near-field zone.^{43,44} For this purpose, we have fabricated a novel integrated device. As schematically shown in Fig. 13.8, an aperture of 8 μm diameter and a planar probe are deposited on the surface of a GaAs/AlGaAs heterostructure chip. The aperture and the probe are insulated by a 50 nm thick SiO_2 layer. The GaAs chip has a 2DEG layer at the heterointerface, whose electron mobility is 18 m^2/Vs and sheet electron density is $4.4 \times 10^{15} \text{ m}^{-2}$ at 77 K. The 2DEG, located 60 nm below the chip surface, works as a THz detector. The source and drain electrodes were extended to the side surfaces of the chip, to each of which an electrical wire was attached.

In this device, the THz evanescent field generated just behind the aperture is directly sensed by the 2DEG detector thanks to the close vicinity to the detector and the aperture. Additionally, the presence of the planar probe changes the spatial distribution of the evanescent field, enhancing the coupling of the evanescent field to the 2DEG detector. This is expected to lead to an increase in the detection sensitivity. An advantage of this device structure is that all the components: an aperture, a probe and a detector are integrated on one GaAs/AlGaAs chip. This scheme eliminates any optical and mechanical alignments between each component, resulting in an easy-to-use and robust system.

Figure 13.9 displays calculations of THz electric field distributions around the aperture using a finite element method. We compared the device with aperture alone with that of aperture combined with probe, where the aperture diameters are the same. In the case of the device with aperture alone, the electric field is concentrated in the vicinity of the aperture. For this reason, the conventional aperture-based technique generally



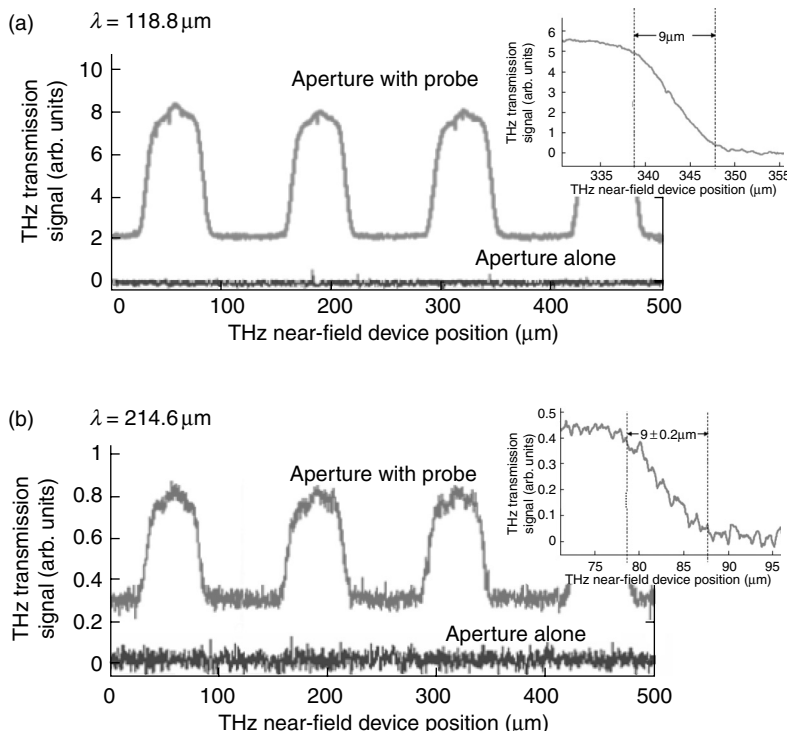
13.9 Calculations of THz electric field distributions near the aperture of the near-field THz imager. (a) The device with the aperture alone and (b) that with the aperture and probe were compared.

has the problem of low transmission through the aperture. On the other hand, when the probe is present just behind the aperture, the electric field expands into the interior region of the GaAs substrate. This result indicates that the presence of the probe changes the distribution of the evanescent field, enhancing the coupling between the evanescent field and the 2DEG THz detector.

In order to confirm experimentally the above effect and evaluate spatial resolution, we measured the THz transmission distribution by scanning the device across a sample. As a THz illumination source, the THz gas laser pumped by the CO₂-gas laser was used. The THz radiation was chopped at 16 Hz and the synchronous amplitude modulation of the voltage change of the 2DEG was measured with a lock-in amplifier. The sample was made up of a THz transparent substrate, the surface of which was covered at regular intervals by THz-opaque Au film. The widths of THz opaque and transparent regions across the scan direction are 80 μm and 50 μm, respectively. We compared the probe-integrated aperture and the aperture alone.

Figure 13.10 clearly shows that in the former situation, a large signal is seen, whereas in the latter situation, no signal is observed. This feature does not depend on the wavelength of the incident THz wave. The enhancement factor of the signal amplitude between the two devices was 41 for $\lambda = 118.8 \mu\text{m}$ and 67 for $\lambda = 214.6 \mu\text{m}$. These results are consistent with the calculations of Fig. 13.9, demonstrating that the detection sensitivity has been improved due to the enhancement of the THz evanescent field distribution caused by the presence of the probe.

From the decay curves shown in the inset of Fig. 13.10, spatial resolution of the near-field THz device is observed to be 9 μm. The resolution does not depend on the wavelength of the THz wave and is far beyond the diffraction limit $\lambda/2$ (107.3 μm) for the wavelength of $\lambda = 214.6 \mu\text{m}$. These features are characteristic of near-field effect, thus indicating that

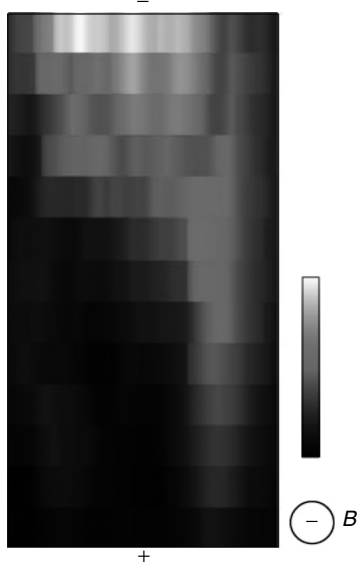


13.10 THz transmission signal as a function of the position of the near-field THz imager for (a) $\lambda = 118.8 \mu\text{m}$ and (b) $\lambda = 214.6 \mu\text{m}$. The insets show magnification of the decay curves of the signals.

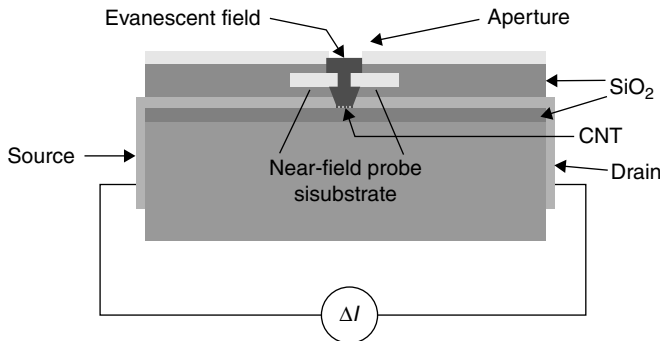
the present device works as a near-field THz imager. We have recently achieved higher resolution of 500 nm ($\sim\lambda/430$) by using a 2DEG with a smaller aperture size.

Figure 13.11 displays a near-field image of THz emission distribution in another 2DEG sample on a GaAs/AlGaAs heterostructure at a current of 160 μA , taken with the above device (resolution: 9 μm).⁴⁵ The THz emission here occurs as a consequence of inter-Landau-level transitions of electrons in the 2DEG under magnetic field. The length and width of the 2DEG channel are 400 μm and 200 μm . The result reveals asymmetric distribution between the source- and drain-contact sides, which does not simply follow electric field distribution in quantum Hall devices. This feature can be attributed to a very long equilibrium length of excited electrons.^{46,47}

To further improve spatial resolution, it is critical to achieve high detection sensitivity and high spatial resolution simultaneously. This is because reducing a sensing area leads to further reduction in the THz intensity to be detected. For the resolution improvement, the use of the CNT THz detector is promising, because it exhibits much higher sensitivity and has a much



13.11 Near-field image of THz emission distribution in another 2DEG sample at a current of $160\ \mu\text{A}$. The 2DEG-channel length and width are $400\ \mu\text{m}$ and $200\ \mu\text{m}$. In this measurement, a magnetic field was applied perpendicular to the 2DEG plane and the Landau-level filling factor for the sample was 1.83. This THz map was obtained using the imager depicted in Fig. 13.8. (Reprinted with permission from Reference 45.)



13.12 Sketch of the improved structure of the near-field THz imager with a carbon nanotube detector. (Reprinted with permission from Reference 45.)

smaller sensing area ($\sim 100\ \text{nm}$), compared to the 2DEG detector. When the CNT detector is integrated with an aperture and a probe as schematically represented in Fig. 13.12, the resulting device would show ultra-high sensitivity and nanometer resolution.⁴⁵

13.4 Conclusion

In this chapter, I have presented novel THz detectors and imagers based on the micro- and nanoscale carbon devices and semiconductors, such as CNTs and 2DEGs. At present, the CNT-based THz detectors are categorized into the three types: bolometric detection, PAT, and single photon-electron converter. The last type of detector has provided THz detection with high sensitivity and frequency selectivity. As an application of the THz detector, the near-field THz imager is introduced. Using the new integrated device structure where the micro/nano-sized 2DEG detector is directly coupled with the THz evanescent field, highly sensitive detection of the THz evanescent field and near-field THz imaging have been achieved. For the next step, the use of the CNT THz detector would enable ultra-sensitive and nanometer-resolution THz imaging.

Regarding the application of the THz detector and imager, materials science and biochemistry are interesting research targets. In these fields, the detection of very weak THz radiation from electrons in materials and biomolecules is expected to reveal much information concealed behind materials properties and life activities.

13.5 Acknowledgments

This work was supported by the Japan Science and Technology Agency, Research Foundation for Opto-Science and Technology, the Canon Foundation, the Funding Program for Next Generation World-Leading Researchers, and the Grants-in-Aid for Scientific Research of the Ministry of Education, Culture, Sports, Science and Technology.

13.6 References

1. B. Ferguson and X-C. Zhang, ‘Materials for terahertz science and technology’, *Nature Materials* **1**, 26 (2002).
2. M. Tonouchi, ‘Cutting-edge terahertz technology’, *Nature Photonics* **1**, 97 (2007).
3. B. S. Williams, ‘Terahertz quantum-cascade lasers’, *Nature Photonics* **1**, 517 (2007).
4. S. Komiyama, O. Astafiev, V. Antonov, H. Hirai and T. Kutsuwa, ‘A single-photon detector in the far-infrared range’, *Nature* **403**, 405 (2000).
5. J. Wei, D. Olaya, B. S. Karasik, S. V. Pereverzev, A. V. Sergeev and M. E. Gershenson, ‘Ultrasensitive hot-electron nanobolometers for terahertz astrophysics’, *Nature Nanotechnology* **3**, 496 (2008).
6. L. Ozyuzer, A. E. Koshelev, C. Kurter, N. Gopalsami, Q. Li, M. Tachiki, K. Kadowaki, T. Yamamoto, H. Minami, H. Yamaguchi, T. Tachiki, K. E. Gray, W.-K. Kwok and U. Welp, ‘Emission of coherent THz radiation from superconductors’, *Science* **318**, 1291 (2007).

7. S. Ariyoshi, C. Otani, A. Dobroiu, H. Matsuo, H. Sato, T. Taino, K. Kawase and H. Shimizu, 'Terahertz imaging with a direct detector based on superconducting tunnel junctions', *Appl. Phys. Lett.* **88**, 203503 (2006).
8. J. W. Song, G. R. Aizin, J. Mikalopas, Y. Kawano, K. Ishibashi, N. Aoki, J. L. Reno, Y. Ochiai and J. P. Bird, 'Bolometric THz detection in pinched-off quantum point contacts', *Appl. Phys. Lett.* **97**, 083109 (2010).
9. K. S. Yngvesson, 'Ultrafast two-dimensional electron gas detector and mixer for terahertz radiation', *Appl. Phys. Lett.* **76**, 777 (2000).
10. A. D. Semenov, H.-W. Hübers, H. Richter, M. Birk, M. Krocka, U. Mair, Y. B. Vachtomin, M. I. Finkel, S. V. Antipov, B. M. Voronov, K. V. Smirnov, N. S. Kaurova, V. N. Drakinski and G. N. Gol'tsman, 'Superconducting hot-electron bolometer mixer for terahertz heterodyne receivers', *IEEE Trans. Applied Superconductivity* **13**, 168–171 (2003).
11. R. Saito, G. Dresselhaus and M. S. Dresselhaus, *Physical Properties of Carbon Nanotubes*; Imperial College Press: London, 1998.
12. M. E. Itkis, F. Borondics, A. Yu and R. C. Haddon, 'Bolometric infrared photo-response of suspended single-walled carbon nanotube films', *Science* **312**, 413 (2006).
13. K. Fu, R. Zannoni, C. Chan, S. H. Adams, J. Nicholson, E. Polizzi and K. S. Yngvesson, 'Terahertz detection in single wall carbon nanotubes', *Appl. Phys. Lett.* **92**, 033105 (2008).
14. Y. Kawano, T. Fuse, S. Toyokawa, T. Uchida and K. Ishibashi, 'Terahertz photon-assisted tunneling in carbon nanotube quantum dots', *J. Appl. Phys.* **103**, 034307 (2008).
15. Y. Kawano, T. Uchida and K. Ishibashi, 'Terahertz sensing with a carbon nanotube/two-dimensional electron gas hybrid transistor', *Appl. Phys. Lett.* **95**, 083123 (2009).
16. P. K. Tien and J. P. Gordon, 'Multiphoton process observed in the interaction of microwave fields with the tunneling between superconductor films', *Phys. Rev.* **129**, 647 (1963).
17. J. M. Hergenrother, M. T. Tuominen, J. G. Lua, D. C. Ralpha and M. Tinkham, 'Charge transport and photon-assisted tunneling in the NSN single-electron transistor', *Physica B* **203**, 327 (1994).
18. B. Leone, J. R. Gao, T. M. Klapwijk, B. D. Jackson, W. M. Laauwen and G. de Lange, 'Electron heating by photon-assisted tunneling in niobium terahertz mixers with integrated niobium titanium nitride striplines', *Appl. Phys. Lett.* **78**, 1616 (2001).
19. T. H. Oosterkamp, L. P. Kouwenhoven, A. E. A. Koolen, N. C. van der Vaart, and C. J. P. M. Harmans, 'Photon sidebands of the ground state and first excited state of a quantum dot', *Phys. Rev. Lett.* **78**, 1536 (1997).
20. T. H. Oosterkamp, T. Fujisawa, W. G. van der Wiel, K. Ishibashi, R. V. Hijman, S. Tarucha and L. P. Kouwenhoven, 'Microwave spectroscopy of a quantum-dot molecule', *Nature* **395**, 873 (1998).
21. J. R. Tucker and M. J. Feldman, 'Quantum detection at millimeter wavelengths', *Rev. Mod. Phys.* **57**, 1055–1113 (1985).
22. F. Thiele, U. Merkt, J. P. Kotthaus, G. Lommer, F. Malcher, U. Rossler and G. Weimann, 'Cyclotron masses in n-GaAs/Ga_{1-x}Al_xAs heterojunctions', *Solid State Commun.* **62**, 841 (1987).

23. S. H. Tessmer, P. I. Glicofridis, R. C. Ashoori, L. S. Levitov and M. R. Melloch, 'Subsurface charge accumulation imaging of a quantum Hall liquid', *Nature* **392**, 51 (1998).
24. Y. Kawano, Y. Hisanaga, H. Takenouchi and S. Komiyama, 'Highly sensitive and tunable detection of far-infrared radiation by quantum hall devices', *J. Appl. Phys.* **89**, 4037 (2001).
25. Y. Kawano, Y. Hisanaga and S. Komiyama, 'Cyclotron emission from quantized hall devices: injection of nonequilibrium electrons from contacts', *Phys. Rev. B* **59**, 12537 (1999).
26. Y. Kawano and S. Komiyama, 'Spatial distribution of non-equilibrium electrons in quantum Hall devices: imaging via cyclotron emission', *Phys. Rev. B* **68**, 085328 (2003).
27. F. Miyamaru, M. Kamijo, K. Takano, M. Hangyo, H. Miyazaki and M. W. Takeda, 'Characteristics and generation process of surface waves excited on a perfect conductor surface', *Opt. Exp.* **18**, 17576 (2010).
28. M. Ohtsu, ed. *Near-Field Nano/Atom Optics and Technology* (Springer-Verlag, Berlin/New York/Tokyo, 1998).
29. L. Novotny and B. Hecht, 'Principles of Nano-Optics', Cambridge University Press, Cambridge, UK (2006).
30. T. Saiki, S. Mononobe, M. Ohtsu, N. Saito and J. Kusano, 'Tailoring a high-transmission fiber probe for photon scanning tunneling microscope', *Appl. Phys. Lett.* **68**, 2612 (1996).
31. F. Zenhausern, Y. Martin and H. K. Wickramasinghe, 'Scanning interferometric apertureless microscopy: optical imaging at 10 Angstrom resolution', *Science* **269**, 1083 (1995).
32. W. C. Symons III, K. W. Whites and R. A. Lodder, 'Theoretical and experimental characterization of a near-field scanning microwave microscope (NSMM)', *IEEE Trans. Microwave Theory Tech.* **51**, 91 (2003).
33. M. Tabib-Azar and Y. Wang, 'Design and fabrication of scanning near-field microwave probes compatible with atomic force microscopy to image embedded nanostructures', *IEEE Trans. Microwave Theory Tech.* **52**, 971 (2004).
34. S. Hunsche, M. Koch, I. Brener and M. C. Nuss, 'THz near-field imaging', *Opt. Commun.* **150**, 22 (1998).
35. O. Mitrofanov, M. Lee, J. W. P. Hsu, I. Brener, R. Harel, J. Federici, J. D. Wynn, L. N. Pfeiffer and K. W. West, 'Collection-mode near-field imaging with 0.5-THz pulses', *IEEE J. Selected Topics in Quantum Electronics* **7**, 600 (2001).
36. N. C. J. van der Valk and P. C. M. Planken, 'Electro-optic detection of subwavelength terahertz spot sizes in the near field of a metal tip', *Appl. Phys. Lett.* **81**, 1558 (2002).
37. H. T. Chen, R. Kersting and G. C. Cho, 'Terahertz imaging with nanometer resolution', *Appl. Phys. Lett.* **83**, 3009 (2003).
38. A. J. Huber, F. Keilmann, J. Wittborn, J. Aizpurua and R. Hillenbrand, 'Terahertz near-field nanoscopy of mobile carriers in single semiconductor nanodevices', *Nano Lett.* **8**, 3766 (2008).
39. T. Yuan, J. Z. Xu and X.-C. Zhang, 'Development of Terahertz wave microscopes', *Infrared Phys. Technol.* **45**, 417–425 (2004).
40. R. Lecaque, S. Gre'sillon, N. Barbey, R. Peretti, J.-C. Rivoal and C. Boccara, 'THz near-field optical imaging by a local source', *Opt. Commun.* **262**, 125–128 (2006).

41. A. Doi, F. Blanchard, H. Hirori and K. Tanaka, ‘Near-field THz imaging of free induction decay from a tyrosine crystal’, *Opt. Exp.* **18**, 18419–18424 (2010).
42. J. Cunningham, M. Byrne, P. Upadhyay, M. Lachab, E. H. Linfield and A. G. Davies, ‘Terahertz evanescent field microscopy of dielectric materials using on-chip waveguides’, *Appl. Phys. Lett.* **92**, 032903–1–3 (2008).
43. Y. Kawano and K. Ishibashi, ‘An on-chip near-field terahertz probe and detector’, *Nature Photonics* **2**, 618–621 (2008).
44. Y. Kawano, ‘Terahertz detectors: quantum dots enable integrated terahertz imager’, *Laser Focus World* **45**(7), 45–47, 50 (2009).
45. Y. Kawano and K. Ishibashi, ‘On-chip near-field terahertz detection based on a two-dimensional electron gas’, *Physica E* **42**, 1188 (2010).
46. S. Komiyama, Y. Kawaguchi, T. Osada and Y. Shiraki, ‘Evidence of nonlocal breakdown of the integer quantum hall effect’, *Phys. Rev. Lett.* **77**, 558 (1996).
47. Y. Kawano and T. Okamoto, ‘Macroscopic channel-size effect of nonequilibrium electron distributions in quantum hall conductors’, *Phys. Rev. Lett.* **95**, 166801 (2005).

Terahertz integrated devices and systems

T. OUCHI, Canon Inc., Japan

DOI: 10.1533/9780857096494.2.423

Abstract: This chapter describes two types of semiconductor based integrated devices which operate in the terahertz (THz) region. One is transmission line type on-chip THz sensors for biology. In this structure, two photoconductive switches of GaAs thin layers and microstrip line are integrated on one Si substrate. Marker-free DNA hybridization detection was achieved at the level of a few femto-moles. The other integrated device is an InGaAs/InAlAs triple-barrier resonant tunneling diode, with current injection operation integrated with a patch antenna which realized sub-terahertz oscillation at room temperature.

Key words: biosensor, transmission line, terahertz oscillator, resonant tunneling diode.

14.1 Integrated terahertz biosensor chip

Highly sensitive biosensors are necessary for developing clinical applications. Biosensor chips using terahertz (THz) radiation have the potential to realize high-performance bio-sensing. In this section, an integrated device which has a THz generator and detector with a THz waveguide and a measurement system are described, including evaluation of the performance.

14.1.1 Transmission line sensors

Recent progress in THz technology has extended into bio-sensing, in which only trace amounts of a specimen may be available. To date, DNA sensor chips based on micro arrays are well known as a highly sensitive and fast sequencing method (Southern, 1996). These sensors need suitable markers, such as fluorescent materials, for detecting hybridization. These markers are able to provide commercially femto-molar detection chips (e.g., Affymetrix, Inc.) but the fluorescent species have a lifetime, conformation change, and sometimes toxicity. Other approaches based on electrochemical, optical (surface plasmon, nanoparticles, fibers, etc.), piezoelectric methods, as well as magnetic particles have been studied to achieve higher sensitivity and functional biosensors (Teles and Fonseca, 2008).

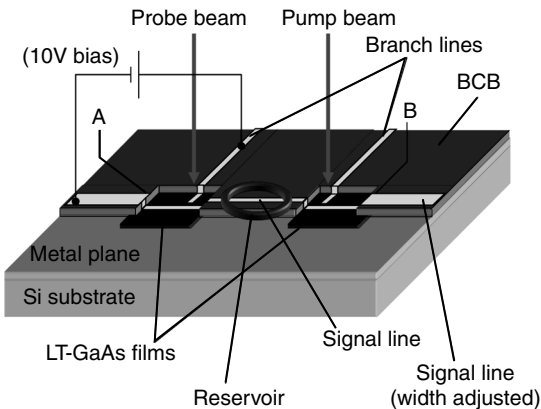
On-chip THz integrated devices based on THz waveguides such as transmission lines are useful for high-sensitive marker-free biosensors. Because waveguides confine the propagating THz electric field, these devices are less sensitive to atmospheric humidity and more sensitive to the characteristics of the specimen than free-space spectroscopy. Once bio-samples are applied on the transmission line, the condition of THz electric field propagation is changed by the permittivity variation caused by the specimen. Nagel *et al.* (2002a) proposed microstrip line (MSL) based THz integrated devices for detecting DNA hybridization. In order to achieve high sensitivity, they fabricated a parallel-coupled (Nagel *et al.*, 2002b) or ring resonator (Nagel *et al.*, 2003) connected to an MSL. Nagel and Kurz (2006) also realized low-cost disposable chips using corrugated waveguides as high-Q resonators. Cunningham *et al.* (2005) demonstrated band-stop filters embedded in MSLs for the sensor array. As other transmission lines, coplanar strip line devices with 2.5 THz bandwidth were integrated with transferred low-temperature-grown (LT)-GaAs layers for photoconductive switches (Desplanque *et al.*, 2004). To measure liquid samples, a polyethylene vessel on a transmission line was fabricated by Ohkubo *et al.* (2006).

These studies showed the feasibility of marker-free detection without any fluorescent materials. The next sections describe a biosensor chip in which the transmission line integrates a specimen reservoir, resulting in a femtomolar sensitivity which is promising as a new THz biosensor chip.

14.1.2 Structure and design of transmission line sensors

Figure 14.1 shows the schematic structure of transmission line sensors (Kasai *et al.*, 2009). The structure contains two photoconductive (PC) switches for generating and detecting THz pulses, connected by an MSL. A specimen placed on the MSL interacts with propagating THz waves. Details of the device structure are as follows. Two 2 µm thick low-temperature-grown (LT)-GaAs layers are transferred onto a Si substrate using Au-Sn solder bonding (Ouchi *et al.*, 2006). Between the LT-GaAs layers, a 600 µm length MSL is fabricated with a Ti/Au signal line and benzo-cyclo-butene (BCB) layer as a dielectric material. Branch lines are formed on the LT-GaAs layer for driving PC switches. A specimen reservoir (400 µm diameter, 6.5 µm height) made of SU-8 is fabricated on the MSL. Adding a specimen to the reservoir increases the total effective refractive index of the MSL, which in turn delays the THz pulses propagating along the MSL. The function of the reservoir is to ensure that the specimen is concentrated around the MSL without spreading.

The electric field of the propagating THz pulses is confined around the MSL. Therefore, keeping the specimen in a reservoir around the MSL improves sensitivity. The reservoir diameter defines the interaction length between the MSL and the specimen, so reproducibility and quantitative

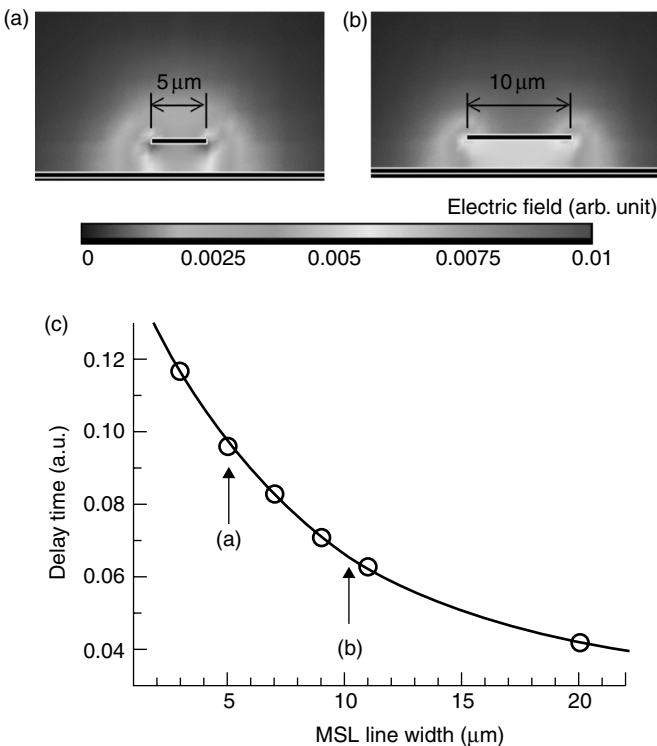


14.1 Schematic structure of on-chip transmission line sensors.
(Reprinted with permission from Kasai *et al.*, 2009. Copyright 2009, The Japan Society of Applied Physics.)

analysis are achieved simultaneously. In order to reduce the reflection of THz pulses at bumps of the BCB windows, the width of the MSL is adjusted in the vicinity of the BCB windows to achieve impedance matching. Reducing reflection prevents THz pulse widening, which improves the resolution of the peak shift measurement.

To obtain a highly sensitive sensor chip, the width of the MSL was designed using numerical calculations. Electric field distributions of the THz radiation were derived by a transmission line modeling (TLM) simulation (Microstripes by AET Inc.) as shown in Fig. 14.2a and b. For simulation purposes, the dielectric permittivity of the BCB was assumed to be 2.4. The results for MSL widths of 5 and 10 μm are described. The delay time of the THz pulses caused by interaction with a specimen was calculated as shown in Fig. 14.2c. The refractive index of the specimen was assumed to be 1.6, approximately the same as that of glycerin. It was assumed that an infinitely thick glycerin sample is placed on the MSL. The delay time increased monotonically with decreasing MSL line width, which meant higher sensitivity.

A wide MSL confines the electric field of THz radiation tightly within the BCB layer. On the other hand, the electric field along a narrow MSL penetrates further in the air (see Fig. 14.2a and b). An effective refractive index for the MSL is determined by the ratio of electric field distribution between dielectrics. The effective refractive index of the narrow MSL depends more on the dielectric permittivity of the environment surrounding the MSL compared with that of the wide MSL. Therefore a glycerin droplet on the narrow MSL yields a large change of effective refractive index. To confirm these simulation results, two THz integrated devices were fabricated: one with a narrow (5.8 μm), and one with a wide (11.1 μm), signal line MSL.

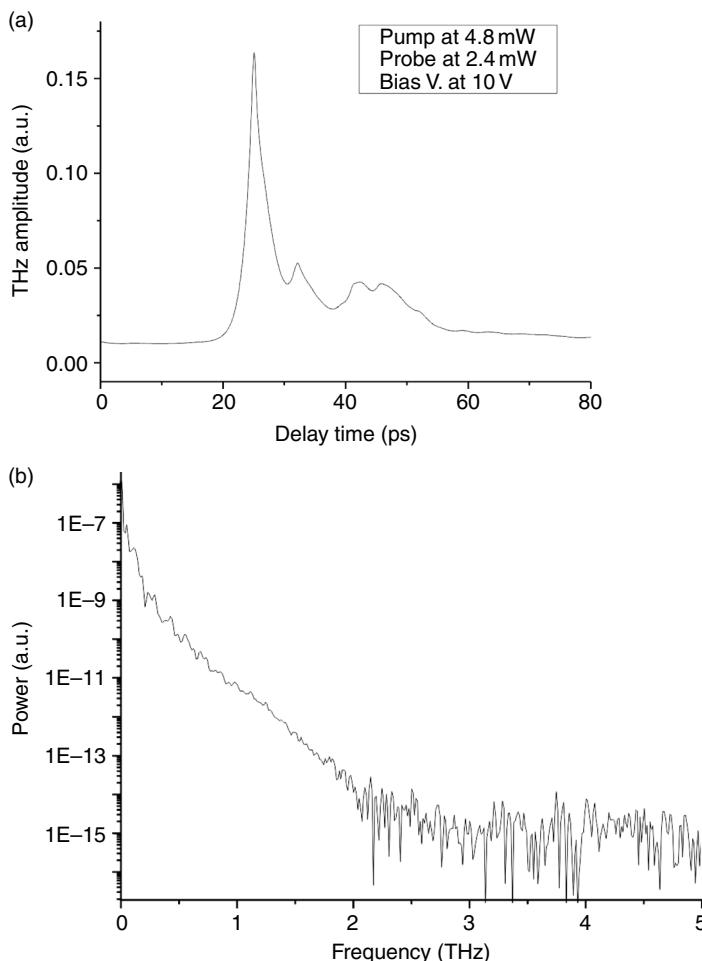


14.2 Numerical calculation results using TLM method: electric field distribution for microstrip line (MSL) of (a) 5 μm width and (b) 10 μm width. (c) Normalized delay time shift of THz pulse peak against the MSL line width for a glycerin sample; $n = 1.6$, thickness = infinite, length = 500 μm . (Reprinted with permission from Kasai *et al.*, 2009. Copyright 2009, The Japan Society of Applied Physics.)

14.1.3 Experiments and results of a THz biosensor chip

THz time-domain spectroscopy with a femtosecond mode-locked Ti:Sapphire laser (Coherent, Inc. Vitesse, 80-fs pulse duration) was constructed to measure the sensor chips. A laser beam was divided into pump and probe beams, which were focused on the PC switches on the chip. The average pump and the probe beam powers were 4.8 and 2.4 mW, respectively. The bias voltage on the transmitter PC switch was 10 V. To measure temporal waveforms, the irradiation time of the probe beams to the PC switch was varied using a linear stage and optical mirrors, resulting in the simultaneous acquisition of the amplitude and the phase of the THz signal (Tani *et al.*, 1997).

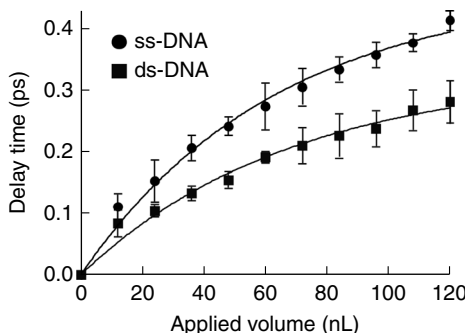
The measured THz waveform and its fast Fourier transform (FFT) spectrum are shown in Fig. 14.3a and b, respectively. The pulse duration is 3.5 ps (full width at half maximum), and the FFT spectrum extends to 2 THz with



14.3 (a) Temporal THz waveform and (b) FFT spectrum of the fabricated device. THz pulse duration is 3.5 ps and FFT bandwidth is about 2 THz.

a dynamic range of 70 dB. Small peaks following the first main pulse are pulses reflected from the BCB window bump. Impedance matching significantly reduces reflection pulses; however, a remaining slight mismatch causes these reflections.

To compare sensitivities of the two devices, a glycerin sample was placed in the reservoir using an electrical micro injector (Narishige Co. Ltd., IM-300). The delay per unit length (1 mm) of the narrow MSL (1.58 ps/mm) was almost two times larger than that of the wide MSL (0.72 ps/mm) and was in good agreement with the simulation (see Fig. 14.2c). Thus, the narrower signal line MSL device was confirmed to have higher sensitivity.



14.4 Delay time variation of THz pulse depending upon applied volume of DNA specimen. Clear difference between ss- and ds-DNA was observed at 24 nL. (Reprinted with permission from Kasai *et al.*, 2009. Copyright 2009, The Japan Society of Applied Physics.)

DNA hybridization detection was demonstrated using Vector pcDNA3 (5.4 kb, 0.5 µg/µL, 0.14 µmol/L) (Brucherseifer *et al.*, 2000) by the 5.8-µm width MSL device. The delay times of the THz pulses caused by double strand (ds-) DNA and a thermally denatured single strand (ss-) DNA were compared. The ss-DNA solution was obtained from a part of the ds-DNA solution by raising the temperature to 95°C for 5 min and then rapidly cooling on ice to prevent renaturation. A droplet (approximately 12 nL) of the DNA solution was placed in the reservoir using the injector. The relative humidity and temperature of the atmosphere were controlled to 30% and 24°C so that the solution dried within a few seconds. The THz waveforms were then measured. Another droplet was added and allowed to dry and the THz waveform measured again. This procedure was then repeated several more times.

Figure 14.4 shows the dependence of the THz pulse delay on the applied volume of DNA solution. The error bars are standard deviations based on the results of two identical repetitions of the experiment. Precipitated ss-DNA yields a longer delay than ds-DNA, which means ss-DNA has higher refractive index. Note that the addition of a second droplet (a total amount of 24 nL, which corresponds to 3.4 femto-moles) yields a 0.10 ps difference in delay times, which is enough to identify the specimen conformation. A different injector which can inject smaller droplets will give a better indication of the real sensitivity of this device. The saturation characteristics are attributable to the electromagnetic wave penetration limit toward the air from the MSL, that is, DNA layers thicker than the penetration depth do not interact with THz radiation.

This device has high sensitivity as a DNA hybridization sensor (at least 3.4 femto-moles) owing to the MSL design adjustment and the specimen reservoir. The reservoir prevents specimen spreading, and allows for quantitative

analysis. The experimental results show that these THz integrated devices will realize trace quantity specimen bio-sensing. In the future, we need a low-cost and fast sequencing system using, for example array transmission line structures as well as femtosecond fiber lasers.

14.2 Terahertz oscillators integrated with patch antennas

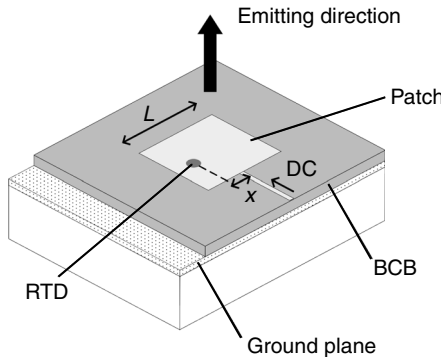
Room temperature operation in THz region is highly expected to solid-state THz oscillators. Plane antenna is suitable for resonator and radiator of THz oscillators by integrating with electronic gain devices. In this and next sections THz oscillators based on resonant tunneling diode with patch antenna are explained to show the feasibility of the THz sources.

14.2.1 THz semiconductor oscillators

Solid-state THz oscillators are desirable as key components for many THz applications. Semiconductor based THz oscillators such as semiconductor lasers, quantum cascade lasers (QCLs) (Faist *et al.*, 1994) and resonant tunneling diodes (RTDs) (Brown *et al.*, 1991) have been studied extensively. Oscillation characteristics such as output power, oscillation frequency, and operation temperature are improving rapidly. Other than these, direct extractions from oscillators, and up-conversion from lower frequencies by frequency multiplication amplifiers can provide sub-terahertz emission. Sub-terahertz amplifier gain has been achieved using heterojunction bipolar transistors (HBTs) (Hafez *et al.*, 2005, Jain *et al.*, 2011), and monolithic integration of SiGe HBTs showed over 0.3 THz output by the frequency multiplier chain (Ojefors *et al.*, 2011). These solid-state devices are expected to be small and highly efficient THz sources in the near future.

QCLs and RTDs need heterojunction semiconductors for intra- or inter-sub-band transitions integrated with resonant structures of metal. THz oscillation at 4.4 THz from a QCL was first reported by Köhler *et al.* (2002). Recently nearly 1 THz oscillation (Kumar *et al.*, 2011) and high power output (Mahler *et al.*, 2010) were realized under low temperature operation. The THz waveguide was formed by a double surface plasmon structure of metal. The major issue of QCLs to this point is the difficulty of room temperature operation.

RTD-based oscillators are expected to realize solid-state THz sources in room temperature (RT) operation (Orihashi *et al.*, 2005, Asada *et al.*, 2008). An oscillation of 712 GHz has been reported using InAs/AlSb double-barrier RTDs in a waveguide tube (Brown *et al.*, 1991). Recently, a fundamental oscillation up to 1.04 THz has been observed using InGaAs/AlAs double-barrier RTDs with a slot antenna (Suzuki *et al.*, 2010). Although



14.5 Schematic structure of RTD oscillators integrated with patch antenna.

output power over $100 \mu\text{W}$ was reported at 550 GHz (Shiraishi *et al.*, 2011), higher power and efficiency are still desirable.

14.2.2 Design of RTD oscillators

A novel type of resonant structure for RTD oscillators with a patch antenna can realize higher efficiencies (Sekiguchi *et al.*, 2010). The device structures of InGaAs/InAlAs RTD oscillators with a patch antenna are shown in Fig. 14.5. An RTD post, buried within a dielectric, is sandwiched between the patch and the ground plane on InP substrates. The oscillation frequency is decided by the resonant length L of the patch. The resonant length L is determined by a value of $\lambda/2\sqrt{\epsilon_r}$ (Kraus and Marhefka, 2001), where λ is the oscillation wavelength in a vacuum and ϵ_r is the relative permittivity of the dielectric. The input resistance of the patch can be tuned, by shifting the RTD post over a distance x away from the center of the patch, proportionally to $\sin(2\pi x/L)$ (Kumar and Ray, 2003). Bias voltage on the RTD post is supplied at the center null point of the patch. A parallel resistance is put between the bias supply lines in order to prevent parasitic oscillation due to return pass of the bias supply lines.

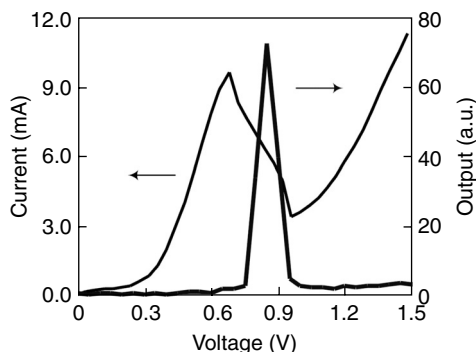
The oscillation output of the RTD oscillators is maximized when the impedance of the antenna is matched to the RTDs. Although the patch antenna needs high gain RTDs due to its large load, the antenna that has several tens of ohms can satisfy the matching condition. The patch antenna of planar structures on substrates is easy to fabricate even for the array scheme. Since almost all fields emit toward the upper side of the substrate, dielectric lenses are not essential. As the oscillation output of the slot antenna fabricated by Suzuki *et al.* (2010) emits mainly into the substrate, the lens on the opposite surface is required to avoid substrate modes.

In the actual device, the RTD post of 2 to 4 μm -diameter on the InP substrate is formed by electron beam lithography and dry-etching techniques. An approximately 3 μm -thick layer of BCB is used to provide the magnitude of impedance of the patch antenna at about 50 Ω . Ti/Pd/Au metal in contact with the RTD post and Ti/Au metal in contact with the *n*-type InP substrate are adopted as the patch and the ground plane, respectively.

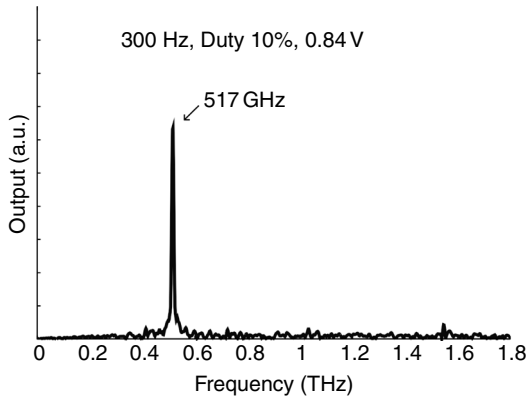
InGaAs/InAlAs triple-barrier RTDs were used as a gain structure for THz frequency range (Asada, 2001), which suppresses the broadening of sub-bands at quantum wells. Therefore, these types of RTDs enable resonant sharpness to be narrower compared with double-barrier RTDs (Nakagawa *et al.*, 1986). As a result, large negative differential conductance is expected against small peak current density. The triple-barrier RTD is designed to get negative differential conductance similar to double-barrier RTDs. The epitaxial layers consist of (from the top down), n^+ InGaAs ($\text{Si} = 1 \times 10^{19} \text{ cm}^3$, 100 nm), n -InGaAs ($\text{Si} = 2 \times 10^{18} \text{ cm}^3$, 50 nm), InGaAs spacer (undoped, 5 nm), AlAs barrier (undoped, 1.3 nm), InGaAs quantum well (undoped, 7.6 nm), InAlAs barrier (undoped, 2.6 nm), InGaAs quantum well (undoped, 5.6 nm), AlAs barrier (undoped, 1.3 nm), InGaAs spacer (undoped, 5 nm), n -InGaAs ($\text{Si} = 2 \times 10^{18} \text{ cm}^3$, 50 nm), and n^+ InGaAs ($\text{Si} = 1 \times 10^{19} \text{ cm}^3$, 3400 nm) on the *n*-type InP substrate. The InGaAs and InAlAs layers are lattice-matched to InP substrates.

14.3 Results and discussion of fabricated resonant tunneling diodes

The current-voltage and THz output characteristics of the fabricated RTDs at RT are shown in Fig. 14.6. The peak current density is about 280 kA/cm^2 and the peak–valley ratio is about 3. This is consistent with the calculation



14.6 Current–voltage characteristics of fabricated RTDs at room temperature. Differential negative resistances were observed on both bias sides. RTD post diameter was 2 μm .

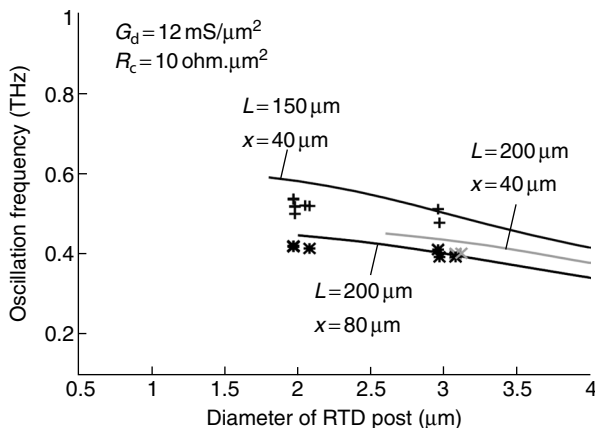


14.7 Oscillation spectrum of fabricated RTDs. A resonant length of antenna is 150 μm , RTD post position and diameter are 40 μm and 2 μm , respectively. Applied bias voltage is 0.84 V at room temperature. (Reprinted with permission from Sekiguchi *et al.*, 2010. Copyright 2010, American Institute of Physics.)

based on the density matrix theory (Asada, 2001). This negative resistance profile corresponds to the tunneling from the first sub-band of the 5.6 nm quantum well to the second sub-band of the 7.6 nm quantum well. THz output was observed in the negative resistance region.

The measurement system of the device is as follows. The oscillation output is observed from the upper side of the patch antenna. The output power and spectra are measured using a liquid He-cooled Si composite bolometer and a Fourier transformed infrared (FT-IR) spectrometer, respectively. The device operates at RT under pulsed bias conditions (the pulse duration is 0.3 ms and the repetition frequency is 300 Hz) to eliminate noise from the bolometer by the lock-in technique. An experimental example of the sub-THz oscillation is shown in Fig. 14.7. A fundamental oscillation of 517 GHz was measured at 0.8 V bias where the RTD post area was $3.1 \mu\text{m}^2$ (2 μm -diameter), the resonant length of the patch was $L = 150 \mu\text{m}$, and the RTD post position was $x = 40 \mu\text{m}$.

Figure 14.8 shows relation between the oscillation frequency, RTD post area, and some design parameters (resonant length L and the RTD post position x) including the device explained above. Cross markers exhibit measured points of fabricated devices. Details of equivalent circuits of RTD oscillators are described in Asada *et al.* (2008). Small signal admittance of the RTD post at 0.8 V bias is obtained from the equivalent circuit element where negative differential conductance $G_d = 12 \text{ mS}/\mu\text{m}^2$, capacitance including transit time delay $C_d = 2.9 \text{ fF}/\mu\text{m}^2 + \tau G_d$, and contact resistance $R_c = 10 \Omega/\mu\text{m}^2$ are assumed. In the term for the transit time delay, τ



14.8 Calculation (lines) and experimental (crosses and stars) results of fundamental oscillation frequencies as a function of RTD post size. (Reprinted with permission from Sekiguchi *et al.*, 2010. Copyright 2010, American Institute of Physics.)

is reduced by $\tau_{\text{dep}}/2 + \tau_{\text{rtd}}$ with $\tau_{\text{dep}} = 0.1$ fs, and $\tau_{\text{rtd}} = \hbar/\Gamma$. Γ indicates the resonant widths of each resonant peak.

The admittance of the patch antenna is obtained from a three-dimensional full-wave electromagnetic field simulator (HFSS by ANSYS Inc.). The experimental results comply with the analysis. The negative differential conductance decreases with decreasing area of the RTD post, and oscillation is limited at the points where the real part of the admittance of the antenna is equal to the negative differential conductance. Therefore, different oscillation limits are found for different x/L . The oscillations at higher frequencies are expected at shorter resonant length L of the patch. Compared with the analysis results, the oscillation frequency degradation might be due to parasitic capacitance of the fabricated devices. As for the 4 μm -diameter post, oscillations are not observed. This is because 20 Ω parallel resistances used between bias lines are by far higher than the negative differential resistance (Reddy *et al.*, 1995). However, at -0.4 V bias for the 4 μm -diameter post, a fundamental oscillation of 336 GHz was measured where the resonant length of the patch was $L = 200$ μm and the RTD post position was $x = 80$ μm . Different oscillations at each bias polarity are unique properties of asymmetric triple-barrier RTDs.

In these devices, the output powers 1 μW to 10 μW were measured where only the coupling of the simulated emitting pattern with parabolic mirror was taken into account. No dielectric lenses on the device are used. However, the power loss due to absorption and misalignment in the optical system and coupling of the detection pattern of the bolometer are excluded. Therefore, absolute power measurements will be necessary to

evaluate the efficiency accurately. This RTD-based solid-state source is a promising approach for THz applications such as imaging, inspections and telecommunications.

14.4 References

- Asada M (2001), ‘Density-matrix modeling of terahertz photon-assisted tunneling and optical gain in resonant tunneling structures’, *Jpn. J. Appl. Phys.*, **40**, 5251–5256.
- Asada M, Suzuki S, and Kishimoto N (2008), ‘Resonant tunneling diodes for sub-terahertz and terahertz oscillators’, *Jpn. J. Appl. Phys.*, **47**, 4375–4382.
- Brown E R, Sonderstrom J R, Parker C D, Mahoney L J, Molvar K M, and McGill T C (1991), ‘Oscillations up to 712 GHz in InAs/AlSb resonant tunneling diodes’, *Appl. Phys. Lett.*, **58**, 2291–2293.
- Brucherseifer M, Nagel M, Bolivar P H, Kurz H, Bosserhoff A, and Buttner R (2000), ‘Label-free probing of the binding state of DNA by time-domain terahertz sensing’, *Appl. Phys. Lett.*, **77**, 4049–4051.
- Cunningham J, Wood C, Davies A G, Hunter I, and Linfield E H (2005), ‘Terahertz frequency range band-stop filters’, *Appl. Phys. Lett.*, **86**, 213503.
- Desplanque L, Lampin J F, and Mollot F (2004), ‘Generation and detection of terahertz pulses using post-process bonding of low-temperature-grown GaAs and AlGaAs’, *Appl. Phys. Lett.*, **84**, 2049–2051.
- Faist J, Capasso F, Sivco D L, Sirtori C, Hutchinson A L, and Cho A Y (1994), ‘Quantum cascade laser’, *Science*, **264**, 553–556.
- Hafez W, Snodgrass W, and Feng M (2005), ‘12.5 nm base pseudomorphic heterojunction bipolar transistors achieving $f_T=710$ GHz and $f_{MAX}=340$ GHz’, *Appl. Phys. Lett.*, **87**, 252109.
- Jain V, Lobisser E, Baraskar A, Thibeault B J, Rodwell M J W, Griffith Z, Urteaga M, Loubychev D, Snyder A, Wu Y, Fastenau J M, and Liu W K (2011), ‘InGaAs/InP DHBTs in a dry-etched refractory metal emitter process demonstrating simultaneous $f/f_{max} \sim 430/800$ GHz’, *IEEE Trans. Electron. Devices*, **58**, 24–26.
- Kasai S, Tanabashi A, Kajiki K, Itsuji T, Kurosaka R, Yoneyama H, Yamashita M, Ito H, and Ouchi T (2009), ‘Micro strip line-based on-chip terahertz integrated devices for high sensitivity biosensors’, *Appl. Phys. Express*, **2**, 062401.
- Köhler R, Tredicucci A, Beltram F, Beere H E, Linfield E H, Davies A G, Ritchie D A, Iotti R C, and Rossi F (2002), ‘Terahertz semiconductor-heterostructure laser’, *Nature*, **417**, 156–159.
- Kraus J D, and Marhefka R J (2001), *Antennas for All Applications 3rd ed.*, McGraw-Hill, 304–346.
- Kumar G and Ray K P (2003), *Broadband Microstrip Antennas*, Artec House, Boston London, 29–88.
- Kumar S, Chun Wang I, Chan C W I, Hu Q, and Reno J L (2011), ‘A 1.8-THz quantum cascade laser operating significantly above the temperature of ω/k_B ’, *Nature Physics*, **7**, 166–171.
- Mahler L, Tredicucci A, Beltram F, Walther C, Faist J, Beere H E, and Ritchie D A (2010), ‘High-power surface emission from terahertz distributed feedback lasers with a dual-slit unit cell’, *Appl. Phys. Lett.*, **96**, 191109.

- Nakagawa T, Imamoto H, Kojima T, and Ohta K (1986), 'Observation of resonant tunneling in AlGaAs/GaAs triple barrier diodes', *Appl. Phys. Lett.*, **49**, 73–75.
- Nagel M, Bolivar P H, Brucherseifer M, and Kurz H, (2002a), 'Integrated THz technology for label-free genetic diagnostics', *Appl. Phys. Lett.*, **80**, 154–156.
- Nagel M, Bolivar P H, Brucherseifer M, Kurz H, Bosserhoff A, and Buttner R (2002b), 'Integrated planar terahertz resonators for femtomolar sensitivity label-free detection of DNA hybridization', *Appl. Opt.*, **41**, 2074–2078.
- Nagel M and Kurz H (2006), 'Corrugated waveguide based genomic biochip for marker-free THz read-out', *Int. J. Infrared and Millimeter Waves*, **27**, 517–529.
- Nagel M, Richter F, Bolivar P H, and Kurz H (2003), 'A functionalized THz sensor for marker-free DNA analysis', *Phys. Med. Biol.*, **48**, 3625–3636.
- Ohkubo T, Onuma M, Kitagawa J, and Kadoya Y (2006), 'Micro-strip-line-based sensing chips for characterization of polar liquids in terahertz regime', *Appl. Phys. Lett.*, **88**, 212511.
- Ojefors, E, Heinemann, B, Pfeiffer, U.R. (2011), 'Active 220- and 325-GHz frequency multiplier chains in an SiGe HBT technology', *IEEE Trans. Microw. Theory Tech.*, **59**, 1311–1318.
- Orihashi N, Suzuki S, and Asada M (2005), 'One THz harmonic oscillation of resonant tunneling diodes', *Appl. Phys. Lett.*, **87**, 233501.
- Ouchi T, Kasai S, Kurosaka R, Itsuji T, Yoneyama H, Yamashita M, Kawase K, and Ito H (2006), 'Terahertz integrated transmission line sensors using a bonded epitaxial GaAs layer on silicon substrates', *Proceeding IRMMW-THz 2006*, TueP-40.
- Reddy M, Yu R Y, Kroemer H, Rodwell M J W, Martin S C, Muller R E, and Smith R P (1995), 'Bias stabilization for resonant tunneling diode oscillators', *IEEE Microwave and Guided Wave Lett.*, **5**, 219–221.
- Sekiguchi R, Koyama Y, and Ouchi T (2010), 'Subterahertz oscillations from triple-barrier resonant tunneling diodes with integrated patch antenna', *Appl. Phys. Lett.*, **96**, 062115.
- Shiraishi M, Shibayama H, Ishigaki K, Suzuki S, Asada M, Sugiyama H, and Yokoyama H (2011), 'High output power (~400uW) oscillators at around 550 GHz using resonant tunneling diodes with graded emitter and thin barriers', *Appl. Phys. Express*, **4**, 064101.
- Southern E M (1996), 'DNA chips: analysing sequence by hybridization to oligonucleotides on large scale', *Trends Genet.*, **12**, 110–115.
- Suzuki S, Asada M, Teranishi A, Sugiyama H, and Yokoyama H (2010), 'Fundamental oscillation of resonant tunneling diodes above 1 THz at room temperature', *Appl. Phys. Lett.*, **97**, 242102.
- Tani M, Matsuura S, Sakai K, and Nakashima S (1997), 'Emission characteristics of photoconductive antennas based on low-temperature-grown GaAs and semi-insulating GaAs', *Appl. Opt.*, **36**, 7853–7859.
- Teles F R R, and Fonseca L P (2008), 'Trends in DNA biosensors', *Talanta*, **77**, 606–623.

Terahertz frequency metrology based on frequency comb techniques

T. YASUI, The University of Tokushima, Japan

DOI: 10.1533/9780857096494.2.436

Abstract: For a long time there has been a gap in frequency metrology in the terahertz (THz) region of the spectrum, between the optical and electrical regions, due to the lack of a frequency standard and traceability in this region. This chapter describes the concept of a new THz frequency metrology method based on a frequency comb, which is designed to fill this gap. Three techniques embodying the concept are also described: a THz-comb-referenced spectrum analyzer, an optical-comb-referenced THz synthesizer and a THz-comb-referenced spectrometer. Via coherent frequency linking among microwave, optical and THz waves, these three techniques are traceable to a microwave frequency standard and hence possess the same frequency uncertainty as that in the optical and electrical regions. Traceability of these techniques to the microwave frequency standard will ensure reliability of the frequency scale in the THz spectrum, which will expand the scope of various THz applications.

Key words: frequency metrology, traceability, optical comb, THz comb, photoconductive mixing.

15.1 Introduction

Terahertz (THz) electromagnetic waves, lying at the boundary between optical and electrical waves, have emerged as a new mode for sensing, spectroscopy, communication and other applications (Mittleman, 2003; Tonouchi, 2007). Along with recent progress in THz technology and science, the requirements of THz metrology have increased in various applications of THz photonics because metrology is an important technical infrastructure guaranteeing reliability of measurement in industry (Kleine-Ostmann *et al.*, 2008; Yasui *et al.*, 2011a). In particular, frequency is an important quantity to be measured in THz metrology because it is a fundamental physical quantity of electromagnetic waves. In contrast to electrical and optical regions, reliable frequency metrology has not yet been established in the THz region, due to the fact that source and detector technologies are still

immature in this frequency region. Such a ‘THz gap’ in frequency metrology could hinder the growth of various THz applications. If reliable THz frequency metrology could be established based on the national frequency standard, the scope of THz applications would be greatly expanded as a result of the high reliability achieved.

An ideal approach for establishing reliable THz frequency metrology is to use a transition frequency in an atom for a frequency standard. For example, a frequency standard at 9.2 GHz was established based on the hyperfine transition in the cesium atom, which is the basis of the definition of time in the International System of Units (SI). In the THz region, a scheme for establishing a frequency standard based on three-photon coherent population trapping in stored ions has been proposed (Champenois *et al.*, 2007); however, realizing this scheme will be challenging in practice. Another practical approach for frequency metrology is to transfer the frequency uncertainty of other electromagnetic-wave regions, where reliable frequency standards have already been established, to the THz region. To achieve this, frequency linking between two electromagnetic-wave regions is required. Recently, an optical frequency comb was used to distribute the frequency uncertainty of a microwave frequency standard to the optical region directly (Udem *et al.*, 2002). Furthermore, the concept of a frequency comb has been extended to the THz region (Yasui *et al.*, 2006). These techniques show promise for realizing reliable frequency metrology in the THz region.

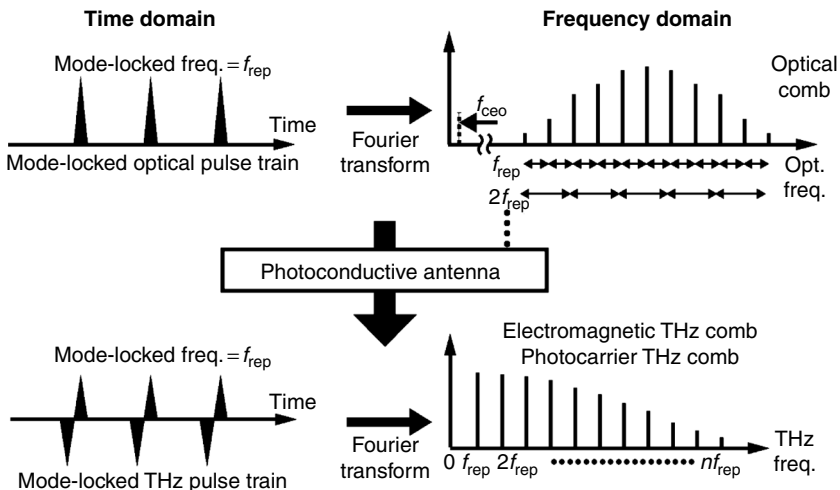
In this chapter, three techniques for THz frequency metrology based on a frequency comb are reviewed. Coherent frequency linking among the microwave, optical and THz regions, achieved by frequency comb techniques, is described in Section 15.2. A THz-comb-referenced spectrum analyzer for precise frequency measurement of continuous-wave (CW) THz waves is presented in Section 15.3. Section 15.4 describes the demonstration of an optical-comb-referenced THz synthesizer using photomixing of two optical frequency synthesizers phase-locked to a microwave frequency standard. In Section 15.5, a THz-comb-referenced spectrometer is described, in which each mode of the THz comb is used as a frequency marker for a broadband THz spectrum. Section 15.6 summarizes our work and discusses some goals for future research.

15.2 Coherent frequency linking with a frequency comb

Figure 15.1 illustrates the principles of an optical comb and a THz comb in the time and frequency domains. A femtosecond mode-locked (fs-ML) laser generates a sequence of pulses that are essentially copies of the

same pulse separated by an interval equal to the inverse of the mode-locked frequency, f_{rep} (Yasui *et al.*, 2011a). The highly stable fs-ML pulse train is synthesized by a series of regular frequency spikes separated by f_{rep} in the optical frequency domain. This structure is referred to as a frequency comb. Since the frequency comb structure can be used as a precision frequency ruler in the optical region, the fs-ML-laser-based optical frequency comb has received a lot of interest as a powerful metrological tool capable of covering the optical region by virtue of precise laser stabilization (Udem *et al.*, 2002). Recently, the concept of the frequency comb has been extended to the THz region by combining fs-ML pulse trains with a photoconductive process (Yasui *et al.*, 2006). When a photoconductive antenna (PCA) for THz generation is irradiated by the fs-ML optical pulse train, a free-space-propagating, mode-locked THz pulse train is radiated from the PCA. This THz pulse train is composed of a regular comb of sharp lines of electromagnetic waves in the THz frequency domain, namely, an electromagnetic THz comb (EM-THz comb). On the other hand, when the fs-ML optical pulse train is incident on a PCA used for THz detection, the instantaneous generation of photocarriers is repeated in the PCA in synchronization with the optical pulse train. The resulting mode-locked THz pulse train of photocarriers constructs a frequency comb structure of photocarriers in the THz region, namely, a photocarrier THz comb (PC-THz comb). In this way, the optical comb is down-converted to the THz region without any change in its frequency spacing. The resulting THz comb is a harmonic frequency comb without any frequency offset, composed of a fundamental component and a series of harmonic components of the mode-locked frequency f_{rep} . This is the biggest difference compared with an optical frequency comb having a carrier-envelope offset frequency (f_{ceo}), which has to be stabilized. Since the optical comb and THz comb are considered to be a set of several thousand or several tens of thousands of narrow-linewidth, single-mode CW waves, they provide attractive features for frequency metrology, such as simplicity, broadband selectivity, high spectral purity and absolute frequency calibration. Therefore, if f_{rep} and f_{ceo} can be well stabilized by laser control, the optical and THz combs can be used as precise frequency rulers in the optical and THz regions, respectively.

Figure 15.2 shows the concept of THz frequency metrology based on the frequency comb. Atomic clocks in the microwave region have been widely used as standards of time and frequency. However, it has been difficult to transfer the frequency uncertainty of the atomic clocks to the optical region due to the large frequency gap between the microwave and optical regions. Although such a gap has been bridged by a frequency chain (Schnatz *et al.*, 1996), it is a rather bulky and complicated apparatus. Furthermore, the frequency uncertainty deteriorates while passing

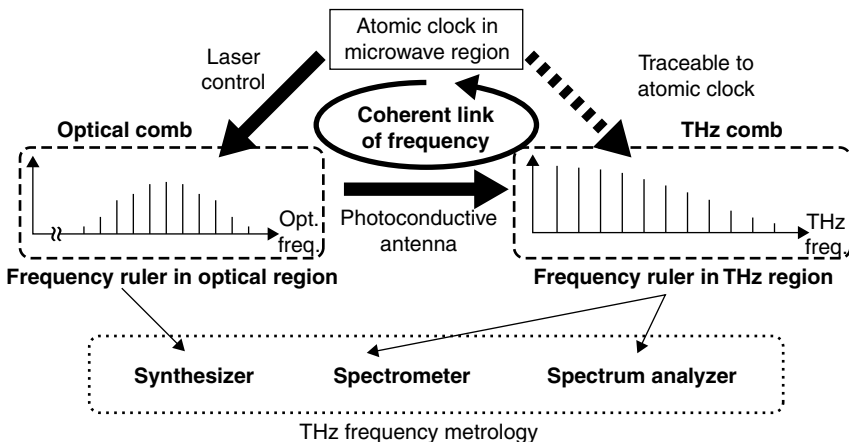


15.1 Optical comb and THz comb.

through many intermediate oscillators in the chain. Recently, an optical comb has emerged as a powerful tool for frequency linking between the microwave and optical regions directly, without losing the frequency uncertainty, by achieving precise laser stabilization with an atomic clock (Udem *et al.*, 2002). Furthermore, the frequency comb has been extended to the THz region using a PCA, as shown in Fig. 15.1 (Yasui *et al.*, 2006). Here, the most important point is that frequency linking among the microwave, optical and THz regions is based on a coherent process, involving laser control and a photoconductive antenna. The resulting coherent frequency linking enables us to share the same frequency uncertainty in three different regions of the electromagnetic spectrum. Therefore, based on a THz comb or optical comb, one can construct a THz frequency metrology system that is directly connected to a frequency standard in the microwave region. In other words, THz frequency metrology traceable to the SI base unit of time can be established.

15.3 Terahertz-comb-referenced spectrum analyzer

A spectrum analyzer is a fundamental frequency measurement instrument widely used for radio frequency (RF), microwave and millimeter waves. However, it is still difficult to use in the THz region, although steady efforts are being made to extend its frequency range. The electrical heterodyne method with a superconductor-insulator-superconductor mixer

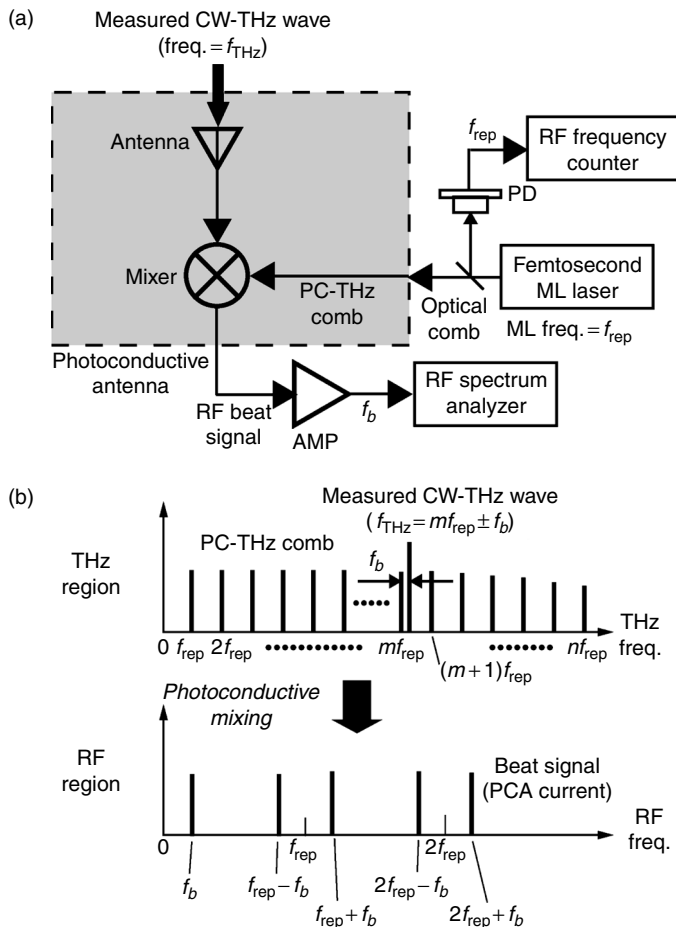


15.2 Coherent link of frequency using the frequency comb.

(Kohjiro *et al.*, 2008) or a hot-electron-bolometer mixer (Baselmans *et al.*, 2004) enables frequency measurement of CW waves in the sub-THz and THz regions. Conversely, the optical interferometric method can be used as an optical spectrum analyzer in the THz region. However, those methods often require cryogenic cooling of the mixer or detector to suppress thermal noise, which is a major obstacle to practical use. Recently, a new type of spectrum analyzer based on a harmonic mixing technique with a frequency comb has been proposed and developed. This device can measure the absolute frequency and spectral shape of CW-THz waves in real time without the need for cryogenic cooling (Yokoyama *et al.*, 2008; Yasui *et al.*, 2009).

15.3.1 Principle of operation

In the field of microwave technology, harmonic mixing technique based on electro-optic sampling has been often used to down-convert microwave spectrum to RF spectrum using the comb spectrum of the mode-locked laser with a nonlinear detection technique (Kolner and Bloom, 1986; Gopalakrishnan *et al.*, 1993). Furthermore, this technique has been extended to the THz region (Gaal *et al.*, 2007). We here modified this technique to down-convert THz spectrum to RF spectrum using photoconductive detection. Our THz spectrum analyzer is based on a heterodyne technique as shown in Fig. 15.3a. In this heterodyne method, the PC-THz comb is used as an RF signal with multiple frequencies covering from the sub-THz to THz regions, whereas a measured CW-THz wave works as a local oscillator. Since each mode of THz comb has a low power, the



15.3 (a) Principle of THz-comb-referenced spectrum analyzer and (b) the corresponding spectral behavior in THz and RF regions.

moderate power is required for the measured CW-THz wave to get the beat signal at good signal-to-noise ratio (Yokoyama *et al.*, 2008; Yasui *et al.*, 2009). Moreover, combining PCAs and PC-THz combs enables heterodyne mixing covering from the sub-THz to THz regions without the need for cryogenic cooling.

Consider a PCA detector triggered by an fs-ML laser beam with repetition frequency f_{rep} . Figure 15.3b illustrates the corresponding spectral behaviors in THz and RF regions. The probe pulse train emitted from the fs-ML laser constructs an optical frequency comb in the frequency domain, whose mode spacing is equal to a mode-locked frequency (see Fig. 15.1). When the PCA is triggered by such pulse train, the PC-THz comb is induced in the

PCA. Next, consider what happens when a measured CW-THz wave (frequency = f_{THz}) is incident on a PCA detector triggered by the probe pulse train. The photoconductive mixing process in the PCA generates a group of beat signals between the CW-THz wave and the PC-THz comb in the RF region. Focus on a beat signal at the lowest frequency (= f_b), namely f_b beat signal. Since this f_b beat signal is generated by mixing the CW-THz wave (frequency = f_{THz}) with the m -th mode of the PC-THz comb (frequency = mf_{rep}) nearest in frequency to the CW-THz wave, f_{THz} is given as follows:

$$f_{\text{THz}} = mf_{\text{rep}} \pm f_b. \quad [15.1]$$

Since f_{rep} and f_b can be measured by RF frequency instruments, f_{THz} can be determined if the value of m and the sign of f_b are measured. To this end, the mode-locked frequency is changed from f_{rep} to $f_{\text{rep}} + \delta f_{\text{rep}}$ by adjustment of the laser cavity length with the laser control system. This results in a change of the beat frequency to $f_b + \delta f_b$. Since $|\delta f_b|$ is equal to $|m\delta f_{\text{rep}}|$, the value of m is determined as:

$$m = \frac{|\delta f_b|}{|\delta f_{\text{rep}}|}. \quad [15.2]$$

and $\delta f_b/\delta f_{\text{rep}}$ and f_b have opposite signs. Finally, the absolute frequency of the measured CW-THz wave can be determined by measuring f_{rep} , f_b , δf_{rep} and δf_b because

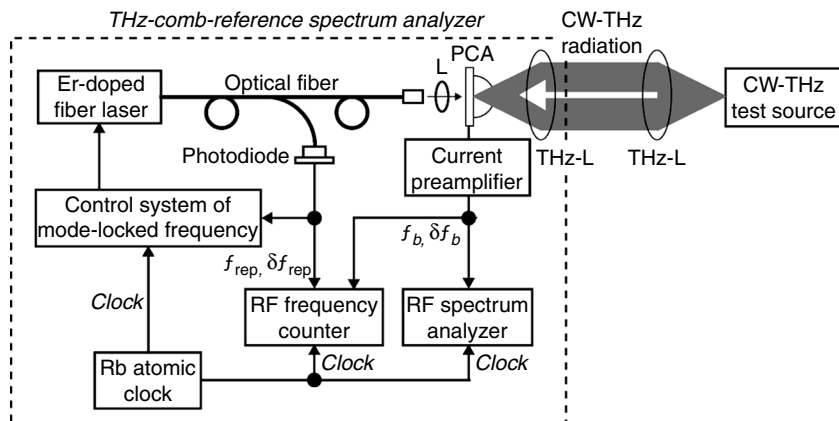
$$f_{\text{THz}} = mf_{\text{rep}} + f_b \quad \left(\frac{\delta f_b}{\delta f_{\text{rep}}} < 0 \right) \quad [15.3a]$$

and

$$f_{\text{THz}} = mf_{\text{rep}} - f_b \quad \left(\frac{\delta f_b}{\delta f_{\text{rep}}} > 0 \right). \quad [15.3b]$$

15.3.2 Experimental set-up

Figure 15.4 shows a schematic diagram of the experimental set-up. The THz-comb-referenced spectrum analyzer was composed of a home-built, fs-ML Er-doped fiber laser (center wavelength = 1550 nm, pulse duration = 40 fs and $f_{\text{rep}} = 56\,122\,206$ Hz) (Inaba *et al.*, 2006), a PCA for THz detection and

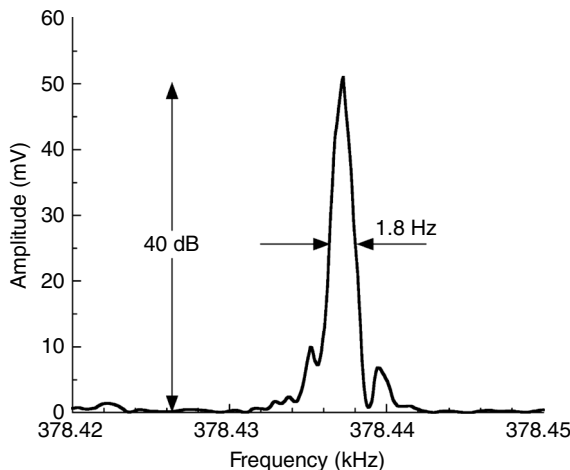


15.4 Experimental set-up of THz-comb-referenced spectrum analyzer.
L: lens; PCA: bowtie-shaped, low-temperature-grown InGaAs/InAlAs photoconductive antenna; THz-L: THz lenses.

RF frequency instruments. The mode-locked frequency f_{rep} was stabilized using a laser control system referenced to a rubidium (Rb) atomic clock (Stanford Research Systems FS725 with frequency = 10 MHz, accuracy = 5×10^{-11} , stability = 2×10^{-11} at 1 s). The output of the fiber laser was delivered to a bowtie-shaped, low-temperature-grown InGaAs/InAlAs PCA for a 1550 nm laser light (Menlo Systems GmbH, BT10) by an optical fiber. This results in generation of the PC-THz comb in the PCA equivalent to the Rb atomic clock. The CW-THz wave from a test source was propagated in free space through a pair of THz lens (Pax Co., Tsurupica), and was then incident on the PCA. Photoconductive heterodyne mixing between the CW-THz wave and the PC-THz comb in the PCA generates a group of beat signals in the RF region. The f_b beat signal is amplified by a high-gain current preamplifier (bandwidth = 10 MHz and sensitivity = 10^5 V/A) and was measured with an RF spectrum analyzer (Agilent E4402B with a frequency range of 100 Hz to 3 GHz) and an RF frequency counter (Agilent 53132A with a frequency range to 225 MHz) to determine its spectral shape and center frequency. A portion of the laser light is detected with a photodetector, and its mode-locked frequency ($= f_{rep}$) is measured using the RF frequency counter. The RF spectrum analyzer and RF frequency counter are synchronized to the Rb atomic clock.

15.3.3 Results

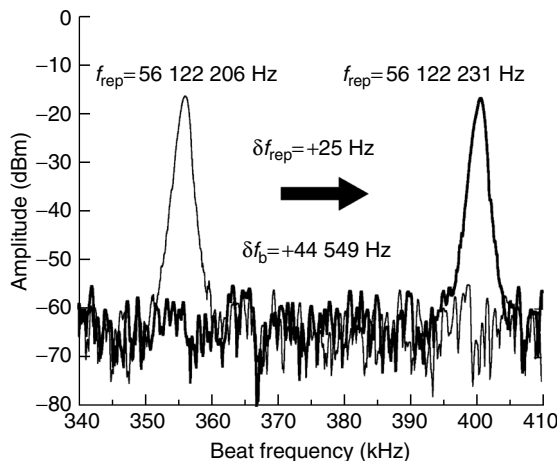
The first test source (output power = 4 dBm = 2.5 mW, frequency range = 75–110 GHz and linewidth < 0.6 Hz) is achieved by combination of an



15.5 Spectrum of the f_b beat signal of the AFMC source measured by the RF spectrum analyzer (RBW = 1 Hz and sweep time = 690 ms).

active frequency multiplier chain (Millitech AMC-10-R0000 with multiplication factor = 6) and a microwave frequency synthesizer (Agilent E8257D with frequency = 12.5–18.33 GHz), referred to as an AFMC source. Since the frequency synthesizer is synchronized to the Rb atomic clock, output frequency of this AFMC source is accurate and stable. We first evaluated the spectral linewidth of the f_b beat signal when the output frequency of the AFMC source was set to 100 GHz. Figure 15.5 shows a linear-scale spectrum of this signal, measured by the RF spectrum analyzer (resolution bandwidth (RBW) = 1 Hz and sweep time = 690 ms). The resulting linewidth of the beat signal was 1.8 Hz. This result indicates that each mode of the PC-THz comb has sufficiently narrow linewidth to perform the frequency measurement with high precision. On the other hand, the signal-to-noise ratio (SNR) of the f_b beat signal reached 40 dB. From this SNR and the output power of the test source (namely +4 dBm = 2.5 mW), the detection limit of the THz power is estimated to –36 dBm, or 250 nW. Comparison of SNR between the f_b beat signals obtained by PCAs and electro-optic sampling is given in detail elsewhere (Yasui *et al.*, 2009).

To determine the absolute frequency of the test source, it is necessary to measure the deviation of f_b before and after changing f_{rep} . The initial f_{rep} and f_b values were measured to be 56 122 206.03 Hz and 356 156 Hz as indicated as the left spectrum in Fig. 15.6 (RBW = 1 kHz and sweep time = 902 ms). Then, the frequency f_{rep} was changed by δf_{rep} (+25 Hz) using the laser control system. This resulted in a change of the beat frequency by δf_b of 44 549 Hz (see the right spectrum in Fig. 15.6). Since $|\delta f_b|$ is equal to $|m\delta f_{\text{rep}}|$, m is determined as



15.6 Spectra of the f_b beat signal when the laser mode-locked frequency (f_{rep}) is set at 56 122 206 Hz (left curve) and 56 122 231 Hz (right curve) (RBW = 1 kHz and sweep time = 902 ms).

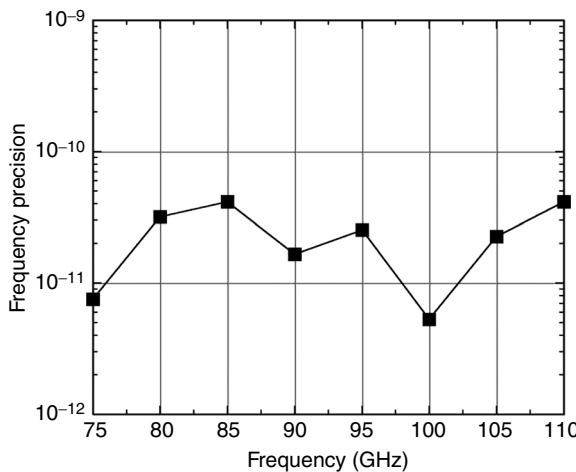
$$m = \frac{|\delta f_b|}{|\delta f_{\text{rep}}|} = \frac{|+44\,549|}{|+25|} = 1781.96 \approx 1782. \quad [15.4]$$

Since the sign of $\delta f_b/\delta f_{\text{rep}}$ (positive in this case) is opposite to that of f_b , the value of f_{THz} was determined as follows:

$$f_{\text{THz}} = mf_{\text{rep}} - f_b = 1782 * 56\,122\,206.03 - 356\,156 = 100\,009\,414\,989.46 \text{ Hz.} \quad [15.5]$$

Since the actual set frequency of the AFMC source was 100 009 414 988.9 Hz from the output frequency of the microwave synthesizer, the error between the set and measured frequencies was only 0.56 Hz. When precision of frequency measurement is defined as the ratio of the error to f_{THz} , the corresponding precision was 5.6×10^{-12} .

To evaluate the precision of frequency measurement in available frequency range of the AFMC source, we determined the absolute frequency of the source while tuning its output frequency from 75 to 110 GHz at 5 GHz intervals. The resulting precision for eight different measurement frequencies is shown in Fig. 15.7, in which the precision is defined as a ratio of the frequency error to the set frequency of the test source. A mean precision of 2.4×10^{-11} was obtained for this source, which is limited by the performance of the Rb atomic clock used. The frequency precision will be further

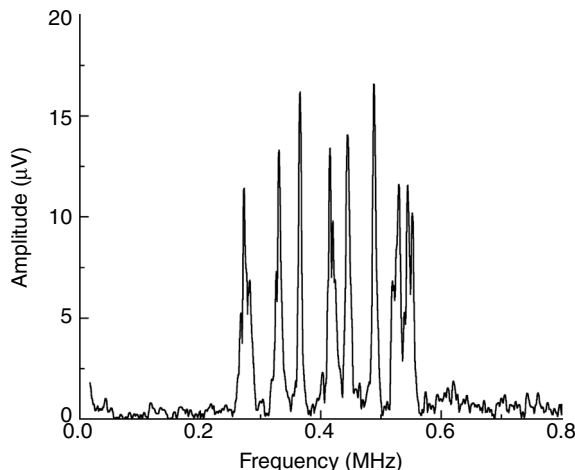


15.7 Precision of frequency measurement in available frequency range of the AFMC source.

improved if we use a frequency standard having less uncertainty, such as cesium atomic clock.

The second test source was produced by photomixing of two CW near-infrared lasers at adjacent wavelengths with a uni-traveling-carrier photodiode (UTC-PD) (Nagatsuma *et al.*, 2009). The two CW lasers were external cavity wavelength-tunable laser diodes with an emission wavelength of 1550 nm and operated in free-running mode (Koshin Kogaku Co., LS-601A-15S1; spectral linewidth \leq 100 kHz, frequency fluctuation $<$ 100 MHz/h). The optical frequency difference between them was set to be approximately 120 GHz. The outputs of the lasers were combined using a fiber coupler, amplified with an Er-doped fiber amplifier, and then photomixed by an F-band UTC-PD (NTT Electronics, available frequency = 90–140 GHz) equipped with a horn antenna. The output power was set to be 100 μ W at a frequency of 120 GHz. We used the THz-comb-referenced spectrum analyzer for monitoring this photomixing source. The resulting spectrum of the beat signal is shown in Fig. 15.8 (RBW = 1 kHz, sweep time = 13 ms). The detailed spectral behavior of the beat signals is shown as a video elsewhere (Yasui *et al.*, 2009). In contrast to the stable AFMC source, the beat frequency of the photomixing source exhibits large fluctuations within a spectral window of 0.8 MHz. This is because the two CW lasers used for the photomixing are operating in free-running mode without any frequency control.

Although the frequencies of the above test sources were in the low-frequency THz region due to the limitation of our available CW-THz sources,



15.8 Spectrum of the f_b beat signal of the photomixing source (RBW = 1 kHz and sweep time = 13 ms).

it is natural to believe that this THz spectrum analyzer can be extended to the higher frequency THz region. This is because the spectral bandwidth of the THz spectrum analyzer is limited mainly by spectral sensitivity of the PCA. For example, the spectral characteristics of the LT-GaAs-PCA as a THz detector have been investigated using THz time-domain spectroscopy (THz-TDS), for which a bandwidth over 100 THz was achieved (Katayama *et al.*, 2010). Therefore, the THz-comb-referenced spectrum analyzer can cover the entire THz spectral region.

15.4 Optical-comb-referenced terahertz synthesizer

Accurate, stable and/or tunable single-frequency signal generation is an essential technique in developing the THz clock and synthesizer. One promising method for widely tunable CW-THz sources is photomixing two CW near-infrared lasers of adjacent wavelengths with a photomixer, such UTC-PD (Nagatsuma *et al.*, 2009) or PCA (Matsuura *et al.*, 1997). However, if the two CW lasers are operated in the free-running mode, it is difficult to generate an accurate and stable frequency in the CW-THz wave as shown in Fig. 15.8. One attractive frequency reference for simultaneous control of these two CW lasers is an optical frequency comb (Udem *et al.*, 2002). An accurate, stable, phase-locked CW-THz wave has been discretely generated at four different frequencies (0.30, 0.56, 0.84 and 1.1 THz) by photomixing of two CW lasers locked to a single optical

comb based on a mode-locked Ti: Sapphire laser (Quraishi *et al.*, 2005). Furthermore, the output frequency was tuned continuously by scanning the frequency interval of the optical comb while locking the CW lasers to the comb; however, the range of continuous tuning was limited to several kilohertz. In the case where the two CW lasers share the same optical comb, when scanning the frequency interval of the comb, the optical frequencies of the two CW lasers change simultaneously. This common-mode change cancels most of the optical frequency change in the two CW lasers. As a result, the continuous tuning range of the CW-THz wave is much smaller than that of the optical frequency in the CW lasers. One promising approach to increase the continuous tuning range while maintaining excellent frequency uncertainty is photomixing two independent optical frequency synthesizers (OFS) phase-locked to a microwave frequency standard (Yasui *et al.*, 2010b, 2011b).

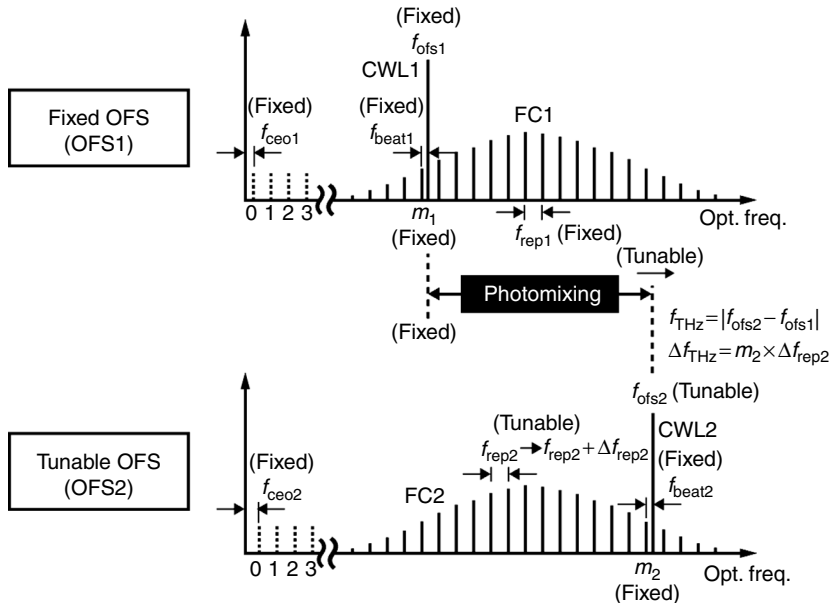
15.4.1 Principle of operation

An OFS is realized by phase-locking a tunable single-frequency CW laser to one of the optical comb modes (Takahashi *et al.*, 2009). When the frequency spacing and carrier-envelope-offset frequency in the optical comb and the beat frequency between the CW laser and one of the comb modes are fully phase-locked to the microwave frequency standard, the optical frequency of the OFS can be determined at the uncertainty of the frequency standard via the optical comb. Furthermore, the optical frequency can be widely and continuously tuned by scanning the comb spacing while maintaining the phase-locking. Therefore, if the outputs from a tunable OFS and a fixed OFS are optically heterodyned with a photomixer, the generated CW-THz radiation is widely and continuously tunable while its frequency is always determined, referenced to the microwave frequency standard.

Let us consider the optical frequency $f_{\text{ofs}1}$ of a fixed OFS (OFS1), composed of a CW laser (CWL1) and a fiber-based optical comb (FC1), as shown in the upper part of Fig. 15.9. The optical frequency $f_{\text{ofs}1}$ is represented by (Takahashi *et al.*, 2009)

$$f_{\text{ofs}1} = f_{\text{ceo}1} + m_1 f_{\text{rep}1} + f_{\text{beat}1}, \quad [15.6]$$

where $f_{\text{ceo}1}$ and $f_{\text{rep}1}$ are the carrier-envelope offset frequency and repetition rate of FC1, respectively, m_1 is the mode number of the comb to which CWL1 is phase-locked, and $f_{\text{beat}1}$ is the beat frequency between CWL1 and the m_1 -th mode. In the fixed OFS, f_{ceo} , $f_{\text{rep}1}$, m_1 and $f_{\text{beat}1}$ are all stabilized at



15.9 Principle of THz synthesizer based on photomixing of two OFSs.

fixed values by precise laser control referenced to a microwave frequency standard. Therefore, f_{ofs1} can be determined at the uncertainty of the optical comb.

On the other hand, the optical frequency f_{ofs2} of a tunable OFS (OFS2), composed of another CW laser (CWL2) and another fiber comb (FC2), as shown in the lower part of Fig. 15.9, is given by

$$f_{ofs2} = f_{ceo2} + m_2 f_{rep2} + f_{beat2}, \quad [15.7]$$

where f_{ceo2} and f_{rep2} are the carrier-envelope offset frequency and repetition rate of FC2, respectively, m_2 is the mode number of the comb to which CWL2 is phase-locked, and f_{beat2} is the beat frequency between CWL2 and the m_2 -th mode. If the comb spacing is changed from f_{rep2} to $f_{rep2} + \Delta f_{rep2}$ while keeping f_{ceo2} at a fixed value, all the modes of FC2 expand in a manner similar to the bellows of an accordion, and thus the frequency of the m_2 -th mode changes by the product of m_2 and Δf_{rep2} . Therefore, f_{ofs2} can also be tuned continuously by $m_2 \Delta f_{rep2}$ if CWL2 remains phase-locked to the m_2 -th comb mode. In the tunable OFS, f_{ceo2} , m_2 and f_{beat2} are fixed at certain values while f_{rep2} is tuned precisely, via the precise laser control referenced to the frequency standard. Even though OFS2 is used for continuous

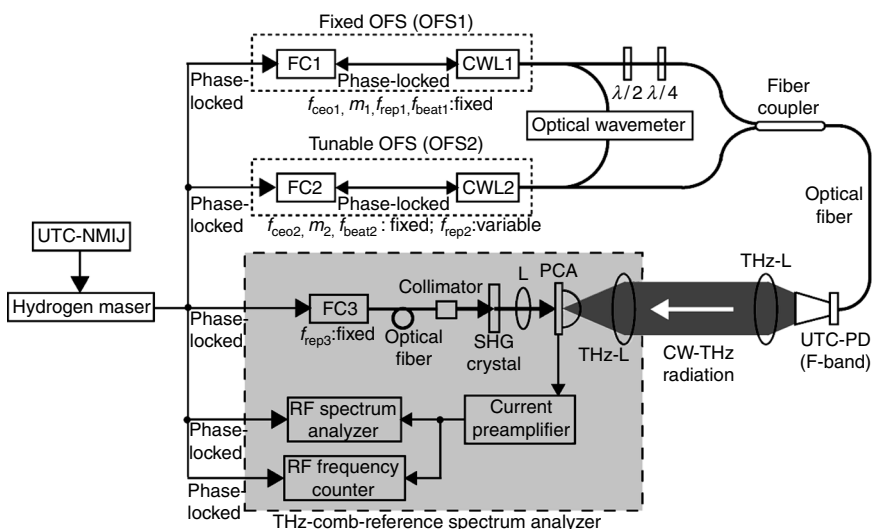
tuning, its absolute frequency $f_{\text{ofs}2}$ can be determined within the uncertainty of the optical comb by simply monitoring $f_{\text{rep}2}$ in real time with a frequency counter.

When a THz synthesizer is realized by photomixing OFS1 and OFS2 with a photomixer, its output frequency (f_{THz}) is given by

$$\begin{aligned} f_{\text{THz}} &= |f_{\text{ofs}2} - f_{\text{ofs}1}| \\ &= |(f_{\text{ceo}2} + m_2 f_{\text{rep}2} + f_{\text{beat}2}) - (f_{\text{ceo}1} + m_1 f_{\text{rep}1} + f_{\text{beat}1})|. \end{aligned} \quad [15.8]$$

Here, it is important to emphasize that the absolute value of f_{THz} can be determined at the uncertainty of the microwave frequency standard by measuring $f_{\text{ceo}1}$ (fixed), $f_{\text{ceo}2}$ (fixed), $f_{\text{rep}1}$ (fixed), $f_{\text{rep}2}$ (variable), m_1 (fixed), m_2 (fixed), $f_{\text{beat}1}$ (fixed) and $f_{\text{beat}2}$ (fixed). This is the main advantage over traditional THz synthesizers. The continuous tuning range of f_{THz} (Δf_{THz}) is represented as:

$$\Delta f_{\text{THz}} = \Delta f_{\text{ofs}2} = m_2 \Delta f_{\text{rep}2}. \quad [15.9]$$



15.10 Experimental set-up. FC1, FC2 and FC3: fiber combs; CWL1 and CWL2: CW near-infrared lasers; $\lambda/2$: half-wave plate; $\lambda/4$: quarter-wave plate; UTC-PD: uni-traveling-carrier photodiode for photomixing; THz-L: THz lenses; L: lens; PCA: photoconductive antenna; SHG crystal: second-harmonic-generation crystal; UTC-NMIJ: coordinated universal time operated by the National Metrology Institute of Japan.

The value of m_2 reaches 3 880 000 when the optical frequency of CWL2 is 194 THz (corresponding wavelength = 1550 nm) and $f_{\text{rep}2}$ is 50 MHz. For example, when $\Delta f_{\text{rep}2} = 500$ kHz, which is 1 % of $f_{\text{rep}2}$, Δf_{THz} could reach about 2 THz from Equation [15.9]. Therefore, the proposed method can also be used for widely and continuously tunable THz synthesizers.

15.4.2 Experimental set-up

The experimental set-up of the THz synthesizer is shown in the upper part of Fig. 15.10. We first constructed two OFSs operating at a wavelength of 1542 nm for photomixing. The fixed OFS (OFS1) was composed of a distributed feedback fiber laser (CWL1; Koheras A/S, Inc., AdjustiK E15-PM) and a custom-built optical comb including a mode-locked Er-doped fiber laser (Inaba *et al.*, 2006), namely, a fiber comb (FC1). On the other hand, the tunable OFS (OFS2) was composed of an external cavity laser diode (CWL2; Optical Comb, Inc., LT-5001) and another fiber comb (FC2). The frequencies $f_{\text{ceo}1}, f_{\text{ceo}2}, f_{\text{rep}1}, f_{\text{rep}2}, f_{\text{beat}1}$ and $f_{\text{beat}2}$ were all phase-locked to the microwave frequency reference synthesized from a hydrogen maser linked to coordinated universal time (UTC), operated by the National Metrology Institute of Japan (UTC-NMIJ). Details of the phase-locking process in the OFSs are given elsewhere (Takahashi *et al.*, 2009). The mode numbers m_1 and m_2 were selected depending upon the frequency of the generated CW-THz radiation. An optical wavemeter (Advantest Corp., Q8326) was used to determine m_1 and m_2 . The continuous tuning range of $\Delta f_{\text{ofs}2}$ was achieved up to 990 GHz by expanding the tuning range of CWL2 using a combination of a piezoelectric (PZT) actuator and a linear translation stage.

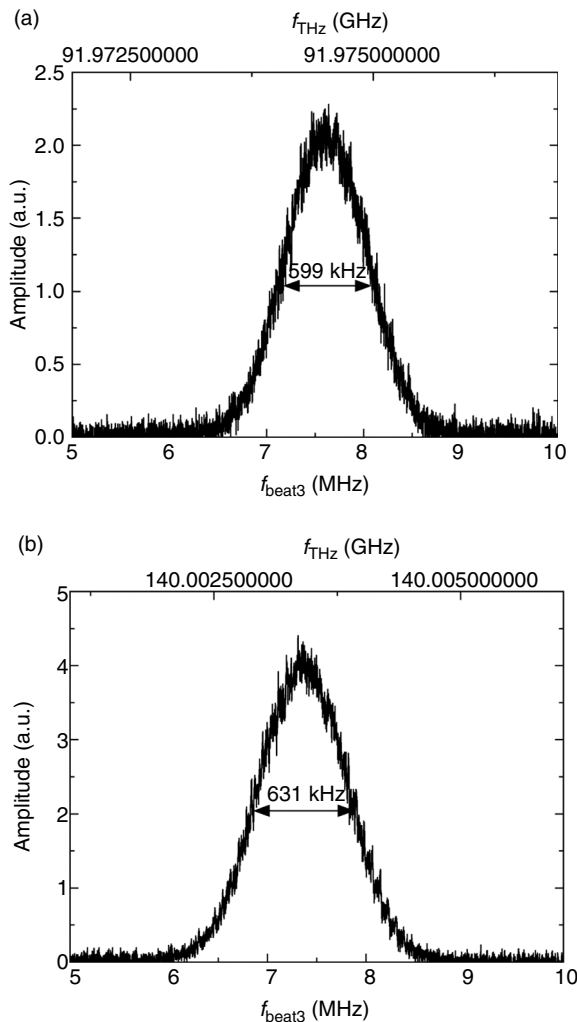
Promising photomixers for the THz synthesizer included a UTC-PD (Nagatsuma *et al.*, 2009) and a PCA (Matsuura *et al.*, 1997). The former had the advantages of high power characteristics and good compatibility with laser sources in the 1.5 μm telecommunication band, whereas the latter could achieve higher frequency response and broader tunability by use of 0.8 μm laser sources. Furthermore, the available frequency range in the UTC-PD could be extended to over 1 THz (Nagatsuma *et al.*, 2009). We here used an F-band UTC-PD (NTT Electronics, frequency range = 90–140 GHz) as a photomixer for actual proof of the proposed method; however, it should be emphasized that it is easily possible to use another UTC-PD or PCA in place of the F-band UTC-PD, if THz synthesizers with higher frequency and/or broader tunability are required. After adjusting the polarization overlap with a half-wave plate ($\lambda/2$) and a quarter-wave plate ($\lambda/4$), the output beams from OFS1 ($f_{\text{ofs}1} = 194.4$ THz, power = 7.3 mW) and OFS2 ($f_{\text{ofs}2} = 194.3$ THz, power = 9.4 mW) were combined with a fiber coupler and then optically heterodyned with a fiber-coupled, F-band UTC-PD

equipped with a horn antenna. We estimated from the observed photocurrent value (7 mA) and the set bias voltage (-2.5 V) of the UTC-PD that the average power of generated CW-THz radiations was around 250 μ W in the F-band.

To evaluate the spectral characteristics of the THz synthesizer, we used a THz-comb-referenced spectrum analyzer (Yokoyama *et al.*, 2008; Yasui *et al.*, 2009) composed of a third fiber comb whose frequency f_{rep} was stabilized (FC3 with $f_{\text{rep}3} = 56\,122\,639$ Hz), a bow-tie-shaped, low-temperature-grown GaAs PCA for THz detection, and RF frequency instruments, as shown in the lower part of Fig. 15.10. The frequency $f_{\text{rep}3}$ and RF frequency instruments were synchronized to the microwave frequency reference. The free-space-propagating CW-THz radiation passing through a pair of THz lenses (Pax Co., Tsurupica) was made incident on the PCA. The PCA was triggered by second-harmonic-generation (SHG) light (center wavelength = 775 nm, average power = 10 mW) from FC3. This resulted in the generation of the PC-THz comb of FC3 in the PCA. Photoconductive heterodyne mixing between the CW-THz radiation and the PC-THz comb in the PCA generated beat signals in the RF region. The beat signal of the current from the PCA was amplified by a high-gain current preamplifier (bandwidth = 10 MHz, sensitivity = 10^5 V/A) and was measured with an RF spectrum analyzer (Agilent E4402B) and frequency counter (Agilent 53132A). Details of the THz-comb-referenced spectrum analyzer are given in Section 15.3. The spectral behavior and frequency instability of the CW-THz radiation were measured with the THz-comb-referenced spectrum analyzer. On the other hand, the absolute frequency of the CW-THz radiation was determined based on Equation [15.8].

15.4.3 Results

To evaluate the spectral characteristics in the THz synthesizer, we first generated frequency-locked CW-THz radiation at upper and lower frequency limits within the F-band, ranging from 90 to 140 GHz. Figures 15.11a and b show spectra of the beat signal for CW-THz radiation around 91.97 GHz and 140.0 GHz, respectively. The lower horizontal axes gave the frequency scale ($f_{\text{beat}3}$) measured with the RF spectrum analyzer. One can clearly confirm that the CW-THz radiation spectra have similar Gaussian-like shapes at these two frequencies. The linewidth of the CW-THz radiation was 599 kHz at 91.97 GHz and 631 kHz at 140.0 GHz when a Gaussian function was fitted to the spectral shape by regression analysis based on the Levenberg–Marquardt algorithm. If a combination of narrower-linewidth CW lasers with fast feedback control is employed for the OFSs, the linewidth of the CW-THz radiation will be further decreased.



15.11 Spectra of CW-THz radiation at (a) 91.97 GHz and (b) 140.0 GHz.

We next assigned an absolute frequency to each CW-THz spectrum in Fig. 15.11. In the THz-comb-referenced spectrum analyzer, the absolute frequency of the CW-THz radiation (f_{THz}) is given by Equations [15.3a] or [15.3b]. When the CW-THz radiation had sufficiently narrow linewidth, its absolute frequency was determined at an uncertainty of 10^{-11} as described in Section 15.3. However, when the linewidth of the CW-THz radiation became broader, around 1 MHz, fitting analysis of the beat signal spectrum to determine its center frequency included an error of a few kHz (Yasui *et al.*, 2010b; Yasui *et al.*, 2011b). This resulted in an uncertainty of

Table 15.1 Parameters of OFS1 and OFS2 when $f_{\text{THz}} = 91\ 974\ 517\ 201\ \text{Hz}$

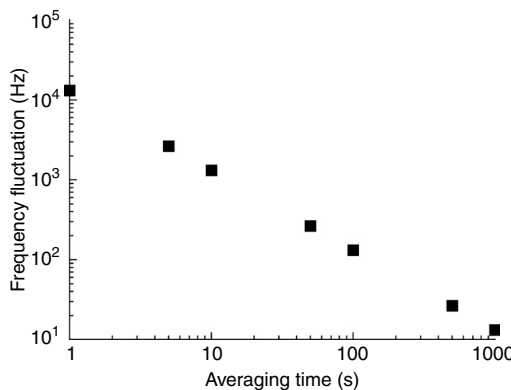
	f_{ceo} (Hz)	m	f_{rep} (Hz)	f_{beat} (Hz)	f_{ofs} (Hz)
OFS1	10 683 000	3 889 263	49 985 122.0	-21 384 000	194 405 274 844 086
OFS2	10 683 000	3 812 171	50 971 800.5	69 960 000	194 313 300 326 885

Table 15.2 Parameters of OFS1 and OFS2 when $f_{\text{THz}} = 140\ 003\ 403\ 918\ \text{Hz}$

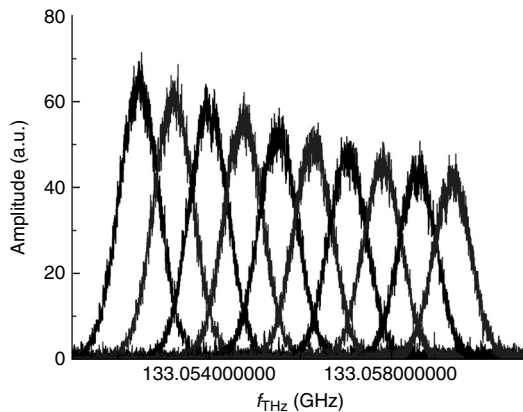
	f_{ceo} (Hz)	m	f_{rep} (Hz)	f_{beat} (Hz)	f_{ofs} (Hz)
OFS1	10 683 000	3 889 264	49 985 129.0	-21 384 000	194 405 352 054 056
OFS2	10 683 000	3 811 224	50 971 884.1	69 960 000	194 265 348 650 138

10^{-3} in the absolute frequency measurement even though the actual frequency of the CW-THz radiation was more stable and accurate. Conversely, if all parameters in Equations [15.6] and [15.7] are known, the absolute frequency of the CW-THz radiation can be simply determined from Equation [15.8] without the need for the THz-comb-reference spectrum analyzer. Therefore, we decided to determine the absolute frequency using Equation [15.8]. Parameters of OFS1 and OFS2 are summarized in Tables 15.1 and 15.2 when $f_{\text{THz}} = 91.97\ \text{GHz}$ and $140.0\ \text{GHz}$ in Fig. 15.11. From these values, center frequencies for those two CW-THz radiation spectra were $91\ 974\ 517\ 201\ \text{Hz}$ and $140\ 003\ 403\ 918\ \text{Hz}$, respectively. The upper horizontal axes in Fig. 15.11a and b show the actual scale of the absolute frequency determined by Equation [15.8]. Here, it is important to note that their absolute frequency is traceable to the hydrogen maser because two OFSs are fully phase-locked to the maser and the phase-noise in photomixer is negligible.

We also evaluated the frequency instability of the CW-THz radiation set at $132.0\ \text{GHz}$ by measuring the frequency fluctuation of the beat signal ($f_{\text{beat}3}$) with the RF frequency counter. Figure 15.12 shows the fluctuation of the beat frequency, represented by the Allan standard deviation σ_A (Allan, 1966), with respect to various averaging times τ . A power law relationship in the form $\sigma_A = \tau^{-1}$ between averaging time τ and frequency fluctuation σ_A was found. The inverse proportionality between them clearly indicates that the output frequency of the THz synthesizer was phased-locked to the hydrogen maser. Here, we consider whether the frequency fluctuation of the THz synthesizer is consistent with that of the OFS. The THz synthesizer had a frequency fluctuation of about $10\ \text{kHz}$ at an averaging time of $1\ \text{s}$ (see Fig. 15.12). Conversely, since the frequency uncertainties of $f_{\text{ceo}1}$ (or $f_{\text{ceo}2}$), $f_{\text{rep}1}$ (or $f_{\text{rep}2}$) and $f_{\text{beat}1}$ (or $f_{\text{beat}2}$) in OFS1 (or OFS2) were respectively 10^{-17} , 10^{-12} and 10^{-13} at an averaging time of $1\ \text{s}$ (Takahashi *et al.*, 2009), the frequency fluctuation in the OFS was estimated to be a few hundreds of Hz from the uncertainty of $m_1 f_{\text{rep}1}$ (or $m_2 f_{\text{rep}2}$), which is mainly due to the uncertainty of the frequency synthesis of $f_{\text{rep}1}$ (or $f_{\text{rep}2}$). We consider that the discrepancy of frequency fluctuation between THz and optical synthesizers is mainly due



15.12 Frequency fluctuation of CW-THz radiation at 132.0 GHz with respect to averaging time.

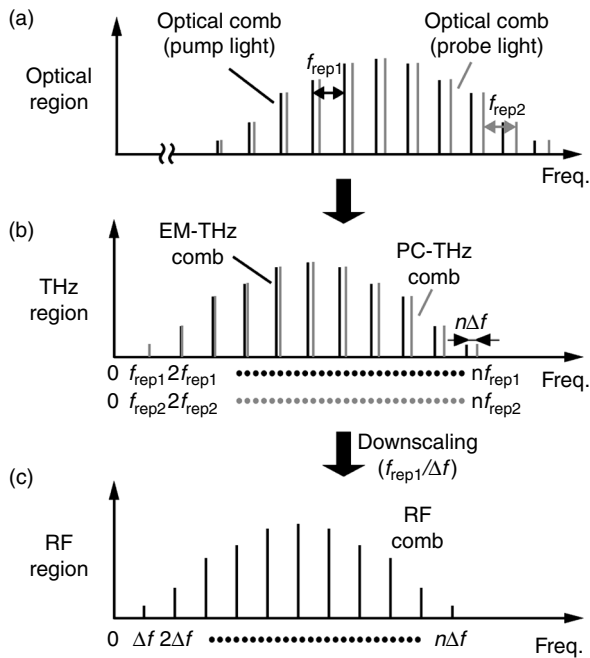


15.13 Incremental tuning of CW-THz radiation around 133 GHz when scanning $f_{\text{rep}2}$ at 0.2 Hz intervals.

to electrical noise caused in the amplification processes of the considerably weak beat signal in the THz-comb-referenced spectrum analyzer.

Next, we show the result of incremental tuning of the CW-THz radiation around 133 GHz by scanning $f_{\text{rep}2}$ at 0.2 Hz intervals. The resulting consecutive spectra of the CW-THz radiation are shown in Fig. 15.13 (sweep time = 2.483 s, RBW = 10 kHz, number of integrated signals = 50), in which the horizontal coordinate is scaled by Equation [15.8]. It is important to note that a tiny increment of 0.2 Hz in $f_{\text{rep}2}$ caused a large change of 762 281.6 Hz in f_{Thz} due to a large tuning rate in Equation [15.9] ($m_2 = 3\ 811\ 408$ in this demonstration). This tuning rate is three orders of magnitude larger than that of the previous THz synthesizer using the single comb (Quraishi *et al.*, 2005).

Furthermore, we demonstrated continuous tuning of the CW-THz radiation over 1 GHz elsewhere (Yasui *et al.*, 2011). We believe that it



15.14 Spectral behavior of frequency combs in (a) optical, (b) THz, and (c) RF regions.

should be possible to further extend the tuning range to 990 GHz in the THz frequency region by use of a broadband photomixer, such as a PCA (Matsuura *et al.*, 1997), because we have already achieved continuous tuning of 990 GHz in the tunable OFS.

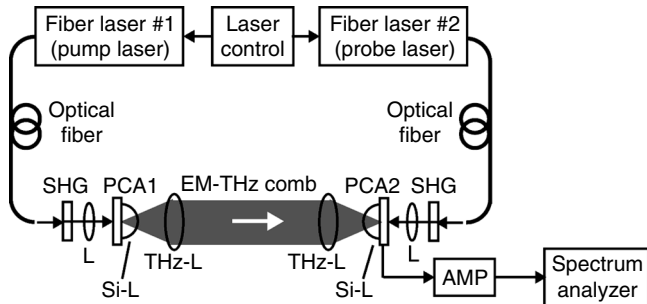
15.5 Terahertz-comb-referenced spectrometer

THz-TDS is a popular spectroscopic technique for obtaining a broadband THz spectrum. In this method, marking of a frequency scale in the THz spectrum is performed by a mechanical scanning time delay with a motor-driven translation stage. However, poor positioning precision and limited stroke length of the translation stage hinder the achievement of high spectral resolution and accuracy in THz-TDS. This sometimes leads to inconsistency of frequency scales in the THz spectrum among different THz-TDS systems. On the other hand, THz frequency domain spectroscopy (THz-FDS) with a tunable narrow-linewidth CW-THz wave is a promising spectroscopic technique to achieve high spectral resolution. Unfortunately, the spectral range covered by this method is much narrower than that in THz-TDS. The accuracy of the frequency scale in

this method depends on the performance of an optical wavemeter for measuring the wavelengths of two CW near-infrared lasers for photo-mixing, which is typically 10^{-6} to 10^{-7} . In this way, the conventional spectroscopic techniques have both merits and demerits. If we could only combine the merits of both THz-TDS and THz-FDS, and also mark the frequency scale of the spectrum accurately based on a frequency standard, the ultimate THz spectrometer with high accuracy, high resolution, and a broad spectral range would be achieved. Coherent linking of frequency with a frequency comb, described in Section 15.2, has the potential to achieve this ultimate THz spectrometer, because the THz comb has both characteristics of CW-THz waves and a broadband THz radiation, and the absolute frequencies of all comb modes are traceable to the microwave frequency standard. To realize this concept, we developed a multi-frequency-heterodyning THz-comb-referenced spectrometer (Yasui *et al.*, 2006; Yasui *et al.*, 2010a).

15.5.1 Principle of operation

Let us consider THz generation from a PCA emitter excited by a femtosecond laser (pump laser; mode-locked frequency f_{rep1}) and THz detection using a PCA detector gated by another femtosecond laser (probe laser; mode-locked freq. = f_{rep2}). Figure 15.14 illustrates spectral behaviors in (a) optical, (b) THz and (c) RF regions. In the frequency domain, since the PCA generation of the THz pulse can be considered as an ultra-wideband demodulation of an optical frequency comb, the optical comb is down-converted to the THz region without any change to the frequency spacing. The resulting THz comb of electromagnetic wave, namely EM-THz comb, is a harmonic frequency comb without a frequency offset, composed of a fundamental component (freq. = f_{rep1}) and a series of harmonic components (freq. = $2f_{\text{rep1}}, 3f_{\text{rep1}}, \dots, nf_{\text{rep1}}$) of a mode-locked frequency. Next, we consider what happens when the mode-locked frequency of the probe laser ($f_{\text{rep2}} = f_{\text{rep1}} + \Delta f$) is slightly detuned from that of the pump laser (f_{rep1}) by a certain frequency offset (Δf). Instantaneous photoconductive gating by the probe laser induces a frequency comb of photocarrier, namely PC-THz comb, having a different frequency spacing (freq. = $f_{\text{rep2}}, 2f_{\text{rep2}}, 3f_{\text{rep2}}, \dots, nf_{\text{rep2}} = (f_{\text{rep1}} + \Delta f), 2(f_{\text{rep1}} + \Delta f), 3(f_{\text{rep1}} + \Delta f), \dots, n(f_{\text{rep1}} + \Delta f)$) in the PCA detector, which is also existed in THz frequency region. Under this condition, it is possible to detect the EM-THz comb as a result of the photoconductive process occurring between the EM-THz and PC-THz combs, giving rise to the multi-frequency-heterodyning effect. This results in the generation of a secondary frequency comb in the RF region, termed the RF comb (freq. = $\Delta f, 2\Delta f, 3\Delta f, \dots, n\Delta f$). Since the RF comb is a replica of the EM-THz comb



15.15 Experimental set-up. SHG: second-harmonic-generation crystal; L: lenses; PCA1 and PCA2: dipole-shaped LTG-GaAs photoconductive antennas; Si-L: hemispherical silicon lenses; THz-L: THz lenses; AMP: current preamplifier.

only downscaled by $f_{\text{rep}}/\Delta f$ in frequency, one can utilize the THz comb easily via direct observation of the RF comb using an RF spectrum analyzer and calibration of the frequency scale.

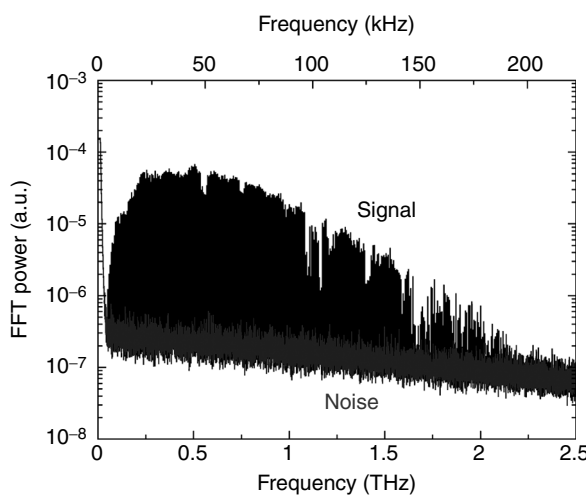
15.5.2 Experimental set-up

Figure 15.15 shows a schematic diagram of the experimental set-up. We constructed two self-starting, stretched-pulse mode-locked, Er-fiber lasers (center wavelength = 1550 nm, pulse duration = 50 fs and mean power = 90 mW) (Inaba *et al.*, 2006) for use as laser sources (pump and probe lasers) to generate and detect EM-THz comb. The individual mode-locked frequencies of the two lasers ($f_{\text{rep}1} = 56\,124\,000$ Hz and $f_{\text{rep}2} = 56\,124\,005$ Hz) and the frequency difference between them ($\Delta f = f_{\text{rep}2} - f_{\text{rep}1} = 5$ Hz) were stabilized by two independent PI (proportional and integral) control systems with reference to a rubidium (Rb) frequency standard (accuracy = 5×10^{-11} , instability = 2×10^{-11} at 1 s). The instability of the mode-locked frequency was equal to that of the Rb frequency standard whereas the timing jitter between the two lasers was less than 300 fs. Excellent stability of $f_{\text{rep}1}$, $f_{\text{rep}2}$ and Δf enables generating stable frequency combs and achieving an exact multi-frequency-heterodyning process. Output light from the pump laser was delivered by an optical fiber and was converted by SHG to half its original wavelength using an SHG crystal ($\beta\text{-BaB}_2\text{O}_4$). The resulting 775-nm SHG light was focused on the gap of a dipole-shaped low-temperature-grown GaAs (LTG-GaAs) PCA for THz generation (PCA1; length = 7.5 μm , width = 10 μm , gap = 5 μm). The EM-THz comb from PCA1 propagated in free space through two pairs of hemispherical silicon lenses (Si-L) and THz lenses (THz-L), and was then incident on another dipole-shaped LTG-GaAs PCA (PCA2)

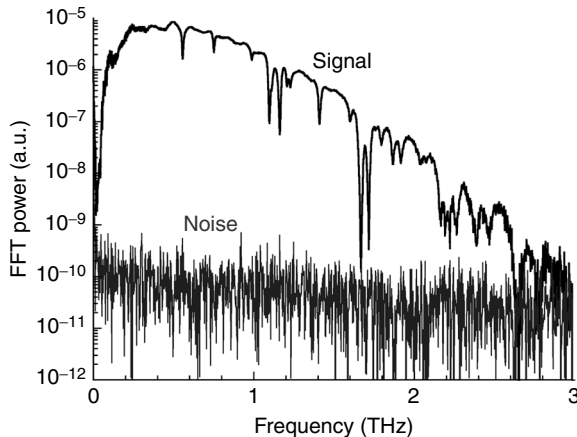
gated by the SHG light of the probe laser, which had the PC-THz comb. A fully fiber-coupled THz spectrometer would be achieved without the need for frequency doubling if a PCA for a 1550 nm light were used (Sartorius *et al.*, 2008). As a result of multi-frequency-heterodyning photoconductive detection, the RF comb was directly measured with an RF spectrum analyzer (Agilent Technologies, E4402B) after passing through a high-gain current preamplifier (AMP). One can reconstruct the EM-THz comb exactly by calibrating the RF comb with the frequency downscale factor ($= f_{\text{rep}}/\Delta f = 11\,224\,800$).

15.5.3 Results

Figure 15.16 shows a power spectrum of the RF comb obtained using the proposed method (measurement time = 100 s), in which the upper horizontal axis gives the frequency scale in the RF spectrum analyzer. One can confirm that the RF comb is distributed within a frequency range of 200 kHz. The actual frequency values in the THz comb spectrum are scaled according to the lower horizontal axis by using the frequency downscale factor. The tail of the observed spectrum was achieved to 2 THz. The spectrum painted over is actually composed of a series of frequency spikes regularly separated by the mode-locked frequency. Considering a spectral range of 2 THz and a frequency spacing of 56.1 MHz, the THz spectrum is composed of over 35 000 comb modes. Several absorption lines caused by atmospheric water vapor were clearly observed as dips in the spectrum of Fig. 15.16.



15.16 Power spectrum of EM-THz comb. FFT, fast Fourier transform.



15.17 Power spectrum of THz radiation measured by ASOPS-THz-TDS.

To confirm the validity of the observed spectrum, we also measured the power spectrum of the pulsed THz radiation at the same experimental condition using asynchronous-optical-sampling THz-TDS (ASOPS-THz-TDS) (Yasui *et al.*, 2005, 2010a). In the case of the ASOPS-THz-TDS, the signal of THz radiation was measured in time domain using a fast digitizer triggered by a sum-frequency-generation cross-correlation signal (not shown in Fig. 15.15), in place of the RF spectrum analyzer. Figure 15.17 shows the power spectrum of the THz radiation and the noise, in which signal averaging of 500-sweep sequences was carried out by the digitizer. Spectral shape and bandwidth in Fig. 15.16 was almost equal to those in Fig. 15.17. The reason for difference of dynamic range in power is mainly due to a difference in efficiency of signal acquisition between the spectrum analyzer and the digitizer. Detail discussion on this point is given elsewhere (Yasui *et al.*, 2010a).

15.6 Conclusions and future trends

We described the concept of THz frequency metrology based on a frequency comb, together with three concrete techniques embodying this concept. The most important point in our approach is that the coherent linking of the frequency established by the frequency comb enables us to realize THz frequency metrology traceable to the SI base unit of time. Also, the fiber-based techniques used here, including fiber lasers and optical fibers, have the advantage of being portable, alignment-free, robust and flexible. First, the THz-comb-referenced spectrum analyzer was achieved by photoconductive mixing of a CW-THz wave with a PC-THz comb. Based on

the stable PC-THz comb generated in a PCA, the absolute frequency of the CW-THz wave was determined at a precision of 10^{-11} , which is limited by the performance of the Rb atomic clock used. Furthermore, the detailed spectral behavior of the CW-THz waves was monitored in real time. Second, a widely and continuously tunable THz synthesizer traceable to the hydrogen maser linked to UTC-NMIJ was demonstrated by photomixing of two independent OFSs. A combination of dual optical combs and the photomixing technique achieved a frequency uncertainty of 10^{-12} in the THz frequency range. Furthermore, photomixing of a tunable OFS and a fixed one enabled us to extend the continuous tuning range of the CW-THz radiation up to 1.26 GHz while maintaining unprecedented frequency uncertainty. Third, a THz-comb-referenced spectrometer traceable to the microwave frequency standard was constructed using dual THz combs. The EM-THz comb was downscaled to the RF region by using a multi-frequency-heterodyning technique and was then measured directly with an RF spectrum analyzer. Frequency modes constituting the THz comb will be used as frequency markers, having an interval of 56 MHz, for a broadband THz spectrum.

Our approach for THz frequency metrology enables us to treat the frequency in the THz region as a universal quantity based on the national frequency standard, in the same manner as in the optical and electrical regions. Therefore, the so-called THz gap problem will be essentially solved. Establishment of THz frequency metrology will cause a ripple effect in various fields of THz technology and applications. For example, to achieve universal identification power in spectroscopic applications, uncertainty of the frequency scale in the THz spectrum should be certified by referencing to the SI base unit of time, that is, a microwave frequency standard. Our THz frequency metrology will play an important role in frequency calibration and traceability of various types of commercial THz instruments, such as sources, detectors and systems. The absolute frequency of CW-THz sources can be accurately determined by THz spectrum analyzers, whereas the frequency scale of a THz spectrometer can be precisely calibrated by THz synthesizers. The precisely calibrated THz spectrometer will increase the identification power in spectroscopic applications based on THz spectral fingerprints. Also, the highly spectroscopic performance made possible by using a THz comb will contribute to the development of precise THz spectrometers and preparation of a precise spectral database atlas. Furthermore, when THz waves are used as carrier waves for broadband wireless communications, the transmission frequency should be highly accurate and stable in order to secure the necessary and sufficient bandwidth for broadband communication without interference with other applications, such as astronomy or sensing. A THz synthesizer can be used to generate an accurate and stable transmission frequency. In this way, THz

frequency metrology will spread to various THz applications based on a high-reliability frequency scale.

15.7 References

- Allan DW (1966), ‘Statistics of atomic frequency standards’, *Proc. IEEE*, **54**, 221–230.
- Baselmans JJA, Hajenius M, Gao JR, Klapwijk TM, de Korte PAJ, Voronov B, and Gol’tsman G (2004), ‘Doubling of sensitivity and bandwidth in phonon cooled hot electron bolometer mixers’, *Appl. Phys. Lett.*, **84**, 1958–1960.
- Champenois C, Hagel G, Houssin M, Knoop M, Zumsteg C, and Vedel F (2007), ‘Terahertz frequency standard based on three-photon coherent population trapping’, *Phys. Rev. Lett.*, **99**, 013001.
- Gaal P, Raschke MB, Reimann K, and Woerner M (2007), ‘Measuring optical frequencies in the 0–40 THz range with non-synchronized electro-optic sampling’, *Nature Photon.*, **1**, 577–580.
- Gopalakrishnan GK, Burns WK, and Bulmer CH (1993), ‘Microwave-optical mixing in LiNbO₃ modulators’, *IEEE Trans. Microwave Theory and Techniques*, **41**, 2383–2391.
- Inaba H, Daimon Y, Hong F-L, Onae A, Minoshima K, Schibli TR, Matsumoto H, Hirano M, Okuno T, Onishi M, and Nakazawa M (2006), ‘Long-term measurement of optical frequencies using a simple, robust and low-noise fiber based frequency comb’, *Opt. Express*, **14**, 5223–5231.
- Katayama I, Akai R, Bito M, Shimosato H, Miyamoto K, Ito H, and Ashida M (2010), ‘Ultrabroadband terahertz generation using 4-N,N-dimethylamino-4 - N -methyl-stilbazolium tosylate single crystals’, *Appl. Phys. Lett.*, **97**, 021105.
- Kleine-Ostmann T, Schrader T, Bieler M, Siegner U, Monte C, Gutschwager B, Hollandt J, Müller R, Ulm G, Pupeza I, and Koch M (2008), ‘THz metrology’, *Frequenz*, **62**, 135–146.
- Kohjiro S, Kikuchi K, Maezawa M, Furuta T, Wakatsuki A, Ito H, Shimizu N, Nagatsuma T, and Kado Y (2008), ‘A 0.2–0.5 THz single-band heterodyne receiver based on a photonic local oscillator and a superconductor-insulator-superconductor mixer’, *Appl. Phys. Lett.*, **93**, 093508.
- Kolner BH and Bloom DM (1986), ‘Electro-optic sampling in GaAs integrated circuits’, *IEEE J. Quantum Electron.*, **22**, 79–93.
- Matsuura S, Tani M, and Sakai K (1997), ‘Generation of coherent terahertz radiation by photomixing in dipole photoconductive antennas’, *Appl. Phys. Lett.*, **70**, 559–561.
- Mittleman DM (2003), *Sensing with THz radiation*, Berlin, Springer.
- Nagatsuma T, Ito H, and Ishibashi T (2009), ‘High-power RF photodiodes and their applications’, *Laser Photon. Rev.*, **3**, 123–137.
- Quraishi Q, Griebel M, Kleine-Ostmann T, and Bratschitsch R (2005), ‘Generation of phase-locked and tunable continuous-wave radiation in the terahertz regime’, *Opt. Lett.*, **30**, 3231–3233.
- Sartorius B, Roehle H, Künzel H, Böttcher J, Schlak M, Stanze D, Venghaus H, and Schell M (2008), ‘All-fiber terahertz time-domain spectrometer operating at 1.5 μm telecom wavelengths’, *Opt. Express*, **16**, 9565–9570.

- Schnatz H, Lipphardt B, Helmcke J, Riehle F, and Zinner G (1996), 'First phase-coherent frequency measurement of visible radiation', *Phys. Rev. Lett.*, **76**, 18–21.
- Takahashi H, Nakajima Y, Inaba H, and Minoshima K (2009), 'Ultra-broad absolute-frequency tunable light source locked to a fiber-based frequency comb', Technical Digest of *Conference on Lasers and Electro-Optics 2009*, Optical Society of America, Washington DC, paper CTuK4.
- Tonouchi M (2007), 'Cutting-edge terahertz technology', *Nature Photon.*, **1**, 97–105.
- Udem Th, Holzwarth R, and Hänsch TW (2002), 'Optical frequency metrology', *Nature*, **416**, 233–237.
- Yasui T, Saneyoshi E, and Araki T (2005), 'Asynchronous optical sampling terahertz time-domain spectroscopy for ultrahigh spectral resolution and rapid data acquisition', *Appl. Phys. Lett.*, **87**, 061101.
- Yasui T, Kabetani Y, Saneyoshi E, Yokoyama S, and Araki T (2006), 'Terahertz frequency comb by multi-frequency-heterodyning photoconductive detection for high-accuracy, high-resolution terahertz spectroscopy', *Appl. Phys. Lett.*, **88**, 241104.
- Yasui T, Nakamura R, Kawamoto K, Ihara A, Fujimoto Y, Yokoyama S, Inaba H, Minoshima K, Nagatsuma T, and Araki T (2009), 'Real-time monitoring of continuous-wave terahertz radiation using a fiber-based, terahertz-comb-referenced spectrum analyzer', *Opt. Express*, **17**, 17034–17043.
- Yasui T, Nose M, Ihara A, Kawamoto K, Yokoyama S, Inaba H, Minoshima K, and Araki T (2010), 'Fiber-based, hybrid terahertz spectrometer using dual fiber combs', *Opt. Lett.*, **35**, 1689–1691.
- Yasui T, Takahashi H, Iwamoto Y, Inaba H, and Minoshima K (2010), 'Continuously tunable, phase-locked, continuous-wave terahertz generator based on photomixing of two continuous-wave lasers locked to two independent optical combs', *J. Appl. Phys.*, **107**, 033111.
- Yasui T, Yokoyama S, Inaba H, Minoshima K, Nagatsuma T, and Araki T (2011), 'Terahertz frequency metrology based on frequency comb', *IEEE J. Selected Topics in Quantum Electron.*, **17**, 191–201.
- Yasui T, Takahashi H, Kawamoto K, Iwamoto Y, Arai K, Araki T, Inaba H, and Minoshima K (2011), 'Widely and continuously tunable terahertz synthesizer traceable to a microwave frequency standard', *Opt. Express*, **19**, 4428–4437.
- Yokoyama S, Nakamura R, Nose M, Araki T, and Yasui T (2008), 'Terahertz spectrum analyzer based on a terahertz frequency comb', *Opt. Express*, **16**, 13052–13061.

Semiconductor material development for terahertz applications

M. MISSOUS, The University of Manchester, UK

DOI: 10.1533/9780857096494.2.464

Abstract: Analysis of the performance characteristics of low-temperature-grown GaAs (LT-GaAs) and detailed characterisation of undoped and Be-doped LT-In_{0.53}Ga_{0.47}As-In_{0.52}Al_{0.48}As structures is undertaken in order to correlate the structural point defect behaviour with obtained electrical, optical and THz properties. By a judicious combination of doping and annealing temperatures, materials with sub-picosecond lifetimes and resistivity of $\sim 1 \times 10^7$ ohm/square have been obtained on LT-In_{0.53}Ga_{0.47}As-In_{0.52}Al_{0.48}As with THz performances that include sub-picosecond recombination times and over 50 dB THz power spectrum dynamic range. The LT-In_{0.53}Ga_{0.47}As-In_{0.52}Al_{0.48}As system shows promise for next generation efficient and portable all-fibre THz imaging systems.

Key words: LT-GaAs, LT-In_{0.53}Ga_{0.47}As-In_{0.52}Al_{0.48}As, epitaxy, THz, photomixers, photoconductive switches.

16.1 Introduction

This chapter deals with detailed descriptions of the material properties of semiconductor photoconductor devices suitable for use as emitters and detectors of THz radiation. The materials space of semiconductors devices that have potential as sources and detectors is very large indeed; however, the key materials addressed here are those that have shown most promise for use in commercial applications. With this in mind, semiconductor components for use in both THz time-domain pulsed systems (TDS) and continuous wave (CW) optical fibre based systems operating at wavelengths of 0.8 and 1.55 μm will be described.

The use of THz radiation in both astronomy and chemical analysis has been well documented in the past, albeit at the expense of using large systems. However, the potential, and indeed widespread usage of THz radiation in various applications, such as imaging and spectroscopy, is now imminent in such diverse fields as biology and medical sciences, information and communications systems, non-evasive and non-destructive measurements, and security screening among many others.

This explosion in applications in recent years has been largely the result of innovations in photonics and semiconductor materials. The key breakthroughs recently have been in the first instance in the development of THz time-domain spectroscopy systems, but also increasingly of CW systems using photomixing of high power semiconductor lasers both at 800 and 1550 nm, the latter opening the way to a widespread use of all-fibre coupled systems.

16.1.1 THz radiation

It is generally acknowledged that the THz region is the frequency spectrum that spans the range from roughly 300 GHz to 10 THz,¹ though other definitions range from 100 GHz to 30 THz. In both cases, this frequency domain is located between high frequency solid state (semiconductor) electronics and far infrared optics. At room temperature, all objects emit thermal energy (black-body) in the THz range and, while less penetrating than X-rays, its millimetre-scale penetration depth ability into many organic materials, coupled with its damage-free (non-ionising) features, makes THz radiation very useful for biological and medical applications. The fact that THz radiation is transparent to many optically opaque materials, such as clothes and plastics, makes THz imaging systems important for security screening.^{2–5} The high absorbance of THz radiation by water, which can sometimes limit its domain of application, nevertheless makes it useful in distinguishing materials depending upon their water content. All these aspects of THz radiation are addressed in detail elsewhere in this book.

Recent interest in the use of THz radiation has thus been a key driver in the development of sources that are able to emit such radiation with high output power, ideally well above 10 µW for practical portable systems. Most research efforts have been expanded in either extending the microwave electronics region towards higher frequencies, and/or by developing photonic devices in the lower frequency regime.

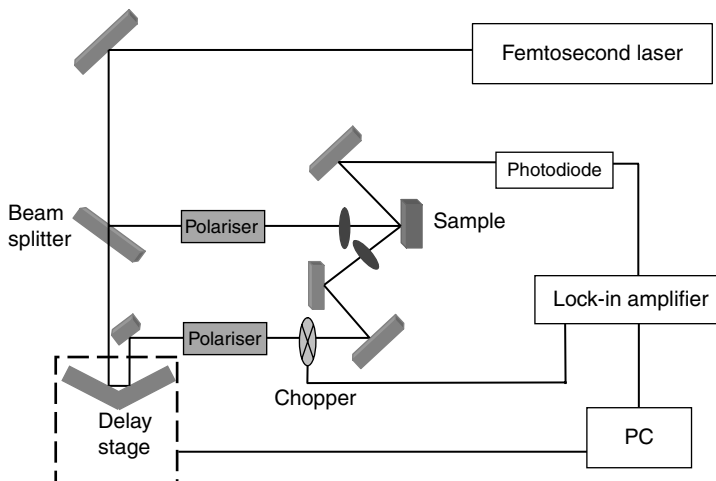
Semiconductor microwave technology is making great strides in realising electronic solid state THz sources, such as oscillators and amplifiers. Millimetre wave and sub-millimetre wave monolithic integrated circuits (MMIC), high frequency Gunn diodes, IMPATT and resonant tunnelling diodes have all been developed and used for emission at the long wavelength end of the THz region^{6–9} while, at the upper frequency end, photonic techniques are used to develop sources based on Quantum Cascade Lasers.¹⁰ However, among all existing THz sources the most widely used ones belong to the innovative field of THz optoelectronics and are laser driven. These sources are based on the frequency down-conversion from the optical region and rely on semiconductor photoconductive (PC) switch techniques

pioneered by Auston and Lee.^{11,12} There are two techniques to generate THz radiation in the above semiconductor-based approaches: one produces broadband pulsed THz radiation and is based on femtosecond pulsed lasers, such as Ti:Sapphire,^{13,14} driving photoconductive switches, while the other produces narrowband continuous wave THz radiation and is based on photomixing two CW lasers, whose frequency difference is tuned to the THz region, in a photoconductor.¹⁵ Although the former technique is an efficient one, the sheer complexity of the femtosecond laser set-up and the high cost of such a laser restrict its application for laboratory usage. On the other hand, the CW technique is cost effective and makes the fabrication of portable and highly efficient THz imaging systems possible. However, the output power is limited to $\sim 1\mu\text{W}$ (per device) at present, due to the finite breakdown voltage and to thermal failure. The frequency range of such sources is typically 0.2–2 THz, or higher depending on the laser pulse parameters, while the output power ranges from nanowatts to a few microwatts.

On the detector front, electro-optic detectors can be based on either thermal or electronic detection, respectively. In the case of thermal detectors, THz radiation is detected in a radiation absorber attached to a heat sink. The radiation energy is then converted to heat, where a sensitive thermometer measures the increase of heat generated by the radiation. Electronic detectors such as Hot Electron Bolometers (HOB) and superconductor-insulator-superconductor (SIS) mixers are robust and reliable,^{16,17} however the cryogenic temperature conditions required for their operation are a major drawback.

16.2 Generation and detection of broadband pulsed terahertz radiation

One of the most commonly used techniques for generating and detecting THz radiation is broadband pulsed THz using photoconductive antennas. This technique is the most efficient for converting visible/near infrared pulses to THz radiation^{18,19} and is used extensively in applications such as THz spectroscopy and imaging. The most commonly used spectroscopy system is the TDS. A schematic of a THz pump-probe set-up is shown in Fig. 16.1. The Ti:Sapphire laser provides pulses with durations in the femtosecond range with wavelengths at around 800 nm. The output beam from the laser is split into a pump and probe beam, respectively. The pump beam is focused onto the surface of the photoconductor emitter, while the probe beam is focused onto the photoconductor detector. Parabolic mirrors at the side of the emitter are used to collimate the emitted THz pulse and drive it onto the sample under test. The parabolic mirrors are used to collect the transmitted THz pulse and focus it onto the photoconductor detector.^{20–22}

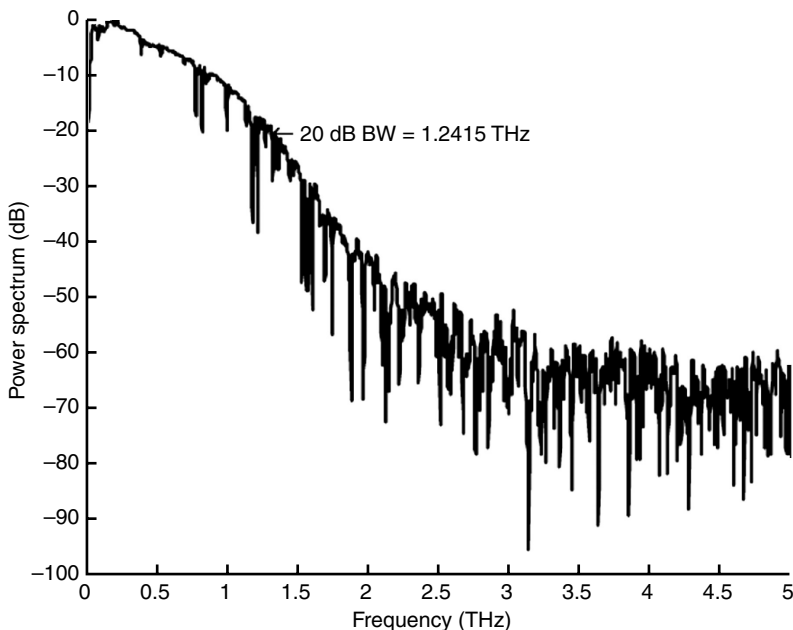


16.1 Schematic of THz pump-probe set-up.

The THz emitter generates a pulse which is distorted by selective absorption as it passes through the sample, causing a delay in its arrival time at the detector. By varying the time at which the sample pulse arrives at the detector, portions of the THz pulses can be detected and built into a complete image of the pulse in the time domain. The data acquired is then processed using fast Fourier transform analysis in order to convert the delay time into frequency.

The photoconductor is, for the most part, a semiconductor structure grown at low temperature using molecular beam epitaxy (MBE), the only non-equilibrium growth technique by which such materials can be synthesised. The most widely used material is the so-called low-temperature-grown GaAs (LT-GaAs), whose growth and material properties are discussed later. Both emitter and detector structures can be made not only from the same semiconductor layers but also from the same layout, with the only difference in use being that the emitter is biased while the detector is not. Antenna structures are carefully designed, as the geometry is critical for the THz generation and detection. The antennas' electrodes are vacuum evaporated on the surface of the low-temperature-grown semiconductor layer using Ti/Au, Ti/Pd/Au, NiCr/Au or AuGe/Ni/Au metals. Antenna structures are usually based on Bow-Tie, Zig-Zag, interdigitated electrodes, spiral or dipole geometries.

The physical mechanisms for THz emission and detection are well documented.²³ In brief, electron–hole pairs are generated in the photoconductor as a result of the above band-gap energy supplied by the pulsed femtosecond laser. The generated photocarriers are accelerated in the presence of



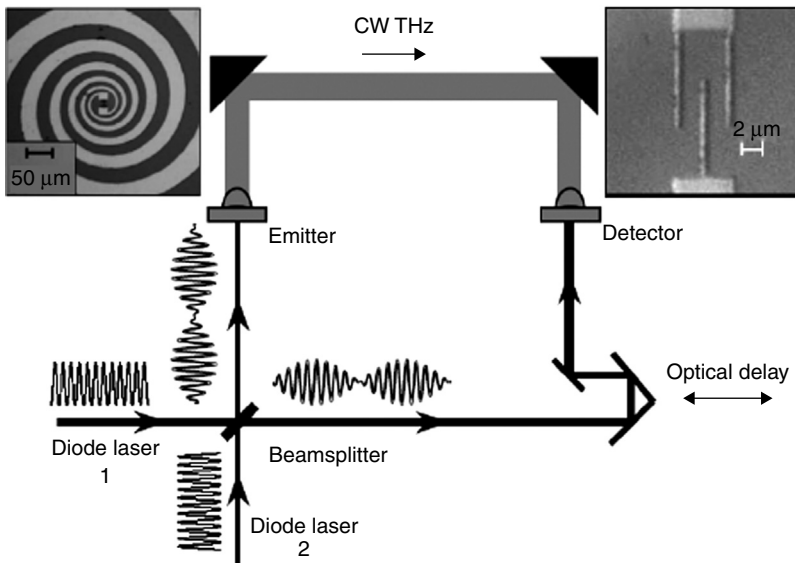
16.2 THz power spectrum of dipole antennas fabricated on the LT-GaAs. VMBE2018 at $\lambda = 800$ nm.

the bias electric field across the antenna terminals. This acceleration is in phase with the bias field and decays with a time constant determined by the carrier lifetime, yielding a pulsed photocurrent in the photoconductor antenna. Current modulation occurs in the sub-picosecond regime and there is thus emission of a sub-picosecond electromagnetic transient, which is the THz pulse. The photoconductor antenna acts as a sampling gate, which samples the waveform of the THz pulse when its carrier lifetime is much shorter than the THz pulse. The incident THz radiation generates an electric field, which accelerates the photocarriers. This acceleration is detected as a photocurrent, which is proportional to the electric field of the focused THz radiation. It is then amplified with a low-noise current amplifier and fed to a lock-in amplifier. The THz pulse waveform is obtained by measuring the average photocurrent versus time delay between the THz pulses and the gating optical pulses. Amplitude and phase spectrum are extracted from Fourier analysis of the temporal profile of the received THz pulse.²⁴ When LT-GaAs materials fabricated into dipole antennas act as photoconductor for both emission and detection respectively, a response of 2 or 3 THz is obtained with power spectrum dynamic range of 70 dB or greater, as shown in Fig. 16.2.

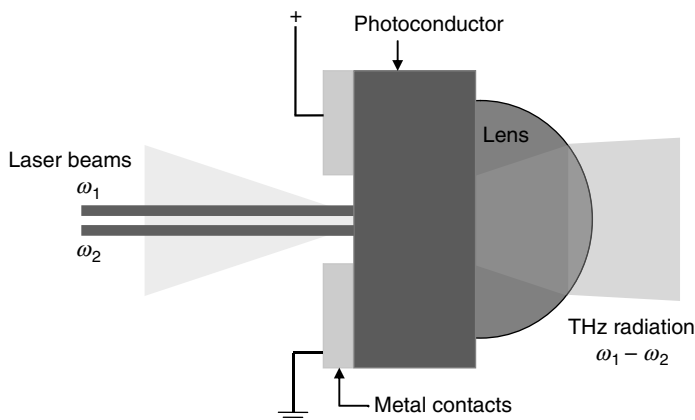
16.3 Generation of continuous wave terahertz radiation using photomixing

In this technique, the CW THz generation relies on a photomixing process, based on optical heterodyne down-conversion. This process occurs by illuminating the photomixer (photoconductor) with two CW lasers, which have a frequency difference in the THz region. The conductance of the photomixer is then modulated at that frequency and the THz radiation is emitted through the antenna structure. Compared to photoconductors used in TDS, these devices should meet stricter characteristics such as very high dark resistivity, high carrier mobility and sub-picosecond carrier lifetime. Although there have been great improvements in the growth of III-V optoelectronic devices, the resulting output THz power is still too low for widespread usage in portable battery-operated applications. One limiting factor for maximum output power is the thermal damage threshold, due to excessive biasing and high incident laser power. A typical CW THz system depicting the photomixing process is shown in Fig. 16.3. The antenna structure of the photomixers is based on spiral geometry with interdigitated electrode fingers at the central point.^{25,26}

The most widely used photomixer material to date is LT-GaAs, as this material meets most of the requirements needed for efficient photomixing.



16.3 Schematic diagram of the CW THz system including the combining beamsplitter, optical delay line and THz emitter and detector. Left inset shows spiral antenna while the right inset shows the interdigitated fingers at the central feed of the spiral.²⁵



16.4 Complete view of a THz emitter from which CW THz radiation can be generated using photomixing techniques.

Photomixing is achieved using two single-mode lasers. The beams from the two lasers are combined with a 50/50 beamsplitter and focused onto the antenna gap of the emitter. The output radiation is then focused onto the detector. Silicon hyperhemispherical lenses are attached at the substrate sides of the emitter and detector in order to collimate and focus the generated THz radiation. The stability of the frequency of the emitted radiation is determined by the stability of the pump lasers. Figure 16.4 illustrates the main components of the photoconductive device used as a photomixer for CW THz generation. The metal contacts used to apply an external field, are part of the antenna, and their design influences the characteristics of the emitted radiation. The portion of THz radiation that emerges from the back of the semiconductor is usually collimated using a high resistivity ($> 10 \text{ K}\Omega$) silicon lens to minimise the effect of the free-carrier absorption.

The role of the silicon lens is not only to collimate the emitted radiation, but also to couple it out of the GaAs substrate into free space as, without the lens, the high refractive index of GaAs ($n \sim 3.61$) at 1 THz causes strong diffraction of the outgoing THz radiation at the substrate-air interface.

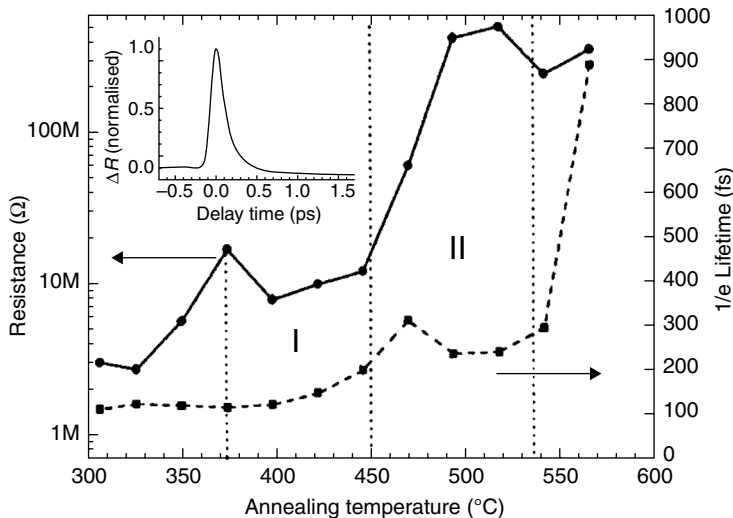
16.4 Photoconductive semiconductor materials

A semiconductor photoconductive material (also sometimes referred to as a ‘switch’) is an electrical device that changes its conductivity as a result of irradiation with light. In a semiconductor material, any absorbed light with a photon energy greater than the band gap energy generates free carriers, which then contribute to the conductivity.

16.4.1 Low temperature GaAs

At present the most successful photomixer material is low temperature GaAs (LT-GaAs), the reason being that it meets all the requirements for efficient emitters and detectors – that is, short carrier lifetime, high resistivity, high electron mobility and high electric breakdown field.^{27,28} Short carrier lifetime is desirable so that the crystal properties can respond on sub-picosecond time scale. High resistivity and breakdown voltage in the emitters allows the application of large external bias, while high resistivity minimises the dark current in detectors. What makes these characteristics possible is the formation of deep energy levels in the middle of the energy band-gap of the semiconductor material during the growth at low temperatures, that is, $\leq 250^\circ\text{C}$, using the MBE technique. The growth of a semiconductor layer at low temperature results in the incorporation of excess As atoms, which lead to the formation of point defects such as As antisites defects (As(Ga)), As interstitials (As(i)) and Ga vacancies (V(Ga)) with density exceeding $10^{17}\text{--}10^{20}\text{ cm}^3$.²⁹ These defects manifest themselves primarily as a strain in the epitaxial layer whose effect is readily measurable using Double Crystal X-Ray Diffraction (DCXRD). The concentration of the point defects is, to first order, determined by the growth temperature and the overpressure of arsenic during growth. These vacancy defects have been studied in detail³⁰ and shown to be deep-donor-like and deep-acceptor-like defects. The thermal energy at room temperature is not sufficient to ionise these deep energy levels, and as a consequence they do not contribute to the conduction mechanism.³¹ Instead they are responsible for the shorter recombination carrier lifetime and compensation process. The compensation process is the process whereby the deep levels capture the free carriers from the shallow-energy levels, leading to a net reduction of the free-carrier density. An important deep energy defect in GaAs is the so-called EL2, which is located roughly 0.75 eV below the conduction band³² and is a deep donor-like, thermally very stable, and acts as an electron trap.³³ It also gives rise to semi-insulating properties and therefore high resistivity.

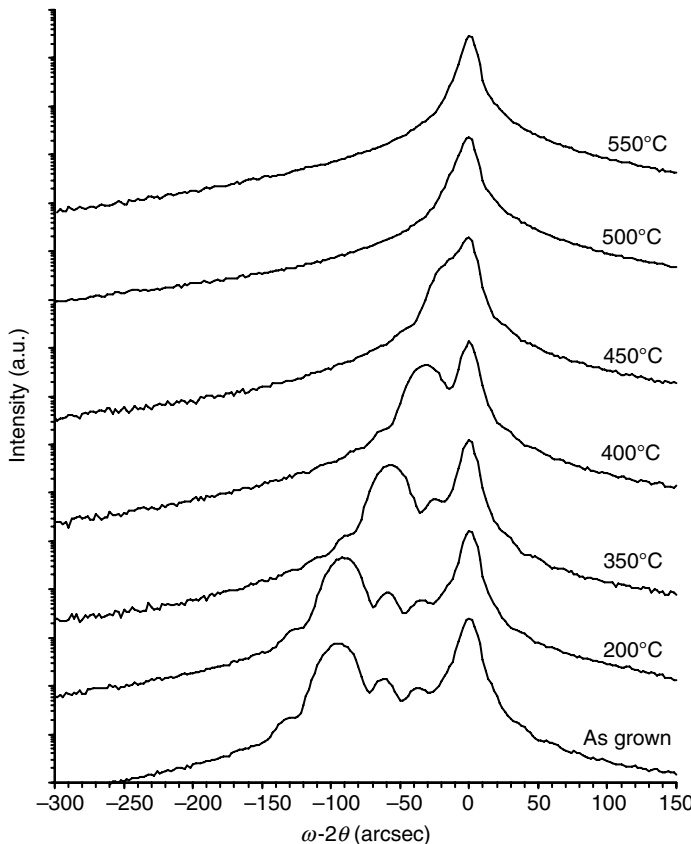
LT-GaAs can be grown as high quality mono-crystals³⁴ despite its high non-stoichiometry. If, however, the growth is at temperatures below 180°C , the epitaxial layer becomes polycrystalline or amorphous. During the low temperature growth, mid gap states are formed by incorporation of excess arsenic as point defects. These cause the electrons to be rapidly trapped from the conduction band to the mid gap states, resulting in very short recombination lifetimes. Hopping conduction in the very dense defect band causes low resistivity, around $0.2\text{--}2\ \Omega\text{cm}$. However, post-growth annealing³⁵ improves the crystal structure of the epilayers and concomitantly the strain in the lattice caused by the excess arsenic antisites vanishes that is, the layer relaxes totally. The effects of post-growth annealing on the LT-GaAs



16.5 Resistance together with carrier lifetime measurements as a function of the anneal temperature for a photoconductive device. Inset is a reflectance, R , curve for annealing at a temperature of 350°C .³⁶

material significantly alter the structural and electrical properties of the material, starting from a low annealing temperature of $\sim 350^{\circ}\text{C}$ up to temperatures of $\sim 650^{\circ}\text{C}$, with higher annealing temperatures leading to a dramatic increase of the carrier lifetime.³⁶ Such a process allows the formation of precipitates from the excess arsenic incorporated as point defects, which in turn become the primary carrier traps. The precipitates act as buried Schottky barriers, increasing the material resistivity through the creation of overlapping depletion regions. The large density of states in the precipitates results also in the elimination of the saturation effects experienced in the as-grown material. Figure 16.5 shows typical measurements of the resistance of a processed LT-GaAs photoconductive device along with the carrier lifetime as a function of the annealing temperature.³⁶ As the annealing temperature is increased above 550°C , the point defects are eliminated and the lattice constant relaxes to that of the substrate.

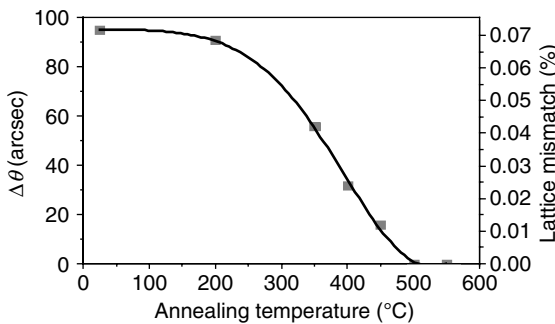
The post-growth annealing effects on the structural, optical and electrical characteristics of LT-GaAs material have been studied using techniques such as X-ray diffraction, infrared absorption and Hall measurements, which all provide useful information about excess As precipitation, absorption wavelength and carrier mobility. The DCXRD rocking curves show that the epitaxial layers are crystalline and that there is a lattice mismatch between the substrate and the epilayers. Figure 16.6 shows the X-ray rocking curves for an as-grown and annealed LT-GaAs layer.



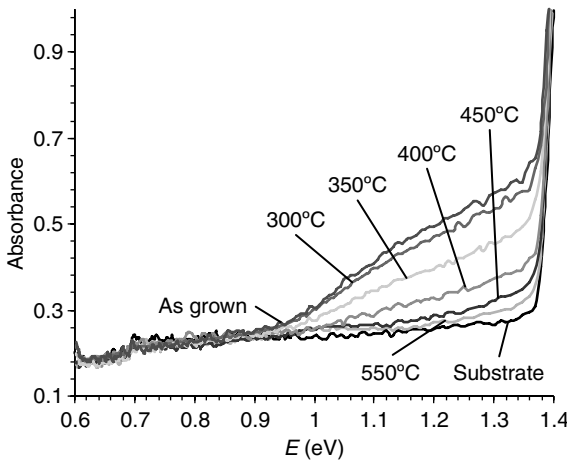
16.6 Double Crystal X-Ray rocking curves for as-grown and annealed LT-GaAs.

Two peaks are found in all the as-grown samples, which are attributable to the GaAs substrate and the LT-GaAs epilayer. The splitting of the peaks is an indication of the lattice mismatch and thus the built-in strain. As the growth temperature decreases the strain is increased. The post-growth annealing at temperatures greater than roughly 550°C results in one peak only is consistent with total relaxation of the epilayer, which then adopts the same lattice constant as that of the GaAs substrate. This implies that the excess arsenic atoms undergo at the very least a phase transformation via the creation of arsenic precipitates. The large densities of point defects are then dramatically reduced (but not totally eliminated).

By measuring the peak separation, the lattice mismatch as a function of the annealing temperature can be plotted as shown in Fig. 16.7.



16.7 Peak separation and lattice mismatch between LT-GaAs layer and substrate as a function of annealing temperature.



16.8 Absorption spectra of LT-GaAs at different annealing temperatures.

The absorption spectra of LT-GaAs layer annealed at different temperatures are shown in Fig. 16.8. For each spectrum, the absorbance, which is the product of the absorption coefficient (α) and the thickness (d) of the sample, is plotted as a function of the photon energy. Absorption due to the deep level impurities, that is, As antisite defects, lies in the region between the absorption due to the band-to-band transitions at around 1.4 eV, and the background absorption due to the free carriers at about 0.6 eV, which is below the photo-ionisation energy of EL2. The concentration of As antisite defects which are incorporated in the LT-grown samples has been shown to behave like the EL2 defects in semi-insulating GaAs, and the LT-GaAs materials show a strong absorption at about 1.24 eV (~1 μ m) as the EL2

related defects change their states to a metastable EL2* state. Martin's calibration curve at room temperature for EL2 concentration is:³⁷

$$[\text{EL2}] = 7.8 \times 10^{15} \alpha(1.24) \quad (\text{cm}^{-3}) \quad [16.1]$$

Due to the similarity of behaviour between EL2 and As antisite defects, this calibration can be used to estimate the concentration of As antisite defects in the LT-GaAs epitaxial layers. For instance, when light is incident on the LT-GaAs sample there will be absorption due to EL2 in the substrate and arsenic antisite defects in the LT-grown GaAs layer and hence Equation [16.1] becomes:

$$[\text{As}_{\text{Ga}}] = 7.8 \times 10^{15} [\alpha_{\text{L+S}}(1.24) - \alpha_{\text{s}}(1.24) - \alpha_{\text{L+S}}(0.6)] \quad (\text{cm}^{-3}) \quad [16.2]$$

where

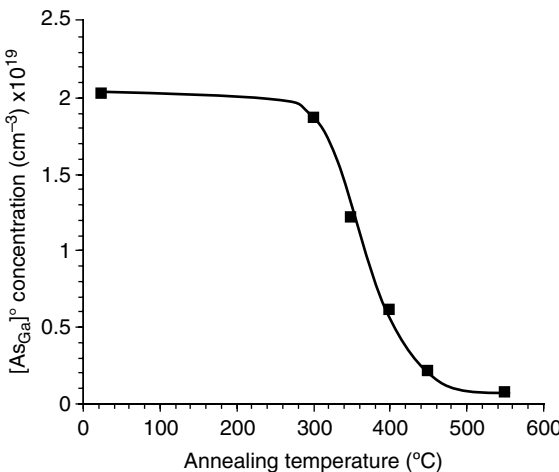
$\alpha_{\text{L+S}}(1.24)$ is the absorption coefficient of the sample (layer + substrate) at 1.24 eV

$\alpha_{\text{s}}(1.24)$ is the absorption coefficient of the substrate at 1.24 eV

$\alpha_{\text{L+S}}(0.6)$ is the background coefficient (due to the free electrons) at 0.6 eV, as this energy is below the photo-ionisation energy of the EL2.

The effect of increasing the annealing temperature on the absorption due to the arsenic antisite defects is depicted in Fig. 16.8, which shows clear reduction in their concentration, and this reduction agrees well with the DCXRD results shown in Fig. 16.6.

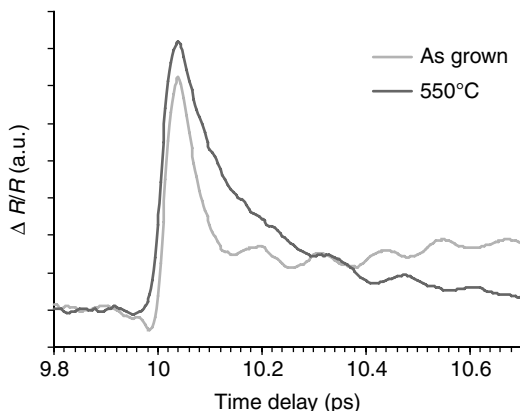
The concentrations of the neutral arsenic antisite defects $[\text{As}_{\text{Ga}}]^\circ$ in the LT-grown epitaxial layers, in addition to the EL2 concentration in the GaAs substrate, can be estimated from the above spectra using Martin's calibration at room temperature. The concentration of the EL2 defects in the substrate of the LT-GaAs sample (after removing the LT-GaAs layer using wet etching) is $9.96 \times 10^{15} \text{ cm}^{-3}$ whereas the concentration of $[\text{As}_{\text{Ga}}]^\circ$ defects in the as-grown LT layer is $\sim 2 \times 10^{19} \text{ cm}^{-3}$. The concentration of the arsenic point defects estimated from the DCXRD measurements is around $3.5 \times 10^{20} \text{ cm}^{-3}$ using Yu *et al.*'s calibration.³⁸ Therefore, by comparing the concentration of the neutral arsenic antisite defects estimated from the absorption measurements with that from the DCXRD studies, it can be inferred that the arsenic interstitial As_i are the dominant defects in the LT layer as the $[\text{As}_{\text{Ga}}]^\circ$ is only 5.8% of the total arsenic defect concentration. Figure 16.9 depicts the reduction of the $[\text{As}_{\text{Ga}}]^\circ$ in the LT-GaAs layer as a function of the annealing temperature, and shows decay towards an equilibrium substrate value at 550°C.



16.9 Neutral As antisite concentration $[\text{As}_{\text{Ga}}]^{\circ}$ in the LT-GaAs layer as a function of annealing temperature.

The transmission coefficient varies exponentially for annealing temperatures between 400°C and 500°C. Below 400°C there is no change in the transmission coefficient, while above 500°C there is saturation. The rise in the transmission coefficient is due to the reduction of the arsenic point defects, while the saturation is taken as indication of the formation of the precipitates. The derivative of the transmission spectra gives the absorption spectra, where it becomes apparent that the centres of the absorption band are shifted towards the conduction band by increasing the annealing temperature. The changes in the absorption band are attributed to the relaxation of the lattice due to partial removal of arsenic point defects, which in turn affects the coupling energy of the defects with the lattice.

Another important parameter that determines the efficiency of THz photoconductors is carrier mobility. In stoichiometric GaAs material grown at high temperature the mobility of free electrons is dominated, at room temperature, by phonon and ionised impurity scattering with the lattice. In LT-GaAs, the high density of lattice imperfections due to its non-stoichiometric characteristics influences the mobility which is now mainly defined by the elastic carrier scattering on neutral and ionised defects. Look *et al.* were among the first researchers to report values for the mobility in LT-GaAs material using the Hall Effect method.^{39–41} These studies showed that the conductivity of LT-GaAs layers has two components: band conductivity due to free-carrier motion, and hopping conductivity. For the as-grown material the reported mobility at room temperature was below 1 cm²/Vs, pointing to the fact that conduction takes place through hopping in the dense EL2 defect bands. At high annealing temperatures, and with the resulting decrease in the point



16.10 Time-resolved differential reflectivity of as-grown and 550°C annealed LT-GaAs sample.

defect densities, the conduction band carrier transport becomes predominant and the conduction band mobility increases to values of 200–400 cm²/Vs. Another study by Betko *et al.*^{42,43} reported Hall hopping mobility of around 0.14–0.45 cm²/Vs for as-grown material using the same method. The band Hall mobility was reported to be 500–6000 cm²/Vs depending upon the growth temperature. The sheet resistivity and the Hall mobility increase with increasing annealing temperature, yielding values that are very close to those of the semi-insulating (SI) substrate. The sign of the Hall coefficient was negative for all the samples indicating electron transport. At high annealing temperatures the values reach those of the SI substrate, and this can make the analysis of the data complicated. One way to overcome this is to separate the LT-GaAs layer from its substrate. However, such a solution requires a special structure with an AlAs etch-separation layer. Another solution is to use the data obtained from the LT-GaAs and the SI substrate after etching away the LT-GaAs layer.

In addition to high resistivity, the carrier lifetime plays a very important role in the performance of photoconductive materials. As mentioned previously, post-growth annealing increases resistivity for the LT-grown samples, but it may also increase the carrier lifetime. Figure 16.10 shows the change in the material reflectivity of an LT-GaAs sample (as-grown and 550°C annealed) as a function of the time delay of the probe beam after excitation with 800 nm laser beam. The lifetime of the generated carriers was measured at the initial 1/e point of the reflectivity decay to be 60 and 140 fs for the as-grown and 550°C annealed samples respectively.

These are among the shortest lifetimes ever reported and in line with the previous work performed in Reference 36.

16.4.2 ErAs:GaAs superlattices

Another approach for generating LT-GaAs-like characteristics, but in a controllable manner, has been the use of composite material such as Er:GaAs, in which thin layers of ErAs are embedded in GaAs during growth. ErAs is a semi-metallic material similar to arsenic with a lattice constant close to that of GaAs (1.6% difference). This composite material is produced by depositing one monolayer of ErAs during MBE growth of GaAs at around 535°C.⁴⁴ The ErAs self-assembles into nm islands and the GaAs growth proceeds with high crystalline integrity between the ErAs layers. The nanoparticles act as non-radiative recombination centres due to their semi-metallic characteristics, which are very similar to the arsenic precipitates in LT-GaAs. Pump-probe experiments show that the response times of the ErAs:GaAs samples are in the sub-picosecond range and controlled by the superlattice period, which can be attributed to carrier capture by the ErAs islands. The fact that the response time can be engineered makes this material desirable for device applications such as THz sources and high speed optoelectronic circuits, though its electrical properties (resistivity and mobility) have not been studied in detail.

16.4.3 LT-In_{0.53}Ga_{0.47}As-In_{0.52}Al_{0.48}As

LT-GaAs remains the most intensively studied material for ultrafast optoelectronic applications; however, its rather large band-gap energy imposes certain limits for lasers that can be used with it, and which on the whole tend to be specialist and very expensive components. The challenge thus is the synthesis of materials that combine the desirable properties of the LT-GaAs, such as ultrashort carrier lifetime, high carrier mobility and high dark resistivity, while at the same time being able to be excited at the practical and cost-effective telecommunication wavelengths of 1.3 and 1.55 μm. The key material which can be excited at these wavelengths is In_{0.53}Ga_{0.47}As grown lattice matched on InP substrate. As in the case of LT-GaAs, the low temperature growth of In_{0.53}Ga_{0.47}As results in the formation of native defects due to excess arsenic incorporation, and which, as a consequence, results in ultrafast recombination and photo-response. In contrast to GaAs based materials, however, LT-In_{0.53}Ga_{0.47}As shows highly conductive behaviour, due to the fact that the growth-induced defect levels are very close to the conduction band edge,^{45,46} yielding very low resistivity material. Such behaviour is not suitable for THz applications, and one solution for increasing the resistivity is to compensate the free-electron concentration by doping the material with a shallow acceptor element, such as Beryllium (Be). By adding Be dopants, the Fermi-level shifts into the middle of the band

gap and there is thus an increase in resistivity. There are two difficulties with this approach: firstly, perfect balancing of the Be doping and the background carrier concentration is difficult and secondly, the small band gap of $\text{In}_{0.53}\text{Ga}_{0.47}\text{As}$ (~ 0.75 eV) is not conducive to large resistivity.

A much more promising approach consists of embedding the $\text{In}_{0.53}\text{Ga}_{0.47}\text{As}$ material between the larger band gap (~ 1.45 eV) $\text{In}_{0.52}\text{Al}_{0.48}\text{As}$ layers, which are grown under the same conditions as the $\text{In}_{0.53}\text{Ga}_{0.47}\text{As}$. In this case, the resistivity is found to be further increased and the response time is reduced to the femtosecond range.^{47,48} $\text{In}_{0.52}\text{Al}_{0.48}\text{As}$ is chosen as it is lattice matched to $\text{In}_{0.53}\text{Ga}_{0.47}\text{As}$, has a higher band gap, is transparent at $1.55\ \mu\text{m}$ and does not contribute to photoconductivity. The resistivity is increased due to the large deep electron levels in $\text{In}_{0.52}\text{Al}_{0.48}\text{As}$ that can trap the free electrons that form in the $\text{In}_{0.53}\text{Ga}_{0.47}\text{As}$ quantum well close to the interface by tunnelling effects.⁴⁹ In order for this trapping effect to be effective, the $\text{In}_{0.53}\text{Ga}_{0.47}\text{As}$ layer must be as thin as $100\text{--}150\ \text{\AA}$ so that the distance between the electrons and the trapping centres is short. The trade off for such a thin photoconductive layer is the fairly weak absorption of radiation. One way to enhance the absorbance is by repeating the photoconductive layer and trapping layer many times. The latter results in a LT- $\text{In}_{0.53}\text{Ga}_{0.47}\text{As}$ - $\text{In}_{0.52}\text{Al}_{0.48}\text{As}$ multiple quantum wells structure.

It has been shown that Be doping of LT InGaAs increases the resistivity and retains the sub-picosecond absorption recovery after annealing, and this has been attributed to Be–As complexes formation. However, the absorption response cannot be a reliable measure of the trapping or the recombination time of photogenerated carriers due to photo-induced absorption induced by excited-state transitions.⁵⁰ Chen *et al.*⁵¹ reported the existence of a long-lived residual photoconductivity, which is reduced by Be doping. In this study the technique of time-resolved THz transmission spectroscopy was used to determine the recombination dynamics of three LT $\text{In}_{0.53}\text{Ga}_{0.47}\text{As}$ - $\text{In}_{0.52}\text{Al}_{0.48}\text{As}$ multi quantum well structures. The quantum well was repeated 50 times and the layer thicknesses were $84\ \text{\AA}$ and $100\ \text{\AA}$ for the well and the barrier, respectively. The three samples were either undoped, doped with $5 \times 10^{17}\ \text{cm}^{-3}$ Be, or doped with $2 \times 10^{18}\ \text{cm}^{-3}$ Be, respectively. THz transmission spectra of the as-grown and low-doped samples indicates carrier lifetimes above the sub-picosecond range. An increase in the Be concentration to $2 \times 10^{18}\ \text{cm}^{-3}$ results in a dramatic reduction of the residual conductivity. The initial transient response in conjunction with the measured static THz transmission and the photogenerated carrier density allowed the initial and residual change of the conductivity, $\Delta\sigma_i$, and $\Delta\sigma_r$, static mobility μ_{THz} and static electron density N_{THz} to be obtained through numerical modelling. The values of mobility decreased from $\sim 2700\ \text{cm}^2/\text{Vs}$ from the as-grown sample to less than $1000\ \text{cm}^2/\text{Vs}$ for the heavily Be-doped one. The consequence of annealing the samples was a significant decrease

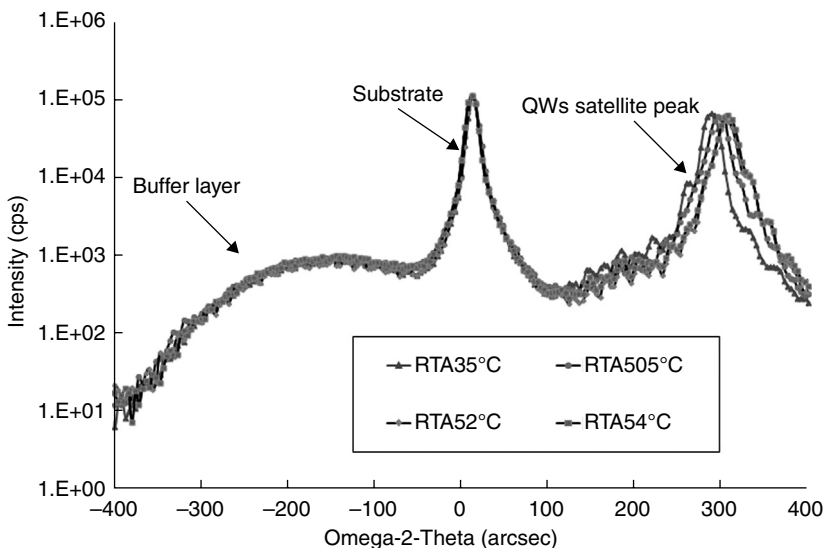
in the residual carrier density for the low-doped sample. Furthermore, modelling revealed a reduction of the static carrier concentration with a slight increase of mobility. It was also found that the Be–As complex remained constant during the annealing as the initial conductivity lifetime did not change appreciably.

Be-doped multi quantum wells $\text{In}_{0.53}\text{Ga}_{0.47}\text{As}$ – $\text{In}_{0.52}\text{Al}_{0.48}\text{As}$ structures grown at low temperatures in the range of 100 to 200°C and with a period of 100 have also been studied by Kuenzel *et al.*⁵² The effect of the Be doping resulted in a reduction of the response time in the femtosecond range. By contrast, annealing the material resulted in an increase of the response time from 230 fs for the as-grown sample to 1.5 ps for the annealed one. Annealing reduces the defect concentration by the diffusion of arsenic antisites from Ga sites and the formation of arsenic clusters and thus, carrier trapping becomes slower. A high resistivity of around $10^6 \Omega/\text{sq}$ and mobilities in the range of 500–1500 cm²/Vs are also reported in the same study.

Detailed structural (using DCXRD), transport (using Hall Effect measurements) and electrical properties of a series of low-temperature-grown (~220°C) MBE lattice matched $\text{In}_{0.53}\text{Ga}_{0.47}\text{As}$ – $\text{In}_{0.52}\text{Al}_{0.48}\text{As}$ superlattice structures, doped with various levels of Be, has been recently reported.⁵³ The key findings have led to materials whose lifetimes are ~1 psec and whose resistivities are an order of magnitude higher than the best reported to date in this material system⁵² and approaching those of LT-GaAs.

A series of LT-InGaAs-InAlAs layers were grown by MBE on SI, iron-doped InP substrates. The multi quantum well structures were inspired by designs by Chen *et al.*⁵⁴ and incorporated first in a 900 Å InAlAs buffer layer grown at 520°C on top of which a superlattice structure of InGaAs (120 Å) and InAlAs (90 Å) was repeated 50 times and grown at a nominal temperature of 220–230°C. The set of samples contained a control, undoped wafer (VMBE2001) and four samples with Be doping of 2.5, 6.5, 1.5 and $2 \times 10^{18} \text{ cm}^{-3}$ to closely follow the compensation process. Following growth, the samples were annealed *ex situ* at temperatures between 300°C and 600°C, in a rapid thermal annealer in a nitrogen atmosphere, and in contact with a SI GaAs wafer to passivate the surface and inhibit arsenic loss. The anneal duration was 10 min, which was found to be the time required for achieving full equilibrium defect concentration.

X-ray diffraction was used to examine the defects incorporated by the low temperature growth, and changes induced by the annealing process. Figure 16.11 shows the DCXRD spectra evolution of the undoped material as a function of annealing. It is clear from the rocking-curve spectra that there is a sizeable movement of the QW satellite peak as the annealing temperature is increased corresponding to a *decrease* in the QW thickness, which we associate with arsenic precipitation; this is the first evidence and report of a direct observation of this phenomenon in LT-InGaAs-InAlAs QWs.

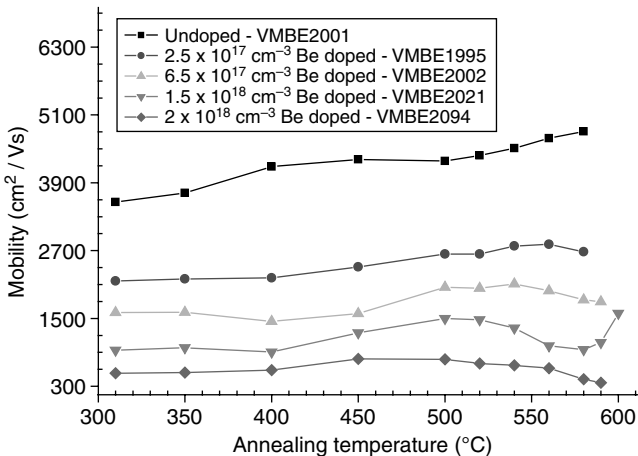


16.11 DCXRD of undoped sample (VMBE2001) as a function of annealing.

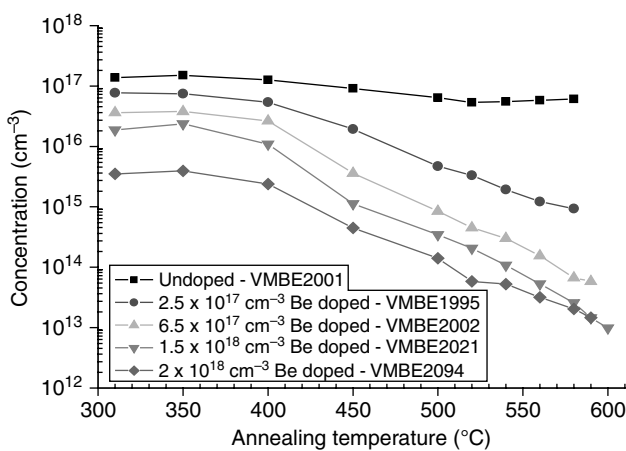
This behaviour was observed in all samples studied, suggesting that the fundamental point-defects behaviour is similar in all samples and is not affected by the Be doping, at least for the levels used here. As the Be atoms sit preferentially on gallium sites, one would have expected competition from arsenic antisites for this, but this does not seem to happen, at least for the Be doping levels used.

The samples were all subjected to photoluminescence measurements at room temperature to ascertain any optical activity in these materials. Both the undoped and lower doped samples showed signs of optical activities, in sharp contrast to LT-GaAs materials, suggesting that the native defects in LT-InGaAs-InAlAs are not sufficient to completely inhibit band-to-band recombination. The situation changes dramatically after annealing though, suggesting that the compensating mechanism and the short lifetime obtained are related to the arsenic precipitation process again in contrast to LT-GaAs.

While there is undeniable reordering and restructuring of arsenic, the electrical properties of the undoped wafer, unlike those of LT-GaAs, remain largely unaffected. The incorporation of various levels of Be ($\sim 2 \times 10^{17}$ to $2 \times 10^{18} \text{ cm}^{-3}$) changes the background levels (always n-type) when subjected to annealing in the structures from a high 10^{16} cm^{-3} to a low 10^{13} cm^{-3} (Fig. 16.12) but with an accompanying drop in mobility from a high of 5000 to a low $500 \text{ cm}^2/\text{Vs}$ (Fig. 16.13), the latter being comparable to those obtained on LT-GaAs material. The doped wafers (Be doping $> 2 \times 10^{17} \text{ cm}^{-3}$) all



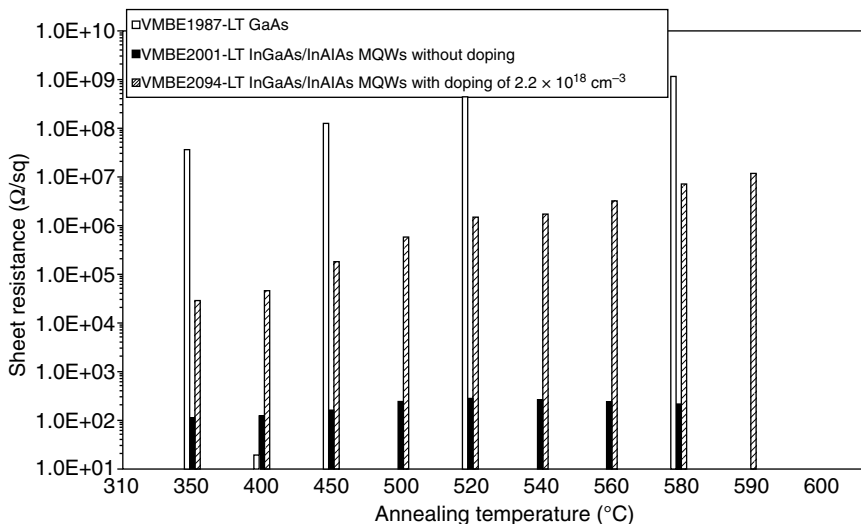
16.12 Carrier concentrations as function of annealing.



16.13 Mobility as a function of annealing.

showed $< 1 \text{ ps}$ carrier recombination lifetime, sometimes almost irrespective of annealing temperature and in the light of the DCXRD data above suggests that a combination of native defects and Be doping is the key mechanism for the sub-picoseconds recombination processes.

The sheet resistance of all the wafers investigated is shown in Fig. 16.14 and compared with a control LT-GaAs layer. Note that the upper annealing temperatures are much higher than hitherto used in the literature. The usual 500–520°C anneal misses at least an order of magnitude drop in the carrier concentration and consequent increase in resistivity.

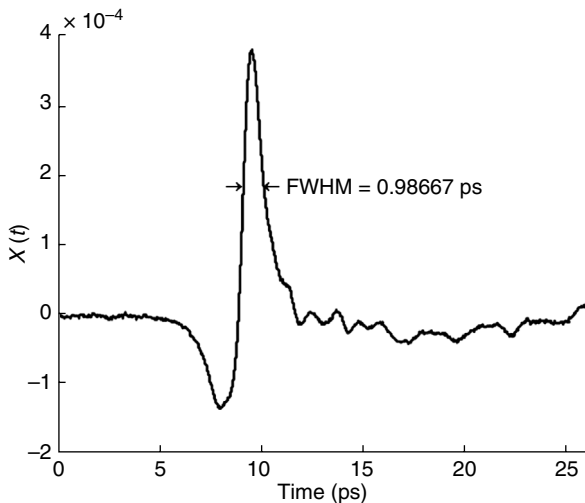


16.14 Sheet resistance as a function of annealing for the various samples compared with LT-GaAs. MQW, multi quantum well.

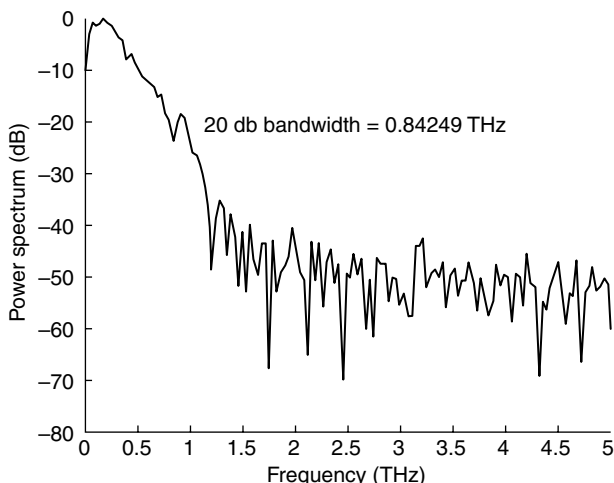
A terahertz time domain measurement system was used to characterise a series of terahertz photoconductive antennas (THz PCAs) made on the multi quantum well LT-InGaAs-InAlAs material described above. These antennas used simple dipole structures with no anti-reflective coating. A pair of collimating hyper hemispherical lenses made of high resistivity Si were attached to the back side of the transmitter and the receiver antennas. The system used a 1550 nm FemtoFibre FFS short pulse laser from Optica Photonics AG and with infra red optical pulse duration of 100 fs.

A total system response using photoconductive antennas made from the highest resistivity InGaAs-InAlAs samples is shown in Fig. 16.15, where the time decay is below 1 ps. A strong THz signal is detected with its frequency content extending up to 3 THz with more than 50 dB dynamic range for the THz power spectrum for the highest resistivity sample (Fig. 16.16). The resistance of the dipole structures exceeded 300 kΩ in this case. The high resistivity achieved in these samples translates in excellent THz performances, even though the carrier life time should be improved to match that of LT-GaAs as they are still too high for sub picoseconds THz pulse detection. An improved material system with shorter carrier lifetime and with the same level of resistivity and free-carrier mobility looks very promising for high bandwidth, high dynamic range THz signal generation and detection at the 1550 nm wavelength range.

A more recent study reports the first all-fibre THz time-domain spectrometer for operation at 1.5 μm, and based on Be-doped LT-In_{0.53}Ga_{0.47}



16.15 THz system response using annealed high resistivity $\text{In}_{0.53}\text{Ga}_{0.47}\text{As}-\text{In}_{0.52}\text{Al}_{0.48}\text{As}$ photoconductive samples as both emitters and detectors. InGaAs transmitter and InGaAs receiver at 1550 nm.



16.16 THz power spectrum of annealed high resistivity $\text{In}_{0.53}\text{Ga}_{0.47}\text{As}-\text{In}_{0.52}\text{Al}_{0.48}\text{As}$ dipole antennas. InGaAs transmitter and InGaAs receiver at 1550 nm.

As-In_{0.52}Al_{0.48}As MQWs.⁵⁵ The demonstrated ultrafast photo-response at 1.5 μm is around 750 fs. The evolution of the dark sheet resistance from Be-doped In_{0.53}Ga_{0.47}As to the use of multi quantum wells led to a high value of $10^6 \Omega/\text{sq}$. In this study the system performance was evaluated with the

THz path purged with dry nitrogen in order to avoid the effects on the THz waves by the absorption of the water vapour in the air. The detectable frequencies extend up to 3 THz.

16.4.4 ErAs: $\text{In}_{0.53}\text{Ga}_{0.47}\text{As}$ - $\text{In}_{0.52}\text{Al}_{0.48}\text{As}$

Composite ErAs into InGaAs have also been attempted but these result in lower resistivity material with long carrier lifetimes.⁵⁶ Other attempts have been directed at the growth of layers of ErAs islands embedded in an InGaAs/InAlAs matrix.^{57,58}

X-ray measurements on structures with different ErAs deposition amounts revealed smooth crystalline overgrowth of the ErAs islands for depositions up to 2.4 ML. Above this thickness, an appreciable loss of crystalline coherency was observed. Hall measurements showed that the sheet resistance was increased as the ErAs deposition was increased. The highest sheet resistance ($\sim 37 \times 10^3 \Omega/\text{sq}$) at room temperature was reported for a sample of 3 ML ErAs deposition. This value is some two orders of magnitude lower than those using crystalline $\text{In}_{0.53}\text{Ga}_{0.47}\text{As}$ - $\text{In}_{0.52}\text{Al}_{0.48}\text{As}$. The room temperature mobilities ranged from 1500 to 5700 cm^2/Vs . The temperature dependence of the mobility was found to be depended on the amount of the ErAs in the sample. This conduction behaviour is fundamentally different from that observed in similar ErAs:GaAs structures and therefore further investigations are required in order to determine the mechanisms for such a behaviour.

16.5 Conclusions

The search for a compact, efficient and cost-effective THz sources or THz generation and detection systems is still an on-going concern. This chapter has reviewed the most promising material systems that will power up future portable THz systems. It has also illustrated directions of research which use both LT-GaAs and LT-InGaAs-InAlAs materials that will surely lead to suitable systems. The InGaAs-InAlAs material system in particular, with its ability to be excited at the very important wavelength of $1.55 \mu\text{m}$, shows most promise.

The Holy Grail of THz emitter system is 1mW of power generation at room temperature using CW techniques. At the moment the best systems achieve $\sim 1\text{--}10 \mu\text{W}$, so there is a 100-fold improvement needed. However, the prize for such an achievement would be the opening up of a whole new industry for fast THz imaging, a field akin to Silicon CCD cameras, but of course addressing completely different markets including biological and security applications. The devices reported in this chapter are a step towards realising this aim.

16.6 Acknowledgements

I gratefully acknowledge the UK's Engineering and Physical Sciences Research Council for funding this research. I am also indebted to my past and current research students (Dr M. Alduraibi and I. Kostakis) for expert help with material characterisation and device processing. I am also grateful to Dr Daryoosh Saeedkia from T-Era Consulting for expert THz measurements.

16.7 References

1. A. G. Davies, E. H. Linfield, and M. B. Johnston, 'The development of terahertz sources and their applications', Institute of Physics Publishing, *Phys. Med. Biol.*, **47**, 3679–3689 (2002).
2. J. E. Bjarnason, T. L. J. Chan, A. W. M. Lee, M. A. Celis, and E. R. Brown, 'Millimeter-wave, Terahertz, and mid-infrared transmission through common clothing', *Appl. Phys. Lett.*, **85**, 519–521 (2004).
3. Y.-S. Jin, G.-J. Kim, and S.-G. Jeon, 'Terahertz dielectric properties of polymers', *J. Korean Phys. Soc.*, **49**, 513–517 (2006).
4. K. Kawase, Y. Ogawa, H. Minamide, and H. Ito, 'Terahertz parametric sources and imaging applications', *Semicond. Sci. Technol.*, **20**, 258–265 (2005).
5. P. H. Siegel, 'Terahertz technology', *IEEE T. Microw. Theory*, **50**(3), 910–928 (2002).
6. H. Eisele, 'Recent advances in the performance of InP Gunn devices and GaAs TUNNETT diodes for the 100–300 GHz frequency range and above', *IEEE T. Microw. Theory*, **48**, 626 (2000).
7. N. Karpowicz, H. Zhong, C. Zhang, K.-I. Lin, J.-S. Hwang, J. Xu, and X.-C. Zhang, 'Compact continuous-wave subterahertz system for inspection applications', *Appl. Phys. Lett.*, **86**(5), 054105 (2005).
8. T. Fong and H. Kuno, 'Millimeter-wave pulsed IMPATT sources', *IEEE T. Microw. Theory*, **27**, 492–499 (1979).
9. E. R. Brown, J. R. Soderstrom, C. D. Parker, L. J. Mahoney, K. M. Molvar, and T. C. McGill, 'Oscillations up to 712 GHz in InAs/AlSb resonant-tunneling diodes', *Appl. Phys. Lett.*, **58**(20), 2291–2293 (1991).
10. R. Köhler, A. Tredicucci, F. Beltram, H. E. Beere, E. H. Linfield, A. Giles Davies, D. A. Ritchie, R. C. Iotti, and F. Rossi, 'Terahertz semiconductor heterostructure laser', *Nature*, **417**, 156 (2002).
11. D. H. Auston, 'Picosecond optoelectronic switching and gating in silicon', *Appl. Phys. Lett.*, **26**, 101–103 (1975).
12. C. H. Lee, 'Picosecond optoelectronic switching in GaAs', *Appl. Phys. Lett.*, **30**, 84–86 (1977).
13. Z. Jiang and X.-C. Zhang, 'Terahertz imaging via electro-optic effect', *IEEE T. Microw. Theory*, **47**, 2644 (1999).
14. Q. Wu, T.D. Hewitt, and X.-C. Zhang, 'Two dimensional electro-optic imaging of THz beams', *Appl. Phys. Lett.*, **69**, 1026 (1996).
15. E.R. Brown, K.A. McIntosh, K.B. Nichols, and C.L. Dennis, 'Photomixing up to 3.8 THz in low temperature-grown GaAs', *Appl. Phys. Lett.*, **66**, 285 (1995).

16. S. Cherednichenko, P. Khosropanah, E. Kollberg, M. Kroug, and H. Merkel, 'Terahertz superconducting hot-electron bolometer mixers', *Physica C Superconductivity*, **372**, 407–415 (2002).
17. D. E. Prober, 'Superconducting terahertz mixer using a transition edge micro bolometer', *Appl. Phys. Lett.*, **62**(17), 2119–2121 (1993).
18. I. Brener, D. Dykaar, A. Frommer, L. N. Pfeiffer, J. Lopata, J. Wynn, K. West, and M. C. Nuss, 'Terahertz emission from electric field singularities in biased semiconductors', *Opt. Lett.*, **21**, 1924 (1996).
19. G. Zhao, R. N. Schouten, N. van der Valk, W. Th. Wenckebach, and P. C. M. Planken, 'Design and performance of a THz emission and detection setup based on a semi-insulating GaAs emitter', *Rev. Sci. Instrum.*, **73**, 1715 (2002).
20. C. Baker, I. S. Gregory, W. R. Tribe, E. H. Linfield, A. G. Davies, M. Missous, 'Terahertz pulsed imaging with 1.06 μm laser excitation', *Appl. Phys. Letters*, **83**(20), 4199–4201 (2003).
21. Y. C. Shen, P. C. Upadhyya, H. E. Beere, E. H. Linfield, A. G. Davies, I. S. Gregory, C. Baker, W. R. Tribe, and M. J. Evans, 'Generation and detection of ultrabroadband terahertz radiation using photoconductive emitters and receivers', *Appl. Phys. Lett.*, **85**, 164 (2004).
22. Y. C. Shen, P. C. Upadhyya, E. H. Linfield, H. E. Beere, and A. G. Davies, 'Ultrabroadband terahertz radiation from low-temperature-grown GaAs photoconductive emitters', *Appl. Phys. Lett.*, **83**, 3117 (2003).
23. K. Sakai (Ed): 'Terahertz optoelectronics', *Topics Appl. Phys.*, **97**, 1–30 (2005).
24. M. Tani, S. Matsuura, K. Sakai, and S. Nakashima, 'Emission characteristics of photoconductive antennas based on low-temperature-grown GaAs and semi-insulating GaAs', *Appl. Opt.*, **36**, 7853 (1997).
25. C. Baker, I. S. Gregory, M. J. Evans, W. R. Tribe, E. H. Linfield, and A. M. Missous, 'All optoelectronic terahertz system using low temperature grown InGaAs photomixers', *Optics Express*, **13**(23), 9639–9644 (2005).
26. K. Sakai (Ed): 'Terahertz optoelectronics', *Topics Appl. Phys.*, **97**, 157–202 (2005).
27. I. S. Gregory, C. Baker, W. R. Tribe, H. E. Beere, and M. Missous, 'High resistivity annealed low – temperature GaAs with 100 fs lifetimes', *Appl. Phys. Lett.*, **83**(20), 4199–4201 (2003).
28. P. Kordos, M. Marso, and M. Mikulics, 'Performance optimization of GaAs-based photomixers as sources of THz radiation', *Appl. Phys. A-Mater.*, **87**, 563–567 (2007).
29. M. Luysberg, H. Sohn, A. Prasad, P. Specht, Z. Liliental-Weber, and E. R. Weber, 'Effects of the growth temperature and As/Ga flux ratio on the incorporation of excess As into low temperature grown GaAs', *J. Appl. Phys.*, **83**(1), 561–566 (1998).
30. S. Y. Chiang and G. L. Pearson, 'Properties of vacancy defects in GaAs single crystals', *J. Appl. Phys.*, **45**, 2986–2991 (1975).
31. B. G. Yacobi, *Semiconductor Materials: An Introduction to Basic Principles*, New York: Kluwer Academic/Plenum Publishers, 2003.
32. G. M. Martin, 'Optical assessment of the Main Electron Trap in Bulk Semi – Insulating GaAs', *Appl. Phys. Lett.*, **39**, 747–748 (1981).
33. G. M. Martin, J. P. Farges, G. Jacob, J. P. Hallais, and G. Poiblaud, 'Compensation mechanisms in GaAs', *J. Appl. Phys.*, **51**, 2840–2852 (1980).

34. M. Kaminska, Z. Liliental-Weber, E. R. Weber, T. George, J. B. Kortright, F. W. Smith, B-Y. Tsaur, and A. R. Calawa, 'Structural properties of As-rich GaAs grown by molecular beam epitaxy at low temperatures', *Appl. Phys. Lett.*, **54**(19), 1881–1883 (1989).
35. M. R. Melloch, N. Otsuka, J. M. Woodall, A. C. Warren, and J. L. Freeouf, 'Formation of arsenic precipitates in GaAs buffer layers grown by molecular beam epitaxy at low substrate temperatures', *Appl. Phys. Lett.*, **57**(15), 1531–1533 (1990).
36. I. S. Gregory, C. Baker, W. R. Tribe, H.E Beere, and M. Missous, 'High resistivity annealed low – temperature GaAs with 100 fs lifetimes', *Appl. Phys. Lett.*, **83**(20), 4199–4201 2003.
37. G. M. Martin, 'Optical assessment of the main electron trap in bulk semi-insulating GaAs', *Appl. Phys. Lett.*, **39**, 747–748 (1981).
38. K. M. Yu, M. Kaminska, and Z. Lilientalweber, 'Characterization of GaAs-layers grown by low-temperature molecular-beam epitaxy using ion-beam techniques', *J. Appl. Phys.*, **72**, 2850–2856 (1992).
39. D. C. Look, D. C. Walters, M. O. Manasreh, J. R. Sizelove, C. E. Stutz, and K. R. Evans, 'Anomalous Hall-effect results in low-temperature molecular beam-epitaxial GaAs: Hopping in a dense EL2-like band', *Phys. Rev. B*, **42**(6), 3578–3581 (1990).
40. D. C. Look, G. D. Robinson, J. R. Sizelove, and C. E. Stutz, 'Electrical properties of molecular beam epitaxial GaAs grown at 300–450 °C', *J. Electron. Mat.*, **22**(12), 1425–1428 (1993).
41. D. C. Look, D. C. Walters, G. D. Robinson, J. R. Sizelove, M. G. Mier, and C. E. Stutz, 'Annealing dynamics of molecular-beam epitaxial GaAs grown at 200 °C', *J. Appl. Phys.*, **74**(1), 306–310 (1993).
42. J. Betko, P. Kordos, S. Kuklovsky, A. Förster, D. Gregusová, and H. Lüth, 'Electrical properties of molecular beam epitaxial GaAs layers grown at low temperature', *Mater. Sci. Eng. B*, **28**, 147–150 (1994).
43. J. Betko, M. Morvic, J. Novak, A. Forster, and P. Kordos, 'Hall mobility analysis in low-temperature-grown molecular-beam epitaxial GaAs', *Appl. Phys. Lett.*, **69**(17), 21 (1996).
44. C. Kadow, S. B. Fleischer, J. P. Ibbetson, J. E. Bowers, and A. C. Gossard, 'Subpicosecond carrier dynamics in low-temperature grown GaAs on Si substrates', *Appl. Phys. Lett.*, **75**(17), 2575–2577 (1999).
45. H. Kunzel, J. Bottcher, R. Gibis, G. Urmann, 'Material properties of GaInAs grown on InP by low-temperature molecular beam epitaxy', *Appl. Phys. Lett.*, **61**, 1347 (1992).
46. R. A. Metzger, A. S. Brown, L. G. McCray, and J. A. Henige, 'Structural and electrical properties of low temperature GalnAs', *J. Vac. Sci. Technol.*, **B11**, 798 (1993).
47. K. Biermann, D. Nickel, K. Reimann, M Woerner, Elsaesser, and H. Kuenzel, 'Ultrafast optical nonlinearity of low-temperature grown GalnAs/AlInAs quantum wells at wavelength around 1.55 μm', *Appl. Phys. Lett.*, **80**, 1936 (2002).
48. R. Takahashi, Y. Kawamura, and H. Iwamura, 'Ultrafast 1.55 μm all-optical switching using low-temperature-grown multiple quantum wells', *Appl. Phys. Lett.*, **68**, 153 (1996).

49. P.S. Whitney, W. Lee, and C.G. Fonstad, 'Capacitance transient analysis of molecular-beam epitaxial n-InGaAs and n-InAlAs', *J. Vac. Sci. Technol.*, **B5**, 796 (1987).
50. Y. Kostoulas, L. J. Waxer, I. A. Walmsley, G. W. Wicks, and P. M. Fauchet, 'Femtosecond carrier dynamics in low temperature grown Ga_{0.51}In_{0.49}P', *Appl. Phys. Lett.*, **66**, 1821 (1995).
51. Y. Chen, S. S. Prabhu, S. E. Ralph, and D. T. McInturff, 'Trapping and recombination dynamics of low-temperature-grown InGaAs/InAlAs multiple quantum wells', *Appl. Phys. Lett.*, **72**(4), 439–441 (1998).
52. H. Kuenzel, J. Boettcher, K. Biermann, H. Hensel, H. Roehle, and B. Sartorius, 'Low temperature MBE-Grown In(Ga,Al)As/InP structures for 1.55 μm THz photoconductive antenna applications', *20th International Conference on Indium Phosphide and Related Materials*, IPRM 2008 (IEEE, New York, 2008), pp. 1–4
53. M. Missous, 'Advanced MBE low temperature grown materials for CW THz generation and detection', *IEEE Sensors 2011*, 184–186 (2011).
54. Y. Chen, S. S. Prabhu, S. E. Ralph, and D. T. McInturff, 'Trapping and recombination dynamics of low-temperature-grown InGaAs/InAlAs multiple quantum wells', *Appl. Phys. Lett.*, **72**(4), 439 (1998).
55. B. Sartorius, H. Roehle, H. Künzel, J. Böttcher, M. Schlak, D. Stanze, H. Venghaus, and M. SchellB, 'All-fiber terahertz time-domain spectrometer operating at 1.5 μm telecom wavelengths', *Opt. Express*, **16**(3), 9567 (2008).
56. S. Sethi and P. K. Bhattacharya, 'Characteristics and device applications of erbium doped III-V semiconductors', *J. Electron. Mater.*, **25**, 467 (1996).
57. D. C. Driscoll, M. Hanson, C. Kadov and A. C. Gossard, 'Electronic structure and conduction in metal-semiconductor digital composite: ErAs:InGaAs', *Appl. Phys. Lett.*, **78**(12), 1703–1705 (2001).
58. M. P. Hanson, D. C. Driscoll, E. Muller, and A. C. Gossard, 'Microstructure and electronic characterisation of InGaAs containing layers of self assembled ErAs nanoparticles', *Physica E*, **13**, 602–605 (2002).

Terahertz applications in tomographic imaging and material spectroscopy: a review

T. SHIBUYA and K. KAWASE,
Nagoya University and RIKEN, Japan

DOI: 10.1533/9780857096494.3.493

Abstract: This chapter begins by reviewing several research projects which were considered to be useful for industrial application in the IRMMW - THz 2010 conference. Next, our recent studies of industrial applications are introduced: a computed tomography system using terahertz (THz) to millimeter waves, and a time-of-flight (TOF) THz tomography system. In the study of the tomography system, non-destructive investigation of the soot-removal filter installed in the internal combustion engine is demonstrated. Finally, a component analysis method for powder material using THz waves is introduced.

Key words: industrial application, computed tomography, time-of-flight tomography, componential analysis.

17.1 Introduction

Terahertz (THz) radiation can penetrate dielectric materials, including plastics, ceramics, crystals and colorants, similar to electric waves, allowing it to be applied to transmission or tomographic imaging.^{1–5} In addition, spectrum information can be acquired using THz waves, similar to infrared technologies. Using transparency or spectral information features, THz applications are expected to improve as research advances in numerous sectors, including manufacturing, pharmaceuticals, materials, semiconductors and security.

Tonouchi *et al.*⁶ developed the scanning laser THz emission microscope (LTEM), applying it to studying the dynamic response of semi-insulating GaAs (SI-GaAs) and low-temperature-grown GaAs (LT-GaAs) photoconductive antennas. In an LTEM, THz waves are radiated from a laser-induced transition current at the P–N junction in an integrated circuit. Non-contact and non-destructive failure analyses are possible using LTEM, because of the field intensity distribution of the THz-wave change during integrated circuit disconnection. Recently, LTEM systems with sub-

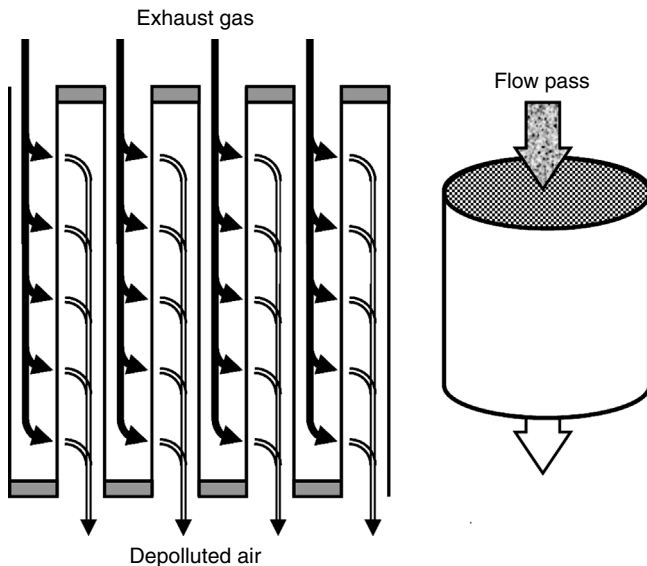
micrometer spatial resolutions have been developed. They have been used to diagnose actual large-scale integrated circuits (LSI) and could be used in LSI failure analyses, similar to laser-superconducting quantum interference device (SQUID) microscopy. Wallace *et al.*⁷ addressed medical imaging advances in pharmaceuticals using THz waves. Microscopic imaging can provide structural and functional information from preserved tissue specimens, but is used mainly in histopathology. Conversely, medical imaging methods, including magnetic resonance imaging (MRI) and computed tomography (CT), provide macroscopic images of living tissues, albeit with much lower resolution and specificity. THz-wave technology is expected to resolve these issues, due to its efficient resolution of medical imaging and tissue spectral information. Currently, imaging living tissue with high water content is difficult. However, adding THz-wave technology to medical imaging tools could increase the output power and signal-to-noise ratio (SNR) of the systems. Moreover, tomography using THz waves has been developed for non-destructive investigations, including in aerospace devices and art.^{8,9} Tomographic imaging has also been introduced in industrial applications, such as automobile part examinations and quantitative analyses of powdered chemicals.

17.2 Tomographic imaging applications

Tomography can acquire three-dimensional (3D) images within the THz frequency, similar to the photonic or X-ray regions of the electromagnetic spectrum. Two systems are CT, using millimeter-terahertz waves, and TOF-THz tomography. The THz-CT technique is similar to X-ray CT; however, it can image the internal structures of soft materials more easily. TOF tomography uses a THz pulse with a width <1 ps, and a depth resolution of tens of microns is possible. In addition, it can measure samples that are opaque in the visible region.

17.2.1 Computed tomography

CT can measure the internal structures of samples. It was developed for X-rays, but can be applied using THz radiation, resulting in more sensitive measurement of soft materials, due to reduced transmission at THz frequencies. Unlike X-rays, THz radiation causes scattering and diffraction, as well as some additional complications. We applied THz-CT to inspecting engine filters non-destructively. Air pollution from internal combustion engine emissions is a substantial problem. In particular, soot particulates from vehicle emissions, consisting primarily of carbon, are harmful to human health. Soot-removal filters installed in exhaust systems can reduce

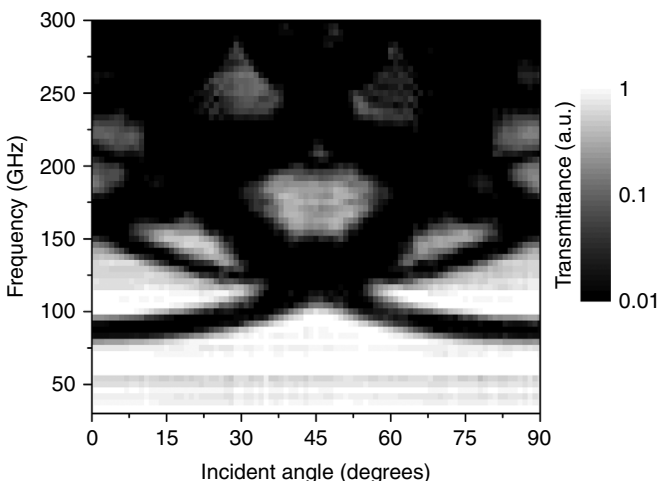


17.1 Cross-section (left) and overview (right) of a soot-removal filter.

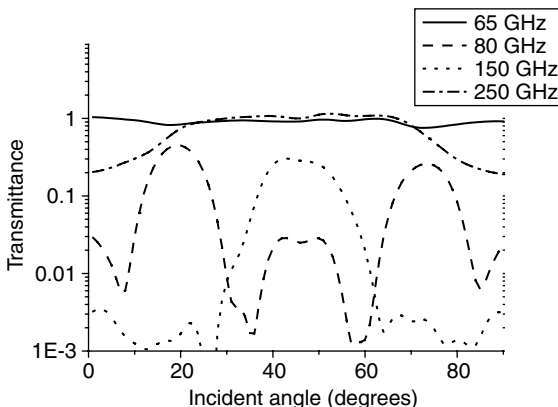
emissions. Measuring the soot distribution in soot-removal filters is important, because soot accumulation is invisible, but closely related to fuel costs. Figure 17.1 shows a simple overview of a filter. Exhaust is filtered through ceramic walls and discharged into the atmosphere. Developing an efficient filter is difficult, as it is hard to characterize the soot distribution in the filter, since that requires dismantling or destroying the filter. A non-destructive technique for measuring the accumulated soot distribution is preferable.

To construct a tomographic image, filter transmittance must be measured from all azimuthal angles. Transmittance was mapped as a function of the angle of incidence and frequency (Fig. 17.2). The dependence of transmittance on the angle of incidence is shown in Fig. 17.3 at 65, 80, 150, 175 and 250 GHz. The transmittance was strongly dependent on the angle of incidence at higher frequencies, resulting in behavior similar to that observed in photonic crystals, with pronounced dips. These dips in transmittance were caused by photonic band-gaps in the periodic filter structure, whereas the transmittance was almost flat at 65 GHz. Therefore, 65 GHz was used as the CT system operating frequency so that the position of soot deposits could be determined without artifacts from the filter structure affecting the image.

A schematic diagram of a CT imaging system is shown in Fig. 17.4. The source was a 65-GHz Gunn oscillator. The output was collimated using a

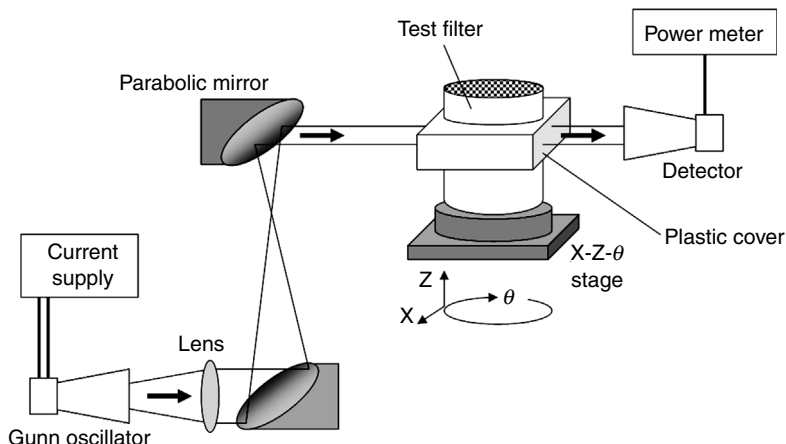


17.2 Transmittance mapping as a function of the angle of incidence and frequency; transmittance is indicated with a pseudocolor plot.

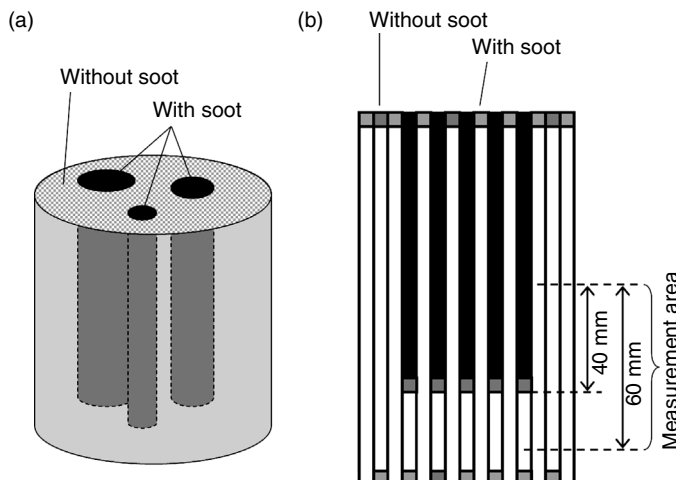


17.3 Transmittance as a function of the angle of incidence at several frequencies. There are strong dips in the transmittance at higher frequencies.

horn antenna and dielectric lens. The beam diameter was reduced using two parabolic mirrors to a full-width at half-maximum beam of 9.4 mm, and the sample was placed on an X-Z- θ stage in the collimated beam path. Since the sample was cylindrical, it behaved as a rod lens and was enclosed in a Teflon cover to prevent refraction at the sample/air interface. A test filter with a non-uniform soot distribution was used (Fig. 17.5). A reconstructed 3D image was obtained using filtered back-projection (Fig. 17.6).¹ The

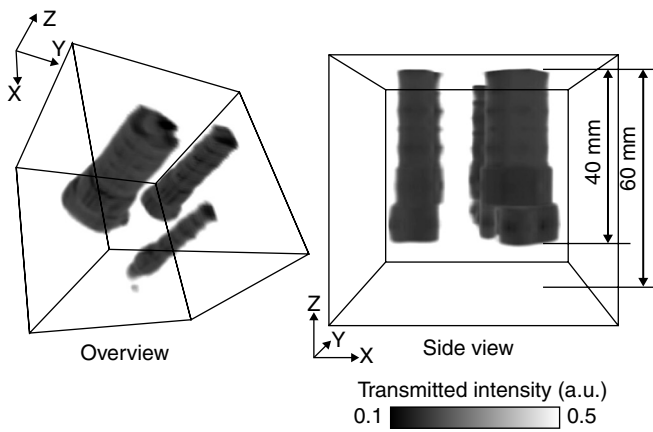


17.4 Schematic diagram of the 3D-CT image-acquisition system.



17.5 Schematic diagram of the test sample of a soot-removal filter. (a) Soot accumulates in the three 110-mm-long cylindrical regions shown in black, at a density of 4.7 g/L. The final 40 mm of the filter contains no soot. (b) The microstructure of the sample soot-removal filter. Soot is located in the inlet regions of the filter, as shown by the black sections, and the sooty regions terminate part way along the length of the filter. The 60-mm-long measurement region is illustrated.

regions of accumulated soot were defined clearly. Some resolution loss and image distortion occurred from diffraction due to the mismatch of the refractive indices of the filter and Teflon cover, as well as artifacts of the Fourier transform.



17.6 Reconstructed 3D-CT image of the soot-removal filter.

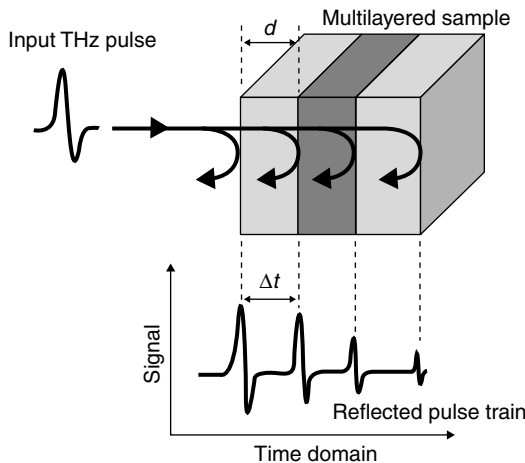
17.2.2 Time-of-flight tomography

TOF-THz tomography is based on a reflection THz-time-domain spectroscopy (TDS) system. Since electromagnetic fields in sub-picosecond THz pulses are measured directly with THz-TDS, multilayered structures of samples can be imaged by detecting the pulses reflected from the interfaces between layers. This is valuable in industrial applications, as the transmission characteristics of THz radiation enable the inspection of multilayered paints in industrial products or tablet coatings^{11,12} that cannot be measured using optical coherence tomography (OCT), which is based on an optical light source.¹³ Figure 17.7 illustrates a TOF-THz tomography system. In multilayered structures (Fig. 17.7), the pulse is partially reflected due to the refractive index discontinuity at each interface, and details of the multilayered structure can be inferred from the reflected pulse train. Assuming that the THz pulse is normally incident on the sample, the delay, Δt , of the reflected pulse is determined using:

$$\Delta t = \frac{2n_g d}{c}, \quad [17.1]$$

where n_g , d , and c are the refractive index, thickness of each layer, and speed of light, respectively. If the refractive index of the layers is known, d can be determined by measuring the delay time of each pulse:

$$d = \frac{c\Delta t}{2n_g}. \quad [17.2]$$



17.7 Principle of TOF-THz tomography.

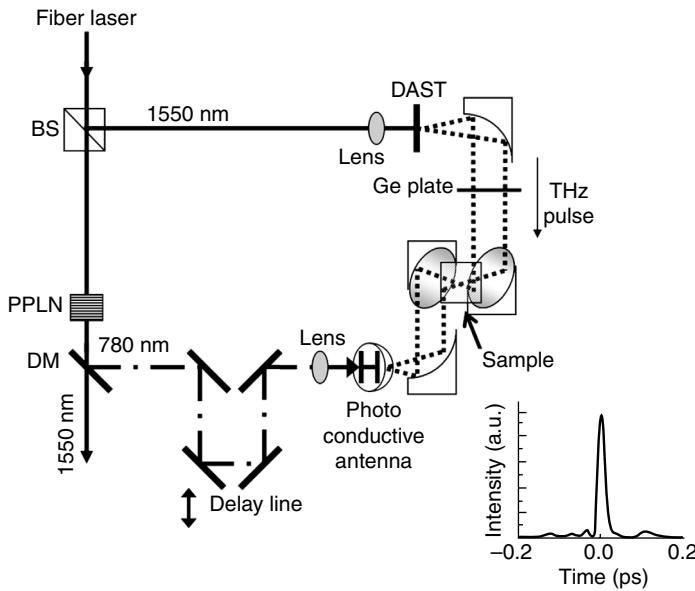
This can readily be extended to samples where the THz pulse is incident on the sample at angle θ :

$$d = \frac{c\Delta t}{2n_g} \cos \theta. \quad [17.3]$$

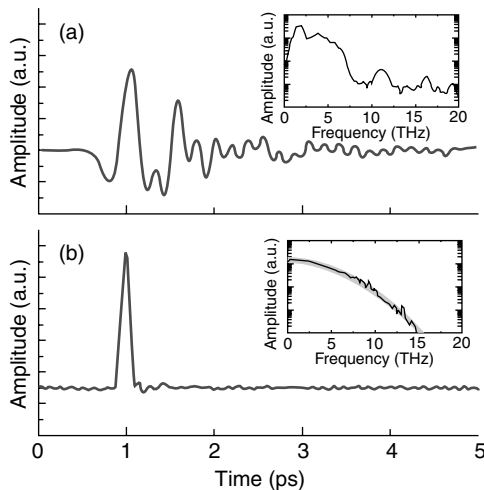
Tomographic resolution depends on the width of the incident THz pulse, and is improved using short pulses. Using non-ideal THz pulses, such as top-hat functions, ghost images can appear in the tomographic image. These can be eliminated using signal processing, for example by using deconvolution algorithms.

We developed a TOF tomography system with improved depth resolution using a femtosecond (fs) fiber laser system as the pump source.¹⁴ We developed an all-fiber laser system that produced 17-fs optical pulses with a wavelength of 1.56 μm , and generated and detected broadband pulses from 0.1 to 27 THz (Fig. 17.8; the inset shows the compressed optical pulses). The average power of the pulses was 200 mW and the repetition rate was 48 MHz.

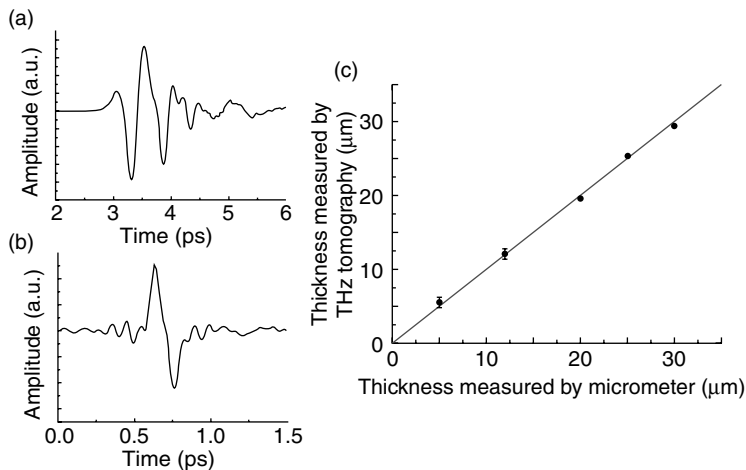
Figure 17.9a shows the reflected THz signal with an aluminum plate in the sample position. The maximum amplitude was about 1 ps, followed by oscillating components for several picoseconds due to a peculiar absorption characteristic of the diethylaminosulfur trifluoride (DAST) crystal. This anomalous reflected waveform made it more difficult to detect interfaces than using a THz pulse generated with a photoconductive antenna, and signal processing was required to improve the data. Figure 17.9b shows the processed waveform using the data in Fig. 17.9a, with one peak. Figure



17.8 Experimental set-up of a high-resolution TOF-THz tomography system using a fiber laser. The inset shows the waveform of a 17-fs fiber laser. BS: beam splitter; PPLN: periodically poled lithium niobate; DM: dichroic mirror; PCA: photoconductive antenna; Ge, germanium plate; DAST: diethylaminosulfur trifluoride.



17.9 Reflected THz pulse: (a) raw data and (b) after signal processing. The insets show the corresponding Fourier transforms. The gray curve in the inset of (b) indicates the Fourier transform of a Gaussian pulse.

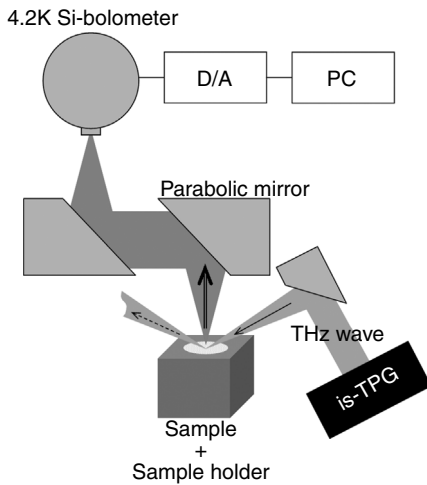


17.10 Axial resolution evaluation using Teflon films. (a) A typically measured reflected pulse, (b) the reflected pulse after signal processing, and (c) the thickness of the Teflon films measured with TOF-THz compared to that measured with a micrometer.

17.10 shows the TOF-THz measurements of 5-, 12-, 20-, 25- and 30-μm-thick Teflon films. Figure 17.10a and 17.10b show the reflected THz pulses before and after signal processing from the 12-μm-thick Teflon film. The two interfaces defining the film were observed clearly in the processed signal. Figure 17.10c shows the tomographic measurements of the thickness of the Teflon films. The depth resolution of this system was better than $10/n$ μm, where $n = 1.9$, the refractive index of the Teflon membrane. This technology could lead to systems capable of inspecting the thickness of thin films, such as paint, human skin, and fruit and vegetable peel.

17.3 Quantitative analysis of powdered chemicals

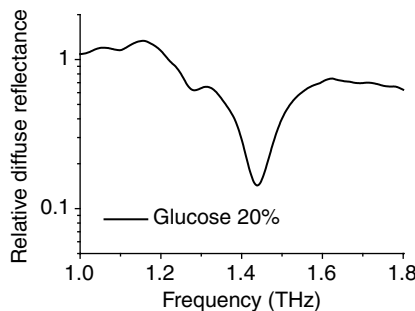
Using the characteristics of THz waves, such as their permittivity, and the spectrum characteristics of many materials, non-destructive investigations of illicit drugs and explosives concealed in envelopes have been developed.⁴ Depending on the sample thickness and shape, measurement can be difficult. In particular, powdered samples are difficult to measure because they create strong scattering. To measure powdered samples, the diffuse reflectance method is effective for infrared spectrum measurement. Since diffuse reflected radiation involves an absorbing component, the spectrum associated with the absorption coefficient can be obtained with a reflection measurement. Grain size must be adjusted to several micrometers when using



17.11 Experimental set-up for measuring diffuse reflectance.

infrared in diffuse reflection measurements, as many reagents have diameters from tens to hundreds of micrometers. By contrast, THz radiation has wavelengths from tens to hundreds of micrometers and is suitable for scattering measurements without complicated preprocessing.

We have demonstrated spectrum measurements of powdered sugar using diffuse reflection.⁴ The spectrum of different sugar concentrations was measured, and a calibration curve was obtained. The Kubelka–Munk theory¹⁵ and multivariate data analysis¹⁶ were used for the spectrum analysis. Spectrum measurements were acquired even when the samples were covered with paper, suggesting the utility of this technique in non-destructive investigations, such as mail security checks and pharmaceutical chemical quality reviews. The experimental set-up is shown in Fig. 17.11. We used an injection-seeded terahertz parametric generator (is-TPG)¹⁷ that emitted higher-output THz waves from about 1–2 THz as the THz-wave source. The THz waves were focused on the sample surface with a parabolic mirror. There was a 15° angle between the sample surface and the incident THz waves. Vertical diffuse reflected THz waves from the sample were focused to the detector by parabolic mirrors.¹⁸ A large-aperture parabolic mirror with a numerical aperture (NA) of 0.6 was used considering the detection efficiency. Specular reflection from the sample was undetectable. The spectrum was obtained by scanning the wavelength of the is-TPG seed light with a measuring range from 1.0 to 1.8 THz and a 5-GHz frequency resolution. A 4.2 K Si-bolometer was used as the detector. Powdered glucose and maltose with particle sizes classified from 100 to 300 µm using a sieve shaker were used as samples. A powder sample was packed into the sample holder, an



17.12 Relative diffuse reflection spectrum of 20 wt% glucose powder.

aluminum cube with a 5-mm-wide, 5-mm-deep cylinder hole. White polyethylene powder, which has little absorption in the THz region, was used as a reference powder. The relative diffuse reflectance was derived from

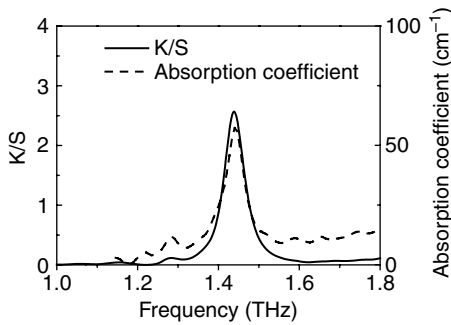
$$R_d = \frac{I_{\text{sample}}}{I_{\text{ref}}} \quad [17.4]$$

where I_{sample} and I_{ref} are the detected intensities of the sample and reference powders, respectively.

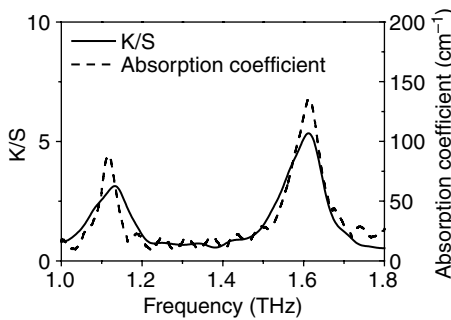
The measured relative diffuse reflection spectrum of 20 wt% glucose powder is shown in Fig. 17.12. There were well-defined absorption peaks around 1.28 and 1.44 THz. Using the Kubelka–Munk theory, the relative diffuse reflectivity was converted into a parameter that was proportional to the absorption coefficient. The Kubelka–Munk formula is:

$$\frac{K}{S} = \frac{(1-R_d)^2}{2R_d} \quad [17.5]$$

where K and S are the absorption and scattering coefficients, respectively. Using this equation, the parameter proportional to the sample concentration can be obtained if the particle size distribution is constant. Figure 17.13 shows the converted spectrum using the relative diffuse reflection spectrum and Equation [17.4] is called the Kubelka–Munk (KM) spectrum. The absorption spectrum is shown as a dashed line for comparison. The absorption coefficient spectrum is referred and calculated from the THz database provided by RIKEN.¹⁹ A KM spectrum was obtained from a powder sample, while an absorption spectrum was obtained from pellet samples, which exhibited little scattering. The same absorption peaks at 1.28 and 1.44 THz were observed. The absolute value of the parameter differed greatly between the KM and absorption coefficient spectra because the KM spectrum was the ratio of the



17.13 Comparison of the absorption and KM spectra of 20 wt% glucose.



17.14 Comparison of the absorption and KM spectra of maltose.

absorption and scattering coefficient. There was some difference in the baseline shape, because of dispersion of the scattering coefficient.

Figure 17.14 shows the KM and absorption coefficient spectrums of maltose. The center position of the absorption peak of the KM spectrum corresponded to the absorption coefficient spectrum. The line width of the absorption peak at 1.12 THz broadened more than the absorption spectrum, because the line width of the THz source broadened. Parametric THz-wave generation was achieved by satisfying the angle phase-matching condition in the nonlinear optical crystal used in the is-TPG source.²⁰ The injection seeding efficiency decreased and the line width of the generated THz wave broadened because the phase-matching angle and parametric gain decreased at lower frequencies.

Calibration curves were created from KM spectrum measurements of different concentrations of powder samples. Samples with concentrations of 2, 4, 6, 8, 10, 20, 40, 60 and 80 wt% were prepared. To create the calibration curve, we conducted a multivariate analysis of the KM spectrum using the absorption coefficient spectrum as a reference. The non-negative

least squares method was used for the multivariate analysis. For the analysis, the KM spectrum intensity $I(f) = K/S$ observed at f THz can be expressed as a linear combination of the absorbance spectra $D(f)$ and concentration parameter P :

$$\left\{ \begin{array}{l} I(f_1) = D_1(f_1)P_1 + D_2(f_1)P_2 + \dots + D_M(f_1)P_M \\ I(f_2) = D_1(f_2)P_1 + D_2(f_2)P_2 + \dots + D_M(f_2)P_M \\ \vdots \\ I(f_N) = D_1(f_N)P_1 + D_2(f_N)P_2 + \dots + D_M(f_N)P_M \end{array} \right. \quad [17.6]$$

where N and M are the measuring frequency and component numbers, respectively. These simultaneous equations can be rewritten as the linear matrix equation:

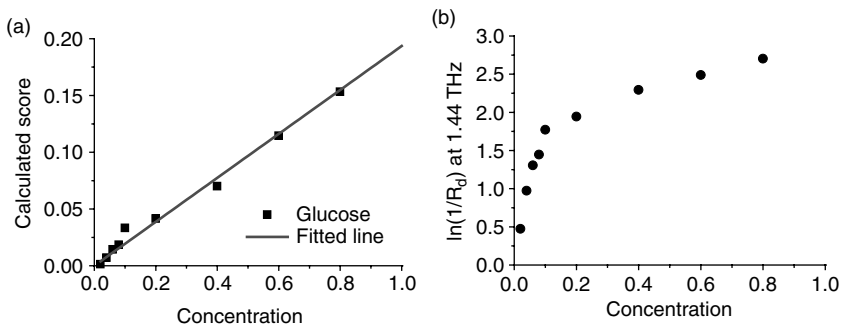
$$[I] = [D][P] \quad [17.7]$$

The absolute of the concentration cannot be calculated, because $[I]$ is the ratio of the absorption and scattering coefficients. The calibration curve can be calculated by deriving $[P]$, because the sample particle size distribution is constant and the scattering coefficient can be treated as a constant. When this matrix equation is solved for $N > M$ using the least squares method, the matrix $[P]$ can be described by:

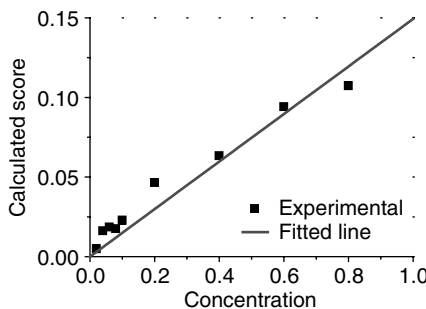
$$[P] = ([D^t][D])^{-1}[D^t][I] \quad [17.8]$$

where t denotes the transpose. The $[P]$ calculated for glucose powder was derived using Equation [17.8] and the glucose KM and absorption coefficient spectrums (Fig. 17.15a). The linearity between the concentration and calculated $[P]$ was confirmed within the measured range of concentrations from 2% to 80%. A relatively high correlation coefficient of 0.987 was obtained (Fig. 17.15a). Conversely, the relationship between the concentration of glucose powder and the naturalized logarithm of the inverse relative diffuse reflectivity was nonlinear (Fig. 17.15b). Figure 17.16 shows the relationship between the concentration and the calculated score using maltose powder, with a correlation coefficient of 0.932, which might have been lower than that of glucose due to a relatively large spectral shape error at low frequencies. Quantitative density measurements of powder samples with constant particle size distributions might be possible using this calibration curve.

We demonstrated non-destructive measurements of powder concealed by paper. The THz wave was not scattered by paper much compared to

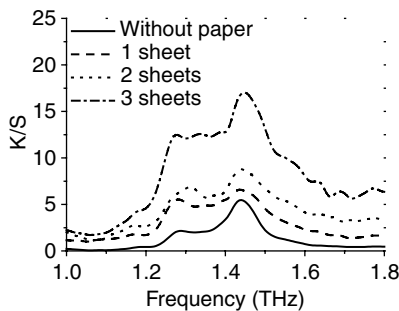


17.15 Relationship between the powdered glucose concentration and (a) the calculated score using the KM spectrum and multivariable analysis, and (b) the naturalized logarithm of the inverse relative diffuse reflectivity.

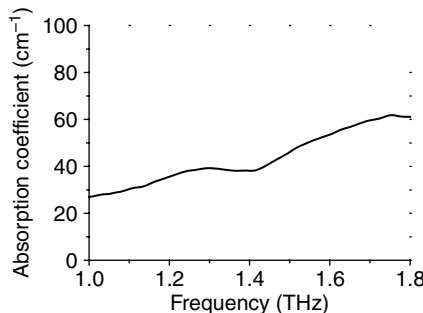


17.16 Relationship between the powdered maltose concentration and calculated score using the KM spectrum and multivariable analysis.

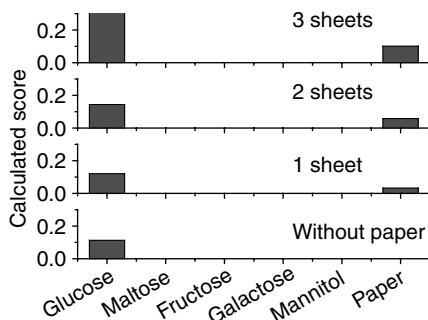
infrared radiation because its wavelength was 10–100 times longer. One application of this technology is detecting illicit drugs hidden in envelopes. Figure 17.17 shows the KM spectrum of 40 wt% powdered glucose unconcealed and concealed by one, two and three sheets of paper. The K/S parameter increased with the number of sheets of paper. Component identification was demonstrated using a multivariate analysis with Equation [17.6]. We used the absorption coefficient spectra of glucose, maltose, fructose, galactose, mannitol and paper as reference spectra for matrix $[D]$ in Equation [17.6]. The absorption spectrum of paper used in this experiment was measured as shown in Fig. 17.18. Other sugar spectra were from the RIKEN THz database. Figure 17.19 shows the results of the multivariate analysis. Other than the paper component, only glucose components were detected. A relatively large K/S parameter was



17.17 KM spectrum of 40 wt% powdered glucose unconcealed and concealed by one, two and three sheets of paper.



17.18 Measured absorption spectrum of the concealing paper.



17.19 Calculated score of each component when measuring powdered glucose concealed by 1–3 sheet(s) of paper or unconcealed. Only glucose was detected.

indicated (Fig. 17.19) for the sample covered by three sheets of paper because of the large decrease in the SNR and the influence of multiple reflections from the sheets. Regardless, the study confirmed that the component parameter of the paper increased with the number of sheets of

paper. Non-destructive component analysis of powder samples using the given database was confirmed.

17.4 Conclusion

Applied research using THz radiation is increasing, and is expected to be useful in various fields. Realizing its industrial application depends on developing high-power sources and sensitive room-temperature detectors. In the THz-wave source region, a high-power source can be realized using Cherenkov phase-matching conditions. Conversely, in the THz-wave detector region, the advances have been remarkable, such as the room-temperature micro-bolometer detector array. It is expected that practical industrial applications using THz radiation will be achieved following these developments.

17.5 References

1. B. Hu and M. Nuss, *Opt. Lett.*, **20**, 1716 (1995).
2. D. Mittleman, M. Gupta, R. Neelamani, R. Baraniuk, J. Rudd, and M. Koch, *Appl. Phys. B – Laser Opt.*, **68**, 1085 (1999).
3. R. Woodward, B. Cole, V. Wallace, R. Pye, D. Arnone, E. Linfield, and M. Pepper, *Phys. Med. Biol.*, **47**, 3853 (2002).
4. K. Kawase, Y. Ogawa, Y. Watanabe, and H. Inoue, *Opt. Express*, **11**, 2549 (2003).
5. A. Dobroiu, M. Yamashita, Y. Ohshima, C. Otani, and K. Kawase, *Appl. Opt.*, **43**, 5637 (2004).
6. M. Tonouchi, S. Fujiwara, D. Kaneko, I. Kawayama, and H. Murakami, *Proc. 35th Int. Conf. on Infrared, Millimeter and Terahertz Waves*, Tu-E2.2 (2010).
7. V. Wallace, E. Pickwell-MacPherson, and C. Reid, *Proc. 35th Int. Conf. on Infrared, Millimeter and Terahertz Waves*, PL09 (2010).
8. K. Fukunaga, Y. Kohdzuma, M. J. Kim, Y. Fujii, and Y. Fujiwara, *Proc. 35th Int. Conf. on Infrared, Millimeter and Terahertz Waves*, Th-P02 (2010)
9. H. Quast, A. Keil, and T. Loeffler, *Proc. 35th Int. Conf. on Infrared, Millimeter and Terahertz Waves*, We-A2.4 (2010)
10. G. T. Herman, *Image Reconstruction From Projections — The Fundamentals of Computerized Tomography* (Academic, New York, 1980).
11. H. Zhao, X. Guang, and J. Huang, *Physica E*, **40**, 3025 (2008).
12. B. Wang and G. Wang, *Appl. Phys. Lett.*, **87**, 013107 (2005).
13. W. Lin and G. Wang, *Appl. Phys. Lett.*, **91**, 143121 (2007).
14. J. Takayanagi, H. Jinno, S. Ichino, K. Suizu, M. Yamashita, T. Ouchi, S. Kasai, H. Otake, H. Uchida, N. Nishizawa, and K. Kawase, *Opt. Express*, **17**, 7549 (2009).
15. P. Kubelka, *J. Opt. Soc. Am.*, **38**, 448 (1948).
16. C.L. Lawson and R.J. Hanson, *Solving Least Squares Problems* (Prentice-Hall, Upper Saddle River, NJ, 1974) p. 161.
17. K. Imai, K. Kawase, M. Hiroaki, and H. Ito, *Opt. Lett.*, **27**, 2173 (2002).

18. T. Shibuya, M. Yamashita, Y. Ogawa, C. Otani, and K. Kawase, *Rev. Laser Eng.* **33**, 10 (2005).
19. Terahertz Project (2007) ‘Terahertz Database’ Available from: <http://thzdb.org>
20. Y. Nakagomi, K. Suizu, T. Shibuya, and K. Kawase, *Jpn. J. Appl. Phys.*, **49**, 102701 (2010).

Terahertz applications in the aerospace industry

M. J. BOHN, Air Force Institute of Technology, USA and
D. T. PETKIE, Wright State University, USA

DOI: 10.1533/9780857096494.3.510

Abstract: Aerospace applications for terahertz (THz) imaging will be examined in this chapter. The outer skin of the aircraft consists of thin (~ millimeter) sheets of fiber composites that are bonded to honeycombed composites for structural support. During the manufacturing process, quality-assurance inspections could be performed on these thin sheets using a transmissive THz system. A transmissive system can accurately determine the optical path length of the sheet which provides useful information regarding the epoxy homogeneity and regions of delamination. For inspections after the aircraft has been manufactured, reflective THz geometry is required because there are often structural components beneath the layer of interest that obstruct the penetration of the transmitted THz wave. Experiments demonstrating the utility of both of these techniques using both pulsed and continuous (CW) THz systems will be explained in detail. Results from CW THz experiments will also be presented and compared to the pulsed THz experiments. The chapter concludes with an experimental study comparing traditional non-destructive imaging techniques to THz imaging systems.

Key words: terahertz, millimeter wave, time domain spectroscopy, glass fiber composite, aerospace composite, non-destructive evaluation.

18.1 Introduction

Only months after the tragedy of 9/11, Flight 587 crashed into a Queen's borough in New York City killing 260 passengers on board, the second worst air accident in US history, and prompted fears of another terrorist attack (Wald and Baker, 2001). The National Transportation Safety Board (NTSB) quickly released statements that this tragedy was not a terrorist attack, but their investigation led to some interesting questions concerning the use of composite materials in aircraft because the vertical stabilizer which fell off and caused the accident was made from composite parts (NTSB, 2001). Generally, the outer skin of the aircraft consisted of glass reinforced fiber

plastics (GRFP) typically employing a polyimide resin. The rudder and vertical stabilizer consisted of long strands of carbon or glass held together by an epoxy. The aircraft, N14053, was involved in a number of interesting events. Prior to departing the Airbus factory in Toulouse, France on 12 July, 1988, the vertical stabilizer delaminated and had to be repaired with additional rivets and layers of fiber composite. Airbus instructed American Airlines that no further inspections were required of this repaired component. The vertical stabilizer is attached at six points with both composite and aluminum lugs and titanium bolts. The NTSB inspection revealed that the composite lugs failed while the metal components did not. In 1994, the aircraft experienced severe turbulence, resulting in injuries to 47 passengers over Puerto Rico. Afterwards, the aircraft was visually inspected and no structural damage was discovered (Wald and Baker, 2001).

The NTSB later found that the pilot/pilot training and the sensitivity of the rudder pedal caused the accident and not the composites used in the aircraft (NTSB, 2001). These deficiencies have been addressed by the airline and aircraft manufacturer and hopefully a repeat of this tragedy will be avoided. Nevertheless, there are lessons to be learned from aircraft N14053 with respect to the testing of fiber composites. There are three distinct situations where non-destructive testing should be performed on aircraft components: during the manufacturing process for quality assurance, scheduled periodic inspections as part of a preventative maintenance plan, and inspections after a reported incident. Note that all three of these examples are represented in aircraft N14053. A quality-assurance inspection using a THz system would have revealed the extent of the delaminations in the vertical stabilizer and could have been used to verify the quality of the repair of the delaminated section. Routine maintenance inspections would have insured that the delamination was not creeping and expanding. Finally, after the severe turbulence experienced over Puerto Rico in 1994, an inspection using a reflective THz system could have been used to determine if any cracks had formed during the abnormal stresses induced by the turbulence.

Glass fiber reinforced plastics (GFRP) and carbon fiber reinforced plastics (CFRP) are increasingly being used as structural components in aircraft, because of their high strength-to-weight ratios, improved aerodynamic performance and reduced corrosion compared with other structural materials. Composites can be weakened by various defects and stress during the lifecycle of an aircraft (specific examples are provided by the history of aircraft N14053), and routine maintenance of composite materials requires rather complicated inspection and repair techniques. THz radiation has the unique ability to penetrate composites and identify defects such as voids, delaminations, mechanical damage or heat damage (Chan, Deibel and Mittleman, 2007; Cooney and Blackshire, 2006; Kemp *et al.*, 2010; Petkie

et al., 2009; Redo-Sanchez *et al.*, 2006; Reiten, Hess and Cheville, 2006; Rutz *et al.*, 2006a; Rutz *et al.*, 2006b; Stoik, 2008; Stoik, Bohn and Blackshire, 2008; Wang and Zhang, 2004; Wietzke *et al.*, 2007; Zimdars *et al.*, 2006). THz offers a non-invasive, non-contact, non-ionizing method of assessing composite part condition and can overcome some of the shortcomings of other non-destructive techniques such as X-rays, ultrasound, video inspection, eddy currents and thermographic techniques. THz time domain spectroscopy (TDS) has been investigated as a possible method of quality control of polymeric compounds and their composites by imaging (Rutz *et al.*, 2006a; Rutz *et al.*, 2006b). THz, in both continuous-wave (CW) and pulsed modes, has also been studied as a means of evaluating damage to carbon fiber composites (Redo-Sanchez *et al.*, 2006).

A THz imaging system can provide a non-destructive, standoff imaging technique capable of detecting corrosion on metallic surfaces under obscurants, and defects in composite materials on aerospace structures (Kemp *et al.*, 2010; Petkie *et al.*, 2009; Stoik, 2008; Stoik *et al.*, 2008). In addition to higher transmission occurring at the lowest frequencies and higher optical resolution at the highest frequencies, signatures associated with defects will significantly change due to the relative scale of the wavelength to the physical structure of the defect in addition to changes in the complex dielectric constant of both the obscurants and defects. Some successful examples that illustrate the potential for non destructive evaluations (NDE) applications include products from the companies Picometrix and Teraview, both of which have developed THz NDE commercial systems for specific applications (www.picometrix.com/, www.teraview.com/).

This chapter will examine the application of THz imaging for aerospace applications. The outer skin of the aircraft consists of thin (~ millimeter) sheets of fiber composites that are bonded to honeycombed composites for structural support. During the manufacturing process, quality-assurance inspections could be performed on these thin sheets using a transmissive THz system, because the sheet is thin enough to permit THz transmission and the optical path is not obscured by structural components. The transmissive system can accurately determine the optical path length of the sheet, which can be useful to determine if the epoxy is curing properly or if there are regions of delamination. For inspections after the aircraft has been manufactured, reflective THz geometry is required because often there are structural components beneath the layer of interest that obstruct the penetration of the transmitted THz wave. Experiments demonstrating the utility of both of these techniques, using both pulsed and CW THz systems will be explained in detail. CW electronic systems have some advantages over a pulsed system; namely they can be made more compact and less expensive. Results from CW THz experiments will also be presented and compared to the pulsed THz experiments. Finally the chapter will conclude

with an experimental study comparing traditional non-destructive imaging techniques to THz imaging systems.

18.2 Non-destructive evaluation of aircraft composites using transmissive terahertz time domain spectroscopy

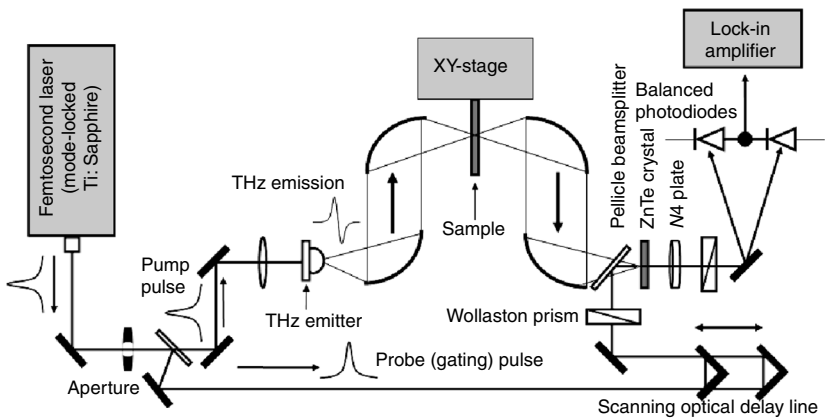
In this section, aircraft glass fiber composites are examined with various forms of damage with a transmissive THz TDS system. The samples represent the outer shell of the panel of an aircraft, consisting mostly of the glass fiber composite with a thin outer coating on the order of several millimeters. Refractive indices and absorption coefficients in the THz frequency range were measured using THz TDS in transmission configuration. Note that the attenuation of the THz radiation should consist of both absorption and scattering, but for these samples, the scattering coefficient has been estimated to be less than 1% of the absorption coefficient and therefore can be neglected (Stoik, 2008; Stoik *et al.*, 2008). Changes in the THz signal were observed due to material blistering, coating loss and/or residue caused by heat damage, and could be isolated with THz imaging. Hidden voids and delaminations could be located by TDS imaging using amplitude and phase analysis techniques.

18.2.1 Theory and experiment

The THz TDS set-up used to collect the material parameter data and perform the imaging is shown in Fig. 18.1. A Ti:Sapphire laser produced mode-locked, 100 femtosecond pulses which were used to excite a photoconductive switch biased with 48 volts. The transmitted THz pulse was detected using an electro-optic technique (ZnTe crystal). A Fourier transform could then be taken of the pulse to determine the amplitude spectrum of the THz pulse. Material properties such as the index of refraction $n(\omega)$ could be calculated from the spectrum using the following equation:

$$n(\omega) = \frac{1 - |r(\omega)|^2}{1 + |r(\omega)|^2 - 2|r(\omega)|\cos\phi(\omega)} \quad [18.1]$$

where $|r(\omega)|$ is the ratio of the sample to the reference pulse, $\phi(\omega)$ is the phase difference between the sample and the reference, c is the speed of light, and d_{sam} is the sample thickness. The absorption coefficient $\alpha(\omega)$ could then be calculated simultaneously with the index of refraction using the following formula:



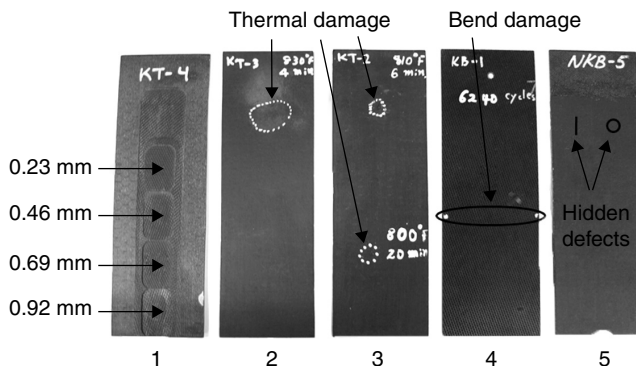
18.1 THz TDS system used in transmission configuration for imaging and material parameter measurements.

$$\alpha(\omega) = -\frac{2}{d_{\text{sam}}} \ln \left[\frac{|E_{\text{sam}}(\omega)|}{T(\omega)|E_{\text{ref}}(\omega)|} \right] \quad [18.2]$$

where $|E_{\text{sam}}(\omega)|$ is the magnitude of the THz field collected through the sample, $|E_{\text{ref}}(\omega)|$ is the magnitude of the THz field collected through air, and $T(\omega)$ is the fraction of the electric field transmitted through the air-sample interface.

Polyimide is a resin which has the characteristic of being very resilient to thermal loads, maintaining its properties for long periods of continuous use at 230°C, and for short excursions as high as 480°C. One of the problems with designing aircraft is that the heat from jet engines can cause damage to the external structure of the aircraft. Composite samples were prepared that were heated to various temperatures close to the maximum specifications for polyimide for short durations. These samples are labeled 2 and 3 in Fig. 18.2. The first sample was heated to 440°C for 4 min, creating a blister on the sample about 2 cm × 1.5 cm. The second sample was heated in two places: 430°C for 6 min and 425°C for 20 min.

Another goal was to determine if various forms of damage could be imaged with a THz TDS system in transmission set-up. Three additional samples were prepared to test the ability of a THz TDS imaging system to detect the damage. The first composite specimen, labeled 1 in Fig. 18.2, was used as a thickness standard coupon to test the response of THz TDS imaging techniques to various sample thicknesses. Another coupon, labeled 5, was prepared to try to detect hidden flaws and delaminations. This coupon consisted of two laminated pieces: the bottom piece was prepared by etching four layers and then creating a 6 mm slit and a 3 mm flat bottom hole



18.2 Photographs of the five glass fiber samples: (1) thickness calibration sample, (2) and (3) heat-damaged samples, (4) mechanical stress sample, and (5) hidden defect sample showing the hidden location of two of the eight defects.

(~70 μm depth) in each of the four layers. The top layer was created by etching four layers with the same thicknesses and then attached to the bottom layer in the opposite direction with epoxy, being careful not to allow any epoxy into the flaws. Finally, a third sample, labeled 4 in Fig. 18.2, was prepared by bending a piece of glass fiber about a fixed axis a total of 6240 cycles to investigate bending damage with THz TDS imaging.

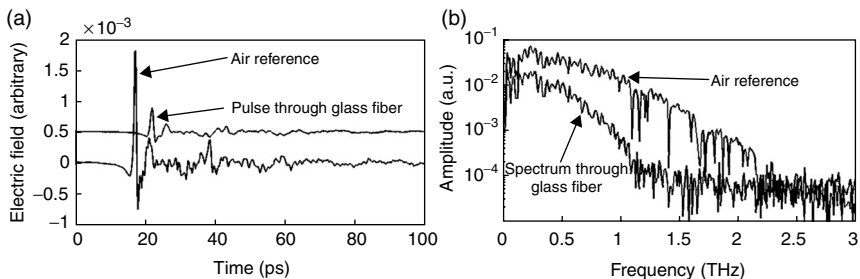
18.2.2 Results and discussion

Undamaged glass fiber samples

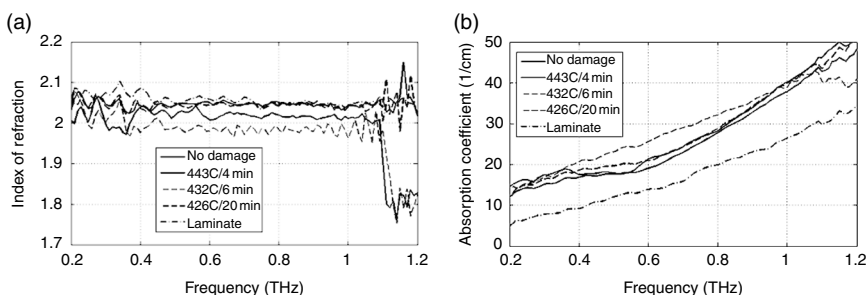
In preparation for measuring material parameters, we first measured a THz pulse and its amplitude spectra for the air reference and compared it with the pulse and spectrum through undamaged glass fiber shown in Fig. 18.3. In an effort to determine the scattering effects of THz radiation in a glass fiber composite, samples of polyimide and glass fiber weave were also prepared and studied.

Material property measurements of heat-damaged samples

After measuring the indices of refraction for the glass, polyimide and composite, we investigated the heat-damaged samples to determine their material parameters, see Fig. 18.4. The index of refraction for the unaltered composite remained relatively constant in the THz frequency range at 2.05 ± 0.01 while the absorption coefficient was measured as $17.5 \pm 0.8 \text{ cm}^{-1}$ (0.5 THz), $27.5 \pm 1.1 \text{ cm}^{-1}$ (0.8 THz) and $38 \pm 1.6 \text{ cm}^{-1}$ (1 THz). These results are consistent with other measurements made on glass fiber samples, where the



18.3 THzTDS (a) pulse and (b) amplitude spectra for air reference and glass fiber.

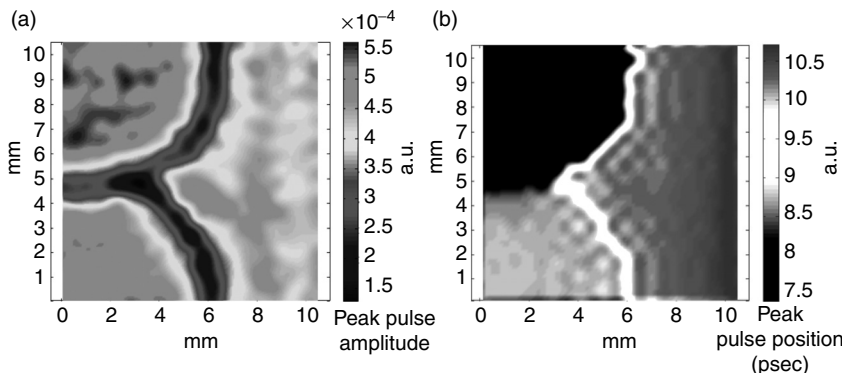


18.4 THzTDS material parameter measurements for heat damage areas showing (a) indices of refraction and (b) absorption coefficients.

index of refraction was 2.05–2.1 and the absorption coefficient was 12 cm^{-1} (0.5 THz) and 26–32 (0.8 THz) (Rutz *et al.*, 2006b). These results also compare well with CW transmission experiments on the identical samples (see Fig. 18.22). The results in Fig. 18.22 do not include Fresnel reflection losses, and when this factor is included the CW results are $\sim 19 \pm 2\text{ cm}^{-1}$ (0.5 THz) and $\sim 30 \pm 2\text{ cm}^{-1}$ (0.8 THz) for the undamaged samples(Petkie *et al.*, 2009). The damage area heated to 430 °C for 6 min may have been affected by either a removal of the outer coating or a residue created during the heating process. The low variability of these measurements suggest that heating the samples at these high temperatures does not alter the material parameters of the complex index of refraction, but introduces structural changes, such as blistering of the glass fiber and/or coating.

2-D transmissive imaging of defects

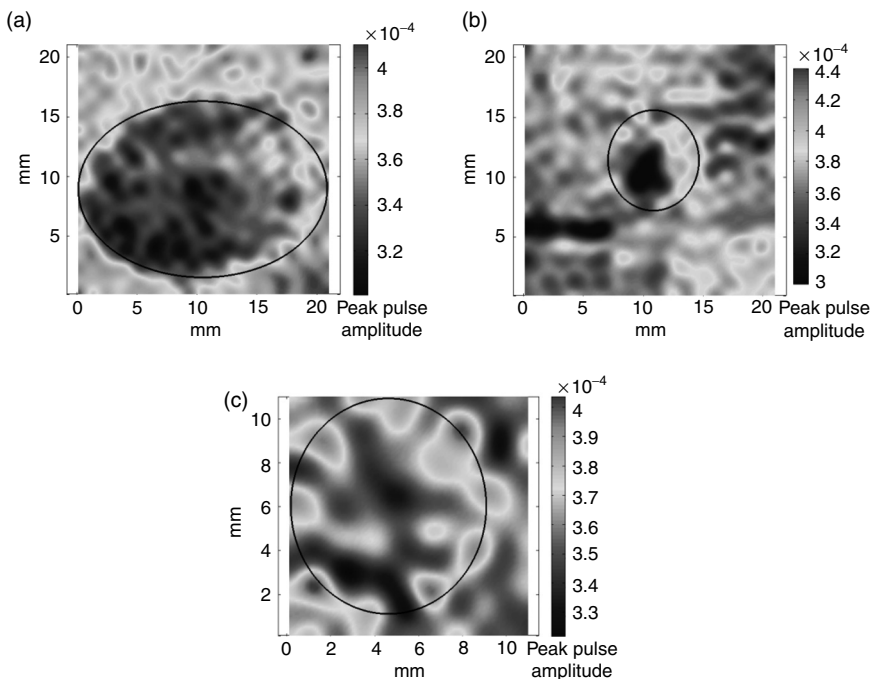
This subsection describes the THz imaging results from scanning the various defects described above. Images were created using the THz TDS set-up in Fig. 18.1 with a raster scanner to move the sample through the



18.5 THz TDS images of the section of the glass fiber that had been milled to two different thicknesses using (a) peak pulse amplitude and (b) peak pulse position techniques.

THz beam. The THz spot size was measured to be 1.5 mm and individual pixels were $1 \times 1 \text{ mm}^2$ in all of the scans except the calibration sample with $0.5 \times 0.5 \text{ mm}^2$ pixels. The first sample was prepared to calibrate the system based on material thickness (coupon 1 in Fig. 18.2). A THz image was taken of a $1 \times 1 \text{ cm}^2$ section of overlapping milled out areas with different thicknesses. The image is shown in Fig. 18.5 where (a) represents the peak pulse amplitude and (b) shows the pulse position at each pixel (Mittleman, 2003). The decrease in amplitude of the pulse at the edges is a result of THz scattering (Mittleman, 2003). Similar images can be shown using the area under the curve from the amplitude spectrum in the frequency domain. The differing heights of the edges of the milled out areas causes a frequency dependence in amplitude intensity. The periodic modulation in Fig. 18.5b is a result of the interpolation technique to smooth out the pixels and does not match the pattern of the glass weave within the composite.

The next task was to image the heat-damaged samples. The images formed by the peak amplitude of the THz pulses are shown in Fig. 18.6, with the heat-damaged areas within the circles (of the white marker dots of Fig. 18.2). Figure 18.6a shows the sample that was heated to 440°F for 4 min over $\sim 2 \times 1.5 \text{ cm}^2$ area. It has a visibly noticeable bubble or blister on its exterior, which roughly corresponds with the black area within the black oval. The other two burn areas are shown in Fig. 18.6b and c, neither of which showed visual evidence of blistering. The white circular dots in Fig. 18.6c and less noticeable white dots in Fig. 18.6b correspond to the white marker dots (shown in Fig. 18.2) made on the samples to show the extent of the heat-damaged area. The THz image of the damage area in Fig. 18.6c was inconclusive in showing evidence of the thermal damage.

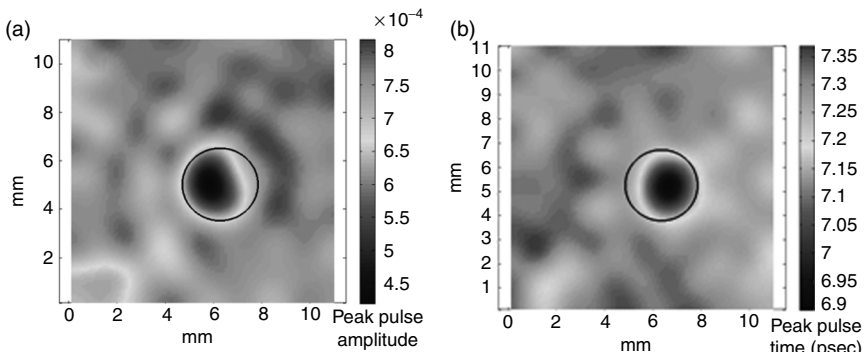


18.6 THz TDS images for three heated areas on glass fiber samples:
 (a) 440°C for 4 min, (b) 430°C for 6 min, and (c) 425°C for 20 min.

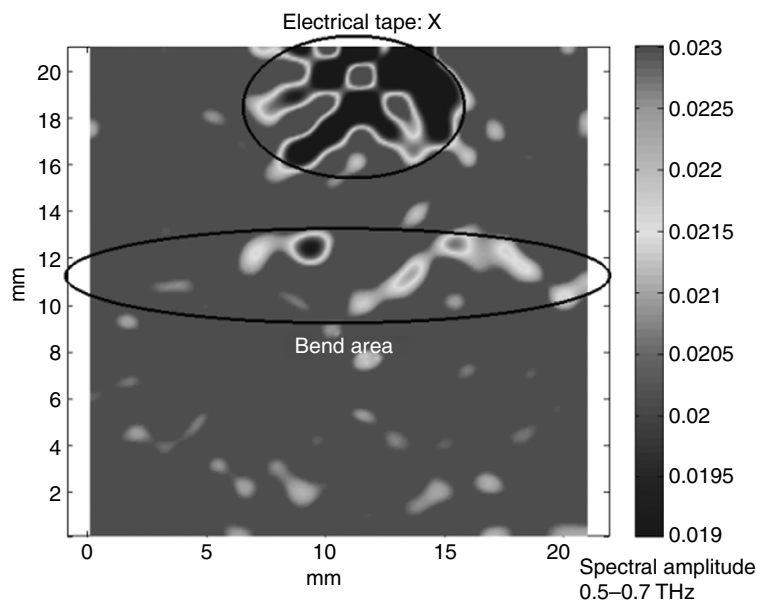
Voids were also investigated, which simulate either manufacturing defects or damage caused by stress over time. THz images are shown in Fig. 18.7 for a circular void (3 × 3 mm) which employed a simple time domain amplitude technique to detect the void (Mittleman, 2003). The voids show an area of reduced amplitude, most likely due to the multiple reflections from the air/composite interface.

Finally, an attempt was made to show damage caused by mechanical fatigue as a result of 6240 bending cycles. Visually, one could observe a thin area of discoloration on one side of the glass fiber strip and one could see a small amount of cracking and buckling on the back side. In Fig. 18.8, the image of the sample shows an area of reduced amplitude corresponding roughly to the axis of bending. Electrical tape, in the shape of an ‘x’, was attached at the top of the image area for reference.

In summary, aircraft glass fiber composite samples/coupons with various forms of damage were examined using a transmissive THz TDS imaging system. Indices of refraction and absorption coefficients in the THz frequency range were measured using THz TDS in transmission configuration for comparison of damaged and undamaged material states. Results showed that localized heat damage did not change the complex indices of refraction of



18.7 THz TDS images of 3 mm diameter milled area hidden between two glass-fiber-strips using (a) peak pulse amplitude and (b) peak pulse position.



18.8 THz TDS image of bend damage across the central bend axis.

the composite samples noticeably; however, changes in the THz signal were observed due to material blistering and/or residue deposited. The approximate depth of a delamination could be determined in the time domain by measuring the timing of a Fabry-Pérot reflection through a thin slice of the composite. A hidden circular void was imaged and there was also evidence that areas of damage from mechanical bending stress and simulated hidden cracks could be detected with THz TDS imaging.

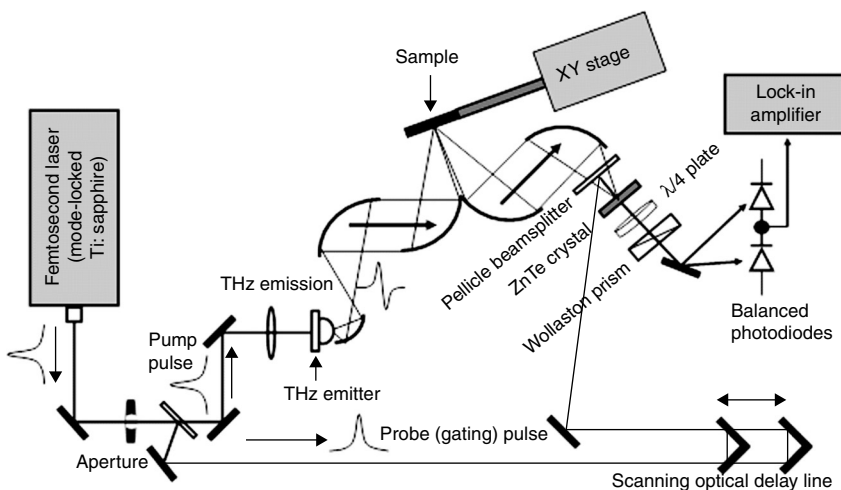
THz TDS in transmission set-up was effective in locating voids at any depth or thickness, but had difficulty in finding damage that was smaller than THz wavelengths. Heat-damaged spots could be detected and the dielectric properties of polyimide appeared to remain unaltered at burn temperatures below 480°C. A THz TDS system in reflection mode would be a more likely candidate for inspection of GFRP on aircraft and would be more effective in determining the depth of damage areas – see Section 18.3. The glass fiber composite absorbs a significant amount of the THz radiation, attenuating the signal, and limiting the use of Fabry–Pérot reflections for depth measurements. In reflection mode, the magnitude of the first surface reflection and subsequent reflections would be approximately the same, which should enable a greater ability to locate the depth of a void.

18.3 Non-destructive evaluation of aircraft composites using reflective terahertz time domain spectroscopy

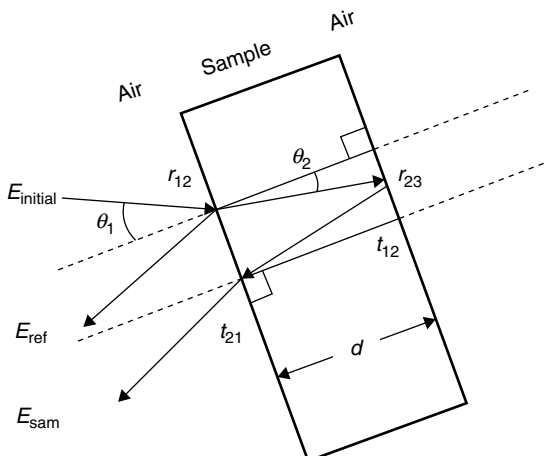
The same aircraft glass fiber composites studied in transmission were also studied with a THz TDS in a reflective configuration (Jackson *et al.*, 2008; Stoik, 2008; Stoik *et al.*, 2008). Refractive indices and absorption coefficients in the THz frequency range were measured using THz TDS in reflection configuration. Hidden voids and thermal blisters could be located by TDS imaging using amplitude and phase analysis techniques. The depth of the delaminations could be measured via the timing of Fabry–Pérot reflections after the main pulse. There was little evidence that areas of damage from bending stress and simulated hidden cracks (linear slit voids) could be detected with THz TDS reflective imaging. Finally, an entire glass fiber composite panel, consisting of a 2.5 cm honeycombed area sandwiched between two of the glass fiber composite strips tested earlier, was imaged. Surface damage such as punctures, paint removal, and burn on thermally damaged areas were detected.

18.3.1 Theory and experiment

The THz TDS reflective set-up used to collect the material parameter data and perform the imaging is shown in Fig. 18.9, and is very similar to the set-up for transmission seen in Fig. 18.1. The THz pulse was reflected at $\theta_r = 20^\circ$, see Fig. 18.10, from the sample and was detected using an electro-optic technique (ZnTe crystal). A Fourier transform could then be taken of the pulse to determine the amplitude spectrum of the THz pulse. The average group velocity of the pulse was calculated by using the optical path length



18.9 THz TDS system used in reflection configuration for imaging and material parameter measurements.



18.10 Diagram of the geometry of the surface reflection and the first Fabry-Pérot reflection in THz-TDS reflection configuration.

difference between the front and back reflections in the time domain, see Fig. 18.10. The average group refractive index is defined by:

$$n_g = (T_b - T_f)c/2d = n_0 + \omega \frac{dn}{d\omega} \Big|_{\omega} \quad [18.3]$$

where T_b is the time of the pulse off the back surface and T_f is the time of the pulse off the front surface, c is the speed of light, d is the sample thickness, n_0 is the average index of refraction and ω is the frequency. Since it has been demonstrated (Rutz *et al.*, 2006b) that the index of refraction of GFRP is constant throughout the THz range of interest (0.2 to 2.5 THz), it is assumed that the group index is nominally equal to the phase index (i.e., $n_g = n_0$).

An alternate method to determine the absorption coefficient was demonstrated in reflection configuration, where the pulses from the front and back surfaces could be isolated in the time domain and then a Fourier transform of each could be taken. The absorption coefficient, α , could then be calculated using the following formula:

$$\alpha(\omega) = \frac{\cos(\theta_2)}{d} \ln \left(\frac{|r_{12}(\theta_1)E_{\text{sam}}(\omega)|}{|t_{12}(\theta_1)t_{21}(\theta_2)r_{23}(\theta_2)E_{\text{ref}}(\omega)|} \right) \quad [18.4]$$

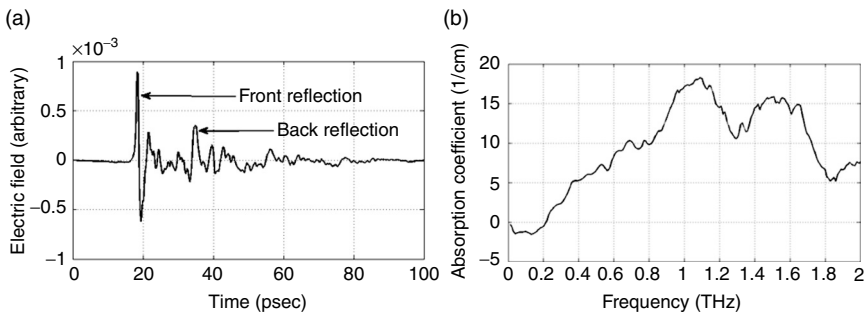
where E_{sam} is the magnitude of the THz field collected through the sample, E_{ref} is the magnitude of the THz field collected through air, and each of the Fresnel coefficients shown in Fig. 18.10 is a function of the incident angle, θ .

THz TDS in reflection configuration could be used to measure the complex indices of refraction of the aircraft composites to determine if these material parameters have fundamentally changed due to heat exposure from the engines – the same damaged samples were used in this study as the transmissive study above.

18.3.2 Results and discussion

Glass fiber composite material parameter measurements with reflection configuration

In preparation for measuring material parameters, we first measured a THz pulse reflected from the uncoated composite coupon in Fig. 18.11. In Fig. 18.11a one can clearly see the initial reflection from the surface and the subsequent reflection off the back surface. The index of refraction was determined to be 2.03 ± 0.02 using Equation [18.2]. The absorption coefficient was then measured to be $7 \pm 2 \text{ cm}^{-1}$ at 0.5 THz and $18 \pm 2 \text{ cm}^{-1}$ at 1.0 THz with the results shown in Fig. 18.11b. This is comparable to other measurements made on composite samples in transmission configuration – see the subsection ‘Material property measurements of heat-damaged samples’, where the index of refraction was 2.05–2.1 and the absorption coefficient was 12 cm^{-1} (at 0.5 THz) and 26 to 32 cm^{-1} (at 0.8 THz) (Stoik *et al.*, 2008).



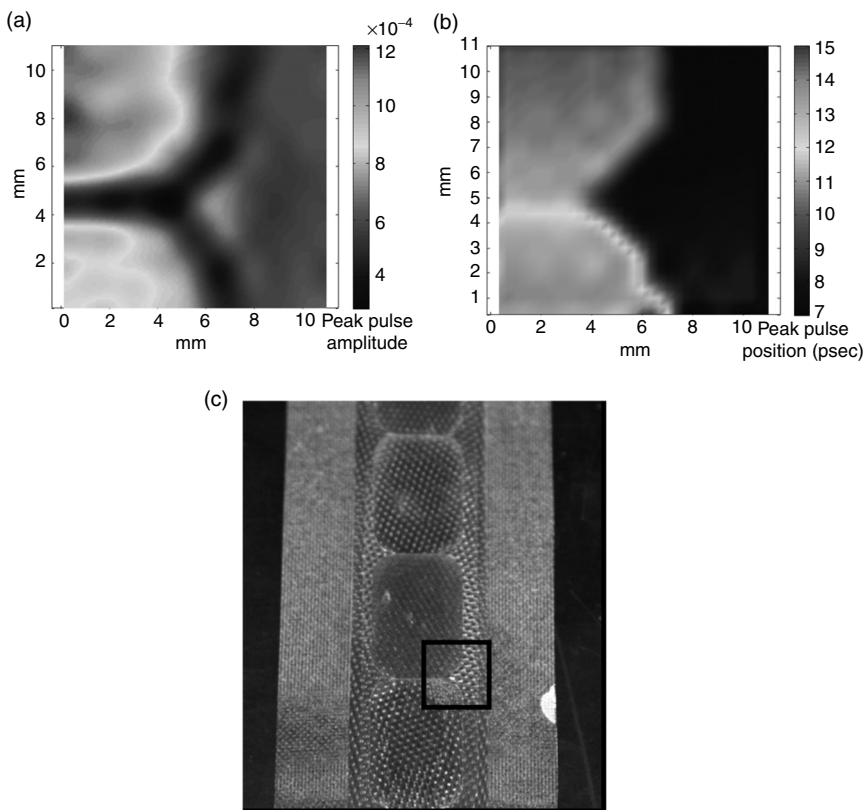
18.11 THzTDS (a) pulses reflected from the front and back surface, (b) absorption coefficient for uncoated composite.

Reflective imaging of glass fiber composite coupon defects

This subsection describes the THz imaging results from scanning the various defects outlined above. Imaging was accomplished using the THz TDS set-up in Fig. 18.9 with a raster scanner to move the sample through the THz beam. The THz spot size was measured to be 3.5 mm and individual pixels were $1 \times 1 \text{ mm}^2$ in each of the scans. The first sample was prepared to calibrate the system based on material thickness. A THz image was taken of a $1 \times 1 \text{ cm}^2$ section of overlapping milled areas with different thicknesses. The image is shown in Fig. 18.12 where (a) represents the peak pulse amplitude, and (b) shows the pulse position at each pixel (Jepsen *et al.*, 2008). The decrease in amplitude of the pulse at the edges is a result of THz scattering (Jepsen *et al.*, 2008). Similar images can be created using the area under the curve from the amplitude spectrum in the frequency domain. The different edge thicknesses of the milled areas cause a frequency dependence in amplitude intensity because the THz scattering from an edge is frequency dependent.

After imaging the calibration sample, the next task was to image the thermally damaged samples. The images of the burn samples formed by the peak amplitude of the THz pulses are shown in Fig. 18.13 with the visibly heat-damaged areas identified by the circles. Figure 18.13a and d show the sample that was heated at 440°C for 4 min over $\sim 1.5 \times 2 \text{ cm}^2$ area. The sample in Fig. 18.13a and d has a bubble or blister on its exterior visible to the naked eye which roughly corresponds with the black area within the black oval.

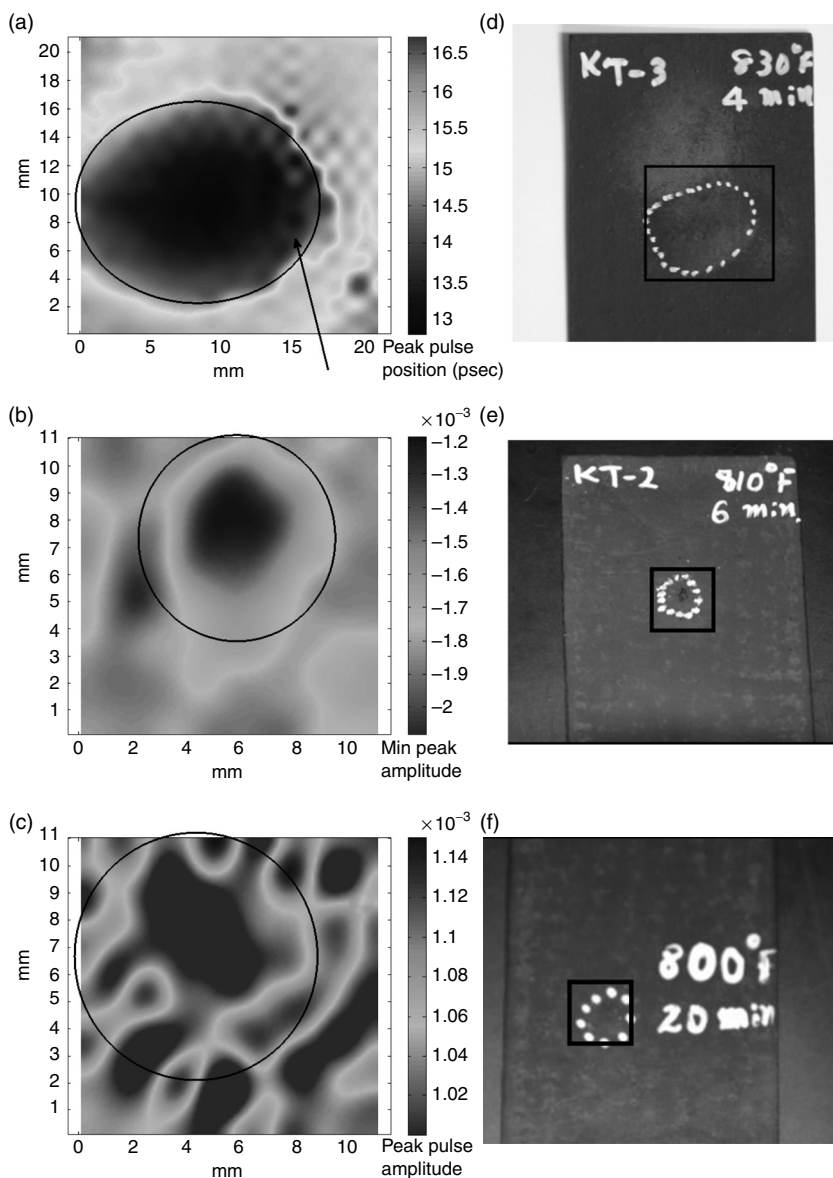
Comparisons of the THz time-domain signal of pixels from the heated regions were compared with those from outside the heated regions. Multiple peaks in the THz time-domain signal at many of the pixel locations provided evidence of air gaps. An example of the time-domain signal from the pixel highlighted in Fig. 18.13a is shown in Fig. 18.14a. For comparison, a side profile of the thermal damage is shown using an X-ray computed tomography image in Fig. 18.14b. The time delay between the two peaks equates



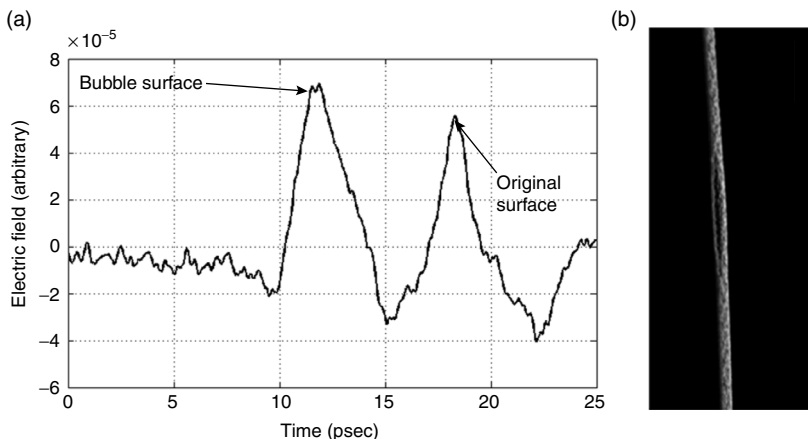
18.12 THzTDS images of a section of the composite milled to two different thicknesses using peak pulse amplitude (a) and peak pulse position (b) techniques. (c) Photograph of the calibration sample showing the scanned area.

to a distance of 480 microns. This is roughly equivalent to the 500 microns difference measured between the thermal blister and the undamaged sample using a micrometer caliper. The other two heated areas are shown in Fig. 18.13b–f, neither of which displayed any visual evidence of blistering. The black area within the circle in Fig. 18.13b is roughly equivalent to the position of the residue in the heated area. The circular dots in Fig. 18.13c correspond to the white marker dots (see Fig. 18.2f) made on the samples to show the extent of the heated area.

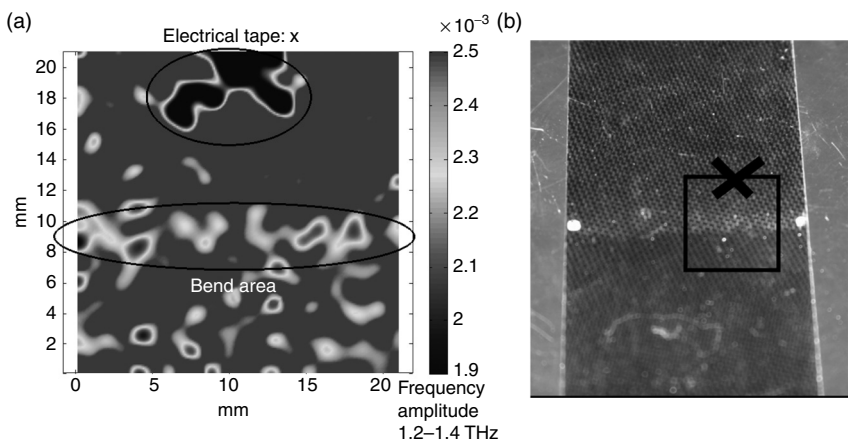
Next, the sample with the mechanical damage caused by bending the composite 6240 cycles was imaged in the reflection set-up. The image in Fig. 18.15a was constructed using the area under the curve from the amplitude spectrum between 1.2–1.4 THz. There is a slightly greater density of lower amplitude radiation around the bend axis, but it is not conclusive.



18.13 THz TDS images and photos for three heat-damaged areas on composite samples: (a) and (d) 440°C for 4 min; (b) and (e) 430°C for 6 min; and (c) and (f) 425°C for 20 min heated to 440°C for 4 min over roughly 1.5 × 2 cm² area.

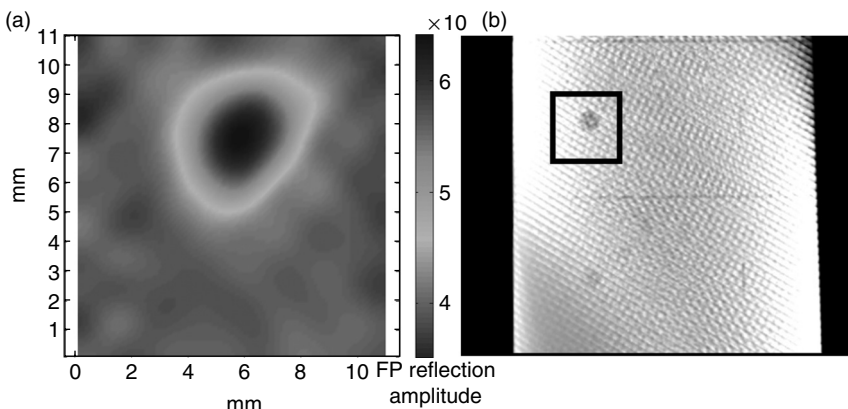


18.14 (a) THz TDS time-domain signal of the THz signal collected from the pixel located in Fig. 18.15a. (b) An X-ray computed tomography scan of the side profile of the large thermal blister.



18.15 (a) THz TDS reflection image using the amplitude of frequencies (1.2–1.4 THz) showing bend damage across the central bend axis. (b) Photograph of scanned area.

Voids were also investigated, which simulate either manufacturing defects or stress damage. The results of a THz image are shown in Fig. 18.16 for a circular void ($3 \times 3 \text{ mm}^2$) using an imaging technique which measured the relative amplitude of the first Fabry–Pérot reflection after the main pulse in the time domain. An X-ray computed tomography image of the composite sample is shown in Fig. 18.16b, which shows the positions of the hidden circular and slit voids. The same technique could not conclusively locate the slit void.

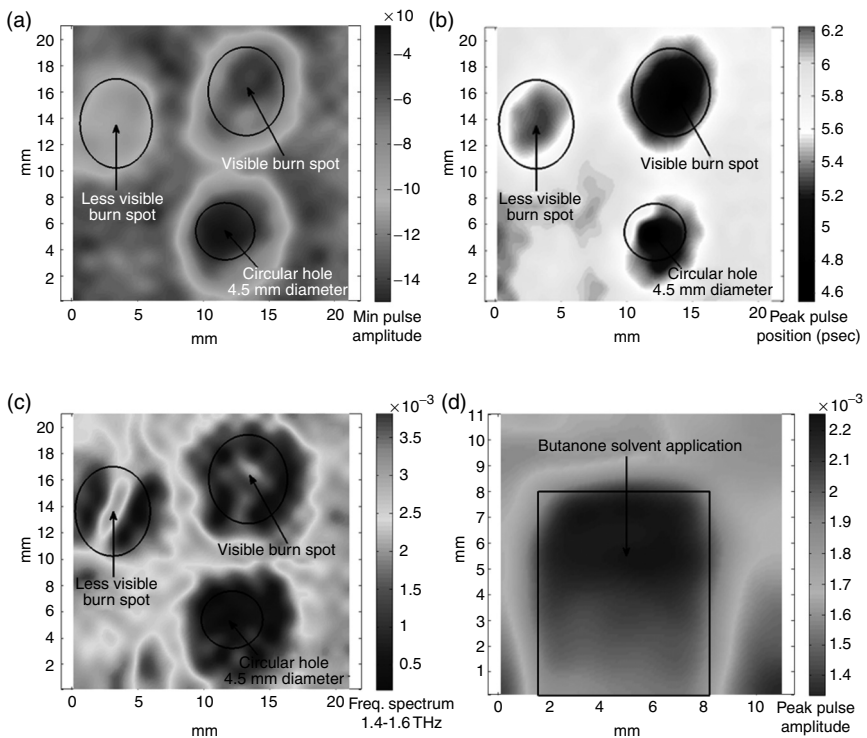


18.16 (a) THz TDS images of 3-mm-diameter milled circle hidden between two composite strips using first Fabry–Pérot reflection. (b) X-ray computed tomography image showing the position of the hidden circular and slit voids.

Reflective imaging of glass fiber composite panel defects

In the previous subsection, all of the THz images were taken on thin coupons (several millimeters) of composite with various forms of damage. On an aircraft, the composite sheets are attached to both sides of a much thicker honeycomb structure, which is then attached to form the exterior of the aircraft. A THz TDS transmission scan was attempted on an entire panel (~3 cm thick); however, insufficient energy penetrated through the panel to form an image. Since THz TDS in reflection does not require penetration through the panel, it can still be used to detect damage to the exterior GFRP sheet. Two panels were prepared for imaging and analysis with THz radiation: one with thermal damage and holes punched in its surface, and the other panel with a portion of its paint removed with a butanone solvent.

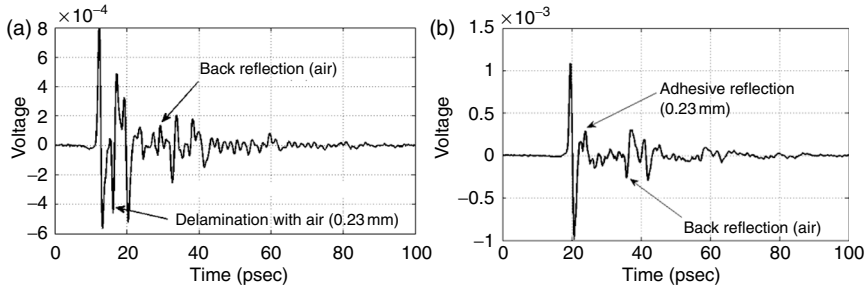
The first panel had holes (4.5 mm diameter) punched through the composite representing puncture damage and thermal damage between the holes. The scanned area of the panel included one hole and two thermally damaged areas (see Fig. 18.17a–c). A visually obvious thermally damaged region is located on the right half. The other thermally damaged region is not visible to the naked eye; in fact, it was not noticed until after THz TDS imaging. THz images of the panel can be seen in Fig. 18.17, where the (a) minimum peak amplitude, (b) maximum peak position, and (c) amplitude spectrum (1.4–1.6 THz) were used to construct the images. The second panel had a solvent, butanone, applied to the exterior surface of the panel to dissolve the paint. The area that was dissolved was about 7 mm wide and can be seen in Fig. 18.17d.



18.17 THzTDS reflection image of entire panel with puncture hole (4.5 mm diameter) and two regions of thermal damage. Images were constructed using the (a) minimum peak pulse amplitude, (b) maximum peak pulse position, and (c) the integrated frequency spectrum amplitude from 1.4 to 1.6 THz. (d) THzTDS image of a panel with the exterior coating removed with butanone solvent.

Depth of discontinuities analysis using reflection configuration

Depth analysis was performed on data collected on the delaminated portion of coupon 5 shown in Fig. 18.2. During the data collections it was quickly apparent that the adhesive–composite interface provided a large enough index discontinuity to create a back reflection. The air–composite interface provided a large reflected signal because the greater Δn resulted in a higher reflection coefficient. Figure 18.18 shows two examples of the time-domain pulse returns showing the reflections from the two discontinuities. The ZnTe ($n = 3.2$, thickness = 1 mm) reflection was measured at the same position (~21 psec after the main pulse) on all of the temporal plots and was clearly distinguishable from the back reflection of the composite sample. The sign of the ZnTe reflection was not reversed from the main pulse while the sign of the back reflection was reversed because of the difference in the change of index of refraction at the interface.



18.18 THz TDS time-domain plots showing reflections from discontinuities: (a) air and (b) adhesive.

The Fourier transform was used to show the depth of delaminations in the laminated sample. A comparison of the returns from discontinuities at various depths is shown in Fig. 18.19a–f. The dashed lines were added to show the similarity of the backside reflections in each scan along with the pulse reflection from the ZnTe etalon effect. A separate calculation was made to remove the TDS system effects. This was accomplished by making a separate measurement of the THz pulse reflection from aluminum and then subtracting out the aluminum transfer function from the sample. This procedure removed most of the main pulse and the ZnTe reflection. A series of depth measurements can be seen in Fig. 18.19g–l for the various thicknesses. Each series of plots was measured from a different side of the sample, showing minimal difference from each side.

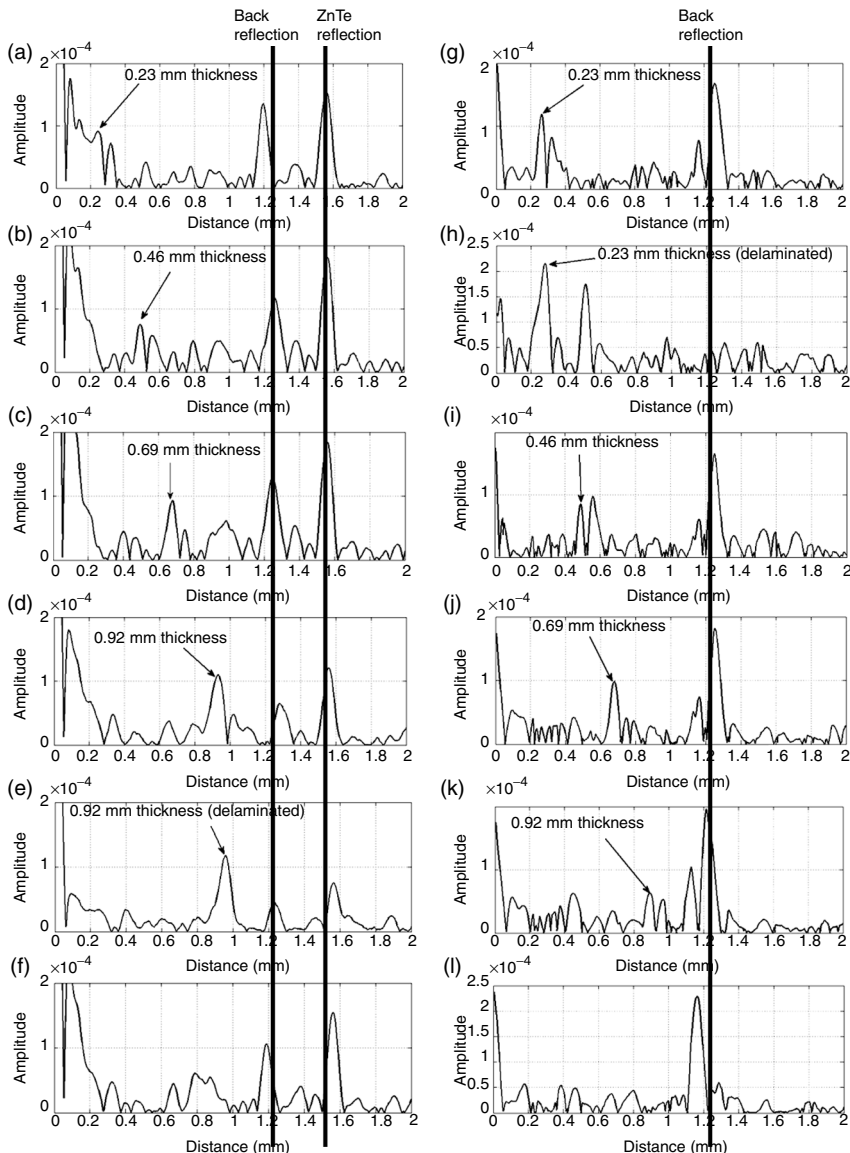
The attenuation of the THz signal can be estimated based on the measured absorption coefficient of the composite and the Fresnel coefficients from the two air–sample interfaces. To show the relative strength of the first Fabry–Pérot etalon reflection to the surface reflection, the following equation was used:

$$\frac{E_{\text{FP_Ref}}}{E_{\text{sam}}} = \frac{t_{12}(\theta_1)t_{21}(\theta_1)r_{23}(\theta_1)}{r_{12}(\theta_1)} \exp\left(-\frac{\alpha(\omega)}{2}(2d)\right) \quad [18.5]$$

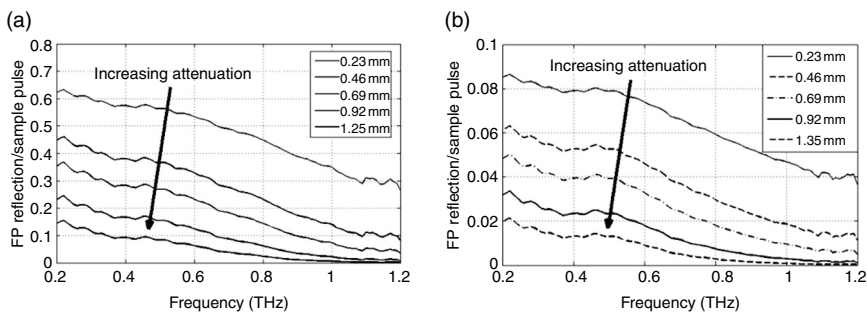
where the Fresnel coefficients geometry was shown previously in Fig. 18.12 and are defined by

$$r_{12} = \frac{n_1 \cos(\theta_1) - n_2 \cos(\theta_2)}{n_1 \cos(\theta_1) + n_2 \cos(\theta_2)}, \quad t_{12} = 1 + r_{12} \quad [18.6]$$

and



18.19 Results using the Fourier technique in Equation [18.4] showing the discontinuities present in a composite sample laminated at various thicknesses: (a) 0.23 mm, (b) 0.46 mm, (c) 0.69 mm, (d) 0.92 mm, (e) 0.92 mm delaminated, and (f) no lamination. Results using the Fourier technique with the TDS system characteristics subtracted are shown from (g) to (l).



18.20 Chart showing the calculated relative strength of the first Fabry–Pérot reflection after traveling through various thicknesses of composite material for THzTDS in (a) reflection configuration and (b) transmission configuration.

$$r_{23} = \frac{n_2 \cos(\theta_2) - n_3 \cos(\theta_3)}{n_2 \cos(\theta_2) + n_3 \cos(\theta_3)}, \quad t_{21} = 1 + r_{21}. \quad [18.7]$$

The graph in Fig. 18.20a shows the relative strength of the first Fabry–Pérot reflection at various depths from an air–composite discontinuity to the strength of the front pulse. These relative amplitudes of the Fabry–Pérot reflections compared favorably with the amplitudes of the measured data from the laminate sample. A similar chart is shown for an air–composite interface in Fig. 18.20b in transmission configuration (Fletcher *et al.*, 2007).

In summary, an aircraft composite with various forms of damage was examined using a reflective THz TDS system. Indices of refraction and absorption coefficients in the THz frequency range for composite were measured using a reflection configuration. Thermal damage and a hidden circular void could be identified in a THz image, but there was little evidence that areas of damage from mechanical bending stress could be detected with THz TDS reflective imaging. Next, the THz TDS reflective configuration was used to image an entire panel, consisting of two composite strips surrounding a honeycomb center. Surface damage, such as puncture holes, thermal damage and paint removal could be detected, but no reflections occurred below the thin composite layer down into the honeycomb. The approximate depth of a delamination could be determined in the time domain by measuring the timing of a Fabry–Pérot reflection through a thin slice of the composite.

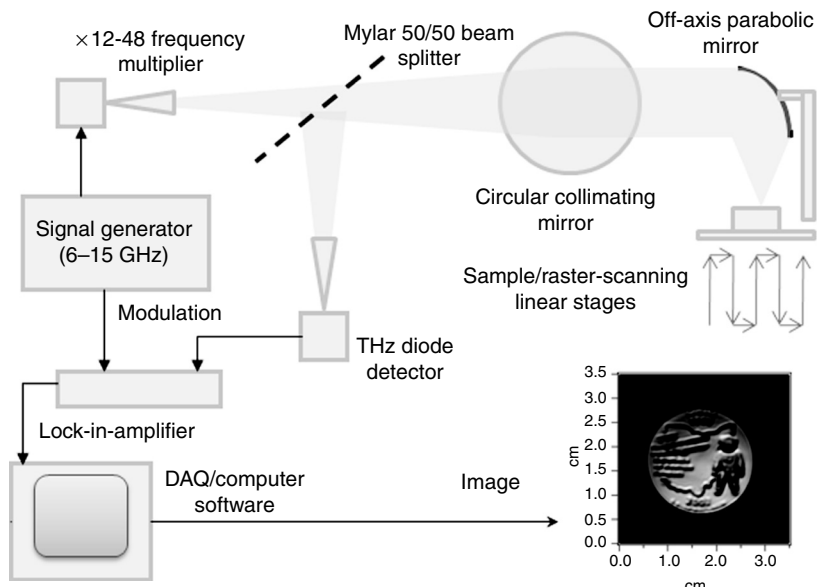
18.4 Continuous-wave non-destructive terahertz imaging for aerospace applications

The aircraft glass–fiber composites studied in transmission and reflection modalities with THz TDS imaging methods were also studied with several CW systems spanning the 140–900 GHz frequency range. With these systems, transmission measurements were made over this entire range and the samples were imaged near 100 GHz and 600 GHz to study the signatures of the various defects. The results of the CW studies for several samples are presented and discussed in this section, while images of the defects in all of the samples are presented and discussed in comparison with other NDE imaging methods in the next section.

18.4.1 Theory and experiment

Several similar systems were used to generate and detect THz radiation in the 140–900 GHz region. An Agilent PSG signal generator (6–15 GHz) and a voltage tuned YIG oscillator (20–40 GHz) were used to drive Virginia Diodes Inc. (VDI) frequency multiplier chains (www.vadiodes.com) to reach this spectral range. For transmission measurements, the YIG oscillator was used with different combinations of frequency multipliers and VDI zero biased detectors (ZBD) to cover five frequency bands: 140–225, 220–325, 325–460, 450–700 and 600–900 GHz. For imaging, two systems operating near 100 GHz and 600 GHz were used in conjunction with the Agilent synthesizer and ZBD detectors. In all cases, the sources were amplitude modulated and lock-in amplification techniques were used to improve the signal-to-noise ratio. For transmission measurements, a free-space configuration consisting of two lens (2-inch diameter and 50 mm focal length) were used to focus the THz radiation onto particular sections of the sample and to couple the radiation to the source and detector horns. The spot size was approximately several millimeters (proportional to the wavelength) on the sample. The transmission was calculated by comparing the transmission through a sample to that through air. The absorption coefficient was then calculated based on the transmission measurement and sample thickness (on the order of 1–2 millimeters). It is important to note that losses due to scattering and Fresnel reflections from the front surface in the transmission measurements also contributed to overall losses. While scattering losses were in general not considered significant in this work, an index of $n = 2.05$ leads to a 12% front surface Fresnel reflection loss and consequently an overestimate of the absorption coefficient when not taken into account.

Each reflection-based imaging system was very similar and schematically shown in Fig. 18.21. The source and detector horns were coupled to the same optical system by a 50/50 Mylar beamsplitter. A spherical mirror collimated



18.21 Imaging system used to acquire the 100 GHz and 600 GHz images. (DAQ - data acquisition.)

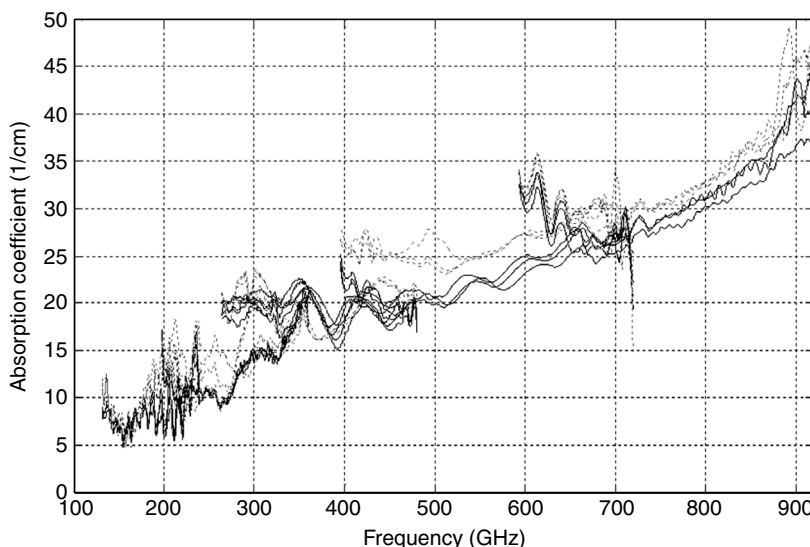
the THz beam and directed the radiation to a 90 degree off-axis parabolic mirror that focused the radiation onto the sample. The parabolic mirror was four inches in diameter with a six inch effective focal length. The sample was raster scanned on x-y stages and the THz radiation had a normal incident angle on the samples. The stages were stepped in the x-direction, typically by 0.25–0.5 mm, and moved in a constant velocity mode in the y-direction, where the DAQ's digitization rate determined the spatial sampling size that was approximately one-half to one-tenth the wavelength. Image acquisition times were on the order of thirty minutes or less for sample sizes of approximately 10 cm × 20 cm. LabView was used to control the stages and collect data, while Igor Pro, along with its imaging toolboxes, was used for image analysis. In cases with larger step sizes in comparison to the wavelength, linear interpolation routines were used to smooth the appearance of the images. The glass fiber samples are transmissive to THz radiation and were either backed with a flat aluminum plate (a ‘mirror’) or with Ecosorb (good absorber) and were held in place with clamps since any adhesive could affect the samples. The images represent the intensity of the reflected/scattered THz radiation back to the optical system and detector. For Ecosorb-backed samples, the reflected radiation would be from the samples only. For metal-backed samples, the measured signal would be reflections from the sample as well as two-transmission through the sample

having reflected off the metal plate. Highly coherent CW systems are subject to standing waves that create system artifacts that are the equivalent of Fabry-Pérot fringes in the transmission measurements or interference bands in the images. Frequency modulation techniques can be implemented to mitigate the standing wave artifacts (Petkie *et al.*, 2005).

18.4.2 Results and discussion

Transmission measurements

Transmission measurements for the glass fiber polyamide composite samples were performed at several different locations on each sample in both the damaged and undamaged regions to estimate the variability of the measurements. Measured absorption coefficients are presented in Fig. 18.22 for sample 2 shown in Fig. 18.2. Larger variations in the absorption coefficients occur toward the ends of each of the five multiplier bands where the power drops off significantly. The general trend of the absorption coefficient is to increase from $\sim 5 \text{ cm}^{-1}$ near 100 GHz to $\sim 40 \text{ cm}^{-1}$ near 900 GHz and is representative of all the samples. These measurements are also consistent with the THz TDS measurements shown in Fig. 18.4. This particular sample had a region heated to 443°C for 4 min, where a blister/delamination formed, as discussed in the



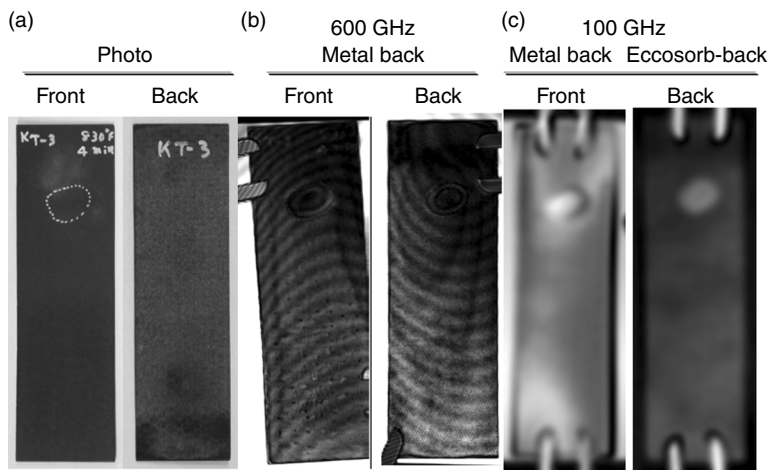
18.22 Absorption coefficient measurements on sample 2 (KT-3) of Fig. 18.2 comparing several measurements from undamaged (solid curves) and the heat-damaged regions (dashed curves).

previous sections. The CW measurements in the frequency region above 500 GHz show that the heat-damaged region has a slightly higher absorption coefficient by $2\text{--}5 \text{ cm}^{-1}$. However, as was discussed with the THz TDS measurements, we will not claim this is due to a change in the material properties since the delamination and change in the physical structure of the sample play a significant role in the measurements through changes in specular and diffuse reflections/scattering and interference effects.

The data in Fig. 18.22 show etalon patterns that span from $\sim 140\text{--}700 \text{ GHz}$ in many of the scans that are a result of internal reflections within the sample. All the etalon patterns with a sufficient signal-to-noise ratio were fitted using a lossy thin film model and yielded an index of refraction of $n = 2.04 \pm 0.01$, in agreement with the value measured with the THz TDS techniques in Section 18.2.

Reflective imaging of heat-damaged glass fiber composite samples at 100 GHz and 600 GHz

The $2'' \times 6''$ glass fiber composite samples were imaged near 100 and 600 GHz. The sample presented in Fig. 18.23 is same as the one discussed in the previous section and was subjected to 443°C for a 4 min duration that caused delamination of the material on the side exposed to the extreme temperature. Figure 18.23 shows photos of the front and back of the sample. As discussed above, a set of images was collected with the samples backed by either a smooth plate of aluminum (mirror) or a sheet of Eccosorb (absorber). The white dots on the front of the sample in the photo indicate



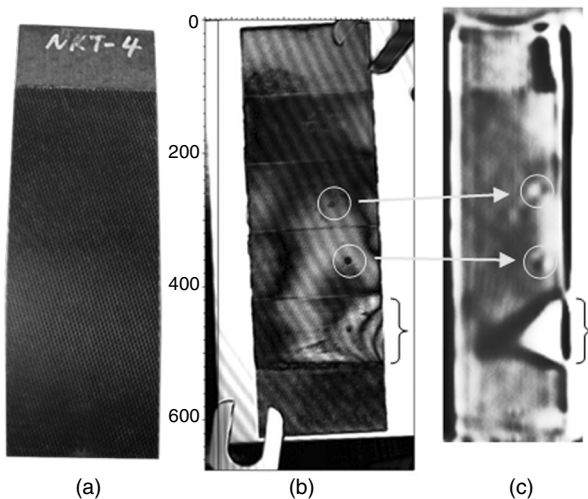
18.23 Photograph (a), $\sim 600 \text{ GHz}$ (b) and $\sim 100 \text{ GHz}$ (c) images of a glass-fiber composite sample.

the region with thermal damage with a delamination present on the front of the sample and no evidence of the thermal damage on the back of the sample. Both 600 GHz images were with a metal backing. Images from the front and back of the sample show the damaged region has a signature due to the delamination. Likewise, the damaged region is also clearly evident in the 100 GHz images. Note that the image on the far right was taken from the unheated side of the sample with an Eccosorb backing.

The contrast of a defect can change drastically depending on the relative size of the defect with respect to the wavelength, the sample thickness, and the material backing the sample (metal or Eccosorb). This is illustrated in the differences between the images shown in Fig. 18.23. The thermal damage in the 600 GHz image has an interference pattern that matches the shape of the heat-damaged region and the delamination. The interference fringes caused by the blister are consistent with the delamination separation of $\sim 500 \mu\text{m}$ (\sim two fringes in optical depth), as measured by THz TDS and X-ray CT techniques as shown in Fig. 18.4. The 100 GHz image of this defect does not show the same signature due to the longer wavelength ($\sim 3 \text{ mm}$) in comparison to the depth of the delamination, but it does show a significant contrast due to constructive interference (1/3 of a fringe in optical depth) as well as changes in the surface topology due to the blister. Furthermore, the metal-backed 100 GHz image has a greater intensity than the 600 GHz metal-backed image due to the differences in the absorption coefficient at these frequencies. In addition to this, while the 600 GHz image has a greater spatial resolution and consequently reveals more features, the blister defect due the thermal damage has a higher contrast in the 100 GHz image. Each defect in each material will have a ‘sweet spot’ in the THz-CW frequency domain that will provide the greatest contrast and ability to detect specific defects.

Reflective imaging of hidden defects in glass fiber composite samples at 100 GHz and 600 GHz

The THz-CW images of a sample with hidden defects are shown in Fig. 18.24 (sample 5 of Fig. 18.2), each taken with a metal backing from the front side of the sample. The hidden 3 mm diameter circular voids are clearly visible in each image, with two being indicated by the circles. Also visible in the lower right hand side of each image is the unintended delamination caused by improper bonding (shown by the brackets). The internal sample layers (five horizontal lines in the 600 GHz image) that are part of the constructed sample are easily visible in the 600 GHz image and only partially visible in the 100 GHz image. The hidden vertical slit defects are only barely visible in some of the 600 GHz CW images and at a greatly reduced contrast in comparison to the 3 mm diameter circular voids (Fig. 18.29 in



18.24 Three images of polyamide sample NKT-4, showing hidden circular defects (circled) and delamination (lower right corner indicated by brackets). (a) Photograph, (b) 600 GHz, (c) 100 GHz.

Section ‘Continuous-wave 600 GHz images’). Polarization will play a significant role in the optimization of illumination strategies to more readily identify such slit defects. The differences in the 100 GHz vs the 600 GHz images are due primarily to the differences in the material properties at these two frequencies as well as the size of the defects compared to the wavelengths. The diagonal bands in the 600 GHz image are artifacts of system standing waves.

In summary, THz-CW images of several glass fiber composite samples using two different frequencies provide a good demonstration of the utility of CW THz systems for non-destructive testing and the importance of waveform diversity. An optimized THz NDE system will ultimately depend on the defect properties, sample properties and obscurant characteristics. For instance, the scale of the features, surface roughness, the absorption and scattering associated with any obscurants, and the change in the sample’s physical structures and material properties due to a particular defect, will all impact the quality of the THz image and the ability to identify the defects.

18.5 Comparison of non-destructive imaging for glass fiber reinforced plastics

The objective of this section is to compare the non-destructive evaluation capabilities of THz radiation with conventional NDE techniques: X-ray, X-ray CT, ultrasound and flash IR thermography. Each technique was

applied to the evaluation of delaminated, heated or otherwise damaged glass–fiber composite samples (Fig. 18.2). The six NDE methods and their respective advantages and disadvantages were explored, and a comparison of imaging results is provided. This work will focus on a comparison of the different NDE imaging techniques for visually identifying defects.

18.5.1 Experimental procedures

Radiographic inspection

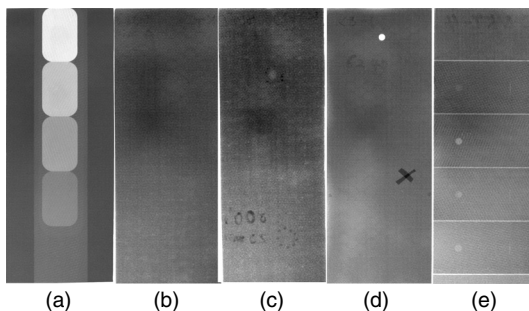
A X-TEK HMX 160 X-ray CT chamber was used for all radiographic testing. Enclosed within the shielded chamber are an X-ray tube, a variable-element target, a three degree of freedom (DOF) sample mount, and a digital detector. An 85 kV, 60 μ A electron beam incident on a molybdenum target was used to generate the X-rays used in all radiographic imaging.

Each composite test sample was mounted vertically, and the images produced were a 32 frame average recorded at 1 fps. X-ray CT images were formed via 720 projections at 1 fps using 0.5° angle increments to provide a 3-D scan. Each image plane was then inspected for defects by exterior and cross-sectional slice views, zooming through the image slice-by-slice (in 0.14 mm increments), adjusting the contrast as required before saving and exporting 2D images. No effort was given to scan individual defect areas for greater image resolution and penetrants/ dyes were not used.

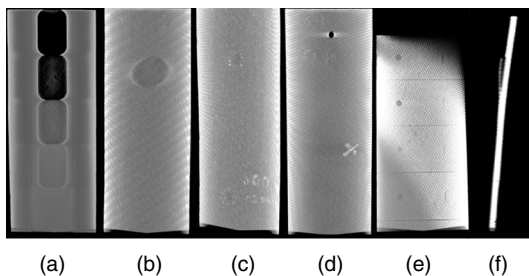
The X-ray inspection techniques imaged the glass fiber microstructure and defects according to cumulative density changes by producing 2-D shadowgraphic image projections (Fig. 18.25). Light areas correspond to higher material transmittance and dark areas to greater X-ray absorption and scatter. Sample thickness variations and fiber concentrations were easily detected along with one thermal damaged area that included some surface damage. The just discernible hexagonal shapes are the epoxy remains from when these samples were face plates of aerospace honeycomb sandwich structures. The CT scans (Fig. 18.26) were able to improve upon the 2-D X-ray projections by exploiting 3-D sample scans offering the ability to resolve sub-surface and side delaminations. As expected, X-ray and X-ray CT were both unable to detect the fiber breakage and matrix yielding of mechanical damage without the aid of dye penetrants.

Ultrasonic inspection

The immersive ultrasound system used was an AMDATA 5-Axis System with a thick, flat aluminum plate leveled about 10 in. below the water's surface. A 5 MHz transducer with a 3-in. focal length was used to generate and detect the acoustic pulses. The scan settings used included a software



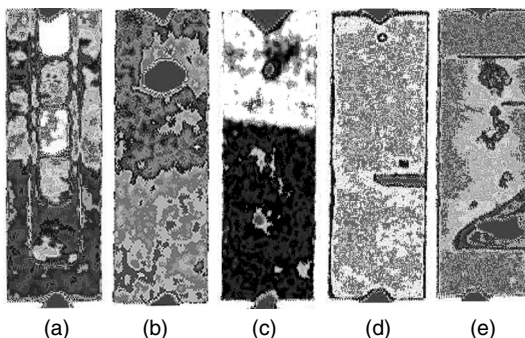
18.25 Radiographic X-ray through scans of glass fiber samples showing: (a) thickness variation, (b) heat treatment for 4 min at 440°C, (c) heat treatment for 6 min at 430°C and heat treatment for 20 min at 425°C, (d) cracking, and (e) circular and slit voids.



18.26 X-ray CT scans of glass fiber samples showing: (a) thickness variation, (b) heat treatment for 4 min at 440°C, (c) heat treatment for 6 min at 430°C and heat treatment for 20 min at 425°C, (d) cracking, (e) circular and slit voids, and (f) cross-section of delamination.

time-gate in order to only measure the reflected signal return from the aluminum plate. This ensured all measured signals had passed through the sample twice. The image output settings were set to display C-scans of maximum positive amplitude signal values versus location. Each sample was secured above the aluminum plate by placing 1/2 in. thick lead weights, which appear in the C-scan images as triangular shapes at the ends of each sample.

The images shown in Fig. 18.27 are the result of false gray-mapping of the signal amplitude returning from the reflector plate located beneath the samples. Gray indicates the loss of signal while white indicates areas of maximum return signal amplitude and black indicates the lowest return. Samples (a), (b) and (c) have an inhomogeneous front surface coating not present on samples (d) and (e), resulting in their lower signal returns. The milled sections of (a) and the thermal damage in (b) and (c) are quite apparent. The width and shape of the bending damage detected in (d) implies elastic



18.27 Ultrasonic scans of glass fiber samples at 5 MHz for (a) thickness variation, (b) heat treatment for 4 min at 440°C, (c) heat treatment for 6 min at 430°C and heat treatment for 20 min at 425 °C, (d) cracking, and (e) voids and delamination.

yielding in the polyimide matrix, interestingly only along half the bend axis. The edge delamination appearing as a triangular section located in the bottom right hand corner is clearly defined in (e), along with artifacts along the sample centerline which are likely disbonds between fiber and matrix layers formed when the milled laminae were epoxied back together. Very little pressure was applied during curing to prevent epoxy seepage into the voids.

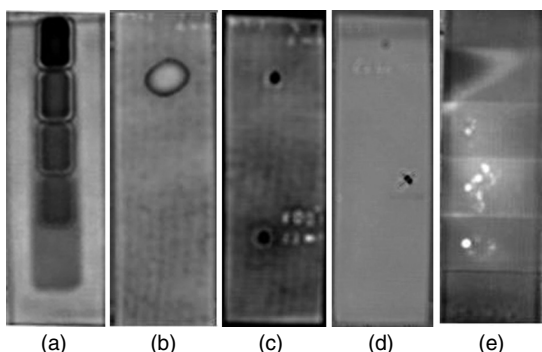
Thermographic inspection

Thermal Wave Imaging, Inc.'s ThermoScope IITM was used in conjunction with MOSAIQ 4.0 software. The flash heat lamp was co-located with a high speed IR camera for single-surface scanning. The flash duration was set to 4.9 ms and the capture rate to 60 Hz. The samples were set flat on two raised wooden slats to thermally isolate them, and the camera positioned a focal length away from sample surface.

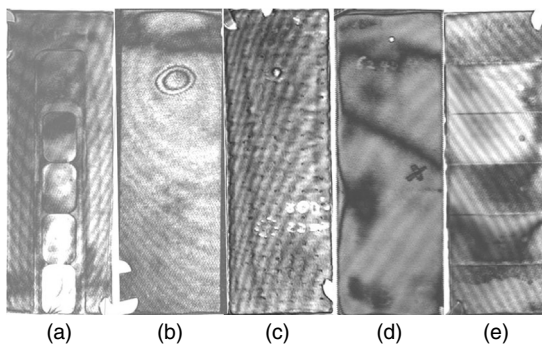
The thickness variations in Fig. 18.28a and thermal damage in Figures 18.28b and 18.28c are quickly recognized while the bending damage in Fig. 18.28d is easily missed. The brief contrast before feature disappearance implies surface cracking only. In Fig. 18.28e, only the two slit voids closest to the surface were detected consistent with decreased resolution at greater depths and more lateral conduction. The circular artifacts in Fig. 18.28e had the same thermal properties as the voids again implying disbonds and not less dense bonding material.

Continuous-wave 600 GHz images

Although presented earlier in this chapter, these results are summarized here along with some additional THz images. The thickness variations in Fig. 18.29a



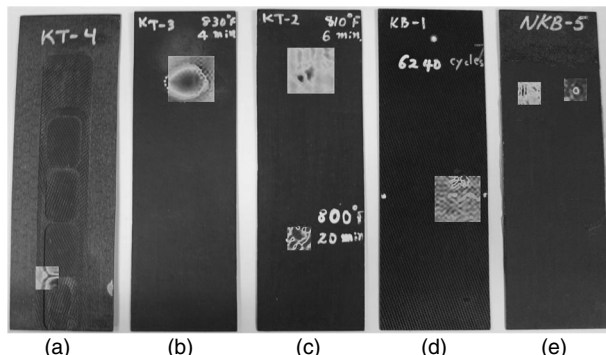
18.28 Flash IR thermographic images of time-derivative surface temperatures for glass fiber composite samples showing: (a) thickness variation, (b) heat treatment for 4 min at 440°C, (c) heat treatment for 6 min at 430°C and heat treatment for 20 min at 425°C, (d) cracking, and (e) voids and delamination.



18.29 CWTHz images of glass fiber samples: (a) thickness variation, (b) heat treatment for 4 min at 440°C, (c) heat treatment for 6 min at 430°C and heat treatment for 20 min at 425°C, (d) cracking, and (e) voids and delamination.

show clearly in the CW images, as well as damage to the sample created in the process of milling out the different thicknesses that is invisible to visual inspection. This damage appears as a group of dark lines at the bottom of the sample which appear to be the result of bending or cracking. The thermal damage on Fig. 18.29b and c, the delaminations in panel (e) and the circular voids in panel (e) are all clearly visible. The slit voids in Fig. 18.29e are practically invisible and the bending damage in panel (c) is less than obvious, but is somewhat visible along the right side of the image, as in the ultrasonic image.

The interference patterns/bands visible in the images are system artifacts produced by standing waves and multiple reflections in the imaging system itself rather than thin film effects in the samples and can be removed by the implementation of frequency modulations techniques (Petkie *et al.*, 2005).



18.30 Pulsed THz imagery of glass fiber samples showing $1 \times 1 \text{ cm}^2$ and $2 \times 2 \text{ cm}^2$ scans of reflected peak pulse signal amplitudes overlaid on the respective test samples: (a) thickness variation, (b) heat treatment for 4 min at 440°C , (c) heat treatment for 6 min at 430°C and heat treatment for 20 min at 425°C , (d) cracking, and (e) voids and delamination.

Pulsed terahertz imaging

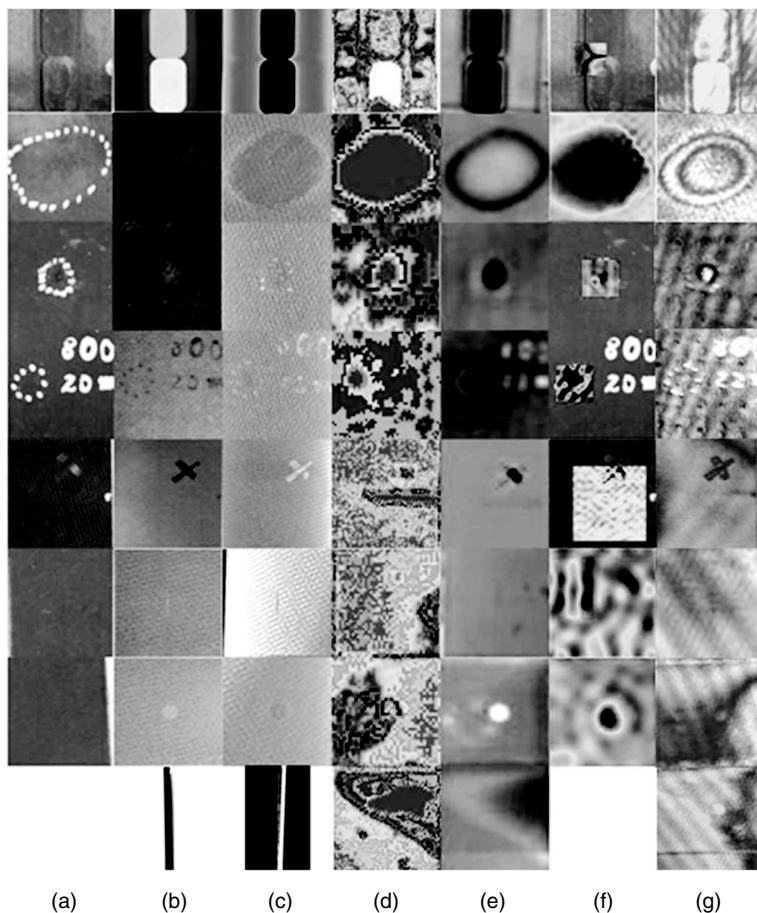
The custom pulsed THz results were presented earlier in this chapter and are summarized here. Figure 18.30 shows pulsed THz scans of the defect areas overlaying sample photographs.

18.5.2 Comparisons

Figure 18.31 is a composite image that aids in comparing the different NDE techniques. The thickness variations show clearly in all imaging methods, although the finer gradations are less obvious in the two X-ray methods Fig. 18.31b and c. Ultrasound Fig. 18.31d and flash IR thermography (e) show thermal damage the best. In the CW THz images Fig. 18.31g and the ultrasound images (d), the stress damage from bending is visible across half the sample whereas it is invisible, or nearly so, in the other images. The circular voids and the delaminations are easily detected by all methods except the ultrasound image, which is masked by the improper epoxy bonding. The slit voids are only clear in the X-ray (b) and X-ray CT (c) images. In the two THz methods, the slit voids are nearly visible and can be seen with a trained eye or possibly brought out by image processing. Overall, the ultrasound and CW THz imaging methods provide the clearest detection of defects, although other methods may perform better on a specific defect.

18.6 Conclusion

THz radiation can exhibit some uniquely different characteristics for non-destructive evaluation from other evaluation techniques. Microwaves have the ability to penetrate composites, but their spatial resolution is more



18.31 Comparison of glass fiber defects imaged with (a) photography, (b) X-ray, (c) X-ray CT, (d) ultrasound, (e) flash IR thermography, (f) pulsed THz imaging and (g) CW THz imaging.

limited due to their longer wavelengths. Infrared techniques can have better spatial resolution than THz, but less penetration depth. THz can penetrate composites without contacting it, with submillimeter transverse resolution, and can detect surface defects, hidden voids, delaminations and bending damage in composites. The depth resolution for defects is much better than the spatial resolution, and very thin composite samples can be analyzed with THz TDS.

There are advantages and disadvantages to using either the TDS transmission or reflection configuration. It was easier to get a smaller THz spot size onto the sample using a transmission configuration. This was primarily due to the small F-number parabolic mirrors and the cumbersome stages

used to steer them. Custom optical parts could alleviate this problem for reflection configurations. It was also easier to measure the material properties of the composite using a transmission configuration. With an exterior coating, the reflective technique for measuring the material properties was ineffective. Reflection mode is certainly a more likely candidate for a maintenance technique, but the transmission set-up could aid in the design and quality control of glass–fiber composite sheets. Reflection mode would also be a more effective technique in determining the depth of delaminations. This is due to reflection mode signals traveling a shorter distance through the attenuating composite, and also to the relative similarity in the amplitude of Fresnel reflections between a void and the initial pulse. This can be easily seen from the calculations plotted in Fig. 18.20. The relative amplitude of the first Fabry–Pérot reflection is calculated to be an order of magnitude larger in reflection configuration than in transmission.

Six NDE methods were used to inspect aerospace GFRP samples that contained various forms of damage. The conventional NDE methods of X-ray, X-ray CT, ultrasound and flash IR thermography were compared to the emerging technology of THz imaging to evaluate its utility in composite material inspection. Although the comparisons made are by no means a complete picture of these NDE methods' full capabilities in GFRP evaluation, we have made distinctions in their abilities to detect common damage mechanisms in GFPRs. Ultrasonic inspection was the best overall for damage detection. Next best in effectiveness was flash IR thermography followed by THz imaging, X-ray CT and X-ray. For inspections of thin glass–fiber composite structures in an operational environment, only flash IR thermography or a commercial THz imaging system would be practical for high-resolution defect imaging. Although not available for this comparison study, laser ultrasound would likely be another alternative.

A fast scanning commercial THz system was not available to be employed, but the results from our custom set-ups demonstrate the NDE capabilities of THz imaging. Pulsed THz imaging, when coupled with its TDS ability, is able to provide more NDE capability than any other single technology. It effectively provides three damage detection schemes in a single scan via return signal amplitude, phase and spectrum. It is capable of detecting all of the common aerospace composite defects: surface damage, delaminations, air voids, cracking and thermal damage. CW THz imaging also produces similar damage detection capabilities with a fraction of the scanning time. The only disadvantage of a CW imaging system, in comparison to a pulsed system, is its limited spectroscopic information and the difficulty of determining the depth of the delamination or damage. Outperforming X-ray inspection, these technologies definitely have a future in the non-destructive evaluation and inspection of polymer matrix composite structures.

18.7 References

- Chan W L, Deibel J and Mittleman D M (2007), 'Imaging with terahertz radiation', *Reports on Progress in Physics*, **70**, 1325–1379.
- Cooney A and Blackshire J L (2006), 'Advanced Imaging of hidden damage under aircraft coatings', *Proceedings of SPIE*, **6179**, 617902.
- Fletcher J R, Swift G P, Dai D, Chamberlain J M and Upadhyay P C (2007), 'Pulsed terahertz signal reconstruction', *Journal of Applied Physics*, **102**, 113105.
- Jackson J B, Mourou M, Whitaker J F, Duling I N, Williamson S L, Menu M and Mourou G A (2008), 'Terahertz imaging for non-destructive evaluation of mural paintings', *Optics Communications*, **281**, 527–532.
- Jepsen P U, Jensen J K and Moller U (2008), 'Characterization of aqueous alcohol solutions in bottles with THz reflection spectroscopy', *Optics Express*, **16**, 9318–9331.
- Kemp I, Peterson M, Benton C and Petkie D T (2010), 'Sub-mm wave imaging techniques for non-destructive aerospace materials evaluation', *IEEE Aerospace and Electronic Systems Magazine*, **25**, 17–19.
- Mittleman D (2003), 'Terahertz imaging', in Mittleman D, *Sensing with Terahertz Radiation*, New York, Springer, 117–154.
- NTSB (2001), 'In-Flight Separation of Vertical Stabilizer American Airlines Flight 587 Airbus Industrie A300–605R, N14053, Belle Harbor, New York, November 12, 2001'. Washington, D.C.: National Transportation Safety Board. Available from: <http://www.ntsb.gov/doclib/reports/2004/AAR0404.pdf> [Accessed 10 April 2012].
- Petkie D T, De Lucia F C, Casto C, Helminger P, Jacobs E L, Moyer S K, Murrill S, Halford C, Griffin S and Franck C (2005), 'Active and passive millimeter- and sub-millimeter-wave imaging', *Proceedings of SPIE*, **5989**, 359–366.
- Petkie D T, Kemp I V, Benton C, Boyer C, Owens L, Deibel J A, Stoik C D and Bohn M J (2009), 'Nondestructive terahertz imaging for aerospace applications', *Proceedings of SPIE*, **7485**, 74850D.
- Redo-Sanchez A, Karpowicz N, Xu J and Zhang X C (2006), 'Damage and defect inspection with terahertz waves', Fourth International Workshop on Ultrasonic and Advanced Methods for Nondestructive Testing and Material Characterization, 19 June 2006, UMass Dartmouth, N. Dartmouth, MA. Available from: <http://www.ndt.net/article/v11n07/papers/08.pdf> [Accessed 10 April 2012].
- Reiten M T, Hess L and Cheville R A (2006), 'Nondestructive evaluation of ceramic materials using terahertz impulse ranging', *Proceedings of SPIE*, **6179**, 617905.
- Rutz F, Hasek T, Koch M, Richter H and Ewert U (2006a), 'Terahertz birefringence of liquid crystal polymers', *Applied Physics Letters*, **89**, 221911.
- Rutz F, Koch M, Khare S, Moneke M, Richter H and Ewert U (2006b), 'Terahertz quality control of polymeric products', *International Journal of Infrared and Millimeter Waves*, **27**, 547–556.
- Stoik C D (2008), Dissertation, 'Nondestructive Evaluation of Composite Materials using Terahertz Time Domain Spectroscopy', *Air Force Institute of Technology*, Wright Patterson Air Force Base.
- Stoik C D, Bohn M J and Blackshire J L (2008), 'Nondestructive evaluation of aircraft composites using transmissive terahertz time domain spectroscopy', *Optics Express*, **16**, 17039–17051.

- Wald M L and Baker A (2001), 'A Workhorse of the Skies, Perhaps With a Deadly Defect', *The New York Times*, November 19, 2001.
- Wang S and Zhang X C (2004), 'Pulsed terahertz tomography', *Journal of Physics D-Applied Physics*, **37**, R1–R36.
- Wietzke S, Jordens C, Krumbholz N, Baudrit B, Bastian M and Koch M (2007), 'Terahertz imaging: a new non-destructive technique for the quality control of plastic weld joints', *Journal of the European Optical Society*, **2**, 07013.
www.picometrix.com/ [Accessed 10 April 2012]
- www.teraview.com/ [Accessed 10 April 2012]
- www.vadiodes.com [Accessed 10 April 2012]
- Zimdars D, White J, Stuk G, Chernovsky A, Fichter G and Williamson S (2006), 'Large area terahertz imaging and non-destructive evaluation applications', *Fourth International Workshop on Ultrasonic and Advanced Methods for Nondestructive Testing and Material Characterization*, 19 June 2006, UMass Dartmouth, N. Dartmouth, MA. Available from: <http://www.ndt.net/article/v11n07/papers/07.pdf> [Accessed 10 April 2012].

Terahertz applications in the wood products industry

M. E. REID, I. D. HARTLEY and T. M. TODORUK,
University of Northern British Columbia, Canada

DOI: 10.1533/9780857096494.3.547

Abstract: An overview of terahertz (THz) technology for the wood products industry is presented. The basic application areas that are amenable to exploiting emerging THz technology are examined. In doing so, the basics of wood structure are presented so that THz–wood interactions can be discussed. This will set the context for discussing a THz scanner that was deployed in a successful pilot study in 2008, which measured oriented strand board (OSB) mat density in the production process, and allowed mill operators to adjust the process based on real-time feedback provided by the THz scanner.

Key words: terahertz technology, non-destructive evaluation, wood science, oriented strand board, sensor technology, density mapping, industrial applications.

19.1 Introduction

The THz portion of the electromagnetic spectrum has remained one of the last frontiers in optics, having only recently been exploited in industry for real-world applications (Mittleman, 2003). This is because technology for the efficient generation and detection of electromagnetic radiation at these frequencies has been difficult to develop, as it requires either extremely fast electronics or long-wavelength photonics. Over the past several decades, hybrid techniques combining electronics and photonics have made possible industrial applications at these wavelengths, and many new applications for this technology are being studied, as highlighted throughout this book. This chapter examines new directions in the wood products industry made possible by emerging THz technology.

There are several characteristics of THz–matter interactions that drive applications development. First, most non-conductive dry materials are transparent at THz frequencies. This is true also of radiation at both microwave and X-ray frequencies. However, in comparison to microwaves, which have wavelengths in the order of cms, THz wavelengths are sub-mm,

Table 19.1 Electromagnetic radiation characteristics matrix as a probe for wood products

Source	Transparency	Resolution	Safety	Sensitivity to fiber orientation
X-ray	Good	Good	Poor	Poor
Optical/UV	Poor	Good	Good	Good
Infrared	Poor	Good	Good	Good
Terahertz	Good	Good	Good	Good

offering substantially better spatial resolution in a transmission imaging mode. In comparison to X-ray systems, THz technology is substantially less invasive. THz radiation is non-ionizing and poses no threat to biological systems exposed to levels that typically appear in THz time-domain spectroscopy systems (Walker *et al.*, 2002), and therefore does not require the strict regulation that X-ray technologies do when implemented in a working environment. In addition to this, the polarization state of THz radiation is sensitive to fibrous structures, which offers more information about the system being probed than can be obtained with X-rays. Therefore, THz technology offers the possibility for transmission imaging that can simultaneously probe internal fiber structure of non-conductive dry materials with sub-mm spatial resolution.

Wood is a natural system to pursue for applications development using THz technology because the key characteristics that allow one to probe wood in a useful way are transparency, spatial resolution and sensitivity to gross fiber structure. Using these key characteristics, one can see why there is a lot of excitement about THz technology for wood products' applications, as highlighted in Table 19.1.

Another extremely important characteristic for industrial applications is system speed. For the purposes of this chapter, the context of using THz technology will be in the form of THz time-domain spectroscopy (THz-TDS). While there are other methods of performing THz spectroscopy and imaging using continuous wave sources such as quantum cascade lasers (Williams, 2007), the applications discussed in this chapter require broad-band pulsed THz radiation primarily in the lower frequency THz range (0.01–1 THz). To this end, it has only been in the past five years that speeds of 100 waveforms per second and higher acquisition rates have been commercially available, which is approaching the speeds necessary for practical applications in many industries (see Section 19.7 for an overview of commercially available THz-TDS systems). Finally, fiber-coupled THz emitters and detectors have made it possible to remove the sensitive electronics and optics components of a THz-TDS system from the sensing area, thereby allowing THz-TDS systems to operate in environments substantially less controlled than the

laboratory, which has been a key to seeing THz technology implemented in the manufacturing industry.

In summary, the ability to image non-conductive dry materials in transmission with sub-mm spatial resolution with sensitivity to fiber structure makes THz technology ideally suited for applications in the wood products industry. Commercially available THz-TDS systems are currently achieving the speeds necessary for scanning applications in industry, and future developments are expected to open up more applications in imaging. It is indeed an exciting time for applications development with THz technology.

19.2 Applications of terahertz technology in the wood products industry

In this section, a review of the state of the art in THz science of wood and related areas from the literature will be presented. This information will be used to project those areas in the wood products industry that will most benefit from using THz technology.

The earliest application of THz science to the wood industry was the examination of non-contact density mapping of solid wood (Koch *et al.*, 1998). Using THz time-domain transmission imaging in the frequency range from 0.1 to 2.5 THz, wood was found to be transparent, with inhomogeneities in density being visible in the transmission profile. These inhomogeneities correspond to wood's anatomical and gross physical structure such as annual growth rings, and this application demonstrated sub-annual ring spatial resolution, although it is limited by the thickness of the sample (Koch *et al.*, 1998). An extremely good correlation was observed between transmitted THz power and wood density, demonstrating for the first time the ability to use THz technology to accurately image and profile wood density at THz frequencies. More recently, sensitivity to wood density was used for non-contact dendrochronology using time-domain THz reflection imaging (Jackson *et al.*, 2009). Reflection imaging was performed on both the tangential (parallel to the annual growth ring direction) and cross-sectional (parallel to the grain fiber direction) faces in a tomography mode. Fresnel reflections were seen clearly at the boundaries between earlywood and latewood, as there is a large density gradient at these boundaries. This application demonstrated a spatial resolution for ring profiling of 0.1 mm. Reflection THz imaging was also used to examine density variations in a pure reflection mode (non-tomography mode), and was even demonstrated to reveal ring structure when concealed by paint layers. This method was not limited by the thickness of the sample; however, fiber alignment with the polarization of the THz beam had to be optimized to reduce signal attenuation (Jackson *et al.*, 2009; Fukunaga *et al.*, 2010). Although these studies focused on art conservation (as the method offered the unique capability of imaging

through concealing layers, and was non-destructive), dendrochronology and tree-ring analysis is a prominent application in wood science.

THz technology has also proven useful as a non-destructive evaluation tool in the wood products industry. THz-TDS and imaging between 0.1 and 2 THz were applied to the non-destructive evaluation of natural cork (Hor *et al.*, 2008). THz technology was found to be an equivalent or superior technique compared to the use of visible inspection and X-ray tomography which are currently used, and the presence of voids, cracks and defects in the cork are evident in the THz images. The main limitation is the spatial resolution, which was found to be 0.5 mm, but was limited by the pixel step size. For example, by halving the pixel step size, the spatial resolution should be increased two-fold (Hor *et al.*, 2008). The same techniques were used to non-destructively probe and image the diffusion of water through natural cork samples, although a 0.3 mm resolution was obtained (Teti *et al.*, 2011). This is particularly interesting because it demonstrates the strong sensitivity of THz radiation to moisture (which strongly absorbs at THz frequencies), which is a feature that shows up in many applications of THz technology, including applications to wood products where moisture content is an extremely important physical property.

Non-destructive testing of wooden timbers used as building materials was examined in transmission imaging and spectroscopy at frequencies around 0.2 THz (Oyama *et al.*, 2009). While the spatial resolution was limited as a result of the lower frequencies used, the spatial resolution that was achieved is considerably higher than what can be obtained using other conventional methods such as using microwave technology. At this frequency, transmission images are constructed, and the detection of invisible defects and knots within timber proves possible due to their density variation. Beyond this, due to the high absorption of THz by water, water content measurements of timber using THz technology is also practicable (Oyama *et al.*, 2009).

THz technology is unique in that it is able to probe the gross fiber structure of wood and wood products (Reid and Fedosejevs, 2006 and Jordens *et al.*, 2009). The possibility for fiber-orientation analysis relies on the crystalline structure of cellulose that makes up wood fibers. Using transmission THz-TDS, in the frequency range of 0.2 to 1.6 THz, the sensitivity of THz radiation to fiber orientation was studied using both lens paper and solid wood, both of which have a preferential fiber orientation. The orientation of the fibers with respect to the polarization of the THz beam was mapped out, demonstrating the possibility of using THz radiation for fiber-orientation analysis (Reid, 2006). This is possible because of the strong birefringence at THz frequencies, and its dependence on the orientation of the wood grain. Subsequently, further developments in fiber-orientation analysis are showing promise for applications at THz frequencies (Jordens *et al.*, 2009).

Substantial progress has been made in the pulp and paper industry as well. As the drying process has a high impact on the final paper quality, accurate, in-line measurements of moisture content during processing is necessary. As THz radiation offers high sensitivity to water, and insensitivity to scattering from the paper surface, THz spectroscopy is a prime candidate for moisture content monitoring of paper. THz transmission time-domain spectroscopy was performed in the frequency range of 0.1 to 2.5 THz, as well as at the fixed frequency of 0.6 THz. It was determined that the amplitude and phase measurements allowed for accurate moisture content measurements on paper in the laboratory setting (Banerjee *et al.*, 2008). In the pulp and paper industry, there are three parameters that are extremely important in the manufacturing process: moisture content, basis weight and thickness. Advances have been made in order to measure both the composition of the paper and the thickness of the sheet simultaneously to an accuracy comparable to existing sensor technology. THz-TDS with a bandwidth of 1.5 THz can be used to measure the complex transmission amplitude, which can be fitted to a physical model to determine these parameters. Most impressive is that THz sensing has been demonstrated with sub- μm thickness resolution (using wavelengths of hundreds of μm), while simultaneously probing moisture and basis weight in real time (Mousavi *et al.*, 2009).

Another area of great interest for THz technology is the wood–plastic composites industry, where the optical properties (Scheller *et al.*, 2007), sorption properties (Jordens *et al.*, 2010), and dispersion, homogeneity and mechanical properties (Krumbholz *et al.*, 2011) have been investigated at THz frequencies. The main optical property used for the investigation was the refractive index. Numerous refractive index mixing equations were evaluated for modeling the complex index of refraction for heterogeneous dielectrics using THz-TDS, where it was found that the shape-dependent Bruggman model provided the most accurate fit (Scheller *et al.*, 2007). As many physical properties are related to the refractive index, this modeling may prove useful in other aspects of the wood products industry. The sorption of water into wood–plastic composites was studied using THz-TDS between 0.2 and 1.0 THz. The dielectric properties were determined over this range and showed that below the fiber saturation point (a moisture content of approximately 30% dry basis), both the refractive index and absorption coefficient increased with moisture content of the sample. This shows that THz radiation is highly sensitive to bound water, and the effective medium theory used suggests that the interaction of free water can also be accounted for (Jordens *et al.*, 2010). As this suggests that THz technology is very sensitive to both free and bound water, this opens substantially more possibilities in the wood products industry, as both the manufacturing process and properties of the finished product depend on the moisture content, for example finished case-goods for residential uses. For composite

wood products, the degree of dispersion also influences properties during processing and application of the product. This relates to the homogeneity, particle size and amount of agglomerations of fillers in the product, and substantially affects the mechanical characteristics. THz-TDS was investigated in the frequency range from 0.1 to 0.4 THz as a non-destructive and contact-free method to estimate the filler content and degree of dispersion simultaneously. Reported techniques suggest that the absorption coefficient integrated over a finite frequency interval accurately represented the degree of dispersion, and a clear correlation was seen between this and the mechanical properties, such as the impact strength, flexural modulus and tensile strength of the product. THz-TDS also proved useful in detecting larger agglomerates on the order of hundreds of micrometers, as well as small particles on the order of a few micrometers. Also, the refractive index showed distinct differences between the well and poorly dispersed samples as a function of filler content as the refractive index of wood is higher than that of the surrounding material; so as filler content increases, the refractive index did as well (Krumbholz *et al.*, 2011).

Finally, THz-TDS has been used for disease detection and identification in solid wood. Two strains of nematode pine disease and their affect on pine wood was investigated using THz-TDS in the frequency range of 0.2 to 3.0 THz. Physical modeling was used to extract the absorption coefficient, refractive index and extinction coefficient, which were compared between two separate strains of the disease, as well as diseased and non-diseased pine wood. It was determined that while the two strains of nematode disease did absorb THz radiation differently, no absorption peaks were observed, and therefore, no spectral fingerprint existed. It was found, however, that differences in the absorption coefficient and refractive index could be used to identify diseased and non-diseased wood, as well as distinguish the two separate strains of the disease (Liu *et al.*, 2010).

The ability of THz radiation to (i) penetrate wood, (ii) probe material density, (iii) probe moisture contents and (iv) probe fiber orientation make THz technology highly attractive for many wood and composite wood product applications. The strength of solid wood, and composite wood products such as OSB and plywood, derive primarily from the orientation and density of the fiber that compose the structure. For this reason, it is natural to expect this technology to penetrate these industries, and is the subject of Section 19.6, which discusses the THz OSB scanner that was developed.

19.3 Wood structure and morphology

Wood of different tree species falls into two main groups: angiosperm trees, commonly called hardwoods, consisting of the leaf bearing trees, and gymnosperm trees, commonly called softwoods, consisting of the needle and

cone bearing trees (Desch and Dinwoodie, 1996). The alignment and chemical constituents of wood in both hardwoods and softwoods have somewhat similar structural elements. Therefore, it is necessary to consider both types of wood in order to determine the origin of birefringence at THz frequencies. The structure will be described in more detail below.

19.3.1 Softwoods

In most softwoods, there are two main types of cells (wood elements) present: tracheid cells, which provide physical support and conduction of water and sap; and parenchyma cells, which provide storage of nutrients during tree growth. Tracheid cells are long, hollow and needle shaped, and are generally 2.5–5 mm in length, although they can be as long as 10 mm. The tracheid cells are packed tightly together, aligned in radial and tangential orientations, and provide an overall grain direction for the wood. The parenchyma cells are major components in the rays and are oriented radially in a cross section of the wood (Desch and Dinwoodie, 1996).

19.3.2 Hardwoods

In most hardwoods, there are four main types of cells (wood elements) present: tracheid cells, which provide physical support and conduction of water and sap; parenchyma cells, which provide storage of nutrients; fibers, which provide support; and vessels, which provide conduction of sap. The majority of the mechanical elements are provided by the fibers. The fibers are narrow, spindle-shaped cells, similar to tracheids, usually about 1 mm in length. The orientation of these cells provides the grain or fiber orientation (Desch and Dinwoodie, 1996).

All of the cell walls in hardwoods and softwoods have similar structures. The cell walls are made up of layers consisting of structures called microfibrils; the layers are aligned differently in each of the layers of the cell wall.

19.3.3 Chemical constituents of wood

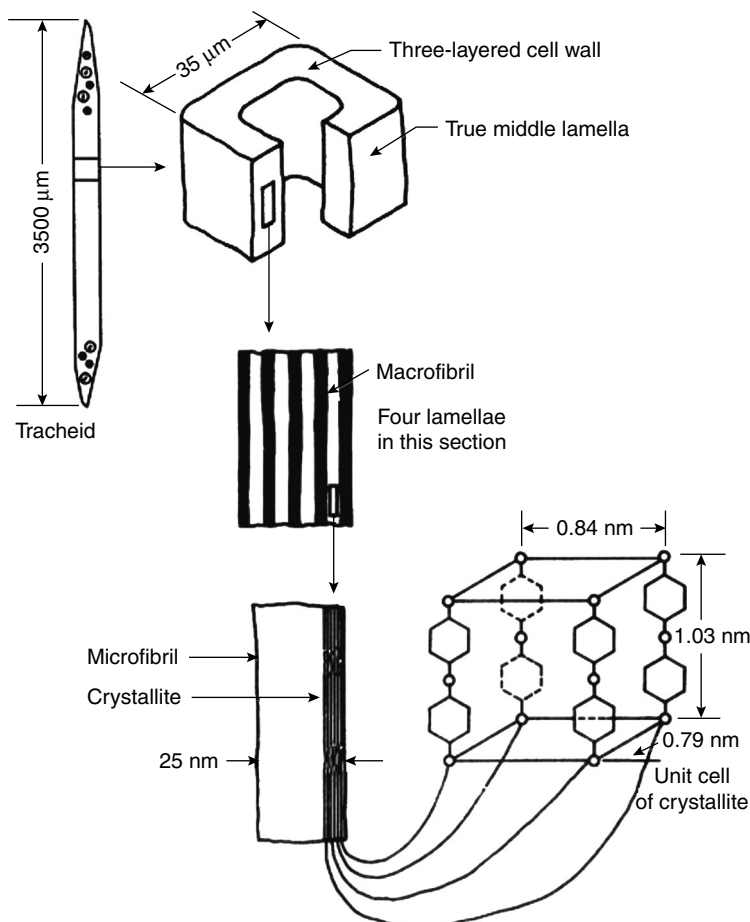
Wood is primarily composed of three chemical constituents, namely cellulose, hemicellulose and lignin. The cellulose in wood is a polymer of the glucose monomer ($C_6H_{10}O_5$)_n with crystalline and amorphous components, at an approximate 70:30 ratio, and has a degree of polymerization, *n*, between 8000 and 10 000. The hemicellulose and lignin chemicals contribute to the mechanical properties of the wood. Hemicelluloses are carbohydrates of 15% to 20% of galactoglucomannans and about 10% of arabinoglucuronoxylan for softwood. In hardwood, the hemicellulose comprises of 20% to

30% of glucoronoxyan and approximately 5% glucomannan. The degree of polymerization is lower than that of cellulose, containing about 200 units. Lignin is a complex, 3D aromatic molecule of phenyl groups with no crystalline regions. The softwood lignin is comprised of guaiacyl-type unit. The hardwood lignin is comprised of guaiacyl and syringyl units (Desch and Dinwoodie, 1996).

Within the cell wall of the wood elements, for example the softwood tracheid, there are three secondary layers denoted S1, S2 and S3 and one primary layer denoted P, including another layer called the middle lamella. Each cell wall layer comprises microfibrils which are aligned at specific angles (Desch and Dinwoodie, 1996). The microfibrils are made up of a cellulose core with lignin and hemicellulose acting as the glue. The size of the microfibril is generally accepted to fall between 10 to 25 nm in cross section.

In terms of the size of the layers in the cell wall, the S1 layer constitutes less than 10% of the cell wall thickness, and the S3 layer constitutes approximately 1% of the cell wall thickness, leaving the S2 layer being the bulk of the wall at 85% or more. The remaining 4% of the cell wall is the primary layer. The orientation of the microfibrils is strongly related to the performance parameters of the wood, such as mechanical properties and dimensional change. The approximate longitudinal microfibril angle in S1, S2 and S3 is 50–70°, 10–30° and 60–90°, respectively. The orientation of the microfibrils in the P-layer is random (Desch and Dinwoodie, 1996). A diagram of wood structure is shown in Fig. 19.1.

As previously discussed, birefringence in wood can be caused by the intrinsic birefringence, based on the crystalline nature of the cell wall, and form birefringence, based on the periodic structure of the cells. The overall structure of hardwood and softwood is important in determining the relative contribution from form and intrinsic birefringence, for a number of reasons. First of all, the wood density corresponds strongly to the intrinsic birefringence, because it is based on the components and structures of the cell walls, as well as the size of the cells. Second, the repetitive structure of the wood corresponds strongly to the form birefringence. If there are random orientations of the cells, there would be less form birefringence. Based on this, hardwood would exhibit less form birefringence, as the cell array is less uniform and consistent than that in softwoods. Furthermore, determining the source of the birefringence is important, as it provides information as to whether or not THz radiation can probe the gross fiber structure, or the microscopic structure of the cell wall (crystallinity and microfibril angle, for example). If there is significant form birefringence, THz radiation could probe the gross fiber structure, which would be beneficial in composite wood products industries, such as OSB. In these industries, the fiber alignment within the product is strongly correlated to the strength of the product; hence being



19.1 The relationship between the structure of wood at different levels of magnitude. The unit cell is the classical model of cellulose I proposed by Meyer and Misch (1937). (Layout adapted from J. F. Stau (1971) Flow in wood, reproduced by permission of Paul M. Winstorfer, PhD, Dean, College of Natural Resources and Environment, Virginia Tech, Blacksburg, VA.)

able to probe this alignment would provide in-line strength measurements. Another important variable in the wood products industry is moisture content. Moisture content is expected to significantly affect THz measurements. Water strongly absorbs THz radiation, so it is important that the moisture content of the wood is studied in detail, especially when considering industrial applications. Furthermore, the effect of the moisture content on the birefringence needs to be quantified in order to understand the dependencies before other parameters can be analyzed in more detail.

The importance of identifying the source of birefringence in wood at THz frequencies has been highlighted, and will be discussed in detail in Section 19.5. First, however, the THz properties of wood will be examined.

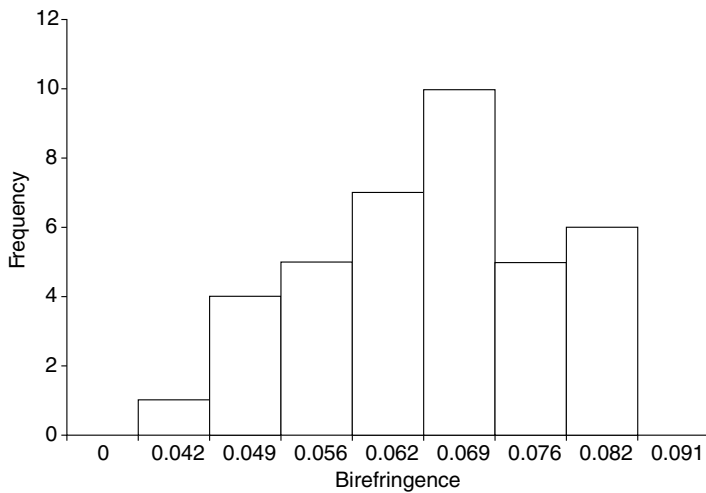
19.4 Far infrared properties of wood

Many crystalline substances, such as wood, are optically anisotropic, where their optical properties are not the same in all directions. Specifically, a material which displays two different indices of refraction is birefringent, and a material which absorbs different polarizations of light differently is dichroic (Hecht, 2002). Wood exhibits both strong birefringence and dichroism at THz frequencies (Reid and Fedosejevs, 2006; Todoruk *et al.*, 2008; Todoruk *et al.*, 2012), and it is these two properties that make THz sensitive to fiber structure and orientation within wood.

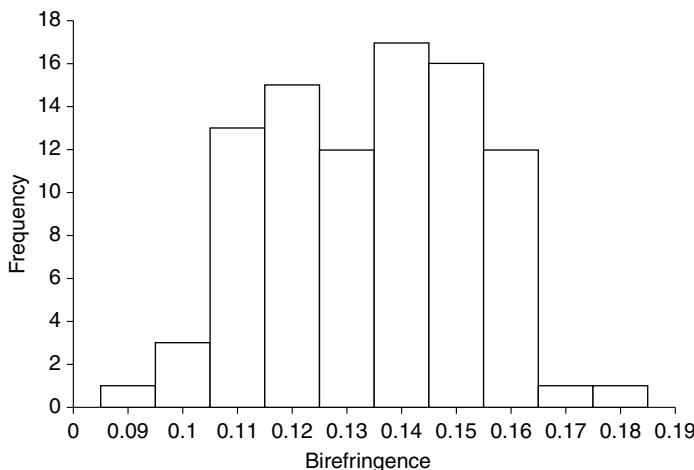
The birefringence measured in wood at THz frequencies varies substantially both within and between species (Todoruk *et al.*, 2008), as shown in Figs 19.2 and 19.3. As a proportion of the measured refractive indices, the birefringence observed is reported to be exceptionally strong (Reid and Fedosejevs, 2006). Polarized THz time-domain spectroscopy performed with the polarization at incremented angles to the wood grain showed that the strongest birefringence and dichroism occur when the two are perpendicular, as shown in Fig. 19.4 (Reid and Fedosejevs, 2006; Todoruk *et al.*, 2008). This suggests that THz radiation is sensitive to the gross fiber structure seen in wood and wood products (Reid and Fedosejevs, 2006; Jordens *et al.*, 2009). The angularly resolved refractive index is plotted in Fig. 19.4 for spruce, which has a large birefringence of approximately 0.07.

Figure 19.5 shows the angularly resolved absorption coefficient which is plotted for spruce. The absorption coefficient also varies substantially with the angle between the polarization of the THz beam and the wood grain, indicating that wood is also dichroic, and that the dichroism is sensitive to the wood grain. Spruce has a large difference in the absorption coefficient between orthogonal polarizations, exhibiting a change of 3.8 cm^{-1} as the polarization changes with respect to the wood grain. The dependence of absorption coefficient and index of refraction on polarization suggests a strong sensitivity to the gross fiber structure seen in wood.

As wood is a complex material, moisture content varies substantially, both within a given piece of wood as well as between pieces of wood within the same environment. Hydroscopicity depends on many factors, such as previous drying, mechanical stress, extractives present, species, as well as the growing location and conditions (Desch and Dinwoodie, 1996). As moisture

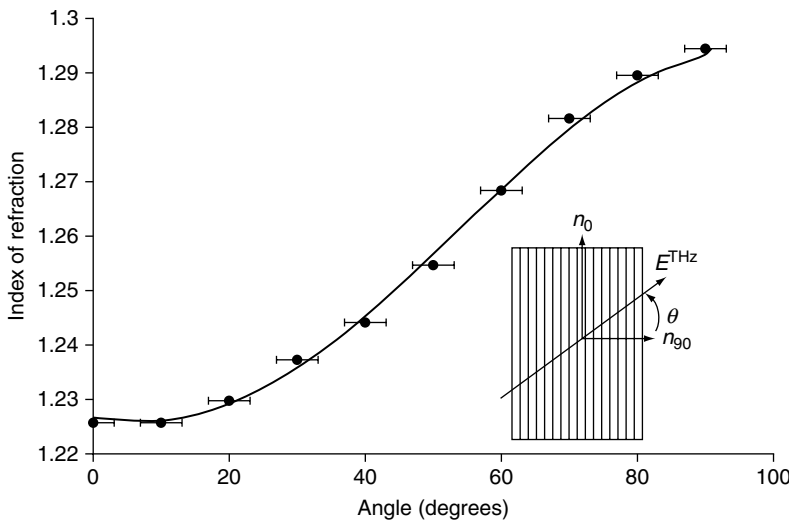


19.2 Polarized THz-TDS was performed on 38 dry maple (*Acer saccharum*) samples and the birefringence was extracted. The distribution of birefringence within maple was seen to be $\Delta n = 0.063 \pm 0.011$.



19.3 Polarized THz-TDS was performed on 91 dry fir (*Abies amabilis*) samples and the birefringence was extracted. The distribution of birefringence within fir was seen to be $\Delta n = 0.130 \pm 0.019$.

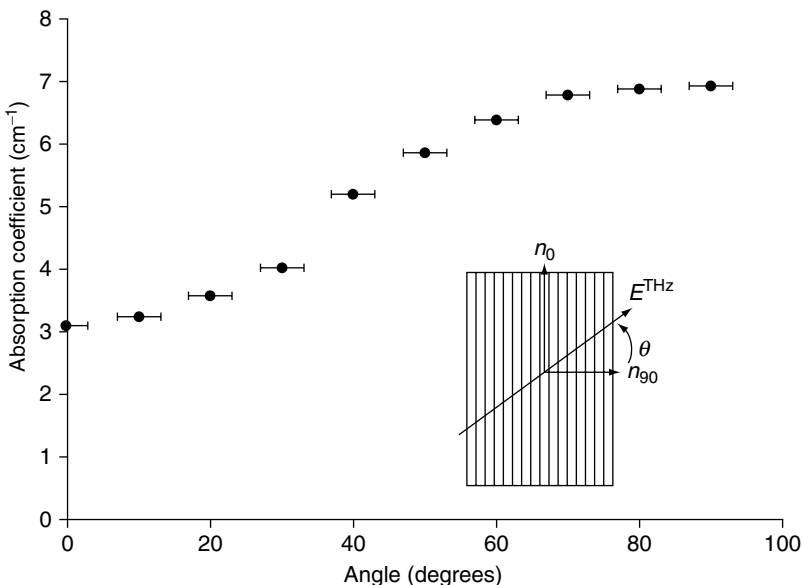
content is also a key factor in the wood products industry, and both the manufacturing process and final product performance depend strongly on it, the ability to probe moisture content is a key asset in these types of applications.



19.4 Polarized THz-TDS was performed on dry spruce (*Picea glauca* var. *albertiana*) varying the angle between the grain orientation and the polarization direction of the THz beam according to the inset figure. The refractive index was extracted, and the birefringence (Δn) is 0.069. The solid line is a theoretical fit of the dependence on the refractive index with respect to the orientation angle using the ellipsoid model of wave normals. The errors in the refractive index are small, and comparable in size to the data point size. The notation that is used in the inset defines the angle θ (x-axis) of the figure. In the inset, n_0 and n_{90} correspond to the index of refraction measured with a THz field that is polarized parallel (n_0) and perpendicular (n_{90}) to the visible grain. The angle θ on the x-axis of the figure measures the angle that the polarization of the THz field makes with respect to the perpendicular direction (n_{90}).

A detailed study of the effects of moisture content on the refractive index and birefringence was performed on various species of wood (Todoruk *et al.*, 2012). This study was performed in order to determine the source of the strong birefringence at THz frequencies, but also demonstrates the sensitivity of various signatures of wood at THz frequencies. This will be discussed in the context of the birefringence of wood next.

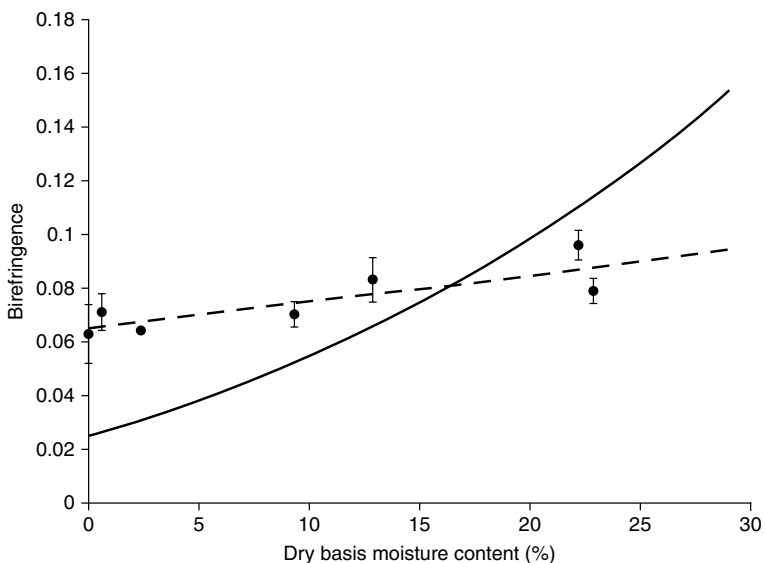
The large birefringence can result from the microscopic structure of wood in the crystalline microfibrils, or from the macroscopic periodic structure of the wood cells themselves. For applications, it is important to understand where this sensitivity comes from. The birefringence of maple (*Acer* spp.) and fir (*Abies* spp.) were examined at different moisture contents, and it was found that the measured birefringence was directly dependent on the moisture content, while the birefringence of aspen (*Populus* spp.) was not. This suggests that form birefringence has a large contribution to the measurable birefringence in maple and fir, but not in aspen (Figs 19.6–19.8).



19.5 Polarized THz-TDS was performed on dry spruce (*Picea glauca* var. *albertiana*) varying the angle between the grain orientation and the polarization direction of the THz beam according to the inset figure. The absorption coefficient was extracted, and the dichroism ($\Delta\alpha$) is 3.83 cm^{-1} . The absorption coefficient (y-axis) values are per cm. The errors in the absorption coefficient are small, and comparable in size to the data point size.

The addition of water into wood changes the dielectric function of the cellulose matrix because it is substantially modified by the presence of water. In crystalline materials, water interacts only with the surface, and does not change the structure of the molecule, so the intrinsic birefringence is not expected to change with the addition of water. As seen in Figs 19.6 and 19.7, the birefringence of maple and fir do change with the addition of water, which suggests that form birefringence does have a significant contribution to the measured birefringence in these species. Figure 19.8 shows that the birefringence of aspen does not appear to change with varying moisture content, suggesting that form birefringence has a minimal contribution to the measured birefringence. In Figs 19.6–19.8, the solid line represents a theoretical estimation of the dependence of form birefringence on moisture content (Zhou and Knighton, 1997). In all cases, the measured birefringence is higher than the theoretical estimate, suggesting that intrinsic birefringence also contributes to the measured birefringence values.

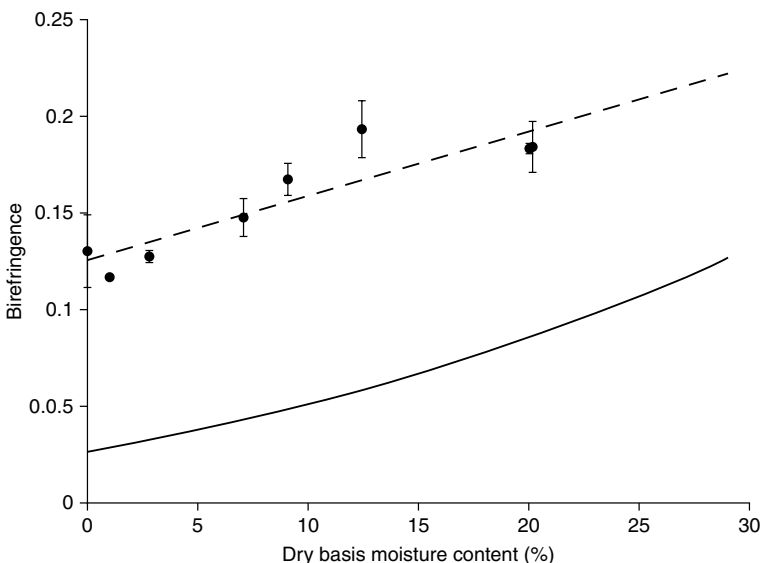
The dichroism of wood is also affected by moisture content and may have potential applications in the wood products industry, but certainly is important for any application where moisture contents are not tightly controlled.



19.6 Polarized THz-TDS was performed on maple (*Acer saccharum*) samples (thickness 3 mm) conditioned in humid environments (relative humidity = 15%, 23%, 32%, 52%, 66%, 87% and 93%). The birefringence was extracted and the dry basis moisture content was calculated based on the mass of the wet and dry samples. The solid curve represents a theoretical estimation of the dependence of form birefringence on moisture content (Zhou and Knighton, 1997) and the dashed line (slope = 0.10) is a linear regression fit to the data points in order to analyze the trend in the dependence of birefringence on moisture content.

Figure 19.9 shows the dependence of the absorption coefficient on moisture content for aspen wood. For both parallel and perpendicular orientations of the wood grain to the polarization of the THz beam, the absorption coefficients increased with moisture content, as expected. As the two increased at a different rate, the dichroism is also dependent on the moisture content. It is interesting that the dichroism grows by more than a factor of 3 over from 3% to 20% moisture content. This is most likely a result of the nature of the strong interaction of the water with the cell wall material, and the difference between bound and free water.

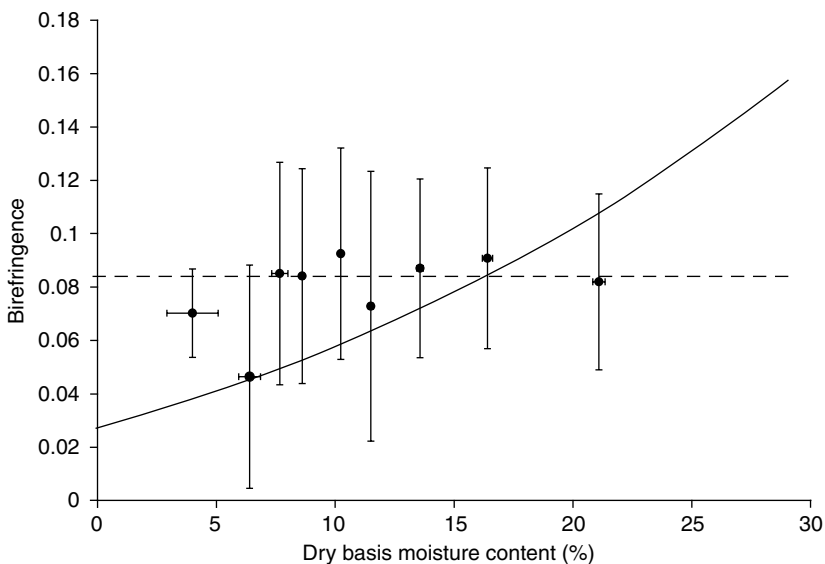
Based on the physical structure of wood, the birefringence observed can be due to intrinsic birefringence, resulting from the dielectric properties of the wood material present in cell walls, or it can be due to form birefringence, resulting from the repetitive array of cylindrical cells present in the wood structure as might be suggested by the dependence on moisture content discussed above (Figs 19.6–19.8).



19.7 Polarized THz-TDS was performed on fir (*Abies amabilis*) samples (thickness 3 mm) conditioned in humid environments (relative humidity = 15%, 23%, 32%, 52%, 66%, 87% and 93%). The birefringence was extracted and the dry basis moisture content was calculated based on the mass of the wet and dry samples. The solid curve represents a theoretical estimation of the dependence of form birefringence on moisture content (Zhou and Knighton, 1997) and the dashed line (slope = 0.33) is a linear regression fit to the data points in order to analyze the trend in the dependence of birefringence on moisture content.

In order to determine the source of birefringence, wood samples from three different species were saturated with liquids with refractive index values which span values above and below that of cellulose. When changing the saturation medium, the intrinsic contribution should remain constant, provided that the submersion medium is itself isotropic, while the form birefringence contribution changes. When the observed birefringence is plotted against the refractive index of the submersion medium, if both types of birefringence are present, there will be a minimum in birefringence reached, but not zero. The measured birefringence would be equal to the intrinsic birefringence when the form birefringence is zero, which would occur when the refractive indices of the submersion medium and cell wall are equal (Born and Wolf, 1999).

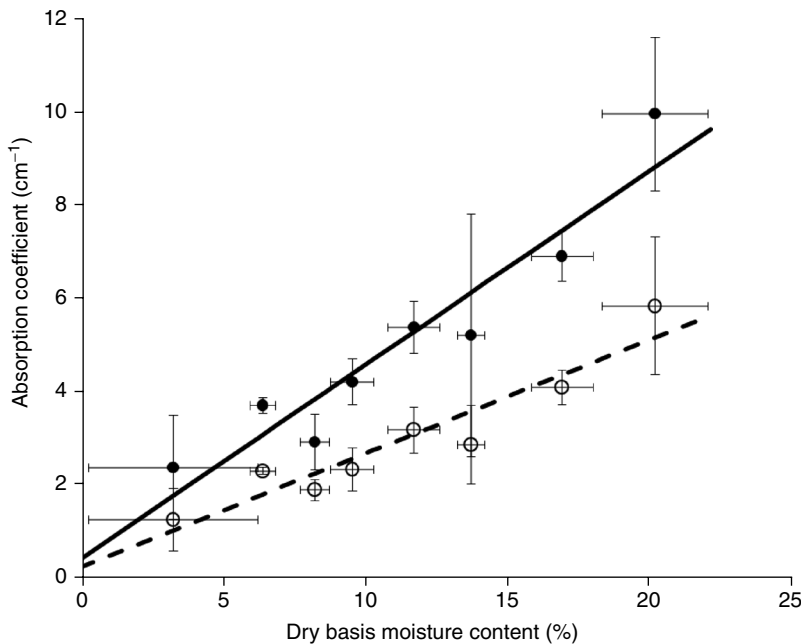
Submersion of maple, fir, aspen, red oak (*Quercus rubra*), white oak (*Quercus alba*), and spruce (*Picea* spp) in hexane ($n = 1.378$), toluene ($n = 1.498$), and quinoline ($n = 1.669$) was performed, although only maple, fir and aspen are discussed here, as the other species follow similar trends to maple and fir (Todoruk *et al.*, 2012). Figures 19.10–19.12 plot the measured



19.8 Polarized THz-TDS was performed on trembling aspen (*Populus tremuloides*) samples (thickness 0.5 to 1.3 mm) conditioned in humid environments (relative humidity = 15%, 23%, 32%, 52%, 66%, 87% and 93%). The birefringence was extracted and the dry basis moisture content was calculated based on the mass of the wet and dry samples. The solid curve represents a theoretical estimation of the dependence of form birefringence on moisture content (Zhou and Knighton, 1997) and the dashed line is a horizontal linear fit to the data points.

birefringence as a function of the refractive index of the pore filler, with the points corresponding to a pore filler of air, hexane, toluene and quinoline, respectively. The relative contributions of both form and intrinsic birefringence was extracted from these plots. It was determined that the relative contributions of form and intrinsic birefringence were approximately 60% and 40%, respectively, for maple, and 55% and 45%, respectively, for fir. For aspen, the relative contribution of form birefringence was only approximately 20%, and intrinsic birefringence approximately 80%. As the form birefringence can be measured at THz frequencies, the gross physical structure of wood can be probed, and as the intrinsic birefringence can be measured, the crystallinity and microfibril angle can be probed, which allows more applications for non-contact and non-destructive testing for wood and wood products.

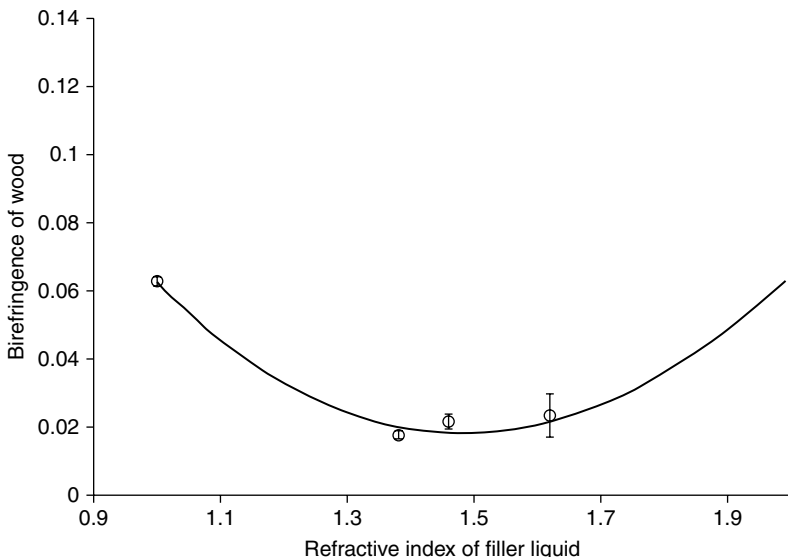
And so for most species of wood, the large birefringence results from a combination of form and intrinsic birefringence. Therefore THz technology can probe both microscopic (crystallinity and microfibril angle for example) and macroscopic (pore and gross fiber structure) properties. This opens up a host of significant application areas for wood science. As such, it is useful to



19.9 Polarized THz-TDS was performed on trembling aspen (*Populus tremuloides*) samples (thickness 0.5 to 1.3 mm) conditioned in humid environments (relative humidity = 15%, 23%, 32%, 52%, 66%, 87% and 93%). The absorption coefficient (y-axis) is in units of cm^{-1} . The parallel and perpendicular absorption coefficients were extracted and the dry basis moisture content was calculated based on the mass of the wet and dry samples. The filled points represent the absorption coefficient when the polarization of the THz beam is perpendicular to the grain orientation of the sample and the open points represent the absorption coefficient when the polarization of the THz beam is parallel to the grain orientation of the sample. The solid line is a linear regression fit to the perpendicular data points (slope = 0.415) and the dashed line is a linear regression fit to the parallel data points (slope = 0.243) in order to analyze the trend in the dependence of birefringence on moisture content.

understand other technologies that are currently employed in wood science to look at similar physical quantities, in order to make a forecast of where THz technology might make the most impact.

Technologies, such as microwaves, infrared radiation and X-rays are currently being used in both wood science and in the wood products industry. Microwaves have been successfully used for defect detection and evaluation of the characteristics of wood (Martin *et al.*, 1987), density measurements of wood-based composites (James *et al.*, 1985; King and Basuel, 1993), and measurements of fiber orientation (Schajer and Orhan, 2005; James *et al.*,

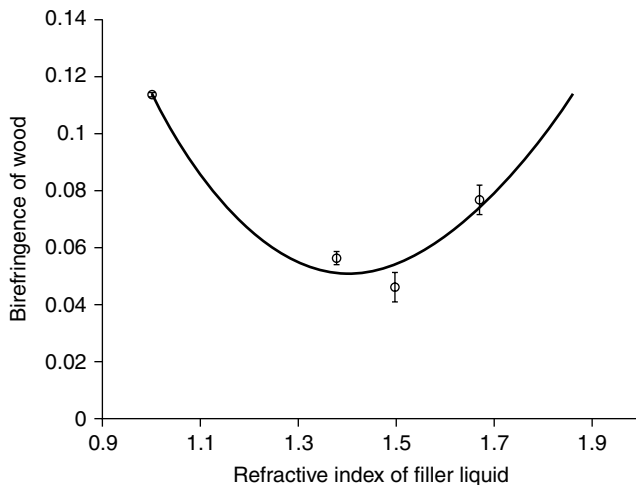


19.10 Polarized THz-TDS was performed on maple (*Acer saccharum*) saturated with liquids with refractive index values that span that of cellulose. The dependence of the birefringence on the refractive index of the pore filler is plotted. The solid line represents a non-linear regression fit assuming changes result from form birefringence. The four points correspond to sample averages of a pore filler of air, hexane, toluene, and quinoline, and the minimum of the curve corresponds to the intrinsic birefringence observed in the sample. The error bars on the refractive index of the filler liquids were calculated to be 0.004.

1985). The difficulty with using microwave technology is that spatial resolution is limited by the wavelengths used, and in the case of microwaves, is restricted to tens of centimeters.

Infrared radiation, in comparison, has been successfully used for estimating the chemical composition of wood (Jones *et al.*, 2006), species differentiation (Nault and Manville, 1997; Flate *et al.*, 2006; Huang *et al.*, 2008), moisture sensing (Defo *et al.*, 2007; Tsuchikawa, 2007; Adedipe and Dawson-Andoh, 2008), and quantification of resin content in OSB (Taylor and Via, 2009). While this technology works well for many applications, it is restricted to a surface measurement technology only as wood is opaque at infrared frequencies.

X-ray technology, on the other hand, can penetrate wood and wood products and has been successfully used for density measurements (Lindgren, 1991), for internal defect scanning of logs (Rinnhofer *et al.*, 2003), and for void detection in wood composites (Sugimori and Lam, 1998). The main limitation to using X-ray technology in the wood products industry is the



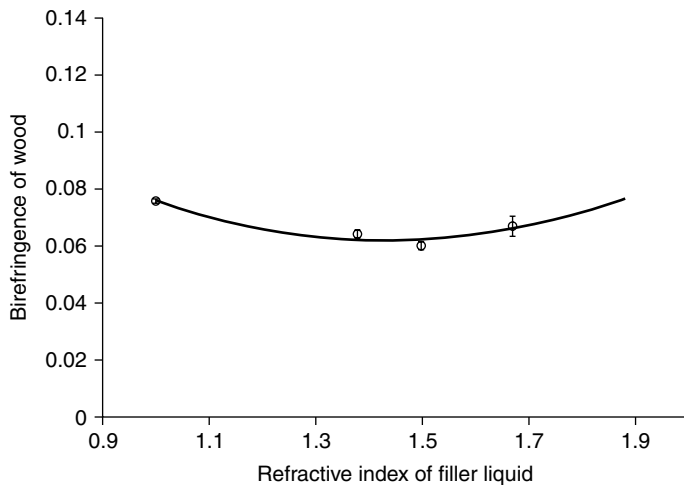
19.11 Polarized THz-TDS was performed on fir (*Abies amabilis*) saturated with liquids with refractive index values that span that of cellulose. The dependence of the birefringence on the refractive index of the pore filler is plotted. The solid line represents a non-linear regression fit assuming changes result from form birefringence. The four points correspond to sample averages of a pore filler of air, hexane, toluene, and quinoline, and the minimum of the curve corresponds to the intrinsic birefringence observed in the sample. The error bars on the refractive index of the filler liquids were calculated to be 0.004.

substantial regulation surrounding its implementation in a working environment due to health-related concerns. THz technology, on the other hand, poses no substantial health risk at levels typically present in a THz-TDS system (Walker *et al.*, 2002). In addition to this, X-ray technology is not sensitive to fiber structure as THz radiation is, and in many situations (such as in the manufacturing of OSB as discussed in Section 19.6) cannot be used for density monitoring without substantial changes to the manufacturing process.

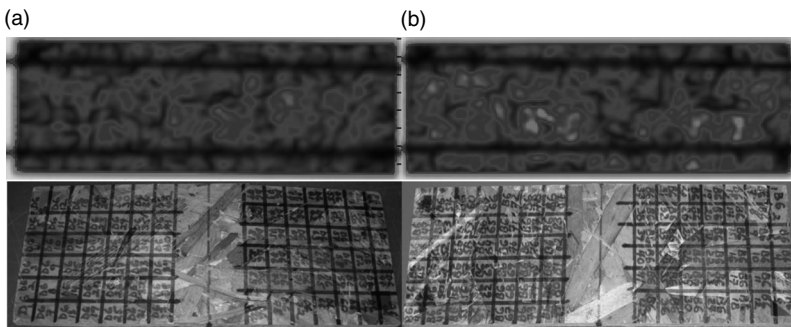
From the discussion above, where THz technology will have the largest impact in the wood products industry is a key question. It is likely to be found where safe transmission imaging of dry wood and wood fiber is required with a good spatial resolution.

19.5 Probing wood characteristics at terahertz frequencies

Sensitivity of THz radiation to many properties of wood was examined and two examples are presented that highlight *how* THz radiation can be used to probe the properties of wood. The point of these examples is that once it



19.12 Polarized THz-TDS was performed on aspen (*Populus tremuloides*) saturated with liquids with refractive index values that span that of cellulose. The dependence of the birefringence on the refractive index of the pore filler is plotted. The solid line represents a non-linear regression fit assuming changes result from form birefringence. The four points correspond to sample averages of a pore filler of air, hexane, toluene, and quinoline, and the minimum of the curve corresponds to the intrinsic birefringence observed in the sample. The error bars on the refractive index of the filler liquids were calculated to be 0.004.



19.13 THz (top) and optical (bottom) image of 12.5" x 4" OSB. The average densities of the boards are 43.5 lbs/ft³ (a) and 37 lbs/ft³ (b). The images are density maps based on the phase of the transmitted THz pulse (index of refraction). Darker color represents denser board. The two dark horizontal lines in the THz images are supports for imaging the boards.

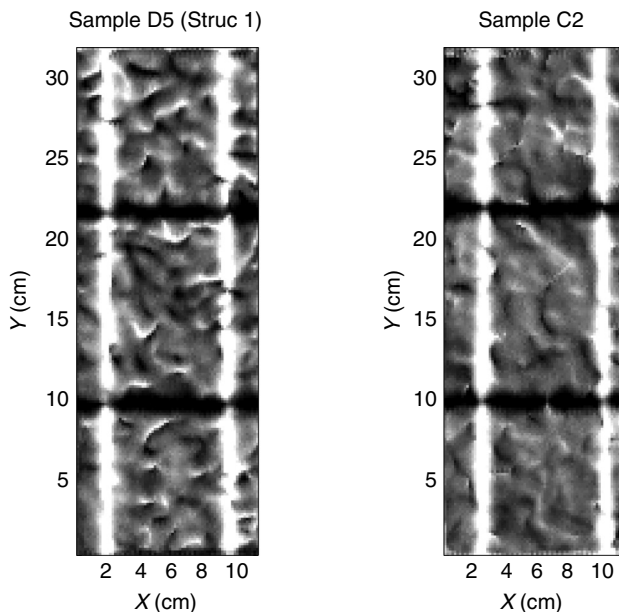
is understood how the properties of wood affect the THz radiation, an imaging modality can be employed to image those properties.

The initial work on THz properties of wood (Koch *et al.*, 1998) showed that the attenuation of THz radiation through a wood sample depends on the density of that sample. That is to say, by imaging the *amount* of THz radiation that gets through a piece of wood, a density image can be produced. This was used to produce a density map with a spatial resolution sufficient to show the ring structure (early and late wood having different densities) of the wood. This essentially makes use of the absorption coefficient. As we saw, the absorption coefficient depends on moisture content as well as on the polarization direction of the THz radiation with respect to the grain of the wood. Another method for producing a density map is to use the index of refraction, which is less sensitive to changes in moisture content, with a fixed polarization direction. An example of a density profile measured in this way is presented in Fig. 19.13. This is a density map of two pieces of OSB. The details of what OSB is, and how it is manufactured, are discussed in Section 19.6. Optical images of those pieces are seen in Fig. 19.13 (bottom). The dark lines are support bars used to support the boards while imaging them. The two boards have different average densities, 43.5 lbs/ft³ (696.8 kg/m³) (Fig. 19.13a) and 37 lbs/ft³ (592.7 kg/m³) (Fig. 19.13b), which appear in the images. The resolution is of the order of 1 mm where the boards were 12.5" × 4" (31.8 cm × 10.16 cm) in size. The key point to make is that either the absorption coefficient (attenuation) or index of refraction (pulse delay or phase of the THz beam) can be used to image density, as both are correlated to density for a fixed moisture content and polarization.

As discussed in Section 19.5, wood is dichroic and birefringent, meaning that the fiber orientation can be probed by examining either the anisotropic absorption or anisotropic phase of a transmitted THz beam. If this can be probed in an imaging modality, then a map of fiber orientation can be constructed.

Two fiber-orientation anisotropy images are presented in a dichroism map in Fig. 19.14, where each was formed by taking two THz transmission images with orthogonal polarizations (transmission maps converted to absorption coefficient maps), and subtracting the two images. This then provides a measurement (in cm⁻¹), which corresponds to the degree of dichroism. It is somewhat difficult to interpret, because an actual map of the fiber orientation would require precise knowledge of the birefringence of the material, which in this case is highly variable. However, the anisotropy of the overall fiber structure can be shown, as complete misalignment of the fibers would lead to no measured dichroism.

What is interesting here is that the board on the left is more dense (43 lbs/ft³) than the one on the right (41 lbs/ft³). However, interpreting the images as a lighter value demonstrates more dichroism (in such a way that there is



19.14 The lighter the pixel, the more anisotropic the fiber distribution (more fiber in the vertical direction) and the darker the pixel, the more isotropic the fiber distribution. The vertical and horizontal lines are supports used for collecting images. These images are formed by taking the difference of two absorption coefficient maps taken with orthogonal THz polarizations.

more alignment of the fibers to the vertical direction) and the darker values show less dichroism (more isotropic, in this case more fibers in the horizontal direction), the board on the left has more fibers aligned in the vertical direction in the middle of the board than the one on the left. In breaking these samples on a strength testing apparatus, the break strength of the one on the right was 291 lbs (132 kg) and the one on the left was 320 lbs (145 kg). It is interesting to note that the orientation of the fibers, *in addition to the average density*, plays a role in the overall strength of the boards. Indeed, this is why manufacturers of OSB preferentially align the fibers to give strength in a particular direction.

As discussed in most of this chapter, wood is an extremely complicated material. As such, there is much work that remains to be done in order to fully understand the microscopic and macroscopic interactions of THz radiation with wood, including wood–water interactions. However, when some of the variables can be controlled, such as keeping a controlled moisture content, there are industrial applications of THz technology to wood products that can be realized right now. Applications to the OSB industry are a good example, and showcased by the pilot study that will be described in Section 19.6.

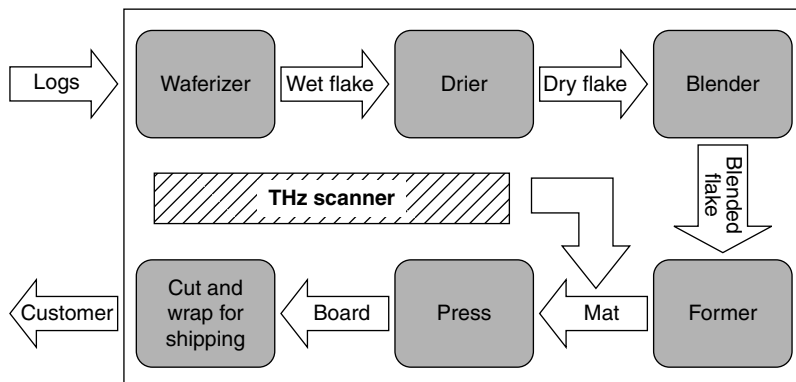
19.6 Terahertz sensing in the oriented strand board industry

This section examines the OSB process, highlighting the need for density monitoring during manufacturing. The use of THz technology is then explored as a tool for online density monitoring.

19.6.1 The OSB process

OSB is used for roofing, siding and flooring applications in home construction, with the notable feature of being composed of ‘strands’ of wood which are pressed together with resin to form a structural panel. In order to understand how THz technology can impact this industry, and the significance of the pilot project which will be discussed, it is important to visualize the OSB manufacturing process.

Soon after the bark has been removed from the logs, they are brought into an OSB facility, first put through a set of knives that chop the wood into chips, called ‘flake’, which are usually around $1.5'' \times 4''$ ($3.8\text{ cm} \times 10.2\text{ cm}$) and less than 1 mm thick (Fig. 19.15). Because the logs are usually wet to aid in the waferization process, the flake is passed through driers to bring the moisture content down to a few percent. The flake is passed through a series of blenders, which add resin and wax to the flake. The product is passed through a series of ‘formers’ which allow the flake to pass onto a caul screen or caul plate, which pulls the mat of flake along a conveyor belt but imparts to the flake a preferred orientation in the plane of the conveyor belt. The mat of flake is built up first through a surface former with the preferred



19.15 Schematic diagram illustrating the OSB manufacturing process, and the location of the THz scanner discussed in this chapter.

orientation of the flake in the direction of the movement of the conveyor belt (the machine direction), to give strength to the board in that direction. It then passes through one or more core formers, which lay down flake onto the mat which has a preferred direction perpendicular to the machine direction to give strength in this direction. Finally, the mat passes through a surface former, which adds a surface layer with a preferred orientation parallel to the first layer. This mat of flake is then passed into a heated press at high pressure and temperature to form the structural panel. The finished board is then cut to size, wrapped and shipped to customers.

19.6.2 The challenge in the OSB process

In the manufacturing of OSB, the largest cost is the cost of the fiber (wood). In order for an OSB manufacturer to operate efficiently, it is critical that the amount of wood used is at a minimum while maintaining the structural properties that allow them to meet certification standards. The strength of the final board depends most strongly on the amount of wood flake used in the process and the orientation of the wood flake in the boards. It is for this reason that OSB manufacturers are monitoring the uniformity of the wood distribution in the mat prior to pressing. This is because the density of the mat varies across the manufacturing line, and the low density portion of the mat must be able to make boards that are strong enough to meet certification standards. Everything above the lowest density across the mat is therefore wasted wood. For this reason, OSB manufacturers invest heavily in technologies that provide a picture of the density profile of the OSB mat.

The only technology commercially available to monitor the density profile of OSB mats is based on X-ray technology. This poses a significant problem for OSB facilities using metal caul screens (or plates) to transport the mat to the press; the density fluctuations in the caul screens completely overwhelm the density fluctuations of the mat itself, and render the technology useless for these mills. Later in this section, a comparison of THz scanning and X-ray scanning technology will be drawn for the purpose of measuring OSB mat density profiles.

19.6.3 The THz solution

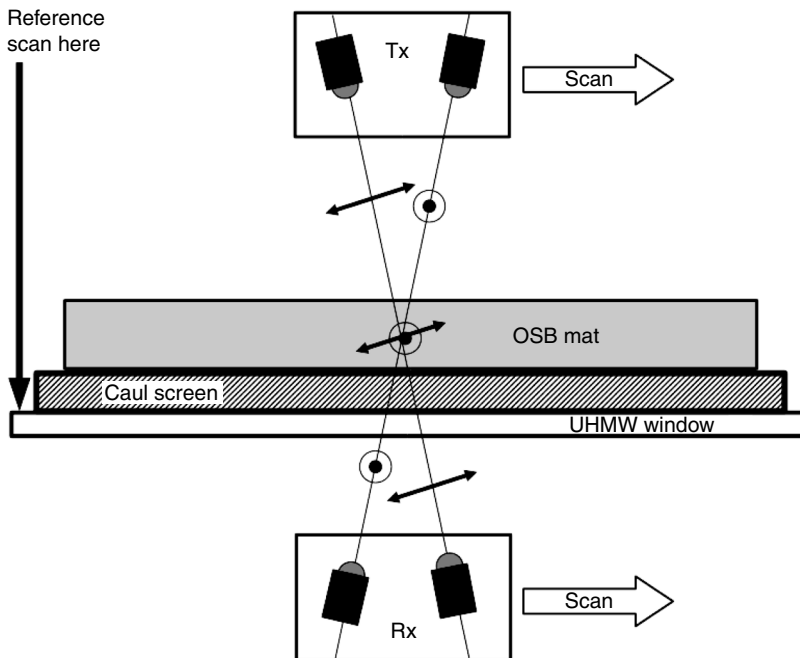
The financial significance of monitoring the density of the mat to OSB facilities drove the need to develop a scanning system based on THz technology. The transparency and spatial resolution make THz the ideal wavelength range to probe the density profile of the mat. As discussed earlier in this chapter, the sensitivity to moisture content can be problematic for many applications. So too it is for measuring the density profile of an OSB mat. However, the

moisture content of the flake in the OSB process is extremely controlled and is uniform, which allows calibration measurements for the controlled moisture content present. The moisture content is controlled to aid in heat transfer in the pressing process, since wood is a poor thermal conductor. Further, we were able to exploit the unique properties of THz radiation to probe through the metal caul screens to get a measurement of the density of the mat itself, which is not possible with X-ray technology as discussed in the previous section. For this reason, the only OSB mills that employ X-ray density monitors use rubber sheet to transfer the mats to the press, which can be calibrated for a relatively accurate X-ray measurement of mat density.

The environment on the manufacturing line in an OSB mill is not conducive to the deployment of sensitive optical equipment. Considerations for dust, substantial vibrations and temperature fluctuations on the order of 30°C within hours had to be made. For this reason, implementation of new technology in this industry is difficult and challenging. The pilot study discussed here is a showcase, showing that THz technology is now at a point suitable for deployment in the manufacturing industry.

The scanning system was built and operated in a transmission geometry for the manufacturing line of OSB facility. It was constructed from a pair of orthogonally polarized transmitters, each coupled to a receiver on the opposite side of the OSB mat. The scanning heads scanned at a speed of 500 mm/s, and created a density profile of the OSB mat in the transverse direction (across the manufacturing line). The THz emitters and detectors were fiber-optically and electrically connected to the laser system and electronics were housed in a temperature-controlled and sealed enclosure. A THz ‘window’ was constructed on the manufacturing line using 1” (2.54 cm) thick ultra high molecular weight (UHMW) polymer. The THz beam therefore scanned through the mat, the caul screens and the UHMW windows. Measurements were calibrated by subtracting out the effects of the caul screen and UHMW windows on a monthly basis, and temperature fluctuations and system power drifts were corrected for every scan by taking a reference scan prior to each measurement scan across the line. The THz system itself was composed of a Picometrix T-Ray 4000 unit, modified to produce 1000 THz waveforms per second, each with an 80 ps scan range. Each polarization channel operated at this speed, was analyzed in real time to produce measurements of mat density across the manufacturing line. A schematic of the scanning system is shown in Fig. 19.16.

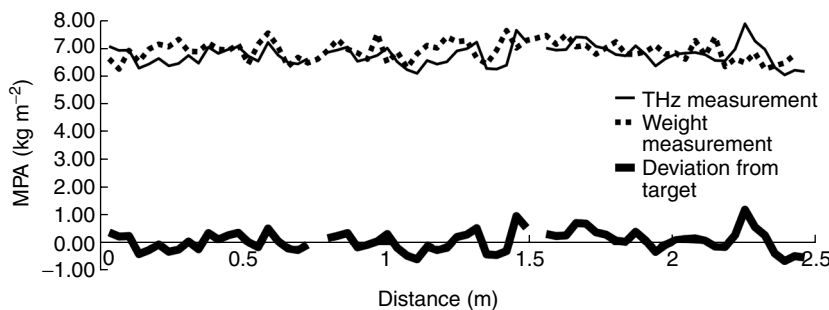
The system was deployed in June 2009 at the Ainsworth 100 Mile House OSB facility in 100 Mile House, British Columbia, Canada. It was in operation until February 2010, at which point it was removed for upgrading. During the pilot, the system operated almost continuously with no problems encountered with the THz system itself, which is indicative that the technology has matured to the point where industrial applications are feasible.



19.16 Schematic of the THz scanning system. Two orthogonally polarized emitter/detector pairs scan perpendicular to the machine direction (which is off the page). The mat density is measured by subtracting the effects of the caul screen and UHMW windows, and temperature fluctuations and system drift are corrected at each scan with a reference trace before each scan.

19.6.4 The result

Before the THz scanning system was considered to be reliable by mill operators, the technology had to be proven to facility quality-control specialists. An exhaustive series of tests were performed, where the profile of the OSB mat was measured with the THz system, marked with an ink-dye at the location of measurements, and the final board was tested for density. The measurements and testing conducted demonstrate that the THz scanning system can scan with an accuracy of 3% after calibration, and continue to scan with a precision of better than 0.7%. The data collected indicated that there are changes to the mat after the position of the THz scanner, which complicate comparisons between mat measurements and finished board measurements. Therefore these absolute accuracy measurements are conservative, and could potentially be smaller, limited by the ability to accurately cut samples of the final OSB to locations that were actually scanned.



19.17 MPA as a function of position on the manufacturing line. Dashed curve is the measured value by weighing the finished OSB product and relating the position back to the THz measurement (thin solid line). The thick solid line is the difference between the THz-measured MPA and the target MPA during manufacturing at that time, showing where too much/too little wood is being used.

with a positional accuracy of 3.5 cm or better. A sample scan comparing the THz measurement and hand cut measurement is presented in Fig. 19.17. Note that the 'MPA' is the mass per unit area in kg m². The thick solid line is the difference between the THz measurement and the target MPA, which is what the mill operators are interested in for improving efficiency. The thick solid line is quite consistent over time, and is what was used by mill management to change the process.

It is important to recognize that it is the precision of the measurement that is important here, as variations from the average density profile on the order of $\pm 6\%$ are what the mill operators are trying to control. Therefore, measuring variations from the average on the order of $\pm 6\%$ with a precision of 0.7% is possible and extremely useful, irrespective of whether or not the exact density is known. In order to evaluate the efficacy of the THz scanning system, it is useful to compare it to other technologies that perform the same task. There are two manufacturers of an X-ray scanning system for density profiling of OSB mats. Based on the specifications published online, one of the manufacturers claims the density profiling has the ability to image density with an accuracy of 0.1% at speeds similar to what was conducted in our pilot study using the THz scanner when a scanning head was used. It is likely that this number was determined in the laboratory environment, as calibration is required to account for the rubber mats used to transport the OSB mat. This would be consistent with the quoted value of 3% by the second manufacturer, and in-line with the conservative estimate for the THz OSB scanner described here. Further, the tests that were used to

'prove-out' the THz scanning system for the purpose of making process changes were designed for the purpose of instilling confidence in the mill operators, rather than scientific rigor, which is part of performing an industrial pilot. While a direct comparison of the two technologies is not possible in the pilot that was conducted, because the X-ray systems are not compatible of working with processes that use caulk screens, it would be interesting to test the THz scanner in an OSB facility that also has X-ray densitometers for a direct comparison.

Finally, it should be noted that this project was based only on density measurements. To incorporate fiber-orientation anisotropy measurements was not possible for various reasons, and so the full capability of THz technology for this industry has not fully been recognized. It is, however, also worth noting that OSB is one of the most complicated composites that exist. And so it is quite exciting that THz technology is able to give us useful information on such a complex system, and gives us the expectation that there will be many applications of this new technology.

As with any prototype system, many difficulties were encountered. The majority of the difficulties had to do with the environment. Nonetheless, the pilot demonstrated that: (i) THz technology is now at a point where it can be deployed in the manufacturing industry, and (ii) the sensitivity for density monitoring in OSB manufacturing is sufficient to be used for process optimization.

19.7 Future trends

Much work remains to get a better understanding of the interaction of THz radiation with wood, and how it can be used as a probe of various properties of wood. While this exciting science is getting started, a host of new applications will wait. And as these applications develop, new technology will have to keep up to the demand. Since 2008–9, when the OSB pilot was conducted, the Authors are aware of two other large-scale pilot projects for THz technology in manufacturing industries to 2011. These applications are primarily driven by the availability of fast, fiber-coupled THz time-domain spectrometers. What is meant by 'fast' is that the THz signals are acquired at a repetition rate of more than 1 per second. This is necessary for most applications, especially if imaging is involved. To this end, it is useful to see what manufacturers offer THz-TDS systems that operate at repetition rates above 1 Hz, a summary of which is presented in Table 19.2. The system employed in the OSB scanner discussed in Section 19.6 was a Picometrix T-Ray 4000 system, which operates at 1000 Hz with 80 ps of delay per waveform.

Table 19.2 Manufacturers of THz-TDS systems that operate at repetition rates greater than 1 Hz

Manufacturer	System	Description	Bandwidth	Repetition rate	Website
Ekspia	T-SPEC	THz-TDS for spectroscopy. Photconductive emitter/detector, free-space coupling	0.1–3.5 THz	Up to 10 Hz	www.ekspia.com
Menlo Systems	TERA K15	Fiber-coupled THz spectroscopy and imaging kit. Photoconductive emitter/detector	3 THz	Approximately 4 Hz	www.melosystems.com
Picomatrix	T-RAY 4000	Fiber-coupled THz-TDS for spectroscopy and imaging. Photconductive emitter/detector	0.2–2 THz (3 THz available)	100 Hz (custom 1000 Hz available)	www.picomatrix.com
Teraview	TPS Spectra 3000	THz for spectroscopy and imaging. Fiber-coupled emitter/detector option. Stand-off reflection/transmission mode	0.06–4 THz		www.teraview.com

19.8 References

- Adepape O E and Dawson-Andoh B (2008), ‘Predicting moisture content of yellow-poplar (*Liriodendron tulipifera L.*) veneer using near infrared spectroscopy’, *For. Prod. J.*, **58**(4), 28–33.
- Banerjee D, von Spiegel W, Thomson M D, Schabel S and Roskos H G (2008), ‘Diagnosing water content in paper by terahertz radiation’, *Opt. Exp.*, **16**(12), 9060–9066.
- Born M and Wolf E (1999), *Principals of Optics*, 7th (expanded) ed., Cambridge, University Press.
- Defo M, Taylor A M and Bond B (2007), ‘Determination of moisture content and density of fresh-sawn red oak lumber by near infrared spectroscopy’, *For. Prod. J.*, **57**(5), 68–72.
- Desch H E and Dinwoodie J M (1996), *Timber: Structure, Properties, Conversion and Use*, Houndsills-Basingstoke-Hampshire-London, MacMillan Press.
- Flæte P O, Haartveit E Y and Vadla K (2006), ‘Near infrared spectroscopy with multivariate statistical modeling as a tool for differentiation of wood from tree species with similar appearance’, *New Zealand J. of For. Sci.*, **26**(2/3), 382–392.
- Fukunaga K, Hosako I and Picollo M (2010), ‘Terahertz spectroscopy applied to the analysis of artists materials’, *Appl. Phys. A.*, **100**(3), 591–597.
- Hecht E (2002), *Optics*, San Francisco, Pearson Education, Inc. as Addison Wesley.
- Hor Y L, Federici J F and Wample R L (2008), ‘Nondestructive evaluation of cork enclosures using terahertz millimeter wave spectroscopy and imaging’, *Appl. Opt.*, **47**(1), 72–78.
- Huang A, Zhou Q, Liu J, Fei B and Sun S (2008), ‘Distinction of three wood species by fourier transform infrared spectroscopy and two-dimensional correlation IR spectroscopy’, *J. Mol. Struct.*, **883–884**, 160–166.
- Jackson J B, Mourou M, Labaune J, Whitaker J F, Duling I N III, Williamson S L, Lavier C, Menu M and Mourou G A (2009), ‘Terahertz pulse imaging for tree-ring analysis: a preliminary study for dendrochronology applications’, *Meas. Sci. Technol.*, **20**(7), 075502–075512.
- James W L, Yen Y-H and King R J (1985), *A microwave method for measuring moisture content density, and grain angle of wood*, University of Wisconsin–Madison, Forest Products Laboratory, United States Department of Agriculture.
- Jones P D, Schimleck L R, Peter G F, Daniels R F and Clark A (III) (2006), ‘Nondestructive estimation of wood chemical composition of sections of radial wood strips by diffuse reflectance near infrared spectroscopy’, *Wood Sci. Technol.*, **40**, 709–720.
- Jordens C, Scheller M, Wichmann M, Mikulics M, Wiesauer K and Koch M (2009), ‘Terahertz birefringence for orientation analysis’, *Appl. Opt.*, **48**(11), 2037–2044.
- Jordens C, Wietzke S, Scheller M and Koch M (2010), ‘Investigation of the water absorption in polyamide and wood plastic composite by terahertz time-domain spectroscopy’, *Polym. Test.*, **29**(2), 209–215.
- King R J and Basuel J C (1993), ‘Measurement of basis weight and moisture content of composite boards using microwaves’, *For. Prod. J.*, **43**(9), 15–22.
- Koch M, Hunsche S, Schauacher P, Nuss M C, Feldmann J and Fromm J (1998), ‘THz-imaging: a new method for density mapping of wood’, *Wood Sci. Technol.*, **32**(6), 421–438.

- Krumbholz N, Hochrein T, Vieweg N, Radovanovic I, Pupeza M S, Kretschmer K and Koch M (2011), 'Degree of dispersion of polymeric compounds determined with terahertz time-domain spectroscopy', *Polym. Eng. Sci.*, **51**(1), 109–116.
- Lindgren L O (1991), 'Medical CAT-scanning: X-ray absorption coefficients, CT-numbers and their relation to wood density', *Wood Sci. Technol.*, **25**, 341–349.
- Liu Y, Tan J, Jiang L, Shi S, Jin B and Ma J (2010) 'Study on terahertz time-domain spectroscopy of pine wood nematode disease', *International Conference on Microwave Technology and Computational Electromagnetics*, Beijing, China, Nov. 3–6, 2009, 271–275.
- Martin P, Collet R, Barthelemy P and Roussy G (1987), 'Evaluation of wood characteristics: internal scanning of the material by microwaves', *Wood Sci. Technol.*, **21**, 361–371.
- Mittleman D (2003), *Sensing with Terahertz Radiation*, Berlin-Heidelberg-New York, Springer-Verlag.
- Mousavi P, Haran F, Jez D, Santosa F and Dodge J S (2009), 'Simultaneous composition and thickness measurement of paper using terahertz time-domain spectroscopy', *Appl. Opt.*, **48**(33), 6541–6545.
- Nault J R and Manville J F (1997), 'Species differentiation of two common lumber mixes by diffuse reflectance fourier transform infrared (DRIFT) spectroscopy', *Wood Fib. Sci.*, **29**(1), 2–9.
- Oyama Y, Zhen L, Tanabe T and Kagaya M (2009), 'Sub-terahertz imaging of defects in building blocks', *NDT and E Int.*, **42**(1), 28–33.
- Reid M and Fedosejevs R (2006), 'Terahertz birefringence and attenuation properties of wood and paper', *Appl. Opt.*, **45**(12), 2766–2772.
- Rinnhofer A, Petutschnigg A and Andreu J-P (2003), 'Internal log scanning for optimizing breakdown', *Comput. Electron. Agr.*, **41**(1–3), 7–21.
- Schajer G S and Orhan F B (2005), 'Microwave non-destructive testing of wood and similar orthotropic materials', *Subsurf. Sens. Technol. Appl.*, **6**(4), 293–313.
- Scheller M A, Wietzke S, Jansen C, Mittleman D M and Koch M (2007), 'Heterogeneous dielectrics in the lower terahertz frequency range: evaluation and extension of physical models', *The Joint 32nd International Conference on Infrared and Millimeter Waves and the 15th International Conference on Terahertz Electronics*. Cardiff, Sept. 2–9, 2007, 542–543.
- Sugimori M and Lam F (1998), 'Macro-void distribution analysis in strand-based wood composites using and x-ray computer tomography technique', *J. Wood Sci.*, **45**, 254–257.
- Taylor A and Via B K (2009), 'Potential of visible and near infrared spectroscopy to quantify phenol formaldehyde resin content in oriented strand board', *Eur. J. Wood Prod.*, **67**, 3–5.
- Teti A J, Rodriguez D E, Federici J F and Brisson C (2011), 'Non-destructive measurement of water diffusion in natural cork enclosures using terahertz spectroscopy and imaging', *J. Infrared Millim. Te.*, **32**(4), 513–527.
- Todoruk T M, Schneider J, Hartley I D and Reid M (2008), 'Birefringence of wood at terahertz frequencies', *Proc. SPIE Photonics North 2008*, Montreal, Canada, June 2–4, 2008.
- Todoruk T M, Hartley I D and Reid M E (2012), 'Origin of birefringence in wood at terahertz frequencies', *IEEE Trans. THz Sci. Technol.*, **2**(1), 123–130.

- Tsuchikawa S (2007), ‘A review of recent near infrared research for wood and paper’, *App. Spec. Rev.*, **42**, 43–71.
- Walker G.C., Berry E., Zinov’ev N. N., Fitzgerald A. J., Miles R. E., Chamberlain M., and Smith M. A. (2002), ‘Terahertz imaging and international safety guidelines,’ *Physics of Medical Imaging, Proc. SPIE*, **4682**, 683–690.
- Williams B.S. (2007), ‘Terahertz quantum-cascade lasers,’ *Nature Photonics*, **1**, 517–525.
- Zhou Q and Knighton R W (1997), ‘Light scattering and form birefringence of parallel cylindrical arrays that represent cellular organelles of the retinal nerve fiber layer’, *Appl. Opt.*, **36**(10), 2273–2285.

Terahertz applications in the pharmaceutical industry

Y.-C. SHEN, University of Liverpool, UK
and B.B. JIN, Nanjing University, China

DOI: 10.1533/9780857096494.3.579

Abstract: The chapter begins with a brief introduction of the typical experimental set-up used for terahertz time-domain spectroscopy and imaging measurements. It then describes ways of sample preparation and data analysis, before discussing a few case studies of terahertz applications in the context of pharmaceutical industry and science.

Key words: terahertz, pharmaceutical, spectroscopy, imaging.

20.1 Introduction

The terahertz (THz) region of the electromagnetic spectrum spans the frequency range between the mid-infrared (mid-IR) and the millimetre/microwave. The centre portion of the THz region ($0.1\text{--}4\,\text{THz}$, $3.3\text{--}133\,\text{cm}^{-1}$) offers a number of very useful properties desired for pharmaceutical applications: (1) THz radiation gives rise to individual ‘fingerprints’ spectra for many crystalline materials including active pharmaceutical ingredients (API), making THz spectroscopy a useful tool for pharmaceutical material characterisation; (2) THz radiation can penetrate deep into pharmaceutical tablets as most common pharmaceutical amorphous materials are semitransparent to THz radiation, thus THz imaging can be used to map internal structures of pharmaceutical products; (3) the photon energy of THz radiation is millions of times smaller than that of X-rays, thus it is safe to use as it will be unlikely to cause any damage to the sample under study. The combination of these properties makes THz spectroscopy and imaging a potentially very powerful technique for characterising the physical structures and chemical compositions of pharmaceutical solid dosage forms.

Spectroscopy in near- and mid-IR region has been widely used by the pharmaceutical industry since it became technically feasible in the 1950s with the development of Fourier transform infrared (FTIR) spectroscopy. However, spectroscopy measurement in THz region has historically been difficult, owing to the lack of any suitable source and detector. The blackbody

radiation source such as mercury arc lamps, which is used in FTIR spectroscopy, becomes increasingly inefficient when approaching THz frequency. An extremely sensitive cryogenically cooled bolometer is thus necessary to detect this weak THz signal (Chantry 1971; Ikeda *et al.* 2010). Furthermore, the measurement result in THz frequency is sensitive to the thermal fluctuation of the sample under investigation and/or its surrounding materials. Due to these difficulties, THz spectroscopy has generally been ignored by the pharmaceutical industry until recently (Heinz *et al.*, 2009).

With the advances in ultrafast laser technology, the past ten years have seen a revolution in THz devices and systems (Ferguson *et al.*, 2002). Of particular significance is the development of THz time-domain spectroscopy (THz-TDS) and THz time-domain imaging (THz-TDI) systems. One of the most distinct features of THz-TDS and THz-TDI techniques is the coherent generation and detection of short pulse broadband THz radiation by using an ultrafast femtosecond laser system. There are three main advantages to using pulsed THz radiation and the associated coherent-detection scheme. (1) This technology directly measures the transient *electric field*, not simply the intensity of the THz radiation. This yields THz spectra with far better signal-to-noise ratio and dynamic range compared with the FTIR method (Han *et al.*, 2001). High-quality THz spectra are now routinely obtained in less than 20 ms without the need for a cryogen-cooled bolometer, making THz spectroscopy more easily and widely accessible. (2) Because of the time-gated *coherent-detection* technology used, the extraneous ambient noise (originating from the *incoherent* blackbody radiation from the sample and its surroundings) is minimised. This, for the first time, allows the use of THz spectroscopy for characterising heated samples under extreme conditions (Cheville and Grischkowsky, 1995) and for *in situ* studies of phase transitions of pharmaceutical solids (Zeitler *et al.*, 2006a, 2006b). (3) The use of pulsed radiation and the associated coherent-detection scheme preserves the time-gated phase information, upon which THz imaging has been developed, for characterising the internal structures of a sample quantitatively and non-destructively.

The enormous inherent potential of THz technology led to a rapid development of THz systems, and the availability of commercial THz spectroscopy and imaging products has opened up many exciting opportunities in the pharmaceutical sector (Zeitler *et al.*, 2007b; Shen, 2011). This chapter intends to supply the basic information necessary to understand and to apply the methods of THz spectroscopy and imaging, to design the experimental procedures, to perform measurements on pharmaceutical samples and finally to analyse the measurement results. We will first describe the general principles of the instruments and their accessories, and then discuss the guidelines for sample preparation and data analysis, and finally present some example applications in the context of the pharmaceutical sector.

20.2 Terahertz time-domain spectroscopy (THz-TDS): spectroscopy set-up and analysis

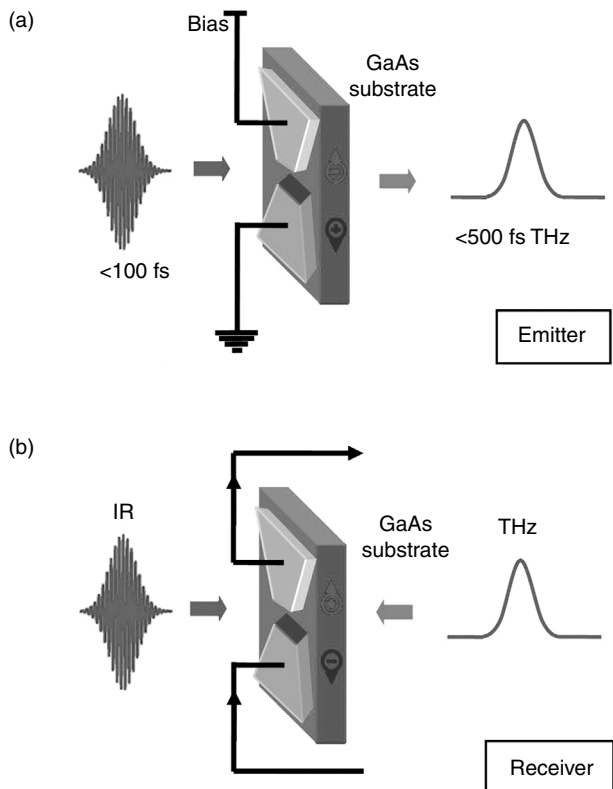
THz-TDS is a new powerful spectroscopic technique in which the properties of a material are probed with short pulses of THz radiation. In this chapter, we will first describe the experimental set-up for THz generation and detection, followed by sample preparations, data analysis with a focus on how to make use of both the amplitude and phase information of the measured THz signal, and finally a few case studies of its pharmaceutical applications.

20.2.1 Spectroscopy set-up

THz emitter and receiver

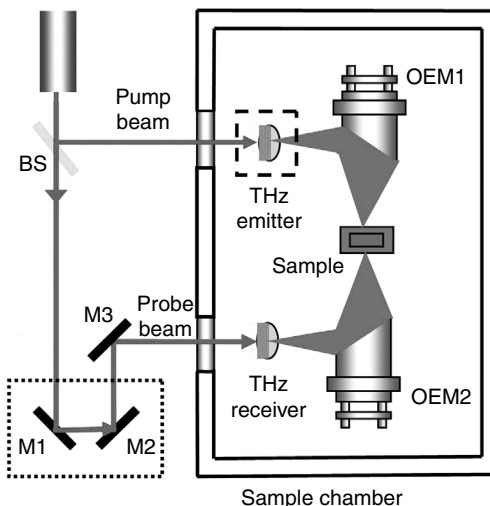
The core technology behind THz-TDS is the coherent generation and detection of short pulses of broadband THz radiation by using an ultrafast femtosecond laser system. A detailed overview of different techniques for THz generation and detection has been published by Ferguson and Zhang (2002), and more recently by Jansen *et al.*, (2010) and Jepsen *et al.*, (2011). To date, the most commonly used device for the generation of ultrashort THz pulses is photoconductive antenna (Auston *et al.*, 1984). In this technique, a biased photoconductive antenna is illuminated using an above-band-gap femtosecond pulse of near-infrared (NIR) light (Fig. 20.1a). Electron–hole pairs are generated in the semiconductor crystal (usually a low-temperature grown GaAs crystal), and these photo-generated carriers are then accelerated by the applied electric field. The physical separation of the electrons and holes forms a macroscopic space-charge field oriented opposite to the biasing field, and thus the total net electrical field undergoes rapid changes. The fast temporal change in the electric field produces a transient current, which generates a pulse of electromagnetic radiation in the THz frequency range.

For the detection of the broadband THz pulse, a NIR probe light is used to optically gate an *unbiased* photoconductive detector antenna (Fig. 20.1b). In the dark, the photoconductive receiver antenna is highly resistive. The carriers generated by the NIR laser pulse causes the resistance to drop significantly in a femtosecond time scale. In this sense, the photoconductive receiver antenna is ‘switched on’ only when the photo-generated carriers are present. In contrast to the THz emitter antenna, the detector antenna is not biased by an external circuit. The electric field required to drive a photocurrent in the antenna structure is supplied by the THz pulses, which arrive in synchronism with the NIR probing light. The photocurrent from the antenna is proportional to the time integration of the product of



20.1 (a) Generation and (b) detection of broadband THz pulses in a gallium arsenide (GaAs) photoconductive antenna. Electron–hole pairs are excited in the GaAs crystal using an above-band gap femtosecond pulse (usually < 100 fs pulses centred at a wavelength of 780 nm, with a 78 MHz repetition rate). For THz emitter antenna that is biased, these photo-generated carriers are accelerated by the applied electric field. This produces a transient current, which generates a pulse of electromagnetic radiation in the THz frequency range. In contrast to the THz emitter antenna, the THz detector antenna is not biased. The photo-generated carriers are actually driven by the electric field of the THz pulse, which arrives in synchronism with the NIR light. Both the amplitude and the phase of the THz electric field could be obtained by measuring the resultant photocurrent in the antenna.

the incident THz electric field and the total number of photo-generated carriers in the photoconductive antenna. In the limit of an ideal photoconductive antenna with carrier lifetime much shorter than the duration of the THz field, the detected current is directly proportional to the THz field strength.



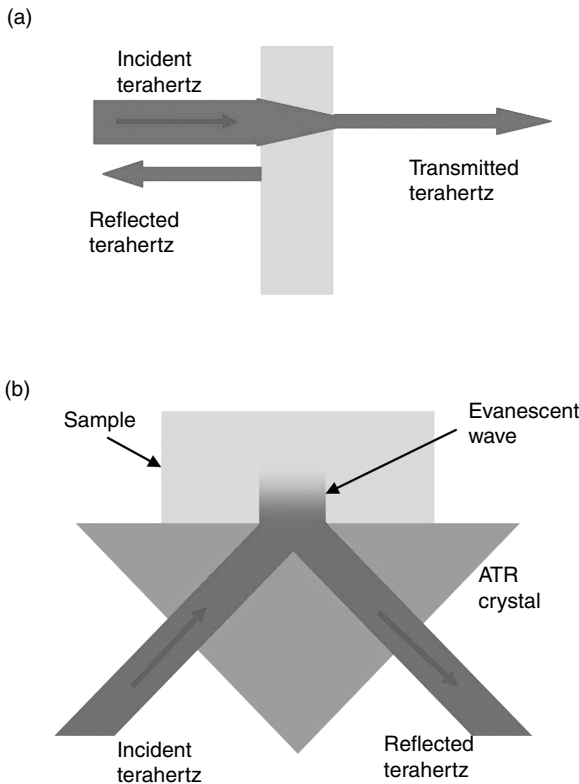
20.2 Schematic diagram of a THz-TDS instrument. BS: beam splitter; M1–M3: metallic mirror; OEM1 and OEM2: off-axis elliptic mirrors.
(Reproduced from Shen, 2011.)

Transmission THz-TDS

The THz time-domain spectroscopy (THz-TDS) in transmission configuration is the main technique used to investigate the solid-state properties of most pharmaceutical materials. Figure 20.2 shows the schematic diagram of a typical experimental set-up. Briefly, a beam splitter separated the NIR light into two beams: an excitation beam and a probe beam. The excitation beam is used to pump a THz emitter antenna for generating a short pulse of broadband THz radiation. The generated THz pulse is focused and transmitted through the sample, before being detected using a THz receiver antenna, which is gated by the probe beam from the same ultrafast laser system. In this way, the time-resolved electric field of the THz pulse could be recorded by scanning the time delay between the THz pulse and the NIR probe beam using a variable delay stage. The achieved spectral resolution is determined by the scanned time delay (distance) of the variable delay stage. Usually the entire system for THz generation and detection is either purged with dry nitrogen gas or evacuated throughout measurement to reduce the water vapour absorption.

Reflection and ATR THz-TDS

Reflection THz-TDS measurements (Fig. 20.3a) are used where a transmission geometry is not suitable, for example in measurements of highly absorbing samples or where information about the dielectric properties of



20.3 (a) The reflected THz radiation, rather than the transmitted THz radiation, was measured in a reflection THz-TDS system. (b) Schematic illustration of the THz-ATR (attenuated total reflection) sampling technique. When a beam of THz light irradiates the crystal-sample interface (from below) at an angle greater than the critical angle, total internal reflection occurs at the crystal-sample interface. Such total internal reflection forms the evanescent wave that extends into and interacts with the sample material. Note that total internal reflection occurs only when the refractive index of the crystal is larger than that of the sample under study. For THz-ATR spectroscopy, silicon crystal is most widely used because it has very low dispersion and transmission losses in the THz region with a refractive index of 3.42, which is larger than that of most pharmaceutical solids.

the different layers of an optically thick sample, such as a coated tablet, are of interest (Pickwell and Wallace, 2006; Shen and Taday 2008). The source and detector used for reflection THz-TDS are the same as those used for transmission measurements. The main differences lie in the geometry of the parabolic mirrors used to focus the THz radiation onto the sample, the reference measurement of a perfectly reflecting sample (usually a metallic

mirror), and in the analysis of the resulting spectra. Reflection THz systems are mostly used for imaging applications, and will be discussed in more detail in Section 20.3.1.

Another technique that can be used to measure pharmaceutical materials is attenuated total reflection (ATR) THz-TDS (Fig. 20.3b). The core component in ATR configuration is a Dove prism, which is usually made of high-resistivity silicon because of its high refractive index, low dispersion and transmission loss. When the incident angle of THz beam is greater than the critical angle, total internal reflection occurs, resulting in an evanescent THz field that penetrates above the upper surface of the prism, where it interacts with the sample. The dielectric properties of the sample could be determined from the difference between the THz signal measured with and without the presence of the sample. ATR configuration can provide reliable THz spectra of solid samples, provided that adequate pressure is applied to remove possible air gaps between the sample and the surface of the prism. The ATR technique requires small amounts of sample and no sample preparation, and thus it provides a simplified method for the collection of THz spectra, ideal for the rapid screening of pharmaceutical samples (Newnham and Taday, 2008).

Generally speaking, terahertz pulsed spectroscopy (TPS) transmission measurement provides quantitative THz spectra, whilst THz-ATR measurement is most suitable for rapid screening many samples. In addition, a waveguide configuration could be used to obtain a sharper spectral signature (Laman *et al.*, 2008), although one has to prepare an ordered polycrystalline film on the metal plate which forms part of the waveguide.

20.2.2 Sample preparation and data analysis

In transmission THz-TDS measurements, the transient THz electric field, $E(t)$, is measured in time-domain as a function of the time delay between the THz pulse and the probing optical pulses. Fourier transform of $E(t)$ gives the electric field component in the frequency domain $E(v) = A(v)e^{j\phi(v)}$, where $A(v)$ is the amplitude and $\phi(v)$ is the phase. To avoid complications in data analysis, usually measurements are conducted on both a sample and a reference. In the simplest transmission experiment, where air is used for the reference measurement, one would have the following equation (Fischer *et al.*, 2005):

$$\frac{E_s(v)}{E_r(v)} = T(n) \exp \left(-\frac{\alpha(v)d}{2} + j \frac{(n(v)-1)d}{c} 2\pi v \right) \quad [20.1]$$

where the subscripts s and r represent the sample and the reference, respectively, and d is the sample thickness, ν is the frequency of the radiation, c is the speed of light in vacuum, and $T(n) = \frac{4n(\nu)}{(n(\nu)+1)^2}$ is a factor which accounts for refection losses at the sample surfaces. Both the refractive index $n(\nu)$, and the power absorption coefficient $\alpha(\nu)$, can be derived as:

$$n(\nu) = 1 + \frac{c}{2\pi\nu d} (\phi_s(\nu) - \phi_r(\nu)) \quad [20.2]$$

$$\alpha(\nu) = -\frac{2}{d} \ln \left(\frac{1}{T(n)} \left| \frac{E_s(\nu)}{E_r(\nu)} \right| \right) \quad [20.3]$$

Most pharmaceutical materials of interest are granulated powder samples. As compared with NIR and mid-IR spectroscopy, THz spectroscopy utilises a much longer wavelength and is thus less prone to scattering by micrometer-sized particles. Nevertheless, the effect of scattering on THz-TDS measurements cannot be ignored, particularly for granulated materials with particle size comparable to the wavelength of the THz radiation (Wu *et al.*, 2007; Shen *et al.*, 2008). In order to obtain high-quality and reliable THz spectra, the granulated material should be ground using a pestle and mortar to reduce particle size; the resulting fine powder is then usually mixed with polyethylene (PE) fine powder, and finally compressed into a pellet for acquiring THz spectrum.

High-density PE is a good binding material and is nearly transparent, with a frequency-independent refraction index of 1.53 in THz region (Walther *et al.*, 2003). A circular pellet of about 3 mm thickness and 13 mm diameter usually provides acceptable THz spectra for most pharmaceutical powder samples. A pellet with a thickness of larger than 3 mm has the advantage of preventing the acquisition of multiple reflections of the THz pulse, which would lead to etaloning artefact in the recorded spectra (Strachan *et al.*, 2004; Zeitler *et al.*, 2005). For quantitative spectroscopy measurement, both the reference pellet (containing 360 mg PE powder) and the sample pellets (containing a mixture of 40 mg sample powder and 360 mg PE powder) should be prepared and measured under the same condition. The thickness of the reference and sample pellets should be recorded both before and after the THz-TDS measurement, together with the compression force used to prepare the pellet. Usually a compression force of two-tons provides good quality pellets for THz spectroscopy measurement, and it was found

that this compression force did not induce any polymorphic change in the sample (Strachan *et al.*, 2004).

The THz pulse transmitted through the sample and the reference pellets experienced different amount of dispersion and absorption. The electric field component in the frequency domain $E(v)$ can be expressed as:

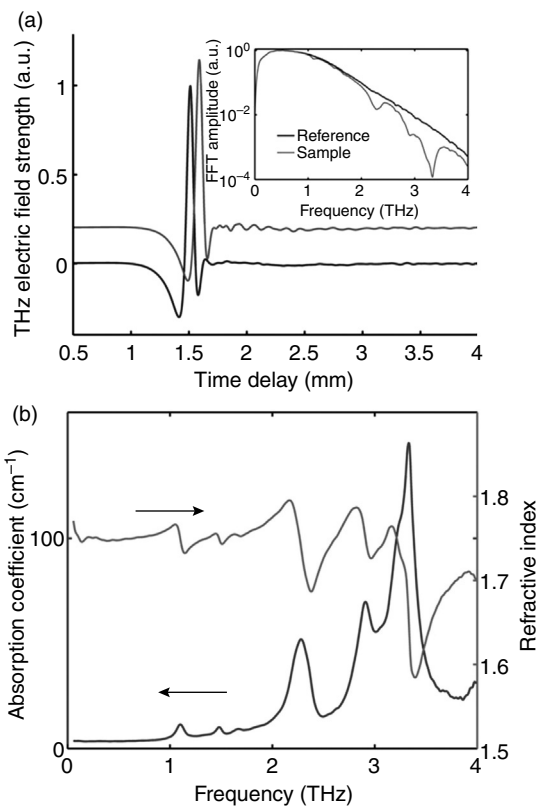
$$E_r(v) = E_0(v) \frac{4\tilde{n}_r}{(\tilde{n}_r + 1)^2} \exp\left(-\frac{(\alpha d)_r}{2} + j \frac{(nd)_r + d_{rs}}{c} 2\pi v\right) \quad [20.4]$$

$$E_s(v) = E_0(v) \frac{4\tilde{n}_s}{(\tilde{n}_s + 1)^2} \exp\left(-\frac{(\alpha d)_s + (\alpha d)_r}{2} + j \frac{(nd)_r + (nd)_s}{c} 2\pi v\right) \quad [20.5]$$

where d_{rs} is the thickness difference between the reference and sample pellet, and \tilde{n}_r and \tilde{n}_s are the effective refractive indices of the reference and the sample pellets, respectively. The absorbance $(\alpha d)_r$ is defined as the product of the absorption coefficient and the thickness of the pellet. Note that the sample pellet is made from a mixture of sample and PE powders. Therefore the $(\alpha d)_s$ and $(\alpha d)_r$ in Equation [20.5] should be understood as the THz absorbances introduced by the sample powder and the PE powder within the sample pellet, respectively. Similarly, the $(nd)_s$ and $(nd)_r$ in Equation [20.5] should be understood as the optical path lengths introduced by, respectively, the sample powder and the PE powder within the sample pellet. In this way, the refractive index $n(v)$ and the power absorption coefficient $\alpha(v)$ of the sample can still be calculated using Equations [20.2] and [20.3], where the factor which accounts for refection losses has the form:

$$T'(n) = \frac{\tilde{n}_s (\tilde{n}_r + 1)^2}{\tilde{n}_r (\tilde{n}_s + 1)^2}.$$

Figure 20.4a shows typical THz waveforms measured after transmission through a reference pellet and a sample pellet, respectively. The measurement was done at room temperature. The reference pellet contains 360 mg pure PE powder, whilst the sample pellet contains a mixture of 360 mg PE filler material and 40 mg mannitol powder. There are ripple-like features in the THz waveform of the sample pellet, and these features were caused by the resonant absorption of the sample. The inset of Fig. 20.4a shows the corresponding fast Fourier transform (FFT) amplitude, where characteristic spectral dips at 1.1, 1.5, 2.3, 2.9 and 3.3 THz are clearly visible in the sample FFT amplitude. The coherent-detection scheme used in THZ-TDs allows both the absorption coefficient and the refractive index to be determined



20.4 (a) THz waveforms measured after propagating through a sample pellet (360 mg PE and 40 mg mannitol) and a reference pellet (360 mg PE). The inset shows their corresponding FFT amplitude. (b) The extracted absorption coefficient and the refractive index of the mannitol sample.

without the need to apply the Kramers-Kronig dispersion relationship. Figure 20.4b shows the extracted absorption coefficient and the extracted refractive index spectra of the mannitol sample.

Note that the thicknesses of the sample and reference pellet were used in the calculation of the absorption coefficient and the refractive index spectra. Each pellet was formed by compressing powder mixtures, and the compression force may affect the pellet thickness, thus the obtained refractive index and absorption coefficient. Furthermore, it is evident from the inset of Fig. 20.4a that the dynamic range, DR , defined as the strength of the reference signal with respect to the noise floor of the experiment, is frequency dependent. The highest absorbance that can be obtained is expressed as (Jepsen *et al.*, 2011)

$$(\alpha d)_{\max} = 2 \ln \left(DR \frac{4n_r}{(n_r + 1)^2} \right) \quad [20.6]$$

It is therefore important to check the frequency-dependent dynamic range of a specific measurement when reporting the obtained absorption coefficient of the sample. We note that a novel iterative algorithm could be used for accurate optical material parameter determination from THz-TDS measurement (Pupeza *et al.*, 2007).

20.3 Terahertz time-domain spectroscopy (THz-TDS): identification, quantification and analysis

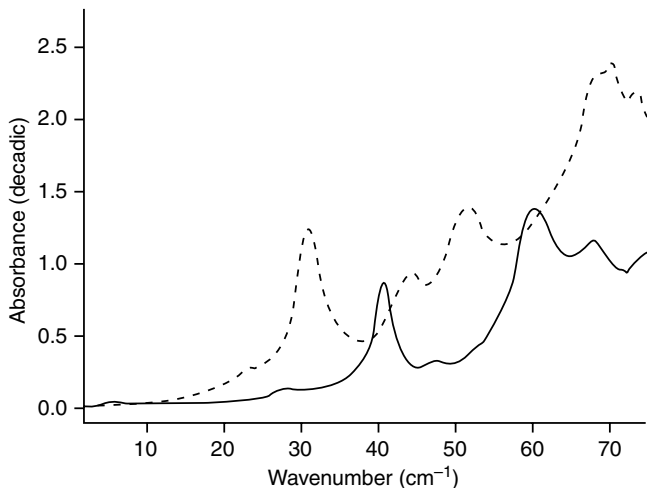
THz spectroscopy directly probes the lattice phonon modes that is ideal for quantitative characterisation of crystalline pharmaceuticals such as polymorphs and hydrates.

20.3.1 Identification and quantification of polymorphs and hydrates

Polymorphs discrimination

Crystal polymorphs are defined as substances that are chemically identical but exist in more than one crystal form. Polymorphism is of particular importance in the pharmaceutical industry, as many APIs receive regulatory approval only for a single crystal form or polymorph. Furthermore, polymorphism in drugs can affect such physicochemical properties as dissolution rate, solubility, bioavailability and manufacturability (Brittain, 2007). The detection of polymorphs in the drug discovery and manufacturing process is thus very important for quality control and assurance.

The first application of THz-TDS for polymorph discrimination was reported by Taday *et al.*, (2003), where two different polymorphs of ranitidine hydrochloride could be readily discriminated using their THz spectra. Strachan *et al.*, (2004) studied a number of pharmaceutical compounds, and found that the different polymorphic forms of carbamazepine (CBZ) exhibit distinct THz absorbance spectra (Fig. 20.5). Absorption features within the mid-IR region are dominated by intra-molecular vibrations of sample molecules. In contrast, absorption features in THz region are dominated by inter-molecular vibrations, corresponding to motions associated with coherent, delocalised movements of large numbers of atoms and molecules (Walther *et al.*, 2003; Day *et al.*, 2006). Such collective phonon modes only exist in materials with periodic structure. A consequence of this is that crystalline



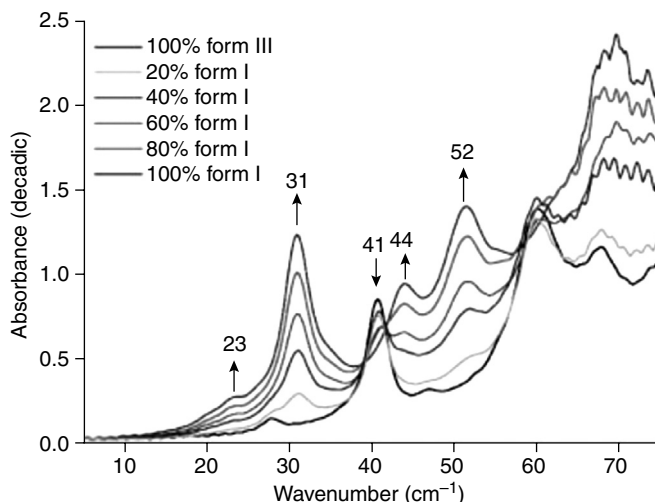
20.5 THz absorbance spectra of CBZ form III (solid line) and form I (dashed line). The sample pellet contains a mixture of 50% CBZ w/w in PE. (Reproduced from Strachan *et al.*, 2004.)

samples have distinct THz spectra, whilst amorphous materials are too disordered to sustain phonon modes, hence are relatively transparent in the THz spectral region. It was indeed found that in contrast to crystalline indomethacin, which has spectral signatures, amorphous indomethacin shows no sharp absorption feature (Strachan *et al.*, 2004).

In other studies, Zeitler *et al.* (2006a) reported that all five known polymorphs of sulfathiazole were readily distinguished by their THz spectra. Ge *et al.* (2009) observed distinct THz absorption features for all five forms of the modified furosemide and one commercial product. The recent work by Ikeda *et al.* (2010) and Chakkittakandy *et al.* (2010) also concludes that THz spectroscopy is a particularly useful and effective tool for characterising crystalline pharmaceuticals as it probes the lattice phonon modes directly.

Hydrates analysis

Not only can the THz spectrum be used to distinguish between different polymorphic forms, but it can also be used to differentiate between different hydrate forms. It was found that THz spectroscopy is able to discriminate between different lactose hydrates (Zeitler *et al.*, 2006b), theophylline monohydrate and its anhydrous forms (Upadhyay *et al.*, 2006; Liu *et al.*, 2007; Balbuena *et al.*, 2008), anhydrous and hydrate forms of ampicillin, D-glucose (Liu *et al.*, 2007), and the anhydrous and monohydrate caffeine molecules and crystals (Liu *et al.*, 2007; Balbuena *et al.*, 2008). Recently, THz spectroscopy was also used to characterise ceftazidime and its generic versions



20.6 THz pulsed spectra of binary mixture of CBZ forms I and III (20% intervals, 0 to 100% form I). The arrows indicate spectra changes as form III concentration decreases and form I concentration increases. Each spectrum is the average of three spectra (from three independent samples) that were smoothed using the Savitzky–Golay algorithm to remove etaloning artefacts (13 smoothing points). (Reproduced from Strachan *et al.*, 2005.)

(Kawase *et al.*, 2009). THz results show small, but significant, difference in the states of ceftazidime hydrate between the original and generic versions. It was concluded that THz spectroscopy can be used to evaluate the stability of medicines, as well as to monitor/control their quality.

Pharmaceutical quantification

As summarised in a recent review paper (Shen, 2011), many pharmaceutical polymorphs and hydrates have distinct THz spectral features. These crystal ‘fingerprints’ could be used for quantitative evaluation of pharmaceuticals. Strachan *et al.* (2004, 2005) demonstrated that not only could the different polymorphs be qualitatively discriminated from each other using their unique THz spectral feature, but each compound of a pharmaceutical mixture could also be quantified using chemometric methods (Fig. 20.6). The limits of detection achieved for carbamazepine form III, enalapril maleate form II and crystalline fenoprofen calcium were 1.23% w/w, 0.69% w/w and 2.69% w/w, respectively. In a similar study, Nishikiori *et al.* (2008) reported that DL-tartaric acid and its enantiomers (L- and D-tartaric acid) have different absorption features and this allows L-tartaric acid in L- and DL-tartaric acid mixture to be quantified. Wu *et al.*, (2008) demonstrated the feasibility of integrating THz spectroscopy and chemometrics for the

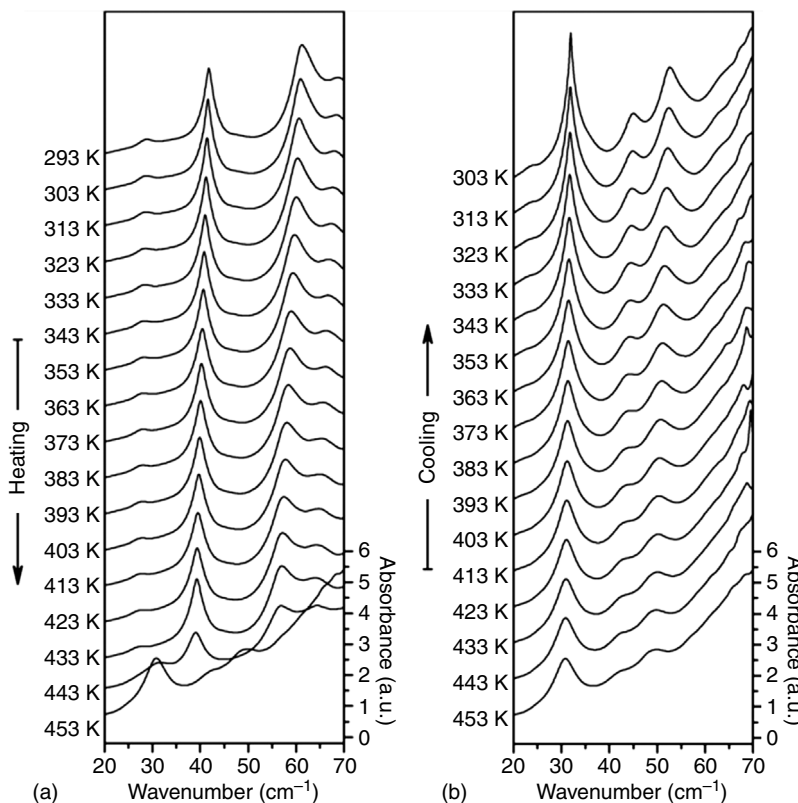
purpose of quantifying pharmaceutical tablet concentrations. Otsuka *et al.* (2010) reported that the two forms of mefenamic acid have distinct THz spectra, and this allows the amount of form I and II to be quantified using a chemometric model based on the partial least squares method. All these results demonstrated the feasibility of using THz-TDS, in combination with chemometrics, for quantifying pharmaceuticals. However, most of these studies used purposely prepared samples and the validation of THz-TDS for quantifying the amount of APIs in real world solid dosage forms are yet to be published.

20.3.2 Analysis of solid phase transformation

Solid phase transformations proceed directly from one solid-state form to the other, without any intermediate liquid phases. They may occur during any stage of pharmaceutical processing and upon storage of a solid dosage form. Early detection and quantification of these transformations is important, since the physical form of an API can significantly influence its processing behaviour and biopharmaceutical properties such as solubility, dissolution rate and bioavailability (Aaltonen *et al.*, 2008; Heinz *et al.*, 2009a, 2009b).

The first study to use temperature-dependent THz-TDS to characterise the solid phase transformation of the pharmaceutical crystal was reported by Zeitler *et al.* (2005). Figure 20.7 shows the THz spectra measured during the heating (from 293 K to 433 K) and cooling (from 453 K to 303 K) of the carbamazepine sample. It was found that the solid-state transformation of carbamazepine form III to form I was reversible. In a further study, Zeitler *et al.*, (2007c) studied *in situ* the relaxation and crystallisation of amorphous carbamazepine using a variable temperature THz-TDS. Even though THz spectra of disordered materials in the glassy state exhibit no distinct spectral features, the crystallisation leads to distinct spectral features allowing the crystallisation and the subsequent polymorphic phase transition at higher temperature to be studied in detail. Other phase transition processes studied using THz-TDS include sulfathiazole (Zeitler *et al.*, 2006a, 2006b) and theophylline (Upadhyay *et al.*, 2006). Liu and Zhang (2006) used THz-TDS to characterise the dehydration kinetics of polycrystalline hydrates. The dehydration kinetics was found to obey the contracting area equation of the solid-state reaction.

Nguyen *et al.* (2007) applied THz-TDS for quantitative monitoring of dynamic process of cocrystal formation (formed mechanochemically by grinding together phenazine and mesaconic acid). Limwikrant *et al.* (2009) used THz-TDS for the characterisation of ofloxacin-oxalic acid complex. The distinctive THz spectra showed that the vibrational modes of the complex are different from those of the starting materials, suggesting that THz-TDS



20.7 THz absorption spectra of CBZ form III during the temperature dependent measurements. The plots are offset in absorbance for clarity. (a) Heating from 293 K to 453 K, transformation of form III to I takes place. (b) Cooling the transformed sample of CBZ form I from 453 to 303 K. (Reproduced from Zeitler *et al.*, 2005.)

is an alternative tool to evaluate complex formations through weak interactions. All these studies demonstrated that THz-TDS is an effective new tool to characterise the kinetics of solid phase transformation.

The photon energy of THz radiation is in the range of a few meV (one thousand times smaller than that of UV light and one million times smaller than that of X-ray). This makes TPS intrinsically safe to use, because no photochemical effect is expected at such a low energy level. However, the precise modelling and assignment of the corresponding vibration modes with such a low energy is extremely challenging, because one has to take into consideration all the weak yet complex intermolecular interactions in crystalline materials. Consequently, a detailed interpretation of the spectral changes that occurred during conversion of the respective API is rather difficult. Nevertheless, a number of groups have begun to attempt to interpret/

assign the spectral features observed in the THz region (Allis *et al.*, 2006; Day *et al.*, 2006; Jepsen and Clark, 2007; Balbuena *et al.*, 2008; Hakey *et al.*, 2009; Heinz *et al.*, 2009a; Hooper *et al.*, 2009; Li *et al.*, 2010). With improvements in computer power and the further development of coding that can readily handle more complex systems, such as unit cells and many-molecule problems, a full understanding of the spectral changes observed in variable temperature TPS will be possible. This in turn will have a significant impact in improving the ultimate understanding of pharmaceutical materials, formulations and processes.

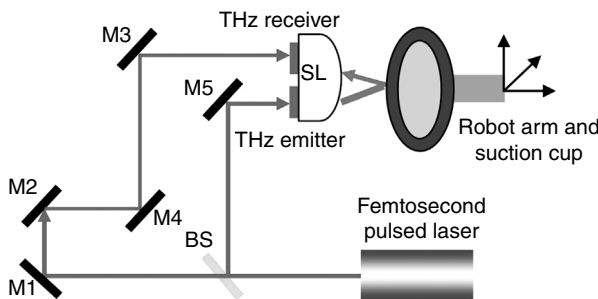
20.4 Terahertz time-domain imaging (THz-TDI): imaging set-up and analysis

The ability to generate THz radiation from a point source coupled with the fact that many pharmaceutical excipients are semitransparent in this region has resulted in the development of imaging systems capable of non-destructive, three-dimensional investigations of solid dosage forms. In this chapter, we will first describe the THz imaging set-up, followed by how to construct various THz images from the measured THz signal, and finally a few examples of its applications in the context of pharmaceutical sector.

20.4.1 Imaging set-up

Like THz spectroscopy system, the THz time-domain imaging (THz-TDI) system employs the same core technology for coherent generation and detection of short pulses of broadband THz radiation. As shown in Fig. 20.8, a beam splitter separated the NIR light into two beams: an excitation beam and a probe beam. THz pulses emitted from a biased photoconductive THz emitter antenna were collimated and focused onto the sample by a silicon lens system. The reflected and backscattered THz pulses are then collected and focused, using the same silicon lens system, onto an *unbiased* photoconductive THz receiver antenna for laser-gated THz detection. For THz imaging measurement, THz waveform is taken at many points mapped over the whole surface of a sample, and at each pixel an entire THz waveform is recorded as a function of time delay using a variable delay stage. Thus THz-TDI provides three-dimensional information: the x- and y-axis describe vertical and horizontal dimensions of the sample and the z-axis represents the time delay (depth) dimension. In addition, Fourier transform of the measured time-domain THz waveform provides THz spectral information in the frequency dimension (the fourth dimension), which could then be used to map out the chemical distribution of a specific pharmaceutical of a sample.

Most pharmaceutical tablets have a curved surface. In order to image these whole tablet samples, a six-axis robot system was employed (Zeitler *et al.*,

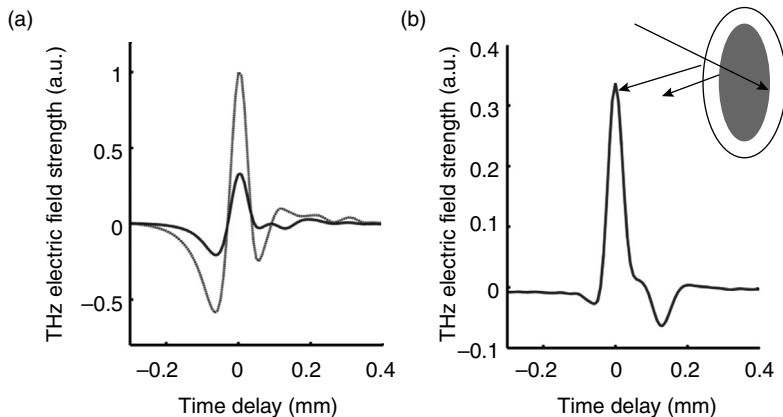


20.8 Schematic diagram of a THz time-domain imaging (THz-TDI) system. SL: silicon lens system; BS: beam splitter; M1–M5: metallic mirrors. Both the THz emitter and detector were directly attached to a specially designed silicon lens system. This minimises the THz path length in free space thus nitrogen purging is no longer required during the measurement. A six-axis robot system was used to move the sample according to a pre-generated surface model, ensuring that the sample is always at the THz focus position with sample surface always perpendicular to the THz probe beam throughout the measurement. (Reproduced from Shen, 2011.)

2007a; Shen and Taday, 2008). In this specific THz-TDS system (TPIimaga, 2000; TeraView Ltd, Cambridge, UK), a laser gauge employing a visible laser beam with a wavelength of 670 nm was used to precisely model the surface shape/curvature of the tablet under investigation. The generated surface model was subsequently used for THz imaging measurement. This ensures that the sample is always at the THz focus position with sample surface always perpendicular to the THz probe beam throughout the imaging process. Consequently, no sample preparation is required, and most pharmaceutical solid dosage forms with common shapes and surface curvatures can be imaged using this commercial product (Zeitler *et al.*, 2007a). Furthermore, both the THz emitter and detector antennas were directly attached to a specially designed silicon lens system (Fig. 20.8). As the distance between the THz lens and the sample is less than 8 mm, the effects of water vapour absorption were significantly reduced. Consequently, no nitrogen purging is necessary during THz-TPI measurement, and this greatly simplifies THz-TDI measurements.

20.4.2 Data analysis and interpretation

A THz pulse incident on a tablet surface penetrates through different coating layers. At each interface or abrupt change in refractive index, a portion of the THz pulse is reflected back to the detector. By measuring the arrival time of these surface and interface reflections, structural information such as layer thickness can be determined. This provides the contrast mechanism



20.9 (a) A typical raw THz waveform measured for a single-layer coated tablet (solid line) and a reference mirror (grey line). (b) The processed THz waveform where the surface reflection and the interface reflection features are clearly distinguishable. The coating layer thickness is directly calculated as the time delay between the surface reflection and interface reflection (divided by the refractive index of the coating). The inset shows schematically how THz pulse was reflected from the surface and interface of a tablet.

to map the drug and interfaces from different coating layers or subsurface structures within the tablet.

The measured raw THz waveform (Fig. 20.9a) is the convolution of the sample response and the system response of the instrument used, making the data interpretation difficult. In order to obtain the true sample response $E_{\text{THz}}(t)$, a deconvolution process was used to remove the instrument response. The deconvolution is performed by dividing, in the frequency domain, the raw THz waveform measured from the sample by a reference waveform recorded from a reference surface (usually a metal mirror) as follows:

$$E_{\text{THz}}(t) = \text{FFT}^{-1} \left\{ \frac{E_s(v)}{E_r(v)} S_{\text{filter}}(v) \right\} \quad [20.7]$$

where $S_{\text{filter}}(v)$ is a numerical band pass filter which is used to remove high- and low-frequency noise; $E_s(v)$ and $E_r(v)$ is the Fourier transform of the raw THz waveform measured from a sample and a mirror reference, respectively. Figure 20.9b shows a typical processed THz waveform recorded from a coated tablet. The data interpretation of this processed THz waveform becomes straightforward and intuitive. The maximum at 0.0 mm is due to the THz reflection at the tablet surface (air/coating interface).

The second peak at 0.13 mm arises from the THz reflection at the coating/core interface. The formation of a negative reflection peak at around 0.13 mm indicates the decrease in the refractive index at the transition from the tablet coating to the tablet core. Coating thickness of the sample could be determined by simply measuring the arrival time difference of these two THz pulses.

In order to determine the absolute layer thickness, one needs to know precisely the value of the refractive index of each layer. This can be accomplished by establishing a THz spectrum library of all pharmaceutical ingredients and excipients of interest, using THz-TDS as discussed in Section 20.2.2. Alternatively, the refractive index values can be extracted from the measured THz waveform, through the following analysis. For illustration purpose, we assume: (1) the sample has a single coating layer; (2) the multiple reflections within the coating layer is negligible (which is valid for most tablet coating and core materials). Under normal incident condition, the reflection coefficient (defined as the ratio of the electric field of the incident and reflected THz radiation) can be expressed as (Shen and Taday, 2008):

$$\frac{E_s(v)}{E_r(v)} = \Gamma_1(v) + \Gamma_2(v) \cdot \exp(-j2\beta D) \quad [20.8]$$

In the above equation, the first item is the THz reflection at the sample surface whilst the second item represents the THz reflection at the coating/core interface. $\beta(v) = 2\pi v \sqrt{\epsilon_1(v)} / c$ is the propagation constant and D is the layer thickness. If we limit the analysis to sample materials with low absorption coefficient (i.e., $\sqrt{\epsilon(v)} \approx n(v)$) then the Fresnel transmission coefficients are real-valued. In this case, the refractive index of the first coating layer (n_1) can be simply estimated as: $n_1 = (1 + \Gamma_{10}) / (1 - \Gamma_{10})$ where Γ_{10} is the peak intensity of the THz surface reflection. The refractive index of the inner layer (n_2) can also be determined in a similar manner as: $n_2 = n_1 [(1 + r'_2 / 1 - r'_2)]$ where $r'_2 = \Gamma_{20} [(1 + n_1)^2 / 4n_1]$ and Γ_{20} is the peak intensity of the THz reflection at the coating/core interface.

For the THz waveform shown in Fig. 20.9b, $\Gamma_{10} = 0.34$ and $\Gamma_{20} = 0.063$. Consequently, the refractive indices value of the coating and the core were calculated to be 2.01 and 1.73, respectively, and the layer thickness was determined to be 66 μm . Maps of coating thickness could be obtained by repeating the same calculation at each measurement point. This can be done not only for the top coating layer, but also for any subsequent sub-surface layers within the products.

Apart from coating thickness, other THz parameters such as peak intensity Γ_{10} (which is related to the refractive index of the coating, that is, surface

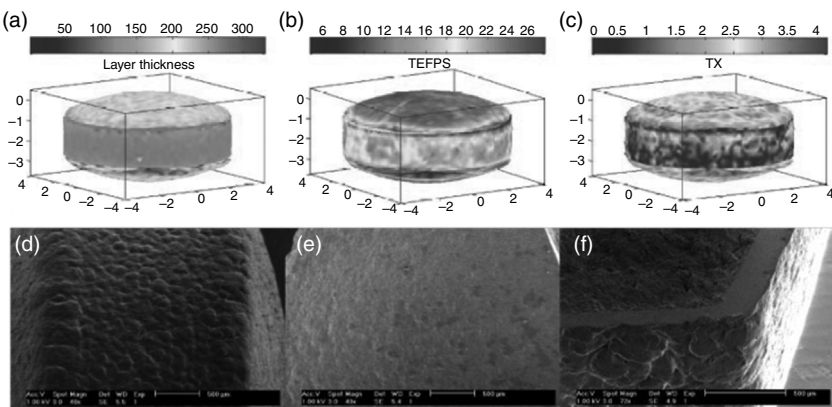
hardness or density) and interface index Γ_{20} (which is related to changes of the refractive index at the coating/core interface) can also be extracted from the same THz waveform. It was found that all these physico-chemical properties of the coating are closely correlated to the tablet dissolution performance (Ho *et al.*, 2009b, 2009c, 2010).

20.4.3 Analysis of tablet and coating properties

Despite the on-going development of more sophisticated solid drug delivery systems, the tablet remains the single most important solid dosage form that is used to administer drugs to a patient. It is the dosage form of choice, because it combines reproducible drug dosage, high stability during storage, and can be economically produced (Wagh *et al.*, 2009). Perhaps more importantly, pharmaceutical tablet coating could be conveniently applied to control the release of API molecules in the human body. For example, enteric coating is used to protect the API against degradation in the stomach and sustained-release coating is used to obtain an optimum release profile, and hence a desirable API absorption rate (Jantzen and Robinson, 2002). The quality of these functional tablet coatings will thus have direct implications on product performance. It is therefore of great interest to characterise coating properties including *coating thickness* and *coating uniformity* as well as tablet properties including *tablet density* and *surface hardness*, for the purposes of quality control and quality assurance.

Coating thickness and uniformity

In a proof-of-principle work, Fitzgerald *et al.* (2005) studied coated pharmaceutical tablets using a table-top THz imaging system. It was found that the coating thickness of the sugar-coated tablets could be determined quantitatively and non-destructively. Using a commercial THz-TDS system, Zeitler *et al.* (2007a) reported that coating thickness and uniformity could be readily obtained for a wide range of commercially available pharmaceutical dosage forms such as film-coated tablets, controlled-release tablets and soft gelatin capsules. In other studies, THz imaging has been used for the analysis of coating thickness and uniformity of sustained-release tablets (Ho *et al.*, 2007), and for investigating the coating characteristics of push-pull osmotic systems (Malaterre *et al.*, 2009). All these studies concluded that THz-TDI could provide spatially resolved quantitative measurements of layer thickness through multiple film coating layers and detect weak spots on the coating that are not visible to the naked eye.



20.10 (a)–(c): Three-dimensional false colour images of a biconvex tablet were constructed using the coating thickness (a), THz electric field peak strength (TEFPS) (b) and interface index (c). The scales in the x, y and z directions are in mm. The coating layer thickness around the central band is much thinner than that on the surfaces of the tablet. The film coat on the central band also has a lower TEFPS and TII than the film coat on the top and bottom domain. The units for the colour scales are in microns for coating thickness (a) and % for both TEFPS (b) and interface index (c). (d)–(f): SEM images of the film coating on the tablet central band (d) and the top and bottom domain (e). Polymer droplet deposition on the surface of the central band (d) is visible, whilst the film coating surface on the top and bottom domain (e) is comparatively smooth. The tablet is slightly tilted in (f) to demonstrate the film coating surface roughness on the central band. The scale bar in the micrographs is 500 microns (reproduced from Ho *et al.*, 2010).

Because the THz-TDI measurement covers the whole tablet surface, aspects of coating defects along with their site, depth and size were identified with virtual THz cross-sections. As an example, Fig. 20.10a–c reveals the intra-tablet variation of coating layer thickness (the coating thickness around the central band was thinner than that on the tablet surfaces). This THz-TDI result was confirmed by scanning electron microscopy (SEM) studies on the same batch of tablets (Fig. 20.10d–f) (Ho *et al.*, 2010). This intra-tablet variation of coating thickness, revealed non-destructively by THz-TDI, is of particular significance. In development of film coating technology, weight gain data during coating are widely used by pharmaceutical industry, and it is assumed that a uniform distribution of the film exists over the whole surface of the tablet and across the whole batch of tablets. The THz-TDI results, validated by the destructive optical microscope and SEM analysis, demonstrated that this may not always be an appropriate assumption (Ho *et al.*, 2007, 2010).

Tablet density and hardness analysis

The ability to quantify the effect of compaction force on the refractive index of the solid oral dosage forms using THz-TDI was first investigated by Palermo *et al.* (2008). They were able to predict the density of compacted mixtures of four excipients by building a multivariate calibration model. Using the chemometric model, the density distribution over the surface of flat tablets was predicted from the THz-TDI maps. In a further study, May *et al.* (2009) studied the ‘hardness’ (crushing strength) of pharmaceutical tablets by using THz-TDI. They observed radically symmetric spatial distributions in tablet density that were attributed to the shape of the punch used in the tablet manufacture. The THz results were found to be in agreement with those from diametric compression tests as well as finite element analysis (FEA) simulations. It was concluded that TPI has an advantage over the traditional diametric compression test (Hoag *et al.*, 2008), which is destructive in nature and provides no spatial distribution information of the tensile strength of the tablet under study. In a related study, Juuti *et al.* (2009) investigated the surface roughness and bulk properties of starch acetate tablets. It was found that the time delay of the THz pulses transmitted through a tablet are correlated with the porosity of the tablet across a range of compression pressure. All these results suggest that THz-TPI is suitable for characterising tablet bulk properties non-destructively.

Tablet performance

One of the key steps for quality control in pharmaceutical industry is the determination of the dissolution profile of drug tablets. Currently, wet dissolution testing has to be performed and this is often a lengthy and costly process. Efforts have been made to implement less costly and time-consuming methods in order to determine or predict dissolution performance of tablets (Zannikosm *et al.*, 1991). Because THz-TDI experiment is non-destructive in nature, it is possible to perform dissolution testing on the same tablet samples that are used for the coating thickness determination.

In a study by Spencer (2008), the mean dissolution time (MDT) was found to correlate with the coating thickness of enteric-layer coated tablets. Ho *et al.* (2008) investigated the potential of using THz data to predict the dissolution performance of sustained-release tablets from lab- and pilot-scale batches. The correlation between coating thickness and MDT was found to be very clear and much stronger than in the study by Spencer *et al.* (2008). In addition, the authors found that the change in coating density is also a good indicator of the dissolution performance of the coated tablet. In a further study by Ho *et al.* (2009b), the whole THz waveform, rather than the derived

coating thickness and coating density, was used to predict the tablet dissolution performance. Using a two-component partial least squares model, it was possible to predict the MDT of the corresponding *in vitro* dissolution whilst the tablets were still intact.

All these results strongly suggest that THz-TDI has potential to be employed as a process analytical tool to probe film uniformity during film coating development and to assess/predict the dissolution performance of the final product. The speed and ease of THz-TDI measurement may make it an attractive replacement for wet dissolution testing, both in product development and eventually for process analysis. However, it was acknowledged that the delayed-release system was very complex and the coating thickness, coating uniformity and density were only a few factors contributing to the dissolution performance amongst others (Ho *et al.*, 2009c).

20.5 Terahertz time-domain imaging (THz-TDI): process monitoring, spectroscopic imaging and chemical mapping

THz-TDI has also been demonstrated as a useful tool for monitoring of the pharmaceutical manufacturing process. In this chapter, we will first discuss its applications for off-line and online monitoring of tablet coating process of film-coated tablets, followed by a detailed discussion on its future prospects for spectroscopic imaging and chemical mapping.

20.5.1 Pharmaceutical process monitoring

Tablet film coating is a pharmaceutical unit operation modifying simple compressed tablets. Tablets are coated to improve their aesthetic appeal, to mask an odour, to disguise the taste, to improve drug stability, or most importantly to achieve a modified drug release profile (Cole, 1995). Slight changes in the coating equipment and coating parameters may cause variations in the physico-chemical properties of the film and may consequently compromise the coating quality (Porter, 2000; Ho *et al.*, 2009a). Monitoring and controlling coating quality is thus important to prevent output risks including batch reprocessing and reject, or even product recall.

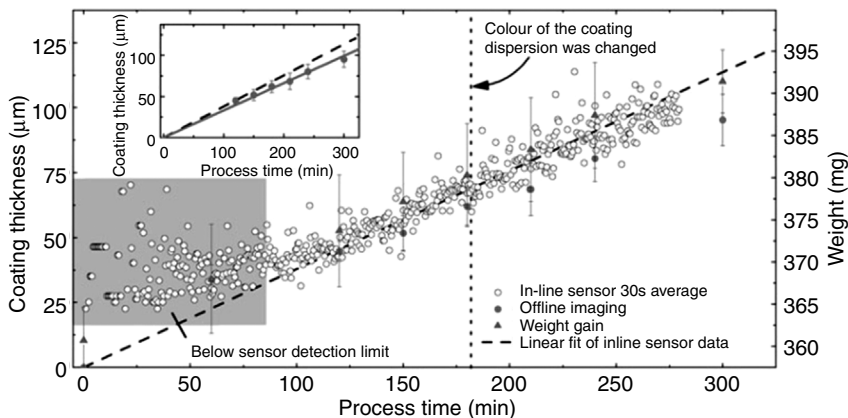
Coating process monitoring – offline

Ho *et al.* (2009a) investigated the ability of THz imaging as an analytical tool for monitoring a film coating unit operation and for assessing the success of a subsequent process scale-up. They found that the coating thickness extracted from non-destructive THz measurement increases

with the amount of polymer applied. However, it was shown that the coating thickness and coating density extracted from THz measurement were more informative on the product quality when compared with the amount of polymer applied. Whilst the coating layer thickness was the governing factor of the subsequent dissolution behaviour for monitoring a specific film coating unit operation, differences in the film coating density showed a more prominent effect on dissolution during process scale-up (Ho *et al.*, 2009a). In other studies, THz imaging was used for the monitoring of the coating process of film-coated tablets, and its results were compared with NIR spectroscopy (Cogdill *et al.*, 2007), NIR imaging (Maurer and Leuenberger, 2009) and NIR optical coherency tomography (Zhong *et al.*, 2011). NIR imaging proved to be better for resolving thinner coating layers and had a higher spatial resolution, whereas THz-TDI had the clear advantage that it provided *direct* thickness values, even for very *thick* coating layers.

Coating process monitoring – inline

Being able to monitor and control the coating process is highly desirable as it will improve manufacturing efficiency and improve the quality of the film coating. Optical sensors, including NIR and Raman spectroscopy, have been developed previously to monitor the coating operation and to determine the process endpoint (Kirsch and Drennen, 1996; Perez-Ramos *et al.*, 2005; El Hagrasny *et al.*, 2006). However, these optical techniques usually require a chemometric model to be built for each coating process and the established chemometric model may need to be recalibrated if either the coating material composition or coating process parameter changes. Recently, May *et al.* (2011) demonstrated for the first time that an inline THz sensor can be used to *directly* quantify the coating thickness of individual tablets in a production scale pan coater. Figure 20.11 shows a typical plot of coating thickness measured as a function of coating time over 300 min coating process, using the inline THz sensor. The coating thicknesses measured using the inline THz sensor, which requires no prior chemometric calibration model, agrees well with those measured using the reference offline THz-TDI method. The ability to measure the coating thickness distribution in the coating pan during process conditions without interfering with the coating process cannot be achieved using any of the currently available NIR or Raman sensor technology, as each measurement point acquired with these techniques inherently represents the temporal and spatial average over a large number of tablets compared to the single tablet measurements made using the THz sensor (May *et al.* (2011)). This exciting new sensor technology could have considerable impact in process understanding, process analytical technology (PAT) and quality-by-design (QbD) developments of film coating



20.11 Coating thickness measured by the inline THz sensor as a function of process time (open circles). For clarity, the measurements are subdivided into bins of 30 s duration and the data points correspond to the average thickness during each 30 s bin. The black dashed line indicates the trend line based on the linear fit over all inline data points above the sensor detection limit indicated in the figure by the shaded region. The filled circles correspond to the coating thickness as measured by the offline THz sensor. Each data point represents the average coating thickness over both surfaces of six tablets removed from the coating pan. The filled triangles indicate the average weight gain of 20 tablets. Before 80 min process time, the coating thickness was below the minimum resolution. After 180 min process time (indicated by the vertical dotted line), the colour of the coating dispersion was changed. Inset shows linear fit of the TPI offline measurements of the tablets after storage compared with the linear fit of the inline data. (Reproduced from May *et al.*, 2011.)

processes, although more research is required to assess the full potential of this new sensor technology.

Solvent diffusion in polymers

Solvent diffusion into polymers is central to their performance, for example as controlled delivery pharmaceutical products. Obradovic *et al.* (2007) studied the ability of THz-TDS to quantify the ingress of acetone into various polymer materials. By monitoring the reflections from the top and bottom surfaces of the discs, as well as the reflection from the interface between acetone-wet polymer and -dry polymer, they were able to quantify the liquid diffusion front as a function of time. In a separate study, Portieri *et al.* (2007) have investigated the hydration process of Hydroxypropyl Methyl Cellulose (HPMC) based coatings matrices. HPMC is a polymer commonly used in the production of tablets to control the release of the drug. A layer of hydrogel is formed by polymer hydration and chain relaxation when the

tablet coating is in contact with water. This layer represents a barrier that retards processes of further water uptake and of drug release. It was found that the shape and integrity of the gel layer formed after adding a drop of 10 µl water onto a HPMC tablet can be mapped using THz-TDI method. Both studies demonstrated that THz-TDI is a useful technique for monitoring the solvent diffusions in solvent and gel formation process.

20.5.2 Spectroscopic imaging and chemical mapping

Spectroscopic imaging and chemical mapping is an exciting new analytical advance that provides comprehensive information characterising complex heterogeneous samples. The basis of chemical mapping is the acquisition of a three-dimensional data set where two axes describe vertical and horizontal spatial dimensions, and the third axis represents the spectral frequency dimension. As aforementioned, many crystalline pharmaceuticals has distinct THz absorption features thus THz-TDI could be used for mapping the distribution of chemicals of a sample.

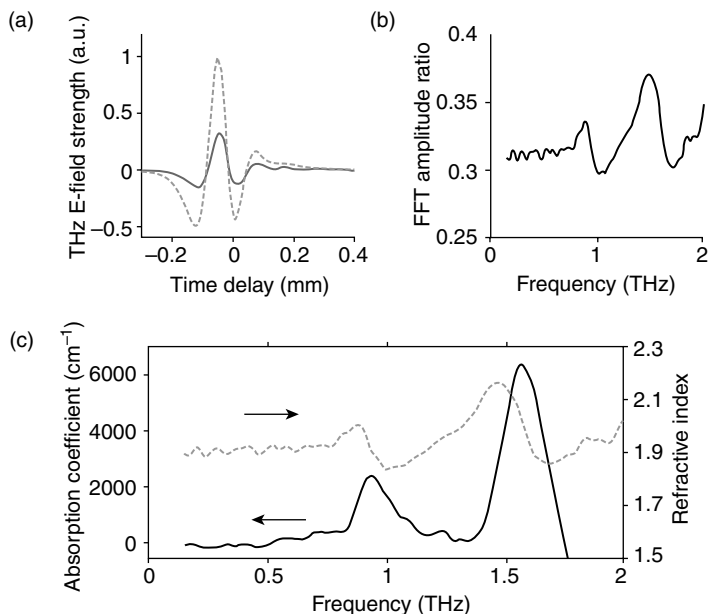
Reflection THz spectrum

Spectroscopic information can also be obtained in reflection THz-TDI measurement. The electric field of THz radiation reflected from a sample or reference was recorded in time-domain, and Fourier transforming the measured THz waveform provided THz spectral information. The absorption coefficient spectrum, $\alpha(v)$, and the refractive index spectrum, $n(v)$, were then calculated as follows:

$$\sqrt{\varepsilon} \equiv n(v) + j \frac{\alpha(v)c}{4\pi v} = \frac{1 - R(v)}{1 + R(v)} \quad [20.9]$$

$R(v) \equiv E_s(v)/E_M(v)$ is the frequency-dependent reflection coefficient, where $E_s(v)$ and $E_M(v)$ are the Fourier transform of the THz waveforms reflected/measured from a sample and a reference mirror, respectively. As an example, Fig. 20.12 shows typical THz waveforms measured for a sample and a reference mirror, together with the extracted absorption coefficient and refractive index spectra of the sample pellet made of theophylline crystalline powder.

It is worthwhile to note that reflection THz-TDS experiment requires a separate measurement on a reference mirror. In practice, it is difficult to place the reference mirror accurately at the same position of the sample. Whereas a small difference Δx between the sample and reference position is not problematic for transmission THz-TDS, for reflection THz-TDS it will introduce a

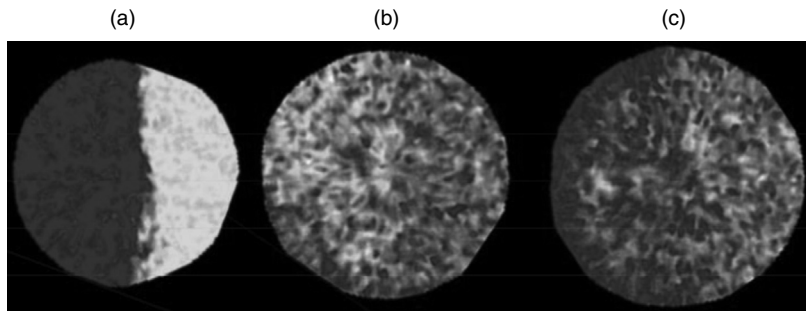


20.12 (a) A typical THz waveform measured for a sample pellet (solid dark line) and reference mirror (dashed light line), using reflection THz-TDI configuration. (b) The FFT amplitude of the sample waveform normalised with the FFT amplitude of the reference waveform. (c) The extracted absorption coefficient (lower curve) and refractive index (upper curve) spectrum of the sample pellet. The sample pellet used was made from pure anhydrous theophylline powder.

phase shift in the frequency-dependent reflection coefficient ($R' = R(\nu)e^{ik(\nu)2\Delta x}$). This leads to an additional slope on the phase difference (Jepsen, 2011). This artefact could be removed numerically by using, for example, a phase shift compensation method (Shen and Taday, 2008). It should also be pointed out that whilst a reflection THz-TDS measurement is suitable for characterising highly absorbing materials, there is still a limit on the highest absorbance that can be precisely determined from a reflection THz-TDS measurement (Jepsen and Fischer, 2005). Fortunately, the absorption coefficient of most pharmaceutical materials is well below the highest absorbance therefore they are measurable using reflection THz-TDS measurement.

Chemical mapping at sample surface

Once the absorption and refractive index spectra are determined, various spectral matching techniques can be used to generate chemical maps. If we define the THz spectrum measured for the sample material as the pixel spectrum $p(1:n)$, and the THz spectrum of a reference material as the target



20.13 Pseudocolour prediction images for the split tablets. The RGB maps have been scaled such that red (R), green (G) and blue (B) intensities are proportional to the concentration of theophylline, lactose and MCC, respectively. The tablet compositions are as follows (left: right): (0–1–0:0–0–1) (a), (3–2–5:5–3–2) (b), (3–5–2:5–3–2) (c). Off-colour domains in the lactose-MCC tablet (a) can be attributed to spectral noise and/or prediction error. Non-primary coloured domains (e.g., yellow, orange, purple) indicate regions of uniform mixtures where the size of domains for individual constituents is below the diffraction limit/ spatial resolution. (Reproduced from Cogdill *et al.*, 2006.)

spectrum $t(1:n)$, where n is the number of the data points of each THz spectrum, the similarity of the pixel spectrum and target spectrum can be calculated using Cosine Correlation Mapping (CCM) method (Schwarz and Staenz, 2001),

$$\cos(\theta) = \sum_{i=1}^n t_i p_i / \sqrt{\sum_{i=1}^n t_i^2} \sqrt{\sum_{i=1}^n p_i^2} \quad [20.10]$$

where θ is the angle between pixel spectrum and the target spectrum, and the value of $\cos(\theta)$ is between 0 and 1. The larger value of $\cos(\theta)$ indicates more similarity between the pixel and target spectra, thus the sample of interest is more like the reference material. The calculated $\cos(\theta)$ values were subsequently used to generate RGB maps. In this way, three different pharmaceuticals could be displayed in a single RGB map. Figure 20.13 shows an example RGB map obtained for tablets that were made by compressing a mixture of theophylline, lactose and microcrystalline cellulose (MCC) powders, where red (R), green (G) and blue (B) intensities are proportional to the concentration of theophylline, lactose and MCC (Cogdill., 2006). In other studies, reflection THz-TDI was used to obtain spatially resolved chemical maps of lactose and sucrose (Shen *et al.*, 2005a), and α -monohydrate and β -anhydrate lactose (Shen and Taday, 2008). Chemical sensing and imaging capability of THz imaging has also been demonstrated using a transmission configuration (Fischer *et al.*, 2005; Walther *et al.*, 2010).

These results conclude that THz-TDI can be used in conjunction with multiple chemometric tools for quantitative chemical mapping of crystalline pharmaceutical materials.

3D chemical mapping

One of the most desirable and promising applications of THz-TDI technology is perhaps the three-dimensional (3D) chemical mapping, because THz technology has the required chemical specificity and penetration capability. There are many potential applications of 3D chemical mapping in the context of pharmaceutical dosage forms: for example, investigating the spatial distribution of APIs inside a tablet after compact or coating, and API stability and moisture uptake during storage of a finished pharmaceutical product (Zeitler and Gladden, 2009). However, there has been very little work reported on 3D chemical mapping, possibly due to the difficulties associated with the spatialtemporal-spectral coupling of THz radiation and the very weak THz signal components that are characteristic to a specific chemical. Nevertheless, under favourable conditions, chemicals buried in a matrix could be detected and identified using their THz spectral signature (Shen *et al.*, 2005b). The method used to separate the structural and the chemical information is to calculate the spectrogram of the THz waveform using a time-partitioned Fourier transform method (Shen, 2005b; Shen and Taday, 2008). However, a full 3D chemical mapping functionality requires advanced technology capable of detecting, separating and recording the extremely weak signatures from the reflected and scattered THz pulses. More research is certainly necessary in order to realise the full potential of the 3D chemical mapping capability of THz-TDI technology.

20.6 Conclusions and future trends

Since the pioneering work by Grischkowsky in the late 1980s, THz technology has advanced considerably with both THz-TDS and THz-TDI instruments now commercially available. The availability of commercial THz products has opened up many exciting opportunities in pharmaceutical industry and science.

Over the past few years or so, THz spectroscopy has become established as a new tool for the physical characterisation of pharmaceutical drug materials and final solid dosage forms. THz spectroscopy has been shown to have a number of advantages: good quality THz waveform/spectrum can be acquired in a couple of milliseconds; as the THz power used is usually below 1 μW , orders of magnitude lower than that used in other techniques such as Raman spectroscopy, physical or chemical changes are unlikely

to be induced in the samples; the photon energy of THz radiation is one million times smaller than that of X-ray and one thousand times smaller than that of UV light; therefore, THz technology is safe to both the user and the sample under investigation. Furthermore, standard sampling techniques common for other vibrational spectroscopic techniques, including transmission, specular reflection, diffuse reflection and ATR, can be used in THz-TPS. This makes THz spectroscopy an effective tool for rapid discrimination and quantification of polymorphs/hydrates, and for analysis of solid form transformation dynamics, in both drug discovery and manufacture stages. However, at present, the interpretation of THz spectra, including the assignment of spectral modes, is rather difficult. This is because the corresponding phonon vibration modes involved in the THz transitions are intrinsically low energy and thus are extremely difficult to model accurately. With improvements in computer power and the further algorithm development, a full understanding and interpretation of the spectral features observed in THz region might be possible. This in turn will have a significant impact in improving the ultimate understanding of pharmaceutical materials, formulations and processes.

On the other hand, THz imaging has been demonstrated to be a useful tool for characterising pharmaceutical tablets and coatings non-destructively and quantitatively. Not only the coating thickness maps of a sample can be determined directly from THz-TDI measurement, but the tablet surface hardness and density maps (complex dielectric constant) can also be extracted from the recorded THz data. Furthermore, THz inline sensor for *direct* coating thickness measurement of individual tablets during coating process *in situ* and in *real-time* has also been demonstrated. THz technology has the advantages of being non-ionising, non-destructive, self-referenced and able to image at depth. However, the achieved lateral resolution, which is wavelength-dependent, is diffraction-limited to be 200 µm and the axial resolution is limited by the THz pulse duration to be 40 µm (Zeitler *et al.*, 2007a; Shen and Taday, 2008). Whilst THz imaging technology has acceptable spatial resolution for certain pharmaceutical applications, NIR and Raman imaging technology, which is more widely adopted by pharmaceutical industry, provide better spatial resolution.

The future THz technology will have to be cheap, as currently the cost of the instrument is prohibitive for many pharmaceutical applications. The recent development of THz quasi-time-domain spectroscopy (THz-QTDS) (Scheller and Koch, 2009) will hopefully boost the industry uptake of THz technology significantly in the near future. In addition, future THz technology will also have to be fast and cover a wider frequency range. The broad bandwidth will not only provide better spectral specificity for higher-resolution imaging and chemical mapping, but also will help to resolve thinner coating layer with higher spatial resolution. We believe THz spectroscopy and

imaging have significant potential to become industry standards for future pharmaceutical endeavours.

20.7 Acknowledgement

The authors acknowledge Mr Yue Dong and Ms Chen Li for preparing some of the figures.

20.8 References

- Aaltonen, J., Gordon, K.C., Strachan, C.J., and Rades, T., 2008. Perspectives in the use of spectroscopy to characterise pharmaceutical solids. *Int. J. Pharm.* **364**, 159–169.
- Allis, D.G., Prokhorova, D.A., Korter, T.M., 2006. Solid-state modeling of the terahertz spectrum of the high explosive HMX. *J. Phys. Chem. A* **110**, 1951–1959.
- Auston, D.H., Cheung, K.P., and Smith, P.R., 1984. Picosecond photoconducting hertzian dipoles. *Appl. Phys. Lett.* **45**, 284–286.
- Balbuena, P.B., Blocker, W., Dudek, R.M., Cabrales-Navarro, F.A., and Hirunsit, P., 2008. Vibrational spectra of anhydrous and monohydrated caffeine and theophylline molecules and crystals. *J. Phys. Chem. A* **112**, 10210–10219.
- Brittain, H.G., 2007. Polymorphism and solvatomorphism 2005. *J. Pharm. Sci.* **96**, 705–728.
- Chakkittakandy, R., Corver, J.A. and Planken, P.C., 2010. Terahertz spectroscopy to identify the polymorphs in freeze-dried mannitol. *J. Pharm. Sci.* **99**, 932–940.
- Chantry, G.W. 1971. *Submillimetre Spectroscopy; A Guide to the Theoretical and Experimental Physics of the Far Infrared*. First edition. Academic Press Inc.
- Cheville, R. A. and Grischkowsky, D., 1995. Far-infrared terahertz time-domain spectroscopy of flames. *Opt. Lett.* **20**, 1646–1648.
- Cogdill, R.P., Short, S.M., Forcht, R., Shi, Z., Shen, Y.C., Taday, P.F., Anderson, C.A., and Drennen, J. K., 2006. An efficient method-development strategy for quantitative chemical imaging using terahertz pulse spectroscopy. *J. Pharm. Innov.* **1**, 63–75.
- Cogdill, R.P., Shen, Y.C., Taday, P.F., Creekmore, J.R., Anderson, C.A., and Drennen III, J.K., 2007. Comparison of terahertz pulse imaging and near-infrared spectroscopy for rapid, non-destructive analysis of tablet coating thickness and uniformity. *J. Pharm. Innov.* **2**, 29–36.
- Cole, G.C., 1995. Introduction and overview of pharmaceutical coating. In: Cole, G., Hogan, J., Michael, A., editors. *Pharm. Coat. Tech.* **1**, 1–5.
- Day, G.M., Zeitler, J.A., Jones, W., Rades, T., and Taday, P.F., 2006. Understanding the influence of polymorphism on phonon spectra: lattice dynamics calculations and terahertz spectroscopy of carbamazepine. *J. Phys. Chem. B* **110**, 447–456.
- Ferguson, B., and Zhang, X.C., 2002. Materials for terahertz science and technology. *Rev. Art. Nat. Mater.* **1**, 26–33.
- Fischer, B. M., Hoffmann, M., Helm, H., Modjesch, G., and Jepsen, P. U., 2005. Chemical recognition in terahertz time-domain spectroscopy and imaging. *Semiconductor Sci. Technol.* **20**, S246–S253.
- Fitzgerald, A.J., Cole, B.E., and Taday, P.F., 2005. Nondestructive analysis of tablet coating thicknesses using terahertz pulsed imaging. *J. Pharm. Sci.* **94**, 177–183.

- Ge, M., Liu, G.F., Ma, S.H., and Wang, W.F., 2009. Polymorphic forms of furosemide characterized by THz time domain spectroscopy. *Bull. Kor. Chem. Soc.* **30**, 2265–2268.
- Hakey, P.M., Allis, D.G., Hudson, M.R., Ouellette, W., and Korter, T.M., 2009. Investigation of (1R,2S)-(-)-Ephedrine by Cryogenic terahertz spectroscopy and solid-state density functional theory. *Chem. Phys. Chem.* **10**, 2434–2444.
- Han, P.Y., Tani, M., Usami, M., Kono, S., Kersting, R., and Zhang, X.C., 2001. A direct comparison between terahertz time-domain spectroscopy and far-infrared Fourier transform spectroscopy. *J. Appl. Phys.* **89**, 2357–2359.
- Heinz, A., Gordon, K.C., McGoverin, C.M., Rades, T., and Strachan, C.J., 2009a. Understanding the solid-state forms of fenofibrate – A spectroscopic and computational study. *Eur. J. Pharm. Biopharm.* **71**, 100–108.
- Heinz, A., Strachan, C.J., Gordon, K.C., and Rades, T., 2009b. Analysis of solid-state transformations of pharmaceutical compounds using vibrational spectroscopy. *J. Pharm. Pharmacol.* **61**, 971–988.
- Ho, L., Muller, R., Romer, M., Gordon, K.C., Heinamaki, J., Kleinebudde, P., Pepper, M., Rades, T., Shen, Y.C., Strachan, C.J., Taday, P.F., and Zeitler, J.A., 2007. Analysis of sustained-release tablet film coats using terahertz pulsed imaging. *J. Controlled Release*. **119**, 253–261.
- Ho, L., Mueller, R., Gordon, K.C., Kleinebudde, P., Pepper, M., Rades, T., Shen, Y.C., Taday, P.F., and Zeitler, J.A., 2008. Applications of terahertz pulsed imaging to sustained-release tablet film coating quality assessment and dissolution performance. *J. Controlled Release*. **127**, 79–87.
- Ho, L., Muller, R., Gordon, K.C., Kleinebudde, P., Pepper, M., Rades, T., Shen, Y.C., Taday, P.F., and Zeitler, J.A., 2009a. Terahertz pulsed imaging as an analytical tool for sustained-release tablet film coating. *Eur. J. Pharm. Biopharm.* **71**, 117–123.
- Ho, L., Muller, R., Gordon, K.C., Kleinebudde, P., Pepper, M., Rades, T., Shen, Y.C., Taday, P.F., and Zeitler, J.A., 2009b. Monitoring the film coating unit operation and predicting drug dissolution using terahertz pulsed imaging. *J. Pharm. Sci.* **98**, 4866–4876.
- Ho, L., Cuppok, Y., Muschert, S., Gordon, K.C., Pepper, M., Shen, Y., Siepmann, F., Siepmann, J., Taday, P.F., and Rades, T., 2009c. Effects of film coating thickness and drug layer uniformity on in vitro drug release from sustained-release coated pellets: a case study using terahertz pulsed imaging. *Int. J. Pharm.* **382**, 151–159.
- Ho, L., Mueller, R., Krueger, C., Gordon, K.C., Kleinebudde, P., Pepper, M., Rades, T., Shen, Y., Taday, P.F., and Zeitler, J.A., 2010. Investigating dissolution performance critical areas on coated tablets: a case study using terahertz pulsed imaging. *J. Pharm. Sci.* **99**, 392–402.
- Hoag, S.W., Dave, V.S., Moolchandani, V., 2008. Compression and compaction, in pharmaceutical dosage forms: tablets, Vol. 1: Unit operations and mechanical properties, L.L. Augsburger, S.W. Hoag, Eds., *Information Healthcare*, 555–630.
- Hooper, J., Mitchell, E., Konek, C., and Wilkinson, J., 2009. Terahertz optical properties of the high explosive beta-HMX. *Chem. Phys. Lett.* **467**, 309–312.
- Ikeda, Y., Ishihara, Y., Moriwaki, T., Kato, E., and Terada, K., 2010. A novel analytical method for pharmaceutical polymorphs by terahertz spectroscopy and the optimization of crystal form at the discovery stage. *Chem. Pharm. Bull.* **58**, 76–81.

- Jansen, C., Wietzke, S., Peters, O., Scheller, M., Vieweg, N., Salhi, M., Krumbholz, N., Jordens, C., Hochrein, T., and Koch, M., 2010. Terahertz imaging: applications and perspectives. *Appl. Optics*. **49**, E48–E57.
- Jantzen G.M., and Robinson J.R., 2002. Sustained and controlled-release drug delivery systems. In: Bunker GS, Rhodes CT, editors. *Modern pharmaceutics*. 4th ed. New York: Marcel Dekker. 501–528.
- Jepsen, P.U. and Fischer, B.M., 2005. Dynamic range in terahertz time-domain transmission and reflection spectroscopy. *Opt. Lett.* **30**, 29–31.
- Jepsen, P.U. and Clark, S.J., 2007. Precise ab-initio prediction of terahertz vibrational modes in crystalline systems. *Chem. Phys. Lett.* **442**, 275–280.
- Jepsen, P. U., Cooke, D.G., Kock, M., 2011. Terahertz spectroscopy and imaging – Modern techniques and applications. *Laser Photonics Rev.* **5**, 124–166.
- Juuti, M., Tuononen, H., Prykari, T., Kontturi, V., Kuosmanen, M., Alarousu, E., Ketolainen, J., Myllyla, R., and Peiponen, K.E., 2009. Optical and terahertz measurement techniques for flat-faced pharmaceutical tablets: a case study of gloss, surface roughness and bulk properties of starch acetate tablets. *Meas. Sci. Tech.* **20**, 015301.
- Kawase, M., Saito, T., Ogawa, M., Uejma, H., Hatsuda, Y., Kawanishi, S., Hirotani, Y., Myotoku, M., Ikeda, K., Takano, K., Hangyo, M., Yamamoto, K., and Tani, M., 2009. Terahertz absorption spectra of original and generic ceftazidime. *Anal. Sci.* **25**, 1483–1485.
- Kirsch J.D., and Drennen J.K. 1996. Near-infrared spectroscopic monitoring of the film coating process. *Pharm. Res.* **13**, 234–237.
- El Hagras A., Chang S.-Y., Desai D., and Kiang S. 2006. Application of Raman spectroscopy for quantitative in-line monitoring of tablet coating. *Am. Pharm. Rev.* **9**, 40–45.
- Laman, N., Harsha, S.S., and Grischkowsky, D., 2008. Narrow-line waveguide terahertz time-domain spectroscopy of aspirin and aspirin precursors. *Appl. Spectrosc.* **62**, 319–326.
- Limwikrant, W., Higashi, K., Yamamoto, K., and Moribe, K., 2009. Characterization of ofloxacin–oxalic acid complex by PXRD, NMR, and THz spectroscopy. *Int. J. Pharm.* **382**, 50–55.
- Liu, H.B. and Zhang, X.C., 2006. Dehydration kinetics of D-glucose monohydrate studied using THz time-domain spectroscopy. *Chem. Phys. Lett.* **429**, 229–233.
- Liu, H.B., Chen, Y.Q., and Zhang, X.C., 2007. Characterization of anhydrous and hydrated pharmaceutical materials with THz time-domain spectroscopy. *J. Pharm. Sci.* **96**, 927–934.
- Malaterre, V., Pedersen, M., Ogorka, J., Gurny, R., Loggia, N., and Taday, P.F., 2009. Terahertz pulsed imaging, a novel process analytical tool to investigate the coating characteristics of push–pull osmotic systems. *Eur. J. Pharm. Biopharm.* **74**, 21–25.
- Maurer, L. and Leuenberger, H., 2009. Terahertz pulsed imaging and near infrared imaging to monitor the coating process of pharmaceutical tablets. *Int. J. Pharm.* **370**, 8–16.
- May, R., Han, L., Alton, J., Zhong, S., Elliott, J.A., Byers, C., Gladden, L., Evans, M. J., Shen, Y. and Zeitler, J., 2009. Pharmaceutical tablet hardness measurements with THz pulsed imaging, in *IEEE Int. Conf. IR.MMW.THz. Waves* (Busan, South Korea, 2009).

- May, R.K., Evans, M.J., Zhong, S., Warr, I., Gladden, L.F., Shen, Y.C. and Zeitler, J.A. 2011. Terahertz in-line sensor for direct coating thickness measurement of individual tablets during film coating in real-time. *J. Pharm. Sci.* **100**, 1535–1544.
- Newnham, D.A. and Taday, P.F., 2008. Pulsed terahertz attenuated total reflection spectroscopy. *Appl. Spectro.* **62**, 394–398.
- Nguyen, K.L., Friš i , T., Day, G.M., Gladden, L.F., and Jones, W., 2007. Terahertz time-domain spectroscopy and the quantitative monitoring of mechanochemical cocrystal formation. *Nat. Mater.* **6**, 206–209.
- Nishikiori, R., Yamaguchi, M., Takano, K., Enatsu, T., Tani, M., de Silva, U.C., Kawashita, N., Taragi, T., Morimoto, S., Hangyo, M., and Kawase, M., 2008. Application of partial least square on quantitative analysis of L-, D-, and DL-tartaric acid by terahertz absorption spectra. *Chem. Pharm. Bull.* **56**, 305–307.
- Obradovic, J., Collins, J.H.P., Hirsch, O., Mantle, M.D., Johns, M.L., and Gladden, L.F., 2007. The use of THz time-domain reflection measurements to investigate solvent diffusion in polymers. *Polymer*. **48**, 3494–3503.
- Otsuka, M., Nishizawa, J.I., Shibata, J., and Ito, M., 2010. Quantitative evaluation of mefenamic acid polymorphs by terahertz-chemometrics. *J. Pharm. Sci.* **99**, 4048–4053.
- Palermo, R., Cogdill, R.P., Short, S.M., Drennen, J.K., and Taday, P.F., 2008. Density mapping and chemical component calibration development of four-component compacts via terahertz pulsed imaging. *J. Pharm. Biomed. Anal.* **46**, 36–44.
- Perez-Ramos, J.D., Findlay, W.P., Peck, G., and Morris, K.R. 2005. Quantitative analysis of film coating in a pan coater based on in-line sensor measurements. *AAPS Pharm. Sci. Tech.* **6**, E127–E136.
- Pickwell, E. and Wallace, V.P., 2006. Biomedical applications of terahertz technology. *J. Phys. D-App. Phys.* **39**, R301–R310.
- Portieri, A. and Taday, P., and Shen, Y.C., 2007. *Terahertz pulsed imaging for non-invasive and non-destructive analysis of the hydration dynamics of HPMC matrix. 58th PGH. Conf. Anal. Appl. Spectro. (PITTCON 2007, Chicago, USA)*.
- Porter, S.C., 2000. *Scale-Up of film Coating*, Taylor & Francis, New York.
- Pupeza, I., Wilk, R., and Koch, M., 2007. Highly accurate optical material parameter determination with THz time-domain spectroscopy. *Opt. Express*, **15**, 4335–4350.
- Scheller, M. and Koch, M., 2009. Terahertz quasi time domain spectroscopy. *Opt. Express* **17**, 17723.
- Schwarz, J. and Staenz, K., 2001. Adaptive threshold for spectral matching of hyperspectral data. *Canadian J. Remote Sensing* **27**, 216–224.
- Shen, Y.C., Taday, P. F., Newnham, D. A., Pepper, M., 2005a. Chemical mapping using reflection terahertz pulsed imaging. *Semiconductor Sci. Technol.* **20**, S254–S257.
- Shen, Y.C., Taday, P.F., Newnham, D.A., Kemp, M.C., and Pepper, M., 2005b. 3D chemical mapping using terahertz pulsed imaging. *SPIE Proceedings* **5727**, 24–31.
- Shen, Y.C., Taday, P.F., and Pepper, M., 2008. Elimination of scattering effects in spectral measurement of granulated materials using terahertz pulsed spectroscopy. *Appl. Phys. Lett.* **92**, 051103.
- Shen, Y.C. and Taday, P.F., 2008. Development and application of terahertz pulsed imaging for nondestructive inspection of pharmaceutical tablet. *IEEE. J. Sel. Top. Quant. Electro.* **14**, 407–415.

- Shen, Y.C., 2011. Terahertz pulsed spectroscopy and imaging for pharmaceutical applications: A review. *Int. J. Pharm.* **417**, 48–60.
- Spencer, J.A., Gao, Z.M., Moore, T., Buhse, L.F., Taday, P.F., Newnham, D.A., Shen, Y.C., Portieri, A., and Husain, A., 2008. Delayed release tablet dissolution related to coating thickness by terahertz pulsed image mapping. *J. Pharm. Sci.* **97**, 1543–1550.
- Strachan, C.J., Rades, T., Newnham, D.A., Gordon, K.C., Pepper, M., and Taday, P.F., 2004. Using terahertz pulsed spectroscopy to study crystallinity of pharmaceutical materials. *Chem. Phys. Lett.* **390**, 20–24.
- Strachan, C.J., Taday, P.F., Newnham, D.A., Gordon, K.C., Zeitler, J.A., Pepper, M., and Rades, T., 2005. Using terahertz pulsed spectroscopy to quantify pharmaceutical polymorphism and crystallinity. *J. Pharm. Sci.* **94**, 837–846.
- Taday, P.F., Bradley, I.V., Arnone, D.D., and Pepper, M., 2003. Using terahertz pulse spectroscopy to study the crystalline structure of a drug: a case study of the polymorphs of ranitidine hydrochloride. *J. Pharm. Sci.* **92**, 831–838.
- Upadhyaya, P.C., Nguyen, K.L., Shen, Y.C., Obradovic, J., Fukushige, K., Griffiths, R., Gladden, L.F., Davies, A.G., and Linfield, E.H., 2006. Characterization of crystalline phase-transformations in theophylline by time-domain terahertz spectroscopy. *Spectr. Lett.* **39**, 215–224.
- Wagh, M.P., Sonawane, Y.H., and Joshi, O.U., 2009. Terahertz technology: a boon to tablet analysis. *Ind. J. Pharm. Sci.* **71**, 235–241.
- Walther, M., Fischer, B.M., and Jepsen, P.U., 2003. Noncovalent intermolecular forces in polycrystalline and amorphous saccharides in the far infrared. *Chem. Phys.* **288**, 261–268.
- Walther, M., Fischer, B.M., Ortner, A., Bitzer, A., Thoman, A., and Helm, H., 2010. Chemical sensing and imaging with pulsed terahertz radiation. *Anal. Bioanal. Chem.* **397**, 1009–1017.
- Wu, H.Q., Heilweil, E.J., Hussain, A.S., and Khan, M.A., 2007. Process analytical technology (PAT): Effects of instrumental and compositional variables on terahertz spectral data quality to characterize pharmaceutical materials and tablets. *Int. J. Pharm.* **343**, 148–158.
- Wu, H.Q., Heilweil, E.J., Hussain, A.S., and Khan, M.A., 2008. Process analytical technology (PAT): quantification approaches in Terahertz spectroscopy for pharmaceutical application. *J. Pharm. Sci.* **97**, 970–984.
- Zannikoski, P., Li, W., Drennen, J., and Lodder, R., 1991. Spectrophotometric prediction of the dissolution rate of carbamazepine tablets. *Pharm. Res.* **8**, 974–978.
- Zeitler, J.A., Newnham, D.A., Taday, P.F., Strachan, C.J., Pepper, M., Gordon, K.C., and Rades, T., 2005. Temperature dependent terahertz pulsed spectroscopy of carbamazepine. *Thermo. Acta.* **436**, 71–77.
- Zeitler, J.A., Newnham, D.A., Taday, P.F., Threlfall, T.L., Lancaster, R.W., Berg, R.W., Strachan, C.J., Pepper, M., Gordon, K.C., and Rades, T., 2006a. Characterization of temperature induced phase transitions in the five polymorphic forms of sulfathiazole by terahertz pulsed spectroscopy and differential scanning calorimetry. *J. Pharm. Sci.* **95**, 2486–2498.
- Zeitler, J.A., Kogermann, K., Rantanen, J., Rades, T., Taday, P.F., Pepper, M., Aaltonen, J., and Strachan, C.J., 2006b. Drug hydrate systems and dehydration processes studied by terahertz pulsed spectroscopy. *Int. J. Pharm.* **334**, 78–84.

- Zeitler, J.A., Shen, Y.C., Baker, C., Taday, P.F., Pepper, M., and Rades, T., 2007a. Analysis of coating structures and interfaces in solid oral dosage forms by three dimensional terahertz pulsed imaging. *J. Pharm. Sci.* **96**, 330–340.
- Zeitler, J.A., Taday, P.F., Newnham, D.A., Pepper, M., Gordon, K.C., and Rades, T., 2007b. Terahertz pulsed spectroscopy and imaging in the pharmaceutical setting – a review. *J. Pharm. Pharmacol.* **59**, 209–223.
- Zeitler, J.A., Taday, P.F., Pepper, M., and Rades, T., 2007c. Relaxation and crystallization of amorphous carbamazepine studied by terahertz pulsed spectroscopy. *J. Pharm. Sci.* **96**, 2703–2709.
- Zeitler, J.A., Taday, P.F., Newnham, D.A., Pepper, M., Gordon, K.C., and Rades, T., 2008. Terahertz pulsed spectroscopy and imaging in the pharmaceutical setting – a review. *J. Pharm. Pharmacol.* **59**, 209–223.
- Zeitler, J.A. and Gladden, L.F., 2009. In vitro tomography and non-destructive imaging at depth of pharmaceutical solid dosage forms. *Eur. J. Pharm. Biopharm.* **71**, 2–22.
- Zhong, S., Shen, Y.C., Ho, L., May, R.K., Zeitler, J.A., Evans, M., Taday, P.F., Pepper, M., Rades, T., Gordon, K.C., Müller, R., and Kleinebudde, P., 2011. Nondestructive testing of pharmaceutical coatings by terahertz pulsed imaging and optical coherency tomography. *Opt. Laser Eng.* **49**, 361–365.

Terahertz applications in art conservation

K. FUKUNAGA, National Institute of Information and Communications Technology, Japan

DOI: 10.1533/9780857096494.3.615

Abstract: Terahertz (THz) spectroscopy and imaging techniques have been applied to investigate cultural heritage objects. In particular, time domain THz imaging using a THz pulse as a probe makes it possible to observe cross-sectional images and/or sliced images of artworks. The information about the internal structure of artworks is useful for conservation planning. This chapter introduces heritage science and the advantages of using the THz frequency region with several case studies.

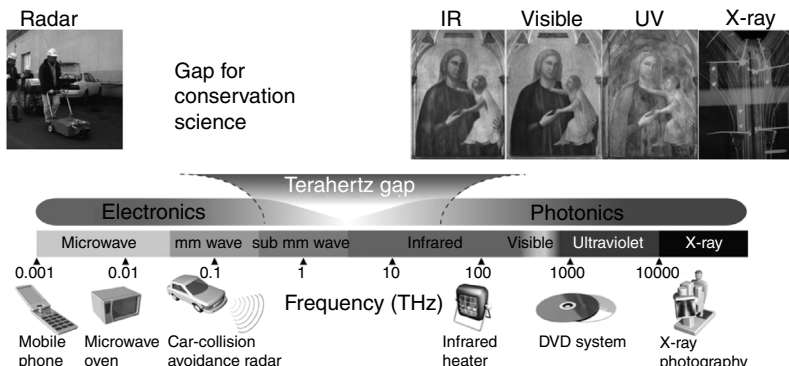
Key words: time domain, imaging, non-destructive test, heritage science, field test.

21.1 Introduction

This chapter introduces applications of terahertz (THz) spectroscopy and imaging techniques for the investigation of cultural heritage objects.

21.1.1 The terahertz (THz) gap in heritage science

The deterioration or damage of cultural heritage objects is inevitable, due to the natural ageing of materials, uncondusive atmospheric conditions, insects, natural disasters, human activities and so on. To maintain the value of our cultural heritage objects, conservation is required. The term ‘conservation’ covers not only keeping artwork under proper conditions, but also cleaning, repairing supporting materials, supplying missing colours and varnishing the surface of paintings. The conservation process for artworks is similar to the process of medical diagnosis and treatment for people: the first step is visual observation by an expert, then non-destructive or non-contact observation with electronic imaging machines. Thus, photographic examination has been commonly used for art conservation in the wide frequency range from X-ray to infrared. Near and mid infrared spectroscopy has been also used in laboratories to identify materials used in artworks.^{1,2} Microwave and millimetre wave radar are used for detecting objects in the



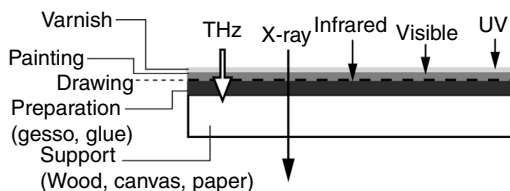
21.1 THz gap in heritage science research field.

soil by archaeologists. As shown in Fig. 21.1, there is a THz gap also in the field of heritage science. THz waves should be useful for investigating cultural objects if the equipment were transportable and affordable.

21.1.2 Advantage of THz waves

THz waves can be used for heritage science for two objectives: spectroscopy for material study and imaging the internal structure of objects. THz spectroscopy is similar to the far infrared version of the more common Fourier transform infrared spectroscopy (FTIR). An advantage of THz spectroscopy is that a specimen can be analysed even if it is in an opaque package, because THz waves can penetrate into most dielectric materials. Terahertz time domain spectroscopy (THz-TDS) with THz pulse spectroscopy directly gives the permittivity of a specimen without performing Kramers-Kronig analysis, because the pulse has both phase and amplitude values. The details of THz-TDS are explained in Chapter 10 of this book. When it comes to imaging, THz transmission imaging has previously been used to perform spectroscopic imaging of illegal drugs in envelopes. In THz reflection imaging, on the other hand, a THz pulse can be used as a probe to show the internal structure of an object by detecting reflection pulses from each discontinuity inside the object.

Figure 21.2 shows a typical structure of a western painting. Electromagnetic waves have been used for various analyses depending on their characteristics. The X-ray passes through almost all artworks and gives images of the internal structure, just like a medical examination of our body. However, organic materials, such as dried plants in a ceramic vase, are difficult to detect and layer structure with similar materials, such as two types of clays, is hardly recognised. Element analysis by X-ray fluorescence spectroscopy



21.2 Structure of a painting and electromagnetic waves.

(XRF) is also commonly used to identify pigments. Ultraviolet (UV) rays are useful for examining the condition of varnish, and they also give material information by fluorescence reflection. Infrared (IR) is used to analyse materials in reflection mode, although sampling is often required for precise examination with a common FTIR in transmission mode. In addition to these non-destructive tests, a cross-section image is observed when destructive sampling is allowed. The cross-section image is extremely useful for studying the techniques employed in the original artwork and any previous conservation processes undertaken.

THz waves penetrate to the preparation layer where mid-infrared waves cannot reach. The biggest advantage of using THz waves is that THz-TDS imaging can give a cross-sectional image non-destructively, and the area information on the layer of interest can be examined by extracting the particular pulse in the output signals. Most cultural heritage objects are handmade and their materials are quite pure, so the spatial resolution and the sensitivity of today's THz technology already meets the requirements in the majority of cases. Various practical applications of studying cultural heritage objects using THz spectroscopy have been performed, and Jackson *et al.* summarises activities in a recent review paper.³

21.2 Material analysis using terahertz waves

21.2.1 Spectral database

FTIR is commonly used to identify unknown materials, and databases developed by using pure chemicals are commercially available and usually come with software in the system at shipment. For heritage science, the infrared and Raman users group (IRUG) (<http://www.irug.org/>) established an online spectral database of art materials, including historic pigments from real cultural objects. However, in the case of THz spectroscopy, FTIR manufacturers have not prepared a database for their far infrared options. National Institute of Information and Communications Technology (NICT) and Riken have made a THz spectral database (<http://thzdb.org/>), and we are preparing to invite contributions from around the world. The current website introduces

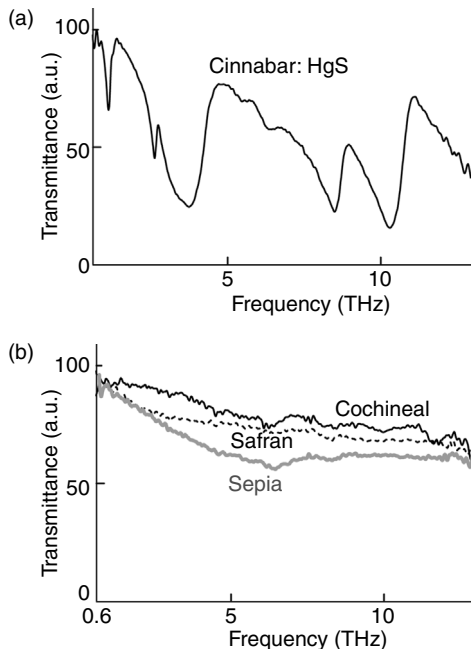
spectra of mineral pigments, organic dyes, natural binders (resin, oil, animal glues), synthetic materials, and their mixtures measured by far infrared FTIR or FT-THz in transmission mode. Figure 21.3a shows examples of spectra of three pigments obtained by Model VIR-F(JASCO, Tokyo). Cinnabar is HgS, which has been used from ancient times to the present, and a similar red colour can be made by using cadmium red, a mixture of CdS and CdSe. Pure CdS purchased as a chemical reagent and cadmium yellow pigment show exactly the same spectra in THz region, and have a relatively broad peak at around 8 THz, as in the spectra of cadmium red. Further investigation is required to understand the physics appearing in each peak. The spectra of organic materials, on the other hand, do not show particular peaks, as shown in Fig. 21.3b, and a chemometrics technique could be useful to extract information.⁴ Chemometrics is based on a pure mathematical technique developed for statistical analysis. In analytical chemistry, it is used to extract a particular tendency by gathering large number of spectra.

21.2.2 THz spectroscopy of real objects

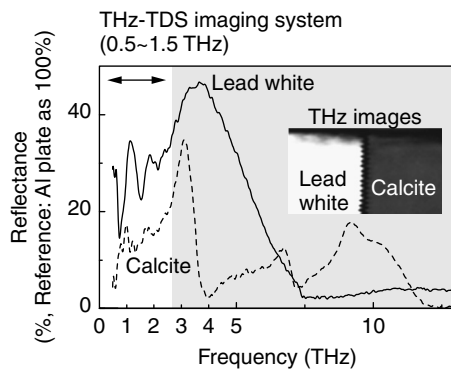
In almost all cases real objects, such as paintings, are observed in reflection mode. Although the reflection spectra are not as clear as those obtained in transmission mode, the reflection level itself can be used to distinguish materials as a map, even though the substance is not identifiable by THz imaging alone. Figure 21.4 shows reflection spectra of two white pigments, and the imaging results were obtained by a commercial THz imaging system. The highest level of the reflection in power integration is shown as 100% white in the grey scale images. As shown in the inset image in the figure, these two white pigments – lead white ($2\text{PbCO}_3\cdot\text{Pb}(\text{OH})_2$) and calcite (CaCO_3) – can be clearly distinguished. By accumulating a database of reflection characteristics from various art materials, spectroscopic imaging can be practically realised in the future.

21.2.3 Case studies

Figure 21.5 shows a case study of the spectroscopic imaging of a fragment of a mural painting from the Dazhao Temple (Inner Mongolia).⁵ The fragment was analysed by Raman spectroscopy in 2002, and orange colour at the point indicated in the visible photograph in Fig. 21.5a was found as minium, a lead-based mineral pigment. There is a belt which looks like the same orange but was not analysed at that time. As shown in Fig. 21.5b, the THz reflection from the belt is not the same as the THz reflection from the minium part, and it proved that the two oranges were made of different materials. We then observed the orange belt by XRF and confirmed that it was neither minium nor cinnabar, but it could be an organic material.

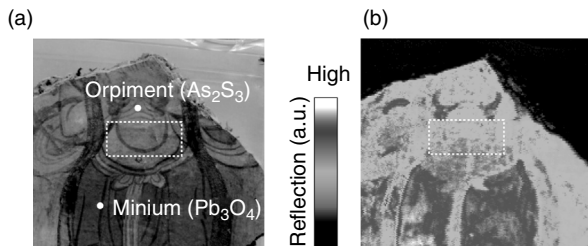


21.3 Example of spectra of colouring substances: (a) mineral pigments and (b) organic dyes.



21.4 Reflection spectra and an imaging result of two white pigments.

Here, it should be noted that both Raman spectroscopy and XRF measure a ‘point’. Although these techniques are very effective for identifying a substance, the results will depend on the measurement point selected, and making an image by performing point measurements takes days. THz imaging, on the other hand, takes around 30 min for a specimen of 15 cm × 15 cm, and it gives useful information about where you need to perform element



21.5 THz imaging of a fragment of Inner Mongolian wall painting: (a) visible and (b) THz image.

analysis to identify a substance. When only minimal destructive examination is allowed, THz imaging will be helpful to decide which part of the specimen to take samples from.

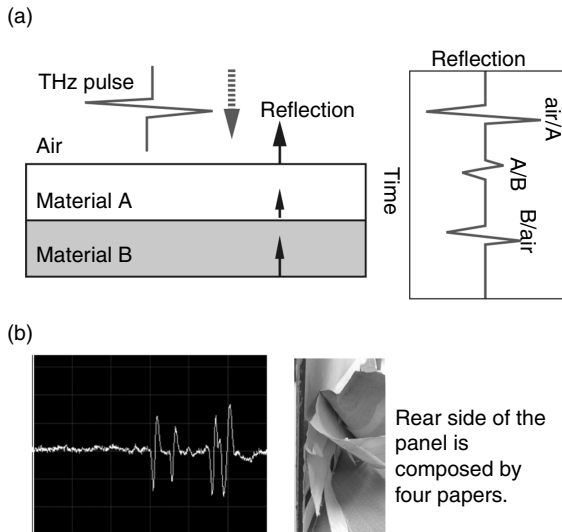
21.3 Observation of the internal structure of artworks using terahertz waves

21.3.1 Non-destructive cross-section by terahertz time domain spectroscopy (THz-TDS) system

As described in Section 21.2, THz time domain imaging has advantages for investigating the preparation layers of artworks, in particular paintings. Further details of the THz time domain system are described in the Chapter 10 of this book. When a THz pulse is applied to a multi-layered object made of materials A and B, in this case (Fig. 21.6a), the reflection pulses from each interface, air/A, A/B, B/air, appear as a sequence of pulses, and the amplitude and the phase are determined by the refractive index of the materials at each interface. It also means the material information at the internal interface could be estimated from the output signal. Figure 21.6b shows the output signal from the back side of an old Japanese panel screen, which was to be removed for conservation. The four peaks indicate that the number of paper layers in the back side was four, and we confirmed this by removing papers from the back surface. The THz-TDS system can be synchronised with a scanning stage, resulting in three dimensional imaging by reconstructing data sets. Spectroscopic information can be extracted by applying Fourier transformation.

21.3.2 Case studies using the THz-TDS system

We had the opportunity to study a masterpiece of Giotto di Bondone, 'Polittico di Badia' (1300), in the permanent collection of the Uffizi Gallery in Florence, Italy. The artwork was under conservation in 2008, and we applied the THz imaging technique to investigate the internal structure. The

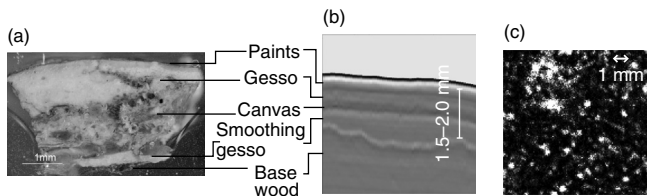


21.6 Internal structure observation by using the THz-TDS system: (a) time domain measurement by THz pulse and (b) paper layer observation.

following examples were obtained by using T-Ray 4000 (Picometrix, Ann Arbor). Figure 21.7b is a non-invasive cross-sectional image from the centre part, compared with the visible cross-section of a sample taken from another part near the edge (Fig. 21.7a). These figures clearly show that there are two gesso layers. It proves that Giotto followed the medieval technique with two gesso layers; a gesso layer was made directly on a carved wood base to flatten it because the plane had not been invented. A canvas was placed on that first gesso layer; subsequently, another gesso layer was made as a preparation for painting. We also investigated an area image of the canvas by extracting the reflection pulse from the particular layer; as shown in Fig. 21.7c, a regular pattern of fabric was clearly obtained. According to conservators and historians, this technique had been used in the medieval era. We had conducted other scientific analyses, including photographic examinations (IR, UV, X-ray), FTIR analysis of varnish by sampling, cross-section observation by scanning electron microscopy/electron probe X-ray micro-analysis (SEM-EPMA), fiber optic reflectance spectroscopy (FORS), and so on. The results interested historians and conservators, and a book dedicated to the conservation of the Polittico di Badia is being published.⁶

21.4 Prospective development of terahertz technology as a tool for heritage science

Almost all conservators with whom we have worked so far say that it is extremely useful to know the condition of a painting behind the surface.



21.7 Non-invasive THz cross-section image (b) compared with a microscope observation by sampling (a), of a tempera masterpiece, 'Polittico di Badia'. (a) Visible observation by a microscope, (b) non-invasive cross-section image by THz image, and (c) THz image of the canvas layer. Note: The photograph and the THz cross-section image are not exactly the same point of observation. The thickness of the smoothing gesso depends on the condition of the base wood.

Information on the surface, such as the materials of pigments, can be analysed by existing methods, and sampling is possible when the artwork has become a research objective. However, information regarding the condition of preparation and support layers is important for conservation. For paintings, in particular, THz time domain imaging is the only non-invasive technique to observe layer structures and give area information of the layer of interest.

Recently, THz computed tomography (CT) has been applied to archaeological objects. Abraham *et al.* have developed a transportable THz-CT system with a Gunn diode continuous wave source of 0.1 THz, and applied it to investigate the remains in Egyptian vases.⁷ The results clearly show that THz-CT can reveal remains which cannot be seen by X-ray-CT, such as organic plants seeds, although substance information may not be obtained without frequency response. When it comes to imaging with material analysis, spectroscopic imaging by using a THz camera with false colour description will be developed in the near future. A micro-bolometer camera which operates at video rate is available and THz sources using quantum cascade lasers (QCLs) can be developed and applied to distinguish art materials.⁸ By allotting a colour to each frequency, a substance map could be obtained. Since the camera unit itself is handheld size, it will allow us to use THz imaging even in excavation sites in the near future.

21.5 References

1. D. Pinna, M. Galeotti, and R. Mazzeo, *Scientific Examination for the Investigation of Paintings. A Handbook for Conservator-restorers*, Centro Di, Firenze, 2009.
2. M. R. Derrick, D. Stulik, and J. M. Landry, *Infrared Spectroscopy in Conservation Science*, The Getty Conservation Institute, Los Angeles, 1999.
3. J. B. Jackson, J. Bowen, G. Walker, J. Labaune, G. Mourou, M. Menu, and K. Fukunaga, 'A survey of terahertz applications in cultural heritage conservation science', *IEEE Transaction on Terahertz Science and Technology*, **1**(1), 220–231, 2011.

4. T. Trafela, M. Mizuno, K. Fukunaga, and M. Strlic, 'Terahertz spectroscopy and chemometrics for quantitative determination of chemical properties and dating of historic paper', Proceedings of IRMMW-THz, No. C1.2, 2010.
5. K. Fukunaga, I. Hosako, Y. Kohdzuma, T. Koezuka, M.-J. Kim, T. Ikari, and X. Du, 'Terahertz analysis of an East Asian historical mural painting', *Journal of European Optics Society*, **5**(10024), 2010.
6. A. Tartuferi, ed. 'Giotto, Il Restauro di "Politico di Badia/ The Restoration of the Badia Polyptych', Mandragora, Firenze, 2012.
7. J.P. Caumes, A. Younus, S. Salort, B. Chassagne, B. Recur, A. Ziéglé, A. Dautant, and E. Abraham, 'Terahertz tomographic imaging of XVIIth Dynasty Egyptian sealed pottery', *Applied Optics*, **50**, 3604–3608, 2011.
8. K. Fukunaga, N. Sekine, I. Hosako, N. Oda, H. Yoneyama, and T. Sudou, 'Real-time terahertz imaging for art conservation science', *Journal of European Optics Society*, **3**(08027), 2008.

Applications of terahertz technology in the semiconductor industry

Y. CAI, Z. WANG and D. GOYAL, Intel Corporation, USA

DOI: 10.1533/9780857096494.3.624

Abstract: Electro-optical terahertz pulse reflectometry (EOTPR), an electro-optical system driven by an ultrafast laser source, has enabled terahertz to be successfully applied in fault isolation and defect detection for microelectronics. This system has 10 µm resolution with high speed test signal, high bandwidth measurement of the system's response and low time base jitter. Numerous successful failure analysis cases have demonstrated the unique capabilities of EOTPR and its advantages over conventional time domain reflectometry.

Key words: electro-optics, photoconductive switch, rise time, resolution, signal/noise ratio, fault isolation, failure analysis, Cu bump and solder bump.

22.1 Introduction

An ultrafast electrical pulse can be generated by femtoseconds laser and detected by either electro-optic (EO) materials or a photoconductive switch. The pulse can have extremely high temporal resolution, which may be utilized for characterizing high speed integrated circuits (Valdmanis and Mourou, 1988; Frankel *et al.*, 1992; Pfeifer *et al.*, 1996; Nagel *et al.*, 2011) and as characterization methods for semiconductor manufacture. One example is EOTPR, a fault isolation system based on terahertz generation and detection circuits (Cai *et al.*, 2010). It is a non-destructive method that can locate the faults (open or short) in an electrical circuit with very high resolution and accuracy. The principle of EOTPR is to measure and display, as a function of time, reflections from the electrical signals being input into the device under test (DUT). The reflected signals contain information on the location and nature of discontinuities that have caused impedance mismatch. The method of applying EOTPR to fault isolation is waveform comparison – the waveform of the failed unit is evaluated against the record of a known-good CPU or chipset, to identify the failure mode as well as the failing location within the circuit. A CPU or chipset usually consists of an Si die on the top, substrate on the bottom and a bump connection in-between, which is the

interconnection between the Si die and the package formed by reflow of solder balls onto the copper bumps on the die. The failures may be located within the Si die or package, and occasionally right at the bump. Currently, the widely used electrical fault isolation tool is Tektronix TDS 8000/8200, of which the rise time is 35 ps with a 20 GHz plug-in time domain reflectometry (TDR) module. The resolution of this type of TDR had been evaluated to be around 500 µm, which is the minimum distance between two known open failures that can result in appreciable difference in reflected signals when plotted side-by-side. With this TDR resolution, it can be determined whether the failure is in the Si die or in the package; nevertheless, substantial physical failure analysis (FA) work including polishing and cross-section, is still needed to pinpoint the failures, resulting in long FA throughput time (TPT). In addition, there are some occasions when this TDR system cannot accurately detect failure locations, thus giving misleading information, especially when the failures are in the vicinity of bump. Other TDR modules with higher bandwidth sampling heads and lower rise times show a resolution improvement of no more than twice that of the existing model.

EOTPR was developed for the successful failure analysis for future generation packages. It is a unique method of combining electro-optics (EO) (Yang and Whitaker, 2002) and TDR into EOTPR for its attributes of jitter freeness and high resolution. The basic idea is to use an ultrafast laser to excite the photoconductive switch (PCS) and generate a high speed electrical pulse which propagates into the DUT; after being reflected, it is sampled by either the EO crystal with Pockels effect, or the PCS. Two independent proof-of-concept systems, based on EO and PCS, have been successfully demonstrated; both of them were characterized to have 10 µm resolution and less than 6 ps rise time. In 2009 the first industry compatible EOTPR system based on PCS sampling was installed in Intel labs. The nomenclature ‘EO’ is still retained to acknowledge the first prototype based on EO and the significant research effort that went into this. The system has achieved 10 µm resolution, 5.7 ps rise time, 94 dB signal/noise ratio and 150 mm testing range. This system has three distinct advantages over a conventional fully-electronic sampling TDR system: (a) very high speed test signal; (b) very high time base resolution and low time base jitter, and (c) high bandwidth measurement of the system’s response. A validation study has demonstrated superior system performance compared to conventional TDR and the results are discussed in following sections.

22.1.1 Principle of electro-optical terahertz pulse reflectometry (EOTPR)

TDR systems based on EO and PCS sampling schemes have been developed because both of them provide wide bandwidth and high resolution.

Electro-optic sampling and photoconductive switch sampling

EO sampling is a non-contacting probe technique through field interaction. It provides the highest bandwidth, and can be performed over a wide range of optical wavelengths. Nevertheless, it is susceptible to temperature swings. Apart from that, since this method relies on the EO effect (induced birefringence), electrical coupling to such devices is indirect and can result in an inefficient sample of the signal of interest (Frankel *et al.*, 1991).

PCS sampling provides the highest sensitivity and is a contacting (though high-impedance) probe technique. It can directly measure the voltage of the electrical signal and can be configured to also generate a pico-second electrical pulse (David *et al.*, 1998). It is relatively simple to construct, and uses relatively standard semiconductor materials. However, its low optical-to-electrical efficiency can require high-power laser.

Electro-optic sampling

When an electric field (E) of RF/microwave is applied to a birefringent crystal (a crystal that has different indices of refraction along different crystal axes), the refractive indices in different directions will be differentially varied by the electric field, leading to change in polarization of an optical beam propagating through this crystal; thus, the information from the RF/microwave signal can be transferred to the optical beam. This is called EO sampling, also known as Pockels effect (Yang and Whitaker, 2002). If this optical beam is a succession of ultrafast laser pulses that are variably delayed against signal to be measured, EO sampling has the highest time domain resolution due to the short duration of the laser pulse, for instance, 100 fs. Usually a polarization control optical circuit converts this polarization change into an intensity change that can be presented as below:

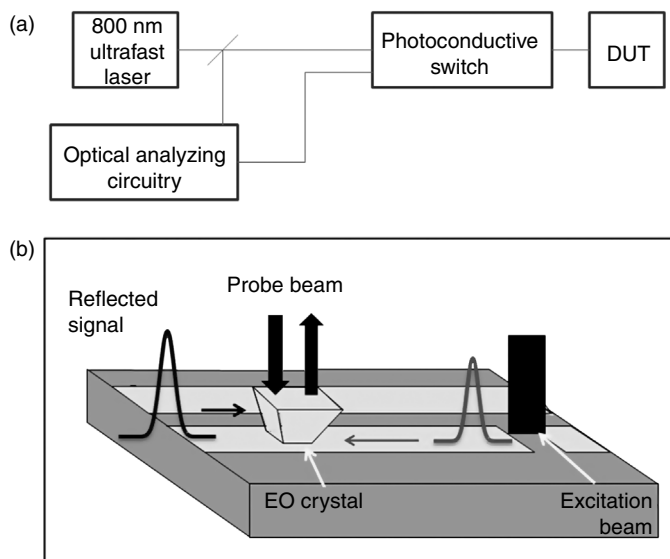
$$I = I_0 \sin^2 \left(\frac{\Gamma_0 + \Delta\Gamma}{2} \right) \quad [22.1]$$

where I_0 is the input intensity, Γ_0 is the static birefringence and $\Delta\Gamma$ is phase retardation due to the EO effect and the electrical field (Yang and Whitaker, 2002). The optical intensity change due to the measured sinusoidal electric field at a given time can then be derived below:

$$I = \frac{I_0}{2} \left[1 + \sin \left(\pi \frac{E_z^0 \sin(\omega_m t)}{E_\pi} \right) \right] \quad [22.2]$$

where I_0 is the input intensity, E_z^0 and ω_m are the measured electric field amplitude and frequency, respectively, E_π is the half-wave electric field, and t is time (Yang and Whitaker, 2002).

The EO sampling system developed is shown in Fig. 22.1. It is an optical fibre based system, which consists of a laser, optical analysis circuitry (delay rail, polarization optics, acoustic-optic modulator), PCS and EO sampling head. The ultrafast laser is a Ti:Sapphire laser with 800 nm wavelength that outputs a laser pulse train of 100-fs duration. The laser pulse train is divided by a beamsplitter into two beams: an excitation beam for generating a high speed electrical pulse, and a probe beam for acquiring the reflected signal from the DUT. After beamsplitting, the excitation beam enters the EO sampling head. The EO sampling head consists of a PC switch, optical fibre for the excitation beam, EO crystal (LiTaO_3) connected with the optical fibre for the probe beam, a 110 GHz high frequency probe, a 110 GHz high speed connector and DC bias circuit, all of which are assembled in an aluminium housing piece. The PC switch, based on LT-GaAs, is a co-planar stripe line with a 14 μm opening on one trace. The excitation beam shines onto the opening and generates an electrical pulse that will propagate into the DUT through the high frequency probe (110 GHz), be reflected back by an open or short, then be picked up by the EO crystal and probe beam.



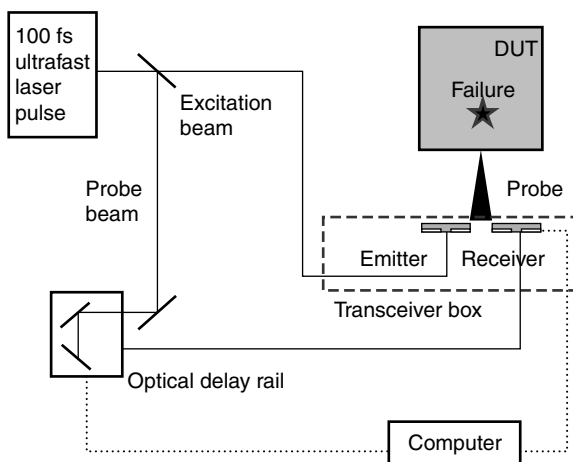
22.1 (a) Schematic of the EO sampling system. (b) Schematic of EO sampling head.

This system is characterized by its resolution. The definition of resolution is to differentiate appreciable change of reflected signals on a gold co-planar waveguide (CPW) line from an open end when the CPW is moved by certain distance, for instance 50 µm. The measurement results demonstrated that this EO sampling system can resolve 50 µm on gold CPW by translating the CPW respective to the EO probe (Cai *et al.*, 2010).

Photoconductive switch sampling

Although EO sampling has higher bandwidth than PCS sampling, it suffers from high temperature sensitivity and indirect measurement of the birefringence field (Frankel *et al.*, 1991). Therefore, PCS sampling configuration was selected for the final system built, which is called EOTPR, where EO acknowledges the first prototype based on electro-optics and TP identifies the nature of use of a terahertz pulse.

The system contains an ultrafast laser source, transceiver, optical delay line, a high speed probe, optical delay rail and computer for readout and display (see Fig. 22.2). The essence of the instrument's operation is the use of a transceiver box to convert a high speed optical pulse (transmitted from the laser source through an umbilical cord) into an electrical transient test signal, which is then sent through the specific test structure of the DUT, and then a subsequent reconversion to the optical domain from reflected electrical waveforms which gives relevant information about the DUT. The transceiver box consists of two LT-GaAs PCSs: the emitter to produce a high speed electrical test pulse, and the receiver to measure the returning electrical signal as a high speed sampling gate. The two switches are integrated



22.2 Terahertz emission and PCS detection.

within an optical fibre-coupled module that is coupled to a high frequency (110 GHz) probe. The two PCS devices are excited by a sub-picosecond laser pulse that is split in two and delivered to the two switches. Jitter free equivalent time sampling of the electrical waveform is accomplished by varying the delay between the two pulses using the linear stage and rapid scan delay line. The profile of the reflected electrical waveform can then be constructed.

For terahertz generation, a train of ultrafast laser pulses strike onto a biased PCS, which then produces a very fast electrical pulse. This signal is then fed into the system. The emitter PCS is biased at a few volts. The high speed (< 100 fs) optical pulse induces transient conductivity in the device, which launches a fast transient into a microstrip circuit. The signal will be reflected back whenever there are any discontinuities or impedance mismatch. Acquisition of the reflected signal from the probe tip and DUT follows an inverse process: the optical pulse incident on the receiver PCS induces transient conductivity in the device, which gates the incident signal through to the pre-amplifier and acquisition system. Measurement of the entire reflected waveform is obtained by varying the relative optical delay between the emitter and the receiver beams (often referred to as equivalent time sampling). The photocarrier lifetime in the PCS is approximately 1ps, but a rather slower transient with typically < 6 ps rise time.

Conventional (fully-electronic sampling) TDR has resolution difficulties because measurement of the distance from probe to the defect requires very high speed time resolution for sampling signals travelling at a speed close to that of light, and is almost impossible for an electronic sampling system. EOTPR, instead, measures the distance travelled by an electromagnetic wave in the air, which is essentially jitter free and is correlated to the distance travelled by the same electromagnetic wave in the DUT. The resolution of the distance-to-defect measurement is therefore determined by the resolution of a simple distance measurement in free space, which can be achieved relatively easily on the optical delay rail. Consequently, this equivalent time sampling system has very high time base resolution with very low jitter. Combined with a very narrow sampling window of the optically gated receiver PCS (< 1 ps), EOTPR provides a very high measurement bandwidth. Table 22.1 is a simple table comparing some major characteristics between EOTPR and conventional TDR.

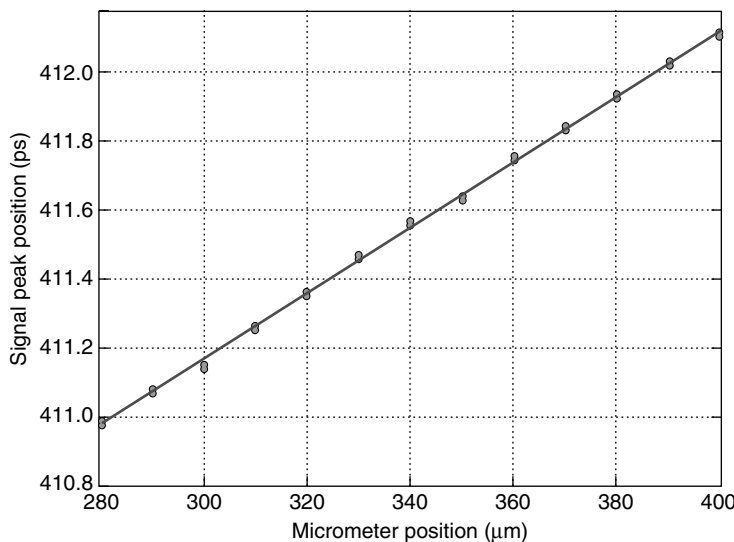
22.2 Characterizations of electro-optical terahertz pulse reflectometry (EOTPR)

EOTPR is characterized for four specifications: (a) resolution, (b) rise time, (c) signal-to-noise ratio, and (d) testing range on packaged units.

Table 22.1 Comparison between EOTPR and conventional TDR

	EOTPR	Conventional TDR
Rise time	5.7 ps	35–40 ps
Resolution	10 µm	500 µm
Feature resolved	C4* bump	Package or die

* C4 is 'Controlled Collapse Chip Connection'.



22.3 Reflection signal peak position versus micrometer position.

22.2.1 Resolution

This test measures the changes of reflected signals on an impedance characterization structure on packages when the high frequency probe is moved by only 10 µm. A 110 GHz probe was placed in contact with an impedance characterization structure ($50\ \Omega$) and moved over a distance of 100 µm in one direction in approximately 10 µm increments. The movement was actually carried out by moving the device on a micrometer-controlled stage with the probe remaining stationary. At each position, the reflection waveform was measured over the delay range of the rapid scan delay line. This was repeated 15 times at each position, before the waveguide was moved by another 10 µm. The peak positions of each waveform acquired at the 11 positions were then plotted in Fig. 22.3. The plot shows qualitatively that TDR waveform moves in one direction as the impedance characterization structure is moved with respect to the high frequency (HF) probe. A linear relationship can be drawn between the maximum peak position in each of the reflected signals and the micrometer

position. Statistical analysis of the peak positions shows that the level of confidence for the reflection waveform shift to a different position when the probe is moved by 10 µm is larger than the six-sigma value of 99.9999980%.

22.2.2 Rise time

The rise time is defined as the time for the reflected pulse from the end of the HF probe to rise from 10% to 90% of its maximum value. This rise time of the reflection from the probe tip of open-circuit is 5.7 ps. This rise time is a characteristic property of the system, including the effect of the high speed probe, cable and transceiver box. It is directly related with the resolution of this system – the lower the rise time, the better the resolution.

22.2.3 Signal/noise ratio (SNR)

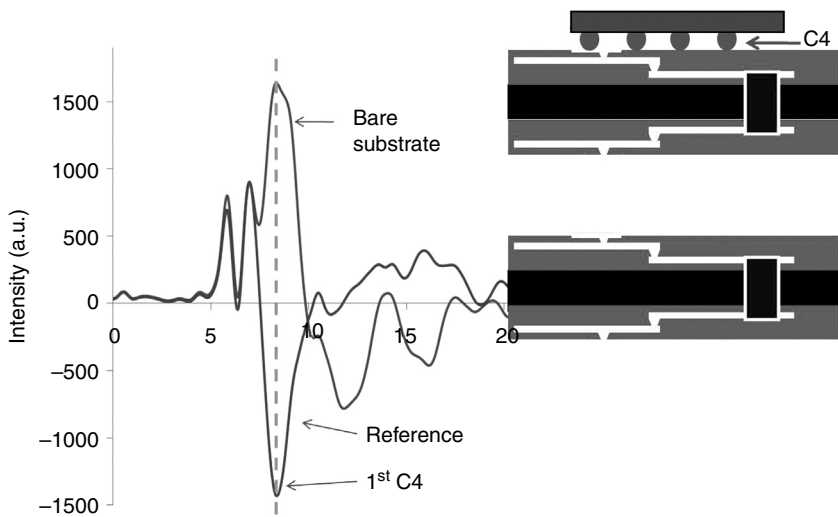
The SNR is a very important parameter as the resolution depends on higher SNR value. SNR is defined as $20 \log_{10}(s/\sigma)$. Here s is the maximum amplitude in the averaged time domain signal. σ is an estimate of the noise remaining in the average time domain signal. The specification value is for measurement of the reflected impulse from the end of the HF probe when it is open-circuit, and measured over the full range of the rapid scan delay line with the impulse centred in the measurement window and averaged for 45 s. The tool achieves 94 dB with this amount of averaging. In addition to better measurement resolution, this level of higher SNR is beneficial for reduction in the time required to make a measurement. In fact, this tool has an SNR of 64 dB without averaging, which is good enough for fast real-time measurement.

22.2.4 Test range

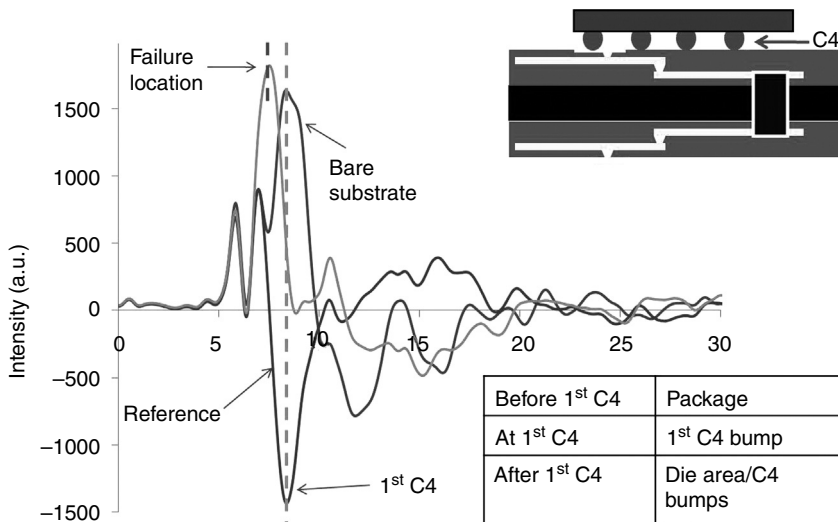
In order to collect signals from the longest traces of packages, this EOTPR system is required to measure faults at distance up to 150 mm through the contacting probe. This testing range specification was checked by measuring reflections from components with known electrical lengths corresponding to the peaks which demonstrated that the TPR system is able to measure over a significantly greater range than the length of 150 mm.

22.2.5 Waveform interpretation

Since pulses are sent into the DUT, it is expected to see a peak as the response. For EOTPR, a peak means open failure and a negative peak means bump, short, etc. For instance, a signal propagates from the test pin all the way into the die through the bump: if this were a bare substrate, it would be reflected



22.4 Identifying C4 location.



22.5 Reflection peak of failure within package.

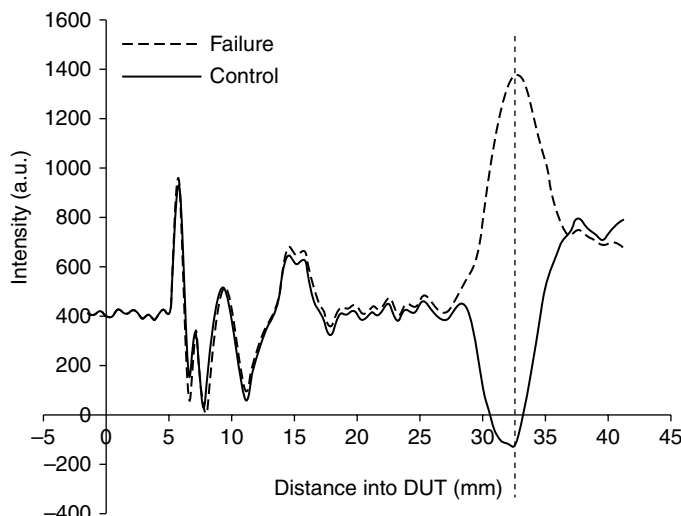
back right at the bump location and a peak would show up at the bump; if the signal passes the bump and goes into Si, a negative peak appears at the bump (Fig. 22.4). If there is a failure in the package and the pulse has not reached the bump, a peak will show up before the bump. In contrast, reflections show up on the right side of the bump if the failure is within the Si dies (Fig. 22.5). By determining the peak position of the reflected signal relative to the bump position, one can easily identify the failure location.

22.3 Examples of failure analysis using electro-optical terahertz pulse reflectometry (EOTPR)

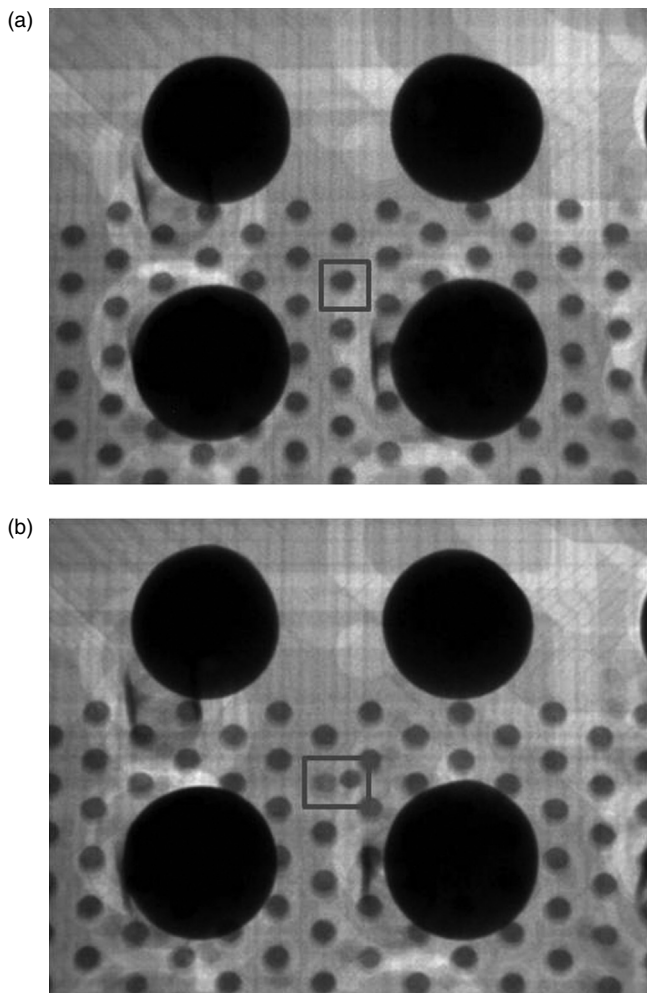
EOTPR waveform is different from that of conventional TDR. Here positive peaks represent open failure; negative peaks represent C4 joint, leakage, or short, etc. For a given circuit structure, a set of reflection peaks from a passing unit can be obtained as a reference, with which reflection peaks from failing units are compared and the failing locations can be calculated. The raw data from EOTPR consists of signal strength plotted against time in picoseconds. This plot can be converted to position by using a value of velocity factor that is calculated from the dielectric constant, assuming that the entire package (including, traces, vias, planes, etc.) is embedded within a homogeneous and infinite large dielectric material with a prescribed dielectric constant. A number of units with real failures were measured with EOTPR and the results were confirmed by physical failure analysis (FA). Examples of successful FA using EOTPR are described below including misaligned bump connection, trace open caused by dielectric crack, non-wet bump, and short/leakage failure in the substrate.

22.3.1 Misaligned bump connection

As shown in Fig. 22.6, an open failure was found in a product structure through electrical testing. The unit was measured with EOTPR and the resulting waveform (failure) was compared with that of a control unit. Of the control waveform, there is a big negative peak around 32.5 mm on x-axis

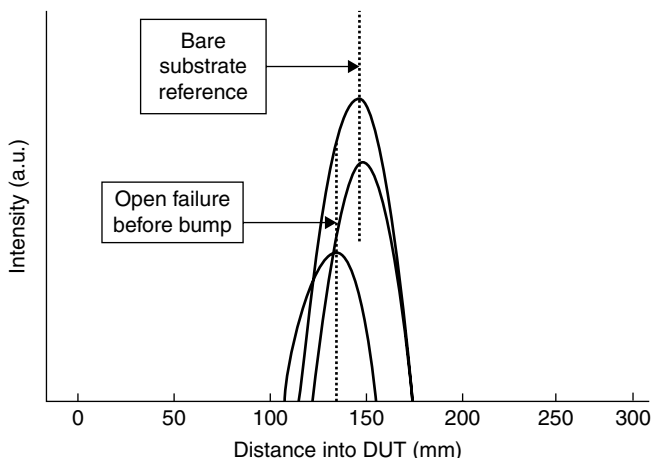


22.6 EOTPR waveform of an open failure in a product.



22.7 X-ray shows misaligned or disjoined bump that caused an open failure. (a) Control unit and (b) failed unit.

while at the same location a sharp positive peak shows up in the failed unit waveform. The big negative of the control unit can be attributed to the bump since the incident signal begins to enter the Si die at the bump and meets a large capacitance. The sharp positive peak at the location of the bump for the failed unit means that the incident signal does not enter into Si die; rather it is reflected back and displayed as a sharp positive peak. Therefore, there must be an open failure at the bump. The follow-up X-ray images did confirm that this open failure had been caused by a misaligned or disjoined bump, as shown in Fig. 22.7. In the top X-ray image, one dark



22.8 Open failure predicted by EOTPR.

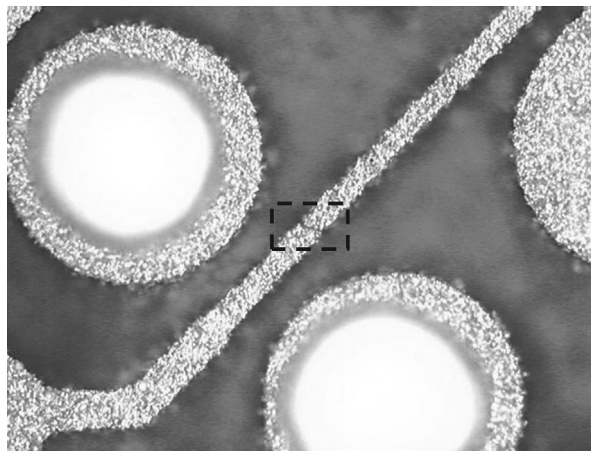
ball (the bump) shows up at the location of the prescribed bump (in a box); however, in the bottom image there are two dark balls showing up at this location, which indicates the solder bump and Cu bump were disjoined and did not merge into one. Therefore, the incident signal could not propagate into Si die and thus led to the open failure.

22.3.2 Open failure due to dielectric crack

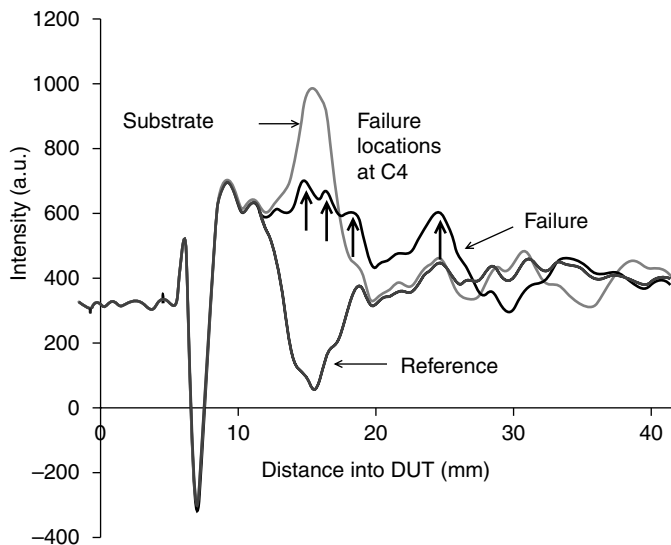
A failed CPU was determined to have an open failure by electrical test. EOTPR identified the failure was on a metal trace at one specific location within the package (Fig. 22.8). After the dielectric material was removed and the metal trace was exposed, it was confirmed that this open failure had been caused by a broken trace within the package as a result of dielectric crack, of which the location was predicted by EOTPR precisely (Fig. 22.9). With conventional TDR, this type of failure could be mistakenly assumed to be within the Si die, which would lead to unsuccessful failure analysis if the package was ground off according to TDR results.

22.3.3 Non-wet bump

A failed test vehicle was found to have an open failure at die corner bumps. EOTPR waveform indicated that this open failure should occur at bumps and identified the bump locations (Fig. 22.10). Subsequent 3D X-ray image confirmed that several non-wet bumps, as predicated by EOTPR, had caused this open failure as shown in Fig. 22.11; a non-wet (failed) bump still maintains spherical shape while a properly formed bump should render like a disc.



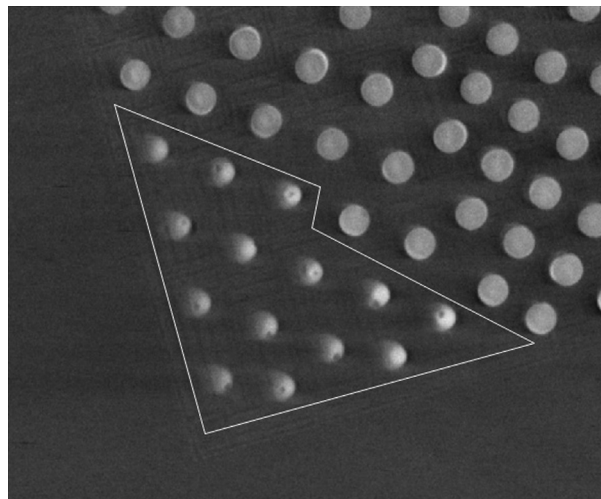
22.9 Trace open caused by dielectric crack.



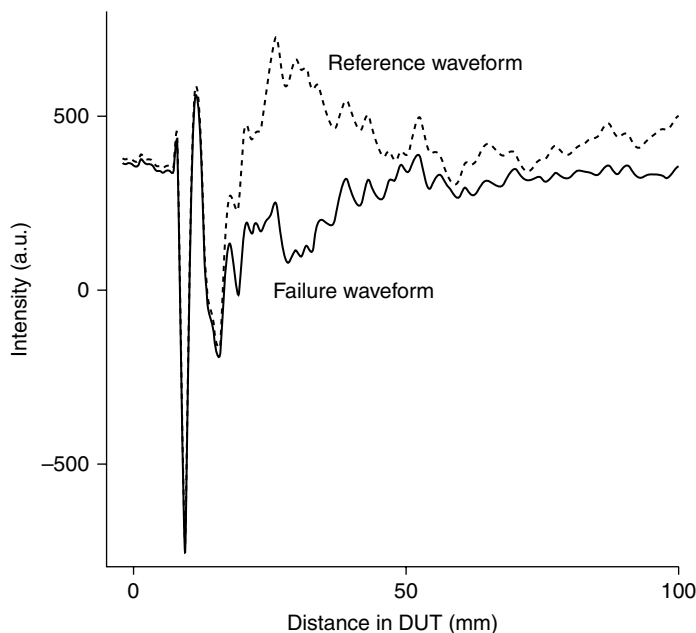
22.10 Open failure at C4 bumps detected by EOTPR.

22.3.4 Short/leakage failure in the substrate

By electrical test, a short/leakage failure was detected between two metal planes within a CPU package. EOTPR waveforms were acquired from test pin L22; however, there were many peaks/valleys showing up which made it difficult to identify the failure location (Fig. 22.12). However, some simple data processing helped to solve this problem; the substrate waveform

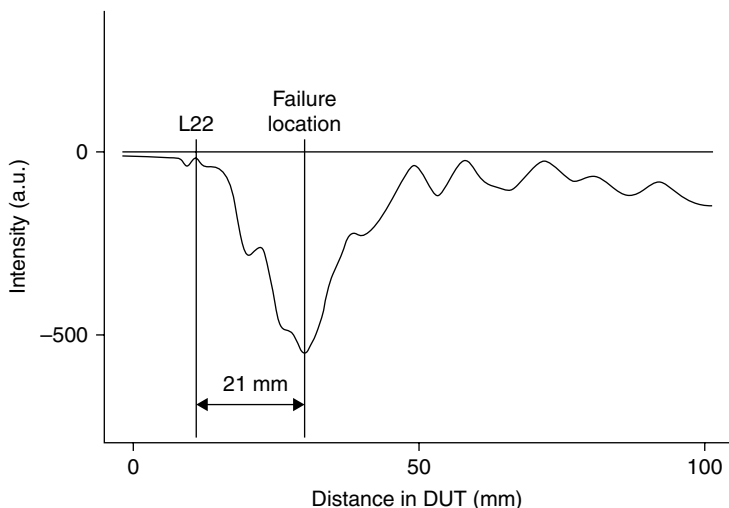


22.11 3D X-ray detected the non-wet C4 bumps (the enclosed spheres).



22.12 Waveforms of short/leakage before subtraction.

was subtracted from failure waveform so that the failure location could be manifested. The processed EOTPR waveform showed the leakage failure location to be at 21 mm from test pin L22 (Fig. 22.13). The unit was polished from die side until the dielectric layer between the two metal planes.



22.13 Waveform after subtraction pinpointed the failure location.

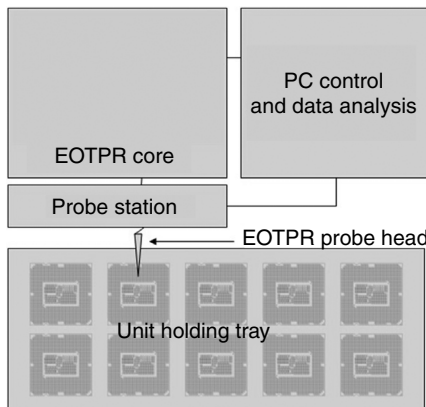
A circle with radius of 21 mm was drawn from Pin L22 and the area around this circle was searched. Finally at a location 21 mm from L22, a Cu particle was found which had caused this plane-to-plane leakage.

22.4 Conclusions and future trends

Until now, EOTPR has been successfully implemented in FA flow and used as a standard analytical tool in assembly and test development. EOTPR possesses some unique capabilities for fault isolation: determination of failure locations around incoming first level interconnection bump – whether it is within the Si die or the package; precise identification of the locations of trace cracks in the vicinity of bumps (which is impossible with conventional TDR); identifications of the location of open failure for Daisy Chain; fault isolation on certain short and leakage cases.

Future development of THz technology for applications in microelectronic industry will be focusing on several major areas as described in this section.

As the resolution of THz technology is continuously improving, applications of THz technology can be expanded from the fault isolation and failure analysis field into quality-assurance areas in microelectronic manufacturing, where substrate metal line and interconnection joint quality can be monitored based on their response to the THz signal as an indicator of process healthiness. Figure 22.14 shows a schematic of an example of quality-assurance test system, which consist of EOTPR core system, a probe station with EOTPR probe head, and a sample holder that can handle a high volume



22.14 Schematic of an example of the Quality Assurance Test System.

manufacturing sample size. The system can vary in design dependent on the particular manufacturing environment.

Terahertz technology has also advanced dramatically in industry applications such as imaging or sensing (Chan *et al.*, 2007). However, due to its high reflectivity from metals, THz imaging has limited application in high density interconnection packaging technology, where it can only be used as an imaging tool to inspect defects that are embedded in the build up organic layers, such as delaminations in the electronic package encapsulation layers, and it is also limited by its resolution, due to current THz focusing techniques. Further development in this area is still needed to fully realize its capability.

In addition, electronic packages are becoming more and more sensitive to moisture absorption, where catastrophic failures, such as pop corning, could occur during the surface mounting reflow process due to high moisture content in microelectronic components. THz spectroscopy could play an important role in measuring and monitoring the moisture absorption in electronic packages due to its sensitivity to water content (Siegel, 2002).

As industry is adopting more and more SOC (system on a chip) designs and mixed processes and technologies, electrical field mapping (Yang and Whitaker, 2002; Seo *et al.*, 2007) could be another area where THz technology could be utilized to study complex circuit responses including optical interconnects.

22.5 References

- Cai, Y., Wang, Z., Dias, R., and Goyal, D., 'Electro optical terahertz pulse reflectometry – an innovative fault isolation tool', *Electronic Components and Technology Conference (ECTC), 2010 Proceedings 60th*, Las Vegas, NV, USA, 1309–1315 (2010).

- Chan, W., Deibel, J., and Mittleman, D., ‘Imaging with terahertz radiation’, *Rep. Prog. Phys.*, **70**, 1325–1379 (2007).
- David, G., Yun, T.-Y., Crites, M.H., Whitaker, J.F., Weatherford, T.R., Jobe, K., Meyer, S., Bustamante, M.J., Goyette, B., Thomas, S., III., and Elliott, K.R., ‘Absolute potential measurements inside microwave digital IC’s using a micromachined photoconductive sampling probe’, *IEEE T. Microw. Theory*, **46**, 2330–2337 (1998).
- Frankel, M.Y., Whitaker, J.F., and Mourou, G.A., ‘Optoelectronic transient characterization of ultrafast devices’, *IEEE J. Quantum Electron.*, **28**(1), 2313–2324 (1992).
- Frankel, M.Y., Whitaker, J.F., Mourou, G.A., and Valdmanis, J.A., ‘Experimental characterization of external electrooptic probes’, *IEEE Microw. Guided W.*, **22**(1), 60–62 (1991).
- Nagel, M., Michalski, A., and Kurz, H., ‘Contact-free fault location and imaging with on-chip terahertz time-domain reflectometry’, *Opt. Express*, **19**(13), 12509 (2011).
- Pfeifer, T., Heiliger, H.-M., Loffler, T., Ohlhoff, C., Meyer, C., Lupke, G., Roskos, H.G., and Kurz, H., ‘Optoelectronic on-chip characterization of ultrafast electric devices: measurement techniques and applications’, *IEEE J. Sel. Top. Quant.*, **2**, 586–604 (1996).
- Seo, M.A., Adam, A.J.L., Kang, J.H., Lee, J.W., Jeoung, S.C., Park, Q.H., Planken, P.C.M., and Kim, D.S., ‘Fourier-transform terahertz near-field imaging of one-dimensional slit arrays: mapping of electric-field, magnetic-field, and Poynting vectors’, *Opt. Express*, **15**, 11781–11789 (2007).
- Siegel, P.H., ‘Terahertz technology’, *IEEE T. Microw. Theory*, **50**, 910–928 (2002).
- Valdmanis, J.A. and Mourou, G., ‘Subpicosecond electrooptic sampling: principles and applications’, *IEEE J. Quantum Electron.*, **22**(1), 69–78 (1986).
- Yang, K. and Whitaker, J., ‘Electro-optic sampling and field mapping’, in *Ultrafast Lasers: Technology and Applications*, CRC press, 473–519 (2002).

- aerospace industry
continuous-wave non-destructive
terahertz imaging, 532–7
non-destructive imaging for glass
fibre reinforced plastics, 537–42
- reflective terahertz time domain
spectroscopy of aircraft
composites, 520–31
- terahertz applications, 510–44
- transmissive terahertz time domain
spectroscopy of aircraft
composites, 513–20
- air–composite interface, 528
- aircraft composites
reflective terahertz time domain
spectroscopy, 520–31
results and discussion, 522–31
theory and experiment, 520–2
- transmissive terahertz time domain
spectroscopy, 513–20
results and discussion, 515–20
theory and experiment, 513–15
- AMDATA 5-Axis System, 538
- annual growth ring, 549
- anti-resonant reflecting optical fibres,
45–6
- apertures scanning near-field optical
microscopy (ASNOM), 95
- ARROW fibre, 45
- art conservation
artwork internal structure
observation using THz waves,
620–1
- development of THz technology as
tool for heritage science, 621–2
- material analysis using THz waves,
617–20
- overview, 615–17
- terahertz gap in heritage science,
615–16
- terahertz waves advantage, 616–17
- terahertz applications, 615–22
- asynchronous optical sampling
(ASOPS), 296
- asynchronous-optical sampling
THz-TDS (ASOPS-THz-TDS),
460
- attenuated total reflection terahertz
time-domain spectroscopy (ATR
THz-TDS), 583–5
- sampling technique, 584
- Auston switches, 299
- backward wave oscillators (BWOs), 4
- beam shaping, 189–90
- measured THz transmission spectra
and image from spatial light
modulator, 191
- beat signal, 442
- Beer-Lambert law power attenuation,
203
- benzocyclobutene, 414
- bipolar complementary metal oxide
semiconductor (BICMOS), 232
- birefringence, 550, 553, 554–6, 556–64,
567
- bit-error-rate tester (BERT), 183
- bolometers, 7, 404
- Bragg fibres, 46–51
fabrication based on high-index
composite materials, 46–8
fabrication procedures, 49
- PE-based polymer compound
refractive index and power
absorption loss, 48
- schematic of hollow Bragg fibre, 47

- Bragg fibres (*cont.*)
 modal properties in high-index
 -contrast polymer, 48–51
 modal properties in high-index
 contrast polymer Bragg fibres
 experimentally measured
 transmission, 50
 fundamental mode and modal loss
 in TiO_2 -doped PE/PE hollow
 core, 51
- broadband pulsed terahertz radiation
 generation and detection, 466–8
 THz power spectrum of dipole
 antennas, 468
 THz pump-probe set-up, 467
- Bruggeman model, 47
- bump
 misaligned connection, 633–5
 control and failed unit, 634
 waveform of an open failure in
 product, 633
 non-wet, 635
 C4 bumps detected by 3D X-ray,
 637
 open failure at C4 bumps detected
 by EOTPR, 636
- carbon nanotubes, 405–12
 bolometric THz detection, 405–6
 carbon nanotube quantum dot
 (CNT-QD) and electron
 tunnelling processes, 408
 near-infrared detector with carbon
 nanotube films, 406
 THz detector with carbon nanotube
 transistors, 407
 THz detector with CNT/2DEG
 hybrid structure, 410–11
 THz photon-assisted tunnelling,
 406–9
 ultra-sensitive readout of
 THz-excited carriers, 409–12
- carbon reinforced fibre plastic (CRFP),
 511
- cellulose, 553
- channel narrowing, 150
- chemical mapping, 605–7
 pseudocolour prediction images for
 the split tablets, 606
- 3D chemical mapping, 607
- chromatic dispersion, 302
- circular holes, 99–101
 effective dipole moments, 101–4
 electric and magnetic dipole
 moments above and below
 surface view, 102
 normalised tangential magnetic and
 electric field distributions, 103
 schematic set-up with oblique
 incidence and surface current
 distribution, 104
- near-field imaging, 99–101
 diffraction of a plane wave, 101
 THz electric near-field, 100
- CMOS field effect transistors
 technology, design and
 implementation, 243–9
 array of 50 patch-antenna-coupled
 detectors, 249
- CMOS antenna integration, 246–8
- CMOS technology with respect to
 THz focal-plane arrays, 244–6
 cross-section through the back-end
 of a CMOS chip, 245
 detector design and
 implementation, 248–9
- coating process monitoring
 inline, 602–3
 coating thickness measured by
 the inline THz sensor and TPI
 offline linear fit, 603
 offline, 601–2
 coherent frequency linking, 437–9
 optical and THz comb, 439
- complementary metal oxide
 semiconductor (CMOS), 232
- computed tomography (CT), 494–8, 622
 3D-CT image-acquisition system, 497
 reconstructed 3D-CT image of
 soot-removal filter, 498
 soot-removal filter, 495
 test sample of a soot-removal
 filter, 497
 transmittance, 496
- COMSOL Multiphysics, 30, 42
- conductor-dielectric-conductor
 multilayer, 77
- continuous-wave, 437, 512

- continuous-wave laser, 448–9
 continuous-wave mode, 10–14, 15–16
 THz-PCA with small active area and equivalent circuit model, 12
 continuous-wave non-destructive terahertz imaging, 532–7
 results and discussion, 534–7
 absorption coefficient measurements, 534
 transmission measurements, 534–5
 theory and experiment, 532–4
 continuous-wave photomixing, 177
 continuous-wave terahertz, 439–42, 443, 447–8
 radiation, 469–70
 beamsplitter, optical delay line and THz emitter and detector, 469
 coordinated universal time, 451
 coplanar waveguide (CPW), 628
 Cosine Correlation Mapping (CCM), 606
 Coulomb screening effect, 14–15
 coupler fibre, 41
 covert battlefield, 173–7
 channel cooling together with spread spectrum techniques, 176
 schematic of communication link utilising ultra-wide THz bandwidth, 175
 crystal fingerprints, 591
 current narrowing, 150–1
 current peak shift, 405
 current readout mode, 234
 cut-off frequency, 235
 cyclotron resonance spectrometer, 135–6
 spectra InSb bulk emitter and InGaAs HEMT emitter, 136
 Debye model, 218–19
 decay length, 75
 density functional theory (DFT), 225
 density matrix theory, 432
 dielectric-conductor-dielectric multilayer, 77
 dielectric crack
 open failure predicted by EOTPR, 635
 trace open, 636
 dielectric phase-locked resonator oscillator (DPRO), 181
 difference frequency generation (DFG), 18
 digital video broadcast (DVB), 199
 directional coupler method, 41–4
 finite-element calculated modal properties, 44
 power as function of relative displacement and fibre attenuation data fit, 43
 schematic of set-up for measurement of fibre transmission losses, 42
 dispersion, 34–5, 67–72
 dispersion relation of SPPs, 72
 non-porous and porous PE fibres and temporal evolution of output signal, 36
 real and imaginary components of wavenumber of SPPs, 70
 dispersion law, 125
 distributed Bragg reflector (DBR) diode lasers, 350
 distributed feedback (DFB) diodes, 350
 Dove prism, 585
 Drude model, 64–7, 278
 real and imaginary components of permittivity of gold, 66
 real and imaginary components of single crystalline bulk InSb permittivity, 67
 drug coating, 598–601
 thickness and uniformity, 598–9
 biconvex tablet false colour and film coating, 599
 drug tablet, 598–601
 density and hardness, 600
 performance, 600–1
 dual-mode DFB laser, 354–5
 dual-wavelength optical parametric oscillators (OPO), 356–7
 Dyakonov–Shur equations, 236–7, 238
 Dyakonov–Shur model, 242
 edge emission, 138
 effective wavelength, 334
 EL2, 471, 473–5
 electrical noise-equivalent power (NEP_e), 252

- electrical responsivity, 250
 electro-optic crystal, 96
 electro-optic modulator (EOM), 346
 electro-optical terahertz pulse reflectometry (EOTPR)
 characterisation, 629–33
 failure analysis, 633–8
 principle, 625–9
 electro-optics (EO), 624–5, 626–8
 sampling system and head, 627
 electromagnetic potential theory, 8
 electromagnetic surface mode, 70
 electromagnetic terahertz comb (EM-THz comb), 438, 457–8, 461
 electromagnetic waves, 99
 electron beam sources, 4
 ErAs:GaAs, 478
 ErAs:In_{0.53}Ga_{0.47}As-In_{0.52}Al_{0.48}As, 485
 fabricated resonant tunnelling diodes, 431–4
 calculation and experimental results of fundamental oscillation frequencies, 433
 current–voltage characteristics of fabricated RTD, 431
 oscillation spectrum of fabricated RTD, 432
 Fabry-Pérot reflection, 519–20, 526, 529, 544
 Fabry-Pérot resonant, 38
 far infrared, 295
 wood properties, 556–65
 femtosecond fibre laser system, 499
 femtosecond mode-locked laser, 437–8, 441
 femtosecond mode-locked optical pulse train, 438
 fiber-based optical comb, 448–9
 fibre-based terahertz imaging, 40
 scanning imaging system, 40
 fibre-coupled terahertz time-domain spectroscopy systems (THz-TDS), 295–324
 comparison with other systems and techniques, 318–24
 fibre-based continuous wave (cw) systems, 321–4
 fibre-based pulsed systems – Picometrix Inc., 318–19
 fibre-coupled system using 1.5 μm pump wavelength, 321
 layout of cw THz system, 323
 mesa-structured InGaAs/InAlAs PCAs, 322
 pulsed systems at 1.5 microns pump wavelength, 319–21
 system layout of Picometrix Inc.
 fibre-coupled modules, 319
 experimental layout and system characterisation, 303–11
 19" rack containing all electronics and optics, 310
 average power dependent pulse length after propagation, 308
 components, heads and system, 309–10
 dependency of the minimally obtainable laser pulse duration after propagation, 307
 experimental layout of fibre-coupled THz-TDS system, 304
 laser pulse interferometric autocorrelation, 307
 laser pulse width after propagation, 306
 measurement heads, 310
 non-linear effects, 308
 recorded reference pulse measured in transmission, 311
 stretcher based on angular dispersion, 305
 system characterisation, 310–11
 fibre-based THz systems
 measurement results, 312–18
 angle dependent measurements, 312–13
 angular-resolved reflection
 measurement of metallised sand paper, 313
 compact and monolithic sensor for ATR spectroscopy, 317
 fibre-coupled monolithic attenuated total reflection (ATR)-sensor, 316–18

- goniometer with Tx/Tx modules, 312
 high-speed measurement of cyclotron resonance in pulse magnetic field, 313–16
 relative transmitted THz amplitude of the ATR sensor, 318
 time-dependent magnetic field, 315
 fibre guiding, 300–3
 fibre patch cord used to guide the laser pulses to the measurement head, 301
 future trends, 324
 laboratory THz time-domain spectroscopy system experimental layout, 298
 photoconductive antenna, 299
 recorded electric field in the time-domain and spectral amplitude, 297
 fibre coupling, 312
 fibre-orientation analysis, 550
 field effect transistor (FET), 121
 experimental set up, 141
 GaAs/AlGaAs photoresponse, 141
 steady state instability with dc current, 125–8
 dimensionless instability increment, 127
 oblique modes and edge emission, 127–8
 terahertz radiation detection, 128–35
 characteristic length, 131–2
 high frequency regime, 130
 low frequency regime, 130–1
 nonlinearity mechanism, 132
 phenomenological approach, 134–5
 schematics as THz detector and equivalent circuit, 129
 simplified theory, 132–3
 THz detection experimental studies, 141–52
 broadening, 148–50
 channel narrowing, 150
 current narrowing, 150–1
 gate leakage current, 142
 high magnetic field studies, 151–2
 loading effects, 143–5
 optical length choice, 145
 photoresponse modelling, 142
 resonant detection, 147–8
 room temperature imaging, 146–7
 Silicon FETs, 145–6
 temperature dependence, 142–3
 THz emission studies, 135–40
 cyclotron resonance spectrometer, 135–6
 edge emission, 138
 Fourier-transform spectrometer, 136–7
 terahertz emission threshold, 137–8
 tunable emission, 139–40
 field effect transistor (FET) detectors characterisation and optimisation, 249–59
 calculated real and imaginary parts of the impedance of FET, 254
 drain coupling and parasitic equivalent-circuit components, 255
 electrical and optical responsivity, 250–1
 limitations for impedance matching and tuning, 253–5
 measured voltage responsivity vs gate voltage, 251
 method for device characterisation, 255
 NEP as function of gate voltage, 253
 noise-equivalent power (NEP), 251–2
 optical responsivity of detectors for emission frequencies, 258
 response time, 252–3
 responsivity enhancement by current bias, 259
 results for MOSFET THz detectors, 256–9
 finger spacing, 331–2
 finger width, 332
 Fourier-transform near-field imaging, 107

- Fourier-transform spectrometer, 136–7
 free electron lasers (FELs), 4
 free-space damping
 fog, rain and snow, 163–5
 calculated atmospheric attenuation
 in THz and IR band, 163
 predicted IR in THz and sub-THz
 attenuation due to spherical
 airborne particles, 166
 free spectral range (FSR), 353–4
 frequency modulation (FM), 190
 frequency multipliers, 4–5
 Fresnel reflection, 549
 Friis formula, 160
- GaAs devices, 330–8
 antenna design, 333–6
 ion-implanted GaAs, 336–7
 low-temperature-grown GaAs, 336
 nanocomposite GaAs, 337–8
 photomixer design, 331–3
 gate leakage current, 142
 calculated room temperature
 photoresponse of GaAs/AlGaAs
 FET at 600 GHz, 143
 gate-source coupling, 234
 glass fibre composite
 material parameter measurement
 with reflection configuration,
 522–3
 THz TDS, 523
 reflective imaging of coupon defects,
 523–7
 amplitude of frequencies showing
 bend damage and scanned area,
 526
 milled circle analysis using
 Fabry-Pérot reflection, 527
 milled composite using peak pulse
 amplitude, 524
 three heat-damaged areas on
 composite samples, 525
 THz TDS time-domain signal and
 side profile of the large thermal
 blister, 526
 reflective imaging of heat-damaged
 samples, 535–6
 600 and 100 GHz sample images,
 535
- reflective imaging of hidden defects,
 536–7
 polyamide sample NKT-4
 circular defects and
 delamination, 537
 reflective imaging of panel defects,
 527–8
 panel with puncture hole and
 regions of thermal damage, 528
 glass reinforced fibre plastic (GRFP),
 510–11, 537–42
 comparison, 542
 different NDE techniques, 543
 experimental procedures, 538–42
 continuous-wave 600 GHz images,
 540–1
 CW THz images of glass-fibre
 samples, 541
 flash IR thermographic images of
 time-derivative surface, 541
 pulsed terahertz imaging, 542
 pulsed THz imagery of glass fibre
 samples, 542
 radiographic inspection, 538
 radiographic X-ray through scans
 of glass-fibre samples, 539
 thermographic inspection, 540
 ultrasonic inspection, 538–40
 ultrasonic scans of glass-fibre
 samples, 540
 X-ray CT scans of glass-fibre
 samples, 539
 group velocity dispersion (GVD), 34,
 302
 Gunn electron devices, 4
- H-shaped dipole, 299
 Hall effect, 476–7, 480
 hardwoods, 553
 hemicellulose, 553–4
 heritage science
 terahertz gap, 615–16
 THz technology development, 621–2
 heterodyne detectors, 7–8
 heterodyne (frequency conversion)
 detection, 405
 heterojunction bipolar transistors
 (HBT), 429
 high-definition television (HDTV), 158

- high electron mobility transistor (HEMT), 137, 179
- high frequency regime, 130
- long gate, 130
 - short gate, 130
- high magnetic field studies, 151–2
- experimental photoresponse and magnetoresistance vs 300GHz oscillations, 151
- hollow-core fibres, 45–51
- anti-resonant reflecting optical fibres, 45–6
 - PE and PTFE tube cross-section images, 46
 - Bragg fibres, 46–51
- homodyne detectors, 6–7
- hybrid plasmonic switching devices, 287–9
- hydrates, 590–1
- hydroxypropyl methyl cellulose (HPMC), 603–4
- ideal current responsivity, 239
- III/V-tunnelling-diode arrays, 267
- indium gallium arsenide (InGaAs), 320
- indoor THz communication channel, 166–9
- infrared lock-in thermography, 392
- InGaAs/InP devices, 338–44
- photodiode emitters, 339–41
 - nipnip photodiodes, 339
 - UTC photodiodes, 340–1
 - WIN photodiodes, 339–40
 - receiver photodiodes, 342–4
 - receiver photomixers, 341–2
- integrated circuits, 183–4, 198
- output power vs frequency from several semiconductor, 184
- integrated terahertz biosensor chip, 423–9
- delay time variation of THz pulse depending upon applied volume of DNA specimen, 428
 - numerical calculation results using TLM method, 426
 - on-chip transmission line sensors, 425
 - structure and design of transmission line sensors, 424–6
- temporal THz waveform and FFT spectrum of the fabricated device, 427
- THz biosensor chip experiments and results, 426–9
- transmission line sensors, 423–4
- Inter-Symbol Interference (ISI), 168
- intermediate frequency (IF), 7
- International System of Units, 437
- ion-implanted GaAs, 336–7
- junction-gate field-effect transistors (JFET), 235
- kinetic inductances, 129
- kinetic THz absorption (KITA) technique, 219
- Kirchoff formalism
- near-field estimate, 110–16
 - FDTD analysis, 115
 - field enhancements in rectangular holes, 116
 - nanoslit and nanoantenna, 112–16
 - SEM image of a 70nm-width nanogap perforated on gold film, 113
 - THz nanogap concept, 114
- relation between near- and far-field, 110–12
- diffraction geometry for screen with square aperture, 111
 - THz far-field set-up and reference aperture, 112
- Kubelka–Munk spectrum, 503–5
- Kubelka–Munk theory, 502, 503
- Labview program, 309
- lignin, 553–4
- Lithium Niobate modulator, 185
- loading effects, 143–5
- registered signal amplitude and phase for different frequencies, 144
- local oscillator (LO), 181
- localised surface plasmon resonances (LSPRs), 82
- long-range surface plasmon polaritons (LRSPPs), 78
- low frequency regime, 130–1
- long gate, 130–1

- low frequency regime (*cont.*)
 ac voltage dependence and dc
 photo-induced voltage, 131
 short gate, 130
- low-temperature-grown GaAs, 336, 458, 467, 468, 469, 471–7
- absorption spectra different
 annealing temperatures, 474
- anneal temperature for a
 photoconductive device, 472
- double crystal X-ray rocking curves, 473
- neutral As antisite concentration
 as function of annealing
 temperature, 476
- peak separation and lattice mismatch, 474
- time-resolved differential reflectivity, 477
- LT-In_{0.53}Ga_{0.47}As-In_{0.52}Al_{0.48}As, 478–85
 carrier concentrations as a function
 of annealing, 482
- DCXRD of undoped sample as a
 function of annealing, 481
- mobility as a function of annealing, 482
- sheet resistance as a function of
 annealing, 483
- THz power spectrum of annealed
 high resistivity dipole antennas, 484
- THz system response using annealed
 high resistivity photoconductive
 samples, 484
- Maxwell's equation, 97
- mean dissolution time (MDT), 600–1
- metal-semiconductor FET (MESFET), 235
- micro-electro mechanical systems
 (MEMS), 190
- microbolometer arrays, 266
- microstrip antennas, 246
- microwave frequency multipliers, 180–3
 THz source and receiver from
 reference 62, 181
- THz transmission link scheme and
 balanced mixer characteristics at
 625 GHz, 182
- modulators
 terahertz waves, 184–90
 beam shaping and steering,
 189–90
 experimental set-up for outdoor
 data communication and
 subsystem details, 187
- generator independent modulation
 schemes, 186–9
- generator specific modulation
 schemes, 185–6
- Schottky diode mixer systems, 186
- molecular beam epitaxy (MBE), 320, 467
- monolithic microwave integrated circuit
 (MMIC), 5, 378
- Monte Carlo simulations, 167
- Mousley-Vilar equation, 162
- multilayered structures, 76–81
 long-range and short-range
 surface plasmon polaritons in
 slab, 77–81
- LRSPPs and SRSPPs wavenumber
 real and imaginary components,
 78, 79
- propagation and decay length, 80
- surface charges and electric field
 lines of LRSPPs and SRSPPs, 80
 time-average field profiles of
 LRSPPs and SRSPPs, 81
- multiplied microwave systems, 199
 BER curves for long/short PRBSs
 with and without decision
 threshold optimisation, 200
- N14053 aircraft, 511
- nanocomposite GaAs, 337–8
- nanoscale terahertz detector, 404–12
 carbon nanotube quantum dot
 (CNT-QD) and electron
 tunnelling processes, 408
 carbon nanotubes, 405–12
 nanoscale superconductor THz
 bolometer, 405
 near-infrared detector with carbon
 nanotube films, 406
- PAT process for double-coupled QD, 409

- superconductor and semiconductor, 404–12
- THz detector with carbon nanotube transistors, 407
- THz detector with CNT/2DEG hybrid structure, 410–11
- near-field imaging
 - fundamental aspects of terahertz sensing, 91–116
 - subwavelengths holes, 99–110
 - terahertz measurements, 95–9
 - ASNOM technique schematic and scattering-type SNOM, 96
 - detector antenna electrode structure and two near-field detection techniques, 98
 - experimental set-up for scanning optical microscopes, 95
 - THz electric field and magnetic near-field profile at 1THz for slit array, 98
 - THz near-field microscopy set-up, 97
 - terahertz sensing fundamentals
 - Kirchoff formalism for near-field estimate, 110–16
 - near-field microscopy, 37
 - near-field THz imager, 412–18
 - calculations of THz electric field distributions, 416
 - illustration of integrated near-field THz imager, 415
 - improved structure with carbon nanotube detector, 418
 - integrated near-field THz imager, 415–18
 - near-field image of THz emission distribution in another 2DER sample, 418
 - THz transmission signal as function of near-field THz imager position, 417
 - near-field THz imaging, 413–14
 - types, 414
 - nipnip photodiodes, 339
 - noise equivalent temperature difference (NETD), 6
 - non-destructive cutback technique, 41–4
 - non-linear length, 303
 - non-return-to-zero (NRZ), 183
 - nonlinear crystals
 - difference frequency mixing, 19–22
 - parametric interaction, 18–19
 - nonlinearity mechanism, 132
 - oblique modes
 - calculated instability increments for normal fundamental and boundary mode, 128
 - oblique plasma waves, 127
 - Ohm's law, 122
 - optical array responsivity, 250
 - optical coherence tomography (OCT), 498
 - optical-comb-referenced terahertz synthesiser, 447–56
 - experiment result, 452–6
 - CW-THz radiation frequency fluctuation, 455
 - CW-THz radiation incremental tuning, 455
 - CW-THz radiation spectra, 453
 - CW-THz radiation spectral configuration, 456
 - OFS1 and OFS2 parameters, 454
 - experimental set-up, 451–2
 - schematic diagram, 450
 - principle of operation, 448–51
 - photomixing of two OFS, 449
 - optical fibres, 301
 - optical length choice, 145
 - photoresponse of Si-MOSFETs vs gate length, 145
 - optical noise-equivalent power (NEP_o), 252
 - optical responsivity, 250
 - optically pumped far-infrared gas lasers, 5
 - optically thin metallic hole arrays, 274–8
 - opto-electronic, 177–80
 - schematic of sub-THz generation using optical frequency comb, 179
 - opto-electronic approaches, 232

- opto-electronic THz communication systems, 192–8
- photonic MMW/UTC-PD opto-electronic systems, 195, 197–8
- time-domain systems as communication links, 192–5
- different date rate eye diagrams and error-free operation, 196
- experimental set-up using external THz modulator, 194
- optoelectronic detectors, 8
- optoelectronic techniques
- signal detection in THz-PCAs, 15–17
 - continuous-wave mode, 15–16
 - continuous-wave vs pulsed mode, 17
 - pulsed mode, 16–17
- signal generation in THz-PCAs, 8–15
- aperture illuminated by laser beam, 9
 - continuous-wave mode, 10–14
 - coulomb and radiation screening effect, 14–15
 - pulsed mode, 14
- terahertz waves generation and detection, 3–22
- detector technologies, 6–8
- difference frequency mixing in nonlinear crystals, 19–22
- parametric interaction in nonlinear crystals, 18–19
- signal detection in THz-PCAs, 15–17
- sources, 5–6
- oriented strand board (OSB), 569–74
- process, 569–70
 - schematic diagram, 569
- process challenge, 570
- result, 572–4
- MPA, 573
- THz solution, 570–2
- scanning system, 572
- passive imaging, 231–2
- periodically poled lithium niobate (PPLN) crystal, 357
- pharmaceutical industry
- future trends, 607–9
 - terahertz applications, 579–609
- terahertz time-domain imaging (THz-TDI), 594–601, 601–7
- terahertz time-domain spectroscopy (THz-TDS), 581–9, 589–94
- pharmaceutical quantification, 591–2
- THz pulsed spectra of binary mixture of CBZ forms I and III, 591
- photocarrier terahertz comb (PC-THz comb), 438, 440–2, 443
- photoconductive antenna (PCA), 299, 438, 440–2, 451, 466, 581
- photoconductive semiconductor, 470–85
- photoconductive switch, 624–5
- sampling, 626, 628–9
 - EOTPR vs. conventional TDR, 630
- terahertz emission and PCS detection, 628
- photoconductors, 404
- photodiode emitters, 339–41
- nipnip photodiodes, 339
 - UTC photodiodes, 340–1
 - WIN photodiodes, 339–40
- photomixing, 327, 469–70
- CW THz radiation generation, 470
- photon-assisted tunnelling (PAT), 405
- photon sidebands, 406
- photoresponse modelling, 142
- photovoltaic effect, 128
- photovoltaic signal, 141
- planar diode chips, 186
- plasma wave velocity, 124
- plasma waves
- low-dimensional structures, 122–5
 - 2D electron gas, 123
 - bulk plasma, 123
 - gated 2D electron gas, 124–5
 - wires, 125
- plasmon oscillation, 272
- plasmonic mixing, 235–43
- device model, 235–6
 - distributed resistive-self-mixing regime, 238–41
 - frequency dependence of the efficiency factor, 243
- plasmonic mixing regime, 241–3
- resistive mixing regime, 236–8
- spatial distribution of gate-to-channel voltage oscillations, 237

- voltage response and ideal current responsivity, 239
- plasmonic mixing regime
 - frequency dependence of the efficiency factor, 243
 - high-frequency enhancement of the sensitivity, 241–2
 - resonant mixing, 242–3
- plastic waveguides
 - challenges of terahertz fibre optics, 29–39
 - dispersion, 34–5
 - losses, 29–34
 - porous core subwavelength fibres, 30–2
 - solid core subwavelength fibres, 30
- composite materials, 51–4
 - extracted refractive index and metamaterial film permittivity, 54
 - optical micrographs of metal and semiconductor arrays, 53
 - SEM image of fabricated wire-array fibres cross-sections, 53
- terahertz experimental characterisation
 - THz-TDS set-up for waveguide measurements, 55
- terahertz waves transmission and propagation, 28–58
 - devices based on subwavelength fibres, 39–44
 - experimental characterisation, 54–6
 - hollow-core fibres, 45–51
- polarisation-maintaining (pm)
 - single-mode (sm) fibre, 301
- polarisation mode dispersion, 301
- polymorphism, 589
- polymorphs, 589–90
 - THz absorbance spectra of CBZ form III and I, 590
- polypeptides, 225
- printed circuit board (PCB), 379
- propagation length, 74
- pseudo random bit sequence (PRBS), 195
- pulse pattern generator (PPG), 191
- pulsed mode, 14, 16–17
- pulsed terahertz, 542
- pyroelectric cameras, 266
- pyroelectric detectors, 7
- quadrature amplitude modulation (QAM), 190
- quantum cascade lasers (QCL), 183, 198
- quantum detection, 406
- quantum well, 479–80
- quasi time domain spectroscopy (QTDS), 355–6
- radiation screening effect, 14–15
- radio-over-fiber (RoF) systems, 197
- Raman-shifted Stokes photon, 18
- ray-tracing techniques, 167
- Rayleigh scattering, 165
- receiver photodiodes, 342–4
- receiver photomixers, 341–2
- rectangular holes, 105–7, 107–10
- reflection configuration
 - depth of discontinuities analysis, 528–31
 - calculated relative strength of the first Fabry-Pérot reflection, 531
 - discontinuities in a composite sample laminated at various thickness, 530
 - THz TDS time-domain plots showing reflections from discontinuities, 529
- glass fibre composite material
 - parameter measurement, 522–3
- reflection imaging, 549
- reflection terahertz time-domain spectroscopy, 583–5, 604–5
- measurement, 584
- THz waveform, absorption coefficient and refractive index extraction, 605
- reflective terahertz time domain spectroscopy, 520–31
 - results and discussion, 522–31
 - theory and experiment, 520–2
 - geometry of the surface and first Fabry-Pérot reflection, 521
 - reflection configuration for imaging and material parameter measurement, 521

- refraction index, 161, 552
 resistive mixer regime, 130
 resistive mixing, 233–5
 resolution, 630–1
 reflection signal peak position *versus*
 micrometer position, 630
 resonant detection, 147–8
 high mobility photoresponse and
 position of signal maximum vs
 gate voltage, 149
 photoresponse vs gate, voltage
 experimental and theory,
 148
 resonant electron tunnelling
 microscopy, 392
 resonant terahertz field enhancement,
 272–93
 active control of terahertz surface
 plasmon polaritons, 282–93
 active transition from silicon
 photonic crystal to metallic hole
 array, 283–7
 frequency-dependent THz
 transmission, 286
 hybrid plasmonic switching devices
 with metamaterial properties,
 287–9
 measured transmitted THz pulses,
 284
 optical images of hole array,
 291
 photo-excited silicon measured
 dielectric function, 285
 plasmonic MM (silicon, aluminium
 and sapphire), 288
 simulated spectra at different
 pump fluences, 289
 superconducting plasmonics,
 290–3
 YBCO hole array measured
 and simulated amplitude
 transmission response, 292
 fundamentals of surface plasmon
 polaritons at terahertz
 frequencies, 273–4
 terahertz waves through metallic hole
 arrays, 274–82
 amplitude transmission of THz
 pulses, 281
 array-on-silicon samples measured
 amplitude transmission, 279
 Fourier-transformed spectra of
 transmitted THz pulses, 276
 frequency-dependent skin depth of
 metals Ag, Al and Pb, 275
 optically thin metallic hole arrays,
 274–8
 Pb arrays measured amplitude
 transmission, 277
 resonance frequencies of Al-air
 SPP mode, 282
 SPP mode for arrays made from
 different metals, 280
 surface plasmonic sensors, 280–2
 surface waves metallic permittivity
 dependent transmission, 278–80
 resonant tunnelling diode (RTD), 4,
 183–4
 RF source, 264
 RGB map, 606
 rise time, 631
 RTD oscillators
 design, 430–1
 integrated with patch antenna, 430
 satellite-to-satellite channel, 170–3
 channel capacity vs ground and an
 airborne vehicle link frequency,
 170
 simulated transmission and eye
 diagrams for transmission
 distances and rain rate, 172
 simulating distortions to eye
 diagrams from atmospheric
 attenuation, 171
 scanning electron microscope (SEM),
 108
 scanning near-field optical microscopy
 (SNOM), 95
 scanning photoconductive antenna, 37
 Schottky barrier, 472
 Schottky diode mixer systems, 186
 Schottky diodes, 267
 scintillations
 experimental characterisation of rain
 and fog on THz communication
 links, 200–6
 link degradation, 161–3

- air turbulence causes refractive index fluctuations resulting to speckles, 162
- rain and fog experimental characterisation on THz communication links
- attenuation of THz link and IR link with time and log(BER), 204
- IR photodetectors outputs and log(BER) of IR and THz due to fog, 205
- measured BER for 120 GHz wireless link vs rain attenuation, 201
- schematic of co-propagating THz and IR links, 202
- self-phase-modulation (SPM), 308
- semiconductor, 65–6, 404–12
- broadband pulsed terahertz radiation generation and detection, 466–8
 - continuous wave terahertz radiation generation using photomixing, 469–70
 - material development for terahertz applications, 464–85
 - overview, 464–6
 - photoconductive semiconductor materials, 470–85
 - semiconductor industry
 - electro-optical terahertz pulse reflectometry (EOTPR) characterisation, 629–33
 - electro-optical terahertz pulse reflectometry (EOTPR) failure analysis, 633–8
 - future trends, 638–9
 - quality assurance test system, 639
 - overview, 624–9
 - electro-optical terahertz pulse reflectometry (EOTPR) principle, 625–9
 - terahertz applications, 624–39
- sensing
- fundamental aspects of terahertz near-field imaging, 91–116
 - terahertz near-field imaging fundamentals
 - Kirchoff formalism for near-field estimate, 110–16
- measurements, 95–9
 - subwavelength holes, 99–110
- Separated-Transport Recombination photodiode (STR-PD), 178
- shallow water equations, 127
- Shannon-Hartley theorem, 170
- Shannon-Nykqvist sampling theorem, 260
- short/leakage failure, 636–8
- waveforms after subtraction, 638
 - waveforms before subtraction, 637
- short-range surface plasmon polaritons (SRSPPs), 78
- Shubnikov-de Haas oscillations, 132
- signal-to-noise ratio (SNR), 199, 259, 631
- silicon FETs
- THz detection, 145–6
 - responsivity of frequency for gate voltage 0.2V, 146
- single-electron transistor (SET), 408
- single-mode CW waves, 438
- softwood, 553
- solid phase transformation, 592–4
- THz absorption spectra of CBZ form III, 593
- solid-state sources, 4
- solvent diffusion, 603–4
- Sommerfeld's solution, 100
- soot-removal filter, 495
- spectral database, 617–18
- spectra of mineral pigments and organic dyes, 619
- spectroscopy, 493–508
- powdered chemicals quantitative analysis, 501–8
 - absorption vs. KM spectra of 20 wt% glucose, 504
 - experimental set-up for measuring diffuse reflectance, 502
 - powdered glucose concentration relationship, 506
 - powdered maltose concentration relationship, 506
 - relative diffuse reflection spectrum of 20 wt% glucose powder, 503

- spectroscopy (*cont.*)
 unconcealed and concealed KM
 spectrum of 40 wt% powdered
 glucose, 507
 unconcealed and concealed
 powdered glucose component
 calculated score, 507
- split ring resonator (SRR), 189
- square holes, 104–5
- square-law detection, 234
- square root law, 123
- standing wave ratio (SWR), 256
- steering, 189–90
- subwavelength fibres
 devices, 39–44
 directional couplers and
 non-destructive cutback
 technique, 41–4
 fibre-based terahertz imaging, 40
- packaging, 35–9
 amplitude transmission spectra
 and average power attenuation
 losses, 39
 cross section and close-up view
 of suspended and porous core
 fibre, 37
 near-field microscopy images and
 suspended solid core fibre, 38
- porous core, 30–2
 fabrication, 32–4
 fabrication procedure, sacrificial
 polymer and microstructured
 technique, 33
 subwavelength porous and solid
 core PE fibre, 31
 transmission and cutback loss
 measurements, 32
- subwavelength-sized photoconductive
 antenna, 98–9
- subwavelengths holes, 99–110
 circular, 99–101
 circular holes effective dipole
 moments, 101–4
 rectangular, 105–7
 schematic and normalised-to-area
 transmittance vs wavelength,
 106
 x-component of electric near-fields,
 108
- rectangular holes with nano-sized
 width, 107–10
- metallic nanobarrier, point
 measurements spectra and
 electric near-field SEM image,
 110
- SEM image of THz nanoantenna
 and electric near-field
 x-component, 109
- square, 104–5
 electric field distribution and
 three-dimensional vector
 mapping, 105
- superconducting plasmonics, 290–3
- superconductor, 404–12
- surface plasmon polaritons (SPP), 273
 characteristic lengths, 72–6
 real and imaginary components of
 wavenumber vs frequency, 73
 SPPs decay length, 75
 SPPs propagation length, 75
 SPPs refraction index and
 wavelengths, 74
 SPPs time-average field properties
 and instantaneous field profile, 76
- fundamental aspects, terahertz
 frequencies, 62–84
 Drude model, 64–7
 multilayered structures, 76–81
- planar surfaces, 67–76
 dispersions, 67–72
 schematic representation of surface
 charge and electric field lines, 68
 wavelength, propagation and decay
 length, 72–6
- plasmonics new trends, 81–4
 designed surface plasmon
 polaritons in perforated metals,
 81–2
 localised surface plasmon
 polaritons, 82–4
- surface plasmonic sensors, 280–2
- switch *see* photoconductive
 semiconductor
- TDR-based fault isolation, 387
- temperature dependence, 142–3
- GaAs/AlGaAs FET calculated
 photoresponse at 600 GHz, 143

- terahertz array imagers, 231–67
 characterisation and optimisation of field effect transistor detectors, 249–59
 developments towards a THz camera, 260–5
 50-pixel array, 260
 package with sunflower seeds used for THz imaging demonstration, 263
 packaged camera chip, 264
 real-time coherent imaging emulation with a 10-kilopixel virtual camera, 263–5
 real-time direct imaging emulation with a 10-kilopixel virtual camera, 261–3
 THz heterodyne imaging, 265
 THz imaging modalities in transmission mode, 262
 field effect transistor (FET)
 detectors characterisation and optimisation, 249–59
 calculated real and imaginary parts of the impedance of FET, 254
 drain coupling and parasitic equivalent-circuit components, 255
 electrical and optical responsivity, 250–1
 limitations for impedance matching and tuning, 253–5
 measured voltage responsivity vs gate voltage, 251
 method for device characterisation, 255
 NEP as function of gate voltage, 253
 noise-equivalent power (NEP), 251–2
 optical responsivity of detectors for emission frequencies, 258
 response time, 252–3
 responsivity enhancement by current bias, 259
 results for MOSFET THz detectors, 256–9
 overview of other focal-plane technologies, 266–7
- plasmonic mixing, 235–43
 device model, 235–6
 distributed resistive-self-mixing regime, 238–41
 frequency dependence of the efficiency factor, 243
 plasmonic mixing regime, 241–3
 resistive mixing regime, 236–8
 spatial distribution of gate-to-channel voltage oscillations, 237
 voltage response and ideal current responsivity, 239
 resistive mixing, 233–5
 technology, design and
 implementation of CMOS field effect transistors, 243–9
 array of 50 patch-antenna-coupled detectors, 249
 CMOS antenna integration, 246–8
 CMOS technology with respect to THz focal-plane arrays, 244–6
 cross-sectional through the back-end of a CMOS chip, 245
 detector design and implementation, 248–9
 terahertz biosensing techniques, 217–27
 binding-state dependent, 222–3
 refractive indices, power absorption and dielectric constants of TSH and single-stranded helix, 222
 characteristic resonances of biomolecules and molecular imaging, 223–5
 molar absorption coefficient and refractive index of the nucleobases, 224
 sensing of proteins, 219–22
 difference in absorption of protein, 220
 measured absorption coefficients of HEWL and HEWL + triacetylglucosamine, 221
 sensing of water dynamics by terahertz waves, 218–19
 water-mediated terahertz molecular imaging, 225–7

- terahertz biosensor chip
experiments and results, 426–9
- terahertz comb-referenced
spectrometer, 456–60
experimental set-up, 458–9
principle of operation, 457–8
- terahertz comb-referenced spectrum
analyser, 439–47
coherent link of frequency using
frequency comb, 440
- experiment result, 443–7
experimental set-up, 445
 f_b beat signal spectra of
photomixing source, 447
 f_b beat signal spectra of the AFMC
source, 444
frequency measurement precision,
446
- experimental set-up, 442–3
schematic diagram, 443
- principles of operation, 440–2
principle and spectral behaviour, 441
- terahertz continuous-wave photomixer
systems, 327–64
coherent signal detection, 344–50
continuous-wave spectroscopy
set-up, 345
dynamic range of
frequency-domain spectroscopy
set-up, 346
frequency-domain set-up with a
pair of fibre stretchers, 348
frequency-domain set-up with
electro-optic phase modulator,
347
frequency scan across two water
vapour absorption lines, 349
phase variation in controlled
frequency steps, 348–50
phase variation with electro-optic
modulator, 346–7
phase variation with fibre stretcher,
347–8
- continuous-wave emitter and
detector technologies, 329–44
different antenna designs, 333
fibre-pigtail end photomixers, 335
GaAs devices, 330–8
InGaAs/InP devices, 338–44
- LT-InGaAs receiver module, 343
photomixer with interdigitated
finger electrodes, 331
uni-travelling-carrier photodiode,
341
- UTC diode operation modes as
terahertz receiver, 344
- waveguide-integrated photodiode,
340
- laser sources, 350–8
comparison, 358
- DFB laser diode schematic, 351
- DFB lasers temperature tuning,
352
- dual-mode and multi-mode laser
diodes, 354–6
- dual-mode distributed feedback
laser diode, 355
- dual-wavelength optical parametric
oscillators (OPO), 356–7
- quadrature interferometer and
beat signal linewidth, 353
- quasi-time-domain spectroscopy,
356
- twin-distributed feedback (DFB)
lasers, 350–2
- two-colour OPO, 357
- planar photomixer and p-i-n
photodiode, 328
- selected applications, 358–64
ceramic knife blade photograph
and 500 GHz image, 362
imaging, 361–4
- QTDS imaging of airbag
cover, 363
- real and imaginary part of
 α -lactose monohydrate dielectric
constant, 361
- spectroscopy of solids, 360–1
- terahertz spectra of mixture
of hydrocyanic acid and
hydrochloric acid, 359
- trace gas detection, 358–9
- terahertz emitter with planar
photomixer, 328
- terahertz detectors
room temperature, 121–52
low-dimensional structures plasma
waves, 122–5

- radiation detection by FET, 128–35
 steady state instability with dc current in FETs, 125–8
 THz detection experimental studies by FETs, 141–52
 THz emission studies from FETs, 135–40
 technologies, 6–8
 heterodyne, 7–8
 homodyne, 6–7
 optoelectronic, 8
 terahertz emission threshold, 137–8
 emission intensity as source-drain bias function in magnetic field, 137
 terahertz emitter, 581–2
 broadband pulses generation and detection, 582
 terahertz fluorescent writing, 386
 terahertz frequency
 fundamental aspects of near-field imaging and sensing, 91–116
 Kirchoff formalism for near-field estimate, 110–16
 measurements, 95–9
 radiation of induced electric and magnetic-dipole moment, 93–5
 subwavelengths holes, 99–110
 fundamental aspects of surface plasmon polaritons, 62–84
 Drude model, 64–7
 multilayered structures, 76–81
 planar surfaces, 67–76
 plasmonics new trends, 81–4
 near-field and far-field, 91–3
 enhanced field of a perfectly conducting sphere, 92
 magnetic field distribution, 93
 terahertz frequency comb
 coherent frequency linking, 437–9
 future trends, 460–2
 optical-comb-referenced terahertz synthesiser, 447–56
 referenced spectrometer, 456–60
 referenced spectrum analyser, 439–47
 terahertz frequency metrology, 436–62
 coherent frequency linking, 437–9
 future trends, 460–2
 optical-comb-referenced terahertz synthesiser, 447–56
 referenced spectrometer, 456–60
 referenced spectrum analyser, 439–47
 terahertz gap, 403, 436–7
 heritage science, 615–16
 research field, 616
 terahertz integrated devices, 423–33
 fabricated resonant tunnelling diodes, 431–4
 calculation and experimental results of fundamental oscillation frequencies, 433
 current-voltage characteristics of fabricated RTD, 431
 oscillation spectrum of fabricated RTD, 432
 integrated terahertz biosensor chip, 423–9
 delay time variation of THz pulse depending upon applied volume of DNA specimen, 428
 numerical calculation results using TLM method, 426
 on-chip transmission line sensors, 425
 structure and design of transmission line sensors, 424–6
 temporal THz waveform and FFT spectrum of the fabricated device, 427
 THz biosensor chip experiments and results, 426–9
 transmission line sensors, 423–4
 THz oscillators integrated with patch antennas, 429–31
 RTD oscillators design, 430–1
 RTD oscillators integrated with patch antenna, 430
 THz semiconductor oscillators, 429–30

- terahertz molecular imaging (TMI), 218
 terahertz nano-devices, 403–19
 nanoscale terahertz detector, 404–12
 carbon nanotube quantum dot (CNT-QD) and electron tunnelling processes, 408
 carbon nanotubes, 405–12
 nanoscale superconductor THz bolometer, 405
 near-infrared detector with carbon nanotube films, 406
 PAT process for double-coupled QD, 409
 superconductor and semiconductor, 404–12
 THz detector with carbon nanotube transistors, 407
 THz detector with CNT/2DEG hybrid structure, 410–11
 near-field THz imager, 412–18
 calculations of THz electric field distributions, 416
 illustration of integrated near-field THz imager, 415
 improved structure with carbon nanotube detector, 418
 integrated near-field THz imager, 415–18
 near-field image of THz emission distribution in another 2DER sample, 418
 near-field THz imaging, 413–14
 THz transmission signal as function of near-field THz imager position, 417
 types of near-field THz imaging systems, 414
 terahertz near-field approaches, 374–97
 failure analysis in integrated electronic structure based on THz time-domain reflectometry, 386–92
 applied optical pump/probe set-up for terahertz time-domain measurements, 389
 measured time-domain signal for vertical probe-tip to sample distance of 10 µm, 391
 measured time position of the reflected signal against waveguide shift, 393
 minimum distance between neighbouring still resolvable discontinuities vs signal rise time, 388
 future trends, 396–7
 high-resolution imaging of free-carrier concentrations for photovoltaic material inspection, 392–6, 397
 design for carrier concentration measurements, 394
 THz amplitude contrast, 395
 two-dimensional THz NF raster scan, 397
 two-dimensional THz raster scan of the edge region, 396
 nanophotonic second-order nonlinear-optic waveguides with THz near-field probing, 382–6
 nanophotonic silicon devices spatio-temporal NF measurements, 384
 plasma-activated silicon waveguide spatio-temporal field demonstration, 385
 spatial resolved measurement of locally activated silicon waveguide, 386
 novel micro-machined THz near-field probe-tips, 377–82
 active PC NF cantilever structures exemplary designs, 382
 active PC probing devices basic fabrication steps, 381
 front-end components of an active cantilever-based PC NF probing device, 380
 state-of-the-art, 375–7
 terahertz oscillators integrated with patch antennas, 429–31
 RTD oscillators design, 430–1
 RTD oscillators integrated with patch antenna, 430
 terahertz photoconductive antennas (THz-PCA), 5
 terahertz pulse, 468, 586, 587

- terahertz quasi-time-domain spectroscopy (THz-QTDS), 608
- terahertz radiation, 465–6
- terahertz receiver, 581–2
- broadband pulses generation and detection, 582
- terahertz semiconductor lasers, 5
- terahertz semiconductor oscillators, 429–30
- terahertz spectroscopy, 618
- reflection spectra and an imaging result of two white pigments, 619
- terahertz spectrum, 586
- terahertz (THz)
- aerospace industry applications, 510–44
 - continuous-wave non-destructive terahertz imaging, 532–7
 - non-destructive imaging for glass fibre reinforced plastics, 537–42
 - reflective terahertz time domain spectroscopy of aircraft composites, 520–31
 - transmissive terahertz time domain spectroscopy of aircraft composites, 513–20
 - application in tomographic imaging and material spectroscopy, 493–508
 - powdered chemicals quantitative analysis, 501–8
- art conservation applications, 615–22
- artwork internal structure observation using THz waves, 620–1
 - development as tool for heritage science, 621–2
 - material analysis using THz waves, 617–20
 - overview, 615–17
- biosensing techniques, 217–27
- binding-state dependent, 222–3
 - characteristic resonances of biomolecules and molecular imaging, 223–5
 - sensing of proteins, 219–22
 - sensing of water dynamics by terahertz waves, 218–19
- pharmaceutical industry and science
- applications, 579–609
 - future trends, 607–9
- terahertz time-domain imaging (THz-TDI), 594–601, 601–7
- terahertz time-domain spectroscopy (THz-TDS), 581–9, 589–94
- semiconductor industry applications, 624–39
- electro-optical terahertz pulse reflectometry (EOTPR)
- characterisation, 629–33
- electro-optical terahertz pulse reflectometry (EOTPR) failure analysis, 633–8
- future trends, 638–9
- overview, 624–9
- semiconductor material development, 464–85
- broadband pulsed terahertz radiation generation and detection, 466–8
- continuous wave terahertz radiation generation using photomixing, 469–70
- overview, 464–6
- photoconductive semiconductor materials, 470–85
- wood product industry applications, 547–75
- future trends, 574
 - overview, 547–9
 - probing wood characteristics, 565–68
 - sensing in oriented strand board (OSB), 569–74
 - technology, 549–52
 - wood far infrared properties, 556–65
 - wood structure and morphology, 552–6
- terahertz time domain, 483
- terahertz time-domain imaging (THz-TDI), 580, 594–601, 601–7
- data analysis and interpretation, 595–8
- THz waveform, 596
- imaging set-up, 594–5

- terahertz time-domain imaging (*cont.*)
 schematic diagram, 595
 pharmaceutical process monitoring,
 601–4
 spectroscopic imaging and chemical
 mapping, 604–7
 tablet and coating properties, 598–601
- terahertz time-domain spectroscopy
 (THz-TDS), 177, 296, 447, 456–7,
 498, 512, 513–20, 520–31, 532,
 534–5, 543, 548–9, 550–2, 556,
 565, 574, 581–9, 589–94
 case studies, 620–1
 non-invasive THz vs. microscope
 observation of ‘Politico di
 Badia,’ 622
 non-destructive cross-section
 analysis, 620
 internal structure observation, 621
 polymorphs and hydrates
 identification and quantification,
 589–92
 sample preparation and data analysis,
 585–9
 waveform measurement,
 absorption coefficient and
 refractive index extraction, 588
- set-up, 581–5
 instrument, 583
 transmission, 583
 solid phase transformation analysis,
 592–4
- terahertz waves
 advantage, 616–17
 painting structure and
 electromagnetic waves, 617
 artwork internal structure
 observation, 620–1
 material analysis, 617–20
 case studies, 618–20
 terahertz imaging of Inner
 Mongolian wall painting, 620
 optoelectronic techniques, 3–22
 detector technologies, 6–8
 difference frequency mixing in
 nonlinear crystals, 19–22
 parametric interaction in nonlinear
 crystals, 18–19
- signal detection in THz-PCAs,
 15–17
 signal generation in THz-PCAs,
 8–15
 technology sources, 4–5
 transmission and propagation of
 plastic waveguides, 28–58
 composite materials, 51–4
 devices based on subwavelengths
 fibres, 39–44
 experimental characterisation, 54–6
 fibre optics challenges, 29–39
 hollow-core fibres, 45–51
- terahertz wireless communications,
 156–208
 atmospheric propagation, 159–65
 free-space damping including fog,
 rain and snow, 163–5
 scintillations as link degradation,
 161–3
 THz radiation directionality, 160–1
- channels modeling
 covert battlefield, 173–7
 indoor, 166–9
 satellite-to-satellite/
 satellite-to-ground, 170–3
- examples, 192–200
 link measurement summary, 193
 experimental characterisation of rain,
 fog, and scintillations, 200–6
 future trends, 206–8
 technology road map, 207
- hardware sources and detectors,
 177–84
 microwave frequency multipliers,
 180–3
 opto-electronic, 177–80
 quantum cascade lasers, 183
 THz integrated circuits, 183–4
- modelling of channel, 165–77
 motivation, 157–9
 signal modulation formats, 190–2
 wave modulators, 184–90
 Schottky diode mixer systems, 186
 THz beam shaping and steering,
 189–90
 THz generator specific modulation
 schemes, 185–6

- THz independent specific modulation schemes, 186–9
- test range, 631
- thermal spectral voltage-noise density, 251
- thermoelectric devices, 267
- ThermoScope II, 540
- 3D through silicon via (3D-TSV), 387
- time-domain spectroscopy (TDS), 99
- time-of-flight tomography, 498–501
- axial resolution evaluation using Teflon films, 501
 - experimental set-up, 500
 - principle, 499
 - reflected THz pulse, 500
- tomography, 493–508
- imaging applications, 494–501
 - powdered chemicals quantitative analysis, 501–8
 - absorption *vs.* KM spectra of 20 wt% glucose, 504
 - experimental set-up for measuring diffuse reflectance, 502
 - powdered glucose concentration relationship, 506
 - powdered maltose concentration relationship, 506
 - relative diffuse reflection spectrum of 20 wt% glucose powder, 503
 - unconcealed and concealed KM spectrum of 40 wt% powdered glucose, 507
 - unconcealed and concealed powdered glucose component calculated score, 507
- Topas, 35
- transceivers, 314
- transmission line sensors, 423–4
- structure and design, 424–6
- transmissive terahertz time domain spectroscopy, 513–20
- results and discussion, 515–20
- bend damage across the central bend axis, 519
 - heat-damaged samples
 - material property measurement, 515–16
- material parameter measurements for heat damage areas, 516
- milled area hidden between two glass-fibre strips, 519
- milled glass fibre using peak pulse amplitude, 517
- pulse and amplitude spectra of air reference and glass fibre, 516
- three heated areas on glass fibre samples, 518
- undamaged glass fibre samples, 515
- theory and experiment, 513–15
- five glass fibre samples, 515
 - imaging and material parameter measurement transmission configuration, 514
- transmitter voltage swing (TVS), 195
- Triple-Stack Nanocellular Architecture, 159
- tunable emission, 139–40
- emission frequency experimental data and calculations, 140
 - spectra for GaN/AlGaN transistor at drain voltage 4V and different gate voltages, 139
- twin-distributed feedback (DFB) lasers, 350–4
- excursion: a quadrature interferometer for frequency control, 352–4
- two-dimensional electron gas (2DEG), 409, 411
- ultrafast photoconductive (PC) switches, 377
- uni-travelling carrier photodetector, 177
- uni-travelling-carrier photodiode, 340–1, 446, 447, 451
- United States Department of Defense (DOD), 173
- United States Federal Strategic Spectrum Plan, 158
- waveform interpretation, 631–3
- identifying C4 location, 632
 - reflection peak of failure within package, 632

- Wideband Network Waveform (WNW), 173
- WIN photodiodes, 339–40
- wireless local area network (WLAN), 158
- wireless personal area network (WPAN), 158
- wood
- far infrared properties, 556–65
 - polarisated THz-TDS performed on aspen, 566
 - polarisated THz-TDS performed on dry fir, 557
 - polarisated THz-TDS performed on dry maple, 557
 - polarisated THz-TDS performed on dry spruce, 558, 559
 - polarisated THz-TDS performed on fir, 561, 565
 - polarisated THz-TDS performed on maple, 560, 564
 - polarisated THz-TDS performed on trembling aspen, 562, 563
- probing characteristics at THz frequencies, 565–68
- THz and optical image of OSB, 566
- two fibre-orientation anisotropy, 568
- structure and morphology, 552–6
- chemical constituents, 553–6
- relationship at different levels of magnitude, 555
- wood elements, 553
- wood–plastic composite, 551
- wood product industry
- future trends, 574
 - manufacturers of THz-TDS systems, 575
- overview, 547–9
- electromagnetic radiation characteristics matrix, 548
- probing wood characteristics at THz frequencies, 565–68
- terahertz applications, 547–75
- THz sensing in oriented strand board (OSB), 569–74
- THz technology applications, 549–52
- wood far infrared properties, 556–65
- wood structure and morphology, 552–6
- X-TEK HMX 160, 538
- yttrium barium copper oxide (YBCO), 290
- ZEMAX simulation tool, 261
- Zenneck waves, 273
- ZnTe crystal, 513, 520